David A. Yuen
Shigenori Maruyama
Shun-ichiro Karato
Brian F. Windley
Editors

Superplumes: Beyond Plate Tectonics

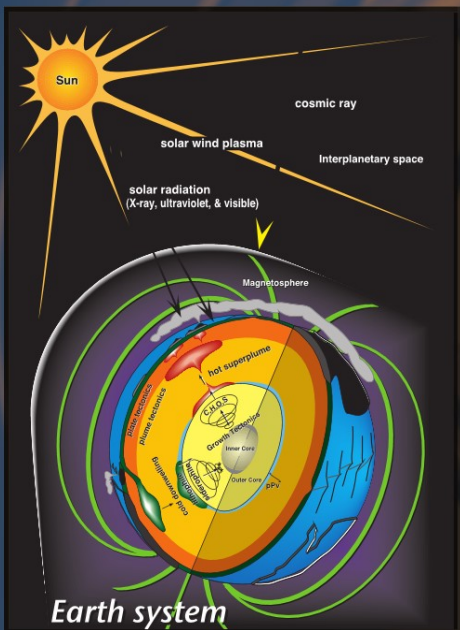

Springer

Superplumes: Beyond Plate Tectonics

Edited by

DAVID A. YUEN
University of Minnesota, U.S.A.

SHIGENORI MARUYAMA
Tokyo Institute of Technology, Japan

SHUN-ICHIRO KARATO
Yale University, Connecticut, U.S.A.

and

BRIAN F. WINDLEY
University of Leicester, U.K.

Springer

A C.I.P. Catalogue record for this book is available from the Library of Congress.

ISBN 978-1-4020-5749-6 (HB)
ISBN 978-1-4020-5750-2 (e-book)

Published by Springer,
P.O. Box 17, 3300 AA Dordrecht, The Netherlands.

www.springer.com

Book cover: The Earth system consists of 6 sub-systems: (1) growth tectonics in the core; (2) plume tectonics in the lower mantle; (3) plate tectonics in the upper mantle; (4) Solar-driven hydro-biosphere; (5) atmosphere; and (6) magnetosphere, penetrating through all of these domains. The Earth behaves as a nonlinear system in response to either external or internal forcing. The surface environment of (4) and (5) is controlled by the solar energy in a daily time span, whereas the solid Earth is driven by internal heating over a much longer time span, up to a time scale of billions of years. With a cooling Earth, the Earth system has changed with catastrophic events due to the linked subsystem, and drastically affected the evolution of the surface environment and of life. The superplume sits atop the hot liquid outer core to drive the Earth as a main heat engine in maintaining geodynamics. (graphics by Shio Watanabe)

Printed on acid-free paper

All Rights Reserved
© 2007 Springer
No part of this work may be reproduced, stored in a retrieval system, or transmitted in any form or by any means, electronic, mechanical, photocopying, microfilming, recording or otherwise, without written permission from the Publisher, with the exception of any material supplied specifically for the purpose of being entered and executed on a computer system, for exclusive use by the purchaser of the work.

TABLE OF CONTENTS

PREFACE

Forty years ago when plate tectonics was first discovered, there was a major shift in thinking in the Earth Sciences. Little was known at that time about the deep mantle because of the lack of knowledge about material properties, the absence of any seismic tomography or concepts such as mantle convection. Thus the theory of plate tectonics was built on surface observations and kinematic constraints. The theory of plate tectonics is not independent but consists of several assumptions. Examples are the origin of arc magma, MORB or OIB, and the distribution of earthquakes and the plate margin processes are all part of plate tectonics theory.

In the intervening years much progress has been made in all three burgeoning areas of mineral physics, seismic tomography and mantle dynamics, thanks to the technological advances in synchrotron radiation and supercomputers.

Mineral physics studies have provided some of the key parameters that control the style of mantle convection. The style of convection in the Earth's mantle is largely controlled by complex material properties including the changes in density and viscosity associated with a large variation in the pressure and temperature of the Earth's interior. These key physical properties have become the target of both experimental and theoretical studies in mineral physics. Starting from the early 90s, the advances in high-performance computational capability has allowed us to incorporate these mineral physics findings into large-scale computational modeling of mantle convection; and these studies have highlighted the complexities of mantle convection caused by the variation in density due to both thermal and chemical anomalies (and viscosity) in the Earth's deep interior.

By the same token, the development of seismic tomography has also revealed the rich dynamics of the Earth's deep interior. For example, the tomographic images of the deep mantle published by Dziewonski's seismic tomography in the 1980's, have unveiled the existence of two low seismic velocity anomalies underneath the central Pacific and Africa, which had not been expected and was very enigmatic. These objects with a diameter exceeding 1000 km were called superplumes and have piqued the interests of many in the geophysical, geological and geochemical communities. High-resolution tomography published by Fukao and his colleagues also revealed athe rich detail about the interaction between convection and transition zone.

Based partly on the tomographic images made by Fukao et al. (1992), Maruyama in 1994 has speculated that superplumes may indeed have played a bigger role than plate tectonics in driving mantle dynamics. He obtained funds from the Japanese government to examine this superplume idea as the next important paradigm as a possibility and planned a series of workshops at Riken, Japan in 1997, the superplume symposium at the San Francisco AGU in 2000, and the superplume II workshop at Tokyo Institute of Technology in January 2002.

In Japan, the Superplume Project was initiated and supported by STA (Science and Technology Agency, Japan) from 1996 to 2001. As a summary of the second Superplume workshop in 2002, a special issue of *Physics of the Earth and Planetary Interior* appeared in the summer of 2004.

As part of the research supported by the superplume project for deep mantle, Hirose and his co-workers have discovered in the summer of 2004 a new phase, post-perovskite in diamond-anvil cell apparatus at elevated temperatures of 2500 K and pressures of 120 GPa. This has stimulated much research and thought about the role played by the post-perovskite transition in maintaining the seismic heterogeneity of the D″ layer and superplumes at the same time. Radiative thermal conductivity may be needed in the deep mantle to promote the development of the superplume. There is still much work needed to test the influence of superplumes on the plate tectonics in the upper mantle.

How do the two systems communicate with each other? At the same time, how does the growing inner core impact on the development of a superplume and on the initial onset of superplumes in the deep mantle? To answer these questions, surface records of the Earth's history are the critical source of information. In this book, about 50% is geology and petrology combining with geophysics, by which superplume dynamics of the terrestrial planets is speculated.

In this book, we summarize our current knowledge of the whole mantle through time from diverse points of view in order to stimulate this nascent concept of superplume and to investigate it further as a testable model in the future.

We would like to dedicate this book to the memory of our Hungarian colleague, Laszlo Cserepes, who passed away before the Superplume II Workshop. Laszlo was one of the pioneers of mantle convection modeling and developed the concept of different types of mantle plumes, including the superplume. All the editors acknowledge the staff at Springer who provided a timely opportunity for this book.

D.A. Yuen
S. Maruyama
S. Karato and
B.F. Windley

LIST OF CONTRIBUTORS

Robert C. Anderson
Jet Propulsion Laboratory
4800 Oak Grove Drive
MS 230-235
Pasadena,
California 91109
USA
randerson@jpl.nasa.gov

Victor R. Baker
Department of Hydrology and
Water Resources
(and The Lunar and Planetary
Laboratory)
The University of Arizona
Tucson,
Arizona 85721-0011
USA
baker@hwr.arizona.edu

K.L. Buchan
Geological Survey of Canada
601 Booth St., Ottawa, K1A 0E8
Canada
kbuchan@nrcan.gc.ca

Frédéric Deschamps
Institute of Geophysics
ETH Zurich
8093 Zurich
Switzerland
deschamps@erdw.ethz.ch

D.W. Desnoyers
Geological Survey of Canada
601 Booth St., Ottawa, K1A 0E8
Canada
don.desnoyers@nrcan-rncan.gc.ca

James M. Dohm
Department of Hydrology and
Water Resources
The University of Arizona
Tucson, Arizona 85721-0011
USA
jmd@hwr.arizona.edu

Richard E. Ernst
Geological Survey of Canada
601 Booth St., Ottawa
Ontario K1A 0E8
Canada
Now at Ernst Geosciences
43 Margrave Avenue
Ottawa K1T 3Y2
Canada
richard.ernst@ernstgeosciences.com

Edward J. Garnero
School of Earth and Space Exploration
Arizona State University
Tempe Arizona 85287-1404
USA
garnero@asu.edu
Web: http://garnero.asu.edu

Ulrich Hansen
Institut für Geophysik
University of Münster
48149 Münster
Germany
hansen@earth.uni-muenster.de

Kei Hirose
Department of Earth and
Planetary Sciences
Tokyo Institute of Technology
O-okayama 2-12-1, Meguro,
Tokyo 152-8551
Japan
kei@geo.titech.ac.jp

Anne M. Hofmeister
Department of Earth and
Planetary Science
Washington University
1 Brookings Drive, St. Louis
Missouri 63130
hofmeist@wustl.edu

Miaki Ishii
Harvard EPS Hoffman Lab
20 Oxford Street
Cambridge, Massachusetts 02138
USA
ishii@eps.harvard.edu

Yukio Isozaki
Department of Earth Science
and Astronomy
Graduate School of Arts
and Sciences
The University of Tokyo
3-8-1 Komaba, Meguro
Tokyo 153-8902, Japan
isozaki@chianti.c.u-tokyo.ac.jp

Masanori C. Kameyama
Earth Simulator Center
JAMSTEC
Kanazawa-ku
Yokohama 237-0061
Japan
kameyama@jamstec.go.jp

Shun-Ichiro Karato
Department of Geology and Geophysics
Yale University
P.O. Box 208109
Connecticut 06520-8109
USA
shun-ichiro.karato@yale.edu

Tetsu Kogiso
Institute for Research on Earth
Evolution (IFREE)
Japan Agency for Marine-Earth
Science and Technology (JAMSTEC)
Yokosuka 237-0061, Japan
kogisot@jamstec.go.jp

Tetsuya Komabayashi
Department of Earth and
Planetary Sciences
Tokyo Institute of Technology
O-okayama 2-12-1, Meguro
Tokyo 152-8551
Japan
tkomabay@geo.titech.ac.jp

Tsuyoshi Komiya
Department of Earth and
Planetary Sciences
Tokyo Institute of Technology
O-okayama 2-12-1, Meguro
Tokyo 152-8551
Japan
tkomiya@geo.titech.ac.jp

Shigenori Maruyama
Department of Earth and
Planetary Sciences
Tokyo Institute of Technology
O-okayama 2-12-1, Meguro
Tokyo 152-8551
Japan
smaruyam@geo.titech.ac.jp

Ctirad Matyska
Department of Geophysics
Faculty of Mathematics and Physics
Charles University
18000 Prague 8, Czech Republic
cm@karel.troja.mff.cuni.cz

Allen McNamara
School of Earth and Space Exploration
Arizona State University
Tempe, Arizona 85287-1404
USA
allen.mcnamara@asu.edu

Marc Monnereau
UMR5562, C.N.R.S.
Universite Paul Sabatier Toulouse III
14 Avenue Ed. Belin
314000 Toulouse, France
marc.monnereau@dtp.obs-mip.fr

Soichi Omori
Research Center for Evolving
Earth and Planet
Department of Earth and
Planetary Sciences
Tokyo Institute of Technology
O-okayama 2-12-1, Meguro
Tokyo 152-8551
Japan
omori@geo.titech.ac.jp

Tsutomu Ota
Institute of Study of the
Earth's Interior
Okayama University
Misasa, Yamada 827
Tottori 682-0193
Japan
tsutom@pheasant.misasa.okayama-
u.ac.jp

Kuniko Munekata
Department of Earth and
Planetary Sciences
Tokyo Institute of Technology
O-okayama 2-12-1, Meguro
Tokyo 152-8551
Japan
kuniko0325@sepia.plala.or.jp

Sebastian Rost
School of Earth and Environment
Earth Sciences
The University of Leeds
Leeds, LS6 9JT
UK
earsro@earth.leeds.ac.uk

Norihito Suzuki
Department of Earth and
Planetary Sciences
Tokyo Institute of Technology
O-okayama 2-12-1, Meguro
Tokyo 152-8551
Japan
norihito.suzuki@exxonmobil.com

Paul J. Tackley
Institute of Geophysics
ETH Zurich
8093 Zurich
Switzerland
ptackley@ethz.ch

Michael S. Thorne
Arctic Region Supercomputing Center
University of Alaska Fairbanks
909 Koyukuk Drive, Suite 105
P.O. Box 756020
Fairbanks, Alaska 99775-6020
USA
mthorne@gi.alaska.edu

Jeannot Trampert
Faculty of Earth Sciences
Utrecht University
3508 TA Utrecht
The Netherlands
jeannot@geo.uu.nl

Jun Tsuchiya
Geodynamics Research Center
Ehime University
2-5 Bunkyo-cho
Matsuyama 790-8577
Japan
junt@sci.ehime-u.ac.jp

Taku Tsuchiya
Geodynamics Research Center
Ehime University
2-5 Bunkyo-cho
Matsuyama 790-8577
Japan
takut@sci.ehime-u.ac.jp

Yuko Uchio
Public Relations Department
National Science Museum, Japan
Ueno Park 7-20, Taito
Tokyo 110-8718
Japan
yuchio@kahaku.go.jp

Atsushi Utsunomiya
Institute of Earth Sciences
Academia Sinica
P.O. Box 1-55, Nankang
Taipei 11529
Taiwan
uchii@earth.sinica.edu.tw

Renata M. Wentzcovitch
Department of Chemical Engineering
and Materials Science
University of Minnesota
421 Washington Av. SE
Minneapolis, Minnesota 55455
USA
wentzcov@cems.umn.edu

Brian F. Windley
Department of Geology
University of Leicester
University Load
Leicester LE1 7RH
UK
brian.windley@btinternet.com

David A. Yuen
Department of Geology and Geophysics
and Minnesota Supercomputing
Institute
University of Minnesota
Minneapolis, Minnesota 55455-0219
USA
daveyuen@gmail.com

Dapeng Zhao
Geodynamics Research Center
Ehime University
Matsuyama 790-8577
Japan
zhao@sci.ehime-u.ac.jp

PART I

THE THERMAL AND COMPOSITIONAL STRUCTURE OF THE EARTH

INTRODUCTION

Part I consists of chapters giving seismological and mineral physics observations on the structure of the Earth's interior (Fig. 1). During the last two decades, there has been a major revolution in the way in which we understand how the Earth and the other planets might have evolved. The two most influential driving forces leading this revolution are (i) high-resolution imaging of the Earth's deep interior mainly by seismology, and (ii) high-pressure mineral physics studies. High-resolution seismological studies have established that there are large heterogeneities in deep interior of Earth including huge low velocity anomalies in the lower mantle beneath Africa and the South Pacific, sometimes referred to as *superplumes* (Fig. 2).

Zhao shows the 3-D P-wave tomographic images for the two superplumes, in addition to the several other plumes with or without tails at core-mantle boundary (hereafter abbreviated as CMB). Moreover, the stagnant slabs are commonly present at 410–660 km depth range (mantle transition zone) in most of the deep subduction zones throughout the world, by this improved tomographic method, based primarily on P waves and other body-wave phases.

To infer the origin of a superplume, an understanding of the post-perovskite phase change in the lower mantle holds the key (Fig. 3). Hirose summarizes the phase relations in both pyrolite and MORB compositions from surface to CMB conditions, and emphasizes the importance of the recently discovered post-perovskite phase, that is stable in D″ layer. Furthermore, the solubility of light elements such as Si, O, Mg in iron liquid is reviewed.

Due to the uncertainties in the pressure-scale under extremely-high pressure conditions (Hirose et al., 2006), it is necessary to calculate the Clapeyron slope of perovskite/post-perovskite transformation by first-principles quantum mechanical calculations. Tsuchiya et al. present a critical review of this debate, and recommend a value of 7.5 MPa/K. However, there are still large variations due to the particular method used in these calculations.

If the catastrophic collapse of once stagnant low-temperature slabs at the mantle transition zone occurs and moves into the lower mantle, the core dynamics must also be strongly affected by a cold slab avalanche due to its refrigerating effect on the liquid core. The direction of flow in the outer core is from north to south in the bundle of

D. A. Yuen et al. (eds.), Superplumes, 3–6.
© 2007 *Springer.*

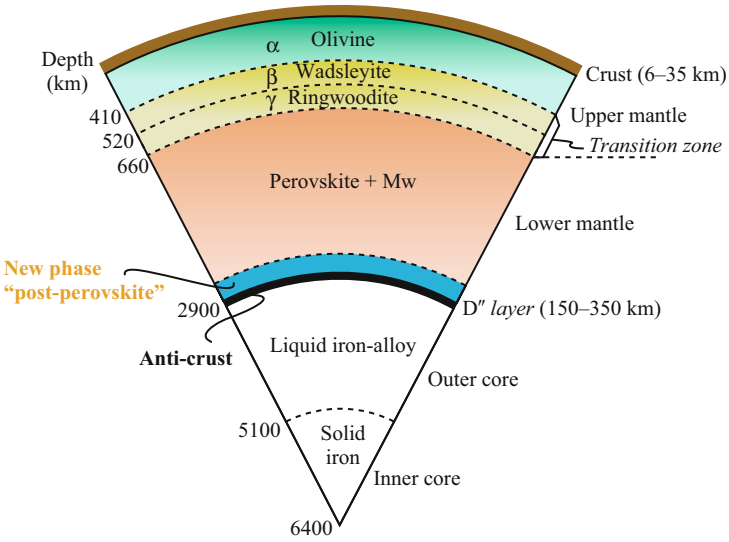

Figure 1. Change of mineral assemblage in the mantle with depth. The seismological boundaries are delineated in the solid Earth.

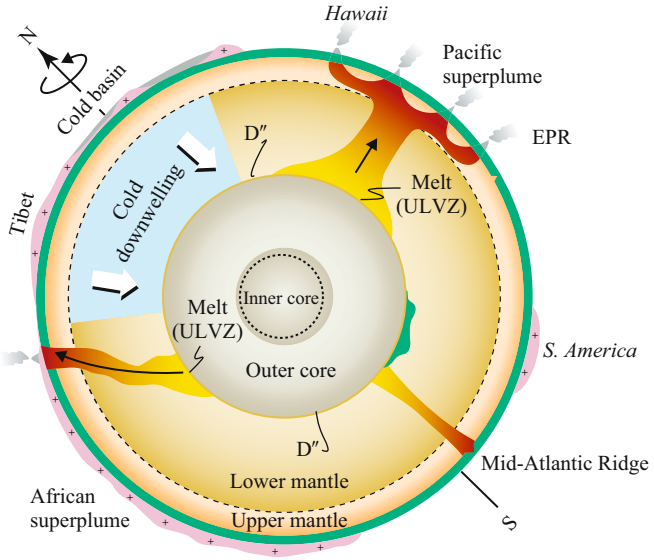

Figure 2. General pattern of mantle convection of the Earth. Two superplumes in the Pacific and Africa, and one super-downwelling underneath Asia form the major convection pattern. The mantle under the Tibet-China-Japan-W. Pacific is the coldest region but most of it is enriched in water by subduction. At 410 km depth small amounts of melt may accumulate. Majorite may also be present as a thin layer at 500–600 km depth, but only in a high-T region such as the central Pacific and Africa.

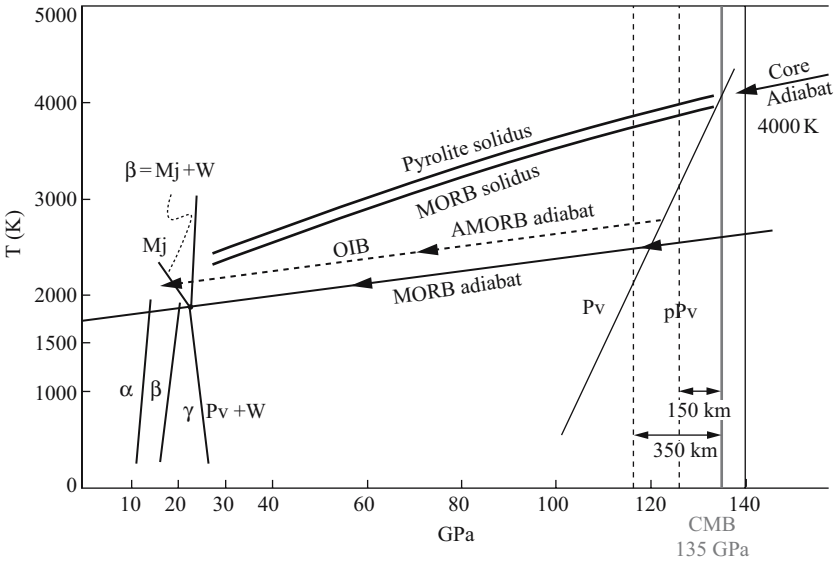

Figure 3. Stability of the post-perovskite phase. The Clapeyron slope of the perovskite/post-perovskite is still being debated.

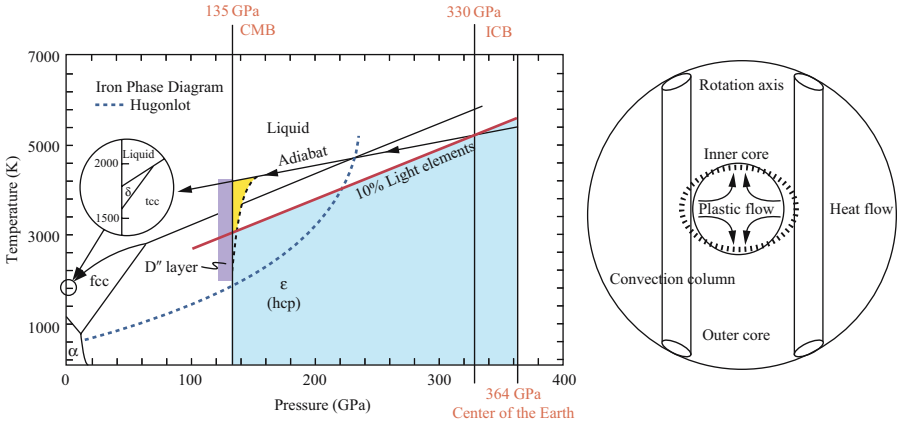

Figure 4. Dynamics of the core. Left: A phase diagram of Fe down to the center of the Earth (Anderson, 2003). ICB may be 5000 K. The core adiabat shows 4000 K at CMB, whereas the coldest zone on the top of the D″ layer (350 km thick) underneath Asia indicates 2000 K. A large temperature gradient is inferred to be present at the CMB. Right: North–south directed columnar dynamo convections in the outer core cool the equatorial solid inner core to cause the plastic flow in the central core (Yoshida et al., 1996).

convective columns, which may cause the preferential growth at the equatorial zone of the solid inner core to the polar regions (Yoshida et al., 1996). This controls the convective plastic flows in the solid inner core (Fig. 4). The concepts of an isotropic upper outer core and an anisotropic lower inner core, and the argument of a possible phase transition of Fe are introduced.

M. Ishii reviews the recent progress on core dynamics, in addition to her own recent works. The structure of the solid inner core can be determined by seismology in great detail. Unlike the liquid outer core, the solid inner core has a rich structure that contains potentially important clues to understanding the evolution and dynamics of the Earth. Ishii's paper provides a good guideline to the use of seismological literature on the core in order to understand the dynamics and evolution of this planet.

REFERENCES

Anderson, O.L. (2003) The three dimensional phase diagram of iron. In V. Dehart, V. et al. (eds.) Earth's Core; Dynamics, Structure and Rotation, Geodynamic Series, 31, AGU, 83–103.

Hirose, K., R. Sinmyo, N. Sata, and Y. Ohishi (2006) Determination of post-perovskite phase transition boundary in MgSiO3 using Au and MgO pressure standards. *Geophys. Res. Lett.*, 33, L01310, 10.1029/2005GL024468.

Yoshida, S., I. Sumita, and M. Kumazawa (1996) Growth model of the inner core coupled with outer core dynamics and the resulting elastic anisotropy. *J. Geophys. Res.*, 101, 28085–28103.

CHAPTER 1

MULTISCALE SEISMIC TOMOGRAPHY OF MANTLE PLUMES AND SUBDUCTING SLABS

DAPENG ZHAO

Geodynamics Research Center, Ehime University, Matsuyama 790-8577, Japan;
E-mail: zhao@sci.ehime-u.ac.jp

Abstract
Local, regional and global tomographic studies of mantle plumes and subducting slabs are reviewed. Applications of the well-established local and teleseismic tomography methods to subduction zones have resulted in clear images of subducting slabs and magma chambers in the upper mantle wedge beneath active arc volcanoes, indicating that geodynamic systems associated with arc magmatism and back-arc spreading are related to deep processes, such as convective circulation in the mantle wedge and dehydration reactions of the subducting slab. Evidence also shows that arc magma and slab dehydration may also contribute to the generation of various types of earthquakes in subduction zones. Most of the slab materials are stagnant in the mantle transition zone before finally collapsing down to the core-mantle boundary as a result of large gravitational instability from phase transitions. Because most hotspots are located in poorly instrumented continental and oceanic regions, 3-D crust and upper mantle structure is determined for only a few hotspots such as Iceland, Yellowstone and Eifel which are covered by seismic networks. Plume-like low-velocity anomalies are revealed in the upper mantle under those hotspots. Global tomographic studies of deep mantle plumes have just started, and more efforts are needed to image the conduits of the lower-mantle plumes. A thorough understanding of the seismic structure of mantle plumes and subducting slabs will only be achieved by a combination of more effective seismic imaging techniques and dense coverage of global seismic networks, particularly in the oceans.

1 INTRODUCTION

Seismic tomography is a technique for determining the three-dimensional (3-D) structure of the Earth's interior by combining information from a large number of crisscrossing seismic waves triggered by natural or artificial seismic sources (Fig. 1). According to the data used, there are body-wave tomography and surface-wave tomography. According to the scales of the study areas, there are global tomography

D. A. Yuen et al. (eds.), Superplumes, 7–30.
© 2007 *Springer.*

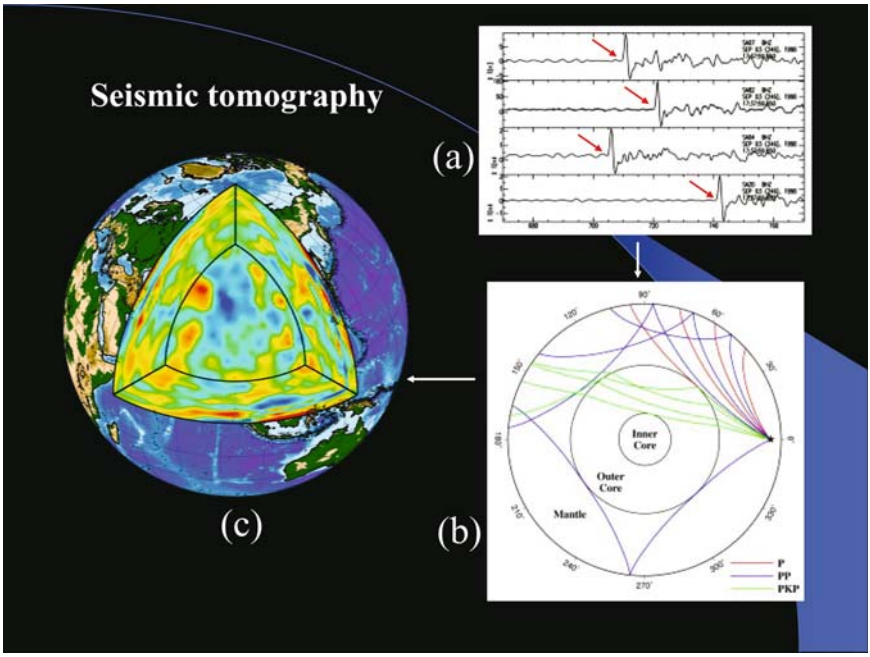

Figure 1. A conceptual diagram of seismic tomography. A large number of arrival times are collected from observed seismograms (a), then a ray tracing technique is used to compute theoretical travel times and ray paths in the Earth's interior (b). Inverting the travel time residuals (differences between the measured and theoretical travel times) results in the three-dimensional distribution of seismic velocity in the Earth (c).

and local/regional tomography. The pioneer studies of the body-wave tomography are Aki and Lee (1976) and Aki et al. (1977) for the local and regional scale, and Dziewonski et al. (1977) and Dziewonski (1984) for the global scale. The surface-wave tomography was initiated by Nakanishi and Anderson (1982), Woodhouse and Dziewonski (1984), and Tanimoto and Anderson (1984). Generally speaking, surface-wave tomography has a lower resolution because of the long wavelength nature of surface waves, and so it is more appropriate for global or large-scale regional studies. By contrast, body-wave tomography can have a much higher spatial resolution because of the short wavelengths of body waves, and it can be applied to multiscale (local, regional and global) studies of the Earth's structure. However, surface-wave tomography is more powerful than body-wave tomography for studying the upper mantle structure under oceanic regions because few stations exist in the oceans. Due to the sparse and uneven coverage of the global seismic networks, global tomographic models still have a low resolution (>500 km), but the models provide information on the deep structure of the Earth. By contrast, local and regional tomographic models for some regions like Japan and California have a much higher

resolution (20–40 km), thanks to the dense seismic networks and much seismicity there, but they are mainly for the crust and/or shallow mantle structures. Because of these advantages and limitations of each of the tomographic approaches, it is necessary to study mantle plumes and subducting slabs by combining useful information from the multiscale tomographic models.

Subducting lithospheric slabs and ascending mantle plumes could be the two complementary features of mantle convection (Nataf, 2000). Subducting slabs represent the main downwellings of mantle convection, while the main upwellings of mantle convection are concentrated in hot columnar features, i.e., plumes. Not all kinds of thermal convection must assume this structural form for the upwellings, but a long series of theoretical investigations has by now established the consensus that ascending flow in the mantle is organized in plume-like structures (Cserepes and Yuen, 2000). The mantle plume hypothesis was proposed forty years ago by Wilson (1963) and Morgan (1971) to explain hotspot volcanoes such as Hawaii and Iceland. A mantle plume is a buoyant mass of material in the mantle that rises because of its buoyancy. On reaching the base of the lithosphere, the plume heads may reach diameters of 500–3000 km, while plume tails are typically 100–500 km in diameter. Hotspots are the surface manifestation of mantle plumes and are focused zones of melting. They are characterized by high heat flow, active volcanism, variable topographic highs depending on plume depth, and hotspot tracks with the age of magmatism and deformation increasing with distance from a hotspot (Condie, 2001). Hotspots and mantle plumes hold the key to several crucial issues of mantle dynamics, and geoscientists are now fully aware of their geodynamical importance (Maruyama, 1994; Condie, 2001). Maruyama (1994) proposed a plume tectonics theory, emphasizing the dominant role of plumes and particularly superplumes in the dynamic evolution of the Earth. In the multidisciplinary effort engaged in understanding hotspots and plumes better, the first task assigned to seismologists is the detection of mantle plumes (Nataf, 2000).

The principles and early developments of seismic tomography were summarized and reviewed by Thurber and Aki (1987), Iyer (1989) and Zhao (2001a). Studies of global and surface-wave tomography were covered by Montagner (1994) and Romanowicz (2003). Shallow and deep structures of subduction zones are reviewed by Zhao (2001b) and Fukao et al. (2001), respectively. Nataf (2000) reviewed the seismic studies of mantle plumes in the twentieth century. In this chapter I review the recent advances in the multiscale tomographic studies of subducting slabs and mantle plumes.

2 LOCAL AND REGIONAL TOMOGRAPHY

Seismologists have mainly used two methods to conduct local and regional tomographic imagings. One is local earthquake tomography (LET) which uses arrival times from local earthquakes recorded by a network of seismic stations; both earthquakes and seismic stations are located in the study area (e.g., Aki and Lee, 1976;

Thurber, 1983; Zhao et al., 1992). The other is teleseismic tomography which uses relative travel time residuals from teleseismic events (distant earthquakes or nuclear explosions) recorded by a seismic network (e.g., Aki et al., 1977). In the latter case, seismic stations are located within the study area, while seismic events are located far from the study area, usually 30–100 degrees (1 degree = 111.2 km) from the edge of the study region. The two methods have inherent advantages and drawbacks. LET can determine the shallow structure of an area to a depth above which earthquakes occur or diving rays (like Pn waves) propagate, but cannot determine the deeper structure. In contrast, teleseismic tomography can determine the deep structure of an area (the maximum modeling depth is about 1.5 times the aperture of the seismic network used), but usually cannot determine the shallow structure since teleseismic rays basically travel in a vertical direction and do not crisscross well near the surface. To resolve this problem, local earthquake arrival times and teleseismic data can be used jointly (e.g., Zhao et al., 1994, 1997). This joint inversion approach preserves the advantages of the two separate approaches and overcomes their drawbacks. Moreover, the horizontally propagating local rays and vertically traveling teleseismic rays crisscross well in the shallow portion of the model, which improve the resolution there.

2.1 Crust and upper mantle structure of subduction zones

Subduction zones have long been recognized as key elements in plate tectonics. Subduction and arc magmatism are fundamental processes in the evolution of the Earth. They play critical roles in the present day differentiation of the Earth's material and are believed to be the major sites of the generation of the continental crust. Subduction is also significant in the water and carbon cycles. So far numerous seismological studies have been made in order to understand the subduction processes, and the 3-D crust and upper mantle structure of most subduction zones has been investigated by using LET or teleseismic tomography methods (see reviews by Zhao, 2001b and Stern, 2002). According to these previous studies, seismological features of subduction zones can be summarized as follows.

All kinds of earthquakes occur in the crust and upper mantle under subduction zones. Shallow earthquakes mainly occur in the upper crust down to about 20 km depth. In the lower crust and uppermost mantle low-frequency microearthquakes ($M < 2.0$) occur only in localized small areas right beneath active volcanoes, which are considered to be associated with the activity of arc magma chambers (Ukawa and Obara, 1993; Hasegawa and Yamamoto, 1994). Recently it has been found that low-frequency microearthquakes occur widely in the forearc regions of Southwest Japan and Cascadia subduction zones, which are considered to be associated with the dehydration process of subducting slabs (Obara, 2002; Rogers and Dragert, 2003). Intermediate-depth and deep-focus earthquakes occur only in the subducting slabs which are colder than the surrounding mantle by a few hundred degrees, and they form a clear Wadati-Benioff deep seismic zone. In some regions the Wadati-Benioff zone may show a two-layered structure (double seismic zone) (Hasegawa et al.,

1978). A majority of seismicity in subduction zones, particularly the large and great earthquakes, occur in the dipping main thrust zone from the oceanic trench down to 40–60 km depth, which reflect the seismic and mechanical coupling between the subducting oceanic plate and the overlying continental plate (e.g., Kanamori, 1971; Stern, 2002).

The subducting oceanic slabs are imaged clearly by seismic tomography as high-velocity anomalies with P and S wave velocities 4–8% faster than the surrounding mantle (Zhao et al., 1992, 1994) (Fig. 2). The subducting slabs also exhibit lower attenuation (high-Q) than the surrounding mantle (Tsumura et al., 2000; Stachnik et al., 2004). The thickness of the slabs seems to depend on the slab age; it is 30–35 km under Kyushu and Southwest Japan (Zhao et al., 2000; Zhao, 2001b), 50 km under Alaska (Zhao et al., 1995), and 90–100 km under NE Japan and Tonga (Zhao et al., 1994, 1997) (Fig. 2).

Structural heterogeneity is expected to exist within the subducting slabs, and it is actually revealed by detailed analysis of seismic waves passing through the slabs. A thin low-velocity (low-V) layer is detected on the top of the slab, which is interpreted to be the subducting oceanic crust (Matsuzawa et al., 1986). Abers (2005) investigated the structure of the low-V layer under seven circum-Pacific arcs and detected a wave guide extending to greater than 150 km depth with a low-V channel 2–8 km thick and with velocity reductions as large as 14% compared with the surrounding mantle,

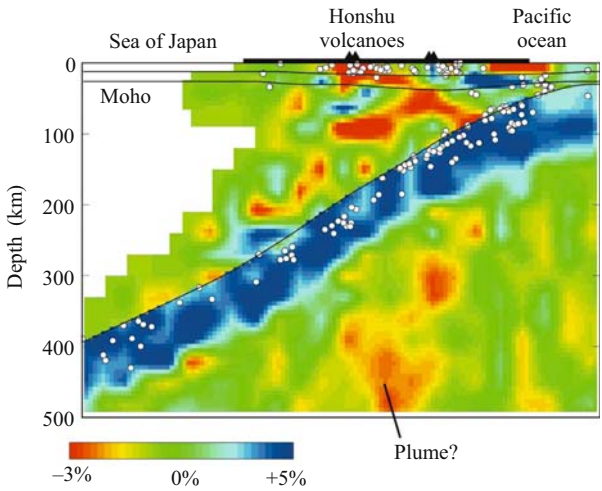

Figure 2. East–west vertical cross section of P-wave velocity structure along a profile passing through central Japan. Red and blue colors denote slow and fast velocities, respectively. The velocity perturbation scale is shown at the bottom. White dots denote earthquakes that occurred within a 40-km width from the profile. The thick bar and solid triangles denote the land area and active arc volcanoes, respectively. The three curved lines show the Conrad and the Moho discontinuities and the upper boundary of the subducting Pacific plate (Zhao, 2004).

although there is substantial variability with depth. It is found that intermediate-depth earthquakes in the lower plane of the double seismic zone under NE Japan occur in relatively higher-velocity areas within the slab (Zhao et al., 1992). The existence of a metastable olivine wedge within the subducting slab was proposed to explain the occurrence of the intermediate-depth and deep-focus earthquakes (Green and Burnley, 1989; Kirby, 1991). However, it is still debatable whether such a metastable olivine wedge really exists and, and even if it does exist, whether it can be detected (Koper et al., 1998).

Prominent low-V and low-Q (high attenuation) zones are imaged by seismic tomography in the upper mantle wedge above the subducting slab in all the subduction zones investigated so far, which represent the arc magma chambers associated with the slab dehydration and convective circulation process in the mantle wedge (Zhao et al., 1992, 1997; Zhao, 2001b) (Fig. 2). Shear wave splitting analyses have shown that strong seismic anisotropy exists in the mantle wedge (Nakajima and Hasegawa, 2004). Tamura et al. (2002) found along-arc variation of the low-V zones in the mantle wedge under NE Japan, suggesting that mantle melting and the production of magmas may be controlled by locally developed hot regions within the mantle wedge that have the form of inclined, 50 km wide fingers. The hot fingers in the mantle wedge under NE Japan are also modelled by numerical simulations (Honda and Saito, 2003).

So far 3-D seismic structure of the crust and upper mantle has been determined under the land areas of many subduction zones. The structure of the forearc region under oceanic areas, however, is less well known because earthquakes under the oceans are not located accurately due to the lack of seismic stations. Umino et al. (1995) detected sP depth phase from seismograms of earthquakes under the Pacific Ocean recorded by land seismic stations in NE Japan and used the sP phase to relocate the sub-oceanic events accurately, since the sP phase is very sensitive to the focal depth. This approach is used to relocate many earthquakes under the NE Japan forearc beneath the Pacific Ocean; and then P and S wave data from earthquakes beneath both the land and Pacific Ocean are combined to determine 3-D P and S velocity structures under the entire NE Japan arc from the Japan trench to the Japan Sea coast (Zhao et al., 2002; Mishra et al., 2003; Wang and Zhao, 2005). Their inversion results revealed strong lateral heterogeneities on the upper boundary of the Pacific slab under the forearc region, which show a good correlation with the spatial distribution of large interplate earthquakes. Widespread slow anomalies are visible in the forearc mantle above the subducting Pacific slab, which may reflect the serpentinization of the forearc mantle associated with the dehydration process of the subducting slab. Fluids from the slab dehydration and lateral heterogeneity on the slab boundary can certainly affect the nucleation of large interplate earthquakes in the forearc region (Zhao et al., 2002). These studies have the important implications that detailed tomographic images can be obtained outside a seismic network if earthquakes occur there. Applying the new approach to other subduction zones would greatly advance our understanding of the structure and dynamics of the forearc regions.

2.2 Upper mantle structure of hotspots and mantle plumes

Hotspots have an irregular but nonrandom distribution over the Earth's surface. They are preferentially located near the divergent plate boundaries (mid-ocean ridges), and are preferentially excluded from regions near the convergent plate boundaries, in particular, subduction zones (Stefanick and Jurdy, 1984; Richards et al., 1988; Weinstein and Olson, 1989). There is little agreement on the total number of hotspots. Several hotspot lists have been published and the number of hotspots included on these lists ranges from about 20 to more than 100 (Morgan, 1972; Wilson, 1973; Crough and Jurdy, 1980; Vogt, 1981). On recent lists the number of hotspots converges to 44 (Steinberger, 2000) to 47 (Richards et al., 1988). The origin of these hotspots is generally attributed to mantle plumes (Wilson, 1963; Morgan, 1971), but some intraplate volcanism may be explained by plate tectonic processes in the upper mantle and the mantle transition zone (Anderson, 2000; Foulger, 2003).

Compared with subduction zones, the seismic structure of the crust and mantle is less well known for most of the hotspots and mantle plumes. The main reason for this seems to be that most of the hotspots are located in the oceanic regions and the African continent where few seismic stations exist, posing problems for seismic imaging. The upper mantle structure under only a few hotspots has been studied by seismic imaging.

The best studied hotspot is Iceland, partly because the island is large enough to install permanent and portable seismic networks for imaging its 3-D upper mantle structure (Tryggvason et al., 1983; Wolfe et al., 1997; Foulger et al., 2000; Allen et al., 2002; Hung et al., 2004). These studies show that a cylindrically shaped low-V zone extends from the shallow upper mantle to 400 km depth beneath central Iceland. The low-V anomalies in the depth range of 250–400 km are elongated in the N-S direction, which is interpreted as an indication of the upper mantle origin of the upwelling beneath the hotspot (Foulger et al., 2000). Hung et al. (2004) used finite frequency tomography to image the Iceland plume. Their results show a columnar low-V zone having a lateral dimension of ~250–300 km extends to 670 km depth, deeper than that resolved by the ray-based studies. Receiver function analyses using P to S conversions from upper mantle discontinuities show that the mantle transition zone beneath central and southern Iceland is thinned, consistent with the hypothesis that the Iceland plume originates from deeper than 700 km (Shen et al., 2002).

Hawaii is a prototypal hotspot and has the largest buoyancy flux of all active plumes (Sleep, 1990). It is one of the most thoroughly studied hotspots in the world by various geophysical, geochemical and petrological methods, yet there remain fundamental geodynamic questions regarding the nature of mantle flow and plume-lithosphere interaction in the region. Several seismic studies in the Hawaiian region have characterized aspects of the local mantle structure. Tomographic inversions of teleseismic data have yielded images of low-V anomalies down to 350 km depth, which have been taken to indicate the presence of melt migrating upward to the active volcanoes (Ellsworth and Koyanagi, 1977; Tilmann et al., 2001; Wolfe et al., 2002). The inversions did not resolve a cylindral low-V plume in the upper mantle beneath the

islands of Hawaii, but resolution tests indicate that this outcome could be the result of the sparse and nearly linear distribution of seismic stations combined with the incomplete azimuthal coverage of the earthquake sources (Wolfe et al., 2002). Measurements of Rayleigh wave dispersion have been carried out to assess the presence of a hot asthenosphere emanating from the plume and the degree of downstream lithospheric erosion (Woods and Okal, 1996; Priestley and Tilmann, 1999; Laske et al., 1999). Mantle discontinuities beneath the islands have been mapped using receiver functions (Li et al., 2000). While these results have been promising, the limited distribution of seismic stations in these experiments has left open the full nature of the mantle seismic structure beneath the Hawaiian hotspot. A determination of the detailed 3-D structure of the upper mantle beneath the Hawaiian hotspot will require a simultaneous deployment of both ocean-bottom and land seismometers (Wolfe et al., 2002).

Yellowstone is the best known continental hotspot. As it propagated across eastern Idaho to its current location in NW Wyoming, it left behind a swath of magmatically altered crust, the eastern Snake River Plain, which lies along the axis of a SW broadening wake-like swell. This behavior is consistent with mantle melt release at a focused site that is stationary in a hotspot reference frame, and with the hot and buoyant residuum flattening against the base of the lithosphere as it is dragged to the SW by the motion of the North American plate. Several teleseismic tomography studies have been made for this region (Evans, 1982; Saltzer and Humphreys, 1997; Schutt and Humphreys, 2004; Yuan and Dueker, 2005). A 100-km diameter upper mantle plume is imaged that extends from the Yellowstone volcanic caldera to 500 km depth. A monotonic decrease in the velocity perturbation of the plume from −3.2% at 100 km to −0.9% at 450 km is consistent with a uniform thermal anomaly of 180°C (Yuan and Dueker, 2005).

Ritter et al. (2001) and Keyser et al. (2002) showed P and S wave images of the upper mantle below the Quaternary Eifel volcanic fields, Germany, determined by teleseismic tomography. They measured the data at a dedicated seismic network of more than 200 stations. Their results show a columnar low-V anomaly in the upper mantle. The 100 km wide structure extends to at least 400 km depth and is equivalent to ∼150–200 K excess temperature. This clear evidence for a plume below a region of comparatively minor volcanism suggests that deep mantle plumes could be more numerous than commonly assumed (Malamud and Turcotte, 1999), which may often be associated with small volcanic fields or may have no volcanic surface expression at all. Global tomographic studies show a wide plume-like structure in the lower mantle below Central Europe, but no clear connection through the transition zone to the shallow mantle (Goes et al., 1999; Zhao, 2001c).

Pilidou et al. (2004) showed a S-wave velocity and azimuthal anisotropy model for the upper mantle beneath the North Atlantic and surrounding region derived from analyses of over 3000 fundamental and higher mode Rayleigh waveforms. Their model has a horizontal resolution of a few hundred kilometers extending to 400 km depth. Low-V anomalies in the vicinity of the Eifel hotspot extend to about 400 km depth. Strong slow anomalies exist in the North Atlantic upper mantle beneath the

Iceland and Azores hotspots. Both anomalies are, above 200 km depth, 5–7% low and are elongated along the Mid-Atlantic ridge. The fast propagation direction of S waves in the Atlantic south of Iceland correlates well with the E-W ridge-spreading direction at all depths and changes to a direction close to N-S in the vicinity of Iceland.

2.3 Intraplate volcanism in Northeast Asia

Several active intraplate volcanoes, e.g., Wudalianchi and Changbai, exist in NE Asia (Figs. 3 and 4). The Wudalianchi volcano erupted in AD 1719 and 1721. The Changbai volcano erupted in AD 1050, 1120, 1193 and 1410. The origin of these volcanoes is still unclear. Some researchers considered them to be hotspots (e.g., Turcotte and Schubert, 1982), while others invoked the asthenospheric injection to explain them (Tatsumi et al., 1990). Recently 3-D seismic images of the mantle down

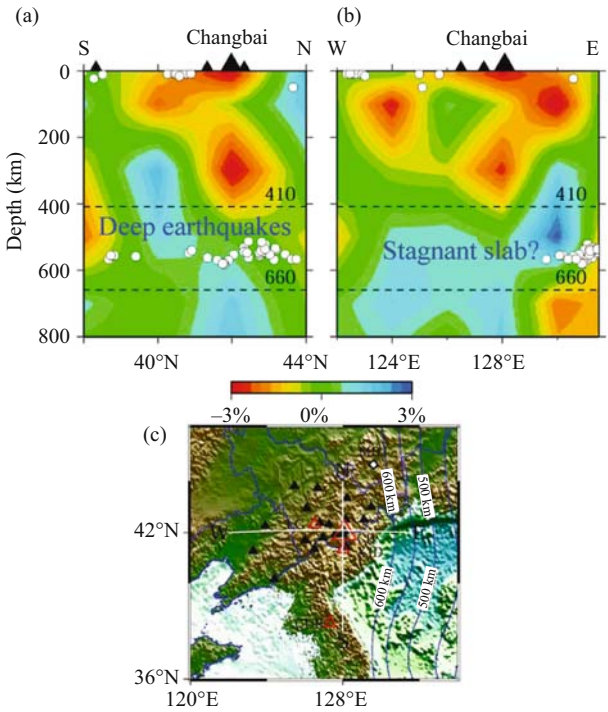

Figure 3. North–south (a) and east–west (b) vertical cross sections of P-wave velocity images under the Changbai intraplate volcano in NE Asia (Zhao et al., 2004). Red and blue colors denote slow and fast velocities, respectively. The velocity perturbation scale is shown below the cross sections. Black triangles in (a) and (b) denote the intraplate volcanoes. White dots denote earthquakes that occurred within 100 km of the profiles. The two dashed lines denote the 410 and 660 km discontinuities. (c) Locations of the cross sections in (a) and (b). Black and red triangles denote seismic stations and volcanoes, respectively. The contour lines show the depths of the Wadati-Benioff deep seismic zone.

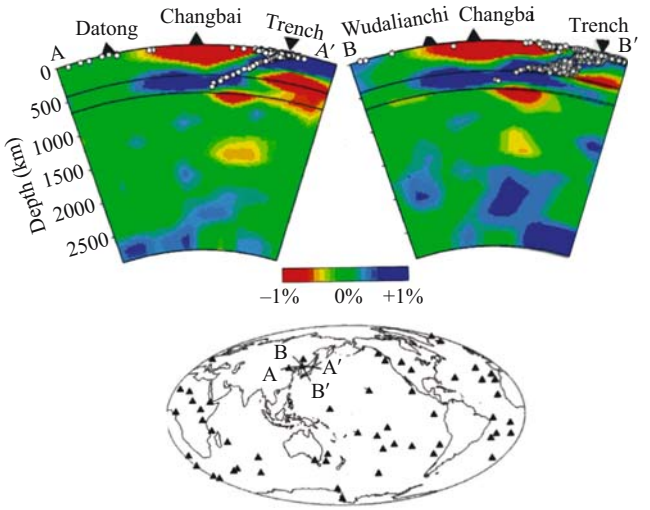

Figure 4. Vertical cross sections of P-wave velocity images determined by a global tomographic inversion (Zhao, 2004). Locations of the cross sections are shown in the insert map. Red and blue colors denote slow and fast velocities, respectively. The velocity perturbation scale is shown below the cross sections. Black triangles denote volcanoes. The reversed triangles show the location of the Japan Trench. White dots denote earthquakes that occurred within 150 km of the profiles. The two solid lines denote the 410 and 660 km discontinuities.

to 800 km depth are determined beneath the Changbai volcano by applying teleseismic tomography to relative travel time residuals recorded by a portable seismic network (Zhao et al., 2004; Lei and Zhao, 2005) (Fig. 3). The results show a columnar low-V anomaly extending to 400 km depth under the Changbai volcano. High-velocity anomalies are visible in the mantle transition zone, and deep earthquakes occur at depths of 500–600 km under the region, suggesting that the subducting Pacific slab is stagnant in the transition zone, as imaged clearly also by global tomography (Zhao, 2004) (Fig. 4).

The tomographic images under NE Asia are quite similar to those under the Fiji-Tonga region where the back-arc volcanoes in Fiji and the Lau spreading center are located above very slow anomalies in the mantle wedge right above the subducting Tonga slab (Zhao et al., 1997). These results suggest that the active volcanoes in NE Asia are not hotspots like Hawaii but a sort of back-arc volcanoes which are closely related to the subduction process of the Pacific slab. Low-V anomalies in the back-arc region are generally associated with the back-arc magmatism and volcanism caused by the deep dehydration process of the subducting slab and the convective circulation process of the mantle wedge (Zhao et al., 1994, 1997; Zhao, 2001b). These processes lead to the large-scale upwelling of the asthenospheric materials under NE Asia and cause intraplate volcanism and continental rift systems in the region. The extensional rift systems and faults widely existing in NE Asia may be the surface manifestation

of the deep dynamic processes (Tatsumi et al., 1990). Tatsumi et al. (1990) first proposed the asthenospheric injection to explain the formation of the Wudalianchi and Changbai volcanoes, but they did not consider the stagnant Pacific slab under the region because such a slab structure was unknown at that time. Zhao et al. (2004) emphasized the role of the stagnant Pacific slab in the formation of the intraplate volcanism in NE Asia.

2.4 The Baikal rift zone

The Baikal rift zone is composed of a branched chain of Late Cenozoic half-grabens extending over a distance of about 1500 km in Siberia with significant seismic and volcanic activities. It is situated at the boundary of the Siberian platform (craton) to the northwest and the Mongolian fold belt to the southeast. Lake Baikal occupies only about a third of the rift zone. It is the deepest lake (1620 m) in the world and contains 20% of the world's fresh water. The Baikal rift is probably the most debated of all rifts in terms of its origin. Most Russian scientists support the active rift hypothesis that theorizes an anomalous upper mantle that formed beneath the continental lithosphere and led to the development of the rift. The passive hypothesis suggests the rift began as a result of the collision of India with Asia. These disagreements are mainly caused by the fact that the deep structure of the Baikal rift zone has not been understood well, although many researchers have studied the crust and upper mantle structure under this region using various geophysical methods including seismic tomography.

Zhao et al. (2006) carefully collected a large number of high-quality arrival time data from original seismograms of teleseismic events recorded by a portable seismic network; they used a modified tomographic inversion method (Zhao, 2001c) to determine the P-wave velocity images under the Baikal rift zone. Their results show a prominent low-velocity anomaly extending down to 600 km depth under the Baikal rift zone and high-velocity anomalies in the lithosphere under the Siberian craton. The low-velocity anomalies are interpreted as a mantle upwelling (plume) which has played an important role in the initiation and evolution of the Baikal rift zone. The rift formation may also be controlled by other factors such as older (prerift) linear lithosphere structures favorably positioned relative to the upwelling and favorable orientation of the far-field forces caused by the India-Asia collision.

3 GLOBAL SEISMIC TOMOGRAPHY

During the last two decades, many global tomographic studies have been made to determine the whole mantle 3-D structure (Dziewonski, 1984; Inoue et al., 1990; Zhang and Tanimoto, 1993; Su et al., 1994; Vasco et al., 1995; Grand et al., 1997; van der Hilst et al., 1997; Bijwaard et al., 1998; Boschi and Dziewonski, 1999; Ritsema et al., 1999; Zhao, 2001c, 2004). Forward waveform modeling has complemented tomographic studies, providing details of structural features as well as smaller-scale patterns of heterogeneity (see reviews by Lay et al., 1998 and Garnero, 2000). These studies have greatly improved our understanding of the structure and dynamics of

the Earth's deep interior. In past studies of travel-time tomographic inversions for the mantle structure, a few researchers have carefully measured their own arrival time data (Woodward and Master, 1991; Su et al., 1994; Grand et al., 1997); many others have used the large International Seismological Center (ISC) data set. Although the ISC data have been critiqued because of uncertainties in travel time picking methods, a careful reprocessing of the data (Engdahl et al., 1998) has resulted in global images of mantle structure from ISC P times that look remarkably similar to those from non-ISC S times (Grand et al., 1997).

So far most of the global tomographic studies have concentrated on the imaging of deep subducting slabs, and much has been found out about the cold parts of the mantle convection. The upwelling plumes, the hot portion of the mantle convection, however, have been focused only by a few recent global tomographic studies (Bijwaard and Spakman, 1999; Zhao, 2001c, 2004; Montelli et al., 2004).

3.1 Deep structure of subducting slabs

Many seismological studies in the last two decades have addressed the issue of the fate of subducting oceanic slabs, in particular, the behavior of slabs around the 670 km discontinuity. Earlier researchers (e.g., Creager and Jordan, 1984, 1986) thought that slabs simply plunge directly through the 670 km discontinuity. Later, tomographic images showed complex behavior of the subducted slabs (e.g., Zhou, 1996; Grand et al., 1997; van der Hilst et al., 1997; Bijwaard et al., 1998; Fukao et al., 2001; Zhao, 2001c, 2004). Their results do not support a simple slab penetration, but show a strong resistance when the slab encounters the 670 km discontinuity. The slab bends horizontally, and accumulates there for a long time (ca. 100–140 m.y.), and then finally collapses to fall down as blobs onto the core mantle boundary (CMB) as a result of very large gravitational instability from phase transitions (Machetel and Weber, 1991; Honda et al., 1993; Cadek et al., 1994; Maruyama, 1994) (Fig. 4). But there are still different opinions on the depth range of the slab stagnancy. Fukao et al. (2001) suggested that slabs are stagnant in the so-called Bullen transition zone at depths of 400–1000 km. In contrast, the tomographic images of Boschi and Dziewonski (1999) and Zhao (2001c, 2004) show that strong and wide high-velocity anomalies exist in the mantle transition zone (410–670 km) under the subduction regions. In the top portion of the lower mantle, the circum-Pacific high-velocity zone becomes less clear or disappears. Zhao (2004) conducted several synthetic tests and confirmed it to be a reliable feature.

Receiver functions and waveform modeling analyses show complicated features in the depth range of 660–780 km at the tip of the stagnant slab as well as reflectors/scatters in the lower mantle under the subduction region in the western Pacific (Niu and Kawakatsu, 1996; Tajima et al., 1998; Kaneshima and Helffrich, 2003; Ai et al., 2003). This phenomenon is considered to be caused by the pieces of slab blobs collapsing down to the lower mantle.

Many tomographic models show the images of the old Farallon slab in the lower mantle under North America, and it is generally agreed that the Farallon slab has

sunk deeply through the lower mantle reaching the CMB (e.g., Grand et al., 1997; Bijwaard et al., 1998; Fukao et al., 2001; Zhao, 2004). Other deeply sinking slabs are the presumed Indian (Tethys) slab under Himalaya and the Bay of Bengal as well as Mesozoic slabs under Siberia (Van der Voo et al., 1999a,b). These remanent slabs are not connected to the surface plates or to the presently subducting slabs and appear to sink independently from the latter. The presence of these deeply sinking slabs implies that the pre-Eocene subduction occurred in much the same way as in the present day to accumulate slab bodies in the transition zone and that the consequent unstable down flow occurred extensively through the transition region in the Eocene epoch to detach many of the surface plates from the subducted slabs at depths and hence caused the reorganization of the global plate motion (Fukao et al., 2001).

An unexpected feature in Figure 4 is that prominent slow anomalies appear beneath the subducting Pacific slab and extend down to the lower mantle. This feature was also imaged by Fukao et al. (2001). To understand this feature better, Zhao (2004) conducted a high-resolution tomographic inversion using arrival times of local and teleseismic rays recorded by the dense seismic networks on the Japan Islands. The tomographic image obtained has a spatial resolution of 25–35 km for the crust and mantle wedge and 40–50 km for the subducting slab and the mantle under the slab down to a depth of 500 km (Fig. 2). The subducting Pacific slab and arc-magma related slow anomalies in the mantle wedge are imaged clearly. Prominent slow anomalies are visible in the depth range of 260–500 km under the subducting Pacific slab. The sub-slab slow anomalies have a lateral extent of 70–160 km. Reconstruction tests and resolution analyses confirmed that they are a reliable feature. It is unclear what the sub-slab slow anomalies represent. There are two possibilities: one is that they represent a hot upwelling portion of a local-scale convection associated with the subduction of the Pacific slab; the other is that they show a small mantle plume rising from the lower mantle (see also Fig. 4). Malamud and Turcotte (1999) suggested that more than 5000 plumes exist in the mantle and the large number of seamounts represents the surface evidence for small plumes. If this conjecture is correct, it is not surprising that small plumes appear under the subducting slab, as detected by the tomographic imagings (Figs. 2 and 4).

3.2 Deep mantle plumes

Although most of the global tomographic studies in the last two decades have showed that seismic velocity is slower in the lower mantle under South-Central Pacific and Africa where most hotspots are located, little effort was made to exploit the tomographic models to address the deep structure and origin of mantle plumes. Bijwaard and Spakman (1999) were perhaps the first attempt to address this issue. Their global P-wave tomographic model revealed a continuous low-V anomaly of 500–600 km wide in the lower mantle under the Iceland hotspot, which was interpreted as the Iceland plume originating from the CMB. Ritsema et al. (1999) developed a global S-wave tomographic model derived from surface-wave and body-wave data. Their model shows that vertically continuous low-V anomalies in the upper mantle are

present beneath Afar, Bowie, Easter, Hawaii, Iceland, Louisville, McDonald and Samoa hotspots but not beneath the other 29 hotspots in the list of Sleep (1990). Low-V zones are also visible in the lower mantle under some of the hotspots, but the authors were not certain about those features due to the limited resolution of their model (see also Ritsema and Allen, 2003).

Zhao (2001c) developed a global P-wave tomography model particularly for detecting mantle plumes. He inverted about one million data of P, pP, PP and PcP waves selected from the reprocessed ISC data set (Engdahl et al., 1998). His model shows two superplumes under South Pacific and Africa, which have lateral extents of thousands of kilometers and exist in the whole mantle (Fig. 5). Continuous whole-mantle plumes are also detected under Hawaii, Iceland and Kerguelen hotspots (Fig. 5). The Hawaiian plume is not part of the Pacific superplume, but it is possible that there are some heat or material interchanges between them in the mid-mantle depth (Zhao, 2004; Lei and Zhao, 2006). Some small-scaled plumes are also found, which originate from the transition zone or mid-mantle depths. An important result of Zhao (2001c, 2004) is that slow anomalies under hotspots usually do not show a straight pillar shape, but exhibit winding images (Fig. 5), which suggests that plumes are not fixed in the mantle but can be deflected due to the influence of mantle flow, as was

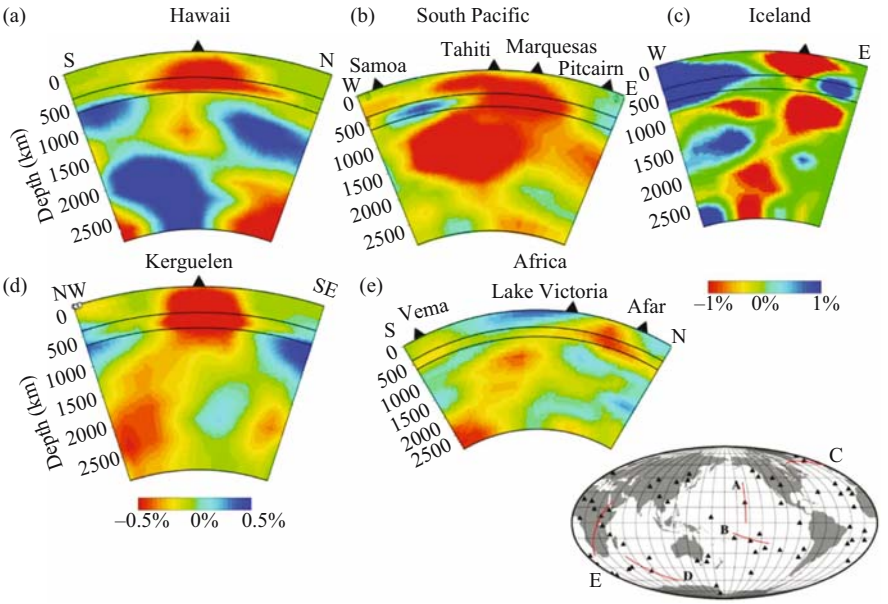

Figure 5. Vertical cross sections of P-wave velocity images under Hawaii (a), South Pacific (b), Iceland (c), Kerguelen (d), and Africa (e) derived from the global tomographic model of Zhao (2004). Locations of the cross sections are shown in the insert map. Red and blue colors denote slow and fast velocities, respectively. The velocity perturbation scale is shown below (c) and (d). Black triangles denote the hotspot volcanoes. The two solid lines in each of the cross sections denote the 410 and 660 km discontinuities.

pointed out earlier by numerical simulation studies (e.g., Griffiths and Richards, 1989; Loper, 1991; Steinberger, 2000). Other seismic imagings (Bijwaard and Spakman, 1999; Shen et al., 2002) and paleomagnetic studies (Tarduno and Cottrell, 1997) also suggested the deflection of plumes. As a consequence of the deflection of mantle plumes, hotspots would not be fixed in the long geological history but could wander on the Earth's surface, though their relative moving velocities are much smaller than those of the lithospheric plates (Molnar and Stock, 1987; Griffiths and Richards, 1989; Tarduno and Cottrell, 1997; Steinberger, 2000).

Montelli et al. (2004) determined a global P-wave tomographic model using a finite-frequency modeling and irregular model parameterizations. Their model shows a collection of plumes in the mantle. Deep plumes are present beneath Ascension, Azores, Canary, Cape Verde, Cook Island, Easter, Kerguelen, Samoa and Tahiti. Plumes rising from the base of the mantle but not yet reaching the surface are located in the Coral Sea, east of Solomon and south of Java. Plumes beneath Eifel, Etna and Seychelles remain mostly confined to the upper mantle. Several plume images extend only down to the mid-mantle. For these plumes a deep origin cannot be simply ruled out because resolution tests show that they could have a very thin, not resolvable, tail. Also, none of the imaged plumes exhibits the typical mushroom-shaped structure. Their model also shows that the plumes are wide, with radii as large as 300–400 km. However, the effectiveness of the finite-frequency tomography and the tomographic model of Montelli et al. (2004) have been questioned and criticized recently (de Hoop and van der Hilst, 2005; van der Hilst and de Hoop, 2005).

In addition to global tomography, several waveform modeling studies also suggested the lower mantle or CMB origin of the Hawaiian plume (Ji and Nataf, 1998; Russell et al., 1999) and the Iceland plume (Helmberger et al., 1998; Shen et al., 2002). Foulger et al. (2000) proposed that the Iceland plume extends down to the mantle transition zone and no deeper. However, their tomographic images were based on the data recorded by a local seismic network and so have no resolution below the transition zone.

It is still a debated issue what causes the hotspots and whether plumes exist. Instead of the plume hypothesis, some mechanisms associate hotspot formation to propagating cracks, abandoned ridges, leaky transforms or other damaged regions of the lithosphere that is under extention and above a partially molten upper mantle (McDougall, 1971; Turcotte and Oxburgh, 1973; Anderson, 2000; Fougler, 2003). Convection due to thermal gradients at the margins of cratonic lithosphere and passive infilling processes along the mid-ocean ridge produce 3-D instabilities that may be indistinguishable from plume upwellings (King and Anderson, 1995; King and Ritsema, 2000; Korenaga and Jordan, 2002).

3.3 Heterogeneity in the lowermost mantle

The lowermost 200 km of the mantle (known as the D″ region) has long been characterized by seismologists as distinctive in its properties from the overlying deep mantle. The D″ and CMB regions have undoubtedly played a significant role

in both the core and mantle dynamic systems throughout the 4.50-Gyr evolution of the Earth (Lay et al., 1998). Numerous studies have revealed the presence of anomalous features in the D″ region, such as intermittent stratification, shear-wave anisotropy and ultra-low-velocity layer (see reviews by Lay et al., 1998 and Garnero, 2000). These seismic observations and their spatial systematics raise many questions about primary processes in the CMB region and possible importance of the CMB layer for dynamic processes throughout the planet, including an intimate relationship to subducted slabs and mantle plumes as well as surface structures, which define challenging research frontiers for experimental and computational geophysics. But the precise role of the CMB region remains a topic of vigorous research and debate requiring improved resolution of the structure and processes operating there.

The D″ and CMB regions are thought to be the graveyard of subducted slabs and the birth place of mantle plumes. It has been proposed that the large slow regions in the mantle beneath the central Pacific and Africa, observed in all tomographic models, are related to superplumes generated by thermal boundary layer instabilities at the CMB (Stacey and Loper, 1983; Sleep, 1990; Thompson and Tackley, 1998). It was also found that some parts of the D″ regions under south-central Pacific and Africa exhibit ultralow velocities, which are interpreted as partial melts (Williams and Garnero, 1996). Some chemical heterogeneity, possibly involving core material (iron), may be present as well (Knittle and Jeanloz, 1991). It is dynamically possible for the heavier iron to be pulled upward by strong enough thermal buoyant forces, as shown in numerical simulations (Hansen and Yuen, 1988; Yuen et al., 1993; Cadek et al., 1994).

Prominent high-velocity patches are also visible in the lowermost mantle. Waveform modeling studies show that some areas have a contrast of 7–8% with respect to adjacent "hot" mantle, which cannot be explained by thermal effects alone (Breger and Romanowicz, 1998). A portion of ancient slab lying at the CMB is not likely to be responsible for this velocity contrast because reconstructions of ancient subduction zones do not predict the presence of a remnant lithosphere in D″ under the south-central Pacific (Lithgow-Bertelloni and Richards, 1998), and such a fossil slab might not produce a sufficient velocity contrast (Wysession et al., 1998). The fast and localized anomaly could represent a high-velocity product of the decomposition of perovskite at temperatures and pressures corresponding to the lowermost mantle (Stixrude, 1998) or of core-mantle reactions (Knittle and Jeanloz, 1991; Stixrude, 1998); and it may be related to the selective entrainment of chemically distinctive material into the thermal plume (Kellogg and King, 1993). Because significant shear wave splitting has been observed for waves traveling through the central Pacific region (Vinnik et al., 1998), the large velocity contrast could also be related to anisotropy. The blocks of fast material on the CMB could be responsible for the intermittent reflections observed at the top of D″ (Garnero, 2000).

Recently a post-perovskite transition in $MgSiO_3$ was found by in situ X-ray diffraction in a diamond anvil cell at ~2500 K and 125 GPa (Murakami et al., 2004). This condition is similar to that expected in the D″ layer. This post-perovskite structure

was also identified by first principles calculations (Tsuchiya et al., 2004). This phase transition is important for understanding the state of the deep lower mantle, particularly that of the D″ layer, e.g., its wide topography and strong anisotropy.

4 DISCUSSION AND CONCLUSIONS

The distribution of both earthquakes and seismic stations on Earth is nonuniform. Earthquakes occur mainly in plate boundary regions; intermediate-depth and deep-focus earthquakes occur only in subduction zones. Seismic stations are installed mainly in a few developed countries on the land areas. In the broad oceanic regions and the African and South American continents, there are few permanent stations; though portable stations were deployed there for short periods of time. This nonuniform nature of the distribution of the seismic sources and stations requires a multiscale approach to seismic imaging. Regions that are covered densely by stations and/or seismicity can be imaged with a high resolution by using teleseismic and local tomography, while poorly instrumented regions can only be imaged roughly by global or large-scale regional tomography. This situation will last for quite a long time. However, a recent study shows that high-resolution local tomography can be obtained without a dense seismic network if reflected and converted waves can be detected from seismograms and used in the tomographic inversion (Zhao et al., 2005).

Compared with other tectonic units on Earth, subduction zones have been well studied by seismological methods. The 3-D seismic structure of the crust and upper mantle under the continental margins and the land areas of island arcs is determined for most of the subduction zones, which revealed the high-velocity subducting slabs and low-velocity anomalies in the mantle wedge under the active arc volcanoes. The formation of arc magmatism and volcanism has been well understood in the last two decades, thanks to the advances in seismic imaging in addition to the petrological and geochemical studies.

There is, however, much to be done for the further understanding of the structure and dynamics of subduction zones. First, little is known on the forearc region of most subduction zones. Determination of the detailed structure of the forearc regions is important for understanding the initial stage of subduction and the seismic and mechanical coupling between the subducting oceanic plate and the overlying continental plate. Most of the large and great earthquakes in the world occur in the forearc regions of subduction zones. Clarification of the generating mechanism of the damaging interplate earthquakes also requires a detailed study of the forearc regions. Second, the back-arc regions need further studies, which are important for understanding the mechanism of back-arc spreading, deep slab dehydration, depth extent of the mantle wedge magma, as well as the relationship between the arc magmatism and the intraplate volcanism in the continental region behind the marginal seas (e.g., the active volcanoes in NE Asia). Third, the detailed structure of the subducting slab should be investigated, which is important for resolving the puzzle of the double seismic zone, the presence or absence of the metastable olivine wedge, and the mechanism of deep-focus earthquakes. Fourth, the structure of the

lower slab boundary and the mantle under the slab is poorly known. Is the lower boundary of the slab a sharp seismic discontinuity as its upper boundary? If not, how thick is the transitional zone around the lower slab boundary? Is the mantle under the slab homogeneous or heterogeneous? If heterogeneity exists there, what is the cause? These questions should be addressed in future studies of subduction zones.

The plume hypothesis is very attractive in explaining the hotspot magmatism and it is now widely recognized. However, direct evidence for actual plumes is weak, and many questions remain unanswered. Do plumes actually exist? What do they look like? How wide are they? How hot are they? Do they really rise from the CMB? All of them? Are they tilted on their way up? Are there different kinds of plumes? (Nataf, 2000). To answer these questions, seismic imaging will play a critical role. So far detailed 3-D crust and upper mantle structure is determined for only a few hotspots such as Iceland, Yellowstone and Eifel. Such information is scarce for most of the hotspots, even the best known one, Hawaii. Since the local and teleseismic tomography methods have been well established and proved to be quite effective, the main remaining work for studying the upper mantle structure of hotspots is the instrumentation. Portable seismic networks should be deployed in every continental hotspot area. For imaging the oceanic hotspots and plumes, ocean bottom seismic networks are necessary, though they are much more expensive and difficult to deploy than the instrumentation on the land.

Global seismic tomography is the most effective tool to determine the deep structure of subducting slabs and mantle plumes. So far most global tomographic studies have been conducted for determining the long-wavelength structures of the mantle and for imaging the slabs, those for detecting plumes have just started. Because most hotspots are located far from the existing seismic stations and earthquake sources, special efforts are needed to collect useful data and to devise tomographic inversions for imaging mantle plumes. A large number of multiple reflected waves from the surface (or ocean floor), such as PP, PPP, SS and SSS waves, should be collected, which, together with surface wave data, can help to image the upper mantle plumes under the oceanic regions. Multiple reflected waves from the CMB (e.g., PcP, PcP2, ScS, ScS2) and diffracted waves at the CMB (Pdiff, Sdiff) should be collected for imaging the plumes in the lower mantle. These later phase data can be collected multitudinously with the modern waveform processing technologies.

Continuous efforts are also needed to improve the theoretical aspects of seismic imaging. The development of an improved theoretical framework, coupled with more powerful computers, has opened the way to new tomographic methods and the possibility of exploiting more fully the richness of broadband seismograms (Romanowicz, 2003). It is clear that the full understanding of the seismic structure of mantle plumes and subducting slabs will only be achieved by a combination of more effective seismic imaging techniques and dense coverage of global seismic networks, particularly in the oceans. The challenge is great, but with ingenuity and cooperation we can anticipate exciting new advances in seismic imaging and the understanding of the Earth's structure and dynamics in the next one to two decades.

ACKNOWLEDGEMENTS

This work was partially supported by Grant-in-aid for Scientific Research (B-11440134 and A-17204037) from the Ministry of Education and Science, Japan, and a special COE grant from Ehime University. The author is grateful to S. Maruyama, D. Yuen, C. Matyska and S. Omori for thoughtful discussion and review comments.

REFERENCES

Abers, G. (2005) Seismic low-velocity layer at the top of subducting slabs: Observations, predictions, and systematics. *Phys. Earth Planet. Inter.*, 149, 7–29.

Ai, Y., T. Zheng, W. Xu, Y. He, and D. Dong (2003) A complex 660 km discontinuity beneath northeast China. *Earth Planet. Sci. Lett.*, 212, 63–71.

Aki, K., and W. Lee (1976) Determination of three-dimensional velocity anomalies under a seismic array using first P arrival times from local earthquakes, 1. A homogeneous initial model. *J. Geophys. Res.*, 81, 4381–4399.

Aki, K., A. Christoffersson, and E. Husebye (1977) Determination of the three-dimensional seismic structure of the lithosphere. *J. Geophys. Res.*, 82, 277–296.

Allen, R., G. Nolet, W. Morgan et al. (2002) Imaging the mantle beneath Iceland using integrated seismological techniques. *J. Geophys. Res.*, 107(B12), JB000595.

Anderson, D. (2000) The thermal state of the upper mantle: No role for mantle plumes. *Geophys. Res. Lett.*, 27, 3623–3626.

Bijwaard, H., and W. Spakman (1999) Tomographic evidence for a narrow whole mantle plume below Iceland. *Earth Planet. Sci. Lett.*, 166, 121–126.

Bijwaard, H., W. Spakman, and E. Engdahl (1998) Closing the gap between regional and global travel time tomography. *J. Geophys. Res.*, 103, 30055–30078.

Boschi, L., and A. Dziewonski (1999) High- and low-resolution images of the Earth's mantle: Implications of different approaches to tomographic modeling. *J. Geophys. Res.*, 104, 25567–25594.

Breger, L., and B. Romanowicz (1998) Three-dimensional structure at the base of the mantle beneath the central Pacific. *Science*, 282, 718–720.

Cadek, O., D.A. Yuen, V. Steinbach, A. Chopelas, and C. Matyska (1994) Lower mantle thermal structure deduced from seismic tomography, mineral physics and numerical modeling. *Earth Planet. Sci. Lett.*, 121, 385–402.

Condie, K. (2001). Mantle Plumes and Their Record in Earth History, Cambridge University Press, Cambridge, UK, 306pp.

Creager, K., and T. Jordan (1984) Slab penetration into the lower mantle. *J. Geophys. Res.*, 89, 3031–3049.

Creager, K., and T. Jordan (1986) Slab penetration into the lower mantle beneath the Mariana and other island arcs of the Northwest Pacific. *J. Geophys. Res.*, 91, 3573–3589.

Crough, S., and D. Jurdy (1980) Subducted lithosphere, hotspots, and the geoid. *Earth Planet. Sci. Lett.*, 48, 15–22.

Cserepes, L., and D. Yuen (2000) On the possibility of a second kind of mantle plume. *Earth Planet. Sci. Lett.*, 183, 61–71.

de Hoop, M., and R. van der Hilst (2005) On sensitivity kernels for wave equation transmission tomography. *Geophys. J. Int.*, 160, 621–633.

Dziewonski, A. (1984) Mapping the lower mantle: Determination of lateral heterogeneity in P velocity up to degree and order 6. *J. Geophys. Res.*, 89, 5929–5952.

Dziewonski, A., B. Hager, and R. O'Connell (1977) Large-scale heterogeneities in the lower mantle. *J. Geophys. Res.*, 82, 239–255.

Ellsworth, W., and R. Koyanagi (1977) Three-dimensional crust and mantle structure of Kilauea volcano, Hawaii. *J. Geophys. Res.*, 82, 5379–5394.

Engdahl, E., R. van der Hilst, and R. Buland (1998) Global teleseismic earthquake relocation with improved travel times and procedures for depth determination. *Bull. Seismol. Soc. Am.*, 88, 722–743.

Evans, J. (1982) Compressional wave velocity structure of the upper 350 km under the eastern Snake River Plain near Rexburg, Idaho. *J. Geophys. Res.*, 87, 2654–2670.

Foulger, G. (2003) Plumes, or plate tectonic processes? *Astron. Geophys.*, 43, 6.19–6.23.

Foulger, G., M. Pritchard, B. Julian, and J. Evans (2000) The seismic anomaly beneath Iceland extends down to the mantle transition zone and no deeper. *Geophys. J. Int.*, 142, F1–F5.

Fukao, Y., S. Widiyantoro, and M. Obayashi (2001) Stagnant slabs in the upper and lower mantle transition region. *Rev. Geophys.*, 39, 291–323.

Garnero, E. (2000) Heterogeneity of the lowermost mantle. *Annu. Rev. Earth Planet. Sci*. 28, 509–537.

Goes, S., W. Spakman, and H. Bijwaard (1999) A lower mantle source for Central European volcanism. *Science*, 286, 1928–1931.

Grand, S., R. van der Hilst, and S. Widiyantoro (1997) Global seismic tomography: A snapshot of convection in the Earth. *GSA Today*, 7, 1–7.

Green, H., and P. Burnley (1989) A new self-organizing mechanism for deep-focus earthquakes. *Nature*, 341, 733–737.

Griffiths, R., and M. Richards (1989) The adjustment of mantle plumes to changes in plate motion. *Geophys. Res. Lett.*, 16, 437–440.

Hansen, U., and D. Yuen (1988) Numerical simulation of thermal chemical instabilities at the core-mantle boundary. *Nature*, 334, 237–240.

Hasegawa, A., and A. Yamamoto (1994) Deep, low-frequency microearthquakes in or around seismic low-velocity zones beneath active volcanoes in northeastern Japan. *Tectonophysics*, 233, 233–252.

Hasegawa, A., N. Umino, and A. Takagi (1978) Double-planed deep seismic zone and upper-mantle structure in the northeastern Japan arc. *Geophys. J. R. Astron. Soc.*, 54, 281–296.

Helmberger, D., L. Wen, and X. Ding (1998) Seismic evidence that the source of the Iceland hotspot lies at the core-mantle boundary. *Nature*, 396, 251–258.

Honda, S., and M. Saito (2003) Small-scale convection under the back-arc occurring in the low viscosity wedge. *Earth Planet. Sci. Lett.*, 216, 703–715.

Honda, S., D.A. Yuen, S. Balachandar, and D. Reuteler (1993) Three-dimensional instabilities of mantle convection with multiple phase transitions. *Science*, 259, 1308–1311.

Hung, S., Y. Shen, and L. Chiao (2004) Imaging seismic velocity structure beneath the Iceland hotspot: A finite frequency approach. *J. Geophys. Res.*, 109, B08305.

Inoue, H., Y. Fukao, K. Tanabe, and Y. Ogata (1990) Whole mantle P wave travel time tomography. *Phys. Earth Planet. Inter.*, 59, 294–328.

Iyer, H. (1989) Seismic tomography. In James, D. (ed.) The Encyclopedia of Solid Earth Geophysics, Van Nostrand Reinhold, New York, pp. 1131–1151.

Ji, Y., and H. Nataf (1998) Detection of mantle plumes in the lower mantle by diffraction tomography: Hawaii. *Earth Planet. Sci. Lett.*, 159, 99–115.

Kanamori, H. (1971) Great earthquakes at island arcs and the lithosphere. *Tectonophysics*, 12, 187–198.

Kaneshima, S., and G. Helffrich (2003) Subparallel dipping heterogeneities in the mid-lower mantle. *J. Geophys. Res.*, 108(B5), JB001596.

Kellogg, L., and S. King (1993) Effect of mantle plumes on the growth of D″ by reaction between the core and mantle. *Geophys. Res. Lett.*, 20, 379–392.

Keyser, M., J. Ritter, and M. Jordan (2002) 3D shear-wave velocity structure of the Eifel plume, Germany. *Earth Planet. Sci. Lett.*, 203, 59–82.

King, S., and D. Anderson (1995) An alternate mechanism of flood basalt volcanism. *Earth Planet. Sci. Lett.*, 136, 269–279.

King, S., and J. Ritsema (2000) African hot spot volcanism: Small-scale convection in the upper mantle beneath cratons. *Science*, 290, 1137–1140.

Kirby, S. (1991) Mantle phase changes and deep-earthquake faulting in subducting lithosphere. *Science*, 252, 216–224.

Knittle, E., and R. Jeanloz (1991) Earth's core-mantle boundary: Results of experiments at high pressure and temperatures. *Science*, 251, 1438–1443.

Koper, K., D. Wiens, L. Dorman, J. Hildebrand, and S. Webb (1998) Modeling the Tonga slab: Can travel time data resolve a metastable olivine wedge? *J. Geophys. Res.*, 103, 30079–30100.

Korenaga, J., and T. Jordan (2002) Effects of vertical boundaries on infinite Prandtl number thermal convection. *Geophys. J. Int.*, 147, 639–659.

Laske, G., J. Morgan, and J. Orcutt (1999) First results from the Hawaiian SWELL pilot experiment. *Geophys. Res. Lett.*, 26, 3397–3400.

Lay, T., Q. Williams, and E. Garnero (1998) The core-mantle boundary layer and deep Earth dynamics. *Nature*, 392, 461–468.

Lei, J., and D. Zhao (2005) P-wave tomography and origin of the Changbai intraplate volcano in Northeast Asia. *Tectonophysics*, 397, 281–295.

Lei, J., and D. Zhao (2006) A new insight into the Hawaiian plume. *Earth Planet. Sci. Lett.*, 241, 438–453.

Li, X., R. Kind, K. Priestley, S. Sobolev, and F. Tilmann (2000) Mapping the Hawaiian plume conduit with converted seismic waves. *Nature*, 405, 938–941.

Lithgow-Bertelloni, C., and M. Richards (1998) The dynamics of Cenozoic and Mesozoic plate motions. *Rev. Geophys.*, 36, 27–78.

Loper, D. (1991) Mantle plumes. *Tectonophysics*, 187, 373–384.

Machetel, P., and P. Weber (1991) Intermittent layered convection in a model mantle with an endothermal phase change at 670 km. *Nature*, 350, 55–57.

Malamud, B., and D. Turcotte (1999) How many plumes are there? *Earth Planet. Sci. Lett.*, 174, 113–124.

Maruyama, S. (1994) Plume tectonics. *J. Geol. Soc. Jpn.*, 100, 24–49.

Matsuzawa, T., N. Umino, A. Hasegawa, and A. Takagi (1986) Upper mantle velocity structure estimated from PS-converted wave beneath the north–eastern Japan arc. *Geophys. J. R. Astron. Soc.*, 86, 767–787.

McDougall, L. (1971) Volcanic island chains and sea floor spreading. *Nature*, 231, 141–144.

Mishra, O., D. Zhao, N. Umino, and A. Hasegawa (2003) Tomography of northeast Japan forearc and its implications for interplate seismic coupling. *Geophys. Res. Lett.*, 30(16), GL017736.

Molnar, P., and J. Stock (1987) Relative motions of hotspots in the Pacific, Atlantic, and Indian oceans since late Cretaceous time. *Nature*, 327, 587–591.

Montagner, J. (1994) Can seismology tell us anything about convection in the mantle? *Rev. Geophys.*, 32, 115–138.

Montelli, R., G. Nolet, G. Master, F. Dahlen, E. Engdahl, and H. Hung (2004) Finite-frequency tomography reveals a variety of plumes in the mantle. *Science*, 303, 338–343.

Morgan, W. (1971) Convection plumes in the lower mantle. *Nature*, 230, 42–43.

Morgan, W. (1972) Deep motions and deep mantle convection. *Geol. Soc. Am. Mem.*, 132, 7–22.

Murakami, M., K. Hirose, K. Kawamura, N. Sata, and Y. Ohishi (2004) Post-perovskite phase transition in MgSiO3. *Science*, 304, 855–858.

Nakajima, J., and A. Hasegawa (2004) Shear-wave polarization anisotropy and subduction-induced flow in the mantle wedge of northeastern Japan. *Earth Planet. Sci. Lett.*, 225, 365–377.

Nakanishi, I., and D. Anderson (1982) World-wide distribution of group velocity of mantle Rayleigh waves as determined by spherical harmonic inversion. *Bull. Seismo. Soc. Am.*, 72, 1185–1194.

Nataf, H. (2000) Seismic imaging of mantle plumes. *Annu. Rev. Earth Planet. Sci.*, 28, 391–417.

Niu, F., and H. Kawakatsu (1996) Complex structure of mantle discontinuities at the tip of the subducting slab beneath northeast China. *J. Phys. Earth*, 44, 701–711.

Obara, K. (2002) Nonvolcanic deep tremor associated with subduction in southwest Japan. *Science*, 296, 1679–1681.

Pilidou, S., K. Priestley, O. Gudmundsson, and E. Debayle (2004) Upper mantle S-wave speed heterogeneity and anisotropy beneath the North Atlantic from regional surface wave tomography: The Iceland and Azores plumes. *Geophys. J. Int.*, 159, 1057–1076.

Priestley, K., and F. Tilmann (1999) Shear-wave structure of the lithosphere above the Hawaiian hotspot from two-station Rayleigh wave phase velocity measurements. *Geophys. Res. Lett.*, 26, 1493–1496.

Richards, M., B. Hager, and N. Sleep (1988) Dynamically supported geoid highs over hotspots: Observation and theory. *J. Geophys. Res.*, 93, 7690–7708.

Ritsema, J., and R. Allen (2003) The elusive mantle plume. *Earth Planet. Sci. Lett.*, 207, 1–12.

Ritsema, J., H. Jan der Heijst, and J. Woodhouse (1999) Complex shear wave velocity structure imaged beneath Africa and Iceland. *Science*, 286, 1925–1928.

Ritter, J., M. Jordan, U. Christensen, and U. Achauer (2001) A mantle plume below the Eifel volcanic field, Germany. *Earth Planet. Sci. Lett.*, 186, 7–14.

Rogers, G., and H. Dragert (2003) Episodic tremor and slip on the Cascadia subduction zone: The chatter of silent slip. *Science*, 300, 1942–1943.

Romanowicz, B. (2003) Global mantle tomography: Progress status in the past 10 years. *Ann. Rev. Earth Planet. Sci.*, 31, 303–328.

Russell, S., T. Lay, and E. Garnero (1999) Small scale lateral shear velocity and anisotropy heterogeneity near the core-mantle boundary beneath the central Pacific imaged using broadband ScS waves. *J. Geophys. Res.*, 104, 13183–13199.

Saltzer, R., and E. Humphreys (1997) Upper mantle P wave velocity structure of the eastern Snake River Plain and its relationship to geodynamic models of the region. *J. Geophys. Res.*, 102, 11829–11842.

Schutt, D., and E. Humphreys (2004) P and S wave velocity and Vp/Vs in the wake of the Yellowstone hot spot. *J. Geophys. Res.*, 109, B01305.

Shen, Y., S. Solomon, I. Bjarnason, and G. Nolet (2002) Seismic evidence for a tilted mantle plume and north–south mantle flow beneath Iceland. *Earth Planet. Sci. Lett.*, 197, 261–272.

Sleep, N. (1990) Hotspots and mantle plumes: Some phenomenology. *J. Geophys. Res.*, 95, 6715–6736.

Stachnik, J., G. Abers, and D. Christensen (2004) Seismic attenuation and mantle wedge temperatures in the Alaska subduction zone. *J. Geophys. Res.*, 109(B10), B10304.

Stacey, F., and D. Loper (1983) The thermal boundary layer interpretation of D″ and its role as a plume source. *Phys. Earth Planet. Inter.*, 33, 45–50.

Stefanick, M., and D. Jurdy (1984) The distribution of hot spots. *J. Geophys. Res.*, 89, 9919–9925.

Steinberger, B. (2000) Plumes in a convecting mantle: Models and observations for individual hotspots. *J. Geophys. Res.*, 105, 11127–11152.

Stern, R. (2002) Subduction zones. *Rev. Geophys.*, 40(4), RG000108.

Stixrude, L. (1998) Elastic constants and anisotropy of MgSiO3 perovskite, periclase, and SiO2 at high pressure. In Gurnis, M., B. Buffett, K. Knittle, M. Wysession (eds.) The Core-Mantle Boundary, AGU, pp. 83–96.

Su, W., R. Woodward, and A. Dziewonski (1994) Degree 12 model of shear velocity heterogeneity in the mantle. *J. Geophys. Res.*, 99, 6945–6980.

Tajima, F., Y. Fukao, M. Obayashi, and T. Sakurai (1998) Evaluation of slab images in the northwestern Pacific. *Earth Planets Space*, 50, 953–964.

Tamura, Y., Y. Tatsumi, D. Zhao, Y. Kido, and H. Shukuno (2002) Hot fingers in the mantle wedge: new insight into magma genesis in subduction zones. *Earth Planet. Sci. Lett.*, 197, 105–116.

Tanimoto, T., and D. Anderson (1984) Mapping convection in the mantle. *Geophys. Res. Lett.*, 11, 287–290.

Tarduno, J., and R. Cottrell (1997) Paleomagnetic evidence for motion of the Hawaiian hotspot during formation of the Emperor seamounts. *Earth Planet. Sci. Lett.*, 153, 171–180.

Tatsumi, Y., S. Maruyama, and S. Nohda (1990) Mechanism of backarc opening in the Japan Sea: Role of asthenospheric injection. *Tectonophysics*, 181, 299–306.

Thompson, P., and P. Tackley (1998) Generation of mega-plumes from the core-mantle boundary in a compressible mantle with temperature-dependent viscosity. *Geophys. Res. Lett.*, 25, 1999–2002.

Thurber, C. (1983) Earthquake locations and three-dimensional crustal structure in the Coyote Lake area, central California. *J. Geophys. Res.*, 88, 8226–8236.

Thurber, C., and K. Aki (1987) Three-dimensional seismic imaging. *Ann. Rev. Earth Planet. Sci.*, 15, 115–139.

Tilmann, F., H. Benz, K. Priestley, and P. Okubo (2001) P-wave velocity structure of the uppermost mantle beneath Hawaii from travel time tomography. *Geophys. J. Int.*, 146, 594–606.

Tryggvason, K., E. Husebye, and R. Stefansson (1983) Seismic image of the hypothesized Icelandic hot spot. *Tectonophysics*, 100, 97–118.

Tsuchiya, T., J. Tsuchiya, K. Umemoto, and R. Wentzcovitch (2004) Phase transition in MgSiO3 perovskite in the earth's lower mantle. *Earth Planet. Sci. Lett.*, 224, 241–248.

Tsumura, N., S. Matsumoto, S. Horiuchi, and A. Hasegawa (2000) Three-dimensional attenuation structure beneath the northeastern Japan arc estimated from spectra of small earthquakes. *Tectonophysics*, 319, 241–260.

Turcotte, D., and E. Oxburgh (1973) Mid-plate tectonics. *Nature*, 244, 337–339.

Turcotte, D., and G. Schubert (1982) Geodynamics, John Wiley and Sons Press, New York, 450pp.

Umino, N., A. Hasegawa, and T. Matsuzawa (1995) sP depth phase at small epicentral distances and estimated subducting plate boundary. *Geophys. J. Int.*, 120, 356–366.

Ukawa, M., and K. Obara (1993) Low frequency earthquakes around Moho beneath the volcanic front in the Kanto district, central Japan. *Bull. Volcanol. Soc. Jpn.*, 38, 187–197.

van der Hilst, R., and M. de Hoop (2005) Banana-doughnut kernels and mantle tomography. *Geophys. J. Int.*, 163, 956–961.

van der Hilst, R., S. Widiyantoro, and E. Engdahl (1997) Evidence for deep mantle circulation from global tomography. *Nature*, 386, 578–584.

Van der Voo, R., W. Spakman, and H. Bijwaard (1999a) Mesozoic subducted slabs under Siberia. *Nature*, 397, 246–249.

Van der Voo, R., W. Spakman, and H. Bijwaard (1999b) Tethyan subducted slabs under India. *Earth Planet. Sci. Lett.*, 171, 7–20.

Vasco, D., L. Johnson, and R. Pulliam (1995) Lateral variations in mantle velocity structure and discontinuities determined from P, PP, S, SS, and SS-SdS travel time residuals. *J. Geophys. Res.*, 100, 24037–24059.

Vinnik, L., L. Breger, and B. Romanowicz (1998) Anisotropic structures at the base of the mantle. *Nature*, 393, 564–567.

Vogt, P. (1981) On the applicability of thermal conduction models to mid-plate volcanism, comments on a paper by Gass et al. *J. Geophys. Res.*, 86, 950–960.

Wang, Z., and D. Zhao (2005) Seismic imaging of the entire arc of Tohoku and Hokkaido in Japan using P-wave, S-wave and sP depth-phase data. *Phys. Earth Planet. Inter.*, 152, 144–162.

Weinstein, S., and P. Olson (1989) The proximity of hotspots to convergent and divergent plate boundaries. *Geophys. Res. Lett.*, 16, 433–436.

Williams, Q., and E. Garnero (1996) Seismic evidence for partial melt at the base of Earth's mantle. *Science*, 273, 1528–1530.

Wilson, J. (1963) A possible origin of the Hawaiian islands. *Can. J. Phys.*, 41, 863–870.

Wilson, J. (1973) Mantle plumes and plate motions. *Tectonophysics*, 19, 149–164.

Wolfe, C., I. Bjarnason, J. VanDecar, and S. Soloman (1997) Seismic structure of the Iceland mantle plume. *Nature*, 385, 245–247.

Wolfe, C., S. Solomon, P. Silver, J. VanDecar, and R. Russo (2002) Inversion of body-wave delay times for mantle structure beneath the Hawaiian islands: Results from the PELENET experiment. *Earth Planet. Sci. Lett.*, 198, 129–145.

Woodhouse, J., and A. Dziewonski (1984) Mapping the upper mantle: Three-dimensional modeling of earth structure by inversion of seismic waveforms. *J. Geophys. Res.*, 89, 5953–5986.

Woods, M., and E. Okal (1996) Rayleigh-wave dispersion along the Hawaiian swell: A test of lithospheric thinning by thermal rejuvenation at a hotspot. *Geophys. J. Int.*, 125, 325–339.

Woodward, R., and G. Master (1991) Lower mantle structure from ScS-S differential travel times. *Nature*, 352, 231–233.

Wysession, M., T. Lay, and J. Revenaugh (1998) The D″ discontinuity and its implications. In Gurnis, M., B. Buffett, K. Knittle, M. Wysession (eds.) The Core-Mantle Boundary, AGU, pp. 273–297.

Yuan, H., and K. Dueker (2005) Teleseismic P-wave tomogram of the yellowstone plume. *Geophys. Res. Lett.*, 32(7), L07304.

Yuen, D., O. Cadek, A. Chopelas, and C. Matyska (1993) Geophysical inferences of thermal-chemical structures in the lower mantle. *Geophys. Res. Lett.*, 20, 899–902.

Zhang, Y., and T. Tanimoto (1993) High-resolution global upper mantle structure and plate tectonics. *J. Geophys. Res.*, 98, 9793–9823.

Zhao, D. (2001a) New advances of seismic tomography and its applications to subduction zones and earthquake fault zones. *The Island Arc*, 10, 68–84.

Zhao, D. (2001b) Seismological structure of subduction zones and its implications for arc magmatism and dynamics. *Phys. Earth Planet. Inter.*, 127, 197–214.

Zhao, D. (2001c) Seismic structure and origin of hotspots and mantle plumes. *Earth Planet. Sci. Lett.*, 192, 251–265.

Zhao, D. (2004) Global tomographic images of mantle plumes and subducting slabs: Insight into deep Earth dynamics. *Phys. Earth Planet. Inter.*, 146, 3–34.

Zhao, D., A. Hasegawa, and S. Horiuchi (1992) Tomographic imaging of P and S wave velocity structure beneath northeastern Japan. *J. Geophys. Res.*, 97, 19909–19928.

Zhao, D., A. Hasegawa, and H. Kanamori (1994) Deep structure of Japan subduction zone as derived from local, regional and teleseismic events. *J. Geophys. Res.*, 99, 22313–22329.

Zhao, D., D. Christensen, and H. Pulpan (1995) Tomographic imaging of the Alaska subduction zone. *J. Geophys. Res.*, 100, 6487–6504.

Zhao, D., Y. Xu, D. Wiens, L. Dorman, J. Hildebrand, and S. Webb (1997) Depth extent of the Lau back-arc spreading center and its relation to subduction processes. *Science*, 278, 254–257.

Zhao, D., K. Asamori, and H. Iwamori (2000) Seismic structure and magmatism of the young Kyushu subduction zone. *Geophys. Res. Lett.*, 27, 2057–2060.

Zhao, D., O.P. Mishra, and R. Sanda (2002) Influence of fluids and magma on earthquakes: Seismological evidence. *Phys. Earth Planet. Inter.*, 132, 249–267.

Zhao, D., J. Lei, and R. Tang (2004) Origin of the Changbai intraplate volcanism in Northeast China: Evidence from seismic tomography. *Chinese Sci. Bull.*, 49, 1401–1408.

Zhao, D., S. Todo, and J. Lei (2005) Local earthquake reflection tomography of the Landers aftershock area. *Earth Planet. Sci. Lett.*, 235, 623–631.

Zhao, D., J. Lei, T. Inoue, A. Yamada, and S. Gao (2006) Deep structure and origin of the Baikal rift zone. *Earth Planet. Sci. Lett.*, 243, 681–691.

Zhou, H. (1996) A high-resolution P wave model for the top 1200 km of the mantle. *J. Geophys. Res.*, 101, 27791–27810.

CHAPTER 2

SEISMOLOGICAL CONSTRAINTS ON THE STRUCTURE OF THE EARTH'S CORE

MIAKI ISHII

Department of Earth and Planetary Sciences, Harvard University 20 Oxford Street, Cambridge, Massachusetts 02138, USA;
E-mail: ishii@eps.harvard.edu

Abstract
Our knowledge of the Earth's core has improved dramatically since its discovery, and this chapter attempts to provide a review of the current understanding as constrained by seismological observations. We also illustrate difficulties in studying this region, and uncertainties in the constraints. A short discussion of seismic data used to investigate the core is followed by sections focusing on properties of the outer core, the inner-core boundary, and the inner core. The range of observed values for compressional and shear wave speeds, density, and attenuation are presented.

1 INTRODUCTION

The Earth's core is a difficult entity to study. The mantle protects it from our direct sampling, and its extreme conditions, i.e., temperature and pressure above 3000 K and 135 GPa, respectively, are a challenge to recreate in a laboratory or with a computer simulation. The core properties are therefore best studied by remote observations at the Earth's surface. For example, the magnetic field provides information about the dynamics of the fluid outer core, and seismic energy passing through the core tells us of elasticity, anelasticity, and density of the fluid outer core and solid inner core. In this paper, we review seismological constraints on the core, accumulated in almost 100 years of investigations. Since properties of the core often play a vital role in understanding the dynamics, composition, and mineralogy, reliability of seismological estimates are addressed whenever possible.

D. A. Yuen et al. (eds.), Superplumes, 31–68.
© 2007 *Springer.*

1.1 Seismologically observable parameters

Seismic tomography relies upon elastic energy that samples the Earth's interior, hence parameters that can be directly constrained from seismological observations are elasticity, anelasticity, and density. Typically, the Earth's interior is assumed to be isotropic, and elasticity is discussed in terms of the wave speeds of compressional and shear waves. The relationships between seismic wave speeds and rigidity (or shear modulus, μ) and incompressibility (or bulk modulus, κ) are given by

$$\alpha^2 \rho = \kappa + \frac{4}{3}\mu, \quad \text{and} \quad \beta^2 \rho = \mu,$$

where α and β are the compressional and shear wave speeds, respectively, and ρ is the density. Rigidity μ is zero for liquid, hence we can determine the solidity of a region by observing shear-wave propagation within the given region. The outer core, with $\beta = \mu = 0$, must be liquid, whereas the inner core, with $\beta > 0$, is solid (Fig. 1a, b).

Anelasticity of the Earth's interior is given by the quality factor Q of compressional waves (Q_α) and shear waves (Q_β). The inverse of the quality factor is defined as the fractional loss of energy in a period of oscillation, i.e.,

$$Q^{-1} \propto \Delta E/E,$$

where ΔE is the amount of energy dissipated and E is the initial energy. This implies that high values of Q correspond to low attenuation and vice versa. The parameters Q_α and Q_β can be related to the quality factors of shear (Q_μ) and bulk (Q_κ) moduli as (Anderson and Hart, 1978; Dahlen and Tromp, 1998)

$$Q_\alpha^{-1} = \begin{cases} \left[1 - \frac{4}{3}\left(\frac{\beta}{\alpha}\right)^2\right] Q_\kappa^{-1} + \frac{4}{3}\left(\frac{\beta}{\alpha}\right)^2 Q_\mu^{-1} & \text{when } \mu \neq 0, \\ Q_\kappa^{-1} & \text{when } \mu = 0, \end{cases} \quad \text{and} \quad (1)$$

$$Q_\beta^{-1} = Q_\mu^{-1}.$$

Throughout this paper, we use elastic, anelastic, and density profiles given in a one-dimensional model PREM (Dziewoński and Anderson, 1981; Fig. 1) as the reference model to which we compare various seismological estimates. This model is constrained by both types of seismic data, i.e., body waves and normal modes, which are described in the next section. It should be noted that PREM is not a purely seismic model: it is derived using additional observations such as the Earth's mass and moment of inertia and uses theoretical predictions based upon mineral physics (e.g., Birch, 1952).

In general, because seismic data are results of elastic wave propagation, they cannot be used to investigate rheology of the Earth's interior. There is one exception, however, where the viscosity may be constrained from seismic data (discussed in

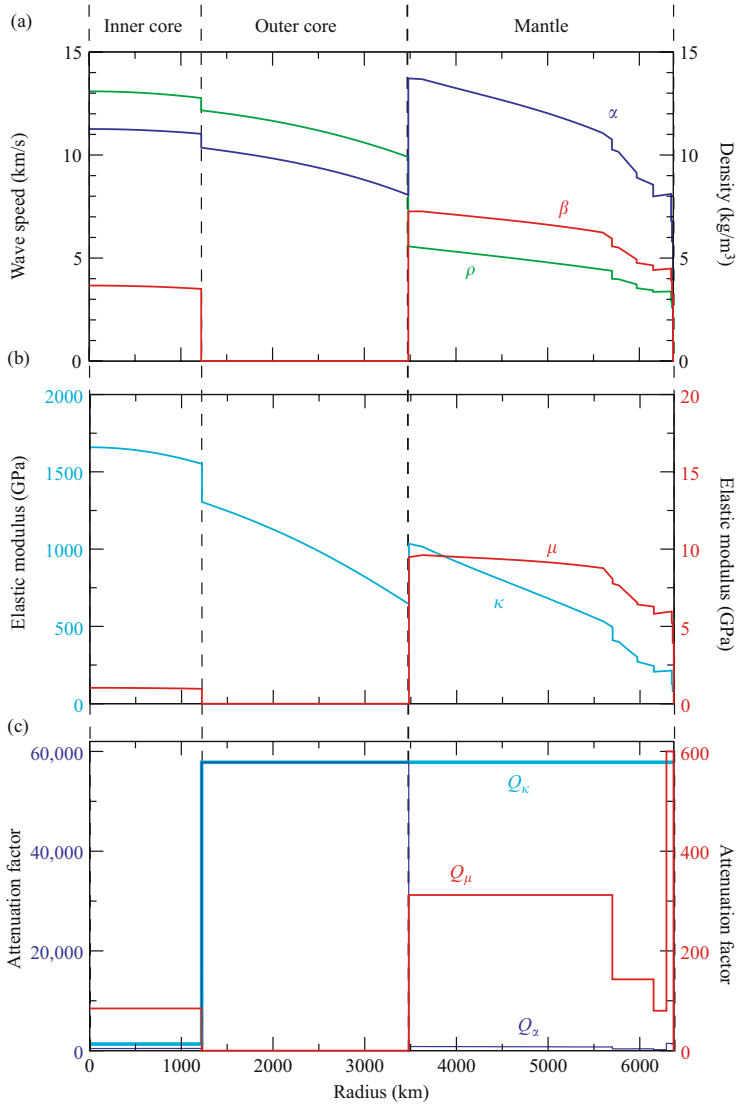

Figure 1. Depth-Dependent Structure of the Earth. (a) The elastic parameters α, β, and density ρ as a function of radius as given in the one-dimensional model PREM (Dziewoński and Anderson, 1981). This model is derived mainly from seismic observations with some additional information, such as the moment of inertia, and theoretical predictions. The wave speeds are given in km/s (left vertical axis) and the density is given in kg/m^3 (right vertical axis). (b) Same as in (a) except for rigidity or shear modulus (μ) and incompressibility or bulk modulus (κ). The two moduli are given in GPa. Note that the vertical scale is different for μ (right vertical axis) and κ (left vertical axis). (c) Same as in (a) except for the quality factors Q_α, Q_μ, and Q_κ. Note that the scales for Q_α and Q_κ (left vertical axis) are 100 times smaller than Q_μ (right vertical axis), and that $Q_\alpha = Q_\kappa$ in the outer core because $\mu = 0$ (Eq. 1).

the Outer Core section). Seismic data also cannot directly give us information such as temperature and flow of material, but these properties may be investigated if results from seismological studies are combined with those from other fields, such as geodynamics and mineral physics.

2 DATA

There are two types of seismological observations used in studies of the Earth's deep interior. The first is the body-wave data, i.e., information obtained from seismic energies traveling from a source (usually an earthquake) to a seismometer. These are relatively short-period data with periods measured typically in seconds. The second type of data is the free oscillations or normal modes of the Earth. After a large earthquake, the planet "rings" like a bell, and various resonance frequencies can be recorded. The resonance frequencies of modes that are useful in core studies are measured in mHz, i.e., periods in minutes, and are considered long- or very long-period data. These two seismological observations sample the internal structure in a different way, and are usually treated separately.

2.1 Body waves

Every type of seismic energy traversing the Earth is given a shorthand name. Isotropic solid material supports compressional and shear waves, and the letters *P* and *S* are assigned, respectively, to ray paths of these waves within the mantle. The compressional wave in the outer core is given the letter *K*, the same wave in the inner core is *I*, and the shear wave in the inner core is called *J*. Tracing the waves from a source to a receiver, one can write core-sampling seismic waves as *PKIKP* (compressional wave through the mantle, the outer core, the inner core and back), *SKS* (shear wave in the mantle, compressional wave in the core, converted back to shear wave in the mantle), and so on. In addition, energy reflected from the core-mantle boundary and the inner-core boundary are written with *c* and *i*, respectively, to indicate reflection. This leads to wave names such as *PcP* (compressional wave reflected at the core-mantle boundary) and *PKiKP* (compressional wave within the mantle and the outer core reflected at the inner-core boundary).

This naming convention is not quite sufficient for the outer core. Because of the large difference in the compressional wave speed between the mantle and the outer core (Fig. 1a), seismic stations at certain distances from the earthquake will receive two *PKP* waves, sampling the top and bottom of the outer core (Fig. 2a). When the travel times of core-sampling waves are plotted as a function of the epicentral distance (Fig. 2b) one can identify points where two *PKP* phases merge, such as at the point *C* where the *PKP* wave sampling the deep outer core becomes indistinguishable from the *PKiKP*. Using the cusp points, the two *PKP* phases are identified as PKP_{BC} (*PKP* sampling deep outer core), and PKP_{AB} (*PKP* sampling shallow outer core). Following

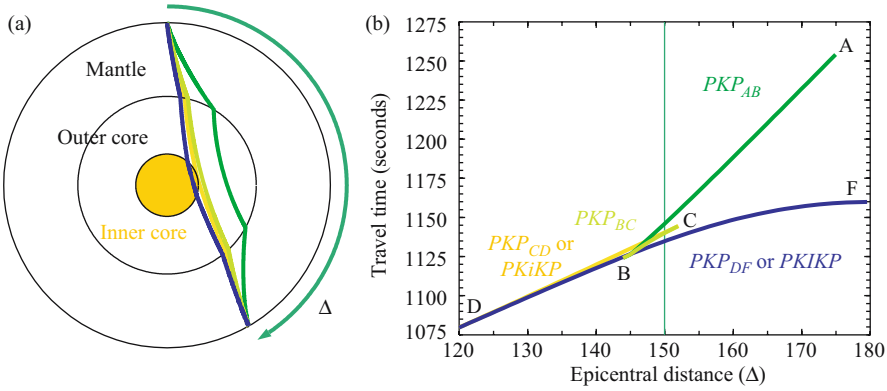

Figure 2. Core Phases. (a) Ray paths of core sampling seismic phases PKP_{BC} (dark green), PKP_{AB} (green), *PKiKP* or PKP_{CD} (yellow), and *PKIKP* or PKP_{DF} (blue) at 150° epicentral distance (Δ) calculated using PREM (Dziewoński and Anderson, 1981). (b) Travel time of the four *PKP* phases as a function of epicentral distance with the same color scheme as in (a). The alphabets A, B, C, and D are assigned at each cusp, and are used to identify various *PKP* phases.

this convention, *PKiKP* and *PKIKP* are also referred to as PKP_{CD} and PKP_{DF}, respectively. Sometimes, both outer and inner core phases are grouped together and referred to as the *PKP* branch.

The travel time of a seismic wave gives information about the seismic wave speed along the ray path, i.e.,

$$\text{travel time} = \int_s \frac{1}{v(s)}\, ds,$$

where $v(s)$ is the wave speed along the ray path s. With a large number of travel-time measurements from different source and receiver locations, models of the compressional and shear wave speeds within the Earth can be obtained.

The amplitude of various phases also provides information about attenuation of the Earth's interior (Fig. 1c). The amplitude spectrum of a given phase $A(f)$, where f is the frequency, can be expressed as (Niazi and Johnson, 1992)

$$A(f) = S(f)Ge^{-\pi f t^*},$$

where $S(f)$ is the source spectrum, and G accounts for frequency independent factors along the ray path such as the geometrical spreading and the effects of transmission and reflection coefficients at discontinuities. The parameter t^* is given by

$$t^* = \text{travel time/quality factor} = T/Q.$$

Typically, the spectral ratio of two phases $R(f) = A_1(f)/A_2(f)$ is considered to eliminate the source spectrum, and

$$\ln[R(f)] = \ln\left(\frac{G_1}{G_2}\right) - \pi f \left(\frac{T_1 - T_2}{Q}\right).$$

The situation becomes complicated with the presence of scatterers, because they have significant influence on the amplitude. Therefore, the values of Q_α and Q_β obtained from the analysis of compressional and shear wave amplitudes, respectively, trade off with the strength and abundance of scatterers. Due to this ambiguity, scattering and viscoelastic attenuation effects are sometimes grouped together, and the measured t^* is referred to as the apparent t^* to clarify that this includes the combined effects of attenuation and scattering.

Clearly, the amplitude study is more complex than the travel-time analysis, but the ultimate modeling involves the full fitting of waveforms such as the one shown in Figure 3. There are studies of mantle heterogeneity where waveforms are included in the inversion (e.g., Megnin and Romanowicz, 2000), but they have not yet been used in inversions for the core structure. Waveforms in core study are used for comparisons with synthetic seismograms where an input model is modified in a trial-and-error fashion until a good agreement between the two is achieved.

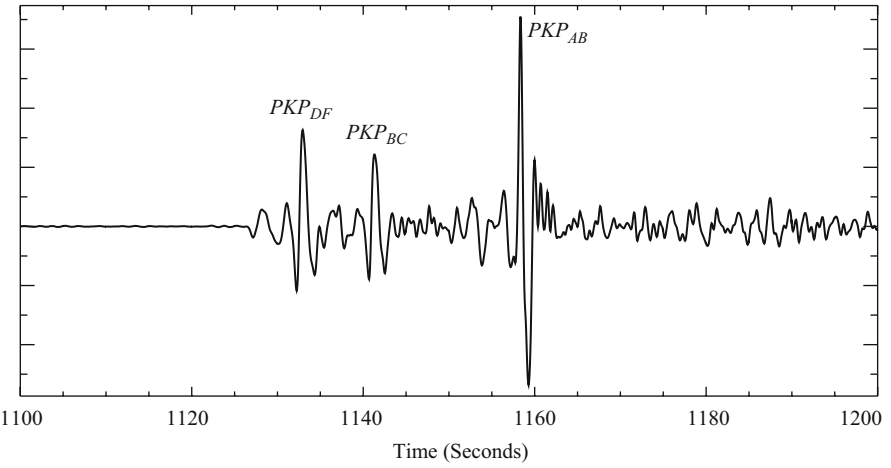

Figure 3. Seismogram with Core Phase Arrivals. A vertical-component seismogram recorded at station DWPF (Disney Wilderness Preserve, Florida) located approximately 154° from the July 25, 2004 earthquake in Southern Sumatra, Indonesia (magnitude 7.3, 582 km depth). The phases *PKIKP* or PKP_{DF}, PKP_{BC}, and PKP_{AB} are identified. This time series is obtained from IRIS (Incorporated Research Institutions for Seismology) Data Management Centre, and has been bandpass filtered between 0.3 and 3 Hz.

2.2 Free oscillations

A seismic spectrum from a large earthquake show clear peaks associated with various resonance frequencies or normal modes of the Earth (Fig. 4). Each mode has a unique set of eigenfunctions (Fig. 5), and the characteristic frequency of a mode is determined by how the mode samples the elasticity and the density of the Earth's interior (Dahlen and Tromp, 1998). Just as there are two types of seismic waves (compressional and shear waves), there are two types of modes, spheroidal (S) and toroidal (T) modes. The mode names ${}_nS_l$ and ${}_nT_l$ consist of the type of mode (S or T), the overtone number n (corresponding to the number of zero crossings made by the mode's eigenfunction in radial direction), and the angular degree l (spherical harmonic degree of the mode's lateral pattern). Combining the measurements of mode frequencies and eigenfunctions, one can make estimates of the elastic parameters and density as a function of radius.

Since a mode is simply a decaying sinusoid, a seismogram $u(t)$ can be expressed as a sum of all modes, i.e.,

$$u(t) = \sum_{k=1}^{\infty} A_k \, e^{i\omega_k t} e^{-\gamma_k t},$$

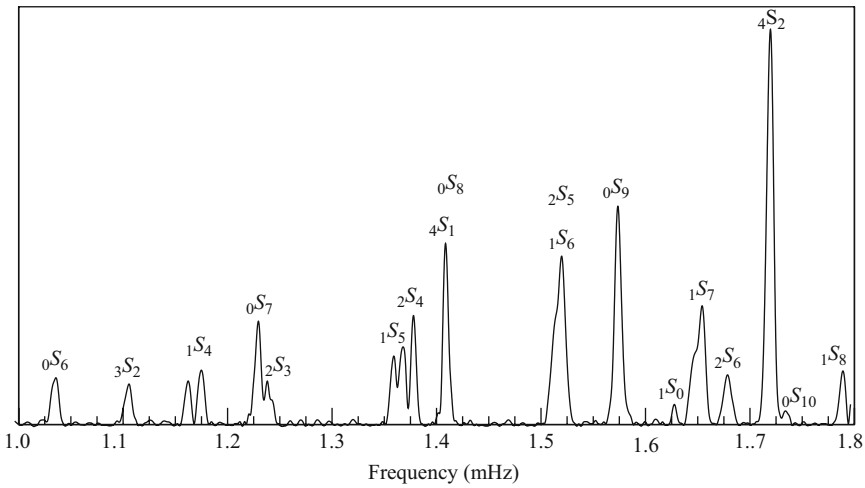

Figure 4. Seismic Spectrum. A seismic spectrum obtained from a vertical-component seismogram recorded at station GSC (Goldstone, California) from the June 9, 1994 earthquake in Northern Bolivia (magnitude 8.2, 647 km depth). 100 hours of the time series (starting 2 hours after the event time) are Hanning-tapered and Fourier-transformed. Each peak is labeled with corresponding mode name. Because this is the vertical component, toroidal modes do not appear in this spectrum.

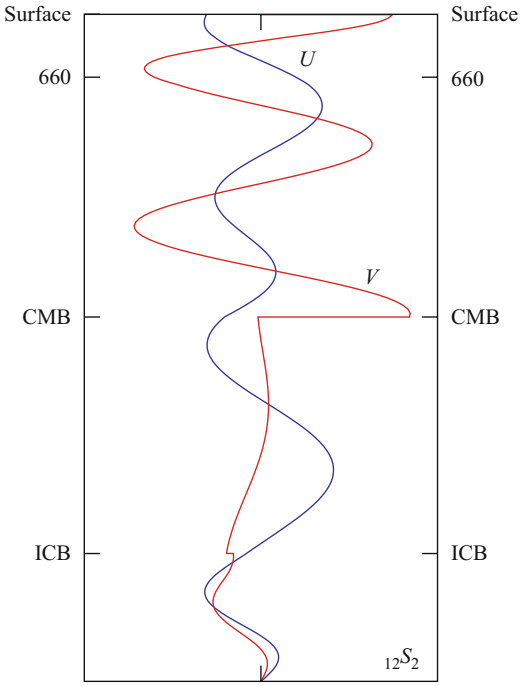

Figure 5. Eigenfunctions of $_{12}S_2$. Eigenfunctions U (associated with the radial displacement) and V (associated with lateral displacement) of the mode $_{12}S_2$ calculated using PREM (Dziewoński and Anderson, 1981). The plot has the amplitude of the eigenfunctions in the x-direction and radius in the y-direction with labels for the inner-core boundary (ICB), core-mantle boundary (CMB), and the 660-km discontinuity (660). This particular mode is dominated by the lateral displacement V in the mantle, and hence is considered to be an *ScS*-equivalent mode.

where A_k gives the initial amplitude and phase of the k'th mode, ω_k is the characteristic frequency, and γ_k is the decay constant. This decay constant is related to the quality factor of the mode Q_k as

$$\gamma_k = \frac{\omega_k}{2Q_k}.$$

In turn, Q_k is related to internal Q_α and Q_β or Q_κ and Q_μ in a similar manner as the characteristic frequency is related to α, β, and ρ.

The values of ω_k and Q_k are interpreted in terms of radially-varying global averages in elasticity, density, and anelasticity (e.g., PREM, Dziewoński and Anderson, 1981). Deviations from these one-dimensional models, such as lateral variations within the mantle, are observed as splitting of the resonance peaks. For example, the mode $_1S_4$ in Figure 4 is visibly split into two. After correcting for splitting due to the Earth's rotation and ellipticity (Woodhouse and Dahlen, 1978), one can obtain splitting coefficients $_kc_{st}$ for the k'th mode associated with the internal structure. These

are visualized as the splitting function σ_k as (Giardini et al., 1987)

$$\sigma_k(\theta,\phi) = \sum_{s,t} {}_k c_{st} Y_{st}(\theta,\phi),$$

where $Y_{st}(\theta,\phi)$ gives the value of the spherical harmonics at angular degree s, order t, and at colatitude θ and longitude ϕ. An example splitting function is shown in Figure 6(a). The splitting coefficients are linearly related to small perturbations δm from a reference model,

$${}_k c_{st} = \sum_i \int_0^a {}_k K_s^i(r) \delta m_i(r)\, dr,$$

where ${}_k K_s^i$ is the sensitivity of the k'th mode to perturbations in i different model parameters m_i, and the integration is over the radius r from the centre to the surface a of the Earth. For lateral variations in wave speeds and density, m_i becomes α, β, and ρ (Fig. 6b). The sensitivity functions ${}_k K_s^i(r)$ is unique to each mode, and can be calculated using the mode's eigenfunctions and their radial derivatives (Woodhouse, 1980; Li et al., 1991).

Physically, the splitting function represents the radial average of the internal structure as sensed by the particular mode. Because a mode is a standing wave, i.e., a

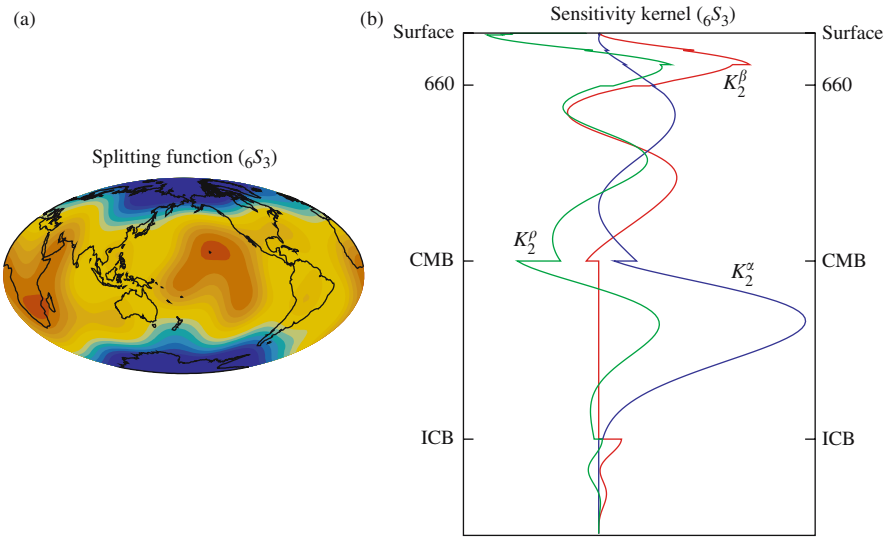

Figure 6. Normal-Mode Splitting. (a) An example splitting function for an inner-core sensitive mode ${}_6S_3$ obtained by Resovsky and Ritzwoller (1998). (b) Sensitivity kernels of the mode ${}_6S_3$ to shear wave speed (K_2^β, red), compressional wave speed (K_2^α, blue), and density (K_2^ρ, green) structure at spherical harmonic degree 2.

result of constructive and destructive interference of seismic energy traveling around the globe, the signal due to the odd degree structure is cancelled out. This means that ${}_kK_s^i$ with odd s is identically zero, and no inferences can be made about the odd-degree variations within the Earth. In order to gain odd-degree information, one needs to consider splitting of coupled modes such as a mode pair ${}_1S_5{-}{}_2S_4$. Efforts to estimate c_{st} of coupled modes have been made, but discrepancies exist between measurements from different groups (e.g., Resovsky and Ritzwoller, 1995). Furthermore, the number of odd-degree splitting coefficients available today are not yet sufficient to provide strong constraints on the internal structure.

Lateral variations in the quality factor are observed in a similar manner as the variations in elasticity. They appear simply as the imaginary part of the splitting function coefficients, c_{st}, and are linearly related to attenuation within the Earth. However, the imaginary part is difficult to obtain, and so far, no reliable estimates have been reported.

3 OUTER CORE

The existence of the core was first proposed by Oldham (1906) when he observed that no compressional waves arrived in the epicentral distances above $\sim 100°$ (the shadow zone). This observation indicated that there is a significant drop in the wave speed (c.f. Fig. 1a), and Gutenberg (1913) ascribed this jump to be at 2900-km depth. In this section, we review the depth-dependent elastic properties and density, as well as attenuation, within the outer core, and discuss seismological constraints on lateral heterogeneity. A brief discussion on the estimate of viscosity near the inner-core boundary is also included.

3.1 Compressional wave speed and density

Early studies of the seismic wave speed within the core relied heavily on observations of the compressional waves that have been reflected multiple times on the underside of the core-mantle boundary (Engdahl, 1968; Fig. 7). These waves are named *PKKP*, *PKKKP*, and so on (for waves traveling as compressional energy in the mantle), but often, they are abbreviated as *P*2*KP*, *P*3*KP*, or *PnKP*. The integer n indicates the number of the K legs, hence $n-1$ gives the number of underside reflections. Since these waves sample the outer core many times, they are very sensitive to the compressional wave speed of the outer core. Of course, the simple *PKP* phases are also used to investigate the structure of the outer core.

The efforts to resolve depth-dependent profile of the compressional wave speed within the outer core started in early 1960's (e.g., Bolt, 1962; Adams and Randall, 1964). These models often included multiple discontinuities within the outer core, and yet the number and depths of these discontinuities varied from model to model (e.g., Bolt, 1962; Adams and Randall, 1964; Ergin, 1967; Engdahl, 1968; Buchbinder, 1971; Jordan, 1973; Müller, 1973; Qamar, 1973). Some of these models were quite complex, including a low wave speed layer within the liquid core (e.g., Ergin, 1967).

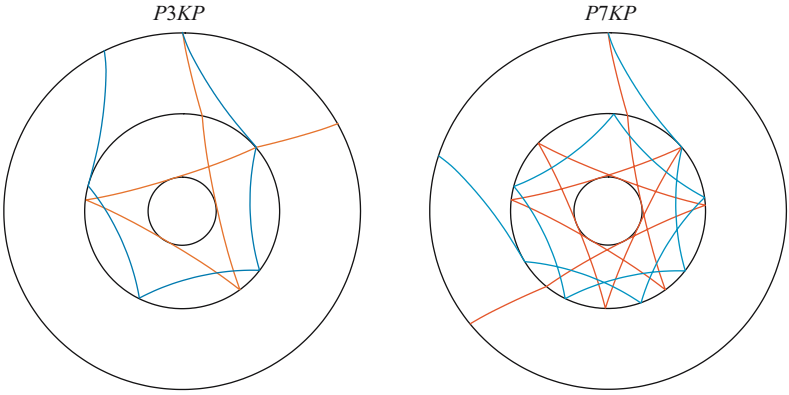

Figure 7. Multiple Underside Reflections at the Core-Mantle Boundary. Ray paths of *P*3*KP* and *P*7*KP*, phases that are suitable for investigating the outer-core properties.

However, the complications in data leading to such models have been demonstrated as resulting from scatterers in the lowermost mantle and irregularities or topography on the core-mantle boundary (Cleary and Haddon, 1972; Doornbos and Vlaar, 1973; Jordan, 1973). After this demonstration, smooth models of the outer core as a function of radius became more standard, and a model of Hales and Roberts (1971) has often been used as the reference model. In this paper, we compare various models of the outer core against the profile of PREM (Dziewoński and Anderson, 1981).

The compressional wave speed at the top of the core is 8.06 km/s according to PREM. This value appears to be a well-constrained parameter. From the earliest estimate of 8.10 km/s (Jeffreys, 1939), it has not changed by more than 1–2%. The lowest value is around 7.9 km/s (Hales and Roberts, 1971), and the highest value is around 8.26 km/s (Hales and Roberts, 1970; Randall, 1970). Most studies give numbers between 7.95 and 8.20 km/s (Jordan, 1973; Qamar, 1973; Johnson and Lee, 1985; Lay and Young, 1990; Souriau and Poupinet, 1991; Garnero et al., 1993; Tanaka and Hamaguchi, 1993a,b; Garnero and Helmberger, 1995; Kennett et al., 1995). Estimates obtained after the mid 1980's consistently prefer a value that is slightly lower than the PREM value.

As demonstrated by the early confusion in data interpretation (e.g., discontinuities vs. scatterers), the gradient of the wave speed is harder to constrain than the absolute wave speed at the top of the core. It is also dependent upon the choice of the radial parametrisation. PREM treats the outer core as one layer, and uses polynomials to express the radial variation (Dziewoński and Anderson, 1981). Consequently, the wave speed varies smoothly with radius. This profile explains most seismic observations, but it seems to require minor modifications. Because the wave speed at the top of the core is now slightly lower than the PREM value, current models prefer slightly higher gradient in the upper outer core (Souriau and Poupinet, 1991; Garnero and

Helmberger, 1995; Kennett et al., 1995). In addition, studies in the 1990's favor a reduced gradient in the lower outer core compared to PREM (Souriau and Poupinet, 1991; Song and Helmberger, 1992,1995b; Kaneshima et al., 1994; Kennett et al., 1995). The lower gradient implies that the compressional wave speed at the bottom of the outer core is also lower than the PREM value of 10.36 km/s, and is often inferred to be between 10.22 and 10.30 km/s (e.g., Choy and Cormier, 1983; Song and Helmberger, 1992; Kennett et al., 1995). Finally, the density profile within the outer core is mainly constrained by the normal-mode data (Masters, 1979). The smooth profile of PREM agrees well with the mode observations, and no significant evidence for a change in the density profile has been suggested.

3.2 Lateral variations and anisotropy

The possibility of a laterally heterogeneous outer core was first discussed in the 1970's. Comparing *PnKP* with $n \leq 7$, and *SmKS* with $m \leq 2$, Buchbinder (1972a) and Kind and Müller (1977) concluded that the outer core is laterally homogeneous. However, body-wave studies of outer core heterogeneity have been inconclusive. There are studies where heterogeneity is less than $\pm 0.1\%$, or below detection (Morelli and Dziewoński, 1987; Souriau and Poupinet, 1991; Roudil and Souriau, 1993; Garnero and Helmberger, 1995; Koper et al., 2003; Soldati et al., 2003; Souriau et al., 2003). This is consistent with an observation that the outer core is free of small-scale scatterers (based upon precursors of *PKP* and *PKKP*; Shearer et al., 1998). On the other hand, there are models with one to a few percent wave-speed variations (Kohler and Tanimoto, 1992; Vasco and Johnson, 1998; Boschi and Dziewoński, 2000; Romanowicz et al., 2003; Soldati et al., 2003).

In 1981, normal modes with sensitivity to the core were shown to be split anomalously (Masters and Gilbert, 1981). Even though the normal-mode data, which constrain large-scale structures, favor the top few hundred kilometers of the outer core to be homogeneous (Giardini et al., 1987), the anomalous splitting observation motivated models of the outer core with a few percent lateral variations in the compressional wave speed and density (Ritzwoller et al., 1986, 1988; Giardini et al., 1987; Widmer et al., 1992). These models explained the anomalous splitting, but had some unsatisfactory features such as large topography on the inner-core and core-mantle boundaries (Giardini et al., 1987; Ritzwoller et al., 1988), and an unusual ratio of compressional wave speed to density (Widmer et al., 1992). A later study showed that the anomalous splitting is mainly due to inner-core anisotropy and that outer core heterogeneity is not necessary to explain mode observations (Tromp, 1993, 1995a). Nonetheless, significant lateral variations are still inferred using normal-mode data (Romanowicz and Bréger, 2000), but the level of heterogeneity is considerably lower than earlier models (e.g., Ritzwoller et al., 1986) that are constructed before inner-core anisotropy is introduced (Tromp, 1993).

The discrepancy in the level of outer core heterogeneity arises partly from trade offs between outer core structure and other parts of the Earth, such as the mantle. Normal-mode results can be biased by large-scale mantle heterogeneities (Ritzwoller

et al., 1988), and when the inner-core sensitive modes are included in the outer-core modeling, signatures of inner-core anisotropy can be mapped into the outer core. Body-wave results can similarly be biased by mantle heterogeneity, including small-scale features such as slabs (Cormier, 1989; Kohler and Tanimoto, 1992; Roudil and Souriau, 1993; Garnero and Helmberger, 1995), mantle anisotropy (Silver and Chan, 1988; Boschi and Dziewoński, 2000), and topography on the core-mantle boundary (Morelli and Dziewoński, 1987; Kohler and Tanimoto, 1992). Significant drop in the level of outer-core heterogeneity has been reported once these factors are taken into account (Kohler and Tanimoto, 1992; Boschi and Dziewoński, 2000).

Recently, the question of outer core heterogeneity has been revisited with a specific interest on the tangent cylinder structure (Proudman, 1916; Taylor, 1917). One study put forth a relatively complex model with one percent variation in compressional wave speed and density (Romanowicz et al., 2003). However, other studies report no significant change in wave speed within the cylinder (Souriau et al., 2003; Ishii and Dziewoński, 2005). Anisotropy within the tangent cylinder and at polar caps beneath the core-mantle boundary have also been tested using body-wave data, and the investigators conclude that data do not support the existence of strong anisotropy within these structures (Souriau et al., 2003).

3.3 Finite rigidity in the outer core

The anomalous splitting of core-sensitive modes (Masters and Gilbert, 1981) has also led to a study where a finite rigidity layer ($\beta \sim 0.1$ km/s) of less than 100 km is proposed at the base of the outer core (Mochizuki and Ohminato, 1989). Other studies have suggested that finite rigidity at the base of the liquid core can reconcile the anomalous splitting without invoking significant heterogeneity in the bulk part of the outer core or anisotropy in the inner core (Romanowicz and Bréger, 2000; Tsuboi and Saito, 2002). However, no normal-mode study has convincingly shown the necessity of a finite rigidity layer.

In contrast, there has been a report of finite rigidity zones directly beneath the core-mantel boundary based upon *ScP* waveforms sampling a small region (Rost and Revenaugh, 2001). The authors argue that these data are best explained by a core-rigidity patch of 120–180 m thickness with shear wave speed of 0.6–0.8 km/s, and density reduction of 40% relative to PREM. Such a structure is too small and thin to be resolved by the normal-mode data, and further body-wave studies may provide more insight into the robustness, nature, and distribution of these core-rigidity zones.

3.4 Attenuation

The observations of multiply reflected waves such as *P*4*KP* and *P*7*KP* (e.g., Engdahl, 1968; Buchbinder, 1972a) suggest that energy dissipation in the outer core is low. Indeed, the outer core has almost the highest Q value in the Earth (Dziewoński and Anderson, 1981; Fig. 1c). Body-wave inferences of Q_α within the outer core are based upon the amplitude ratios of various phases, e.g., *SKS*/*ScS* (Suzuki and

Sato, 1970), *P/PKPPKP* (Sacks, 1971), *P7KP/P4KP* (Qamar and Eisenberg, 1974), and *P4KP/PcP* (Tanaka and Hamaguchi, 1996). Early estimates of the quality factor cover a wide range, but are typically below 10,000; 100–300 (Suzuki and Sato, 1970), 4000 (Buchbinder, 1971), 3000–10,000 (Sacks, 1971), >2200 (Adams, 1972), and 5000–10,000 (Qamar and Eisenberg, 1974). These values are underestimated due to improper treatment or complete neglect of the reflection and transmission coefficients at the core-mantle boundary (Tanaka and Hamaguchi, 1996). Once the body-wave data are corrected for the core-mantle boundary effects, the value of Q_α (10,000 to infinity, Cormier and Richards, 1976) agrees well with high values inferred from the normal-mode data (16,600, Masters et al., 1983; 12,000, Widmer et al., 1991; practically infinity, Romanowicz and Durek, 2000).

The frequency dependence of attenuation in the outer core has been suggested both from the body-wave (Tanaka and Hamaguchi, 1996) and normal-mode (Anderson, 1980) data. Resolvability of such feature, however, is refutable with the current data set. For a similar reason, depth dependence has not been modeled for attenuation within the outer core.

3.5 Viscosity

The viscosity of the liquid core near the inner-core boundary is the only exception where Earth's rheology can potentially be constrained by seismic data. In 1961, Slichter proposed the existence of a normal mode associated with the translation of the solid inner core within the liquid outer core (Slichter, 1961a,b; Smith, 1976). Because the translational motion of the inner core displaces the liquid surrounding it, the frequency of this mode depends on the change in density between the outer and inner core, as well as viscosity at the base of the outer core (Smylie and McMillan, 1998; Smylie, 1999). There were efforts to determine the frequency and splitting of this mode using super-conducting gravimeter (Smylie, 1992; Courtier et al., 2000). The viscosity inferred from the observed frequencies is 1.22×10^{11} Pa · s (Smylie, 1999; Smylie and McMillan, 2000), a value that is rather high for liquid. Furthermore, reports of Slichter mode detection (Smylie, 1992; Courtier et al., 2000) have been highly controversial, and been criticized for improper use of an input parameter (Crossley et al., 1992; Crossley, 1993, 2003), for a method which relies heavily upon *a priori* estimates of the Slichter mode frequencies, and for calculation of frequency using incomplete theoretical considerations (Rieutord, 2002). These factors question the reliability of the Slichter-mode observation, and hence the value of viscosity obtained based upon the observed frequency.

4 INNER-CORE BOUNDARY

The inner core was first discovered by Lehman in 1936 when she reported arrival of compressional wave energy in the core shadow zone (see the Outer Core section), and proposed that it can be explained if there is an inner core with a radius less than that of the moon (Lehman, 1936). This energy was later identified as the reflection

from the inner-core boundary (*PKiKP*). This section will focus on this discontinuity, which is not as significant as other internal boundaries of the Earth such as the core-mantle boundary. Nonetheless, it has unique seismological implications, and has been studied in detail using reflected waves *PKiKP*, and *PKIIKP* in conjunction with *PKP* phases and core reflected phase *PcP*.

4.1 Radius

Lehman's estimate of the inner-core radius of less than 1738 km was followed by values that were considerably smaller. Jeffreys (1939) proposed a value of 1250 km, and later studies prefer a value around 1220 km. For example, Bolt suggested 1216 and 1220 km (Bolt, 1962, 1964). In 1970's, estimates were made using the combination of body waves and normal modes, and in some cases, including the Earth's mass and the moment of inertia. These estimates give 1226 km (Buchbinder, 1971), 1229–1250 km (Gilbert et al., 1973), 1215 km (Jordan, 1973), 1213 km (Qamar, 1973), and 1220–1230 km (Engdahl et al., 1974). The PREM is one of the models with additional non-seismological constraints, and it gives a value of 1221 km for the inner-core radius (Dziewoński and Anderson, 1981). This value seems to satisfy most data, even though later studies prefer slight modification (e.g., 1207–1242 km, Stark et al., 1986; 1216 ± 3 km, Souriau and Souriau, 1989).

4.2 Topography

Large topography on the inner-core boundary was initially suggested by Poupinet et al. (1983) in order to explain early arrivals of north-south traveling *PKIKP* waves. They proposed the inner core to be prolate with polar radius that is 200 km larger than equatorial radius. Considerations of anomalous splitting of core-sensitive modes have also led to similar inner-core topography models with more than 25 km variation (Giardini et al., 1987; Ritzwoller et al., 1988). However, a prolate inner core is dynamically unstable, and subsequent studies of *PKiKP* and *PKIIKP* show that the inner core is oblate with only a small perturbation from the hydrostatic figure (polar radius smaller by 1.6–5.0 km; Souriau and Souriau, 1989), and that the boundary is very smooth without significant undulations (Rial and Cormier, 1980; Cormier and Choy, 1986). The observations leading to large topography are now explained in terms of inner-core anisotropy.

4.3 Sharpness of the boundary

The sharpness of an internal boundary can be estimated by the frequency content of the reflected wave energy: the higher the frequency of the wave, the sharper the boundary. The inner-core boundary has been continuously demonstrated to be a sharp boundary based upon short-period *PKiKP*, with a width of less than 5 km (Engdahl et al., 1974; Cummins and Johnson, 1988; Souriau and Souriau, 1989). Studies with additional *PKIIKP* data arrive at a similar conclusion (Bolt and O'Neill, 1965; Bolt

and Qamar, 1970; Engdahl et al., 1970; Bolt, 1977; Song and Helmberger, 1995b), suggesting that the sharpness is a well-constrained characteristic of the inner-core boundary.

4.4 Changes in wave speeds and density

The discontinuity in wave speed and density at the inner-core boundary can be estimated through reflection and transmission coefficients. The reflection and transmission coefficients are sensitive to changes in shear wave speed and density, but they are most sensitive to the change in compressional wave speed. This is because only the compressional waves are transmitted through the outer core, and reliable observations of the inner-core shear waves are not yet available for determining the transmission efficiency at the inner-core boundary. Furthermore, there is a strong trade off between shear wave speed and density. Therefore, most body-wave studies make an assumption about the jump in shear wave speed and density ($\Delta\beta$ and $\Delta\rho$, respectively) and analyse the data for a change in the compressional wave speed ($\Delta\alpha$). Consequently, $\Delta\beta$ and $\Delta\rho$ estimates are constrained mainly by normal-mode frequencies.

The estimates of $\Delta\alpha$, the change in the compressional wave speed, is rather tightly bound to be between 0.5 and 0.8 km/s (Buchbinder, 1971; Müller, 1973; Qamar, 1973; Cormier and Richards, 1977; Rial and Cormier, 1980; Choy and Cormier, 1983; Häge, 1983; Johnson and Lee, 1985; Song and Helmberger, 1992, 1995b). PREM takes a middle value of 0.67 km/s (Dziewoński and Anderson, 1981). On the other hand, estimates of the jump in the shear wave speed (hence the shear wave speed at the top of the inner core) range from 0 km/s (Choy and Cormier, 1983) to an upper bound of 4 km/s (Müller, 1973), although values between 2.5 and 3.0 km/s are preferred by most studies (Häge, 1983; Cummins and Johnson, 1988; Shearer and Masters, 1990). Inferences of shear wave speed from the normal-mode data all cluster around 3.5 km/s (Derr, 1969; Dziewoński, 1971; Dziewoński and Anderson, 1981; Masters and Gilbert, 1981; Masters and Shearer, 1990), demonstrating the robustness of the estimates obtained from mode frequencies.

Except for the earliest estimate which suggested the density jump to be between 1 and 2 g/cm^3 (Derr, 1969), normal-mode data propose less than 1 g/cm^3 difference between the outer and inner core density (Jordan and Anderson, 1974; Anderson and Hart, 1976; Masters, 1979; Dziewoński and Anderson, 1981; Masters and Shearer, 1990). The value inferred from the controversial Slichter mode observations also falls in this range (Smylie, 1992). The density jump estimate is slightly higher using the body-wave data, and values larger than 1 g/cm^3 are preferred (Bolt and Qamar, 1970; Buchbinder, 1972b; Souriau and Souriau, 1989; Adushkin et al., 1997). Nonetheless, Shearer and Masters (1990) suggest that values less than 1 g/cm^3 can also be consistent with body-wave observations.

The discrepancy between normal-mode and body-wave estimates can be a result of the trade off between shear wave speed and density, as well as due to anisotropy in the inner core. It should be noted that the mode values are averages over a broad

depth range. Hence the actual change in wave speed and density across the sharp inner-core boundary may be different from normal-mode estimate if the wave speed and density profiles on either side of the boundary have large gradient.

5 INNER CORE

Soon after its discovery (Lehman, 1936), the solidity of the inner core was proposed based upon mineral physical considerations (Birch, 1940). However, it took another twenty years for seismological observations to confirm this proposal (Dziewoński, 1971). The observed frequencies of deeply penetrating normal modes were difficult to reconcile without a solid inner core, i.e., without finite shear wave speed. Since then, studies of the inner core have revealed various types of complexities, but the source and mechanisms creating most of these complexities are not understood.

5.1 Average wave speed and density

The compressional wave speed within the inner core, especially its depth dependence, is mainly constrained by the *PKIKP* travel times. These observations require compressional wave speed to be 11.0 ± 0.2 km/s at the top of the inner core (Buchbinder et al., 1973; Müller, 1973; Qamar, 1973; Masse et al., 1974; Choy and Cormier, 1983; Cummins and Johnson, 1988; Song and Helmberger, 1992; Kaneshima et al., 1994). The data also suggest an increase in wave speed with depth to a value around 11.3 km/s at the centre of the Earth (Adams and Engdahl, 1974; Kaneshima et al., 1994). PREM with both body-wave and normal-mode constraints has a value of 11.02 km/s at the inner-core boundary which increases smoothly to 11.26 km/s (Dziewoński and Anderson, 1981). This is nearly identical to the model ak135 which is constructed from travel-time observations: 11.04 km/s increasing smoothly to 11.26 km/s (Kennett et al., 1995). Because the increase in wave speed with depth is small, the ray path within the inner core is almost linear (Fig. 2a).

The shear wave speed and density of the inner core are obtained from the free-oscillation data. As discussed in the Inner-Core Boundary section, normal-mode data give a value around 3.5 km/s for shear wave speed at the top of the inner core (Dziewoński, 1971; Dziewoński and Anderson, 1981; Masters and Gilbert, 1981). Further modeling allows for a gradual increase in this parameter with depth, and PREM suggests 3.50 km/s at the inner-core boundary and 3.67 km/s at the centre of the core. Similarly, the density in PREM starts with 12.76 g/cm^3 and increases to 13.09 g/cm^3. However, because the normal-mode eigenfunctions must be zero at the centre of the Earth, the mode sensitivity to wave speed and density also vanishes at the bottom of the inner core. Therefore, shear wave speed and density at the bottom of the inner core are only weakly constrained.

With the inner core being solid, shear wave, the *J* phase, should be able to propagate through the inner core. However, the conversion from compressional wave to shear wave at the inner-core boundary is highly inefficient, and, as a consequence, the amplitude of inner-core shear energy is very low (Bullen, 1951). Despite this fact,

observation of *PKJKP* phase at a relatively high frequency was reported soon after the demonstration of inner-core solidity (Julian et al., 1972). This was later questioned by Doornbos (1974) who argued that the high attenuation of the inner core forfeits high-frequency observation of the shear wave in the inner core. After more than two decades of quiescence, two independent studies reported observations of the *J* phase: *PKJKP* (Okal and Cansi, 1998) and *pPKJKP* and *SKJKP* (Deuss et al., 2000). Improvements in data recording, coverage, and theory played important roles in the revived interest. These two studies also calculated the shear wave speed, and obtain similar values of 3.65 km/s (Okal and Cansi, 1998) and 3.6 km/s (Deuss et al., 2000). Curiously, however, different *J* phases (*PKJKP*, *pPKJKP* and *SKJKP*) are observed by the two groups analyzing the same events. Deuss et al. (2000) argues that higher-frequency data analyzed by Okal and Cansi (1998) suffer from the same attenuation problem as the earlier Julian et al. (1972) study, and that the *PKJKP* arrival is a mis-identification of another phase. The observation of the *J* phase is still in its infancy, and additional studies will provide better understanding of shear waves in the inner core.

5.2 Anisotropy

A peculiar behavior of seismic data penetrating deep into the core was reported in the early 1980's. The core-sensitive normal modes exhibited anomalous splitting which, when visualized as a splitting function, had a strong zonal pattern (Masters and Gilbert, 1981; Fig. 6a). In addition, a collection of *PKIKP* travel times showed that the waves traveling in the north-south direction arrived consistently earlier than those travelling in the east-west direction (Poupinet et al., 1983; Fig. 8). The Poupinet et al. (1983) paper proposed prolateness and heterogeneity within the inner core to explain the observation. Similarly, the anomalous splitting of modes were modeled with topography on the inner-core and the core-mantle boundaries, as well as heterogeneity in the inner and outer core (e.g., Ritzwoller et al., 1986; Giardini et al., 1987; Widmer et al., 1992). For example, Giardini et al. (1987) argued that a model with considerable topography both on the core-mantle and inner-core boundaries ($>$25 km) and a heterogeneity of more than 6% near the inner-core boundary can fit the anomalous splitting. As we have seen, these models were physically and dynamically questionable, and did not agree with models of the inner-core and the core-mantle boundary obtained through other seismic data.

Morelli et al. (1986) and Woodhouse et al. (1986) demonstrated that a more reasonable model can be constructed by introducing the simplest form of anisotropy. This anisotropy, often referred to as cylindrical anisotropy or transverse isotropy, is described with an axis of symmetry and the angle the seismic ray makes with this axis (the ray angle). With the axis of symmetry aligned with the rotation axis, the difference between the arrival times of the north-south and east-west paths can be explained by having high wave speed when the ray angle is zero and low wave speed when the ray angle is 90° from the axis. At the same time, this type of anisotropy predicts strong zonal pattern for splitting function of inner-core sensitive modes, consistent with observations.

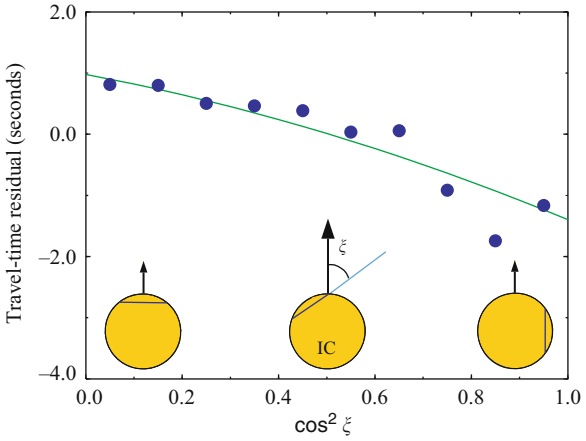

Figure 8. PKIKP Travel Times. Averaged absolute travel time residuals (blue circles) from the International Seismological Centre (ISC) Bulletins between 1964 and 1994. The data have been averaged using $\cos^2$ of the ray angle ξ, and the averaged travel-time residuals (after correcting for source and mantle/crustal structure) are shown as a function of $\cos^2 \xi$. The epicentral distance range for this data set is between 150° and 153°, i.e., the wave samples the upper couple of hundred kilometers of the inner core. The compressional wave ray paths are shown as blue lines within the yellow inner core to illustrate that the waves traveling perpendicular to the Earth's rotation axis (black arrow) arrive later than expected (positive travel-time residuals), and waves traveling parallel to the rotation axis arrive earlier than expected (negative travel-time residuals).

Models of inner-core anisotropy can be divided into three groups. Those based upon normal-mode splitting data prefer relatively weak, 1–2%, anisotropy (e.g., Li et al., 1991; Tromp, 1993, 1995b; Ishii et al., 2002a), and if a depth dependence is included, the strength of anisotropy diminishes rapidly in the lower inner core (e.g., Woodhouse et al., 1986; Romanowicz et al., 1996). The second type of model has similar anisotropy level as models based upon mode data, but anisotropy increases considerably near the centre of the Earth (Morelli et al., 1986; Shearer et al., 1988; Shearer, 1994; Su and Dziewoński, 1995). These models are constructed using the absolute travel times of the *PKIKP* wave. The disadvantages of using the *PKIKP* travel times for inner-core modeling are the possible contamination from mantle heterogeneities and earthquake mislocation. Studies that use the *PKIKP* data correct for these effects, but these corrections may be insufficient. To minimize this uncertainty, differential travel times of the PKP_{BC} and *PKIKP* (PKP_{DF}) have been introduced (Shearer and Toy, 1991; Creager, 1992). These two ray paths are nearly identical except for a part of *PKIKP* sampling the inner core (Fig. 2), and subtracting travel times of *PKIKP* from PKP_{BC} provides travel time associated only with inner-core structure. These data therefore require no correction for effects due to mantle and source location. The disadvantage of this data set is that PKP_{BC} is observable in a limited epicentral distance range, implying that the PKP_{BC}–PKP_{DF} data constrain only the

upper part of the inner core (Fig. 2). To complement this data set, the other outer-core phase, PKP_{AB}, was considered (Song and Helmberger, 1993b; Vinnik et al., 1994). Measurements of PKP_{AB}–PKP_{DF} are available up to antipodal distances, allowing us to probe the deepest part of the Earth. The models of inner-core anisotropy based upon these differential travel-time data (PKP_{BC}–PKP_{DF} and PKP_{AB}–PKP_{DF}) are characterized by strong anisotropy (often more than 3%) that increases with depth (e.g., Creager, 1992; Song and Helmberger, 1993b; Vinnik et al., 1994; Song, 1996, 2003; Creager, 1999, 2000; Li and Richards, 2003; Souriau and Poupinet, 2003).

The main differences between the models based upon the three types of data are the strength and depth dependence of anisotropy. The discrepancy in depth profile between body-wave and normal-mode models is an artifact of inversion. The normal-mode sensitivity to structure vanishes at the centre of the Earth, and the current mode data set consists of modes that are practically insensitive to the lowermost part of the inner core. A typical inversion scheme forces the model to be zero or very small within a poorly constrained region, resulting in a decrease in anisotropy with depth. If a different inversion scheme is used, one can obtain relatively strong anisotropy in the central inner core (Beghein and Trampert, 2003). However, the robustness of a model with high value in the null space is questionable. Alternatively, one can combine normal-mode and body-wave data for a simultaneous inversion. These models fit the mode data while having a slight increase in anisotropy with depth (Tromp, 1995b; Romanowicz et al., 1996; Ishii et al., 2002a). This confirms that the decrease in anisotropy with depth, a characteristic of many mode models, is an artifact of the inversion and not a real feature.

The source of the second discrepancy, the strength of anisotropy, is not as obvious as the depth dependence. Both normal-mode and *PKIKP* travel-time data favor relatively weak anisotropy, in contrast to strong anisotropy inferred from differential travel times. Part of this difference appears to come from difference in sampling (Ishii et al., 2002b). Normal modes, by their nature, sample and average the whole inner core. The *PKIKP* travel times also have a good coverage, and biasing due to uneven sampling is relatively low. On the other hand, differential travel times are not as readily available as the *PKIKP* data, and the coverage is uneven. In particular, there are some paths with large travel-time anomaly, such as the one between the South-Sandwich Islands and Alaska, for which abundant measurements are available. With an incomplete coverage, these anomalous data may bias inferences of global average anisotropy. Indeed, a joint inversion of mode, *PKIKP*, and differential travel-time data results in a model with relatively weak anisotropy of about 1.8% (Ishii et al., 2002a). This model does not fit the differential travel times as well as it does the mode or *PKIKP* data, but the poorer fit is partly due to the small number of anomalous paths. When these are removed or treated with less importance, predictions from the model agree well with averaged differential travel-time data (Ishii et al., 2002a).

Another source of discrepancy is the effect of mantle heterogeneity. In many differential travel-time studies, the signal due to mantle heterogeneity is assumed to have been completely removed by the differencing operation. However, this may not be adequate if the mantle has considerable amount of small-scale variations. This is of

particular concern for PKP_{AB}–PKP_{DF} data for which the two ray paths are substantially different in the lower mantle (Bréger et al., 1999, 2000a,b; Ishii et al., 2002b; Luo et al., 2002; Rost and Garnero, 2004). The PKP_{AB}–PKP_{DF} data are indeed very sensitive to structure near the base of the mantle, and they have been used to model heterogeneities in the D″ (e.g., Song and Helmberger, 1993a; Bréger et al., 1999, 2000b). Furthermore, structures with strong wave-speed variations along the ray path, such as slabs, have been found to affect the differential travel times significantly, even though these features may be in the upper mantle where ray paths are close together (Weber, 1990; Helffrich and Sacks, 1994). To account for the mantle, investigators have began to invert jointly for structure within the mantle and inner core (e.g., Song, 2000a; Sun and Song, 2002).

Not all scatter in the data can be explained by mantle variations, however, and what remains may be associated with lateral heterogeneity in the inner core. For example, non-zonal components of the mode splitting functions can be related to large-scale lateral variations, and local averaging of the absolute *PKIKP* travel times can give similar information at various length scales. These features are addressed in the next few sections.

5.3 Hemispheric variations and isotropic layer near the inner-core boundary

The upper few hundred kilometers of the inner core are relatively well-sampled by mode, *PKIKP*, and PKP_{BC}–PKP_{DF} data. Based upon the body-wave data, two additional complexities to the inner core have been proposed: an isotropic layer immediately below the inner-core boundary (Song and Helmberger, 1995a), and hemispheric difference between the east and west (Tanaka and Hamaguchi, 1997). These are treated together in this section, because some studies suggest that the thickness of the isotropic layer has hemispheric variation.

The difference between the eastern and western hemispheres is well-documented using both *PKIKP* and differential travel times (e.g., Tanaka and Hamaguchi, 1997; Creager, 1999; Garcia and Souriau, 2000; Niu and Wen, 2001; Ishii et al., 2002b; Romanowicz et al., 2003). The waves that sample the eastern hemisphere have smaller travel-time variations than those that sample the western hemisphere. There are additional indications that the division is not quite hemispherical, and quasi-eastern (roughly between 40 and 160 or 180°E) and quasi-western (roughly between 180 and 40°E) hemisphere division has been proposed (Tanaka and Hamaguchi, 1997; Creager, 1999, 2000; Niu and Wen, 2001; Souriau and Poupinet, 2003). There is also a suggestion that the transition between the two hemispheric regions is sharp (Souriau and Poupinet, 2003). Unfortunately, normal-mode data cannot complement the body-wave information for investigation of hemispheric variation. Such structure is of spherical harmonic degree 1, and the current database of isolated mode measurements are insensitive to odd-degree variations.

Even though the observation of hemispheric difference is indisputable, its interpretation differs considerably between studies. The initial report of hemispheric variation

proposed perturbations in isotropic compressional wave speed of $+0.29 \pm 0.15\%$ and $-0.66 \pm 0.20\%$ in the eastern and western regions, respectively (Tanaka and Hamaguchi, 1997). A study based upon *PKiKP–PKIKP* differential travel times supports this result with the eastern hemisphere $\sim$1% faster than the western hemisphere at the top of the inner core (Niu and Wen, 2001; Garcia, 2002; Luo et al., 2002). Others have suggested that the data can be explained by a change in the thickness of the isotropic layer between east ($\sim$400 km thickness) and west (100–200 km thickness) (Garcia and Souriau, 2000; Souriau and Poupinet, 2003). Finally, there are models that prefer a combination of change in anisotropy and layer thickness: anisotropy of less than 1% and thickness of 60–400 km in the eastern region, and 0–4% anisotropy within a 100–200 km layer in the western region (Creager, 1999, 2000; Li and Richards, 2003). Some of these studies argue that there is no variation in isotropic wave speed in the upper-most inner core (Creager, 1999).

Whether the top of the inner core is isotropic or anisotropic is an issue not fully resolved. Although a global isotropic layer of thickness between 50 and 400 km is favored by many investigators (Song and Helmberger, 1995a; Garcia and Souriau, 2000; Garcia, 2002; Souriau and Poupinet, 2003) with possible lateral variations in thickness (Ouzounis and Creager, 2001; Isse and Nakanishi, 2002; Niu and Wen, 2002), weak anisotropy of $\leq$1% cannot be ruled out (McSweeney et al., 1997; Bréger et al., 1999; Creager, 1999, 2000; Sun and Song, 2002; Li and Richards, 2003). Weak anisotropy also agrees with *PKIKP* travel-time data (Shearer, 1994; Ishii et al., 2002a). Normal-mode data can be fit with a global isotropic layer with thickness less than 100 km, but a weak anisotropy at the top of the inner core will fit the data equally well (Durek and Romanowicz, 1999; Ishii et al., 2002a).

A sharp discontinuity, which may be related to the transition from isotropic to anisotropic layers, has been proposed at about 200 km depth beneath the inner-core boundary based upon triplication of the *PKIKP* data (Song and Helmberger, 1998; Song and Xu, 2002). This observation is spatially limited, and the depth of the transition may vary laterally (e.g., Creager, 2000). The sharpness of this transition zone is not well-constrained, and the observation of a triplication does not preclude a rapid change in the level of anisotropy. The first-order discontinuity is often an artifact of model parametrisation, and a broader transition zone can also accommodate the data (Ouzounis and Creager, 2001).

5.4 Lateral variations and the axis of symmetry

In this section, we focus on smaller-scale variations than at the hemispheric scale, and also on constraints on the location of the axis of symmetry. These two parameters, as will be discussed in the next section, are vital components in estimating the inner-core rotation rate. Indications of aspherical structure within the inner core has been noted in early investigations of inner-core anisotropy (e.g., Shearer and Toy, 1991). At large scales (wavelengths $>$200 km), some studies propose relatively strong heterogeneity of $\sim\pm$1% (Su and Dziewoński, 1995; Kaneshima, 1996), but others suggest only a weak heterogeneity of $<$0.3% (McSweeney et al., 1997; Garcia and Souriau,

2000; Souriau and Poupinet, 2003). At smaller scales (a few hundred kilometers), the inferred level of wave speed variation increases (Cormier and Choy, 1986; Garcia and Souriau, 2000; Collier and Helffrich, 2001; Souriau and Poupinet, 2003; Rost and Garnero, 2004). At an even smaller scale, scatterers that are few kilometers in size are observed using energy that arrive before *PKKP* but after *PKiKP* (Shearer et al., 1998; Vidale and Earle, 2000).

In addition to lateral variations in wave speed, strong gradients in compressional wave speed have also been reported from regional studies (Creager, 1997; Song, 2000a; Xu and Song, 2003). Such gradients could result from isotropic wave speed variations, but they can also arise from a tilt in the symmetry axis: two rays that travel with the same angle with respect to the rotation axis would have different ray angles, hence different wave speed, if the symmetry axis is tilted. Therefore, there is a trade-off between the tilt of the symmetry axis and lateral variation in isotropic wave speed. Studies that report a tilt in the axis favor a tilt of about 10° from the rotation axis (Su and Dziewoński, 1995; McSweeney et al., 1997; Isse and Nakanishi, 2002), although the earliest value was half these estimates (Creager, 1992). The exact longitudinal location of the axis, however, varies considerably between 100 and 160°E (Creager, 1992; Su and Dziewoński, 1995; McSweeney et al., 1997; Isse and Nakanishi, 2002).

The difficulty in constraining the location of the symmetry axis comes from two sources. First, the uneven sampling of the inner core biases the estimate (Souriau et al., 1997; Souriau, 1998b; Ishii and Dziewoński, 2003). Second, especially for a regional study, the trade off between lateral variation and the tilt of the axis is too strong to obtain a reliable constraint. Indeed, there are studies that argue for a tilt that is either below the detection level or close to the axis of rotation (Dziewoński and Su, 1998; Creager, 1999, 2000; Souriau and Poupinet, 2003). Because the tilt of the symmetry axis is not well-constrained, inner-core anisotropy is often studied assuming that the Earth's rotation axis is the axis of symmetry.

5.5 Rotation

Soon after there was a prediction that the inner core rotates faster than the mantle based upon numerical simulations of the geomagnetic field (Glatzmaier and Roberts, 1995, 1996; Kuang and Bloxham, 1997), seismic studies reported observations of this phenomenon (Song and Richards, 1996; Su et al., 1996). However, the inferred rates differed by almost a factor of three: 1.1°/yr by Song and Richards (1996) and 3°/yr by Su et al. (1996). This difference illustrates the difficulties in estimating the inner-core rotation rate.

If the inner core was cylindrically anisotropic with the symmetry axis aligned with the rotation axis, it would be impossible to detect differential rotation of the inner core with respect to the mantle. The properties of such inner core sampled by the seismic waves would remain the same over time even if the differential rotation rate was high. In order for the rotation to be detected, there must be some longitudinal change in seismic wave speed. This can come from cylindrical anisotropy with a tilted axis of symmetry, lateral variations in wave speed, or small scatterers. As discussed in the

previous section, the first condition is difficult to constrain reliably, and can easily be biased by uneven sampling (e.g., Souriau et al., 1997). Indeed, this problem has been recognized as the source of large rotation rate of 3°/yr (Souriau et al., 1997; Souriau, 1998b), and re-analysis of the same data set led to the conclusion that the inner-core differential rotation is below the uncertainty (Dziewoński and Su, 1998). Another important unknown in the determination of the rotation rate is earthquake mislocation. Because the distribution of seismometers change with time, estimates of the hypocentral location may contain time-dependence that may map into estimates of inner-core rotation. Efforts to address this ambiguity include simultaneous inversions for the rotation rate and earthquake locations (Song, 2000a), and doublet analysis (Poupinet et al., 2000). The doublet analysis uses a pair of earthquakes separated by time but with a similar source mechanism and hypocentral location (Poupinet et al., 2000). Comparison of the data from these two events should suffer little from the source mislocation, and changes in travel times over the time period can be attributed to change due to inner-core rotation. However, there is a disagreement as to which pair of earthquakes qualify as a doublet, and estimates of inner-core rotation vary accordingly (Poupinet et al., 2000; Song, 2001; Zhang et al., 2005).

Despite these factors of uncertainty, inferences of inner-core rotation have been made, mainly by using body-wave data that sample small parts of the inner core. The results can be divided into two groups. One argues that the rotation is not required or that it cannot be significantly different from zero (Souriau, 1998b; Poupinet et al., 2000; Isse and Nakanishi, 2002). Another group argues that there is a significant rotation above the uncertainty level (Song and Richards, 1996; Creager, 1997, 2000; Ovtchinnikov et al., 1998; Song, 2000a,b, 2003; Song and Li, 2000; Vidale et al., 2000; Collier and Helffrich, 2001; Li and Richards, 2003; Xu and Song, 2003; Zhang et al., 2005). The rotation rates obtained by these studies generally range between 0.2 and 1.0°/yr in the eastward direction (Fig. 9). The eastward direction is supported even by studies from the first group, most of which conclude that if the inner core is rotating (with rates below the detection limit), it is in the eastward direction.

There are also studies that base their estimates on global sampling, either body-wave measurements from earthquakes and stations distributed globally (Dziewoński and Su, 1998; Souriau and Poupinet, 2000, 2003) or on normal-mode data (Sharrock and Woodhouse, 1998; Laske and Masters, 1999, 2003). Due to scatter and various uncertainties in the data, the global body-wave studies typically have larger error estimates than regional studies, and result in a rotation rate below the detection level, i.e., 0 ± 1°/yr. On the other hand, normal-mode studies analyze the time dependence of the non-zonal components of the splitting function of inner-core sensitive modes. The initial study by Sharrock and Woodhouse (1998) suggested a westward rotation below 2.5°/yr, but later studies prefer a rate below the uncertainty level (0.01 ± 0.21°/yr, Laske and Masters, 1999), or slightly above the noise level (0.13 ± 0.11°/yr, Laske and Masters, 2003).

Collier and Helffrich (2001) suggest an alternative to the eastward super-rotation in an attempt to reconcile some of the scatter in the data. They analyzed PKP_{BC}–PKP_{DF}

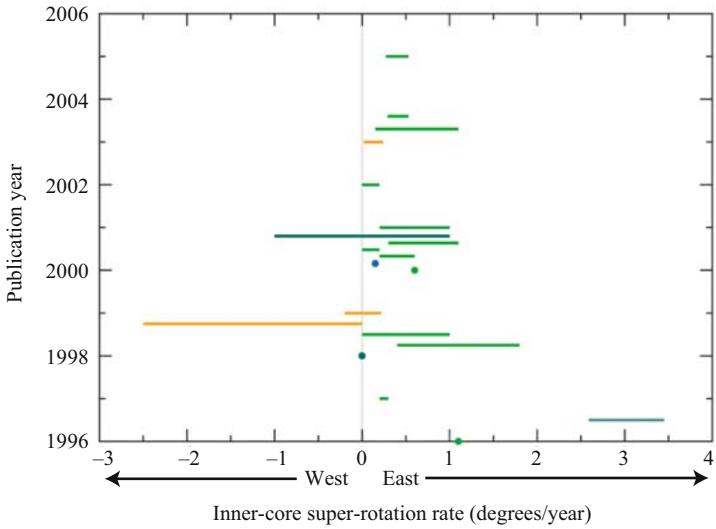

Figure 9. Summary of the Inner-Core Super-Rotation Estimates. Various estimates of the inner-core super rotation plotted by the publication date of each study (Song and Richards, 1996; Su et al., 1996; Creager, 1997, 2000; Souriau et al., 1997; Ovtchinnikov et al., 1998; Sharrock and Woodhouse, 1998; Souriau, 1998a; Laske and Masters, 1999, 2003; Poupinet et al., 2000; Song, 2000a,b, 2001, 2003; Song and Li, 2000; Souriau and Poupinet, 2000, 2003; Vidale et al., 2000; Collier and Helffrich, 2001; Isse and Nakanishi, 2002; Li and Richards, 2003; Xu and Song, 2003; Zhang et al., 2005). The estimates are color-coded by the type of data used: normal modes (orange), absolute travel times (dark green), differential travel times (light green), and scatterers (blue).

data from a path between the south-west Pacific and the United Kingdom. The time-dependence of the data can be explained by an eastward rotation of 0.2–1.0°/yr. A better fit, however, is obtained by rotational oscillation of the inner core with a time scale of about 280 days. According to this study, the inner core rotates westward by 1.42 ± 0.38°/yr between 1987 and 1992, and eastward by 1.50 ± 0.26°/yr between 1992 and 1997 (Collier and Helffrich, 2001). This additional complication is undoubtedly more challenging to constrain than an uni-directional rotation, and it has not yet been confirmed by any other studies.

5.6 Attenuation

The estimates of the attenuation factor Q in the inner core are derived both from normal-mode and body-wave data. Because the inner core is solid, there are two attenuation factors Q_α and Q_β in terms of wave speeds, or Q_κ and Q_μ in terms of elastic moduli. The relationship between these two sets of parameters is given in Equation (1). Because Q_β and Q_μ are identical, we will only discuss Q_α, Q_κ, and Q_μ in this section.

The attenuation factors based upon normal-mode data are often given in terms of elastic moduli, i.e., Q_μ and Q_κ. Various inferences of Q_μ are consistently between 3000 and 3500 (Buland and Gilbert, 1978; Masters and Gilbert, 1981; Masters et al., 1983; Fukao and Suda, 1989; Suda and Fukao, 1990a,b), although two studies propose much smaller values around 100 (Giardini et al., 1988; Widmer et al., 1991). The constraints on Q_κ are not as readily available from normal-mode studies. The slow decay of inner-core modes suggests a high value of Q_κ, and a value much higher value than Q_μ has been proposed (15,700, Masters et al., 1983).

Normal-mode estimates of Q can be biased by two factors. First, mis-identification of inner-core modes, with other modes that have similar characteristic frequency, can lead to erroneous inferences (Suda and Fukao, 1990b; Widmer et al., 1991). To avoid such confusion and contamination from nearby mantle modes, analysis of inner-core mode usually use records that start hours after the earthquake occurrence. This allows mantle modes to be attenuated away, making observation of inner-core modes easier. The second factor for bias in Q estimates comes from mode coupling. Some modes exchange energy between one another, and this can alter the appearance and location of the mode frequency peak. Masters et al. (1983) have considered this coupling effect and provide Q_μ and Q_κ of 3140 and 15,700, respectively.

There is a significant discrepancy between the attenuation factors obtained from normal-mode and body-wave data. The body-wave analysis typically uses the amplitude ratio of PKP_{DF} (or *PKIKP*) and PKP_{BC} phases to estimate the value of Q_α. These estimates cover a wide range of values from below 100–600 (Buchbinder, 1971; Doornbos, 1974, 1983; Bolt, 1977; Cormier, 1981; Choy and Cormier, 1983; Niazi and Johnson, 1992; Bhattacharyya et al., 1993; Tseng et al., 2001; Cormier and Li, 2002; Li and Cormier, 2002). To compare these values of Q_α to the attenuation factors from the mode studies (Q_μ and Q_κ), one needs to convert Q_μ and Q_κ into Q_α (Eq. 1). The value of (β^2/α^2) in the inner core is about 0.1, and using conservative values of Q_μ and Q_κ of 3000 and 15,000, respectively, Q_α based upon mode study is calculated to be about 10,000. On the other hand, a weak constraint on Q_μ is obtained from the *PKIKP* wave, and the preferred value is about 30 (Cormier, 1981; Doornbos, 1983), in contrast to 3000 from mode studies.

One possible source of this discrepancy is in sampling of the inner core by different data. The estimates from the mode data have been averaged in lateral and radial directions, whereas most body-wave values are based upon regional sampling of the upper inner core. It is possible that attenuation varies laterally and radially. The issue of depth-dependent Q_α in the upper 400–500 km has been investigated by several groups using the body-wave data. Although there are studies which report no variation with depth (Cormier, 1981; Niazi and Johnson, 1992), most analyses agree that Q_α increases with depth within the upper 500 km of the inner core from about 100–600 (Doornbos, 1974; Choy and Cormier, 1983; Song and Helmberger, 1995a; Souriau and Roudil, 1995; Tseng et al., 2001; Cormier and Li, 2002; Li and Cormier, 2002). There is also an indication that the top-most 50 km of the inner core has a highly attenuating layer with Q_α below 100 (Song and Helmberger, 1992; Garcia, 2002).

Below 500 km, the body-wave constraint on Q_α is weak, nonetheless, it is argued to be below 2000 (Doornbos, 1974).

Due to limitations in the data coverage, lateral variation in Q_α is not pursued zealously. The hemispheric difference in the inner-core property has, nevertheless, motivated investigations for similar behaviour in Q_α. The results are inconclusive. One study rejects such a large-scale lateral variation in Q_α (Li and Cormier, 2002), but another reports that Q_α in the eastern hemisphere is considerably higher than in the western hemisphere (Tseng et al., 2001). Anisotropy in Q_α has also been considered using regional data set, and higher attenuation is observed for waves travelling nearly parallel to the spin axis (Creager, 1992; Song and Helmberger, 1993b; Souriau and Romanowicz, 1996; Cormier et al., 1998; Li and Cormier, 2002). However, the correlation between wave speed and attenuation is not very high when a global data set is considered (Souriau and Romanowicz, 1997; Cormier and Li, 2002).

Incorporating depth dependence, or lateral/anisotropical variations does not appear to reconcile the value of Q_α based upon body-wave data with that inferred from mode studies. An alternate explanation for this discrepancy is the frequency dependence of Q_α. If Q_α is strongly dependent upon frequency, the discrepancy in values obtained by body waves (short period) and normal modes (long period) may be explained. Investigation of the frequency dependence requires data with a wide range of frequency, hence is difficult to model reliably. Some body-wave studies suggest a weak dispersion (Doornbos, 1983; Cummins and Johnson, 1988; Cormier et al., 1998; Li and Cormier, 2002), whereas others observe no frequency dependence (Cormier, 1981; Bhattacharyya et al., 1993; Souriau and Roudil, 1995). Alternatively, if the inner core is dominated by small-scale scatterers, the body-wave amplitudes can be affected significantly and reduce the Q_α estimates (Cormier and Li, 2002). There are indications of scatters in the inner core (Shearer et al., 1998; Vidale and Earle, 2000; Cormier and Li, 2002), and this might help explain the differences between the Q_α values based upon body-wave and normal-mode data. Another source of bias in body-wave inferences is the effects of structure at the base of the mantle. The amplitudes of PKP_{DF} and PKP_{BC} are sensitive to attenuation in laterally varying D″ region and ultra-low velocity zones. These effects are unlikely to explain the large discrepancy between body-wave and normal-mode inferences, but they may explain the scatter in the Q_α estimates based upon body-wave data.

5.7 Innermost inner core

The deepest few hundred kilometers of the Earth is not well-sampled by currently available normal-mode data set. As described in an earlier section, normal-mode sensitivity is practically zero in the central couple hundred kilometers, and a mode model in this region is unreliable (e.g., Beghein and Trampert, 2003). Thus, any inference in the central inner core must rely on the *PKIKP* data recorded at nearly antipodal distances. The peculiarity of *PKIKP* travel-time behavior from these distances has been noted in early studies of inner-core anisotropy (Morelli et al., 1986; Su and

Dziewoński, 1995). With an improved data set, Ishii and Dziewoński (2002) proposed that the deepest 300 km of the inner core behaves slightly different from the region above, and introduced the innermost inner core. Anisotropy in the top 920 km of the inner core propagate waves faster in the north-south direction, and slower in the east-west direction. In the model of the innermost inner core, the direction of the fastest wave speed remains the same as the overlying inner core, but the direction of the slowest wave propagation is about 45° from the north-south direction. Note that this model does not require higher-order anisotropy or change in the location of the symmetry axis.

There are additional indications that the property of the inner core near the centre differs from the bulk solid core. Using an array of stations in Antarctica, Wiens et al. (2003) observed a change in *PKIKP* data as the epicentral distance increased toward the antipode. Cormier and Stroujkova (2004) specifically used waveform data to examine the model of Ishii and Dziewoński (2002) and concluded that the waveform data are not consistent with a sharp discontinuity at 300 km radius. Instead, they suggest either a gradual change in anisotropy or a discontinuity around 450 km radius. The latter is consistent with a proposed change in attenuation property (Cormier and Li, 2002; Li and Cormier, 2002). Although a discontinuity at 450 km radius is inconsistent with the data set used by Ishii and Dziewoński (2002), a gradual change in anisotropy is admissible. The sharp change in anisotropy at 300 km radius is artificially imposed, and the absolute travel-time data set from the International Seismological Centre (ISC) Bulletin does not have the power to resolve the sharpness of the transition. Finally, an attempt has been made to determine the tilt of the symmetry axis in the innermost inner core, but due to the same data coverage problem as discussed earlier, the results are inconclusive (Ishii and Dziewoński, 2003).

6 SUMMARY

The two types of seismic observations, body waves and free oscillations, need to be treated differently, and should be chosen according to the particular property that is being investigated. For example, data coverage and small-scale variations can bias the global average of elastic properties if body-wave data are used. On the other hand, normal-mode data will not be very useful in a search for small-scale features. Nonetheless, a good model should explain the bulk part of both body-wave and free-oscillation observations once frequency effects have been considered. After all, these two data sets are sampling the same Earth.

The global average of the outer core wave speed and density appears to be well-constrained by seismic data. These parameters vary smoothly with depth, and earlier inferences of discontinuities and low wave speed layers have been explained by scatterers in the lowermost mantle and topography on the core-mantle boundary. Compared to the PREM model (Dziewoński and Anderson, 1981), the compressional wave speed at the top of the core should be slightly lower, and the wave-speed gradient should be slightly higher in the upper outer core and slightly lower in the lower outer core. The estimates of Q for the whole outer core also seems to agree well between

models. Both body-wave and normal-mode studies prefer values higher than 10,000, indicating that the outer core is not an efficient attenuator of seismic energy. The deviations from the one-dimensional model have been studied, and a wide range of estimates in the strength of lateral heterogeneity exists. One group of studies argues that the heterogeneities are below or close to the detection limit, i.e., within the uncertainty level. Another group argues for a few percent variations. Resolving three-dimensional structure is further complicated by the trade offs with other parts of the Earth, such as structure in the mantle and anisotropy in the inner core. However, there is evidence that the top of the outer core is close to being homogeneous with the possible exception of small and thin patches of finite rigidity zones. Finally, it is possible to obtain an estimate of viscosity at the base of the liquid core through seismological constraints, but the current observation of the Slichter mode, and hence the inference of viscosity, is highly controversial.

The transition from liquid to solid core occurs sharply with a width of less than 5 km, and is located around 1220-km radius. Initially, this boundary was thought to have strong undulations; however, later studies showed that this was an artifact due to inner-core anisotropy. Based upon waves reflected from the inner-core boundary, it appears smooth, while being slightly oblate with 1.5–5.0 km difference between polar and equatorial radii. The change in the compressional wave speed across this boundary is mainly constrained by body-wave data, and is between 0.5 and 0.8 km/s. The changes in shear wave speed and density are derived mostly from normal-mode data, and they are about 3.5 km/s and less than 1 g/cm^3, respectively.

The depth profiles of compressional and shear wave speeds as well as density within the inner core is relatively well determined. The shear wave speed and density exhibit small increase with depth. This is mainly constrained by normal-mode observations, but they generally agree with the limited number of body-wave inferences. The compressional wave speed is obtained using both normal-mode and body-wave data, and it increases only slightly with depth. These parameters are best resolved near the inner-core boundary, and their uncertainties increase with depth.

The peculiar behavior of inner-core sensitive data have been attributed to various parts and properties of the Earth, for example, as coming from outer-core heterogeneity or topography on the core-mantle boundary. We currently understand it as an expression of anisotropy of the inner core, and models have been proposed based upon normal-mode, absolute and differential travel-time data. Near the inner-core boundary, material is only weakly anisotropic, or even isotropic. As depth increases, many models favor an increase in the strength of anisotropy. In some studies, the central part of the inner core has been argued as having a different anisotropic behavior, even though the form of anisotropy and the axis of symmetry remains the same as the overlying layer. However, the central inner core is poorly sampled, and such issues as the width of the transition and exact form of anisotropy require further investigation.

Lateral variations within the inner core have been studied with great interest, because there is distinct signal in the data, and because they are essential in deducing the location of the symmetry axis and differential rotation of the inner core. At large scales, the inner core exhibits a clear dichotomy between the eastern and western

hemispheres. Nevertheless, interpretation of this signal ranges from mantle heterogeneity to isotropic or anisotropic variations in the inner and/or outer core. At smaller scales, lateral variations in anisotropy and isotropic wave speeds have both been proposed, but rejection or confirmation of either model has been difficult, due to limitations in data coverage. Similarly, the location of the symmetry axis has not been determined with confidence. There are some indications that it may be tilted with respect to the rotation axis, but once various factors are considered, the uncertainty becomes too large to make statistically significant inferences.

Because investigation of inner-core differential rotation requires either a tilted symmetry axis or lateral variation, resolvability has been a controversial issue. Consequently, estimates vary from zero to 3°/yr. Careful consideration of biasing factors has shown that rates much larger than 1°/yr can be disregarded. If the inner core does rotate with respect to the mantle, most studies suggest that the acceptable rate is less than or about 1°/yr in the eastward direction.

The parameter that is least constrained in the inner core is attenuation. There is a factor of 10–100 difference between values obtained from normal-mode and body-wave observations. The source of this discrepancy has not been clearly identified, and it may simply be that the attenuation in the inner core is strongly frequency dependent, or that the effects of small-scale scatterers are significant. Based upon the body-wave data, attenuation may be laterally heterogeneous, anisotropic, depth dependent, and/or layered. However, we need much larger data set in order to understand the strength and variation of attenuation and other properties within the inner core. Because of its small size (it is only about 0.7% of the Earth's volume), seismic energy can reach the inner core only if the wave leaves the source with less than 6° take-off angle for a shallow source. It is a difficult target to observe, but we have learned so much since its discovery. With continued efforts, we will have even better understanding of this mysterious region of the Earth.

ACKNOWLEDGEMENTS

The author would like to thank the editor, Dave Yuen, and two anonymous reviewers for constructive suggestions, and Karen Felzer and Hiromi Yoshina-Ishii for comments that improved the manuscript.

REFERENCES

Adams, R.D. (1972) Multiple inner core reflections from a Novaya Zemlya explosion. *Bull. Seismol. Soc. Am.*, 62, 1063–1071.

Adams, R.D., and E.R. Engdahl (1974) P-wave velocities in the Earth's core; an interim report. *Phys. Earth Planet. Inter.*, 9, 36–40.

Adams, R.D., and M.J. Randall (1964) The fine structure of the Earth's core. *Bull. Seismol. Soc. Am.*, 54, 1299–1313.

Adushkin, V.V., V.A. An, V.M. Ovchinnikov, and D.N. Krasnoshchekov (1997) On the density jump at the inner boundary of the Earth's core from observations of PKiKP waves at distances of about 6 degrees. *Transactions (Doklady) Russ. Acad. Sci. Earth Sci. Sections*, 354, 595–598.

Anderson, D.L. (1980) Bulk attenuation in the Earth and viscosity of the core. *Nature*, 285, 204–207.
Anderson, D.L., and R.S. Hart (1976) An Earth model based on free oscillations and body waves. *J. Geophys. Res.*, 81, 1461–1475.
Anderson, D.L., and R.S. Hart (1978) Q of the Earth. *J. Geophys. Res.*, 83, 5869–5882.
Beghein, C., and J. Trampert (2003) Robust normal mode constraints on inner-core anisotropy from model space search. *Science*, 299, 552–555.
Bhattacharyya, J., P.M. Shearer, and G. Masters (1993) Inner core attenuation from short-period PKP(BC) versus PKP(DF) wave forms. *Geophys. J. Int.*, 114, 1–11.
Birch, A.F. (1940) The alpha-gamma transformation of iron at high pressures, and the problem of the Earth's magnetism. *Am. J. Sci.*, 238, 192–211.
Birch, A.F. (1952) Elasticity and constitution of the Earth's interior. *J. Geophys. Res.*, 57, 227–286.
Bolt, B.A. (1962) Gutenberg's early PKP observations. *Nature*, 196, 122–124.
Bolt, B.A. (1964) The velocity of seismic waves near the Earth's center. *Bull. Seismol. Soc. Am.*, 54, 191–208.
Bolt, B.A. (1977) The detection of PKIIKP and damping in the inner core. *Annali di Geofisica*, 30, 507–519.
Bolt, B.A., and M.E. O'Neill (1965) Times and amplitudes of the phases PKiKP and PKIIKP. *Geophys. J. R. Astron. Soc,*, 9, 223–231.
Bolt, B.A., and A. Qamar (1970) Upper bound to the density jump at the boundary of the Earth's inner core. *Nature*, 228, 148–150.
Boschi, L., and A.M. Dziewoński (2000) Whole Earth tomography from delay times of P, PcP, and PKP phases: Lateral heterogeneities in the outer core or radial anisotropy in the mantle? *J. Geophys. Res.*, 105, 13675–13696.
Bréger, L., B. Romanowicz, and H. Tkalčić (1999) PKP(BC−DF) travel time residuals and short scale heterogeneity in the deep Earth. *Geophys. Res. Lett.*, 26, 3169–3172.
Bréger, L., B. Romanowicz, and S. Rousset (2000a) New constraints on the structure of the inner core from P′P′. *Geophys. Res. Lett.*, 27, 2781–2784.
Bréger, L., H. Tkalčić, and B. Romanowicz (2000b) The effect of D″ on PKP(AB−DF) travel time residuals and possible implications for inner core structure. *Earth Planet. Sci. Lett.*, 175, 133–143.
Buchbinder, G.G.R. (1971) A velocity structure of the Earth's core. *Bull. Seismol. Soc. Am.*, 61, 429–456.
Buchbinder, G.G.R. (1972a) Travel times and velocities in the outer core from PmKP. *Earth Planet. Sci. Lett.*, 14, 162–168.
Buchbinder, G.G.R. (1972b) An estimate of inner core density. *Phys. Earth Planet. Inter.*, 5, 123–128.
Buchbinder, G.G.R., C. Wright, and G. Poupinet (1973) Observations of PKiKP at distances less than 110°. *Bull. Seismol. Soc. Am.*, 63, 1699–1707.
Buland, R., and F. Gilbert (1978) Improved resolution of complex eigenfrequencies in analytically continued seismic spectra. *Geophys. J. R. Astron. Soc.*, 52, 457–470.
Bullen, K.E. (1951) Theoretical amplitudes of the seismic phase PKJKP. *Mon. Not. R. Astron. Soc. Geophys. Suppl.*, 6, 163–167.
Choy, G.L., and V.F. Cormier (1983) The structure of the inner core inferred from short-period and broadband GDSN data. *Geophys. J. R. Astron. Soc.*, 72, 1–21.
Cleary, J.R., and R.A.W. Haddon (1972) Seismic wave scattering near the core-mantle boundary: A new interpretation of precursors to PKP. *Nature*, 240, 549–551.
Collier, J.D., and G. Helffrich (2001) Estimate of inner core rotation rate from United Kingdom regional seismic network data and consequences for inner core dynamical behaviour. *Earth Planet. Sci. Lett.*, 193, 523–537.
Cormier, V.F. (1981) Short-period PKP phases and the anelastic mechanism of the inner core. *Phys. Earth Planet. Inter.*, 24, 291–301.
Cormier, V.F. (1989) Slab diffraction of S waves. *J. Geophys. Res.*, 94, 3006–3024.
Cormier, V.F., and G.L. Choy (1986) A search for lateral heterogeneity in the inner core from differential travel times near PKP-D and PKP-C. *Geophys. Res. Lett.*, 13, 1553–1556.

Cormier, V.F., and X. Li (2002) Frequency-dependent seismic attenuation in the inner core: 2. A scattering and fabric interpretation. *J. Geophys. Res.*, 107, doi:10.1029/2002JB001796.

Cormier, V.F., and P.G. Richards (1976) Comments on "The damping of core waves" by Anthony Qamar and Alfredo Eisenberg. *J. Geophys. Res.*, 81, 3066–3068.

Cormier, V.F., and P.G. Richards (1977) Full wave theory applied to a discontinuous velocity increase: The inner core boundary. *J. Geophys.*, 43, 3–31.

Cormier, V.F., and A. Stroujkova (2004) Waveform search for the innermost inner core. *Earth Planet. Sci. Lett.*, 236, 96–105.

Cormier, V.F., L. Xu, and G.L. Choy (1998) Seismic attenuation of the inner core: Viscoelatic or stratigraphic? *Geophys. Res. Lett.*, 25, 4019–4022.

Courtier, N., B. Ducarme, J. Goodkind, J. Hinderer, Y. Imanishi, N. Seama, H. Sun, J. Merriam, B. Bengert, and D.E. Smylie (2000) Global superconducting gravimeter observations and the search for the translational modes of the inner core. *Phys. Earth Planet. Inter.*, 117, 3–20.

Creager, K.C. (1992) Anisotropy of the inner core from differential travel times of the phases PKP and PKIKP. *Nature*, 356, 309–314.

Creager, K.C. (1997) Inner core rotation rate from small-scale heterogeneity and time-varying travel times. *Science*, 278, 1284–1288.

Creager, K.C. (1999) Large-scale variations in inner core anisotropy. *J. Geophys. Res.*, 104, 23127–23139.

Creager, K.C. (2000) Inner core anisotropy and rotation. In Karato, S., A.M. Forte, R.C. Lieberman, G. Masters, and L. Stixrude (eds.) Earth's Deep Interior: Minral Physics and Tomography from the Atomic to the Global Scale, American Geophysical Union, Washington DC, pp. 89–114.

Crossley, D.J. (1993) Core modes and Slichter modes; fact and fancy. *Marees Terrestres. Bulletin d'Informations*, 117, 8628–8638.

Crossley, D.J. (2003) Can a stably stratified layer in the core be detected using seismic normal modes or Earth rotation? In Dehant, V., K.C. Creager, S. Karato, and S. Zatman (eds.) Earth's Core: Dynamics, Structure, Rotation, American Geophysical Union, Washington DC, pp. 241–250.

Crossley, D., M.G. Rochester, and Z.R. Peng (1992) Slichter modes and Love numbers. *Geophys. Res. Lett.*, 115, 1202–1207.

Cummins, P., and L.R. Johnson (1988) Short-period body wave constraints on properties of the Earth's inner core boundary. *J. Geophys. Res.*, 93, 9058–9074.

Dahlen, F.A., and J. Tromp (1998) Theoretical Global Seismology, Princeton University Press, Princeton, New Jersey.

Derr, J.S. (1969) Internal structure of the Earth inferred from free oscillations. *J. Geophys. Res.*, 74, 5202–5220.

Deuss, A., J.H. Woodhouse, H. Paulssen, and J. Trampert (2000) The observation of inner core shear waves. *Geophys. J. Int.*, 142, 67–73.

Doornbos, D.J. (1974) The anelasticity of the inner core. *Geophys. J. R. Astron. Soc.*, 38, 397–415.

Doornbos, D.J. (1983) Observable effects of a seismic absorption band in the Earth. *Geophys. J. R. Astron. Soc.*, 75, 693–711.

Doornbos, D.J., and N.J. Vlaar (1973) Regions of seismic wave scattering in the Earth's mantle and precursors to PKP. *Nature*, 243, 58–61.

Durek, J.J., and B. Romanowicz (1999) Inner core anisotropy inferred by direct inversion of normal mode spectra. *Geophys. J. Int.*, 139, 599–622.

Dziewoński, A.M. (1971) Solidity of the inner core of the Earth inferred from normal mode observations. *Nature*, 234, 465–466.

Dziewoński, A.M., and D.L. Anderson (1981) Preliminary reference Earth model. *Phys. Earth Planet. Inter.*, 25, 297–356.

Dziewoński, A.M., and W. Su (1998) A local anomaly in the inner core. *EOS Trans. Am. Geophys. Un. Suppl.*, 79, S218.

Engdahl, E.R. (1968) Seismic waves within Earth's outer core; multiple reflection. *Science*, 161, 263–264.

Engdahl, E.R., E.A. Flinn, and C.F. Romney (1970) Seismic waves reflected from the Earth' inner core. *Nature*, 228, 852–853.

Engdahl, E.R., E.A. Flinn, and R.P. Masse (1974) Differential PKiKP travel times and the radius of the inner core. *Geophys. J. R. Astron. Soc.*, 39, 457–463.

Ergin, K. (1967) Seismic evidence for a new layered structure of the Earth's core. *J. Geophys. Res.*, 72, 3669–3687.

Fukao, Y., and N. Suda (1989) Core modes of the Earth's free oscillations and structure of the inner core. *Geophys. Res. Lett.*, 16, 401–404.

Garcia, R. (2002) Constraints on upper inner-core structure from waveform inversion of core phases. *Geophys. J. Int.*, 150, 651–664.

Garcia, R., and A. Souriau (2000) Inner core anisotropy and heterogeneity level. *Geophys. Res. Lett.*, 27, 3121–3124.

Garnero, E.J., and D.V. Helmberger (1995) On seismic resolution of lateral heterogeneity in the Earth's outermost core. *Phys. Earth Planet. Inter.*, 88, 117–130.

Garnero, E.J., D.V. Helmberger, and S.P. Grand (1993) Constraining outermost core velocity with SmKS waves. *Geophys. Res. Lett.*, 20, 2463–2466.

Giardini, D., X.-D. Li, and J.H. Woodhouse (1987) Three-dimensional structure of the Earth from splitting in free-oscillation spectra. *Nature*, 325, 405–411.

Giardini, D., X.-D. Li, and J.H. Woodhouse (1988) Splitting functions of long-period normal modes of the Earth. *J. Geophys. Res.*, 93, 13716–13742.

Gilbert, F., A.M. Dziewoński, and J.N. Brune (1973) An informative solution to a seismological inverse problem. *Proc. Nat. Acad. Sci.*, 70, 1410–1413.

Glatzmaier, G.A., and P.H. Roberts (1995) A three-dimensional convective dynamo solution with rotating and finitely conducting inner core and mantle. *Phys. Earth Planet. Inter.*, 91, 63–75.

Glatzmaier, G.A., and P.H. Roberts (1996) Rotation and magnetism of Earth's inner core. *Science*, 274, 1887–1891.

Gutenberg, B. (1913) Über die Konstitution des Erdinnern, erschlossen aus Erdbebenbeobachtungen. *Z. Geophys.*, 14, 1217–1218.

Häge, H. (1983) Velocity constraints for the inner core inferred from long-period PKP amplitudes. *Phys. Earth Planet. Inter.*, 31, 171–185.

Hales, A.L., and J.L. Roberts (1970) The travel times of S and SKS. *Bull. Seismol. Soc. Am.*, 60, 461–489.

Hales, A.L., and J.L. Roberts (1971) The velocities in the outer core. *Bull. Seismol. Soc. Am.*, 61, 1051–1059.

Helffrich, G., and I.S. Sacks (1994) Scatter and bias in differential PKP travel times and implications for mantle and core phenomena. *Geophys. Res. Lett.*, 21, 2167–2170.

Ishii, M., and A.M. Dziewoński (2002) The innermost inner core of the earth: Evidence for a change in anisotropic behavior at the radius of about 300 km. *Proc. Natl. Acad. Sci. USA*, 22, 14026–14030.

Ishii, M., and A.M. Dziewoński (2003) Distinct seismic anisotropy at the centre of the Earth. *Phys. Earth Planet. Inter.*, 140, 203–217.

Ishii, M., and A.M. Dziewoński (2005) Constraints on the outer core tangent cylinder using normal-mode splitting measurements. *Geophys. J. Int.*, 162, 787–792.

Ishii, M., J. Tromp, A.M. Dziewoński, and G. Ekström (2002a) Joint inversion of normal mode and body wave data for inner core anisotropy: 1. Laterally homogeneous anisotropy. *J. Geophys. Res.*, 107, doi:10.1029/2001JB000712.

Ishii, M., A.M. Dziewoński, J. Tromp, and G. Ekström (2002b) Joint inversion of normal mode and body wave data for inner core anisotropy: 2. Possible complexities. *J. Geophys. Res.*, 107, doi:10.1029/2001JB000713.

Isse, T., and I. Nakanishi (2002) Inner-core anisotropy beneath Australia and differential rotation. *Geophys. J. Int.*, 151, 255–263.

Jeffreys, H. (1939) The times of the core waves. *Mon. Nat. R. Astr. Soc. Geophys. Suppl.*, 4, 594–615.

Johnson, L.R., and R.C. Lee (1985) Extremal bounds on the P velocity in the Earth's core. *Bull. Seismol. Soc. Am.*, 75, 115–130.

Jordan, T.H. (1973) *Estimation of the radial variation of seismic velocities and density in the Earth*. Ph.D. Thesis, California Institute of Technology, Pasadena CA.

Jordan, T.H., and D.L. Anderson (1974) Earth structure from free oscillations and travel times. *Geophys. J. R. Astron. Soc.*, 36, 411–459.

Julian, B.R., D. Davies, and R.M. Sheppard (1972) PKJKP. *Nature*, 235, 317–318.

Kaneshima, S. (1996) Mapping heterogeneity of the uppermost inner core using two pairs of core phases. *Geophys. Res. Lett.*, 23, 3075–3078.

Kaneshima, S., K. Hirahara, T. Ohtaki, and Y. Yoshida (1994) Seismic structure near the inner core-outer core boundary. *Geophys. Res. Lett.*, 21, 157–160.

Kennett, B.L.N., E.R. Engdahl, and R. Buland (1995) Constraints on seismic velocities in the Earth from traveltimes. *Geophys. J. Int.*, 122, 108–124.

Kind, R., and G. Müller (1977) The structure of the outer core from SKS amplitudes and travel times. *Bull. Seismol. Soc. Am.*, 67, 1541–1554.

Kohler, M.D., and T. Tanimoto (1992) One-layer global inversion for outermost core velocity. *Phys. Earth Planet. Inter.*, 72, 173–184.

Koper, K.D., M.L. Pyle, and J.M. Franks (2003) Constraints on aspherical core structure from PKiKP−PcP differential travel times. *J. Geophys. Res.*, 108, doi:10.1029/2002JB001995.

Kuang, W., and J. Bloxham (1997) An Earth-like numerical dynamo model. *Nature*, 389, 371–374.

Laske, G., and G. Masters (1999) Limits on differential rotation of the inner core from an analysis of the Earth's free oscillations. *Nature*, 402, 66–69.

Laske, G., and G. Masters (2003) The Earth's free oscillations and the differential rotation of the inner core. In Dehant, V., K.C. Creager, S. Karato, and S. Zatman (eds.) Earth's Core: Dynamics, Structure, Rotation, American Geophysical Union, Washington DC, pp. 5–21.

Lay, T., and C.J. Young (1990) The stably-stratified outermost core revisited. *Geophys. Res. Lett.*, 17, 2001–2004.

Lehman, I. (1936) P′. *Pub. Bur. Cent. Seism. Int.*, A14, 3–31.

Li, X., and V.F. Cormier (2002) Frequency-dependent seismic attenuation in the inner core: 1. A visco-elastic interpretation. *J. Geophys. Res.*, 107, doi:10.1029/2002JB001795.

Li, A.Y., and P.G. Richards (2003) Study of inner core structure and rotation using seismic records from Novaya Zemlya underground nuclear tests. In Dehant, V., K.C. Creager, S. Karato, and S. Zatman (eds.) Earth's Core: Dynamics, Structure, Rotation, American Geophysical Union, Washington DC, pp. 23–30.

Li, X.-D., D. Giardini, and J.H. Woodhouse (1991) Large-scale three-dimensional even-degree structure of the Earth from splitting of long-period normal modes. *J. Geophys. Res.*, 96, 551–577.

Luo, S.-N., S. Ni, and D. Helmberger (2002) Relationship of D″ structure with the velocity variations near the inner-core boundary. *Geophys. Res. Lett.*, 29, doi:10.1029/2001GL013907.

Masse, R.P., E.A. Flinn, R.M. Seggelke, and E.R. Engdahl (1974) PKIIKP and the average velocity of the inner core. *Geophys. Res. Lett.*, 1, 39–42.

Masters, G. (1979) Observational constraints on the chemical and thermal structure of the Earth's deep interior. *Geophys. J. R. Astron. Soc.*, 57, 507–534.

Masters, G., and F. Gilbert (1981) Structure of the inner core inferred from observations of its spheroidal shear modes. *Geophys. Res. Lett.*, 8, 569–571.

Masters, T.G., and P.M. Shearer (1990) Summary of seismological constraints on the structure of the Earth's core. *J. Geophys. Res.*, 95, 21691–21695.

Masters, G., J. Park, and F. Gilbert (1983) Observations of coupled spheroidal and toroidal modes. *J. Geophys. Res.*, 88, 10285–10298.

McSweeney, T.J., K.C. Creager, and R.T. Merrill (1997) Depth extent of inner-core seismic anisotropy and implications for geomagnetism. *Phys. Earth Planet. Inter.*, 101, 131–156.

Megnin, C., and B. Romanowicz (2000) The three-dimensional shear velocity structure of the mantle from the inversion of body, surface and higher-mode waveforms. *Geophys. J. Int.*, 143, 709–728.

Mochizuki, E., and T. Ohminato (1989) On the anomalous splitting of Earth's free oscillations. *Geophys. Res. Lett.*, 16, 1415–1416.

Morelli, A., and A.M. Dziewoński (1987) Topography of the core-mantle boundary and lateral homogeneity of the liquid core. *Nature*, 325, 678–683.

Morelli, A., A.M. Dziewoński, and J.H. Woodhousee (1986) Anisotropy of the inner core inferred from PKIKP travel times. *Geophys. Res. Lett.*, 13, 1545–1548.

Müller, G. (1973) Amplitude studies of core phases. *J. Geophys. Res.*, 78, 3469–3490.
Niazi, M., and L.R. Johnson (1992) Q in the inner core. *Phys. Earth Planet. Inter.*, 74, 55–62.
Niu, F., and L. Wen (2001) Hemispherical variations in seismic velocity at the top of the Earth's inner core. *Nature*, 410, 1081–1084.
Niu, F., and L. Wen (2002) Seismic anisotropy in the top 400 km of the inner core beneath the "eastern" hemisphere. *Geophys. Res. Lett.*, 29, doi:10.1029/2001GL014118.
Okal, E.A., and Y. Cansi (1998) Detection of PKJKP at intermediate periods by progressive multi-channel correlation. *Earth Planet. Sci. Lett.*, 164, 23–30.
Oldham, R.D. (1906) The constitution of the interior of the earth as revealed by earthquakes. *Quart. J. Geol. Soc. Lond.*, 62, 456–475.
Ouzounis, A., and K.C. Creager (2001) Isotropy overlying anisotropy at the top of the inner core. *Geophys. Res. Lett.*, 28, 4331–4334.
Ovtchinnikov, V.M., V.V. Adushkin, and V.A. An (1998) On the velocity of differential rotation of the Earth's inner core. *Dokl. Akad. Nauk.*, 362, 683–686.
Poupinet, G., R. Pillet, and A. Souriau (1983) Possible heterogeneity of the Earth's core deduced from PKIKP travel times. *Nature*, 305, 204–206.
Poupinet, G., A. Souriau, and O. Coutant (2000) The existence of an inner core super-rotation questioned by teleseismic doublets. *Phys. Earth Planet. Inter.*, 118, 77–88.
Proudman, J. (1916) On the motions of solids in a liquid possessing vorticity. *Proc. R. Soc. Lond. A*, 92, 408–424.
Qamar, A. (1973) Revised velocities in the Earth's core. *Bull. Seismol. Soc. Am.*, 63, 1073–1096.
Qamar, A., and A. Eisenberg (1974) The damping of core waves. *J. Geophys. Res.*, 79, 758–765.
Randall, M.J. (1970) SKS and seismic velocities in the outer core. *Geophys. J. R. Astron. Soc.*, 21, 441–445.
Resovsky, J.S., and M.H. Ritzwoller (1995) Constraining odd-degree Earth structure with coupled free-oscillations. *Geophys. Res. Lett.*, 22, 2301–2304.
Resovsky, J.S., and M.H. Ritzwoller (1998) New and refined constraints on deep Earth structure from generalized spectral fitting: Application to free oscillations below 3 mHz. *J. Geophys. Res.*, 103, 783–810.
Rial, J.A., and V.F. Cormier (1980) Seismic waves at the epicenter's antipode. *J. Geophys. Res.*, 85, 2661–2668.
Rieutord, M. (2002) Slichter modes of the Earth revisited. *Phys. Earth Planet. Inter.*, 131, 269–278.
Ritzwoller, M., G. Masters, and F. Gilbert (1986) Observations of anomalous splitting and their interpretation in terms of aspherical structure. *J. Geophys. Res.*, 91, 10203–10228.
Ritzwoller, M., G. Masters, and F. Gilbert (1988) Constraining aspherical structure with low-degree interaction coefficients: Application to uncoupled multiplets. *J. Geophys. Res.*, 93, 6369–6396.
Romanowicz, B., and L. Bréger (2000) Anomalous splitting of free oscillations: A reevaluation of possible interpretations. *J. Geophys. Res.*, 105, 21559–21578.
Romanowicz, B., and J.J. Durek (2000) Seismological constraints on attenuation in the Earth: A review. In Karato, S., A.M. Forte, R.C. Lieberman, G. Masters, and L. Stixrude (eds.) Earth's Deep Interior: Minral Physics and Tomography from the Atomic to the Global Scale, American Geophysical Union, Washington DC, pp. 161–179.
Romanowicz, B., X.-D. Li, and J. Durek (1996) Anisotropy in the inner core: Could it be due to low-order convection? *Science*, 274, 963–966.
Romanowicz, B., H. Tkalčić, and L. Bréger (2003) On the origin of complexity in PKP travel time data. In Dehant, V., K.C. Creager, S. Karato, and S. Zatman (eds.) Earth's Core: Dynamics, Structure, Rotation, American Geophysical Union, Washington DC, pp. 31–44.
Rost, S., and E.J. Garnero (2004) A study of the uppermost inner core from PKKP and P′P′ differential traveltimes. *Geophys. J. Int.*, 156, 565–574.
Rost, S., and J. Revenaugh (2001) Seismic detection of rigid zones at the top of the core. *Science*, 294, 1911–1914.
Roudil, P., and A. Souriau (1993) Liquid core structure and PKP station anomalies derived from PKP(BC) propagation times. *Phys. Earth Planet. Inter.*, 77, 225–236.

Sacks, I.S. (1971) Anelasticity of the outer core. In *Year Book*, 69, Carnegie Institution of Washington, Washington DC, pp. 414–416.
Sharrock, D.S., and J.H. Woodhouse (1998) Investigation of time dependent inner core structure by the analysis of free oscillation spectra. *Earth Planets Space*, 50, 1013–1018.
Shearer, P.M. (1994) Constraints on inner core anisotropy from PKP(DF) travel times. *J. Geophys. Res.*, 99, 19647–19660.
Shearer, P.M., and G. Masters (1990) The density and shear velocity contrast at the inner core boundary. *Geophys. J. Int.*, 102, 491–498.
Shearer, P.M., and K.M. Toy (1991) PKP(BC) versus PKP(DF) differential travel times and aspherical structure in the Earth's inner core. *J. Geophys. Res.*, 96, 2233–2247.
Shearer, P.M., K.M. Toy, and J.A. Orcutt (1988) Axi-symmetric Earth models and inner-core anisotropy. *Nature*, 333, 228–232.
Shearer, P.M., M.A.H. Hedlin, and P.S. Earle (1998) PKP and PKKP precursor observations; implications for the small-scale structure of the deep mantle and core. In Gurnis, M., M.E. Wysession, E. Knittle, and B.A. Buffett (eds.) The Core-Mantle Boundary Region, American Geophysical Union, Washington DC, pp. 37–55.
Silver, P.G., and W.W. Chan (1988) Implications for continental structure and evolution from seismic anisotropy. *Nature*, 335, 34–39.
Slichter, L.B. (1961a) The fundamental free mode of the Earth's inner core. *Proc. Nat. Acad. Sci.*, 47, 186–190.
Slichter, L.B. (1961b) Concerning a free mode of the earth's inner core possibly observed during the Chilean earthquake. *Science*, 133, 1369.
Smith, M.L. (1976) Translational inner core oscillations of a rotating, slightly elliptical Earth. *J. Geophys. Res.*, 81, 3055–3065.
Smylie, D.E. (1992) The inner core translational triplet and the density near Earth's center. *Science*, 255, 1678–1682.
Smylie, D.E. (1999) Viscosity near Earth's solid inner core. *Science*, 284, 461–463.
Smylie, D.E., and D.G. McMillan (1998) Viscous and rotational splitting of the translational oscillations of Earth's solid inner core. *Phys. Earth Planet. Inter.*, 106, 1–18.
Smylie, D.E., and D.G. McMillan (2000) The inner core as a dynamic viscometer. *Phys. Earth Planet. Inter.*, 117, 71–79.
Soldati, G., L. Boschi, and A. Piersanti (2003) Outer core density heterogeneity and the discrepancy between PKP and PcP travel time observations. *Geophys. Res. Lett.*, 30, doi:10.1029/2002GL016647.
Song, X. (1996) Anisotropy in central part of inner core. *J. Geophys. Res.*, 101, 16089–16097.
Song, X. (1997) Anisotropy of the Earth's inner core. *Rev. Geophys.*, 35, 297–313.
Song, X. (2000a) Joint inversion for inner core rotation, inner core anisotropy, and mantle heterogeneity. *J. Geophys. Res.*, 105, 7931–7943.
Song, X. (2000b) Time dependence of PKP(BC)−PKP(DF) times: Could this be an artifact of systematic earthquake mislocations? *Phys. Earth Planet. Inter.*, 122, 221–228.
Song, X. (2001) Comment on "The existence of an inner core super-rotation questioned by teleseismic doublets" by Georges Poupinet, Annie Souriau, and Olivier Coutant. *Phys. Earth Planet. Inter.*, 124, 269–273.
Song, X. (2003) Three-dimensional structure and differential rotation of the inner core. In Dehant, V., K.C. Creager, S. Karato, and S. Zatman (eds.) Earth's Core: Dynamics, Structure, Rotation, American Geophysical Union, Washington DC, pp. 45–63.
Song, X., and D.V. Helmberger (1992) Velocity structure near the inner core boundary from waveform modeling. *J. Geophys. Res.*, 97, 6573–6586.
Song, X., and D.V. Helmberger (1993a) Effect of velocity structure in D″ on PKP phases. *Geophys. Res. Lett.*, 20, 285–288.
Song, X., and D.V. Helmberger (1993b) Anisotropy of Earth's inner core. *Geophys. Res. Lett.*, 20, 2591–2594.

Song, X., and D.V. Helmberger (1995a) Depth dependence of an isotropy of Earth's inner core. *J. Geophys. Res.*, 100, 9805–9816.

Song, X., and D.V. Helmberger (1995b) A P wave velocity model of Earth's core. *J. Geophys. Res.*, 100, 9817–9830.

Song, X., and D.V. Helmberger (1998) Seismic evidence for an inner core transition zone. *Science*, 282, 924–927.

Song, X., and A.Y. Li (2000) Support for differential inner core superrotation from earthquakes in Alaska recorded at South Pole station. *J. Geophys. Res.*, 105, 623–630.

Song, X., and P.G. Richards (1996) Seismological evidence for differential rotation of the Earth's inner core. *Nature*, 382, 221–224.

Song, X., and X. Xu (2002) Inner core transition zone and anomalous PKP(DF) waveforms from polar paths. *Geophys. Res. Lett.*, 29, doi:10.1029/2001GL13822.

Souriau, A. (1998a) New seismological constraints on differential rotation of the inner core from Novaya Zemlya events recorded ar DRV, Antarctica. *Geophys. J. Int.*, 134, F1–F5.

Souriau, A. (1998b) Is the rotation real? *Science*, 281, 55–56.

Souriau, A., and G. Poupinet (1991) A study of the outermost liquid core using differential travel times of the SKS, SKKS and S3KS phases. *Phys. Earth Planet. Inter.*, 68, 183–199.

Souriau, A., and G. Poupinet (2000) Inner core rotation: A test at the worldwide scale. *Phys. Earth Planet. Inter.*, 118, 13–27.

Souriau, A., and G. Poupinet (2003) Inner core rotation: A critial appraisal. In Dehant, V., K.C. Creager, S. Karato, and S. Zatman (eds.) Earth's Core: Dynamics, Structure, Rotation, American Geophysical Union, Washington DC, pp. 65–82.

Souriau, A., and B. Romanowicz (1996) Anisotropy in inner core attenuation: A new type of data to constrain the nature of the solid core. *Geophys. Res. Lett.*, 23, 1–4.

Souriau, A., and B. Romanowicz (1997) Anisotropy in the inner core: Relation between P-velocity and attenuation. *Phys. Earth Planet. Inter.*, 101, 33–47.

Souriau, A., and P. Roudil (1995) Attenuation in the uppermost inner core from broad-band GEOSCOPE PKP data. *Geophys. J. Int.*, 123, 572–587.

Souriau, A., and M. Souriau (1989) Ellipticity and density at the inner core boundary from subcritical PKiKP and PcP data. *Geophys. J. R. Astron. Soc.*, 98, 39–54.

Souriau, A., P. Roudil, and B. Moynot (1997) Inner core differential rotation: Facts and artefacts. *Geophys. Res. Lett.*, 24, 2103–2106.

Souriau, A., A. Teste, and S. Chevrot (2003) Is there any structure inside the liquid outer core? *Geophys. Res. Lett.*, 30, doi:10.1029/2003GL017008.

Stark, P.B., R.L. Parker, G. Masters, and J.A. Orcutt (1986) Strict bounds on seismic velocity in the spherical earth. *J. Geophys. Res.*, 91, 13892–13902.

Su, W., and A.M. Dziewoński (1995) Inner core anisotropy in three dimensions. *J. Geophys. Res.*, 100, 9831–9852.

Su, W., A.M. Dziewoński, and R. Jeanloz (1996) Planet within a planet: Rotation of the inner core of Earth. *Science*, 274, 1883–1887.

Suda, N., and Y. Fukao (1990a) Structure of the inner core inferred from observations of seismic core modes. *Geophys. J. Int.*, 103, 403–413.

Suda, N., and Y. Fukao (1990b) Observation of quasi-core modes: Further evidence of high Q_μ in the inner core *J. Phys. Earth*, 38, 391–397.

Sun, X., and X. Song (2002) PKP travel times at near antipodal distances: Implications for inner core anisotropy and lowermost mantle structure. *Earth Planet. Sci. Lett.*, 199, 429–445.

Suzuki, Y., and R. Sato (1970) Viscosity determination in the Earth's outer core from ScS and SKS phases. *J. Phys. Earth*, 18, 157–170.

Tanaka, S., and H. Hamaguchi (1993a) Degree one heterogeneity at the top of the Earth's core, revealed by SmKS travel times. In Mouel, J.L., D.E. Smylie, and T. Herring (eds.) Dynamics of Earth's Deep Interior and Earth Rotation, American Geophysical Union, Washington DC, pp. 127–134.

Tanaka, S., and H. Hamaguchi (1993b) Velocities and chemical stratification in the outermost core. *J. Geomagnetism Geoelectricity*, 45, 1287–1301.

Tanaka, S., and H. Hamaguchi (1993c) Travel times and velocities in the outer core based on the global observations of SmKS seismic phases. *Tohoku Geophys. J.*, 34, 55–87.

Tanaka, S., and H. Hamaguchi (1996) Frequency-dependent Q in the Earth's outer core from short-period P4KP/PcP spectral ratio. *J. Phys. Earth*, 44, 745–759.

Tanaka, S., and H. Hamaguchi (1997) Degree one heterogeneity and hemispherical variation of anisotropy in the inner core from PKP(BC)−PKP(DF) times. *J. Geophys. Res.*, 102, 2925–2938.

Taylor, G.I. (1917) Motion of solids in fluids when the flow is not irrotational. *Proc. R. Soc. Lond.*, A93, 99–113.

Tromp, J. (1993) Support for anisotropy of the Earth's inner core from free oscillations. *Nature*, 366, 678–681.

Tromp, J. (1995a) Normal-mode splitting due to inner-core anisotropy. *Geophys. J. Int.*, 121, 963–968.

Tromp, J. (1995b) Normal-mode splitting observations from the Great 1994 Bolivia and Kuril islands earthquakes: Constraints on the structure of the mantle and inner core. *GSA Today*, 5, 140–141, 148–151.

Tseng, T., B. Huang, and B. Chin (2001) Depth-dependent attenuation in the uppermost inner core from the Taiwan short period seismic array PKP data. *Geophys. Res. Lett.*, 28, 459–462.

Tsuboi, S., and M. Saito (2002) Existence of finite rigidity layer at the base of the Earth's liquid outer core inferred from anomalous splitting of normal modes. *Earth Planets Space*, 54, 167–171.

Vasco, D.W., and L.R. Johnson (1998) Whole Earth structure estimated from seismic arrival times. *J. Geophys. Res.*, 103, 2633–2671.

Vidale, J.E., and P.S. Earle (2000) Fine-scale heterogeneity in the Earth's inner core. *Nature*, 404, 273–275.

Vidale, J.E., D.A. Dodge, and P.S. Earle (2000) Slow differential rotation of the Earth's inner core indicated by temporal changes in scattering. *Nature*, 405, 445–448.

Vinnik, L., B. Romanowicz, and L. Bréger (1994) Anisotropy in the center of the inner core. *Geophys. Res. Lett.*, 21, 1671–1674.

Weber, M. (1990) Subduction zones; their influence on traveltimes and amplitudes of P-waves. *Geophys. J. Int.*, 101, 529–544.

Widmer, R., G. Masters, and F. Gilbert (1991) Spherically symmetric attenuation within the Earth from normal mode data. *Geophys. J. Int.*, 104, 541–553.

Widmer, R., G. Masters, and F. Gilbert (1992) Observably split multiplets—data analysis and interpretation in terms of large-scale aspherical structure. *Geophys. J. Int.*, 111, 559–576.

Wiens, D., A. Nyblade, S. Anandakrishnan, and P. Shore (2003) Near-antipode PKPdf observations from the Trans-Antarctic Mountains Seismic Experiment (TAMSEIS): Constraints on inner-core anisotropy from a seismic deployment in Antarctica. *EOS Trans. Am. Geophys. Un. Suppl.*, 84 Fall Meeting, Abstract S31B-04.

Woodhouse, J.H. (1980) The coupling and attenuation of nearly resonant multiplets in the Earth's free oscillation spectrum. *Geophys. J. R. Astron. Soc.*, 61, 261–283.

Woodhouse, J.H., and F.A. Dahlen (1978) The effect of a general aspherical perturbation on the free oscillations of the Earth. *Geophys. J. R. Astron. Soc.*, 53, 335–354.

Woodhouse, J.H., D. Giardini, and X. Li (1986) Evidence for inner core anisotropy from free oscillations. *Geophys. Res. Lett.*, 13, 1549–1552.

Xu, X., and X. Song (2003) Evidence for inner core super-rotation from time-dependent differential PKP traveltimes observed at Beijing Seismic Network. *Geophys. J. Int.*, 152, 509–514.

Zhang, J., X. Song, Y. Li, P.G. Richards, X. Sun, and F. Waldhauser (2005) Inner core differential motion confirmed by earthquake waveform doublets. *Science*, 309, 1357–1360.

CHAPTER 3

POST-PEROVSKITE PHASE TRANSITION AND THE NATURE OF THE D″ LAYER

KEI HIROSE

Department of Earth and Planetary Sciences, Tokyo Institute of Technology, Meguro, Tokyo 152-8551, Japan;
E-mail: kei@geo.titech.ac.jp

Abstract
Recent experimental and theoretical studies have shown that $MgSiO_3$ perovskite, a predominant mineral in the lower mantle, transforms to a post-perovskite phase at pressure and temperature conditions expected in the D″ region. The D″ layer has long been the most enigmatic region in the Earth's interior, due to a number of large seismic anomalies that are not consistent with the known properties of $MgSiO_3$ perovskite. Discovery of a phase transformation from perovskite to post-perovskite significantly improves our understanding of the nature of the Earth's lowermost mantle. In addition, the post-perovskite phase transition destabilizes the hot thermal boundary layer at the base of the mantle and induces extensive formation of mantle plumes, because it has a large positive Clapeyron slope. If the plumes originate in the core-mantle boundary (CMB) region, chemical compositions of such plumes are naturally distinct from the bulk of the mantle. The D″ layer most likely has significant chemical heterogeneities at various scales caused by accumulation of subducted slabs, partial melting, and reaction with the outer core.

1 INTRODUCTION

Many mantle plumes originate in the core-mantle boundary (CMB) region (e.g., Zhao, 2004). The D″ layer that occupies the bottom several 100 km of the mantle is one of the least understood regions in the Earth's interior. Seismic observations show a number of unexplained features, which are not reconciled with the known properties of $MgSiO_3$ perovskite that have long been believed to be stable to the bottom of the mantle. Phase transition of a particular mantle mineral in the D″ region was not known until recently.

Developments in X-ray diffraction (XRD) measurements at synchrotron facilities combined with laser-heated diamond-anvil cell (LHDAC) techniques have enabled

D. A. Yuen et al. (eds.), Superplumes, 69–82.
© 2007 *Springer.*

us to search for a phase transition at a high P-T condition corresponding to the CMB region. The phase transformation from $MgSiO_3$ perovskite to post-perovskite was discovered by a drastic change in the XRD pattern above 125 GPa and 2500 K, corresponding to 2700-km depth in the mantle (several 100 km above the CMB) (Murakami et al., 2004). The post-perovskite transition was later confirmed by theory, and its elastic properties were also calculated (Tsuchiya et al., 2004a,b; Iitaka et al., 2004; Oganov and Ono, 2004).

Discovery of this phase transition in the lowermost mantle has significant implications for its nature and dynamics (Hirose et al., 2006b). A number of seismic anomalies observed in the D″ layer cannot be due to a thermal anomaly alone. Since a phase transition was not known, these anomalies were often interpreted as chemical heterogeneities (Karato and Karki, 2001). However, many of these observations may be reconciled with the post-perovskite phase (Wookey et al., 2005). Moreover, this phase transition is a significantly large exothermic reaction. It destabilizes the bottom thermal boundary layer, although density increase at the phase change is small (Nakagawa and Tackley, 2004; Matyska and Yuen, 2005).

The understanding of thermal and chemical anomalies in D″ is very important if we are to understand the nature of mantle plumes. Here I review the experimental and theoretical studies on the post-perovskite phase transition and its implications for the D″ layer. Since the D″ region is a thermal and compositional boundary, it is naturally expected that it includes large chemical heterogeneities. I discuss the possible chemical heterogeneities and their origins that may be reflected in the distinct chemical compositions of plumes originating from the CMB region.

2 POST-PEROVSKITE PHASE TRANSITION IN THE LOWERMOST MANTLE

Post-perovskite phase transition in pure $MgSiO_3$ has been investigated by both high-pressure experiments and theoretical calculations. Experimental results have shown that the phase transformation also occurs in natural peridotitic mantle and mid-oceanic ridge basalt (MORB) compositions at pressures similar to that in pure $MgSiO_3$ (Hirose et al., 2006a).

2.1 Peridotite composition

The post-perovskite phase transition in natural KLB-1 peridotite (pyrolitic mantle) composition was investigated experimentally by Murakami et al. (2005) and Ono and Oganov (2005). The phase diagram is shown in Figure 1. In recent high-pressure experimental studies based on in-situ XRD measurements, the largest source of pressure uncertainty derives from the choice of pressure scale (P-V-T equation of state) used to calculate the pressure of experiments. The post-perovskite phase transition boundary presented in Figure 1 was modified from the results of Murakami et al. (2005), by converting pressure to that based on a MgO scale (Speziale et al., 2001). The MgO scale may be the most practical pressure scale because it has been

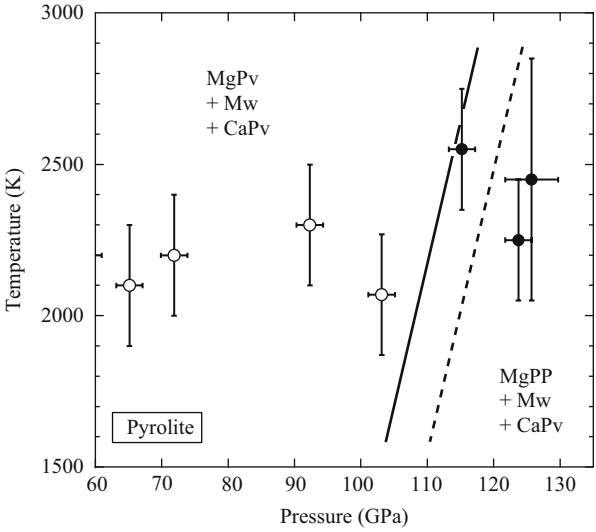

Figure 1. Phase relations in the pyrolitic mantle (KLB-1 peridotite) composition (Murakami et al., 2005). Open and solid circles indicate the phase assemblages of $MgSiO_3$-rich perovskite (MgPv) + magnesiowüstite (Mw) + $CaSiO_3$-rich perovskite (CaPv) and $MgSiO_3$-rich post-perovskite (MgPP) + Mw + CaPv, respectively. Post-perovskite phase transition boundary is shown by the solid line. Pressure was determined by Au pressure scale in these experiments. The broken line indicates the post-perovskite phase transition boundary when pressure is recalculated by the MgO pressure scale. The Clapeyron slope is assumed to be +11.5 MPa/K, the same as that in pure $MgSiO_3$ (Hirose et al., 2006a).

extensively studied and is the least controversial (Fei et al., 2004). In fact, the post-spinel transformation boundary determined by Speziale's MgO scale matches the depth of the 660-km seismic discontinuity. If this pressure scale is accurate, the post-perovskite phase transition occurs at about 119 GPa and 2400 K, consistent with the location of the D″ seismic discontinuity around 2600-km depth (Wysession et al., 1998).

Changes in mineral assemblage and proportion in KLB-1 peridotite composition are summarized in Figure 2. The pyrolitic composition consists of Al-bearing $(Mg,Fe)SiO_3$ perovskite together with minor amounts of (Mg,Fe)O magnesiowüstite and $CaSiO_3$ perovskite in the lower mantle except at its bottom. It contains 72% post-perovskite, 21% magnesiowüstite, and 7% $CaSiO_3$ perovskite$CaSiO_3$ perovskite (by weight) near the base of the mantle (Murakami et al., 2005). The post-perovskite phase is depleted in iron, and iron partitions predominantly into magnesiowüstite (Kobayashi et al., 2005; Murakami et al., 2005). The strong partitioning of iron into magnesiowüstite can cause unique geophysical and geochemical properties in the D″ region. The iron content strongly affects the viscosity, electrical conductivity, radiative heat transfer, and melting reaction. The electrical conductivity of the lowermost mantle may be lower than that of the overlying mantle due to the depletion in iron in the predominant mineral. The radiative heat transfer may be effective through the

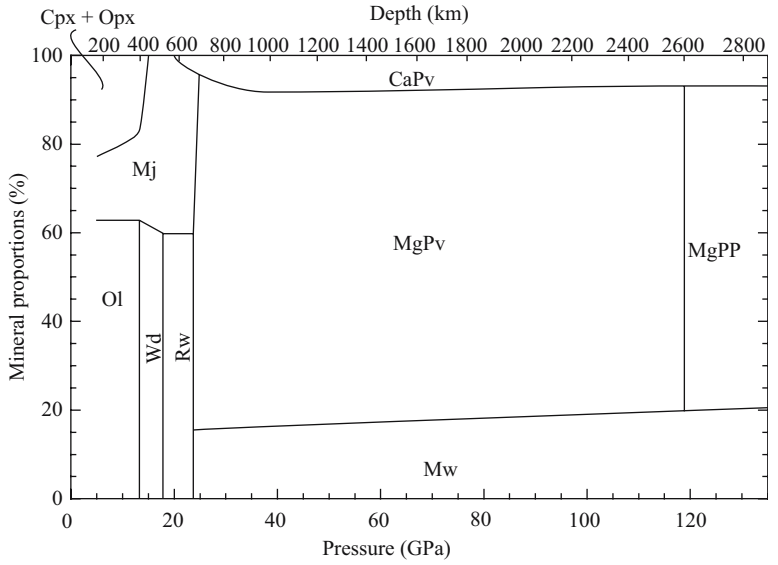

Figure 2. Changes in mineral assemblage and proportion in pyrolitic mantle composition. Cpx: clinopyroxene; Opx: orthopyroxene; Mj: majorite garnet; Ol: olivine; Wd: wadsleyite; Rw: ringwoodite; CaPv: $CaSiO_3$ perovskite;$CaSiO_3$ perovskite MgPv: $MgSiO_3$-rich perovskite; MgPP: $MgSiO_3$-rich post-perovskite; Mw: magnesiowüstite.

Fe-depleted post-perovskite that is much more transparent than perovskite. Badro et al. (2004) also argued that radiative heat transfer is important in the deep lower mantle due to a spin transition of Fe.

2.2 MORB composition

Phase relations in MORB composition were determined on the basis of XRD measurements to the bottom of the mantle (Fig. 3) (Hirose et al., 2005). The MORB composition consists of $MgSiO_3$-rich perovskite, SiO_2 stishovite, $CaSiO_3$ perovskite,$CaSiO_3$ perovskite and $CaFe_2O_4$ (Ca-ferrite)-type Al-phase in the upper part of the lower mantle below 720-km depth (Kesson et al., 1994; Hirose et al., 1999). Stishovite transforms to $CaCl_2$-type SiO_2 phase around 1500-km depth and further to α-PbO_2-type structure at 2600-km depth. The most abundant mineral of Mg-perovskite also undergoes transformation to a post-perovskite phase at about 2600-km depth. Both $CaSiO_3$ perovskite$CaSiO_3$ perovskite and $CaFe_2O_4$-type Al-phase are stable down to the bottom of the mantle. MORB composition consists of 38% post-perovskite, 23% α-PbO_2-type SiO_2 phase, 23% $CaSiO_3$ perovskite, $CaSiO_3$ perovskite and 16% $CaFe_2O_4$-type Al-phase (in weight) in the lowermost mantle. The changes in mineral assemblage and proportion are summarized in Figure 4.

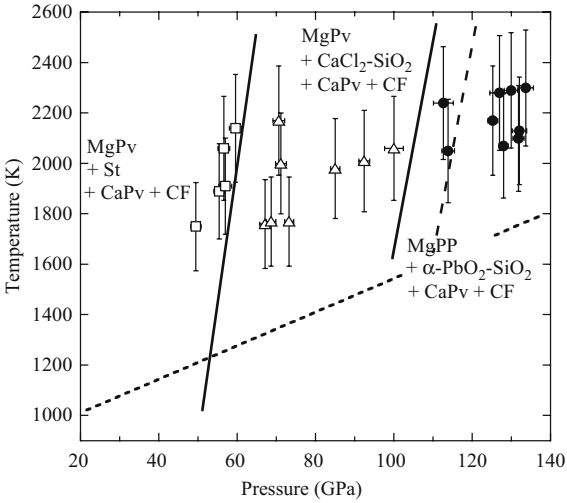

Figure 3. Phase relations of MORB composition (Hirose et al., 2005). Squares and triangles indicate the phase assemblage of $MgSiO_3$-rich perovskite (MgPv) + stishovite (St) or $CaCl_2$-type SiO_2 phase + $CaSiO_3$-rich perovskite (CaPv) + $CaFe_2O_4$-type Al-phase (CF). Circles represent the assemblage of $MgSiO_3$-rich post-perovskite (MgPP) + α-PbO_2-type SiO_2 phase + CaPv + CF. Pressure was determined by Au pressure scale in these experiments. Long-dashed line indicates the post-perovskite phase transition boundary when pressure is converted to that based on the MgO scale. The dotted curve shows the tetragonal to cubic phase transition boundary in Ca-perovskite.

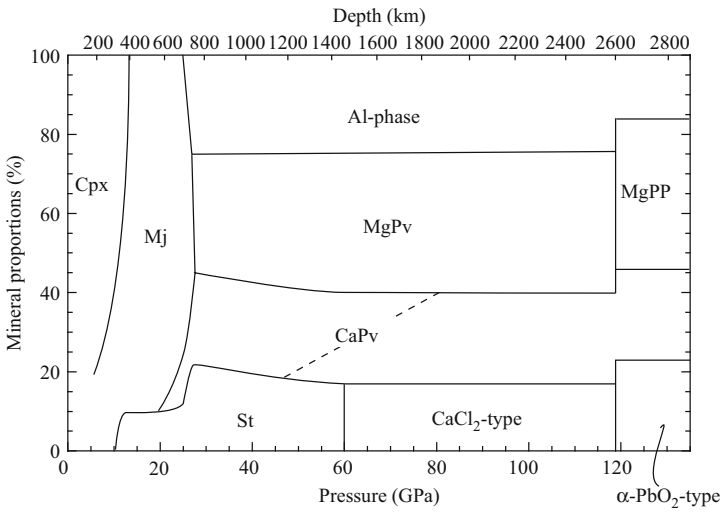

Figure 4. Change in mineral proportions in subducted MORB crust. Abbreviations are similar to those in Figures 2 and 3. The broken line indicates tetragonal to cubic phase transition of Ca-perovskite that could occur in cold subducting slabs.

3 NATURE OF D″ LAYER

3.1 Origin of D″ discontinuity

The D″ seismic discontinuity is observed at the top of D″ layer, which is located around 2600 to 2700-km depth (119–125 GPa) (Lay and Helmberger, 1983; Wysession et al., 1998). A seismic velocity increase at the D″ discontinuity is typically 2.5–3.0% for both S- and P-waves, although the discontinuity is not observed in many localities especially for P-wave. Since a phase transition of a major mantle mineral was not previously known, it was believed that such a velocity increase is caused by remnant subducted slabs (cold anomaly) or a large-scale chemical heterogeneity.

The D″ discontinuity may be reconciled with the post-perovskite phase transition. The transition pressure in a peridotitic (pyrolitic) mantle composition (Fig. 1) matches the depth of the D″ discontinuity. Calculations at $T = 0\,\mathrm{K}$ indicate that velocity increase is 1.0% for S-wave and -0.1% for P-wave at the phase transition, when both perovskite and post-perovskite are isotropic aggregates (Iitaka et al., 2004; Tsuchiya et al., 2004b; Oganov and Ono, 2004). Stackhouse et al. (2005) showed that velocity increase is larger at higher temperatures for S-wave, whereas temperature has little effect on the P-wave discontinuity. These are generally consistent with the observations that the discontinuity in the S-wave speed is much more observable than the P-wave discontinuity. However, the 3% velocity increase is larger than calculated, especially for P-wave. This may be due to a preferred orientation of post-perovskite that is a more elastically anisotropic mineral than perovskite. These observations are consistent with transversely isotropic aggregates of post-perovskite with (010) plane parallel to the mantle flow. The post-perovskite phase has a layered-sheet structure that is stacked along the b axis. A slip between such layers causes lattice preferred orientation with the (010) plane parallel to the shear direction. However, the large elastic constant for shear along the layering plane suggests that such deformation mechanism of post-perovskite is still controversial (see Hirose et al., 2006b).

The D″ layer is possibly a graveyard of subducted slabs and has a basaltic chemical composition. The pressure of the post-perovskite phase transition in MORB also matches the depth of the D″ discontinuity (Fig. 3). It is notable that the phase transformation from $CaCl_2$-type SiO_2 to α-PbO_2-type structure occurs at a pressure very similar to that of the post-perovskite phase transition. Theoretical calculations suggested that these two phase transitions have opposite effects on the changes in seismic wave velocities; S-wave and P-wave speeds change by -1% and $+1\%$ at the phase transition of a silica phase, respectively. If the effects of both the transitions are combined, only $\sim$0.6% and $\sim$0.3% velocity increases are expected for S- and P-wave, respectively, when phase proportions of the Mg-perovskite and SiO_2 phase in MORB are considered. These velocity increases are much less than those observed at the D″ discontinuity, but it may be consistent with the fact that the discontinuity is not observed in many localities (Wysession et al., 1998).

3.2 Thermal structure in D″

The temperature variation at the D″ discontinuity may be estimated from its topography and the Clapeyron slope of the post-perovskite phase transition. The location of the D″ seismic discontinuity varies from 2550 to 2750-km depth (Wysession et al., 1998). The Clapeyron slope was first determined by theory to be +7.5 to +10 MPa/K (Oganov and Ono, 2004; Tsuchiya et al., 2004a). Experiments consistently showed +11 MPa/K, based on the Speziale's MgO scale (Hirose et al., 2006a). If the D″ discontinuity is caused by the post-perovskite phase transition, such topography is formed by a temperature variation of 1000–1500 K.

Some seismic evidence indicates a presence of two discontinuities in D″ beneath Eurasia and the Caribbean (Thomas et al., 2004a,b). The shallower one is a positive velocity discontinuity, followed by a negative discontinuity at a deeper level. These observations were interpreted as indicating that perovskite transforms to post-perovskite at a shallower discontinuity and then the post-perovskite transforms back to perovskite at a deeper level. This is called the "double-crossing" model (Hernlund et al., 2005). If this model is correct, the geotherm near the CMB can be tightly constrained from the location of the post-perovskite phase transition boundary (Fig. 5). In regions where double discontinuities are observed, the $MgSiO_3$ perovskite should be stable at the base of the mantle. Experiments based on the most practical MgO pressure scale suggest that perovskite is stable above 3800 K at the base of the mantle

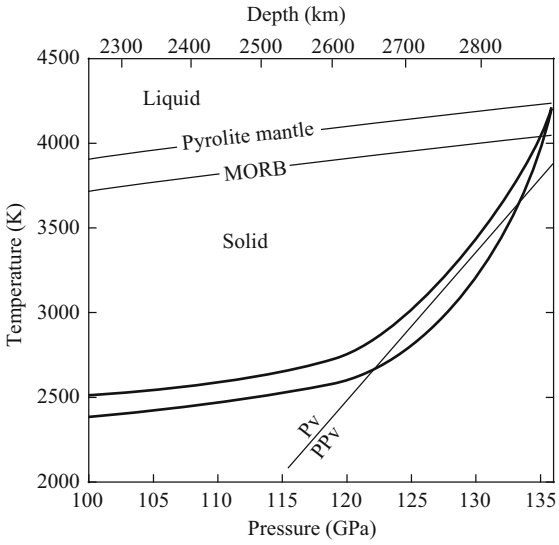

Figure 5. Temperature profiles in the deep lower mantle. The temperature at the CMB may be higher than the melting temperature of MORB and possibly peridotitic mantle (Hirose et al., 1999; Zerr et al., 1998). Post-perovskite transforms back to perovskite in the deep D″ layer.

(Hirose et al., 2006a). The average of the LDA and GGA calculations by Tsuchiya et al. (2004a) shows a transition temperature of 4200 K. These values are consistent with the previous estimation of about 4000 K, based on the melting temperature of iron at the inner core boundary (Boehler, 1996).

3.3 Possible chemical heterogeneity in D″

Since the D″ region is a compositional and thermal boundary layer, it is naturally expected that there should be complex chemical heterogeneities. It had been believed that the anti-correlation between anomalies in S-wave velocity and bulk-sound velocity is strong evidence for a large-scale chemical heterogeneity in D″ (e.g., Masters et al., 2000; Karato and Karki, 2001). Such anti-correlation, however, can be reconciled with the post-perovskite phase transition (Iitaka et al., 2004; Oganov and Ono, 2004). Ishii and Tromp (1999) found the anti-correlation between density and velocity anomalies from the analysis of free oscillations. If true, this must be due to chemical heterogeneity. However, Romanowicz (2001) suggested that the resolving power of free oscillations is weak and ambiguous in the lowermost mantle, and that the correlation between density and velocity anomalies is not well constrained. Nevertheless, the D″ region exhibits a variety of small-scale (<10 to 100-km) seismic heterogeneities, and their origins are still unknown.

3.3.1 Accumulation of basaltic crust at CMB

Subduction of basaltic crust gives rise to a strong chemical heterogeneity in the mantle. The amount of the basaltic component that has ever subducted into the Earth's interior over geological time possibly sums up to several tens percent of the whole mantle. The density relationship with the surrounding mantle is important for the fate of subducted MORB crust. The basaltic crust is denser than the average upper mantle; it becomes buoyant at 660 to 720-km depth, due to the persistence of garnet in a basaltic composition (Irifune and Ringwood, 1993; Hirose et al., 1999). Such crust is again denser than the normal mantle below 720-km depth to the bottom (Hirose et al., 2005) (Fig. 6). This is contrary to some earlier predictions by Kesson et al. (1998) and Ono et al. (2001), in which mineral volumes were not measured at high pressures.

Subducted MORB crust is denser than the PREM density (Dziewonski and Anderson, 1981) by several percent at the base of the mantle (Fig. 6). It has already been demonstrated on the basis of dynamical simulations that the 2% density contrast strongly induces segregation of MORB crust from the rest of the slab (e.g., Christensen and Hofmann, 1994; Nakagawa and Tackley, 2005). Such segregated dense MORB crusts may have accumulated at the base of the mantle and formed a chemically dense layer.

3.3.2 Partial melting of the lowermost mantle

Partial melting near the base of the mantle has been suggested by the presence of an ultra-low seismic wave velocity zone at the base of the mantle (e.g., Lay et al.,

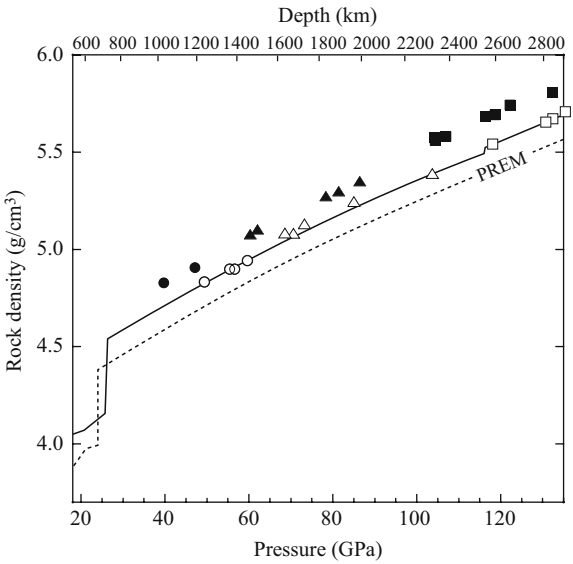

Figure 6. Density profile of subducted MORB crust (Hirose et al., 2005). Circles: MgPv + St + CaPv + CF; triangles: MgPv + $CaCl_2$-type SiO_2 + CaPv + CF; squares: MgPP + α-PbO_2-type SiO_2 + CaPv + CF. Closed and open symbols indicate 300 K and high temperature (1750–2290 K) data, respectively. Pressure was determined by the Au pressure scale in these experiments; but it was recalculated by using MgO scale only for high-temperature data above 100 GPa. The broken line indicates the PREM density (Dziewonski and Anderson, 1981). The subducted MORB crust is denser than the average lower mantle below 720-km depth through the bottom of the mantle.

1998). Such an ultra-low velocity anomaly is present even at 200-km above CMB in the African superplume (Wen, 2001).

The double-crossing model suggests that the temperature is ~4000 K at the base of the mantle, which is high enough for the pyrolitic mantle to melt (Zerr et al., 1998). A basaltic composition has a lower melting temperature, and therefore the subducted MORB crust possibly melts prior to the mantle (Hirose et al., 1999). Ohtani and Maeda (2001) suggested that a basaltic melt is denser than the surrounding mantle and therefore should segregate downwards and form a melt pond on top of the outer core. A chemical reaction between such a silicate melt and liquid outer core would occur very effectively. The silicate melt would change chemical composition and then be solidified by the consequence of a chemical reaction with the core. These are schematically shown in Figure 7.

These partial melting, reaction, and solidification processes produce a significant chemical heterogeneity in D″. Melting should have been more extensive in the past when the temperature was higher. The melting phase relations and melt compositions formed by partial melting of natural peridotite and MORB compositions are known only up to 33 GPa (Ito et al., 2004; Hirose and Fei, 2002). In the peridotitic mantle

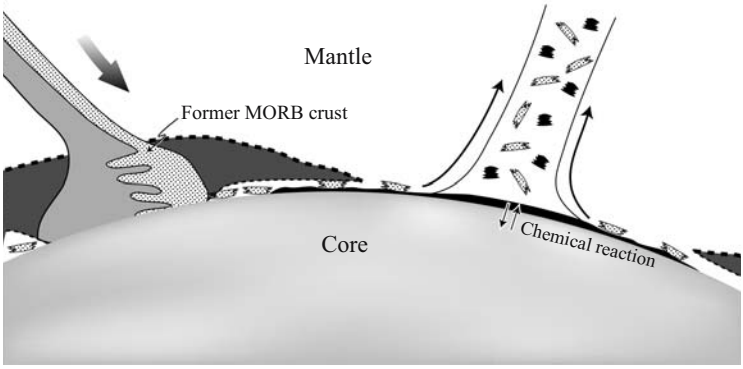

Figure 7. Schematic illustration of the core-mantle boundary region. Melt formed by partial melting of mantle and subducted MORB crust could segregate downward and accumulate on top of the outer core. It chemically reacts with molten iron core, which causes depletion in FeO and SiO_2 components in silicate melt and solidification. A complex melting zone, including solid residue, silicate partial melt, and crystal cumulate, is shown in black. Plumes originating from the CMB region may include such melting products and the former MORB crust.

composition, $MgSiO_3$-rich perovskite is the last phase to disappear with an increasing degree of partial melting above 31 GPa, and is therefore enriched in a solid residue. By contrast, $CaSiO_3$ perovskite$CaSiO_3$ perovskite appears on the liquidus in a MORB composition at 27 GPa, followed by stishovite. Previous chemical reaction experiments showed that large amounts of FeO and SiO_2 components can be dissolved from a silicate melt to the liquid outer core (Knittle and Jeanloz, 1991; Takafuji et al., 2005). Such a silicate melt may crystallize to a perovskite-poor (magnesiowüstite-rich) solid assemblage with a Fe-depleted composition.

4 IMPLICATIONS FOR PLUMES

4.1 Effects of post-perovskite phase transition

The post-perovskite phase transition has significant effects on the dynamics of the lowermost mantle due to the high positive Clapeyron slope. Numerical simulations demonstrate that such an extremely large exothermic reaction near the CMB destabilizes the hot thermal boundary layer and increases heat transport that causes a higher temperature in the whole mantle by several hundred degrees (Nakagawa and Tackley, 2004; Matyska and Yuen, 2005).

Both theory and experiments showed the Clapeyron slope to be +8 to +11 MPa/K (Tsuchiya et al., 2004b; Oganov and Ono, 2004; Ono and Oganov, 2005; Hirose et al., 2006a), which is larger by a factor of 3–4 than those of the post-spinel phase transition. On the other hand, a density jump is 1–1.5%: that is only about 1/5 of that of a post-spinel phase transition. Therefore, the post-perovskite phase transition

has similar effects on mantle dynamics to the post-spinel phase transition at 660-km depth, although the effect is opposite.

Mars also has a phase transition just above the CMB. This is a strong endothermic reaction from spinel to perovskite. It causes therefore a different style of mantle convection from that of the Earth. This endothermic reaction traps the bottom thermal boundary layer in Mars and allows only one large plume (superplume) upwelling through this transition boundary (Weinstein, 1995; Harder and Christensen, 1996). In contrast, the strong exothermic reaction near the CMB in the Earth leads to the formation of a large number of weak (small) plumes from the CMB region (Nakagawa and Tackley, 2004; Matyska and Yuen, 2005). Superplumes observed beneath the central Pacific and Africa could be clusters of small plumes (Schubert et al., 2004), although the resolution of seismic tomography images is not enough to prove it.

4.2 The distinct chemistry of plumes

Plumes have large chemical variations compared to the MORB source mantle (see review by Hofmann, 1997). Such variations found in oceanic island basalts (OIBs) are generally consistent with the involvement of recycled continental and oceanic crust components. This is a natural consequence if plumes originate in the D″ region where subducted oceanic lithosphere may have accumulated.

However, the wide chemical variations of OIBs cannot be due to recycled components alone. The geochemical "Ca-perovskite signature" is found in natural plume mantle xenoliths (Hirose et al., 2004). Some clinopyroxenes from Samoa, Austral, and Hawaii have trace element patterns that resemble those of Ca-perovskite experimentally obtained in molten MORB (Fig. 8). Such a Ca-perovskite signature of natural clinopyroxenes could be inherited from Ca-perovskite, which had been formed by partial melting of subducted MORB crust in the D″ layer. It is noted that MORB crust includes a large amount of Ca-perovskite (∼25%) in the lowermost mantle and that Ca-perovskite is the last phase to disappear with an increasing degree of partial melting. Moreover, the HIMU (high U/Pb) characteristic of these Samoan and Austral Islands is also consistent with the partitioning of U, Th, and Pb to Ca-perovskite. It has often been discussed whether they could have been caused by dehydration during subduction (Kelly et al., 2005), but alternatively they could be formed by partial melting of the MORB crust in the presence of Ca-perovskite.

Brandon et al. (1998) reported coupled enrichments in Os isotopes ($^{186}Os/^{188}Os$ and $^{187}Os/^{188}Os$), which are caused by enrichments in Pt and Re relative to Os in plume-related materials. They argued for the involvement of core material in plumes, although such enrichments can also be observed in altered oceanic crust. Humayun et al. (2004) reported excess iron in a Hawaiian plume from the analyses of Fe/Mn ratios. They suggested that it may be due to the core-mantle interaction, although it is difficult to distinguish it from the effect of recycled basaltic crust. Clearly, we need partitioning data between silicate melt/solid and between metal/silicate at high P-T conditions relevant to the CMB region. This could help us to find more

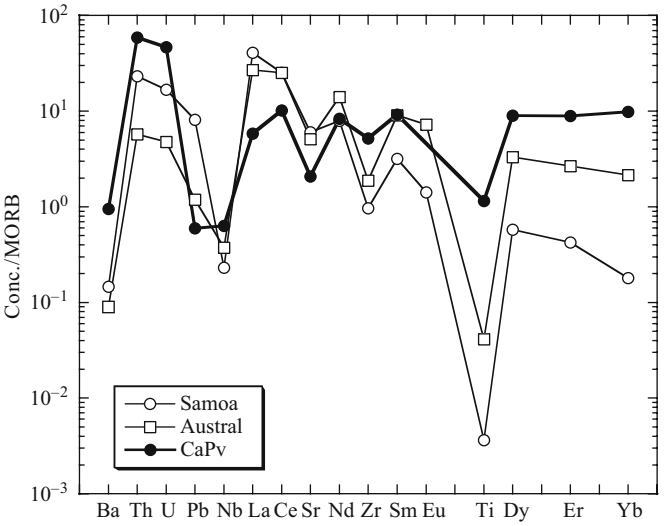

Figure 8. Trace element patterns of natural clinopyroxenes in plume mantle xenoliths from Samoa and Austral Islands (Hauri et al., 1993), compared with those of experimentally obtained Ca-perovskite in molten MORB (Hirose et al., 2004).

geochemical evidence for chemical fractionation in the mantle and for core-mantle chemical reaction at the CMB.

ACKNOWLEDGEMENTS

I am grateful to S. Maruyama and T. Kogiso for discussions on plume dynamics and chemistry. Comments on the manuscript by B. Windley were very helpful.

REFERENCES

Badro, J., J.P. Rueff, G. Vanko, G. Monaco, G. Fiquet, and F. Guyot (2004) Electronic transitions in perovskite: Possible nonconvecting layers in the lower mantle. *Science*, 305, 383–386.

Boehler, R. (1996) Melting temperature of the Earth's mantle and core: Earth's thermal structure. *Annu. Rev. Earth Planet. Sci.*, 24, 15–40.

Brandon, A., R. Walker, J. Morgan, M. Norman, and H.M. Prichard (1998) Coupled ^{186}Os and ^{187}Os evidence for core-mantle interaction. *Science*, 280, 1570–1573.

Christensen, U.R., and A.W. Hofmann (1994) Segregation of subducted oceanic crust in the convecting mantle. *J. Geophys. Res.*, 99, 19867–19884, doi:10.1029/94JB03403.

Dziewonski, A.M., and D.L. Anderson (1981) Preliminary reference Earth model. *Phys. Earth. Planet. Inter.*, 25, 297–356.

Fei, Y., J.V. Orman, J. Li, W.V. Westrenen, C. Sanloup, W. Minarik, K. Hirose, T. Komabayashi, M. Walter, and K. Funakoshi (2004) Experimentally determined postspinel transformation boundary in Mg_2SiO_3

using MgO as an internal pressure standard and its geophysical implications. *J. Geophys. Res.*, 109, B02305, doi:10.1029/2003JB002562.

Harder, H., and U.R. Christensen (1996) A one-plume model of Martian mantle convection. *Nature*, 380, 507–509.

Hernlund, J.W., C. Thomas, and P.J. Tackley (2005) A doubling of the post-perovskite phase boundary and structure of the Earth's lowermost mantle. *Nature*, 434, 882–886.

Hirose, K., Y. Fei, Y. Ma, and H. Mao (1999) The fate of subducted basaltic crust in the Earth's lower mantle. *Nature*, 397, 53–56.

Hirose, K., and Y. Fei (2002) Subsolidus and melting phase relations of basaltic composition in the uppermost lower mantle. *Geochim. Cosmochim. Acta*, 66, 2099–2108.

Hirose, K., N. Shimizu, W. van Westrenen, and Y. Fei (2004) Trace element partitioning in Earth's lower mantle and implications for the geochemical consequences of partial melting at the core-mantle boundary. *Phys. Earth Planet. Inter.*, 146, 249–260.

Hirose, K., N. Takafuji, N. Sata, and Y. Ohishi (2005) Phase transition and density of subducted MORB crust in the lower mantle. *Earth Planet. Sci. Lett.*, 237, 239–251.

Hirose, K., R. Sinmyo, N. Sata, and Y. Ohishi (2006a) Determination of post-perovskite phase transition boundary in $MgSiO_3$ using Au and MgO internal pressure standards. *Geophys. Res. Lett.*, 33, L01310, doi:10.1029/2005GL024468.

Hirose, K., S. Karato, V. Cormier, J. Brodholt, and D. Yuen (2006b) Unsolved problems in the lowermost mantle. *Geophys. Res. Lett.*, 33, L12S01, doi:10.1029/2006GL025691.

Hofmann, A.W. (1997) Mantle geochemistry: The message from oceanic volcanism. *Nature*, 385, 219–229.

Humayun, M., L. Qin, and M. Norman (2004) Geochemical evidence for excess iron in the mantle beneath Hawaii. *Science*, 306, 91–94.

Iitaka, T., K. Hirose, K. Kawamura, and M. Murakami (2004) The elasticity of the $MgSiO_3$ post-perovskite phase in the Earth's lowermost mantle. *Nature*, 430, 442–445.

Irifune, T., and A.E. Ringwood (1993) Phase transformations in subducted oceanic crust and buoyancy relationships at depths of 600–800 km in the mantle. *Earth Planet. Sci. Lett.*, 117, 101–110.

Ishii, M., and J. Tromp (1999) Normal-mode and free-air gravity constraints on lateral variations in velocity and density of Earth's mantle. *Science*, 285, 1231–1236.

Ito, E., A. Kubo, T. Katsura, and M.J. Walter (2004) Melting experiments of mantle materials under lower mantle conditions with implications for magma ocean differentiation. *Phys. Earth Planet. Inter.*, 143–144, 397–406.

Karato, S.-I., and B.B. Karki (2001) Origin of lateral variation of seismic wave velocities and density in the deep mantle. *J. Geophys. Res.*, 106, 21771–21784, doi:10.1029/2001JB000214.

Kelly, K.A., T. Plank, L. Farr, J. Ludden, and S. Hubert (2005) Subduction cycling of U, Th, and Pb. *Earth Planet. Sci. Lett.*, 234, 369–383.

Kesson, S.E., J.D. Fitz Gerald, and J.M.G. Shelley (1994) Mineral chemistry and density of subducted basaltic crust at lower-mantle pressures. *Nature*, 372, 767–769.

Kesson, S.E., J.D. Fitz Gerald, and J.M. Shelley (1998) Mineralogy and dynamics of a pyrolite lower mantle. *Nature*, 393, 252–255.

Kobayashi, Y., T. Kondo, E. Ohtani, N. Hirao, N. Miyajima, T. Yagi, T. Nagase, and T. Kikegawa (2005) Fe-Mg partitioning between $(Mg,Fe)SiO_3$ post-perovskite, perovskite, and magnesiowüstite in the Earth's lower mantle. *Geophys. Res. Lett.*, 32, L19301.

Knittle, E., and R. Jeanloz (1991) Earth's core-mantle boundary: Results of experiments at high pressures and temperatures. *Science*, 251, 1438–1443.

Lay, T., and D.V. Helmberger (1983) A lower mantle S-wave triplication and the velocity structure of D″. *Geophys. J. R. Astron. Soc.*, 75, 799–837.

Lay, T., Q. Williams, and E. Garnero (1998) The core-mantle boundary layer and deep mantle dynamics. *Nature*, 392, 461–468.

Masters, G., G. Laske, H. Bolton, and A. Dziewonski (2000) The relative behavior of shear velocity, bulk sound velocity, and compressional velocity in the mantle: Implications for chemical and thermal structure. In Karato, S. et al. (ed.) Earth's Deep Interior, AGU, Washington, D.C., pp. 63–88.

Matyska, C., and D.A. Yuen (2005) The importance of radiative heat transfer on superplumes in the lower mantle with the new post-perovskite phase change. *Earth Planet. Sci. Lett.*, 234, 71–81.

Murakami, M., K. Hirose, K. Kawamura, N. Sata, and Y. Ohishi (2004) Post-perovskite phase transition in $MgSiO_3$. *Science*, 304, 855–858.

Murakami, M., K. Hirose, N. Sata, and Y. Ohishi (2005) Post-perovskite phase transition and crystal chemistry in the pyrolitic lowermost mantle. *Geophys. Res. Lett.*, 32, L03304, doi:10.1029/2004GL021956.

Nakagawa, T., and P. Tackley (2004) Effects of a perovskite–post perovskite phase change mantle boundary in compressible mantle. *Geophys. Res. Lett.*, 31, L16611, doi:10.1029/2004GL020648.

Nakagawa, T., and P.J. Tackley (2005) The interaction between the post-perovskite phase change and a thermo-chemical boundary layer near the core–mantle boundary. *Earth Planet. Sci. Lett.*, 238, 204–216.

Oganov, A.R., and S. Ono (2004) Theoretical and experimental evidence for a post-perovskite phase of $MgSiO_3$ in Earth's D″ layer. *Nature*, 430, 445–448.

Ohtani, E., and M. Maeda (2001) Density of basaltic melt at high pressure and stability of the melt at the base of the lower mantle. *Earth Planet. Sci. Lett.*, 193, 69–75.

Ono, S., E. Ito, and T. Katsura (2001) Mineralogy of subducted basaltic crust (MORB) from 25 to 37 GPa, and chemical heterogeneity of the lower mantle. *Earth Planet. Sci. Lett.*, 190, 57–63.

Ono, S., and A.R. Oganov (2005) In situ observations of phase transition between perovskite and $CaIrO_3$-type phase in $MgSiO_3$ and pyrolitic mantle composition. *Earth Planet. Sci. Lett.*, 236, 914–932.

Romanowicz, B. (2001) Can we resolve 3D density heterogeneity in the lower mantle? *Geophys. Res. Lett.*, 28, 1107–1110.

Schubert, G., G. Masters, P. Olsen, and P. Tackley (2004) Superplumes or plume clusters? *Phys. Earth Planet. Inter.*, 146, 147–162.

Speziale, S., C. Zha, T.S. Duffy, R.J. Hemley, and H.K. Mao (2001) Quasi-hydrostatic compression of magnesium oxide to 52 GPa: Implications for the pressure-volume-temperature equation of state. *J. Geophys. Res.*, 106, 515–528.

Stackhouse, S., J.P. Brodholt, J. Wookey, J.-M. Kendall, and G.D. Price (2005) The effect of temperature on the seismic anisotropy of the perovskite and post-perovskite polymorphs of $MgSiO_3$. *Earth Planet. Sci. Lett.*, 230, 1–10.

Takafuji, N., K. Hirose, M. Mitome, Y. Bando (2005) Solubilities of O and Si in liquid iron in equilibrium with $(Mg,Fe)SiO_3$ perovskite and the light elements in the core. *Geophys. Res. Lett.*, 32, L06313, doi:10.1029/2005GL022773.

Thomas, C., J.M. Kendall, and J. Lowman (2004a) Lower-mantle seismic discontinuities and the thermal morphology of subducted slabs. *Earth Planet. Sci. Lett.*, 225, 105–113.

Thomas, C., E.J. Garnero, and T. Lay (2004b) High-resolution imaging of lowermost mantle structure under the Cocos plate. *J. Geophys. Res.*, 109, B08307, doi:10.1029/2004JB003013.

Tsuchiya, T., J. Tsuchiya, K. Umemoto, and R.M. Wentzcovitch (2004a) Phase transition in $MgSiO_3$ perovskite in the Earth's lower mantle. *Earth Planet. Sci. Lett.*, 224, 241–248.

Tsuchiya, T., J. Tsuchiya, K. Umemoto, and R.M. Wentzcovitch (2004b) Elasticity of post-perovskite $MgSiO_3$. *Geophys. Res. Lett.*, 31, L14603, doi:10.1029/2004GL020278.

Weinstein, S.A. (1995) The effects of a deep mantle endothermic phase change on the structure of thermal convection in silicate planets. *J. Geophys. Res.*, 100, 11719–11728, 10.1029/95JE00710.

Wen, L. (2001) Seismic evidence for a rapidly varying compositional anomaly at the base of the Earth's mantle beneath the Indian Ocean. *Earth Planet. Sci. Lett.*, 194, 83–95.

Wookey, J., S. Stackhouse, J.M. Kendall, J. Brodholt, and G.D. Price (2005) Efficacy of the post-perovskite phase as an explanation for lowermost-mantle seismic properties. *Nature*, 438, 1004–1007.

Wysession, M.E., T. Lay, J. Revenaugh, Q. Williams, E. Garnero, R. Jeanloz, and L. Kellog (1998) The D″ discontinuity and its implications. In Gurnis, M. et al. (ed.) The Core-Mantle Boundary Region, Geodynamics Ser., Vol. 28, AGU, Washington, D.C., pp. 273–297.

Zerr, A., A. Diegeler, and R. Boehler (1998) Solidus of Earth's deep mantle. *Science*, 281, 243–246.

Zhao, D. (2004) Global tomographic images of mantle plumes and subducting slabs: Insight into deep earth dynamics. *Phys. Earth Planet. Inter.*, 146, 3–34.

CHAPTER 4

POST-PEROVSKITE $MgSiO_3$ INVESTIGATED BY FIRST PRINCIPLES

TAKU TSUCHIYA[1], JUN TSUCHIYA[1], AND RENATA M. WENTZCOVITCH

Chemical Engineering and Materials Science, Minnesota Supercomputing Institute for Digital Simulation and Advanced Computation, University of Minnesota, Minneapolis, MN 55455, USA
[1]*Now at Geodynamics Research Center, Ehime University, Matsuyama 790-0903, Japan;*
E-mail: takut@sci.ehime-u.ac.jp

Abstract
A high-pressure phase transition in iron free $MgSiO_3$ perovskite, the most abundant Earth forming mineral phase, was discovered and reported in 2003–2004. Here, we summarize our theoretical and computational studies on this phase transition and on the physical properties of the newly found post-perovskite phase. The theoretical approach is based on density functional theory and on the plane-wave pseudopotential method. We focus here on the structural, elastic, vibrational, and thermodynamic properties of the post-perovskite phase. The predicted Clapeyron slope of this transition and several elastic properties of the high-pressure phase strongly suggest that this new phase is an important candidate for a primary constituent in D″.

1 INTRODUCTION

Phase transitions of Earth-forming materials dominate the structure and dynamics of the Earth (e.g., Helffrich and Wood, 2001). Major changes in seismic velocity traveling through the Earth's mantle can be attributed to phase transitions of the constituent minerals. Exploration and investigation of high-pressure phase change in the predominant MgO-FeO-SiO_2 system have therefore been one of the central problems in the Earth sciences for a long time. The high-pressure *Pbnm*-perovskite polymorph of $MgSiO_3$ (hereafter pv) (Liu, 1974) is believed to be the most abundant mineral in the Earth's lower mantle (Knittle and Jeanloz, 1987). The possibility of a phase transition in this polymorph has been controversial for several years. Reports of its dissociation into SiO_2 and MgO at 70–80 GPa and 3000 K (Meade et al., 1995; Saxena et al., 1996), or of a possibly subtle phase change above 83 GPa and 1700 K

D. A. Yuen et al. (eds.), Superplumes, 83–104.
© 2007 *Springer.*

(Shim et al., 2001), or of no phase transition at all (Fiquet et al., 2000) up to 94 GPa and 2500 K, have appeared in the literature. Although the pressure–temperature (P-T) conditions in these experiments were quite high, none of them had achieved the thermodynamics state expected in the D″ region. Recently, a post-perovskite (ppv) transition in $MgSiO_3$ was found by in situ X-ray diffraction in a diamond anvil cell at ∼2500 K and ∼125 GPa (Murakami et al., 2004). This P-T condition is similar to that expected in the D″ layer near the core-mantle boundary (CMB). The ppv structure was independently identified by first principles variable cell shape calculations and its thermodynamic properties were obtained by means of quasiharmonic free energy calculations (Tsuchiya et al., 2004b; Tsuchiya et al., 2005a). The predicted Clapeyron slope of the ppv transition was $\sim 7.5 \pm 0.5$ MPa/K, which is surprisingly close to that claimed to be necessary for a solid–solid transition to account for the D″ discontinuity (Sidorin et al., 1999). These results, also supported by another study (Oganov and Ono, 2004), suggest that the ppv phase might be the most abundant mineral in the D″ region. The ppv phase transition with this large positive Clapeyron slope could enhance mantle convection (Nakagawa and Tackley, 2004) and substantially affect generation of superplume (Matyska and Yuen, 2005). Therefore, understanding of the ppv transition and the properties of the ppv phase is essential for understanding the deep lower mantle, particularly of the D″ region (Lay and Helmberger, 1983; Lay et al., 1998; Wysession et al., 1998; Wysession et al., 1999). Knowledge of seismic velocities and elastic anisotropy at relevant pressures is also important for understanding the characteristic velocity discontinuities and anisotropy observed in D″. Here we summarize our first principles computational results obtained so far, in particular, the structural, thermodynamic, and elastic properties of ppv $MgSiO_3$.

2 THEORETICAL METHODS

Within this theoretical framework a solid is viewed as an interacting many-particle system of nuclei and electrons. To solve the many-particle problem exactly is impossible. Some simplifications and approximations are needed to obtain solutions with reasonable computational efficiency. First principles approaches are those that solve the fundamental equations of quantum mechanics with a bare minimum of approximations. Here we briefly describe the essence of a method based on the density functional theory, which has found wider application in the study of the Earth's interior.

Density functional theory (DFT), originally developed by Hohenberg and Kohn (1964) and Kohn and Sham (1965), is, in principle, an exact theory of the ground state and allows us to reduce the interacting many-electron problem to a single-electron problem (the nuclei being treated as an adiabatic background). Within this theory the charge density is the central quantity and the ground state total energy of a system is a unique functional of the charge density $n(\mathbf{r})$:

$$E[n(\mathbf{r})] = F[n(\mathbf{r})] + \int V_{\text{ion}}(\mathbf{r}) n(\mathbf{r})\, d\mathbf{r}. \tag{1}$$

Here functional $F[n]$ contains the electronic kinetic energy and all the electron–electron interactions and is independent of the external potential, which is usually the Coulomb potential V_{ion} due to ions (or nuclei) plus possibly other external fields. A key to the application of DFT in handling the interacting electron gas was given by Kohn and Sham (1964) by splitting up the kinetic energy of a system of interacting electrons into the kinetic energy of noninteracting electrons plus some remainder which can be conveniently incorporated into the exchange-correlation energy, whose explicit form is not known and contains all the many-body effects in an interacting system.

Using the variational principle implied by properties of the energy functional, one can derive the effective single-electron Schrödinger equation, well known as the Kohn–Sham (KS) equation. The KS equation constitutes a self-consistent field problem; that is, the self-consistent solutions (electronic wave functions and eigenvalues) can be obtained by iteratively solving the KS equation. Then the total energy E can be computed. To solve the KS equations exactly requires knowledge of the exact exchange-correlation functional. For the simple case of the uniform electron gas, the explicit expression for the exchange component is known from the Hartree–Fock theory; but the correlation component is known only numerically from quantum Monte-Carlo calculations (Ceperley and Alder, 1980; Perdew and Zunger, 1981). The charge density in real materials is not uniform, so the exchange-correlation functional cannot be calculated precisely. The local density approximation (LDA) (Kohn and Sham, 1964) replaces the exchange-correlation potential at each point **r** by that of a homogeneous electron gas with a density equal to the local density at point **r**.

The LDA works remarkably well for a wide variety of materials, especially for silicates; the equation of state, elastic constants, and other properties often agree with experiment to within a few percent. Agreement with laboratory measurements is not perfect, however, and some systematic discrepancies are apparent for some materials. Attempts to improve LDA through consideration of non-local corrections have met with some success. The generalized gradient approximation (GGA) (Perdew et al., 1996) is a marked improvement over LDA for certain cases of transition metals (Bagno et al., 1989; Stixrude et al., 1994) and hydrogen bonded system (Hamann, 1997). There is some evidence that GGA improves the energetics of silicates and oxides but structures tend to be underbound: the volume calculated with GGA tends to be larger than that measured experimentally (Hamann, 1996; Demuth et al., 1999; Tsuchiya and Kawamura, 2001). For $MgSiO_3$ LDA and GGA calculations including zero-point motion tend to overestimate equilibrium volumes and underestimate bulk moduli, with deviations being much smaller with the former (see Wentzcovitch et al., 2004a and references therein).

There are various self-consistent methods for solving the Kohn–Sham equation differing from each other mainly in two aspects: (1) inclusion of all electrons in the calculations or use of pseudopotentials, and (2) details of the basis functions used to expand the electronic wave functions. In all "all-electron" full potential approaches, no approximations are made to the shape of the charge density or the potential and they are generally accepted as highly accurate and suitable to all types of crystals

irrespective of their bonding nature. However, representation of the rapidly varying core states makes all-electron calculations relatively intensive computationally. The idea behind the plane-wave-pseudopotential-method (PWPP), by which all the results shown in this article were obtained, is that the precise representation of the core states is not essential because they do not participate in bonding. The strong potential due to the nucleus and core electrons is replaced by a soft, more slowly varying potential with the same scattering properties (pseudopotential). This approach speeds up calculations substantially because (1) only valence electrons are treated explicitly and (2) the pseudocharge density and potential vary much more slowly in space. The latter feature in particular allows one to use plane waves as the basis functions to represent the electronic wave function at each wave vector **k**. Evaluation of total energies, forces, and stresses with the plane wave basis set is particularly efficient (Nielsen and Martin, 1985). Construction of the pseudopotential is a non-unique process, but differences between different pseudopotentials (Hamann et al., 1979; Vanderbilt, 1990; Troullier and Martins, 1991), and between PWPP and all electron calculations, are often smaller than the uncertainties due to approximations to the exchange-correlation potential.

Properties of materials in their ground state are obtained through variational calculations that minimize the total energy of the system with respect to all degrees of freedom, electronic and ionic. The charge density is the quantity that must be varied for minimization with respect to electronic degrees of freedom, and ionic positions and lattice parameters are the corresponding ionic ones. One can then obtain various physical properties starting from the stable structure; elastic constant tensor, thermodynamic property and so on.

The plane wave pseudopotential approach, which combines accuracy, computational efficiency, and formal simplicity, has been developed to the point of being used in the context of molecular dynamics (MD) simulations. This facilitated the implementation of a variable-cell-shape-MD (VCSMD) formalism (Wentzcovitch et al., 1993). This type of simulation is particularly useful in high-pressure studies. Its flexible periodic boundary conditions can capture dynamically even structural phase transitions under pressure and is useful in investigations of complex low-symmetry structures typical of the Earth-forming minerals.

In contrast, the central quantity in lattice dynamics (LD) calculations is the dynamical matrix

$$D^{\alpha\beta}_{\kappa\kappa'}(\mathbf{q}) = \frac{1}{\sqrt{m_\kappa m_{\kappa'}}} \sum_l \Phi^{\alpha\beta}_{\kappa\kappa'}(0l) \exp[-i\mathbf{q} \cdot (x_0 - x_l)]. \tag{2}$$

Here the interatomic force constants $\Phi^{\alpha\beta}_{\kappa\kappa'}(0l)$ include ionic and electronic contributions, the former being calculated from Evald sums and the latter being expressed as

$$\Phi^{\alpha\beta}_{\kappa\kappa'}(0l) = \int \left[\frac{\partial \rho(\mathbf{r})}{\partial u^\alpha_\kappa(0)} \frac{\partial V_{\text{ion}}(\mathbf{r})}{\partial u^\beta_{\kappa'}(l)} + \rho(\mathbf{r}) \frac{\partial^2 V_{\text{ion}}(\mathbf{r})}{\partial u^\alpha_\kappa(0) \partial u^\beta_{\kappa'}(l)} \right] d^3r, \tag{3}$$

where $\rho(\mathbf{r})$ is the electron density, $V_{\text{ion}}(\mathbf{r})$ is the ionic potential, and $\partial\rho(\mathbf{r})/\partial u_\kappa^\alpha(0)$ represents the density response of the system to a displacement of the κ atom in the reference cell ($l = 0$) along the α direction. This linear electron density response can be calculated self-consistently using density functional perturbation theory (Baroni et al., 2001). At a given pressure (or volume), first the structure is fully optimized. Then the dynamical matrices are computed, and are used for interpolation to obtain bulk phonon dispersions. These methods have been successfully applied to MgO, SiO_2 polymorphs, $MgSiO_3$ ilmenite and perovskite (Karki et al., 2000a; Karki et al., 2000b; Wentzcovitch et al., 2004a; Tsuchiya et al., 2004a).

In polar semiconductors and insulators, phonons are coupled to macroscopic electric field in the long-wavelength limit. The non-analytical contribution of the macroscopic electric field to the force constant tensor is given by

$$\frac{4\pi e^2}{V}\frac{(\mathbf{q}\cdot\mathbf{Z}_\kappa^*)_\alpha(\mathbf{q}\cdot\mathbf{Z}_{\kappa'}^*)_\beta}{\mathbf{q}\cdot\boldsymbol{\varepsilon}_\infty\cdot\mathbf{q}}, \tag{4}$$

where the tensors $\mathbf{Z}^*$ and $\boldsymbol{\varepsilon}_\infty$ are, the Born effective charges and macroscopic high-frequency static dielectric constant which are calculated self-consistently, respectively (Baroni et al., 2001).

When the volume dependence of the thermal energy is represented within the quasi-harmonic approximation (QHA) (Wallace, 1972), the internal energy and Helmholtz free energy take the following forms,

$$U(V,T) = U_0(V) + \frac{1}{2}\sum_{\mathbf{q},i} h\omega_i(\mathbf{q},V) + \sum_{\mathbf{q},i}\frac{1}{e^{h\omega_i(\mathbf{q},V)/k_BT}-1} \tag{5}$$

and

$$F(V,T) = U_0(V) + \frac{1}{2}\sum_{\mathbf{q},i} h\omega_i(\mathbf{q},V) + k_BT\sum_{\mathbf{q},i}\ln\left[1-e^{-h\omega_i(\mathbf{q},V)/k_BT}\right], \tag{6}$$

where the first, second, and third terms are the static lattice, zero-point and thermal contributions, respectively. This approximation neglects the temperature dependence of phonon frequencies at the constant volume condition. Other thermodynamic quantities (pressure P, vibrational entropy S, specific heats C_P, C_V, thermal expansivity α, bulk moduli B_T, B_S, Grüneisen parameter, etc.) are derived from their thermodynamic or statistical mechanical definitions. At zero pressure, the predicted temperature dependence of α appears to be significantly biased by the QHA leading to unusually large values at very high temperatures. As pressure rises, α rapidly decreases at each temperature, and also the effects of temperature are increasingly suppressed, thus converging to a nearly constant value in the limit of high pressure and high temperature.

The determination of the elastic constants proceeds: (1) at a given pressure (or volume) the crystal structure is first fully optimized using MD; (2) the lattice is slightly deformed by applying a small strain. The stress in the strained configuration

is calculated, and the values of the elastic constants follow from the linear stress–strain relation

$$\sigma_{ij} = c_{ijkl}\varepsilon_{kl}. \tag{7}$$

In these calculations, (1) the ionic positions need to be reoptimized in the strained lattice in order to incorporate any couplings between strains and vibrational modes in the crystal (Nastar and Willaime, 1995); (2) the elastic constants need to be computed in the appropriate limit of zero strain. At finite strain, higher-order terms in the stress–strain relationship become important. To calculate the elastic constants in the linear regime, strains of different magnitude or sign are applied, and the zero-strain limit is determined by extrapolation or interpolation. This linear regime is the most relevant in geophysics.

3 POST-PEROVSKITE CRYSTAL STRUCTURE

The search for the ppv structure was guided by two general principles: (a) polyhedron types and interconnections that would be reasonable at ultrahigh pressures; and (b) extrapolation of the compressive mechanism of the *Pbnm*-pv structure. Edge-sharing rutile-like columns form a more compact octahedral arrangement, but the stoichiometry requires these columns to be connected by the octahedral apices. This produces the SiO_3 layers. These layers should then be intercalated by magnesium ions with the highest possible coordination (Fig. 1). These criteria produce a family of structures. All attempted structures were fully optimized above 120 GPa using variable cell shape damped molecular dynamics; and their enthalpies were then compared with *Pbnm*-pv's. The structure (last figure in Fig. 1) is the only one we found

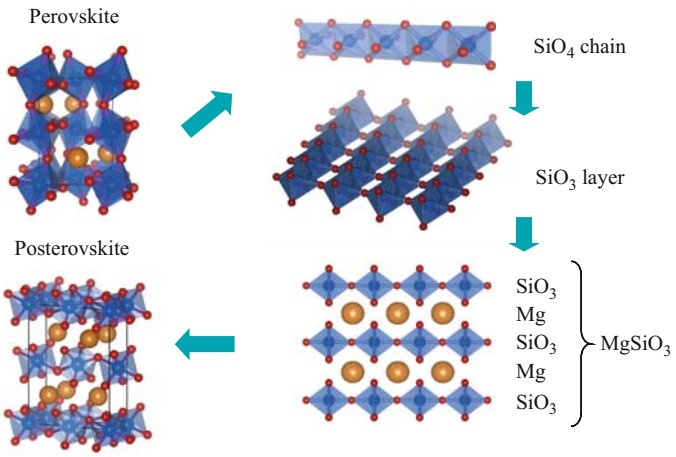

Figure 1. Strategy of the structural search for ppv. Small and large spheres are oxygen and magnesium ion; octahedron corresponds with SiO_6 unit. Detailed calculated crystallographic data of ppv, along with those of pv, are given in Tsuchiya et al. (2004b).

with lower enthalpy than pv in static LDA and/or GGA calculations. This is the structure of $CaIrO_3$ (Hyde and Andersson, 1989), the same one found experimentally (Murakami et al., 2004). This structure is base-centered orthorhombic (BCO) with space group *Cmcm*. Magnesium ions are located in approximately eightfold-coordinated sites, at the center of irregular hendecahedra. It has four formulae unit per conventional cell ($Z_c = 4$) like the *Pbnm* pv structure, two unit per primitive cell (monoclinic, $Z_p = 2$), but it is very anisotropic. Static isotropic compression using LDA revealed a transition pressure of 98 ± 3 GPa (109 ± 4 GPa using the GGA).

The relationship between this *Cmcm* and the *Pbnm* structures (Fig. 2) can be understood on the basis of the extrapolated compressive behavior of $MgSiO_3$-pv (Wentzcovitch et al., 1995). The angles between the octahedral edges bisected by the (110) plane in the *Pbnm* structure decrease faster than other similar angles. The *Cmcm* structure can be produced by forcing these angles to close faster under strain ε_6. Figure 2 shows structures that result by applying strains ε_6 in the *Pbnm*-pv first equilibrated at 120 GPa. For sufficiently large strains, these angles vanish and form edge-sharing rutile columns when one of the oxygens in each pair of edges defining these angles is removed. This process forces layer formation. In the third direction, perpendicular to the columns and to the layers, octahedra remain connected at the apices. According to this transition mechanism, the $[100]_{ppv}$, $[010]_{ppv}$, and $[001]_{ppv}$ directions in the *Cmcm* structure correspond to the $[110]_{pv}$, $[1\bar{1}0]_{pv}$, and $[001]_{pv}$ in the *Pbnm* structure, respectively. Structural parameters obtained in static LDA calculations at 120 GPa are given elsewhere (Tsuchiya et al., 2004b).

Figure 3 shows compression curves of pv and ppv at various temperatures. In the relevant pressure range, ppv is always denser than pv. At the transition pressure, which of course depends on temperature, volume decreases approximately by 1.5%.

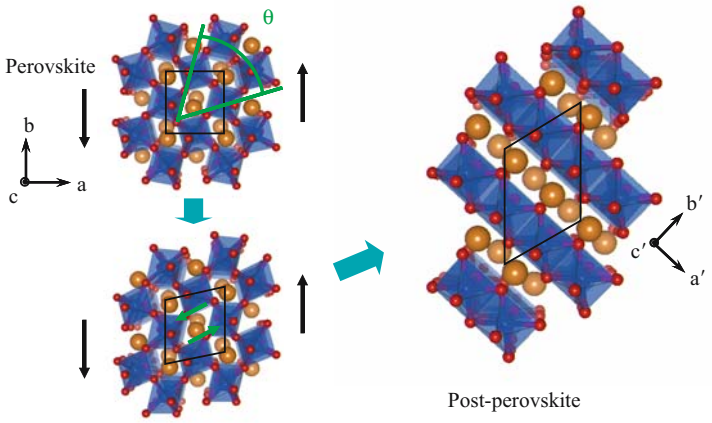

Figure 2. Structural relation between pv and ppv under shear deformation of ε_6. θ indicates the octahedra tilting angle which decreases the fastest with hydrostatic compression of pv.

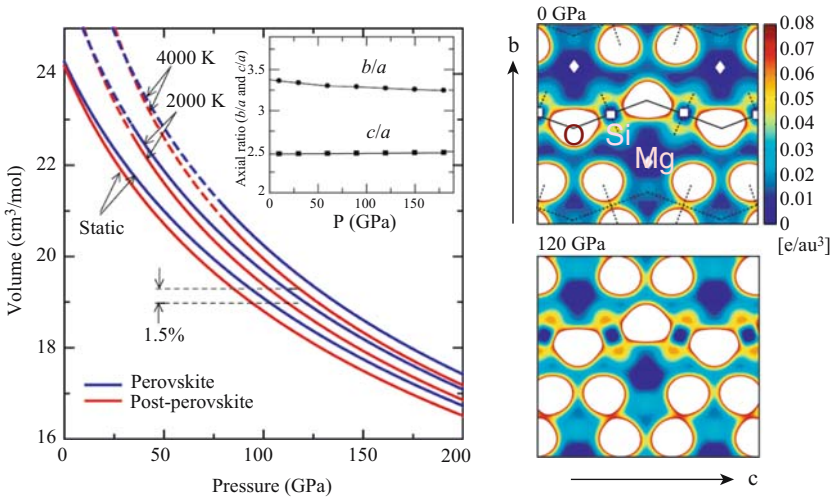

Figure 3. PT compression behavior of pv and ppv. Isothermal compression curves are shown in the left panel together with the change in axial ratios in the inset. Volume decrease across the transition is ~1.5%. Pseudocharge densities across (100) at 0 and 120 GPa are also shown on the right hand side.

Ppv compresses very anisotropically. The *b* axis perpendicular to the SiO_3 layers compresses faster than the others. The inset shows the pressure dependence of the *b*/*a* and *c*/*a* ratios in this phase as obtained from static calculations. As expected, the structure is more compressible along [010]. Right hand parts of Figure 3 are the charge density in the (100) plane that cut across the SiO_3 layers. Vertical is the *b* direction. Magnesium (diamonds) is almost completely ionized. Strong Si (square)-O (center of white hole) bonds are within the layers. Mg-O bonds connecting the layers are ionic and weak. Therefore the structure is more compressive along *b*.

4 VIBRATIONAL AND THERMODYNAMIC PROPERTIES

4.1 Phonons

Vibrational and thermodynamic properties are helpful for better understanding the basic properties of the ppv phase and to further explore the importance of this phase as a D″ constituent. Comparison between the thermal expansivity, specific heat, and entropy of pv and of the ppv phase is essential to clarify the effect of this transformation on mantle dynamics also. However, experimental measurements of these properties under lower mantle conditions are not yet possible. Here we use the QHA combined with first principles calculations of the vibrational density of states to compute the free energy of $MgSiO_3$ ppv and derive several thermodynamic properties of interest up to 180 GPa. We then compare with the same properties previously calculated in

the pv phase (Karki et al., 2000a; Karki et al., 2001). There are 30 vibrational modes at any point in the BZ because $Z_p = 2$.

The predicted dispersion curves along several symmetry directions and vibrational density of states (VDoS) at 0 and 120 GPa are shown in Figure 4a. Though 0 GPa is obviously outside of its stability fields, these results are informative and indicative of the mechanical/vibrational stability of this phase. Under decompression the lowest acoustic branch starts drooping down around the Y point of the BZ (Fig. 4a). This behavior is associated with the easier elongation of the *b* axis under decompression. Zone center optic phonon frequencies are shown in Figure 4b as a function of pressure. They are grouped with respect to symmetry which has been determined by the factor group analysis. No phonon instability is found in the entire range of pressure even at 0 GPa. The diagonal components of the dielectric tensor are 3.53, 3.22, and 3.24 at zero pressure, and 3.27, 3.04, and 3.03 at 120 GPa. Born effective charges for Mg are close to the formal ionic charges of magnitudes equal to two and are weakly anisotropic: Z^* [Mg] = (2.00, 2.36, 2.13) at zero pressure and Z^* [Mg] = (1.85, 2.14, 2.00) at 120 GPa. However, those for Si and O are very anisotropic: Z^* [Si] = (3.98, 2.93, 3.60), Z^* [O(1)] = (−1.45, −1.55, −2.50), and Z^* [O(2)] = (−2.26, −1.87, −1.62) at zero pressure, and Z^* [Si] = (3.79, 2.99, 3.51), Z^* [O(1)] = (−1.49, −1.55, −2.34), and Z^* [O(2)] = (−2.08, −1.79, −1.59) at 120 GPa.

4.2 Thermodynamic properties

We then proceeded with calculations of phonon dispersions and vibrational densities of states (VDoS) (see Fig. 4a) to obtain Gibbs free energies within the QHA. At 300 K, the zero-pressure bulk modulus, $B_0 = 216$ GPa, is substantially smaller than pv's, 246 GPa. However, the pressure derivative of the bulk modulus, $B_0' = 4.4$, is distinctly larger than pv's, 4.0, where these EoS parameters were determined using the fourth-order finite strain equation. The zero-pressure Grüneisen parameter, ∼1.7, and the Debye temperature, $\Theta_D \sim 1100$ K, are fairly comparable to those of pv. Comparison between the volumes of both phases at the same P-T conditions indicates that the ppv phase is always denser than pv (see Fig. 3).

The coefficient of thermal expansion α is determined from the temperature dependence of the volume at each pressure (Fig. 5). At zero pressure, the predicted temperature dependence of α appears to be significantly biased by the QHA leading to unusually large values at very high temperatures. As pressure rises, α rapidly decreases at each temperature, and also the effects of temperature are increasingly suppressed, thus converging to a nearly constant value in the limit of high pressure and high temperature. At lower pressure, the thermal expansion coefficient of pv is quite smaller than ppv's. The difference between pv and ppv decreases with increasing pressure. Above 100 GPa, α of pv and of ppv are nearly the same.

Because of the expected high temperatures in the mantle, the validity of QHA is often questioned. However, it should be valid up to a temperature between the Θ_D

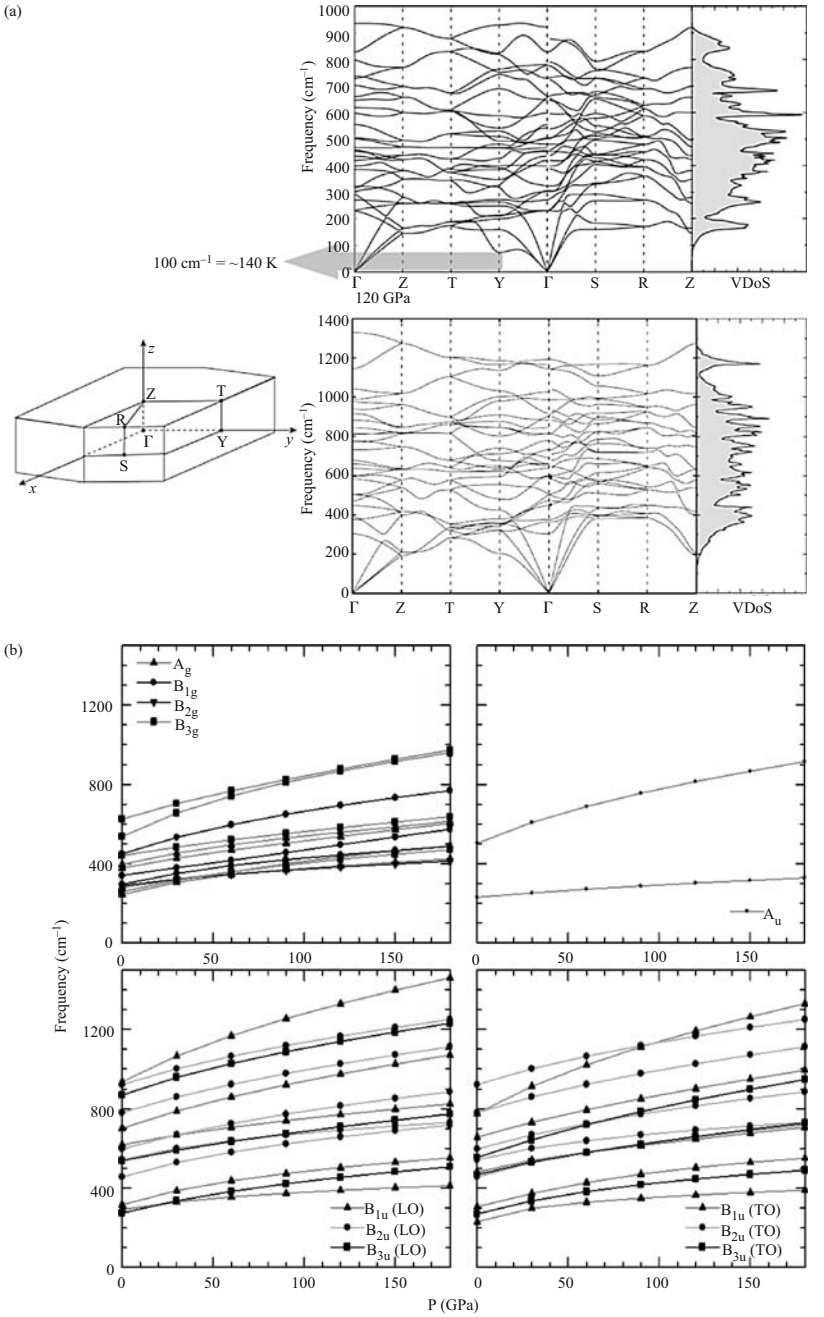

Figure 4. Vibrational frequencies in ppv. (a) Phonon dispersion relation at 0 (up) and 120 GPa (down) together with the *Cmcm* Brillouin zone. (b) Pressure dependence of zone center optic phonons.

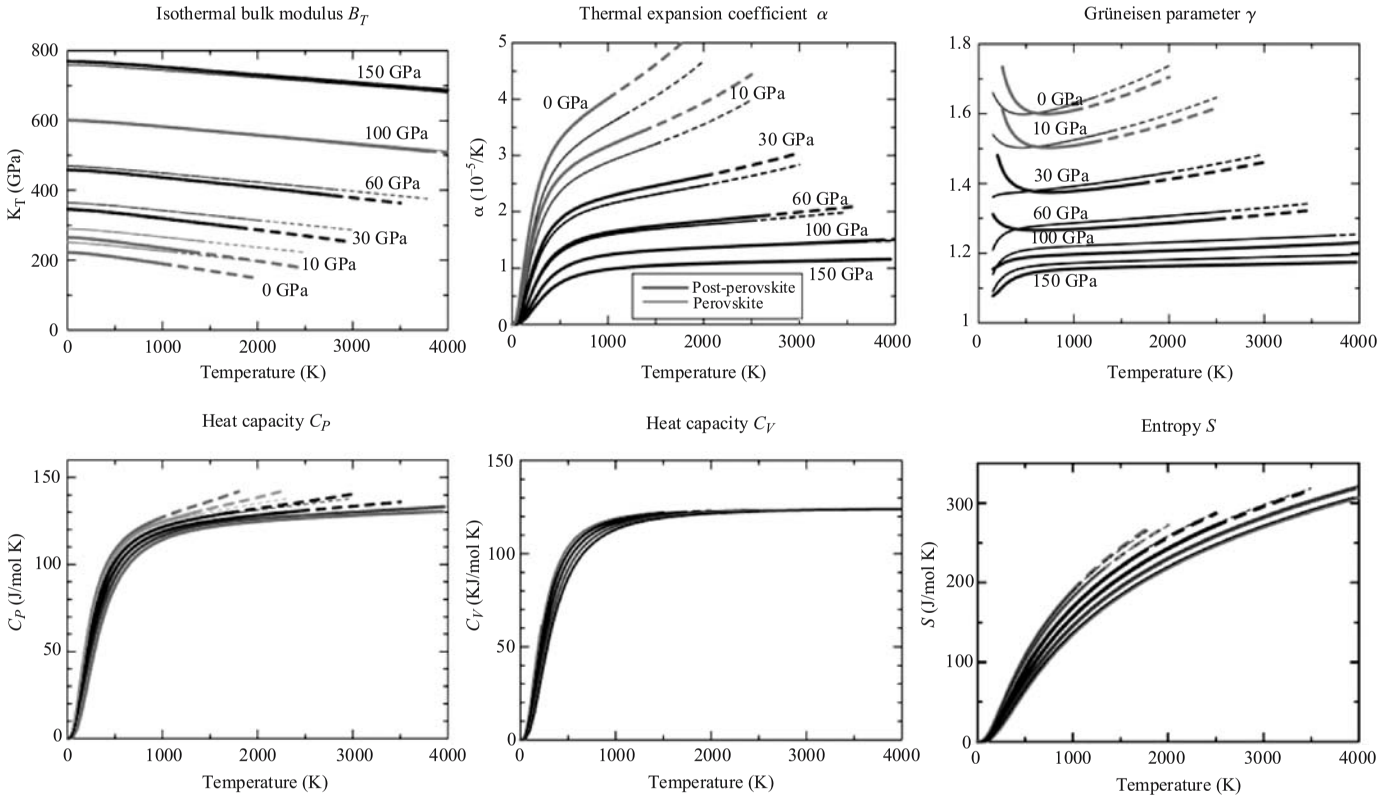

Figure 5. Thermodynamic properties of pv and ppv as a function of temperature. Thick and thin lines are for ppv and pv, respectively. Most of them are indistinguishable at the pressures in ppv stability field.

and the melting temperature (T_M), the latter being considerably higher than expected mantle temperatures. The calculations of thermal properties of MgO (Karki et al., 2000b) and $MgSiO_3$ (Wentzcovitch et al., 2004b) have indicated that the QHA is valid for these phases throughout the lower mantle regime. A posteriori inspection of their thermal expansivities, $\alpha(T)|_P$, offers a criterion for the QHA validity domain. Experimentally $\alpha(T)|_P$, displays linear behavior at high T's but the QHA introduces an unphysical divergence after some inflection point at $T = T_I(P)$. We take $T_I(P)$ as the upper limit for which our results should be considered predictive. This criterion indicates the QHA is valid for pv and ppv within the P, T regime of the lower mantle, except perhaps at the top of the lower mantle, i.e., at $P = 23$ GPa and $T = 1900 \sim 2000$ K. On the basis of this criterion alone, the valid temperature and pressure conditions of the QHA for ppv appears to be similar to that of pv. This criterion appears to be quite strict for the free energies themselves, but perhaps not sufficiently strict for quantities involving temperature derivatives such as the constant volume specific heat, C_V, α, etc. The thermal Grüneisen parameter γ may be particularly sensitive to this approximation since it involves two temperature derivative quantities, α and C_V. Below 30 GPa, ppv's γ increases rapidly, and so does its temperature dependence. This behavior seems anomalous and might be caused by the inadequacy of the QHA for this quantity in this regime.

The specific heat at constant pressure (C_P) calculated from $C_P = C_V(1 + \alpha\gamma T)$ and the entropy (S) are also shown in Figure 5, respectively. The difference between C_V of pv and ppv are rather negligible at each pressure. The entropy S of ppv is slightly smaller than that of pv at stable pressure conditions giving a Clapeyron slope, $dP_T/dT = \Delta S/\Delta V \sim 7.5$ MPa/K for the ppv transition. The thermodynamic properties reported here are important inputs for geodynamic modeling. Our calculations indicate that the thermal expansivity, specific heat, thermal Grüneisen parameter etc., change very little across the ppv transition. Although it has been pointed out that small changes in thermal expansivity lead to significant variations in mantle convection pattern and its time evolution (Ita and King, 1998), it appears that the changes here are quite insignificant for such effects to happen.

4.3 Phase equilibrium

In static calculations, LDA tends to underestimate transition pressures and GGA results are usually in better agreement with experiments. The main source of these deviations is the description of the exchange correlation energy in density functional theory. The inclusion of zero-point motion in the calculation of a phase boundary with positive Clapeyron slope shifts the boundary to higher pressures, $\sim$2 GPa in this case. It is therefore reasonable to anticipate that the true transition pressure falls between the phase boundaries given by LDA and GGA. Direct comparison of the Gibbs free energies of both phases produces the phase boundary. The dP_T/dT at 2500 K is $\sim 7.5 \pm 0.3$ MPa/K in complete agreement with the value derived from the Clausius–Clapeyron equation.

5 ELASTICITY

Ppv $CaIrO_3$-type structure is anisotropic. Its elastic properties are also expected to be anisotropic. From the overall behavior of the elastic constants, of which specific values are reported elsewhere as a function of pressure (Tsuchiya et al., 2004c), it is clear that the structure is quite anisotropic and that anisotropy is strongly pressure dependent. Two particular features can be immediately noticed: (1) c_{22} is considerably smaller than c_{11} and c_{33} at relevant pressures; and (2) c_{66} is quite large compared with c_{55} and c_{44}. The first feature is typical of layered minerals. It shows that this structure is more compressive in the direction perpendicular to the layers (layers parallel to (010)). The second feature is very intriguing. It indicates that a lateral shift of layers ((010) planes) parallel to the edge sharing octahedral columns (along [100]) faces the greatest resistance. This is counterintuitive. In a typical layered structure, lateral shear of layers, along any direction, should offer less resistance than the deformation of the layers themselves, here represented by c_{55}. In this structure, the smallest shear elastic constant is c_{44}. It expresses the resistance along [001], i.e., to the lateral shift of layers in the direction perpendicular to the octahedral columns.

The pressure dependence of the isotropic bulk (B) and shear (G) moduli obtained from the Voigt–Ruess–Hill averages (Hill, 1963) are shown in Figure 6 along with those of the pv structure. It can be seen that B of both phases are very similar throughout most of the pressure range of the lower mantle. The larger B_0 of ppv, 4.3, compensates to produce similar bulk moduli at lower mantle pressures. In contrast, ppv has considerably larger G than pv in the pressure range corresponding to the

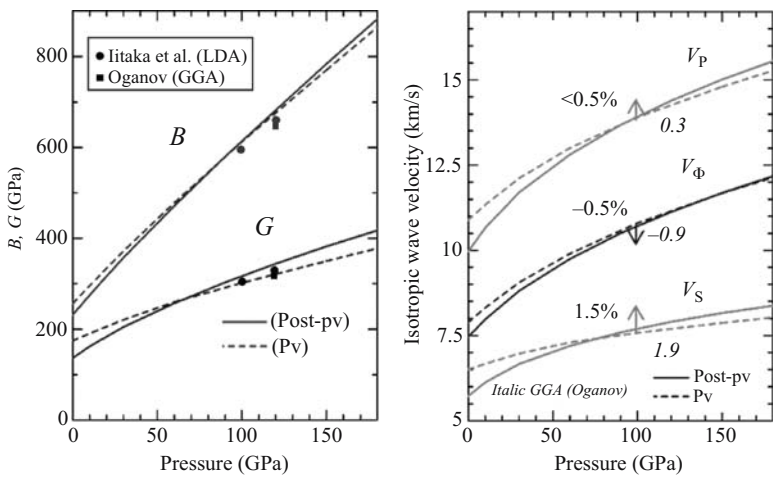

Figure 6. Aggregate elastic moduli and velocities of pv and ppv as a function of pressure. Results are supported well by other works (Iitaka et al., 2004; Oganov and Ono, 2004).

lower part of the lower mantle (7% larger at 120 GPa) even though ppv's G is smaller than pv's at 0 GPa. This large G is caused by the large c_{66}. The isotropic averaged compressional (P), shear (S) and bulk (Φ) wave velocities are plotted in Figure 6. At zero pressure, all velocities are smaller than those of pv, while at high pressure, V_P and V_S of ppv are distinctly larger than those of pv. V_Φ is quite comparable. The discontinuity in V_P, V_S and V_Φ at the static P_T of 100 GPa are 0.5, 1.5 and -0.5%, respectively. The large shear wave velocity of ppv is clearly caused by its large G, despite the larger density of this phase. Negative change in V_Φ is because of density increase and unchanged bulk modulus. The ppv transition should be observed preeminently through S wave anomalies.

The single crystal elastic wave velocities were obtained by solving Cristoffel's equation (Musgrave, 1970). Wave velocities depend on propagation direction and on polarization. For ppv, the difference between V_P and V_S is relatively small compared to the same difference found in pv (Wentzcovitch et al., 1998). This is also caused by the relatively larger G of ppv. Fast and slowest directions change very much with pressure. At 0 GPa V_P is largest and smallest along [100] and [110] respectively. This results from large c_{11} and small c_{66} respectively. At 120 GPa, the slowest direction of the P wave changes to [010], consistent with the small c_{22}. The fastest S waves propagate along [110] and [101], and the slowest along [010] and [001] at 0 GPa. In contrast, at 120 GPa, the fastest directions is along [101] while the slowest are along [100] and [001] (Tsuchiya et al., 2004c).

Azimuthal anisotropy for P (A_P) and S (A_S) waves, defined as $A_P = (V_{Pmax} - V_{Pmin})/V_P \times 100$ and $A_S = (V_{Smax} - V_{Smin})/V_S \times 100$, are plotted in Figure 7. First, they decrease up to about 100 GPa and then remain almost constant. However, at the

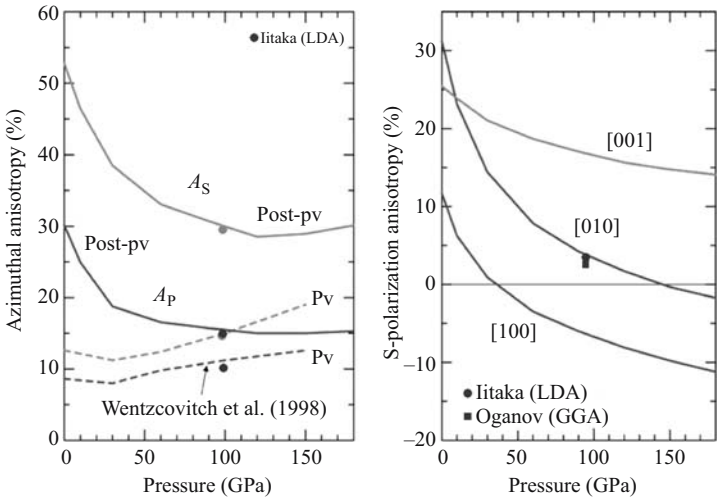

Figure 7. Elastic anisotropies in pv and ppv as a function of pressure.

stable pressure range of ppv, A_P and A_S are much larger than pv's (A's are more than 50% larger). Single crystal anisotropy gives the upper limit on the realistic anisotropy of aggregates. The magnitude of anisotropy due to the lattice preferred orientation (LPO) in aggregates is, in general, much smaller (by a factor of 2–3). Another point relevant for extracting information about mantle flow from seismic observations is the anisotropy produced by transversely isotropic aggregates. This type of aggregate may be caused by LPO's produced under shear flow and can occur at boundary layers. Shear stresses related with changes in flow direction are expected to be particularly large near the CMB. A transversely isotropic medium with a principal vertical axis is characterized by five elastic moduli determined from single-crystal elastic constants (Wentzcovitch et al., 1998).

Transverse anisotropy in V_S is defined as $A_S^T = (V_{SH} - V_{SV})/V_S \times 100$, where $V_{SH}(V_{SV})$ is horizontally (vertically) polarized V_S propagating horizontally. V_S is the usual isotropic averages. Results are also plotted in Figure 7 for aggregates with a, b, and c vertical alignment. It can be seen that A_S^T can be positive or negative depending on the crystalline axes orientation. Contrary to expectations for a layered structure with the slip plane parallel to the layers, A_S^T is small in magnitude ($\sim$3% at P_T) and becomes negative at high pressure for [010] aligned vertically. This is because of the counterintuitively large c_{66} at high pressures. The positively largest A_S^T ($\sim$17% at P_T) is achieved with [001] oriented vertically, i.e., layers oriented vertically. Again this is caused by the large values of c_{66} for vertical orientation of layers. These properties have been supported by other calculations (Stackhouse et al., 2005).

The phonon dispersions displayed in Figure 4a reveal an interesting fact about ppv. Although there is an acoustic branch that softens under decompression, at 0 GPa all phonons are still stable. This type of acoustic phonon softening is typical of materials that amorphize under decompression (or compression). The frequencies along this branch (except around Γ), are in the range of 100 cm^{-1}, i.e., $\sim$140 K. This means that below this typical temperature these phonons are not very populated and therefore ppv may be retrieved metastably at 0 GPa, unless there is some nonobvious elastic instability.

6 DISCUSSION

This transition is important for understanding the state of the deep lower mantle, particularly that of the D″ region, the lowest 300 km of the lower mantle (Sidorin et al., 1999; Lay and Helmberger, 1983; Lay et al., 1998; Wysession et al., 1998; Wysession et al., 1999). The D″ layer has wide topography (Lay and Helmberger, 1983). Properties of this region vary strongly laterally, including its considerable anisotropy (Wysession et al., 1998). Chemical heterogeneity, partial melting, phase transitions or a combination of all of these have been proposed as possible mineralogical origins of these features and it is likely that all of them indeed play a role in this region. It is also believed that the anisotropy observed in S_H and S_V waves traveling through D″ at least in part could be attributed to LPO of strained minerals aggregates (Karato, 1998; McNamara et al., 2002). In particular, it has been argued on

the basis of seismic and geodynamic considerations that a solid–solid phase change with a Clapeyron slope of ∼6 MPa/K (Sidorin et al., 1999) could cause the observed topography. Our Clapeyron slope of 7.5 ± 0.3 MPa/K is quite close to this value. The major effects of a ppv transition on the dynamics in the lowermost mantle have already been investigated and reported (Nakagawa and Tackley, 2004). This exothermic transition with a large and positive Clapeyron slope enhances mantle convection and accelerates heat release from the core. This results in raising the overall mantle geotherm by ∼200 K and also helps to produce small unstable plumes. Large thermal conductivity possibly associated with radiative thermal conduction would be necessary to stabilize superplumes (Matyska and Yuen, 2005). If geotherm is sufficiently high ($T > 4000 \sim 4500$ at 135 GPa), the ppv transition pressure shifts into the outer core condition. No ppv is therefore expected in the mantle at the stage of hot early Earth. When the ppv transition pressure fell into the mantle pressures and ppv appeared in the mantle along with cooling of the Earth, mantle and core dynamics would have begun to be activated. Geophysical importance of advent of ppv in the history of Earth's evolution is now being investigated (Maruyama et al., 2007).

Determination of the rheological change across the transformation is now the key issue for assessing the effects of such transformation more realistically. Obviously, effects of minor elements (Al, Fe) partitioning on all properties across the transition also must be considered. This fact might be of minor significance considering that the D″ region is a thermochemical boundary layer with strong heterogeneities. The presence of alloying elements, such as aluminum and iron, is likely to affect the transition pressure and the Clapeyron slope, particularly if minor element partitioning between $MgSiO_3$ and other coexisting phases is affected. For instance, silicon and magnesium polyhedral volumes increase and decrease, respectively, across the transformation (Tsuchiya et al., 2004b). This might affect element partitioning. It was reported that iron-bearing pv would transform at lower pressures (Mao et al., 2004). However, the relationship between high- to low-spin transition in iron (Badro et al., 2003, 2004) and the ppv transition, proposed to occur simultaneously at least in part, is still highly unclear. In contrast, recent results suggest that the Al incorporation does not affect the transition pressure significantly (Murakami et al., 2005; Ono et al., 2005b; Tsuchiya et al., 2005b). The structural relationship between the *Pbnm* and the *Cmcm* phases found here suggests that also shear stresses are likely to affect the transition pressure (in both directions). Shear stresses, although very small compared to those in our investigation, are expected to occur particularly near the CMB. Also, the possibility of an intervening pv phase with different symmetry (Shim et al., 2001) could increase the ppv transition pressure, though this observation itself seems to be interpreted as a cause other than pv modification (Ono et al., 2005a).

Our best estimate of the transition temperature in pure $MgSiO_3$-pv through the pressure range of 125–133 GPa is 2750–3800 ± 250 K (Tsuchiya et al., 2004b). These temperatures are consistent with the existence of a ppv transition before the core-mantle boundary where temperatures can reach ∼4100 K (Williams and Jeanloz, 1990; Boehler, 1993) and point to the possibility of 1000 K lateral temperature variations in this region. However, D″ is very likely a thermo-chemical boundary layer

(Lay et al., 2004). Therefore the effects of composition and stress state on this transition still need to be investigated before an attempt is made to relate the D″ topography and lateral temperature variations through the ppv transition.

Although the elastic wave properties shown here are static 0 K results and high temperature results are necessary before a more reliable analysis of the importance of ppv to D″ can be attempted, these results give the first glimpses on the elastic properties of the newly found phase. First, the stability field of ppv appears to correspond well with that expected in the D″ layer. We see here that, at the transition point, the discontinuity in V_S should be considerably larger than in V_P. This is consistent with reports that the velocity anomaly at the D″ discontinuity is more preeminent in V_S than in V_P (Wysession et al., 1998). In contrast, the discontinuity in V_Φ is negative. This indicates that the ppv transition can cause the anticorrelation between S and bulk velocities observed in tomographic images at the bottom of mantle (Masters et al., 2000), which is one of the most enigmatic properties observed in this region. The D″ region is also known to be much more anisotropic than the lower mantle (Lay et al., 1998) and the anisotropy style, i.e., $V_{SH} > V_{SV}$ or vice-versa, varies considerably from place to place (Pulliam and Sen, 1998).

LPO in this structure can be a source of anisotropy in this region. Here we show that ppv's static azimuthal anisotropy (Fig. 7) is much larger (by 50%) than pv's. This is primarily caused by the small and very large values of c_{22} and c_{66}, respectively. The contrast between pv's and ppv's anisotropies could, in principle, produce seismically detectable anisotropy changes across the transition in addition to velocity discontinuities. We also see that the transverse shear anisotropy is very large in magnitude for more than one LPO, in addition to changing sign. Although real fabrics with LPO formed under shear stresses should have some azimuthal anisotropy in the shear plane and should not be completely transversely isotropic, and a better understanding of the rheological properties of ppv is necessary before anything can be stated with more confidence, here we can anticipate from the property of the transversely isotropic medium that LPO's produced by vertical or horizontal flows in D″ could produce quite distinct shear wave splittings. This appears to be consistent with the documented lateral variation of anisotropy in D″ (Lay et al., 1998). The anisotropy style observed underneath the circum-Pacific, i.e., $V_{SH} > V_{SV}$, could be produced by vertical alignments mainly of [001], but perhaps also of [010] (Fig. 7). The former is however much more significant than the latter, contrary to expectations for this layered structure. These elastic properties of ppv indicate that at high pressures the usual notion of a layered structure is not simply applicable to this phase.

Magnesiowüstite (Mg,Fe)O, the expected secondary abundant phase, is also very anisotropic, and another likely candidate for the origin of seismic anisotropy in the D″ (Karki et al., 1999; Yamazaki and Karato, 2002). Mw aggregates with [100] oriented vertically could produce much larger (>20%) positive S wave splitting at the D″ condition. (100) is the expected natural slip plane in this mineral and, thus, even in smaller amount, mw cold be the main source of LPO derived anisotropy in D″. In this case, significant change in the deformation mechanism of mw, from dislocation to diffusion creep, must accompany the ppv transition. However, the elasticity of

mw including low-spin to high-spin transition in iron is still unknown. The proper description of electronic transitions such as this one, is a major challenge in theoretical mineral physics today.

In summary, we have shown that $MgSiO_3$-ppv is a highly anisotropic phase. Aggregates of this phase with mw could be a source of LPW derived anisotropy in D″. For more complete understanding of the origin of D″ anisotropy, detailed information on elasticity and plasticity of these two phases aggregates (ppv+mw) at high temperatures, including the effects of Fe, still need to be considered. To this list one should add $CaSiO_3$-pv. Despite its small abundance, its elasticity is quite "suspicious" because of the large number of nearly stable pv-distortions in this mineral. This indicates this mineral is stabilized by anharmonic fluctuations and is constantly on the verge of stress induced structural transitions (Caracas et al., 2005). After all these factors have been properly addressed the importance of chemical stratification and partial melting in generating the observed anisotropy style where the ppv transtition is most likely to occur, $V_{SH} > V_{SV}$ (Kendall and Silver, 1996), can be more fully appreciated.

7 CONCLUSIONS

A new polymorph of $MgSiO_3$ with the $CaIrO_3$ structure and more stable than the *Pbnm*-pv phase has been identified by first principles computations. The $CaIrO_3$ structure is shown to be related with the *Pbnm*-pv structure through a shear strain σ_6. This very simple structural relationship suggests that the ppv phase transition pressure might be affected by shear stresses. Quasiharmonic high-temperature calculations of the thermodynamic phase boundary gives a Clapeyron slope of ∼7.5 MPa/K at ∼2750 K and ∼125 GPa. These P-T conditions are close to those anticipated in the D″ region and this Clapeyron slope is close to that anticipated if the D″ topography were related to a solid–solid transformation. Thermodynamic properties of ppv are very similar to those of pv at relevant pressures. Some of them are indistinguishable. The anticorrelated anomaly in V_S and V_Φ and the positive S wave splitting have been known as particular observables in the deep mantle which have never been explained well. The ppv transition can produce this type of anticorrelation. A transversely isotropic medium of ppv with [001] oriented vertically can produce the very large positive S wave splitting. These results strongly suggest that the ppv transition might be associated with the D″ discontinuity and that this polymorph might be the most abundant phase in D″.

REFERENCES

Badro, J., G. Fiquet, F. Guyot, J.-P. Rueff, V.V. Struzhkin, G. Vanko, and G. Monaco (2003) Iron partitioning in Earth's mantle: Toward a deep lower mantle discontinuity. *Science*, 300, 789–791.

Badro, J., J.-P. Rueff, G. Vanko, G. Monaco, G. Fiquet, and F. Guyot (2004) Electronic transitions in perovskite: Possible nonconvecting layers in the lower mantle. *Science*, 305, 383–386.

Bagno, P., O. Jepsen, and O. Gunnarsson (1989) Ground-state properties of third-row elements with nonlocal density functionals. *Phys. Rev. B*, 40, 1997–2000.

Baroni, S., S. de Gironcoli, A. Dal Corso, and P. Giannozzi (2001) Phonons and related crystal properties from density-functional perturbation theory. *Rev. Mod. Phys.*, 73, 515–562.

Boehler, R. (1993) Temperature in the earth's core from melting-point measurements of iron at high static pressures. *Nature*, 363, 534–536.

Caracas, R., R. Wentzcovitch, G.D. Price, and J. Brodholt (2005) $CaSiO_3$Perovskite at lower mantle pressures. *Geophys. Res. Lett.*, 32, 06306.

Ceperley, D., and B. Alder (1980) Ground state of the electron gas by a stochastic method. *Phys. Rev. Lett.*, 45, 566–569.

Demuth, T., Y. Jeanvoine, J. Hafner, and J.G. Angyan (1999) Polymorphism in silica studied in the local density and generalized-gradient approximations. *J. Phys.: Condens. Matter*, 11, 3833–3874.

Fiquet, G., A. Dewaele, D. Andrault, M. Kunz, and T. Le Bihan (2000) Thermoelastic properties and crystal structure of MgSiO3 perovskite at lower mantle pressure and temperature conditions. *Geophys. Res. Lett.*, 27, 21–24.

Hamann, D.R. (1996) Generalized gradient theory for silica phase transitions. *Phys. Rev. Lett.*, 76, 660–663.

Hamann, D.R. (1997) H2O hydrogen bonding in density-functional theory. *Phys. Rev. B*, 55, R10157–R10160.

Hamann, D.R., M. Schlüter, and C. Chiang (1979) Norm-conserving pseudopotentials. *Phys. Rev. Lett.*, 43, 1494–1497.

Helffrich, G.R., and B.J. Wood (2001) The Earth's mantle. *Nature*, 412, 501–507.

Hill, R. (1963) Elastic properties of reinforced solids: Some theoretical principles. *J. Mech. Phys. Solids*, 11, 357–372.

Hohenberg, P., and W. Kohn (1964) Inhomogeneous electron gas. *Phys. Rev.*, 136, B864–871.

Hyde, B., and S. Andersson (1989) Inorganic Crystal Structures, Wiley, New York.

Iitaka, T., K. Hirose, K. Kawamura, and M. Murakami (2004) The elasticity of the $MgSiO_3$ post-perovsktie phase in the Earth's lowermost mantle. *Nature*, 430, 442–445.

Ita, J., and S.D. King (1998) The influence of thermodynamic formulation on simulations of subduction zone geometry and history. *Geophys. Res. Lett.*, 25, 1463–1466.

Karato, S. (1998) Some remarks on the origin of seismic anisotropy in the D″ layer. *Earth Planets Space*, 50, 1019–1028.

Karki, B.B., R.M. Wentzcovitch, S. de Gironcoli, and S. Baroni (1999) First-principles determination of elastic anisotropy and wave velocities of MgO at lower mantle conditions. *Science*, 286, 1705–1707.

Karki, B.B., R.M. Wentzcovitch, S. de Gironcoli, and S. Baroni (2000a) Ab initio lattice dynamics of $MgSiO_3$ perovskite at high pressure. *Phys. Rev. B*, 62, 14750–14756.

Karki, B.B., R.M. Wentzcovitch, S. de Gironcoli, and S. Baroni (2000b) High-pressure lattice dynamics and thermoelasticity of MgO. *Phys. Rev. B*, 61, 8793–8800.

Karki, B.B., R.M. Wentzcovitch, S. de Giuroncoli, and S. Baroni (2001) High-pressure elastic properties of major materials of earth's mantle from first principles. *Geophys. Res. Lett.*, 28, 2699–2702.

Kendall, J.-M., and P.G. Silver (1996) Constraints from seismic anisotropy on the nature of the lowermost mantle. *Nature*, 381, 409–412.

Knittle, E., and R. Jeanloz (1987) Synthesis and equation of state of $(Mg,Fe)SiO_3$ perovskite to over 100 gigapascals. *Science*, 235, 668–670.

Kohn, W., and L.J. Sham (1965) Self-consistent equations including exchange and correlation effects. *Phys. Rev.*, 140, A1133–A1138.

Lay, T., E.J. Garnero, and Q. Williams (2004) Partial melting in a thermo-chemical boundary layer at the base of mantle. *Phys. Earth Planet. Int.*, 146, 441–467.

Lay, T., and D.V. Helmberger (1983) A lower mantle S wave triplication and the shear velocity structure of D″. *Geophys. J. R. Astron. Soc.*, 75, 799–838.

Lay, T., Q. Williams, and E.J. Garnero (1998) The core-mantle boundary layer and deep earth dynamics. *Science*, 392, 461–468.

Liu, L.-G. (1974) Silicate perovskite from phase transformation of pyrope-garnet at high pressure and temperature. *Geophys. Res. lett.*, 1, 277–280.

Mao, W.L. et al. (2004) Ferromagnesian postperovskite silicates in the D″ layer of the Earth. *Proc. Natl. Acad. Sci.*, 101, 15867–15869.

Maruyama, S., D.A. Yuen, and B.F. Windley (2007) Dynamics of plumes and superplumes through time. In Yuen, D.A., S. Maruyama, S. Karato, and B.F. Windley (eds.) Superplumes: Beyond Plate Tectonics, Springer, Dordrecht, pp. 441–502.

Masters, G., G. Laske, H. Bolton, and A. Dziewonski (2000) The relative behavior of shear velocity, bulk sound speed, and compressional velocity in the mantle: Implications for chemical and thermal structure. In Karato, S., A. Forte, R. Liebermann, G. Masters, and L. Stixrude (eds.) Earth's Deep Interior, Geophysical Monograph, Vol. 117, American Geophysical Union, Washington, DC, pp. 63–87.

Matyska, C., and D.A. Yuen (2005) The importance of radiative heat transfer on superplumes in the lower mantle with the new post-perovskite phase change. *Earth Planet. Sci. Lett.*, 234, 71–81.

McNamara, A.K., P.E. van Keken, and S. Karato (2002) Development of anisotropic structure in the Earth's lower mantle by solid-state convection. *Nature*, 416, 310–314.

Meade, C., H.K. Mao, and J. Hu (1995) High-temperature phase transition and dissociation of (Mg,Fe)SiO_3 perovskite at lower mantle pressures. *Science*, 268, 1743–1745.

Murakami, M. et al. (2004) Post-perovskite phase transition in $MgSiO_3$. *Science*, 304, 855–858.

Murakami M., K. Hirose, N. Sata, and Y. Ohishi (2005) Post-perovskite phase transition and mineral chemistry in the pyrolitic lowermost mantle. *Geophys. Res. Lett.*, 32, L03304, doi:10.1029/2004GL021956.

Musgrave, M.J.P. (1970) Crystal Acoustics, Holden-Day, Boca Raton, Fla.

Nakagawa, T., and P.J. Tackley (2004) Effects of a perovskite-post perovskite phase change near core-mantle boundary in compressible mantle convection. *Geophys. Res. Lett.*, 31, L16611, doi:10.1029/2004GL020648.

Nastar, M., and F. Willaime (1995) Tight-binding calculation of the elastic constants of fcc and hcp transition metals. *Phys. Rev. B*, 51, 6896–6907.

Nielsen, O.H., and R.M. Martin (1985) Stresses in semiconductors: Ab initio calculations on Si, Ge, and GaAs. *Phys. Rev. B*, 32, 3792–3805.

Oganov, A.R., and S. Ono (2004) Theoretical and experimental evidence for a postperovskite phase of $MgSiO_3$ in Earth's D″ layer. *Nature*, 430, 445–448.

Ono, S., T. Kikegawa, and Y. Ohishi (2005a) A high-pressure and high-temperature synthesis of platinum carbide. *Solid State Comm.*, 133, 55–59.

Ono S., Y. Ohishi, M. Isshiki, and T. Watanuki (2005b) In situ X-ray observations of phase assemblages in peridotite and basalt compositions at lower mantle conditions: Implications for density of subducted oceanic plate. *J. Geophys. Res.*, 110, B02208, doi:10.1029/2004JB003196.

Perdew, J.P., K. Burke, and M. Ernzerhof (1996) Generalized gradient approximation made simple. *Phys. Rev. Lett.*, 77, 3865–3868.

Perdew, J., and A. Zunger (1981) Self-interaction correction to density functional approximations for many-electron systems. *Phys. Rev. B*, 23, 5048–5079.

Pulliam, J., and M.K. Sen (1998) Seismic anisotropy in the core-mantle transition zone. *Geophys. J. Int.*, 135, 113–128.

Saxena, S.K. et al. (1996) Stability of perovskite ($MgSiO_3$) in the earth's mantle. *Science*, 274, 1357–1359.

Shim, S.-H., T.S. Duffy, and G. Shen (2001) Stability and structure of $MgSiO_3$ perovskite to 2300-kilometer depth in earth's mantle. *Science*, 293, 2437–2440.

Sidorin, I., M. Gurnis, and D.V. Helmberger (1999) Evidence for a ubiquitous seismic discontinuity at the base of the mantle. *Science*, 286, 1326–1331.

Stackhouse, S. et al. (2005) The effect of temperature on the seismic anisotropy of the perovskite and post-perovskite polymorphs of $MgSiO_3$. *Earth Planet. Sci. Lett.*, 230, 1–10.

Stixrude, L., R.E. Cohen, and D.J. Singh (1994) Iron at high pressure: Linearized-augmented-plane-wave computations in the generalized-gradient approximation. *Phys. Rev. B*, 50, 6442–6445.

Troullier, N., and J.L. Martins (1991) Efficient pseudopotentials for plane-wave calculations. *Phys. Rev. B*, 43, 1993–2006.

Tsuchiya, J., T. Tsuchiya, and R.M. Wentzcovitch (2005a) Vibrational and thermodynamic properties of $MgSiO_3$ postperovskite. *J. Geophys. Res.*, 110, B02204, doi:10.1029/2004JB003409.

Tsuchiya, J., T. Tsuchiya, and R.M. Wentzcovitch (2005b) Post-Rh_2O_3(II) transition and the high *P*, *T* phase diagram of alumina. *Phys. Rev. B*, 72, 020103(R).

Tsuchiya, T., R. Caracas, and J. Tsuchiya (2004a) First principles determination of the phase boundaries of high-presusre polymorphs of silica. *Geophys. Res. Lett.*, 31, L11610, doi:10.1029/2004GL019649.

Tsuchiya, T., and K. Kawamura (2001) Systematics of elasticity: Ab initio study in B1-type alkaline earth oxides. *J. Chem. Phys.*, 114, 10086–10093.

Tsuchiya, T., J. Tsuchiya, K. Umemoto, and R.M.Wentzcovitch (2004b) Phase transition in $MgSiO_3$ perovskite in the Earth's lower mantle. *Earth Planet. Sci. Lett.*, 224, 241–248.

Tsuchiya, T., J. Tsuchiya, K. Umemoto, and R.M. Wentzcovitch (2004c) Elasticity of post-perovskite $MgSiO_3$. *Geophys. Res. Lett.*, 31, L14603, doi:10.1029/2004GL020278.

Vanderbilt, D. (1990) Soft self-consistent pseudopotentials in a generalized eigenvalue formalism. *Phys. Rev. B*, 41, 7892–7895.

Wallace, D. (1972) Thermodynamics of Crystals, Wiley, New York.

Wentzcovitch, R.M., B.B. Karki, M. Cococcioni, and S. de Gironcoli (2004a) Thermoelastic properties of $MgSiO_3$ perovskite: Insights on the nature of earth's lower mantle. *Phys. Rev. Lett.*, 92, 018501.

Wentzcovitch, R.M., B.B. Karki, S. Karato, and C.R.S. Da Silva (1998) High pressure elastic anisotropy of $MgSiO_3$ perovskite and geophysical implications. *Earth Planet. Sci. Lett.*, 164, 371–378.

Wentzcovitch, R.M., J.L. Martins, and G.D. Price (1993) Ab initio molecular dynamics with variable cell shape: Application to MgSiO3. *Phys. Rev. Lett.*, 70, 3947–3950.

Wentzcovitch, R.M., N. Ross, and G.D. Price (1995) Ab initio study of $MgSiO_3$ and $CaSiO_3$ perovskites at lower-mantle pressures. *Phys. Earth Planet. Inter.*, 90, 101–112.

Wentzcovitch, R.M., L. Stixrude, B.B. Karki, and B. Kiefer (2004b) Akimotite to perovskite phase transition in $MgSiO_3$. *Geophys. Res. Lett.*, 31, L10611, doi:10.1029/2004GL019704.

Williams, Q., and R. Jeanloz (1990) Melting relations in the iron-sulfur system at ultrahigh pressures: Implications for the thermal state of the earth. *J. Geophys. Res.*, 95, 19299–19310.

Wysession, M.E. et al. (1998) Implications of the D″ discontinuity. In Gurnis, M., M.E. Wysession, E. Knittle, B. Buffett (eds.) The Core-Mantle Boundary Region, Geodynamic Series, Vol. 28, American Geophysical Union, Washington, DC, pp. 273–297.

Wysession, M.E. et al. (1999) Lateral variations in compressional/shear velocities at the base of the mantle. *Science*, 284, 120–124.

Yamazaki, D., and S. Karato (2002) Fabric development in (Mg,Fe)O during large strain, shear deformation: Implications for seismic anisotropy in Earth's lower mantle. *Phys. Earth Planet. Inter.*, 131, 251–267.

PART II

SEISMOLOGICAL EVIDENCE AND BOUNDARY LAYERS IN THE MANTLE

INTRODUCTION

Part II contains two chapters that discuss issues related to the properties of the various mantle boundary layers. The lithosphere is a surface boundary layer, which is formed at a mid-oceanic ridge, where extensive cooling and hydration cause a steep geothermal gradient, hence called a surface boundary layer. Lithospheric plate subducts at the trench into the deep mantle, carrying surface water, which depends on the geotherm

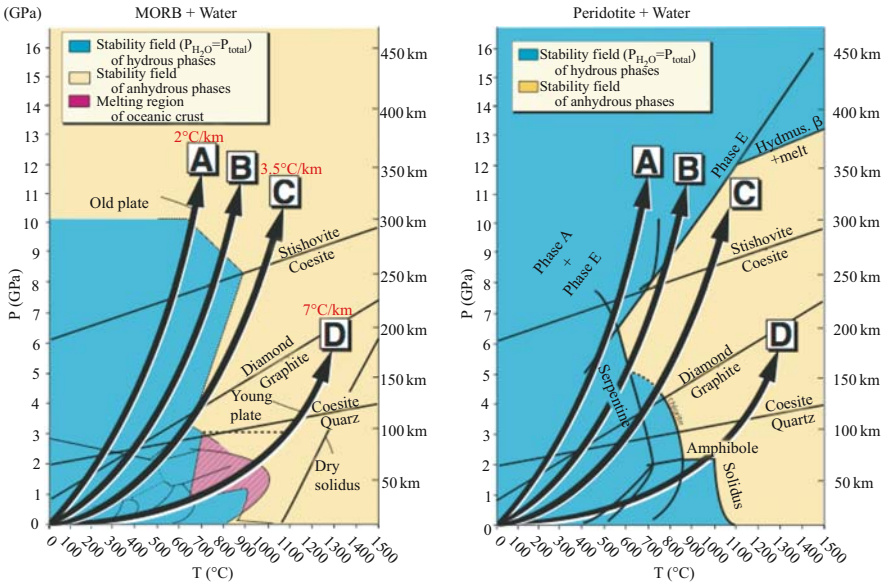

Figure 1. Two phase diagrams of MORB + Water and Peridotite + Water systems (A), and the mechanism of water transportation into the mantle (B). Along the subduction zone geotherms A,B,C, and D, the hydrated MORB crust transported the seawater into deep mantle. The colder the slab, the more the seawater is transported into deeper mantle, as the Earth has cooled through time. The sequence from D to A corresponds to the Earth from Archean (D), through Proterozoic (C and B) to Phanerozoic (A).

D. A. Yuen et al. (eds.), Superplumes, 107–112.
© 2007 *Springer.*

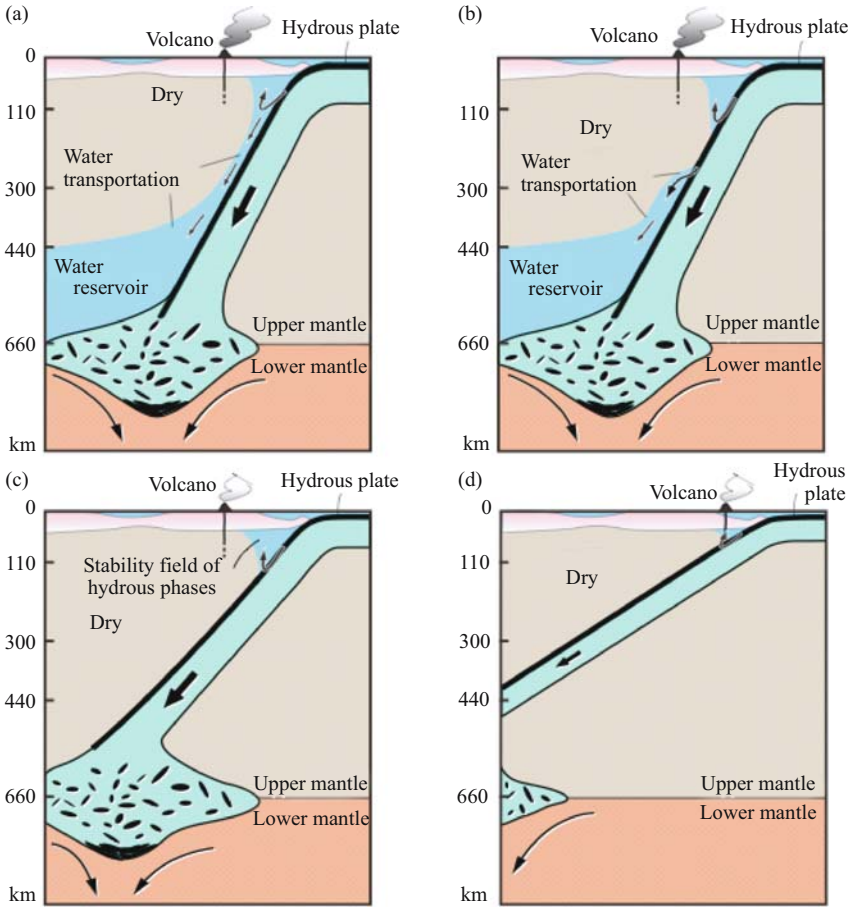

Figure 2. The fate of circulating water on the Earth. Depending on the subduction zone geotherms, A, B, C and D in Figure 1, the surface water returns back to the surface, or circulates into the deep mantle.

of the slab. The role of water is critically important in mantle dynamics because of the power of water to reduce the viscosity of minerals and to drop the melting temperature of the mantle.

Omori and Komabayashi summarize the phase diagram of the MASH system as an analog of slab peridotite, and clarify the nature of the dehydration reaction at mantle depth. Depending on the geotherms, four different mechanisms of water transportation may be expected. At the highest geothermal gradient similar to the Archean, the hydrated MORB crust dehydrates to release water at a shallow depth to yield a hydrous magma such as adakite. In contrast, a hydrated slab carries water into the mantle transition zone if the slab is low in temperature such as those in present-day

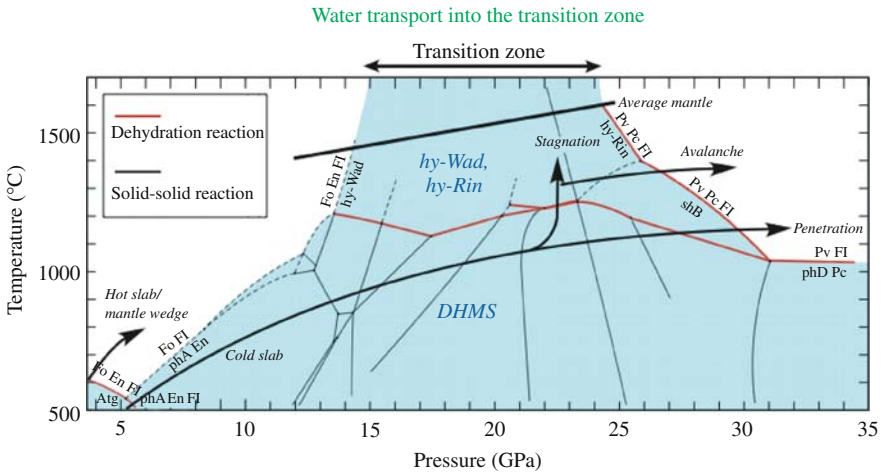

Figure 3. Stability fields of dense hydrous silicates (DHMS), hydrous wadsleyite (hy-Wad) and hydrous ringwoodite (hy-Rin) in the mantle (modified after Komabayashi and Omori, 2006). Note two critical points. First, water can be transported into the deep mantle only along the geotherm above at point P = 5.2 GPa, T = 540°C. This point is called a choke point (Kawamoto, 2004). Second, the high-T side abrupt enlargement of the stability field of DHMSs into MBL (410–660 km) is due to the hydrous wadsleyite and hydrous ringwoodite with high water content (2–3%). This causes a huge water tank in the MBL which is five times of the volume of the Ocean. Several geotherms are shown. If the slab is stagnant at 660 km depth, the hydrated slab would be heated up underneath to cross-cut the dehydration reaction (red). Dehydrated water is trapped in the crystalline hydrous phases.

Tonga, Kamchatska, and NE Japan to Mariana. These two processes are two extreme cases (Figs. 1 and 2).

Throughout geologic time, the mechanism of water transportation has changed, due to the variation in temperature. As seen in changing P-T conditions recorded on the regional metamorphic rocks along consuming plate boundaries, the subduction zone geotherm has evolved rapidly and cooled down after 750–600 Ma (Fig. 3). In other words, the rapid change of the transportation mechanism of water into mantle occurred around the Proterozoic/Phanerozoic boundary. This change caused the drastic environmental change from the end-Precambrian to the Cambrian eras (Maruyama and Liou, 2005).

In the western Pacific and East Asia, the upper mantle is lowest in temperature, as observed in the thickness of the mantle transition zone, about 200–300 K lower than that of the standard mantle transition zone, yet on-going with active magmatism, seismicity, and deformation along the fragmented continental blocks or oceanic micro-plates. These presumably reflect the ubiquitous occurrence of water-rich fluids in the whole of the upper mantle and crust in these regions (Fig. 4).

In addition to the surface and mantle transition zone, the D″ layer at the bottom of the mantle is critical for the origin of superplume and other types of plumes in

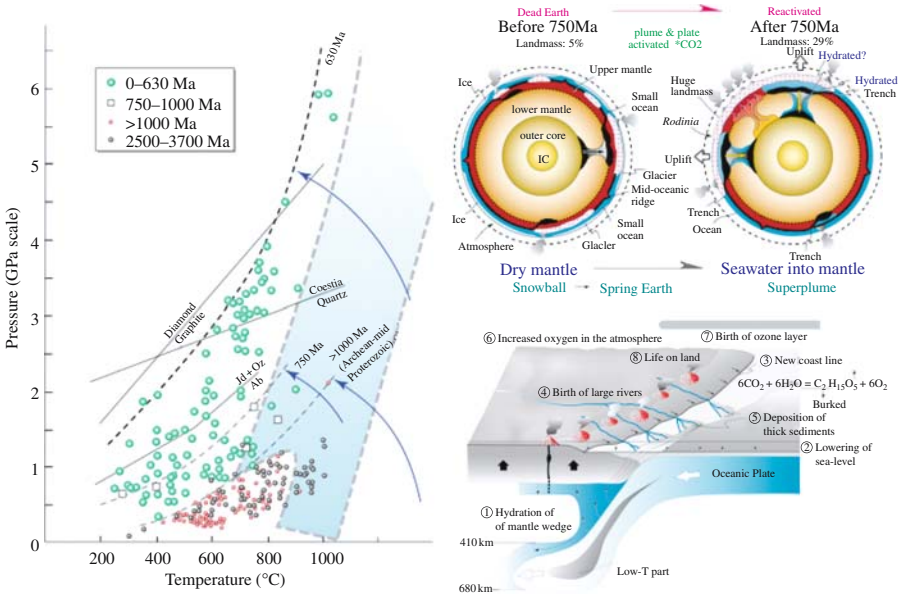

Figure 4. Left: P-T conditions of regional metamorphic rocks in space and time (Maruyama et al., 1996). A rapid temperature drop occurred at the subduction zone during 750–600 Ma, which enabled the surface water to move into deep mantle down to 660 km depth (right). Right-above: By the initiation of return-flow of the surface water into the mantle, mantle dynamics changed drastically at 750–600 Ma. Dry mantle changed into wet mantle to break up the supercontinent Rodinia. The snowball Earth was changed into the Phanerozoic Earth, causing the viscosity drop to promote mantle convection and, by lowering the melting temperature, to activate the magmatism to transport CO_2 to the surface. Right-below: By this event, the surface environment changed drastically and there emerged a large landmass, extensive erosion, burial of organic matter, change of seawater composition, increase of oxygen in atmosphere, and large multi-cellular animals (Maruyama and Liou, 2005).

the lower mantle. Garnero et al. summarize their own outstanding works to focus the physical and chemical processes on CMB as the most dynamic boundary layer, with 2000 K temperature difference below and above the D″ layer. In addition to their own interpretation of D″ dynamics, a series of figures, (1) D″ shear wave velocity perturbations, (2) strongest D″ lateral seismic velocity gradients, (3) hotspots and D″ density anomalies, (4) dense piles which are formed from geodynamic causes, (5) geodynamical D″ temperature anomalies, (6) ULVZ thickness, (7) seismically derived D″ density anomalies, (8) D″/CMB PKP scattering intensity, and (9) paleomagnetic VGP reversal paths are shown to illustrate CMB dynamics.

REFERENCES

Kawamoto, T. (2004) Hydrous phase stability and partial melt chemistry in H_2O saturated KLB-1 peridotite up to the uppermost lower mantle conditions. *Phys. Earth Planet. Inter.*, 143–144, 387–395.

Komabayashi, T., and S. Omori (2006) Internally consistent thermodynamic data set for dense hydrous magnesium silicates up to 35 GPa, 1600°C: Implications for water circulation in the Earth's deep mantle. *Phys. Earth Planet. Inter.*, 156, 89–107.

Maruyama, S., and J.G. Liou (2005) From snowball to Phanerozoic Earth. *Inter. Geol. Rev.*, 47, 775–791.

Maruyama, S., J.G. Liou, and M. Terabayashi (1996) Blueschists and eclogites of the world, and their exhumation. *Inter. Geol. Rev.*, 38, 485–594.

CHAPTER 5

SUBDUCTION ZONE: THE WATER CHANNEL TO THE MANTLE

SOICHI OMORI AND TETSUYA KOMABAYASHI

Department of Earth and Planetary Sciences, Tokyo Institute of Technology, 2-12-1 O-okayama, Meguro-ku, Tokyo, 1528551, Japan;
E-mail: omori@geo.titech.ac.jp

Abstract

We review the role of subduction zones as water carriers from the Earth's surface to the mantle. A phase diagram for the hydrous peridotite in the MgO-Al_2O_3-SiO_2-H_2O system and a model distribution of the dehydration reaction in the subducting peridotite are shown to discuss a mode of water transportation via the subduction zone. Stagnation of the slab has significance for dehydration in the mantle transition zone, therefore water transport into the lower-mantle is limited in most of the subduction zones except where slab penetration into the lower mantle is observed. The dehydration induction model for the intraslab earthquakes was introduced to estimate sites of dehydration in the mantle without thermal modeling. Subduction-zone earthquakes show two organized structures in their depth-distribution down to 700 km depth and in the hypocenter distribution geometry at the intermediate depths (50–300 km). The former is represented by three types of depth-distribution of earthquakes in the world's subduction zones; and the latter has been known as the double seismic zone (DSZ). The dehydration-induction earthquake model is reviewed to show a close link between the locations of metamorphic dehydration reactions in the subducting oceanic peridotite and hypocenter distribution. The phenomenon of earthquakes in subduction zones possibly reflects water transportation into the mantle by the subducting slab. The hypothesis involves hydration of the oceanic peridotite down to 50 km depth from the ocean floor. A possible mechanism of the hydration process has been proposed. The hydration of the oceanic peridotite implies a new water channel to the mantle which is more suitable to carry water than previously proposed mantle wedge material. Water transportation has a significant role in the Earth's dynamics. Irreversible cooling of the Earth's interior leads to decline of material circulation in the solid Earth. Instead cooler mantle allows much water to be carried into the deeper mantle, and rheological activation will be expected. The subduction of hydrous minerals provides a negative feedback to stabilize the mantle-surface material activity.

D. A. Yuen et al. (eds.), Superplumes, 113–138.
© 2007 *Springer.*

1 INTRODUCTION

The subduction zone is the most important subsystem in the plate tectonics paradigm. Subducting plates are distinct in terms of their temperature and chemical composition. A plate is subjected to continuous cooling during its traverse from an oceanic ridge to a subduction zone. Subduction of such a cold plate generates relatively low-temperature domains in the mantle, which have roles for making a down-flow and storing water molecules in the mantle. A plate mainly consists of oceanic crust and herzbergitic-lherzoritic peridotite, which are differentiated by partial melting at the oceanic ridge. Hydrothermal alteration near the oceanic ridge brings hydroxyl components into hydrous minerals in the oceanic crust and probably in the peridotitic lithosphere. The hydroxyl in the hydrous minerals can survive subduction metamorphism depending on a thermal condition of the subduction zone and thereby conveying water into the deep mantle. It is known that water can change the mechanical properties of mantle rocks (Karato et al., 1986; Hirth and Kohlstedt, 1996; Chen et al., 1998, Karato and Jung, 1998): subducting plates thus bring thermal, chemical and mechanical heterogeneity to the mantle from the subduction zone. Such heterogeneities in the mantle are considered to be essential for plume or superplumes generation (Karato, 2007; Maruyama et al., 2007; in this book). In this way the generation and subduction of plates are important elements in the plume tectonics paradigm.

Chemical and thermal processes in subduction zones have been studied extensively, ever since the beginning of the plate tectonics paradigm. Comprehensive reviews of these studies can be found in many papers and text books (e.g., Bebout et al., 1996). Water transportation via the crustal layer of the slab and mantle wedge peridotite has been discussed in previous studies (e.g., Schmidt and Poli, 1998; Okamoto and Maruyama, 1999; Maruyama and Liou, 2005, Introduction of the Part II of this book). In this chapter, we focus on new insights in regard to the behavior of water in the subducting slab peridotite and mantle transition zone (MTZ): these include thermodynamically consistent phase diagram for the hydrous phases, stagnant slabs, water transportation into the MTZ, a relation between seismicity and dehydration reaction, and extensive hydration to the deep oceanic plate.

2 PHASE RELATION IN THE MgO-Al_2O_3-SiO_2-H_2O PERIDOTITE

The stability of hydrous minerals in mantle peridotite and the basaltic composition are the most important issues in regard to the role of the subduction zone as a channel of water. For the basaltic system, experimental studies have revealed the stability of hydrous minerals (e.g., Schdmit and Poli, 1998; Okamoto and Maruyama, 1999; Poli and Schmidt, 2002). The chemical system MgO-SiO_2-H_2O (MSH) is a basic approximation of peridotite+water and has been studied now for 40 years (Ringwood and Major, 1967; Yamamoto and Akimoto, 1977; Akaogi and Akimoto, 1980; Liu, 1987; Kanzaki, 1991; Luth, 1995; Shieh et al., 1998; Wunder, 1998; Bose and Navrotsky, 1998; Frost and Fei, 1998; Gasparik, 1993; Inoue, 1994; Irifune et al.,

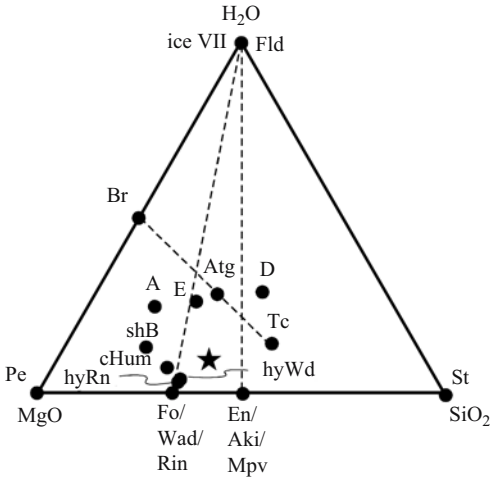

Figure 1. Ternary composition diagram in the MgO-SiO_2-H_2O system showing the chemographic relation of the hydrous phases.

1998; Ohtani et al., 2000; Angel et al., 2001; Komabayashi et al., 2004; Komabayashi et al., 2005a; Komabayashi et al., 2005b). Figure 1 shows chemographic relations of the hydrous phases in the MSH system. The dominant site of the hydroxyl in the MSH system changes according to pressure; below 6 GPa in a cold subduction geotherm, a serpentine mineral (antigorite) is the major hydrous phase. In higher-P conditions, high-pressure hydrous phases which are dense hydrous magnesium silicates (DHMSs), also hydrous wadsleyite, and hydrous ringwoodite can store water. Antigorite phase relations have been investigated by both experimental and theoretical studies, and the P-T conditions of the reactions have been determined (Ulmer and Trommsdorff, 1995; Wunder and Schreyer, 1997; Bose and Navrotsky, 1998; Bromiley and Pawley, 2003; Komabayashi et al., 2005a). However phase relations of high-P hydrous phases have previously been studied by high-pressure experiments which did not determine precise phase boundaries. Therefore, thermodynamic analyses are required to fully describe the stability relations of the high-P hydrous phases. The theoretical investigation of phase stability in the MSH system at high P-T conditions was done to construct a comprehensive phase diagram in the MSH system, involving the effect of high-solubility of the rock component in the fluid in mid-lower mantle conditions (Komabayashi and Omori, 2006).

For a better approximation of the peridotite+water system, Al_2O_3 should be added to the MSH system. The addition of aluminum to the MSH system expands the stability of antigorite (Bromiley and Pawley, 2003). In the system MgO-Al_2O_3-SiO_2-H_2O (MASH), aluminous hydrous phases, chlorite and Mg-sursassite, are stable in post-antigorite P-T conditions (Fockenberg, 1998; Grevel et al., 2001; Bromiley and

Pawley, 2002; Bromiley and Pawley, 2003; Pawley, 2003). Chlorite breaks down in high-T conditions by a continuous reaction which forms an Mg-tschermak component in enstatite. The MASH system approximates about 90% of the constituents of the mantle. The rest of the major components are FeO and CaO. When these components are included in the model, most of the reactions in the MASH become continuous reactions which involve compositional change in the solid-solution minerals. In this case, the reaction curves in the MASH would become specific bands in the P-T space, and would be located at somewhat different positions. However, experimental works (Litasov et al., 2003; Kawamoto, 2004) and their compilations (Hacker et al., 2003; Iwamori, 2004) in the FeO- and/or CaO- bearing systems could not detect significant differences in the dehydration reactions compared with the MASH in regard to water transportation to the deep mantle. Therefore, we consider that the MASH approximation of the mantle+water system is a reasonable approximation.

Figure 2 illustrates a P-T diagram showing all possible dehydration reactions during the subduction of the model hydrated mantle in the MASH system. This diagram was constructed by thermodynamic calculations in the MASH system (Omori et al., 2004) for lower-P ($P < 10$ GPa) conditions and in the MSH system for higher-P ($P > 10$ GPa) conditions (Komabayashi et al., 2005a; Komabayashi, 2006). Compositions, abbreviations, and thermodynamic data sources of the phases are shown in Table 1; and reaction formulae are shown in Table 2. In the diagram, two kinds of dehydration reaction are shown by different colors. One color shows the reactions which occur in water-saturated conditions and the other color shows a less hydrated conditions assuming complete removal of fluid from the system after the dehydration. Then the behavior of the fluid and effective bulk water content in the subducting slab will be discussed in a later section.

Note that the reaction Fo + Fld = phA + En (reaction 44) was termed the "water-line" (Liu, 1987) because it bounds the P-T region in the upper mantle where all the H_2O components in the system behave as a free fluid. In addition, Komabayashi et al., (2005b) showed that the reaction Fo + Fld = cHu + En (reaction 2) is another "water-line". In spite of their importance to water transportation, there are large discrepancies among previous experimental results on the antigorite dehydration reactions and the "water-line" (Ulmer and Trommsdorff, 1995; Luth, 1995; Wunder and Schreyer, 1997; Wunder, 1998; Bose and Navrotsky, 1998; Bromiley and Pawley, 2003). The reported invariant point in these studies ranges from 4.5 to 6.2 GPa and 550 to 620°C. Possible sources for these discrepancies have been considered to be due to differences in composition of the starting natural antigorite and other experimental factors (Mysen et al., 1999; Wunder and Schreyer, 1997; Bromiley and Pawley, 2003; Komabayashi et al., 2005a).

Another important phase relation related to the behavior of water in the mantle was proposed by Bina and Navrotsky (2000). At very low temperatures (below 300°C at 7 GPa), the dehydration reaction of antigorite intersects the melting curve of iceVII (e.g., Fei et al., 1993), leading to formation of iceVII at the breakdown of antigorite by the reaction Atg = phA + En + iceVII.

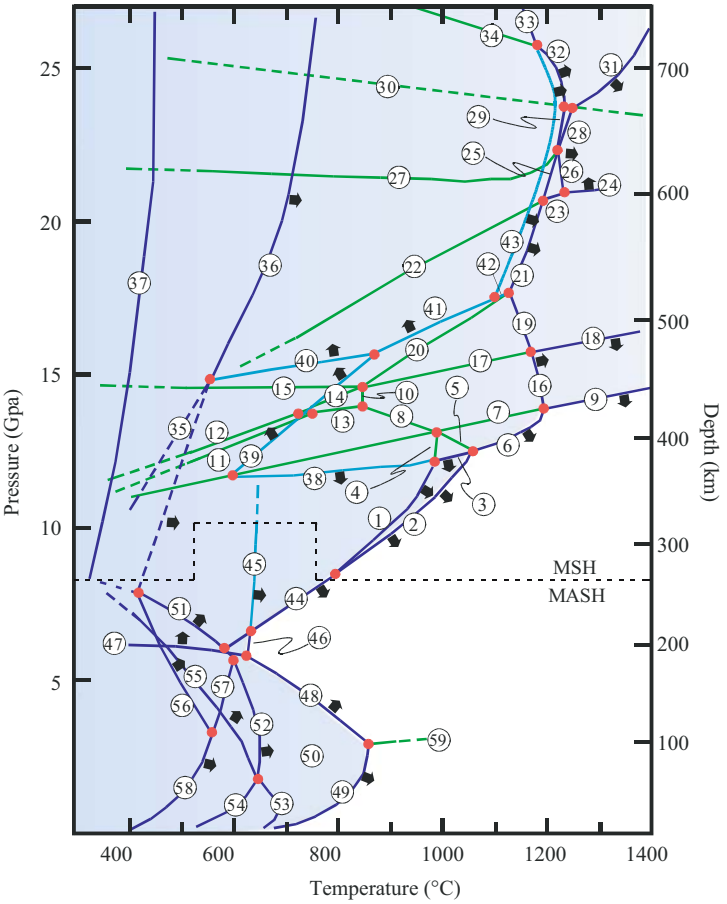

Figure 2. Phase diagram for the hydrous peridotite in the MgO-Al_2O_3-SiO_2-H_2O system (after Omori et al., 2004; Komabayashi, 2006). Blue curves correspond to the dehydration reactions which can occur in the water undersaturated composition. Light blue curves are the dehydration reactions which occur in the water saturated composition. Green curves represent reactions only among solid phases.

3 COLD PLATE SUBDUCTION, STAGNATION OF THE SLAB, AND WATER TRANSPORTATION

3.1 Cold subduction of the slab

It is essential for water transportation into the deep mantle that the subducting plate subject to a relatively low-T conditions compared with the normal mantle temperature. This is because the stability of the hydrous phase is temperature-dependent and is limited to relatively low-T conditions (Fig. 2). If a P-T path of a part of the plate intersects the reaction including H_2O toward the side in which H_2O is stable, a

Table 1. Abbreviations and compositions of the phases in the model hydrous-peridotite

Abbreviation	Phase	Chemical formula	Data source
A	phase A	$Mg_7Si_2O_8(OH)_6$	1
Aki	Akimotoite	$Mg_2Si_2O_6$	8
Atg	Antigorite	$Mg_{48}Si_{34}O_{85}(OH)_{62}$	1
Ath	Anthophyllite	$Mg_7Si_8O_{22}(OH)_2$	1
Br	Brucite	$Mg(OH)_2$	1
Chl	Clinochlore	$Mg_5Al_2Si_3O_{10}(OH)_8$	1, 4
cHum	Clinohumite	$Mg_9Si_4O_{16}(OH)_2$	1, 5
D	phase D	$MgSi_2O_4(OH)_2$	8
E	phase E	$Mg_{2.3}Si_{1.28}O_{3.65}(OH)_{2.42}$	8
En	Enstatite (ortho, high-P clino, low-P clino)	$Mg_2Si_2O_6$	1, 6
Fld	fluid	H_2O (+silicate components)	1
Fo	Forsterite	Mg_2SiO_4	1
hyRn	Hydrous ringwoodite	$Mg_{1.89}Si_{0.98}O_{3.7}(OH)_{0.3}$	8
hyWd	Hydrous wadsleyite	$Mg_{1.89}Si_{0.98}O_{3.7}(OH)_{0.3}$	8
Mpv	Mg-silicate perovskite	$Mg_2Si_2O_6$	8
Msur	Mg-sursassite	$Mg_5Al_5Si_6O_{21}(OH)_7$	3, 7
Mts	Mg-tschermak pyroxene	$MgAl_2SiO_6$	1
Pe	Periclase	MgO	8
Prp	Pyrope	$Mg_3Al_2Si_3O_{12}$	1, 4
Rin	Ringwoodite	Mg_2SiO_4	8
shB	superhydrous phase B	$Mg_{10}Si_3O_{14}(OH)_4$	8
Sp	Spinel	$MgAl_2O_4$	1, 4
St	Stishovite	SiO_2	1
Tc	Talc	$Mg_3Si_4O_{10}(OH)_2$	1
Wad	Wadsleyite	Mg_2SiO_4	8

1: Holland and Powell (1998); 2: Vs and bulk modulus were taken from Faust and Knittle (1994), ΔHf°_{298} and S°_{298} were estimated from Wunder (1998); 3: Cp was approximated by oxide sum; 4: bulk modulus and thermal expansion were modified to fit Ulmer and Trommsdorff (1999); 5: ΔHf°_{298} and S°_{298} were estimated from Pawley (2000); 6: ΔHf°_{298} and S°_{298}, Vs, bulk modulus and thermal expansion were estimated from Shinmei et al. (1999); 7: ΔHf°_{298} and S°_{298}, Vs, bulk modulus and thermal expansion were estimated from Fockenberg (1998) and Grevel et al. (2001); 8: Komabayashi and Omori (2006).

dehydration will occur, and H_2O in the rock will be released as a fluid phase. Therefore we will first summarize what is known about the temperature in the subduction zone.

A subducting plate is composed of oceanic lithosphere. The lithosphere is a thermal boundary layer of the outermost shell of the solid earth. The surface is presently in contact with sea water of about 4°C. The lithosphere-asthenosphere boundary at 50–100 km depth is considered to be at about 1000°C (Fig. 3a). The oceanic plate is continuously cooled during its traverse from a mid-oceanic ridge to a trench. During the cooling, the thickness of the plate increases simultaneously with time. An empirical relation applies to the thermal structure of an oceanic plate and its age. Stein and Stein (1996) estimated the thickness and thermal structure of the plate before subduction by performing a numerical simulation. Recently, the possibility that the oceanic plate is re-heated in its traverse was shown by observations of volcanic activities in the oceanic plate (e.g., Wessel, 1997; Hirano et al., 2001). When

Table 2. Reactions in Figure 1. Numbers correspond to that on the reaction curves in Figure 1

No	Reaction
1	A + En = cHu + Fld
2	cHu + En = Fo + Fld
3	E = cHu + En + Fld
4	A + En = cHu + E
5	cHu + En = E + Fo
6	E = Fo + En + Fld
7	hyWd = Fo + En + E
8	A + En = hyWd + E
9	hyWd = Fo + En + Fld
10	En + shB = E + hyWd
11	shB + D = A + En
12	shB + St = En + D
13	A + En = shB + E
14	shB + St = E + En
15	shB + En = hyWd + St
16	E = hyWd + En + Fld
17	hyWd + St = E + En
18	hyWd + St = En + Fld
19	E = hyWd + St + Fld
20	shB + St = E + hyWd
21	shB + St = hyWd + Fld
22	hyRn + shB + St = hyWd
23	hyRn + St + Fld = hyWd
24	hyWd + St = Aki + Fld
25	shB + St = hyRn + Fld
26	hyRn + St = Aki + Fld
27	hyRn + St = Aki + shB
28	shB + Aki = hyRn + Fld
29	shB + St = Aki + Fld
30	Aki = Pv
31	shB + Pv = hyRn + Fld
32	shB + St = Pv + Fld
33	shB + D = Pv + Fld
34	shB + St = D + Pv
35	D + Br = A + Fld
36	D + Br = shB + Fld
37	IceVII = Fld
38	A + En + Fld = E
39	A + D + Fld = E
40	shB + Fld = A + D
41	shB + D + Fld = E
42	shB + St + Fld = E
43	D = shB + St + Fld
44	A + En = Fo + Fld
45	A + En + Msur = Prp + Fld

(*Continued*)

Table 2. (*Continued*)

No	Reaction
46	Fo + En + Msur = Prp + Fld
47	Chl + Atg = Msur + A + Fld
48	En + Chl = Fo + Prp + Fld
49	Chl = En + Fo + Sp + Fld
50	Chl + En = Mg-ts + Fo + Fld
51	Atg = A + En + Fld
52	Atg = Fo + En + Fld
53	Ath + Fo = En + Fld
54	Tc + Fo = Ath + Fld
55	Atg + Tc = En + Fld
56	Atg + Br = A + Fld
57	A + Atg = Fo + Fld
58	Atg + Br = Fo + Fld
59	Fo + Prp = En + Sp

an oceanic plate subducts, a unique thermal structure is formed in the subduction zone. Many studies have made numerical simulations of the thermal structure of the subduction zone down to a depth of 200 km (e.g., Peacock, 1996; Iwamori, 1998; Yamasaki and Seno, 2003). These results are qualitatively in agreement. Figure 3a shows an example of calculated thermal structure in the NE-Japan where the Pacific plate with an age of 130 Ma is subducting (Yamasaki and Seno, 2003). While the thermal structure before subduction is preserved at shallower depths, the plate mantle-wedge boundary is heated as it descends, and the lowest-temperature part shifts to the inside of the plate. Thereby inside the plate the isotherm shows a parabolic shape which is convex in the subduction direction. Parameters that could contribute significantly to the degree of heating in the slab are thermal conductivity and viscous heating. Examples of P-T paths of portions of the plate, at the surface, 30 km depth, and 50 km depth from the surface, are shown in Figure 3b. The stability of the hydrous phases will be discussed along such P-T paths of the portions of the slab, although there remain substantial uncertainties in the thermal calculations of the subduction zone.

3.2 Stagnant slab in the MTZ

In many subduction zones, it has been shown by seismic tomography that the subducted oceanic plate is stagnating in the mantle transition zone (Fukao et al., 2001; Zhao, 2004; Zhao et al., 2006 in this book). It is expected that the mantle transition zone in which the oceanic plate stagnates is at a low temperature compared with the circumference. In the thermal structure of the subduction zone, which reached the steady state, the slab subducts while keeping the relatively cold condition as mentioned above. Pressure increases systematically with depth. The T/P of the rock in

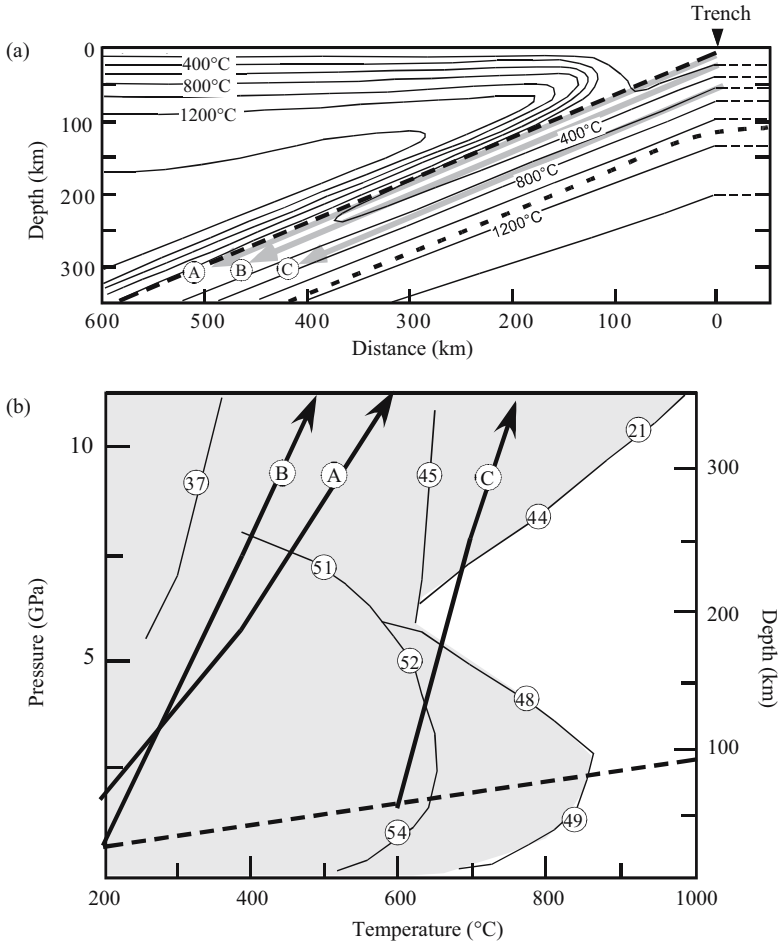

Figure 3. (a) An example of calculated thermal condition in the NE Japan (Yamasaki and Seno, 2003). (b) P-T paths of portions in the subducting slab projected onto the P-T plane from Figure 2a.

the plate becomes low because heat-conduction is relatively slow compared with the subduction velocity. However, the plate that stagnates in the MTZ will receive heating under the isobaric conditions. Thus, it is expected such nearly isobaric heating drives a dehydration event in the MTZ.

The top 410 km boundary of the mantle transition zone is thought to correspond to the phase transition from olivine to wadesleyite, and that the lower 660 km boundary corresponds to the reaction in which ringwoodite decomposes into Mg-perovskite and Mg-wüstite. Since these phase transitions have some temperature dependency, and when seismic tomography determines the changes of the up-and-down boundary

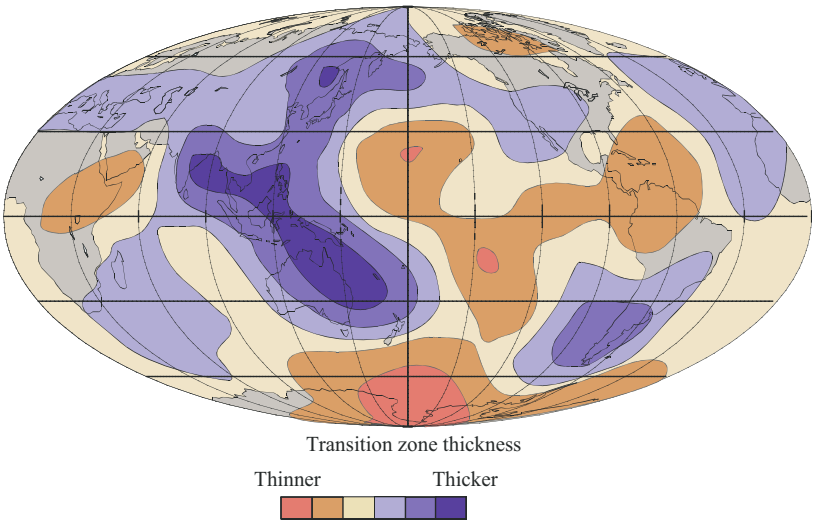

Figure 4. Thickness of the mantle transition zone estimated by Flanagan and Shearer (1998).

precisely, we can estimate a relative temperature difference with the surrounding mantle.

Since the olivine-wadesleyite transition has a positive P/T slope and decomposition of ringwoodite has a negative slope, when a part of MTZ is at a low temperature, the thickness of the low-T part will become thick. A thickness distribution of the mantle transition zone based on Flanagan and Shearer (1998) is shown in Figure 4. There are three characteristic features in the thickness distributions of MTZ: (1) an about 200–300K low-T area is seen as characteristic of the Pacific Rim and the Tethys area; (2) an area of 100–200 K higher temperature than the circumference is the typical of the central Pacific Ocean and Africa; and (3) the high-T area branches conversely into three directions, and corresponds to a very fast spreading rate of the mid-oceanic ridge. Feature (1) conforms with the prediction that the mantle transition zone achieves low-temperature because of the subducted slab.

Because the 660 km boundary is a thermal boundary accompanied by a phase transition, a large temperature gradient should exist near this boundary. The temperature gradient must be the largest at the place where the slab accumulates. Figure 5 shows an estimated thermal structure in the MTZ where the subducted slab from the Japan trench stagnates. The temperature was estimated by coupling observations of the depth of the “660 km” boundary with the phase diagram. Near the tip of the slab, a large temperature gradient exceeding 700 K/50 km exists both horizontally and vertically (Fig. 5). This depends on the total amount of subducted plate and the lapsed time from the beginning of the subduction whether such a large thermal gradient is a steady state or not. Therefore, it is difficult to generalize. However, when the slab stagnates in the MTZ, a change in T/P of the slab from low to high is the

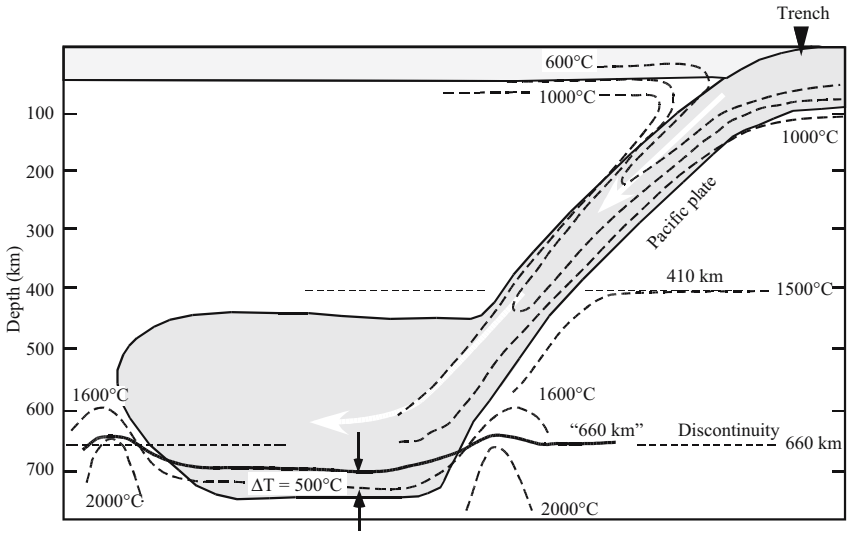

Figure 5. Estimated thermal structure of the MTZ with stagnant slab in Hokkaido area, Japan. Upper- and lower-boundaries of the MTZ are drawn using seismic data from Shearer and Masters (1992).

inevitable temperature-pressure history which the subducted plate follows. This will have a major influence on the stability of the hydrated minerals in the plate.

3.3 Water transportation into the deep mantle

The relative allocation between the dehydration reactions and a P-T path of a part of the subducting slab determines the fate of the water in the slab. For the water subduction into the deep mantle, the most important phase relation of antigorite occurs at about 5 GPa and 550° C (Fig. 2). The antigorite dehydration reaction intersects a reaction Fo + Fld = phA + En (water-line: reaction 44) to form an invariant point where Atg, Fo, En, phA, and Fld are stable. Subducting antigorite thus transfers water to phase A only when the subduction geotherms are lower than this invariant point. If the subduction geotherms are higher, antigorite dehydrates to Fo + En + Fld (reaction 52), and the solid phase assemblage becomes nominally dry. Therefore, the P-T location of this invariant point determines the fate of subducting water. Beyond the "water-line", water storage capacities of the solid phase assemblages are significantly larger because DHMS are stabilized, so that up to several weight percent of H_2O can be stored in the solid phases, and no free fluid exists. In the subducting slab, fluid released by a dehydration reaction may move upward due to its relative low density. In the P-T area which is higher-P than the waterline, the fluid will react with the surrounding peridotite and form new hydrous minerals until the rock is saturated

with H_2O. Such a rehydration would change the effective bulk water-content, so that it should also be considered in discussing water transportation in the subduction zone.

There are some difficulties in estimating the effective bulk water-content of the slab. These arise because the distribution of water should be heterogeneous in the slab. It is thought that the fluid formed by a certain dehydration reaction will move upwards. The fluid should react with the surrounding rock to form a new hydrous phase, if a portion is not saturated with water and lies in the stability field of a certain hydrous phase. When the fluid moves through mineral grain boundaries, the effective bulk water content becomes small. Hydrated minerals with comparatively small water contents are formed over a wide area. On the other hand, when the fluid is heterogeneously distributed, as in the case of vein, the effective bulk water content apparently becomes large. The portion of higher water content is locally formed, and the hydrated mineral containing much of the water act as condensed water storage. Nishiyama (1992) proposed the term "mantle hydrology". These hydrological aspects of dehydration are important when water transportation is argued. Until now, there have been some studies which discussed the moving of water in terms of wet angles of olivine under hydrostatic pressure (e.g., Watson and Bernan, 1987; Mibe et al., 1998). In peridotite under high- P and high-T condition, it is found that the permeability of the mineral grain boundary is high. However, the actual slab is under a stress. Moreover, the slab may have many fractures and faults that were formed at a mid-oceanic ridge and traverse to a trench. This means that mechanical heterogeneity exists inside the slab. Therefore, the idea could not be discarded that fluid is possibly concentrated along a mechanically weak line and forms a concentrated hydration vein.

Based on the above considerations, the maximum water content of rock of peridotite composition is assumed to be the local water content in slab, taking into account the dehydration-rehydration process in the slab, in the following arguments of this chapter. However, note that this assumption does not necessarily suggest a high water content exists over the whole slab.

Possible P-T relations of the coldest thermal-center in the subducting slab were semi-quantitatively modeled. Figures 6a and b present model P-T conditions for the coldest part of the subducting slab and the corresponding depth-range for dehydration events, respectively. It is assumed that the dehydration reaction proceeds under near equilibrium conditions. There are three important features in Figure 6b as follows:

1) Isobaric heating of the stagnant slab causes an effective dehydration. Therefore the maximum depth of dehydration is limited to 550–660 km, and no water, or less, could enter the lower-mantle. In such cases, the maximum depth of dehydration is independent of the temperature during subduction. In the case of direct slab penetration into the lower-mantle, dehydration can even occur at the depth of over 660 km.

2) There is a concave area that lacks dehydration in the 200–500 km depth-range and at intermediate slab-temperature.

3) The hottest slab does not experience deep dehydration reactions, because it exhausts all water at a shallow ($P < 6$ GPa) depth.

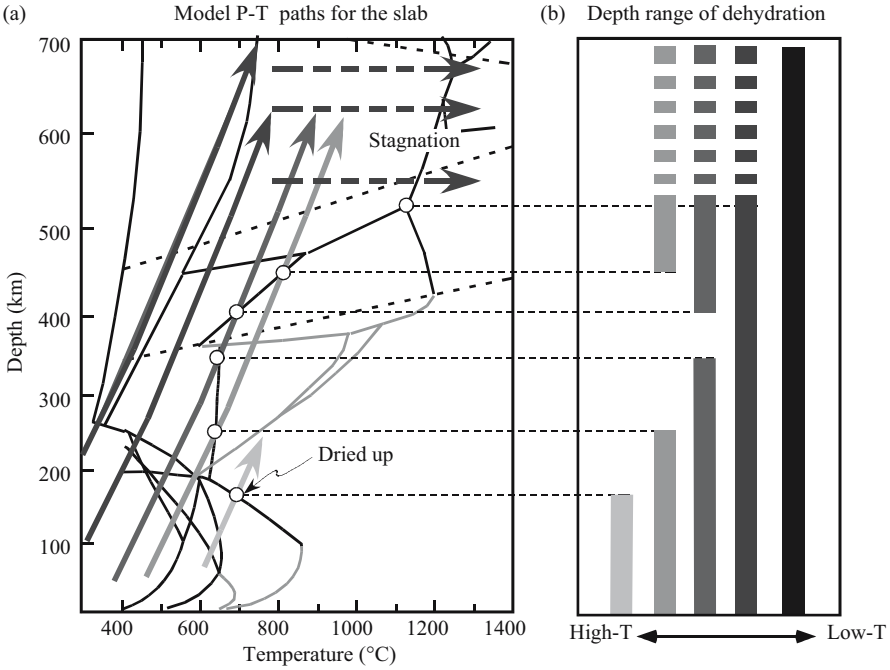

Figure 6. (a) Model P-T paths for the subducting slab. (b) Depth ranges of dehydrations in the slab.

A phase transformation from fluid H_2O to iceVII changes the phase relations in the low-T region, because the reactions in the stability field of fluid H_2O will become solid–solid reactions in the iceVII stability field. Therefore, if the slab temperature at the breakdown of antigorite is lower than the melting curve of iceVII, whole water in antigorite will be transferred into the deeper mantle by phase A and iceVII (Bina and Navrotsky, 2000).

4 DEEP SEISMICITY AND WATER

4.1 Experimental basis for the dehydration-induced earthquake hypothesis

Experimental work by Raleigh and Paterson (1965) presented the first observations that suggested a genetic relation between the decomposition of serpentine-group minerals, which are the most abundant hydrous minerals in ultramafic rocks in the Earth's surface, and earthquakes. They observed ductile to brittle transformation of serpentinite when the serpentine-group minerals decomposed and water was released. In addition, Meade and Jeanloz (1991) and Dobson et al. (2002) observed acoustic emission from compressed serpentinite down to lower mantle depths. They considered that dehydration and amorphism of serpentine-group minerals induced

brittle fracturing. Serpentine-group minerals are the most dominant product of the hydration of peridotite: therefore, these laboratory phenomena are considered to be related to the earthquakes in the mantle peridotite. However, these experiments have only been conducted on serpentine-group minerals, and it is not demonstrated whether these phenomena are common in all dehydration events in rocks.

In addition to the dehydration embrittlement of serpentine, a number of studies have investigated changes in the physical properties of mantle minerals under hydrous conditions. The viscosity of olivine is reduced by a factor of more than 100 under such hydrous conditions (Karato et al., 1986; Hirth and Kohlstedt, 1996; Chen et al., 1998, Karato and Jung, 1998), and the presence of only 10–100 ppm water can drastically weaken olivine crystals. Such observations suggest that water release by the dehydration of hydrous minerals within slab peridotites may cause local weakening under specific stress conditions, and induce very high-speed shearing which could be compared to a brittle deformation. The possible reactivation of deep-seated faults, as suggested by Kirby (1995) and Silver et al. (1995), probably occurs by the same mechanism.

A model to explain the origin of the intermediate-depth double seismic zone (DSZ) in the Wadati-Benioff zone by dehydration of serpentine was proposed by Nishiyama (1992) and Seno and Yamanaka (1996); and subsequent research by Peacock (2001), Omori et al. (2002) and Yamasaki and Seno (2003) discussed the details about this hypothesis. Omori et al. (2002) substantiated the hypothesis by demonstrating a close link between the predicted topology of dehydration reactions in a multi-component system and the distribution of intermediate-depth earthquakes.

4.2 Mesoscopic link between the double seismic zone and dehydrations

After the first discovery of a DSZ in NE Japan (Umino and Hasegawa, 1975), DSZs have been reported from most subduction zones. However, NE Japan is still the best studied area, because of dense and high-precision observations. The upper plane of the DSZ in NE Japan is separated from the lower plane by about 30–50 km, and the two planes gradually merge near a depth of 180 km (Fig. 7a). In NE Japan, the upper plane is partly within the oceanic crust, but the lower plane is definitely within the slab mantle (Zhao et al., 1997).

To explain the origin of the DSZ, the dehydration-induced earthquake model is favored, because it seems to be able to explain both the faulting under high-P and T conditions and the morphology of the hypocenter distribution of the DSZ. Previous studies (Nishiyama, 1992; Seno and Yamanaka, 1996; Peacock, 2001, Yamasaki and Seno, 2003) emphasized the similarity of the morphology of the DSZ and the location of antigorite (a member of the serpentine-group minerals) decomposition. However, the range of P-T conditions of lower-zone earthquakes is too wide to be explained by the simple dehydration of antigorite, even when the possible uncertainties of hypocentral determination, upon modeling the thermal structure in the phase diagram, and some kinetic effects on dehydration, are taken into account. Therefore a multi-component and multi-dehydration model was suggested by Omori et al. (2002). They

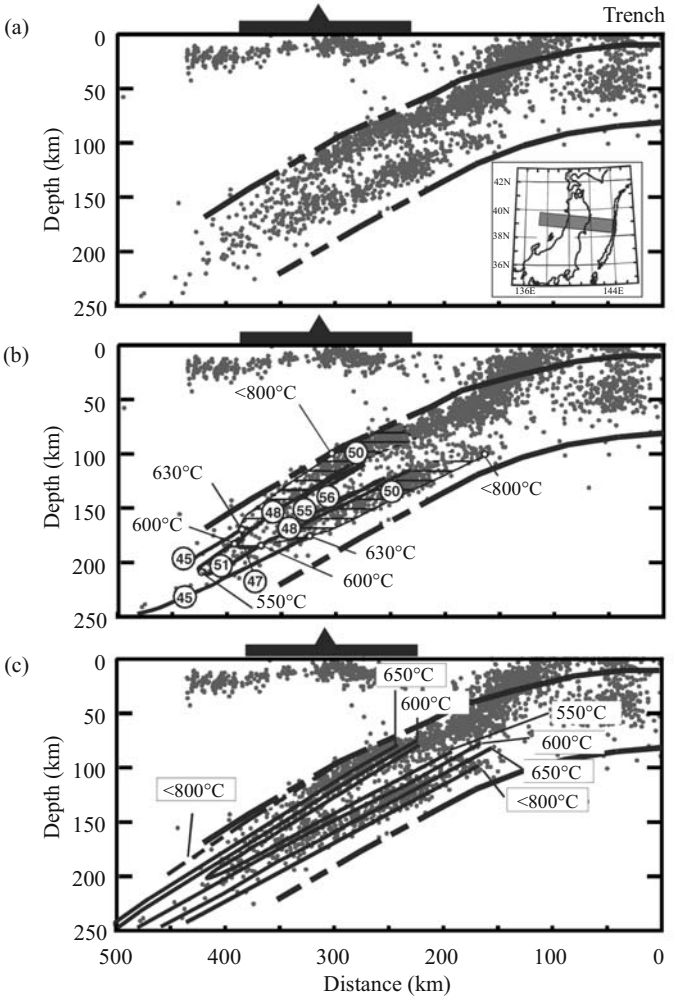

Figure 7. (a) The double seismic zone in the northeast Japan subduction zone. (b) An empirical link between the dehydrations in the slab peridotite and the double seismic zone. (c) Temperature in the subducting slab estimated by the dehydration induction model for the double seismic zone.

considered that the discrepancies between the simulations and observed geometry of the DSZ resulted from ignoring the dehydration reactions in a multi component system, as well as significant uncertainties in the numerical model for the thermal structure.

In the P-T diagram of Figure 2, there are fifteen dehydration reactions (Nos. 44–58) at the intermediate depth (<250 km): therefore the geometry of the DSZ should reflect the net of multi-reactions, if dehydration induces the earthquake. Figure 7a

shows a best-fit link between the dehydration reactions and the hypocenter distribution in the DSZ. In this link, the lower-zone of the DSZ consists of the dehydrations of antigorite and clinochlore (reactions 48, 50 and 52). The dehydration of clinochlore by reaction 50 is a continuous reaction which consumes clinochlore to form the Mg-tschermak component in enstatite. Therefore H_2O is released continuously. The thickness of the lower-zone is explained by the range of this continuous reaction. The convergence of the two zones at 180 km depth is represented by the dehydration of clinochlore to form Mg-surssasite by reaction 47, which is nearly temperature-independent below 650˚ C. The temperature estimated from the link (Fig. 7b) shows a similar geometry to the temperature given by numerical simulation, although the absolute value of the temperature of a part of the slab is generally higher than shown in previous simulations (e.g., Iwamori, 1998; Peacock, 2001).

4.3 Global depth distribution of earthquakes and dehydrations

Frohlich (1989) showed the bimodal depth-distribution of the world's subduction-zone seismicities by a sum of the hypocenter distributions of various subduction zones having different properties. Subduction velocity, subduction angle, and age of the plate are important properties in regard to the nature of water transport in the subduction zone, because these affect the temperature in the subducting slab. Hence, it is necessary to see the distribution of the hypocenters from place to place, to investigate the relation between the hypocenter distribution and dehydration events in the subducting slab. For this purpose, Omori et al. (2004) examined sixty-four profiles from eleven subduction zones (Fig. 8) using hypocenter data provided from the International Seismological Centre, ISC Catalogue from 1980 to 1998, except those for NE Japan, which were taken from Japan University Network Earthquake Catalog (JUNEC) Hypocenters File, 1985–1993. The profiles are classified into three types. Type 1 is for the subduction zones having only shallow to intermediate-depth earthquakes (eastern Kamchatka, Sumatra, Alaska, Mexico, and southern Chile); type 2 is for the subduction zones showing clear bimodal depth-distributions (western Kamchatka, Bolivia and northern Chile); and, type 3 is for the subduction zones having deep earthquakes, but without obvious bimodal depth-distributions (Kurile, NE-Japan, Mariana and Tonga). The dehydration induction model also explains such differences in the distribution of seismicities.

The predicted depth of dehydration events shows different patterns depending on the thermal condition of the slab. To compare such a pattern of dehydration with the hypocenter distribution, it is necessary to recompile the depth-distribution profiles in each subduction zone (Fig. 8) on the basis of a thermal index for each of profile. In previous studies, some qualitative relations between the subduction-zone properties and the temperature have been found. The age of the oceanic plate at the trench (At) can be considered as a first order approximation of the subduction zone temperature, since older plates are colder and younger plates are hotter (Stein and Stein, 1996). The subduction velocity (V) and angle (a) are also basic parameters for the subduction

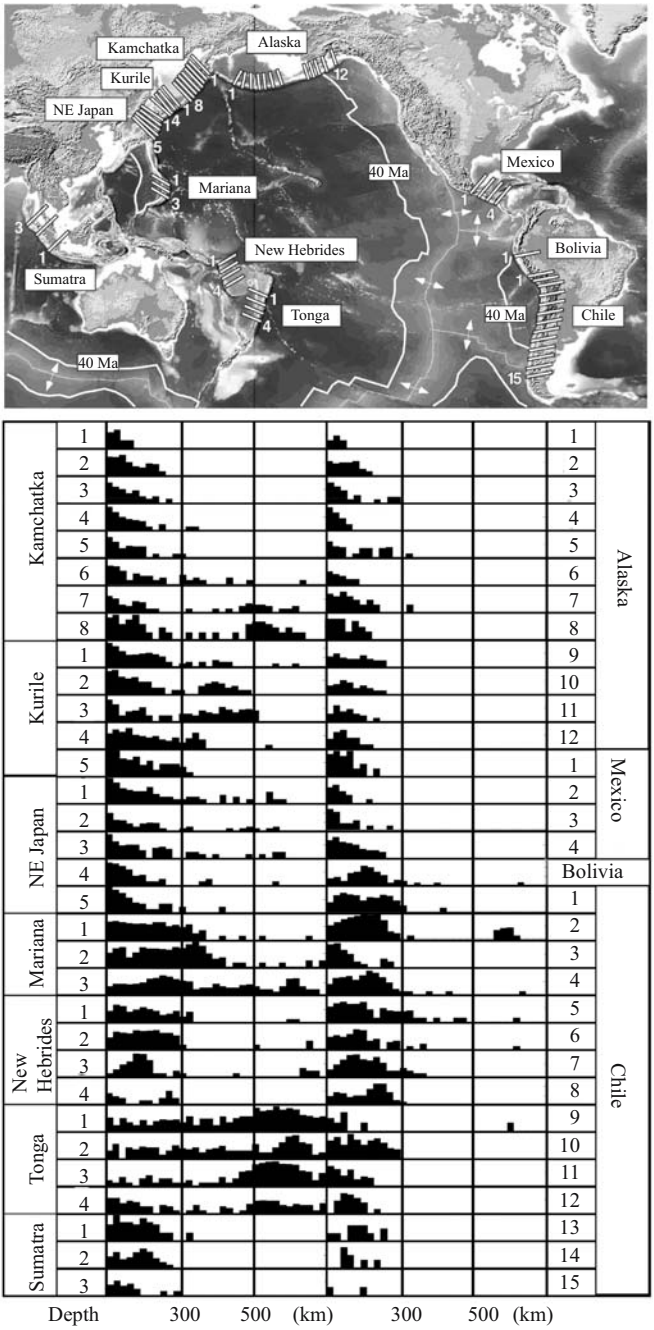

Figure 8. Global depth distributions of the subduction zone earthquakes.

zone temperature. Fast and steep subduction leads to a cooler slab compared to slow and flat subduction. The thermal parameter ($\varphi = VAt \sin a$) is an empirical thermal index, which includes At-V-a contributions, proposed by Kirby et al. (1991). It is known that there is a case when the age of the subducting plate is different from that at the trench and that in the subducted portion, due to relative motions between mid-oceanic ridges and trenches. Thus, Omori et al. (2004) introduced a secular change for the age of plate, and modified the thermal parameter to $\varphi(d) = VA(d)\sin a$, where d is a depth of a portion of the slab and A(d) is the age of the plate at that depth. All subduction-zone parameters were taken from Gorbatov and Kostoglodov (1997).

Figures 9a and b shows a comparison of the depth range of dehydration with the rearranged depth distribution of subduction-zone earthquakes using the $\varphi(d)$ as the relative temperature-index. The three features of the depth-distributed dehydration events outlined in the previous section are also evident in the $\varphi(d)$-d diagram (Fig. 9b); these are the maximum depths of deep dehydration, the concaved aseismic area, and the absence of deep dehydration in the hottest slabs. In Figure 9b, the

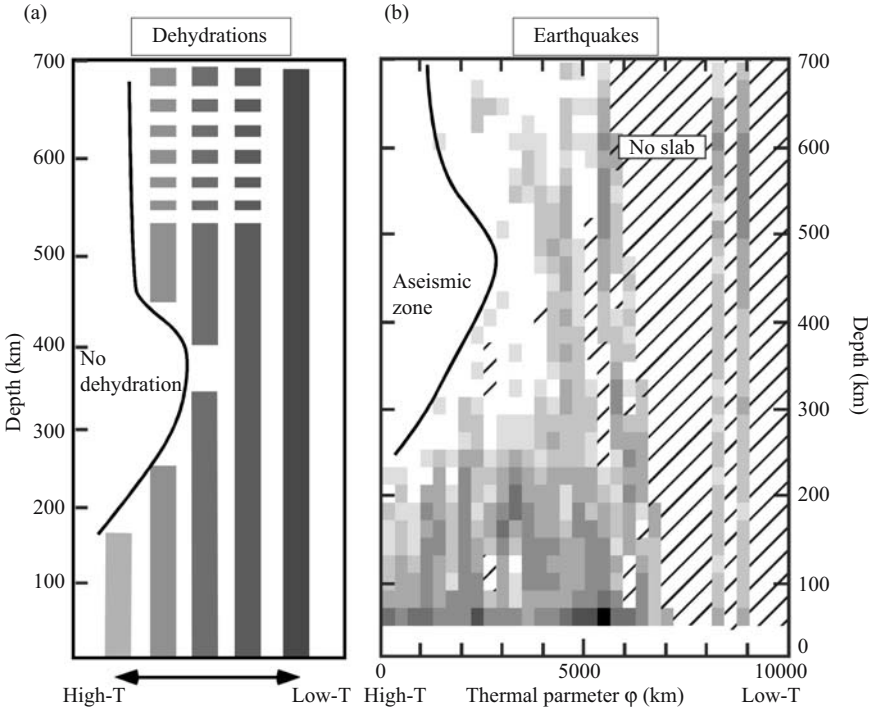

Figure 9. (a) Estimated depth distributions of the dehydration events in the subduction zone versus thermal condition in the slab. (b) Thermal parameter-depth of hypocenter diagram for the world's subduction zone earthquakes.

maximum depth of deep earthquakes is independent of the thermal parameter $\varphi > 4500$ km; and there is an aseismic area deeper than 640 km and $2800 < \varphi < 4500$ km. However, the maximum depth of deep earthquakes at φ around 1500–2800 km is still within the lower mantle-transition zone. This observation is a most consistent with the depth-distributed dehydration reactions. A possible explanation for the deep-aseismic area between $2800 < \varphi < 4500$ km is that dehydration reactions are promoted by the isobaric heating in the stagnant slab. In such a case, a higher-temperature slab can reach dehydration at a high-temperature, while cooler slabs will not achieve the temperature of dehydration. Additionally, the degree of heating depends on the subduction zone history, such as the degree of cooling of the mantle transition layer by the subducted slab. Due to such factors there will be some discrepancies between the dehydration distribution in natural subduction zones and that predicted by the simple model. The distinctive structure of a concaved aseismic area at $1200 < \varphi < 1500$ km, between 300–600 km depth, in Figure 9b is compared with the non-dehydration area in Figure 9a. The slabs that have φ around 8000 km, such as those in the Tonga subduction zone, show a continuous distribution of earthquakes from shallow to maximum depths. This type of distribution corresponds to dehydration distribution in the very low-T model (Fig. 9a). Such a distribution is also observed around $\varphi = 5000$ km; however, the continuity of slabs of $\varphi = 5000$–7500 km is not clear due to the lack of the slabs in this area. In the low-φ slab, the maximum depth of seismicity is limited to below about 250 km, and is consistent with the lack of deep dehydration in the high-T model slab.

The dehydration induction model for the deep seismicity suggests the dehydrations in the mantle transition zone and the existence of water above the stagnant slab. Recently, Ichiki et al. (2006) estimated that the upper-mantle under NE-China (250–400 km depth) contains 500–1000 ppm H/Si of H_2O by the electrical conductivity and P-wave velocity. This result supports the dehydration in the stagnant slab in the NE-Japan subduction zone, where the cold-130Ma Pacific plate is subducting.

5 DEEP HYDRATION OF THE PLATE

The hydration of peridotite in subduction zones is an important issue for water subduction. Mantle wedge peridotite is believed to be hydrated by water released from the subducting hydrated mid-oceanic ridge basalt (MORB) layer (e.g., Poli and Schmidt, 1995; Schmidt and Poli, 1998; Okamoto and Maruyama, 1999). This has been discussed in relation to island arc magmatism (e.g., Schmidt and Poli, 1998) and the hydrous low-T plume model (Gerya and Yuen, 2003). In contrast, hydration of subducting slab peridotite is controversial because there are neither plausible observations nor mechanical models showing that the slab is hydrated to substantial depth (Kerrick, 2002), although previous studies implicitly included hydrated slab peridotite in their water transport models (Shieh et al., 1998; Irifune et al.,1998; Frost and Fei, 1998; Frost, 1999; Ohtani et al., 2000; Ohtani et al., 2001; Angel et al., 2001).

Substantial hydration of slab peridotite down to 30–50 km depth from the plate surface was suggested in regard to the origin of the double seismic zone observed in the

slab, on the basis of the dehydration embrittlement hypothesis (Seno and Yamanaka, 1996; Peacock, 2001; Omori et al., 2002). Observations of seismic-velocity and a calculated Poisson's ratio provide evidence for hydration in the mantle (Christensen, 1996; Kamiya and Kobayashi, 2000). In the Kanto area of Japan, the Poisson's ratio in the Pacific plate subducted beneath Tokyo indicates substantial serpentinization of the peridotite up to 100 km from the top of the slab (Omori et al., 2002). Although such tomographic studies are limited in this area, the hydration of oceanic periodtite before subduction is a possible phenomenon, even in the fast-spreading Pacific ocean.

The hydration of the sub-oceanic uppermost mantle has been the focus of considerable discussion ever since Hess (1962). The petrogenesis of MORB suggests the existence of an almost dry mantle in the 30–20 km depth range at the mid-ocean ridge. However, a few possible mechanisms have been proposed to account for the hydration of the oceanic lithospheric mantle during its traverse from a mid-ocean ridge to a subduction zone, as has been determined by tomographic studies.

Peacock (2001) suggested that seawater could be injected deep into the crust along major faults in a subducting plate that was ruptured by trench-outer rise events. The close association between a double seismic zone and present-day deep events beneath the trench-outer rise was described by Seno and Yamanaka (1996). Kanamori (1971) suggested that significant normal faulting, caused by bending of the lithosphere, may rupture the oceanic plate up to 70 km depth below the trench. However, the observed maximum depth of the outer-rise event is limited to ca. 50 km (Seno and Yamanaka, 1996). Ranero et al. (2003) also discussed the role of bending-related faulting along a trench on the water penetration into the subducting plate to substantial depth. If the fault reaches considerable depth, and if water can infiltrate through such a fault, the oceanic mantle could be sufficiently hydrated to the depth of the lower plane of the double seismic zone.

Seawater could also infiltrate into the oceanic mantle via transform faults (Francis, 1981), or by high-temperature alteration of ultramafics in the upper-mantle beneath an oceanic fracture zone (Kimball et al., 1985). A topographic anomaly (ca. +400 m) parallel to oceanic fracture zones is a common oceanic feature (Bonatti, 1978). Bonatti (1978) proposed that serpentinite diapirism was related to such vertical tectonism. This observation supports the idea of water infiltration through transform faults, however these observations are limited to slow spreading ridges in the Atlantic Ocean. If such topographic anomalies are caused by serpentinite diapirism alone, then, on the basis of isostatic balance, a +400 m anomaly can only be explained by ca. 4 km depth of complete serpentinization. The degree of the anomaly is a function of the ratio and of the depth-limit of serpentinization. If a 1 volume percent of serpentinization down to 50 km depth is assumed, the expected topographic anomaly is about +30 m. Therefore, the lack of obvious topographic anomalies in the Pacific Ocean floor does not preclude the hydration of peridotite of the oceanic plate, because the degree of serpentinization in fast-spreading plates is considerably less than in the Atlantic Ocean.

The depth-limit for the penetration of sea water through a fault or fracture zone is not known. It is likely that there may be some barriers during penetration (Kerrick,

2002); namely, a fluid under lithostatic pressure is considered to move upward; and, crack sealing by interaction of wall rock and water may be a possible barrier to deep penetration. However, during the formation of serpentine from water+peridotite, there is a significant volume decrease that may induce a form of chemical-pumping. Moreover, vertical tectonism associated with serpentinization may assist the hydration of the slab peridotite. Although such factors are difficult to assess quantitatively, the idea of water infiltration into the deep oceanic plate should not be discarded.

6 IMPLICATIONS FOR THE EARTH'S DYNAMICS

In the present Earth, stagnation of the slab is observed in most subduction zones, and most water is considered to be released in the mantle transition zone. However, where the slab has penetrated into the lower mantle in low-temperature subduction zones, such as Tonga, earthquakes at 700 km depth are observed, and transportation of the water to the upper part of the lower mantle is suggested.

A cold and stagnated subduction zones are evident in the western Pacific and East Asia, where the upper mantle has the lowest temperature worldwide, as observed in the thickness of the mantle transition zone (Fig. 4). This zone has a temperature of about 200–300K lower than that of a standard mantle transition zone; and yet this region has active magmatism, seismicity, and deformation in fragmented continental blocks and oceanic micro-plates. Predictably this reflects the ubiquitous occurrence of water-rich fluids in the upper mantle and crust of this region. High-resolution seismic tomography of this area shows a low-V anomaly just above the MTZ connected to the intracontinental volcano of Changbai, NE Asia (Lei and Zhao, 2005; Zhao et al., 2007). This observation supports the view of dehydration in the stagnant slab and indicates that water transported from the surface significantly affects the upper mantle dynamics.

Water transportation also has a significant role in the history of Earth's dynamics. Irreversible cooling of the Earth's interior leads to a decline of material circulation in the solid Earth. Instead, a cooler mantle allows much water to be carried into the deeper mantle, and rheological activation, such as a cold plume suggested by Gerya and Yuen (2003), is expected. Thus, subduction and dehydration of hydrous minerals have the role of negative feedback to stabilize the mantle-surface thermal and material system. Maruyama and Liou (2005) suggested that such an activation in the upper-mantle occurred at the Precambrian-Cambrian boundary thereby recovering the Earth from the snowball to make it habitable.

In the future, further cooling will cause more effective water transportation to Earth's deep mantle. In this case, dehydration in the upper mantle will cease. When the MTZ become cool enough, upper mantle dynamics would be significantly reduced. The surface water will enter to the lower-mantle in such cold condition, and some dehydration reactions are expected in the deeper part of the lower-mantle. Dehydration in the lower-most mantle will activate lower-mantle dynamics so that a plume or superplume will continue in the old and cold planet. This speculation suggests the important role for superplumes in the late stage of a terrestrial planet. In comparative

planetology concerning Mars and the Earth, the role of water in the mantle may play an important role for contrasting fates of these planets and life (Baker et al., 2007; Dohm et al., 2007 in this book).

ACKNOWLEDGEMENTS

We are grateful to S. Maruyama for discussions. We also thank A. Hasegawa, T. Matsuzawa, and D. Zhao for earlier discussions about the double seismic zone in NE-Japan. The manuscript was improved by constructive comments by V. Baker.

REFERENCES

Akaogi, M., and S. Akimoto (1980) High-pressure stability of a dense hydrous magnesian silicate $Mg_{23}Si_8O_{42}H_6$ and some geophysical implications. *J. Geophys. Res.*, 85, 6944–6948.

Angel, R.J., D.J. Frost, N.L. Ross, and R.J. Hemley (2001) Stabilities and equations of state of dense hydrous magnesium silicates. *Phys. Earth Planet. Inter.*, 127, 181–196.

Baker, V., S. Maruyama, and J. Dohm (2007) Tharsis superplume and the geological evolution of early Mars. In Yuen, D.A., S. Maruyama, S. Karato, and B.F. Windley (eds.) Superplumes: Beyond Plate Tectonics, Springer, Dordrecht, pp. 507–522.

Bebout, G.E., D.W. Scholl, S.H. Kirby, and J.P. Platt (eds.) (1996) Subduction Top to Bottom, Geophysical Monograph, American Geophysical Union, 96, 384p.

Bina, C.R., and A. Navrotsky (2000) Possible presence of high-pressure ice in cold subducting slabs. *Nature*, 408, 844–847.

Bonatti, E. (1978) Vertical tectonism in oceanic fracture zones. *Earth Planet. Sci. Lett.*, 37, 369–379.

Bose, K., and A. Navrotsky (1998) Thermochemistry and phase equilibria of hydrous phases in the system $MgO\text{-}SiO_2\text{-}H_2O$: Implications for volatile transport to the mantle. *J. Geophys. Res.*, 103(B5), 9713–9719.

Bromiley, G.D., and A.R. Pawley (2002) The high-pressure stability of Mg-sursassite in a model hydrous peridotite: A possible mechanism for the deep subduction of significant volumes of H_2O. *Contrib. Mineral. Petrol.*, 142, 714–723.

Bromiley, G.D., and A.R. Pawley (2003) The stability of antigorite in the systems $MgO\text{-}SiO_2\text{-}H_2O$ (MSH) and $MgO\text{-}Al_2O_3\text{-}SiO_2\text{-}H_2O$ (MASH): The effects of Al^{3+} substitution on high-pressure stability. *Am. Mineral.*, 88, 99–108.

Chen, J., T. Inoue, D.J. Weidner, Y. Wu, and M.T. Vaughan (1998) Strength and water-weakening of mantle minerals, olivine, wadsleyite and ringwoodite. *Geophys. Res. Lett.*, 25, 575–578.

Christensen, N. (1996) Poissons's ratio and crustal seismology. *J. Geophys. Res.*, 101, 3139–3156.

Dobson, D.P., P.G. Meredith, and S.A. Boon (2002) Simulation of subduction zone seismicity by dehydration of serpentine. *Science*, 298, 1407–1410.

Dohm, J., V. Baker, and R. Anderson (2007) Traits and evolution of the Tharsis superplume, Mars. In Yuen, D.A., S. Maruyama, S. Karato, and B.F. Windley (eds.) Superplumes: Beyond Plate Tectonics, Springer, Dordrecht, pp. 523–536.

Faust, J., and E. Knittle (1994) Static compression of chondrodite: Implications for water in the upper mantle. *Geophys. Res. Lett.*, 21, 1935–1938.

Fei, Y., H.-k. Mao, and R.J. Hemley (1993) Thermal expansivity, bulk modulus, and melting curve of H_2O-ice VII to 20 GPa. *J. Chem. Phys.*, 99(7), 5369–5373.

Flanagan, M.P., and P.M. Shearer (1998) Global mapping of topography on transition zone velocity discontinuities by stacking SS precursors. *J. Geophys. Res.*, 103, 2673–2692.

Fockenberg, T. (1998) An experimental study of the pressure-temperature stability of MgMgAl-pumpellyite in the system $MgO\text{-}Al_2O_3\text{-}SiO_2\text{-}H_2O$. *Am. Mineral.*, 83, 220–227.

Francis, T.J.G. (1981) Serpentinization faults and their role in the tectonics of slow spreading ridges. *J. Geophys. Res.*, 86, 11616–11622.

Frohlich, C. (1989) The nature of deep-focus earthquakes. *Ann. Rev. Earth Planet. Sci.*, 17, 227–254.

Frost, D.J. (1999) The stability of dense hydrous magnesium silicates in Earth's transition zone and lower mantle. In Fei, Y., C.M. Bertka, and B.O. Mysen (eds.) Mantle Petrology: Field Observations and High Pressure Experimentation: A Tribute to Francis R. (Joe) Boyd, The Geochemical Society, pp. 283–296.

Frost, D.J., and Y. Fei (1998) Stability of phase D at high pressure and high temperature. *J. Geophys. Res.*, 103(B4), 7463–7474.

Fukao, Y., S. Widiyantoro, and M. Obayashi (2001) Stagnant slabs in the upper and lower mantle transition region. *Rev. Geophys.*, 39, 291–323.

Gasparik, T. (1993) The role of volatiles in the transition zone. *J. Geophys. Res.*, 98(B3), 4287–4299.

Gerya, T.V., and D.A. Yuen (2003) Rayleigh-Taylor instabilities from hydration and melting propel 'cold plumes' at subduction zones. *Earth Planet. Sci. Lett.*, 212, 47–62.

Gorbatov, A., and V. Kostoglodov (1997) Maximum depth of seismicity and thermal parameter of the subducting slab: General emprical relation and its application. *Tectonophys*., 277, 165–187.

Grevel, K.-D., J. Majzlan, A. Navrotsky, W.A. Kahl, and D.W. Fasshauer (2001) Thermodynamic data of the high-pressure phase $Mg_5Al_5Si_6O_{21}(OH)_7$ (Mg-sursassite). *Phys. Chem. Mineral.*, 28, 475–487.

Hacker, B.R., G.A. Abers, and S. Peacock (2003) Subduction factory 1. Theoretical mineralogy, densities. Seismic wave speeds, and H_2O contents. *J. Geophys. Res.*, 108, 2029, doi:10.1029/2001JB001127.

Hess, H.H. (1962) History of ocean basins. In A.E.J.E. Angel et al. (eds.) Petrological Studies: A Volume in Honor of A.F. Buddington, GSA, pp. 599–620.

Hirano, N., Y. Ogawa, K. Kawamura, M. Hattori, and K. Saito (2001) A new type of intra-plate volcanism; young alkali-basalts discovered from the subducting Pacific Plate, Northern Japan Trench. *Geophys. Res. Lett.*, 28, 2719–2722.

Hirth, G. and D.L. Kohlstedt (1996) Water in the oceanic upper mantle -implications for rheology, melt extraction and the evolution of the lithosphere. *Earth Planet. Sci. Lett.*, 144, 93–108.

Holland, T.J.B., and R. Powell (1998) An internally-consistent thermodynamic data set for phases of petrological interest. *J. Metamorphic Geol.*, 16, 309–343.

Ichiki, M., K. Baba, M. Obayashi, and H. Utada (2006) Water content and geotherm in the upper mantle above the stagnant slab: Interpretation of electrical conductivity and seismic P-wave velocity models. *Phys. Earth Planet. Inter.*, 155, 1–15.

Inoue, T. (1994) Effect of water on melting phase relations and melt composition in the system Mg_2SiO_4-$MgSiO_3$-H_2O up to 15 GPa. *Phys. Earth Planet. Inter.*, 85, 237–263.

Irifune, T., N. Kubo, M. Isshiki, and Y. Yamasaki (1998) Phase transformations in serpentine and transportation of water into the lower mantle. *Geophys. Res. Lett.*, 25(2), 203–206.

Iwamori, H. (1998) Transportation of H_2O and melting in subduction zones. *Earth Planet. Sci. Lett.*, 160, 65–80.

Iwamori , H. (2004) Phase relations of peridotites under H_2O-saturated conditions and ability of subducting plates for transportation of H_2O. *Earth Planet. Sci. Lett.*, 227, 57–71.

Kamiya, S., and Y. Kobayashi (2000) Seismological evidence for the existence of serpentinized wedge mantle. *Geophys. Res. Lett.*, 27, 819–822.

Kanamori, H. (1971) Seismological evidence for a lithospheric normal faulting—The Sanriku earthquake of 1933. *Phys. Earth and Planet. Inter.*, 4, 289–300.

Kanzaki, M. (1991) Stability of hydrous magnesium silicates in the mantle transition zone. *Phys. Earth Planet. Inter.*, 66, 307–312.

Karato, S. (2007) Microscopic models for the effects of hydrogen on physical and chemical properties of Earth materials. In Yuen, D.A., S. Maruyama, S. Karato, and B.F. Windley (eds.) Superplumes: Beyond Plate Tectonics, Springer, Dordrecht, pp. 321–356.

Karato, S., and H. Jung (1998) Water, partial melting and the origin of the seismic low velocity and high attenuation zone in the upper mantle. *Earth Planet. Sci. Lett.*, 157, 193–207.

Karato, S., M.S. Paterson, and J.D. Fiz Gerald (1986) Rheology of synthetic olivine aggregates -influence of grain-size and water. *J. Geophys. Res.*, 91, 8151–8176.

Kawamoto, T. (2004) Hydrous phase stability and partial melt chemistry in H_2O-saturated KLB-1 peridotite up to the uppermost lower mantle conditions. *Phys. Earth Planet. Inter.*, 143–144, 387–395.

Kerrick, D. (2002) Serpentinite seduction. *Science*, 298, 1344–1345.

Kimball, K.L., F.S. Spear, and H.J.B. Dick (1985) High temperature alteration of abyssal ultramafics from the Islas Orcadas fracture zone, South Atlantic. *Contrib. Mineral. Petrol.*, 91, 307–320.

Kirby, S. (1995) Intraslab earthquakes and phase changes in subducting lithosphere. *Rev. Geophys., supplement*, 33, 287–297.

Kirby, S., W.B. Durham, and L.A. Stern (1991) Mantle phase changes and deep-earthquake faulting in subducting lithosphere. *Science*, 252, 216–225.

Komabayashi, T., K. Hirose, K.-i. Funakoshi, and N. Takafuji (2005a) Stability of phase A in antigorite (serpentine) composition determined by in-situ X-ray pressure observations. *Phys. Earth Planet. Inter.*, 151, 276–289.

Komabayashi, T., S. Omori, and S. Maruyama (2004) Petrogenetic grid in the system MgO-SiO_2-H_2O up to 30 GPa, 1600°C: Applications to hydrous peridotite subducting into the Earth's deep interior. *J. Geophys. Res.*, 109, B03206, doi:10.1029/2003JB002651.

Komabayashi, T., S. Omori, and S. Maruyama (2005b) Experimental and theoretical study of stability of dense hydrous magnesium silicates in the deep upper mantle. *Phys. Earth Planet. Inter.*, 153, 191–209.

Komabayashi, T., and S. Omori (2006) Internally consistent thermodynamic data set for dense hydrous magnesium silicates up to 35 GPa, 1600°C: Implications for water circulation in the Earth's deep mantle. *Phys. Earth Planet.*, 56, 89–107.

Lei, J., and D. Zhao (2005) P-wave tomography and origin of the Changbai intraplate volcano in Northeast Asia. *Tectonophysics*, 397, 281–295.

Litasov, K., E. Ohtani, F. Langenhorst, H. Yurimoto, T. Kubo, and T. Kondo (2003) Water solubility in Mg-perovskites and water storage capacity in the lower mantle. *Earth Planet. Sci. Lett.*, 211, 189–203.

Liu, L.-G. (1987) Effects of H_2O on the phase behaviour of the forsterite-enstatite system at high pressures and temperatures and implications for the Earth. *Phys. Earth Planet. Inter.*, 49, 142–167.

Luth, R.W. (1995) Is phase A relevant to the Earth's mantle? *Geochim. Cosmochim. Acta*, 59 (4), 679–682.

Maruyama, S., and J.G. Liou (2005) From Snowball to Phaneorozic Earth. *Inter. Geol. Rev.*, 47, 775–791.

Maruyama, S., D.A. Yuen, and B.F. Windley (2007) Dynamics of plumes and superplumes through time. In Yuen, D.A., S. Maruyama, S. Karato, and B.F. Windley (eds.) Superplumes: Beyond Plate Tectonics, Springer, Dordrecht, pp. 441–502.

Meade, C., and R. Jeanloz (1991) Deep-focus earthquakes and recycling of water into Earth's mantle. *Science*, 252, 68–72.

Mibe, K., T. Fujii, and A. Yasuda (1998) Connectivity of aqueous fluid in the Earth's upper mantle. *Geophys. Res. Lett.*, 25, 1233–1236.

Mysen, B.O., P. Ulmer, J. Konzett, and M.W. Schmidt (1999) The upper mantle near convergent plate boundaries. In R.J. Hemley (ed.), Ultrahigh-pressure Mineralogy, Vol. 37, pp. 97–138.

Nishiyama, T. (1992) Mantle hydrology in a subduction zone: A key to episodic geologic events, double Wadati-Benioff zones and magma genesis, In Mathematical Seismology VII, Report of The Institute of Statistical Mathematics, Tokyo, 34, 31–67.

Ohtani, E., H. Mizobata, and H. Yurimoto (2000) Stability of dense hydrous magnesium silicate phases in the systems Mg_2SiO_4-H_2O and $MgSiO_3$-H_2O at pressures up to 27 GPa. *Phys. Chem. Minerals*, 27, 533–544.

Ohtani, E., M. Toma, K. Litasov, T. Kubo, and A. Suzuki (2001) Stability of dense hydrous magnesium silicate phases and water storage capacity in the transition zone and lower mantle. *Phys. Earth Planet. Inter.*, 124, 105–117.

Okamoto, K., and S. Maruyama (1999) The high-pressure synthesis of lawsonite in the MORB + H_2O system. *Am. Mineral.*, 84, 362–373.

Omori, S., S. Kamiya, S. Maruyama, and D. Zhao (2002) Morphology of the intraslab seismic zone and devolatilization phase equilibria of the subducting slab peridotite. *Bull. Earthq. Res. Inst. Univ. Tokyo*, 76, 455–478.

Omori, S., T. Komabayashi, and S. Maruyama (2004) Dehydration and earthquakes in the subducting slab: Empirical link in intermediate and deep seismic zones. *Phys. Earth Planet. Inter.*, 146, 297–311.

Pawley, A. (2000) Stability of clinohumite in the system MgO-SiO_2-H_2O. *Contrib. Mineral. Petrol.*, 138, 284–291.

Pawley, A. (2003) Chlorite stability in mantle peridotite: The reaction clinochlore + enstatite = forsterite + pyrope + H_2O. *Contrib. Mineral. Petrol.*, 144, 449–456.

Peacock, S. (1996) Thermal and petrologic structure of subduction zones. In Bebout et al. (eds.) Subduction Top to Bottom, AGU Geophys. Monogr., 96, 119–133.

Peacock, S. (2001) Are the lower planes of double seismic zones caused by serpentine dehydration in subducting oceanic mantle ? *Geology*, 29, 299–302.

Poli, S., and M.W. Schmidt (1995) H_2O transport and release in subduction zones: Experimental constraints on basaltic and andesitic systems. *J. Geophys. Res.*, 100(B11), 22299–22314.

Poli, S., and M. Schmidt (2002) Petrology of subducted slabs. *Ann. Rev. Earth Planet. Sci*., 30, 207–235.

Raleigh, C.B., and M.S. Paterson (1965) Experimental deformation of serpentinite and its tectonic implications. *J. Geophys. Res.*, 70, 3965–3985.

Ranero, C.R., J. Phipps Morgan, K. McIntosh, and C. Reichert (2003) Bending-related faulting and mantle serpentinization at the Middle America trench. *Nature*, 425, 367–373.

Ringwood, A.E., and A. Major (1967) High-pressure reconnaissance investigations in the system Mg_2SiO_4-MgO-H_2O. *Earth Planet. Sci. Lett.*, 2, 130–133.

Schmidt, M.W., and S. Poli (1998) Experimentally based water budgets for dehydrating slabs and consequences for arc magma generation. *Earth Planet. Sci. Lett.*, 163, 361–379.

Seno, T., and Y. Yamanaka (1996) Double seismic zones, compressional deep trench-outer rise events, and superplumes. In Bebout et al., (eds.) Subduction Top to Bottom, AGU Geophys. Monogr., 96, pp. 347–355.

Shearer P.M., and T.G. Masters (1992) Global mapping of topography on the 660-km discontinuity. *Nature*, 355, 791–796.

Shieh, S.R., H.-k. Mao, R.J. Hemley, and L.C. Ming (1998) Decomposition of phase D in the lower mantle and the fate of dense hydrous silicates in subducting slabs. *Earth Planet. Sci. Lett.*, 159, 13–23.

Shinmei, T., N. Tomioka, K. Fujino, K. Kuroda and T. Irifune (1999) In situ X-ray diffraction study of enstatite up to 12 GPa and 1473 K and equations of state. *Am. Mineral.*, 84, 1588–1594.

Silver, P.G., S.L. Beck, T.C. Wallace, C. Meade, S.C. Myers, D.E. James, and R. Kuehnel (1995) Rupture characteristics of the deep Bolivian earthquake of 9 June 1994 and the mechanism of deep-focus earthquakes. *Science*, 268, 69–73.

Stein, S., and C.A. Stein (1996) Thermo-mechanical evolution of oceanic lithosphere: Implications for the subduction process and deep earthquakes. In Bebout et al. (eds.) Subduction Top to Bottom, AGU Geophys. Monogr., 96, pp. 1–17.

Ulmer, P., and V. Trommsdorff (1995) Serpentine stability to mantle depths and subduction-related magmatism. *Science*, 268, 858–861.

Umino, N. and A. Hasegawa (1975) On the two-layered structure of deep seismic plane in northeastern Japan arc (in Japanese with English abstract). *J. Seis. Soc. Jpn.*, 27, 125–139.

Watson E.B., and J.M. Brenan (1987) Fluids in the lithosphere, 1. Experimentally-determined wetting characteristics of CO_2-H_2O fluids and their implications for fluid transport, host-rock physical properties, and fluid inclusion formation. *Earth Planet. Sci. Lett.*, 85, 497–515.

Wessel, P. (1997) Sizes and ages of seamounts using remote sensing: Implications for intraplate volcanism. *Science*, 277, 802–805.

Wunder, B. (1998) Equilibrium experiments in the system MgO-SiO_2-H_2O (MSH): Stability fields of clinohumite-OH [$Mg_9Si_4O_{16}(OH)_2$], chondrodite-OH [$Mg_5Si_2O_8(OH)_2$] and phase A ($Mg_7Si_2O_8(OH)_6$). *Contrib. Mineral. Petrol*., 132, 111–120.

Wunder, B., and W. Schreyer (1997) Antigorite: High-pressure stability in the system MgO-SiO_2-H_2O (MSH). *Lithos*, 41, 213–227.

Yamamoto, K., and S. Akimoto (1977) The system MgO-SiO_2-H_2O at high pressures and temperatures-stability field for hydroxyl-chondrodite, hydroxyl-clinohumite and 10 _-phase. *Am. J. Sci.*, 277, 288–312.

Yamasaki, T., and T. Seno (2003) Double seismic zone and dehydration embrittlement of the subducting slab. *J. Geophys. Res.*, 108, doi: 10.1029/2002JB001918.

Zhao, D. (2004) Global tomographic images of mantle plumes and subducting slabs: Insight into deep Earth dynamics. *Phys. Earth Planet. Inter.*, 146, 3–34.

Zhao, D., S. Maruyama, and S. Omori (2007) Mantle dynamics of Western Pacific and East Asia: Insight from seismic tomography and mineral physics. *Gondwana Research*, 11, 120–131.

Zhao, D., T. Matsuzawa, and A. Hasegawa (1997) Morphology of the subducting slab boundary in the northeastern Japan arc. *Phys. Earth Planet. Inter.*, 102, 89–104.

CHAPTER 6

FINE-SCALE ULTRA-LOW VELOCITY ZONE LAYERING AT THE CORE-MANTLE BOUNDARY AND SUPERPLUMES

EDWARD J. GARNERO, MICHAEL S. THORNE[1], ALLEN MCNAMARA, AND SEBASTIAN ROST[2]

School of Earth and Space Exploration, Arizona State University, Tempe, Arizona 85287-1404, USA; E-mail: garnero@asu.edu

[1]*Now at Arctic Region Supercomputing Center, University of Alaska, Fairbanks, Alaska 99775-6020, USA*

[2]*Now at School of Earth and Environment Earth Sciences, The University of Leeds, Leeds LS6 9JT, UK*

Abstract

Ultra-low velocity layering at the Earth's core-mantle boundary (CMB) has now been detected using a variety of seismic probes. *P*- and *S*-wave velocity reductions of up to 10's of percent have been mapped in a thin (5–50 km) layer, which commonly underlies reduced seismic shear wave speeds in the overlying few 100 km of the mantle. Ultra-low velocity zones (ULVZ) contain properties consistent with partial melt of rock at the very base of the mantle. Strong evidence now exists for a significant density increase in the layer (∼5–10% greater than reference models), which must be included in dynamical scenarios relating ULVZ partial melt to deep mantle plume genesis. 3-D geodynamical calculations involving an initially uniform dense layer in the lowermost few 100 km of the mantle result in thermo-chemical piles that are geographically well-correlated with seismic tomography low velocities, when past plate motions are imposed as a surface boundary condition. The hottest lower mantle regions underlay edges of the dense thermo-chemical piles. A scenario is put forth where these piles geographically correlate with ultra-low velocity zones, and subsequent mantle plume genesis.

1 INTRODUCTION

In the past decade increasing evidence has been put forth linking the seismic structure of the deepest mantle to overall mantle dynamics and chemistry on a variety of scale lengths (e.g., 100–3000 km, see Wysession, 1996; van der Hilst and Kárason; 1999; Wysession et al., 1999; Masters et al., 2000; Garnero, 2000; Deschamps and

D. A. Yuen et al. (eds.), Superplumes, 139–158.
© 2007 *Springer.*

Table 1. Seismically observed lower mantle layering features

Deep mantle feature	Thickness at base of mantle (km)	Velocity perturbation (%)		Notes
		δV_S	δV_P	
D″ discontinuity	200–300	2 to 3	$\sim< 1$	δV_P discontinuity difficult to detect
D″ anisotropy	200–300	1 to 2	Unconstrained	Mechanism still poorly resolved
ULVZ	5–30	−10 to −30	−5 to −10	ULVZ density an important parameter
Large low velocity provinces	500–1500	−3 to −12	−1 to −3	Sharp sides, likely chemically distinct

Trampert, 2003; Lay et al., 2004; Lay and Garnero, 2004). It has been known for over 50 years that the structure of the lowermost few hundred km of the mantle, the D″ region (Bullen, 1949) differs from overlying mantle structure. Recent studies using regional forward modeling of seismic waveforms and travel times reveal complex structure on a variety of both radial and lateral scale lengths, in contrast to the bulk of the lower mantle. Features detected in D″ include evidence for a seismic velocity discontinuity (the D″ discontinuity) some 200–300 km above the CMB (e.g., see Wysession et al., 1998), anisotropy in the lowermost few 100 km of the mantle (e.g., Kendall and Silver, 1998; Lay et al., 1998; Kendall, 2000), as well as thin ultra-low velocity layering in the deepest 5–50 km of the mantle (e.g., see Thorne and Garnero, 2004). The seismic characteristics of these features are summarized in the Table 1. A principal challenge is to constrain the origin of these features, as well as their possible connection to the evolution and dynamic behavior of the lower mantle. In this regard, incorporating information from other geophysical disciplines will be crucial.

For decades, the general presence of two long wavelength low velocity regions at the base of the mantle has been noted (e.g., Dziewonski, 1984; Romanowicz, 1991). This degree-two pattern of velocity reductions is particularly evident for shear velocities (V_S). These low velocity regions generally underlie the locations of surface hot spot volcanism, and do not underlie regions of past or present subduction (e.g., Morgan, 1971, 1972; Hager et al., 1985; Duncan and Richards, 1991), suggesting an interaction between the shallowest and deepest mantle. The large-scale low velocities detected through seismic tomography have been dubbed "super" or "mega" plumes (e.g., Tackley, 2000). However, it has not been demonstrated that these low-velocity regions actually constitute a plume (as in upwelling) as opposed to a pile (as in some form of dense and possibly stable dreg).

One challenge in distinguishing between a plume upwelling and stable dense pile lies in the difficulties of seismically resolving the detailed nature of high- or low-velocities in the mid-mantle. Tomographic imaging typically resolves structure on the order of 1000+ km laterally (see Fig. 1), while plumes may be an order of magnitude smaller. For example, a plume conduit in the mid mantle could have a diameter of roughly 100–400 km (e.g., Ji and Nataf, 1998). Although tomographic imaging

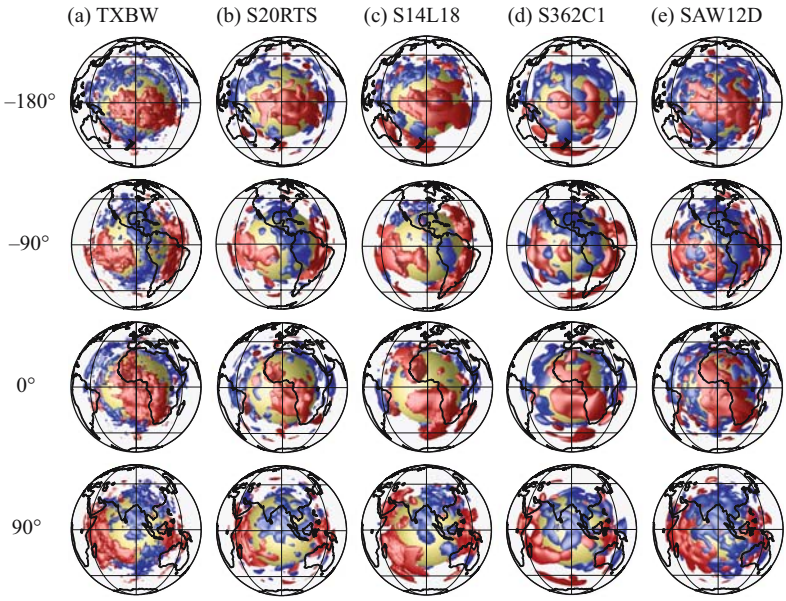

Figure 1. Iso-contoured shear velocity heterogeneity in the lower mantle from five different tomographically derived models: (a) TWBX (Grand, 2002), (b) S20RTS (Ritsema and van Heijst, 2000), (c) S14L18 (Masters et al., 2000), S362C1 (Gu et al., 2001), and SAW (Mégnin and Romanowicz, 2000). Iso-velocity surfaces are shown, where the low velocity (red) and high velocity (blue) surfaces represent at −0.8 and +0.8%, respectively, relative to global 1-D reference velocity structures. Longitude of the viewing perspective is shown to the left of each row. The −180° and 0° views display the degree 2 low shear velocity anomalies beneath the Pacific Ocean and southern Atlantic Ocean/Africa, respectively. Iso-velocity contours are shown for the bottom 1800 km of the mantle. The core-mantle boundary is shown in yellow.

has typically been unable to resolve structures with length scales as small as plume conduits, recent finite frequency based tomographic imaging of Montelli et al. (2004) reports mapping of low compressional velocities (V_P) from the Earth's surface to large mantle depths beneath several hot spots. At the time of this writing, tomographic imaging of V_S structure has not yet corroborated this result.

Body wave studies are able to provide a greater level of detail in seismic imaging than tomography, especially near the core-mantle boundary (CMB) where various reflections, refractions, and diffractions of seismic energy occur. However, a main restriction in high-resolution body wave studies is the geographic coverage limitations imposed by earthquake-to-seismic recording network configurations. It is particularly challenging if high numbers of seismometers (e.g., >20) are desired over small surface spatial scales (e.g., <100–300 km). Nonetheless, recent body wave analyses have complemented the earlier findings from tomographic inversions of global travel time data sets, adding detail to some of the long wavelength features observed in tomographic models (see recent discussions by Lay et al., 2004; Lay and Garnero,

2004; Garnero, 2004). One notable example is the evidence for multi-pathing (i.e., the presence of two distinct seismic arrivals) in broadband data that sample near the edge of the African low-Velocity anomaly (e.g., Helmberger and Ni, 2005). Multi-pathing is consistent with a sharp (i.e., 10's of km) transition from ambient mantle into the low velocity region. Similar evidence now exists for the Pacific Ocean low velocity anomaly (Ford et al., 2006; To et al., 2005).

In the remainder of this chapter, we discuss scenarios that relate these large-scale low velocity provinces to ultra-low velocity zone (ULVZ) structure and whole mantle plumes. At present, considerable uncertainty exists in precisely constraining elastic properties through seismic imaging, and hence propagations uncertainties to the geodynamic modeling. However, several possibilities can be discussed that form a self-consistent dynamical and chemical system.

2 DEEP MANTLE SEISMIC AND GEODYNAMIC STRUCTURES

2.1 Long wavelength deep mantle patterns

As displayed in Figure 1, large-scale features dominate tomographically derived S-wave velocity perturbations in the lower mantle. Many regional seismic studies have documented structure at scales much smaller than those seen in Figure 1 (see review by Garnero, 2000). It is still unresolved whether tomography accurately depicts the general shape of deep mantle heterogeneity or a smoothed version of much smaller scale, higher amplitude heterogeneity. Nonetheless, several higher resolution studies using waveform and travel time information have recently documented sharp edges to the low velocity patterns seen in tomography (Wen, 2001; Ni et al., 2002; Ni and Helmberger, 2003a,b; Helmberger and Ni, 2005; Ford et al., 2006; To et al., 2005). Thus, the general shapes of the degree-two lows seen in tomography may in fact approximate a smoothed version of Earth's large-scale velocity reductions in the deepest mantle. Though it is important to emphasize that regional studies do not mandate this possibility.

It is instructive to compare various available deep mantle seismic and geodynamic findings, in order to better understand possible dynamical implications of the detected seismic structures, particularly as they relate to ULVZ's. Figure 2a shows D″ shear velocity perturbations (δV_S) for the TXBW model (as in Fig. 1a). Only heterogeneities with amplitudes stronger than $\pm 0.5\%$ are shown. The edges of the degree two low velocity anomalies in this tomographic study contains the strongest lateral gradients in shear wave speeds (as shown in Fig. 2b); these regions of strongest S-wave velocity lateral gradients show a strong correlation to surface hot spot volcanism locations (Thorne et al., 2004), and are detected far from predicted deep mantle locations of subducted material (Fig. 2c). This suggests a connection between subduction and lower mantle structure, that is, whole mantle convection. Furthermore, the strong lateral velocity gradients at the edges of the lowest-velocity regions of the lower mantle point towards the existence of thermo-chemical heterogeneity as source for the detected low velocities.

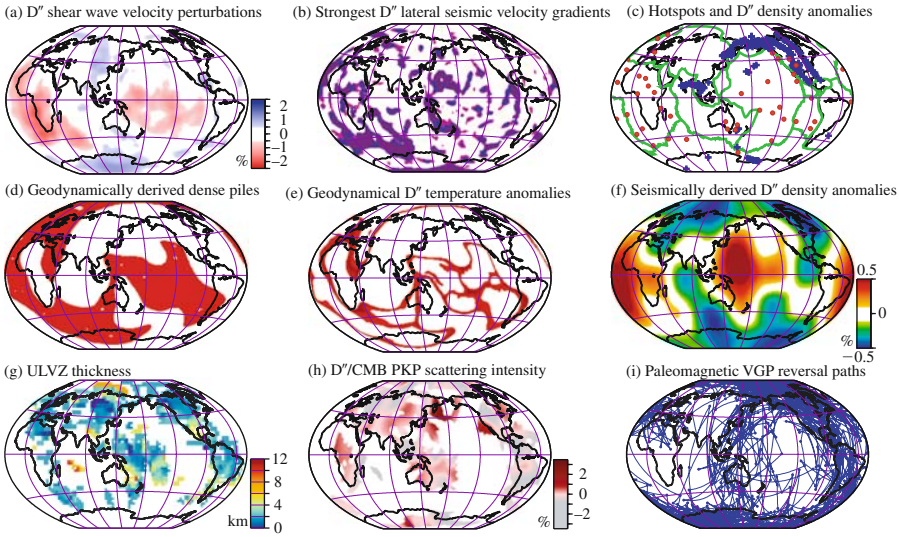

Figure 2. Comparison of several deep mantle data sets and models: (a) D″ shear velocity perturbations according to the TWBX model (Grand, 2002). The values between −0.5 and +0.5% have been omitted to emphasize the stronger heterogeneity signals. (b) The lateral gradients in δV_S of panel (a), as measured in Thorne et al. (2004). The colors correspond to the 30% of the CMB's surface area occupied by the strongest lateral gradients. These patterns, when compared with panel (a), indicate the strongest gradients in D″ surround the low shear velocities, i.e., the edges of low velocities. (c) Hotspots (red), plate boundaries (green), and predicted deep mantle locations of subducted dense material (from Lithgow-Bertelloni and Richards, 1998). (d) Dense thermo-chemical piles from the numerical geodynamics calculations of McNamara and Zhong (2005). The highest temperatures in these simulations are shown in (e), which dominate the edges of the dense piles in (d), along with some lineations within piles that demark internal convection cells. (f) Predicted lower mantle density anomalies of Trampert et al. (2004). (g) ULVZ thickness, assuming $(\delta V_P, \delta V_S, \delta\rho) = (-10\%, -30\%, 0\%)$, adapted from the modeling of Thorne and Garnero (2004). The thickest ULVZ regions are red. (h) PKP scattering strength from Hedlin and Shearer (2000). The strongest scattering occurs for the red colors.

Thermochemical mantle models are geodynamically attractive to explain the large degree two negative seismic anomalies in the lower mantle because geodynamical modeling of isochemical systems has revealed that hot upwellings tend to form more-globally ubiquitous small scale structures (e.g., Bunge et al., 1998, 2002). In other words, past studies have demonstrated the difficultly in generating two large thermal anomalies by thermal convection alone. Several geodynamical studies have been performed that investigate the 3-D morphology and size of possible thermochemical structures in the deep mantle (Olson and Kincaid, 1991; Tackley 1998, 2002; Davaille 1999; Davaille et al., 2002, Jellinek and Manga, 2002, 2004; McNamara and Zhong, 2004a,b, 2005). Depending on the thermochemical parameters used, a dense mantle component will take the form of either rounded, rising, unstable superplumes or linear, stable piles. Under the assumption that stable, dense piles

exist in the lower mantle, McNamara and Zhong (2005) have performed fully 3-D spherical numerical thermochemical convection calculations which incorporate the Earth's 120 My tectonic plate history (from Lithgow-Bertelloni and Richards, 1998) as surface boundary conditions. Starting with initially uniform dense layers of various thicknesses and density contrasts (~2–5%), the final shape and distribution (representing the present day) of thermochemical piles as a function of this plate history forms tends to resemble to first order the large, negative seismic anomalies observed in tomography. It is found that resultant thermochemical piles form a NW-SE trending linear African pile. In contrast, dense material forms a superposition of linear piles in the Pacific resulting in a more-rounded structure there. Also, thermochemical piles tend to have a low cooling efficiency and are therefore large thermal anomalies in addition to being compositional anomalies.

In addition, the geodynamical models predict internal convection within the Pacific anomaly in which upwellings form inside the pile along the edges, likely guided by viscous coupling with the less-dense mantle component. As a result, the internal edges of thermochemical piles are expected to be the hottest regions in the mantle, and if there is any partial melting in the lower mantle, it would certainly be expected to occur inside thermochemical piles at their edges. It is interesting to note the conceptual agreement between the spatial correlation of the strongest lateral velocity gradients in δV_S (Fig. 2b) occurring near the edges of the low δV_S piles (Fig. 2a), and the highest deep mantle temperatures (Fig. 2e) occurring near the edges of the high density thermo-chemical piles (Fig. 2d).

As observed in the previous geodynamical modeling studies, upwellings are produced at the highest peaks of thermochemical piles or superplumes. The modeling of McNamara and Zhong (2005) predicts a Pacific anomaly which is actually a superposition of linear ridges. The ridges form the external edges of the complete anomaly, and as a result, the modeling predicts mantle plumes to form along the tops of these ridges. Therefore, the highest number of mantle plumes in the Pacific is expected to form near the edges of the large Pacific anomaly.

Several further lines of evidence exist for the large scale δV_S depressions shown in Figure 1 and Figure 2a having a chemical origin that is distinct from the surrounding lower mantle material (e.g., see arguments by Samuel et al., 2005). The V_P and V_S velocity perturbation maps appear to be decoupled; including portions of the degree 2 low δV_S having anomalously high P wave speeds (Masters et al., 2000; Deschamps and Trampert, 2003; Ishii and Tromp, 2004; Trampert et al., 2004). It seems unlikely that the decoupling of P and S-wave velocities could solely be the result of thermal perturbation in an isochemical lower mantle. Furthermore, it seems unlikely that sharp lateral transitions (e.g., probably near or less than 100 km) in the low δV_S anomalies can be maintained over extended periods of time by thermal effects. On the other hand chemical variations can easily explain the observed structure as some form of iron enrichment may relate to the lowered shear wave speeds, increased density, and hotter temperatures in this region. We note though that at present no consensus on the origin and constitution of the potentially dense, low-velocity piles has been reached.

Several groups have put forth evidence for density perturbations in the deep mantle (e.g., Masters et al., 2000; Ishii and Tromp, 1999, 2004, Trampert et al., 2004), though some controversy exists regarding the details (Kuo and Romanowicz, 2002; Masters and Gubbins, 2003). Figure 2f shows a density perturbation model of Trampert et al. (2004), which is appropriate for the lowest 1000 km of the lower mantle. The pattern seen in this particular density map roughly correlates well with the geographical locations of the δV_S reductions, though trade-offs in density modeling have been highlighted in previous modeling (e.g., Deschamps and Trampert, 2003; Trampert et al., 2004). Better constraint on the density structure of the degree 2 low velocity anomalies is important, as it relates to a fundamental question regarding the nature of these structures. They have been characterized as "superplumes" for over a decade now (e.g., Su and Dziewonski, 1997), but if they are dense and stable at the base of the mantle and not actively upwelling (as buoyant plumes would do), they may be more appropriately characterized as "piles", or "megapiles" (e.g., Tackley, 1998, 2002; McNamara and Zhong, 2004a). In this chapter, we further explore the megapile possibility, since dynamical calculations have shown the necessity of high densities (along with elevated viscosity) in order to reproduce the long wavelength shape of the degree 2 δV_S reductions (e.g., Tackley, 1998, 2000; McNamara and Zhong, 2004a). We are nonetheless aware that the existing seismological data are presently not sufficient to constrain the detailed internal structure of the low-velocity features. We note an additional inherent shortcoming in seismic imaging of Earth's interior that restricts its application to geodynamical problems: at best, a present day snapshot in time is all that is available. Thus, unfortunately, we are not able to constrain the temporal evolution or specific time signatures of the different seismic features.

2.2 Short wavelength deep mantle patterns

A variety of phenomena have been seismically mapped in the deep mantle at scale lengths much shorter than tomographically derived heterogeneity. These include strong variability in horizontal layering and anisotropy (e.g., see Wen, 2001; Rokosky et al., 2004; Thomas et al., 2004; Garnero et al., 2004), and highly variable ULVZ and CMB properties (e.g., Shearer et al., 1998; Rost and Revenaugh, 2001, 2003; Niu and Wen, 2001; Koper and Pyle, 2004; Rondenay and Fischer, 2003; Thorne and Garnero, 2004; Wang and Wen, 2004; Rost et al., 2005). The lateral gradient map in Figure 2b shows small-scale features that cannot be observed in the δV_S maps. Nonetheless, this is expected for a derivative of the data, rather than actual detected small-scale structure. Figure 2g displays ULVZ thickness, from the modeling experiments in Thorne and Garnero (2004) using diffracted phases as probes to ULVZ structure. Roughly one-third of the CMB is sampled, and these results argue that the ULVZ is not globally contiguous as a relatively thick layer (e.g., >5 km). In fact, it appears that the ULVZ structure is most anomalous in relatively localized regions. For example, very localized, anomalous (i.e., thick ULVZ) regions exist in the Indian Ocean and between New Zealand and Australia with lateral dimensions

of 100–200 km. The Australian location was imaged as having a ∼50 km lateral dimension ULVZ in a recent study by Rost et al. (2005) using short period seismic array recordings of hundreds of Fiji-Tonga earthquakes. It is obvious that significant heterogeneities exist at scales more than an order of magnitude less than presently resolvable by tomography, which nonetheless can be resolved by high resolution, regional studies.

Another expression of small-scale heterogeneity found in the seismic wavefield is scattering of seismic energy. It has been appreciated for some time that the D″ region has an exceptionally strong scattering potential for short period seismic energy (e.g., Bataille et al., 1990; Bataille and Lund, 1996; Flatté and Wu, 1988; Vidale and Hedlin, 1998; Hedlin and Shearer, 2000; Cormier, 1999, 2000). Figure 2h displays the results of a study imaging D″ (or CMB) scattering strength, using PKP precursors (Hedlin and Shearer, 2000). An important point is that the variations are much smaller (∼500 km) than in global tomography (∼1000–3000 km), although the exact magnitudes of scattering strength depend on several factors in the inversion. Strong scattering regions (red colors) are difficult to correlate to specific features in the other maps. A comparison with global features found in the other geophysical studies shown in this figure is not possible since the scatterer map is not globally continuous Nonetheless, comparison with ULVZ thickness (Fig. 2g) suggests the thickest ULVZ zones are closer to high scattering zones than not. This suggests that the possibly partially molten ULVZ may be related to small scale stirring, that give rise to effective scattering at short seismic wavelengths (∼1 Hz).

It is instructive to view ULVZ structure in a well-sampled region in the southwest Pacific. Figure 3 shows the combined findings of different ULVZ studies. Figure 3a displays the δV_S tomography map of Grand (2002), along with CMB sampling of ScP data with or without precursors, which have been used to map a very localized ULVZ (∼50 km in lateral dimension, 8.5 km thick, and V_P and V_S drops of 8 and 25%, respectively, and density increase of 10%) (Rost et al., 2005). This ULVZ is located close to the edge of the low shear velocities mapped by tomography (Figs. 3a, and 2a). This ULVZ location is also in a region of strong lateral δV_S gradients (Fig. 2b), and where the temperatures in the geodynamical calculation (Fig. 2e) are predicted to be the highest (beneath the edge of the thermochemical dense pile, Fig. 2d). This isolated ULVZ location is corroborated by the anomalous waveform behavior of SPdKS data (Fig. 3b) (from Thorne and Garnero, 2004). These data commonly vary on the lateral scales of 10's of km at the CMB. At a scale intermediate to this fine scale variability and that seen in tomography, Fresnel zones of SPdKS can be used to represent ULVZ likelihood, a simple measure of records requiring a ULVZ structure versus records best explained in the absence of a ULVZ (Fig. 3c); this general region displays high variability in ULVZ likelihood. Thus, if ULVZ are indeed related to very local thermal and chemical anomalies in the dense thermo-chemical piles, it is natural to expect high variability at the shortest scales in the ULVZ structure. It is noteworthy that even finer scale CMB structure may exist. For example, a region a few 100 km to the north has been mapped with a core-side localized anomaly (Rost and Revenaugh, 2001). Thus we further allow for the possibility that the core-mantle

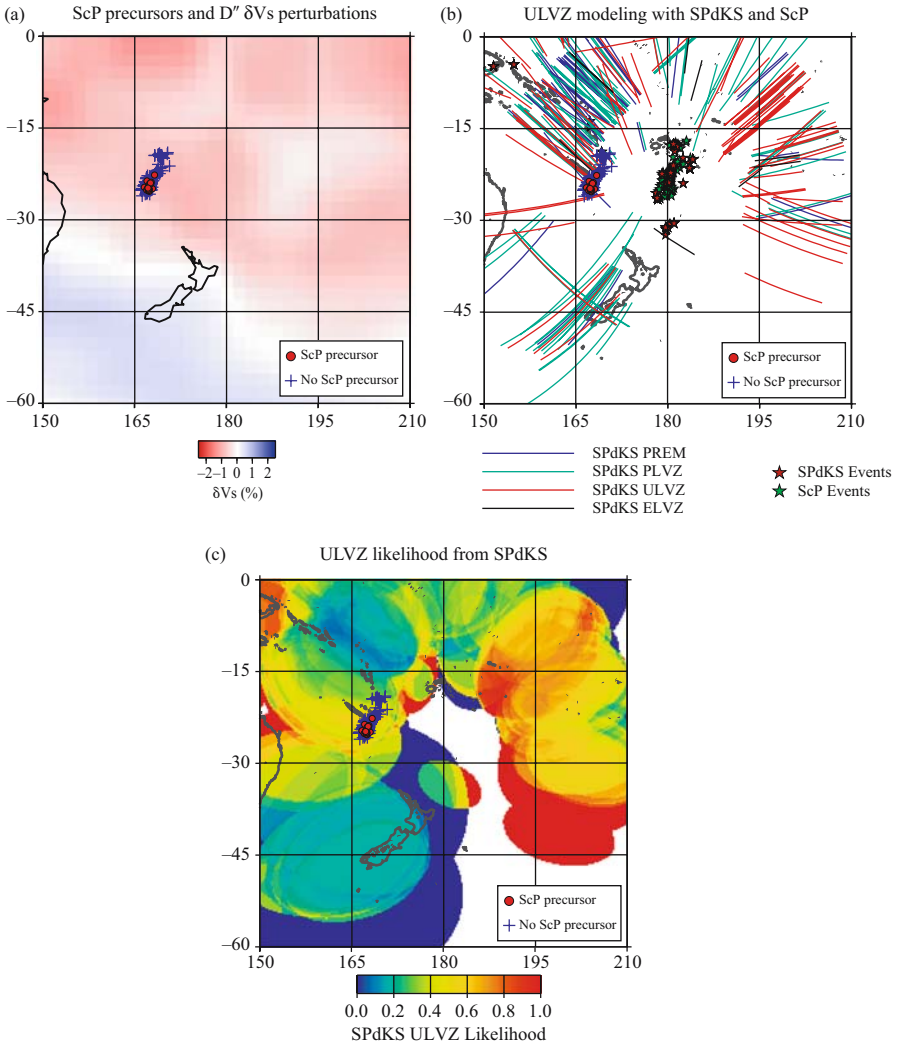

Figure 3. ULVZ behavior in the southwest Pacific (the region shown includes New Zealand and eastern-most Australia). (a) δV_S of Grand (2002) with ScP sampling of Rost et al. (2005) also shown, indicating a CMB zone possessing a very localized ULVZ (red circles). (b) The same ScP data, displayed with SPdKS data of Thorne and Garnero (2004), which also show strongly anomalous behavior in this general region. Line segments correspond to the P_{diff} arcs in SPdKS. Paths are color-coded for: PREM (fpr the Preliminary Reference Earth Model, Dziewonski and Anderson, 1981, shown as blue lines, indicating no ULVZ), PLVZ (Probable Low Velocity Zone, based on a statistical measure of the improvement of fit to the data from ULVZ predictions compared to PREM, light green), ULVZ (red), and ELVZ (Extreme Low Velocity Zone, where records were more anomalous than any of our tested ULVZ structures, colored black). (c) ScP data as in (a), superimposed on top of Fresnel zone estimations of the P_{diff} arcs in SPdKS, color-coded for ULVZ likelihood, as measured by a simple ratio of the number of records requiring ULVZ models to match the data divided by the total number of records, in every 5° × 5° region.

transition (and not just fine layering above it) is extremely anomalous, especially in regions as depicted in Figure 3, which may include chemical reactions between the mantle and core material (e.g., Knittle and Jeanloz, 1989, 1991).

Synthetic seismograms computed for the ScP waveform data used in imaging the SW Pacific ULVZ by Rost et al. (2005) required an increase in density (+10%) of the ULVZ in order to fit the waveforms. Further evaluation of data used by Thorne and Garnero (2004), summarized in Table 2, also suggest that anomalous SPdKS data are best fit by models containing density increases. Density increases affect the impedance contrast between the ULVZ and the overlying mantle, which (a) increases the relative amplitude ratio between the reflection off the top of the ULVZ and ScP, and (b) increases the amplitude of an internal ULVZ multiple that constructively interferes with SPdKS relative to SKS. The Thorne and Garnero (2004) study did an exhaustive model space search to characterize constraints, trade-offs, and uncertainties in global ULVZ modeling. To assess general ULVZ model fits to the data, one can tabulate the number of data that are well fit by any particular model category, such as including (or not) an elevated density in the ULVZ, mantle or core-side ULVZ, and so on. Table 2 shows that 154 individual records were best fit by synthetic seismograms computed for ULVZ models. Of these 154 records, 106 were best fit by synthetics for ULVZ models with a density increase. Furthermore, these ULVZ models with density increases display the best data-to-model fit as indicated by the normalized cross-correlation coefficient in Table 2. Although tradeoffs exist in modeling ULVZ

Table 2. ULVZ modeling misfit statistics. Misfit is represented by the average (for all observations) difference between the cross-correlation coefficient (*CCC*) of each observation and its best fit (*bf*) synthetic seismogram (CCC^{bf}) and the *CCC* of the same observation and models of the model class categories (*m*) listed below (CCC^{m}). Thus larger misfit numbers indicate poorer performance of this model or class of models in comparison to models best fitting the whole data set. Only observations for which the best-fit model had a $CCC > 0.85$ were included. This yielded a total number of records (*NR*) of 273

Model type	Misfit ($< \overline{CCC} >^{a}$)	NR^{b}_{bf}
PREM	4.85	47
ULVZ ($\delta\rho = 0$)	0.72	48
ULVZ ($\delta\rho > 0$)	0.30	106
ULVZ ($\delta V_S = \delta V_P$)	0.52	119
ULVZ ($\delta V_S = 3\delta V_P$)	1.16	35
CRZ	0.59	57
CMTZ	1.47	15

[a] $<\overline{CCC}> = \dfrac{\sum_{i=1}^{n}\left(CCC_i^{bf} - CCC_i^{m}/CCC_i^{bf}\right)*100\%}{n}$.

[b] NR_{bf} – Number of records best fit by this model space.

properties such as density (e.g., Garnero and Helmberger, 1998), these ScP and SPdKS data sets both indicate that to adequately model ULVZ structure elevated densities are typically necessary.

3 THERMO-CHEMICAL AND GEODYNAMICAL POSSIBILITIES

A connection between dense thermo-chemical piles in the deep mantle and depressed seismic shear wave speeds has been suggested (McNamara and Zhong, 2005). Here, we have raised the possibility that ULVZ may be more likely to occur near the edges of such lower mantle features, as the highest deep mantle temperatures may be located there (Fig. 2). In this section, we further explore the possible origins of generating a ULVZ, and how this might relate to other important mantle processes.

For nearly a decade, it has been argued that the 3 to 1 reduction of δV_S to δV_P in the ULVZ indicates a partial melt origin, based on mineral physics grounds (e.g., Williams and Garnero, 1996; Berryman, 2000; Akins et al., 2004), and that this relates to plume genesis from the ULVZ layer, which is manifest in the high correlation of surface hotspots and ULVZ structure (Williams et al., 1998). A recent revisiting of this topic has revealed that hotspots are in fact more likely to overlie the strongest lateral gradients in δV_S (Thorne et al., 2004). Thus, ULVZ structure can indeed be related to plume initiation at or near the CMB. Though it is important to acknowledge that plumes are likely be perturbed from vertical conduits due to mantle convection (e.g., Steinberger, 2000); exactly to what extent is unresolved at present.

Several possible relationships between ULVZ and lower mantle structures are explored in Figure 4. Important considerations are: (i) is the ULVZ partial melt of some principle D″ component, such as post-perovskite structure silicate (Murakami et al., 2004; Tsuchiya et al., 2004; Oganov and Ono, 2004; Shim et al., 2004), or dense thermo-chemical piles (Tackley, 1998; 2000; McNamara and Zhong, 2004a) or layering (Lay et al., 2004; Lay and Garnero, 2004); (ii) is the ULVZ some distinct material, such as chemical reaction products between the mantle and core (e.g., Poirier, 1993; Song and Ahrens, 1994; Manga and Jeanloz, 1996); or (iii), is the ULVZ regionally localized, or global, being imperceptibly thin in regions. The scenarios in Figure 4 are meant to be provocative, illustrating some of the end-member possibilities, though certainly not exhaustive, mainly owing to the lack of solid constraints on elastic structure that would help to distinguish between scenarios. Though it is important to note that present methods would not be able to detect a ULVZ layer less than a few km thick, unless its properties were exceedingly anomalous (e.g., see Garnero and Helmberger, 1998; Thorne and Garnero, 2004; Rost and Revenaugh, 2003; Rost et al., 2005).

While there has been a suggestion that partially molten ULVZ material may relate to plume genesis, it is perhaps premature to seismically constrain the connectivity of whole mantle (or nearly whole mantle) plumes to deep mantle superplumes. The work of Montelli et al. (2004) has mapped low velocity conduits throughout the mantle in key locations, but do not show evidence for large scale deep mantle superplumes (or megapiles) underlying the conduits. Shear velocity tomography models (e.g., Fig. 1)

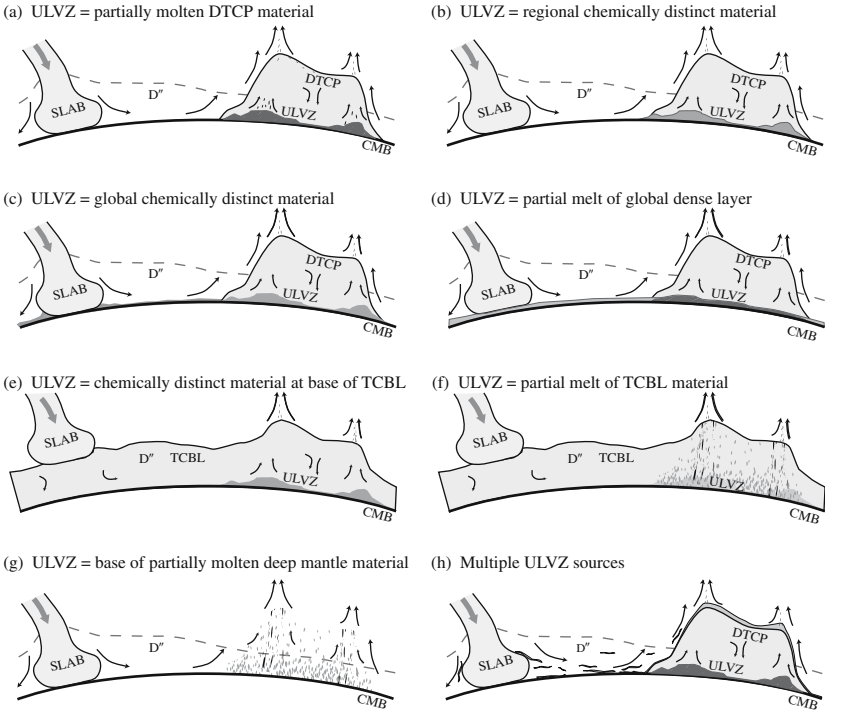

Figure 4. Schematic representation of ULVZ in relationship to dense thermo-chemical piles, or "DTCP", global thermo-chemical layering, and a purely thermal possibility. The different panels are intended to highlight the various possibilities of ULVZ as either chemically similar or distinct from its surrounding rock. (a) ULVZ is partially molten DTCP material, and thus is geographically restricted to DTCP regions. (b) As in (a), but the ULVZ material is distinct from DTCP. (c) ULVZ is a global chemically distinct (and dense) layer, it is thickest (and detectable) in the hottest deep mantle regions. (d) As in (c), except the ULVZ is detectable owing to partial melt of the dense layer. (e) ULVZ is chemically distinct, and ponds beneath the hottest regions in a global thermo-chemical deep mantle layer. (f) The ULVZ is partial melt of a global thermo-chemical lower mantle layer. In this panel the partial melt is portrayed as mixing throughout the layer. (g) ULVZ is partial melt of the post-perovskite material. (h) The possibility of multiple ULVZ sources is portrayed, combining (a) with dense melt from former harzburgitic oceanic crust delaminating from descending slabs.

show evidence for the degree 2 anomalies, but resolution is not quite high enough to track smaller scale plumes from these features up through the mantle. We anticipate important advances in this area over the next several years as data coverage increases in important areas, such as the central Pacific.

Nonetheless, insight from geodynamical numerical calculations and laboratory experiments provide important starting points for synthesizing the seemingly diverse results from seismic studies. Plumes appear to most easily generate from topographical ridges or points (e.g., Jellinek and Manga, 2002, 2004; McNamara and Zhong,

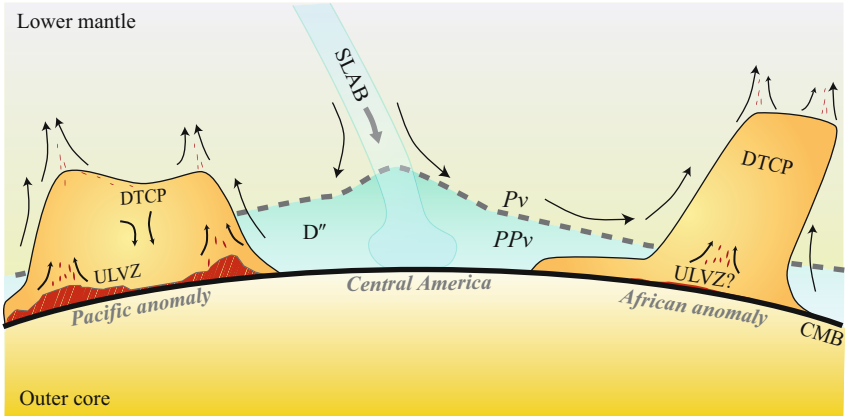

Figure 5. Hypothetical west-to-east cross-section (viewing to the north, approximately equatorial) of the lower mantle that incorporates dense thermo-chemical piles (DTCP), ultra-low velocity zones (ULVZ), and the perovskite (*Pv*) to the post-perovskite (*PPv*) structure solid-solid phase change (dashed line is the implied phase boundary). ULVZ are within the DTCP, which contain the hottest lower mantle temperatures; overlying ridge like topography atop the DTCP is the most likely location for mantle plume initiation.

2004a; 2005). Thus, ridges near the edges of dense thermo-chemical piles that overly the hottest deep mantle areas and possibly ULVZs (see Fig. 2), may be the most likely zones for mantle plume initiation. Figure 5 reiterates this possibility for a hypothetical cross-section across the equator from the Pacific through Central America and through to Africa. Extensive evidence exists for ULVZ beneath portions of the Pacific low-velocity anomaly, but ULVZ underplating of the African anomaly is less clear. The work of Ni and Helmberger (2003a, b) and Helmberger and Ni (2005) argue for the absence of any ULVZ layering, while Wen (2001) and Wang and Wen (2004) (for example) argue that the base of the large African anomaly has shear velocity reductions up to −12%, which is essentially a mild ULVZ structure. Thus, Figure 5 leaves open the possibility that the African anomaly may be distinctly different from the Pacific anomaly.

4 DISCUSSION

Other important possibilities exist for the nature of large scale upwellings in the mantle, i.e., superplumes, which potentially have far reaching consequences (Maruyama, 1994; Maruyama et al., 1994). Several shapes to upwellings are possible, and include the possibility of only a weak seismic signature of the excess plume temperature (e.g., Farnetani and Samuel, 2005). The recent important discovery of the post-perovskite phase (see summary by Lay et al., 2005) must also be considered in relationship to ULVZ, as this is potentially the dominant lower mantle mineral on the mantle side of

the CMB. While significant seismic and geodynamic evidence exists for the presence of lowermost mantle thermochemical anomalies, at large and short scale lengths (e.g., see Masters et al., 2000; Lay et al., 2004; Saltzer et al., 2004; Van Thienen et al., 2005; Samuel et al., 2005), a significant portion of the deep mantle (i.e., away from the degree 2 low velocities) may indeed be the post-perovskite structure. The partially molten post-perovskite may indeed be consistent with the seismic velocity reductions imaged for ULVZ structure. Though it is important to reiterate that ULVZ structure is more commonly detected in association with the lower velocity regions of the deep mantle. The possibility of a double crossing of the post-perovskite phase boundary (Hernlund et al., 2005) due to the thermal boundary layer right at the CMB raises an interesting question: if the temperature right at the CMB is hot enough to partially melt perovskite or post-perovskite, should seismic detection of a high and low velocity reflector within D″ (e.g., as in Thomas et al., 2004, which Hernlund et al., 2005, argue for support of the phase boundary double crossing) be accompanied by ULVZ structure? If yes, this has not been detected as of yet, but future work should target better resolution of this possibility. We clarify that the post-perovskite structure in solid phase does not contain any known significant velocity reduction that matches those seen in ULVZ modeling ($\delta V_P \sim -10\%$, $\delta V_S \sim -30\%$).

5 CONCLUSIONS

In this chapter, we have discussed ultra-low velocities at the CMB, and their possible relationship to deep mantle megapiles or superplumes. Certainly, ULVZ structure may have far reaching effects in Earth's global cycles (Muller, 2002; Dobson and Brodholt, 2005). Though important uncertainties still exist in the seismic modeling. For example, in the SPdKS and PKP modeling, the CMB interacts with waves entering and exiting the core. Thus in many cases, large uncertainties exist regarding the exact location of anomalous structures. This can be improved by adding topside CMB reflection probes, like PcP or ScP precursors (e.g., Mori and Helmberger, 1995; Rost et al., 2005), as well as devising new ULVZ probes, like $PKKP_{AB}^{diff}$ (Rost and Garnero, 2006). Another important point is that most ULVZ modeling to date has utilized 1D wave propagation tools (except for a few notable studies, like Wen and Helmberger, 1998a, b). Future studies need to incorporate improvements in this area.

In this chapter we have summarized recent ULVZ findings in relationship to possible dense thermochemical piles in D″, which may be intimately related to superplumes. The large dense piles may explain the degree 2 low shear velocity heterogeneity reveal by seismic tomography, and help to explain several seismic observations, including sharp sides to these structures and marked differences (even anticorrelation) between P and S heterogeneity—neither of which can be explained by thermal anomalies alone. Geodynamical calculations suggest that the hottest deep mantle temperatures are beneath the edges of the dense piles, which is the most likely region to develop ULVZ with origin of partial melt. Topographical ridges to the dense piles near these edges are the most likely geographical regions to form mantle

plumes. While this scenario presents a self-consistent story for ULVZ, large scale low velocities in the deepest mantle, and plume genesis, several important uncertainties are noted, primarily relating to resolution issues in the seismic imaging and geodynamic modeling.

ACKNOWLEDGEMENTS

We are grateful to the Superplume project for the opportunity to participate, M. Hedlin for the PKP scattering map, F. Deschamps and M. Ishii for density perturbation maps, C. Laj for the VGP reversal data, S. Grand, B. Romanowicz, G. Laske, Y. Gu, and J. Ritsema for their δV_S models, C. Lithgow-Bertelloni for the density anomaly locations, and B. Steinberger for the hot spot locations. The authors thank an anonymous reviewer, whose comments helped improve the manuscript. The work was partially funded by NSF Grant EAR-0135119.

REFERENCES

Akins, J.A., S.-N. Luo, P.D. Asimow, and T.J. Ahrens (2004) Shock-induced melting of $MgSiO_3$ perovskite and implications for melts in Earth's lowermost mantle. *Geophys. Res. Lett.*, 31(14), doi:10.1029/2004GL020237.

Bataille, K., and F. Lund (1996) Strong scattering of short-period seismic waves by the core-mantle boundary and the P-diffracted wave. *Geophys. Res. Lett.*, 23, 2413–2416.

Bataille, K., S. Flatté, and R.S. Wu (1990) Inhomogeneities near the core mantle boundary evidenced from scattered waves: A Review. *Pure Applied Geophys.*, 132, 151–173.

Berryman, J.G. (2000) Seismic velocity decrement ratios for regions of partial melt in the lower mantle. *Geophys. Res. Lett.*, 27, 421–424.

Bullen, K.E. (1949) Compressibility-pressure hypothesis and the Earth's interior. *Mon. Not. Roy. Astron. Soc., Geophys. Suppl.*, 5, 355–368.

Bunge, H.P., M.A. Richards, C. Lithgow-Bertelloni, J.R. Baumgardner, S.P. Grand, and B.A. Romanowicz (1998) Timescales and heterogeneous structure in geodynamic Earth models. *Science*, 280, 91–95.

Bunge, H.P., M.A. Richards, and J.R. Baumgardner (2002) Mantle-circulation models with sequential data assimilation: Inferring present-day mantle structure from plate-motion histories. *Phil. Trans. R. Soc. Lond. A*, 360, 2545–2567.

Cormier, V.F. (1999) Anisotropy of heterogeneity scale lengths in the lower mantle from PKIKP precursors. *Geophy. J. Int.*, 136, 373–384.

Cormier, V.F. (2000) D'' as a transition in the heterogeneity spectrum of the lowermost mantle. *J. Geophys. Res.*, 105, 16193–16205.

Davaille, A. (1999) Simultaneous generation of hotspots and superswells by convection in a heterogeneous planetary mantle. *Nature*, 402, 756–760.

Davaille, A., F. Girard, and M. Le Bars (2002) How to anchor hotspots in a convecting mantle? *Earth Planet. Sci. Lett.*, 203, 621–634.

Deschamps F., and J. Trampert (2003) Mantle tomography and its relation to temperature and composition. *Phys. Earth Planet. Int.*, 140, 277–291.

Dobson, D.P., and J.P. Brodholt (2005) Subducted iron formations as a source of ultralow-velocity zones at the core-mantle boundary. *Nature*, 434, 371–374.

Duncan, R.A., and M.A. Richards (1991) Hotspots, mantle plumes, flood basalts, and true polar wander. *Rev. Geophys.*, 29 (1), 31–50.

Dziewonski, A.M. (1984) Mapping the lower mantle: Determination of lateral heterogeneity in *P* velocity up to degree and order 6. *J. Geophys. Res.*, 89, 5929–5952.

Dziewonski, A.M., and D.L. Anderson (1981) Preliminary reference Earth model. *Phys. Earth and Planet. Inter.*, 25(4), 297–356.

Farnetani, C.G., and H. Samuel (2005) Beyond the thermal plume paradigm. *Geophys. Res. Lett.*, 32, No. 7, L07311, 10.1029/2005GL022360.

Flatté, S.M., and R.S. Wu (1988) Small-scale structure in the lithosphere and asthenosphere deduced from arrival-time and amplitude fluctuations at NORSAR. *J. Geophys. Res.*, 93, 6601–6614.

Ford, S.R., E.J. Garnero, and A.K. McNamara (2006) A strong lateral shear velocity gradient and anisotropy heterogeneity in the lowermost mantle beneath the southern Pacific. *J. Geophys. Res.*, 111, B03306, doi:10.1029/2004JB003574.

Garnero, E.J. (2000) Heterogeneity of the lowermost mantle. *Ann. Rev. Earth Planetary Sci.*, 28, 509–537.

Garnero, E.J. (2004) A new paradigm for Earth's core-mantle boundary. *Science*, 304, doi:10.1126/science.1097849.

Garnero, E.J., and D.V. Helmberger (1998) Further structural constraints and uncertainties of a thin laterally varying ultra-low velocity layer at the base of the mantle. *J. Geophys. Res.*, 103, 12495–12509.

Garnero, E.J., V. Maupin, T. Lay, and M.J. Fouch (2004) Variable azimuthal anisotropy in Earth's lowermost mantle. *Science*, 306(5694).

Grand, S.P. (2002) Mantle shear-wave tomography and the fate of subducted slabs. *Phil. Trans. R. Soc. Lond. A*, 360, 2475–2491.

Gu, Y.J., A.M. Dziewonski, W.J. Su, and G. Ekstrom (2001) Models of the mantle shear velocity and discontinuities in the pattern of lateral heterogeneities. *J. Geophys. Research-Solid Earth*, 106(B6), 11169–11199.

Hager, B.H., R.W. Clayton, M.A. Richards, R.P. Comer, A.M. Dziewonski (1985) Lower mantle heterogeneity, dynamic topography and the geoid. *Nature*, 313(6003), 541–546.

Hedlin, M.A.H., and P.M. Shearer (2000) An analysis of large scale variations in small-scale mantle heterogeneity using Global Seismic Network recordings of precursors to PKP. *J. Geophys. Res.*, 105, 13655–13673.

Helmberger, D.V., and S. Ni (2005) Approximate 3D body wave synthetics for tomographic models. *Bull. Seismol. Soc. Am.*, 95, 212–224.

Hernlund, J.W., C. Thomas, and P.J. Tackley (2005) A doubling of the post-perovskite phase boundary and the structure of the lowermost mantle. *Nature*, 434, 882–886.

Ishii, M., and J. Tromp (1999) Normal-mode and free-air gravity constraints on lateral variations in velocity and density of Earth's mantle. *Science*, 285, 1231–1236.

Ishii, M., and J. Tromp (2004) Constraining large-scale mantle heterogeneity using mantle and inner-core sensitive normal modes. *Phys. Earth Plan. Int.*, 146, 113–124.

Jellinek, A.M., and M. Manga (2002) The influence of a chemical boundary layer on the fixity and lifetime of mantle plumes. *Nature*, 418, 760–763.

Jellinek, A.M., and M. Manga (2004) Links between long-lived hotspots, mantle plumes, D″ and plate tectonics. *Rev. Geophys.*, 42(3), RG3002, 10.1029/2003RG000144.

Ji, Y., and H.C. Nataf (1998) Detection of mantle plumes in the lower mantle by diffraction tomography: Theory. *Earth and Planetary Science Letters*, 159(3–4), 87–98.

Kendall, J.-M., and P. G. Silver (1998) Investigating causes of D″ anisotropy. In Gurnis, M., M. Wyession, E. Knittle, and B. Buffet (eds.) The Core-Mantle Boundary Region, AGU, Washington, D.C., USA, pp. 97–118.

Kendall, J.-M., Seismic anisotropy in the boundary layers of the mantle. In Karato, S., A.M. Forte, R.C. Liebermannm, G. Masters, and L. Stixrude (eds.) Earth's Deep Interior: Mineral Physics and Tomography From the Atomic to the Global Scale, AGU, Washington, D.C., USA, pp. 133–159.

Koper, K.D., and M.L. Pyle (2004) Observations of PKiKP/PcP amplitude ratios and implications for Earth structure at the boundaries of the liquid core. *J. Geophys. Res.*, 109, B03301, doi:10.1029/2003JB002750.

Knittle, E., and R. Jeanloz (1989) Simulating the core-mantle boundary: An experimental study of high-pressure reactions between silicates and liquid iron. *Geophys. Res. Lett.*, 16, 609–612.

Knittle, E., and R. Jeanloz (1991) Earth's core-mantle boundary—Results of experiments at high pressures and temperatures. *Science*, 251, 1438–1443.

Kuo, C., and B. Romanowicz (2002) On the resolution of density anomalies in the Earth's mantle using spectral fitting of normal mode data. *Geophys. J. Inter.*, 150, 162–179.

Lay, T., E.J. Garnero, Q. Williams, L. Kellogg, and M.E. Wysession (1998) Seismic wave anisotropy in the D″ region and its implications, In Gurnis, M., M. Wysession, E. Knittle, and B. Buffett (eds.) The Core-Mantle Boundary Region, AGU, Washington, D.C., U.S.A., pp. 299–318.

Lay, T., and E.J. Garnero (2004) Core-mantle boundary structures and processes. In Sparks, R.S.J., and C.J. Hawkesworth (eds.) The State of the Planet: Frontiers and Challenges in Geophysics, Geophysical Monograph 150, IUGG Volume 19, doi:10.1029/150GM04.

Lay, T., E.J. Garnero, and Q. Williams (2004) Partial melting in a thermo-chemical boundary layer at the base of the mantle. *Phys. Earth Planet. Int.*, 146, 441–467.

Lay, T., D. Heinz, M. Ishii, S.-H. Shim, J. Tsuchiya, T. Tsuchiya, R. Wentzcovitch, and D.A. Yuen (2005) Multidisciplinary impact of the deep mantle phase transition in perovskite structure. *Eos Trans.*, 86, No. 1, 1–15.

Lithgow-Bertelloni, C., and M.A. Richards (1998) Dynamics of cenozoic and mesozoic plate motions. *Rev. Geophys.*, 36, 27–78.

Manga, M., and R. Jeanloz (1996) Implications of a metal-bearing chemical boundary layer in D″ for mantle dynamics. *Geophys. Res. Lett.*, 23, 3091–3094.

Maruyama, S. (1994) Plume tectonics. *J. Geol. Soc. Jpn.*, 100, 24–49.

Maruyama, S., M. Kumazawa, and S. Kawakami (1994) Towards a new paradigm on the Earth's dynamics. *J. Geol. Soc. Jpn.*, 100, 1–3.

Masters, G., and D. Gubbins (2003) On the resolution of density within the Earth. *Phys. Earth Planet. Int.*, 140, 159–167.

Masters, G., G. Laske, H. Bolton, and A. Dziewonski (2000) The relative behavior of shear velocity, bulk sound speed, and compressional velocity in the mantle: Implications for chemical and thermal structure. In Karato, S. (ed.) Earth's Deep Interior, AGU Monograph, 117, pp. 63–87.

McNamara, A.K., and S. Zhong (2004a) Thermochemical structures within a spherical mantle: Superplumes or piles? *J. Geophys. Res.*, 109, B07402, doi:10.1029/2003JB002847.

McNamara, A.K, and S. Zhong (2004b) The influence of thermochemical convection on the fixity of mantle plumes. *Earth and Planet. Sci. Lett.*, 222, 485–500.

McNamara, A.K., and S. Zhong (2005) Thermochemical Piles under Africa and the Pacific. *Nature*, 437, 1136–1139.

Mégnin, C., and B. Romanowicz (2000) The three-dimensional shear velocity structure of the mantle from the inversion of body, surface, and higher-mode waveforms. *Geophys. J. Int.*, 143, 709–728.

Montelli, R., G. Nolet, F. Dahlen, G. Masters, E. Engdahl, and S. Hung (2004) Finite-frequency tomography reveals a variety of plumes in the mantle. *Science*, 303, 338–343.

Morgan, W.J. (1971) Convection plumes in the lower mantle. *Nature*, 230, 42–43.

Morgan, W.J. (1972) Deep mantle convection plumes and plate motions. *Am. Assoc. Petrol. Geol. Bull.*, 56(2), 203–213.

Mori, J., and D.V. Helmberger (1995) Localized boundary layer below the mid-Pacific velocity anomaly from a *PcP* precursor. *J. Geophys. Res.*, 100, 20359–20365.

Muller R.A. (2002) Avalanches at the core-mantle boundary. *Geophys. Res. Lett.*, 29(19), 1935, doi:10.1029/2002GL015938.

Murakami, M., K. Hirose, K. Kawamura, N. Sata, and Y. Ohishi (2004) Post-perovskite phase transition in $MgSiO_3$. *Science*, 304, 855–858.

Ni, S., E. Tan, M. Gurnis, and D.V. Helmberger (2002) Sharp sides to the African Superplume. *Science*, 296, 1850–1852.

Ni, S., and D.V. Helmberger (2003a) Ridge-like lower mantle structure beneath South Africa. *J. Geophys. Res.*, 108, No. B2, 2094.

Ni, S., and D.V. Helmberger (2003b) Seismological constraints on the South African superplume; could be the oldest distinct structure on Earth. *Earth Planet. Sci. Lett.*, 206, 119–131.

Niu, F., and L. Wen (2001) Strong seismic scatterers near the core-mantle boundary west of Mexico. *Geophys. Res. Lett.*, 28, 3557–3560.

Oganov, A.R., and S. Ono (2004) Theoretical and experimental evidence for a post-perovskite phase of $MgSiO_3$ in Earth's D″ layer. *Nature*, 430, 445–448.

Olson, P., and C. Kincaid (1991) Experiments on the interaction of thermal convection and compositional layering at the base of the mantle. *J. Geophys. Res.*, 96(B3), 4347–4354.

Poirier, J.-P. (1993) Core-infiltrated mantle and the nature of the D″ layer. *J. Geomag. Geoelectr.*, 45, 1221–1227.

Ritsema, J., and H.J. van Heijst (2000) Seismic imaging of structural heterogeneity in Earth's mantle: Evidence for large-scale mantle flow. *Science Progress*, 83, 243–259.

Rokosky, J.M., T. Lay, E.J. Garnero, and S.A. Russell (2004) High resolution investigation of shear-wave anisotropy in D″ beneath the Cocos Plate. *Geophys. Res. Lett.*, 31, L07605, doi:10.1029/2003GL018902.

Romanowicz, B. (1991) Seismic tomography of the Earth's mantle. *Ann. Rev. Earth Planet. Sci.*, 19, 77–99.

Rondenay, S., and K.M. Fischer (2003) Constraints on localized core-mantle boundary structure from multichannel, broadband SKS coda analysis. *J. Geophys. Res.*, 108(B11), 2537, doi:10.1029/2003JB002518.

Rost, S., and J. Revenaugh (2001) Seismic detection of rigid zones at the top of the core. *Science*, 294, 1911–1914.

Rost, S., and J. Revenaugh (2003) Small-scale ultra-low velocity zone structure resolved by ScP. *J. Geophys. Res. Solid Earth*, 108, 10.1028/2001JB001627.

Rost, S., and E.J. Garnero (2006) Detection of an ultra-low velocity zone at the CMB using diffracted $PKKP_{ab}$ waves. *J. Geophys. Res.*, 111, B07309, doi:10.1029/2005JB003850.

Rost, S., E.J. Garnero, Q. Williams, and M. Manga (2005) Seismic constraints on a possible plume root at the core-mantle boundary. *Nature*, 435, 666–669 (doi:10.1038/nature03620).

Saltzer, R.L., E. Stutzmann, and R.D. Van der Hilst (2004) Poisson's ration beneath Alaska from the surface to the core-mantle boundary. *J. Geophys. Res.*, 109, doi:10.1029/2003JB002712.

Samuel, H., C.G. Farnetani, and D. Andrault (2005) Heterogeneous lowermost mantle: Compositional constraints and seismological observables. In Bass, J., R.D. van der Hilst, J. Matas, and J. Trampert (eds.) Structure Evolution and Composition of the Earth's Mantle, AGU Geophysical Monograph.

Shearer, P.M., M.A.H. Hedlin, and P.S. Earle (1998) PKP and PKKP precursor observations: Implications for the small-scale structure of the deep mantle and core. In Gurnis, M., M.E. Wysession, E. Knittle, B.A. Buffett (eds.) The Core-Mantle Boundary Region, Washington D.C, American Geophysical Union, pp. 37–55.

Shim, S.-H., T.S. Duffy, R. Jeanloz, and G. Shen (2004) Stability and crystal structure of $MgSiO_3$ perovskite to the core-mantle boundary. *Geophys. Res. Lett.*, 31, L10603, doi:10.1029/2004GL019639.

Song, X., and T.J. Ahrens (1994) Pressure-temperature range of reactions between liquid iron in the outer core and mantle silicates. *Geophys. Res. Lett.*, 21, 153–156.

Steinberger, B. (2000) Plumes in a convecting mantle: Models and observations for individual hotspots. *J. Geophys. Res.*, 105, 11127–11152.

Su, W.J., and A.M. Dziewonski (1997) Simultaneous inversion for 3-D variations in shear and bulk velocity in the mantle. *Phys. Earth Planet. Int.*, 100, 135–156.

Tackley, P.J. (1998) Three-dimensional simulations of mantle convection with a thermo-chemical basal boundary layer: D″? In Gurnis, M., M.E. Wysession, E. Knittle, and B.A. Buffett (eds.) The Core-Mantle Boundary Region, American Geophysical Union, Washington, D.C., USA, pp. 231–253.

Tackley, P. (2000) Mantle convection and plate tectonics: Toward an integrated physical and chemical theory. *Science*, 288, 2002–2007.

Tackley, P.J. (2002) Strong heterogeneity caused by deep mantle layering. *Geochem. Geophys. Geosys.*, 3(4), 1024, doi:10.1029/2001GC000167.

Thomas, C., E.J. Garnero, and T. Lay (2004) High-resolution imaging of lowermost mantle structure under the Cocos Plate. *J. Geophys. Res.*, 109, doi:10.1029/2004JB003013.

Thorne, M.S., and E.J. Garnero (2004) Inferences on ultralow-velocity zone structure from a global analysis of SPdKS waves. *J. Geophys. Res.*, 109, B08301, doi:10.1029/2004JB003010.

Thorne, M., E.J. Garnero, and S. Grand (2004) Geographic correlation between hot spots and deep mantle lateral shear-wave velocity gradients. *Phys. Earth Planet. Int.*, 146, 47–63.

To, A., T.B. Romanowicz, Y. Capdeville, and N. Takeuchi (2005) 3D effects of sharp boundaries at the borders of the African and Pacific Superplumes: Observation and modeling. *Earth Planet. Sci. Lett.*, 233, 137–153.

Trampert, J., F. Deschamps, J. Resovsky, and D.A. Yuen (2004) Probabilistic tomography maps chemical heterogenities throughout the mantle. *Science*, 306, 853–856.

Tsuchiya, T., J. Tsuchiya, K. Umemoto, and R.M. Wentzcovitch (2004) Elasticity of post-perovskite $MgSiO_3$. *Geophys. Res. Lett.*, 31, L14603, doi:10.1029/2004GL020278.

van der Hilst, R.D., and H. Kárason (1999) Compositional heterogeneity in the bottom 1000 kilometers of Earth's mantle: Toward a hybrid convection model. *Science*, 283, 1885–1888.

Van Thienen, P., J. van Summeren, R.D. van der Hilst, A.P. van den Berg, and N.J. Vlaar (2005) Numerical study of the origin and stability of chemically distinct reservoirs deep in Earth's mantle. In van der Hilst, R.D., J. Bass, J. Matas, and J. Trampert (eds.) The Structure, Evolution and Composition of Earth's Mantle, AGU, Geophysical Monograph, pp. 117–136.

Vidale, J.E., and M.A.H. Hedlin (1998) Evidence for partial melt at the core-mantle boundary north of Tonga from the strong scattering of seismic waves. *Nature*, 391, 682–685.

Wang, Y., and L. Wen (2004) Mapping the geometry and geographic distribution of a very-low velocity province at the base of the Earth's mantle. *J. Geophys. Res.*, 109, B10305, doi:10.1029/2003JB002674.

Wen, L. (2001) Seismic evidence for a rapidly-varying compositional anomaly at the base of the Earth's mantle beneath the Indian ocean. *Earth Planet. Sci. Lett.*, 194, 83–95.

Wen, L., and D.V. Helmberger (1998a) Ultra-low velocity zones near the core-mantle boundary from broadband PKP precursors. *Science*, 279, 1701–1703.

Wen, L., and D.V. Helmberger (1998b) A 2D P-SV hybrid method and its application to localized structures near the core-mantle boundary. *J. Geophys. Res.*, 103, 17901–17918.

Williams, Q., and E.J. Garnero (1996) Seismic evidence for partial melt at the base of Earth's mantle. *Science*, 273, 1528–1530.

Williams, Q., J.S. Revenaugh, and E.J. Garnero (1998) A correlation between ultra-low basal velocities in the mantle and hot spots. *Science*, 281, 546–549.

Wysession, M.E. (1996) Imaging cold rock at the base of the mantle: The sometimes fate of Slabs? In Bebout, G.E., D. Scholl, S. Kirby, and J.P. Platt (eds.) Subduction: Top to Bottom, American Geophysical Union, Washington, D.C., USA, pp. 369–384.

Wysession, M., T. Lay, J. Revenaugh, Q. Williams, E.J. Garnero, R. Jeanloz, and L. Kellogg (1998) The D'' discontinuity and its implications. In Gurnis, M., M. Wysession, E. Knittle, and B. Buffett (eds.) The Core-Mantle Boundary Region, AGU, Washington, D.C., U.S.A., pp. 273–298.

Wysession, M.E., A. Langenhorst, M.J. Fouch, K.M. Fischer, G.I. Al-Eqabi, P.J. Shore, and T.J. Clarke (1999) Lateral variations in compressional/shear velocities at the base of the mantle. *Science*, 284, 120–125.

PART III

GLOBAL MATERIAL CIRCULATION AND PETROGENESIS OF SUPERPLUME ROCKS

INTRODUCTION

Petrogenesis of hot-spot magma depends on the physical process of mantle convection and plume dynamics, particularly the compositional variation in the mantle. Right after the consolidation of a magma ocean at 4.6 Ga, two end-member states of chemical composition are considered: (1) If convective flow in a magma ocean was strong enough, then a homogeneous mantle was formed without any chemical stratification between the upper and lower mantles; (2) If a magma ocean was consolidated under the static condition to produce a sufficiently steep chemical gradient by fractional crystallization with time, the lower mantle must be enriched in perovskite, whereas olivine is enriched in the upper mantle. In this case, the lower mantle must be richer in SiO_2, and chemically stratified from bottom to top: wüstite, Mg-perovskite, Ca-perovskite, CF (Na-Al phase), and SiO_2, respectively. In these models a magma ocean is assumed to be in a whole mantle scale, just as the Moon was formed by a giant impact.

Over the past 4.5 Ga, the mantle must have chemically evolved to extract the lighter (continental crust, ocean and atmosphere on the surface) and heavier (anti-crust on the bottom) fractions from the top and to the bottom of the mantle. Figure 1-(3) and (4) show the contrasting image for the present-day compositional variations. If the mantle produced MORB at a rate of Mesozoic-Cenozoic Earth, 20 km^3/yr, over the time back to 2.5 Ga, and three times more during 2.5–4.0 Ga, the whole mantle must have been partially molten once on the way. As the recycled MORB is heavier than the surrounding lower mantle, it must have been accumulated at the bottom with 500 km thickness. This suggests the D″ layer (0–350 km thick) must be enriched in MORB component and have caused the chemical heterogeneity, as pointed out previously. Thick anti-crust may have been present on the bottom of the CMB.

On the other hand, isotope geochemists have long believed that the presence of an OIB source mantle which has never partially melted remained the primordial source since the genesis of the Earth (see Fig. 1). This idea has come mainly from the constraints of Re-Os and He isotopes.

Kogiso argues the source mantle based on the geochemistry of HIMU basalts from the Pacific superplume in French Polynesia and the melting experiments of sandwiched MORB-peridotite. And he suggests the origin of HIMU basalts.

D. A. Yuen et al. (eds.), Superplumes, 161–164.
© 2007 *Springer.*

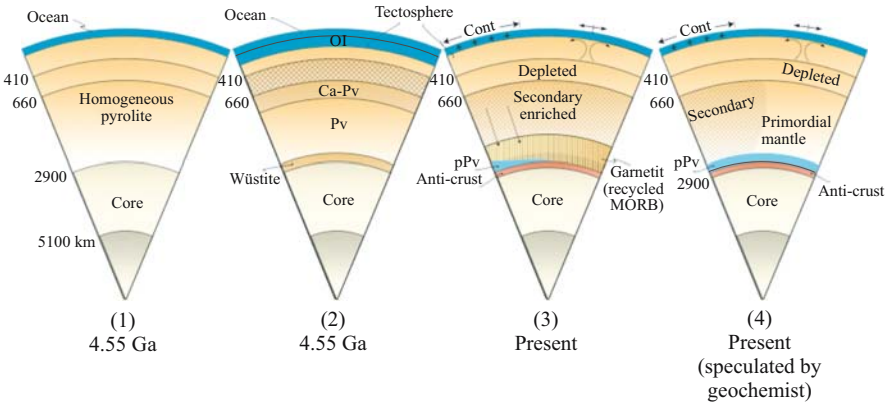

Figure 1. Image of mantle. Compositional profile of mantle right after the consolidation of a magma ocean at 4.5 Ga, homogeneous mantle made by extensive internal convection (1), or chemically stratified mantle by perfect fractional crystallization (2). In this case olivine-enriched upper mantle (Si-poor), and perovskite-enriched lower mantle (Si-rich) are formed. If the present-day rate of MORB-production (20 km^3/yr) had continued over the last 2.5 Ga, and three times more in the Archean, almost whole mantle must have once been molten, to form a 500 km thick D″ layer composed of MORB at the bottom of mantle. If those MORBs on the CMB is partially melted, the anti-crust enriched in Fe-silicates would have developed, similar to a mirror image of granitic continental crust on the surface (3). Based on geochemistry, particularly on Re-Os and He isotope systematics, geochemists have insisted on the presence of un-fractionated primordial mantle in the parts of lower mantle, which has never melted to form MORB since its birth at 4.6 Ga (4). Models (3) and (4) are two end members.

Komiya reviews his own works on Archean to Phanerozoic MORBs and OIBs, in addition to others, and shows the chemical and thermal evolution of the Earth's mantle over 4.0 Ga. The most outstanding events were the mantle overturns taking place at 2.7 and 2.3 Ga. The role of superplumes since 2.3 Ga can also have exerted remarkable influence on the compositional evolution of the mantle. He proposes an illustration of the global material circulation (Fig. 2).

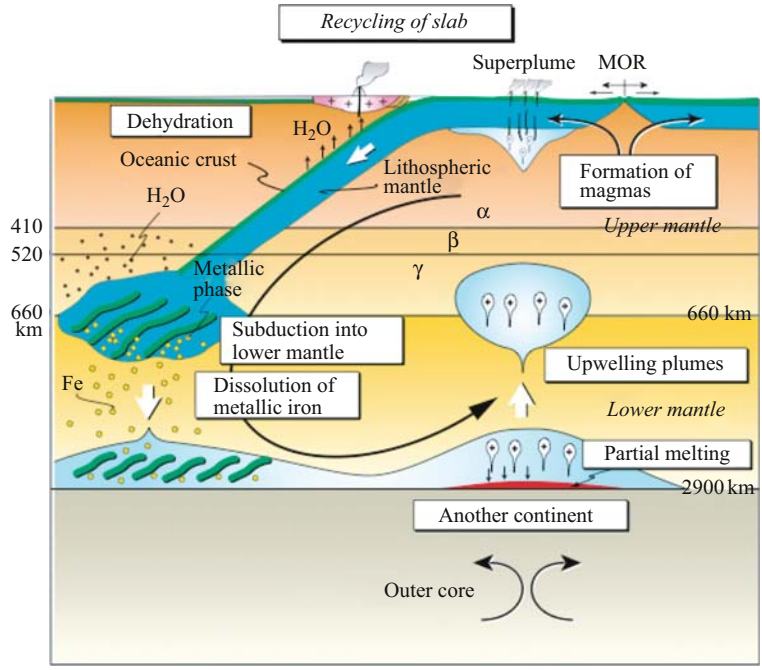

Figure 2. Global material circulation in the Earth's interior. Oceanic lithosphere formed at mid-oceanic ridge by 30% partial melting of lherzolitic mantle, is hydrated by hydrothermal circulation at mid-oceanic ridge, migrates to the trench with time, and subducts into deeper mantle, and finally to the CMB through the transient state at 660 km depth. At the 660 km depth, metallic iron may be formed accompanying with the perovskite formation. Those metallic phases may have moved into the outer core by the melting at the CMB finally. If it happened, FeO in the mantle must have reduced through time, as discussed by Komiya (this issue). On the CMB, slab graveyard is heated up by the core heat, and is chemically differentiated into FeO-rich heavy melt and residual andesitic buoyant plume, which rises up to the surface through the mantle transition zone, as a superplume or plume magma.

CHAPTER 7

A GEOCHEMICAL AND PETROLOGICAL VIEW OF MANTLE PLUME

TETSU KOGISO

Institute for Research on Earth Evolution (IFREE), Japan Agency for Marine-Earth Science and Technology (JAMSTEC), Yokosuka 237-0061, Japan;
E-mail: kogisot@jamstec.go.jp

Abstract
Eruption of basaltic lavas at hotspot volcanoes and oceanic plateaus has been considered to be a manifestation of buoyant plumes ascending through the mantle. The chemical compositions of such plume-related basalts may therefore provide us with key insights into the activity of mantle plumes, including ordinary ones and superplumes, and styles of mantle convection. Isotopic and major-element compositions of ocean island basalts (OIB) strongly suggest that recycling of subducted crustal materials plays an important role in the genesis of OIB. However, isotopic diversity of OIB seems to be too homogeneous to be generated from subducted materials which are expected to have extremely heterogeneous compositions owing to variability in their original compositions, modification history during subduction modification, and mantle residence times. Understanding the origin of the enriched components (EM1, EM2, and HIMU), which characterize the isotopic diversity of OIB, requires detailed knowledge of the dynamic and rheological behavior of mantle and crustal materials under mantle conditions as well as of their chemical characteristics. Major-element compositions of OIB suggest that OIB are generated from peridotite-pyroxenite heterogeneous mixtures at temperatures higher than the normal mantle geotherm. In contrast, major-element compositions of oceanic plateau basalts are similar to those of mid-oceanic ridge basalts (MORB), requiring no excess temperature or significant amounts of extra components such as pyroxenite in their sources. These observations imply that OIB are generated from relatively small hot plumes during normal periods in the Earth's history, whereas oceanic plateau basalts are generated from high-flux and not-hot plumes that are forced to ascend through the upper mantle by flushing of subducted slabs down to the lower mantle. This in turn brings into question the conception that superplumes come from the bottom of the mantle with abnormally high temperatures.

D. A. Yuen et al. (eds.), Superplumes, 165–186.
© 2007 *Springer.*

1 INTRODUCTION

Basalt is the major product of plume-related volcanisms, such as those at hotspot volcanoes, oceanic plateaus and continental flood basalt provinces. Chemical compositions of plume-related basaltic lavas generally reflect not only the chemistry of plume material (e.g., Hofmann, 1997) but also the physical conditions of plume magmatism, including the potential temperature and upwelling rate of the source mantle (Watson and McKenzie, 1991; Sims et al., 1999). In this contribution, I will review the geochemical and petrological features of plume-related oceanic basalts to reveal the chemical properties of mantle plumes, which may in turn provide some constraints on the physical conditions of plume magmatism and the dynamics of mantle plumes, including both ordinary ones and so-called superplumes.

Isotopic ratios and major-element compositions of oceanic basalts are both powerful tools for figuring out the chemical properties of mantle plumes. Isotopic ratios of some key elements, such as Sr, Nd, Pb and Os, reveal important chemical characteristics of basalt sources (Zindler and Hart, 1986), because isotopic ratios of these elements reflect characteristics of the source materials and do not change during partial melting processes. On the other hand, major-element compositions of basalts are controlled by the chemical composition of their sources and the pressures and temperatures prevailing during magma generation, so they have been used for constraining the physical setting of partial melting of basalt sources (McKenzie and Bickle, 1988). Thus, isotopic ratios and major-element compositions of basalts provide complementary information on the chemical and physical manifestations of plumes. While reviewing the isotopic and major-element characteristics of plume-related basalts, I consider how the chemical compositions of plume-related basalts can be (or cannot be) linked to the chemical features of plume source materials and to the physical expressions of mantle plumes.

2 THE ORIGIN OF ISOTOPIC DIVERSITY IN OCEAN ISLAND BASALTS

Basaltic lavas that erupted from hotspot volcanoes, often called ocean island basalts (OIB), have been known to show a wide diversity in their isotopic compositions (Gast et al., 1964; DePaolo and Wasserburg, 1976; White and Hofmann, 1982) compared with mid-oceanic ridge basalts (MORB), indicating that OIB sources are chemically more heterogeneous than the MORB source (Fig. 1a). The isotopic diversity of MORB and OIB sources is often attributed to mixing between one depleted component (DMM: Depleted MORB Mantle) and three distinct "enriched" components: HIMU (high μ = high $^{238}U/^{204}Pb$), EM1, and EM2 (EM = enriched mantle) (Zindler and Hart, 1986), although some authors postulated the existence of "primitive" components in the OIB source, such as FOZO (Focus Zone: Hart et al., 1992), C (common component: Hanan and Graham, 1996) and PHEM (primitive helium mantle: Farley et al., 1992). Many mechanisms have been proposed for the origin of these enriched mantle components, but the most widely accepted model is recycling of subducted

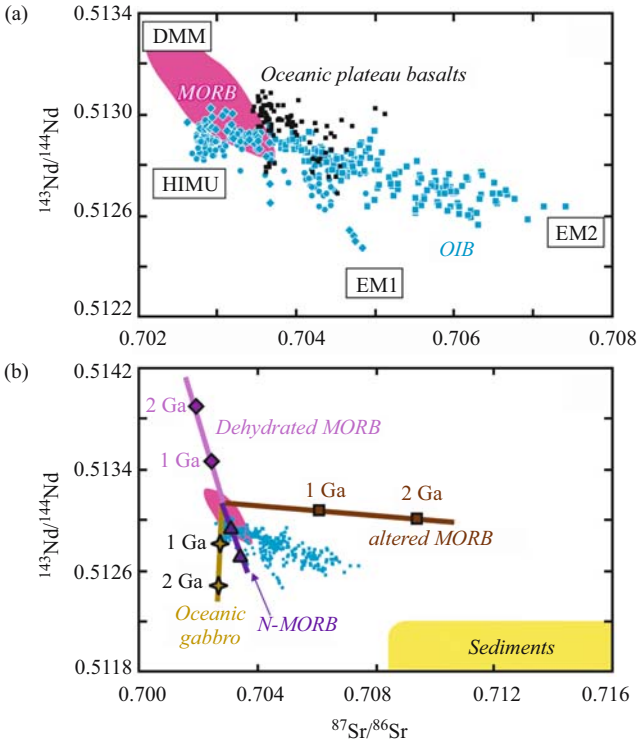

Figure 1. (a) Sr and Nd isotopic variations in OIB (blue) and oceanic plateau basalts (black). Plotted data for OIB are from selected volcanic chains with extreme isotopic signatures (circle: HIMU from St. Helena and Cook-Austral islands, diamond: EM1 from Pitcairn-Gambier islands, square: EM2 from Society and Samoa islands), and data for oceanic plateau basalts are from those in the Pacific ocean (Ontong Java Plateau, Manihiki Plateau, Hess Rise, Nauru Basin, and East Mariana Basin). OIB and oceanic plateau basalts data are from GEOROC database (http://georoc.mpch-mainz.gwdg.de/georoc/ [accessed May 2005]). MORB data (red) are from Melson et al. (1999). (b) Comparison with calculated present-day isotopic compositions of recycled oceanic crust and sediments as a function of subduction age. It is clear that recycled crustal materials can have a much wider range of isotopic compositions than OIB. Calculated data for dehydrated MORB are from Kogiso et al. (1997a), N-MORB, altered MORB and oceanic gabbro are from Stracke et al. (2003) and reference therein, and sediments from Aizawa et al. (1999).

crustal materials (mafic oceanic crust and seafloor sediments) which have been circulated in the convecting mantle and involved in upwelling plumes (Chase, 1981; Hofmann and White, 1982).

2.1 Problems in the recycling model for the origin of OIB

Recycling of subducted crustal components can produce isotopic compositions that are much more extreme than are present in the mantle as inferred from OIB chemistry.

The different components of subducted crust may qualitatively account for the isotope signatures of the enriched components, such as mafic oceanic crust for the radiogenic Pb isotopes of HIMU (e.g., Brenan et al., 1995; Kogiso et al., 1997a) and oceanic sediments for the high $^{87}Sr/^{86}Sr$ ratios of EM2 (Johnson and Plank, 2000). However, it has not been proved yet that recycling of crustal components is quantitatively consistent with observed isotopic variations (Kogiso et al., 1997a; Elliott et al., 1999; Niu and O'Hara, 2003; Stracke et al., 2003). Although some model calculations seem to reproduce quantitatively the isotopic diversity of OIB by recycling of crustal materials (Chauvel et al., 1992; Roy-Barman and Allègre, 1995), such models employ many implicit assumptions particularly regarding the compositions of subducted materials, and these have not been well confirmed. Although a detailed evaluation of previous models for the isotopic heterogeneity of OIB sources is beyond the scope of this contribution, I will consider briefly some of the fundamental difficulties in modeling of the isotopic diversity of OIB sources.

The difficulty in quantitative isotopic modeling of crustal recycling arises from the variability of potential compositions and ages of crustal components. Compositions of subducting crustal material vary significantly owing to variations in their original compositions, degrees of alteration during subduction, and recycling ages of subducted crustal materials, which drastically affect the isotopic evolution of subducted materials during recycling (Fig. 1b). In addition, since dehydration and partial melting during subduction are non-equilibrium and open-system processes, they may enhance compositional variability of subducting materials, although it is difficult to quantitatively estimate the effects of these processes on compositional and isotopic evolution. Thus, crustal materials subducted into the deep mantle can have considerable (and to some extent unpredictable) diversity in chemical and isotopic compositions, which may be much larger than those observed in worldwide OIB. In fact, calculated isotopic compositions of subducted oceanic crust and sediments in many isotope evolution models (Hart and Staudigel, 1989; Kogiso et al., 1997a; Stracke et al., 2003; Tatsumi and Kogiso, 2003) are extensively diverse compared with the OIB isotope variations (Fig. 1b). This seems to imply that enriched components in OIB derive from a rather restricted combination of subducted materials having specific compositions and recycling ages. However, Stracke et al. (2003) demonstrated, based on thorough modeling of isotope evolution, that any specific combinations of composition, subduction modification and age of subducted materials can hardly produce isotopic ratios of the enriched components for several elements at the same time. For example, recycling of N-MORB seems to explain the Sr and Nd isotopic ratios of HIMU (Fig. 1b), but it fails to produce the highly radiogenic Pb isotopes of HIMU. Subducted sediments can produce as high $^{87}Sr/^{86}Sr$ ratios as that of EM2, but it also fails to explain the Pb isotopic ratios (see Fig. 4 of Stracke et al., 2003).

Thus, recycling of crustal materials in the mantle is not quantitatively satisfactory as a model for the isotopic heterogeneity of OIB sources yet. Nevertheless, it is clear that subduction of crustal materials into the mantle is the principal process that introduces chemical heterogeneity into the mantle, because there are no other probable processes that can produce large diversity in isotopic ratios of both lithophile (Sr, Nd)

and chalcophile/siderophile (Pb, Os) elements within the mantle. Contribution of core material (e.g., Brandon et al., 1999) may explain the diversity of Os isotopic ratios of OIB, but it cannot have any effect on Sr and Nd isotopes. Recycling of metasomatised lithosphere can be an alternative explanation (McKenzie and O'Nions, 1983; Pilet et al., 2005), but the chemical consequences of metasomatism within lithosphere are not well constrained quantitatively. Therefore, it still seems reasonable and inevitable that a significant fraction of the isotopic heterogeneity of OIB is related to recycling of crustal materials.

2.2 Length scale of heterogeneity and sampling

A key question to be addressed upon relating subducted material to OIB sources is why OIB isotopic compositions are so "homogeneous" relative to the potential isotopic variability produced by recycled crustal materials (Fig. 1b). The isotopic ratios of subducted crustal materials are expected to extend to extreme values as demonstrated by quantitative model calculations (e.g., Stracke et al., 2003), but those of OIB lavas are always within a limited range. Therefore, there should be some processes that "homogenize" the isotopic ratios in OIB source regions if recycled crustal materials are involved there.

Homogenization of heterogeneity in OIB sources is strongly related to sampling length scale in OIB source regions. The isotopic diversity observed in OIB lavas is one of the results of partial melting processes which sample OIB sources on a certain scale, thereby homogenizing chemical heterogeneity to some extent (Fig. 2). Thus, an important point is the relationship between the sampling length scale of OIB lavas and those of the isotopic heterogeneities in the source. In general, a longer sampling length scale produces more homogeneous isotopic compositions in erupted lavas. One potential example is the difference in isotope diversity between OIB and oceanic plateau basalts. Basalts of large oceanic plateaus, such as Ontong Java, have less variable isotopic compositions than OIB (Fig. 1a). Oceanic plateaus consist of voluminous basaltic lavas that were produced within a relatively short duration (e.g., Tejada et al., 2002), which requires partial melting of an enormous region at once, that is, large length scales of partial melting. This results in averaging much larger dimensions of source regions than OIB, producing lavas with more homogeneous isotope signatures than OIB (Figs. 1a and 2a).

In the actual mantle, length scales of heterogeneity that can be detected by geophysical observations are the order of a kilometer or greater (e.g., Kaneshima and Helffrich, 1999), but geological and geochemical evidence suggests that much finer scales (order of a meter or less) of heterogeneity may exist in basalt source regions (e.g., Allègre and Turcotte, 1986; Saal et al., 1998) although it is difficult to constrain quantitatively. In any case, length scales of sampling (= averaging by partial melting) that produce OIB isotope variations from recycled crustal materials are likely larger than the length scales of source heterogeneity.

It should be noted that even a highly complicated heterogeneity spreading toward several directions in a two-dimensional space (e.g., subducted crustal materials on

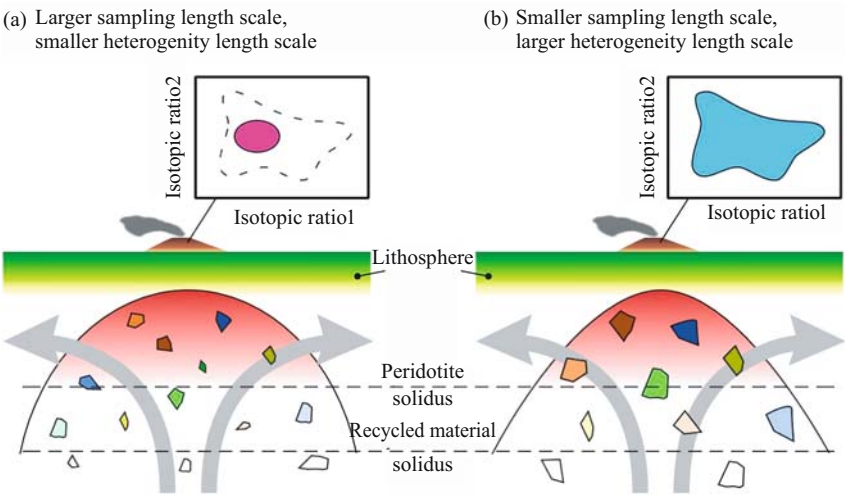

Figure 2. Schematic illustrations of melting of heterogeneous mantle (modified after Ito and Mahoney, 2005b). Recycled crustal materials (fragments with various color and size) are contained in a peridotite matrix. Darkness of the fragments and matrix indicates the extent of partial melting. Dashed lines are solidi of peridotite and recycled materials. Insets are schematic diagrams of isotopic variations in erupted lavas. Lavas generated from a mantle with a smaller length scale of heterogeneity (a) are expected to show less heterogeneous isotopic compositions than those from a mantle with a larger length scale (b).

the $^{87}Sr/^{86}Sr$-$^{143}Nd/^{144}Nd$ plot: Fig. 1a) can be reduced to a simple linear trend by sampling on large length scales (Kellogg et al., 2002). This implies that the mantle does not necessarily contain large regions that match the specific compositions of HIMU, EM1 and EM2. Instead, these enriched components may be produced in OIB lavas by processes that average domains with a wide range of isotopic compositions. This in turn means that the relatively restricted variation of OIB isotopic compositions can be derived from recycled crustal materials which have highly heterogeneous isotopic compositions (Figs. 1 and 2).

In examining the length scales of sampling from a heterogeneous mantle, the difference in solidus temperature between mantle peridotite and recycled materials must be taken into account. Because subducted crustal materials are dominantly mafic crust and subordinate silicic sediments, both of which have lower solidus temperatures than peridotite (e.g., Pertermann and Hirschmann, 2003a), they begin melting at a deeper level than the surrounding peridotite in upwelling heterogeneous plumes (Fig. 2). This may impose a strong bias in sampling of heterogeneous domains. The numerical analyses of Kogiso et al. (2004a) showed that the geochemical signature of recycled materials can be reflected in erupted lavas even if the size of the recycled domains on the order of a meter or smaller, because a partial melt from the recycled domain on that scale can segregate from the residual solid with its original geochemical signature before it is equilibrated with surrounding solid mantle. Moreover, if the lithosphere

above an upwelling heterogeneous plume is thicker, upwelling is blocked at a deeper level and the extent of peridotite melting is limited, resulting in relatively larger contributions of crustal materials to magma genesis. In this context, Ito and Mahoney (2005a,b) used numerical modelling to demonstrate that large isotopic variations in erupted OIB lavas can be produced from a single heterogeneous source with a variable lithosphere thickness. Thus, several factors such as solidus and melting depth may strongly control how efficiently recycled materials in a heterogeneous plume are sampled by erupted magmas, which in turn complicates inferences about the effective sampling length scales in OIB genesis.

In summary, to simulate the isotopic variation in OIB sources in the context of recycling of subducted crustal materials, it is necessary to explore the length scales of recycled materials in the mantle and those of sampling and averaging of the heterogeneity by partial melting. Thorough understanding of melting regimes in OIB generation also provides key insights into the complexities of sampling and averaging of source heterogeneities. These factors should be considered in future efforts to reveal the processes and mechanisms that produce the specific isotopic compositions of the enriched components, such as HIMU and EMs.

2.3 Regional variations of OIB isotopic diversity

The diversity of OIB isotopic compositions changes from ocean to ocean. OIB suites in the Pacific Ocean are characterized by the largest variability in their isotopic compositions among the worldwide OIB (Fig. 3): OIB with the strongest signatures of

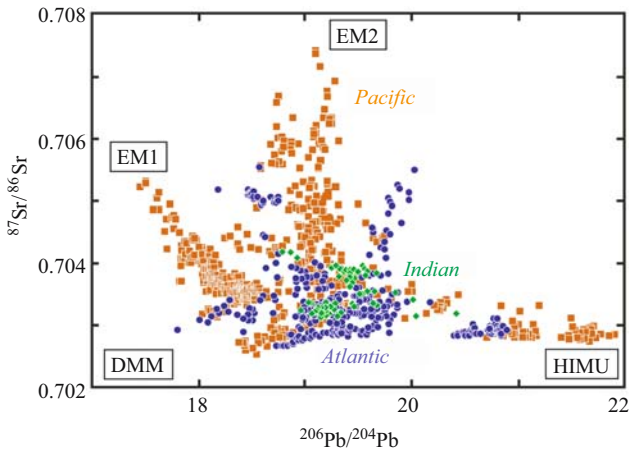

Figure 3. Pb and Sr isotopic variations in OIB from different oceans. OIB data for the Pacific (orange) are from Hawaii, Galapagos, Marquesas, Society, Pitcairn-Gambier, Cook-Austral, and Samoa islands, data for the Indian (green) are from Reunion and Comores islands, and those for the Atlantic (blue) are from Iceland, Azores, Madeira, Cape Verdes, Canary, St. Helena and Tristan da Cuhna. Data source is the GEOROC data base.

EM1, EM2, and HIMU all come from the Pacific Ocean. In contrast, OIB suites from the Atlantic and Indian oceans do not have extreme isotopic signatures that correspond to the enriched components. This indicates that mantle plumes beneath the Pacific Ocean tap the most extreme portion of OIB source regions.

There are several possible explanations for its largest diversity of isotopic compositions in the Pacific mantle. The first is its subduction history. Reconstruction of plate motions by Utsunomiya et al. (2007 this volume) demonstrates that the Pacific Ocean was born by the break up of the supercontinent Rodinia at ~750 Ma. This indicates that subducted crustal materials accumulated beneath Rodinia before ~750 Ma and that since then subduction has not occurred beneath the present Pacific Ocean. In contrast, in the mantle beneath the present Atlantic Ocean, subduction continued until ~250–200 Ma when another supercontinent Pangea broke up; and beneath the Indian Ocean, subduction of Neo-Tethys ceased at 55–45 Ma (Sengör, 1985). Thus, the crustal materials beneath the Pacific have the oldest subduction ages among those within possible OIB source regions. Since subducted materials with old ages can develop extreme isotopic compositions (Fig. 1b), the subducted materials beneath the Pacific Ocean may have the largest isotopic diversity. This may result in the largest isotopic diversity in erupted OIB lavas, if the length scales of sampling of OIB sources by ascending plumes are similar in all oceans (see discussion below). This scenario is, however, not consistent with isotopic model ages of OIB. It requires that the OIB source of each region has a model age similar to the local subduction ages, whereas OIB suites from all regions have much older Pb model ages around 1.8 Ga (Silver et al., 1988).

The second explanation for the largest isotopic diversity in the Pacific domain comes from the difference in length scales of heterogeneity and/or sampling. As Ito and Mahoney (2005a) demonstrated, melting of a single heterogeneous source at various sampling length scales can produce various extents of chemical heterogeneity in erupted lavas, from quite homogeneous to wide variation (Fig. 2). Thus, even if OIB source regions are evenly heterogeneous all over the mantle, the isotopic diversity observed in the Pacific OIB can be the largest in the case where sampling length scale is smaller for Pacific OIB than those of other areas, although the difference in sampling length scale between oceans is difficult to constrain. Alternatively, it may indicate that the length scale of the source heterogeneity is largest beneath the Pacific.

It should be noted that the length scale of recycled crustal materials could be correlated with mantle residence time. Because subducted lithosphere is stirred and stretched by convecting flow in the mantle (e.g., Allègre and Turcotte, 1986; Kellogg et al., 2002), bodies of crustal materials with greater residence times should have smaller widths. Consequently, subducted materials beneath the Pacific Ocean might have smaller length scales than those of other areas. However, it is difficult to estimate how efficiently subducted materials are stretched by mantle convection. The difference in cessation age of subduction between the Pacific and other areas is of the order of 100 million years (Utsunomiya et al., 2007 this volume), but it is not clear whether this time scale is long enough to make a difference in the length scales of subducted materials because of the complicated rheological behaviors of subducted crustal materials (e.g., Riedel and Karato, 1997).

3 CONSTRAINTS FROM MAJOR ELEMENTS OF OCEAN ISLAND BASALTS

OIB show a wide variation in their major-element compositions, from silica-saturated tholeiitic basalts to silica-undersaturated alkali basalts, basanites, and nephelinites (Fig. 4a). OIB lavas in some large hotspot volcanoes, such as Hawaii, are dominated by tholeiitic compositions, whereas those from many hotspots have silica-undersaturated compositions (Hirschmann et al., 2003). Although the variations in OIB major elements are mostly independent of isotopic compositions, concentrations of some major elements are correlated with isotopic ratios (e.g., high Fe and Ca in HIMU basalts: Kogiso et al., 1997b), which have been attributed to recycling of crustal components in OIB sources (Hauri, 1996; Kogiso et al., 1997b). Provided that OIB sources contain recycled crustal materials, as proposed for explaining the OIB isotope diversity, major-element compositions of OIB could be influenced by partial melting of mafic lithologies because subducted crustal materials are dominated by mafic lithologies, such as MORB.

3.1 Melting of pyroxenite and OIB genesis

Recent progress in high-pressure experiments on various types of mafic lithologies (hereafter all called "pyroxenites") have revealed that partial melting of pyroxenites

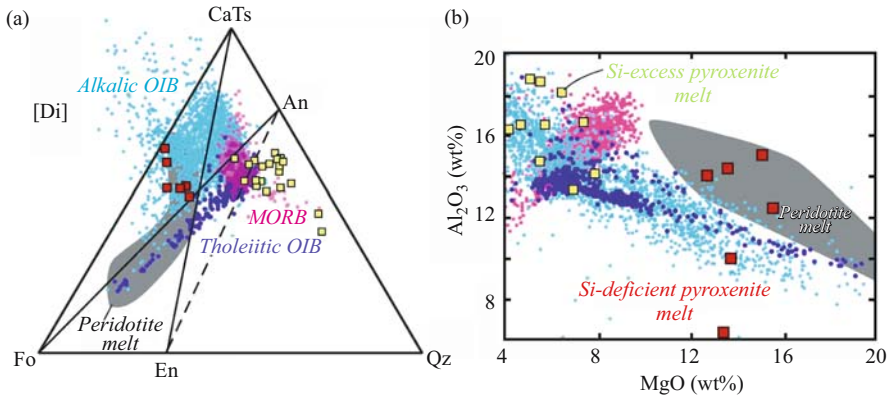

Figure 4. Comparison of major-element composition between OIB and experimental partial melts of pyroxenite and peridotite produced at high pressures (>2 GPa). Larger symbols with solid outline are the pyroxenite partial melts. Experimental data are from the compilation of Kogiso et al. (2004b). Data sources for OIB and MORB are as in Figure 1. (a) Normative plot in the pseudoternary system forsterite (Fo)-Ca-Tschermaks pyroxene (CaTs)-quartz (Qz) projected from diopside [Di] using the method of O'Hara (1968). The anorthite (An)-Fo join is the boundary between silica-undersaturated compositions (left side) and silica-saturated ones (right side). The enstatite (En)-CaTs join is the garnet-pyroxene thermal divide, which separates Si-deficient compositions (left side) from Si-excess ones (right side). (b) Al_2O_3 contents plotted against MgO.

in the mantle can produce a variety of magmas from silica-saturated andesite to strongly silica-undersaturated basanite (Fig. 4) (Pertermann and Hirschmann, 2003b; Kogiso et al., 2003). The major-element variation of pyroxenite-derived partial melts systematically depends on the composition of pyroxenite (Kogiso et al., 2004b): pyroxenites with an excess silica component in terms of the garnet-pyroxene thermal divide (the En–CaTs join of Fig. 4a: O'Hara, 1968) produce silica-rich melts and those deficient in the silica component produce silica-poor melts. The silica-rich melts from silica-excess pyroxenites mostly have a tholeiitic composition, and the silica-poor melts from silica-deficient pyroxenites are mostly alkali basaltic (Fig. 4a).

Note that both tholeiitic and alkali basaltic OIB are characterized by low Al_2O_3 contents compared with experimentally derived partial melts of peridotite (Fig. 4b), suggesting that OIB lavas are not typically produced by simple partial melting of mantle peridotite. Partial melts from both silica-deficient and silica-excess pyroxenites have Al_2O_3 similar to OIB lavas, however (Fig. 4b). In particular, partial melts from a silica-deficient pyroxenite (MIX1G: red squares in Fig. 4) have a composition similar to primitive (= high-MgO) alkalic OIB lavas, not only in Al_2O_3 but also in other major-element contents (Kogiso et al., 2003), indicating that partial melting of silica-deficient pyroxenite significantly contributes to the genesis of alkalic OIB. Partial melts from silica-excess pyroxenites are also similar to tholeiitic OIB lavas, but are too low in MgO to be parental to tholeiitic OIB. Nevertheless, tholeiitic OIB compositions can be produced by mixing of partial melts of silica-excess pyroxenites with MgO-rich melts from peridotite (Fig. 4). Thus, partial melting of pyroxenite lithologies can account for the major-element compositions of both tholeiitic and alkali basaltic OIB.

Pyroxenites in the mantle may originate by many different processes, but a volumetrically dominant potential source is subducted MORB crust (e.g., Hirschmann and Stolper, 1996). The average MORB has a silica-excess composition (Fig. 4a), but it can be converted to silica-deficient compositions by a combination of subduction-related processes and stirring by mantle convection. Dehydration and partial melting of subducting oceanic crust likely release silica-rich aqueous fluid or siliceous melts, resulting in extraction of silica contents from subducting crust. This may ultimately lead to formation of bimineralic pyroxenite, which consists solely of garnet and pyroxene. If such bimineralic pyroxenite is stirred and stretched in the convecting mantle, it will be hybridized, at least partly, with surrounding peridotite and form pyroxenite with silica-deficient compositions (Kogiso et al., 2003). Thus, subducted crust can be a source for both silica-excess and silica-deficient pyroxenites which in turn can be source materials for OIB lavas.

3.2 Melting processes within heterogeneous mantle

The pyroxenite melting experiments mentioned above have simulated equilibrium batch melting of single homogeneous compositions. However, melting processes in actual mantle plumes are likely to be dynamic and include melt segregation and

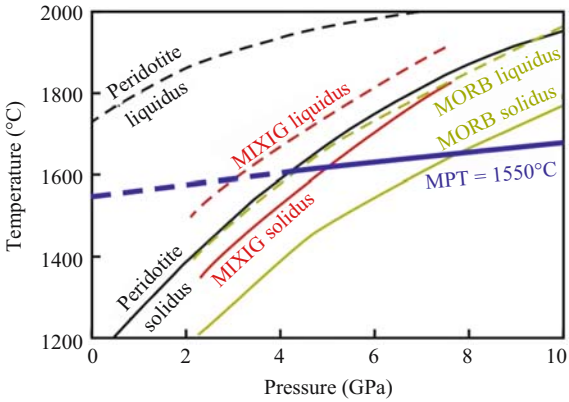

Figure 5. Solidi (solid curves) and liquidi (broken curves) of a silica-excess pyroxenite (MORB: Yasuda et al., 1994), a silica-deficient pyroxenite (MIX1G: Kogiso et al., 2003) and typical peridotite (KLB-1: Takahashi et al., 1993). Also shown is an adiabatic path for a mantle potential temperature (MPT) of 1550°C (Ita and Stixrude, 1992).

consequently fractional or near-fractional melting of heterogeneous lithologies. In such processes, the length scales of heterogeneity and melting region are the important factor to be considered.

Because pyroxenites have lower solidi than peridotite (Fig. 5), pyroxenite-derived melts first segregate from the residue within a heterogeneous mixture of peridotite and pyroxenite, and then migrate upward through solid peridotite up to where peridotite is partially molten (Kogiso et al., 2004a). Before and during segregation, pyroxenite partial melts may react with surrounding solid peridotite, resulting in a significant change in their compositions (e.g., Kelemen et al., 1997). Within a partially molten pyroxenite body, equilibration of the pyroxenite with solid peridotite is promoted by diffusion through both solid peridotite and an interconnected melt network within the pyroxenite body. The larger the pyroxenite body, the longer the time scale of the diffusive equilibration. Therefore, if the pyroxenite body is larger than a certain size, the pyroxenite melt can segregate with its original chemical signatures before equilibrating with surrounding peridotite. Kogiso et al. (2004a) estimated that the critical width of a pyroxenite body for melt segregation without equilibration with the mantle is several meters.

Reaction between the segregated pyroxenite melt and surrounding peridotite during transportation can be controlled by many factors in addition to diffusion, such as melting phase relations in peridotite-melt systems (Kelemen, 1990), melt/rock ratio (Kelemen et al., 1997), reaction kinetics (Morgan and Liang, 2003), and efficiency of melt percolation within a peridotite matrix (Daines and Kohlstedt, 1993; Lundstrom, 2000). It is quite difficult to estimate the combined effect of these factors on melt chemistry, not only because each is controlled by many parameters but also because they are partly dependent on each other. More detailed discussion of melt transport is

beyond the scope of this contribution. However, the factors listed above are of importance near the interface between the pyroxenite melt and surrounding peridotite, so pyroxenite melts passing through wide melt channels may be less affected by reactions. In other words, there may be a critical melt path width required for preservation of a melt composition unaffected during transportation.

3.3 Temperature of OIB genesis

Because solidus temperatures of pyroxenites are generally lower than those of mantle peridotite, at any particular depth a pyroxenite-bearing OIB source can produce partial melts at lower temperatures than peridotite (Fig. 5). The mantle potential temperature of OIB genesis has been estimated to be above 1500°C (McKenzie and O'Nions, 1991; Watson and McKenzie, 1991) based on an assumption that the OIB source is homogeneous peridotite. Lower potential temperatures may be permissible if pyroxenite contributes significantly to OIB sources. However, the experimental pyroxenite-derived melts that are similar to primitive alkalic OIB lavas (Fig. 4) are generated near 1650°C at 5 GPa (Kogiso et al., 2003), which corresponds to a potential temperature of ~1550°C (Fig. 5). MORB-like (silica-excess) pyroxenite, which may be present in the source of some tholeiitic OIB, is partially molten at much lower temperatures (Fig. 5), but such silica-excess pyroxenite cannot produce liquids parental to primitive tholeiitic OIB lavas. Producing primitive tholeiitic OIB requires more MgO-rich liquids, as mentioned in Section 3.1, which in turn requires high temperature components from peridotite melting. Thus, even if OIB sources contain substantial amounts of pyroxenite lithologies, a potential temperature ~200°C higher than the normal oceanic geotherm (McKenzie and Bickle, 1988) is required for OIB genesis, at least under dry conditions.

Enrichment in volatile components, such as H_2O and CO_2, allows generation of OIB at lower temperatures because they strongly depress melting temperatures of mantle materials. OIB sources are known to be more enriched in H_2O than those beneath mid-oceanic ridges (Dixon et al., 2002; Wallace, 1998), leading to the suggestion that "hotspot" magmatism is caused by excess H_2O rather than by excess temperature (Schilling et al., 1980; Bonnatti, 1990; Green et al., 2001). Typical H_2O contents of OIB sources range from 500 to 1000 ppm (e.g., Wallace, 1998; Dixon and Clague, 2001; Nichols et al., 2002). Even such small amounts of H_2O may have a strong effect on melt productivity. Experimental studies show that addition of 0.1–0.2 wt% H_2O drastically enhances melt productivity from peridotite (Hirose and Kawamoto, 1995) and pyroxenite sources (Médard et al., 2006). Moreover, the presence of small amounts of H_2O (<0.1 wt%) does not affect significantly the composition of partial melts (Hirose and Kawamoto, 1995; Gaetani and Grove, 1998), suggesting that the liquids from hydrous peridotite and pyroxenite may be similar to those from their anhydrous equivalents. Therefore, the difference in melting temperature between OIB and MORB may be smaller than expected when both magmas are generated under dry conditions.

Despite the high water contents in OIB sources, a higher temperature is still needed for OIB genesis. This is because the small amount of H_2O in OIB sources may not provide the buoyancy to drive focused upwelling. Provided that OIB magmatism is caused by upwelling of mantle plumes, OIB sources must be conveyed from the deeper part of the mantle. And recycled crustal materials, if present, inhibit upwelling because they are denser than mantle peridotite throughout the upper mantle (Irifune and Ringwoood, 1993; Nishihara et al., 2005). Some other source of buoyancy is necessary to compensate for the negative buoyancy of recycled materials. The presence of water may diminish the density of plume materials to some extent, but the estimated amounts of water in OIB sources (<0.1 wt%) seem too low to have a substantial effect on promoting upwelling, although the effect of H_2O on density is still to be investigated quantitatively. Consequently, a high temperature may be the only likely source of buoyancy for upwelling of mantle plumes that cause hotspot magmatism (see discussion below and Fig. 7).

4 PERSPECTIVES ON THE DYNAMICS OF MANTLE PLUMES

4.1 Link between plume dynamics and isotopic diversity

As mentioned in Section 2, the global isotopic diversity of OIB can be expressed by mixing between the depleted mantle and the enriched components (HIMU, EM1 and EM2) (and possibly enriched components like FOZO). However, it doesn't necessarily guarantee that components actually exist as discrete domains in the mantle with the compositions identical to those observed in erupted OIB lavas, because some processes that average a wider heterogeneity possibly present in OIB sources can make these components appear in OIB chemistry. It is crucial to explain why OIB isotopic compositions are so "homogeneous" relative to the potential isotopic diversity that subducted crustal materials may have, as mentioned above (Fig. 1b). The global and local variations in OIB isotopes (Figs. 1 and 3) result from integration of complicated processes and mechanisms controlled by many factors including the chemical variability of original subducting materials, the geological history of subduction, length scales of heterogeneity in the mantle, and length scales of averaging by partial melting and/or tapping of the heterogeneity. These factors are strongly connected with the rheological properties of mantle materials and recycled crustal materials. That is, an improved understanding of the dynamic behavior of heterogeneous mantle is necessary for interpreting the geochemical data of erupted OIB lavas.

4.2 "PARADOX" about formation of oceanic plateaus

OIB (i.e., lavas erupted at hotspot volcanoes) and oceanic plateau basalts are thought to be products of magmatism caused by decompressional melting within upwelling mantle plumes. As discussed above, it is likely that OIB lavas are generated from mantle plumes that include recycled crustal materials and have higher temperatures

than surrounding mantle. Since both recycled crustal materials and high temperature enhance melt production, the high melt productivity of hotspot magmatism can be attributed to an excess of potential temperature and to fertile components (crustal materials) in the plume sources. Also, an excess temperature is required to compensate for the negative buoyancy of recycled crustal materials.

In contrast, mantle plumes producing large oceanic plateaus have a paradoxical feature. Formation of a large oceanic plateau, such as Ontong Java Plateau, requires production of an enormous amount of basalt within a geologically short period, which in turn seems to require an extremely high potential temperature and/or large amounts of fertile material in the source (Farnetani and Richards, 1994; Cordery et al., 1997; Korenaga, 2005). Nevertheless, major-element compositions of oceanic plateau basalts are quite similar to MORB (Fig. 6). As illustrated in Figure 6, the majority of oceanic plateau basalts plots within the range of MORB composition, suggesting that oceanic plateau basalts and MORB may be generated from similar sources at similar potential temperatures and pressures. Paleogeographic reconstructions by Utsunomiya et al. (2007 this volume) demonstrated that Cretaceous oceanic plateaus in the Pacific were formed near oceanic ridges (Fig. 4 of Utsunomiya et al., 2007 this volume), suggesting that these oceanic plateau basalts and MORB were generated at similar depths. The similarity in MgO content between oceanic plateau basalts and MORB supports the idea that both suites are generated at similar temperatures because MgO contents in partial melts are chiefly controlled by melting temperature (Hirose and Kushiro, 1993). The low MgO contents of oceanic plateau basalts could

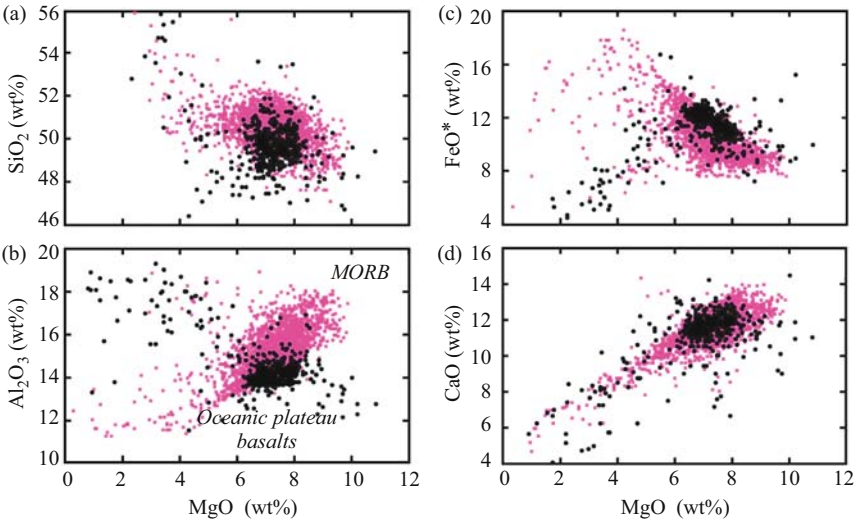

Figure 6. Comparison between oceanic plateau basalts from the Pacific (black) and MORB (red). Data sources are as in Figure 1.

derive from extensive crystal fractionation from more primitive melts produced at a higher temperature from a depleted peridotite like the MORB source (Farnetani et al., 1996). However, it is unlikely that the two suites of basalts having similar compositions (i.e., oceanic plateau basalts and MORB) arrive at similar compositions through different fractionation paths from melts produced at different temperature conditions from a similar source. In fact, extensive crystal fractionation from high-temperature melts of peridotite (Farnetani et al., 1996) cannot explain Ca/Al ratios of oceanic plateau basalts. The low Al_2O_3 contents of oceanic plateau basalts (Fig. 6b) may indicate some contribution from low-Al_2O_3 partial melts of recycled crustal components. Even so, excess temperature is not needed any more for the genesis of oceanic plateau basalts because recycled pyroxenites have lower solidus temperatures (Fig. 5). Thus, it is expected that the mantle plumes that form large oceanic plateaus have potential temperatures (and probably major-element compositions) similar to those of the MORB source.

4.3 Superplume: No excess temperature?

It is certain that fluxes of plumes forming oceanic plateaus are much larger than those of plumes forming hotspot volcanoes, and that is why oceanic plateaus are thought to be products of extremely large plumes. Nevertheless, the chemistry of oceanic plateau basalts doesn't support the idea that the huge fluxes of such "superplumes" are of high-temperature origin. If plateau-forming superplumes don't have excess temperatures enough for ascending through the upper mantle by themselves, then what is the cause of the huge flux of them?

A possible solution for this "oceanic plateau paradox" is that plateau-forming plumes are forced to ascend through the upper mantle as counter flows to the flushing of stagnated subducted slabs at subduction zones (Fig. 7a). Subducted slabs stagnated above the 660-km boundary are considered to descend intermittently into the lower mantle (Christensen and Yuen, 1985; Tackley et al., 1993). Such flushing of upper mantle materials inevitably triggers large-scale upwelling of lower mantle materials through the 660-km boundary, and this could plausibly be the chief cause of the huge-volume magmatism at large igneous provinces, including oceanic plateaus (Maruyama, 1994; Utsunomiya et al., 2007 this volume). Such counter flows from the lower mantle could have higher potential temperatures than the upper mantle, but elevated temperatures are not an inevitable feature of such upwelling. If there is no substantial jump in temperature across the 660-km boundary, a counter flow to slab flushing can have a potential temperature similar to that prevailing in the upper mantle (Fig. 7a). In addition, if the counter flow contains a little more water (<0.1 wt%) than the upper mantle, its viscosity can be orders of magnitude lower than the surrounding mantle (Jung and Karato, 2001), which could result in ascending flows with quite a high flux. Furthermore, since a small amount of water enhances melt production but does not affect major elements of produced melts (Hirose and Kawamoto, 1995; Gaetani and Grove, 1998), a high-flux plume can produce a large amount of magmas with MORB-like composition.

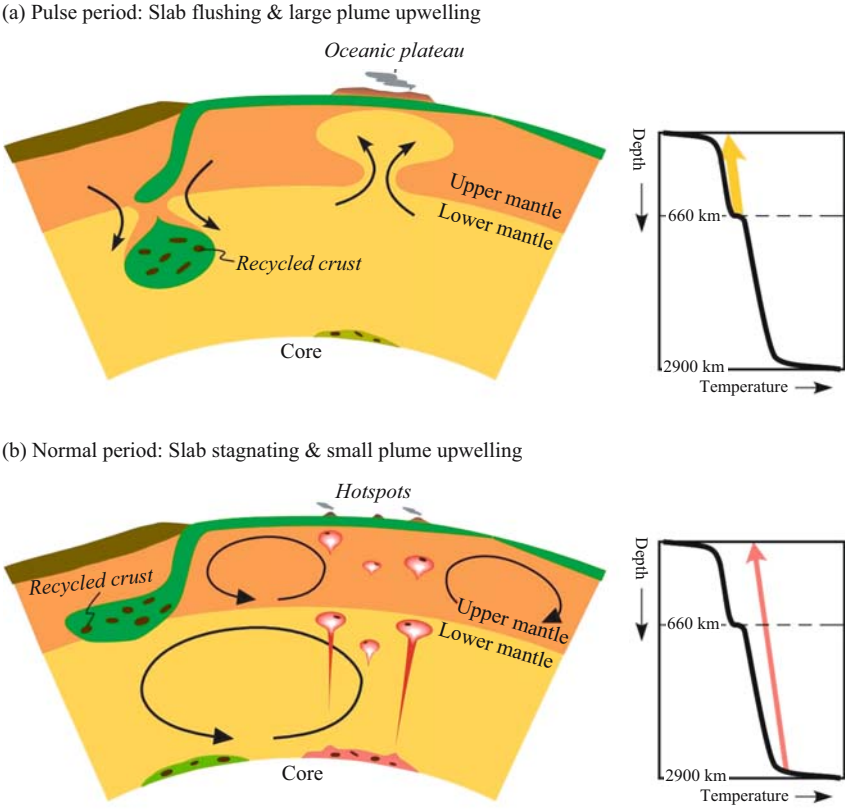

Figure 7. Cartoons of different modes of mantle convection. Insets are schematic diagrams of the mantle geotherm. Arrows indicate temperature profiles of ascending plumes. (a) Pulse period when large oceanic plateaus are formed. Significant temperature excess is not necessary for superplume upwelling because flushing of stagnated slabs forces the superplume to ascend as a counter flow from just below the 660 km boundary. (b) Normal period when oceanic islands are formed at normal hotspots. Subducted slabs stagnate at subduction zones and plumes with excess temperature ascend.

A key point of this scenario is the magnitude of the temperature jump across the 660-km boundary. Stagnation of subducted slabs above the 660-km boundary limits material exchange rate across the 660-km boundary to low, which may increase the temperature gap between the upper and lower mantle (Fig. 7b). Therefore, the stagnation and flushing of subducted slabs may not be a probable explanation for the upwelling of high-flux plumes with normal temperature. Nevertheless, the large temperature gap between the upper and lower mantle can be localized around subduction zones, and the areas far from subduction zones, where plateau-forming plumes upwell, may have a smooth geotherm without any temperature gap at the 660-km boundary. It is unclear whether such a temperature structure can be achieved in the mantle, but,

in any case, it is certain that triggering upwelling of plateau-forming plumes by slab flushing can occur without a large excess of temperature in the plumes.

Another key point is that this scenario requires the lower mantle having a major-element composition similar to that of the upper mantle. As discussed above, oceanic plateau basalts and MORB are likely to be produced at similar pressure–temperature conditions from similar source materials. This doesn't necessarily mean that the lower mantle have the entirely same lithology with the upper mantle. In fact, peridotites with different mineral proportions can produce partial melts with quite similar composition if they have the same mineral assemblage (olivine+orthopyroxene+clinopyroxene+spinel) upon melting (e.g., Pickering-Witter and Johnston, 2000). However, the similarity between oceanic plateau basalts and MORB on the MgO-FeO diagram (Fig. 6c) strongly suggests that both are generated from sources having a similar Fe/Mg ratio, because Fe/Mg ratios in partial melts are highly sensitive to those in their source materials (Hirose and Kushiro, 1993; Kogiso et al., 1998). This means that the lower mantle has a similar composition with the upper mantle at least in terms of Fe/Mg ratio if oceanic plateaus are indeed formed by superplumes from the lower mantle.

4.4 Speculation over styles of mantle convection

The above discussion indicates that OIB and oceanic plateau basalts may be generated from different types of source: OIB are produced from a heterogeneous mixture of peridotite and subducted crustal materials (mainly pyroxenite) at high temperatures compared to MORB, whereas oceanic plateau basalts are formed from material similar to MORB source mantle at normal temperatures. Another important difference between OIB and plateau basalts is in the periodicity of their formation: OIB have been continually erupting on the Earth's surface for several million years with various lengths of interval, whereas oceanic plateaus were formed only at certain periods when the whole mantle was activated (Utsunomiya et al., 2007 this volume).

These differences between OIB and oceanic plateaus may correspond to different modes of mantle convection (Fig. 7). During a normal period, such as the present Earth, active upwelling flow in the mantle creates hot "normal" plumes that cause continual hotspot magmatism producing OIB lavas. Large-scale material exchange between the upper and lower mantle does not occur because subducted slabs are being stagnated above the 660-km boundary (Fig. 7b). This is the reason why only hot plumes are active during a normal period. Such hot plumes may upwell from the core-mantle boundary, because subducted crustal materials, which are to be contained in plumes, will accumulate at the bottom of the lower mantle (Ono et al., 2005). In contrast, during a pulse period such as Cretaceous (Utsunomiya et al., 2007 this volume), stagnated slabs flush down into the lower mantle and resultant "superplumes" upwell through the upper mantle, forming large oceanic plateaus. Because a downwelling flow of stagnant slabs forces a counter flow to ascend into the upper mantle, a superplume may not necessarily be hot. Material with a normal temperature just beneath the 660-km boundary can ascend in a large plume (Fig. 7a).

ACKNOWLEDGEMENTS

I am grateful to Shige Maruyama for inviting me to contribute to this volume. My thoughts on the genesis of plume-related basalts have always been inspired by him since his first paper on superplume appeared in 1994. I also acknowledge constructive and helpful comments by Marc Hirschmann, Brian Windley, and Dave Yuen.

REFERENCES

Aizawa, Y., Y. Tatsumi, and H. Yamada (1999) Element transport by dehydration of subducted sediments: Implication for arc and ocean island magmatism. *The Island Arc*, 8, 38–46.

Allègre, C., and D.L. Turcotte (1986) Implications of a two-component marble-cake mantle. *Nature*, 323, 123–127.

Bonatti, E. (1990) Not so hot 'hot spots' in the oceanic mantle. *Science*, 250, 107–111.

Brandon, A.D., M.D. Norman, R.J. Walker, and J.W. Morgan (1999) ^{186}Os-^{187}Os systematics of Hawaiian picrites. *Earth Planet. Sci. Lett.*, 174, 25–42.

Brenan, J.M., H.F. Shaw, F.J. Ryerson, and D.L. Phinney (1995) Mineral-aqueous fluid partitioning of trace elements at 900°C and 2.0 GPa: Constraints on the trace element chemistry of mantle and deep crustal fluids. *Geochim. Cosmochim. Acta*, 59, 3331–3350.

Chase, C.G. (1981) Oceanic island Pb: Two-stage histories and mantle evolution. *Earth Planet. Sci. Lett.*, 52, 227–284.

Chauvel, C., A.W. Hofmann, and P. Vidal (1992) HIMU-EM: The French Polynesian connection. *Earth Planet. Sci. Lett.*, 110, 99–119.

Christensen, U.R., and D.A. Yuen (1985) Layered convection induced by phase transitions. *J. Geophys. Res.*, 90, 10291–10300.

Cordery, M.J., G.F. Davies, and I.H. Campbell (1997) Genesis of flood basalts from eclogite-bearing mantle plumes. *J. Geophys. Res.*, 102, 20179–20197.

Daines, M.J., and D.L. Kohlstedt (1993) A laboratory study of melt migration. *Philos. Trans. R. Soc. Lond. A*, 342, 43–52.

DePaolo, D.J., and G.J. Wasserburg (1976) Inferences about magma sources and mantle structure from variations of $^{143}Nd/^{144}Nd$. *Geophys. Res. Lett.*, 3, 743–746.

Dixon, J.E., and D.A. Clague (2001) Volatiles in basaltic glasses from Loihi seamount, Hawaii: Evidence for a relatively dry plume component. *J. Petrol.*, 42, 627–654.

Dixon, J.E., L. Leist, C. Langmuir, and J.G. Schilling (2002) Recycled dehydrated lithosphere observed in plume-influenced mid-ocean-ridge basalt. *Nature*, 420, 385–389.

Elliott, T., A. Zindler, and B. Bourdon (1999) Exploring the Kappa conundrum: The role of recycling in the lead isotope evolution of the mantle. *Earth Planet. Sci. Lett.*, 169, 129–145.

Farley, K.A., J.H. Natland, and H. Craig (1992) Binary mixing of enriched and undegassed (primitive?) mantle components (He, Sr, Nd, Pb) in Samoan lavas. *Earth Planet. Sci. Lett.*, 111, 183–199.

Farnetani, C.G., and M.A. Richards (1994) Numerical investigations of the mantle plume initiation model for flood basalt events. *J. Geophys. Res.*, 99, 13813–13833.

Farnetani, C.G., M.A. Richards, and M.S. Ghiorso (1996) Petrological models of magma evolution and deep crustal structure beneath hotspots and flood basalt provinces. *Earth Planet. Sci. Lett.*, 143, 81–94.

Gaetani, G.A., and T.L. Grove (1998) The influence of water on melting of mantle peridotite. *Contrib. Mineral. Petrol.*, 131, 323–346.

Gast, P.W., G.R. Tilton, and C. Hedge (1964) Isotopic composition of lead and strontium from Ascension and Gough Islands. *Science*, 145, 1181–1185.

Green, D.H., T.J. Falloon, S.M. Eggins, and G.M. Yaxley (2001) Primary magmas and mantle temperatures. *Eur. J. Mineral.*, 13, 437–451.

Hanan, B.B., and D.W. Graham (1996) Lead and helium isotope evidence from oceanic basalts for a common deep source of mantle plumes. *Science*, 272, 991–995.

Hart, S.R., and H. Staudigel (1989) Isotopic characterization and identification of recycled components. In Hart, S.R., and L. Gülen (eds.) Crust/Mantle Recycling at Convergence Zones, Kluwer, Reidel, pp. 15–28.

Hart, S.R., E.H. Hauri, L.A. Oschmann, and J.A. Whitehead (1992) Mantle plumes and entrainment: Isotope evidence. *Scienc*e, 256, 517–520.

Hauri, E.H. (1996) Major-element variability in the Hawaiian mantle plume. *Nature*, 382, 415–419.

Hirose, K., and I. Kushiro (1993) Partial melting of dry peridotites at high pressures: Determination of compositions of melts segregated from peridotite using aggregates of diamond. *Earth Planet. Sci. Lett.*, 114, 477–489.

Hirose, K., and T. Kawamoto (1995) Hydrous partial melting of lherzolite at 1 GPa: The effect of H2O on the genesis of basaltic magmas. *Earth Planet. Sci. Lett.*, 133, 463–473.

Hirschmann, M.M., and E.M. Stolper (1996) A possible role for garnet pyroxenite in the origin of the "garnet signature" in MORB. *Contrib. Mineral. Petrol.*, 124, 185–208.

Hirschmann, M.M., T. Kogiso, M.B. Baker, and E.M. Stolper (2003) Alkalic magmas generated by partial melting of garnet pyroxenite. *Geology*, 31, 481–484.

Hofmann, A.W. (1997) Mantle geochemistry: The message from oceanic volcanism. *Nature*, 385, 219–229.

Hofmann, A.W., and W.M. White (1982) Mantle plumes from ancient oceanic crust. *Earth Planet. Sci. Lett.*, 57, 421–436.

Irifune, T., and T.A. Ringwood (1993) Phase transformations in subducted oceanic crust and buoyancy relationships at depths of 600–800 km in the mantle. *Earth Planet. Sci. Lett.*, 117, 101–110.

Ita, J., and L. Stixrude (1992) Petrology, elasticity, and composition of the mantle transition zone. *J. Geophys. Res.*, 97(5), 6849–6866.

Ito, G., and J.J. Mahoney (2005a) Flow and melting of a heterogeneous mantle: 1. Method and importance to the geochemistry of ocean island and mid-ocean ridge basalts. *Earth Planet. Sci. Lett.*, 230, 29–46.

Ito, G., and J.J. Mahoney (2005b) Flow and melting of a heterogeneous mantle: 2. implications for a chemically nonlayered mantle. *Earth Planet. Sci. Lett.*, 230, 47–63.

Johnson, M.C., and T. Plank (1999) Dehydration and melting experiments constrain the fate of subducted sediments. *Geochem. Geophys. Geosyst.*, 13, 1999GC000014.

Jung, H., and S. Karato (2001) Water-induced fabric transitions in olivine. *Science*, 293, 1460–1463.

Kaneshima, S., and G. Helffrich (1999) Dipping low-velocity layer in the mid-lower mantle: Evidence for geochemical heterogeneity. *Science*, 283, 1888–1891.

Kelemen, P.B. (1990) Reaction between ultramafic rock and fractionating basaltic magma I. Phase relations, the origin of calc-alkaline magma series, and the formation of discordant dunite. *J. Petrol.*, 31, 51–98.

Kelemen, P.B., G. Hirth, N. Shimizu, M. Spiegelman, and H.J.B. Dick (1997) A review of melt migration processes in the adiabatically upwelling mantle beneath oceanic spreading ridges. *Philos. Trans. R. Soc. Lond. A*, 355, 283–318.

Kellogg, J.B., S.B. Jacobsen, and R.J. O'Connell (2002) Modeling the distribution of isotopic ratios in geochemical reservoirs. *Earth Planet. Sci. Lett.*, 204, 183–202.

Kogiso, T., Y. Tatsumi, and S. Nakano (1997a) Trace element transport during dehydration processes in the subducted oceanic crust: 1. Experiments and implications for the origin of ocean island basalts. *Earth Planet. Sci. Lett.*, 148, 193–205.

Kogiso, T., Y. Tatsumi, G. Shimoda, and H.G. Barsczus (1997b) High μ (HIMU) ocean island basalts in southern Polynesia: New evidence for whole-mantle scale recycling of subducted oceanic crust. *J. Geophys. Res.*, 102, 8085–8103.

Kogiso, T., K. Hirose, and E. Takahashi (1998) Melting experiments on homogeneous mixtures of peridotite and basalt: Application to the genesis of ocean island basalts. *Earth Planet. Sci. Lett.*, 162, 45–61.

Kogiso, T., M.M. Hirschmann, and D.J. Frost (2003) High pressure partial melting of garnet pyroxenite: Possible mafic lithologies in the source of ocean island basalts. *Earth Planet. Sci. Lett.*, 216, 603–617.

Kogiso, T., M.M. Hirschmann, and P.W. Reiners (2004a) Length scales of mantle heterogeneities and their relationship to ocean island basalt geochemistry. *Geochim. Cosmochim. Acta*, 68, 345–360.

Kogiso, T., M.M. Hirschmann, and M. Pertermann (2004b) High pressure partial melting of mafic lithologies in the mantle. *J. Petrol.*, 45, 2407–2422.

Korenaga, J. (2005) Why did not the Ontong Java Plateau form subaerially? *Earth Planet. Sci. Lett.*, 234, 385–399.

Lundstrom, C.C. (2000) Rapid diffusive infiltration of sodium into partially molten peridotite. *Nature*, 403, 527–530.

Maruyama, S. (1994) Plume tectonics. *J. Geol. Soc. Jpn.*, 100, 24–49.

McKenzie, D., and M.J. Bickle (1988) The volume and composition of melt generated by extension of the lithosphere. *J. Petrol.*, 29, 625–679.

McKenzie, D., and R.K. O'Nions (1983) Mantle reservoirs and ocean island basalts. *Nature*, 301, 229–231.

McKenzie, D., and R.K. O'Nions (1991) Partial melt distributions from inversion of rare earth element concentrations. *J. Petrol.*, 32, 1021–1091.

Médard, E., M.W. Schmidt, P. Schiano, and L. Ottolini (2006) Melting of amphibolite-bearing wehrlites: An experimental study on the origin of ultra-calcic nepheline-normative melts. *J. Petrol.*, 47, 481–504.

Melson, W.G., T. O'Hearn, and P. Kimberly (1999) Volcanic glasses from sea-floor spreading centers and other deep sea tectonic settings: Major and minor element compositions in the Smithsonian WWW Data Set (abstract). *EOS, Trans. Am. Geophys. Un.*, 80(46), F1177.

Morgan, Z., and Y. Liang (2003) An experimental and numerical study of the kinetics of harzburgite reactive dissolution with applications to dunite dike formation. *Earth Planet. Sci. Lett.*, 214, 59–74.

Nichols, A.R.L., M.R. Carrol, and Á. Höskuldsson (2002) Is the Iceland hot spot also wet? Evidence from the water contents of undegassed submarine and subglacial pillow basalts. *Earth Planet. Sci. Lett.*, 202, 77–87.

Nishihara, Y., I. Aoki, E. Takahashi, K.N. Matsukage, and K. Funakoshi (2005) Thermal equation of state of majorite with MORB composition. *Phys. Earth Planet. Inter.*, 148, 73–84.

Niu, Y., and M.J. O'Hara (2003) Origin of ocean island basalts: A new perspective from petrology, geochemistry, and mineral physics considerations. *J. Geophys. Res.*, 108, doi:10.1029/2002JB002048.

O'Hara, M.J. (1968) The bearing of phase equilibria studies in synthetic and natural systems on the origin and evolution of basic and ultrabasic rocks. *Earth-Science Rev.*, 4, 69–133.

Ono, S., Y. Ohishi, M. Issiki, and T. Watanuki (2005) In situ X-ray observations of phase assemblages in peridotite and basalt compositions at lower mantle conditions: Implications for density of subducted oceanic plate. *J. Geophys. Res.*, 110, doi:10.1029/2004JB003196.

Pertermann, M., and M.M. Hirschmann (2003a) Partial melting experiments on a MORB-like pyroxenite between 2 and 3 GPa: Constraints on the presence of pyroxenites in basalt source regions from solidus location and melting rate. *J. Geophys. Res.*, 108, doi:10.1029/2000JB000118.

Pertermann, M., and M.M. Hirschmann (2003b) Anhydrous partial melting experiments on MORB-like eclogite: Phase relations, phase compositions and mineral-melt partitioning of major elements at 2–3 GPa. *J. Petrol.*, 44, 2173–2201.

Pickering-Witter, J., and A.D. Johnston (2000) The effects of variable bulk composition on the melting systematics of fertile peridotitic assemblages. *Contrib. Mineral. Petrol.*, 140, 190–211.

Pilet, S., J. Hernandez, P. Sylvester, and M. Poujol (2005) The metasomatic alternative for ocean island basalt chemical heterogeneity. *Earth Planet. Sci. Lett.*, 236, 148–166.

Riedel, M.R., and S. Karato (1997) Grain-size evolution in subducted oceanic lithosphere associated with the olivine-spinel transformation and its effects on rheology. *Earth Planet. Sci. Lett.*, 148, 27–43.

Roy-Barman, M., and C.J. Allègre (1995) $^{187}Os/^{186}Os$ in oceanic island basalts: Tracing oceanic crust recycling in the mantle. *Earth Planet. Sci. Lett.*, 129, 145–161.

Saal, A.E., S.R. Hart, N. Shimizu, E.H. Hauri, and G.D. Layne (1998) Pb isotopic variability in melt inclusions from oceanic island basalts. Polynesia. *Science*, 282(5393), 1481–1484.

Schiano, P., K.W. Burton, B. Dupre, J.L. Birck, G. Guille, and C.J. Allegre (2001) Correlated Os-Pb-Nd-Sr isotopes in the Austral-Cook chain basalts: The nature of mantle components in plume sources. *Earth Planet. Sci. Lett.*, 186(3–4), 527–537.

Schilling, J.G., M.B. Bergeron, and R. Evans (1980) Halogens in the mantle beneath the North Atlantic. *Philos. Trans. R. Soc. Lond. A*, 297, 147–178.

Sengör, A.M.C. (1985) The story of Tethys: How many wives did Okeanos have? *Episodes*, 8, 3–12.

Silver, P.G., R.W. Carlson, and P. Olson (1988) Deep slabs, geochemical heterogeneity, and the large-scale structure of mantle convection: Investigation of an enduring paradox. *Ann. Rev. Earth Planet. Sci.*, 16, 477–541.

Sims, K.W.W., D.J. DePaolo, M.T. Murrell, W.S. Baldridge, S. Goldstein, D. Clague, and M. Jull (1999) Porosity of the melting zone and variations in the solid mantle upwelling rate beneath Hawaii: Inferences from ^{238}U-^{230}Th-^{226}Ra and ^{235}U-^{231}Ra disequilibria. *Geochim. Cosmochim. Acta*, 63, 4119–4138.

Stracke, A., M. Bizimis, and V.J.M. Salters (2003) Recycling oceanic crust: Quantitative constraints. *Geochem. Geophys. Geosyst.*, 4, doi:10.1029/2001GC000223.

Tackley, P.J., D.J. Stevenson, G.A. Glatzmaier, and G. Shubert (1993) Effects of an endothermic phase transition at 670 km depth in a spherical model of convection in the Earth's mantle. *Nature*, 361, 699–704.

Takahashi, E., T. Shimazaki, Y. Tsuzaki, and H. Yoshida (1993) Melting study of a peridotite KLB-1 to 6.5 GPa, and the origin of basaltic magmas. *Philos. Trans. R. Soc. Lond. A*, 342, 105–120.

Tatsumi, Y., and T. Kogiso (2003) The subduction factory: Its role in the evolution of Earth's crust and mantle. In Larter, R.D., and P.T. Leat (eds.) Intra-oceanic Subduction Systems: Tectonic and Magmatic Processes, Geological Society of London, London, pp. 55–80.

Tejada, M.L., J.J. Mahoney, C.R. Neal, R.A. Duncan, and M.G. Petterson (2002) Basement geochemistry and geochronology of central Malaita, Solomon Islands, with implications for the origin and evolution of the Ontong Java Plateau. *J. Petrol.*, 43, 449–484.

Wallace, P.J. (1998) Water and partial melting in mantle plumes: Inferences from the dissolved H_2O concentrations of Hawaiian basaltic magmas. *Geophys. Res. Lett.*, 25, 3639–3642.

Watson, S., and D. McKenzie (1991) Melt generation by plumes: A study of Hawaiian volcanism. *J. Petrol.*, 32, 501–537.

White, W.M., and A.W. Hofmann (1982) Sr and Nd isotope geochemistry of oceanic basalts and mantle evolution. *Nature*, 296, 821–825.

Utsunomiya, A., T. Ota, B.F. Windley, N. Suzuki, Y. Uchio, K. Munekata, and S. Maruyama (2007) History of the Pacific superplume: Implications for the Pacific paleogeography since the Late Proterozoic. In Yuen, D.A., S. Maruyama, S. Karato, and B.F. Windley (eds.) Superplumes: Beyond Plate Tectonics, Springer, Dordrecht, pp. 363–408.

Yasuda, A., T. Fujii, and K. Kurita (1994) Melting phase relations of an anhydrous mid-ocean ridge basalt from 3 to 20 GPa: Implications for the behavior of subducted oceanic crust in the mantle. *J. Geophys. Res.*, 99, 9401–9414.

Zindler, A., and S. Hart (1986) Chemical geodynamics. *Ann. Rev. Earth Planet. Sci.*, 14, 493–571.

CHAPTER 8

MATERIAL CIRCULATION THROUGH TIME: CHEMICAL DIFFERENTIATION WITHIN THE MANTLE AND SECULAR VARIATION OF TEMPERATURE AND COMPOSITION OF THE MANTLE

TSUYOSHI KOMIYA

Department of Earth and Planetary Sciences, Tokyo Institute of Technology, Tokyo 152-8551, Japan; E-mail: tkomiya@geo.titech.ac.jp

Abstract

In this chapter, we describe that recent progress of our study of Precambrian geology and geochemistry, and present a synthetic view of the evolution of the solid earth including mantle dynamics and surface geology and environment. The recognition of an accretionary complex and oceanic plate stratigraphy in the 3.8 Ga Isua Supracrustal belt clearly indicates the presence of open sea and the operation of plate tectonics in the early Archean. The change of PT paths of subduction-related metamorphism through time shows that a hotter geothermal gradient at the subduction zone more frequently caused slab melting in the Precambrian, and that the transformation of basaltic crust to a heavy residue after slab melting was a driving force of Precambrian-type plate tectonics. We estimated that the potential mantle temperature of the upper mantle was about 1480°C in the Archean and was hotter by ca. 150–200°C than the modern mantle based on composition of 3.8 to 1.9 Ga MORB-related greenstones. The temperature decreased not monotonously but episodically. The high temperature increased its Rayleigh number by about 30 times, and decreased its viscosity by about one-third, but it complementarily raised the amount of accumulated slab material in the mantle transition zone to trigger off their frequent flushing to the lower mantle. The estimated FeO content of the Archean upper mantle was higher, ca. 10 wt% , and was constant until the early Proterozoic, and then it decreased. Segregation of iron grains from subducted oceanic crust during slab penetration into the lower mantle is a plausible mechanism to decrease the FeO content in the mantle. The growth curve of the continental crust obtained from U-Pb ages of detrital zircons indicates the sudden increase at 2.8–2.7 and 2.0–1.7 Ga. The sudden growth of continents, the worldwide presence of LIPs and many continental collisions at those times imply mantle overturn or extensive exchange between the upper and lower mantle materials, caused by successive upwelling and dowelling of giant superplumes. The mantle overturn events influenced both the surface environment and solid earth. The segregation of iron grains produced ferric iron as a by-product to make the mantle oxidized. In addition, the upwelling of the lower mantle materials through superplumes to the upper mantle increased the $Fe^{3+}/\sum Fe$ in the upper mantle to oxidize it. The change of redox condition of influx gases from reduced to oxidized weakened the suppression by reduced gases against biological oxygenation of the surface environment,

D. A. Yuen et al. (eds.), Superplumes, 187–234.
© 2007 *Springer.*

and consequently the surface environment became oxic in the early Proterozoic after a mantle overturn. Moreover, the formation of large continents before and their break-up after the mantle overturn, produced wide habitats for photosynthetic lives, and helped biological oxidation at the surface.

1 INITIATION OF PLATE TECTONICS AND THE DRIVING FORCE

1.1 Geological evidence for initiation of plate tectonics in the Early Archean

Immediately after the establishment of plate tectonics in the early 1970s, Dewey and Spall (1975) proposed another question: "when did the operation of modern-style plate tectonics began on the Earth?" In those days, there were two opposing schools of thought. First, there was the view that the plate tectonic regime begin at the earliest stage of the evolving earth as suggested by the geochemistry of greenstones (Hart et al., 1970; Condie, 1972, 1982), geophysical considerations (Bickle, 1978; Arndt, 1983; Nisbet and Fowler, 1983) and the geological similarities with Phanerozoic orogenic belts (Burke et al., 1976). The other school suggested that the tectonic regime was typified by vertical movement-dominated orogenies until the late Proterozoic (Wynne-Edwards, 1976; Kröner, 1977, 1981; Piper, 1982). The latter school listed the following features disfavoring the concept of plate tectonics in the Archean: absence of (1) ophiolites, (2) Franciscan-type mélange, and (3) blueschists, all of which characterize divergent or consuming plate boundary processes in the modern Earth. Although an Archean ophiolite was recently reported (Kusky et al., 2001), the counterargument is still raised up (Hamilton, 2003; Stern, 2005). Although geological evidence for plate tectonics and accretion of oceanic crust has been reported in some Archean terrains (Kusky, 1989; Hoffman, 1991; Calvert et al., 1995), definitive criteria are still ambiguous (Bickle et al., 1994; Kusky and Winsky, 1995). Plate tectonics requires two necessary factors; rigidity of lithosphere, and its lateral movement. Komiya and others (1999) proposed criteria for the accretion of oceanic materials to continental lithosphere and the operation of plate tectonics. They comprise the formation of an accretionary complex, oceanic plate stratigraphy in an open sea, evidence for subduction, lateral movement from ridge to trench, and rigidity of an oceanic plate.

The Isua supracrustal belt lies approximately 150 km northeast of Nuuk, Greenland (Fig. 1). It is located in the northeastern part of the Akulleq terrane, which is composed of 3880–3660 Ma Amîtsoq gneiss, and 2820 Ma Ikkattoq gneiss. The former contains enclaves of early Archean supracrustal rocks (Akilia association), whereas the latter contains other enclaves of late Archean supracrustal rocks (Malene supracrustals) and anorthosite complex (McGregor, 1993; Nutman et al., 1996). The Isua belt is, at present, exposed as a fault-bounded tectonic slice, and is in tectonic contact with the tonalitic Amîtsoq orthogneiss on both sides (McGregor, 1973;

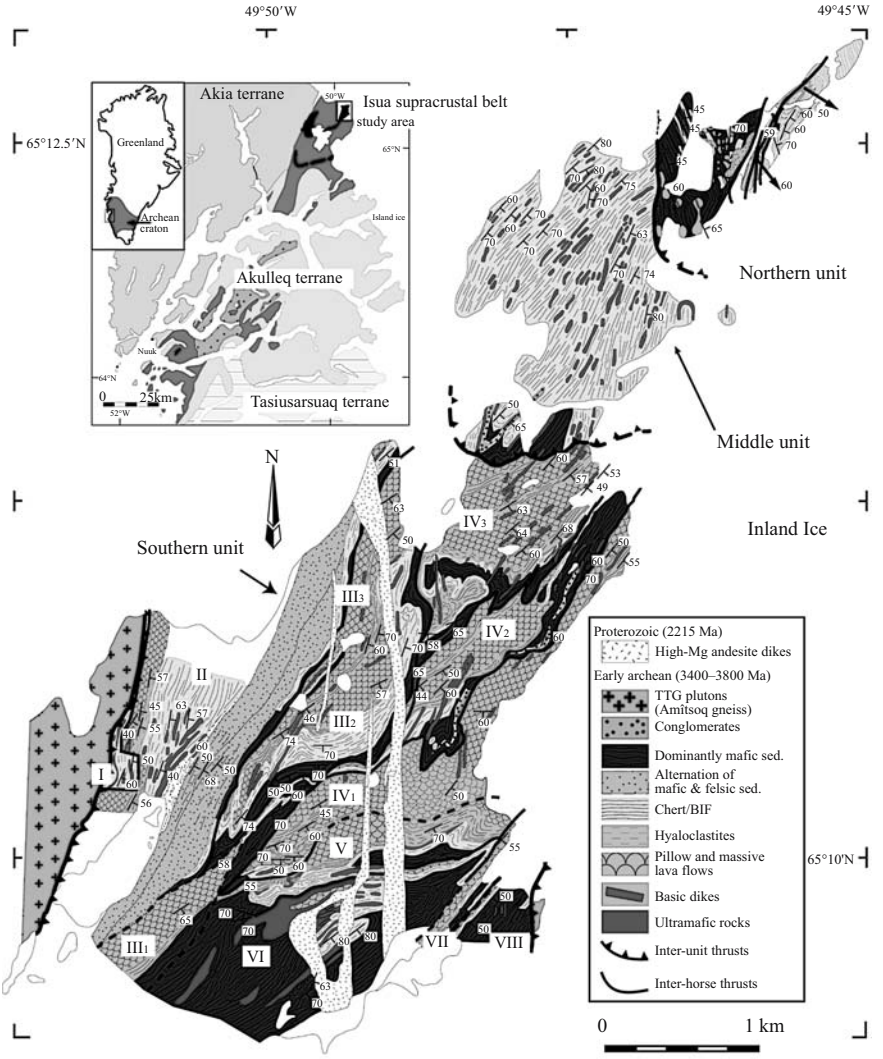

Figure 1. Geologic map of the NE part of the Isua supracrustal belt. The inset is a geotectonic map of southern West Greenland, simplified after McGregor et al. (1991). Three terranes, Akia (gray), Tasiusarsuaq (gray with horizontal bars), and Akulleq are shown. Akulleq terrane is composed of Ikkattoq gneiss (dark gray with white bars), Amîtsoq gneiss (stippled), and supracrustal rocks (black). Post-collision Qôrqut granite (cross) intrudes mainly Akulleq terrane. The Isua supracrustal belt is located in the northeastern corner.

Figure 2. The older basaltic pillow lavas in the Isua supracrustal belt. Some basalts preserve original pillow lava structures in this figure. Each pillow consists of core (gray), mantle (darker gray), rim (white) and matrix (composite from white and dark gray materials).

Bridgwater et al., 1974), but was originally formed as an enclave in the Amîtsoq gneiss. The Isua belt comprises five Early Archean major lithologic units: (1) a mafic-felsic turbidite sequence, including minor interbedded conglomerate, (2) chert and banded iron-formation, (3) pillow lava (Fig. 2), massive lava, pillow breccia, and hyaloclastite, (4) dolerite-gabbro intrusives related to (3), and (5) ultramafic rocks, plus mid-Archean and early Proterozoic intrusions (Fig. 1). The area is subdivided into three units, Northern, Middle, and Southern, by structural breaks defined by low-angle thrusts. The lower half of the Northern Unit is a highly disrupted mélange (Type II, Cowan, 1985), with blocks of greenstone and chert. More than 37 angular to subrounded blocks of greenstone are randomly embedded in a highly sheared muddy matrix, together with several blocks of chert with or without BIF. The upper half is composed of more than four subunits bounded by layer-parallel thrusts. Each subunit is composed of pillow lava or sheet flow greenstone at the bottom, overlain by layered chert/BIF. BIF layers occur at the bottom of the sedimentary sequence, whereas white chert becomes more abundant through the transition of white/blue chert in the upper part. The Middle Unit is mainly composed of dominant NS-trending chert layers, and contains mafic turbidite sequence associated with felsic sandstone, mudstone, calcareous sandy shale, and minor conglomerate near the southern margin.

The Southern Unit displays very clear geological evidence that the Isua supracrustal belt originated from an accretionary complex. It is composed of ultramafic rocks, a basaltic lava flow sequence of massive and pillow lava (Maruyama et al., 1991a) and hyaloclastite, and a sedimentary sequence of pelagic chert and BIF, and terrigenous

turbidite and conglomerate. Cherts and associated sediments form several belts bound by layer-parallel faults, converging in some cases and diverging in others (Fig. 1). Duplex structures are on scales of meters to a few km. At least eight major subunits with horses are defined by the layer-subparallel faults. We reconstructed the original lithostratigraphy within each horse by removing folds and/or thrusts, based on detailed sketches of the outcrops. The reconstructed lithostratigraphies within horses are simple and mutually similar, each consisting of pillow basalt, chert, and turbidite in ascending order (Fig. 3). Major tectonic breaks separating horses on both sides are commonly layer-parallel faults.

The stratigraphic top within each horse always faces southeastward, except in a few strongly folded areas. Petrographic examination of chert indicates that no continental or arc materials occur within the chert beds and underlying pillow lava flows. Detrital materials start to appear in thin laminated chert beds after the end of the major chert deposition, and become common in the turbidite layers. The sequential change of sedimentary lithology, from chert to turbidite, is common to all horses. The

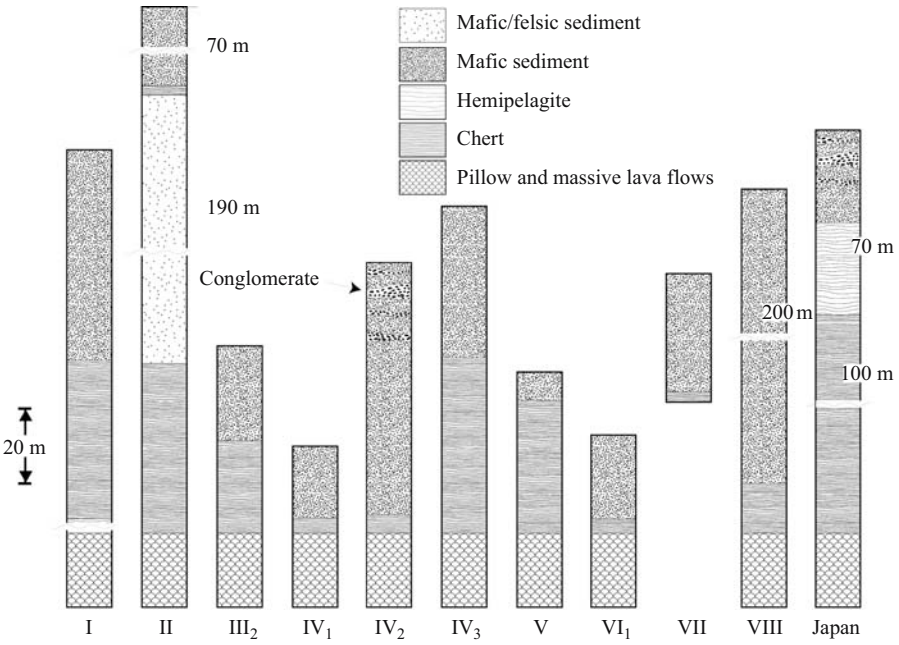

Figure 3. Lithostratigraphies of Duplexes I to VIII. Each lithostratigraphic unit is composed of metabasite, chert, muddy chert and mafic sediment, in ascending order. The metabasite consists of a pile of pillowed basalts with massive basaltic flows and hyaloclastites. A reworked hyaloclastite with rough surfaces and numerous metamorphic garnet megaporphyroblasts occurs at the top. Mafic sediment with graded bedding covers the chert at the top. Muddy chert occurs as a transitional sediment between the chert and the mafic sediment. The reconstructed lithologies are comparable to the Phanerozoic oceanic plate stratigraphy in Japan.

reconstructed lithostratigraphy is remarkably similar to oceanic plate stratigraphy of circum-Pacific accretionary complexes (Isozaki et al., 1990; Matsuda and Isozaki, 1991; Wakita and Metcalfe, 2005). The presence of duplexes indicates the geological structure was formed by layer-parallel shortening, whereas evidence of oceanic plate stratigraphy means lateral movement from pelagic ridge to continental margin. The lines of evidence indicate that the Isua supracrustal belt is the oldest accretionary complex. Komiya and others (1999) demonstrated that in the Southern Unit, and possibly in the whole Isua supracrustal belt, an accretionary complex formed through accretion of oceanic crust to the hangingwall, by duplexing. A sequence of duplexing scenarios can be reconstructed as follows. The structural bottom is Duplex I, and the top is Duplex VIII, as judged by the southward polarity of duplexing. The younger horses develop downward; therefore, the oldest duplex is VIII. Accretion proceeded from Duplex VIII to I with time. Within a given Duplex, the southeastern horse is the oldest. The similar lithostratigraphy within each horse suggests that the oceanic crust segments subducted in the same area and period. The mode of formation of the duplex structure throws light on the direction of the growth of the accretionary prism and the subduction of oceanic lithosphere. The duplex polarity is defined by the direction of convergence of faults, which divide horses, and coincides with plate convergence. The southward convergent morphology of the duplex structure is widespread over the mapped area, indicating that the Isua accretionary prism grew from south to north. A paleogeographic reconstruction is shown in Figure 4 to illustrate the sequential events of the accretionary prisms in the Southern Unit at about 3700–3800 Ma (Komiya et al., 1999). Geologic records preserved within turbidite sediments also provide strong constraints on the type of active plate margin. If they were formed along a large continental margin, they would be dominantly quartzofeldspathic. If they

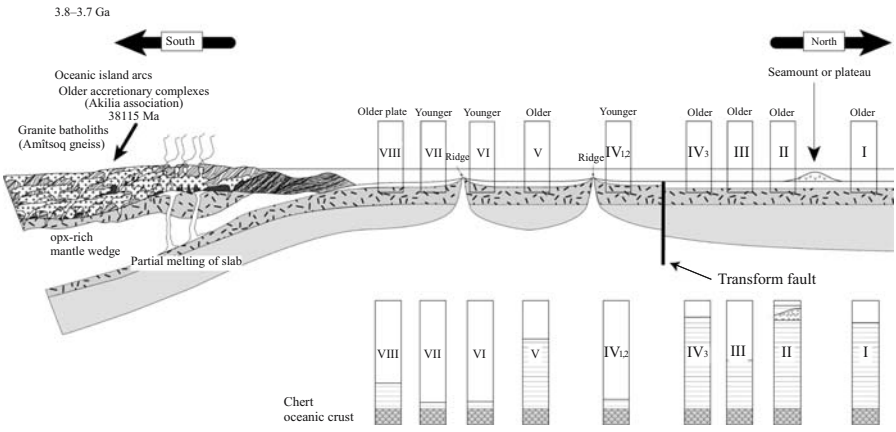

Figure 4. Travel history of Early Archean oceanic lithosphere in the Isua accretionary belt, West Greenland. This diagram shows paleogeographic reconstruction of accreted oceanic lithosphere, followed by successive underthrusting of oceanic crust to form duplexes from Duplex VIII to I with time.

were formed in intra-oceanic environments, such as the present-day western Pacific domains, they would be dominantly mafic in composition. The sedimentary petrology of the turbidite sequences clearly indicates that the Isua accretionary complex was formed in the latter environment, because mafic sediments are dominant in the turbidite sequences. In the Archean, most orogenic belts were formed in intra-oceanic island arcs, and then grew progressively through the collision-amalgamation process.

Evidence of accretion of oceanic materials at subduction zone indicates successive underthrusting of oceanic crust. This suggests that a kind of tectonics similar to the Phanerozoic plate tectonics operated in the Early Archean, but it does not necessarily prove that modern-style plate tectonics were in operation in a strict sense. Evidence of the operation of modern-style plate tectonics on Earth includes: (i) rigid plates, (ii) significant lateral movement of the plate, (iii) multiple plates surrounded by plate boundaries, and (iv) linearity of plate boundaries. However, evidence of (i) and (ii) are necessary and sufficient to identify the existence of modern-style plate tectonics, because horizontal passive movement of rigid plates results in the presence of multiple plates (iii) and in linearity of plate boundaries (iv) (Oldenburg and Brune, 1972; Turcotte and Schubert, 1982). In other words, the rigidity of an oceanic plate is also necessary to discern whether modern-style plate tectonics or a hybrid of plume and plate tectonics operated (Head and Crumpler, 1990). A comparison with tectonics on Venus provides some perspective because Archean tectonics on Earth has been widely regarded as similar to modern Venusian tectonics. Pillowed basalt at the bottom of the oceanic plate stratigraphy preserved in the Isua supracrustal belt indicates that sea water was present and that open sea extended far from any oceanic island arc. Numerical simulations of temperature and composition of ocean and atmosphere demonstrated that formation of a proto-ocean decreases atmospheric pressure to ca. 10 atm and the surface temperature to ca. 20°C (Tajika and Matsui, 1990). These relations support the idea that the surface temperature was cooled down to less than 100°C in the Early Archean. Knowledge of the composition and thickness of oceanic crust, and the temperatures of the mantle and Earth's surface allows us to reconstruct the structure of an oceanic plate (Fig. 5). Geotherms of oceanic lithosphere as a function of age were calculated based on a model of transient half-space cooling (Turcotte and Schubert, 1982) at given parameters of temperature of the mantle and surface, 1450 and 100°C, 1330 and 0°C and 1450 and 470°C for the early Archean and present Earth and Venus, respectively. In addition, transitions of ductile/brittle deformations of peridotite and diabase are calculated as a function of temperature and pressure for a given steady-state strain rate of a representative tectonic strain rate, 10^{-14} s^{-1} (after Hoffman and Ranalli, 1988). The rheological structure of oceanic lithosphere as a function of age were estimated from oceanic geotherms and the ductile/brittle transitions (Fig. 5 b–d), and indicate that an oceanic plate older than 20 m.y. behaves rigidly even in the Early Archean (Fig. 5c right). The evidence suggests that oceanic plates in the Early Archean were rigid, in contrast to the substantial ductile surface of Venus (Fig. 5d). In summary, there is evidence for (i) rigid plates, (ii) significant lateral movements and (iii) subduction of plates in the Early Archean Isua accretionary complex. The evidence proves that modern-style plate tectonics has been in operation

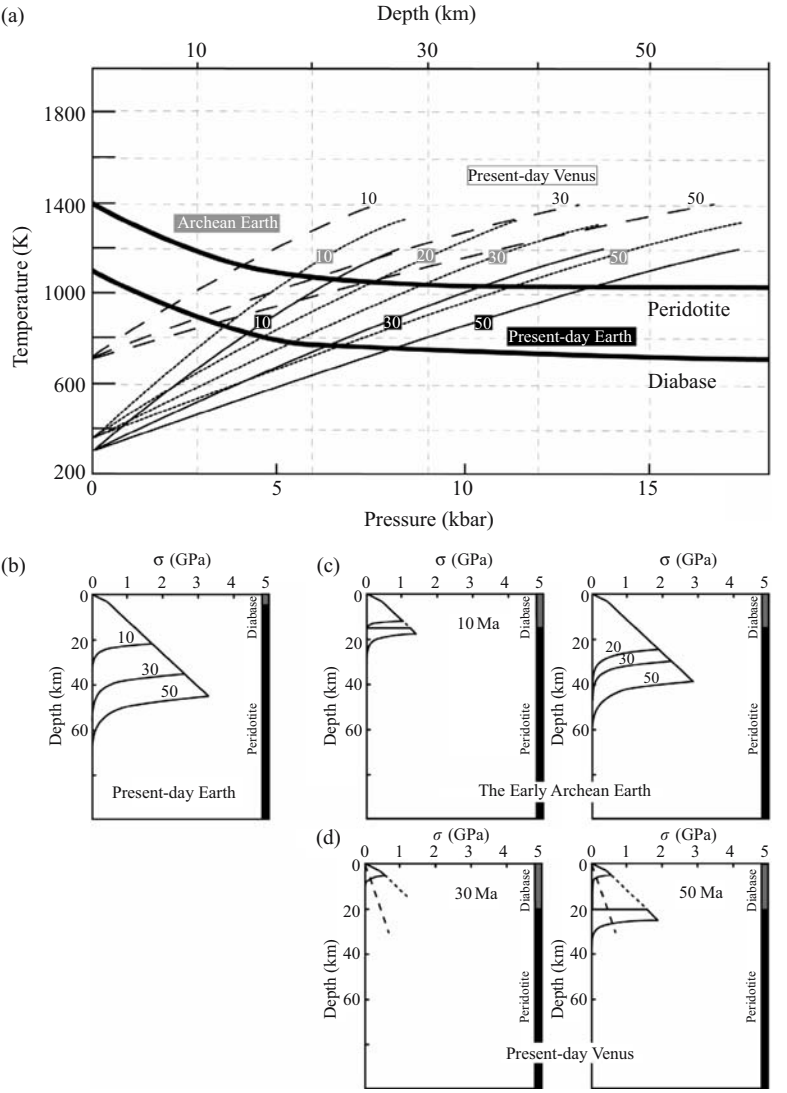

Figure 5. (a) Geothermal gradients of oceanic lithosphere for Earth and Venus at present and in the Archean. The transitions of ductile/brittle behaviour of peridotite and diabase (thick lines) were calculated as a function of temperature and pressure for a given steady-state strain rate of a representative tectonic strain rate, 10^{-14} s^{-1}. Oceanic geotherms for different lithosphere ages given in units of millions of years on the plots are calculated based on a model of transient half-space cooling (Hoffman and Ranalli, 1988). Note that the surface temperature on Venus is 470°C higher than on Earth. (b) Strength profiles in compression for modern oceanic lithosphere as a function of age are given in units of millions of years on the plots. The 7-km thick oceanic crust is modeled as diabase, and the upper mantle as peridotite. (c) Strength profiles in compression are for Archean oceanic lithosphere, 10 m.y. old (left) and 20–50 m.y. old (right). A 15-km thick crust is modeled. (d) Strength profiles in compression for Venusian oceanic lithosphere, 30 m.y. old (left) and 50 m.y. old (right). A 20-km thick crust is modeled (Buck, 1992).

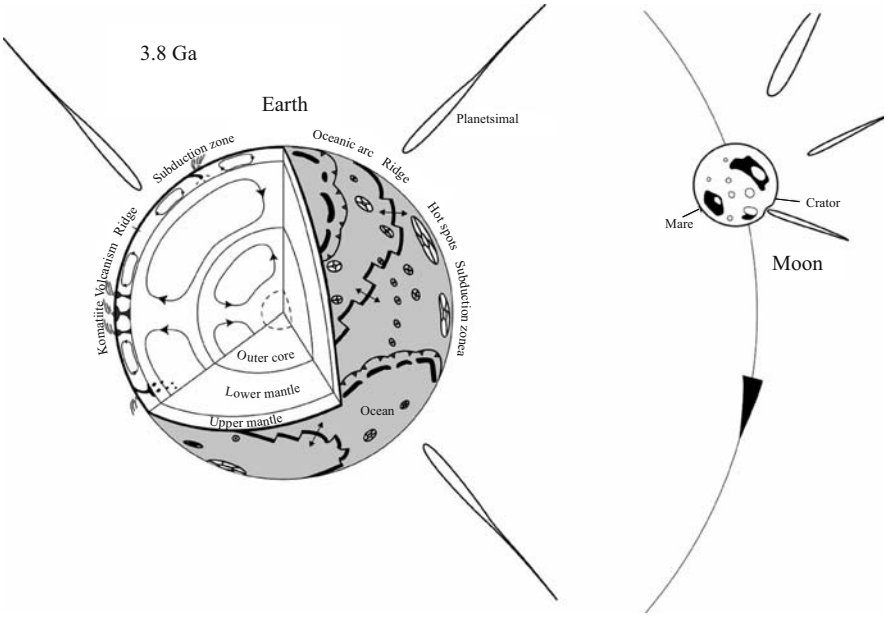

Figure 6. A speculative cartoon showing 3.8 Ga planet Earth and its satellite Moon. Plate tectonics had already started but there was no solid inner core. Double-layered mantle convection with episodic leakage between the upper and lower mantle boundary was predominant. There were no large continents and a number of intra-oceanic island arcs, and abundant off-ridge volcanism related to mantle upwellings. The satellite, Moon, was active only by heavy extra-terrestrial bombardments and related Mare volcanism.

since the Early Archean, and quite different from the Earth's satellite, Moon, which was resurfaced by heavy extraterrestrial bombardment and by related Mare volcanism (Fig. 6).

1.2 Precambrian-type and Phanerozoic-type plate tectonics and the driving force of Precambrian-type plate tectonics

Application of accretionary geology concepts to Archean greenstone belts has revealed that modern-style plate tectonics were already in operation in the Early Archean. However, geophysical calculations of the relationship between the temperature of the mantle and the density of an oceanic plate contradict the geological evidence for the operation of plate tectonics in the Early Archean, because an Archean thin (∼40 km) oceanic plate capped by a thick (∼20 km) oceanic crust may have been lighter than the asthenospheric mantle (Davies, 1992). In the Phanerozoic, oceanic lithosphere is heavier than asthenosphere because of a negligibly thin oceanic crust (Kono and Yoshii, 1975). Therefore, even if the basaltic crust does not transform into eclogite during subduction, the oceanic lithosphere can subduct into the mantle

due to its negative buoyancy. However, in the Archean, Davies (1992) suggested that oceanic lithosphere could not subduct directly into the asthenosphere because it was lighter than the asthenosphere. Therefore, Another driving force would be required for subduction of the oceanic lithosphere into the mantle in the Archean.

Grambling (1981) postulated a secular variation of metamorphic facies series from a compilation of Archean metamorphic data. However, determination of the tectonic setting of metamorphism is essential for investigation of secular change, because the metamorphic facies series strongly depends on the tectonic setting of the metamorphism (Miyashiro, 1973). Recently, the secular change of PT paths of a subducted slab was estimated from a petrological study of the oldest progressive regional metamorphism of the Isua supracrustal belt (Hayashi et al., 2000; Komiya et al., 2002a) and from a compilation of subduction-related metamorphisms (Maruyama et al., 1996; Hayashi et al., 2000). This work was based on a mineralogical and petrological study of metabasites and metapelites affected by Archean progressive metamorphism from the Isua belt, West Greenland, and it proposed a driving force for Archean plate tectonics.

The area of the Isua supracrustal belt is divided into four metamorphic zones based on mineral assemblages and microprobe analyses of coexisting minerals in metabasites and metapelites. Especially we selected mineral assemblages in moderately magnesian metabasites, where chlorite is 50–60 in $Mg^{\#}$ (Fig. 7a), because

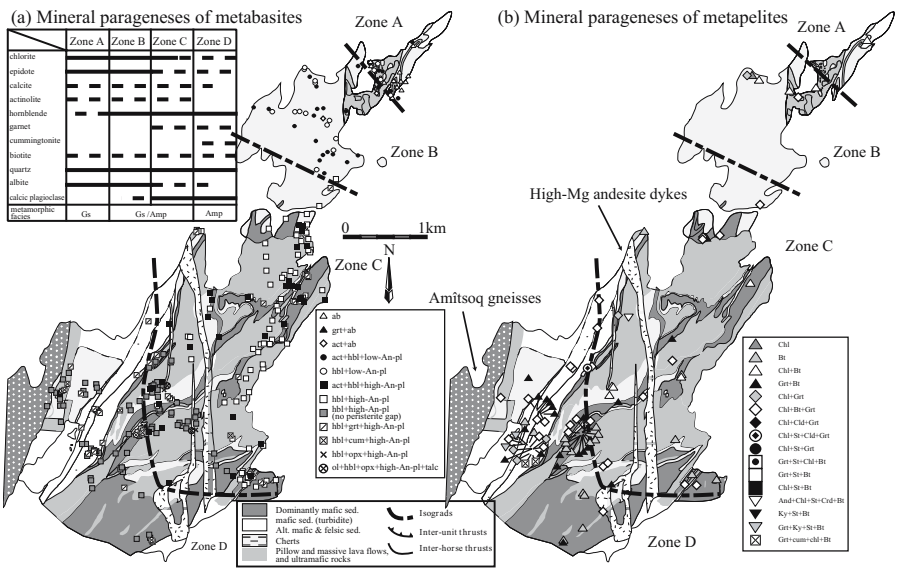

Figure 7. Mineral assemblages of metabasites (a) and metapelites (b) in the northeastern area, which are subdivided into four zones based on mineral assemblages and the anorthite content of plagioclase in metabasite. The metamorphic grade ranges from greenschist facies in the northernmost area through epidote-amphibolite transition to amphibolite facies in the southern Unit.

the composition of calcic amphiboles strongly depends on the whole rock composition (Hayashi et al., 2000). Zone A is defined by the Gs-facies mineral assemblage, Chl + Ep + Ab + Qz, and Zone B by the appearance of Ca-amphiboles, either Act and/or Hbl, together with Ab and/or oligoclase; the mineral assemblage is Chl + Ep + two Ca-amphiboles + peristeritic Pl + Qz, that shows the transition between Gs and Amp facies. Zone C is defined by the appearance of calcic plagioclase, the appearance of a single amphibole of hornblende composition in magnesian samples, and the appearance of Grt coexisting with Hbl in iron-rich samples. The diagnostic mineral assemblage in metabasites is Chl + Ep ± Act + Hbl + Pl + Qz. Zone D is defined by disappearance of two Ca-amphiboles-bearing samples, concomitant with a high anorthite (An) content of plagioclase and a single Ca-amphibole of hornblende composition in moderately magnesian samples; the mineral assemblage is Chl + Ep + Hbl + calcic Pl + Qz. High magnesian rocks contain two amphiboles, cummingtonite (Cum) and Hbl.

About 120 samples have mineral assemblages of typical pelitic systems, and most have mineral assemblages of either Chl + Bt or Grt + Bt, together with Ms and Qz. However, some samples have diagnostic mineral assemblages that enable estimates of metamorphic temperatures and pressures (Komiya et al., 2002a). In Zone A Grt is absent and Chl and Bt are present together with phengite (Phn) and Qz. Grt becomes stable in the northeastern side of Zone B. The mineral parageneses of Chl + Grt or Chl + Bt + Grt are found in some metapelitic rocks, indicating the stable coexistence of Grt and Chl. In Zone C Cld and St occur in aluminous samples together with Grt, Chl, Qz, and Phn. Although the mineral assemblage of other Zone C rocks is the same as that in Zone B, Fe/(Fe + Mg) ratios of the coexisting minerals are much higher than those in Zone B. In Zone D there are two types of mineral paragenesis: most samples contain the same mineral assemblage of Grt + Chl + Bt as in Zone C, but the distinctive parageneses of Ky + St + Bt, Ky + Chl + Bt or St + Grt + Bt and Ky + Grt + Bt or Ky + Chl + Bt occur on the southern side of the Zone (Fig. 7b). In summary, five reactions are expected in the phase diagram of the KFMAS + MnO system (Symmes and Ferry, 1992; Spear, 1993), Chl1 = Grt + Chl2 (ca. 440°C), Chl + Grt + Ky = Cld (ca. 530°C), Cld = St + Grt + Chl + H_2O (ca. 560°C), Grt + Chl = St + Bt + H_2O (ca. 610°C), and St + Chl = Ky + Bt + H_2O (ca. 620°C) (Komiya et al., 2002a). The PT path of the metamorphism was estimated to be in the intermediate-P/T type metamorphic facies series (Fig. 8). The metamorphism is subduction-related, and was caused by late Archean collision-amalgamation of the Akia and Akulleq terranes (e.g., McGregor et al., 1991), or early Archean subduction of oceanic lithosphere. All Archean metamorphic terrains worldwide belong to the intermediate- or low-P/T type metamorphic series (Fig. 8).

The age of a subducting plate has a significant control on the geotherm (e.g., Defant and Drummond, 1990; Peacock, 1996). Comparison of P-T estimates of Archean metamorphism with Phanerozoic subduction metamorphism indicates that the geothermal gradient of Archean subduction zones was over 200°C higher than in the Phanerozoic (Fig. 8). The Phanerozoic geotherm ranges from low to high P/T-type, depending on the age of the subducted slab, but the Archean geotherm does not

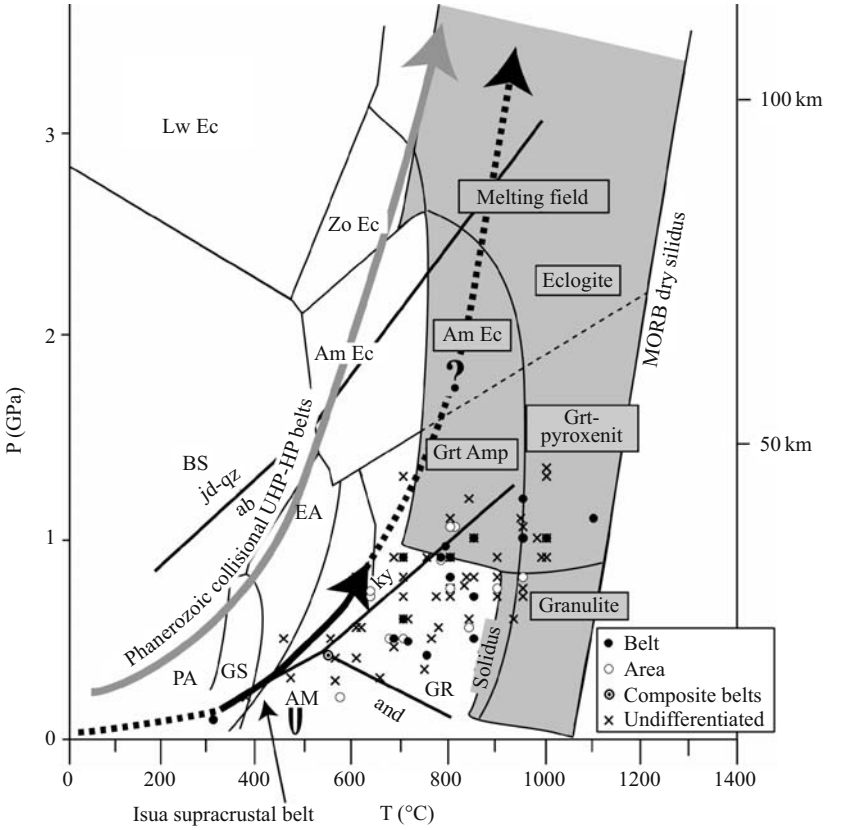

Figure 8. Phase relations of hydrated MORB, modified after Okamoto and Maruyama (1999), and the residual mineral assemblage (shaded region) after partial melting of hydrous Archean basalt (Rapp and Watson, 1995; Vielzeuf and Schmidt, 2001). Also shown are geothermal gradients of Phanerozoic collisional UHP-HP metamorphic belts (Maruyama et al., 1996) and Archean subduction zone metamorphism of the Isua supracrustal belt, accompanied by a recent compilation of P-T estimates of Archean metamorphic belts (Hayashi et al., 2000). Hayashi and others (2000) classified 111 Archean metamorphic terranes into belt, area and composite belts, dependent on the shape. Many Archean metamorphic terrains cannot be simply classified as either "belt" or "area". Among 111 Archean terrains, they identified 20 metamorphic "belts" and 18 "metamorphic areas". The rest of them remain unclassified.

extend to the high P/T side, ranging from low to intermediate P/T-type (Fig. 8). The following three candidates can be considered as a heat source for subduction zone metamorphism with a high geothermal gradient; (1) the overlying mantle wedge and continental crust, (2) the mantle below the oceanic lithosphere and (3) the remaining heat of MORB-formation within the lithosphere. We have calculated the thermal structure of oceanic lithosphere, in order to verify whether the remaining heat of MORB formation within the lithosphere is possible as a heat source for Archean

subduction metamorphism with a high geothermal gradient. The minimum temperature at the base of subducting oceanic crust can be calculated, based on the transient half-space cooling model and diffusivity of 1 $mm^2\ s^{-1}$. In the Phanerozoic, the temperature at the base of a 7-km thick oceanic crust falls below the solidus temperature of hydrated basalt only in 3-m.y after formation at given temperatures of the mantle (1330°C). However, in the case of Archean oceanic lithosphere with a 20 km thick oceanic crust, the temperature at the base of that crust is still higher than the wet solidus even after 15 m.y. at given temperatures of the mantle (1450°C). This calculation indicates that the remaining heat of MORB formation within the lithosphere is a probable heat source for Archean metamorphism with a high geotherm, and even for slab melting.

Although the Isua metamorphism did not reach melting conditions, the simple extension of the P-T path to the higher grades into the melting field in Figure 8 indicates that the hydrated oceanic crust would have been partially melted to produce granitic magma (the protolith of Amîtsoq gneiss). Namely, in the Archean, when the thickness of continental and older oceanic lithosphere combined exceeded ca. 30 km, the high geothermal gradient at the subduction zone led to melting of hydrated oceanic crust to form the tonalite-trondhjemite-granodiorite suite (TTG) (Martin, 1986; Defant and Drummond, 1990) and a denser garnet-bearing residue, such as high-pressure granulite (HGR) and garnet-clinopyroxenite. The calculated densities of basaltic crust, garnet-clinopyroxenite, HGR, and lithospheric and ambient mantle are shown in Figure 9a. The calculation indicates that the average density of lithosphere increases from 3.22 to 3.46 for the oceanic lithosphere with garnet-clinopyroxenite or 3.42 for HGR after slab melting, and that the slab can subduct to mantle depth by the increase of slab-pull force due to TTG melt extraction (Fig. 9a). The calculation suggests that the transformation of basaltic crust to garnet-clinopyroxenite or HGR was a driving force for Archean plate tectonics. There are some differences between plate tectonics in the Archean and at present (Fig. 9). They are (1) thickness of oceanic lithosphere, (2) thickness of the accompanied oceanic crust, (3) average life span of oceanic lithosphere, and (4) the cause of slab-pull (Komiya et al., 2002a). In the Phanerozoic, slab-pull is effective immediately after the birth of oceanic lithosphere, whereas in the Archean slab-pull was achievable only after slab melting. A ratio of the oceanic crust over thickness of the lithosphere of ca. 0.75 is the critical number determining whether slab-pull is effective even just after the birth at a ridge. Geophysical calculation of mantle temperature suggests that the ratio attained the critical value at ca. 1 Ga (Davies, 1992). In addition, compilation of modern and ancient ophiolites also supports the idea that thickness of oceanic crust decreased from ca. 12 to 5 km around 1 Ga (Moores, 1993). This evidence possibly indicates that Phanerozoic-type oceanic lithosphere with a slab-pull force from its birth began to be formed at ca. 1 Ga. In addition, blueschists did not form over the world before the late Proterozoic (Maruyama et al., 1996). The presence of blueschists indicates that the geothermal gradient decreased at subduction zones, and that old oceanic plates began to subduct at that time. This line of evidence and reasoning suggests that plate tectonics switched from a first-stage

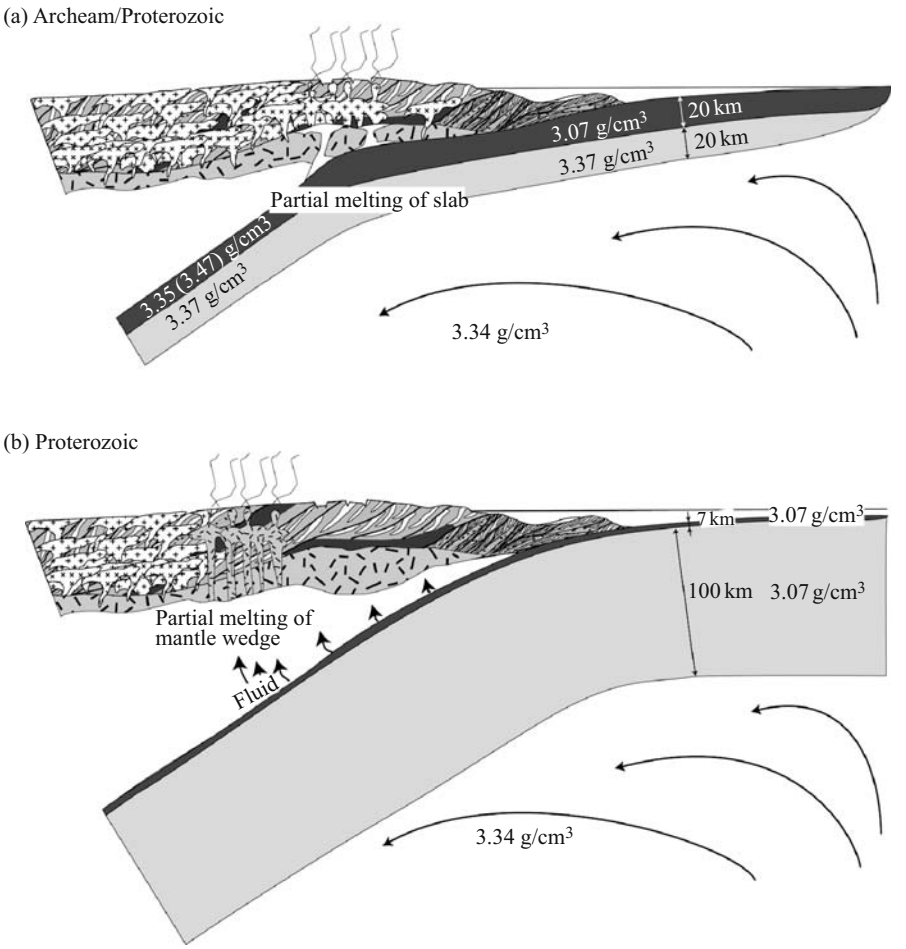

Figure 9. Schematic illustration of subduction zones, showing contrasting tectonic modes of subducting lithosphere. (a) Low-angle subduction of young oceanic lithosphere results in slab melting, supplying felsic magma through the very small volume of mantle wedge to the continent (Precambrian-type). Calculated density profile of Archean oceanic lithosphere indicates formation of highly dense garnet-bearing residues after TTG melt extraction become the slab-pull force. (b) Angle of subduction depends on age of oceanic plate. High-angle subduction of old oceanic lithosphere supplies dehydration fluids to the hanging wall of the mantle wedge (Phanerozoic-type).

with slab melting (Precambrian-type) to a second-stage with/without slab melting (the Phanerozoic-type) in the late Proterozoic. In response to the initiation of Phanerozoic-type plate tectonics, mantle wedges increased in volume by the change from flat- to high-angle subduction, and simultaneously came to be metasomatized by H_2O-rich fluids (Fig. 9b).

2 EVOLUTION OF THE MANTLE THROUGH TIME

It is well-known that the Earth has undergone some major processes since its formation; formation of metallic core, degassing, extraction of continental crust, and differentiation of the silicate mantle. Therefore, it is also necessary to decode the complex events in the Earth's long-term evolution for an investigation of the present-day chemical and physical states of the mantle and continental crust. Working models of present-day mantle dynamics were proposed in the early 1980s after accumulation of geochemical data of mantle-derived rocks and continental crust including Sr and Nd isotopic geochemistry (e.g., Allègre, 1982). In the mid-1980s, the compositional diversity of the mantle was compiled from the compositions of oceanic basalts and continental crust in terms of chemical geodynamics (Zindler and Hart, 1986). In the 1990s mantle tomographies displayed material circulation within the mantle (e.g., Fukao et al., 1992). The combination of geochemical dynamics, mantle tomography and surface geology contributed to establishment of the concept of plume tectonics beyond plate tectonics, and large-scale views of the present mantle (Maruyama, 1994). This section presents our recent studies of the compositional and thermal evolution of the mantle which were the main controls on the evolution of mantle dynamics and surface tectonics through time.

It is important to unravel the evolution of the mantle for an investigation of the geodynamic evolution of the earth because the mantle occupies about 80% of the volume of the whole earth. However, the isotopic evolution of the Earth has been relatively well studied (e.g., Allègre et al., 1980; Galer and Goldstein, 1991; McCulloch and Bennett, 1994), but the thermal evolution of the Earth has not been so well investigated, except for some computational calculations (e.g., Richter, 1985; Davies, 1992; Ogawa, 1997). It was widely accepted in the pre-1970s that the Earth has evolved in an almost steady thermal state, because it was thought that the rate of heat loss from the earth would be similar to the rate of heat production in a chondritic earth (Urey, 1956; Birch, 1958; Tozer, 1965). However, in the 1980s, revised estimates, incorporating correction of the heat loss from oceanic regions, indicated that the heat loss from the Earth is about 30% higher than steady state heat flow from a chondritic earth (Davies, 1980; Pollack, 1980; Sclater et al., 1980). Much geological evidence was also reported for and against the steady state thermal evolution of the Earth. The evidence includes (1) the correspondence of the geothermal gradient of the Archean-aged continental lithosphere to that of Phanerozoic continents (Burke and Kidd, 1978), (2) similarity of the metamorphic facies series between Archean and younger rocks (Windley, 1976; Watson, 1978), (3) the similar height of the mountains in the Archean and at present (England and Bickle, 1984), and (4) presence of the Archean-aged diamonds in kimberlites (Richardson et al., 1984). The counterevidence is the eruption of extremely high temperature magmas of ultramafic komatiitic composition (Green et al., 1975). In the 1990s computer simulations suggested the presence of instability in mantle convection at the Archean-Proterozoic transition, and an episodic or intermittent cooling model of the mantle was highlighted (e.g., Breuer and Spohn, 1995; Davies, 1995). The episodic whole mantle convection model was

also supported by some geological evidence; compilation of U/Pb zircon ages of juvenile continental crust (Condie, 1998, 2000) and of detrital zircons (Rino et al., 2004), secular change of Nd isotopes of greenstones (McCulloch and Bennett, 1994), and geochemistry of different-aged magmas including Nd isotopes, trace elements, rare gas and Pb isotopes (Stein and Hofmann, 1994).

2.1 The secular change of the potential temperature and composition of the MORB source mantle

In the 1990s the potential mantle temperature of the Archean mantle was estimated from the composition of peridotitic komatiites and was higher by 600°C than that of modern MORB (e.g., Takahashi, 1990; Nisbet et al., 1993). However, it is now widely accepted that komatiite was not produced from normal upper mantle, but from plume source mantle or highly wet mantle (e.g., Takahashi and Scarfe, 1985; Campbell et al., 1989; Inoue and Sawamoto, 1992; Parman et al., 1997). Therefore, the potential mantle temperature estimated from the komatiite magma does not represent that of normal upper mantle in the Archean. Abbott and others (1994) estimated the secular variation of the temperature of the upper mantle from the composition of greenstones, and found that the mid-Archean upper mantle was about 250°C higher than the modern upper mantle. But, the estimate may not directly refer to the secular change of the normal upper mantle because they used all of the greenstones, which were derived from mid-oceanic ridges, back-arc basins, primitive island arcs and hotspots. Therefore, it is necessary to determine the tectonic setting of mafic volcanism, because it is well-known that the composition of mafic magmas is strongly dependent on tectonic setting. Many recent investigations of the Phanerozoic circum-Pacific greenstone belts reported a close correlation between the tectonic settings of greenstones defined by chemical discrimination diagrams and the field occurrence of the greenstones. For example, Ueda and others (2000) reported that both MORB and OIB affinity-greenstones occur in a Jurassic to Cretaceous accretionary complex of central Hokkaido in Japan, based on whole-rock compositions including high field strength elements (HFSE), rare earth elements (REE), textures, mineral assemblages and the composition of relict igneous minerals and pseudomorphs of magmatic phenocrysts. Moreover, the MORB-affinity greenstones are covered by thick chert-clastic successions, whereas the OIB-affinity greenstones are intercalated with thin-bedded chert and limestone, or occur as a thick slab or block together with chert and limestone blocks in a black mudstone matrix (Ueda et al., 2000). A detailed review of the occurrence of greenstones in other Phanerozoic accretionary complexes was reported by Isozaki et al. (1990). Maruyama and colleagues worked out determination of the tectonic setting of greenstones in the 3.8 Ga Isua supracrustal belt (Komiya et al., 1999), the 3.5 Ga North Pole area (Maruyama et al., 1991b) and the 3.3 Ga Cleaverville area (Ohta et al., 1996) by comparing them with Phanerozoic greenstone belts. Another inherent problem in geochemical investigations of Archean greenstones is the effect of alteration on original rock compositions. To overcome this problem, it is necessary

to recognize the geochemical effects of such alteration processes as seawater interaction or regional metamorphism prior to any petrographic interpretations as well as to compare the whole rock chemistry with the composition of relict igneous minerals (Komiya et al., 2002c; Komiya et al., 2004).

Figure 10 shows the thermal and compositional evolution of the mantle, estimated by comparing mafic magmas of five different ages with recent melting experiments and multiple saturation experiments of 3.5 Ga MORB from Pilbara (Komiya, 2004). The potential temperature of the source mantles was estimated to be 1480 ± 100 for 3.8 Ga, 1490 ± 70 for 3.5 Ga, 1410 ± 90 for 3.3 Ga, 1500–1566 for 2.5 Ga, and 1470–1500°C for 1.9 Ga mantle and the FeO contents were about 10 wt% . Firstly, the Archean upper mantle potential temperature was only about 100–200°C hotter than the modern equivalent mantle. The estimated temperature is much lower than previous estimates of 1900°C, because they used the composition of peridotitic komatiite for the calculations (Takahashi, 1990; Nisbet et al., 1993). Secondly, the secular variation of the potential mantle temperature of the upper mantle implies that the temperature of the upper mantle has not decreased monotonously but episodically or variably. Although the estimate still has a large error, the potential mantle temperature remained constant from 3.8 to 2.5 Ga, at about 150°C higher than the modern. Moreover, the potential mantle temperature appears to have been lower at 3.3 Ga, whereas it was higher at 2.5 Ga. The thermal variation is possibly consistent with the wide

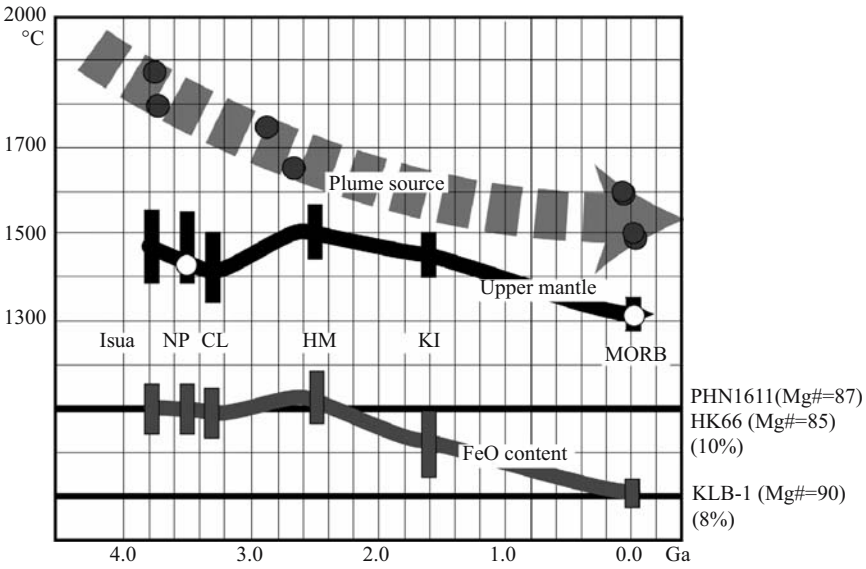

Figure 10. Secular changes of potential mantle temperature (black line) and FeO content (gray line) of the upper mantle, along with potential mantle temperature of a plume source (light gray line, Takahashi, 1990; Nisbet et al., 1993; Sakurai et al., 2001). The left vertical axis represents the potential temperature of the mantle, whereas the right vertical axis represents the FeO content of the upper mantle.

distribution of continental crust (Condie, 1998) and of komatiite rocks (Arndt and Nisbet, 1982) at 2.7 Ga. A steady state of potential mantle temperature through the Archean may be because the hotter lower mantle materials were injected episodically or continuously into the upper mantle. Stein and Hofmann (1994) suggested that the lower mantle material episodically penetrated into the upper mantle because the εNd value of the upper mantle is maintained between primitive and depleted mantle values. In addition, mantle overturn and episodic whole mantle convection is the mechanism suggested by computer simulations (Breuer and Spohn, 1995; Davies, 1995). Although further investigation will be required for the quantification of mantle overturn and the accompanied rejuvenation of the upper mantle, the constancy of potential mantle temperature of the upper mantle also implies episodic whole mantle convection.

2.2 Material circulation model including chemical differentiation and thermal and compositional evolution of the mantle

It has long been thought that the Archean mantle underwent double-layered convection because of the high Rayleigh numbers due to high temperature. In the Archean when the potential mantle temperature was higher by at least 150°C, the viscosity of the mantle became about one-third compared with that of the modern mantle. As a result, the Rayleigh number was about 30 times higher than at present based on the relationship between viscosity and temperature (Honda, 1995). A high Rayleigh number is more compatible with double-layered mantle convection than whole mantle convection (Yuen et al., 1994). In addition, the difference between the depth of phase changes of the subducted basalt and the ambient mantle increases in the hotter mantle (Fig. 11). The combination of these factors suggests that it was more difficult for slab materials to fall down to the lower mantle, and that double-layered mantle convection was preferred rather than whole mantle convection in the Archean. However, whole mantle convection with periodic penetration of subducted materials into the lower mantle is considered to be dominant at present (Fukao et al., 1992), and the mode of the mantle convection is not only controlled by the temperature of the mantle but also by the fate of the accumulated slab. In other words, periodic collapse of an accumulated slab down to the lower mantle causes whole mantle convection (e.g., Maruyama, 1994). Therefore, we can consider whether the intermittent penetration of slab materials into the lower mantle occurred even in the Archean. A higher temperature of mantle in the Archean led to increase of the depth and volume of melting, and thus to a thicker oceanic crust, ca. 15–20 km. On the other hand, the hotter mantle resulted in small plates, and consequently the life-span of oceanic plates was shorter, in order to enable efficient release of the heat flux (Hargraves, 1986; de Wit and Hart, 1993). If the temperature of the mantle were higher by 150°C, about 15 m.y. and 30 km are estimated for the life-span and thickness of the oceanic lithosphere, respectively (Hargraves, 1986; Komiya et al., 1999). Generally speaking, subducted oceanic crust could not penetrate directly into the lower mantle, because basaltic materials change into high-pressure phases at depths of about 40 km greater than the

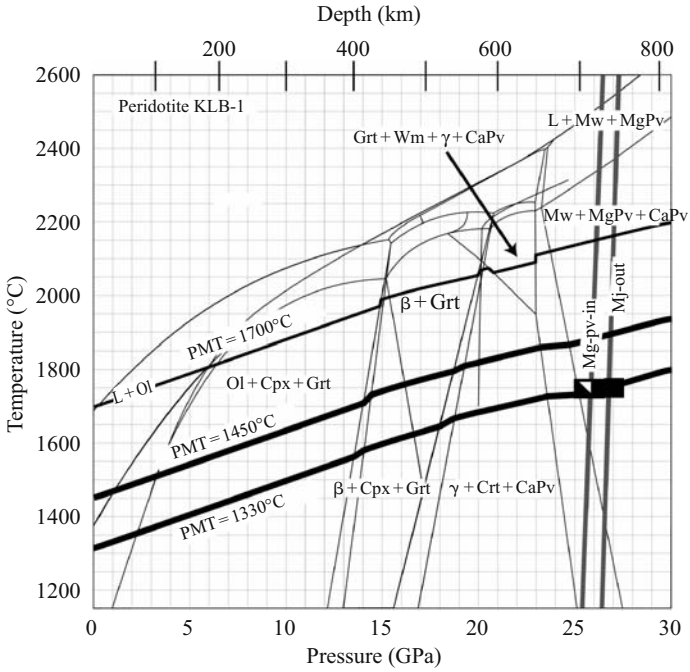

Figure 11. Phase relations of anhydrous peridotite KLB-1 (fine black lines, modified after Figure 1 of Herzberg and Zhang (1996)) and anhydrous Archean MORB (thick gray lines, Hirose et al., 1999). Symbols are defined as follows: L, liquid; Ol, olivine; Opx, orthopyroxene; Cpx, clinopyroxene; Grt, garnet; Mw, magnesiowüstite; MgPv, Mg-perovskite; CaPv, Ca-perovskite; ß, modified spinel (Mg, $Fe)_2SiO_4$, γ, spinel (Mg, $Fe)_2SiO_4$. Also shown are P-T paths of uprising mantle with 1330, 1450, and 1700°C in potential mantle temperature.

ambient peridotite (Hirose et al., 1999). Figure 11 shows the phase relations of KLB-1 in 0–30 GPa, and 1200–2600°C (modified after Herzberg and Zhang, 1996). The P-T paths of the mantle with three different potential mantle temperatures are also drawn: 1330°C (modern upper mantle), 1450°C (the Archean upper mantle) and 1700°C (Archean plume source mantle). The P-T condition of phase change from majorite (Mj)- to perovskite (Pv)-bearing oceanic crust is also shown based on experimental data of Hirose et al. (1999). Although the depth of the upper-lower mantle boundary (ULB) decreases with the potential temperature of the mantle, the difference of potential mantle temperature by 150°C plays an insignificant role on the depth of ULB, by only ca. 7 km (Fig. 11). The high potential mantle temperature of plume source mantle in the Archean promoted upwelling of plumes from the lower mantle (Hirose, 2002), and induced materials in the lower mantle to pass into the upper mantle. By the way, larger quantities of subducted oceanic crust accumulated on the upper-lower mantle boundary in the Archean, because the production rate of oceanic plates was ca. 10 times higher than at present. In particular, significant amounts of subducted

materials built up beneath large continents in the late Archean and early Proterozoic, analogous to the Eurasian continent at present (Engebretson et al., 1992). Assuming that isostasy was valid, the base of a megalith starts to sink into the lower mantle when it grows up to 80 km thick, as estimated from the density contrast between the ambient mantle and subducted basaltic crust (e.g., Irifune and Ringwood, 1987; Hirose et al., 1999). A simple calculation based on the thickness of the oceanic crust and the life-span of the oceanic lithosphere indicates that it took only 100 m.y. for 80-km thick subducted oceanic crust to be stored at the upper-lower mantle boundary in the Archean. In addition, normative calculations of the residue of hydrated basaltic crust after the slab melting suggest that it possibly changes into CaPv + Mj + γ-spinel phases instead of Mj + CaPv + stishovite phases. The residue is heavier than the ambient mantle because of its high concentration of CaPv. There is another remarkable difference between mantle geodynamics in the Archean and at present: the temperature of plume-source mantle. The potential mantle temperature of an Archean plume source mantle reached about 1700°C, but that of modern plume source mantle is about 1500°C. Assuming adiabatic decompression of the plume mantle, the temperature of the former was about 2100°C at 23 GPa and the temperature of the latter is 1900°C. Instead of Mw + MgPv + CaPv, a field of Mj + Mw + γ-spinel + CaPv is present at the higher temperature than about 1950°C at 23 GPa (Fig. 11), and strongly influences the upwelling of the plume-source mantle (Hirose, 2002). A Clapeyron's slope of phase change from Mj + Mw + γ-spinel + CaPv to Mw + MgPv + CaPv is positive, and results in acceleration of upwelling of superplume from lower mantle. Therefore, extensive exchange between upper and lower mantle materials possibly took place in a transition zone from 20 to 24 GPa in the Archean. Seen from the viewpoint of the material exchange, the Archean mantle comprised three layers of upper mantle, transition zone, and lower mantle under the high temperature condition. In addition, if the temperature of the plume-source mantle was higher than 2100°C at 20 GPa, the upwellings of the superplume accelerated at the phase change from ß-spinel + Mj to Mj + Mw + γ-spinel + CaPv, again. As a result, the episodic whole mantle convection was induced by upwelling of superplume. These facts suggest that episodic whole mantle convection, caused by the upwellings of the superplume and collapse of cold subducted materials, operated in the Archean, too.

There may be four plausible mechanisms for the decrease of FeO content through geologic time: core-pumping (Cohen et al., 1980; Dupré and Allègre, 1980); formation of continental crust (e.g., Allègre, 1982); storage of FeO-rich oceanic crust within the mantle (Chase and Patchett, 1988); and iron segregation from the subducted oceanic crust at slab penetration into the lower mantle (this work). However, the core-pumping model is inconsistent with the constancy of compatible siderophile elements such as Ni content through time (Arndt, 1991), and with the abundance of highly chalcophile elements (Newsom et al., 1986). The formation of the continental crust and the storage of the FeO-enriched oceanic crust decrease all lithophile elements including Al_2O_3 and CaO, and are inconsistent with the decrease of only the FeO content. We will discuss below the model of iron segregation from the

subducted oceanic crust at slab penetration into the lower mantle. Recent ultra-high-pressure experiments of natural peridotite and aluminous Mg-perovskite under lower mantle conditions showed that the iron content in Mg-perovskite increases through the coupled substitution of $Al^{3+} + Fe^{3+} = Mg^{2+} + Si^{4+}$ with Al_2O_3 (Wood and Rubie, 1996; McCammon, 1997). Moreover, some ferrous ions were transformed into metallic iron by an electron exchange reaction of $3Fe^{2+} = Fe + 2Fe^{3+}$ accompanying the substitution reaction of $Al^{3+} + Fe^{3+} = Mg^{2+} + Si^{4+}$ (McCammon et al., 1997; Frost et al., 2004). The reactions occur during slab penetration into the lower mantle because the subducted oceanic crust contains high Al_2O_3 and FeO content. Especially, in the Archean, the chemical differentiation by the reactions was more significant because the production rate of oceanic crust in the Archean was higher by 10 times than at present. However, Sun (1984) emphasized that the metallic core has not grown after the Archean, based on the ratio of siderophile to lithophile elements such as the P_2O_5/TiO_2 ratio. Although his work compared Precambrian komatiite and picrite magmas with modern NMORB, comparison between Archean and modern MORB indicates an obvious secular variation of the P_2O_5/TiO_2 ratio (Komiya, 2004). In addition, Hofmann and others (1986) showed that Ce/Pb ratios of modern MORB and OIB are higher than those of the primitive mantle. The high ratio of Ce/Pb of modern MORB and OIB relative to that of the primitive mantle is consistent with the extraction of metallic iron from subducted oceanic lithosphere during slab penetration, if source mantles of MORB and OIB involve residual materials after segregation of metallic iron. Therefore, extraction of metallic iron is consistent with a secular change of incompatible siderophile elements. On the other hand, there are no obvious secular variations of compatible siderophile elements such as NiO (e.g., Arndt, 1991). A difference of behavior between compatible and incompatible siderophile elements can be explained by a difference between the abundance of the compatible elements in the oceanic crust and mantle peridotite, and by the partition coefficients at high pressure. The physicochemical difference between siderophile and lithophile elements, in general, decreases under ultrahigh pressure conditions, and partition coefficients of P and Ni between metallic and silicate liquids decrease to ca. 3.1 and 40 at 27 GPa, 1400°C, $\Delta IW = +2$ (Righter et al., 1997). Also, the NiO content in the oceanic crust is lower by a tenth than in the mantle (e.g., McDonough and Sun, 1995). Therefore, the segregation of metallic iron plays a significant role in the abundance of incompatible siderophile elements such as P, but an insignificant role in the abundance of compatible elements.

Here, we estimate the amount of metallic iron precipitated from subducted oceanic crust during slab penetration into the lower mantle using the parameters given by Komiya (2004). The calculation indicates that assuming that the production rate of metallic iron is half of the production rate of ferric iron, it takes only 3.1 b.y. to reduce the FeO content in the whole mantle from 10.2 to 8.1 wt% at the production rate of MORB in the Archean; and the phosphorus content of the whole mantle also falls from 29 to 21 ppm in only 5 b.y. However, no secular change appears in the NiO content because the NiO content of the whole mantle decreases by only 0.02 wt% in 5 b.y.

This line of evidence indicates that chemical differentiation occurs at the upper-lower mantle boundary, and that a model of iron segregation from subducted oceanic crust during the slab penetration into the lower mantle is plausible to decrease in the FeO content and incompatible siderophile elements in the mantle. If the produced metallic iron sinks and is accumulated on the core, the thickness of the layer of metallic iron would be about 57 km.

Recent ultrahigh-pressure experiments suggested differentiation of subducted oceanic crust at a subduction zone, at the upper-lower mantle and core-mantle boundaries within the mantle as shown in the preceding sections. For example, Hirose and others (2004) suggested that subducted basaltic crusts are molten into denser FeO-rich picritic melt and lighter residue that exists on the core-mantle boundary, and that fractionations of U to Pb and of Lu to Hf occurs because the dense FeO-rich melt accumulates on the core-mantle boundary, whereas the light residue rises toward the upper mantle. However, many current models of material circulation within the mantle suppose that subducted materials do not change within the mantle, and that the mode of the material cycling is immutable through time.

Figure 12 shows the view for global material cycling through time, including chemical differentiation of the subducted materials within the mantle. In the Archean, oceanic lithosphere was thinner, and had a thicker oceanic crust and a shorter life span because of the higher potential mantle temperature. In addition, there were many subduction zones, namely plate boundaries, because the size of plates was smaller. A high geothermal gradient at subduction zones resulted in partial melting of subducted oceanic crust, and changed the oceanic crust into a denser garnet-bearing residue. As a result, large amounts of oceanic crust subducted into the deep mantle and accumulated on the upper-lower mantle boundary. The accumulated materials delaminated at the bottom, and subsided into the lower mantle. Iron grains were segregated from the slab materials during the slab penetration into the lower mantle, and subsided onto the core-mantle boundary. On the other hand, some of the residue was mixed with the surrounding mantle, and other materials sank to the core-mantle boundary. On the core-mantle boundary, the subducted oceanic crust was partially molten, and differentiated into a dense FeO-rich picritic melt and light Ca-perovskite-bearing residue (Hirose et al., 2004). The FeO-rich melt accumulated on the core-mantle boundary, whereas the light Ca-perovskite-bearing residue rose to the upper mantle. The upper-lower mantle boundary intermittently opened during subsidence of slab materials into the lower mantle and enabled injection of superplumes from the lower to the upper mantle. In the Phanerozoic, oceanic lithospheres have become thick and wide, whereas the oceanic crusts are thinner. As a result, the subducted oceanic crust in the Phanerozoic plays a less significant role in the chemical differentiation than in the Archean. Most oceanic crust undergoes dehydration instead of slab melting at a subduction zone, except for very young oceanic plates. Subducted materials accumulate on the upper-mantle boundary, and produce megaliths, which continually sink into the lower mantle, whereas superplumes rise up to the upper mantle from the core-mantle boundary.

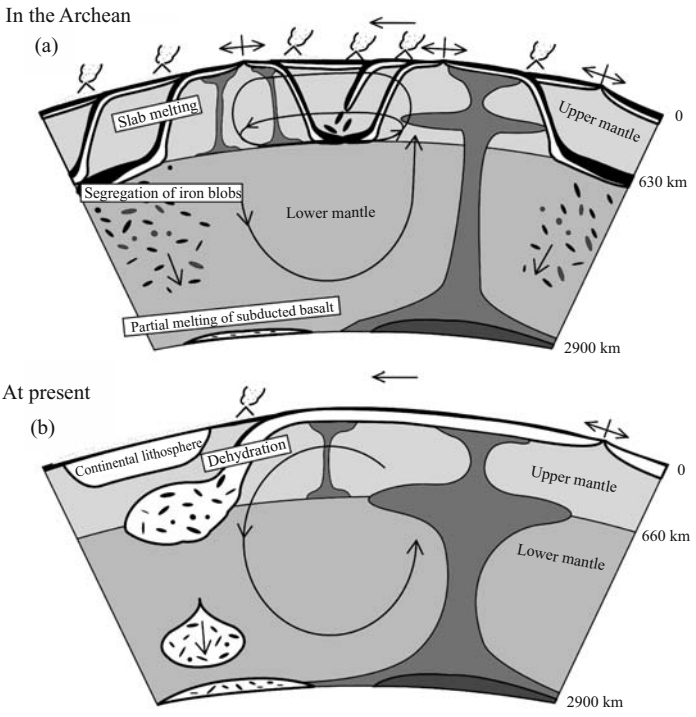

Figure 12. Cartoons of material circulation in the whole mantle in the Archean (a) and in the Phanerozoic (b). In the Archean, thin oceanic lithosphere with thick oceanic crust subducted beneath small oceanic island arcs in many places, and slab materials were widely distributed over the upper-lower mantle boundary. The high production rate of Archean MORB probably resulted in successive subsidence of slab materials into the lower mantle. The formation of the continental crust at subduction zones by slab melting and segregation of iron blobs during slab penetration into the lower mantle have changed the chemical composition of the mantle through geologic time. Partial melting of the subducted oceanic crust on the core-mantle boundary also possibly plays a significant role in the compositional change of the mantle (Hirose et al., 2004). In the Phanerozoic the thick oceanic lithosphere with thin oceanic crust subducts beneath large continental blocks. A huge amount of slab material accumulates beneath a large continent for a long time, and continually subsides into the lower mantle (Fukao et al., 1992).

3 MAJOR EPISODIC INCREASES OF CONTINENTAL CRUSTAL GROWTH AND IMPLICATIONS FOR MANTLE OVERTURNS IN THE EARLY PRECAMBRIAN

The present surface of the Earth is covered with 70% oceanic crust and 30% continental crust. The oceanic crust is basaltic and 0.8–11 km thick, whereas plume-affected crust may be up to 38 km thick (Gladczenko et al., 1997). In contrast, continental crust is about 30–40 km thick, and composed of a felsic to intermediate upper crust and

a basaltic lower crust. The differences in thickness and density between the oceanic and continental crusts result in a unique topographic expression. Earth has a bimodal topographic frequency of elevation, whereas Venus has only one predominant elevation (Phillips et al., 1981). Also, the moon has a bimodal topographic elevation, and a very thick, up to 75 km, continental crust, but its continental crust is anorthositic, dissimilar to the sialic continental crust of the Earth. The moon's anorthositic crust was formed by igneous differentiation of a magma ocean at its birth (Warren, 1985). These relations indicate that the presence of a sialic continental crust is one of the unique characteristics of the Earth. For these reasons, it is important to study the origin and growth rate in order to understand the evolution of the solid Earth (Fowler et al., 2002).

At present, the oldest oceanic crust has an age of about 200 Ma, and is present in the western Pacific and the Atlantic. However, many fragments of oceanic crust were emplaced within accretionary complexes during off-scraping and underplating of oceanic material at the trench (e.g., Isozaki et al., 1990), and fragments of Precambrian oceanic crust also exist in ancient accretionary complexes (e.g., Komiya et al., 1999). In contrast, the oldest sialic continental crust of the earth is ~4.03 Ga orthogneiss in the Acasta Gneiss Complex in the Northwest Territories of Canada (Bowring and Williams, 1999). The oldest minerals in the world are ca. 4.4 Ga detrital zircons from conglomerates of Jack Hills in the Yilgarn craton, western Australia (e.g., Wilde et al., 2001). The rare earth element (REE) patterns and Hf isotopic composition of the zircons indicate that they were derived from continental felsic magma (Kinny et al., 1991; Maas et al., 1992). Recently, oxygen isotope and titanium concentration of the zircons indicate that the parental magma was granitoid, formed from hydrated materials (Cavosie et al., 2005; Watson and Harrison, 2005). This line of evidence indicates that significant continental granitic crust had already formed in the Hadean soon after formation of the Earth. Kamber et al. (2003) argued that preservation of >3.8 Ga material is restricted to cratons with a high U/Pb source character (North Atlantic, Slave, Zimbabwe, Yilgarn and Wyoming), and that the Pb-isotope systematics of these cratons result from reworking of material that was derived from ca. 4.3 Ga Hadean, basaltic crust. We reinvestigated the geology, geochronology and geochemistry of the Acasta Gneiss complex because ancient crustal rocks provide the only direct evidence for evolution of the surface environment and solid earth in the Hadean and Early Archean. We recognized six distinct lithofacies, and at least eight tectonothermal events based on 1/5000 scale geological mapping, detailed study of many outcrops and petrographic investigation of ca. 1000 samples (Komiya et al., 2002b; Iizuka et al., 2006). It mainly comprises early Archean Gray (GG), White (WG) and Layered (LG) Gneisses and middle Archean Foliated Granite (Fig. 13a). GG originated from quartz-diorite, and occurs as enclaves within the WG and LG, which were originally pale-gray tonalitic and white granitic rocks. The gneissic structure of WG is concordant with the shape of the included GG blocks, but completely discordant to those within the GG. The intersection relationship indicates that the GG is older than the well-dated WG (4.0 and 3.7 Ga). In addition, we classified separated zircons into primary, inherited and recrystallized types most effectively using

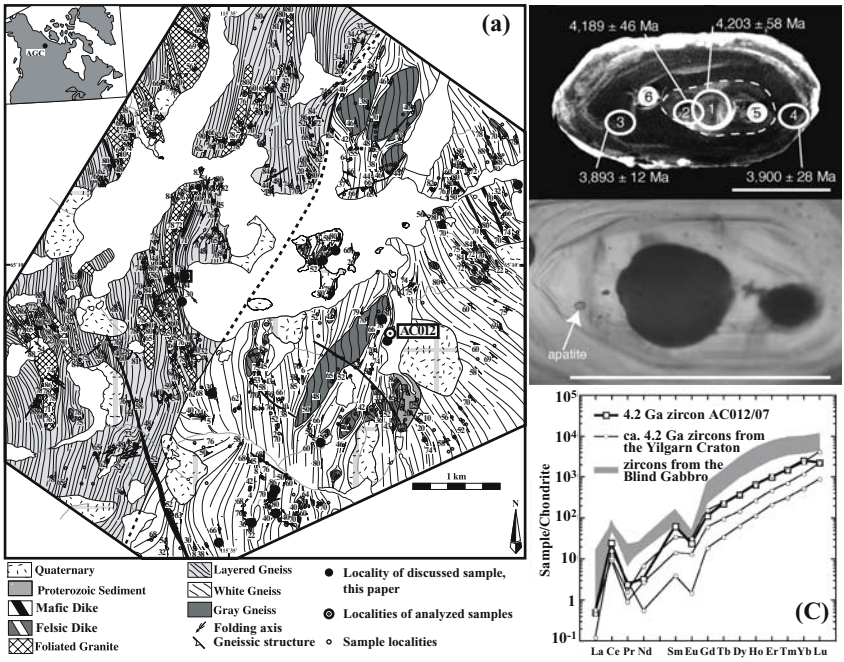

Figure 13. (a) A geological map of the Acasta Gneiss Complex, comprising six distinct lithofacies. (b) A cathodoluminescence image of a zircon with a 4.2 Ga inherited core containing an apatite inclusion. (c) An REE pattern of the inherited core, indicating the host magma was quartz-dioritic.

the Cathodoluminescence (CL) images (Iizuka et al., 2006). The REE patterns of primary zircons within the WG are consistent with those of the host whole rock. The inherited zircons are much older, up to 4203 ± 58 Ma (Fig. 13b), and have REE patterns equilibrated with quartz-dioritic magma based on the discrimination methods (Fig. 13c). The result indicates that the oldest rocks are the 4.2 Ga quartz-dioritic enclaves within the WG, that, when formed, was accompanied by recycling of some portion of the preceding GG. The discovery of the Hadean zircons and wide distribution of quartz-dioritic enclaves in the Acasta Gneiss Complex, including detrital (Wilde et al., 2001) and inherited zircons (Nelson et al., 2000) in the Narryer Complex, implies extensive distribution of continental crust even in the Hadean, consistent with early differentiation of the upper mantle (Bennett et al., 1993).

Many different models of continental growth have been proposed, and can be classified into three groups, according to their methods of estimate and the feature (Fig. 14). The first involves rapid continental formation in the Hadean and Early Archean based on a thermal evolution model and estimate of net growth of continental crust in the Phanerozoic (Fyfe, 1978; Armstrong, 1981; Reymer and Schubert, 1984). Armstrong (1981) first emphasized the significance of recycling crustal materials into the mantle.

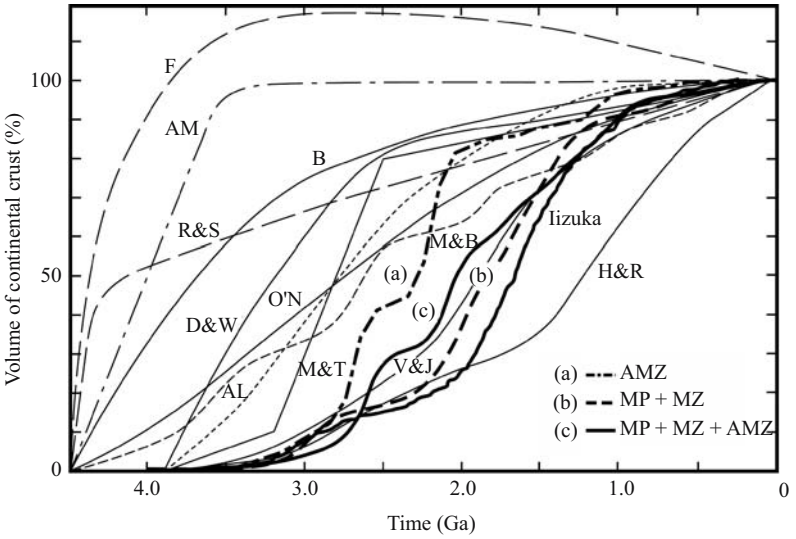

Figure 14. Growth rate estimated from the age population of detrital zircons in the river sands along with crustal growth curves from the literature (Rino et al., 2004); MP, MZ and AMZ represent continental growth rate in the drainage of the Mississippi, Mackenzie, Amazon Rivers, respectively. Iizuka (Iizuka et al., 2005), H & R (Hurley and Rand, 1969), C (Condie, 1998), V & J (Veizer and Jansen, 1979), M & T (McLennan and Taylor, 1982), AL (Allègre, 1982), O'N (O'Nions et al., 1979), M & B (McCulloch and Bennett, 1994), R & S (Reymer and Schubert, 1984), D & W (Dewey and Windley, 1981), B (Brown, 1979), Am (Armstrong, 1981), F (Fyfe, 1978). The continental growth curves are different between the continents. The summarized continental growth curve of two continents indicates episodic growth of continental crust at ca. 2.7 and 2.0 Ga.

According to his model a high proportion of continental crust was produced before the Archean, so that the proportion remained practically constant in later time due to recycling. Reymer and Schubert (1984) estimated the amount of subduction erosion of continental and oceanic materials, and the net amount of continental growth in Phanerozoic subduction zones. They concluded that the net amount of continental growth was small in the Phanerozoic, and suggested that the continental crust was largely produced in the Archean. The second group advocates gradual continental growth since the Archean, and significant growth in the Phanerozoic. These models were made on the basis of the present distribution of the continental crust and its ages (Hurley and Rand, 1969; Condie, 1998). For example, Hurley and Rand (1969) measured the whole-rock Rb-Sr isotopic compositions of the juvenile continental crust in North America, and estimated the continental growth rate from their distribution and their radiometric ages. Condie (1998) compiled the distribution and recent U-Pb zircon ages of juvenile continental crust, and showed a gradual growth of continental crust since the Archean with a few periods of rapid growth of continents. The third group is characterized by the formation of a significant amount of continental crust by

the Archean, and subsequently a gradual increase (Moorbath, 1977; O'Nions et al., 1979; Allègre, 1982; McCulloch and Bennett, 1994). These models were based on the isotopic evolution of the mantle estimated from the geochemistry of greenstones of different ages.

In order to better understand the continental growth history, we have determined the U-Pb age of about 1500 detrital zircons from river sands in three major rivers, the Mississippi, Mackenzie, and Amazon Rivers in the North and South America continents (Fig. 14; Rino et al., 2004). The method for estimating continental growth from the age population of a significant number of detrital zircons in river sands has three advantages (Rino et al., 2004): (1) the almost even collection of zircons from sedimentary rocks and granitic basements in the hinterlands of the major rivers; (2) determination of the age of juvenile crust due to the high closure temperature of the U-Pb systematics of zircons, and the removal of the influence of recycling of crustal materials; and (3) direct determination of the age of continental formation. The processes of recycling of continental materials are classified into three types: intra-crustal recycling, remelting of continental materials and subduction of continental materials into the mantle. Especially, this method is potentially useful for eliminating the effect of intra-crustal recycling. Our estimated continental growth curve displays two clear sudden increases at 2.8–2.5 and 2.3–2.0 Ga (Rino et al., 2004). The discontinuous growth of continental crust indicates episodic crustal growth, because this method minimizes the influence of recycling of crustal materials, and because zircons are almost evenly gathered from the drainage regions. In addition, the result clearly shows that timing and scale of continental growth were different among the continents because age distribution of zircons is different between the North and South American continents. In contrast, extensive continental formations in the Late Archean and early Proterozoic are common in the North and South American continents, which imply global events as shown below.

Iizuka et al. (2005) made in-situ analyses of U-Pb ages and $^{176}Hf/^{177}Hf$ isotopic ratios of over 400 grains of detrital zircons in the Mackenzie River by laser ablation-inductively coupled plasma mass spectrometry (LA-ICPMS). The purpose of the study was to consider the second type of recycling, remelting of continental materials. The U-Pb isotopic data for 416 igneous zircons are summarized in a histogram (Fig. 15b), that shows three peaks, a low 2.6–2.8 Ga peak, a broad 0.9–1.8 Ga peak, and the highest sharp <0.2 Ga peak. The initial $^{176}Hf/^{177}Hf$ isotope ratios for 402 grains of the 416 dated zircons are plotted along with chondritic uniform reservoir (CHUR) and DM evolution curves (Fig. 15a). The DM evolution curve was defined by $(^{176}Hf/^{177}Hf)_i = 0.279724$ and $^{176}Lu/^{177}Hf = 0.0395$, which is consistent with the mean value of the MORB field (0.28323; Nowell et al., 1998) and the initial Hf isotopic composition of the 2.7 Ga juvenile rock (0.28119; Vervoort and Blichert-Toft, 1999). To evaluate the degree of depletion of its parental magma relative to DM, the $\varepsilon Hf(T)_{DM}$ was calculated. Moreover, we calculated mantle extraction model ages (T_{DM}) for all grains, assuming that the parental magmas of the zircons were produced from crustal materials that were originally extracted from the DM, and that the Lu/Hf ratio of the crustal reservoir was the ratio of the upper continental crust

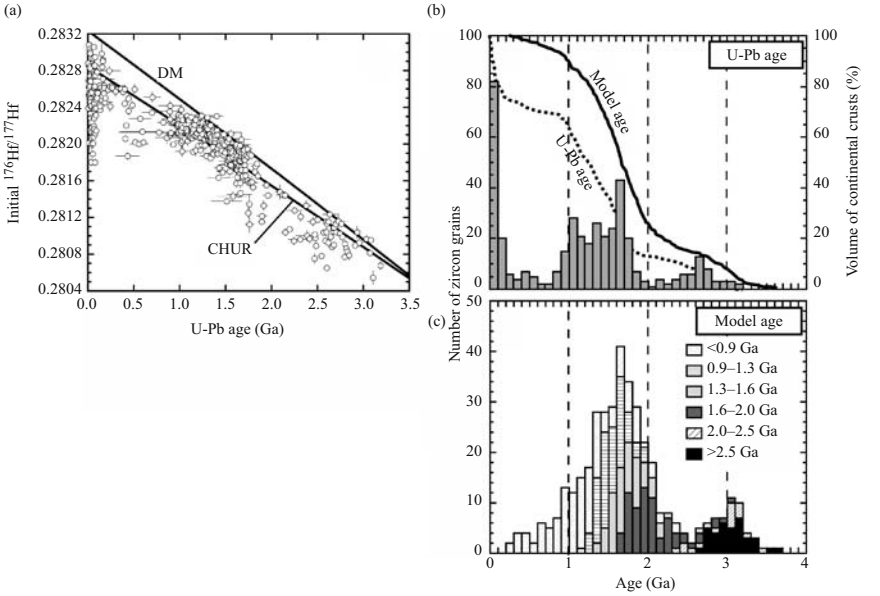

Figure 15. (a) Plot of initial $^{176}Hf/^{177}Hf$ vs. U-Pb age for 402 analyzed zircon grains. For the calculation of initial Hf isotope ratio, the decay constant for ^{176}Lu proposed by Scherer et al. (2001) (1.865×10^{-11} yr^{-1}) was used. CHUR evolution curve is based on CHUR parameter proposed by Patchett et al. (2004). Histograms of U-Pb age of 416 zircon grains (b), and T_{DM} of 402 zircon grains (c). The continental growth curves based on U-Pb age and T_{DM} are also illustrated in (b).

(Lu/Hf = 0.055; Taylor and McLennan, 1985). The histograms of T_{DM} population and the continental growth curves estimated from U-Pb age and T_{DM} population are shown in Figure 15b, c. Figure 15 show that many zircons have negative $\varepsilon Hf(T)_{DM}$, and indicate that the source materials underwent remelting of crustal materials. The highest $\varepsilon Hf(T)_{DM}$ values are scattered along the DM evolution curve, but deviate at some points. The deviation implies that DM was frequently refertilized through time. The continental growth rate in the drainage based on the T_{DM} population indicates that 15% and 78% of the present continental crust were formed by 2.5 and 1.3 Ga, respectively (Fig. 15b). In addition, it also demonstrates that crustal recycling became more significant with time, and $\varepsilon Hf(T)_{DM}$ of all the Phanerozoic zircons have quite a large negative anomaly. Figure 15a, c show that some zircons have negative $\varepsilon Hf(T)_{DM}$ even in the Archean. The T_{DM} of >2.5 Ga zircons range between 2.7 and 3.6 Ga. The Mississippi River drains the Archean Wyoming Craton and western Superior Provinces. The Wyoming Craton comprises abundant metasedimentary rocks, and possesses isotopic evidence for the presence of Middle Archean or older continental crust (Wooden et al., 1988; Frost, 1993). In addition, the granitoids in the craton were formed at 2.55–2.8 Ga, but their Nd model ages are 2.7–3.4 Ga, indicating both formation of some juvenile crust and recycling of older crust at the time (Frost et al.,

1998). On the other hand, continental and oceanic crustal fragments with 2.66–3.2 Ga ages occur in the western Superior Province, and the Nd isotopic data of the felsic volcanic and plutonic rocks also indicates both juvenile crustal formation and recycling of ~3.4 Ga crust (Tomlinson et al., 2004). The T_{DM} data support the previous isotopic studies, which suggest that crustal formation even in the Archean resulted from both the formation of juvenile continental crust and the recycling of older crustal materials. The comparison between the U-Pb age and the T_{DM} population shows firstly that significant Phanerozoic continental growth in the U-Pb age population was not observed in the T_{DM} (Fig. 15c). This fact indicates that most Mesozoic to Cenozoic crusts, at least in the drainage of the Mississippi River, originate from old crustal materials. Secondly, Figure 15c shows that the T_{DM} was predominant between 2.0 and 1.3 Ga, when its proportion reached 53%. This indicates that a huge amount of juvenile crust was formed between 2.0 and 1.3 Ga, and that a significant amount of the crust was subsequently recycled into younger crust. Thirdly, there is no evidence for >3.2 Ga crust in the U-Pb age population, but the T_{DM} histogram shows the existence of early Archean juvenile crust. This indicates that crustal growth started by the early Archean in the drainage basin, but was not preserved except for material in sediments and xenocrysts in younger granitoids. Finally, we emphasize that there is a significant difference between the U-Pb age and T_{DM} histogram, and that crustal recycling was very an important process in continental formation.

After the 1990s, episodic growth models of continental crust came into the limelight (McCulloch and Bennett, 1994; Stein and Hofmann, 1994; Condie, 1995; Davies, 1995; Peltier et al., 1997; Condie, 1998). Condie (2000) suggested that very short-term crustal formation occurred at 2.7, 1.9, and 1.2 Ga. The episodicity of orogeny was originally proposed by Gastil (1960) and Runcorn (1965) from their worldwide compilations of Precambrian isotopic mineral ages. Their age-distributions are supported by recent compilations of mineral ages and the tectonic setting, and explained by episodic thermal activity of the mantle (Barley and Groves, 1992). In addition, some peaks of crustal-age distributions were inferred from the distribution of T_{DM} of juvenile continental crust in the USA (Nelson and DePaolo, 1985), Australia (McCulloch, 1987) and South America (Cordani et al., 2000), from U-Pb ages of zircons (Condie, 1998; Rino et al., 2004), and from Rb-Sr isotope systematics (Hurley and Rand, 1969), and they were interpreted in terms of episodic crustal growth as well as the discontinuous occurrence of the mineral ages (e.g., Moorbath, 1977; McCulloch and Wasserburg, 1979; Nelson and DePaolo, 1985; Stein, 1994 # 207; Condie, 1998; Rino et al., 2004). However, the uneven crustal-age distribution may also be explained by the selective erosional recycling of elevated crust and by the uneven positioning of growth and recycling of continental crust (Gurnis and Davies, 1986; Windley, 2003). We considered the recycling of crustal materials, and quantitatively estimated the rate of continental growth from the U-Pb ages and Hf isotopic compositions of a large number of igneous zircons in river sands as shown above (Rino et al., 2004; Iizuka et al., 2005). The results also indicate significant juvenile continental growth at 2.5–2.8 and 1.8–2.2 Ga. As a result, we shall discuss a mantle overturn hypothesis for the episodic growth of the continental crust.

Several recent geochemical and geological studies have reported anomalous thermal events at 2.7 and 1.9 Ga. Compilation of 304 large igneous provinces (LIPs) since 3.8 Ga showed that the LIPs record is semi-continuous back to at least 3.0 Ga, and there was no obvious periodicity, but that there were apparent increases in plume activity between 0.15 Ga and the present, and between 2.8 and 2.7 Ga (Ernst and Buchan, 2002a,b). Figure 16 illustrates the distribution of LIPs around 2.7–2.8 Ga (references in Rino et al., 2004), and shows that plume activity occurred worldwide. The interpretation of the apparent high distribution of LIPs in the Late Archean is still controversial as to whether it represents an increase of activity of plume magmatism or an exclusive preservation of oceanic LIPs (Ernst and Buchan, 2002b), but the high proportion and worldwide distribution indicate that more active magmatism occurred globally in those days. Many LIPs between 1.9 and 2.1 Ga are also scattered throughout the world. By the way, Maruyama (1994) considered that continental collisions are the herald of subsequent active superplume magmatism, because successive subduction of oceanic materials under a large continent results in the thick accumulation and the formation of a cold plume underneath. Figure 16 also displays late Archean metamorphic belts, and includes collision-type metamorphic belts such as the Limpopo Belt between the Zimbabwe and Kaapvaal Cratons, collisions between the Akulleq, Akia and Tasiusarsuaq terranes in southern West Greenland, and amalgamation of the East and West Pilbara terranes in Australia (references in Rino et al., 2004). In the early Proterozoic, many collisional orogenic belts were also formed. Reconstruction of ancestral supercratons from present cratons based on their

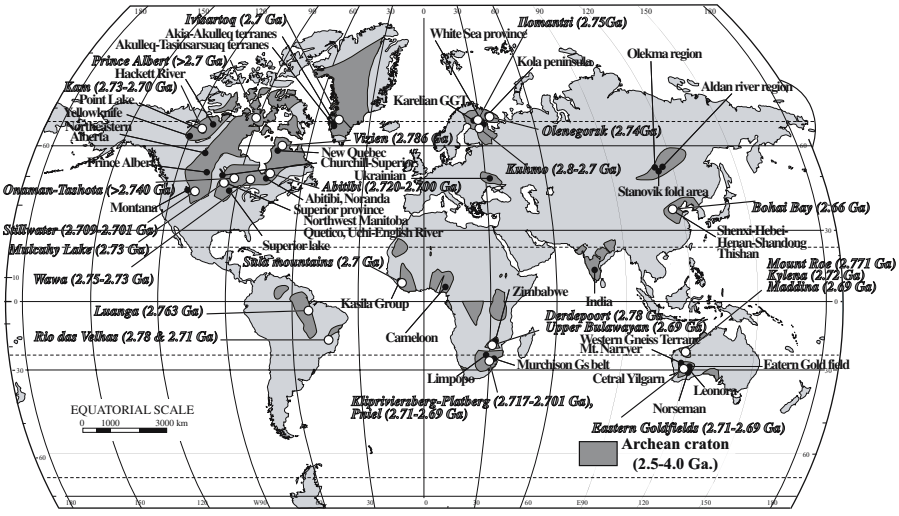

Figure 16. Distribution of large igneous provinces, including continental flood basalts, rift magmatism, komatiitic magmatism, and regional metamorphism between ca. 2.8 and 2.7 Ga (references in Hayashi et al., 2000; Rino et al., 2004). They are scattered in many Archean continents.

geological and geochronological similarities indicates that the cratons can be classified into only a few supercratons in the late Archean and early Proterozoic, when they became relatively large cratons through collision and amalgamation (Bleeker, 2003). This line of evidence suggests that some large continents were formed by collision/amalgamation of cratons and terranes after successive subduction, similar to formation of the modern Eurasian continent, and this implies formation of thick megaliths underneath. The formation of large megaliths in the mantle transition zone and their subsequent collapse causes exchange between upper and lower mantle materials, and influx of fertile and hotter lower mantle materials into the upper mantle. In the Archean, a ca. 150°C hotter mantle resulted in a higher Rayleigh number and an increase of difference of depth of the phase changes between subducted basalt and ambient mantle. In this case, the upper mantle would have behaved as a stagnant lid, and its breakage would have led to a catastrophic mantle overturn because quite large amounts of subducted materials had accumulated before the collapse to the lower mantle. As a consequence, descending slabs would have sunk into the lower mantle (the catastrophic mantle avalanche events of Condie, 1998) and superplumes and plumes would have ascended from the core-mantle boundary to give rise to LIPs (Fig. 17). From our results combined with published data, we suggest that such overturns took place at 2.8–2.6 Ga and at 1.9–1.7 Ga.

The mantle overturn model, which explains the punctuated tectonic evolution of the earth, is based on the thermal evolution of the mantle according to parameterized convection theory. The general model, applied to evolution of the earth, was proposed by McCulloch (1993), developed by Breuer and Spohn (1995) with respect to the Archaean-Proterozoic transition, and constrained by Davies (1995) with numerical calculations. Breuer and Spohn (1995) and Stein and Hofmann (1994) proposed models in which layered mantle convection changes catastrophically to whole-mantle convection during short-lived episodes. The driving forces for such catastrophic movement of mantle materials (mantle overturn) are: thermal instability of the 660 km boundary between cooling upper mantle and lower mantle heated up by radioactive decay (Breuer and Spohn, 1995), and upwelling of a superplume induced by episodic sinking of the accumulated slab materials at the transition zone into the lower mantle (Maruyama, 1994; Stein and Hofmann, 1994; Davies, 1995; Larson and Kincaid, 1996). McCulloch and Bennett (1994) proposed phased growth of a depleted mantle reservoir at the cost of a primitive lower mantle. Compilation of collisional orogenic belts and geological evidence of the presence of large-scale continents at about 2.7 and 1.9 Ga suggests that the mantle overturns were caused by periodic subsidence of subducted oceanic materials under the large continents into the lower mantle.

Mantle overturn was expressed by catastrophic downwelling of cold subducted slabs through the 660-km boundary and by a corresponding upwelling in the form of superplumes from the lower mantle. Where some arose under oceanic plates, they gave rise to oceanic plateaus. The worldwide occurrence of active komatiite magmatism in the late Archean and of OIB-type magmatism in the early Proterozoic (e.g., Stern et al., 1995) supports more active plume-related volcanism at these times (Fig. 16). Where the small plumes arose under a continent, they gave rise to continental

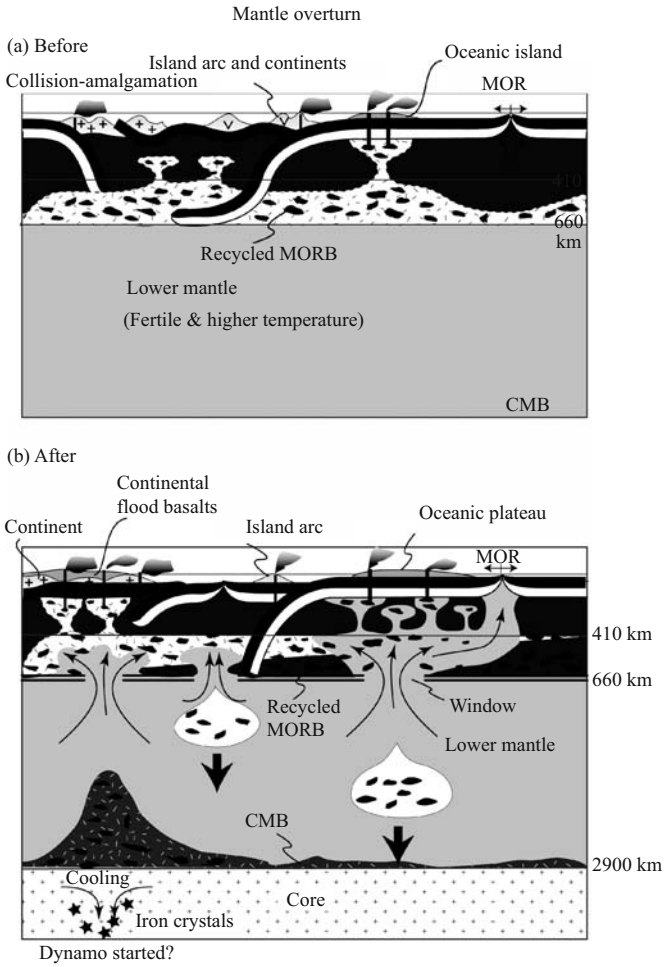

Figure 17. Schematic diagrams of mantle convection systems before and after an overturn (a) In the Archean double-layered convection was dominant because a higher potential mantle temperature of ca. 150°C made the Rayleigh number of the mantle ca. 30 times higher than that of the modern upper mantle. The high potential mantle temperature also resulted in a high productivity of MORB, and accumulated significant amounts of subducted oceanic crust beneath continents. Many island arcs were formed at subduction zones through accretion of oceanic materials and by slab-melting of subducted oceanic basalt to produce TTG magmas. They collided to make continents just before the mantle overturn event. (b) The catastrophic downwelling of the accumulated oceanic crust on the boundary between the upper and lower mantle induced influxes of hotter and more fertile material from the lower mantle. The exchange of materials and the heat transfer between the upper and lower mantle caused active plume-magmatism, and produced large amounts of basalt and komatiite. In addition, continental flood basalts formed on large continents from induced plumes accompanied by entrapment of subducted oceanic crust. After the mantle overturn, the upper mantle became hot and fertile to produce more oceanic crust at mid-oceanic ridges, and consequently more sialic continental crust was formed by partial melting of hydrated basalt at subduction zones.

flood basalts, and cognate mafic dyke swarms (Fig. 16). A recent thermal model of the mantle implies that just before the mantle overturn, the upper mantle was already cooled and depleted so that it could not produce much oceanic crust (Komiya, 2004). Consequently, the productivity of continental crust also decreased at subduction zones at that time. Episodic mantle upwelling gave rise to higher rates of oceanic plate accretion because the influx of hotter and more fertile materials from the lower to the upper mantle produced more basaltic magma at mid-ocean ridges. In this regard, subduction of younger and more oceanic crust led to increased accretion of oceanic materials and/or the slab-melting of them to produce more TTG magmas at subduction zones. This chain of events resulted in formation of more island arcs and episodic continental growth in the Archean.

4 PERSPECTIVE: EVOLUTION OF THE SOLID EARTH AND THE INFLUENCE ON SURFACE ENVIRONMENT

Some elements such as V, Cr, Fe, Ce and Eu have multivalence, and are dependent on their redox state under melting and crystallization conditions. $Fe^{3+}/\sum Fe$ ratio of magma is dependent on the redox state, the temperature, pressure, and composition, and the redox state is the most important among them (e.g., Carmichael, 1991). The oxygen fugacity of the modern upper mantle, especially the MORB-source mantle, ranges around the FMQ buffer, and is estimated from $Fe^{3+}/\sum Fe$ ratios of 0.07 ± 0.03 and 0.023 ± 0.05 for MORB glass and spinel peridotite, respectively (Christie et al., 1986; O'Neill et al., 1993). On the other hand, the $Fe^{3+}/\sum Fe$ ratio of whole rock depends on not only the redox state but also the mineral assemblage (O'Neill et al., 1993; Ballhaus, 1995). For example, peridotite contains little ferric iron because olivine of the major minerals contains no ferric iron, whereas materials in the mantle transition zone have higher $Fe^{3+}/\sum Fe$ ratios because wadsleyite, ringwoodite and majorite contain more ferric iron (O'Neill et al., 1993). Mg-perovskite also contains much ferric iron, simultaneously substituted with aluminum for Mg and Si. As a result, the Fe^{3+}/Fe ratio increases in the deep mantle even at a constant redox state. If lower mantle materials with high $Fe^{3+}/\sum Fe$ ratios ascend to the upper mantle, the upwelling materials have higher ferric iron relative to ambient mantle peridotite, depending on the diffusivity of oxygen or the exchange rate between ferric and ferrous within the mantle. It is widely known that H_2O and CO_2 are easily mobile, but mobility of O_2 or the exchange between Fe^{2+} and Fe^{3+} are restricted (e.g., Chinner, 1960; Mueller, 1960). In addition, there are some mantle materials with the inherited signature of lower mantle materials. For example, clinopyroxenes in xenoliths from Savai'i Western Samoa and Tubuai, Austral islands (Hauri et al., 1993) and from Salt Lake Crater, Hawaii (Salters and Zindler, 1995) inherit trace element patterns from their precursors (Hirose et al., 2004), and some mineral inclusions in lower mantle diamonds have original trace element composition even after phase change from Ca-perovskite to wollastonite (Stachel et al., 2000; Kaminsky et al., 2001). In addition, the lower mantle is inferred to contain 10–20% higher FeO from seismic tomography and mineral physics constraints (e.g., Kellogg et al., 1999), and the fingerprints are still

preserved even after upwelling to the upper mantle and subsequent partial melting (Humayun et al., 2004). These observations imply preserved inheritance of lower mantle conditions even after phase change of minerals because elemental diffusivity is small at the hand-specimen scale. In the case of low diffusivity of oxygen, the materials from the lower mantle would have high oxygen fugacity compared with normal upper mantle because of their high $Fe^{3+}/\sum Fe$. At present, two superplumes arise from the core-mantle boundary in Polynesia and the southern Africa areas. At 2.7 Ga, a mantle overturn event caused upwelling of large amounts of lower mantle materials to the upper mantle. These events possibly oxygenized the upper mantle, and then the surface environment.

Another relevant mechanism is: the mantle was externally oxidized through time. Two different ideas were proposed for the secular change of mantle oxygen fugacity; gradual increase (e.g., Kasting et al., 1993; Eggler and Lorand, 1994; Lécuyer and Ricard, 1999; Kump et al., 2001) and constancy through geological time (Arculus, 1985; Canil, 1997; Delano, 2001). The former estimated the redox state of the mantle from sulfide barometry within peridotitic diamonds from the tectosphere (Kasting et al., 1993; Eggler and Lorand, 1994) and from a box model of the Fe^{3+} cycle between the mantle, subduction zone, continental crust and sediments (Lécuyer and Ricard, 1999). In addition, it is well known that it took half a billion years after emergence of photosynthetic bacteria before a significant amount of O_2 first appeared in the atmosphere. As a hypothesis to account for the delay, oxidation of upper mantle through time is favored, and several models were proposed such as: the upper mantle was oxidized by subduction of hydrated oceanic crust and/or oxidized sediments and the release of reduced volcanic gases (Arculus and Delano, 1987; Kasting et al., 1993). The influx of reduced gases from the ancient reduced mantle suppressed the biological oxygenation of the surface environment that became oxic after the mantle was oxidized (Kasting et al., 1993; Kump et al., 2001). However, the delay can be explained by another mechanisms: an increase of burial rate of organic materials and a decrease of the oxygen consumption in sedimentary rocks caused the oxygen content in the air to rise (Des Marais et al., 1992; Karhu and Holland, 1996), the oxidation of Fe^{2+} to Fe^{3+} in seawater and the deposition of BIF (Cloud, 1972). This paper presents a new idea of oxidation of the mantle by a phase change of subducted oceanic crust to Pv-bearing materials at slab penetration. The process decreases the iron content in the upper mantle by the reaction of ferrous to ferric and metallic iron, as shown above. As a result, the reaction increases the $Fe^{3+}/\sum Fe$ ratio of the silicate mantle, concomitant with the growth of a metallic core, and implies an increase of the oxygen fugacity of the mantle through geological time. However, verification is required to analyze the primary $Fe^{3+}/\sum Fe$ ratio of ancient MORB.

The influence of oxidation of the mantle on the surface environment is still poorly understood. Although still controversial (Ohmoto, 1997; Holland, 1999), it is commonly considered that seawater and the atmosphere were reduced before the late Archean, and were suddenly oxidized in the early Proterozoic (e.g., Cloud, 1972; Kasting, 1993; Holland, 1994; Farquhar et al., 2000). Holland (1994) compiled geological evidence for a sudden increase of atmospheric oxygen in the early

Proterozoic: composition of paleosols, initiation of deposition of red shales, existence of manganese deposits, and termination of deposition of BIF and pyrite- and uraninite-rich sedimentary rocks. Kasting (1993) also collected evidence to constrain the upper and lower bounds of the atmospheric oxygen content, and showed its secular change through time. It is also commonly considered that the redox condition of seawater changed from anoxic in the Archean through euxinic in the early to middle Proterozoic to oxic since the Neoproterozoic due to oxidation by the atmosphere, based on geochemical evidence (Arnold et al., 2004; Kah et al., 2004; Poulton et al., 2004; Rouxel et al., 2005) and schematic views (Kasting, 1993; Anbar and Knoll, 2002). Recently, we made in-situ analyses of major, trace and REE of carbonate minerals with primary sedimentary and precipitation structures in sedimentary carbonate rocks and filled-in amygdules and matrices of pillow lavas to estimate the secular change of the redox condition of seawater (Komiya, 2005). The in-situ analyses eliminate secondary carbonate, contamination of detrital materials, diagenesis and alteration. We estimated the depositional environments from the field occurrence of coexisting basaltic lavas and sedimentary rocks and the fabric of the carbonate themselves, and classified them into shallow and deep (>ca. 1000 m) environmental carbonates. The shallow marine deposits include sedimentary carbonates with stromatolite structure and intercalation with clastic beds, and amygdaloidal carbonates of hot-spot basaltic lava since 3.5 Ga. The deep-sea carbonates comprise those in amygdules and matrices of pillow lavas of MORB-type basalts. Deep-sea carbonates have only faint Ce and Eu anomalies between 3.5 and 1.9 Ga. A negative Ce anomaly of shallow carbonates frequently deviated from that of deep-sea carbonate after 2.78 Ga. The anomaly fluctuated considerably, and was very large at 2.5 and 2.3 Ga. But, the anomaly decreased during/after the Huronian and Marinoan, and probably Sturtian glaciations. This implies a complicated secular change of the redox state in shallow water, whereas the deep-sea environment was anoxic until the Proterozoic. We calculated the oxygen content of shallow and deep seawater based on the Ce concentration and anomaly of carbonate minerals at given parameters of atmospheric pCO_2, and Ca^{2+} of seawater. The Ce concentration of seawater was calculated based on a solid solution model of REE in carbonate and the partition coefficient between carbonate and seawater (Tanaka et al., 2004). The Ce anomaly is dependent on the redox potential and pH of seawater as well as the Ce concentration (Akagi and Masuda, 1998). The variation and distribution of REE complexes in seawater also depends on the pH. We calculated the pH of seawater assuming the evolution curves of atmospheric pCO_2 in the Precambrian (Sleep and Zahnle, 2001) and the Phanerozoic (Royer et al., 2004), and assuming $[Ca^{2+}]_{SW}$ at 3.5 Ga (Foriel et al., 2004) and since the Mesozoic (Demicco et al., 2003), and we estimated a pH of 6.39 at 3.5 Ga to 8.3 at present. We calculated redox potentials from the Ce anomaly and concentration, pCO_2 and pH (Akagi and Masuda, 1998). Assuming that the standard potential is 0.84 (Liu et al., 1988), we estimated the dissolved oxygen content of seawater from the reaction of $2H_2O = O_2 + 4H^+ + 4e^-$. The results are shown in Figure 18, and indicate that oxygen activity of deep-sea water was low and constant until at least 1.9 Ga, probably the Mesozoic, whereas that of shallow seawater increased since

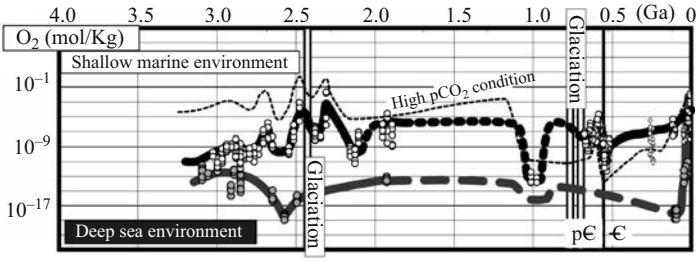

Figure 18. Secular variation of the oxygen contents of shallow marine and deep seawater, respectively. Open circles: carbonate minerals in shallow environment; solid gray circles: deep environment; open diamonds: estimate from composition of Mesozoic carbonate rocks (Tanaka et al., 2003); and open squares: calculated values from modern seawater. Calculations are from Ce anomaly of carbonate minerals through time, secular change of atmospheric CO_2 content (Sleep and Zahnle, 2001 for Precambrian ages; Royer et al., 2004 for Phanerozoic ages), and $[Ca^{2+}]_{SW}$ (Foriel et al., 2004 for 3.5 Ga seawater; Demicco et al., 2003 for the Phanerozoic). Solid solution model of REE in carbonate, and partition coefficient of REE between carbonate and seawater are referred to Tanaka et al. (2004). Standard potential of decomposition of water is 0.84 V (Liu et al., 1988). Temperatures of shallow and deep seawater are assumed to be 15° and 0°C, respectively. A thin dotted line is the oxygen concentration of seawater calculated using a parameter of high atmospheric CO_2, namely average value of a range of atmospheric CO_2 proposed by Kasting (1993). The results show that the oxygen content of deep-sea water was low and constant until at least 1.9 Ga, probably the Mesozoic, whereas that of shallow seawater increased after 2.7 Ga but fluctuated highly. In particular, it reached minima during/after the Snowball Earth events. The oxygen activity became quite high at 2.5 and 2.3 Ga, but it gradually increased in the Phanerozoic.

2.7 Ga but was fluctuated highly. The oxygen activity became quite high at 2.5 and 2.3 Ga, but it eventually increased in the Phanerozoic. Especially, it reached minima during/after Snowball Earth events. However, there are some periods of minima of oxygen content of seawaters, unrelated to Snowball Earth events. Although the causes of them are still unknown, the low oxygen content of seawater around 1.0 Ga probably corresponds to a hiatus in the presence of macrofossils (Hofmann and Chen, 1981; Hofmann and Bengtson, 1992; Hofmann, 1994; Walter et al., 1990; Han and Runnegar, 1992; Kumar, 1995; Zhu and Chen, 1995). High atmospheric CO_2 concentration also explains the small negative Ce anomaly around 1.0 Ga (Fig. 18). Assuming high atmospheric CO_2 concentration through time, namely average value of the estimate by Kasting (1993), we also calculated the dissolved oxygen content of seawater (Fig. 18). The estimate shows the calculated oxygen content of seawater in the Archean was higher than at present, and contradicts many geological observations (Holland, 1994). Therefore, our calculation of dissolved oxygen content of seawater through time favors a low atmospheric CO_2 content through time (e.g., Rye et al., 1995, Sleep and Zahnle, 2001).

BIFs were prominent from 3.8 to 1.8 Ga (Klein et al., 1992). Although there is evidence of oxygenic photosynthetic bacteria, microfossils (e.g., Schopf, 1993) and stromatolites (e.g., Hofmann et al., 1999; Lindsay et al., 2005) only since 3.5 Ga, BIF having been deposited at least since 3.8 Ga. This geological observation is

inconsistent with anoxic seawater in the early Archean. Their formation in an anoxic environment was variably explained by: photochemical reaction (Cairns-Smith, 1978; Braterman et al., 1983; François, 1986; Canuto, 1994), abiotic oxygenic photodissolution (Towe, 1978; Canuto et al., 1982), anaerobic biooxidation of Fe^{2+} (Widdel et al., 1993; Ehrenreich and Widdel, 1994; Hafenbradl et al., 1996; Chaudhuri et al., 2001) and reduction by Fe^{2+} of nitrites and nitrates to prebiotic ammonia (Summers and Chang, 1993; Summers and Lerner, 1998). However, these models are not necessarily consistent with the geological and biological evidence. For example, there is no evidence for such life in the Isua supracrustal belt. High atmospheric pCO_2 resulted in a low pH of the whole seawater, unsuitable for formation of Fe^{3+} as a bi-product of ammonia, whereas the photochemical reaction for Fe^{3+} formation requires quite low pH. BIFs were mostly composed of hematite and iron hydroxide after the middle Archean, whereas BIF in the Isua supracrustal belt mainly contain magnetite. The difference of mineral assemblage is explained by later metamorphism, because hematite is transformed into magnetite at medium-grade metamorphism (Klein, 1983; Dymek and Klein, 1988). However, the mineralogical difference implies a difference of origin. Although generally speaking, hydrothermal fluids have a low pH of 2–6 (Von Damm, 1995), a hydrothermal fluid with a high pH of up to 12 is formed by serpentinization of ultramafic rocks (e.g., Kelley et al., 2005).

Mixing a high pH siliceous hydrothermal fluid and a low pH seawater with a high ferrous content possibly led to precipitation of magnetite and chert under an anoxic environment around a mid-ocean ridge. This hypothesis is consistent with the idea that some BIFs have both negative Ce and positive Eu anomalies. The positive Eu anomaly is caused by precipitation from a hydrothermal fluid (Klinkhammer et al., 1994). Although Dymek and Klein (1988) suggested that a negative Ce anomaly was due to oxic seawater even in the early Archean, the origin of a negative anomaly is still ambiguous. Both anomalies favor the involvement of a hydrothermal fluid with a high pH. If magnetite-type BIF were deposited under an anoxic environment, the BIF in the 3.4 Ga Imataca Complex, Venezuela, is the oldest BIF deposited at least locally in an oxic environment, consistent with the emergence of photosynthetic organisms (James, 1983). However, the photosynthetic organisms did not flourish until the late Archean, because stromatolites became ubiquitous after the late Archean. The prosperity of photosynthetic organisms was also probably due to mantle overturn. The formation of large continents through collision or amalgamation of small continents and island arcs in the late Archean influenced the diversity of life.

Paleomagnetic data show that the intensity of geomagnetism increased in the late Archean (Hale, 1987; Yoshihara and Hamano, 2000) and the increase was caused by formation of the inner core (Stevenson et al., 1983). The geomagnetism was possibly activated by a mantle overturn, because the extensive exchange between the upper and lower mantle materials effectively cooled the core. The intense geomagnetism formed the Van Allen belt, and consequently protected primitive life in the surface environment. However, the ozone layer was still immature, because of low oxygen content in the atmosphere (Kasting, 1993). Therefore, photosynthetic life inhabited tens of meters below the surface of the sea (Berkner and Marshall,

1965). The formation of large continents and their subsequent break-up provided a wide shallow water environment in continental shelves, continental rifts, and intra-continental basins. Especially, the formation of continental rifts and intra-continental basins was indebted to superplume activities; upwelling and downwelling of a super-plume, respectively. Combination of the influence by evolution of a solid earth, which includes oxidation of the mantle through time because of the sink of basaltic materials into the lower mantle and catastrophic upwelling of the lower mantle materials, with the evolution and prosperity of life in plume-related shallow water environments resulted in a sudden increase of atmospheric O_2 in the late Archean to early Proterozoic. The catastrophic evolution of the solid earth was probably induced by mantle overturn.

ACKNOWLEDGEMENTS

This work was partly supported by grants from the Ministry of Education, Culture, Sports, Science and Technology, Japan (No. 04302021, 07238105, 16740284) and by a project on Whole Earth Dynamics from the Science and Technology Agency of Japan. We thank Drs. Takafumi Hirata, Tsuyoshi Iizuka and Shuji Rino for the acquisition of analytical data. We are grateful to Prof. Shigenori Maruyama and Kei Hirose for their constructive comments. The works presented here are based on a number of collaborations with my colleagues including Mamoru Hayashi, Tsuyoshi Iizuka and Shuji Rino. We are grateful to Prof. Brian Windley for his fruitful comments and reviews.

REFERENCES

Abbott, D., L. Burgess, and J. Longhi (1994) An empirical thermal history of the Earth's upper mantle. *J. Geophys. Res.*, 99, 13835–13850.

Akagi, T., and A. Masuda (1998) A simple thermodynamic interpretation of Ce anomaly. *Geochem. J.*, 32, 301–314.

Allègre, C.J. (1982) Chemical geodynamics. *Tectonophysics*, 81, 109–132.

Allègre, C.J., O. Brévart, B. Dupré, and J.-F. Minster (1980) Isotopic and chemical effects produced in a continuously differentiating convecting Earth mantle. *Philos. Trans. R. Soc. Lond. A*, 297, 447–477.

Anbar, A.D., and A.H. Knoll (2002) Proterozoic ocean chemistry and evolution: A bioinorganic bridge? *Science*, 297, 1137–1142.

Arculus, R.J. (1985) Oxidation status of the mantle past and present. *Ann. Rev. Earth Planet. Sci.*, 13, 75–95.

Arculus, R.J., and J.W. Delano (1987) Oxidation state of the upper mantle: Present conditions, evolution, and controls. In Nixon, P.H. (ed.) Mantle Xenoliths, Wiley, New York, pp. 589–599.

Armstrong, R.L. (1981) Radiogenic isotopes: The case for crustal recycling on a near-steady state no-continental-growth Earth. *Philos. Trans. R. Soc. Lond. A*, 301, 443–472.

Arndt, N.T. (1983) Role of a thin, komatiite-rich oceanic crust in the Archean plate-tectonics process. *Geology*, 11, 372–375.

Arndt, N.T. (1991) High Ni in Archean tholeiites. *Tectonophysics*, 187, 411–419.

Arndt, N.T., and E.G. Nisbet (1982) Komatiites, George Allen & Unwin, London, p. 526.

Arnold, G.L., A.D. Anbar, J. Barling, and T.W. Lyons (2004) Molybdenum isotope evidence for widespread anoxia in Mid-Proterozoic oceans. *Science*, 304, 87–90.

Ballhaus, C. (1995) Is the upper mantle metal-saturated? *Earth Planet. Sci. Lett.*, 132, 75–86.
Barley, M.E., and D.I. Groves (1992) Supercontinent cycles and the distribution of metal deposits through time. *Geology*, 20, 291–294.
Bennett, V.C., A.P. Nutman, and M.T. McCulloch (1993) Nd isotopic evidence for transient, highly depleted mantle reservoirs in the early history of the Earth. *Earth Planet. Sci. Lett.*, 119, 299–317.
Berkner, L.V., and L.C. Marshall (1965) On the origin and rise of oxygen concentration in the Earth's atmosphere. *J. Atmospheric Sci.*, 22, 225–261.
Bickle, M.J. (1978) Heat loss from the Earth: A constraint on Archaean tectonics from the relation between geothermal gradients and the rate of plate production. *Earth Planet. Sci. Lett.*, 40, 301–315.
Bickle, M.J., E.G. Nisbet, and A. Martin (1994) Archean greenstone belts are not oceanic crust. *J. Geol.*, 102, 121–138.
Birch, F. (1958) Differentiation of the Mantle. *Geol. Soc. Am. Bull.*, 69, 483–485.
Bleeker, W. (2003) The late Archean record: A puzzle in ca. 35 pieces. *Lithos*, 71, 99–134.
Bowring, S.A., and I.S. Williams (1999) Priscoan (4.00–4.03 Ga) orthogneisses from northwestern Canada. *Contrib. Mineral. Petrol.*, 134, 3–16.
Braterman, P.S., A.G. Cairns-Smith, and R.W. Stolper (1983) Photo-oxidation of hydrated Fe^{2+}-significance for banded iron formations. *Nature*, 303, 163–164.
Breuer, D., and T. Spohn (1995) Possible flush instability in mantle convection at the Archaean-Proterozoic transition. *Nature*, 378, 608–610.
Bridgwater, D., V.R. McGregor, and J.S. Myers (1974) A horizontal tectonic regime in the Archean of Greenland and its implications for early crustal thickening. *Precambrian Res.*, 1, 179–197.
Brown, G.C. (1979) The changing pattern of batholith emplacement during earth history. In Atherton, M.P., and J. Tarney (eds.) Origin of Granite Batholiths, Shiva, Nantwich, UK, pp. 106–115.
Buck, W.R. (1992) Global decoupling of crust and mantle: Implications for topography, geoid and mantle viscosity of venus. *Geophys. Res. Lett.*, 19, 2111–2114.
Burke, K., J.F. Dewey, and W.S.F. Kidd (1976) Dominance of horizontal movements, arc and microcontinental collisions during the later permobile regime. In Windley, B.F. (ed.) The Early History of the Earth, John Wiley & Sons, London, pp. 113–129.
Burke, K., and W.S.F. Kidd (1978) Were Archean continental geothermal gradients much steeper than those of today? *Nature*, 272, 240–241.
Cairns-Smith, A.G. (1978) Precambrian solution photochemistry, inverse segregation, and banded iron formations. *Nature*, 276, 807–808.
Calvert, A.J., E.W. Sawyer, W.J. Davis, and J.N. Ludden (1995) Archaean subduction inferred from seismic images of a mantle suture in the Superior Province. *Nature*, 375, 670–674.
Campbell, I.H., R.W. Griffiths, and R.I. Hill (1989) Melting in an Archaean mantle plume: Heads it's basalts, tails it's komatiites. *Nature*, 339, 697–699.
Canil, D. (1997) Vanadium partitioning and the oxidation state of Archaean komatiite magmas. *Nature*, 389, 842–845.
Canuto, V.M. (1994) Genesis of banded iron-formation. *Economic Geology*, 89, 1384–1397.
Canuto, V.M., J.S. Levine, T.R. Augustsson, and C.L. Imhoff (1982) UV radiation from the young Sun and oxygen and ozone levels in the prebiological palaeoatmosphere. *Nature*, 296, 816–820.
Carmichael, I.S.E. (1991) The redox states of basic and silicic magmas: A reflection of their source regions? *Contrib. Mineral. Petrol.*, 106, 129–141.
Cavosie, A.J., J.W. Valley, S.A. Wilde, and E.I.M.F. (2005) Magmatic $\delta^{18}O$ in 4400–3900 Ma detrital zircons: A record of the alteration and recycling of crust in the Early Archean. *Earth Planet. Sci. Lett.*, 235, 663–681.
Chase, C.G., and P.J. Patchett (1988) Stored mafic/ultramafic crust and early Archean mantle depletion. *Earth Planet. Sci. Lett.*, 91, 66–72.
Chaudhuri, S.K., J.G. Lack, and J.D. Coates (2001) Biogenic Magnetite Formation through Anaerobic Biooxidation of Fe(II). *Appl. Environ. Microbiol.*, 67, 2844–2848.
Chinner, G.A. (1960) Pelitic gneisses with varying ferrous/ferric ratios from Glen Clova, Angus, Scotland. *J. Petrol.*, 1, 178–217.

Christie, D.M., I.S.E. Carmichael, and C.H. Langmuir (1986) Oxidation states of mid-ocean ridge basalt glasses. *Earth Planet. Sci. Lett.*, 79, 397–411.

Cloud, P. (1972) A working model of the primitive Earth. *Am. J. Sci.*, 272, 537–548.

Cohen, R.S., N.M. Evensen, P.J. Hamilton, and R.K. O'Nions (1980) U-Pb, Sm-Nd and Rb-Sr systematics of mid-ocean ridge basalt glasses. *Nature*, 283, 149–153.

Condie, K. (1982) Plate Tectonics and Crustal Evolution, New York, Pergamon, 310p.

Condie, K.C. (1972) A plate tectonics evolutionary model of the South Pass Archaean greenstone belt, southwestern Wyoming. Proc. 24th Int. Geol. Congr., 1, 104–112.

Condie, K.C. (1995) Episodic ages of greenstones: A key to mantle dynamics? *Geophys. Res. Lett.*, 22, 2215–2218.

Condie, K.C. (1998) Episodic continental growth and supercontinents: A mantle avalanche connection? *Earth Planet. Sci. Lett.*, 163, 97–108.

Condie, K.C. (2000) Episodic continental growth models: Afterthoughts and extensions. *Tectonophysics*, 322, 153–162.

Cordani, U.G., K. Sato, W. Teixeira, C.C.G. Tassinari, and M.A.S. Basei (2000) Crustal evolution of the South American platform. In Cordani, U.G., E.J. Milani, A. Thomaz Filho, and D.A. Campos (eds.) Tectonic Evolution of South America, Rio de Janeiro, 31st Inter. Geol. Congr., pp. 19–40.

Cowan, D.S. (1985) Structural styles in Mesozoic and Cenozoic mélanges in the western Cordillera of North America. *Geol. Soc. Am. Bull.*, 96, 451–462.

Davies, G.F. (1980) Thermal histories of convective earth models and constraints on radiogenic heat production in the earth. *J. Geophys. Res.*, 85, 2517–2530.

Davies, G.F. (1992) On the emergence of plate tectonics. *Geology*, 20, 963–966.

Davies, G.F. (1995) Punctuated tectonic evolution of the earth. *Earth Planet. Sci. Lett.*, 136, 363–379.

de Wit, M.J., and R.A. Hart (1993) Earth's earliest continental lithosphere, hydrothermal flux and crustal recycling. *Lithos*, 30, 309–335.

Defant, M.J., and M.S. Drummond (1990) Dehydration of some modern arc magmas by melting of young subducted lithosphere. *Nature*, 347, 662–665.

Delano, J.W. (2001) Redox history of the earth's interior since ~3900 Ma: Implications for prebiotic molecules. *Orig. Life Evol. Biosph.*, 31, 311–341.

Demicco, R.V., T.K. Lowenstein, and L.A. Hardie (2003) Atmospheric pCO2 since 60 Ma from records of seawater pH, calcium, and primary carbonate mineralogy. *Geology*, 31, 793–796.

Des Marais, D.J., H. Strauss, R.E. Summons, and J.M. Hayes (1992) Carbon isotope evidence for the stepwise oxidation of the Proterozoic environment. *Nature*, 359, 605–609.

Dewey, J., and H. Spall (1975) Pre-Mesozoic plate tectonics: How far back in Earth history can the Wilson Cycle be extended? *Geology*, 3, 422–424.

Dewey, J.F., and B.F. Windley (1981) Growth and differentiation of continental crust. *Philos. Trans. R. Soc. Lond. A*, 301, 189–206.

Dupré, B., and C.J. Allègre (1980) Pb-Sr-Nd isotopic correlations and the chemistry of the North Atlantic mantle. *Nature*, 286, 17–22.

Dymek, R.F., and C. Klein (1988) Chemistry, petrology and origin of banded iron-formation lithologies from the 3800 Ma Isua supracrustal belt, West Greenland. *Precambrian Res.*, 39, 247–302.

Eggler, D.H., and J.P. Lorand (1994) Sulfides, diamonds and mantle fO_2. Proc. 5th Int. Kimb. Conf., CPRM Brasilia, Brasilia, pp. 160–169.

Ehrenreich, A., and F. Widdel (1994) Anaerobic oxidation of ferrous iron by purple bacteria, a new type of phototrophic metabolism. *Appl. Environ. Microbiol.*, 60, 4517–4526.

Engebretson, D.C., K.P. Kelley, H.J. Cashman, and M.A. Richards (1992) 180 million years of subduction. *GSA Today*, 2, 93–95, 100.

England, P., and M. Bickle (1984) Continental thermal and tectonic regimes during the Archean. *J. Geol.*, 92, 353–367.

Ernst, R.E., and K.L. Buchan (2002a) Erratum to "Maximum size and distribution in time and space of mantle plumes: Evidence from large igneous provinces". *J. Geodynamics*, 34, 711–714.

Ernst, R.E., and K.L. Buchan (2002b) Maximum size and distribution in time and space of mantle plumes: Evidence from large igneous provinces. *J. Geodynamics*, 34, 309–342.

Farquhar, J., H. Bao, and M. Thiemens (2000) Atmospheric influence of earth's earliest sulfur cycle. *Science*, 289, 756–758.

Foriel, J., P. Philippot, P. Rey, A. Somogyi, D. Banks, and B. Ménez (2004) Biological control of Cl/Br and low sulfate concentration in a 3.5-Gyr-old seawater from North Pole, Western Australia. *Earth Planet. Sci. Lett.*, 228, 451–463.

Fowler, C.M.R., C. Ebinger, and C.J. Hawkesworth (eds) (2002) The early Earth: Physical, chemical and biological development. *Geol. Soc. Lond. Spec. Publ.*, 199, p. 352.

François, L.M. (1986) Extensive deposition of banded iron formations was possible without photosynthesis. *Nature*, 320, 352–354.

Frost, C.D. (1993) Nd isotopic evidence for the antiquity of the Wyoming province. *Geology*, 21, 351–354.

Frost, C.D., B.R. Frost, K.R. Chamberlain, and T.P. Hulsebosch (1998) The Late Archean history of the Wyoming province as recorded by granitic magmatism in the Wind River Range, Wyoming. *Precambrian Res.*, 89, 145–173.

Frost, D.J., C. Liebske, F. Langenhorst, C.A. McCammon, R.G. Trønnes, and D.C. Rubie (2004) Experimental evidence for the existence of iron-rich metal in the Earth's lower mantle. *Nature*, 428, 409–412.

Fukao, Y., M. Obayashi, H. Inoue, and M. Nenbai (1992) Subducting slabs stagnant in the mantle transition zone. *J. Geophys. Res.*, 97, 4809–4822.

Fyfe, W.S. (1978) The evolution of the Earth's crust: Modern plate tectonics to ancient hot spot tectonics. *Chem. Geol.*, 23, 89–114.

Galer, S.J.G., and S.L. Goldstein (1991) Early mantle differentiation and its thermal consequences. *Geochim. Cosmochim. Acta*, 55, 227–239.

Gastil, R.G. (1960) Distribution of mineral dates in time and space. *Am. J. Sci.*, 258, 1–35.

Gladczenko, T.P., M.F. Coffin, and O. Eldholm (1997) Crustal structure of the Ontong Java Plateau: Modeling of new gravity and existing seismic data. *J. Geophys. Res.*, 102, 22711–22729.

Grambling, J.A. (1981) Pressures and temperatures in Precambrian metamorphic rocks. *Earth Planet. Sci. Lett.*, 53, 63–68.

Green, D.H., I.A. Nicholls, M. Viljoen, and R. Viljoen (1975) Experimental demonstration of the existence of peridotitic liquids in earliest Archean magmatism. *Geology*, 3, 11–14.

Gurnis, M., and G.F. Davies (1986) Apparent episodic crustal growth arising from a smoothly evolving mantle. *Geology*, 14, 396–399.

Hafenbradl, D., M. Keller, R. Dirmeier, R. Rachel, P. Ro√ünagel, S. Burggraf, H. Huber, and K.O. Stetter (1996) *Ferroglobus placidus* gen. nov., sp. nov., a novel hyperthermophilic archaeum that oxidizes Fe^{2+} at neutral pH under anoxic conditions. *Arch. Microbiol.*, 166, 308–314.

Hale, C.J. (1987) Palaeomagnetic data suggest link between the Archaean-Proterozoic boundary and inner-core nucleation. *Nature*, 329, 233–237.

Hamilton, W.B. (2003) An alternative Earth. *GSA Today*, pp. 4–12.

Han, T.-M., and B. Runnegar (1992) Megascopic eukaryotic algae from the 2.1 billion-year-old Negaunee Iron-Formation, Michigan. *Science*, 257, 232–235.

Hargraves, R.B. (1986) Faster spreading or greater ridge length in the Archean? *Geology*, 14, 750–752.

Hart, S.R., C. Brooks, T.E. Krogh, G.L. Davis, and D. Nava, 1970, Ancient and modern volcanic rocks: A trace element model. *Earth Planet. Sci. Lett.*, 10, 17–28.

Hauri, E.H., N. Shimizu, J.J. Dieu, and S.R. Hart (1993) Evidence for hotspot-related carbonatite metasomatism in the oceanic upper mantle. *Nature*, 365, 221–227.

Hayashi, M., T. Komiya, Y. Nakamura, and S. Maruyama (2000) Archean regional metamorphism of the Isua supracrustal belt, southern West Greenland: Implications for a driving force of Archean plate tectonics. *Int. Geo. Rev.*, 42, 1055–1115.

Head, J.W., and L.S. Crumpler (1990) Venus geology and tectonics: Hotspot and crustal spreading models and questions for the Magellan mission. *Nature*, 346, 525–533.

Herzberg, C., and J. Zhang (1996) Melting experiments on anhydrous peridotite KLB-1: Compositions of magmas in the upper mantle and transition zone. *J. Geophys. Res.*, 101, 8271–8295.

Hirose, K. (2002) Phase transitions in pyrolitic mantle around 670-km depth: Implications for upwelling of plumes from the lower mantle. *J. Geophys. Res.*, 107, doi: 10.1029/2001JB000597.

Hirose, K., Y. Fei, Y. Ma, and H. Mao (1999) The fate of subducted basaltic crust in the Earth's lower mantle. *Nature*, 397, 53–56.

Hirose, K., N. Shimizu, W. van Westrenen, and Y. Fei (2004) Trace element partitioning in Earth's lower mantle and implications for geochemical consequences of partial melting at the core-mantle boundary. *Phys. Earth Planet. Inter.*, 146, 249–260.

Hoffman, P.F. (1991) On accretion of granite-greenstone terranes. In Robert, F., P.A. Sheahan, and S.B. Green (eds.) Greenstone Gold and Crustal Evolution, Geological Association of Canada, St. John's, Newfoundland, pp. 32–45.

Hoffman, P.F., and G. Ranalli (1988) Archean oceanic flake tectonics. *Geophys. Res. Lett.*, 15, 1077–1080.

Hofmann, A.W., K.P. Jochum, M. Seufert, and W.M. White (1986) Nb and Pb in oceanic basalts: New constraints on mantle evolution. *Earth Planet. Sci. Lett.*, 79, 33–45.

Hofmann, H., and J. Chen (1981) Carbonaceous megafossils from the Precambrian (1800 Ma) near Jixian, northern China. *Can. J. Earth Sci.*, 18, 443–447.

Hofmann, H.J., and S. Bengtson (1992) Stratigraphic distribution of megafossils. In Schopf, J.W., and C. Klein (eds.) The Proterozoic Biosphere, Cambridge University Press, New York, pp. 501–506.

Hofmann, H. (1994) Proterozoic carbonaceous compressions ("metaphytes" and "worms"). In Bengtson, S. (ed.) Early Life on Earth, Columbia University Press, New York, pp. 342–357.

Hofmann, H.J., K. Grey, A.H. Hickman, and R.I. Thorpe (1999) Origins of 3.45 Ga coniform stromatolites in Warrawoona Group, Western Australia. *Geol. Soc. Am. Bull.*, 111, 1256–1262.

Holland, H.D. (1994) Early Proterozoic atmospheric change. In Bengtson, S. (ed.) Early Life on Earth, Columbia University Press, New York, pp. 237–244.

Holland, H.D. (1999) When did the Earth's atmosphere become oxic? *A Reply. The Geochemical News*, 100, 20–22.

Honda, S. (1995) A simple parameterized model of Earth's thermal history with the transition from layered to whole mantle convection. *Earth Planet. Sci. Lett.*, 131, 357–369.

Humayun, M., L. Qin, and M.D. Norman (2004) Geochemical evidence for excess iron in the mantle beneath Hawaii. *Science*, 306, 91–94.

Hurley, P.M., and J.R. Rand (1969) Pre-drift continental nuclei. *Science*, 164, 1229–1242.

Iizuka, T., T. Hirata, T. Komiya, S. Rino, I. Katayama, A. Motoki, and S. Maruyama (2005) U-Pb and Lu-Hf isotope systematics of zircons from the Mississippi River sand: Implications for reworking and growth of continental crust. *Geology*, 33, 485–488.

Iizuka, T., K. Horie, T. Komiya, S. Maruyama, T. Hirata, H. Hidaka, and B.F. Windley (2006) Occurrence of a 4.2 Gyr old zircon in the Acasta Gneiss Complex of northwestern Canada: Geology, v. 34, pp. 245–248.

Inoue, T., and H. Sawamoto (1992) High pressure melting of pyrolite under hydrous condition and its geophysical implication: High-pressure Research. Application to Earth and Planetary Sciences, Tokyo and AGU, Washington D.C., Terra, pp. 323–331.

Irifune, T., and A.E. Ringwood (1987) Phase transformations in a harzburgite composition to 26 GPa: Implications for dynamical behaviour of the subducting slab. *Earth Planet Sci. Lett.*, 86, 365–376.

Isozaki, Y., S. Maruyama, and F. Furuoka (1990) Accreted oceanic materials in Japan. *Tectonophysics*, 181, 179–205.

James, H.L. (1983) Distribution of banded iron-formation in space and time. In Trendall, A.F., and R.C. Morris (eds.) Iron-Formation: Facts and Problems: Developments in Precambrian Geology, Elsevier, Amsterdam, pp. 471–490.

Kah, L.C., T.W. Lyons, and T.D. Frank (2004) Low marine sulphate and protracted oxygenation of the Proterozoic biosphere. *Nature*, 431, 834–838.

Kamber, B.S., K.D. Collerson, S. Moorbath, and M.J. Whitehouse (2003) Inheritance of early Archaean Pb-isotope variability from long-lived Hadean protocrust. *Contrib. Mineral. Petrol.*, 145, 25–46.

Kaminsky, F., O. Zakharchenko, R. Davies, W. Griffin, G. Khachatryan-Blinova, and A. Shiryaev (2001) Superdeep diamonds from the Juina area, Mato Grosso State, Brazil. *Contrib. Mineral. Petrol.*, 140, 734–753.

Karhu, J.A., and H.D. Holland (1996) Carbon isotopes and the rise of atmospheric oxygen. *Geology*, 24, 867–870.

Kasting, J.F. (1993) Earth's early atmosphere. *Science*, 259, 920–926.

Kasting, J.F., D.H. Eggler, and S.P. Raeburn (1993) Mantle redox evolution and the oxidation state of the Archean atmosphere. *J. Geol.*, 101, 245–257.

Kelley, D.S., J.A. Karson, G.L. Fruh-Green, D.R. Yoerger, T.M. Shank, D.A. Butterfield, J.M. Hayes, M.O. Schrenk, E.J. Olson, G. Proskurowski, M. Jakuba, A. Bradley, B. Larson, K. Ludwig, D. Glickson, K. Buckman, A.S. Bradley, W.J. Brazelton, K. Roe, M.J. Elend, A. Delacour, S.M. Bernasconi, M.D. Lilley, J.A. Baross, R.E. Summons, and S.P. Sylva (2005) A serpentinite-hosted ecosystem: The Lost City hydrothermal field. *Science*, 307, 1428–1434.

Kellogg, L.H., B.H. Hager, and R.D. van der Hilst (1999) Compositional stratification in the deep mantle. *Science*, 283, 1881–1884.

Kinny, P.D., W. Compston, and I.A. Williams (1991) A reconnaissance ion-probe study of hafnium isotopes in zircons. *Geochim. Cosmochim. Acta*, 55, 849–859.

Klein, C. (1983) Diagenesis and metamorphism of Precambrian banded iron-formations. In Trendall, A.F., and R.C. Morris (eds.) Iron-Formation: Facts and Problems: Developments in Precambrian Geology, Elsevier, Amsterdam, pp. 417–469.

Klein, C., N.J. Beukes, H.D. Holland, J.F. Kasting, L.R. Kump, and D.R. Lowe (1992) 4. Proterozoic Atmosphere and Ocean. In Schopf, J.W., and C. Klein (eds.) The Proterozoic Biosphere: A Multidisciplinary Study, Cambridge University Press, New York, pp. 135–174.

Klinkhammer, G., C.R. German, H. Elderfield, M.J. Greaves, and A. Mitra (1994) Rare earth elements in hydrothermal fluids and plume particulates by inductively coupled plasma mass spectrometry. *Mar. Chem.*, 45, 179–186.

Komiya, T., S. Maruyama, S. Nohda, T. Masuda, M. Hayashi, and S. Okamoto (1999) Plate tectonics at 3.8–3.7 Ga: Field evidence from the Isua accretionary complex, southern West Greenland. *J Geol.*, 107, 515–554.

Komiya, T., M. Hayashi, S. Maruyama, and H. Yurimoto (2002a) Intermediate-P/T type Archean metamorphism of the Isua supracrustal belt: Implications for secular change of geothermal gradients at subduction zones and for Archean plate tectonics. *Am. J. Sci.*, 302, 804–826.

Komiya, T., T. Iizuka, I. Katayama, Y. Ueno, and Y. Uehara (2002b) Geology of the Acasta Gneiss Complex in Slave Province, northern Canada: Appreciating new geological evidence of the oldest rocks in the world: EOS Trans. AGU, 83(47), Fall Meet. Suppl., Abstract, p. V51B-1243.

Komiya, T., S. Maruyama, T. Hirata, and H. Yurimoto (2002c) Petrology and geochemistry of MORB and OIB in the mid-Archean North Pole region, Pilbara craton, Western Australia: Implications for the composition and temperature of the upper mantle at 3.5 Ga. *Int. Geol. Rev.*, 44, 988–1016.

Komiya, T. (2004) Material circulation model including chemical differentiation within the mantle and secular variation of temperature and composition of the mantle. *Phys. Earth Planet. Inter.*, 146, 333–367.

Komiya, T., S. Maruyama, T. Hirata, H. Yurimoto, and S. Nohda (2004) Geochemistry of the oldest MORB and OIB in the Isua supracrustal belt (3.8 Ga), southern West Greenland: Implications for the composition and temperature of early Archean upper mantle. *The Island Arc*, 13, 47–72.

Komiya, T. (2005) Secular variation of REE patterns of carbonate minerals through the time. EOS Trans. AGU, v. 86, p. Fall Meet. Suppl., Abstract.

Kono, Y., and T. Yoshii (1975) Numerical experiments on the thickening plate model. *J. Phys. Earth*, 23, 63–75.

Kröner, A. (1977) The Precambrian geotectonic evolution of Africa: Plate accretion versus plate destruction. *Precambrian Res.*, 4, 163–213.

Kröner, A. (1981) Precambrian Plate Tectonics. In Kröner, A. (ed.) Precambrian Plate Tectonics, Elsevier, Amsterdam, 57–90.

Kumar, S. (1995) Megafossils from the Mesoproterozoic Rohtas Formation (the Vindhyan Supergroup), Katni area, central India. *Precambrian Res.*, 72, 171–184.

Kump, L.R., J.F. Kasting, and M.E. Barley (2001) Rise of atmospheric oxygen and the "upside-down" Archean mantle. *Geochem. Geophys. Geosyst.*, 2, 2000GC000114.

Kusky, T.M. (1989) Accretion of the Archean Slave province. *Geology*, 17, 63–67.

Kusky, T.M., J.-H. Li, and R.D. Tucker (2001) The Archean Dongwanzi ophiolite complex, North China Craton: 2.505-billion-year-old oceanic crust and mantle. *Science*, 292, 1142–1145.

Kusky, T.M., and P.A. Winsky (1995) Structural relationships along a greenstone/shallow water shelf contact, Belingwe greenstone belt, Zimbabwe. *Tectonics*, 14, 448–471.

Larson, R.L., and C. Kincaid (1996) Onset of mid-Cretaceous volcanism by elevation of the 670 km thermal boundary layer. *Geology*, 24, 551–554.

Lindsay, J.F., M.D. Brasier, N. McLoughlin, O.R. Green, M. Fogel, A. Steele, and S.A. Mertzman (2005) The problem of deep carbon—An Archean paradox. *Precambrian Res.*, 143, 1–22.

Liu, Y.-G., M.R.U. Miah, and R.A. Schmitt (1988) Cerium: A chemical tracer for paleo-oceanic redox conditions. *Geochim. Cosmochim. Acta*, 52, 1361–1371.

Lécuyer, C., and Y. Ricard (1999) Long-term fluxes and budget of ferric iron: Implication for the redox states of the Earth's mantle and atmosphere. *Earth Planet. Sci. Lett.*, 165, 197–211.

Maas, R., P.D. Kinny, I.S. Williams, D.O. Froude, and W. Compston (1992) The Earth's oldest known crust: A geochronological and geochemical study of 3900–4200 Ma old detrital zircons from Mt. Narryer and Jack Hills, Western Australia. *Geochim. Cosmochim. Acta*, 56, 1281–1300.

Martin, H. (1986) Effect of steeper Archean geothermal gradient on geochemistry of subduction-zone magmas. *Geology*, 14, 753–756.

Maruyama, S. (1994) Plume tectonics. *Jour. Geol. Soc. Jpn.*, 100, 24–49.

Maruyama, S., Masuda, S. and Appel, P.W.U. (1991a) The oldest accretionary complex on the Earth, Isua, Greenland. *Geol. Soc. Am., Abstract with programs*, 23, A429-A430.

Maruyama, S., Y. Isozaki, and G. Kimura (1991b) Is the Mid-Archean barite formation from the Pilbara craton, Australia under the deep-sea environment? EOS Trans., 72, p. 532.

Maruyama, S., J.G. Liou, and M. Terabayashi (1996) Blueschists and eclogites of the world and their exhumation. *International Geology Review*, 38, 485–594.

Matsuda, T., and Y. Isozaki (1991) Well-documented travel history of Mesozoic pelagic chert in Japan. *Tectonics*, 10, 475–499.

McCammon, C. (1997) Perovskite as a possible sink for ferric iron in the lower mantle. *Nature*, 387, 694–696.

McCammon, C., M. Hutchison, and J. Harris (1997) Ferric iron content of mineral inclusions in diamonds from São Liz: A view into the lower mantle. *Science*, 278, 434–436.

McCulloch, M.T. (1987) Sm-Nd isotopic constraints on the evolution of Precambrian crust in the Australian continent. In Kröner, A. (ed.) Proterozoic Lithospheric Evolution: Geodynamics, American Geophysical Union, Washington D.C., pp. 115–130.

McCulloch, M.T. (1993) The role of subducted slabs in an evolving earth. *Earth Planet. Sci. Lett.*, 115, 89–100.

McCulloch, M.T., and V.C. Bennett (1994) Progressive growth of the Earth's continental crust and depleted mantle: Geochemical constraints. *Geochim. Cosmochim. Acta*, 58, 4717–4738.

McCulloch, M.T., and G.J. Wasserburg (1979) Sm-Nd and Rb-Sr chronology of continental crust formation. *Science*, 200, 1003–1011.

McDonough, W.F., and S.-S. Sun (1995) The composition of the Earth. *Chem. Geol.*, 120, 223–253.

McGregor, V.R. (1973) The early Precambrian gneisses of the Godthåb district, West Greenland. *Philos. Trans. Royal Soc. Lond. A*, 273, 343–358.

McGregor, V.R. (1993) Descriptive text to 1:100000 Geological map of GREENLAND Qôrqut 64 V.1 Syd.: Copenhagen, Geological Survey of Greenland, 40p.

McGregor, V.R., C.R.L. Friend, and A.P. Nutman (1991) The late Archean mobile belt through Godthåbsfjord, southern West Greenland: A continent-continent collision zone? *Bull. Geol. Soc. Denmark*, 39, 179–197.

McLennan, S.M., and S.R. Taylor (1982) Geochemical constraints on the growth of the continental crust. *J. Geol.*, 90, 342–361.

Miyashiro, A. (1973) Metamorphism and Metamorphic Belts. George Allen & Unwin, London, 492p.

Moorbath, S. (1977) Ages, isotopes and evolution of Precambrian continental crust. *Chem. Geol.*, 20, 151–187.

Moores, E.M. (1993) Neoproterozoic oceanic crustal thinning, emergence of continents and origin of the Phanerozoic ecosystem: A model. *Geology*, 21, 5–8.

Mueller, R.F. (1960) Compositional characteristics and equilibrium relations in mineral assemblages of a metamorphosed iron formation. *Am. J. Sci.*, 258, 449–497.

Nelson, B.K., and D.J. DePaolo (1985) Rapid production of continental crust 1.7 to 1.9 b.y. ago: Nd isotopic evidence from the basement of the North American mid-continent. *Geol. Soc. Am. Bull.*, 96, 746–754.

Nelson, D.R., B.W. Robinson, and J.S. Myers (2000) Complex geological histories extending for $\geq$ 4.0 Ga deciphered from xenocryst zircon microstructures. *Earth Planet. Sci. Lett.*, 181, 89–102.

Newsom, H.E., W.M. White, K.P. Jochum, and A.W. Hofmann (1986) Siderophile and chalcophile element abundances in oceanic basalts, Pb isotope evolution and growth of the Earth's core. *Earth Planet. Sci. Lett.*, 80, 299–313.

Nisbet, E.G., M.J. Cheadle, N.T. Arndt, and M.J. Bickle (1993) Constraining the potential temperature of the Archean mantle: A review of the evidence from komatiites. *Lithos*, 30, 291–307.

Nisbet, E.G., and C.M.R. Fowler (1983) Model for Archean plate tectonics. *Geology*, 11, 376–379.

Nowell, G.M., P.D. Kempton, S.R. Noble, J.G. Fitton, A.D. Saunders, J.J. Mahoney, and R.N. Taylor (1998) High precision Hf isotope measurements of MORB and OIB by thermal ionisation mass spectrometry: Insights into the depleted mantle. *Chem. Geol.*, 149, 211–233.

Nutman, A.P., V.R. McGregor, C.R.L. Friend, V.C. Bennett, and P.D. Kinny (1996) The Itsaq Gneiss Complex of southern West Greenland: The world's most extensive record of early crustal evolution (3,900–3,600 Ma). Precam. Res. Special Issue. *The Oldest Rocks on Earth*, v. 78, pp. 1–39.

O'Neill, H.S.C., D.C. Rubie, D. Canil, C.A. Geiger, C.R. Ross II, F. Seifert, and A.B. Woodland (1993) Ferric iron in the upper mantle and in transition zone assemblages: Implications for relative oxygen fugacities in the mantle. In Takahashi, E., R. Jeanloz, and D. Rubie (eds.) Evolution of the Earth and Planets, IUGG and Am. Geophys. Union, Washington, pp. 73–88.

O'Nions, R.K., N.M. Evensen, and P.J. Hamilton (1979) Geochemical modeling of mantle differentiation and crustal growth. *J. Geophys. Res.*, 84, 6091–6101.

Ogawa, M. (1997) A bifurcation in the coupled magmatism-mantle convection system and its implications for the evolution of the Earth's upper mantle. *Phys. Earth Planet. Inter.*, 102, 259–276.

Ohmoto, H. (1997) When did the Earth's atmosphere become oxic? *Geochem. News*, 93, 12–13, 26–27.

Ohta, H., S. Maruyama, E. Takahashi, Y. Watanabe, and Y. Kato (1996) Field occurrence, geochemistry and petrogenesis of the Archean mid-oceanic ridge basalts (AMORBs) of the Cleaverville area, Pilbara craton, Western Australia. *Lithos*, 37, 199–221.

Okamoto, K., and S. Maruyama (1999) The high-pressure synthesis of lawsonite in the MORB + H_2O system. *Am. Mineral.*, 84, 362–373.

Oldenburg, D.W., and J.N. Brune (1972) Ridge transform fault spreading pattern in freezing wax. *Science*, 178, 301–304.

Parman, S.W., J.C. Dann, T.L. Grove, and M.J. de Wit (1997) Emplacement conditions of komatiite magmas from the 3.49 Ga Komati Formation, Barberton Greenstone Belt, South Africa. *Earth Planet. Sci. Lett.*, 150, 303–323.

Patchett, P.J., J.D. Vervoort, U. Soderlund, and V.J.M. Salters (2004) Lu-Hf and Sm-Nd isotopic systematics in chondrites and their constraints on the Lu-Hf properties of the Earth. *Earth Planet. Sci. Lett.*, 222, 29–41.

Peacock, S.M. (1996) Thermal and petrological structure of subduction zones. In Bebout, G.E., D.W. Scholl, S.H. Kirby, and J.P. Platt (eds.) Subduction: Top to Bottom: Geophys. Monor., Am. Geophys. Union, Washington D.C., pp. 119–133.

Peltier, W.R., S. Butler, and L.P. Solheim (1997) The influence of phase transformations on mantle mixing and plate tectonics. In Crossley, D.J. (ed.) Earth's Deep Interior, Gordon & Breach, Amsterdam, pp. 405–430.

Phillips, R.J., W.M. Kaula, G.E. McGill, and M.C. Malin (1981) Tectonics and evolution of Venus. *Science*, 212, 879–887.

Piper, J.D.A. (1982) The Precambrian palaeomagnetic record: The case for the Proterozoic supercontinent. *Earth Planet. Sci. Lett.*, 59, 61–89.

Pollack, H.N. (1980) The heat flow from the earth: A review. In Davies, P.A., and S.K. Runcorn (eds.) Mechanisms of Continental Drift and Plate Tectonics, Academic Press, New York, pp. 183–192.

Poulton, S.W., P.W. Fralick, and D.E. Canfield (2004) The transition to a sulphidic ocean [sim] 1.84 billion years ago. *Nature*, 431, 173–177.

Rapp, R.P., and E.B. Watson (1995) Dehydration melting of metabasalt at 8–32 kbar: Implications for continental growth and crust-mantle recycling. *J. Petrol.*, 36, 891–931.

Reymer, A., and G. Schubert (1984) Phanerozoic addition rates to the continental crust and crustal growth. *Tectonics*, 3, 63–77.

Richardson, S.H., J.J. Gurney, A.J. Erlank, and J.W. Harris (1984) Origin of diamonds in old enriched mantle. *Nature*, 310, 198–202.

Richter, F.M. (1985) Models for the Archean thermal regime. *Earth Planet. Sci. Lett.*, 73, 350–360.

Righter, K., M.J. Drake, and G. Yaxley (1997) Prediction of siderophile element metal-silicate partition coefficients to 20 GPa and 2800°C: The effects of pressure, temperature, oxygen fugacity, and silicate and metallic melt compositions. *Phys. Earth Planet. Inter.*, 100, 115–134.

Rino, S., T. Komiya, B.F. Windley, I. Katayama, A. Motoki, and T. Hirata (2004) Major episodic increases of continental crustal growth determined from zircon ages of river sands; implications for mantle overturns in the Early Precambrian. *Phys. Earth Planet. Inter.*, 146, 369–394.

Rouxel, O.J., A. Bekker, and K.J. Edwards (2005) Iron isotope constraints on the Archean and Paleoproterozoic ocean redox state. *Science*, 307, 1088–1091.

Royer, D.L., R.A. Berner, I.P. Montañez, N.J. Tabor, and D.J. Beerling (2004) CO2 as a primary driver of Phanerozoic climate. *GSA Today*, 4–10.

Runcorn, S.K. (1965) Changes in the convection pattern in the Earth's mantle and continental drift: Evidence for a cold origin of the Earth. *Philos. Trans. R. Soc. Lond. A*, 258, 228–251.

Rye, R., P.H. Kuo, and H.D. Holland (1995) Atmospheric carbon dioxide concentrations before 2.2 billion years ago. *Nature*, 378, 603–605.

Sakurai, R., T. Komiya, K. Okamoto, K. Shimizu, and K. Hirose (2001) Structural geology and petrology of the Barberton Greenstone Belts, South Africa. 4th International Archean Symposium, pp. 87–89.

Salters, V.J.M., and A. Zindler (1995) Extreme 176Hf/177Hf in the sub-oceanic mantle. *Earth Planet. Sci. Lett.*, 129, 13–30.

Scherer, E., C. Münker, and K. Mezger (2001) Calibration of the Lutetium-Hafnium Clock. *Science*, 293, 683–687.

Schopf, J.W. (1993) Microfossils of the Early Archean Apex Chert: New evidence of the antiquity of life. *Science*, 260, 640–646.

Sclater, J.G., C. Jaupart, and D. Galson (1980) The heat flow through oceanic and continental crust and the heat loss from the earth. *Rev. Geophys. Space Phys.*, 18, 269–311.

Sleep, N.H., and K.J. Zahnle (2001) Carbon dioxide cycling and implications for climate on ancient Earth. *J. Geophys. Res.*, 106, 1373–1399.

Spear, F.S. (1993) Metamorphic Phase Equilibria and Pressure-Temperature-Time Paths, Mineralogical Society of America, Washington, D.C., 799p.

Stachel, T., J.W. Harris, G.P. Brey, and W. Joswig (2000) Kankan diamonds (Guinea) II: Lower mantle inclusion parageneses. *Contrib. Mineral. Petrol.*, 140, 16–27.

Stein, M., and A.W. Hofmann (1994) Mantle plumes and episodic crustal growth. *Nature*, 372, 63–68.
Stern, R.A., E.C. Syme, A.H. Bailes, and S.B. Lucas (1995) Paleoproterozoic (1.90–1.86 Ga) arc volcanism in the Flin Flon Belt, Trans-Hudson Orogen, Canada. *Contrib. Mineral. Petrol.*, 119, 117–141.
Stern, R.J. (2005) Evidence from ophiolites, blueschists, and ultrahigh-pressure metamorphic terranes that the modern episode of subduction tectonics began in Neoproterozoic time. *Geology*, 33, 557–560.
Stevenson, D.J., T. Spohn, and G. Schubert (1983) Magnetism and thermal evolution of terrestrial planets. *Icarus*, 54, 466–489.
Summers, D., and N. Lerner (1998) Ammonia from iron (II) reduction of nitrite and the Strecker synthesis: Do iron (II) and cyanide interfere with each other? *Orig. Life and Evol. Biosph.*, 28, 1–11.
Summers, D.P., and S. Chang (1993) Prebiotic ammonia from reduction of nitrite by iron (II) on the early Earth. *Nature*, 365, 630–633.
Sun, S.-S. (1984) Geochemical characteristics of Archaean ultramafic and mafic volcanic rocks: Implications for mantle composition and evolution. In Kröner, A., G.N. Hansen, and A.M. Goodwin (eds.) Archaean Geochemistry, Springer-Verlag, Berlin, pp. 25–46.
Symmes, G.H., and J.M. Ferry (1992) The effect of whole-rock MnO content on the stability of garnet in pelitic schists during metamorphism. *J. Metamorphic Geol.*, 10, 221–237.
Tajika, E., and T. Matsui (1990) The evolution of the terrestrial environment. In Newsom, H.E., and J.H. Jones (eds.) Origin of the Earth, Oxford University Press, New York, pp. 347–370.
Takahashi, E. (1990) Speculations on the Archean mantle: Missing link between komatiite and depleted garnet peridotite. *J. Geophys. Res.*, 95, 15941–15954.
Takahashi, E., and C.M. Scarfe (1985) Melting of peridotite to 14 GPa and the genesis of komatiites. *Nature*, 315, 566–568.
Tanaka, K., N. Miura, Y. Asahara, and I. Kawabe (2003) Rare earth element and strontium isotopic study of seamount-type limestones in Mesozoic accretionary complex of Southern Chichibu Terrane, central Japan: Implication for incorporation process of seawater REE into limestones. *Geochem. J.*, 37, 163–180.
Tanaka, K., A. Ohta, and I. Kawabe (2004) Experimental REE partitioning between calcite and aqueous solution at 25°C and 1 atm: Constraints on the incorporation of seawater REE into seamount-type limestones. *Geochem. J.*, 38, 19–32.
Taylor, S.R., and S.M. McLennan (1985) The Continental Crust: Its Composition and Evolution, Blackwell, Oxford, 312 p.
Tomlinson, K.Y., G.M. Stott, J.A. Percival, and D. Stone (2004) Basement terrane correlations and crustal recycling in the western Superior Province: Nd isotopic character of granitoid and felsic volcanic rocks in the Wabigoon subprovince, N. Ontario, Canada. *Precambrian Res.*, 132, 245–274.
Towe, K.M. (1978) Early Precambrian oxygen: A case against photosynthesis. *Nature*, 274, 657–661.
Tozer, D.C. (1965) Heat transfer and convection currents. *Philos. Trans. R. Soc. Lond. A*, 258, 252–271.
Turcotte, D.L., and G. Schubert (1982) Geodynamics: Applications of Continuum Physics to Geological Problems, John Wiley & Sons, New York, 450p.
Ueda, H., M. Kawamura, and K. Niida (2000) Accretion and tectonic erosion processes revealed by the mode of occurrence and geochemistry of greenstones in the Cretaceous accretionary complexes of the Idonnappu Zone, southern central Hokkaido, Japan. *The Island Arc*, 9, 237–257.
Urey, H.C. (1956) The cosmic abundance of potassium, uranium, and thorium and the heat balances of the earth, moon, and Mars. *Proc. Natl. Acad. Sci. USA*, 42, 889–891.
Veizer, J., and S.L. Jansen (1979) Basement and sedimentary recycling and continental evolution. *J. Geol.*, 87, 341–370.
Vervoort, J.D., and J. Blichert-Toft (1999) Evolution of the depleted mantle: Hf isotope evidence from juvenile rocks through time. *Geochim. Cosmochim. Acta*, 63, 533–556.
Vielzeuf, D., and M.W. Schmidt (2001) Melting relations in hydrous systems revisited: Application to metapelites, metagreywackes and metabasalts. *Contrib. Mineral. Petrol.*, 141, 251–267.
Von Damm, K.L. (1995) Controls on the chemistry and temporal variability of seafloor hydrothermal fluids. In Humphris, S.E., R.A. Zierenberg, L.S. Mullineaux, and R.E. Thompson (eds.)

Seafloor Hydrothermal Systems: Geophysical Monograph, American Geophysical Union, Washington, pp. 222–247.

Wakita, K., and I. Metcalfe (2005) Ocean Plate Stratigraphy in East and Southeast Asia. *J. Asian Earth Sci.*, 24, 679–702.

Walter, M.R., D. Rulin, and R.J. Horodyski (1990) Coiled carbonaceous megafossils from the Middle Proterozoic of Jixian (Tianjin) and Montana. *Am. J. Sci.*, 290-A, 133–148.

Warren, P.H. (1985) The magma ocean concept and lunar evolution. *Ann. Rev. Earth Planet. Sci.*, 13, 201–240.

Watson, E.B., and T.M. Harrison (2005) Zircon thermometer reveals minimum melting conditions on Earliest Earth. *Science*, 308, 841–844.

Watson, J.V. (1978) Precambrian thermal regimes. *Philos. Trans. R. Soc. Lond. A*, 288, 431–440.

Widdel, F., S. Schunell, S. Heising, A. Ehrenreich, B. Assmus, and B. Schink (1993) Ferrous iron oxidation by anoxygenic phototrophic bacteria. *Nature*, 362, 834–836.

Wilde, S.A., J.W. Valley, W.H. Peck, and C.M. Graham (2001) Evidence from detrital zircons for the existence of continental crust and oceans on the Earth 4.4 Gyr ago. *Nature*, 409, 175–178.

Windley, B.F. (1976) New tectonic models for the evolution of Archean continents and oceans. In Windley, B.F. (ed.) The Early History of the Earth, John Wiley and Sons, London, pp. 105–111.

Windley, B.F. (2003) Continental growth in the Proterozoic: A global perspective. In Yoshida, M., B.F. Windley, and S. Dasgupta (eds.) Proterozoic East Gondwana: Supercontinent Assembly and Breakup, *Geol. Soc. Lond. Spec. Pub.*, pp. 23–33.

Wood, B.J., and D.C. Rubie (1996) The effect of alumina on phase transformations at the 660-kilometer discontinuity from Fe-Mg partitioning experiments. *Science*, 273, 1522–1524.

Wooden, J.L., P.A. Mueller, D.A. Mogk, and D.R. Bowes (1988) A review of the geochemistry and geochronology of Archean rocks of the Beartooth Mountains, Montana and Wyoming: Precambrian and Mesozoic Plate Margins. *Montana Bureau of Mines and Geology Special Publication*, 96, 23–42.

Wynne-Edwards, H.R. (1976) Proterozoic ensialic orogenesis: The millipede model of ductile plate tectonics. *Am. J. Sci.*, 276, 927–953.

Yoshihara, A., and Y. Hamano (2000) Intensity of the Earth's magnetic field in late Archean obtained from diabase dikes of the Slave Province, Canada. *Phys. Earth Planet. Inter.*, 117, 295–307.

Yuen, D.A., D.M. Reuteler, S. Balachandar, V. Steinbach, A.V. Malevsky, and J.J. Smedsmo (1994) Various influences on three-dimensional mantle convection with phase transitions. *Phys. Earth Planet. Inter.*, 86, 185–203.

Zhu, S., and H. Chen (1995) Megascopic multicellular organisms from the 1700-million-year-old Tuanshanzi Formation in the Jixian area, North China. *Science*, 270, 620–622.

Zindler, A., and S. Hart (1986) Chemical geodynamics. *Ann. Rev. Earth Planet. Sci.*, 14, 493–571.

PART IV

DYNAMICS OF SUPERPLUMES

INTRODUCTION

Part IV contains a description of the dynamical issues involved in the generation of superplume in the lower mantle.

Superplume (Fig. 1), as the major physical mechanism for driving dynamics in the lower mantle, is the major subject of this book and therefore deserves some considerations from a dynamical standpoint. However, the physical aspects of superplumes are under debate: whether they are of a thermal or chemical nature or both, or, one big plume, or a cluster of smaller plumes colliding with each other (Schubert et al., 2004).

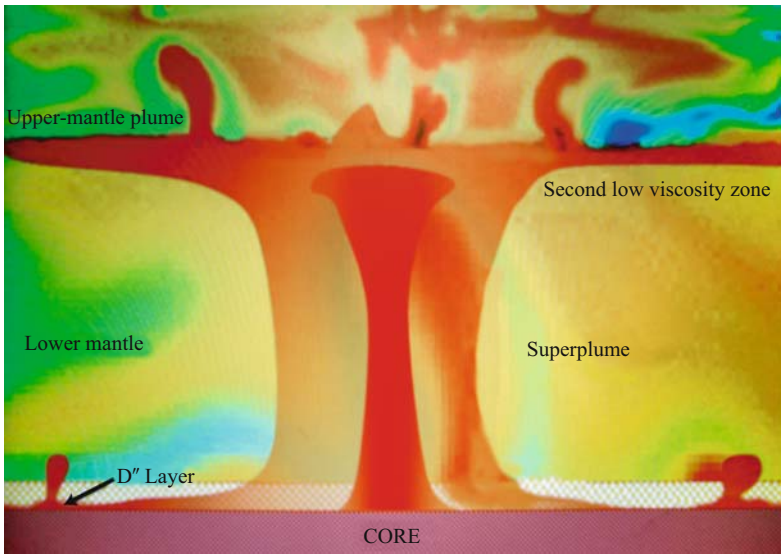

Figure 1. Schematic illustration of the multi-scale nature of mantle plume and superplume based on calculations by Matyska and Yuen (2005) and drawn artistically by Ying-chun Liu.

D. A. Yuen et al. (eds.), Superplumes, 237–238.
© 2007 *Springer.*

Yuen et al. studied the various conditions for thermal convection in the mantle in which superplumes can be generated, particularly by radiative thermal conductivity in the lower mantle in the presence of the post-perovskite phase change. Post-perovskite and the electron spin-transformation of wüstite may play a significant role in promoting the radiative heat transfer. Hofmeister treats the subject matter of thermal conductivity in her chapter, where she outlines the possible applications of radiative and grain-size dependent thermal conductivity in the lower mantle and how this may impact on the growth of superplume and plume enrichment with iron.

Deschamps et al. review the recent progress of the research about thermal and compositional effects in present-day mantle circulation, based on seismic tomography and the separation of the chemical from the thermal effect in the interpretation of today's mantle dynamics.

Karato provides an extensive review of the recent progress in mineral physics on the role of hydrogen in physical properties of minerals. The role of hydrogen is particularly important in relation to the dynamics of the near surface layer (i.e., lithosphere-asthenosphere) and the MBL, but is potentially important also in the dynamics of the D″ layer. Hydrogen can modify the viscosity of minerals by several orders of magnitude, and its role sometimes becomes more important than the thermal effects.

REFERENCES

Matyska, C., and D.A. Yuen (2005) The importance of radiative heat transfer on superplumes in the lower mantle with the new post-perovskite phase change. *Earth Planet. Sci. Lett.*, 234, 71–81.

Schubert, G., G. Masters, P. Olson, and P.J. Tackley (2004) Superplume or plume clusters? *Phys. Earth Planet. Inter.*, 146, 147–162.

CHAPTER 9

DYNAMICS OF SUPERPLUMES IN THE LOWER MANTLE

DAVID A. YUEN[1], MARC MONNEREAU[2], ULRICH HANSEN[3], MASANORI KAMEYAMA[4], AND CTIRAD MATYSKA[5]

[1] *Department of Geology and Geophysics and Minnesota Supercomputing Institute, University of Minnesota, Minneapolis 55455, USA;*
E-mail: daveyuen@gmail.com

[2] *UMR 5562, CNRS—Universiteté Paul Sabatier Toulouse III, 14 Avenue E. Belin, 31400 Toulouse, France*

[3] *Institut für Geophysik, University of Münster, 48149 Münster, Germany*

[4] *Earth Simulator Center, JAMSTEC, Kanazawa-ku, 237-0061 Yokohama, Japan*

[5] *Department of Geophysics, Faculty of Mathematics and Physics, Charles University, 180 00 Prague 8, Czech Republic*

Abstract
Superplumes in the lower mantle have been inferred for a long time by the presence of two very large provinces with slow seismic wave velocities. These extensive structures are not expected from numerical and laboratory experiments nor are they found in thermal convection with constant physical properties under high Rayleigh number conditions. Here we summarize our dynamical understanding of superplume structures within the framework of thermal convection. The numerical studies involve both two- and three-dimensional models in Cartesian and spherical-shell geometries. The theoretical approach is based on models with increasing complexity, starting with the incompressible Boussinesq model and culminating with the anelastic compressible formulation. We focus here on the (1) depth-dependence of variable viscosity and thermal coefficient of expansion (2) radiative thermal conductivity and (3) both upper- and deep-mantle phase transitions. All these physical factors in thermal convection help to create conditions favorable for the formation of partially-layered convection and large-scale upwelling structures in the lower mantle.

1 INTRODUCTION

The notion of superplumes or large-scale structures in the lower mantle has been around for more than twenty years, since the initial tomographic pictures shown by Dziewonski (1984). The surface manifestation of this seismic anomaly was

D. A. Yuen et al. (eds.), Superplumes, 239–268.
© 2007 *Springer.*

recognized and associated with the South Pacific Superswell, which is known as a broad area of shallow seafloor under French Polynesia (McNutt and Judge, 1990). This tantalizing concept, which ran counter to the idea of narrow conduit-like plumes in the deep mantle, proposed earlier by Morgan (1971), has stood the scrutiny of many subsequent tomographic models. So there has now emerged a picture in the lower mantle consisting of two regions with prominent slow seismic velocities, which extend from the core-mantle boundary up to around 1000 km in depth (Su and Dziewonski, 1992; Masters et al., 2000; Li and Romanowicz, 1996; Grand et al., 1997; Zhao, 2001, 2004; Montelli et al., 2004).

These structures have also been interpreted in terms of clusters of plumes (Schubert et al., 2004), arising from plume-plume collisions (Vincent and Yuen, 1988). Maruyama (1994) has discussed the geological and geophysical ramifications of superplumes in mantle evolution and coined the term "plume tectonics" which predicts that eventually these superplumes would control the upper-mantle circulation. Since that time the interest in superplumes has grown immensely, as evidenced by the numerous conferences and a big thirst is fast building up for understanding this interesting phenomenon from physical and geological standpoints.

The appearance of these few obese plumes in the lower mantle can shed light on the physical properties of the lower mantle and indicates that the mantle viscosity cannot be constant throughout the mantle, as the initial work by Hansen et al. (1993) showed a dramatic reduction in the population of lower-mantle plumes with the introduction of depth-dependent thermal expansivity and viscosity. This work was then followed up by Van Keken and Yuen (1995) and Yuen et al. (1996), who emphasized the importance of a high viscosity region in the deep mantle. Davies (2005) has shown that downwellings in the presence of depth-dependent viscosity can induce a few number of plumes in 3-D spherical-shell convection at high Rayleigh numbers. Superplumes can also be considered from the point of view of thermal-chemical convection, as first pointed out by Yuen et al. (1993) from arguments based on the magnitude of seismic velocity anomalies and depth dependence of equation of state parameters in the lower mantle. This phenomenon of accumulation of chemical anomalies in the lower mantle has been corroborated (e.g., Trampert et al., 2004) and investigated numerically by Hansen and Yuen (1989), Tackley (1998), Mc Namara and Zhong (2004) and experimentally by Davaille (1999) and Davaille et al. (2005). Changes in transport properties, such as radiative thermal conductivity (Matyska et al., 1994; Dubuffet and Yuen, 2000; Matyska and Yuen, 2005) and grain-size dependent rheology (Korenaga, 2005) may also broaden lower-mantle plumes considerably.

Although thermal-chemical convection takes place to some degree in the mantle (e.g., Trampert et al., 2004), in this chapter we will direct our attention to thermal convection, because this represents a legitimate end member and we can understand from these exercises a great deal concerning the interaction between the transport properties and phase transitions in nonlinear thermal convection, already a complicated enough phenomenon. Having stated this caveat, we will therefore discuss our results only within the framework of thermal convection.

We will begin in section 2 with a description of our models, which include both two- and three-dimensional models and also have both Cartesian and spherical geometries. We will focus on the influences of variable viscosities, radiative thermal conductivity and phase transitions, which also includes the recently discovered post-perovskite phase transition (Murakami et al., 2004). Section 3 will display the results from these models. Finally we give the conclusions and present our perspectives.

2 MODELS AND FORMULATION

Within our theoretical framework we will employ the viscous fluid model for describing lower-mantle convection and neglect the effects of viscoelasticity (e.g., Mühlhaus and Regenauer-Lieb, 2005) and plasticity (Kameyama et al., 1999; Regenauer-Lieb and Yuen, 2003), which are important for plate dynamics. The conservation equations of mantle convection in this viscous regime can be found in many places, e.g. (Schubert et al., 2002). We will just highlight the salient points here. For the Earth's mantle the conservation of mass is governed by the following dimensionless elliptic partial differential equation in the short-time limit of neglecting elastic waves:

$$\nabla \cdot (\rho \underset{\sim}{\mathbf{V}}) = 0, \tag{1}$$

where ρ is density field non-dimensionalized by the surface density, and $\underset{\sim}{\mathbf{V}}$ is the velocity vector, non-dimensionalized by K/h, where K is the surface thermal diffusivity and h is the mantle thickness. Conservation of mass, as expressed by eqn. (1), is called the anelastic compressible approximation, where ρ, the density depends on the pressure or depth. Within the framework of the incompressible or Boussinesq approximation ρ is taken to be a constant and eqn. (1) becomes $\nabla \cdot \underset{\sim}{\mathbf{V}} = 0$. We note that the Boussinesq approximation is adequate for the upper-mantle, but may be deficient for lower-mantle dynamics, because of the influence of equation of state (see Tan and Gurnis, 2005).

The conservation of momentum for the Earth's mantle does not include either the influences of inertia or rotation because of its high viscosity and just expresses a balance among the viscous stresses, buoyancy and pressure gradient. It is given in non-dimensional form by the elliptic partial differential equation for

$$\nabla \cdot \underset{\approx}{\tau}(\underset{\sim}{\mathbf{V}}) + \mathrm{Ra}\alpha\theta \mathrm{e}_z - \nabla\pi = 0, \tag{2}$$

where $\underset{\approx}{\tau}$ is the Cauchy stress tensor given by the mathematical relationship between $\underset{\approx}{\tau}$ and the spatial derivatives of the velocity field. This relationship belongs to the field of mantle rheology (Ranalli, 1995). The dynamical pressure is given by π. α is thermal expansion coefficient, which can be depth-dependent, θ is the temperature perturbation rendered dimensionless by the temperature drop across the mantle (van den Berg and Yuen, 1998) and Ra is the dimensionless Rayleigh number which measures the vigor of convection.

For the Earth's mantle the spatially averaged Rayleigh number lies between 10^6 and 10^7. The constitutive relationship between the deviatoric stress tensor σ and the velocity is given for Newtonian fluids by:

$$\underset{\sim}{\sigma} = \eta(\mathrm{T}, p, \ldots)\left(\nabla \underset{\sim}{\mathbf{v}} + (\nabla \underset{\sim}{\mathbf{v}})^{\mathrm{T}}\right), \tag{3}$$

where η is called the dynamic viscosity and this particular transport coefficient for momentum depends on the absolute temperature T, the hydrostatic pressure p and other variables, such as grain-size (Solomatov, 1996) and volatile content (Hirth and Kohlstedt, 1996).

The transfer of heat in the mantle is governed by the following dimensionless nonlinear partial differential equation, which has the only time-dependence for thermal convection involving viscous fluids,

$$\rho \frac{\partial \mathrm{T}}{\partial t} = \nabla \cdot (\mathrm{K} \nabla \mathrm{T}) - \rho \underset{\sim}{\mathbf{v}} \cdot \nabla \mathrm{T} - D\alpha w\,(\mathrm{T} + \mathrm{T}_0) + \left(\frac{\mathrm{D}}{\mathrm{Ra}}\right)(\underset{\sim}{\sigma} : \nabla \underset{\sim}{\mathbf{v}}) + R, \tag{4}$$

where T is the dimensionless temperature, w is the vertical velocity, t is time nondimensionalized by the thermal diffusion time across the whole mantle, K is the thermal diffusivity which depends on temperature and pressure (Hofmeister, 1999), R is the dimensionless internal heating rate (e.g., Leitch and Yuen, 1989), T_0 is the temperature of the viscous surface (see Steinbach and Yuen, 1998), D is the dissipation number (Christensen and Yuen, 1985), given by α h/(g Cp), where Cp is the specific heat at constant pressure, g is the gravitational acceleration. In this paper we assume Cp to be a constant, since the mantle temperature is well above the Debye temperature.

The parameters in D appearing in (4) assume the magnitude of the surface values. The energy equation, as expressed above, includes mechanical heating from adiabatic work and viscous heating, as manifested by the dissipation number, which depends on the equation of state. In the Boussinesq approximation the dissipation number is zero and there is no irreversible production of heat from fluid motions. In the extended Boussinesq framework (Christensen and Yuen, 1985), D is non-zero in the energy equation but the continuity equation takes the incompressible limit with a constant density field. For additional details of the non-dimensionalized equations, the reader is referred to Matyska and Yuen (2007).

The two transport properties, η and K, hold the key to the style of mantle convection. The temperature-dependence of mantle viscosity is important for the style of surface deformation because of the sharp variations of viscosity associated with the top thermal boundary layer. In contrast, the variations in the magnitude of temperature-dependence of thermal diffusivity are much smaller than those associated with viscosity, but because K appears in the time-dependent equation governing mantle convection, this positioning of K in the master equation (e.g., Haken, 1983) of the mantle convection system enables it to exert much more subtle influence on mantle convection, which depends on the nature of the heat-transfer mechanism, whether it is lattice conductivity (Yanagawa et al., 2005) or radiative conductivity

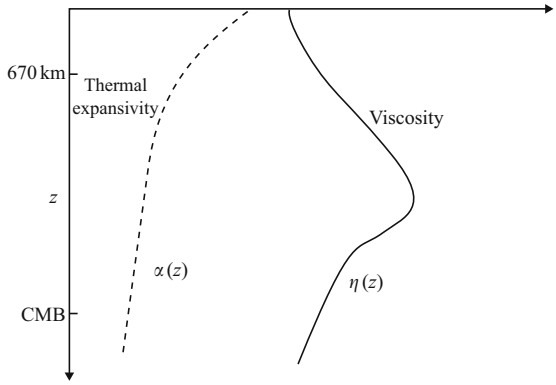

Figure 1. The depth-dependent trends of the coefficient of thermal expansion α and of viscosity η in the mantle. The viscosity profile is taken from the work of Forte and Mitrovica (2001) and Mitrovica and Forte (2004). This viscosity peak in the mid lower-mantle was first shown by Ricard and Wuming (1991). The pressure dependence of α has now been extended to perovskite in the lower mantle (Katsura et al., 2005).

(Dubuffet et al., 2002). In contrast, the viscosity appears as a coefficient in the elliptic equation. Variations in the viscosity with a much larger magnitude are needed to produce significant effects in mantle convection. The depth dependence of α and η stabilizes mantle convection (Hansen et al., 1993) and induces the formation of fewer upwellings. Their general appearances are sketched in Figure 1. We note that α for mantle materials decreases with pressure, which means the potency of thermal buoyancy becomes much weaker in the deep mantle, leading to the situation of dominance by compositional effects (Schott et al., 2002). The pressure-dependence of mantle viscosity depends sensitively on the creep mechanism, but it increases greatly with depth because of the increase in the pressure-work term in the exponential argument of the viscosity (see Sammis et al., 1977).

The rate of decrease in the thermal expansivity with depth is governed by the Anderson-Grueneisen parameter δ (e.g., Anderson, 1995). For olivine, δ was measured to be about 5 (Chopelas and Boehler, 1992), but for perovskite delta has recently been determined to be around 10 for the top 300 km of the lower mantle (Katsura et al., 2005). Such a high value would have profound effects in mantle dynamics, especially for slab penetration and the development of superplumes under the transition zone (Yuen et al., 1996).

The viscosity hill, depicted above, raises some interesting issues. Recent investigations on high-spin to low-spin transition of Fe++ in lower-mantle materials (Badro et al., 2004; Lin et al., 2005; Speziale et al., 2005; Tsuchiya et al., 2006) revealed the possibilities for electronic rearrangements of molecular bonding at pressures corresponding the depth of the viscosity hill, which is located around 1500 to 1800 km at depth (Mitrovica and Forte, 2004). Such a change in the electronic environment in that pressure range would have an unforeseen effect on the activation enthalpy of the lower-mantle assemblage, which would, in turn, invalidate the cherished idea of

a single activation energy and volume, commonly employed in rheological flow law used in modeling (e.g., Tackley, 1996).

We have employed the following numerical models for illustrating the dynamics of superplumes:

(1) Boussinesq, variable viscosity code, based on the finite-volume method and MPI parallelization, in both 2-D and 3-D Cartesian geometries (Trompert and Hansen, 1998).
(2) Anelastic compressible 3-D spherical-shell code, based on finite-differences and spherical harmonics (Monnereau and Yuen, 2002) and Open MP for multiple processors.
(3) Extended-Boussinesq variable viscosity code, based on finite-differences and and conjugate gradient methods in 2-D Cartesian geometry (Matyska and Yuen, 2005; Matyska and Yuen, 2006).
(4) Extended Boussinesq, variable viscosity code, based on finite-volume, pseudo-compressibility, multigrid and MPI parallelization (Kameyama et al., 2005; Kameyama, 2005).

Armed with this array of numerical tools, we can now proceed to explore various aspects of superplume dynamics.

3 RESULTS

3.1 2-D and 3-D Boussinesq models

We will begin with the simplest model taken from the Boussinesq convection equations with both constant thermal conductivity and thermal expansivity. A very wide, two-dimensional box with an aspect-ratio of 36 is taken. The viscosity law employed is temperature-and depth-dependent with the form of

$$\eta(\mathrm{T}, z) = z^n \exp(-100\mathrm{T}) \tag{5}$$

where T is dimensionless temperature and z is the dimensionless depth with $z = 0$ situating at the top. The parameter n controls the steepness of the depth-dependence of the viscosity and the location of the maximum of the viscosity profile, as a consequence of the interplay between the temperature-dependent viscosity and the depth portion of the viscosity. A larger n would move the maximum deeper down toward the core-mantle boundary. The maximum of the horizontally averaged viscosity profile in the lower mantle comes from the interaction between the increasing depth-dependence from the polynomial in z and the decreasing viscosity due to the temperature from the approach to the hot core-mantle boundary. The surface Rayleigh number of the simulations reported in this section is 10^7.

Figure 2 shows the dynamical influence of moving this viscosity hill deeper down. For $n = 2$ there are many upwellings, but with increasing n or greater degree of depth-dependence there is a diminishing number of plumes. Thus we see clearly the stabilizing influence of the depth-dependence of viscosity on mantle convection,

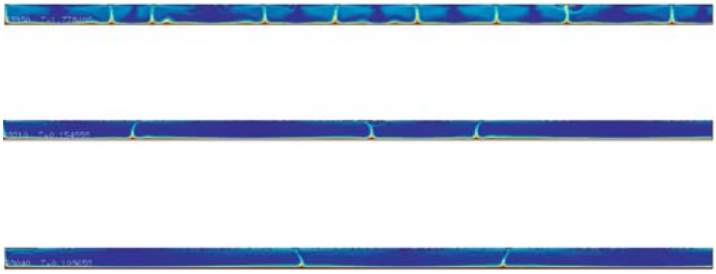

Figure 2. Temperature fields from two-dimensional Boussinesq convection with temperature- and depth-dependent viscosity. A constant thermal coefficient of expansion and constant thermal conductivity are used. Number of grid points used are 128 in the vertical direction and 2048 along the horizontal axis. An aspect-ratio of 36 is taken. We note that the index n in eqn. (5) goes from 2 to 5 to 10 for the three panels.

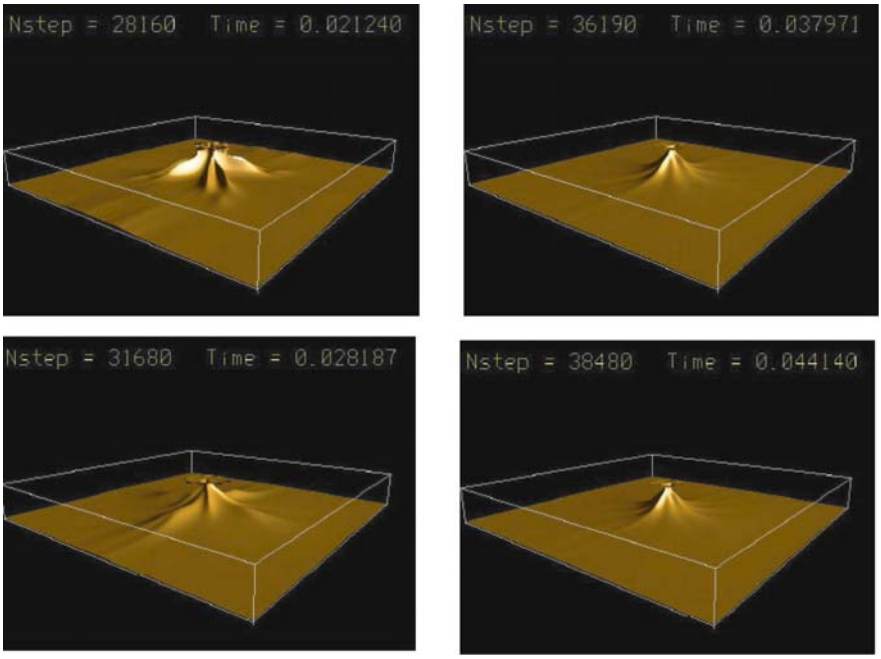

Figure 3. Isosurfaces of the temperature field of 3-D convection at four different times. The isosurface corresponds to T = 0.7, or about 2500 K. A time of 0.01 is around half the age of the Earth. The depth dependence of the viscosity has the form z^5 and the surface Rayleigh number is 10^7. The thermal coefficient of expansion decreases by 1/3 across the mantle in this Boussinesq model with an aspect-ratio of $4 \times 4 \times 1$. The number of grid points is 64 in the vertical and 128×128 on the horizontal plane.

which is a well-known result (Gurnis and Davies, 1986; Hansen et al., 1993). This example reveals that the particular style of plume dynamics and plume population can yield salient information about mantle viscosity stratification.

In plume dynamics it is important to verify the initial 2-D findings in 3-D geometry. Yuen et al., (1996) have already investigated the 3-D dynamical influence arising from

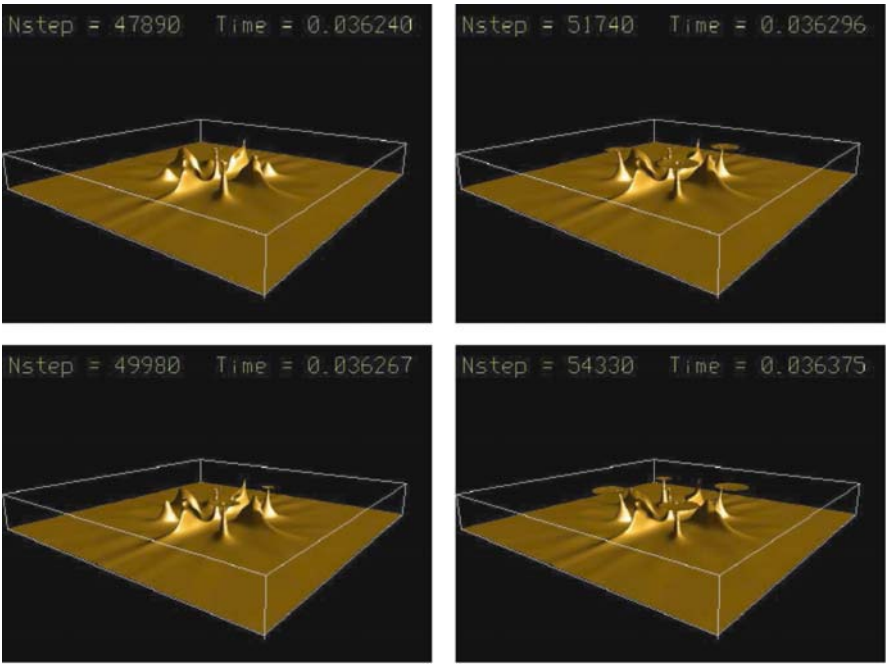

Figure 4. Isosurfaces of the temperature field of 3-D convection with temperature- and depth-dependent viscosity. The depth-dependence of viscosity is the same as in the previous figure but the temperature-dependence is given by exp(−100T). The composite viscosity is a product between the depth-dependent viscosity and the temperature-dependent portion. Otherwise, the rest of the information is the same as in Figure 3.

a viscosity profile, given analytically by a form with a dependence of a polynomial in z modulated by a Gaussian function whose center controls the location of the viscosity hill in the lower mantle. They found in a 3-D box with an aspect-ratio $6 \times 6 \times 1$ that there persisted one single very large plume for around fifty million years. In Figure 3 we verified this earlier result by integrating the solution much longer in time than previously. We note that there is a long evolution of this plume to the final equilibrium configuration shown in the bottom right panel.

It is well-known that temperature-dependent viscosity destabilizes the bottom boundary layer (Yuen and Peltier, 1980) and causes small-scale finite-amplitude instabilities (Christensen, 1984). In Figure 4 we show the long-time development of 3-D convection with the same depth-dependence in viscosity used in Figure 3 but now modulated with a temperature-dependent viscosity of the form exp(−100T).

As expected, we observe the development of small-scale instabilities with a tendency to cluster about a central location, as in a thermal attractor, a consequence

from plume-plume collisions (Vincent and Yuen, 1988). These plumes would march inward and then migrate outward again in a quasi-periodic fashion. Clustering of small-scale plumes in the deep mantle has been invoked by Schubert et al., (2004) as an alternative explanation for superplume province under the central Pacific on the basis of tomographic imaging. We are quite heartened by the recent result by Yoshida and Kageyama (2006), who also demonstrated quite convincingly that for 3-D spherical convection the combination of temperature- and depth-dependent viscosity also preserves the same long-wavelength circulation found here in Cartesian geometry with a similar type of hybrid temperature- and depth-dependent rheology.

3.2 3-D Anelastic compressible spherical-shell model

As in Monnereau and Yuen (2002), we have employed the PREM model (Dziewonski and Anderson, 1981) for the reference density profile and the bulk modulus, which is needed for handling the compressibility of mantle material in long term deformation. The depth-profiles for the density, bulk modulus and the thermal expansivity are exponential functions that fit PREM and are shown in Monnereau and Yuen (2002). The thermal expansivity α is obtained by assuming a constant value of the Grueneisen parameter of unity and a usual value of the specific heat at constant pressure of 1200 J kg^{-1} K^{-1}. The thermal expansivity decreases across the lower mantle by a factor of 2. It decreases a factor of 4 across the mantle. We have not considered the effects of variable thermal conductivity with temperature and pressure (Dubuffet et al., 1999).

The mantle convection models studied here are both heated below, and also internally heated by radiogenic elements, which do not decay with time. There are two Rayleigh numbers, the basal heating Rayleigh number Ra and the internal-heating Rayleigh number, Ra_i. The internal heating has been set to a common value of 25 TW of contributed surface heat released, which corresponds to about 1.5 times the chondritic heating contribution. In Monnereau and Yuen (2002) the internal heating was varied between 0 and 60 TW.

It is well known from past work (e.g., Zhang and Yuen, 1995) that plume dynamics in 3-D spherical convection in basally heated configuration are very much affected by the depth variations of mantle viscosity. The effects of including internal heating, mantle compressibility and viscosity stratification on enhancing the vigor of plume growth have been shown by Zhang and Yuen (1996) and also by Bunge et al. (1996). We have employed eight different viscosity profiles for the purpose of understanding the influence of the deep mantle viscosity stratification on the style of plumes. We have considered profiles ranging from constant viscosity to classical two-layered viscosity models (e.g., Ricard et al., 1984), and extending to more complex viscosity profiles inferred from both geoid anomalies and post-glacial rebound analysis (Mitrovica and Forte, 2004). Walzer et al. (2004) have studied the influence of a family of depth-dependent viscosity profiles in 3-D anelastic compressible convection but did not focus on the development of thick upwellings in the lower mantle.

We have parameterized the viscosity models with a series of layers instead of using analytic functions for describing the sharp variations of the viscosity peaking the mid lower-mantle, as in Zhang and Yuen (1996) or in Yuen et al. (1996). The first five models have been designed to highlight the basic effects of a viscosity hill in the lower mantle. Model 1 is a constant viscosity model. Model 2 is one introduced by Ricard et al. (1984) and Hager and Richards (1989) and has a viscosity increase of 30 across the 660 km phase change. Model 3 is Model 2 including a low viscosity zone (LVZ) of 200 km thick above the CMB. Model 4 and 5 are similar to Model 2 and 3 respectively, but with a viscosity contrast of 300 instead of 30. The three following models have a more complex viscosity structure, taken from recent geoid/postglacial rebound/tomographic analysis. Model 6 (FM) comes from Forte and Mitrovica (2001) in which there are tow prominent viscosity peaks in the lower mantle at a depth of around 900 km and 1800 km. Model 7 (RW) is the viscosity model derived by Ricard and Wuming (1991). The last viscosity model (MF) derives from the recent viscosity profile (Mitrovica and Forte, 2004) based on both geoid anomalies and glacial isostatic readjustment. These viscosity profiles are shown below in Figure 5.

Figure 6 presents the thermal anomaly fields of 3-D spherical convection, i.e., the deviation from the horizontally averaged temperature, of the first 5 cases of the viscosity profiles displayed in Figure 5.

- Case 1: in this constant viscosity case, mantle convection is dominated by downwellings, which is expected with a strong internal heating (77%). The downwellings exhibit a linear shape at the surface, and adopt a cylindrical structure below triple junctions. Only these cylindrical downwellings cross the phase change at 660 km discontinuity. These features fluctuate and do not remain at one place. The hot plumes are less vigorous and remain restricted to the lower mantle.
- Case 2: with the introduction of a stepwise viscosity increase of 30 across the 660 km phase boundary, three large plumes develop and now drive the circulation. Shorter scales than in the previous case feature the downwellings. Their structure remains perceptible in the lower mantle, indicating a decrease of the strength of the phase change barrier. These structures are very close to the one described by Dubuffet et al. (2000) in 3-D Cartesian with the same kind of viscosity profile and 80% of internal heating. Here, it amounts 73% of the total heat flux. It is worth noting that large plumes can develop with intense internal heating and are not only the consequence of pure basal heating. The viscosity increase with depth is well known to cause a cascade to longer wavelengths in the thermal spectrum, but it is much less known to promote large stable hot plumes even when internal heating is dominant. This could be understood, if we point out that another major effect of the viscosity increase with depth is to reduce the ambient temperature and thus to enhance the temperature contrast across the bottom thermal boundary layer. This naturally results from the disequilibrium between the top and the bottom boundary layers introduced by the viscosity contrast. As a matter of fact, the averaged temperature is here 500 K lower than in the previous constant viscosity case for a temperature contrast twice larger.

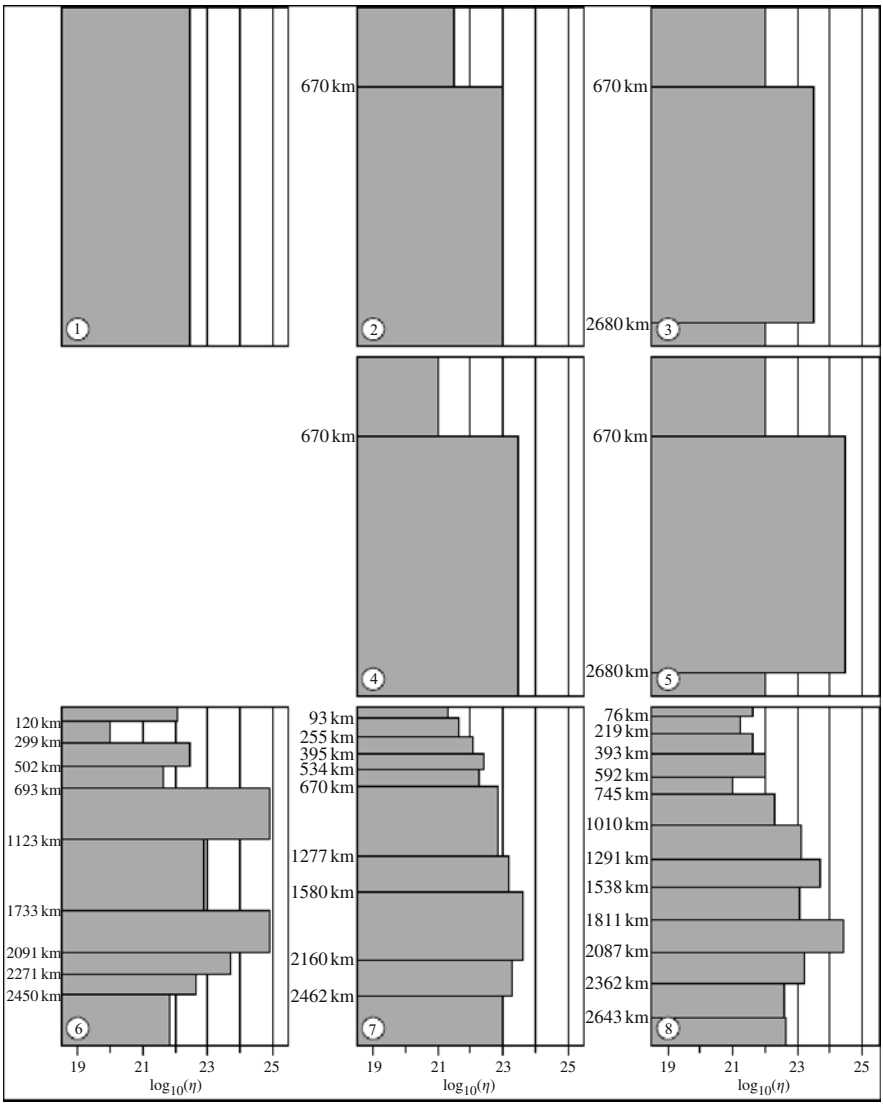

Figure 5. Viscosity profiles used in the 3-D spherical-shell convection model. The first five will be used in Figure 6 and the last three in Figure 7.

- Case 3: we add a 200 km thick low viscosity zone at the CMB, which can be expected, as the viscosity strongly depends on temperature. The viscosities at the CMB and in the upper mantle are the same; so that the disequilibrium between boundary layers previously invoked is strongly reduced, but not entirely because

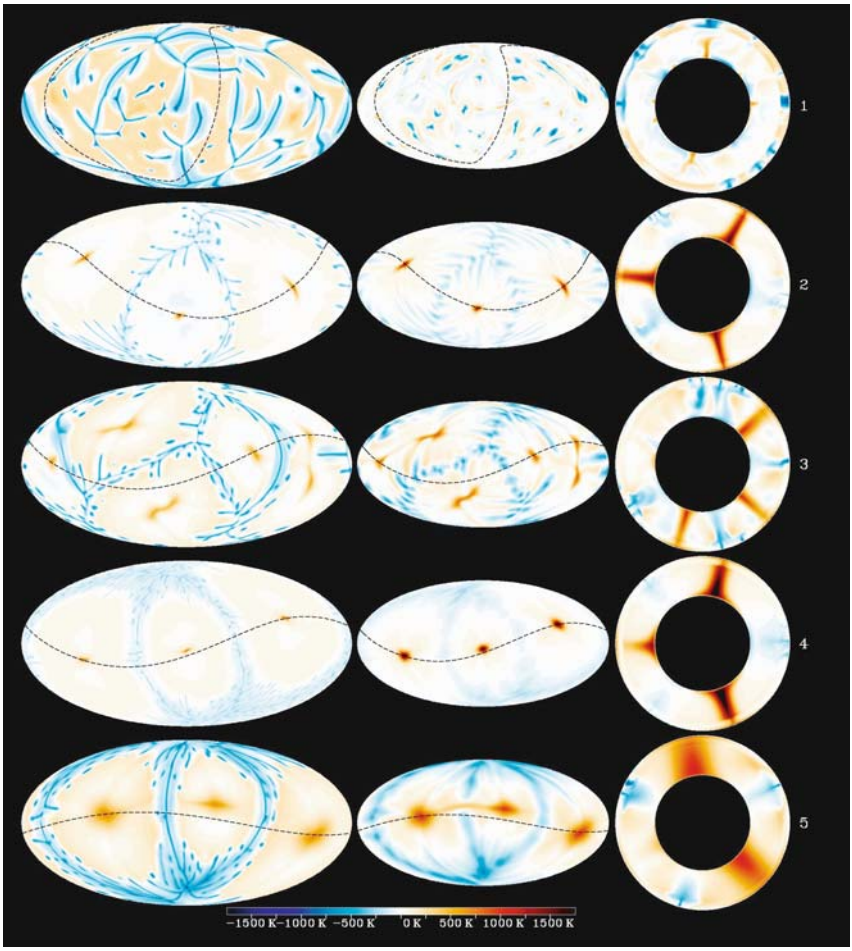

Figure 6. Thermal anomalies of 3-D convection in spherical shell. The horizontal cross-sections associated with the left column are taken at a depth of 500 km, the images of the central column comes from a depth of 1500 km in the mid lower-mantle and the right column contains a global vertical cross section of the entire mantle, whose great circle path is shown in both the upper- and lower-mantle horizontal projections in the left and central columns respectively. Blue color indicates cold downwellings, while the brown color represents hot upwellings. The temperature of the CMB is 3200 K.

of the spherical geometry that produces a similar effect (e.g., Jarvis, 1993). From this point of view, case 1 and 3 may appear analogous. In spite of this similarity, six large plumes develop and the cold structures at the surface keep the features exhibited in case 2. It seems that the high viscosity region in the middle of the mantle plays the role of low-pass filter for the dynamics. This will be highlighted by comparing the two following cases, 4 and 5, where the viscosity profiles exhibit

the same features as in cases 2 and 3 respectively, except in the amplitude of the viscosity contrast.

- Case 4: the viscosity contrast has been raised up to 300. The dynamics develops a structure very similar to case 2, but with shorter wavelength cold currents at the surface. This probably results from the choice of a lower value for the reference viscosity, made in order to keep comparable heat fluxes from one case to another. The main difference is that the hot plumes are now roughly twice thicker than in case 2. We can discern the strong narrowing of these plumes upon crossing the viscosity jump.
- Case 5: in contrast to case 3, the addition of the low viscosity zone at the CMB, does not change the number of plumes. Furthermore, their broad shape is reinforced. They appear like thick vertical cylinders standing atop the CMB.

A viscosity increase with depth is now well known to promote large plumes with long-wavelength circulation in the lower mantle (Hansen et al., 1993), notably through the disequilibrium between boundary layers it introduces. However, if a general depth dependence of the mantle viscosity is expected, the large temperature of the bottom boundary layer should reduce the viscosity and attenuate this effect. We see here that the viscosity stratification effect acts more than a perturbation to the boundary layers and that the presence of a viscosity hill in the middle of the mantle plays the important role of a low pass filter, preventing the onset of short wavelength instabilities at the expense of very broad structures.

Figure 7 displays the temperature anomaly fields of the three remaining cases that correspond to more complex viscosity profiles. At first sight, the expression of mantle convection strongly differs from one case to the other, except in the fact that hot plumes are well established in the lower mantle. There is only one in the case 6, three in case 7, and two in the last case that are distributed along a hot line drawing a great circle at the core surface. The single plume mode that characterizes case 6 has only been found under peculiar conditions: with a small core radius to mantle thickness ratio (Schubert et al., 1990, Moser et al., 1997), or with an endothermic phase change slightly above the CMB (Breuer et al., 1998; Harder and Christensen, 1996). Both situations have been invoked to account for the formation of the Tharsis highlands. These conditions act also in previously described ways: either as a strong imbalance between the local Rayleigh number of boundary layers for the former, or as a low pass filter for the latter. In case 6, the second effect should prevail, enhanced by the presence in the viscosity profile of two maxima peaking three orders of magnitude above the values at the top and the bottom. It is worth noting that, in this case, both upwellings and downwellings are filtered in the same way: the single hot plume being associated with a single cold plume.

More than just the dominance of large hot plumes in the lower mantle, the striking feature rising from the comparison of cases 6, 7 and 8, is the remarkable sensitivity of the upper mantle dynamics to the viscosity profile structure. In case 6, both the hot and cold plumes can cross the whole mantle. The thermal field does not reveal any layering of the dynamics that would be associated with the endothermic phase

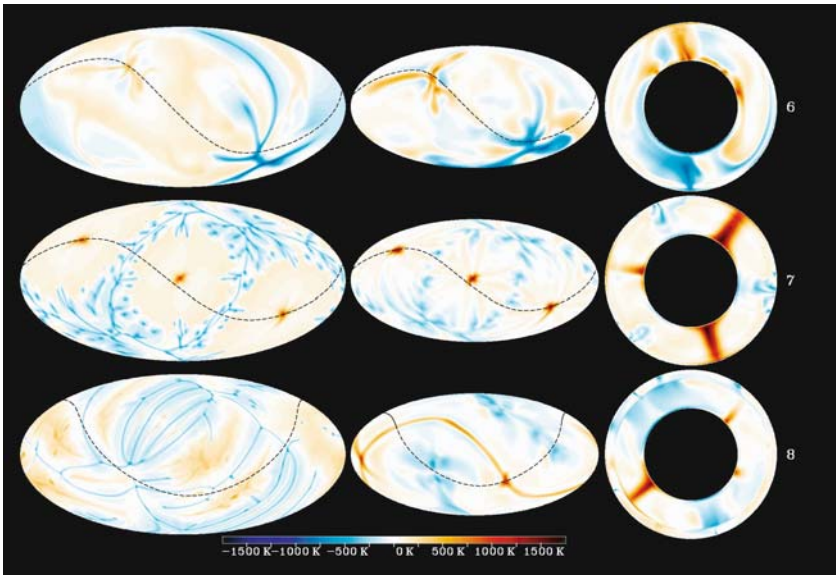

Figure 7. Temperature anomalies of the last three viscosity cases shown in Figure 5. Otherwise, the same information is provided as in Figure 6.

change. In case 7, there is no longer any stratification, but the downwelling structure is quite different from the upwelling one. The asymmetry is close to the one observed in cases 2–5, what would be expected since the viscosity profile proposed by Ricard and Wuming (1991) is also close to the schematic ones introduced in cases 2–5. Case 8 reveals a completely different situation. Here, mantle convection splits into two parts. This is an expected and well-known effect of the endothermic phase change (e.g., Christensen and Yuen, 1985), but that does not necessarily occur, particularly when mantle properties are depth-dependent (Bunge et al., 1996; Monnereau and Rabinowicz, 1996). As a matter of fact, no layering is observed in the previous cases when the viscosity increases with depth. Furthermore, the decoupling, that takes place here, does not behave as the famous intermittent layering highlighted first by Machetel and Weber (1991), where a recurrent rupture of the quite impermeable barrier induced by the phase change precipitates an intense and rapid mass exchange between the upper and lower mantle. Such catastrophic events are more related to the 2-D approximation of numerical experiments, where they have only been observed. Conversely, the mass flux across the phase change is here roughly constant with time, but varies strongly from place to place; the layering is not discontinuous in time but in space. For instance, the surface expression of the huge plumes established in the lower mantle is not a single hot spot as in case 7, but a cluster of small plumes that develop in the area where the lower mantle plume impinges the phase change. It is also worth noting the presence of rolls between two clusters of plumes, oriented perpendicularly

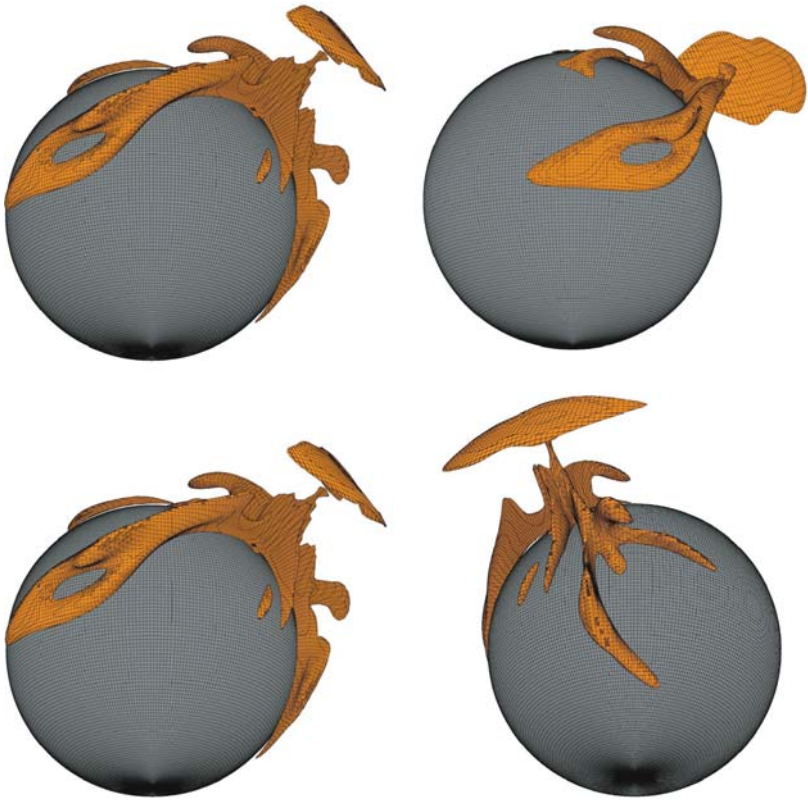

Figure 8. Isosurfaces of hot temperature showing the single plume with a very long ridge-like feature similar to the Great Chinese Wall. The isosurface corresponds to T = 0.7, or about 2700 K.

to the underneath hot line. Such a decoupling between the upper and lower mantle, searched for a long time, mainly results from a low viscosity zone located under the phase change. The role of such a low viscosity zone has been discovered by Kido and Cadek (1997) and well described in a dynamical sense by Cserepes and Yuen (1997). We see in the upper-mantle of case 8 the presence of Richter rolls (Richter and Parsons, 1975) in the left-most panel. These secondary cellular motions are caused by the low-viscosity zone underneath the transition zone. In Figure 8 we take a more detailed look at the ridge-like structures developed in case 8, in which a single plume is found (see Fig. 7).

One striking character of these isosurfaces is that these thermal convective results in spherical geometry appear very similar to ridge-like features obtained in thermal-chemical convection in 3-D Cartesian geometry (e.g., Tackley, 2002). They are similar to the lower-mantle mountain-like feature, reminiscent of the Great Wall of China, which was inferred by Ni and Helmberger (2003), using forward-modelling techniques. See also article by Maruyama et al., in this issue. The factor which

may produce this distinct signature is the steep viscosity stratification in the deep mantle, imposed by the viscosity profile 8, shown in Figure 5. Thus there is a trade-off between thermal-chemical convection and the depth-dependence of viscosity in the production of sharp ridge-like features in lower mantle thermal convection. In laboratory experiments only thermal-chemical aspects can be investigated, while numerical simulations are able to shed light in fluid dynamical situations with depth-dependent properties. The different factors determining the ridge-like features need to be studied in 3-D spherical geometry. Here the influence of the post-perovskite phase transition should also be accounted for, as well as chemical heterogeneities and equations of state of deep mantle components (Tan and Gurnis, 2005). We note that the recent calculations by Yoshida and Kageyama (2006) in 3-D spherical shell show quite convincingly that strong temperature-dependent viscosity cannot override the long-wavelength circulation enforced by depth-dependent viscosity in the lower mantle.

3.3 2-D Extended-Boussinesq Cartesian model with variable viscosity and phase transitions

Up to now, we have not included the effects of phase transitions in both the upper- and lower-mantle, which can surely influence the development of superplumes. The two phase transitions considered are the endothermic spinel to perovskite transition separating the upper- and lower-mantle and the exothermic post-perovskite transition (Murakami et al., 2004; Oganov and Ono, 2004; Tsuchiya et al., 2004) in the deep mantle. The phase transitions have been implemented by using the formulation of an effective thermal expansivity (Christensen and Yuen, 1985). The density changes of the two phase transitions are respectively 8 and 1.5% and the Clapeyron slopes are -3 MPa/K and $+9$ MPa/K. Besides the phase transitions, we will also incorporate a depth-dependent thermal expansivity, which drops by a factor of 2 in the upper mantle but decreases sharply in the shallow portion of the lower mantle right below the transition zone (Katsura et al., 2005) with a total drop of a factor of around 11 across the lower mantle, because of the large value of the Anderson-Grüneisen parameter for perovskite in the shallow part of the lower-mantle (Katsura et al., 2005; R. M. Wentzcovitch, private communication, 2006). We employ a temperature- and depth-dependent viscosity, where the depth-dependent portion is prescribed by a product between a linear function in z and a Gaussian in z which peaks in the middle of the lower mantle and a temperature-dependent portion, which varies exponentially in T. The viscosity hill in the lower mantle at a depth of around 1700 km is about a factor of 150 greater than the viscosity in the upper mantle, while the variations of the temperature-dependent viscosity are around 1000. The full formulation of the viscosity law can be found in Matyska and Yuen (2006).

We have also employed a radiative thermal conductivity $k(\mathrm{T})$ of the canonical form:

$$k(\mathrm{T}) = f \cdot (\mathrm{T} + \mathrm{T}_0)^3 , \tag{6}$$

where f is an enhancement factor, here taken to be 10, and T_0 is the surface temperature, here $T_0 = 0.08$. We have considered three kinds of conductivity model (1) constant thermal conductivity in the entire mantle (2) radiative thermal conductivity just in the D″ layer and constant thermal conductivity in the rest of the mantle (3) radiative thermal conductivity in the entire mantle. We will consider these three cases for thermal conductivity in this section, while all the other thermodynamical and rheological parameters remain the same.

Relatively large aspect-ratio cells are developed but with large asymmetries in the behavior, primarily due to the hotter interior of the right cell. The style of plume dynamics is very much different in the two regions. In the left cell we observe many traveling-wave instabilities, while a large cluster of upwellings is developed in the right cell. Secondary upwellings (see also Yoshida and Ogawa, 2004) are emerging from the spinel to perovskite transition in both right and left cells. The bottom boundary layer is highly unstable due to the exothermic post-perovskite phase transition (Nakagawa and Tackley, 2004a; Matyska and Yuen, 2005).

Next we show the case in which the thermal conductivity is constant everywhere except for a thin post-perovskite layer, in which the thermal conductivity is now radiative.

Comparing Figures 9 and 10, we see the dramatic difference in convection caused by just a thin layer of radiative thermal conductivity. The imposition of a thin radiative layer exerts unexpectedly a substantial influence on the style of mantle convection, because of the ability of radiative transfer to bring up very efficiently an enormous amount of heat from the hot outer core at a temperature of 3880 K. The upwellings developed are very broad in character and heats up the lower mantle. There is a pool of super-heated material (blue color) lodged right under the transition zone in the right cell.

We compare the previous case with a model in which radiative thermal conductivity is prevalent throughout the entire mantle (Fig. 11).

The global presence of radiative thermal conductivity induces thinner upwellings in both cells, because of the better developed bottom boundary layer and stronger thermal buoyancy inside the plumes, which lead to higher velocities and greater contrast between the thinner superplume and the adjacent lower mantle. Moreover, there is a greater mass flux of lower-mantle material penetrating the 670 km discontinuity, which produces bigger upper-mantle plumes. We observe plumes branching off the transition zone, as rendered artistically earlier by Maruyama (1994). Thus the spatial distribution of radiative thermal conductivity can significantly affect the style of superplumes. This has a similar effect, as the spatial distribution of mantle viscosity. The main purpose of this sub-section is to emphasize the importance of variable thermal conductivity on modulating upwellings in the lower mantle. Thermal conductivity can also be enhanced in the D″ layer for other reasons than radiative transfer. For instance, some infiltration of Fe melt (Petford et al., 2005; Kanda and Stevenson, 2006) can also greatly increase the local thermal conductivity of the D″ layer (Manga and Jeanloz, 1996) and also the putative presence of FeS can also increase the local thermal conductivity (Hofmeister and Criss, 2005).

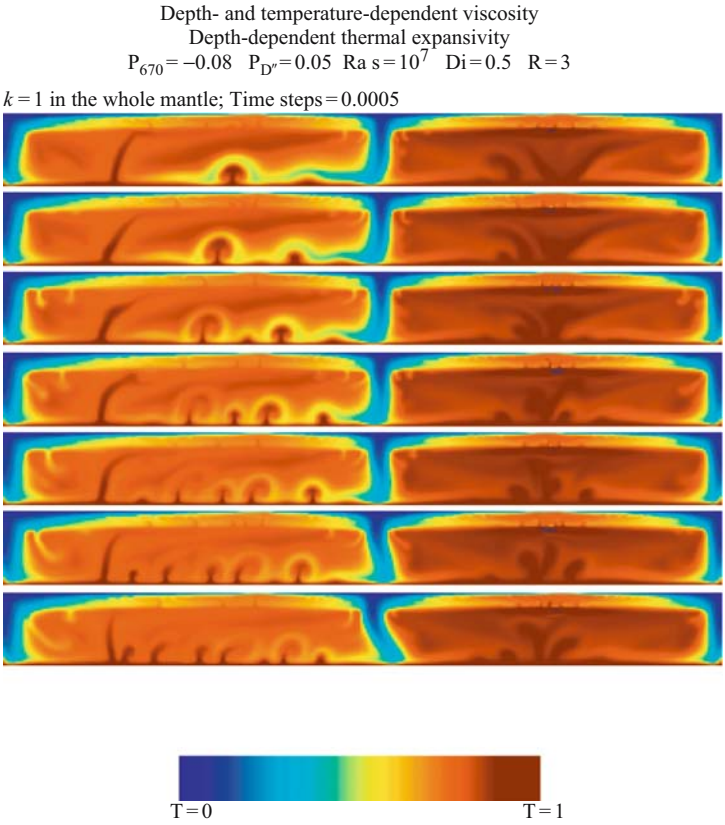

Figure 9. Temperature fields of 2-D extended-Boussinesq convection with constant thermal conductivity, temperature- and depth-dependent viscosity, depth-dependent thermal expansivity, two phase transitions in the upper- and lower- mantle. An aspect-ratio 10 has been assumed. The surface dissipation number is 0.5 and the surface Rayleigh number is 10^7. There is a small amount of internal heating, about 25% of the chondritic value with R = 3. We have used a periodic color scale, i.e., dark blue region below the 660 km boundary shows the places, where the dimensionless temperatures are slightly greater than 1, i.e., greater than the temperature at the core-mantle boundary!

3.4 Three-dimensional extended-Boussinesq convection in Cartesian geometry with variable properties and phase transitions

Now we turn our attention to the 3-D effects in Cartesian geometry in a box having an aspect-ratio of $6 \times 6 \times 1$. We use variable properties in thermal conductivity, viscosity and depth-dependent thermal expansivity along with the two major phase transitions in the upper- and lower-mantles. This particular numerical model, which employs the primitive variable formulation (velocity, pressure and temperature), has already been described in great technical details in Kameyama et al. (2005) and Kameyama

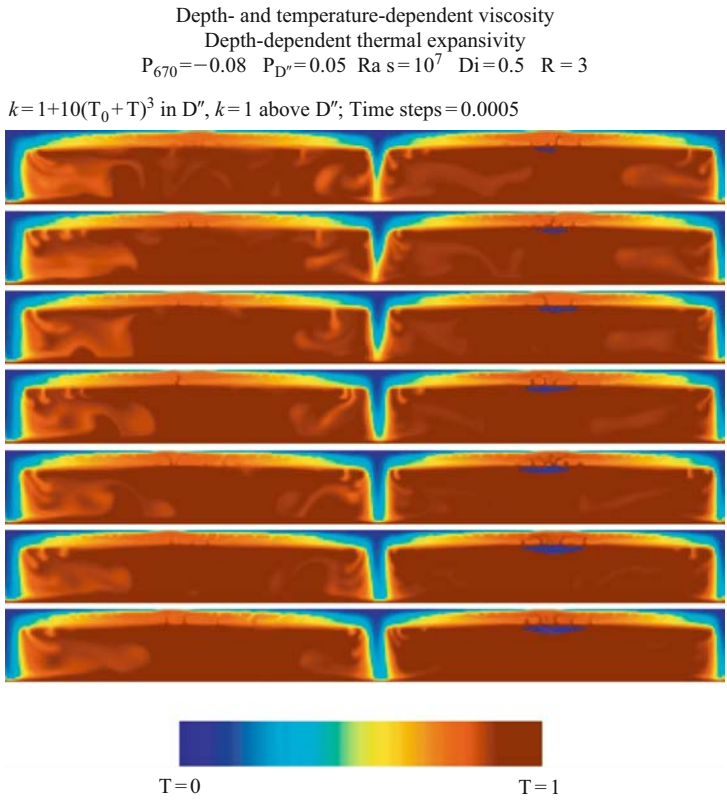

Figure 10. Two-dimensional temperature field from extended-Boussinesq convection with a thin layer (180 km) of radiative thermal conductivity at the bottom. Other parameters are the same as in Figure 9. We have used a periodic color scale, i.e., dark blue region below the 660 km boundary shows the places, where the dimensionless temperatures are slightly greater than 1, i.e., greater than the temperature at the core-mantle boundary!

(2005). The relationship for temperature- and depth-dependent viscosity is similar to the one employed by Matyska and Yuen (2006). This means that the viscosity variation is about a factor of 100 for temperature and 155 for the depth. We have used a temperature-dependent thermal conductivity of the radiative type, very similar to the form given in Matyska and Yuen (2006). The thermal coefficient of expansion is of the same form given in Matyska and Yuen (2005) and decreases by a factor of 8/27 across the mantle. There is a small amount of internal heating with a strength, which is one quarter that of chondritic abundance. The temperature of the CMB is taken to be 3888 K.

For describing the dynamics of the phase transitions, we have employed the formulation of an effective thermal coefficient of expansion (Christensen and Yuen, 1985).

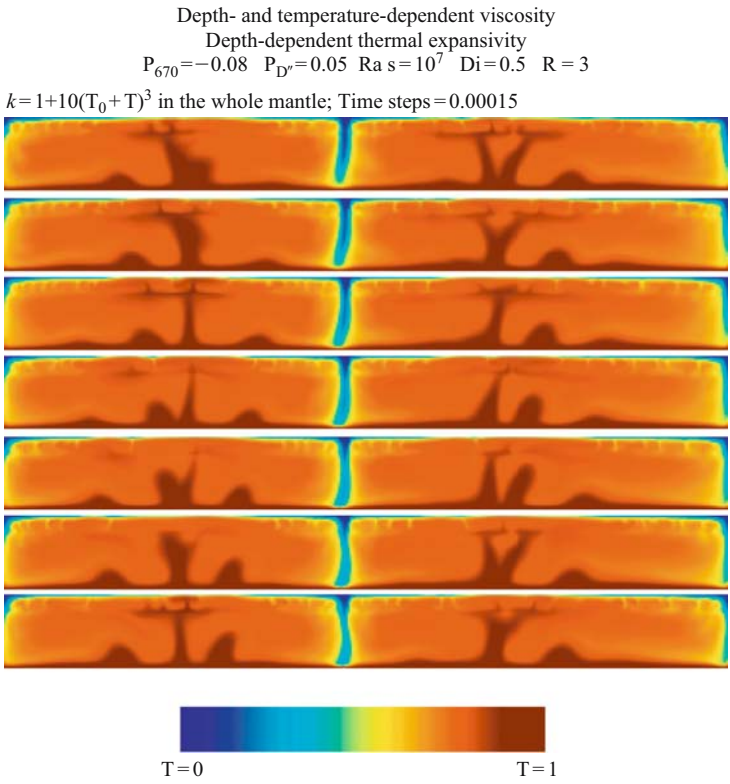

Figure 11. Two-dimensional temperature field from extended-Boussinesq convection with radiative thermal conductivity present throughout the mantle. Other parameters are the same as in Figure 9.

The computational domain consists of 256 × 256 × 64 grid points based on a finite-volume scheme (Kameyama, 2005). This run required over 200,000 time-steps and was carried out on the Earth Simulator computer.

In Figure 12 we show four snapshots of the isosurface of hot upwellings with T = 0.7, covering an interval of time of around 2 Byrs.

The upwellings are unlike the classical type of plumes one would find in laboratory thermal convection or numerical simulations with a simple temperature-dependent rheology (Whitehead and Parsons, 1976; Jellinek et al., 1999; Zhong et al., 2000) and instead they appear closer to those found in thermal-chemical convection (Davaille et al., 2005). These upwellings are characterized by ridge-like structures, similar to the results found in Figure 8 for depth-dependent viscosity in 3-D spherical geometry. The structures develop a dynamical time-dependent pattern, characteristic of being in the thermal-attractor regime (Vincent and Yuen, 1988), with the plumes first marching toward the center and then moving back out. Such a scenario can be likened

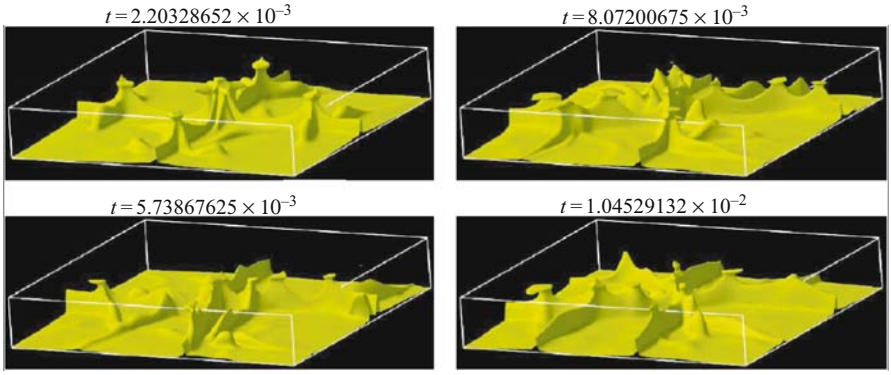

Figure 12. Snapshots of isosurfaces of hot temperature fields in convection with variable properties and two major phase transitions. The temperature of the isosurface corresponds to 2717 K. A dimensionless time of 0.001 represents around 288 Myrs.

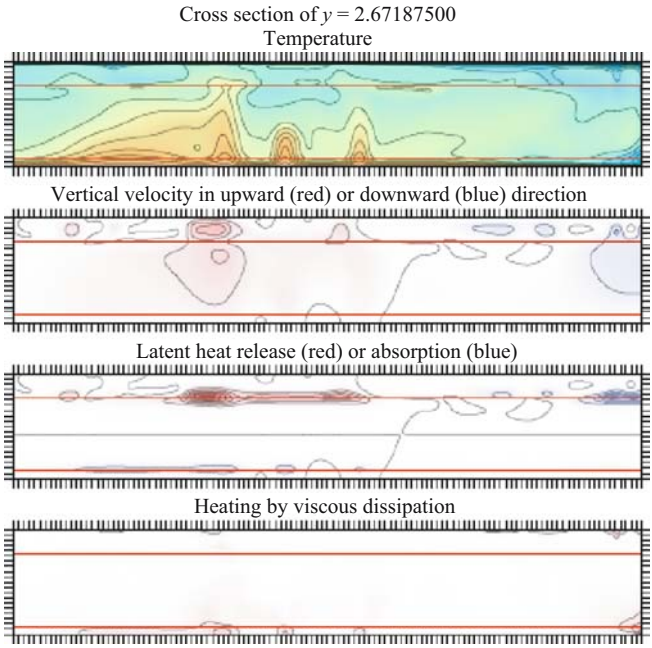

Figure 13. Two-dimensional cross-sections of the temperature, vertical velocity, latent-heat released and viscous dissipation. These fields are taken from the 3-D fields associated with the last time instant in Figure 12. The vertical velocity, latent-heat released and viscous dissipation have been normalized respectively to 57500, 9090 and 155, the maxima of these fields, given in dimensionless units. This is a vertical cross section taken at the horizontal coordinate $y = 2.67$.

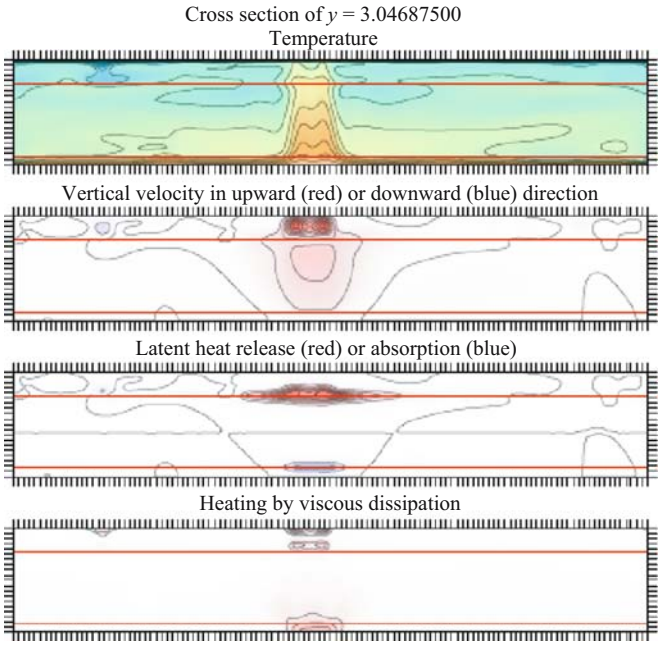

Figure 14. Two-dimensional map of the temperature, vertical velocity, latent-heat budget and viscous dissipation. This is a vertical cross-section taken at $y = 3.05$. Otherwise, the rest is the same as in Figure 13.

to the plume cluster model, as envisioned in Schubert et al. (2004). The proximity of the post-perovskite phase transition to the core-mantle boundary strongly promotes the growth of boundary-layer instabilities with a rich spectral content. The developed upwellings are then moderated by the radiative thermal conductivity (Matyska and Yuen, 2005). Clearly more work is needed in understanding the growth of plume-like structures under these complex physical conditions in the deep mantle.

From the last time instant, we take three 2-D cross-sections in order to understand better the thermo-mechanical structures associated with this type of 3-D thermal convection. These cross sections are taken very close to the intersection of the two ridges near the center of the box (Figs. 13 and 14).

In this perspective we can see from the vertical velocity contours that layered convection prevails with small rolls in the upper mantle. There is a broad-scale upwelling with several small-scale instabilities at the bottom. There is some small-scale shear-heating in the D″ layer and a large-amount of latent-heat released at the base of the transition zone (Steinbach and Yuen, 1994). The fastest plumes are found in the upper mantle.

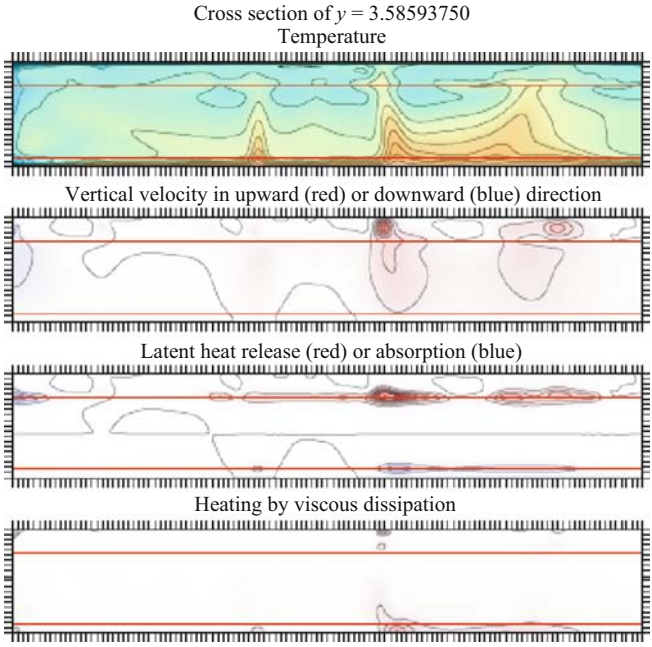

Figure 15. Two-dimensional map of the temperature, vertical velocity, latent-heat budget and viscous heating. This is a vertical cross-section taken at $y = 3.59$. Otherwise, the rest is the same as in Figure 13.

Close to the interaction of the two ridges, we can observe a relatively broad upwelling having a width exceeding 800 km. There is a fast upwelling in the upper mantle associated with this thick root. Large amounts of latent heat released takes place in the transition zone. There is also some shear heating developed in this upwelling. The nature of layered convection with multiple-scales in the flow field is clearly displayed by the vertical velocity field.

The last cross section (Fig. 15) shows again the multi-scale nature of this type of thermal convection with partial layering. There is a large asymmetry in the velocities of the flow field between the upper and lower mantle. We see that small-scale convection takes place in the upper-mantle above the rising superplume in the lower mantle. This shows the need to incorporate as many physical mechanisms as possible in order to account for the diversity of scales in mantle plume dynamics (e.g., Courtillot et al., 2003; Yoshida and Ogawa, 2004).

4 CONCLUSION

In this chapter we have gone over the primary mechanisms in the generation of lower-mantle plumes by thermal convection. We have identified several key ingredients, which will promote the development of superplumes. They include (1) the style of

viscosity increase in the lower mantle, especially that due to the viscosity maximum in the lower mantle at a depth of around 1800 km (e.g., Forte and Mitrovica, 2001) (2) the decrease in the coefficient of thermal expansion (3) the increase of thermal conductivity from radiative contribution in the deep portion of the lower mantle. We may also consider other potential contribution, such as the influence from grain-size dependent rheology (Korenaga, 2005), which has been suggested as a possible mechanism for generating superplumes in the D″ layer, but this hypothesis remains to be verified by either a decisive laboratory experiment or accurate numerical simulations.

The nature of the thermal boundary layer near the CMB would change with time because of the onset of the post-perovskite phase transition in the hot deep mantle with a cooling core, as first suggested by Oganov and Ono (2004). The exothermic phase transition would alter the nature of upward heat transfer by the growth of superplumes, because of the presence of either radiative thermal conductivity and/or grain-size changes from the post-perovskite phase transition. Thus superplumes can transport a great deal of heat from the CMB into the upper mantle, much more than traditional models without the post-perovskite phase transition (e.g., Mittelstädt and Tackley, 2006).

Finally, we should explore next the alternative route of superplumes having a predominant thermal-chemical origin. Up to now, all of thermal-chemical models (e.g., Mc Namara and Zhong, 2004; Nakagawa and Tackley, 2005) have employed simple models in lower-mantle rheology, thermal expansivity, compositional stratification and thermal conductivity. In the future it is necessary to incorporate more realistic multicomponent equations of state (Tan and Gurnis, 2005) and phase diagrams in both the upper- and lower mantles e.g., the majorite transition at high temperatures by Hirose (2002) in order to make a better assessment as to the relative efficacy in producing superplume structures between the thermal and thermal-chemical end-members in a compressible mantle convection.

ACKNOWLEDGEMENTS

We thank stimulating discussions with Cesar da Silva, Renata Wentzcovitch, Anne Hofmeister, and Shigenori Maruyama, which have improved greatly this manuscript. We are grateful to Marina and Katya Shukh and Ying-chun Liu for their skillful help in preparing this chapter. This research has been supported by the Math-Geo, CSEDI and ITR programs of the U.S. National Science Foundation (DAY), the Stagnant Slab Project, Scientific Research in Priority Areas of Ministry of Education, Culture, Sports and Technology of Japan (MK), the Deutsche Forschungs Gemeinschaft (UH), and the Czech Science Foundation grant 205/03/0778 (CM). The calculations presented in this paper were carried out in Earth Simulator at Japan Agency for Marine–Earth Science and Technology, French CNES, Minnesota Supercomputer Institute, Prague and Univ. of Münster in Germany.

REFERENCES

Anderson, O.L. (1995) Equations of State of Solids for Geophysics and Ceramic Science, 405pp, Cambridge Univ. Press.

Badro, J., G. Fiquet, F. Guyot, J.-P. Rueff, V.V. Struzhkin, G. Vanko, and G. Monaco (2003) Iron partitioning in Earth's mantle: Toward a deep lower mantle discontinuity. *Science*, 300, 789–791.

Breuer, D., D.A. Yuen, T. Spohn, and S. Zhang (1998) Three-dimensional models of Martian convection with phase transitions. *Geophys. Res. Lett.*, 25(3), 229–232.

Bunge, H.-P., M.A. Richards, and J.R. Baumgardner (1996) Effect of depth-dependent viscosity on the planform of mantle convection. *Nature*, 379, 436–438.

Chopelas, A., and R. Boehler (1992) Thermal expansivity of the lower mantle. *Geophys. Res. Lett.*, 19, 1983–1986.

Christensen, U.R. (1984) Instability of a hot boundary layer and initiation of thermo-chemical plumes. *Annal. Geophys.*, 2, 311–320.

Christensen, U.R., and D.A. Yuen (1985) Layered convection induced by phase transitions. *J. Geophys. Res.*, 90, 10291–10300.

Courtillot, V., A. Davaille, J. Besse, and J. Stock (2003) Three distinct types of hotspots in the Earth's mantle. *Earth and Planet Sci. Lett.*, 205, 295–308.

Cserepes, L., and D.A. Yuen (1997) Dynamical consequences of mid-mantle viscosity stratification on mantle flows with an endothermic phase transition. *Geophys. Res. Lett.*, 24, 181–184.

Davaille, A. (1999) Simultaneous generation of hotspots and superswells by convection in a heterogeneous planetary mantle. *Nature*, 402, 756–760.

Davaille, A., E. Stutzmann, G. Silveira, J. Besse, and V. Courtillot (2005) Convective patterns under the Indo-Atlantic. *Earth Planet. Sci. Lett.*, 239, 233–252.

Davies, J.H. (2005) Steady plumes produced by downwellings in Earth-like vigor spherical whole mantle convection models. *Geochem. Geophys. Geosys.*, 6(12), Q12001, doi:10.1029/2005GC001042.

Dubuffet, F., D.A. Yuen, and M. Rabinowicz (1999) Effects of a realistic mantle thermal conductivity on the patterns of 3-D convection. *Earth Planet. Sci. Lett.*, 171, 401–409.

Dubuffet, F., and D.A. Yuen (2000) A thick pipe-like heat-transfer mechanism in the mantle: Nonlinear coupling between 3-D convection and variable thermal conductivity. *Geophys. Res. Lett.*, 27(1), 17–20.

Dubuffet, F., M. Rabinowicz, and M. Monnereau (2000) Multiple-scales in mantle convection. *Earth Planet. Sci. Lett.*, 178, 351–366.

Dubuffet, F., D.A. Yuen, and E.S.G. Rainey (2002) Controlling thermal chaos in the mantle by positive feedback from radiative thermal conductivity. *Nonlinear Proc. Geophys.*, 9, 311–323.

Dziewonski, A.M., and D.L. Anderson (1981) Preliminary reference earth model (PREM). *Phys. Earth Planet. Inter.*, 25, 297–356.

Dziewonski, A.M. (1984) Mapping the lower mantle: Determination of lateral heterogeneities in P velocity up to degree and order 6. *J. Geophys. Res.*, 89, 5929–5952.

Forte, A.M., and J.X. Mitrovica (2001) Deep-mantle high-viscosity flow and thermochemical structure inferred from seismic and geodynamic data. *Nature*, 410, 1049–1056.

Grand, S.P., R.D. van der Hilst, and S. Widiyantoro (1997) Global seismic tomography: A snapshot of convection in the Earth. *GSA Today*, 7(4), 1–7.

Gurnis, M., and G.F. Davies (1986) Numerical study of high Rayleigh number convection in a medium with depth-dependent viscosity. *Geophys. J.R. Astr. Soc.*, 85, 523–541.

Hager, B.H., and M.A. Richards (1989) Long-wavelength variations in Earth's geoid: Physical models and dynamical implications. *Phil. Trans. R. Soc. Lond. A*, 328, 309–327.

Haken, H. (1983) Advanced Synergetics, 356pp, Springer Verlag, Berlin.

Hansen, U., and D.A. Yuen (1989) Dynamical influences from thermal-chemical instabilities at the core-mantle boundary. *Geophys. Res. Lett.*, 16, 629–632.

Hansen, U., D.A. Yuen, S.E. Kroening, and T.B. Larsen (1993) Dynamical consequences of depth-dependent thermal expansivity and viscosity on mantle circulations and thermal structure. *Phys. Earth Planet. Inter.*, 77, 205–223.

Harder, H., and U.R. Christensen (1996) A one-plume model of Martian mantle convection. *Nature*, 380, 507–509.

Hirose, K. (2002) Phase transitions in pyrolitic mantle around 670-km depth: Implications for upwellings of plumes from lower mantle. *J. Geophys. Res.*, 107, No. B4, doi:10.1029/2001JB000597.

Hirth, G., and D.L. Kohlstedt (1996) Water in the oceanic upper mantle: Implications for rheology, melt extraction and the evolution of the lithosphere. *Earth Planet. Sci. Lett.*, 144, 93–108.

Hofmeister, A.M. (1999) Mantle values of thermal conductivity and the geotherm from phonon lifetimes. *Science*, 283, 1699–1706.

Hofmeister, A.M., and R.E. Criss (2005) Earth's heat flux revised and linked to chemistry. *Tectonophysics*, 395, 159–177.

Jarvis, G.T. (1993) Effects of curvature in two-dimensional models of mantle convection: Cylindrical polar coordinates. *J. Geophys. Res.*, 98, 4477–4486.

Jellinek, A.M., R.C. Kerr, and R.W. Griffiths (1999) Mixing and compositional stratification produced by natural convection I. Experiments and their application to Earth's core and mantle. *J. Geophys. Res.*, 104(B4), 7183–7201.

Kameyama, M., D.A. Yuen, and S. Karato (1999) Thermal-mechanical effects of low-temperature plasticity (the Peierls mechanism) on the deformation of a viscoelastic shear zone. *Earth Planet. Sci.*, 168, 159–172.

Kameyama, M., A. Kageyama, and T. Sato (2005) Multigrid iterative algorithm using pseudo-compressibility for three-dimensional mantle convection with strongly variable viscosity. *J. Comput. Phys.*, 206, 162–181.

Kameyama, M. (2005) ACuTEMan: A multigrid-based mantle convection simulation code and its optimization to the Earth Simulator. *J. Earth Sim.*, 4, 2–10.

Kanda, R.V.S., and D.J. Stevenson (2006) Suction mechanism for iron entrainment into the lower mantle. *Geophys. Res. Lett.*, 33(2), L02310, doi:10.1029/200GL025009.

Katsura, T. et al. (2005) Precise determination of thermal expansion coefficient of MgSiO3 perovskite at the top of the lower mantle conditions, In Third Workshop on Earth's Mantle, Composition, Structure and Phase Transitions, Saint Malo, France.

Kido, M., and O. Cadek (1997) Inferences of viscosity from the oceanic geoid: Indication of a low viscosity zone below the 660-km discontinuity. *Earth Planet. Sci. Lett.*, 151, 125–138.

Korenaga, J. (2005) Firm mantle plumes and the nature of the core-mantle region. *Earth Planet. Sci. Lett.*, 232, 29–37.

Leitch, A.M., and D.A. Yuen (1989) Internal heating and thermal constraints on the mantle. *Geophys. Res. Lett.*, 16, 1407–1410.

Li, X.D., and B. Romanowicz (1996) Global mantle shear-velocity model developed using nonlinear asymptotic coupling theory. *Geophys. J. R. Astr. Soc.*, 101, 22245–22272.

Lin, J.-F. et al. (2005) Spin transition of iron in magnesiowüstite in the Earth's lower mantle. *Nature*, 436, 377–380.

Machetel, P., and P. Weber (1991) Intermittent layered convection in a model mantle with an endothermic phase change at 670 km. *Nature*, 350, 55–57.

Manga, M., and R. Jeanloz (1996) Implications of a metal-bearing chemical boundary layer in D″ for mantle dynamics. *Geophys. Res. Lett.*, 23(22), 3091–3094.

Maruyama, S. (1994) Plume tectonics. *J. Geol. Soc. Jpn.*, 100(1), 25–49.

Masters, G., G. Laske, H. Bolton, and A. Dziewonski (2000) The relative behavior of shear velocity, bulk sound speed and compressional velocity in the mantle: Implications for chemical and thermal structure. In Karato, S., A.M. Forte, R.C. Liebermann, G. Masters, and L. Stixrude (eds.) Earth's Deep Interior, A.G.U. Monograph, 117, A.G.U., Washington, D.C., pp. 63–87.

Matyska, C., J. Moser, and D.A. Yuen (1994) The potential influence of radiative heat transfer on the formation of megaplumes in the lower mantle. *Earth Planet. Sci. Lett.*, 125, 255–266, 1994.

Matyska, C., and D.A. Yuen (2005) The importance of radiative heat transfer on superplumes in the lower mantle with the new post-perovskite phase change. *Earth Planet. Sci. Lett.*, 234, 71–81.

Matyska, C., and D.A. Yuen (2006) Lower mantle dynamics with the post-perovskite phase change, radiative thermal conductivity, temperature- and depth-dependent viscosity. *Phys. Earth Planet. Inter.*, 154, 196–207.

Matyska, C., and D.A. Yuen (2007) Upper-mantle versus lower-mantle plumes: Are they the same? In press, Foulger G., and D.M. Jurdy (eds.) The Origin of Melting Anomalies: Plumes, Plates and Planetary Processes, Geological Society of America.

Mc Namara, A.K., and S. Zhong (2004) Thermochemical structures within a spherical mantle: Superplumes or piles? *J. Geophys. Res.*, 109, B07402, doi:10.1029/2003JB002847.

McNutt, M., and A. Judge (1990) The superswell and mantle dynamics beneath the South Pacific. *Science*, 248, 969–975.

Mitrovica, J.X., and A.M. Forte (2004) A new inference of mantle viscosity based upon joint inversion of convection and glacial isostatic adjustment data. *Earth Planet. Sci. Lett.*, 225, 177–189.

Mittelstädt, E., and P.J. Tackley (2006) Plume heat flow is much lower than CMB heat flow. *Earth Planet. Sci. Lett.*, 241, 201–210.

Monnereau, M., and M. Rabinowicz (1996) Is the 670 km phase transition able to layer the Earth's convection in a mantle with depth-dependent viscosity? *Geophys. Res. Lett.*, 23, 1001–1004.

Monnereau, M., and D.A. Yuen (2002) How flat is the lower-mantle temperature gradient? *Earth Planet. Sci. Lett.*, 202, 171–183.

Montelli, R., G. Nolet, F.A. Dahlen, G. Masters, E.R. Engdahl and S.-H. Hung (2004) Finite-frequency tomography reveals a variety of plumes in the mantle. *Science*, 303, 338–343.

Morgan, W.J. (1971) Convection plumes in the lower mantle. *Nature*, 230, 42–43.

Moser, J., D.A. Yuen, T.B. Larsen, and C. Matyska (1997) Dynamical influences of depth-dependent properties on mantle upwellings and temporal variations of the moment of inertia. *Phys. Earth Plan. Inter.*, 102, 153–170.

Mühlhaus, H.B., and K. Regenauer-Lieb (2005) Towards a self-consistent plate mantle model that includes elasticity: Simple benchmarks and application to basic modes of convection. *Geophys. J. Int.*, 163, 788–800.

Murakami, M., K. Hirose, K. Kawamura, N. Sata, and Y. Ohishi (2004) Post-perovskite phase transition in MgSiO3. *Science*, 304, 855–858.

Nakagawa, T. and P.J. Tackley (2004a) Effects of a perovskite-post perovskite phase transition near core-mantle boundary in compressible mantle convection. *Geophys. Res. Lett.*, 31, L16611, doi:10.1029/2004GL020648.

Nakagawa, T., and P.J. Tackley (2004b) Effects of thermal-chemical mantle convection on the thermal evolution of the Earth's cores. *Earth Planet. Sci. Lett.*, 220, 107–119.

Ni, S., and D.V. Helmberger (2003) Ridge-like lower mantle structure beneath South Africa. *J. Geophys. Res.*, 108, B2, doi:10.1029/2001JB001545.

Oganov, A.R., and S. Ono (2004) Theoretical and experimental evidence for a postperovskite phase of MgSiO3 in Earth's D″ layer. *Nature*, 430, 445–448.

Petford, N., D.A. Yuen, T. Rushmer, J. Brodholt, and S. Stackhouse (2005) Shear-induced material transfer across the core-mantle boundary aided by the post-perovskite phase transition. *Earth Planet Space*, 57, 459–464.

Ranalli, G. (1995) Rheology of the Earth, 2nd Edition, 413pp, Cambridge Univ. Press.

Regenauer-Lieb, K., and D.A. Yuen (2003) Modeling shear zones in geological and planetary sciences: Solid- and fluid-thermal-mechanical approaches. *Earth Sci. Rev.*, 63(3), 295–349.

Ricard, Y., L. Fleitout, and C. Froidevaux (1984) Geoid heights and lithospheric stresses for a dynamic earth. *Ann. Geophys.*, 2, 267–286.

Ricard, Y., and B. Wuming (1991) Inferring viscosity and the 3-D density structure of the mantle from geoid, topography and plate velocities. *Geophys. J. Int.*, 105, 561–572.

Richter, F.M., and B.E. Parsons (1975) On the interaction of two scales of convection in the mantle. *J. Geophys. Res.*, 80, 2529–2541.

Sammis, C.G., J.C. Smith, G. Schubert, and D.A. Yuen (1977) Viscosity-depth profile in the Earth's mantle: Effects of polymorphic phase transitions. *J. Geophys. Res.*, 85, 3747–3761.

Schott, B., D.A. Yuen, and A. Braun (2002) The influences of compositional and temperature-dependent rheology in thermal-chemical convection on entrainment of the D″-layer. *Phys. Earth Planet. Inter.*, 129, 43–65.

Schubert, G., D. Bercovici, and G.A. Glatzmaier (1990) Mantle dynamics in Mars and Venus: Influence of an immobile lithosphere on three-dimensional mantle convection. *J. Geophys. Res.*, 95, 14105–14129.

Schubert, G., D.L. Turcotte, and P.L. Olson (2001) Mantle Convection in the Earth and Planets, Chapter 6, Cambridge Univ. Press.

Schubert, G., G. Masters, P. Olson, and P.J. Tackley (2004) Superplumes or plume clusters? *Phys. Earth Planet. Inter.*, 146, 147–162.

Solomatov, V. (1996) Can hotter mantle have a larger viscosity? *Geophys. Res. Lett.*, 23, 937–940.

Speziale, S., A. Milner, V.E. Lee, S.M. Clark, M.P. Pasternak, and R. Jeanloz (2005) Iron spin transition in Earth's mantle. *Proc. National Academy Sci. USA*, 102(50), 17918–17922.

Steinbach, V., and D.A. Yuen (1994) Melting instabilities in the transition zone. *Earth Planet. Sci. Lett.*, 127, 67–75.

Steinbach, V., and D.A. Yuen (1998) The influences of surface temperature on upwellings in planetary convection with phase transitions. *Earth Planet. Sci. Lett.*, 162, 15–25.

Su, W.-J., and A. Dziewonski (1992) On the scale of mantle heterogeneity. *Phys. Earth Planet. Inter.*, 74, 29–54.

Tackley, P.J. (1996) Effects of strongly variable viscosity on three-dimensional compressible convection in planetary mantles. *J. Geophys. Res.*, 101, 3311–3332.

Tackley, P.J. (1998) Three-dimensional simulations of mantle convection with a thermo-chemical CMB boundary layer: D″. In Gurnis, M., M. Wysession, and E. Knittle (eds.) The Core-Mantle Boundary Region, American Geophysical Union, Washington D.C., pp. 231–253.

Tackley, P.J. (2002) Strong heterogeneity caused by deep mantle layering. *Geochem. Geophys. Geosyst.*, 3(4), 1, CiteID 1024, doi:10.1029/2001GC000167.

Tan, E., and M. Gurnis (2005) Metastable superplumes and mantle compressibility. *Geophys. Res. Lett.*, 32, L20307, doi:10.1029/2005GL024190.

Trampert, J., F. Deschamps, J. Resovsky, and D.A. Yuen (2004) Probabilistic tomography maps chemical heterogeneities throughout the lower mantle. *Science*, 306, 853–856.

Trompert, R., and U. Hansen (1998) Mantle convection simulations with rheologies that generate plate-like behavior. *Nature*, 395, 686–689.

Tsuchiya, T., J. Tsuchiya, K. Umemoto, and R.M. Wentzcovitch (2004) Phase transition in MgSiO3 perovskite in the lower mantle. *Earth Planet. Sci. Lett.*, 224, 241–248.

Tsuchiya, T., R.M. Wentzcovitch, C.R.S. da Silva, and S. de Gironcoli (2006) Spin transition in magnesiowüstite in Earth's lower mantle. *Phys. Rev. Lett.*, 96,198501.

Van den Berg, A.P., and D.A. Yuen (1998) Modeling planetary dynamics by using the temperature at the core-mantle boundary as a control variable. *Phys. Earth Planet. Inter.*, 108, 219–234.

Van Keken, P.E., and D.A. Yuen (1995) Dynamical influences of high viscosity in the lower mantle induced by the steep melting curve of perovskite: Effects of curvature and time dependence. *J. Geophys. Res.*, 100, 15233–15248.

Vincent, A.P., and D.A. Yuen (1988) Thermal attractor in chaotic convection with high Prandtl number fluids. *Phys. Rev. A*, 38, 328–334.

Walzer, U., R. Handel, and J. Baumgardner (2004) The effects of a variation of the radial viscosity profile on mantle evolution, *Tectonophysics*, 384, 55–90.

Whitehead, J.A., and B. Parsons (1978) Observations of convection at Rayleigh numbers up to 760,000 in a fluid with large Prandtl number. *Geophys. Astrophys. Fluid Dyn.*, 9, 201–217.

Yanagawa, T.K.B., M. Nakada, and D.A. Yuen (2005) Influence of lattice thermal conductivity on thermal convection with strongly temperature-dependent viscosity. *Earth Planets Space*, 57, 15–28.

Yoshida, M., and M. Ogawa (2004) Influence of two major phase transitions on mantle convection with moving and subducting plates. *Earth Planets Space*, 56, 1019–1033.

Yoshida, M., and A. Kageyama (2006) Low-degree mantle convection with strongly temperature- and depth-dependent viscosity in a three-dimensional spherical shell. *J. Geophys. Res.*, 111, B03412, doi:10.1029/2005JB003905.

Yuen, D.A., and W.R. Peltier (1980) Mantle plumes and the thermal stability of the D″ layer. *Geophys. Res. Lett.*, 7, 625–628.

Yuen, D.A., O. Cadek, A. Chopelas, and C. Matyska (1993) Geophysical inferences of thermal-chemical structures in the lower mantle. *Geophys. Res. Lett.*, 20, 889–902.

Yuen, D.A., O. Cadek, P. van Keken, D.M. Reuteler, H. Kyvalova, and B.A. Schroeder (1996) Combined results for mineral physics, tomography and mantle convection and their implications on global geodynamics. In Boschi, E., G. Ekstrom, and A. Morelli (eds.) Seismic Modelling of the Earth's Structure, Editrice Compositori, Bologna, Italy, pp. 463–506.

Zhang, S., and D.A. Yuen (1995) The influences of lower-mantle viscosity stratification on 3-D spherical-shell mantle convection. *Earth Planet. Sci. Lett.*, 132, 157–166.

Zhang, S., and D.A. Yuen (1996) Various influences on plumes and dynamics in time-dependent, compressible, mantle convection in 3-D spherical shell. *Phys. Earth Planet. Inter.*, 94, 241–267.

Zhao, D. (2001) Seismic structure and origin of hotspots and mantle plume. *Earth Planet. Sci. Lett.*, 192, 251–265.

Zhao, D. (2004) Global tomographic images of mantle plumes and subducting slabs: Insight into deep Earth dynamics. *Phys. Earth Planet. Inter.*, 146, 3–34.

Zhong, S., M.T. Zuber, L. Moresi, and M. Gurnis (2000) Role of temperature-dependent viscosity and surface plates in spherical shell models of mantle convection. *J. Geophys. Res.*, 105(B5), 11063–11082.

CHAPTER 10

THERMAL CONDUCTIVITY OF THE EARTH'S DEEPEST MANTLE

ANNE M. HOFMEISTER

Department of Earth and Planetary Sciences, Washington U., 1 Brookings Dr., St. Louis, MO 63130-4899, USA;
E-mail: hofmeist@wustl.edu

Abstract
Thermal transport properties in the lowest mantle are estimated, due to experimental limitations. The lattice component of thermal diffusivity (D) is constrained through measurements of dense phases made using the laser-flash technique, which is accurate ($\pm 2\%$) and unaffected by spurious radiative transfer. Thermal diffusivity is constant once a critical temperature (T_{sat}) of $\sim$1100 to 1500 K is exceeded. The saturated mean free path (λ_{sat}, computed from D_{sat} and sound velocities) nearly equals the primitive lattice parameter $<a>$. This relationship provides temperature independent values of D and k_{lat} for the lower mantle. Pressure derivatives are predicted by the damped harmonic oscillator model. An effective thermal conductivity, $k_{rad}(T)$, due to diffusion of heat by photons is estimated from optical spectra of perovskite at 298 K. To represent the internally heated, grainy mantle, our formulation accounts for grain-size (d) dependences of emissivity and physical scattering, and for interface reflections. An approximate analytical solution is derived which indicates that k_{rad} depends nearly linearly on T in the lower mantle. For perovskite (and probably post-perovskite), k_{rad} has a maximum at $X \sim 0.05$ Fe/(Mg + Fe) for $d \sim 1$ mm. At $X \sim 0.1$, k_{rad} is maximized at $d \sim 3$ mm. Our approximation overestimates k_{rad} at large X and d. For low spin Fe, k_{rad} is low due to grain-size effects, and reaches a maximum at high Fe content. Plumes are expected to form under destabilizing conditions of low thermal conductivity and negative $\partial k/\partial T$. The latter condition is unlikely in the deep mantle, but the following physical properties lower k_{rad}: large grains or very, very small grains, low Fe contents for low spin Fe, or high Fe contents for high spin Fe. High degrees of solid solution reduce k_{lat}. If localized Fe enrichment of the deepest mantle by core material occurs this could create plumes which would carry some core material upwards, thereby enriching the lower mantle in Fe with respect to the upper mantle, and leading to a gravitationally stable, chemically stratified mantle.

D. A. Yuen et al. (eds.), Superplumes, 269–292.
© 2007 *Springer.*

1 INTRODUCTION

Numerical convection models of the Earth have shown that the functional form for thermal conductivity (k) and its close relative thermal diffusivity:

$$D = \frac{k}{\rho C_P}, \tag{1}$$

where ρ is density and C_P is heat capacity at constant pressure (P), strongly influence the character of the solutions through feedback in the temperature equation. Accurately characterizing k or D as a function of T is thus essential to modeling planetary heat flow on diverse scales (e.g., Gerbault, 2000; Branlund et al., 2000; Yuen et al., 2000; Dubuffet et al., 2002; van den Berg et al., 2004; Yanagawa et al., 2005). The functional form of $k(T)$ is determined by summing the contributions from two different microscopic processes: (1) Transport of heat by scattering of phonons within each individual mineral grain is termed lattice conductivity ($k_{\rm lat}$): (2) Heat is also moved when photons emitted by any given grain in the medium are absorbed by nearby grains. Diffusive radiative processes are described by an effective thermal conductivity ($k_{\rm rad}$).

Many studies of $k(T)$ or $D(T)$ utilize contact methods such as that of Ångstrom. A significant problem is that silicates and oxides permit unwanted, direct radiative transfer above $\sim$500–800 K, as indicated by the reversal of the sign of $\partial k/\partial T$ from negative to positive near such temperatures (e.g., Kanamori et al., 1968; Lee and Kingery, 1960). However, the measurements are compromised at significantly lower temperatures because the radiative component increases gradually with temperature, and thus a small component exists at T below the reversal. Such boundary-to-boundary radiative transfer results when the material is transparent in some segment of the near-IR to visible spectrum. Most minerals behave in this manner. Contact methods do not permit differentiation of the two components, which is needed for geodynamic models, and they have systematic errors such those arising from thermal contact resistance, and are limited to $T < 1200$ K (e.g., Parker et al., 1961; Ross et al., 1984).

The present paper constrains the lattice component to $D(T)$ for deep mantle phases by applying the laser-flash technique (Parker et al., 1961) to structural analogues. The method is related to that of Schilling (1999), but accesses higher temperatures, avoids used of thermocouples, and removes remnants of boundary-to-boundary radiative transfer using the quantitative analysis of Mehling et al. (1998). We find D to be constant at mantle temperature and that this saturation value is related to the lattice parameter (Hofmeister, 2006), which is known or calculable.

Calculations of $k_{\rm rad}$ based on spectral data (e.g., Shankland et al., 1979) represent a *diffusive* process that fundamentally differs from boundary-to-boundary radiative transfer and thus cannot be extracted from laboratory measurements of k. Radiative transfer in the mantle is solely diffusive, as assumed in geodynamic models, as shown by estimating the effect of scattering in this grainy medium: If a tiny amount (0.005%) of light back-reflects from grain boundaries, then light is essentially extinguished over

distances of 2 to 200 m. Mantle gradients are below 10 K/km which makes it unlikely that light emitted from any given grain will reach another grain with temperature differing by 1 K. Physical scattering is important which means the grain size (d) cannot be ignored in calculations of k_{rad}. A recent model which includes the effect of d (Hofmeister, 2004a, 2005) is used to set limits on k_{rad} in the deepest mantle. Implications of the results for k_{lat} and k_{rad} on plumes arising from the deep mantle are briefly discussed.

2 LATTICE THERMAL CONDUCTIVITY

2.1 Theory

The quantum mechanical phenomena of phonon–phonon scattering transports heat through the lattice. Models of heat transport in insulators are based on Debye's (1914) analogy of the behavior of phonons to collisions of molecules in a gas, which provided:

$$k_{\mathrm{lat}} = \frac{\rho}{3ZM} C_V u^2 \tau, \tag{2}$$

where ρ is the density, M is the molar formula weight, Z is the number of formula units in the primitive unit cell, τ is the mean free lifetime, and u is an acoustic velocity. The factor ρ/ZM accounts for typical units of heat capacity (per mole of formula unit).

As is the case for heat capacity, models for k_{lat} used either parameters for acoustic modes or parameters for optic modes. Historically, the problem in modeling k_{lat} lies in determining the lifetime, or equivalently the mean free path (λ), of phonon–phonon collisions (Ziman, 1962). Lifetimes in acoustic models are roughly estimated (Roufosse and Klemens, 1973), whereas lifetimes in optic models are extracted from quantitative IR spectra using the damped harmonic oscillator model of Lorentz (Hofmeister, 1999, 2001). The next subsections summarize the form for $k_{\mathrm{lat}}(T)$ predicted by both types of models, and use these to determine the temperature dependence of D.

2.1.1 Acoustic models for the temperature dependence of thermal conductivity

Because heat capacity is a complicated function of T, low- and high-temperature limits have been the focus of acoustic models. The high-T limit is considered here.

For T greater than the Debye temperature (θ), Peierls (1929, 1956) assumed that the mean free path goes $1/T$ which leads to

$$k_{\mathrm{lat}} = B/T \quad \text{for} \quad T > \theta. \tag{3}$$

Dugdale and MacDonald (1955) obtained Equation 3 using dimensional analysis. Their proportionality constant differs from those of Julian (1965) and Roufosse and Klemens (1973) whose values of B differ by a factor of $\sim$7. Because heat capacity is nearly constant for $T > \theta$, Equation 3 gives the limit $D \propto 1/T$.

Equation 3 is invalid if temperature is high enough that the mean free path becomes shorter than the unit cell (e.g., Ziman, 1962). Roufosse and Klemens (1974) obtained

the relationship:

$$k_{\rm lat} = \frac{B}{T}\left[\frac{2}{3}\left(\frac{C}{T}\right)^{1/2} + \frac{1}{3}\frac{T}{C}\right] \quad \text{for } T > \theta, \tag{4}$$

where the constant C is related to the Debye frequency and is proportional to $N^{2/3}$. For simple solids, $N \sim 1$ or 2, C is $\sim$500 K, and deviations from Equation 3 of $\sim$15% are seen only above twice this temperature. For complex crystal structures with $N \sim 10$, C should be 1000–2000 K. Thus Equation 3, rather than Equation 4, should be valid up to the melting temperatures of minerals (Roufosse and Klemens, 1974). Liebfried and Schlöman (1954) independently reached this conclusion.

The above results were obtained by assuming three phonon collisions. For four-phonon events and $T > \theta$, Pomeranchuk (1943) found that $k_{\rm lat} \sim T^{-5/4}$. Klemens (1969) and Ziman (1962) respectively suggested the forms:

$$k_{\rm lat} \sim \frac{1}{BT + CT^2}, \quad \text{or} \quad k_{\rm lat} \sim \frac{1}{BT} + \frac{1}{CT^2}. \tag{5a,b}$$

Because $T > \theta$, the same approximate forms could be used to describe D.

2.1.2 The damped harmonic oscillator model of thermal diffusivity

The optic model is developed in Hofmeister (1999, 2001, 2004b), Geisting and Hofmeister (2002), and Geisting et al. (2004). The lifetime of any given optic mode, $\tau_{\rm i}$, equals $1/2\pi{\rm FWHM_i}$, where FWHM is the full width at half maximum of peaks in the dielectric functions obtained from IR reflectivity data (e.g., Spitzer et al., 1962). The FWHM for each mode describes its interaction with all other vibrational modes in real crystals, including acoustic, and includes the effects of mode mixing, anharmonicity, disorder, impurities, and defects. FWHM can also be obtained from Raman spectra.

Due to a lack of information regarding the specific dependence of frequency on wavevector for each mode, average properties are used:

$$k_{\rm lat} = \frac{\rho}{3ZM}\frac{C_V <u>^2}{2\pi<{\rm FWHM}>}. \tag{6}$$

Because velocities of acoustic and optic modes should be similar inside the Brillouin zone, as inferred from theoretical and measured dispersion relations, acoustic velocities are averaged to provide $<u>$. A simple average of the compression and shear speeds is used here. Other averages are possible, and the specific form for $<u>$ depends somewhat on the crystal structure (Hofmeister, 2004c).

Combining Equations 1 and 6, and neglecting the ($\sim$1–3%) difference between C_P and C_V, provides the temperature dependence of the thermal diffusivity:

$$D(T) = \frac{<u(T)>^2}{6\pi Z<{\rm FWHM}(T)>} = \frac{u(T)\lambda(T)}{3Z}. \tag{7}$$

The factor of M is cancelled because Equation 1 presumes C_P has units J/g-K.

The temperature dependence of D (Eq. 7) is inferred as follows: Sound velocities of dense minerals depend weakly on temperature: $\partial(\ln u)/\partial T$ is near -0.004%/K for dense phases such as garnets (Anderson and Isaak, 1995). Derivatives for dielectric peak widths are ~ 100 times larger, $\partial(\ln \mathrm{FWHM})/\partial T = 0.25\%$/K near 298 K for MgO (Kachare et al., 1972) and thus the temperature dependence of D is derived from the response of FWHM. This information, Equation 7, and observation of finite peak width for MgO at 4 K (Kachare et al., 1972) lead to the following form:

$$\frac{1}{D} = \frac{6\pi Z}{u_0^2}(\mathrm{FWHM}_0 + aT)(1 + bT + cT^2) \approx A + BT + CT^2 + \cdots, \qquad (8)$$

where a, A, etc. are constants (Hofmeister, 2006). The coefficient B dominates and has a positive sign. This form best fit measurements of garnets, which reached the saturation limit (Hofmeister, 2006). If T_{sat} is not reached or $\partial(\ln u)/\partial T$ is not weak, then forms such as $D = a + b/T + c/T^2 + dT^3$ represent the data well (Pertermann and Hofmeister, 2006).

Pressure does not alter the population of the vibrational levels or the other factors thought to influence FWHM. Using Equation 7, and assuming that the mode Grüneisen parameters on average equal the thermal Grüneisen parameter gives

$$\frac{\partial(\ln(D))}{\partial P} = \frac{2}{K_T}\left(\gamma_{\mathrm{th}} + \frac{1}{3}\right). \qquad (9)$$

2.2 Experiment

The fast, contact-free method of Parker et al. (1961) was used to determine thermal diffusivity, wherein a sample in the form of a small slab with parallel faces is held at temperature in a furnace while emissions from the top of the slab are monitored remotely with an IR detector. We use plates with parallel surfaces of thickness of 0.6–2.0 mm and diameters of 8–15 mm with sand-blasted surfaces. The bottom of the slab is heated above the furnace temperature by an optical pulse from an IR laser. Top and bottom surfaces of the sample are graphite coated to enhance absorption of the laser pulse, to shield the detector from laser light, and to increase the intensity of sample emissions (Blumm et al., 1997). Usually, samples are sputter coated with Au or Pt metal before application of graphite to maximize suppression of boundary-to-boundary radiative transfer. As heat from the laser pulse diffuses from the bottom to the top of the sample, the increase in emissions is recorded by the IR detector, in the form of a temperature–time curve. Because boundary-to-boundary transfer is difficult to eliminate at high temperature, its effect on temperature–time curves is incorporated in data analysis (Tan et al., 1991; Andre and Degiovanni, 1995; Mehling et al., 1998; Hofmann et al., 1997). The temperature dependence of D is determined by varying furnace temperature. The pulse must be shorter than the time it takes heat to cross the sample, which is easily achieved with a laser. Because the change in temperature associated with the pulse is small, $\sim$4 K, D is approximately constant during the measurements, simplifying analysis (Parker et al., 1961).

We use a Netzsch LFA 427 apparatus which covers temperatures from ~290 to 2200 K under an Ar atmosphere. Main components are an evacuable furnace with a graphite heating element, water cooled housing, a Nd-GGG laser, and an InSb detector. For a detailed description, see Braeuer et al. (1992) and Blumm and Lemarchand (2002).

Temperatures were monitored using a type D W/Re thermocouple, which was calibrated against Curie transition points of metals. Thermal diffusivity values were calibrated against electrolytic iron, austenitic stainless steel, and Poco graphite standards (Hendersen et al., 1998). Data were collected at intervals of 50 to 100 K as each sample was heated to some maximum temperature. If the sample was not melted, data were also collected during the cool down. Three measurements were made at each temperature step.

2.3 Results

For all minerals studied so far using the laser-flash apparatus, thermal diffusivity decreases rapidly as temperature increases above ambient temperature, such that the slope $\partial D/\partial T$ gradually decreases as T increases until D asymptotically approaches a constant at high temperature (Hofmeister, 2004b, 2006; Pertermann and Hofmeister, 2006). Figure 1 provides examples. The shape of the curve for $D(T)$ depends on chemical composition and structure, but constant D exists at some high temperature for all crystalline substances, except for a few cases where melting occurred while D

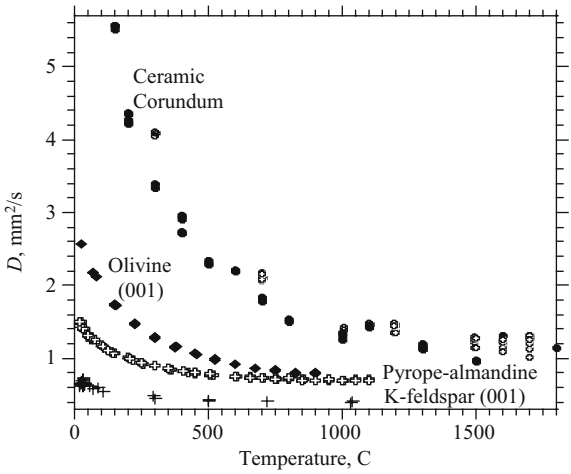

Figure 1. Thermal diffusivity as a function of temperature for minerals with various structures. Filled and open circles = two different samples of ceramic corundum Al_2O_3 with low porosity. Diamond = olivine, $Mg_{0.9}Fe_{0.1}SiO_4$, the (001) face. Plus = feldspar, $KAlSi_3O_8$, the (001) face. Open cross = randomly oriented garnet, $(Mg_{0.43}Al_{0.53}Ca_{0.04})_3Al_2Si_3O_{12}$. Data from Pertermann and Hofmeister (2006) and Hofmeister (2006).

was still decreasing (e.g., calcic garnets). The temperature of saturation is higher for end-member compositions (e.g., Al_2O_3, MgO), than for solid solutions (e.g., most natural garnets) or disordered minerals (e.g., feldspar, Fig. 1).

2.3.1 Comparison of the temperature dependence of D with theory

The observed non-linear decrease in D with temperature (Fig. 1) is not consistent with acoustic models (Eqs. 3–5), although addition of a constant to Equation 5a would provide a form for $D(T)$ that is compatible with our results up to T_{sat}. Acoustic models do not predict a high temperature asymptote for minerals due to their high Debye temperatures (Roufosse and Klemens, 1974).

The dependence of D on temperature is consistent with the damped harmonic oscillator model (Eq. 8). Our measurements (Fig. 1) show that the FWHM controls the temperature dependence of D insofar as u depends weakly on temperature for most dense minerals (Anderson and Isaak, 1995).

Achievement of constant D at high T is also consistent with the damped harmonic oscillator model. In the kinetic theory of gases, lifetimes are connected with the number of molecules per unit volume (e.g., Reif, 1965). At 298 K, FWHM of diverse crystalline structures roughly depends on the number of phonons within the primitive unit cell (Hofmeister, 2004c). As temperature increases, overtone-combination modes are excited. Saturation in the number of modes occurs when T is sufficiently high that the phonon continuum dominates the statistics (Mitra, 1969), and increasing T no longer changes the number of phonons, but rather increases their energy. The flat trend in D at high T occurs when $k_B T \sim h\nu$ of the overtones, where k_B is Boltzmann's constant and h is Planck's constant, which is consistent with phonon saturation. As ρ weakly decreases at high T and C_P weakly increases, k_{lat} (Eq. 1) is also independent of T at roughly double the Debye temperature (Hofmeister and Yuen, under review).

Asymptotic flattening of D is analogous to the Dulong-Petit limit of 3R (the gas constant) for C_P at high T (Fig. 1) and constitutes a threshold (Hofmeister and Yuen, under review). Another threshold temperature divides the strongly T-dependent regime at moderate temperatures ($\sim$250 to $\sim$1200 K) from the cryogenic regime where $1/D \sim T^n$ such that $n \sim 2$–3 (Hofmeister, 2006). An analogy of $1/D$ exists with heat capacity, which is dominated by the behavior of acoustic modes at low T, optic modes at high temperature, and saturation at very high temperature. The regimes for $C_P(T)$ result from populations of energy levels changing with temperature. Phonon–phonon interactions, described by FWHM, should also increase as more energy levels are populated. Thus, $1/D$, being proportional to FWHM, has a T-dependence like that of C_P.

2.3.2 Connection of the saturated mean free phonon path with lattice parameters

The mean free path of the phonons (Fig. 2) was obtained using Equation 7, results for $D(T)$ in Figure 1 and in Hofmeister (2006), and weighted average of the sound speeds

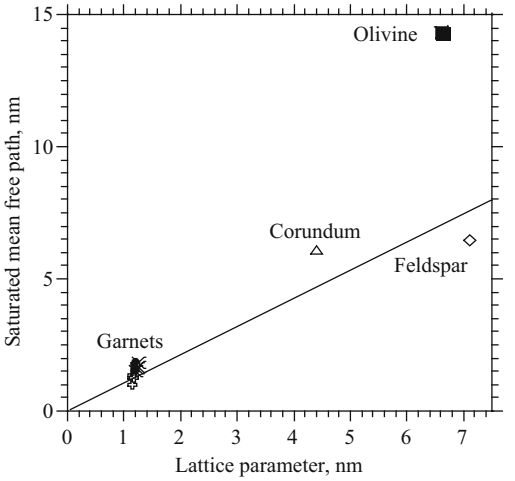

Figure 2. Relationship of the mean free path at saturation (Eq. 7) with lattice parameter for the substances in Figure 1, as labeled, garnet data from Hofmeister (2006). Cross = Mg-Fe-Al garnets; dot = calcic garnets; X = synthetics. Lattice parameters and acoustic velocities $<u> = (u_P + 3u_S)/3$ from the literature (e.g., Smyth and McCormick, 1995; Bass, 1995). Solid line = 1:1 correspondence.

for samples with a large number of vibrational modes (garnet, feldspar), a simple average for a moderate number (olivine) and $<u> = u_P$ for few vibrational modes (corundum), see Hofmeister (2004c). Because acoustic velocities depend linearly and weakly on temperature, $\lambda(T)$ follows $D(T)$. The mean free path is thus constant at high temperature, and approaches the lattice parameter (Fig. 2), which has been considered to a lower limit for λ (Ziman, 1962). It is not clear why olivine departs from the linear trend defined by all other samples. A wider range of mineral structures and chemical compositions needs to be examined to better constrain the dependence of λ on a.

2.3.3 Inference of deep mantle values of lattice thermal conductivity and diffusivity

For mantle materials, high temperatures are expected so constant D (and k_{lat}) will occur throughout the mantle. To determine D_{sat}, we therefore estimate λ_{sat} from Equation 7, using the primitive lattice constants $<a>$ of the phases expected to dominate the lowest mantle. The primitive unit cell, rather than the crystallographic, pertains because the type and number of phonons in a crystalline solid are represented by the vibrations of the primitive unit cell. From Figure 2, this approach approximates D and thus k_{lat}. There is quite a bit of uncertainty involved as olivine does not follow the 1:1 correspondence; although extensive solid solutions closely follow ($\lambda_{sat} = <a>$).

Table 1. Physical properties of $MgSiO_3$

Properties at 120 GPa, 0 K	Perovksite	Post-perovskite	Reference
Space Group	*Pbnm*	*Cmcm*	
Z (primitive)	4	2	
Volume, Å^3 (crystallographic)	122	120	Iitaka et al. (2004)
$<a>$, Å (primitive)	4.96	3.92	Calculated from V
u_P, km/s	∼13.5	∼14	Iitaka et al. (2004)
u_S, km/s	∼7.5	∼7.5	Iitaka et al. (2004)
D_{sat}, mm^2/s	3.92	6.33	This work
$k_{lat,sat}$, W/m-K	5.37	8.7	This work
K_T, GPa	660	654	Iitaka et al. (2004)
Properties at ambient conditions			
K_T, GPa	248	222	Tsuchiya et al. (2004)
dK/dP	3.9	4.2	Tsuchiya et al. (2004)
γ_{th}	1.55	1.64	Tsuchiya et al. (2004)

The relevant physical properties (Table 1) are based on calculations, some of which are confirmed experimentally. Measurements of Organov and Ito (2004) at 118 GPa and 300 K provide a volume for post-perovskite (ppv) that is 1% higher, whereas results of Murakami et al. (2004) are essentially the same as the calculations. Thermal conductivity is determined from Equation 1, using density from PREM $= 5.5$ g/cm^3 (Dziewonski and Anderson, 1981) and $C_P \sim 3R = 24.9$ J/mol, and 101 g/mol for both ppv and perovskite (pv) magnesium end-members.

From Equation 9 and Table 1, the pressure dependence of D is $\sim 0.6\%$/GPa near 120 GPa, and thus is negligible in the core-mantle boundary region. Near 22 GPa, $\partial(\ln(D))/\partial P$ is $\sim 1.2\%$/GPa. Approximating λ as $<a>$ creates more uncertainty than neglecting the effect of pressure over the lower mantle. Thus, the estimates at 120 GPa (Table 1) represent the lower mantle. Notably, ppv is much more effective at transporting heat than pv. As the difference is largely due to disparate sizes of the primitive unit cells, other compositions of these mantle phases, e.g., $(Mg_{0.9}Fe_{0.1})SiO_3$ (Mao et al., 2004), will have similar relative values.

3 RADIATIVE THERMAL CONDUCTIVITY

Realistically modelling the hot lower mantle requires quantifying any heat moved diffusively by photons. This process is described by an effective thermal conductivity (k_{rad}) that cannot be extracted from laboratory measurements because a different type of radiative transfer occurs therein, termed boundary-to-boundary. In the latter process, light from the source warms the thermocouple with negligible participation of the sample (e.g., Kanamori et al., 1968; Lee and Kingery, 1960). By constrast, diffusion of photons occurs by sequential emission and absorption of light from grain-to-grain,

and k_{rad} is calculated from optical spectra. A new formulation (Hofmeister 2004a; 2005) accounts for the frequency dependence of emissivity, in accord with radiative transfer models depicting diverse situations (e.g., Brewster, 1992; Evans, 1992; Kaufmann and Freedman, 2002; Hapke, 1993). The model accounts for the two effects of grain-size (d): physical scattering which shortens the photon's mean free path (Fujisawa et al., 1968), and reflection at interfaces which reduces throughput, especially at frequencies where absorbance is high. As a result, k_{rad} depends strongly and non-linearly on grain-size.

Spectra are currently unavailable for ppv, and available spectra of pv are inadequate for the calculation, having baseline problems due to scattering. Therefore, this paper uses the general behavior of $k_{rad}(T)$ at high temperature to describe the lower mantle.

3.1 Spectra of mantle minerals

Figure 3 shows the three types of optical spectra observed so far for mantle minerals. For details of the technique, see Rossman (1988) and other papers cited in this section.

Olivine has Fe^{2+} in 6-coordination. Octahedral sites have similar sizes in various minerals, and patterns like that of olivine (Fig. 3) were observed for orthopyroxene, clinopyroxene, wadsleyite, silicate spinels, and magnesiowüstite (Burns, 1970; Goto et al., 1980; Rossman, 1988b; Ross, 1997; Smith and Langer, 1982).

Polycrystalline majorite has three weak peaks at low frequency, assigned to Fe^{2+} in the large 8-coordinated site, as in low-pressure garnets (Fig. 3). The high frequency,

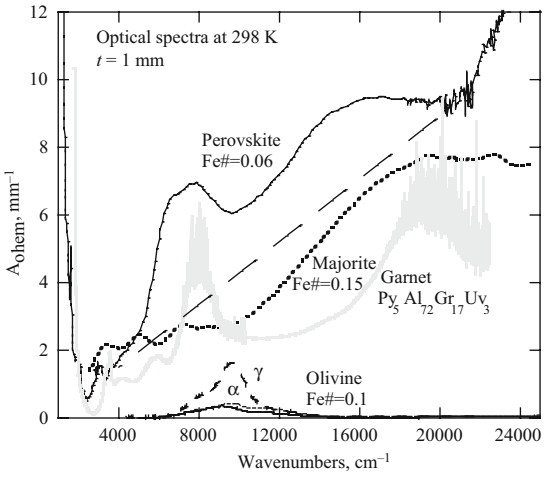

Figure 3. Near-IR to visible spectra of mantle silicates. Light lines = three polarizations of gemmy olivine as marked (Taran and Langer, 2001). Grey = garnet (this work); Heavy dots = majorite (Keppler and McCammon, 1996). Solid line = perovskite (Keppler et al., 1994). Long dashed line = rough baseline for scattering. Iron contents as indicated. Intensities of the high pressure phases are approximate due to uncertainties in both thickness and in the baseline correction.

broad peak was attributed to Fe^{2+}-Fe^{3+} charge transfer (Keppler and McCammon, 1996); but charge transfer bands in low-pressure garnets are narrower (Fig. 3) and seen at high Fe contents (Khomenko et al., 2002). The absorbance of the high ν peak is uncertain as the baseline is equivocal. Due to these problems, $k_{\rm rad}$ of majorite is not computed here.

Polycrystalline perovskite has two d-d electronic transitions of Fe^{2+} from ~6500–8000 cm^{-1} superimposed on a strong scattering curve (Fig. 3) for its 8-coordinated site. A third high frequency band was assigned to charge transfer (Keppler et al., 1994). If Fe ions are is randomly distributed among the octahedral and 12-coordinated sites, then 5% of the Fe^{2+} atoms have Fe^{3+} as neighbors. Probably the juxtaposition is lower: local compensation of charge suggests that octahedral Fe^{3+} should instead be balanced by Fe^{3+} in an adjacent dodecahedra, which is consistent with an uncertain site occupancy of Fe^{3+}(McCammon et al., 1992). Given that the intensity of the ~16,000 cm^{-1} band is similar to those of the low frequency Fe^{2+} transitions, this peak may also be a d-d transition, since three are expected from symmetry. Alternatively, Fe^{3+} is interstitial, e.g., magnetite particles, or on grain boundaries, producing a high frequency band which is not intrinsic to perovskite. Mie scattering from particles does produce peaks at such frequencies (Khomenko et al., 2002). In lieu of single-crystal spectra, radiative transfer for perovskite is calculated with and without the highest frequency band.

Visible spectra have not been measured for post-perovskite, but the cation sites where Fe resides in these two phases are similar (Murakami et al., 2004; Tsuchiya et al., 2004; Mao et al., 2004), suggesting that their absorption spectra will be similar enough that radiative transfer in the lower is not affected by this phase transition.

Visible spectra do not exist for low spin states of any silicate, but it is expected that the pattern consists of very weak bands in the visible and a UV tail.

3.2 Theory

For local radiative equilibrium, optically thick conditions, and non-opaque media:

$$k_{\rm rad}(T) = \frac{4\pi}{3}\int_0^\infty \left(\frac{d}{1+dA(\nu,T)}\right)\frac{c}{\nu^2}\frac{\partial}{\partial T}\left\{[n(\nu,T)]^2[1-{\rm e}^{-dA(\nu,T)}]I_{\rm bb}(\nu,T)\right\}d\nu. \tag{10}$$

where $[d/(1+dA)]$ is the mean free path, n is the index of refraction, c is the speed of light, ν is frequency in cm^{-1}, T is temperature, and $I_{\rm bb}$ is Planck's blackbody function with energy-density provided on a per wavelength basis (Hofmeister, 2004a, 2005). Attenuation of light is described by the true absorption coefficient:

$$A = -\frac{1}{d}\ln\left(\frac{I_{\rm tra}}{I_0}\right), \tag{11}$$

where $I_{\rm tra}$ is the transmitted intensity, I_0 is the incident intensity, and d is thickness or grain-size (Brewster, 1992). The conventions in geophysical literature re followed

except that $\nu = 1/\lambda$, as used in mineral spectroscopy. The factor $[1 - e^{-dA}] = \xi$, the emissivity, was defined by Kirchhoff in ca. 1865. An average grain-size and absorption coefficient are used to describe the mantle, which parallels representation of viscous damping in geodynamic models (Ranalli, 2001).

In evaluating Equation 10, an additional physical process in a grainy medium must be accounted for. Namely, that the amount light exitting the grain is reduced from the incident intensity not only by losses from absorption (Eq. 11), but also due to back reflections (R) at the surface (Hofmeister, 2004a, 2005). This step is necessary because back reflections and high absorbance together produce opaque spectral regions and the model is not valid when the grains are opaque (Clark, 1957). Thus, frequency regions where no light is transmitted must be excluded when integrating Equation 10. How back reflections reduce throughput (and thus radiative transfer) in mantle grains is understood by comparison to laboratory measurements. Absorbance ($a_{\rm chem}$) is obtained from measurements of transmission which include not only $I_{\rm tra}$ (Eq. 11) but also a reduction in throughput due to reflection. Because common logarithms are often used:

$$Ad = 2.3026[a_{\rm chem} + 2\log(1 - R)], \tag{12}$$

where R is computed from the index of refraction mismatch at grain interfaces using Snell's law and Fresnel's equations. Opacity occurs when the product $dA(\nu)$ reaches a critical value, controlled by R, such that the light from any given grain cannot reach its second-nearest neighbor. Such sections are excluded from the integral. This chapter considers the case $dA < 7$ ($R \sim 0.1\%$), corresponding to subhedral grain with $\sim$120° angles, common in mantle rocks. Other cases (Hofmeister, 2005) give similar results.

Given that radiative transfer models are approximate, Equation 10 is simplified based on the dependence of material properties on ν, T, and P. The near-IR to UV spectral range need only be considered, as the lattice modes in the far- to mid-IR, and the metal-oxygen charge transfer bands in the far-UV are too intense to permit radiative transfer. The result (Hofmeister, 2005) is:

$$k_{\rm rad}(T) = \frac{4\pi\, dn^2}{3} \sum \int_{lower}^{upper} \frac{(1 - e^{-dA})}{(1 + dA)\nu^2} \frac{\partial[I_{\rm bb}(\nu, T)]}{\partial T} d\nu, \tag{13}$$

where the sum allows for transparent regions existing above and below the strong bands in the visible. Because A is a complex function of ν (next section) and the cutoff frequencies depending on d and A, Equation 13 is evaluated numerically.

3.2.1 Why the effect of pressure can be neglected

The pressure dependence of the material properties determines $k_{\rm rad}(P)$. Values of $\partial n/\partial P$ are sufficiently small that this aspect can be neglected. The relevant quantity is then $(\partial A/\partial\nu)(\partial\nu/\partial P)$. Although peaks shift with pressure, values of $\partial\nu/\partial P$ at 298 K are near or equal to zero for many bands (Burns, 1982). Moreover, $\partial A/\partial\nu$ is positive at frequencies below the central frequency, but negative above. Combining these effects provides very small values of $\partial k_{\rm rad}/\partial P$, especially when the peak is contained

entirely within the blackbody curve (above ~ 1900 K for Fe^{2+} absorptions of mantle minerals). Thus, $\partial k_{\rm rad}/\partial P$ is unimportant. See Hofmeister (2005) for details.

Furthermore, from the Beer-Lambert law, A is proportional to the concentration. Since concentration is unaffected by pressure, neither should $k_{\rm rad}$ change with pressure.

3.2.2 Use of asymptotic limits to estimate $k_{\rm rad}$

For nearly transparent materials:

$$k_{\rm rad}(T) \cong \frac{4\pi d^2 n^2}{3} \sum \int_{lower}^{upper} \frac{A}{\nu^2} \frac{\partial [I_{\rm bb}(\nu, T)]}{\partial T} d\nu, \quad \text{for } dA \text{ small.} \tag{14}$$

Thus, as $A \to 0$, $k_{\rm rad} \to 0$. Diffusive radiative transfer is absent in a fully transparent medium because a photon cannot heat a grain unless it is absorbed. As $d \to 0$, $k_{\rm rad} \to 0$. This case approximates exceedingly fine-grained ceramics that are effectively opaque due to back reflections. Physical scattering dominates this asymptotic limit.

For dark materials, Equation 13 reduces to the result of Shankland et al. (1979):

$$k_{\rm rad}(T) \cong \frac{4\pi n^2}{3} \sum \int_{lower}^{upper} \frac{1}{A\nu^2} \frac{\partial [I_{\rm bb}(\nu, T)] \partial T}{\partial T} d\nu, \quad \text{for } dA \text{ large.} \tag{15}$$

For an opaque medium ($A \to \infty$) and for any value of d, the correct limit ($k_{\rm rad,dif} \to 0$) is obtained. When dA exceeds a critical value depending on reflectivity and texture (discussed above), $k_{\rm rad,dif} \to 0$. The result of Shankland et al. (1979), derived without considering grain-size, is invalid for very weakly absorbing regions unless grain-size is very, very large.

If A is independent of ν and T, then Equation 14, integrated from $\nu = 0$ to ∞, provides the following simple formula:

$$k_{\rm rad} = \frac{16}{3} \sigma T^3 d^2 A, \quad \text{for } dA \text{ small and constant,} \tag{16}$$

where σ is the Stefan-Boltzmann constant. For constant A, Equation 15 becomes

$$k_{\rm rad} = \frac{16}{3} \sigma T^3 \frac{1}{A}, \quad \text{for } dA \text{ large and constant.} \tag{17}$$

Equation 17 is Clark's (1957) result, which was derived without considering grain-size.

The form for $k_{\rm rad}(A)$ at intermediate values of dA is inferred by combining Equations 16 and 17. Because $\partial k_{\rm rad}/\partial A$ is positive at low dA but negative at high dA, and both limits for $k_{\rm rad}$ are 0, a maximum exists in $k_{\rm rad}(A)$: $k_{\rm rad}$ is largest for moderate A and moderate grain-size, where physical scattering is not overwhelming, significant light is emitted by individual grains in the mantle, and this light is not completely extiguished by neighboring grains. Because A is roughly proportional to

concentration, $k_{\rm rad}$ has a maximum in concentration as well, discussed by Hofmeister and Yuen (under review).

Radiative transfer is more complex than T^3 law in Equations 16 and 17 because A depends on n and T. However, the temperature dependence of $k_{\rm rad}$ can be inferred from these equations (Hofmeister, 2005; Hofmeister and Yuen, under review). The dependence of A on ν weakens the temperature dependence of $k_{\rm rad}$ as it truncates the integral of Equation 13. For small dA, A increasing with T strengthens the temperature dependence of $k_{\rm rad}$ (Eq. 16). The effects of $A(\nu)$ and $A(T)$ roughly cancel at small dA, suggesting for small dA, the T^3 law is roughly correct. But for large dA, A increasing with T decreases $k_{\rm rad}$ (Eq. 17). Dark samples are opaque over larger portions of the integral, which further decreases $k_{\rm rad}$. A much weaker dependence than T^3 is expected for $k_{\rm rad}$ at high T.

3.2.3 An approximate formula that connects $k_{\rm rad}$ with concentration

If the peak is narrow and Ad is low enough that the material is not opaque, then Equation 13 can be evaluated using the trapezoidal rule, providing:

$$k_{\rm rad}(T) = \frac{4dn^2}{3}\frac{[1-\exp(-dA_{\rm ave})]}{(1+dA_{\rm ave})}\Delta\nu\frac{2\pi {\rm h}^2{\rm c}^3\nu_{\rm ave}^4}{k_{\rm B}T^2}\frac{\exp({\rm hc}\nu_{\rm ave}/k_{\rm B}T)}{[\exp({\rm hc}\nu_{\rm ave}/k_{\rm B}T)-1]^2}, \quad (18)$$

where $\nu_{\rm ave}$ and $A_{\rm ave}$ represent the average frequency and average absorption coefficient for a peak that spans the interval $\Delta\nu$ (Hofmeister, 2004b). For a single band, $A_{\rm ave}$ equals the half height $= A_{\rm max}/2$. For broad or multiple peaks, $k_{\rm rad}$ could be calculated by summing the results for a series of segments, for example, $1/10^{\rm th}$ of each peak in the spectrum could be evaulated individually using Equation 18, as well as the near-IR and UV tails. As a first approximation, this paper considers a single peak by generalizing the derivation of Hofmeister (2004b) to cover species other than hydroxyl.

The Beer-Lambert law, which is valid for low to moderate concentrations:

$$X = \sum {\rm II}/(df''), \quad (19)$$

where $\sum$II is the sum of the integrated intensities for the three orthogonal directions, d is thickness or grain size, f, f' or f'' are extinction coefficients, is obtained by calibration (e.g., Rossman 1988b). A simplified version of the Beer-Lambert law is used here:

$$X = A_{\rm max}/f' = A_{\rm ave}/f. \quad (20)$$

The connection of X with A means that the temperature dependence of the spectra can be neglected in this approximation.

The variables in Equation 18 are separable. Combining Equations 18 and 20 gives

$$k_{\rm rad} = \vartheta(T)\frac{8\pi c k_{\rm B} dn^2}{3}\nu_{\rm ave}^2\Delta\nu\frac{1-\exp(-dfX)}{1+dfX}, \quad (21)$$

where the temperature function (ϑ) is given by

$$\vartheta(T) = \left(\frac{s}{T}\right)^2 \frac{\exp(s/T)}{[\exp(s/T) - 1]^2}, \tag{22}$$

and $s = hc\nu_{ave}/k_B$. Materials with absorption bands do not follow the T^3 law of Clark (1957). The next section calculates $\vartheta(T)$ for mantle conditions.

Zeros exist in the derivative of Equation 21 taken with respect to concentration:

$$\frac{\partial[\ln(k_{rad})]}{\partial X} = \frac{df}{[\exp(dfX) - 1]} - \frac{df}{(1 + dfX)}. \tag{23}$$

Equation 23 combined with k_{rad} being positive requires that maxima occur in k_{rad} with X. Given the form of Equations 21 and 23, maxima could also occur in k_{rad} with d. This analysis agrees with the asymptotic behavior of k_{rad} (Section 3.2.2).

To summarize, k_{rad} depends largely on how dark (i.e., Fe-rich) or how pale (i.e., very Fe-poor) individual grains are, more than on the specific spectrum possessed by a given mineral phase. Because completely opaque minerals do not transfer radiation, very Fe-rich minerals have low k_{rad}. Very Fe-poor minerals have low k_{rad} because these are poor emitters, and thus k_{rad} has a maximum at moderate [Fe^{2+}].

3.3 Results

3.3.1 Temperature behavior of k_{rad}

Figure 4 shows that ϑ monotonically increases with T for relevant band positions. The function climbs rapidly near $\sim$ 1500 K for the bands clearly due to d-d transitions of Fe^{2+}, is roughly linear over mantle temperatures, and flattens as T becomes very high. The dependence of s on ν_{ave} means that over mantle temperatures, the d-d transitions in perovskite provide $\vartheta(T)$ that is larger by a factor of 10 over $\vartheta(T)$ for the high frequency band (Fig. 3). Post-perovskite should behave the same.

Figure 4 shows that the temperature component of k_{rad} does not follow the T^3 law for materials with absorption bands. Over the temperature range shown, $\vartheta(T)$ can be fit to a second or third order polynomial, depending on the value of s. Similar behavior was seen for k_{rad} computed for olivine at small d using Equation 13 (Hofmeister, 2005). This correspondence is expected as Equation 22 was derived by assuming that dA is not so large that opacity occurs near ν_{ave}.

3.3.2 Grain size and Fe content dependence of k_{rad}

Calculation of k_{rad} from Equation 21 using the parameters in Table 2 provides approximate values because (1) Fe^{2+} bands are broad, not narrow and (2) surface reflectivity, which can cause opacity for high absorbance, is not accounted for. Large peak breadth contributes some errors, but the amount should be independent of d or X. For low values of absorbance = $dA \propto dX$, the results should be accurate, since opacity is unlikely. For some large value of dA (i.e., of dX), light is not transmitted at frequencies near the center of the peak and this frequency interval should not have been

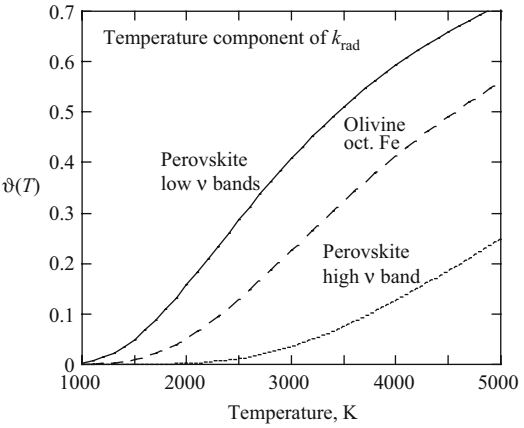

Figure 4. Dependence of ϑ (Eq. 22) on temperature. Three values of s are as follows: $\nu_{ave} = 7138$ cm^{-1} for the d-d transitions of Fe^{2+} in perovskite give $s = 21,870$ K; $\nu_{ave} = 9444$ cm^{-1} for octahedrally coordinated Fe^{2+} [olivine which proxies for (Mg,Fe)O] gives $s = 13,589$ K; and $\nu_{ave} = 15,200$ cm^{-1} for the third band in perovskite gives $s = 21,870$ K. At lower mantle temperatures ($\sim$2000–3000 K), the contribution to k_{rad} from high frequency bands is small, <10%.

Table 2. Spectral properties

	Pv low ν	Olivine	Pv high ν
X, mole%	0.06	0.10	0.06
A_{max}, cm^{-1}	35	8	24
ν_{ave}, cm^{-1}	7138	9444	15,200
$\Delta\nu$, cm^{-1}	3000	2500	6000
n	1.73	1.65	1.73
f, cm^{-1}	290	40	200

included in the integral. As dX increases, the frequency interval becomes larger. Thus, for larger and larger dX, k_{rad} is overestimated. This behavior will affect the trends with d and X.

If the high ν band of perovskite is intrinsic, then the corresponding $\vartheta(T)$ is 1/10th the value calculated for the low ν bands. The remaining components of k_{rad} (cf. Eqs. 21 and 22) depend on ν_{ave}, $\Delta\nu$, d and X. Because the strengths of the d-d transitions and the charge transfer bands in perovskite with high spin Fe^{2+} are essentially the same, the results in Figure 5, lower panels, need only be scaled to account for difference in ν_{ave}, $\Delta\nu$, and $\vartheta(T)$. The results in Figure 5 should be multiplied by 1.9 to provide the total k_{rad} of perovskite. I assume that ppv behaves the same.

Maxima exist in k_{rad} as a function of Fe content (Fig. 5, right-hand side). The position of the maxima depends on the grain size, due to the k_{rad} being a function of the product dX (Eq. 21). Because perovskite has a stronger absorption coefficient

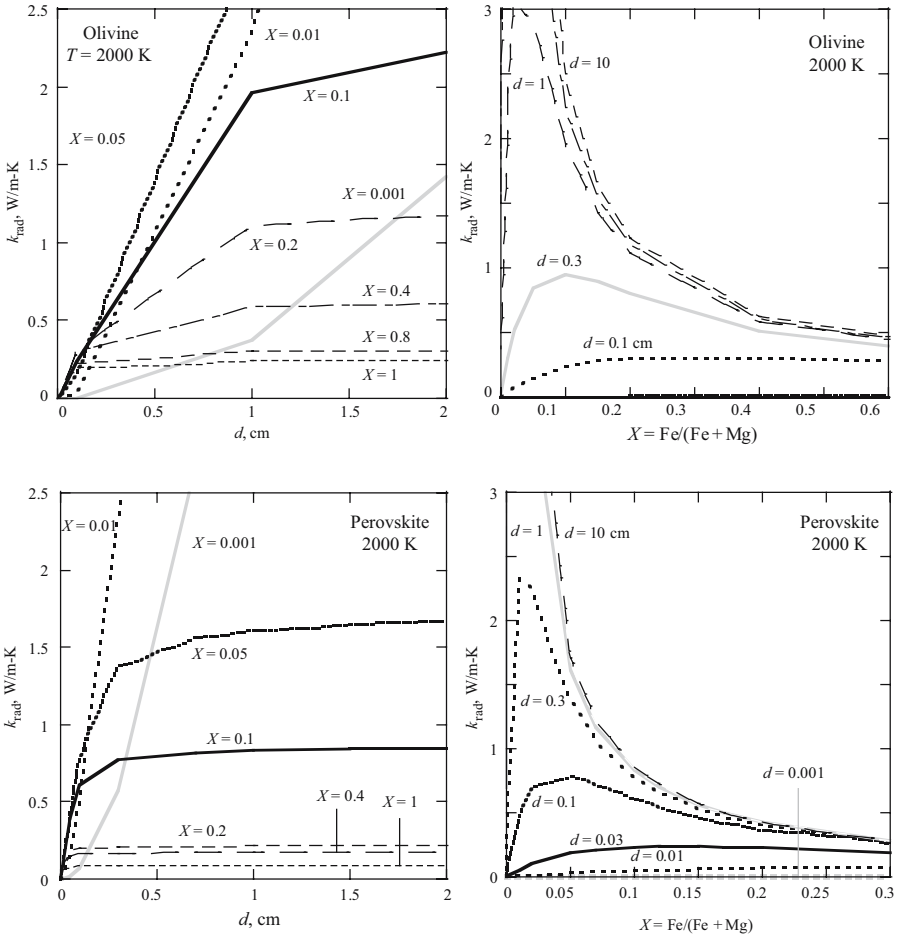

Figure 5. Dependence of $k_{\rm rad}$ (Eq. 21) on d (left panels) and X (right panels). Note difference in axis scales. Curves are labeled with the values of X or d. Upper panels show olivine. Lower panels show perovskite calculated using only the low ν band.

than olivine (i.e., f is larger, Eq. 20), its maxima occur at lower values of X (right panels, Table 3). For most values of d and X, $k_{\rm rad}$ of perovskite is larger than that of olivine, mostly connected to its larger A values. Values of $k_{\rm rad}$ at large dX are overestimated. Accounting for surface reflectivity would sharpen the maxima, but its position should not be affected. At very large dX, the curves would cross, i.e., the $d = 10$ cm curve would approach $k_{\rm rad} = 0$ at smaller X than the $d = 2$ cm curve.

At low concentrations of Fe, $k_{\rm rad}$ increases strongly with grain-size (Fig. 5, left-hand side). For all but the lowest concentrations, a constant value is obtained above about $d = 1$ cm for olivine and above about $d = 0.5$ cm for perovskite. Specifically,

Table 3. Maxima in perovskite k_{rad}

d, cm	X_{max}, Fe/(Mg + Fe)
10	0.001
1	0.01
0.5	0.013
0.1	0.05
0.03	0.12
0.01	0.38

the plateau occurs at d values that inversely correlate with $X = \mathrm{Fe}/(\mathrm{Fe} + \mathrm{Mg})$, i.e., at $X = 0.1$, the plateau is at 0.5 cm whereas at $X = 0.2$, the plateau occurs at $d = 0.2$ cm. The plateau exists because k_{rad} is overestimated at large dX. Instead, a maximum is expected, such that the grain-size where the maximum occurs would decrease as X increases.

3.3.3 Low spin iron

Spectra of silicates with low spin Fe^{2+} are unavailable to the best of our knowledge. However, transformation from the high to low spin state should eliminate the d-d transitions at low ν, but some of the high frequency bands, i.e., transitions to spin-forbidden states, will remain. For perovskite, the band at 15,200 cm^{-1} will disappear if this is a d-d transition, but will remain if it involves Fe^{2+}-Fe^{3+} charge transfer.

If perovskite does indeed have charge transfer, then the low spin state will have $\vartheta(T)$ that is $1/10^{th}$ the value calculated for the d-d transitions of high spin Fe^{2+}. The remaining components of k_{rad} (cf. Eqs. 21 and 22) depend on ν_{ave}, $\Delta\nu$, d and X. Because strengths of the low and high ν bands are essentially the same, the results in Figure 5 for the low ν, d-d bands need only be scaled. From Table 2, the results for high spin perovskite in Figure 5 should be multiplied by 0.9 to depict the low spin state. If charge transfer exists, thermal conductivity is decreased only by a factor of 2 by the spin state transformation, and the shape of the curves, i.e., $k_{rad}(X)$, remains the same.

If the band at 15,200 cm^{-1} is instead the third d-d transition in high spin perovskite, then the low spin state will consist of a UV tail and some weak absorptions in the visible region. Spin forbidden bands are $\sim 1/100^{th}$ the intensity of d-d transitions in the high spin state, and also have much narrow widths which may change f. As a first approximation, widths should be $1/100^{th}$ that of the d-d bands. Frequencies would resemble the high ν band in Table 2. The Y-axis in Figure 5 would therefore be scaled down by a factor of $\sim 1/100^{th}$ to account for the change in s and ϑ. From Equation 20, the X values should be multiplied by a large factor, on the order of 100, to account for lower absorbance. In summary, values of thermal conductivity would be much lower in the high spin state, and the maximum in X is shifted to near the iron end-member, if the high spin spectrum consists only of d-d transitions.

Badro et al. (2004) reached the opposite conclusion that $k_{\rm rad}$ is large for the low spin state of Fe^{2+} owing to its low A values. They neglected to account for the effect of grain-size on radiative transfer (Hofmeister, 2005). To the contrary, the effect of scattering is very strong at low A (Eq. 13) causing $k_{\rm rad}$ to be small for pale materials, including those with low spin Fe^{2+}. This behavior is clear from the asymptotic limit (Eqs. 14 or 16), or by simply considering the size of the mean free path $= d/(1 + dA) \sim d$.

4 DISCUSSION AND CONCLUSIONS

4.1 Summary of lower mantle heat transport properties

Heat transfer in the deepest mantle is connected with mantle convection processes, including the generation and maintenance of plumes. Thermal conductivity (or diffusivity) influences mantle convection models even in the presence of a strongly temperature dependent viscosity (van den Berg et al., 2004; Yanagawa et al., 2005). Providing exact values of k or D for the lower mantle is not currently feasible due to lack of suitable samples, difficult to attain temperatures, and uncertainties in physical properties used to compute k or D. Problems include the chemical composition not being well-constrained because few mantle samples originate near 670 km and nothing has emerged from greater depths (Gasparik, 2000), and because modeling seismic velocity distribution is equivocal due to tradeoffs in T, chemical composition, and phase (Deschampes and Trampart, 2003). Grain-size is crucial, but is also not well-constrained (Ranalli, 2001). Growth is retarded by shear forces arising during flow, which disrupts and deforms the large grains. Yet, grain growth is promoted by high temperatures and slow motions.

Despite the above problems, the phonon contribution is fairly well constrained. Lower mantle conditions are above $T_{\rm C}$, and thus D (or $k_{\rm lat}$) is independent of temperature (Fig. 1), but increases with pressure (Eq. 9; also see Hofmeister, 2007). The large values in Table 1 allow for the high pressure in the deepest mantle. The bulk modulus and thermal Grüneisen parameters of perovskite and ppv are similar, so the pressure effects are similar. Moreover, changes with pressure are relatively unimportant since it is feedback through the temperature equation that strongly influences mantle convection (Dubuffett et al., 2002). However, $k_{\rm lat}$ increasing upon transformation from perovskite to post-perovskite (Table 1) provides positive $\partial k_{\rm lat}/\partial T$, if this transition is spread over sufficient depth that the temperature changes significantly. This exception is important because the positive derivative promotes stability (Dubuffett et al., 2002). Other gradual phase transformations (excepting spin states) and changes in chemical composition could similar provide thermal gradients in the lattice contribution. Although the trends are clear, the absolute value of D is not, due to variation in the dependence of saturated values on lattice constant (Fig. 2).

Diffusion of radiation should largely govern heat transfer in the lower mantle due to its strong dependence on T (Eqs. 13, 21; Fig. 4) which occurs over great depths. Constraining $k_{\rm rad}$ can be difficult owing to its sensitivity to phase, and strong

dependence on chemical composition and grain size (Eq. 13, Fig. 5). Therefore, the mantle is represented by an approximate analytical solution to Equation 13 that is derived in terms of composition and only loosely connected to spectral parameters (Eq. 21). In lieu of spectral data, post-perovskite is assumed to behave the same as perovskite. The absolute values of $k_{\rm rad}$ are uncertain, although the trends are fairly well constrained. Salient features are that $k_{\rm rad}$ depends roughly linearly on T in the lower mantle, and that maxima in $k_{\rm rad}$ occur as a function of $X = {\rm Fe}/({\rm Fe} + {\rm Mg})$ such that the position depends on the grain-size. A broad maximum exists in $k_{\rm rad}$ as a function of d, and its position depends on X. For a maximum to occur at $X = 0.1$, compositions found in the upper mantle, $d \sim 0.3$ mm in the lower mantle (Fig. 5). Similar behavior, but lower values of $k_{\rm rad}$ are expected for the low spin state, such that X of the maximum is shifted towards the Fe end-member. Radiative transfer is weakened by this transition due to the effect of grain-size shortening the mean free path.

4.2 Implications of deepest mantle heat transfer on plumes

As shown by Matyska and Yuen (2005) radiative heat transfer is important in allowing large lower-mantle plumes to develop in the presence of the post-perovskite phase transition. The simple approach taken here considers, as a guideline for plume formation, the overall stability of the core-mantle boundary layer as indicated by the findings of Dubuffett et al. (2002) and the variable nature of thermal conductivity. Plumes are promoted by instabilities: for example, grains with lower thermal conductivity will retain heat and become buoyant. The temperature derivatives play an even more important role, as shown by Yuen and collaborators.

Thermal conductivity due to lattice vibrations in the layer just above the core-mantle boundary appears to be large, due to the combined effects of pressure, large lattice constants, and the transition from pv to ppv, all of which stabilize against convection. However, increasing Fe content decreases $k_{\rm lat}$ (Hofmeister, 2005) and thus decreases stability (promotes convection). This effect is less important, however, than radiative transport which is strongly temperature dependent, positive and thus quite stabilizing. Transition to the low spin state at moderate to high Fe content would increase $k_{\rm rad}$ (if d is unchanged), contributing to stability. However, transition to the low spin state at low Fe content (if d is unchanged) decreases stability because $k_{\rm rad}$ is reduced. Irrespective of the spin state, increasing grain-size increases $k_{\rm rad}$ and contributes to stability, up to a certain d, which depends on X, such that large d and X are destabilizing.

Thus, whether conditions in the core-mantle boundary layer are or are not conducive to plume formation depends on many variables. Plume formation is most likely under destabilizing conditions of large grains (which can actually be small for high Fe^{2+} content, Fig. 5), or very, very small grains, low to moderate Fe contents for low spin iron, or moderate to high contents for high spin iron. Higher degrees of solid solution (e.g., Al or Ca along with Fe in perovskite) would also favor plume formation.

If conditions in the core-mantle boundary layer have evolved to maximize radiative transfer, then provision of additional Fe^{2+} from the core has implications on plume

formation, as discussed by Hofmeister and Yuen, in review) and summarized here. The decrease in k_{rad} at large d, due to finite surface reflectivity and the decrease in k_{rad} as Fe content increases (Fig. 5) suggest that positive feedback exists. Let us assume that the ultralow velocity zone adjacent to the core provides a source of Fe ions. Then, in the boundary layers, flow is slow which allows grain-growth to proceed. The slowest regions within the boundary layers are stagnation points where upwellings (e.g., plumes) would form. Not only does grain growth in the stagnant regions aid incorporation of new, Fe^{2+}-rich material, but moreover, increased grain-size means that very little increase in Fe^{2+} content is needed to reduce radiative transfer and increase buoyancy. Such positive reinforcement suggests that small changes in Fe content or grain size could initiate the process. Whereas grain growth and Fe enrichment work together to initiate the process, it is the connection of reduced viscosity with Fe content which provides the feedback loop which sustains plume development. Feedback can occur regardless of the spin state of Fe ions, but stability of the low-spin state requires higher concentrations and larger grain-sizes to operate.

The above proposal of Hofmeister and Yuen (under review) addresses the seemingly contradictory result of Trampert et al. (2004) which associates high Fe contents with lower mantle underlying the central Pacific, regions thought to be hotter than ambient due to the density being lower. The existence of thermo-chemical plumes (Yuen et al., 1993; Ishii and Tromp, 1999) engendered by iron enrichment further suggests both chemical differentiation of the lower mantle, and a density stratification consistent with layered convection. Evidence for decoupling of the lower and upper mantle systems is summarized by Hamilton (2003), Anderson (2002), and Foulger et al. (2005).

ACKNOWLEDGEMENTS

Support was provided by NSF EAR 0132275 and 0206121.

REFERENCES

Anderson, D.L. (2002) The case for irreversible chemical stratification of the mantle. *Int. Geol. Rev.*, 44, 97–116.

Anderson, O.L., and D.G. Isaak (1995) Elastic constants of mantle minerals at high temperature. In Ahrens, T.J. (ed.) A Handbook of Physical Constants, American Geophysical Union, Washington D.C., pp. 64–96.

Andre, S., and A. Degiovanni (1995) A theoretical study of the transient coupled conduction and radiation heat transfer in glass: Phonic diffusivity measurements by the flash technique. *Int. J. Heat. Transfer.*, 38, 3401–3412.

Bass, J.D. (1995) Elasticity of minerals, melts, and glasses. In Ahrens, T.J. (ed.) A Handbook of Physical Constants, American Geophysical Union, Washington D.C., pp. 45–63.

Blumm, J., J.B. Henderson, O. Nilson, and J. Fricke (1997) Laser Flash measurement of the phononic thermal diffusivity of glasses in the presence of ballistic radiative transfer. *High Temp. High Press.*, 29, 555–560.

Blumm, J., and S. Lemarchand (2002) Influence of test conditions on the accuracy of laser flash measurements. *High Temp. High Press.*, 34, 523–528.

Braeuer, H., L. Dusza, and B. Schulz (1992) New laser flash equipment LFA 427. *Interceram.*, 41, 489–492.

Branlund, J., M.C. Kameyama, D.A. Yuen, and Y. Kaneda (2000) Effects of temperature-dependent thermal diffusivity on shear instability in a viscoelastic zone: Implication for faster ductile faulting and earthquakes in the spinel stability field. *Earth Planet. Sci. Lett.*, 182, 171–185.

Brewster, M.Q. (1992) Thermal Radiative Transfer and Properties, John Wiley and Sons, Inc., New York.

Buettner, R., B. Zimanowski, J. Blumm, and L. Hagermann (1998) Thermal conductivity of a volcanic rock material (olivine-melilitite) in the temperature range between 298 and 1470 K. *J. Volcan. Geothermal. Res.*, 80, 293–302.

Burns, R.G. (1982) Electronic spectra of minerals at high pressures: How the mantle excites electrons. In Schreyer, W. (ed.) High-Pressure Researches in Geoscience, E. Schweizerbartsche Verlag, Stuttgart, pp. 223–246.

Clark, Jr., S.P. (1957) Radiative transfer in the Earth's Mantle. *Trans. Am. Geophys. Union*, 38, 931–938.

Debye, P. (1914) Vortrage über die kinetische Theorie der Materie und der Electriztät. B.G. Teuber, Berlin, pp. 1–196.

Deschamps, F., and J. Trampert (2003) Mantle topography and its relation to temperature and composition. *Phys. Earth Planet. Inter.*, 140, 277–291.

Dubuffet, F., D.A. Yuen, and E.S.G. Rainey (2002) Controlling thermal chaos in the mantle by positive feedback from radiative thermal conductivity. *Nonlinear Proc. Geophys.*, 9, 1–13.

Dugdale, J.S., and D.K.C. MacDonald (1955) Lattice thermal conductivity. *Phys. Rev.*, 98, 1751–1752.

Dziewonski, A.M., and D.L. Anderson (1981) Preliminary reference Earth model. *Phys. Earth Planet. Int.*, 25, 297–356.

Evans, A. (1992) The Dusty Universe, Ellis Horwood, New York, pp. 1–236.

Foulger, G.R., J.H. Natland, D.C. Presnall, and D.L. Anderson (2005) Melting Anomolies: Their Nature and Origin, Geological Society of America, Boulder Colorado, USA, pp. 1–881.

Fujisawa, H., N. Fujii, H. Mizutani, H. Kanamori, and S. Akimoto (1968) Thermal diffusivity of Mg_2SiO_4, Fe_2SiO_4, and NaCl at high pressures and temperatures. *J. Geophys. Res.*, 75, 4727–4733.

Gasparik, T. (2000) Evidence for the transition zone origin of some [Mg,Fe]O inclusions in diamonds. *Earth Planet. Sci. Lett.*, 183, 1–5.

Geisting, P.A., A.M. Hofmeister, B. Wopenka, G.D. Gwanmesia, and B.L. Jolliff (2004) Thermal conductivity and thermodynamic properites of majorite: Implications for the transition zone. *Earth Planet. Sci. Lett.*, 218, 45–56.

Gerbault, M. (2000) At what stress level is the central Indian Ocean lithosphere buckling? *Earth Planet. Sci. Lett.*, 178, 165–181.

Giesting, P.A., and A.M. Hofmeister (2002) Thermal conductivity of disordered garnets from infrared spectroscopy. *Phys. Rev.*, B65, website paper # 144305 (15 pages).

Hamilton, W.B. (2003) An alternative Earth. *GSA Today*, 13, 2–4.

Hapke, B. (1993) Theory of Reflectance and Emittance Spectroscopy, Cambridge University Press, Cambridge, pp. 1–455.

Henderson, J.B., F. Giblin, J. Blumm, and L. Hagemann (1998) SRM 1460 series as a thermal diffusivity standard for laser flash instruments. *Int. Jour. Thermophysics*, 19, 1647–1656.

Hofer, M., and F.R. Schilling (2002) Heat transfer in quartz, orthoclase, and sanidine at elevated temperature. *Phys. Chem. Mineral.*, 29, 571–584.

Hofmann, R., O. Hahn, F. Raether, H. Mehling, and J. Fricke (1997) Determination of thermal diffusivity in diathermic materials by the laser-flash technique. *High Temp. High Press.*, 29, 703–710.

Hofmeister, A.M. (1999) Mantle Values of Thermal Conductivity and the Geotherm from Phonon Lifetimes. *Science*, 283, 1699–1706.

Hofmeister, A.M. (2001) Thermal conductivity of spinels and olivines from vibrational spectroscopy at ambient conditions. *Am. Mineral.*, 86, 1188–1208.

Hofmeister, A.M. (2004a) Enhancement of radiative transfer in the mantle by OH- in minerals. *Phys. Earth Planet. Inter.*, 146, 483–485.

Hofmeister, A.M. (2004b) Thermal conductivity and thermodynamic properties from infrared spectroscopy. In King, P., M. Ramsey, and G. Swayze (eds.) Infrared Spectroscopy in Geochemistry, Exploration Geochemistry, and Remote Sensing, Mineralogical Association of Canada, Ottawa, Ontario, pp. 135–154.

Hofmeister, A.M. (2004c) Physical properties of calcium aluminates from vibrational spectroscopy. *Geochim. Cosmochim. Acta.*, 68, 4721–4726.

Hofmeister, A.M. (2005) The dependence of radiative transfer on grain-size, temperature, and pressure: Implications for mantle processes. *J. Geodynamics*, 40, 51–72.

Hofmeister, A.M. (2006) Thermal diffusivity of garnets at high temperature. *Phys. Chem. Mineral.* 33, 45–62.

Hofmeister, A.M. (2007) Pressure dependence of thermal transport properties. Proceedings of the National Academy of Science, doi: 10.1073/pnas.0610734104.

Iitaka, T., K. Hirose, K. Kawamura, and M. Murakami (2004) The elasticity of the MgSiO3 post-perovskite phase in the Earth's lowermost mantle. *Nature*, 430, 442–445.

Ishii, M., and J. Tromp (1999) Normal-mode and free-air gravity constraints in lateral variations of velocity and density in Earth's mantle. *Science*, 285, 1231–1236.

Julian, C.L. (1965) Theory of heat conduction in rare-gas crystals. *Phys. Rev.*, A137, 128–137.

Kachare, A., G. Andermann, and L.R. Brantley (1972) Reliability of classical dispersion analysis of LiF and MgO reflectance data. *J. Phys. Chem. Solids*, 33, 467–475.

Kanamori, H., N. Fujii, and H. Mizutani (1968) Thermal diffusivity measurement of rock-forming minerals from 300 to 1100 K. *J. Geophys. Res.*, 73, 595–603.

Kaufmann, R., and W.J. Freedman (2002) Universe, W.H. Freeman, New York.

Keppler, H., C.A. McCammon, and D.C. Rubie (1994) Crystal-field and charge-transfer spectra of $(Mg,Fe)SiO_3$ perovskite. *Am. Mineral.*, 79, 1215–1218.

Keppler, H., and C.A. McCammon (1996) Crystal-field and charge-transfer spectra of $(Mg,Fe)SiO_3$ majorite. *Phys. Chem. Mineral.*, 23, 94–98.

Khomenko, V.M., K. Langer, R. Wirth, and B. Weyer (2001) Mie scattering and charge transfer phenomena as causes of the UV edge in the absorption spectra of natural and synthetic almandine garnets. *Phys. Chem. Mineral.*, 29, 201–209.

Klemens, P.G. (1969) Theory of the thermal conductivity of solids. In Tye, R.P. (ed.) Thermal Conductivity, Academic Press, New York, pp. 1–68.

Lee, D.W., and W.D. Kingery (1960) Radiation energy transfer and thermal conductivity of ceramic oxides. *J. Am. Ceram. Soc.*, 43, 594–607.

Liebfried, G., and E. Schlömann (1954) Warmleitund in elektrische isolierenden Kristallen. *Nach Ges Wissenschaften Goettingen Mathematik und Physik* K1, 71–93.

Mao, W., G. Shen, V.B. Prakapenka, Y. Meng, A.J. Campbell, D.L. Heinz, J. Shu, R.J. Hemley, and H.K. Mao (2004) Ferromagnesian postperovskite silicates in the D″ layer. *Proc. Natl. Acad. Sci.*, 39, 15867–15869.

Matyska, C., and D.A. Yuen (2005) The importance of radiative heat transfer on superplumes in the lower mantle with the new post-perovskite phase change. *Earth Planet Sci. Lett.*, 234, 71–81.

McCammon, C.A., D.C. Rubie, C.R. Ross II, F. Siefert, and HStC O'Neill (1992) Mössbauer study of $^{57}Fe_{0.05}Mg_{0.95}SiO_3$ perovskite at 80 and 298 K. *Am. Mineral.*, 77, 894–897.

Mehling, H., G. Huatzinger, O. Nilsson, J. Fricke, R. Hofmann, and O. Hahn (1998) Thermal diffusivity of semitransparent materials determined by the laser-flash method: Applying a new analytical model. *Int. J. Thermophys.*, 19, 941–949.

Mitra, S.S. (1969) Infrared and Raman spectra due to lattice vibrations. In Nudelman, S., and S.S. Mitra (eds.) Optical Properties of Solids, Plenum Press, New York, pp. 333–452.

Murakami, M., K. Hirose, K. Kawamura, N. Sata, and Y. Ohishi (2004) Post-perovskite phase transition in $MgSiO_3$. *Science*, 30, 855–858.

Oganov, A.R., and S. Ono (2004) Theoretical and experimental evidence for a post-perovskite phase of $MgSiO_3$ in Earth's D″ layer. *Nature*, 430, 445–448.

Parker, J.W., J.R. Jenkins, P.C. Butler, and G.I. Abbott (1961) Flash method of determining thermal diffusivity, heat capacity, and thermal conductivity. *J. Appl. Phys.*, 32, 1679–1684.

Peierls, R.E. (1929) Zur kinetische Theorie der Warmeleitung in Kristallen. *Ann der Physik Leipzig*, 3, 1055–1101.

Peierls, R.E. (1956) Quantum Theory of Solids, Clarendon Press, Oxford, 229pp.

Pertermann, M., and A.M. Hofmeister (2006) Thermal diffusivity of olivine-group minerals. *Am. Mineral.*, 91, pp. 1747–1760.

Pomeranchuk, I. (1943) Heat conductivity of dielectrics at high temperatures. *J. Phys. USSR*, 7, 197–201.

Ranalli, G. (2001) Mantle rheology: Radial and lateral viscosity variations inferred from microphysical creep laws. *J. Geodynam.*, 32, 425–444.

Reif, F. (1965) Fundamentals of Statistical and Thermal Physics, McGraw Hill Book Co., New York, pp. 1–651.

Ross, R.G., P. Andersson, B. Sundqvist, and G. Bäckström (1984) Thermal conductivity of solids and liquids under pressure. *Rep. Prog. Phys.*, 47, 1347–1402.

Rossman, G.R. (1988a) Optical spectroscopy. *Rev. Mineral.*, 18, 207–254.

Rossman, G.R. (1988b) Vibrational spectroscopy of hydrous components. *Rev. Mineral.*, 18, 193–206.

Roufosse, M.C., and P.G. Klemens (1973) Thermal conductivity of complex dielectric crystals. *Phys. Rev.*, B7, 5379–5386.

Roufosse, M.C., and P.G. Klemens (1974) Lattice thermal conductivity of minerals at high temperatures. *J. Geophys. Res.*, 79, 703–705.

Schilling, F.R. (1999) A transient technique to measure thermal diffusivity at elevated temperatures. *Eur. J. Mineral.*, 11, 1115–1124.

Shankland, T.J., U. Nitsan, and A.G. Duba (1979) Optical absorption and radiative heat transport in olivine at high temperature. *J. Geophys. Res.*, 84, 1603–1610.

Smyth, J., and T. McCormick (1995) Crystallographic data for minerals. In Ahrens, T.J. (ed.) A Handbook of Physical Constants, American Geophysical Union, Washington D.C., pp. 1–17.

Spitzer, W.G., R.C. Miller, D.A. Kleinman, and L.W. Howarth (1962) Far–infrared dielectric dispersion in $BaTiO_3$, $SrTiO_3$, and TiO_2. *Phys. Rev.*, 126, 1710–1721.

Tan, H.P., B. Maestre, and M. Lallemand (1991) Transient and steady-state combined heat transfer in semitransparent materials subjected to a pulse or step irradiation. *J. Heat. Transfer*, 113, 166–173.

Taran, M.N., and K. Langer (2001) Electronic absorption spectra of Fe^{2+} ions in oxygen-based rock-forming minerals at temperatures between 297 and 600 K. *Phys. Chem. Minerals*, 28, 199–210.

Trampert, J., F. Deschamps, J. Resovsky, and D.A. Yuen (2004) Probabilistic tomography maps chemical heterogeneities in the lower mantle. *Science*, 306, 853–856.

Tsuchiya, T., J. Tsuchiya, K. Umemoto, and R.M. Wentzcovitch (2004) Phase transition in $MgSiO_3$ perovskite in the earth's lower mantle. *Earth Planet. Sci. Lett.*, 224, 241–248.

Van den Berg, A.P., D.A. Yuen, and E.S.G. Rainey (2004) The influence of variable viscosity on delayed cooling due to variable thermal conductivity. *Phys. Earth Planet Inter.*, 142, 283–295.

Yanagawa, T.K.B., M. Nakada, and D.A. Yuen (2005) The influence of lattice thermal conductivity on thermal convection with strongly temperature-dependent viscosity. *Earth Space. Sci.*, 57, 15.

Yuen, D.A., A.P. Vincent, S.Y. Bergeron, F. Dubuffet, A.A. Ten, V.C. Steinbach, and L. Starin (2000) Crossing of scales and nonlinearities in geophysical processes. In Boschi, E., G. Ekstrom, and A. Morelli (eds.) Problems in Geophysics for the New Millenium, Editrice Compositori, Bologna, Italy, pp. 405–465.

Ziman, J.M. (1962) Electrons and Phonons: The Theory of Transport Phenomena in Solids, Clarendon Press, Oxford (Ch 8 and 11), pp. 1–554.

CHAPTER 11

THERMO-CHEMICAL STRUCTURE OF THE LOWER MANTLE: SEISMOLOGICAL EVIDENCE AND CONSEQUENCES FOR GEODYNAMICS

FRÉDÉRIC DESCHAMPS[1,3], JEANNOT TRAMPERT[1], AND PAUL J. TACKLEY[2]

[1] *Department of Earth Sciences, Utrecht University, Budapestlaan 4, PO Box 80021, 3508 TA Utrecht, The Netherlands;*
E-mail: frederic.deschamps@erdw.ethz.ch

[2] *Department of Earth and Space Sciences, University of California, 595 Charles Young Drive East, Los Angeles, California 90095, USA*

[3] *Now at Institute of Geophysics, Swiss Federal Institute of Technology, HPP Honggerberg L8.1, 8083 Zurich, Switzerland*

Abstract

We combine recent progress in seismic tomography and numerical modeling of thermo-chemical convection to infer robust features on mantle structure and dynamics. First, we separate the observed density anomalies into their thermal and compositional contributions. The tomographic maps of thermo-chemical variations were computed using a new approach that combines a careful equation of state modeling of the lower mantle, independent constraints on density from probabilistic tomography, and a full statistical treatment for uncertainties analyses. We then test models of thermo-chemical convection against these density components. We compute synthetic anomalies of thermal and compositional density from models of thermo-chemical convection calculated with the anelastic approximation. These synthetic distributions are filtered to make meaningful comparisons with the observed density anomalies. Our comparisons suggest that a stable layer (i.e., that no domes or piles are generated from it) of dense material with buoyancy ratio $B \geq 0.3$ is unlikely to be present at the bottom of the mantle. Models of piles entrained upwards from a dense, but unstable layer with buoyancy ratio $B \sim 0.2$, explain the observation significantly better, but discrepancies remain at the top of the lower mantle. These discrepancies could be linked to the deflection of slabs around 1000 km, or to the phase transformation at 670 km, not included yet in the thermo-chemical calculations.

D. A. Yuen et al. (eds.), Superplumes, 293–320.
© 2007 *Springer.*

1 INTRODUCTION

Inferring the thermo-chemical structure of the mantle is a key problem in geophysics. Both thermal and chemical sources contribute to lateral variations in density, and the mode of mantle convection strongly depends on the relative strength of these two sources. It is the goal of seismology to map and quantify these contributions. Although seismic data represent our most detailed information on Earth structure, their interpretation raises difficulties that are often underestimated (Trampert and van der Hilst, 2005). For instance, the low shear-wave velocity structures in the deep mantle observed beneath Africa and the Pacific in many tomographic models (e.g., Su and Dziewonski, 1997; Vasco and Johnson, 1998; Masters et al., 2000) are usually referred to as "superplumes" and interpreted as hotter than average, and hence buoyant material (Forte and Mitrovica, 2001; Romanowicz and Gung, 2002). This interpretation implicitly assumes that shear-wave velocity anomalies are a reasonable proxy for temperature and density. It has been argued that in the uppermost mantle compositional effects do not strongly influence seismic velocity (Goes et al., 2000). In the lower mantle, however, pressure effects reduce the influence of temperature, and compositional effects may dominate seismic velocity anomalies (Anderson, 2001). Moreover, we should not forget that even if chemical anomalies do not significantly contribute to seismic velocity anomalies, they may still contribute to density anomalies, which are the important parameters in terms of dynamics.

Lateral variations of temperature and composition play a key role in linking geophysical observations and geodynamics. In recent years, mounting evidence suggested that chemical variations are present in the lower mantle (Ishii and Tromp, 1999; Kellogg et al., 1999; Forte and Mitrovica, 2001; Karato and Karki, 2001; Saltzer et al., 2001; Deschamps and Trampert, 2003), but difficulties remain to quantify thermo-chemical variations from seismology, and to relate them to thermo-chemical convection. Unless independent constraints on mass density are available, the distributions of temperature and composition inferred from tomographic models are not robust (Deschamps and Trampert, 2003).

Recent progresses shed new light on the link between seismology and geodynamics. Probabilistic tomography (Resovsky and Trampert, 2003) estimated independent and robust constraints on the lateral variations of density and seismic velocities, which can be converted into thermo-chemical variations (Trampert et al., 2004). Models of thermo-chemical convection that include the anelastic (e.g., Tackley, 1998) or extended Boussinesq (e.g., Schott and Yuen, 2004) approximation predict more realistic density contrasts. In this chapter, we investigate the geodynamical consequences of these improvements.

2 DENSITY ANOMALIES FROM THERMO-CHEMICAL CONVECTION

A variety of experimental (Olson and Kincaid, 1991; Davaille, 1999) and numerical (Hansen and Yuen, 1988; Christensen and Hofmann, 1994; Kellogg et al., 1999; Tackley, 1998, 2002; Schott and Yuen, 2004) models of thermo-chemical convection

have been developed, showing strong stratification or a more complex structure, depending on the fluid properties and on the buoyancy ratio. A major improvement was to perform calculations that account for fluid compressibility, either using the anelastic (Tackley, 1998), or extended Boussinesq (Schott and Yuen, 2004) approximation. In these approximations, some dissipation is present, and thermo-chemical properties are allowed to vary with depth through the prescription of a reference model. The decrease of thermal expansion with depth, which is well documented from mineral physics data (e.g., Anderson, 1995), is particularly important because it weakens the thermal buoyancy in the lowermost mantle. As a result, chemical stratification and the development of thermo-chemical domes require a smaller buoyancy ratio than in the classical Boussinesq approximation. The mode of convection is therefore controlled by several key parameters, including the buoyancy ratio, the thermal expansion, and the initial composition. Each convection regime predicts a distribution of temperature and composition that we want to test against seismological observations. In this section, we show how to compute the density variations due to the variations of temperature and composition predicted by several models of thermo-chemical convection (Tackley, 2002).

Details of the numerical modeling are described in Tackley (1998, 2002). The equations of conservation of mass, energy and momentum are solved for an anelastic, compressible fluid with infinite Prandlt number. Calculations are made in a 3-D Cartesian box of dimensions $4 \times 4 \times 1$. The fluid is cooled on the top, and heated both from below and from within. The top and bottom boundaries are isothermal, but some cases with zero heat flow at each point (i.e., no bottom heating) have also been considered. The viscosity depends on depth and composition. The viscosity increases smoothly by a factor of 10 across the fluid layer, and an additional viscosity jump equal to 30 is imposed at $z = 660$ km. The dense material is less viscous than the light material by a factor of 100. Calculations involve a depth-dependent reference thermodynamic model (Tackley, 1998), including temperature, density, thermal expansion, and thermal conductivity. The chemical field is represented using 10 million tracer particles dispatched everywhere in the box. Two types of particles are considered, one for regular material, and one for dense material. The fraction of dense particles C in each cell varies between $C = 0$ when the cell is filled with regular material only, and $C = 1$ when the cell is filled with particles of dense material only. The chemical density contrast $\Delta\rho_c^{\max}$ between dense and regular material is acting against the thermal buoyancy due to the thermal density contrast across the fluid layer $\Delta\rho_T^{\max} = \alpha_s \rho_s \Delta T_s$, where α_s and ρ_s are the thermal expansion and density at zero pressure, and ΔT_s the superadiabatic temperature difference between the top and the bottom of the layer. The relative strength of chemical and thermal buoyancies is measured by the global buoyancy ratio

$$B \equiv \frac{\Delta\rho_c^{\max}}{\alpha_s \rho_s \Delta T_s}, \tag{1}$$

which is used to define the chemical Rayleigh number.

The density at temperature T and regular material ($C = 0$) can be computed using the depth-dependent reference state (temperature T_{ref} and thermal expansion α_{ref}),

$$\rho_T = \rho_{\text{ref}}[1 - \alpha_{\text{ref}}(T - T_{\text{ref}})]. \tag{2}$$

The density at temperature T_{ref} and fraction of dense material C can be expressed as a function of the buoyancy ratio (Eq. 1),

$$\rho_c = \rho_s[1 + BC\alpha_s\Delta T]. \tag{3}$$

If $\overline{T}$ and $\overline{C}$ are the average temperature and the average fraction of dense particles at a given depth, the relative thermal and chemical density anomalies are

$$\mathrm{d}\ln\rho_T = -\frac{\alpha_{\text{ref}}(T - \overline{T})}{[1 - \alpha_{\text{ref}}(\overline{T} - T_{\text{ref}})]}, \tag{4}$$

$$\text{and} \quad \mathrm{d}\ln\rho_c = -\frac{B(C - \overline{C})}{(1 + B\overline{C}\alpha_s\Delta T)}\alpha_s\Delta T_s. \tag{5}$$

We computed synthetic $\mathrm{d}\ln\rho_T$ and $\mathrm{d}\ln\rho_c$ for four numerical models with buoyancy ratio equal to 0.2, 0.3 or 0.4 and percentage of dense material equal to 10% or 30% (Table 1). The bottom boundary is isothermal in all cases, except for $B = 0.4$, $X = 10\%$, in which the heat flow is put to zero everywhere on the boundary. Calculations were initialized with a geotherm from similar 2-D calculations that have reached a secular equilibrium. The models we tested are snapshots representative of long-term evolution, and the dimensional evolution times are listed in Table 1. Figure 1 shows isosurfaces of the fraction of dense particles and the non-dimensional temperature, and Figure 2 shows $\overline{T}, \overline{C}$, and the root mean square (RMS) of $\mathrm{d}\ln\rho_T$ and $\mathrm{d}\ln\rho_c$ as a function of depth. For $B = 0.3$, $X = 30\%$, a thick (~ 500 km) stable layer of dense and hot material sediments at the bottom of the fluid (Fig. 1, plots i–l). The RMS of $\mathrm{d}\ln\rho_T$ and $\mathrm{d}\ln\rho_c$ (Fig. 2, green curves) indicate that this layer is thermally and chemically homogeneous, and that most of the lateral variations of temperature and composition are located between 1600 and 2400 km. In the case $B = 0.4$, $X = 10\%$, a stable layer is also present at the bottom of the fluid, but it is much thinner and does not completely cover the bottom boundary (Fig. 1, plots m–p). The Strongest lateral variations of thermal and chemical density are found

Table 1. Four models of thermo-chemical convection[a]

B	X (%)	t (Gy)	Bottom boundary condition	Convective pattern
0.2	10	1.1	Isothermal	Piles
0.3	10	6.0	Isothermal	Discontinuous spokes
0.3	30	2.7	Isothermal	Thick stable layer
0.4	10	4.2	Zero heat flux at each point	Thin stable layer

[a] B is the buoyancy ratio, X the fraction of dense material and t the evolution time.

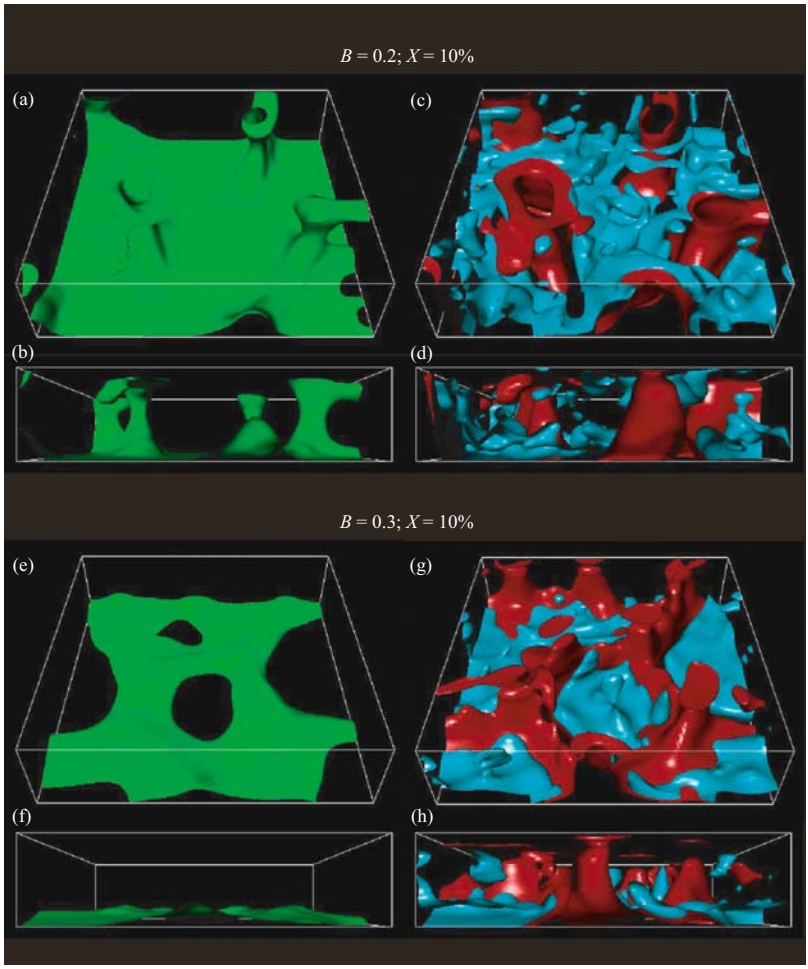

Figure 1. Isosurfaces of non-dimensional temperature (red and blue) and fraction of dense particles (green) for thermo-chemical convection models for various buoyancy ratios (B) and fractions of dense particles (X). Contour levels are $T = 0.0375$ (red), $T = -0.0375$ (blue), and $C = 0.5$ (green). The cases considered are (a–d) $B = 0.2$ and $X = 10\%$; (e–h) $B = 0.3$ and $X = 10\%$; (i–l) $B = 0.3$ and $X = 30\%$ (green curves); and (m–p) $B = 0.4$ and $X = 10\%$.

between 2500 and 2750 km (Fig. 2, blue curves). For $B = 0.3$, $X = 10\%$, the fluid is organized in a discontinuous spoke pattern of dense and hot material (Fig. 1, plots e–h). Strong lateral variations of density are present from $z = 2400$ km down to the bottom of the fluid (Fig. 2, red curves). Note that the two previous cases do not show significant lateral variations of composition for depths shallower than 2000 km. Finally, for $B = 0.2, X = 10\%$, piles are generated in the deep mantle from

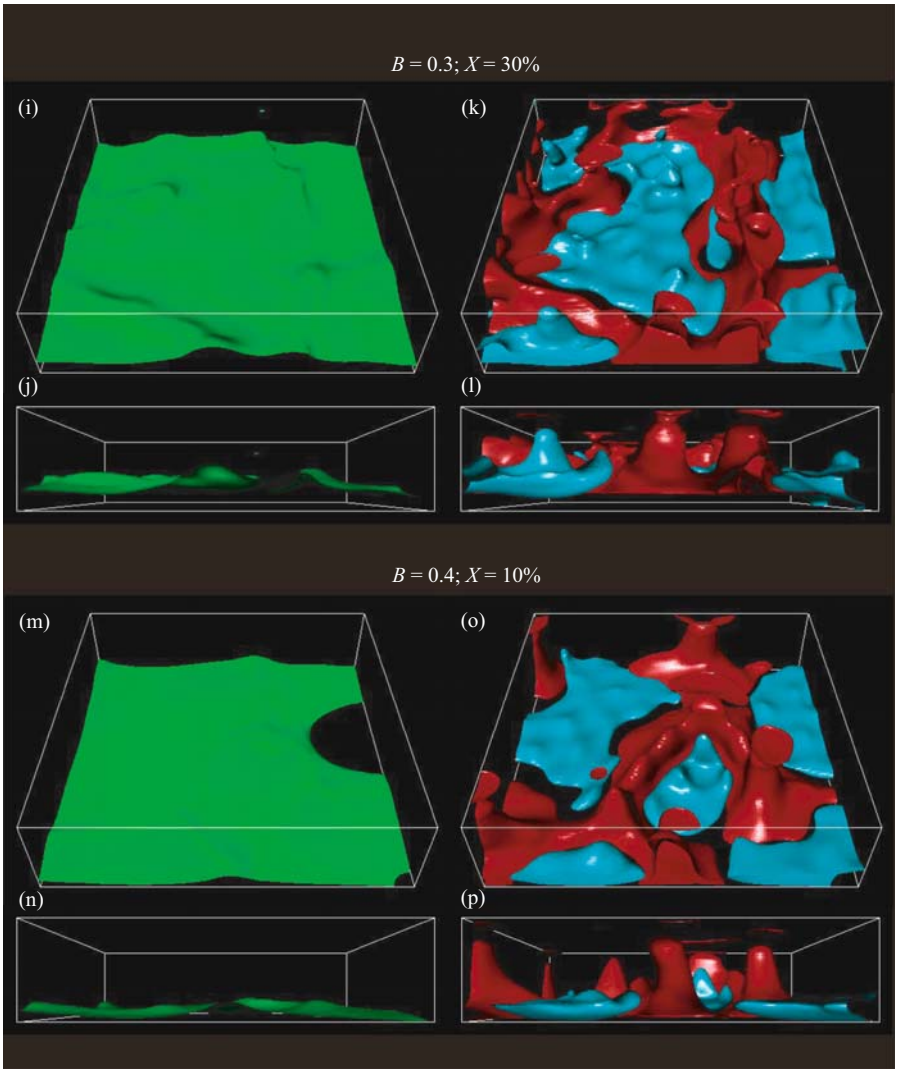

Figure 1. (*Continued*).

a layer of dense material, and are entrained upwards (Fig. 1, plots a–d). Chemical density anomalies are increasing progressively with depth, and drop dramatically to zero in the last 100 km (Fig. 2, orange curve). Some significant variations of density (thermal and chemical) are also observed in the upper half layer of the fluid. It is interesting to note that only this case predicts chemical variations throughout the fluid layer.

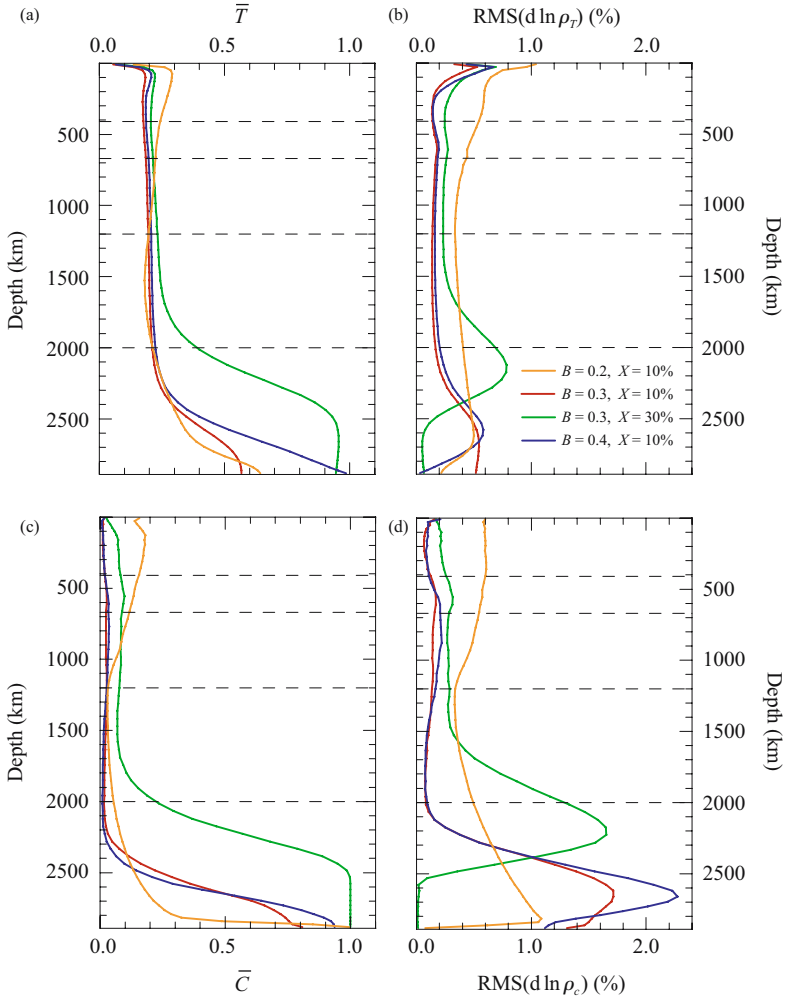

Figure 2. Profiles of (a) average temperature, (b) RMS of lateral variations of thermal density, (c) average fraction of dense particles, and (d) RMS of lateral variations of chemical density, for each model of thermo-chemical convection plotted in Figure 1. Orange curves are for $B = 0.2$ and $X = 10\%$, red curves for $B = 0.3$ and $X = 10\%$, green curves for $B = 0.3$ and $X = 30\%$, and blue curves for $B = 0.4$ and $X = 10\%$.

3 PROBABILISTIC SEISMIC TOMOGRAPHY

Seismic velocities alone cannot resolve the interconnection between temperature and composition. Independent constraints on density anomalies are needed to infer correct variations of temperature and composition. Early constraints on density from normal

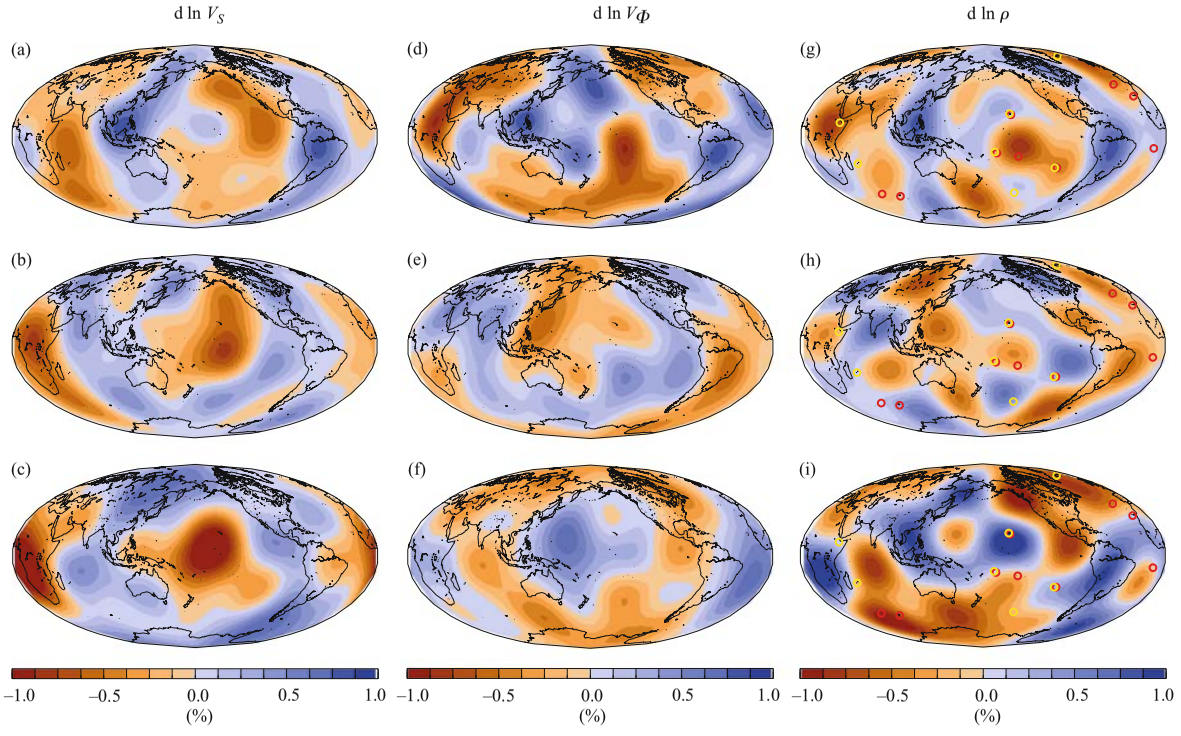

Figure 3. Mean relative anomalies of shear-wave velocity, bulk-sound velocity and density in the lower mantle predicted by probabilistic tomography (Trampert et al., 2004). The lower mantle is parameterized in three layers, from top to bottom $670 \leq z \leq 1200$ km, $1200 \leq z \leq 2000$ km, and $2000 \leq z \leq 2891$ km. Yellow and red dots on density anomalies maps locate hotspots that possibly originate in the deep lower mantle ($z \geq 2000$ km), as identified by Courtillot et al. (2003) and Montelli et al. (2004), respectively.

Table 2. Statistics for tomographic observables and thermo-chemical parameters[a]

Layer (km)		d ln V_S (%)	d ln V_Φ (%)	d ln ρ (%)	dT (K)	dX_{pv} (%)	dFe (%)	d ln ρ_T (%)	d ln ρ_c (%)
670–1200	A	0.77	0.87	0.79	340	11.9	1.8	0.64	0.80
	RMS(σ)	0.16	0.34	0.26	180	5.5	0.75	0.38	0.34
1200–2000	A	0.77	0.57	0.70	311	8.3	1.2	0.41	0.45
	RMS(σ)	0.12	0.22	0.28	112	3.0	0.55	0.15	0.22
2000–2891	A	1.21	0.66	1.05	475	9.3	2.6	0.44	0.95
	RMS(σ)	0.12	0.26	0.48	198	3.6	0.86	0.19	0.37

[a] A is the maximum amplitude of the average model, and RMS(σ) is the root mean square of the uncertainty.

modes were inferred by Ishii and Tromp (1999). More recent studies (Resovsky and Trampert, 2003) have developed the technique of probabilistic seismic tomography, which gives robust likelihoods for long wavelength models (spherical harmonic degree 2, 4, and 6) bulk-sound speed, shear wave speed, density and boundary topography in the mantle, from normal mode splitting and surface wave data. Probabilistic tomography explores the model space using a neighborhood algorithm (Sambridge, 1999a, 1999b) and estimates the likelihood of points in the model space by testing them against observables. The likelihoods of Resovsky and Trampert (2003), hereafter referred to as RT246g, are fully compatible with the observed gravity anomalies, and can thus be seen as a compact representation of the available seismic and gravity data. To a very good approximation, they can be represented as Gaussian distributions, and their standard deviation is remarkably stable within each layer. Figure 3 shows the mean of the distributions for d ln V_S, d ln V_Φ and d ln ρ in each layer, and Table 2 lists the root mean square (RMS) of the uncertainties (defined as one standard deviation around the mean value). In the deepest layer ($2000 \leq z \leq 2891$), there is a general agreement between the d ln V_S, d ln V_Φ of RT246g and those predicted by previous models (Su and Dziewonski, 1997; Vasco and Johnson, 1998; Masters et al., 2000). Like previous studies, RT246g shows regions of low shear-wave velocity beneath Africa and the Pacific. Assuming that d ln V_S scales with lateral variations of temperature, these regions are usually interpreted as "superplumes". However, a quick look to the density anomalies of RT246g (Fig. 3i) clearly shows that these features are denser than the surrounding mantle, and hence not buoyant.

4 LINKING OBSERVABLES TO THERMO-CHEMICAL PARAMETERS

4.1 Sensitivities of density and seismic velocities to temperature and composition

Density and thermo-elastic properties of a lower mantle aggregate depend on temperature, pressure and composition. A careful modeling of these effects is essential to correctly interpret seismological observations. The basic ingredients are the density

and elastic parameters at ambient temperature and pressure, and a set of relations (the equation of state, EOS) that extrapolate these ambient values at mantle temperature and pressure. To calculate thermo-elastic properties at any depth and temperature, we have built a parameterization that combines EOS modeling, experimental values of thermo-elastic parameters at ambient conditions, and existing *ab initio* data calculations (Deschamps and Trampert, 2004). The latter are used to check the consistency of high-temperature and high pressure extrapolations. We are thus able to calculate velocities and density of a given mineralogical composition at mantle pressures and temperatures. Several sources of uncertainties, mainly the error bars on the ambient thermo-elastic parameters and the assumed potential temperature and assemblage composition, contribute to uncertainties on the extrapolated thermo-elastic parameters. The latter are obtained by varying thermo-elastic parameters within their error bars, and average temperature and composition within reasonable range. PREM is used as an additional constraint to reduce the uncertainty range.

By repeating the calculations of elastic moduli and density at high-temperature and high-pressure for slightly different values of temperature and composition, we estimate the partial derivatives (or sensitivities) of density and seismic velocities to temperature and several compositional parameters as a function of depth. The sensitivities plotted in Figure 4 (used in Trampert et al., 2004) account for the most recent corrections for iron (Kiefer et al., 2002; Kung et al., 2002). Compared to previous work (Trampert et al., 2001; Deschamps and Trampert, 2003), sensitivities of shear-wave velocities to composition are different, mainly due to the iron correction for the pressure derivatives of the moduli of magnesio-wüstite (Kung et al., 2002), not included in previous work.

Sensitivities of both shear and bulk sound velocities have similar properties (sign and variation with depth): sensitivities to temperature are negative throughout the mantle and increase with depth; sensitivities to perovskite are positive and decrease with depth; and sensitivities to iron are negative and decrease with depth. A consequence of this similarity is that seismic velocities alone cannot discriminate between thermal and compositional effects. Sensitivities of density (Fig. 4c) are clearly different. The sensitivity to perovskite is negligible, whereas the sensitivity to iron is positive throughout the mantle and increases with depth. Density therefore carries essential information to separate thermal and compositional effects. Another important feature in Figure 4c is that the sensitivity of density to temperature (i.e., the thermal expansion of the aggregate) is decreasing in amplitude with depth. As a consequence, for a fixed temperature anomaly, the strength of the thermal buoyancy is also decreasing with depth.

4.2 Converting density and seismic velocities

Several thermo-chemical sources contribute to the observed anomalies of density and seismic velocities. Knowing the sensitivities of density and seismic velocities

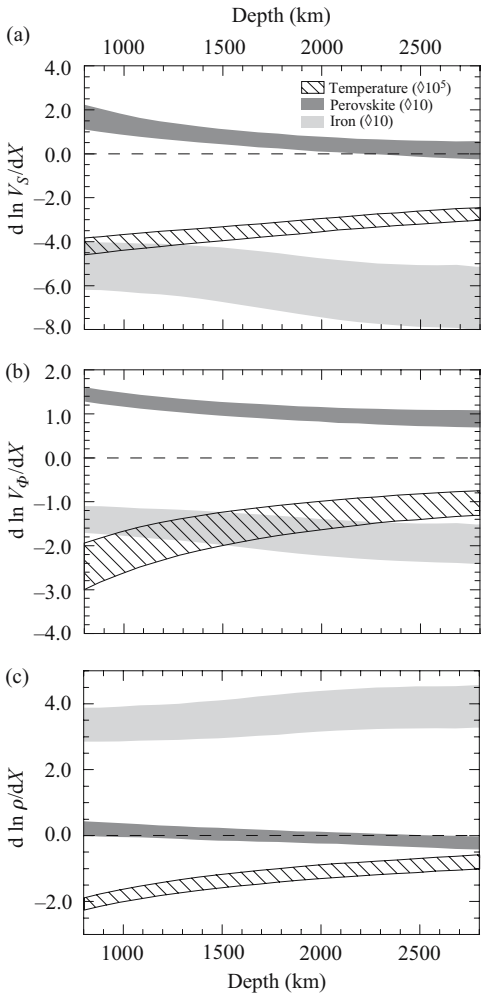

Figure 4. Sensitivities of seismic velocities and density to temperature (dashed areas), perovskite (dark grey areas) and iron content (light grey areas) as a function of depth. Dashed and shaded areas cover one standard deviation around the mean values. Mean and standard deviations are estimated from a collection of possible models that fit PREM within 1%, and are generated by varying thermo-elastic parameters within their error bars, and the average temperature and composition within reasonable ranges. For plotting convenience, sensitivities to temperature are multiplied by 10^5, and sensitivities to perovskite and iron by 10.

to these sources, one can reconstruct synthetic anomalies by adding possible contributions, and compare them to the observed anomalies. A difficulty is to decide which contributions are significant, and which are not. Lateral variations of temperature (dT) are of course a major source. Partial melt is locally generating dramatic

effects, but is limited in extension (Williams and Garnero, 1996) and has therefore limited effects on the global tomography (Deschamps and Trampert, 2003). Compositional (or chemical) variations are a significant contribution, but they consist in a variety of sources that must be treated independently. Since the mantle aggregate consists in a silicate phase (perovskite) and magnesio-wüstite, it is natural to consider the variations in silicate. In the remainder of the chapter, we refer to these variations as variations in the volumetric fraction of perovskite dX_{pv}. In the lower mantle, iron is incorporated in both perovskite and magnesio-wüstite, and induces strong changes in the properties of these minerals. Changes in the elastic moduli (and their derivatives) are moderate for perovskite (Kiefer et al., 2002), but very strong for magnesio-wüstite (Kung et al., 2002). In addition, the density of both perovskite and magnesio-wüstite strongly increases with the iron fraction. Figure 4 clearly shows that the variations in the global volumetric fraction of iron *dFe* strongly contribute to the anomalies of density and seismic velocity. At lower mantle pressure, subducted oceanic crust results in material enriched in calcium compared to average aggregate. If oceanic slabs reach the bottom of the mantle, the fraction of calcium (X_{Ca}) may vary laterally. Calcium is incorporated in perovskite, and induces moderate changes in the elastic properties and very small changes in density. Because in our modeling we considered $CaSiO_3$ as a pole of perovskite, the sensitivities shown in Figure 4 implicitly account for variations in calcium. Practically, however, the differences between these sensitivities and those obtained for $X_{\mathrm{Ca}} = 0$ are not significant. In addition, the sensitivities of density and seismic velocities to calcium are one order of magnitude smaller than those for iron. For these reasons we neglected the contribution of the variations in calcium to the relative anomalies of density and seismic velocities. The fraction of aluminum in perovskite is also expected to vary if subducted crust reaches the lower mantle. The effects of aluminum on the thermo-elastic properties of perovskite are still debated. Jackson et al. (2004) reported important modification in the shear modulus, but no agreement could be found for the bulk modulus (Daniel et al., 2004; Jackson et al., 2004; Yagi et al., 2004). In addition, there are presently no robust estimates for the pressure and temperature derivatives of the elastic moduli. Because the real effects of aluminum are still uncertain, we did not account for them, but potentially they can have a large influence. At first order, it is therefore reasonable to parameterize compositional variations as a function of the variations in perovskite and iron, and the relative anomalies of shear-wave velocity ($\mathrm{d}\ln V_S$), bulk sound velocity ($\mathrm{d}\ln V_\Phi$), and density ($\mathrm{d}\ln \rho$) can be written

$$
\begin{aligned}
\mathrm{d}\ln V_S &= \frac{\partial \ln V_S}{\partial T} dT + \frac{\partial \ln V_S}{\partial X_{pv}} dX_{pv} + \frac{\partial \ln V_S}{\partial Fe} dFe, \\
\mathrm{d}\ln V_\Phi &= \frac{\partial \ln V_\Phi}{\partial T} dT + \frac{\partial \ln V_\Phi}{\partial X_{pv}} dX_{pv} + \frac{\partial \ln V_\Phi}{\partial Fe} dFe, \\
\mathrm{d}\ln \rho &= \frac{\partial \ln \rho}{\partial T} dT + \frac{\partial \ln \rho}{\partial X_{pv}} dX_{pv} + \frac{\partial \ln \rho}{\partial Fe} dFe.
\end{aligned}
\tag{6}
$$

Alternatively, one can use the relative anomalies of compressional-wave velocity ($\mathrm{d}\ln V_P$) instead of $\mathrm{d}\ln V_\Phi$. Equations (6) are the basis for a thermo-chemical interpretation of seismic observations. They can either be used by combining two observables (seismic ratios), or be directly inverted for anomalies of temperature and composition.

5 THERMO-CHEMICAL STRUCTURE: SEISMOLOGICAL EVIDENCES

5.1 First hints from seismic ratios

Several tomographic models based on joint inversion of different seismic data now provide independent constraints on shear and compressive (or bulk sound) velocity anomalies (e.g., Su and Dziewonski, 1997; Kennett et al., 1998; Vasco and Jonhson, 1998; Masters et al., 2000). Seismic ratios combine this information to make a diagnostic of the origin of the observed velocity anomalies. The most commonly used is the ratio of relative shear to compressional velocity anomalies,

$$R_P \equiv \frac{\mathrm{d}\ln V_S}{\mathrm{d}\ln V_P}. \tag{7}$$

Since any scaling $adT + adC$ will result in the same value of R_P, no quantitative information about the amplitude of the variations of temperature (dT) and composition (dC) can be accessed. However, lateral variations of R_P provide clear qualitative evidence for compositional variations in the deep mantle (Master et al., 2000; Saltzer et al., 2001). In a previous study (Deschamps and Trampert, 2003), we showed that a full statistical analysis of the histograms of block-by-block values of R_P provides useful information on the origin of seismic velocity anomalies.

Figure 5 compares histograms predicted by the global model SB10L18 and synthetic histograms computed for several origins of the velocity anomalies using sensitivities from Figure 4. If only temperature variations contribute to the velocity anomalies, the possible ranges of values of R_P are obtained by varying the sensitivities of V_S and V_P to temperature within their error bars. The results (shaded areas) clearly differ from the observed histograms (red curves), which show a strong dispersion at all depths. Accounting for reasonable errors in the tomographic model (Beghein et al., 2002) increases the dispersion in the distribution of R_P (blue curves), but still do not explain the observed dispersion. The observed velocity anomalies can thus not be purely thermal in origin. We also computed distributions of R_P for pure compositional effects, including errors in the tomographic models. For perovskite (green curves), the distributions of R_P have a similar dispersion than for temperature, but peak at smaller values. For iron (orange curves) they are slightly more dispersed than for temperature, and peak at similar values, suggesting that R_P cannot discriminate between temperature and iron variations, hence the need for density information. None of the compositional effects alone can explain

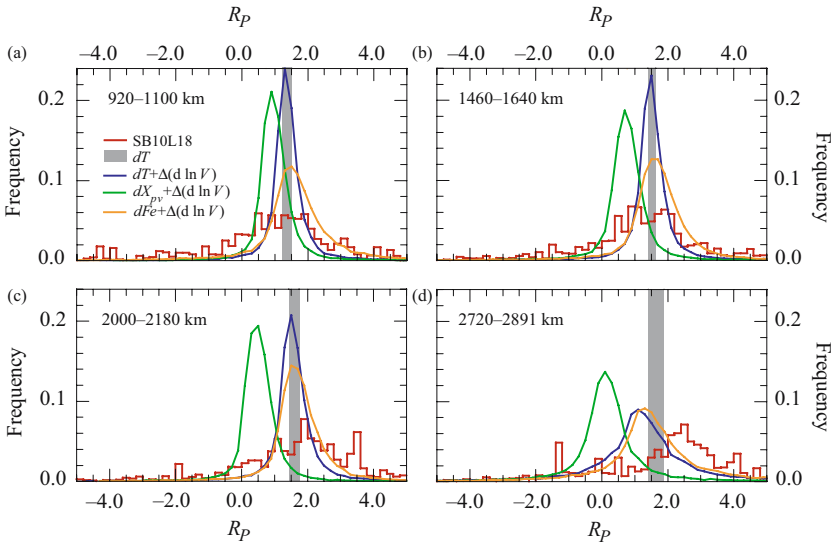

Figure 5. Seismic ratios $R_P = \mathrm{d}\ln V_S/\mathrm{d}\ln V_P$ in the lower mantle. Red curves are block-by-block histograms predicted by SB10L18 (Masters et al., 2000). Dashed areas cover one standard deviation around the mean value obtained for velocity anomalies of a purely thermal origin. Blue curves are obtained by adding simulated errors $\Delta(\mathrm{d}\ln V)$ in the tomographic model to the thermal contribution. Simulated errors have a Gaussian distribution with standard deviation obtained by multiplying the RMS of SB10L18 by the relative error from Beghein et al. (2002). From top to bottom, $\Delta(\mathrm{d}\ln V_S)$ is equal to 2.66×10^{-3}, 1.66×10^{-3}, 1.93×10^{-3}, and 5.84×10^{-3}, and $\Delta(\mathrm{d}\ln V_P)$ is equal to 1.83×10^{-3}, 2.57×10^{-3}, 1.26×10^{-3}, and 3.12×10^{-3}. Green and orange curves are obtained by adding simulated errors $\Delta(\mathrm{d}\ln V)$ to the velocity anomalies due to pure perovskite and pure iron variations, respectively.

the observed histograms, but a combination of thermal and compositional effects might.

Ideally, one would like to vary dT, dX_{pv} and dFe within reasonable ranges, compute associated histograms, and compare them with the observed histograms to decide on bounds for dT, dX_{pv} and dFe that fit the observations best. As noted above, however, combinations of dT, dX_{pv} and dFe that differ by a multiplicative factor give the same value of R_P. While the full histograms of seismic ratios are a good indicator of chemical heterogeneities, a quantitative estimate remains impossible.

5.2 Deterministic inversions of probabilistic seismic tomography

Deterministic inversions of shear-wave and compressional-wave (or bulk-sound) velocity have reported lateral variations of composition in the deep mantle (Forte and Mitrovica, 2001; Deschamps and Trampert, 2003), but a close inspection of the possible sources of uncertainties (including the uncertainties in the sensitivities

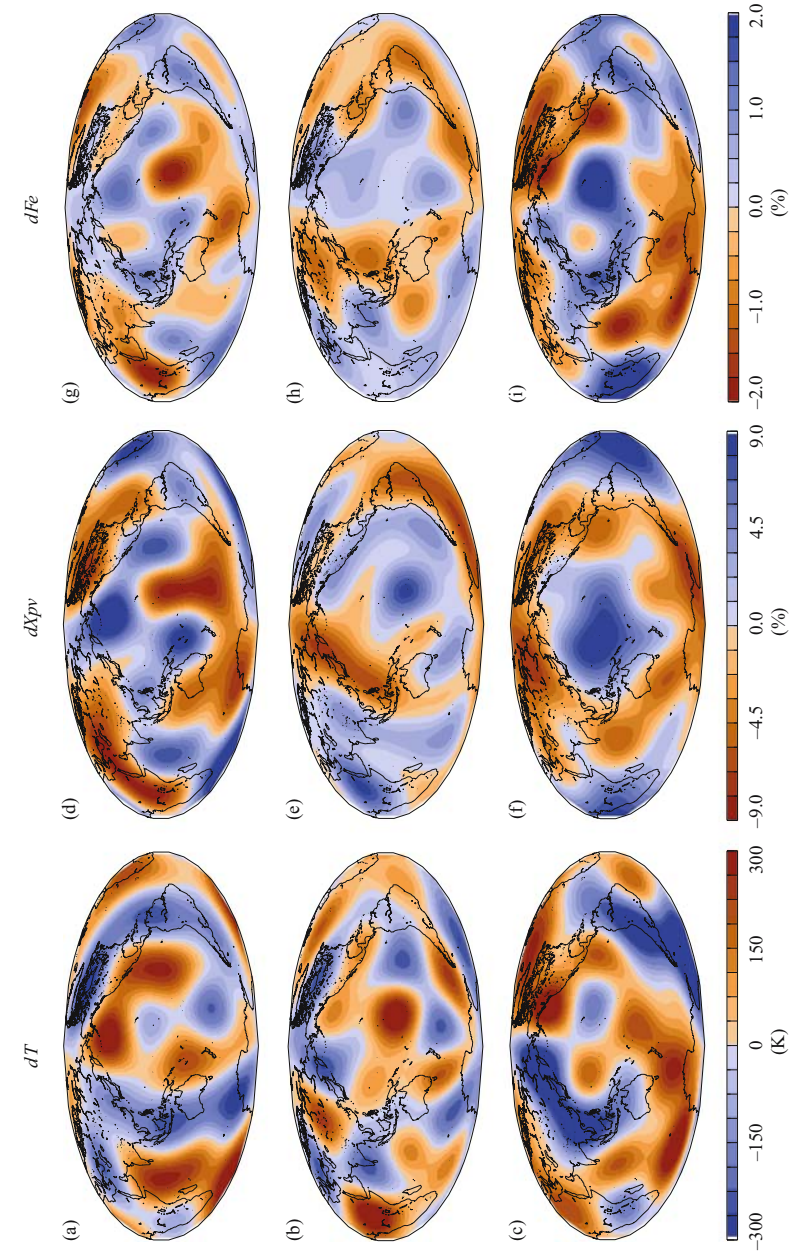

Figure 6. Mean anomalies of temperature, perovskite and iron in the lower mantle derived from Equation 6 and probabilistic seismic tomography (Trampert et al., 2004). The lower mantle is parameterized in three layers, from top to bottom $670 \leq z \leq 1200$ km, $1200 \leq z \leq 2000$ km, and $2000 \leq z \leq 2891$ km.

and reasonable uncertainties in the tomographic model) revealed that these variations are not robust (Deschamps and Trampert, 2003) because of a lack of density information.

In a previous paper (Trampert et al., 2004), we inverted the density and seismic velocity anomalies of RT246g for lateral variations of temperature, perovskite and iron. Since seismic observable and sensitivities are probability density functions, we performed a search that returned likelihoods for anomalies of temperature and composition. Assuming the likelihoods to be Gaussian, they can be represented by a mean and a standard deviation. The error bars on temperature and composition account for errors in the data and in the sensitivities. The latter, however, contribute for less than 10% to the total uncertainties, which are dominated by data errors. The resulting uncertainties are remarkably uniform within each layer (RMS uncertainties are listed in Table 2).

Figure 6 shows the mean of the lateral variations in dT,dX_{pv} and dFe in each layer. Note that, in the deepest layer, the strongest excess in perovskite and iron are found beneath Africa and the Pacific. In the top and mid mantle, amplitudes of temperature and composition anomalies are globally smaller (Table 2). A notable exception are the anomalies of perovskite in the top layer ($670 \leq z \leq 1200$ km), which vary between -8.5% and 11.9% (Fig. 6d). A comparison between Figure 3 and Figure 6 do not show striking similarities between the distributions of $\mathrm{d}\ln V_S$ and dT. The correlations between $\mathrm{d}\ln V_S$ and dT (Table 3) are clearly too low to obtain temperature variations from $\mathrm{d}\ln V_S$ scaling. Further comparisons (Table 3) suggest that $\mathrm{d}\ln V_\Phi$ is an excellent proxy for perovskite variations independent of depth, and that $\mathrm{d}\ln \rho$ maps iron variations very well below $z = 1200$ km.

A striking result is that low velocities in the deep mantle beneath Africa and the Pacific are due to an enrichment in perovskite and iron, which makes them denser than the surrounding mantle. Because sensitivities of shear-wave velocity to iron

Table 3. Correlation between tomographic observables and thermo-chemical parameters[a]

Layer		$\mathrm{d}\ln V_S$	$\mathrm{d}\ln V_\Phi$	$\mathrm{d}\ln \rho$
670–1200 km	dT	−0.564	0.420	−0.524
	dX_{pv}	−0.033	0.907	0.114
	dFe	0.104	0.790	0.716
1200–2000 km	dT	−0.701	0.089	−0.790
	$\mathrm{d}X_{pv}$	−0.332	0.889	−0.281
	dFe	−0.135	0.432	0.898
2000–2891 km	dT	−0.302	−0.102	−0.863
	dX_{pv}	−0.792	0.933	0.277
	dFe	−0.524	0.604	0.942

[a]Correlations are computed for mean values, on the original grid $15° \times 15°$.

(Fig. 4a, light grey area) are negative throughout the lower mantle, this excess in iron results in low V_S-anomalies and could erroneously be interpreted as a temperature increase.

6 THERMO-CHEMICAL STRUCTURE: GEODYNAMICAL CONSEQUENCES

6.1 Observed variations of density

Trampert et al. (2004) clearly demonstrated that strong lateral variations of composition are present throughout the lowermost mantle. It is crucial, from a dynamical point of view, to separate and compare chemical (d ln ρ_c) and thermal (d ln ρ_T) contributions to the density anomalies. At each model point, we randomly sampled the anomalies of temperature and composition (perovskite and iron) within their Gaussian distributions. We similarly sampled the sensitivities of density and generated 20 million models of d ln ρ_T and d ln ρ_c density. Figure 7 shows the average maps of d ln ρ_T and d ln ρ_c in each layer. Again, uncertainties (defined as one standard deviation) are remarkably homogeneous within each layer (RMS of these uncertainties are given in Table 2).

In the bottom layer, d ln ρ_T is small, and varies between -0.31 and 0.44% (Fig. 7c). As previously noted, the small values of d ln ρ_T are due to the decrease of the thermal expansion at great depths (Fig. 4c, dashed area). In comparison, d ln ρ_c are on average twice as large (Fig. 7f), and vary between -0.71% and 0.95%. Due to the small values of the sensitivity of density to perovskite (Fig. 4c, light grey area), variations in perovskite contribute less than 10% to the total d ln ρ_c. The chemical density anomalies are therefore dominated by iron anomalies, as also suggested by the high correlation between the relative density anomalies and the iron anomalies (Table 3). Excess in iron increases the density up to 1.0%, the largest anomalies being observed beneath Africa and the Pacific. Since thermal density anomalies in these regions are of the order of 0.2%, the material is not buoyant. Power spectra of d ln ρ_T and d ln ρ_c reveal that each degree of the spherical harmonic expansion is dominated by chemical density anomalies (Fig. 8c). Moreover, most of the chemical and thermal signals are contained in degree 2. Degrees 4 and 6 are weaker than degree 2 by a factor 4.

Although weaker than in the bottom layer, the chemical density anomalies in the intermediate layer ($1200 \leq z \leq 2000$ km) are of the same order as the thermal density anomalies, and are dominated by degree 2. In general, this layer has small anomalies of temperature and composition.

Thermal and chemical buoyancies become stronger at the top of the lower mantle ($670 \leq z \leq 1200$ km). d ln ρ_T varies between -0.64% and 0.57%, and is stronger, on average, than in the bottom layer. Degree 2 is slightly stronger than in the lowermost layer, but, interestingly, there is more power in the degree 4 than in the degree 2 (Fig. 8a). d ln ρ_c is not as strong as in the lowermost layer, but still varies between -0.80% and 0.67%. Most of the difference in amplitude is due to the degree 2, which

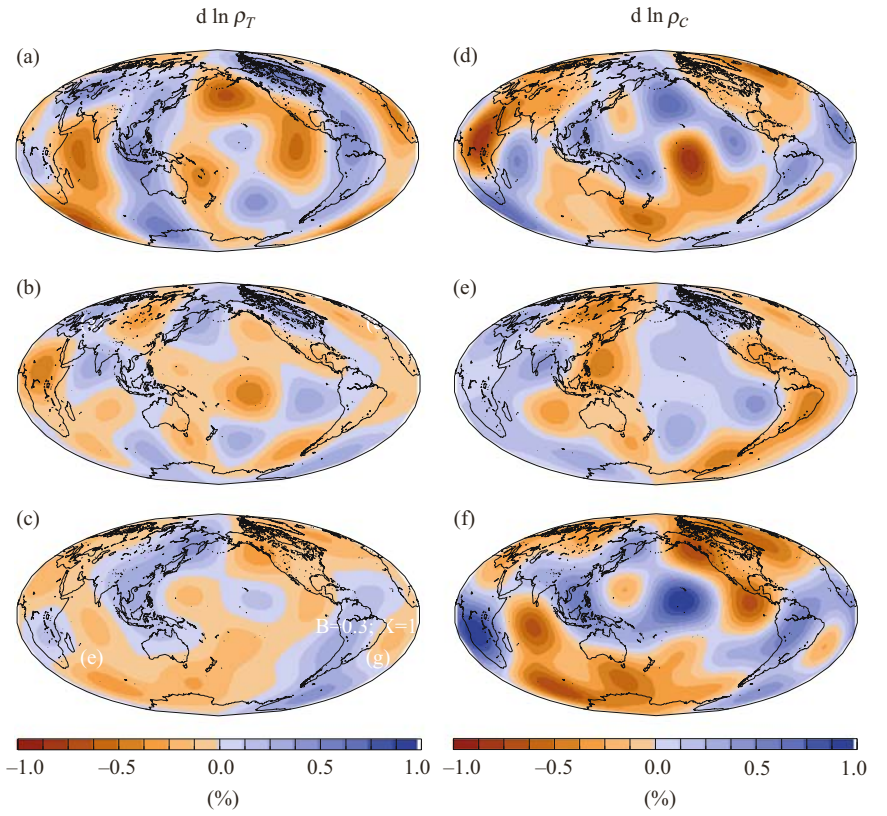

Figure 7. Thermal (a–c) and chemical (d–f) contributions to the relative anomalies of density in the lower mantle. The lower mantle is parameterized in three layers, from top to bottom $670 \leq z \leq 1200$ km, $1200 \leq z \leq 2000$ km, and $2000 \leq z \leq 2891$ km.

is half of that the bottom layer. Note that the anomalies of perovskite now make up 30% of the total d ln ρ_c.

6.2 Comparison with thermo-chemical convection

The numerical models of convection we used are defined on Cartesian grids (see Section 2) and can therefore be transferred to the Fourier domain. To compare them with global tomographic models, which are expanded in spherical harmonics, one must carefully compute the power spectra for each expansion. We did this using a method developed by Chevrot et al. (1998). From the convection models, we first performed a Fourier transform of the d ln ρ_T and d ln ρ_c at each depth, and computed the signal contained in each wave number $k = \sqrt{k_x^2 + k_y^2}$, where k_x and k_y are the

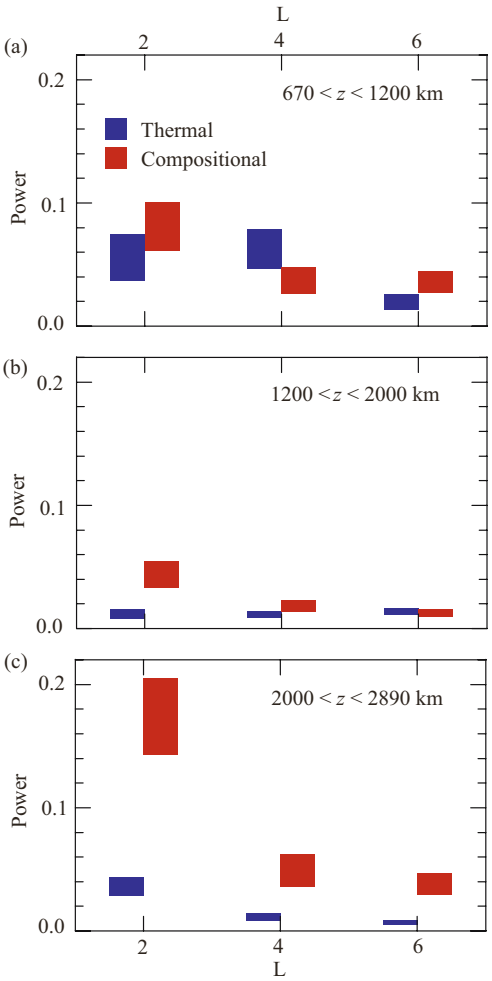

Figure 8. Power spectra of thermal (blue histograms) and chemical (red histograms) density anomalies predicted by probabilistic tomography model RT246g (Trampert et al., 2004) for degrees 2, 4 and 6. Each histogram covers one standard deviation around the mean value of the power.

wave numbers along the x- and y-axis. The signal contained in the spherical harmonic degree ℓ is equal to the sum of the signals contained in the wave numbers k that satisfy $(\ell + 1/2) \leq ka \leq (\ell + 3/2)$ (Chevrot et al., 1998):

$$P(\ell) = \frac{2\pi}{N_x^2 N_y^2 (\ell + 1/2)} \sum_{(\ell+1/2) \leq ka \leq (\ell+3/2)} |\mathrm{d} \ln \rho(k)|^2, \tag{8}$$

where a is the Earth's radius, and N_x and N_y the number of grid points in x and y directions. The tomographic model RT246g represents the lower mantle in three layers, and contains spherical harmonic degrees 2, 4 and 6 only, whereas the numerical models of Tackley (2002) sample the lower mantle with 50 points, and contains signal up to degree 32. To make meaningful comparisons, we averaged the synthetic d ln ρ_T and d ln ρ_c (Eqs. 4–5) in comparable layers as defined by RT246g, and filtered them for spherical harmonic degrees 2, 4 and 6.

The RMS of d ln ρ_T and d ln ρ_c from seismology and convection models are plotted in Figure 9. All the numerical models we considered predicted the RMS of d ln ρ_T and d ln ρ_c that fitted within one standard deviation of the observed RMS. The best fit is obtained for $B = 0.2, X = 10\%$. In the intermediate layer, the RMS of d ln ρ_c for the cases $B = 0.3, X = 10\%$, and $B = 0.4, X = 10\%$ are close to the observed lower bound, but cannot be excluded. Analysis of the RMS is therefore not a conclusive test, at least with the current depth parameterization of probabilistic seismic tomography. Models with finer parameterization will certainly provide a better test, but are not yet available. Clearer conclusions can be drawn from comparing the power spectra of observed and synthetic distributions (Fig. 10). In case of a stable layer of dense material ($B = 0.3$, $X = 30\%$, green histograms), the strongest chemical density anomalies are found between the intermediate and lower layers (Fig. 1d). As a result, spectra of d ln ρ_c in the bottom and intermediate layers are similar one another, which is not observed by RT246g. In particular, degree 2 has too little power in the bottom

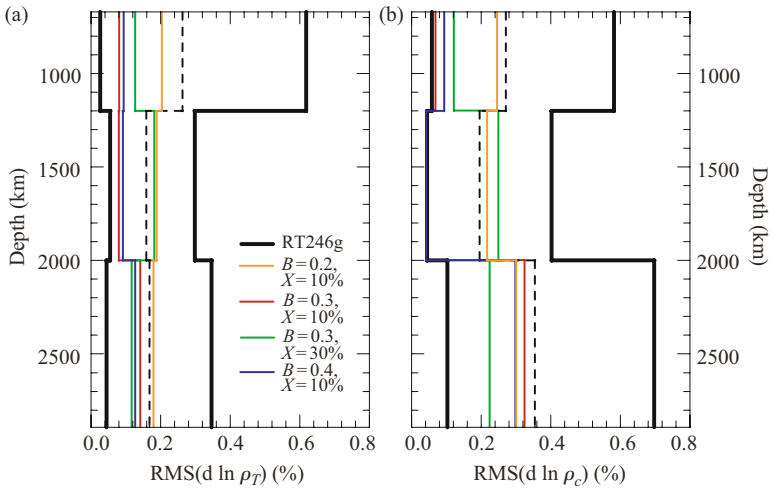

Figure 9. RMS of relative density anomalies due to (a) thermal and (b) compositional effects. The thin dashed curve represents the RMS of the average observed models (Fig. 7), and the thick curves represent de RMS of the models with one standard deviation around these models. Colored curves represent the RMS predicted by 3-D Cartesian numerical models of thermo-chemical convection (Tackley, 2002) with several buoyancy ratio (B) and volumetric fraction of dense material (X). Density anomalies from numerical models of convection are filtered for degrees 2, 4, and 6.

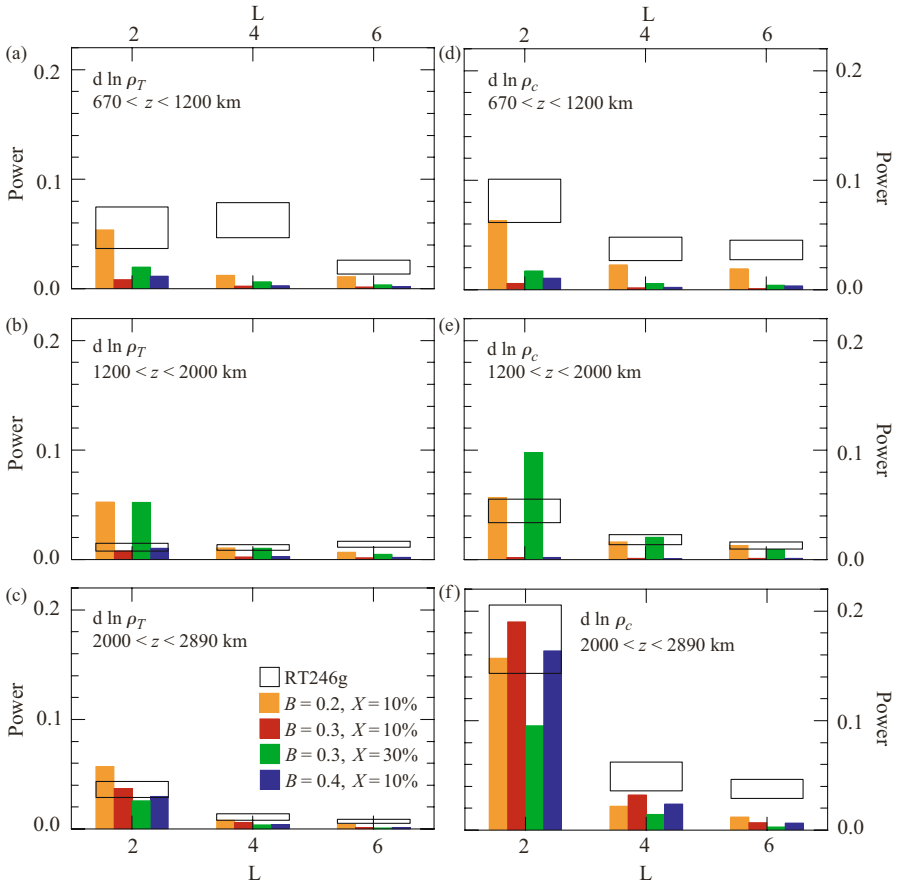

Figure 10. Power spectra of thermal and chemical contributions to the density anomalies derived from numerical models of thermo-chemical convection (Tackley, 1998, 2002), for degrees 2, 4 and 6, and for several buoyancy ratio (B) and volumetric fraction of dense material (C). Because numerical models are defined on a 3-D Cartesian grid, we used the method of Chevrot et al. (1998) to compute their spherical harmonic coefficients (see text). For comparison, the white rectangles cover one standard deviation around the means of the observed power (see Fig. 8).

layer, and too much in the intermediate layer. This case also fails to explain the observed power spectrum of d ln ρ_T and d ln ρ_c in the upper layer, and the degree 2 of d ln ρ_T in the intermediate layer. The thin stable layer ($B = 0.4$, $X = 10\%$, blue histograms) and discontinuous spoke pattern ($B = 0.3$, $X = 10\%$, red histograms) show strong lateral variations of temperature and composition below 2000 km, but not at shallower depths. They explain the observed power spectra in the bottom layer, but not in the intermediate (except the degree 2 of d ln ρ_T) and top layers. Finally, the case $B = 0.2$, $X = 10\%$ (orange histograms) explains most of the power spectra

of d ln ρ_c, at least within two standard deviations (95% certainty). It fits d ln ρ_T less well, most of the discrepancies being due to the degree 2 in the intermediate layer, and to the degree 4 in the top layer.

The previous comparisons suggest that the model with $B = 0.2$ gives the best agreement to the observed density anomalies. As an additional test, we estimated the global buoyancy ratio associated with the observed d ln ρ_T and d ln ρ_c. We considered that the iron fraction of the regular material is equal to 11%, and that the dense material is enriched in iron by 2.0–2.5%, as reported in Section 5. If the mantle aggregate consists in 80% perovskite and 20% magnesio-wüstite, the density and thermal expansion at the surface are $\rho_s = 4240$ kg/m^3 and $\alpha_s = 2 \times 10^{-5}$ K^{-1}, and the chemical density contrast due to the enrichment in iron varies between $\Delta\rho_c^{\max} = 40$ kg/m^3 and $\Delta\rho_c^{\max} = 49$ kg/m^3 (Deschamps and Trampert, 2004). Taking $\Delta T_s = 2500$ K, the thermal density contrast is $\Delta\rho_T^{\max} = 213$ kg/m^3, and the buoyancy ratio varies between $B = 0.19$ and $B = 0.23$.

7 DISCUSSION

The low shear wave velocities observed in the deep mantle below Africa and the Pacific are fully explained by long wavelength lateral variations of composition. Iron increases are responsible for strong (up to 1%) anomalies of density, and variations in perovskite are significant (up to 9%) and explain bulk-sound velocity very well. The comparisons performed in the previous section, however, suggest that these variations are not large enough to maintain a stable chemical layering. If a dense layer is present it must be unstable, i.e., the domes or piles of dense material are generated in the bottom of the mantle and oscillate or are entrained upwards. The current parameterization of probabilistic seismic tomography, however, cannot resolve these structures.

A question that is not addressed in this paper is the origin of the compositional variations. We easily identify three different scenarios. First, early differentiation may have created a dense layer at the bottom of the mantle. Because the buoyancy ratio is not large enough ($B < 0.3$), this layer is unstable, and the material is entrained upwards. A major disadvantage of this scenario is that the layer must have been rapidly entrained and mixed in the mantle, unless it is regularly fed with new material. Gonnerman et al. (2002) showed that even if the initial layer is stable, entrainment of material would progressively decrease the density contrast and lead to a present unstable layer. Second, slabs may penetrate in the lower mantle and reach the CMB, where they sediment in pools (e.g., Christensen and Hofmann, 1994). Again, the density contrast and quantity of sinking material should not be too large to allow the development of instabilities. Slabs could temporarily stack in the mid-mantle, and reach the bottom of the mantle in occasional avalanches (Tackley et al., 1994). There are indeed some indications from classical tomography that significant amounts of slabs are deflected in the top of the lower mantle, around 1000 km (Fukao et al., 2001). The variations of temperature and composition (mainly perovskite) observed by probabilistic tomography at the top of the lower mantle could also be due to

deflected slabs. Finally, iron excess may result from percolation from the core (e.g., Knittle and Jeanloz, 1991). A recent study (Humayun et al., 2004) suggests that the lower mantle beneath Hawaii is enriched in iron by 1–2%. Interestingly, the largest iron anomalies we found are close to 2%, and are located beneath Hawaii (Fig. 6i). The actual influence of iron percolation from the core remains however difficult to estimate. These scenarios are end-members, and a mix of them is more likely required to describe the Earth's mantle. Discriminating between the previous scenarios (or a mix of them) is not possible from the results presented in this paper only, but needs to integrate other types of information, in particular geochemical constraints.

The thermo-chemical distributions from convection we have tested are snapshots of time-dependent calculations, which do not necessarily correspond to the present state of the mantle. A full comparison requires to test series of snapshots at different times. For $B = 0.3$, $X = 30\%$, the layer of dense material remains stable for a long period of time (3 Gy), with similar spectral signature. The spokes pattern ($B = 0.3$, $X = 10\%$) and thin dense layer ($B = 0.4$, $X = 10\%$) modes are also stable over long periods of time (5 Gy and more). For $B = 0.2$, $X = 10\%$, mature piles (such as those plotted in Fig. 1) develop in about 200 My. Once they are formed, piles feed the mantle with dense material until the fluid is chemically homogeneous. Spectral signatures for early stages do not explain the observation as well as mature piles.

Hotspots are a major ingredient of mantle dynamics, but their origin is still debated. Recent tomographic studies (Zhao, 2001, 2004; Montelli et al., 2004) image hotspot tails down to various depths. Several hotspots, including Hawaii, seem to originate in the lowermost mantle, close to the CMB. The resolution of RT246g does not allow detailed inferences on the origin of hotspots, but maps of density anomalies (Fig. 3g–i) clearly show that deep-rooted hotspots, as defined by and Courtillot et al. (2003) and Montelli et al. (2004), do not systematically plot continuously on buoyant material throughout the lower mantle. Within error bars in density anomalies, only one third of these deep hotspots correlate with negative density anomalies in the lowermost mantle, and only two (Iceland and Azores) plot on buoyant material throughout the mantle. It is important to keep in mind that Zhao (2001, 2004) and Montelli et al. (2004) map compressional seismic velocity anomalies only, but not density. Neglecting compositional variations, they assume that the seismic velocity anomalies are purely thermal in origin, i.e., that low velocity regions are related to hot, hence buoyant material. As shown in this chapter and elsewhere (Trampert et al., 2004), chemically dense material dominates thermal buoyancy in the lower mantle, and still results in low velocities. For instance, in the lowermost mantle, the Hawaiian region is associated with dense, non-buoyant material (Fig. 3i) and low shear-wave velocities (Fig. 3c).

The thermo-chemical structure we inferred is based on a parameterization of composition that consists in perovskite and iron variations. Recent developments in mineral physics, which are not accounted for in this study, may complicate the interpretation of seismic information, and modify our inferences. Murakami et al.

(2004) reported a new phase transition from perovskite to post-perovskite around 2700 km. We did preliminary tests using available thermo-elastic data for post-perovskite (Tsuchiya et al., 2004a,b), but we did not find any dramatic differences compared to the sensitivities plotted in Figure 4. The biggest change is for the sensitivities of density to perovskite, which are positive from the depth of the transition down to the CMB. The amplitudes of the sensitivities, however, remain small. Thus, the phase transition to post-perovskite should not dramatically modify the thermo-chemical structure inferred from probabilistic tomography. Still, it may have significant consequences on the lower mantle dynamics (Nakagawa and Tackley, 2005). Interestingly, the large value of its Clapeyron slope (around 8–10 MPa/K) could explain the good correlation (equal to 0.7) between the observed thermal and compositional contributions to density at the bottom of the mantle, which is not predicted by the models of thermo-chemical convection we used. In cold regions (e.g., slabs) perovskite may transform to post-perovskite at shallower depths than in hot regions (if they transform at all before the CMB). In addition, there are indications that Fe-perovskite may transform at shallower depths than Mg-perovskite (Spera et al., 2006). In that case, the chemically dense and cold regions observed in the lowermost mantle would correspond to iron-rich post-perovskite.

Due to heavy computational requirements, the vertical parmeterization of RT246g is limited to three layers in the lower mantle, which reduces the effects of a post-perovskite phase on this study. Further, averaging models of thermo-chemical convection in these layers, we lose important information (compare Figs. 2b and 2d against Fig. 9). A careful statistical analysis, however, allows robust conclusions concerning the lower mantle structure. A thick stable layer of dense material, for instance, implies that the chemical signatures in the mid-mantle ($1200 \leq z \leq 2000$ km) and in the lowermost mantle ($2000 \leq z \leq 2891$ km) are comparable. On the contrary, a thin stable layer would result in no notable chemical signal down to 2000 km. Since none of these features fit within the observed error bars (Fig. 10), a stable layer of dense material is unlikely to be present at the bottom of the mantle. Probabilistic models of seismic tomography with a better vertical parameterization should be available in the near future by performing more efficient parallel calculations. A more serious problem is that RT246g does not include odd degrees, which potentially contain important information. Including odd spherical harmonic degrees is a difficult task because normal mode splitting cannot access these degrees very easily. A last point is that a finer lateral resolution, including degrees higher than 6, is not so essential to correctly understand the lower mantle. The power spectrum of relative density anomalies predicted by models of thermo-chemical convection strongly decreases for degrees higher than 7, as shown in Figure 11 for the case $B = 0.2$ and $X = 10\%$. The power spectra for other models of thermo-chemical convection (not shown here), have a similar decrease. If mantle convection is similar to one of these models, we would expect that degrees higher than 7 are weak, and do not significantly participate to the nature of tomographic models. This is confirmed by recent tomographic models (Gu et al., 2001).

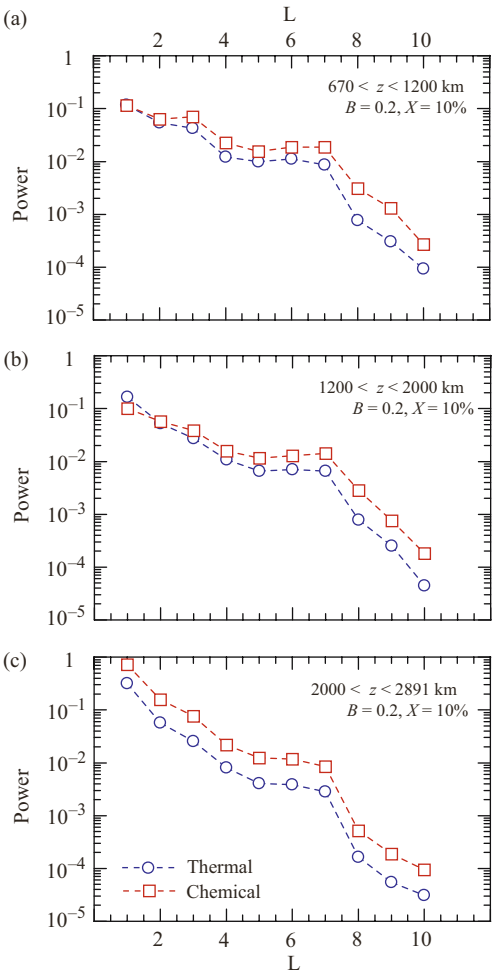

Figure 11. Power spectrum of thermal (blue curves) and chemical (red curves) contributions to the density anomalies predicted by a 3-D Cartesian numerical model of thermo-chemical convection (Tackley, 2002) with buoyancy ratio $B = 0.2$, and volumetric fraction of dense material $X = 10\%$. The power in each spherical harmonic degree is calculated following Chevrot et al. (1998). Degrees $\ell = 1$–10 are represented, and the signal is averaged within each layer defined by the probabilistic model of seismic tomography RT246g.

8 CONCLUSION

Our view of mantle structure and dynamics has rapidly changed during the last decade. A strong indication of dense material (Ishii and Tromp, 1999) or chemical variations in the lower mantle (Forte and Mitrovica, 2001; Saltzer et al., 2001) has now turned

to robust quantitative estimates of the variations of temperature and composition (Trampert et al., 2004). Chemical heterogeneities are clearly present throughout the mantle. In the top layer ($670 \leq z \leq 1200$ km), thermal and chemical signatures could be related to slab deflection. In the lowermost mantle ($2000 \leq z \leq 2891$ km) strong anomalies of iron, whose origin is still to be determined, are present in regions usually referred to as "superplumes". From a geodynamical point of view, the presence of lateral variations of composition is observed in recent models of thermo-chemical convection, which now account for fluid compressibility. Robust comparisons between geophysical observations, mainly seismology, and geodynamical models can now be attempted in order to discriminate between certain modes of convection in the mantle. Preliminary results discussed in this chapter indicate that a stable layer of dense material is unlikely to be present at the bottom of the mantle. Piles of dense material entrained upwards from a dense, unstable layer statistically explain probabilistic tomography better, but discrepancies remain in the top of the lower mantle, possibly linked to the phase transformation around 670 km and/or slabs deflection around 1000 km. Future researches should focus on estimating the influence of recent mineral physics findings on lower mantle seismic velocity and density, exploring and testing scenarios that can produce strong lateral variations of iron at the bottom of the mantle, computing probabilistic models of tomography with finer vertical parameterization, and testing models of thermo-chemical convection that include more complexities, such as a phase transformation at 670 km, or the post-perovskite phase transition in the lowermost mantle.

ACKNOWLEDGEMENTS

We appreciated the constructive reviews of an anonymous reviewer. This research was funded by the Netherlands Research Center for Integrated Solid Earth Sciences (ISES) and Utrecht University.

REFERENCES

Anderson, O.L. (1995) Equations of State of Solids for Geophysics and Ceramic Sciences, Oxford University Press, Oxford, 405pp.

Anderson, D.L. (2001) Top-down tectonics. *Science*, 293, 2016–2018.

Beghein, C., J.S. Resovsky, and J. Trampert (2002) P and S tomography using normal-mode and surface waves data with a neighbourhood algorithm. *Geophys. J. Int.*, 149, 646–658.

Chevrot, S., J.P. Montagner, and R. Snieder (1998) The spectrum of tomographic Earth models. *Geophys. J. Int.*, 33, 783–788.

Christensen, U.R., and A. Hofmann (1994) Segregation of subducted oceanic crust in the convecting mantle. *J. Geophys. Res.*, 99, 19867–19884.

Courtillot, V., A. Davaille, J. Besse, and J. Stock (2003) Three distinct types of hotspots in the Earth's mantle. *Earth Planet. Sci. Lett.*, 205, 295–308.

Daniel, I., J.D. Bass, G. Fiquet, H. Cardon, J. Zhang, and M. Hanfland (2004) Effect of aluminium on the compressibility of silicate perovskite. *Geophys. Res. Lett.*, 31, doi: 10.1029/2004GL020213.

Davaille, A. (1999) Simultaneous generation of hotspots and superswells by convection in a heterogeneous planetary mantle. *Nature*, 402, 756–760.

Deschamps, F., and J. Trampert (2003) Mantle tomography and its relation to temperature and composition. *Phys. Earth Planet. Inter.*, 140, 277–291.

Deschamps, F., and J. Trampert (2004) Towards a lower mantle reference temperature and composition. *Earth Planet. Sci. Lett.*, 222, 161–175.

Forte, A.M., and J.X. Mitrovica (2001) Deep-mantle high-viscosity flow and thermo-chemical structure inferred from seismic and geodynamic data. *Nature*, 410, 1049–1056.

Fukao, Y., S. Widiyantoro, and M. Obayashi (2001) Stagnant slabs in the upper and lower mantle transition region. *Rev. Geophys.*, 39, 291–323.

Goes, S., R. Govers, and P. Vacher (2000) Shallow mantle temperature under Europe from P and S wave tomography. *J. Geophys. Res.*, 105, 11153–11169.

Gonnerman, H.M., M. Manga, and A.M. Jellinek (2002) Dynamics and longevity of an initially stratified mantle. *Geophys. Res. Lett.*, 29, doi:10.1029/2002GL014851.

Gu, Y.J., A.M. Dziewonski, W.J. Su, and G. Ekstrom (2001) Models of the mantle shear velocity and discontinuities in the pattern of lateral heterogeneities. *J. Geophys. Res.*, 106, 11169–11199.

Hansen, U., and D.A. Yuen (1988) Numerical simulations of thermo-chemical instabilities at the core-mantle boundary. *Nature*, 334, 237–240.

Humayun, M., L. Qin, and M.D. Norman (2004) Geochemical evidence for excess iron in the lower mantle beneath Hawai. *Science*, 306, 91–94.

Ishii, M., and J. Tromp (1999) Normal-mode and free-air gravity constraints on lateral variations in velocity and density of Earth's mantle. *Science*, 285, 1231–1236.

Jackson, I. (1998) Elasticity, composition and temperature of the earth's lower mantle: A reappraisal. *Geophys. J. Int.*, 134, 291–311.

Jackson, J.M., J. Zhang, and J.D. Bass (2004) Sound velocities and elasticity of aluminous $MgSiO_3$ perovskite: Implications for aluminium heterogeneity in Earth's lower mantle. *Geophys. Res. Lett.*, 31, doi: 10.1029/2004GL019918.

Jeanloz, R., and E. Knittle (1989) Density and composition of the lower mantle. *Philos. Trans. R. Soc. Lond. A*, 328, 377–389.

Karato, S.I., and B.B. Karki (2001) Origin of lateral variation of seismic wave velocities and density in the deep mantle. *J. Geophys. Res.*, 106, 21771–21783.

Kellogg, L.H., B.H. Hager, and R.D. van der Hilst (1999) Compositional stratification in the deep mantle. *Science*, 283, 1881–1884.

Kennett, B.L.N., S. Widiyantoro, and R.D. van der Hilst (1998) Joint seismic tomography for bulk sound and shear wave speed in the Earth's mantle. *J. Geophys. Res.*, 103, 12469–12493.

Kiefer, B., L. Stixrude, and R.M. Wentzcovitch (2002) Elasticity of $(Mg,Fe)SiO_3$ perovskite at high-pressures. *Geophys. Res. Lett.*, 29, doi: 10.1029/2002GL014683.

Knittle, E., and R. Jeanloz (1991) Earth's core-mantle boundary: Results of experiments at high pressures and temperatures. *Science*, 251, 1438–1443.

Kung, J., B. Li, D.J. Weidner, J. Zang, and R.C. Liebermann (2002) Elasticity of $(Mg_{0.83},Fe_{0.17})O$ ferropericlase at high pressure: Ultrasonic measurements in conjunction with X-radiation techniques. *Earth Planet. Sci. Lett.*, 203, 557–566.

Masters G., G. Laske, H. Bolton, and A.M. Dziewonski (2000) The relative behavior of shear velocity, bulk sound speed, and compressional velocity, in the mantle: Implications for chemical and thermal structure. In Karato, S.I. et al. (eds.) Earth's Deep Interior: Mineral Physics and Tomography from the Atomic to the Global Scale, Geophys. Mon. Ser., 117, pp. 63–87.

Montelli, R., G. Nolet, F.A. Dahlen, G. Masters, E.R. Engdahl, and S.H. Hung (2004) Finite frequency tomography reveals a variety of plumes in the mantle. *Science*, 303, 338–343.

Murakami, M., K. Hirose, K. Kawamura, N. Sata, and Y. Ohishi (2004) Post-perovskite phase transition in $MgSiO_3$. *Science*, 304, 855–858.

Nakagawa, T., and P.J. Tackley (2005) The interaction between the post-perovskite phase change and a thermo-chemical boundary layer near the core-mantle boundary. *Earth Planet. Sci. Lett.*, 238, 204–216.

Olson, P., and C. Kinkaid (1991) Experiment on the interaction of thermal convection and compositional layering at the base of the mantle. *J. Geophys. Res.*, 96, 4347–4354.

Resovsky, J.S., and J. Trampert (2003) Using probabilistic seismic tomography to test mantle velocity-density relationships. *Earth Planet. Sci. Lett.*, 215, 121–134.

Romanowicz, B., and Y. Gung (2002) Superplumes from the core-mantle boundary to the lithosphere: Implications for heat flux. *Science*, 296, 513–516.

Saltzer, R.L., R.D. van der Hilst, H. Kárason (2001) Comparing P and S wave heterogeneity in the mantle. *Geophys. Res. Lett.*, 28, 1335–1338.

Sambridge, M. (1999a) Geophysical inversion with a neighbourhood algorithm—I. Searching a parameter space. *Geophys. J. Int.*, 138, 479–494.

Sambridge, M. (1999b) Geophysical inversion with a neighbourhood algorithm—II. Apraising the ensemble. *Geophys. J. Int.*, 138, 727–746.

Schott, B., and D.A. Yuen (2004) Influences of dissipation and rheology on mantle plumes coming from the D″-layer. *Phys. Earth Planet. Inter.*, 146, 139–145.

Spera, F.J., D.A. Yuen, and G. Giles (2006) Tradeoffs in chemical and thermal variations in the post-perovskite phase transition: Mixed phase regions in the deep lower mantle? *Phys. Earth Planet. Inter.*, 159, 234–246.

Su, W.J., and A.M. Dziewonski (1997) Simultaneous inversion of 3D variations in the shear and bulk velocity in the mantle. *Phys. Earth Planet. Inter.*, 100, 135–156.

Tackley, P.J. (1998) Three-dimensional simulations of mantle convection with a thermo-chemical CMB boundary layer: D″? In Gurnis M. et al. (eds.) The Core-Mantle Boundary Region, Geodynamical Ser., 28, pp. 231–253.

Tackley, P.J. (2002) Strong heterogeneity caused by deep mantle layering. *Geochem. Geophys. Geosys.*, 3, doi: 10.1029/2001GC000167.

Tackley, P.J., D.J. Stevenson, G.A. Glatzmaier, and G. Schubert (1994) Effects of multiple phase transition in a three-dimensional spherical model of convection in Earth's mantle. *J. Geophys. Res.*, 99, 15877–15902.

Trampert, J., P. Vacher, and N. Vlaar (2001) Sensitivities of seismic velocities to temperature, pressure and composition in the lower mantle. *Phys. Earth Planet. Inter.*, 124, 255–267.

Trampert, J., F. Deschamps, J.S. Resovsky, and D.A. Yuen (2004) Probabilistic tomography maps significant chemical heterogeneities in the lower mantle. *Science*, 306, 853–856.

Trampert, J., and R.D. van der Hilst (2005) Quantitative interpretation of global seismic tomography. In van der Hilst et al. (eds) Earth's Deep Mantle: Structure, Composition, and Evolution, Geophys Mon. Ser., 160, pp. 47–62.

Tsuchiya, T., J. Tsuchiya, K. Umemoto, and R.M. Wentzcovitch (2004a) Phase transition in $MgSiO_3$ perovskite in the Earth's lower mantle. *Earth Planet. Sci. Lett.*, 224, 241–248.

Tsuchiya T., J. Tsuchiya, K. Umemoto, and R.M. Wentzcovitch (2004b) Elasticity of post-perovskite $MgSiO_3$. *Geophys. Res. Lett.*, 31, doi: 10.1029/2004GL020278.

Vasco, D.W., and L.R. Johnson (1998) Whole Earth structure estimated from seismic arrival times. *J. Geophys. Res.*, 103, 2633–2671.

Williams, Q., and E.J. Garnero (1996) Seismic evidence of partial melt at the base of the mantle. *Science*, 273, 1528–1530.

Yagi, T., K. Okabe, N. Nishiyama, A. Kubo, and T. Kikegawa (2004) Complicated effects of aluminum on the compressibility of silicate perovskite. *Phys. Earth Planet. Inter.*, 143–144, 81–91.

Zhao, D. (2001) Seismic structure and origin of hotspots and mantle plumes. *Earth Planet. Sci. Lett.*, 192, 251–265.

Zhao, D. (2004) Global tomographic images of mantle plumes and subducting slabs: Insight into deep Earth dynamics. *Phys. Earth Planet. Inter.*, 146, 3–34.

CHAPTER 12

MICROSCOPIC MODELS FOR THE EFFECTS OF HYDROGEN ON PHYSICAL AND CHEMICAL PROPERTIES OF EARTH MATERIALS

SHUN-ICHIRO KARATO

Department of Geology and Geophysics, Yale University, New Haven, Connecticut 06520, USA; E-mail: shun-ichiro.karato@yale.edu

Abstract

Atomistic models of interaction of hydrogen with silicates are reviewed. The most important mechanism of hydrogen dissolution in Mg (Fe)-bearing silicates is the replacement of Mg (Fe) with two protons (a vacancy at M-site trapping two protons ($(2H)_M^{\times}$)). Influence of hydrogen on phase diagrams can be understood from this model. In addition to this fully charge-compensated defect, charged defects are also created by the ionization of a neutral defect, $(2H)_M^{\times}$. Electrical conductivity is due to ionized defect, i.e., free proton. When the concentration of ionized, charged defects exceeds the concentration of charged defects under hydrogen-free environment, then the concentrations of defects at other sub-lattices is also modified leading to the enhancement of a range of properties that are controlled by the motion of defects at silicon or oxygen sub-lattice. The parameterization of creep law in terms of hydrogen content is summarized and applied to the estimation of upper mantle viscosity and fabric transitions. Current knowledge of influence of hydrogen on the rheological properties of deep mantle minerals is reviewed. The role of hydrogen in each mineral in the deep mantle is mineral-specific: solubility of hydrogen and its role in plastic deformation are quite different among the various minerals in the transition zone and the lower mantle. Possible roles of hydrogen in deep Earth dynamics are discussed including the effects of hydrogen on the structure of plumes.

1 INTRODUCTION

Hydrogen is a unique element in terrestrial planets. It occupies only a very small mass fraction of any terrestrial planets (for Earth it occupies less than 0.01 wt%). Yet it has large influence on various physical and chemical properties of Earth materials including melting relations and rheological properties: addition of hydrogen reduces the melting temperature and reduces the rock's resistance to plastic flow (viscosity).

D. A. Yuen et al. (eds.), Superplumes, 321–356.
© 2007 *Springer.*

These two properties are the key to the evolution and dynamics of terrestrial planets, and consequently understanding how hydrogen affects these properties is an important challenge to Earth scientists. This chapter provides a brief review of this subject with emphasis on the latest advances.

At a qualitative or semi-quantitative level, the effects of hydrogen on melting temperature and rheology have been well known for more than ~30 years (melting: Inoue and Sawamoto, 1992; Kusiro et al., 1968; rheology: Karato, 1989; Karato and Jung, 2003; Mei and Kohlstedt, 2000b; Paterson, 1989). The addition of hydrogen (water)[1] to a peridotite reduces the solidus by several hundred degrees, and the addition of hydrogen reduces the creep strength of many silicates more than an order of magnitude.

However, some important details remained unknown until quite recently. They include (i) the influence of hydrogen on phase diagrams such as the one for the olivine-wadsleyite transformation and (ii) the quantitative relationship between hydrogen content and various physical properties such as electrical conductivity, viscosity and seismic wave velocities for upper mantle minerals. In addition, new discoveries have been made on the effects of hydrogen including the high but variable solubility of hydrogen in silicate minerals (e.g., Ingrin and Skogby, 2000), the enhancement of electrical conductivity (Huang et al., 2005; Karato, 1990) and the changes in deformation fabrics in olivine by hydrogen (Jung and Karato, 2001b; Karato, 1995; Katayama et al., 2004). Furthermore the influence of hydrogen on properties of deep mantle minerals is almost unexplored. In addressing these issues, it is critical to understand the atomistic mechanisms by which hydrogen interacts with silicate minerals and melts. The purpose of this chapter is to present a review of our understanding of interaction between hydrogen and silicates at the atomistic level with the emphasis on those in solid silicates. I will first review the models of dissolution of hydrogen in silicates, and then review our current understanding of the way in which hydrogen affects various physical and chemical properties of Earth materials.

2 SOLUBILITY MECHANISMS

The first step in investigating the role of hydrogen in modifying the physical and chemical properties is to understand the mechanisms of dissolution of hydrogen in a given material. In silicates, hydrogen has a strong tendency to be associated with oxygen. In fact for silicate melts, H_2O and OH^- are the only species that are considered in modeling silicate melts (e.g., Burnham, 1979; Silver and Stolper, 1985). However, in silicate minerals, where structures are less flexible than those of melts, free water and free OH^- are less abundant and most of the hydrogen atoms are associated with cation-site vacancies or it could occur as free proton (e.g., Karato, 1989; Paterson, 1989).

[1] The author uses a term "hydrogen" throughout this chapter to indicate that it is hydrogen and not oxygen that affects the physical and chemical properties of silicates. In the literature, the term "water" is used more frequently.

2.1 Hydrogen (water) in silicate melts

For silicate melts, it is often assumed that hydrogen-related species is present either as molecular water (H_2O) or OH^- and an internal chemical equilibrium

$$[H_2O] + [O^{2-}] = 2[OH^-], \tag{1}$$

is considered (e.g., Burnham, 1979; Silver and Stolper, 1985). The concentration of oxygen atoms is assumed to be independent of oxygen fugacity. This is equivalent to the assumption that the charge balance is maintained only by O^{2-} and OH^-. This is in contrast to the case for silicate minerals in which the concentration of hydrogen-related defects is closely related to those of other charged defect species such as ferric iron Fe_M^g or M-site vacancy V_M''.

With this assumption, applying the law of mass action to the following reaction,

$$H_2O\,(\textit{fluid}) \Leftrightarrow H_2O\,(\textit{melt}), \tag{2}$$

one has

$$[H_2O] \propto f_{H_2O}(P,T)\exp\left(-\frac{PV_{H_2O}}{RT}\right), \tag{3}$$

$$[OH^-] \propto f_{H_2O}^{\frac{1}{2}}(P,T)\exp\left(-\frac{PV_{OH}}{RT}\right) \text{ for small water content}([O^{2-}] \approx 1), \tag{4}$$

where f_{H_2O} is the fugacity of water and V_X is the volume change of melt associated with the relevant reaction. As can be seen from Equations (3) and (4), dominant hydrogen-related species in a silicate melt changes with pressure and temperature. Note that the volume change associated with the dissolution of hydrogen-related species likely changes with pressure. The partial molar volume of water at ~1 GPa is $\sim 16 \times 10^{-6}$ m^3/mol (Ochs and Lange, 1997) but it is $\sim 8 \times 10^{-6}$ m^3/mol at ~14 GPa (Matsukage et al., 2005). This has important influence on the melt density as well as the pressure dependence of solubility of hydrogen-related species in melts.

An important recent finding in this area is that water and silicate melt becomes completely miscible above a certain pressure (and temperature) (Mibe et al., 2002). Defining thermodynamic properties of hydrous silicate melts is critical to the understanding of influence of hydrogen on melting (see Section 3.2).

2.2 Hydrogen in solid silicate minerals

Solubility mechanisms of hydrogen in solid silicates are quite different from those in silicate melts. Theoretical analysis of hydrogen-related defects in silicate was made by. (Karato, 1989; Kohlstedt et al., 1996; Mei and Kohlstedt, 2000a; Yan, 1992). Similar to melts, one can consider dissolution of free water (water molecule in the interstitial site of a crystal) or OH^-; but in the case of OH^- one must distinguish OH^- at interstitial site from that at the normal oxygen site. One major difference between

melts and solid silicates is that the structure of solid silicates is more compact, and consequently, there is not much "space" so that hydrogen is often associated with point defects. Considering the fact that the charge neutrality is a strict requirement in any chemical reactions, one can consider five models of dissolution of "water" in silicates containing two types of cations (e.g., Mg_2SiO_4) (Fig. 1):

(i) molecular water at an interstitial site
(ii) two protons from one molecule of water go to M-site, and Mg (or Fe, Ca) from M-site and one oxygen from water goes to the surface
(iii) four protons from two molecules of water go to Si-site, and Si from the Si-site and two oxygens from two water molecules (SiO_2) go to the surface
(iv) two protons go to two O-site oxygens, and one oxygen from water molecule goes to an interstitial site
(v) water reacts with an interstitial oxygen to create an interstitial OH^-.

For each mechanism, one can write an equation for chemical reaction as:

$$H_2O\,(fluid) \Leftrightarrow H_2O_I \qquad \text{for reaction (i)} \qquad (5)$$

$$H_2O\,(fluid) + M_M^{\times} \Leftrightarrow (2H)_M^{\times} + MO \qquad \text{for reaction (ii)} \qquad (6)$$

$$2H_2O\,(fluid) + Si_{Si}^{\times} \Leftrightarrow (4H)_{Si}^{\times} + SiO_2 \qquad \text{for reaction (iii)} \qquad (7)$$

$$H_2O\,(fluid) + 2O_O^{\times} \Leftrightarrow 2\,(OH)_O^{g} + O_I'' \qquad \text{for reaction (iv)} \qquad (8)$$

$$H_2O\,(fluid) + O_I'' + V_O^{gg} \Leftrightarrow 2\,(OH)_I' + V_O^{gg}, \qquad \text{for reaction (v)} \qquad (9)$$

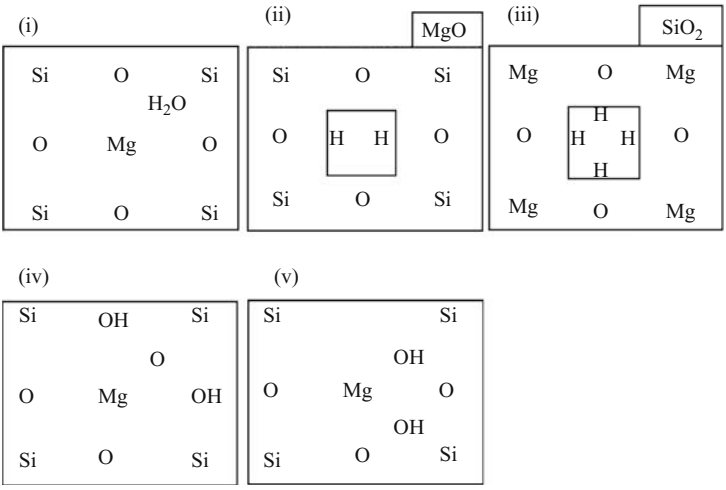

Figure 1. Mechanisms of dissolution of water (hydrogen) in silicates. Note that mechanisms (ii) and (iii) are associated with an explicit volume change. A volume change also occurs to a lesser extent in mechanisms (i), (iv) and (v).

where the Kröger-Vink notation of point defects is used, i.e., X_Y^Z means a species X occupying the Y-site whose effective charge is Z. The effective charge is defined relative to the perfect lattice and a cross means a neutral charge, prime a negative charge and a dot a positive charge.

The law of mass action can be applied to each reaction to yield

$$C_{\mathrm{H}} \propto C_w \propto f_{\mathrm{H_2O}}\,(P,T)\exp\left(-\frac{E_i + PV_i}{RT}\right), \tag{10}$$

$$C_{\mathrm{H}} \propto C_w \propto f_{\mathrm{H_2O}}\,(P,T)\,a_{\mathrm{MO}}^{-1}\exp\left(-\frac{E_{ii} + PV_{ii}}{RT}\right), \tag{11}$$

$$C_{\mathrm{H}} \propto C_w \propto f_{\mathrm{H_2O}}^{2}\,(P,T)\,a_{\mathrm{SiO_2}}^{-1}\exp\left(-\frac{E_{iii} + PV_{iii}}{RT}\right), \tag{12}$$

$$C_{\mathrm{H}} \propto C_w \propto f_{\mathrm{H_2O}}^{\frac{1}{2}}\,(P,T)\left[\mathrm{O}_{\mathrm{I}}''\right]^{\frac{-1}{2}}\exp\left(-\frac{E_{iv} + PV_{iv}}{RT}\right), \tag{13}$$

$$C_{\mathrm{H}} \propto C_w \propto f_{\mathrm{H_2O}}^{\frac{1}{2}}\,(P,T)\left[\mathrm{O}_{\mathrm{I}}''\right]^{\frac{1}{2}}\exp\left(-\frac{E_v + PV_v}{RT}\right), \tag{14}$$

where $C_{\mathrm{H}}(C_w)$ is the concentration of hydrogen (water) in the mineral, $f_{\mathrm{H_2O}}\,(P,T)$ is the fugacity of water that changes with pressure and temperature, a_{MO}, $a_{\mathrm{SiO_2}}$ are the activity of oxides, E_X is the energy change and V_X is the volume change of a solid associated with each reaction, X. Note that both $f_{\mathrm{H_2O}}\,(P,T)$ and $\exp(-(E_x + PV_x)/RT)$ terms strongly depend on pressure (and temperature) and they change with pressure in the opposite ways. Consequently the pressure dependence of hydrogen solubility is controlled by a delicate balance of these two terms. Note also that the concentration of OH^- (Eqs. (13) and (14)) depends on the number of oxygen interstitial atoms that in turn depends on thermo-chemical conditions.

For olivine, Zhao et al. (2004) determined the temperature (and pressure) dependence of hydrogen solubility to get $E_X \sim 50$ kJ/mol and $V_X \sim 10 \times 10^{-6}$ m^3/mol. Note that this value of V_X agrees well with the molar volume of MgO that is consistent with the model (i) above. For wadsleyite, Williams and Hemley (2001) proposed based on highly scattered data that hydrogen solubility *decreases* with temperature. Demouchy et al. (2005) showed that the hydrogen solubility in wadsleyite is only weakly dependent on temperature and pressure in the temperature range in which coexisting fluid is nearly pure water. Using the pressure and temperature dependence of water fugacity, this observation implies that for wadsleyite, we can estimate that $E_X \sim -(50\text{–}80)$ kJ/mol and $V_X \sim (11\text{–}13) \times 10^{-6}$ m^3/mol. Again, the estimated volume change, V_X, is roughly consistent with the volume of MgO supporting the mechanism (i)[2].

[2] Based on the observation of weakly pressure dependence of hydrogen solubility, (Demouchy et al., 2005) argued that the volume change associated with hydrogen dissolution in wadsleyite is nearly zero (which would be *inconsistent* with the model (i)). This inference is incorrect. The pressure dependence of water fugacity must be included in estimating V_X. Similarly, the temperature dependence of water fugacity needs to be included in estimating E_X.

The large difference in E_X between olivine and wadsleyite likely reflects the difference in crystal chemistry as first noted by (Smyth, 1987) (wadsleyite structure favors dissolution of hydrogen).

A comparison of these relationships with experimental observations on hydrogen solubility, as well as the experimental observations of infrared spectroscopy provides a clue as to the dominant defect-type under a given thermo-chemical condition. For quartz (and garnet), the mechanism (iii) i.e., the replacement of Si with four protons is the most important mechanism of hydrogen dissolution (e.g., Cordier et al., 1994; Doukhan and Paterson, 1986), whereas in Mg- (or Fe-) bearing silicate such as olivine, wadsleyite and orthopyroxene, mechanism (ii), i.e., the replacement of two protons with Mg (or Fe) is the most important mechanism of hydrogen dissolution (e.g., Kohlstedt et al., 1996). In the following, I will focus on this particular mechanism since most of minerals we will deal with contain Mg (Fe). Note, however, that the dominant defect type may change when thermo-chemical conditions are changed.

Several comments may be made here. (1) In an earlier study by Bai and Kohlstedt (1993), they investigated the mechanisms of hydrogen dissolution through two-stage thermo-chemical treatment in which a single crystal of olivine was first annealed at high temperatures (∼1573 K) for a given oxygen fugacity and oxide activity. Then the crystal was annealed at lower temperatures (∼1173–1323 K) under hydrous conditions. In this treatment, it is believed that the non-stoichiometry (i.e., Mg/Si, Mg + Fe/O ratios) of a sample is equilibrated with the thermo-chemical conditions in the first stage treatment, and in the second stage, hydrogen reacts with an olivine with fixed stoichiometry. Based on the dependence of concentration of hydrogen on oxygen fugacity and oxide activity in the first stage, Bai and Kohlstedt (1993) concluded that the reaction (v) is the dominant mechanism of hydrogen dissolution in olivine. The distribution of hydrogen after this type of thermo-chemical treatment is only partially in chemical equilibrium with the environment, and the results of such an experiment do not necessarily correspond to the atomic mechanisms of hydrogen dissolution at chemical equilibrium. (2) A proton is in most cases attracted to an oxygen ion to form an OH^- dipole. This is the case even for mechanisms (ii) and (iii). To illustrate this point, a defect such as $(2H)_M^{\times}$ may be written as $\{(OH)_O^{\bullet} - V_M'' - (OH)_O^{\bullet}\}^{\times}$, but this notation obscures the site of a defect. This defect is primarily associated with the M-site and therefore changes the configuration entropy of the system through its effects on the M-site. (3) Throughout this paper, I will use the values of hydrogen contents determined by infrared spectroscopy using the Paterson calibration (Paterson, 1982). There are new calibrations on olivine that suggest that the Paterson calibration may need some corrections (e.g., Bell et al., 2003). However, new calibration is available only for olivine but not for other minerals such as wadsleyite. At the lack of any experimental data showing otherwise, I assume that the corrections are similar for all minerals, so the new calibration will not affect most of the conclusions in this paper except for the absolute values of water (hydrogen) content because all the data are data based on the same calibration.

3 INFLUENCE OF HYDROGEN ON THE PHASE DIAGRAMS

Given the solubility mechanisms of hydrogen in melts and solid minerals, one can make a theoretical analysis of phase relationships such as solid-solid phase transformations or melting. The construction of such a phase diagram depends critically on the expression of a relationship between the hydrogen content and the chemical potential that is determined by the atomistic mechanism of hydrogen dissolution.

3.1 Influence of hydrogen on the olivine-wadsleyite phase boundary

Dissolution of hydrogen reduces the free energy of a material. Experimental studies show that a significantly larger amount of hydrogen can be dissolved in wadsleyite than in olivine (e.g., Kohlstedt et al., 1996; Young et al., 1993). Therefore the dissolution of hydrogen will expand the stability field of wadsleyite relative to that of olivine (the depth of "410-km" boundary will be shallower if a large amount of hydrogen is present). A more subtle effect is the change in the *width* of the "410-km" discontinuity with hydrogen content. When the system is considered to be a binary system, i.e., Mg_2SiO_4-Fe_2SiO_4, there is a range of pressure (at a fixed temperature) during which the phase transformation is completed. When the upper and the lower boundaries are affected by hydrogen differently, then the width of the boundary will be modified by hydrogen.

The degree to which the dissolution of hydrogen affects the free energy depends on the atomistic mechanisms of hydrogen dissolution. In his paper on this topic, (Wood, 1995) used a model of hydrogen dissolution in wadsleyite by (Smyth, 1987, 1994) and in olivine by Bai and Kohlstedt (1993). These models are not consistent with the recent experimental observations as summarized in Section 2, and here I use a model that is consistent with the current experimental observations as discussed in Section 2. In my model, the dissolution mechanism is identical for both olivine and wadsleyite, hydrogen is dissolved mainly as $(2H)_M^{\times}$, and only the magnitude of solubility is different between the two phases. In calculating the phase diagram, I use a simplifying assumption that the system under consideration can be treated as an ideal mixture of three components, Mg, Fe and H for the M-sites. In this approximation, the chemical potential of each component is a function of concentration of each component as

$$\mu_{ij} = \mu_{ij}^0 + RT \log x_{ij}, \tag{13}$$

where μ_{ij} is the chemical potential, μ_{ij}^0 is the chemical potential for a pure material and x_{ij} is the mole fraction of M-sites for a component i (Mg, Fe and H) in phase j (olivine and wadsleyite). Chemical equilibrium demands

$$\mu_{io}^0 + RT \log x_{io} = \mu_{iw}^0 + RT \log x_{iw} \quad \text{for } i = \text{Mg, Fe and H}, \tag{14}$$

where subscript $o(w)$ refers to olivine (wadsleyite). The M-site is shared by three elements so that

$$\sum_i x_{io} = \sum_i x_{iw} = 1. \tag{15}$$

There are six unknowns (three components in a two phase system) with five equations ((14) and (15)). Another necessary parameter is the water fugacity that determines the hydrogen content (in olivine, x_{Ho}). In the first calculation, I fixed the water fugacity, i.e., I assumed the *open system* behavior. I use the various values of hydrogen content in olivine (corresponding to the various values of water fugacity) and the ratio of water content in wadsleyite to olivine is fixed to be $x_{Hw}/x_{Ho} = 10$, which is assumed to be independent of pressure. (This is justifiable because in my model, the mechanism of hydrogen dissolution is identical between olivine and wadsleyite, but not valid for the model assumed by Wood, 1995.) Thermodynamic data for Mg and Fe components of olivine and wadsleyite are from Akaogi et al., 1989. The results are shown in Figure 2a, showing that the depth of transition decreases with the increase in hydrogen content. Both the upper and the lower boundaries move nearly the same amount, and the width of the transition does not change with hydrogen in this case (open system behavior).

When a phase transformation occurs in a *closed system* with hydrogen-undersaturated condition, then a progressive phase transformation will change the concentrations of hydrogen in each phase according to the degree of transformation (water

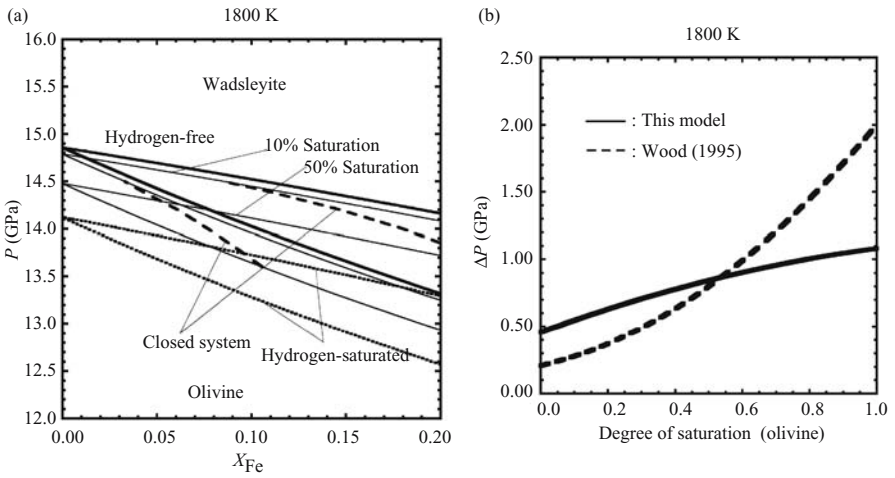

Figure 2. The influence of hydrogen on the olivine-wadsleyite phase boundary. (a) Solid lines: results for an open system. Broken curves: results for a closed system with the total water content of 50% saturation. (b) Variation of the width of the olivine-wadsleyite boundary with hydrogen saturation (saturation in olivine corresponds to ~0.1 wt% water or 1.5×10^4 ppm H/Si).

fugacity will change with the progress of a phase transformation). Consequently, when the pressure just reaches the minimum pressure at which the wadsleyite phase appears, much of the hydrogen is in olivine, whereas the hydrogen concentration in olivine decreases as the volume fraction of wadsleyite increases. Therefore the pressure at which olivine starts to transform to wadsleyite is controlled by the initial water content in olivine, and is significantly lower than the pressure at which this transformation would start in hydrogen-free system. In contrast, the pressure at which this transformation is completed is controlled by the hydrogen content in olivine at this stage that is significantly lower than the hydrogen content at the beginning of the olivine to wadsleyite transformation. (Exactly the same can be applied to a case when a phase transformation starts from wadsleyite.) A phase diagram for this more realistic case can be calculated from the results of fixed hydrogen content by incorporating the mass balance requirement (see broken curves in Figure 2a). As a result of this gradual change in hydrogen content in each phase, there is a broadening of the binary loop as first pointed out by Wood, 1995. The width of the olivine to wadsleyite binary loop calculated in this way is shown in Figure 2b. Note that although the width of the boundary increases with hydrogen content similar to the model by Wood (1995), the degree to which the width increases with hydrogen content is somewhat different between the present model and the model by Wood (1995). This difference is caused mainly by the difference in the model of hydrogen dissolution and the choice of thermodynamic parameters.

A few comments are in order here. (1) The model results for an open, saturated system agree with the experimental observations by Chen et al. (2002); Smyth and Frost (2002) for an open, water-saturated system. But the close system behavior predicted by the model has not been tested experimentally. Chen et al. (2002); Smyth and Frost (2002) compared their results for an open system directly with those by Wood (1995) for a closed system and discussed that their results did not agree with those by Wood (1995). This is misleading. The variation of the width of transformation by hydrogen content predicted by Wood (1995) model occurs only in a closed system but not in an open system. (2) The validity of the assumption of a closed system behavior in real Earth is not necessarily obvious. If the amount of water (hydrogen) in Earth's transition zone exceeds a critical value ($\sim$0.05 wt% , see the next section), the phase transformation from wadsleyite to olivine in a upwelling current could cause partial melting (Bercovici and Karato, 2003). In this case, hydrogen can be removed from the system during the phase transformation and the assumption of a closed system behavior will be violated. (3) A comparison of the model results on the width of the "410-km" boundary with seismological observation is not straightforward due to the fact that the actual depth variation of acoustic properties in a phase loop may not a simple function of the volume fraction of each phase (Stixrude, 1997). In summary, I conclude that the use of the width of the "410-km" discontinuity to infer the water (hydrogen) content as proposed by Wood (1995) (see also van der Meijde et al., 2003) is subjected to large uncertainties. Other techniques such as the use of electrical conductivity or seismic wave velocities (or attenuation) provide a more robust estimate of hydrogen contents (e.g., Karato, 2003; Huang et al., 2005).

3.2 Influence of hydrogen on the melting relation in the olivine- and wadsleyite-rich systems

A similar consideration suggests that the boundary between a solid mineral and a melt should be modified by the addition of hydrogen (water). Whatever the details might be, the addition of hydrogen should expand the stability field of melt and reduces the solidus temperature because a significantly larger amount of hydrogen is dissolved in a melt than in a solid.

Here I will discuss the influence of hydrogen on the melting relation for olivine- and wadsleyite-dominated systems. A particularly interesting issue here is the estimate of the critical amount of water (hydrogen) needed to initiate melting under deep upper mantle conditions which determines the plausibility of the transition-zone melting hypothesis (e.g., Bercovici and Karato, 2003).

A schematic phase diagram of silicate (olivine- or wadsleyite-rich) and water (hydrogen) system is shown in Figure 3. At low temperatures, a fluid phase that coexists with a silicate (olivine or wadsleyite) is more-or-less pure H_2O. Therefore the phase diagram at the lower temperature should be a diagram in which two phases (olivine (wadsleyite) and water) has small mutual solubility. The solidus at low temperatures corresponds, approximately, to the solubility limit of water (hydrogen) in olivine (wadsleyite). The water (hydrogen) solubility in olivine increases with temperature (Zhao et al., 2004). Therefore the solidus for olivine should have a positive slope on a water content versus temperature plane. The intrinsic temperature effect of water (hydrogen) solubility in wadsleyite is not known (see for discussion on this issue, Demouchy et al., 2005); but it is expected to be smaller than olivine because the enthalpy of dissolution of water (hydrogen) in wadsleyite is likely to be smaller than that in olivine. Above a certain temperature, the composition of a fluid phase that coexists with olivine (wadsleyite) changes drastically with temperature: the solubility of silicates in aqueous fluids increases with temperature (also with pressure) (e.g., Mibe et al., 2002). Consequently, the activity of water (hydrogen) in a fluid phase coexisting with olivine or wadsleyite decreases with increasing temperature. This causes the decrease in water (hydrogen) content in olivine or wadsleyite with temperature; and eventually, the curve must go to zero water content at a temperature corresponding to the melting temperature at water-free condition ($\sim$2500 K at $\sim$13 GPa for olivine[3]). Therefore the solidus must have a kink or an inflection point at a certain temperature above which the temperature dependence of silicate content in a fluid is important. If the location of this kink (the inflection point) corresponds to the eutectic point reported by Inoue (1994), then this temperature is $\sim$1500 K at $\sim$13 GPa and the water content in olivine at this point is $\sim$0.1 wt% (I use the temperature and pressure dependence of water (hydrogen) solubility based on Zhao et al. (2004)). The exact calculation of the solidus above this point is difficult because

[3] This temperature is significantly lowered ($\sim$500 K) when the influence of other volatiles such as carbon dioxide is included.

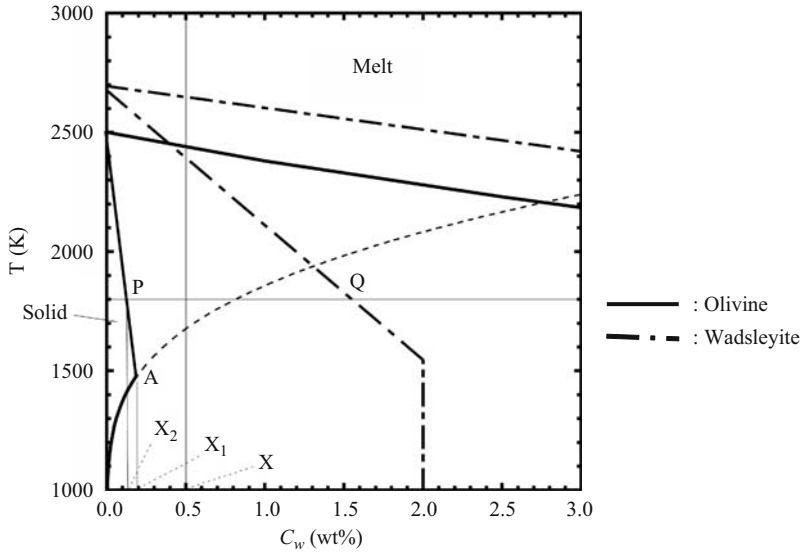

Figure 3. Influence of hydrogen (water) on the melting relationship in an olivine- or wadsleyite-rich system at ~400–450 km depth. Only a silicate-rich portion is shown. The low temperature part of the phase diagram is constrained by the solubility data. The inflection point, A, is constrained by the phase relationship determined by Inoue (1994) and the solubility data by Zhao et al. (2004) to be $X_1 \sim 0.1$ wt% and $T \sim 1500$ K. If the initial water content is $X \sim 0.1 - 1$ wt%, an upwelling material ($T \sim 1800$ K) in the wadsleyite-dominant region will not melt since the boundary between solid and melt for wadsleyite is at the water-rich side (Q). As the material ascends, the volume fraction of olivine increases and the boundary shifts to the water-poor side (P). If this melt-solid boundary intersects a line for a given water content (X), then partial melting will occur. The critical water content for melting is estimated to be $X_2 \sim 0.05$ wt% or less.

we do not know the dependence of free energy of a hydrous silicate melt on water (hydrogen) content precisely.

Although the phase diagram of this system is not precisely known at this time, a useful constraint can be obtained about the critical water (hydrogen) content for partial melting. Imagine an upwelling mass across the "410-km" boundary. The temperature in that mass follows more-or-less the adiabatic gradient (~0.3–0.4 K/km). For a typical mantle temperature, the temperature of an upwelling mass at 410-km is ~1800 K. Consider a rock mass initially in the wadsleyite-rich region (say at 450 km). Because the hydrogen solubility in wadsleyite is significantly higher than that in olivine, the solidus for wadsleyite should be in the water (hydrogen)-rich side. For a typical water content in the transition zone (~0.1 wt%, Huang et al., 2005), water content-temperature conditions will be to the "left" of the curve in this phase diagram, and melting will not occur in a wadsleyite-dominated region. As the volume fraction of wadsleyite decreases with further upwelling, the solidus shifts to the lower water content, and eventually partial melting will occur. Therefore the critical water

content for partial melting is defined by the intersection of a mantle adiabat with the solidus for an olivine-rich system. If Inoue (1994)'s eutectic point and water-free melting points are used, I estimate that this critical water content is ~0.05 wt% or less for an adiabat of ~1800 K. The precise value of X_2 is difficult to constrain because of the lack of detailed knowledge about the thermodynamic properties of hydrous silicate melt under these conditions.

Note also that the estimate of the melting relation presented above is based on the assumption that only hydrogen is an element that enhances melting through the increase in configurational entropy. This is unlikely to be true, and the influence of other elements such as carbon (Dasgupta and Hirschmann, 2006) or potassium (Wang and Takahashi, 2000) should also be considered. In these cases, the conditions for melting are significantly expanded (see Karato et al., 2006).

These two examples illustrate how the knowledge of the dissolution mechanisms of water (hydrogen) may be used to investigate the phase relationships in mantle materials. In these cases, only the dominant hydrogen (water)-related defects play important roles. I conclude that the mechanisms of hydrogen dissolution in solid minerals are well understood and the influence of hydrogen on the phase diagram involving solid minerals is well constrained. In contrast, large uncertainties remain in our understanding of the influence of hydrogen on the free energy of melts.

In the next section, I will focus on the influence of hydrogen on the transport properties of solid minerals, which requires a deeper level of understanding of materials science including the influence of minor hydrogen-related defects.

4 EFFECTS OF HYDROGEN ON DEFECT-RELATED PROPERTIES OF MINERALS

4.1 Point defects

The solubility mechanisms of hydrogen summarized in Section 2 show that in most cases, the majority of the hydrogen is incorporated in minerals as fully charge-compensated defects associated with one particular cation (Mg (Fe), Ca or Si) in a mineral. As far as these defects are neutral (relative to the perfect crystal), the chemical reaction is closed in a particular sub-lattice, and the dissolution of hydrogen does not affect the concentration of defects at other sites. In this regime, the dominant defects that define the charge balance in Fe-bearing minerals are ferric iron Fe^{g}_{M} and M-site vacancy V''_M through $[Fe^{g}_{M}] = 2[V''_M]$ (e.g., Karato, 1974). The defect population is determined basically by the oxidation-reduction reaction. I will call this as the *redox-controlled regime*. However, in reality, the dissolution of hydrogen not only results in neutral defects but also some charged defects through the following type of reaction,

$$(2H)^{\times}_{M} \Leftrightarrow H'_M + H^{g}, \tag{16}$$

where H'_M is a M-site vacancy containing one proton and H^{g} is a free proton.

There are two important consequences of this ionization reaction. First, once a large amount of charged defects such as H'_M are created, then the charge balance of a crystal is modified, and the concentrations of defects at other sub-lattice sites will also be affected. For a reasonable range of conditions, $[(2H)^{\times}_M]/[V''_M] \sim 10^2$–$10^3$, and in such a case, if more than ∼0.1–1 % of $(2H)^{\times}_M$ is ionized by the reaction (16), then the charge balance will be modified. Second, the dominant charge carrying species for electrical conduction will be a minor defect, H^g, if $[H^g]\mu_{H^g} > [(2H)^{\times}_M]\mu_{(2H)^{\times}_M}$ where μ_X is the mobility of a species X. The experimental study by Huang et al. (2005) showed

$$\sigma_{\text{cond}} \propto C_w^{3/4}, \tag{17}$$

where σ_{cond} is electrical conductivity. This result can be interpreted by the conduction due to free protons, H^g, but not by a dominant defect, $(2H)^{\times}_M$, with a charge neutrality condition of $[H'_M] = [Fe^g_M]$ (for conduction due to $(2H)^{\times}_M$, one expects $\sigma_{\text{cond}} \propto C_w$). This means that the ionization reaction is relatively easy although the dominant hydrogen-related species is $(2H)^{\times}_M$[4]. This indicates that the mobility of a free proton is much higher than that of a proton trapped at the M-site. Note that Karato (1990)'s proposal that the electrical conductivity can be directly calculated from the (total) hydrogen content and hydrogen diffusion coefficient using the Nernst-Einstein relation is not justified. Direct conductivity measurements are needed.

In this regime ($[H'_M] = [Fe^g_M]$), concentrations of all other defects are affected by the dissolution of hydrogen. I will call this the *proton-controlled regime*. Consequently, concentrations of all other defects in this regime depend on hydrogen content in the crystal. Therefore plastic deformation that is likely dependent on the diffusion in Si- or O-sublattice is also enhanced by the presence of hydrogen. Figure 4 illustrates the dependence of point defects on chemical environment in these two cases.

The diffusion of atoms in a solid is related to the concentration and diffusivity of relevant defect. Therefore the influence of hydrogen on diffusion is through the effects on defect concentration and through its influence on mobility, viz.,

$$D(C_w) = x_d\,(C_w) \cdot D_d\,(C_w)\,, \tag{18}$$

where $x_d(C_w)$ is the concentration of defect (fraction of defects at a relevant site) and $D_d(C_w)$ is the diffusion coefficient of that defect. In principle, both of these factors can be affected by hydrogen. However, in most cases, the influence of hydrogen on $D_d(C_w)$ is weak, and most of the influence of hydrogen on diffusion is through $x_d(C_w)$ (Hier-Majumder et al., 2005). Consequently, results such as those shown in Figure 4 can be used to calculate the dependence of diffusion coefficients on hydrogen fugacity (or content).

---

[4] This statement means that $[H'_M]?[V''_M]$ and in combination with the results by Hier-Majumder et al. (2005), ('Influence of protons on Fe-Mg interdiffusion in olivine', *Journal of Geophysical Research* **110**, 10.1029/2004JB003292), it implies $[(2H)^{\times}_M]?[H'_M]?[V''_M]$.

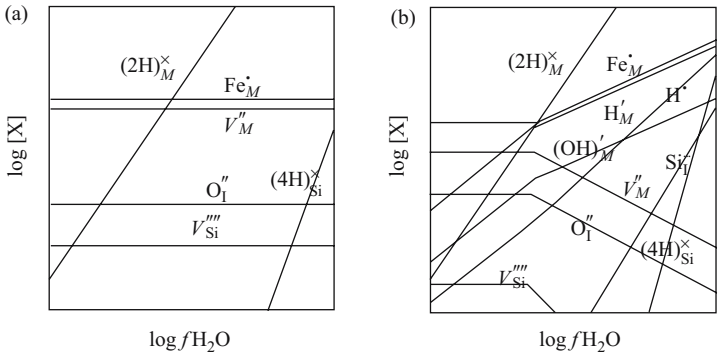

Figure 4. The point defect concentration versus water fugacity diagram for (a) a high ionization potential and (b) a low ionization potential. The Kröger-Vink notation of point defects is used. In case (a), all hydrogen-related point defects are neutral, and the dissolution of hydrogen in one sublattice (say M-sublattice) does not affect the point defect concentration in the other sublattice. In contrast, when the ionization potential is low, then the dissolution of hydrogen at the M-sublattice changes the population of charged defects and hence modifies the concentration of point defects in the other sublattices.

The results summarized above can be directly applied to plastic flow when the deformation is caused by the diffusion of atoms, i.e., diffusion creep. For example, a comparison of the dependence of the rate of deformation on water fugacity with the results of Figure 4 can provide a constraint on the atomic species that controls the rate of deformation. It should be noted that in identifying the atomistic mechanisms of diffusion from such a comparison, the proper parameterization incorporating the effects of both pressure dependence of the fugacity (of water) and the activation volume must be used. In the experimental study such as the one by Mei and Kohlstedt (2000a) at low pressures ($<$0.45 GPa), they could not constrain the activation volume term, and consequently it is difficult to identify the atomistic mechanisms of diffusion convincingly from studies at low pressures.

As can be seen in Figure 5, the dependence of the strain-rate on pressure under hydrogen-saturate conditions is non-monotonic, as was first pointed out by Karato (1989). The strain-rate first increases with pressure due to the effects of increasing water fugacity, but then at higher pressures it decreases with pressure if the activation volume is large. It is important to note that, without knowing the value of activation volume, no laboratory data can be extrapolated to the Earth's interior beyond a few tens of km ($>$1 GPa) (see Fig. 5). Experimental studies at pressures higher than $\sim$2 GPa are needed to place any meaningful constraints on the activation volume. A similar behavior was found by Hier-Majumder et al. (2005) in their study of Mg-Fe diffusion in olivine under hydrogen-saturated conditions to 6 GPa.

It should also be emphasized that in most high-pressure experiments, a large amount of hydrogen is dissolved in a sample even though hydrogen (water) is not added intentionally without a great care being taken (Huang et al., 2005; Nishihara et al.,

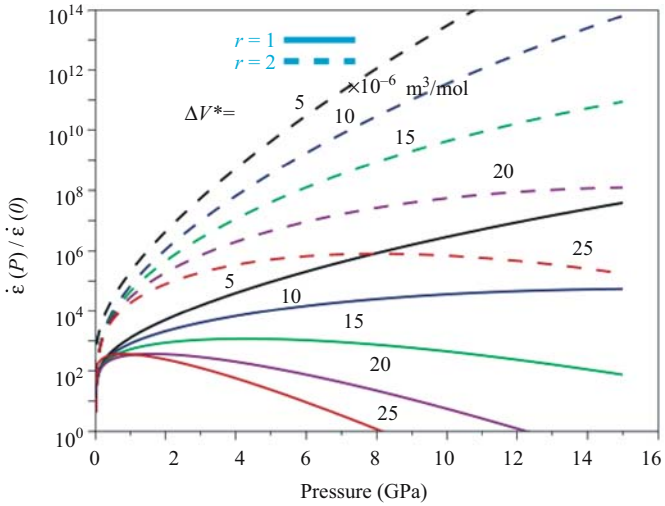

Figure 5. Influence of pressure on the rate of deformation under hydrogen-saturated conditions. The pressure dependence of rate of deformation is controlled both by the water fugacity and the activation volume as $\dot{\varepsilon} \propto f^{r}_{H_2O}(P,T)\exp(-P\Delta V^*/RT)$. Uncertainties in the activation volume, ΔV^*, cause major uncertainties in the estimated strain-rate above ~2 GPa. In other words, a robust constraint on activation volume can only be obtained by the experiments above ~2 GPa.

2006). Consequently, many of the published results on "pressure" effects on diffusion and deformation likely include significant influence of hydrogen. Unusually low activation volumes reported in many previous high-pressure experiments on diffusion (Béjina et al., 2003) or deformation (Li et al., 2004) ($<1\times10^{-6}$ m^3/mol) could be due to unrecognized large effects of hydrogen at high pressures. The hydrogen content in a sample before and after each experiment must be measured and reported in any high-pressure research in this area.

4.2 Dislocations

Dislocations play an important role in plastic deformation, seismic wave attenuation (hence seismic wave velocities) as well as in other kinetic processes such as the kinetics of phase transformation. Hydrogen is known to have a strong influence on dislocation mobility and hence on these physical processes. Currently, the best knowledge about the influence of hydrogen on dislocation mobility comes from the experimental studies of dislocation creep combined with theoretical studies on the interaction of hydrogen with dislocations. Previous papers reviewing the mechanisms of hydrogen effects (on dislocation creep) include Karato (1989) and Paterson (1989). Karato (1989) presented a model of the influence of hydrogen on point defects in olivine (as summarized in Sections 2 and 4.1) and also predicted a non-monotonic

effect of pressure under hydrogen-saturated conditions which is supported by the later experimental study of (Karato and Jung, 2003). Paterson (1989) reviewed the experimental observations and microscopic models of the weakening of quartz by hydrogen. Here I will review the issue of the influence of hydrogen on plastic deformation with the emphasis on the appropriate parameterization of the influence of hydrogen.

Experimental observations in many silicates including quartz, olivine and pyroxenes indicate that plastic deformation due to dislocations is enhanced by the presence of hydrogen. In all cases so far studied, the degree of weakening is positively correlated with the amount of dissolved hydrogen in a given mineral. Also the degree of weakening is correlated with the silica content: the higher the silica content, the more is the weakening by hydrogen. In quartz, this effect is very strong, whereas the weakening effect is modest in olivine.

A generic equation for the rate of deformation by dislocation motion is,

$$\dot{\varepsilon} = \rho b v = \rho b^2 n_i v_i, \tag{19}$$

where $\dot{\varepsilon}$ is strain-rate, ρ is dislocation density, v is dislocation velocity, n_i is the concentration (number per unit length) of "steps" (kinks or jogs) and v_i is their mobility. In writing this equation, we have taken into account the fact that dislocation motion occurs in a step-wise fashion through the motion of individual "steps" such as kinks or jogs. Therefore the dependence of the rate of deformation on hydrogen at steady state[5] can be written as

$$\dot{\varepsilon}(C_w) = \rho b^2 n_i(C_w)\, v_i(C_w)\,. \tag{20}$$

Let us first discuss the dislocation velocity, $v_i(C_w)$. The physical mechanisms that may control the dislocation velocity (mobility) depend on (i) the nature of chemical bonding, (ii) crystal structure, and (iii) the concentration of impurity atoms or secondary phase particles. In most of the silicate minerals or oxides, the nature of chemical bonding is between ionic to covalent. The Si-O is strongly covalent (particularly when it is coordinated with four oxygen ions), whereas Mg-O bond is more ionic. Consequently, the resistance to break chemical bonds is stronger in minerals with high SiO_2 content. In these materials, high-temperature steady-state deformation is controlled, in most cases, either by dislocation climb that is in turn controlled by the diffusion of the slowest moving atomic species or the glide motion of dislocations through the nucleation and migration of double-kinks. In these cases, hydrogen may affect dislocation velocity through two different effects: (i) through the enhancement of the diffusion of the slowest diffusing species, or (ii) through the enhancement of the dislocation glide by reducing the energy for nucleation and/or the migration of kinks.

---

[5] The influence of the non-steady-state deformation is important in minerals with strong covalent bonding (e.g., quartz). In these minerals, the creep strength observed in laboratory experiments is largely controlled by dislocation generation, i.e., $\rho\,(C_w, t)$.

A few words need to be added about the density of steps, $n_i(C_w)$. In a material in which the chemical bonding is strong, the density of jogs or kinks is often controlled by thermal equilibrium. In these cases, the density of these steps depends strongly on the energy of the formation of these steps and the chemical environment. The dependence of the density of these steps on chemical environment can be analyzed by considering the following the chemical reaction, where a dislocation line reacts with some chemically active species such as electron holes or water (hydrogen), viz.,

$$h^{\mathrm{g}},\ \mathrm{H_2O} + \textit{dislocation} \Leftrightarrow \textit{charged or hydrated kinks (jogs)}. \tag{21}$$

For this model, the law of mass action gives

$$n_i(C_w) \propto \left[h^{\mathrm{g}}(C_w)\right]\exp\left(-\frac{\Delta G_i\,(C_w,\sigma)}{RT}\right)\ \textit{or}\ \ [\mathrm{H_2O}]\exp\left(-\frac{\Delta G_i\,(C_w,\sigma)}{RT}\right), \tag{22}$$

where $\Delta G_i(\sigma, C_w)$ is the formation free energy of a step. Heggie and Jones (1986) showed that the energy of the formation and migration of kinks on the dislocation line in quartz is reduced by hydrogen; and hence the kink density (and mobility) will be higher at hydrogen-rich conditions.

Experimental observations supporting both cases have been reported. For olivine polycrystals deformed in the dislocation creep regime at high temperatures and low stresses, the experimental observations can be interpreted by the dislocation climb-controlled model (Fig. 6),

$$\dot{\varepsilon}_{\mathrm{wet}} \propto n_i(C_w)\, v_i(C_w) \propto \left[h^{\mathrm{g}}\right] D \propto \left[h^{\mathrm{g}}\right]\left[\mathrm{Si}_I^{\mathrm{gggg}}\right] \propto f_{\mathrm{H_2O}}^{\frac{5}{4}}, \tag{23}$$

where D is diffusion coefficient (Karato and Jung, 2003; Mei and Kohlstedt, 2000b). Therefore the net strain-rate in this case is given by

$$\dot{\varepsilon} = \dot{\varepsilon}_{\mathrm{dry}} + \dot{\varepsilon}_{\mathrm{wet}}, \tag{24}$$

with

$$\dot{\varepsilon}_{\mathrm{wet}} = A \cdot f_{\mathrm{H_2O}}^{\frac{5}{4}} \propto C_w^{\frac{5}{4}}. \tag{25}$$

This interpretation is not unique, however. Other models such as $\dot{\varepsilon} \propto [(3\mathrm{H})'_{Si}]$ can also explain the observed dependence on water fugacity. Additional observations such as the dependence of strain-rate on oxide activity and on oxygen fugacity need to be used to better constrain the model.

For quartz in which the chemical bonding is a strong covalent bond, and Griggs (1974) proposed that creep is controlled by dislocation glide and that hydrogen reduces the energy for nucleation (and growth) of kinks on dislocation line thereby enhances the dislocation glide mobility. Such a model will also apply to other minerals such as olivine at relatively low temperatures and/or high stresses. In this case, the

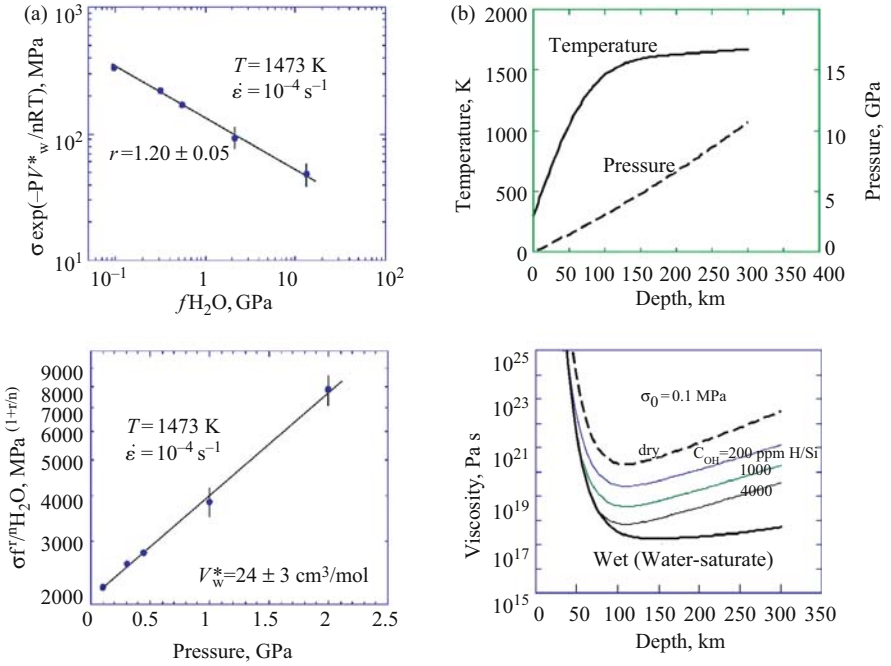

Figure 6. The effects of pressure on dislocation creep in olivine for water (hydrogen)-saturated conditions (after Karato and Jung, 2003). (a) The creep strength can be analyzed using two parameters, r and V^* (ΔV^*), using the relationship, $\dot{\varepsilon} = A\sigma^n f_{H_2O}^r \exp(-PV^*/RT)$. (b) The depth variation of viscosity (for a constant stress) in the upper mantle for a range of water content (bottom) together with the assumed geotherm corresponding to the oceanic environment (age = 100 my) and the pressure-depth relationship (top).

creep rate is proportional to the density of kinks and their mobility and hence (using Eq. (22)),

$$\dot{\varepsilon}_{\text{wet}} \propto [H_2O] \exp\left(-\frac{\Delta G_w(\sigma)}{RT}\right) \propto C_w \exp\left(-\frac{\Delta G_w(\sigma)}{RT}\right), \tag{26}$$

where ΔG_w is the free energy for nucleation and migration of a hydrated double kink. This form of flow law best explains the experimental observations on olivine at relatively high stress levels (Katayama and Karato, 2006a).

So far I have reviewed the influence of hydrogen on the plastic flow of isotropic mineral aggregates. Dislocation creep occurs by the motion of crystal dislocations. By its very definition, the motion of dislocations is anisotropic. Consequently, the influence of hydrogen can also be anisotropic: hydrogen may enhance deformation by different slip systems in a different way. In such a case, the addition of hydrogen will change the relative contribution from different slip systems to the total strain,

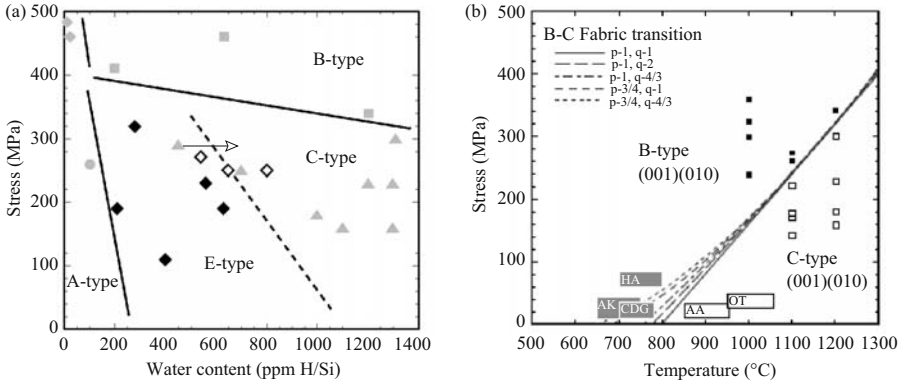

Figure 7. Fabric diagrams for olivine (a) on a stress-water content space at $T \sim 1500$ K (Katayama et al., 2004) and (b) on a stress-temperature space at $C_w \sim 1000$ ppmH/Si (Katayama and Karato, 2006b).

leading to fabric transitions. Hydrogen-induced fabric transitions in olivine was predicted by Karato (1995) and systematically studied by Jung and Karato (2001b), Jung et al. (2006), Karato (1995), Katayama et al. (2004), and Katayama and Karato (2006b) (Fig. 7).

When a fabric transition occurs at relatively low temperatures, the flow laws are best described by an exponential form, i.e., Equation (26). In such a case, the activation free energy for deformation is stress dependent, and in the simplest case, the activation enthalpy, $\Delta H (\Delta G = \Delta H - T\Delta S)$, can be written as

$$\Delta H = \Delta H^o - B\sigma, \tag{27}$$

where ΔH^o is the activation enthalpy at zero stress and B is a constant both of which depend on the slip system. In such a case, the condition for a fabric transition is given by equating the strain-rate for two slip systems as

$$A_1 \exp\left(-\frac{\Delta H_1^o - B_1\sigma}{RT}\right) = A_2 \exp\left(-\frac{\Delta H_2^o - B_2\sigma}{RT}\right). \tag{28}$$

Therefore the fabric boundary is given by

$$RT \log \frac{A_1}{A_2} = \left(\Delta H_1^o - \Delta H_2^o\right) - (B_1 - B_2)\,\sigma. \tag{29}$$

The fabric boundary defined by this equation is insensitive to hydrogen content (as far as a small amount of hydrogen is present), but is sensitive to stress and temperature. This is consistent with the observed fabric transitions from B-type to C-, E-type fabrics (Fig. 7a). This relation is used to extrapolate the experimental data to lower temperatures (the B- to C-type transition) and the results are compared with the

observations on naturally deformed rocks (Fig. 7b). The comparison supports this scaling law.

In contrast, when a fabric transition occurs at high temperature/low stress conditions, then the power-law flow law will apply and then the conditions for a fabric transition will be

$$RT \log \frac{C_1 + D_1 f_{\mathrm{H_2O}}}{C_2 + D_2 f_{\mathrm{H_2O}}} = \Delta H_1^o - \Delta H_2^o. \tag{30}$$

The fabric boundary for this case is controlled essentially by temperature and water fugacity and not by stress. The fabric boundaries between A- and E-type, and between E- and C-type belong to this category (Fig. 7a).

The recognition that hydrogen plays an important role in deformation fabrics has provided a new horizon in interpreting deformation fabrics and seismic anisotropy in terms of flow geometry. In particular, with these new results, the deformation fabrics of rocks from the convergent boundaries and the pattern of seismic anisotropy in these regions can be explained in this model by the regional variation in physical/chemical factors (temperature, water content) rather than the complicated flow patterns (Karato, 2003).

4.3 Grain-boundaries

Hydrogen also affects grain-boundary-related processes. Firstly, grain-boundaries dissolve a higher concentration of hydrogen than the bulk of crystals. Karato et al. (1986) and Mei and Kohlstedt (2000a) noted that fine-grained polycrystalline olivine samples have a larger amount of dissolved hydrogen than their single crystal counterpart. Jung and Karato (2001a) reported that the size of dynamically recrystallized grains in olivine is larger in hydrogen-rich conditions compared to hydrogen-poor conditions. They concluded that this is due to the larger extent of the enhancement of grain-boundary mobility than dislocation mobility using a theory for dynamically recrystallized grain-size by Derby and Ashby (1987). Similarly, Nishihara et al. (2006) found that grain-growth kinetics in wadsleyite is enhanced by hydrogen as (Fig. 8)

$$k = k_{\mathrm{dry}} + k_{\mathrm{wet}}, \tag{31}$$

with

$$k_{\mathrm{wet}} \propto f_{\mathrm{H_2O}}^q \propto C_w^q, \tag{32}$$

with $q \sim 2$ and $L^n - L_0^n = k\,(T, P, C_w)\,t$ (L: grain-size, and t: time). In all cases so far studied, hydrogen enhances grain-boundary processes more than intra-granular processes. Nishihara et al. (2006) suggested that this may be due to the influence of hydrogen not only on diffusion coefficients but also on some grain-boundary properties such as the density of ledges and/or grain-boundary width. Material transport

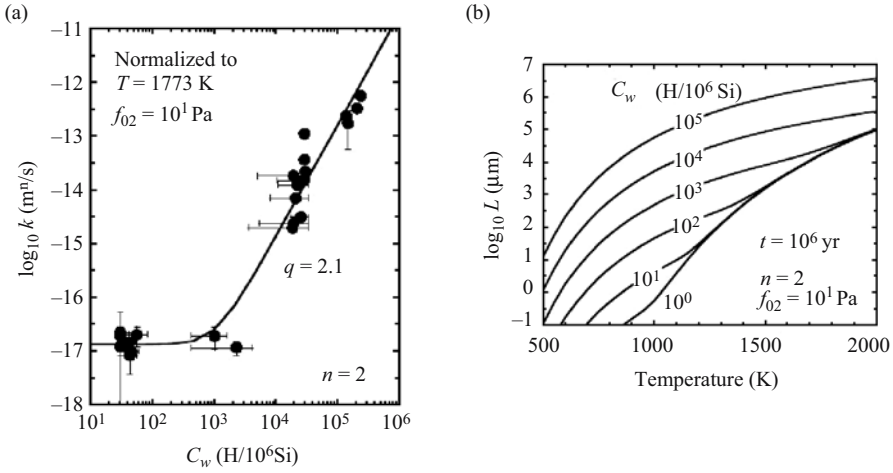

Figure 8. Influence of hydrogen on the rate of grain-growth in wadsleyite (after Nishihara et al., (2006)). (a) The kinetic constant, k, for grain-growth as a function of water content. A constant $k$is defined by $L^n - L_0^n = k\,(T, P, C_w)\,t$ (L: grain-size, L_0: initial grain-size, and t: time). Grain-growth kinetics in wadsleyite shows much stronger dependence on hydrogen content than other properties such as electrical conductivity and diffusion. (b) The grain-size due to grain-growth as a function of annealing temperature and water content. Initial grain-size is assumed to be much smaller than the final grain-size ($L = t^{1/n} k(T, P, C_w)^{1/n}, P = 16$ GPa). A small grain-size, $L < 100\,\mu$m, can be maintained for 1 my only in relatively hydrogen-free and/or low temperature conditions.

across a grain-boundary involves formation of grain-boundary steps "ledges" and migration of steps by diffusion. The density of ledges may increase with water fugacity if the density of ledges is controlled by a reaction similar to (21). Grain-boundary sliding involves formation and migration of ledges and therefore also likely depends strongly on hydrogen content. Strong dependence of grain-growth kinetics on hydrogen content implies that the grain-size in and hence the strength of subducting slabs after the olivine-wadsleyite (or olivine-ringwoodite) phase transformation is likely dependent on hydrogen content as well as on temperature. A small grain-size can be maintained only at relatively hydrogen-free and/or low temperature environment.

5 SOME APPLICATIONS

5.1 Influence of hydrogen on plastic deformation in deep mantle minerals

The Earth's mantle is ∼3000 km thick and plastic deformation in this thick mantle controls the evolution of this planet. One of the most challenging issues in studying the influence of hydrogen on rheological properties is to conduct experimental studies under deep Earth conditions. I have shown that even for the upper mantle minerals it is critical to conduct quantitative deformation experiments above ∼2 GPa in order to

obtain any meaningful data that can be extrapolated to the Earth's interior below a few 10s of km. Although a gas apparatus such as the one developed by Paterson (1990) provides a high resolution mechanical data and has been used in many laboratories (e.g., Mei and Kohlstedt, 2000a; Mei and Kohlstedt, 2000b), the maximum pressure of operation of that apparatus is ∼0.5 GPa. The data obtained under these conditions cannot be used to infer the rheological properties of majority of Earth's mantle.

Currently Karato and Jung (2003) is the only paper in which all the parameters needed for extrapolation to the Earth's deep mantle are determined for olivine (for dislocation creep regime) under controlled hydrogen content. Their experimental studies were conducted to 2.2 GPa (water fugacity ∼13 GPa) and the deviatoric stress was determined using a dislocation density-stress calibration curve. Quantitative experimental studies beyond this pressure range are limited. Two types of high pressure deformation apparatus have been developed: D-DIA (deformation DIA) (Wang et al., 2003) and RDA (rotational Drickamer apparatus) (Xu et al., 2005; Yamazaki and Karato, 2001a). In both cases, controlled deformation of a sample is possible under high pressure and temperature conditions, and the rheological measurements can be performed using a synchrotron X-ray facility. To date, D-DIA has been operated to ∼10 GPa and ∼1600 K (e.g., Li et al., 2004) and RDA has been operated to ∼16 GPa and ∼1800 K (Nishihara et al., 2005). However, quantitative experiments on rheological properties under controlled hydrogen content (water fugacity) have not been performed under these conditions.

Consequently, the influence of hydrogen on rheological properties of minerals in the deep mantle is not well constrained at this time. However, for wadsleyite, we now have a good idea about the atomistic mechanisms of hydrogen dissolution including the nature of charged defects. Processes related to point defects (such as electrical conductivity) in wadsleyite (and ringwoodite) are enhanced by the dissolution of hydrogen. Grain-growth kinetics involving grain-boundary processes in wadsleyite is enhanced by hydrogen. Therefore it is almost certain that plastic deformation in wadsleyite and ringwoodite (either by diffusion of point defects or by dislocation motion) is enhanced by hydrogen. Indirect evidence is available suggesting the enhancement of dislocation motion by hydrogen in wadsleyite (e.g., Kubo et al., 1998). However, there have not been any quantitative experimental studies on the influence of hydrogen on plastic deformation of wadsleyite. Quantitative studies on plastic deformation in wadsleyite (and other deep mantle minerals) are underway in my laboratory. Our preliminary results show a high strength of wadsleyite at water-poor conditions and weakening effects by hydrogen (Nishihara et al., 2005).

Much less is known about the influence of hydrogen in lower mantle minerals. For (Mg,Fe)O, the dominant hydrogen-related defect is either H'_M or $(2H)^{\times}_M$. Deformation of this material occurs either by diffusion of point defects or by dislocation motion, but deformation by dislocation motion is also controlled by diffusion of point defects (kink formation and migration and jog formation are easy in this material because of a small Peierls stress due to weak chemical bonding). Consequently, the influence of hydrogen on deformation of this material can be understood from the results given in Figure 4 the results in Fig. 4 can be applied to (Mg,Fe)O ignoring the defects associated

with Si as far as the charge neutrality condition under hydrogen-rich condition is $[H'_M] = [Fe^g_M]$). In evaluating the influence of hydrogen on deformation in (Mg,Fe)O, I include the following notions: (i) in (Mg,Fe)O, dislocation creep is controlled by dislocation climb that is controlled by diffusion of oxygen. Diffusion of oxygen in (Mg,Fe)O occurs through the diffusion of oxygen vacancies or the diffusion of a neutral defect pair $V''_M - V^{gg}_O$ (see e.g., Ando, 1989). In the former case, the rate of deformation is proportional to $f^{1/2}_{H_2O}$, whereas in the latter, it is insensitive to hydrogen content ($[V''_M - V^{gg}_O] \propto f^0_{H_2O}$). In either case, the influence of hydrogen on plastic deformation by dislocation creep is likely weaker for (Mg,Fe)O than olivine or other silicates. (ii) Diffusion creep in (Mg,Fe)O may be rate-controlled by the volume diffusion of oxygen or by the volume diffusion of Mg (Fe). The latter occurs due to the selected enhancement of oxygen diffusion along grain-boundaries, making the total effective diffusion coefficient of Mg less than that of oxygen (Gordon, 1973). In this case, the creep rate will be proportional to f_{H_2O} (C_w) if $(2H)^\times_M$ is the dominant defect. If one accepts the best documented notion that the volume diffusion of oxygen in (Mg,Fe)O occurs through the diffusion of $V''_M - V^{gg}_O$ and the diffusion creep is rate-controlled by the volume diffusion of Mg (Fe), then the conclusions on the hydrogen effects are (i) hydrogen has no effects on dislocation creep in (Mg,Fe)O, but (ii) hydrogen has effects similar to olivine for diffusion creep (i.e., $\dot{\varepsilon} \propto f_{H_2O}$).

What about silicate perovskites? Virtually nothing is known on the influence of hydrogen on physical properties of silicate perovskites. However, based on the Mössbauer spectroscopy, the dominant point defects in an Al-containing $(Mg,Fe)SiO_3$ perovskite are known to be Al'_{Si} and Fe^g_M (McCammon, 1997). The chemical reaction associated with these defects is

$$\frac{1}{2}Al_2O_3 + \frac{1}{4}O_2 + Fe^\times_M + Si^\times_{Si} \Leftrightarrow Al'_{Si} + Fe^g_M + SiO_2. \tag{33}$$

If the two defects Al'_{Si} and Fe^g_M are the dominant charged defects, then (note that the activity of SiO_2 is fixed by the co-existence of perovskite and magnesiowüsitite)

$$\left[Al'_{Si}\right] = \left[Fe^g_M\right] \propto f^{\frac{1}{8}}_{O_2} a^{\frac{1}{4}}_{Al_2O_3}. \tag{34}$$

The concentrations of these defects are large (more than 10% ; e.g., McCammon, 1997) and hydrogen solubility in perovskite is small (∼10 ppmH/Si or less; e.g., Bolfan-Casanova et al., 2000[6]). Consequently, the incorporation of hydrogen will not change the concentrations of defects at sites other than the one in which hydrogen is incorporated. If analogy with other silicates is a guide, the likely sites at which hydrogen is dissolved in $(Mg,Fe)SiO_3$ perovskite will be either M- or Si-sites (i.e., $(2H)^\times_M$ or $(4H)^\times_{Si}$). Therefore using the model developed in section 4.1 (the results

[6] A much higher "water" solubility was reported by Murakami et al. (2002), but this report is likely in error, because much of the absorption peaks occur at ∼3400 cm^{-1} corresponding to water in fluids or glassy phases. It is likely that their samples contain a number of fluid phase inclusions.

of Fig. 4 can be applied to (Mg,Fe)SiO_3), I conclude that the rate of deformation will be related to water fugacity as $\dot{\varepsilon} - \dot{\varepsilon}_{\rm dry} \propto f_{H_2O}^q \propto C_w^q$ with $q = 1$ if the defects at M-site control the rate of deformation and $q = 2$ if the defects at Si-site control the rate of deformation. In these cases, the influence of hydrogen will be large if plastic deformation under dry conditions is very difficult. The degree to which hydrogen enhances deformation in these cases is primarily controlled by the ratio of the concentration of the point defects at these sites under dry conditions to the concentration of hydrogen-related defects. Judging from the high solubility of trace elements in $CaSiO_3$ perovskite (Corgne and Wood, 2002; Hirose et al., 2004), it is likely that a very small amount of hydrogen (less than 1 ppm H/Si) goes to (Mg,Fe)SiO_3 perovskite in the Earth's lower mantle (a case analogous to hydrogen depletion by partial melting proposed by Karato (1986)). Therefore the influence of hydrogen on plastic deformation in (Mg,Fe)SiO_3 perovskite is likely not very large, unless the concentration of defects under dry conditions is significantly smaller than ~1 ppm.

In evaluating the role of hydrogen in the plastic deformation of the lower mantle phases, it is important to estimate the partitioning of hydrogen as well as the magnitude of hydrogen effect in each phase. The partitioning of hydrogen can be estimated from the experimental results of Bolfan-Casanova et al. (2000) and Bolfan-Casanova et al. (2002), suggesting that more hydrogen is dissolved in (Mg,Fe)O than (Mg,Fe)SiO_3 perovskite. However, I note that Bolfan-Casanova et al. (2002) probably underestimated the hydrogen solubility in (Mg,Fe)O due to the effect of unquenchable hydrogen in their samples.[7] Therefore I conclude that the true partitioning coefficient of hydrogen between (Mg,Fe)O and (Mg,Fe)SiO_3 perovskite is yet to be determined (more hydrogen is likely dissolved in (Mg,Fe)O than was concluded by Bolfan-Casanova et al. (2002). Obviously a lot more research is needed in this area.

5.2 Influence of hydrogen on seismic wave velocities and attenuation

The mechanisms by which hydrogen might influence the seismic wave propagation can be classified into three categories: (i) the addition of hydrogen changes elastic constants due to weak chemical bonding and hence reduces seismic wave velocities, (ii) the addition of hydrogen enhances anelastic relaxation and hence reduces seismic wave velocities and (iii) hydrogen may also modify the relative strength of slip systems and could change the lattice-preferred orientation which changes seismic anisotropy (see Karato, 1995). The third topic is discussed in Section 4.2, so I will briefly review first two topics here assuming elastic isotropy.

[7] The infrared absorption spectra reported by these authors include absorption peaks due to $Mg(OH)_2$ and free water. (Bolfan-Casanova et al., 2002) ignored the hydrogen content associated with these peaks in calculating the hydrogen solubility, but these absorption peaks likely correspond to the hydrogen dissolved in the (Mg,Fe)O lattice at high temperature and pressure that was not quenched. If this is true the actual solubility is ~5–10 times more than the values that they reported.

The basic point is that seismic wave velocities can be modified by hydrogen by two different mechanisms. First is the change in seismic wave velocities through the change in density and (high-frequency) elastic moduli and second is the change in seismic wave velocities through the enhanced attenuation. The direct effect of hydrogen on elasticity was studied using high-frequency elasticity measurements on hydrogen-bearing minerals such as hydrous wadsleyite or hydrous ringwoodite (Inoue et al., 1998; Jacobsen et al., 2004; Yusa and Inoue, 1997[8]). There are some differences in the experimental results particularly on the shear modulus. However, all studies show ∼2–3% reduction in high-frequency seismic wave velocities for 1 wt% addition of water. I conclude that the effects of hydrogen on high-frequency seismic wave velocities could be significant only at relatively high hydrogen content (∼1 wt% water or more). At a smaller hydrogen content (0.1 wt% water or less), this direct influence is less than 0.2–0.3% and consequently, does not play an important role.

How about the indirect influence through anlasticity? (Jackson et al., 1992) conducted the first systematic measurements of seismic wave attenuation under confining pressure. Under their experimental conditions ($T < 1500$ K, $P = 0.3$ GPa), the fugacity of water was ∼0.3 GPa. They observed appreciably higher seismic wave attenuation in samples (dunite, i.e., olivine-dominated polycrystals) that contain more hydrogen than samples from which most of the hydrogen had been removed by heat treatment prior to the experiments. Since many complications occurred in their samples in this pioneering study using a natural dunite, they did not conclude that the difference in attenuation between the two types of sample is due to the difference in hydrogen content. However, in view of our current knowledge on the influence of hydrogen on defect-related properties, this observation is most likely the results of change in hydrogen content in olivine.

A brief theoretical analysis is given below to support the plausibility of this interpretation. First note that seismic wave attenuation under high-temperature, low-frequency regimes obeys the following power-law relationship,

$$Q^{-1}(\omega, T, P, C_w) \propto \omega^{-\alpha}, \tag{35}$$

where ω is the frequency, and α is a constant (∼0.2–0.4). From the dimensional analysis, this implies $Q^{-1}(\omega, T, P, C_w) \propto [\omega \cdot \tau(T, P, C_w)]^{-\alpha}$ where $\tau(T, P, C_w)$ is the relaxation time that depends on the rate of viscous processes involved (T: temperature, P: pressure, C_w: hydrogen content). In most mechanisms of high-temperature attenuation, viscous processes involved in attenuation are similar to long-term creep (Jackson et al., 2000; Karato and Spetzler, 1990), although details can be different. Consequently, $Q^{-1}(\omega, T, P, C_w) \propto \dot{\varepsilon}(T, P, C_w)^{\alpha}$ and therefore $Q^{-1}(\omega, T, P, \text{wet})/Q^{-1}(\omega, T, P, \text{dry}) = [\dot{\varepsilon}(T, P, \text{wet})/\dot{\varepsilon}(T, P, \text{dry})]^{\alpha}$. Alternatively, the relaxation time may be related to the characteristic time for

[8] (Jacobsen et al., 2004)'s results include the influence of Fe/(Fe+Mg) ratio, and the intrinsic effects of hydrogen is smaller than they reported if the effect of Fe/(Fe+Mg) ratio is corrected.

grain-boundary sliding. In this case, $Q^{-1}(\omega, T, P, \text{wet})/Q^{-1}(\omega, T, P, \text{dry}) = [v\,(T, P, \text{wet})/v\,(T, P, \text{dry})]^{\alpha}$ where v is the velocity of grain-boundary sliding (I used a relation $\tau \approx L/v$ with L: grain-size and v: velocity of grain-boundary sliding, and assumed that grain-size did not change with hydrogen content in these experiments). Both dislocation creep and diffusional creep, and all grain-boundary related processes in olivine are known to be enhanced by the dissolution of hydrogen (see previous sections). Therefore it would be surprising if attenuation is *not* enhanced by hydrogen. In the case of (Jackson et al., 1992), the results can be directly compared with the results of (Chopra and Paterson, 1984) who studied the plastic deformation of the exactly same dunite at nearly identical conditions. The results of these studies satisfy the relation $Q^{-1}(\omega, T, P, \text{wet})/Q^{-1}(\omega, T, P, \text{dry}) = [\dot{\varepsilon}\,(T, P, \text{wet})/\dot{\varepsilon}\,(T, P, \text{dry})]^{\alpha}$ reasonably well ($Q^{-1}(\text{wet})/Q^{-1}(\text{dry}) \approx 2$ and $\dot{\varepsilon}\,(\text{wet})/\dot{\varepsilon}\,(\text{dry}) \approx 10$ and hence $Q^{-1}(\omega, T, P, \text{wet})/Q^{-1}(\omega, T, P, \text{dry}) = [\dot{\varepsilon}\,(T, P, \text{wet})/\dot{\varepsilon}\,(T, P, \text{dry})]^{\alpha}$ with $\alpha = 0.3$). Therefore I conclude that the influence of hydrogen (water) on seismic wave attenuation is as well established as the influence of hydrogen on plastic deformation by the study of Chopra and Paterson (1984). A major uncertainty includes the possible influence of grain-boundary sliding. The deformation experiments by Chopra and Paterson (1984) investigated the influence of hydrogen on dislocation creep. Seismic wave attenuation may be due either to dislocation motion or to grain-boundary sliding (Jackson et al., 2000; Karato and Spetzler, 1990). If grain-boundary sliding is important, then a comparison such as $Q^{-1}(\omega, T, P, \text{wet})/Q^{-1}(\omega, T, P, \text{dry}) = [\dot{\varepsilon}\,(T, P, \text{wet})/\dot{\varepsilon}\,(T, P, \text{dry})]^{\alpha}$ is not appropriate if strain-rates are for dislocation creep; and the influence of hydrogen on attenuation will be more important than the case of dislocation-related mechanism.

Combining (31) with an equation for high-frequency, unrelaxed velocity, I get

$$v\,(\omega, T, P, C_w) = v_{\infty}\,(T, P, C_w)\left[1 - \frac{1}{2}\cot\frac{\pi\alpha}{2} Q^{-1}\,(\omega, T, P, C_w)\right], \tag{36}$$

with

$$v_{\infty}\,(T, P, C_w) = \bar{v}_{\infty}\,(P)\,[1 - A\,(P)\,T]\,[1 - B\,(P)\,C_w], \tag{37}$$

and

$$Q^{-1}\,(\omega, T, P, C_w) \propto C_w^{\alpha q}, \tag{38}$$

where $\tau \propto C_w^{-q}$ with $q = 1 - 2$ (1 for dislocation mechanism, 2 for grain-boundary mechanism) and $A\,(P)$ and $B\,(P)$ are constants. This formulation was used in inverting the results of seismic tomography by Shito et al. (2006).

The frequency dependence of seismic wave attenuation in the lower mantle is similar to that in the upper mantle (Shito et al., 2004; Smith and Dahlen, 1981), therefore the sensitivity of attenuation to the relaxation time should be similar between two regions. Assuming a similar functional dependence of attenuation on hydrogen content in the transition zone and the lower mantle minerals, the influence of hydrogen on seismic wave attenuation and velocity in these regions is expected to be large. Figure 9

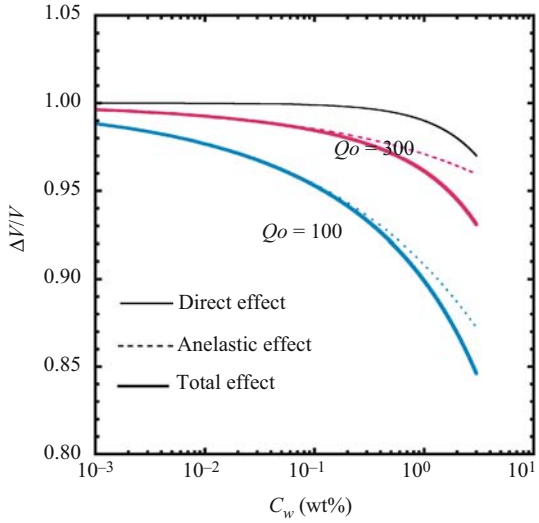

Figure 9. The influence of hydrogen on seismic wave velocities. $\Delta V/V$ is the fraction of velocity variation due to the addition of hydrogen, and C_W is the hydrogen content (wt% water). Qo is the background Q (background Q in the upper mantle is ∼100, whereas in the transition zone and the lower mantle it is ∼300 (in the PREM). A direct effect through the effects on unrelaxed velocity plays a lesser role than anelasticity in most regions of the Earth's mantle, except in regions with very large water content. The hydrogen content exponent is assumed to be $q = 1$.

compares the influence of hydrogen on seismic wave velocities through its effects on unrelaxed velocity (direct effect) and through anelasticity. The data on $B(P)$ are from Inoue et al. (1998), Jacobsen et al. (2004), and Yusa and Inoue (1997), and $\alpha = 0.3$ (e.g., Shito et al., 2004; Smith and Dahlen, 1981) and $q = 1$ are used. I conclude that the hydrogen affects seismic wave velocities mainly through anelasticity in the upper mantle where the background Q is low (∼100). In the transition zone (where the background Q is ∼300), the influence of hydrogen through unrelaxed velocity will be important if the hydrogen content exceeds ∼1 wt% equivalent of water. For hydrogen content less than 0.1 wt% water, the influence through anelasticity is more important. In the lower mantle, because the solubility of hydrogen is so low, a direct effect through unrelaxed velocity is almost definitely unimportant, and the effects through anelasticity would be important if a significantly large variation in hydrogen content (say, ∼0.1 wt% water) is present.

5.3 Some speculations on the role of hydrogen on geodynamic processes and plume structures

Hydrogen can have dramatic effects on the evolution and dynamics of terrestrial planets through its influence on melting temperature and rheological properties. The influence of hydrogen on physical properties on olivine has been studied extensively.

The importance of redistribution of hydrogen by partial melting in the shallow upper mantle has been discussed by Hirth and Kohlstedt (1996), Karato (1986), and Korenaga (2003). In particular, Korenaga (2003) pointed out the importance of shallow mantle dynamics for the evolution of the whole of the Earth because of the large energy dissipation in that region. However, the validity of this model is uncertain because the contribution to energy dissipation from deep mantle deformation is currently poorly constrained. Quantitative studies on hydrogen-related defects and their influence on physical (and chemical) properties (especially rheological properties) in deep Earth minerals are critical in order to advance our knowledge on the dynamics and evolution of terrestrial planets. Here I will review the current knowledge of the role of hydrogen in minerals in the deep interior of the mantle.

One important concept that comes from the atomistic model of hydrogen-related defects in minerals (see Section 5.1) is that in the upper mantle and the transition zone, hydrogen is likely to be dissolved in major minerals (olivine, orthopyroxene, wadsleyite, ringwoodite, and majorite) that control the rheological properties in these regions. In the lower mantle, however, hydrogen is likely in a minor phase, $CaSiO_3$ perovskite, that does not have direct influence on the rheological properties of this region (because of a very small volume fraction, less than $\sim$5%). The amount of $CaSiO_3$ perovskite (i.e., the Ca content) is controlled by the previous history of this region: regions that contain a large amount of materials of paleo-oceanic crust will have a higher content of $CaSiO_3$ perovskite and if dehydration during subduction process is imperfect, this region will have high hydrogen content. Consequently, regions with a high content of $CaSiO_3$ perovskite generally have higher hydrogen content in major minerals as well, and hence are prone to gravitational instability causing plumes due to a reduced viscosity. Plumes coming from these regions will have a higher content of elements that are enriched in the oceanic crust (Ca, Al, Fe). Nolet et al. (2005) suggested Fe-enrichment for plumes based on a plume-flux argument using the results of high-resolution tomographic imaging.

The transition zone minerals such as wadsleyite and ringwoodite can store a large amount of hydrogen. Based on a simple material circulation model, Richard et al. (2002) argued that the transition zone of the Earth might have little water due to the effective removal of hydrogen. However, Bercovici and Karato (2003) suggested that the melting caused by dehydration in an upwelling flow at 410-km could dramatically modify the distribution of hydrogen and other trace elements. In this model, hydrogen (and other trace elements) could be sequestered in the deep mantle through their dissolution in a dense hydrous melt and subsequent transfer to the deep mantle. However, the details of processes of hydrogen transfer in the deep mantle are poorly understood at this time.

Materials transport in the deep mantle occurs partly in the form of concentrated upwelling or downwelling, called "plumes". Recently, Montelli et al. (2004) obtained the first high-resolution images of upwelling plumes using a non-linear inversion scheme incorporating the frequency dependence of seismic wave propagation. Nolet et al. (2005) inverted the tomographic images in terms of thermal and chemical anomalies to estimate the amount of heat transport by plumes. By its very nature,

plumes are associated with thermal as well as chemical anomalies, and the issue of distinguishing them is not trivial. Here I will provide a brief discussion about the possible role of hydrogen on plume structure.

One of the remarkable observations on plumes seen through seismic tomography is that plumes are rather thick and not so hot (Montelli et al., 2004; Nolet et al., 2005). A direct conclusion from the observed thick plume is that the viscosity of plume materials is not much smaller than the viscosity of surrounding materials (Karato, 2000). Let us consider how hydrogen might influence the rheological properties and seismological signatures of plumes.

Since the most robust tomographic imaging is from the lower mantle, I will focus on the lower mantle. Karato et al. (1995) showed that most of the lower mantle deforms by diffusion creep. In such a case, the viscosity of a material strongly depends on the grain-size. Now, in the diffusion creep regime, grain-size is controlled by grain-growth kinetics. Consequently, grain-size will depend on temperature and hydrogen content. We may distinguish two cases: Case I in which the time scale of grain-growth is much larger than the time scale of relevant deformation. In such a case, grain-size can be regarded as a constant and independent of temperature and hydrogen content. Case II is a case in which the time constant of grain-growth is comparable to or smaller than that of deformation. In such a case, temperature and hydrogen content dependence of grain-size must be considered.

Following the suggestion by Solomatov (1996), Korenaga (2005) assumed case II behavior and proposed that the viscosity of plume (source region at least) may have positive correlation with temperature. This notion comes from the fact that once one assumes diffusion creep, then the viscosity depends on grain-size, L, and diffusion coefficient, D, as $\eta(T) \propto L(T)^m D(T)^{-1}$ and hence if grain-size is controlled by grain-growth kinetics, then

$$\eta(T) \propto \exp\left(-\frac{\frac{m}{n}H^*_{gg} - H^*_{\text{diff}}}{RT}\right), \tag{39}$$

where $\eta(T)$ is viscosity, m is the grain-size exponent for diffusion creep ($m = 2$–3), n is the grain-growth exponent, H^*_{gg} is the activation enthalpy for grain-growth, and H^*_{diff} is the activation enthalpy for diffusion. If $m/nH^*_{gg} - H^*_{\text{diff}} > 0$, then the viscosity and temperature will have a *positive* correlation. Although currently available experimental data on grain-growth kinetics and diffusion in the lower mantle minerals do not support this inequality (Yamazaki and Irifune, 2003; Yamazaki et al., 1996; Yamazaki et al., 2001), it is possible that this inequality may be met under some conditions.[9]

[9] Yamazaki et al., 1996 reported a rather large n value ($n = 10$–11) for grain-growth. For this large n, and for the reported values of activation enthalpies, $(m/n)H^*_{gg} - H^*_{\text{diff}} < 0$. But the reported unusually high n values may be an artifact due to elastic interactions of grains or the progressive loss of hydrogen during annealing experiments (for a reasonable range of models, $n = 3$–4 is predicted for the Ostwald ripening mechanisms of grain-growth).

What about the influence of hydrogen? There is evidence that a higher amount of hydrogen is present in the plume source regions (e.g., Nichols et al., 2002; Wallace, 1998). Let us distinguish the two cases discussed above. In case I, the influence of hydrogen on viscosity is simply through diffusion. If viscosity is controlled by that of (Mg,Fe)O by diffusion creep (Yamazaki and Karato, 2001b) and if the bulk diffusion of Mg (Fe) rate-controls the deformation, then we expect $\eta \propto C_w^{-1}$ (see Section 5.1). And hydrogen will also enhance seismic wave attenuation, $Q^{-1} \propto C_w^{\alpha r}$ and hence reduce the seismic wave velocities (see Section 5.2) (α: frequency exponent of Q, r: a hydrogen content exponent for grain-boundary sliding).

Let us now consider a case II where grain-size is controlled by grain-growth kinetics. Using the previous discussions on the influence of hydrogen on viscosity and attenuation, I get the following equations for the influence of hydrogen on these properties,

$$Q^{-1} \propto \tau^{-\alpha} = \left(\frac{L}{v}\right)^{-\alpha} \propto f_{\mathrm{H_2O}}^{-\alpha\left(\frac{q}{n}-s\right)} \propto C_w^{-\alpha\left(\frac{q}{n}-s\right)}, \tag{40}$$

$$\eta \propto L^m D^{-1} \propto f_{\mathrm{H_2O}}^{\frac{mq}{n}-1} \propto C_w^{\frac{mq}{n}-1}, \tag{41}$$

where α is the exponent for the frequency dependence of attenuation, q is the exponent for hydrogen content dependence of grain-growth kinetics, s is the exponent related to the dependence of grain-boundary sliding rate on hydrogen content and m is the grain-size exponent of diffusional creep. In writing these equations, I have made the following assumptions: (1) Seismic wave attenuation is through grain-boundary sliding (e.g., Jackson et al., 2002), and (2) plastic deformation occurs by diffusion creep (e.g., Karato et al., 1995). If we accept typically observed values of these constants ($\alpha \sim 0.3$, $q \sim 2$, $r \sim 2$, $m \sim 3$, $n \sim 3$), then $Q^{-1} \propto C_w^{0.4}$ and $\eta \propto C_w$. So in this case, a high water content will reduce the seismic wave velocity and increases the viscosity due to the combined effect of increased grain-size and increased relevant diffusion coefficients. In both cases, the addition of hydrogen will increase seismic wave attenuation and hence reduces seismic wave velocities. Inferred high viscosity of plumes may partly be due to a higher hydrogen content. The temperature anomalies, and hence the heat flux carried by plumes, will need to be re-calculated using the corrections for hydrogen effects.

I started this review of the relatively well-established aspect of this area of science, namely the solubility mechanisms of hydrogen in silicate minerals and its influence on phase relationships, and ended up with highly speculative discussions on the plausible role of hydrogen in controlling the rheological properties of deep mantle minerals and seismic wave propagation (attenuation). Here I will list some key mineral physics issues that need to be investigated in the near future:

(i) The solubility of hydrogen in minerals must be better determined.
   a. The theoretical basis for hydrogen content versus infrared absorption (e.g., Paterson, 1982) must be better understood.

b. Intrinsic temperature dependence of hydrogen solubility in wadsleyite (and ringwoodite) must be better determined.
c. Hydrogen solubility in the lower mantle minerals ((Mg,Fe)O, (Mg,Fe)SiO_3 perovskite, $CaSiO_3$ perovskite, a post-perovskite phase) needs to be better determined.

(ii) The influence of hydrogen on melt properties including density and melting relations needs to be investigated under deep mantle conditions. I should point out that melting in the transition zone is highly likely due to the influence of volatile components, but the density of melts thus formed can be lighter or heavier than the surrounding solids depending on the melt composition. The variation of melt density on the composition (particularly the amount of water and potassium) controls the fate of melt. This has an important implication for the volcanic activity of deep origin including plumes (Karato et al., 2006).

(iii) The influence of hydrogen on anelasticity needs to be investigated more systematically.

(iv) The influence of hydrogen on the plastic properties of deep mantle minerals needs to be determined.

(v) The kinetics of grain-growth in a multi-phase system such as a perovskite + magnesiowüstite system needs to be investigated more thoroughly including the effects of hydrogen.

It should be emphasized that most of these experimental studies involve development of new experimental techniques and/or careful experimentation in controlling or characterizing the hydrogen contents. It is also emphasized that the results of these studies must be parameterized in an appropriate way in order to justify their applications to Earth science problems. This requires a sound theoretical understanding of basic physics, particularly the scaling laws for a given property. It is through a combination of these mineral physics studies with observational geophysics/geochemistry and geodynamic modeling that we can make a major progress in revealing the evolution and dynamics of Earth and other terrestrial planets.

ACKNOWLEDGEMENTS

This work is supported by NSF grants. The results presented here are based on a number of collaborations with my colleagues including David Bercovici, Xiaoge Huang, Zhenting Jiang, Zhicheng Jing, Haemeyong Jung, Ikuo Katayama, Jun Korenaga, William Landuyt, Kyoko Matsukage, Yu Nishihara, Guust Nolet, Toru Shinmei, Azusa Shito, Phil Skemer, and Yousheng Xu. Thank you all.

REFERENCES

Akaogi, M., E. Ito, and A. Navrotsky (1989) Olivine-modified spinel-spinel transitions in the system Mg_2SiO_4-Fe_2SiO_4: Calorimetric measurements, thermochemical calculation, and geophysical application. *J. Geophys. Res.*, 94, 15671–15685.

Ando, K. (1989) Self-diffusion in oxides. In Karato, S., and M. Toriumi (eds.) Rheology of Solids and of the Earth, Oxford University Press, pp. 57–82.

Bai, Q., and D.L. Kohlstedt (1993) Effects of chemical environment on the solubility and incorporation mechanism for hydrogen in olivine. *Phys. Chem. Miner.*, 19, 460–471.

Béjina, F., O. Jaoul, and R.C. Liebermann (2003) Diffusion at high pressure: A review. *Phys. Earth Planet. Inter.*, 139, 3–20.

Bell, D.R., G.R. Rossman, J. Maldener, D. Endisch, and F. Rauch (2003) Hydroxide in olivine: A quantitative determination of the absolute amount and calibration of the IR spectrum. *J. Geophys. Res.*, 108, doi: 10.1029/2001JB000679.

Bercovici, D., and S. Karato (2003) Whole mantle convection and transition-zone water filter. *Nature*, 425, 39–44.

Bolfan-Casanova, N., H. Keppler, and D.C. Rubie (2000) Water partitioning between nominally anhydrous minerals in the MgO-SiO_2-H_2O system up to 24 GPa: Implications for the distribution of water in the Earth's mantle. *Earth Planet. Sci. Lett.*, 182, 209–221.

Bolfan-Casanova, N., S.J. Mackwell, H. Keppler, C. McCammon, and D.C. Rubie (2002) Pressure dependence of H solubility in magnesiowüstite up to 25 GPa: Implications for the storage of water in the Earth's lower mantle. *Geophys. Res. Lett.*, 29, 89-1/89-4.

Burnham, C.W. (1979) The importance of volatile constituents. In Yorder J.H.S. (eds.) The Evolution of the Igneous Rocks, Princeton University Press, Princeton, New Jersey, pp. 439–482.

Chen, J., T. Inoue, H. Yurimoto, and D.J. Weidner (2002) Effect of water on olivine-wadsleyite phase boundary in the $(Mg,Fe)_2SiO_4$ system. *Geophys. Res. Lett.*, 29, doi: 10.1029/2001GRL014429.

Chopra, P.N., and M.S. Paterson (1984) The role of water in the deformation of dunite. *J. Geophys. Res.*, 89, 7861–7876.

Cordier, P., J.A. Weil, D.F. Howarth, and J.-C. Doukhan (1994) Influence of the $(4H)_{Si}$ defect on dislocation motion in crystalline quartz. *Eur. J. Mineral.*, 6, 17–22.

Corgne, A., and B.J. Wood (2002) $CaSiO_3$ and $CaTiO_3$ perovskite-melt partitioning of trace elements: Implications for gross mantle differentiation. *Geophys. Res. Lett.*, 29, doi: 10.1029/2001GL014398.

Dasgupta, R., and M.M. Hirschmann (2006) Deep melting in the Earth's upper mantle caused by CO_2. *Nature*, 440, 659–662.

Demouchy, S., E. Deloule, D.J. Frost, and H. Keppler (2005) Pressure and temperature-dependence of water solubility in iron-free wadsleyite. *Am. Mineral.*, 90, 1084–1091.

Derby, B., and M.F. Ashby (1987) On dynamic recrystallization. *Scripta Metallurgica*, 21, 879–884.

Doukhan, J.-C., and M.S. Paterson (1986) Solubility of water in quartz. *Bull. Mineral.*, 109, 193–198.

Gordon, R.S. (1973) Mass transport in the diffusional creep of ionic solids. *Journal of the American Ceramic Society*, 65, 147–152.

Griggs, D.T. (1974) A model of hydrolytic weakening in quartz. *J. Geophys. Res.*, 79, 1653–1661.

Heggie, M., and R. Jones (1986) Models of hydrolytic weakening in quartz. *Philosophical Magazine, A.*, 53, L65–L70.

Hier-Majumder, S., I.M. Anderson, and D.L. Kohlstedt (2005) Influence of protons on Fe-Mg interdiffusion in olivine. *J. Geophys. Res.*, 110, doi: 10.1029/2004JB003292.

Hirose, K., N. Shimizu, W. Van Westrenen, and Y. Fei (2004) Trace element partitioning in Earth's lower mantle and implications for geochemical consequences of partial melting at the core-mantle boundary. *Phys. Earth Planet. Inter.*, 146, 249–260.

Hirth, G., and D.L. Kohlstedt (1996) Water in the oceanic upper mantle—implications for rheology, melt extraction and the evolution of the lithosphere. *Earth Planet. Sci. Lett.*, 144, 93–108.

Huang, X., Y. Xu, and S. Karato (2005) Water content of the mantle transition zone from the electrical conductivity of wadsleyite and ringwoodite. *Nature*, 434, 746–749.

Ingrin, J., and H. Skogby (2000) Hydrogen in nominally anhydrous upper-mantle minerals: Concentration levels and implications. *Eur. J. Mineral.*, 12, 543–570.

Inoue, T. (1994) Effect of water on melting phase relations and melt composition in the system Mg_2SiO_4-$MgSiO_3$-H_2O up to 15 GPa. *Phys. Earth Planet. Inter.*, 85, 237–263.

Inoue, T., and H. Sawamoto (1992) High pressure melting of pyrolite under hydrous condition and its geophysical implications. In Syono, Y., and M.H. Manghnani (eds.) High-Pressure Research: Application to Earth and Planetary Sciences, American Geophysical Union, Washington DC, pp. 323–331.

Inoue, T., D.J. Weidner, P.A. Northrup, and J.B. Parise (1998) Elastic properties of hydrous ringwoodite (γ-phase) of Mg_2SiO_4. *Earth Planet. Sci. Lett.*, 160, 107–113.

Jackson, I., J.D. Fitz Gerald, and H. Kokkonen (2000) High-temperature viscoelastic relaxation in iron and its implications for the shear modulus and attenuation of the Earth's inner core. *J. Geophys. Res.*, 105, 23605–23634.

Jackson, I., J.D. Fitz Gerald, U.H. Faul, and B.H. Tan (2002) Grain-size sensitive seismic-wave attenuation in polycrystalline olivine. *J. Geophys. Res.*, 107, doi: 10.1029/2002JB001225.

Jackson, I., M.S. Paterson, and J.D. Fitz Gerald (1992) Seismic wave dispersion and attenuation in Åheim dunite. *Geophys. J. Int.*, 108, 517–534.

Jacobsen, S.D., J.R. Smyth, H.A. Spetzler, C.M. Holl, and D.J. Frost (2004) Sound velocities and elastic constants of iron-bearing hydrous ringwoodite. *Phys. Earth Planet. Inter.*, 143/144, 47–56.

Jung, H., and S. Karato (2001a) Effect of water on the size of dynamically recrystallized grains in olivine. *J. Struct. Geol.*, 23, 1337–1344.

Jung, H., and S. Karato (2001b) Water-induced fabric transitions in olivine. *Science*, 293, 1460–1463.

Jung, H., I. Katayama, Z. Jiang, T. Hiraga, and S. Karato (2006) Effects of water and stress on the lattice preferred orientation in olivine. *Tectonophysics*, 421, 1–22.

Karato, S. (1974) Point defects and transport properties of olivine. MSc, University of Tokyo.

Karato, S. (1986) Does partial melting reduce the creep strength of the upper mantle? *Nature*, 319, 309–310.

Karato, S. (1989) Defects and plastic deformation in olivine. In Karato S., and M. Toriumi (eds.) Rheology of Solids and of the Earth, Oxford University Press, pp. 176–208.

Karato, S. (1990) The role of hydrogen in the electrical conductivity of the upper mantle. *Nature*, 347, 272–273.

Karato, S. (1995) Effects of water on seismic wave velocities in the upper mantle. *Proc. Jpn. Acad.* 71, 61–66.

Karato, S. (2000) Rheology and Dynamics of the Solid Earth, University of Tokyo Press.

Karato, S. (2003) Mapping water content in Earth's upper mantle. In Eiler, J.E. (ed.) Inside the Subduction Factory, American Geophysical Union, pp. 135–152.

Karato, S., D. Bercovici, G. Leahy, G. Richard, and Z. Jing (2006) Transition zone water filter model for global material circulation: Where do we stand? In Jacobsen S.D., and S. van der Lee (eds.) Earth's Deep Water Cycle, American Geophysical Union, submitted.

Karato, S., and H. Jung (2003) Effects of pressure on high-temperature dislocation creep in olivine polycrystals. *Philosophical Magazine, A.*, 83, 401–414.

Karato, S., M.S. Paterson, and J.D. Fitz Gerald (1986) Rheology of synthetic olivine aggregates: Influence of grain-size and water. *J. Geophys. Res.*, 91, 8151–8176.

Karato, S., and H.A. Spetzler (1990) Defect microdynamics in minerals and solid state mechanisms of seismic wave attenuation and velocity dispersion in the mantle. *Rev. Geophys.*, 28, 399–421.

Karato, S., S. Zhang, and H.-R. Wenk (1995) Superplasticity in Earth's lower mantle: Evidence from seismic anisotropy and rock physics. *Science*, 270, 458–461.

Katayama, I., H. Jung, and S. Karato (2004) New type of olivine fabric at modest water content and low stress. *Geology*, 32, 1045–1048.

Katayama, I., and S. Karato (2006a) Effect of water on low-temperature high-stress rheology of olivine. *J. Geophys. Res.*, submitted.

Katayama, I., and S. Karato (2006b) Effects of temperature on the B- to C-type fabric transition in olivine. *Phys. Earth Planet. Inter.*, in press.

Kohlstedt, D.L., H. Keppler, and D.C. Rubie (1996) Solubility of water in the α, β and γ phases of $(Mg,Fe)_2SiO_4$. *Contributions to Mineralogy and Petrology*, 123, 345–357.

Korenaga, J. (2003) Energetics of mantle convection and the fate of fossil heat. *Geophys. Res. Lett.*, 30, doi: 10.29/2003GL016982.

Korenaga, J. (2005) Firm mantle plumes and the nature of the core-mantle region. *Earth Planet. Sci. Lett.*, 232, 29–37.

Kubo, T., E. Ohtani, T. Kato, T. Shinmei, and K. Fujino (1998) Effects of water on the α–β transformation kinetics in San Carlos olivine. *Science*, 281, 85–87.

Kushiro, I., Y. Syono, and S. Akimoto (1968) Melting of a peridotite nodule at high pressures and high water pressures. *J. Geophys. Res.*, 73, 6023–6029.

Li, L., D.J. Weidner, P. Ratteron, J. Chen, and M.T. Vaughan (2004) Stress measurements of deforming olivine at high pressure. *Phys. Earth Planet. Inter.*, 143/144, 357–367.

Matsukage, K.N., Z. Jing, and S. Karato (2005) Density of hydrous silicate melt at the conditions of the Earth's deep upper mantle. *Nature*, 438, 488–491.

McCammon, C. (1997) Perovskite as a possible sink for ferric iron in the lower mantle. *Nature*, 387, 694–696.

Mei, S., and D.L. Kohlstedt (2000a) Influence of water on plastic deformation of olivine aggregates, 1. Diffusion creep regime. *J. Geophys. Res.*, 105, 21457–21469.

Mei, S., and D.L. Kohlstedt (2000b) Influence of water on plastic deformation of olivine aggregates, 2. Dislocation creep regime. *J. Geophys. Res.*, 105, 21471–21481.

Mibe, K., T. Fujii, and A. Yasuda (2002) Composition of aqueous fluid coexisting with mantle minerals at high pressure and its bearing on the differentiation of the Earth's mantle. *Geochim. Cosmochim. Acta*, 66, 2273–2285.

Montelli, R., G. Nolet, F.A. Dahlen, G. Masters, E.R. Engdhal, and S.H. Hung (2004) Finite-frequency tomography reveals a variety of plumes in the mantle. *Science*, 303, 338–343.

Nichols, A.R.L., M.R. Carroll, and A. Höskuldsson (2002) Is the Iceland hot spot also wet? Evidence from water contents of undegassed submarine and subglacial pillow basalts. *Earth Planet. Sci. Lett.*, 202, 77–87.

Nishihara, Y., T. Shinmei, and S. Karato (2006) Grain-growth kinetics in wadsleyite: Effects of chemical environment. *Phys. Earth Planet. Inter.*, 154, 30–43.

Nishihara, Y., D. Tinker, Y. Xu, Z. Jing, K.N. Matsukage, and S. Karato (2005) Plastic deformation of wadsleyite and olivine at high-pressures and high-temperatures using a rotational Drickamer apparatus (RDA). *J. Geophys. Res.*, submitted.

Nolet, G., S. Karato, and R. Montelli (2005) Plume fluxes from seismic tomography: A Bayesian approach. *Earth Planet. Sci. Lett.*, 248, 685–699.

Ochs, F.A.I., and R.A. Lange (1997) The partial molar volume, thermal expansivity, and compressibility of H_2O in $NaAlSi_3O_8$ liquid. *Contributions to Mineralogy and Petrology*, 129, 155–165.

Paterson, M.S. (1982) The determination of hydroxyl by infrared absorption in quartz, silicate glass and similar materials. *Bull. Mineral.*, 105, 20–29.

Paterson, M.S. (1989) The interaction of water with quartz and its influence in dislocation flow—an overview. In Karato S., and M. Toriumi (eds.) Rheology of Solids and of the Earth, Oxford University Press, pp. 107–142.

Paterson, M.S. (1990) Rock deformation experimentation. In Duba, A.G., W.B. Durham, J.W. Handin, and H.F. Wang (eds.) The Brittle-Ductile Transition in Rocks; The Heard Volume, American Geophysical Union, pp. 187–194.

Richard, G., M. Monnereau, and J. Ingrin (2002) Is the transition zone an empty water reservoir? Inference from numerical model of mantle dynamics. Earth Planet. Sci. Lett., 205, 37–51.

Shito, A., S. Karato, K.N. Matsukage, and Y. Nishihara (2006) Toward mapping water content, temperature and major element chemistry in Earth's upper mantle from seismic tomography. In Jacobsen S.D., and S.v.d. Lee (eds.) Earth's Deep Water Cycle, American Geophysical Union.

Shito, A., S. Karato, and J. Park (2004) Frequency dependence of Q in Earth's upper mantle inferred from continuous spectra of body wave. *Geophys. Res. Lett.*, 31, doi: 10.1029/2004GL019582.

Silver, L.A., and E.M. Stolper (1985) A thermodynamic model for hydrous silicate melts. *J. Geol.*, 93, 161–178.

Smith, M.F., and F.A. Dahlen (1981) The period and Q of the Chandler wobble. *Geophys. J. Roy. Astron. Soc.*, 64, 223–281.

Smyth, J.R. (1987) β-Mg_2SiO_4: A potential host for water in the mantle? *American Mineralogist*, 75, 1051–1055.

Smyth, J.R. (1994) A crystallographic model for hydrous wadsleyite (β-Mg_2SiO_4): An ocean in the Earth's interior. *American Mineralogist*, 79, 1021–1024.

Smyth, J.R., and D.J. Frost (2002) The effect of water on the 410-km discontinuity: An experimental study. *J. Geophys. Res. Lett.*, 29, doi: 10.129/2001GL014418.

Solomatov, V.S. (1996) Can hot mantle be stronger than cold mantle? *Geophys. Res. Lett.*, 23, 937–940.

Stixrude, L. (1997) Structure and sharpness of phase transitions and mantle discontinuities. *J. Geophys. Res.*, 102, 14835–14852.

van der Meijde, M., F. Marone, D. Giardini, and S. van der Lee (2003) Seismic evidence for water deep in Earth's upper mantle. *Science*, 300, 1556–1558.

Wallace, P. (1998) Water and partial melting in mantle plumes: Inferences from the dissolved H_2O concentrations of Hawaii basaltic magmas. *Geophys. Res. Lett.*, 25, 3639–3642.

Wang, W., and E. Takahashi (2000) Subsolidus and melting experiments of K-doped peridotite KLB-1 to 27 GPa; Its geophysical and geochemical implications. *J. Geophys. Res.*, 105, 2855–2868.

Wang, Y., W.B. Durham, I.C. Getting, and D.J. Weidner (2003) The deformation-DIA: A new apparatus for high temperature triaxial deformation to pressures up to 15 GPa. *Rev. Sci. Instrum.*, 74, 3002–3011.

Williams, Q., and R.J. Hemley (2001) Hydrogen in the deep Earth. *Ann. Rev. Earth Planet. Sci.*, 29, 365–418.

Wood, B.J. (1995) The effect of H_2O on the 410-kilometer seismic discontinuity. *Science*, 268, 74–76.

Xu, Y., Y. Nishihara, and S. Karato (2005) Development of a rotational Drickamer apparatus for large-strain deformation experiments under deep Earth conditions. In Chen J., Y. Wang, T.S. Duffy, G. Shen, and L.F. Dobrzhinetskaya (eds.) Frontiers in High-Pressure Research: Applications to Geophysics, Elsevier, Amsterdam, pp. 167–182.

Yamazaki, D., and T. Irifune (2003) Fe-Mg interdiffusion in magnesiowüstite up to 35 GPa. *Earth Planet. Sci. Lett.*, 216, 301–311.

Yamazaki, D., and S. Karato (2001a) High pressure rotational deformation apparatus to 15 GPa. *Rev. Sci. Instrum.*, 72, 4207–4211.

Yamazaki, D., and S. Karato (2001b) Some mineral physics constraints on the rheology and geothermal structure of Earth's lower mantle. *American Mineralogist*, 86, 385–391.

Yamazaki, D., T. Kato, E. Ohtani, and M. Toriumi (1996) Grain growth rates of $MgSiO_3$ perovskite and periclase under lower mantle conditions. *Science*, 274, 2052–2054.

Yamazaki, D., T. Kato, M. Toriumi, and E. Ohtani (2001) Silicon self-diffusion in $MgSiO_3$ perovskite at 25 GPa. *Phys. Earth Planet. Inter.*, 119, 299–309.

Yan, H. (1992) Dislocation Recovery in Olivine. Master of Science, University of Minnesota.

Young, T.E., H.W. Green, II., A.M. Hofmeister, and D. Walker (1993) Infrared spectroscopic investigation of hydroxyl in β-$(Mg,Fe)_2SiO_4$ and coexisting olivine: Implications for mantle evolution and dynamics. *Physics and Chemistry of Minerals*, 19, 409–422.

Yusa, H., and T. Inoue (1997) Compressibility of hydrous wadsleyite (β-phase) in Mg_2SiO_4 by high-pressure X ray diffraction. *Geophys. Res. Lett.*, 24, 1831–1834.

Zhao, Y.-H., S.B. Ginsberg, and D.L. Kohlstedt (2004) Solubility of hydrogen in olivine: Dependence on temperature and iron content. *Contributions to Mineralogy and Petrology*, 147, 155–161.

PART V

PLUME DYNAMICS THROUGH EARTH HISTORY

INTRODUCTION

In this Part, the history of Pacific superplume is reviewed together with a series of paleogeographic maps from 1.0 Ga to the present by Ustunomiya et al. The structure and compositional profile of the Pacific superplume is the integrated state since at least the formation of supercontinent Rodinia which was made up right above the present Pacific Ocean and Pacific superplume at 1.0 Ga (Fig. 1). Over 1.0 billions of years, the Pacific superplume evolved to change its structure through several pulsation periods such as the Cretaceous pulse.

The african superplume was born at the initial stage of the break-up of Pangea, ca. 250 Ma, when the largest-scale of mass extinction occurred, one order of magnitude higher than that of the end-Cretaceous dinosaurus extinction. This is the so-called

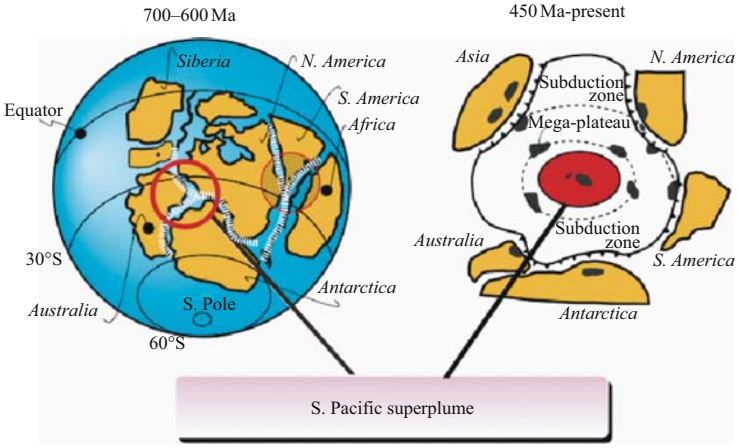

Figure 1. The history of the Pacific superplume since its birth to the present. Left: Simplified paleogeography of Rodinia at 750 Ma at the time of the birth of the Pacific superplume, after Maruyama (1994). The Pacific Ocean was created by 600 Ma by the rifting of Rodinia, and it widened until 500–450 Ma, when circum-Pacific subduction zones developed. Right: Since then, the Pacific Ocean has decreased in size.

D. A. Yuen et al. (eds.), Superplumes, 359–362.
© 2007 *Springer.*

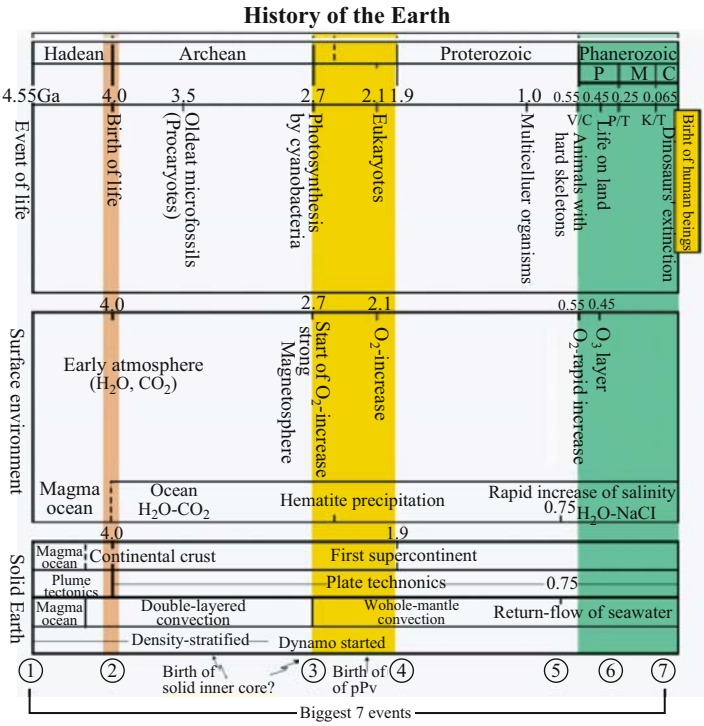

Figure 2. The history of the Earth, showing the biggest 7 events: (1) the birth of the Earth; (2) the birth of the continental crust, and life, and initiation of plate tectonics at 4.0 Ga; (3) the dynamo started by the birth of a solid inner core, and resultant increase of photo-synthetic oxygen in the atmosphere at 2.7 Ga; (4) the birth of the first supercontinent presumably related to the birth of the post-perovskite phase on the CMB; (5) the initiation of the return-flow of seawater into the mantle at 750 Ma, and the resultant appearance of the large continent above sea-level and the diversification of life on the Earth; (6) the Paleozoic/Mesozoic boundary and mass extinction; and (7) the birth of human beings, and their change of the Earth and planets (Maruyama et al., 2001).

Paleozoic/Mesozoic boundary. This is the best-known and largest-scale mass extinction through the Phanerozoic time. More than 96% of large multi-cellular animals died. Summarizing the details of mass extinction at the P/T boundary, and of the paleo-environment in both the Paleo-Pacific Ocean and in China, Y. Isozaki proposes that there was a superplume winter, that occurred twice during this period.

Maruyama and others propose the mechanism of the formation of a superplume, turning the coldest mantle into the hottest mantle by the role of post-perovskite over 1.0 b.y. Through this process, an anti-crust develops as a mirror image of the continental crust on the surface. Moreover, they have speculated about the birth date of post-perovskite at CMB to be 2.3 Ga, based on the growth curve of the continental crust. They have proposed the evolutional sequence of mantle dynamics, from

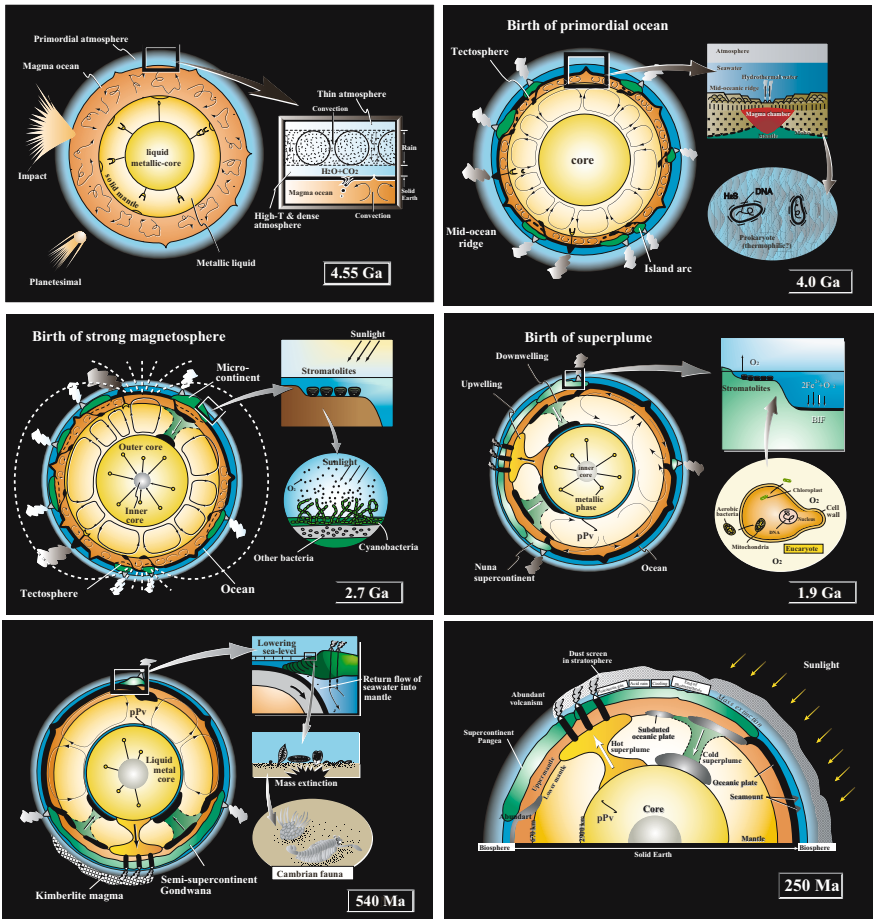

Figure 3. The evolution of the Earth at 4.55 Ga, 4.0 Ga, 2.7 Ga, 1.9 Ga, 0.7–0.6 Ga, 0.25 Ga and the present-day, showing the evolution of the Earth system. The Earth system has evolved by internal buffer to makeing the surface habitable for life, in spite of secular cooling. See also Figure 2 with a summary of the Biggest seven Events.

double-layered convection, catastrophic mantle overturn, birth of post-perovskite at CMB; thereafter the superplume cycle started, and the initiation of the return-flow of seawater into the mantle at the onset of the Phanerozoic era (Figs. 2 and 3).

REFERENCES

Maruyama, S. (1994) Plume tectonics. *J. Geol. Soc. Jpn.*, 100, 24–49.

Maruyama, S., S. Nakashima, Y. Isozaki, and B.F. Windley (2001) History of the Earth and life. In Nakashima, S. et al. (eds.) *Geochemistry and Origin of Life*, Universal Academic Press, Tokyo, pp. 285–325.

CHAPTER 13

HISTORY OF THE PACIFIC SUPERPLUME: IMPLICATIONS FOR PACIFIC PALEOGEOGRAPHY SINCE THE LATE PROTEROZOIC

ATSUSHI UTSUNOMIYA[1,2,4], TSUTOMU OTA[1,5], BRIAN F. WINDLEY[3], NORIHITO SUZUKI[1], YUKO UCHIO[1,6], KUNIKO MUNEKATA[1], AND SHIGENORI MARUYAMA[1]

[1] *Department of Earth and Planetary Sciences, Tokyo Institute of Technology, O-okayama 2-12-1, Meguro, Tokyo 152-8551, Japan*

[2] *Interactive Research Center of Science, Tokyo Institute of Technology, O-okayama 2-12-1, Meguro, Tokyo 152-8551, Japan*

[3] *Department of Geology, University of Leicester, Leicester LE1 7RH, UK*

[4] *Now at Institute of Earth Sciences, Academia Sinica, Nankang, Taipei 11529, Taiwan; E-mail: uchii@earth.sinica.edu.tw*

[5] *Now at Institute of Study of the Earth's Interior, Okayama University, Misasa, Tottori 682-0193, Japan*

[6] *Now at Public Relations Department, Public Relations Division, National Science Museum, Taito, Tokyo 110-8718, Japan*

Abstract

We have reconstructed the paleogeography of continents, oceans and oceanic large igneous provinces (LIPs) since 1000 Ma in order to decode the history of the Pacific Superplume, using the most reliable recent data for accretional geology from orogens associated with ophiolites and greenstone belts, and of geochronologic and paleomagnetic data from each continent. From our reconstructions we have arrived at the following conclusions: (1) the Pacific Superplume was born at 750 Ma and broke-up the supercontinent Rodinia; (2) the African Superplume was born at 200 Ma and broke-up Pangea; (3) the Pacific Superplume was active episodically with culminations at 580–600 Ma, 280–230 Ma and 150–75 Ma; (4) during the formation of Rodinia much oceanic lithosphere from the Tethyan-Indian type ocean was subducted along paleo-trenches of proto-Grenville orogens along a V-shaped, double-sided convergent boundary around the continental lithosphere of Rodinia. These relations suggest that the massive volumes of lithosphere subducted under the Pacific-type orogens triggered the birth of the Pacific Superplume after 200 m.y. at the center of Rodinia.

D. A. Yuen et al. (eds.), Superplumes, 363–408.
© 2007 *Springer.*

1 INTRODUCTION

A super-upwell in the mantle, i.e., "superplume", was first invoked in the early stages of seismic tomography (Dziewonski, 1984; Woodhouse and Dziewonski, 1984; Dziewonski and Woodhouse, 1987). This revealed two low-velocity domains of seismic waves extending continuously between the uppermost and lowermost mantle, originating under the South Pacific and Africa. These major cylindrical structures with a girth extending for ca. 1000 km are much wider than a skimpy jet plume that gives rise to a so-called hot spot on the Earth's surface. Since the early 1990's, the heterogeneity of the velocities in the mantle has been well defined by seismic tomography with a higher resolution than before (e.g., Fukao, 1992). The lower velocity area in the lower mantle is considered to be a superplume that is a huge mantle plume rising from the core-mantle boundary (CMB), and the higher velocity area at ca. 670 km depth is regarded as a megalith that is interpreted as a massive stagnant slab. These images illustrate the process of 'plume tectonics' (Maruyama, 1994). Although plate tectonics only treats the uppermost 100 km of the solid Earth, whole Earth dynamics includes plate tectonics and plume tectonics which is controlled by episodic superplume activities. Whole Earth dynamics operates at three levels: (1) the subsurface domain is controlled by plate tectonics; (2) the lower mantle is controlled by plume tectonics; and (3) growth tectonics takes place in the core. Plate tectonics puts cold slabs into the mantle. A cold slab stagnates at the mantle transition zone for 100–400 m.y., subsequently collapses, and falls to the surface of the outer core; this results in episodic super-downwelling in the whole mantle and a new downflow in the core. A counter flow to the super-downwelling is the super-upwelling of the hot mantle that causes continental break-up, subsequent dispersal, and formation of large igneous provinces (LIPs) that include flood basalts and oceanic plateaus. Fragmented continents collide and amalgamate to form new large composite continents. During such a process a subducting slab descends to the mantle through trenches around a new continent, and this leads to the next super-downwelling beneath the continent.

Seismic tomography only provides a static image of present superplume activity. From the viewpoint of plume tectonics, the history of supercontinents and LIPs is closely related to the superplume activity. In other words, we can draw essential, although indirect, information about the history of a superplume by decoding the geological records of supercontinents and LIPs that remain on the surface of the Earth. The distribution of ancient continents and orogens preserves a record of where oceanic lithosphere subducted and slabs stagnated. The distribution of LIPs represents where mantle upwelling occurred. Furthermore, ophiolites and greenstone belts provide information on the oceanic domains of LIPs and on oceanic lithosphere that disappeared into the mantle.

In this paper, in order to understand the activity of the Pacific Superplume, we discuss the paleogeographic reconstruction of continents and oceans since 750 Ma from an evaluation of the most recent reliable data on regional geology, geochronology and paleomagnetism from each continent. Our reconstruction concerns not only the

distribution of continents, but also of mid-oceanic ridges and trenches. In addition, ancient LIPs, which occur in oceanic regions or are partly trapped in current orogens, are reconstructed with data from accretionary geology. Comparing the Pacific and African Superplumes, we have decoded the general modes of interaction between plume activity and plate tectonics in the Earth's late history.

2 METHODS AND DATA SOURCES FOR RECONSTRUCTION

2.1 Continental reconstructions

Since the development of plate tectonics in the 1970's, numerous paleogeographic maps have been published. In particular, the Paleogeographic Atlas Project (University of Chicago, http://pgap.uchicago.edu/PGAPhome.html), the PLATES project (University of Texas at Austin, http://www.ig.utexas.edu/research/projects/plates/) and the PALEOMAP project (University of Texas at Arlington, http://www.scotese.com) have produced systematic series of paleogeographic maps for several decades. For their constructions they integrated vast amounts of data from paleomagnetism, sea floor linear magnetic anomalies, paleogeography, paleoclimatology and geology. Although the Paleogeographic Atlas Project concentrated on the Mesozoic and Cenozoic, the PLATES and PALEOMAP projects extended from 750 Ma to the present. Although they have reached a general consensus on Cenozoic and Mesozoic continental distributions, their Paleozoic and Neoproterozoic reconstructions are significantly different. Our maps of continental distributions are mainly dependent on the latest paleogeographic maps of the PALEOMAP project (Scotese, 2004). The contributions of individual paleomagnetists and their groups will be referred to specifically in the text.

Figure 1 is a compilation map showing the worldwide distribution of geologic units in continents and oceans of different ages based on published data, in particularly from Liou et al. (1990), Windley (1995), and Maruyama et al. (1996), and references therein. A general view of the compiled map shows that most continents are composed of Precambrian nuclei (cratons) and orogenic belts with zonal growth toward their exteriors. Two types of orogens form at convergent plate boundaries. Collisional orogens result from continent-continent collisions and may involve some arc accretion, and Pacific-type orogens develop as a result of oceanic plate subduction and accretion (e.g., Maruyama, 1997). The temporal and spatial distribution of collisional orogens provides data on the timing of continental amalgamation, and that of Pacific-type orogens supplies direct information on the distribution of trenches. Surely orogenic belts cannot be developed from continental rifts. Only rifts are developed from rifts. A rifting event is accompanied by large-scale magmatism. Their traces of which are preserved as dyke swarms remain on drifted continental margins. At the initial stage of continental rifting, extensive dike swarms are intruded perpendicular to the rift axes, as best documented along the Mesozoic coast lines in the Atlantic Ocean (Ruffman and Greenough, 1990; Hill, 1991). The intrusion ages and distribution of the dykes provide essential information on continental breakup.

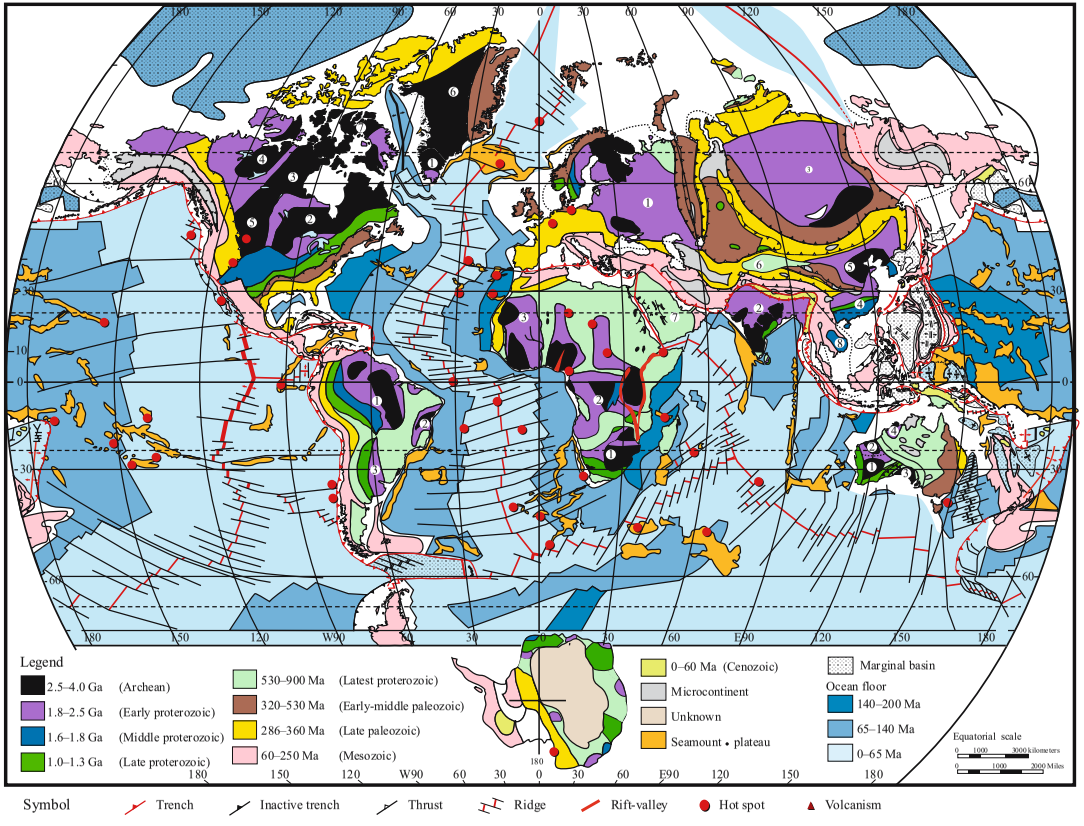

Figure 1. Compilation map of orogenic belts worldwide. Major cratons in each continent are numbered: (Asia-Europe) 1 = Baltica craton; 2 = Indian craton; 3 = Siberian craton; 4 = South China craton; 5 = North China craton; 6 = Tarim block; 7 = Arabian shield; 8 = Indochina block; (Australia) 1 = Yilgarn; 2 = Pilbara; 3 = Gawaler; 4 = Kimberley; (North America) 1 = Nain; 2 = Superior; 3 = Hearne; 4 = Slave; 5 = Wyoming; 6 = Nagssugtoqidian; 7 = Rae; (South America) 1 = Amazonia; 2 = Sao Francisco; 3 = Rio de La Plata; (Africa) 1 = Kalahari; 2 = Congo; 3 = West Africa.

We assessed the maps of the PALEOMAP project by utilizing reliable recent data from continental collisional orogens and correcting them if inconsistent. We decoded the distributions of trenches from Pacific-type orogens and superimposed them on the maps.

2.2 Paleogeographic reconstructions of oceanic domains

The existence of magnetic stripes on the oceanic floor, the distribution of fracture zones, and the assumption that hotspots in the Pacific and Atlantic Oceans are mutually fixed, provided information for the relative motions between the major plates and the distribution of mid-ocean ridges and trenches in the Pacific Ocean (e.g., Engebretson et al., 1985). The paleopositions of oceanic plateaus dispersed in the Pacific Ocean were reconstructed by using the relative motions model (Larson, 1991a). These reconstructions are available only for the last 140 Ma, because most of the older oceanic crust has disappeared into the mantle at subduction zones. But a few fragments of the old oceanic plates remain in the Pacific-type orogens. These fragments occur as on-land ophiolites/greenstone belts (Fig. 2). In this study, we extracted information

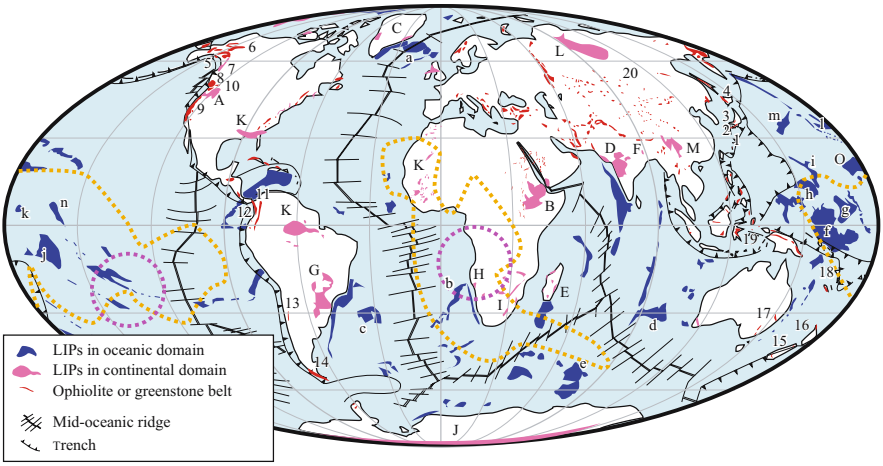

Figure 2. Distribution map of LIPs, ophiolites and greenstone belts over the world (after Coffin and Eldholm, 1994; Mann and Taira, 2004). The regions enveloped by orange and purple dashed lines show the seismic lower velocity zones (Vs) at 2850 m depth in lower mantle and superswell regions, respectively (Courtillot et al., 2003). These express the present superplume roots and active areas. Numbers of ophiolites and greenstone belts listed in Table 2. A = Columbia River basalts; B = Ethiopian and Yemen Traps C = NAVP; D = Deccan Trap; E = Madagascar basalts; F = Rajmahal basalts; *G* = Paraná basalts H = Etendeka basalts; I = Karoo basalts; J = Ferrar basalts; K = CAMP; L = Siberian Trap; M = Emeishan flood basalts. a = Iceland; b = Walvis Ridge; c = Rio Grande plateau; d = Broken Ridge; e = Kerguelen Plateau; f = Ontong Java plateau; g = Nauru Basin; h = East Mariana Basin; i = Pigafetta Basin; j = Manihiki Plateau; k = Magellan Rise; l = Hess Rise; m = Shatsky Rise; n = Line Islands; o = Mid-Pacific Mountains.

on the oceanic domains from the Pacific-type orogens and reconstructed the paleogeography of oceanic domains that included the distribution of mid-ocean ridges, oceanic islands, and oceanic plateaus.

2.2.1 Extraction of oceanic information from pacific-type orogens

Accretionary geology. Compilation of the Pacific-type orogens enabled us to reconstruct the paleo-positions of trenches. Moreover, an accretionary complex in a Pacific-type orogen is a repository of information on oceanic regions, because it captures material from an oceanic plate subducting through a trench. The geologic structure of an accretionary complex is characterized by duplexes (Fig. 3). A duplex has an internal structure in which each faulted-package (horse) is subparallel or oblique to a roof or floor thrust and each duplex is separated by a link thrust. Each horse in the duplex preserves primary stratigraphic relations of oceanic rocks (basal basalt, pelagic bedded chert or micritic limestone, hemipelagic siliceous mudstone or shale capped by trench-fill terrigenous turbidite. This complex structure was unraveled by microfossil mapping (Matsuda and Isozaki, 1991). The ages of the constituents in the

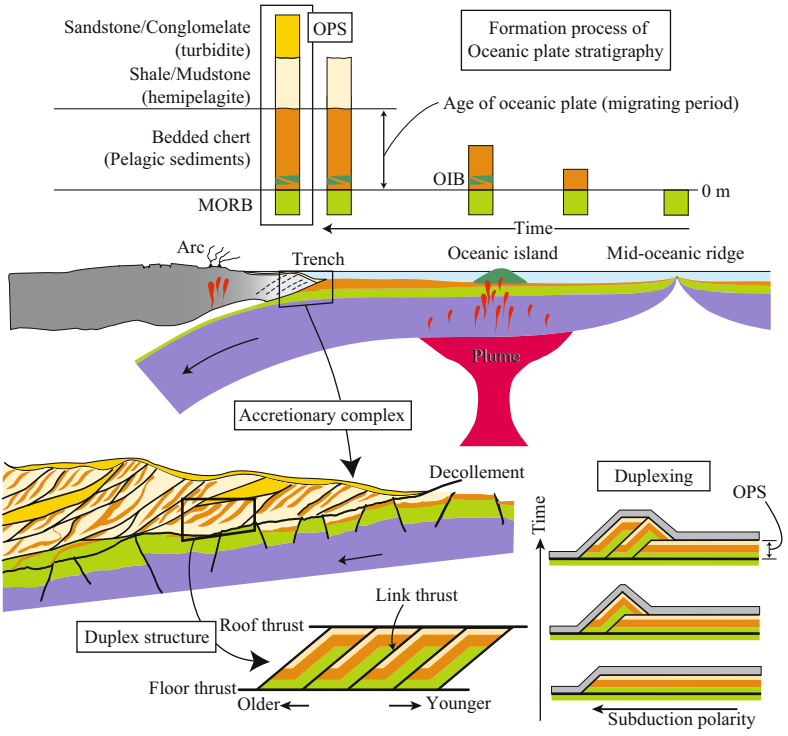

Figure 3. Formation process of oceanic plate stratigraphy and an accretionary complex. See text for explanations.

horses of a particular duplex become younger oceanward, because of their oceanward growth with time: moreover, the duplex develops downward with time. Such primary stratigraphy in an accretionary complex is called "ocean plate stratigraphy" (OPS); it preserves the stratigraphic relations of the rocks and strata of the upper oceanic plate as it moves from ridge to trench. Where the oceanic rocks are covered conformably with terrigenous clastic sediment, the age of that clastic horizon approximates the time of formation of the accretionary complex at the trench. And, accordingly the deposition time of the oceanic sediments is the time interval between the lowermost and uppermost beds of the pelagic and hemi-pelagic sediments, i.e., it indicates the length of time it took for the oceanic plate to move from the mid-oceanic ridge to the trench. That is to say, the deposition time interval of the oceanic sediments is the age of the oceanic plate, which subducts at the trench. Consequently, OPS, which is now exposed on land, provides us with information on how old the oceanic plate is, and when it entered the accretionary complex. The best high-precision method to determine these ages is microfossil dating with radiolarian stratigraphy in the pelagic and terrigenous sediments in Phanerozoic strata (Isozaki et al., 1990; Matsuda and Isozaki, 1991). The reliable Ar-Ar dating is also available to determine the eruption age. In the case of Proterozoic OPS, in which it is difficult to obtain microfossils, the best methods are U-Pb and Pb-Pb dating of heavy minerals such as zircon and a bulk isochron.

Summary of modern volcanic sequences. Information about oceanic materials, i.e., basaltic greenstones and associated sedimentary rocks, in accretionary complexes, is essential to reconstruct the oceanic paleogeography. In this study, we compared the characteristics of modern volcanic sequences in oceanic domains (Table 1) with those of oceanic materials extracted from accretionary complexes, and so worked out their primary tectonic settings such as mid-ocean ridge, off-ridge (oceanic islands, seamounts and oceanic plateaus), fore-arc or back-arc basin, and island arc.

In terms of the geologic features in modern tectonic settings, shallow-marine pelagic sediments such as limestone are suggestive of deposition on a topographic high in the mid-ocean, whereas thick deep-sea pelagic sediments like bedded chert are characteristic of the mid-ocean floor. Terrigenous sediments are expected to be the predominant lithology in a trench near an island arc, where chert and carbonate can be recognized but distinguished from the mid-oceanic sediments, by their thickness and association with terrigenous materials. In this regard, when a mid-ocean ridge reaches a trench, terrigenous sediment rather than pelagic chert will directly cover the mid-oceanic ridge basalts (MORB).

Other key geologic features of modern volcanic sequences are the modes of occurrence of their crustal constituents. Subaerial eruption is characteristic in oceanic islands and island arcs due to their topographic features, whereas pillow lavas indicate submarine settings, i.e., seamounts, mid-ocean ridges and back- and fore-arc basins. The presence of sheeted dykes is conclusive evidence of a spreading center like a mid-ocean ridge. As for the crustal thickness of volcanic sequences (above the Moho depth), there is a distinct contrast between oceanic plateaus and other environment.

Table 1. Geological and petrochemical characteristics of volcanic sequences from different tectonic setting

Tectonic setting	Oceanic plateau (OP)	Oceanic island/seamount (OI/SM)		Mid-ocean ridge (MOR)	Marginal basin (MB; back-/fore-arc basin)	Island arc (IA)
Predominating sediments	Shallow-marine pelagite	Shallow-marine pelagite		Deep-sea pelagite	Hemipelagite, terrigenous clastics	Terrigenous clastics
Crustal thickness	20–40 km	7–15/7–10 km		<7 km	<7 km	7–20 km
Ocean floor metamorphism (gabbro layer)	Granulite facies	Amphibolite facies		Amphibolite facies	Amphibolite facies	Granulite facies
Dyke complex	Not sheeted	Not sheeted		Sheeted	Sheeted	No
Texture of volcanics	Mainly aphyric	Porphyritic		Mainly aphyric	Mainly aphyric	Porphrytic
Fractional control	Ol, Cpx, Pl	Ol, Cpx		Ol, Pl	Ol, Cpx, Pl	Ol, Opx, (Cpx), Amp
Type of basalt	TH, A	A, TH		TH	TH, A	CA, TH, A
(La/Nb)n	≤1	≤1		≤1	from ≤1 to >1	≫1
REE pattern	Mainly flat	LREE enriched + HREE depleted		LREE depleted	Mainly flat	LREE enriched
		Normal hotspot	Superplume-related			
Nb/Y		<5.5(Nb/Zr) + 0.5	>5.5(Nb/Zr) + 0.5			
			Non-HIMU HIMU			
Nb/Zr			<0.23 >0.23			
$^{206}Pb/^{204}Pb$			<20.5 >20.5			

Ol, olivine; Cpx, clinopyroxene; Opx, orthopyroxene; Pl, plagioclase; Amp, amphibole; TH, tholeiite; A, alkaline rock; CA, calc-alkaline rock.

For example, the Ontong Java plateau has an average crustal thickness of about 33 km (e.g., Richardson et al., 2000), and other oceanic plateaus have unusually thick crusts. Based on experimental studies, basaltic rocks with a bulk composition of quartz tholeiite or alkali olivine basalt can be transformed to garnet-bearing granulite at c. 1000°C above 1.2 GPa or 0.8 GPa, respectively (e.g., Ringwood, 1975). The unusual thickness of an oceanic plateau would cause metamorphism at the base of the plateau crust at higher pressure and temperature conditions than at a normal mid-oceanic ridge. The crustal thickness of oceanic plateau could form garnet-bearing granulites like mafic xenoliths found from the northern end of the Kerguelen plateau (Gregoire et al., 1994), although it depends on the availability of fluids and chemical compositions of lower crusts of the plateau. In contrast, the thickness of common oceanic crust does not usually exceed c. 7 km, and the confirmed maximum grade of modern ocean-floor metamorphism is in the amphibolite-facies, except for a very rare case in the Mid Atlantic Ridge (e.g., summary in Ishizuka and Suzuki, 1995). In consequence, the mechanism and process "oceanic plateau metamorphism", mentioned above, differs from those of ocean-floor metamorphism in association with hydrothermal alteration at a mid-ocean ridge.

The petrography and petrology of volcanic rocks also vary in different tectonic settings, depending on the rock type and formation process. Oceanic island basalts (OIB) and island arc basalts (IAB) are porphyritic, whereas oceanic basalts in the other settings are mainly aphyric. The fractionation control of plagioclase following olivine is characteristic in MORB consisting predominantly of low-K tholeiites, whereas OIB are predominantly alkaline rocks and have the crystallization sequence of clinopyroxene following olivine. The crystallization of orthopyroxene and amphibole is a specific feature of IAB associated predominantly with calc-alkaline rocks. However, immature oceanic island arc basalts are predominantly tholeiitic, occasionally associated with boninites and fore- and back-arc-basin basalts, and are similar to MORB. In recent years, it has been established that oceanic plateau basalts (OPB) are generally aphyric and their fractionation is controlled by olivine, plagiolclase and clinopyroxene, depending on the depth of their generation (e.g., Neal et al., 1997), whereas the fractionation of MORB is generally controlled by olivine and plagioclase.

The geochemical characteristics of basaltic rocks can be used to distinguish their parental materials and formation processes. Chondrite-normalized rare earth elements (REE) patterns with depletion of light-rare-earth elements (LREE) are typical of normal-type (N-) MORB (e.g., Sun and McDonough, 1989). OIB have a REE pattern with high LREE-enrichment and the depletion of heavy-rare-earth elements (HREE). Depletion of high-field-strength elements (HFSE) relative to large-ion-lithophile elements (LILE), and distinctive Nb anomalous behaviors in primitive mantle-normalized incompatible elements patterns, are suggestive of calc-alkaline IAB, the sources of which are affected by subduction-zone metasomatism; this is termed a suprasubduction characteristic. Back- and fore-arc-basin basalts have transitional signatures between IAB and N-MORB with relative Nb depletion. Immature oceanic island arc tholeiites also have a negative Nb anomaly. OPB have a flat REE pattern similar to enriched-type (E-) MORB.

Radiogenic isotopic compositions of basalts are a powerful tracer to determine their source materials, because they have not involved a fractionated magmatic process, such as partial melting or fractional crystallization. MORB have depleted components (DM), and OIB have enriched components (EM1, EM2, and HIMU; e.g., Zindler and Hart, 1986). HIMU basalts, which are enriched in radiogenic Pb ($^{206}Pb/^{204}Pb > 20.5$), are restricted to superplume regions (Cook-Austral, Polynesia; St. Helena). OPB have an OIB-like radiogenic isotopic signature.

Criteria for discrimination of tectonic settings of ancient volcanic sequences in accretionary complexes. As described above, modern volcanic sequences have different geologic, petrochemical and isotopic features according to their tectonic settings. Therefore, these features in ancient volcanic sequences trapped in accretionary complexes can help us distinguish their tectonic settings.

In terms of geologic features, sedimentary rocks such as limestone, bedded chert and terrigenous clastics associated with basaltic greenstones in accretionary complexes, and their mutual structural relationships (e.g., conformable or not) provide us with useful information to reconstruct the environment where the greenstones were erupted. When an oceanic plate is trapped in an orogenic belt, rocks from various depths of the plate may be exposed after their uplift and erosion. Metamorphic petrology of such rocks, i.e., the degree of ocean floor metamorphism, enables us to reconstruct their primary geologic structure and original tectonic setting; if there is any evidence of high-pressure granulite-facies ocean floor metamorphism, this must be derived from the lower crust of an oceanic plateau.

The geochemical and isotopic features of modern basaltic rocks from various tectonic settings can be distinguished by several discrimination diagrams (e.g., summary in Wilson, 1989; Rollinson, 1993). However, these discrimination diagrams may not always lead us to confident conclusions for determining the tectonic settings of greenstones. Discrimination diagrams based on compilations of published data only suggest the general petrogenesis of the greenstones, and do not indicate directly their tectonic settings. Moreover, greenstones trapped in orogenic belts have been subjected to secondary modification by hydrothermal alteration and metamorphism during their travel to a trench, after their travel from their birth place. LILE are highly mobile under these processes, and so their contents in greenstones cannot be used to determine their tectonic setting. For the same reason, although the Pb isotopic ratio of HIMU basalts is a conclusive characteristic for distinguishing its origin, Sr and Pb isotopic compositions are easily modified by hydrothermal alteration. But, HFSE such as Nb, Y and Zr, and REEs are generally regarded as immobile against secondary alteration, and the systematics of these elements are useful for discrimination of greenstones. Nd isotope compositions are also available as a discriminant. Tatsumi et al. (1998) pointed out that superplume-related OIB have higher Nb/Y ratios than other OIB at given Nb/Zr ratios, and in particular HIMU basalts have higher Nb/Zr ratios. If Pb isotopic compositions are not available, we can indirectly trace superplume-related volcanism using Nb-Zr-Y systematics that resist alteration.

Cretaceous oceanic plateaus, dispersed at present in the southwestern and western Pacific, formed in the Pacific Superplume region (e.g., Larson, 1991a). However, most basalts from those oceanic plateaus show tholeiite-like geochemical characteristics similar to E-MORB, and are homogeneous in composition (e.g., Mahoney et al., 1993), except for some alkaline basalts with the HIMU signature (Tejada et al., 1996). Therefore, these tholeiitic OPB exhibit different trends on a Nb/Y-Nb/Zr diagram (Tatsumi et al., 1998) from the superplume-related OIB. Such a difference could be caused by the formation process of such a huge amount of plateau basalt; melting a large amount of lithospheric mantle could dilute the geochemical signature of the HIMU end-member in the resultant melt. Except for well analyzed cases (the Solomon islands and the Ontong Java plateau), the petrochemical characteristics of oceanic plateau basalts have been studied by using restricted samples dredged from the ocean floor that provide only limited information on the subsurface of the oceanic plateaus. Because of these problems, it is controversial whether superplume-related plateau basalts can be definitely characterized only by geochemical characteristics such as the HIMU signature and Nb-Y-Zr systematics. So, we must pay attention to other aspects of oceanic plateaus or OPB, i.e., their geologic, petrographic and petrologic features such as crustal thickness, type of phenocrysts, compositional trend by differentiation, and so on (Table 1).

As stated above, a comprehensive examination enables determination of the tectonic settings of greenstones in orogenic belts. With such considerations, we determined the primary tectonic settings of ophiolites and accreted greenstones in orogenic belts mainly in the circum-Pacific region, listed in Table 2. The compilations for the study were taken from the most recent and reliable data available at present, since the quality and quantity of available data are uneven according to area and age.

2.2.2 Procedures of reconstruction of oceanic domains

Cenozoic-mesozoic reconstruction. The distribution of mid-ocean ridges and trenches for the last 200 Ma is well known and plate reconstructions are available, because information on the oceanic domain is immediately retrievable from the extant oceanic floor.

As stated above, the paleopositions of the Cretaceous LIPs in the present oceanic domain can be estimated by using the relative plate motions model (Engebretson et al., 1985; Larson, 1991a); those oceanic LIPs were put back from the present day to their erupted age, following their plate motions. For the ophiolites and greenstones in accretionary complexes of the Pacific-type orogenic belts, at first we distinguished their tectonic settings on the basis of the above-mentioned criteria and available data about their geology, geochronology and petrochemistry. After that, the paleopositions of the ophiolites and greenstones were reconstructed using the relative plate motion model (Engebretson et al., 1985). In a case where a determined setting was an island arc, back- or fore-arc basin, the ophiolites or greenstone belts were generated at a continental margin at that period, and migrated with it until the present. In the case of oceanic settings, we determined the formation age from microfossils from the bottom of the sedimentary section of the OPS, from trapped sediments in lavas,

Table 2. Summary of circum-Pacific ophiolities and greenstone belts

No.	Name	Region	Type	Eruption age	Accretion age, Ma
5	Resurection peninsula and knight island ophiolites (Orca group)	N. America	MOR (TTR)	57 Ma	
1	Melange in shimanto supergroup	E. Asia	MOR (TTR)	Cenomian-earliest paleocene	
18	New caledonia ophiolotite	Oceania	MB, OI, IA	Campanian-upper paleogene, upper paleocene (56–59 Ma)	
16	Tangihua ophiolite (Northland ophiolite)	Oceania	MB	mod-creataceous-paleocene	
11	Caribbean plateau	C. & S. America and Caribbean Sea	OP	90 Ma, 75 Ma	Late cretaceous (85–83 Ma)
12	Gorgona plateau	S. America	OP	90 Ma, 75 Ma	Late Eocene
19	East sulawesi ophiolite		OP	138 Ma	>28 Ma
2	Iratsu massif (Sanbagawa belt)	E. Asia	OP	142–153 Ma	110–120 Ma
4	Sorachi-yezo belt	E. Asia	OP	150 Ma	Barremian
8	Josephine ophiolite	N. America	MB	157 Ma	151 Ma
9	Coast range ophiolite	N. America	IA, SM	160–170 Ma	
7	Wrangellia terrane	N. America	FB	middle ladonian-late karmian	
14	Aysen metamorphic complex	S. America	OP, OI (superplume)	Late triassic, Late devonian	
3	Yakuno ophiolite	E. Asia	OP	282–285 Ma	
6	Angayucham terrane	N. America	OP	Mississipian	Middle jurassic
15	Dun mountain ophiolite	Oceania	MA	280 Ma	
17	Tasmanide ophiolite	Oceania	IA	514 Ma, 524 Ma, 503 Ma, 502 Ma, 530 Ma, 509 Ma, 535 Ma	
10	Trinity ophiolite	N. America	IA-MB	565–570 Ma, 452 Ma, 412 Ma	
13	Precordillera ophiolite	S. America	OP	576 Ma	
20	Kurai greenstone	C. Asia	OP	598 Ma	

or directly from the isotopic age of the volcanics. In a similar way, we determined the emplacement age on the basis of microfossils from the terrigenous horizon of the OPS. From the present day to their emplacement age, we considred that they were considered to have migrated with their relevant continents, whereas from their emplacement age to eruption age, the same method for the LIPs in the present oceanic domain was adopted.

Paleozoic-neoproterozoic reconstruction. Location of mid-oceanic ridges were considered in terms of a model in which the mid-oceanic ridges were present at the center of a small ocean surrounded by continental fragments for the period from continental break-up to initiation of plate subduction. After the beginning of subduction, the locations of mid-oceanic ridges are unknown because we have no method of deciding the relative velocity between the oceanic plates. In such cases, we tentatively arranged the mid-oceanic ridges anywhere in the oceans.

The ophiolites and greenstone belts in accretionary complexes were examined for their tectonic setting based on the criteria mentioned above. In cases where they were generated at a continental margin, they could migrate with the continents. In the case of an oceanic setting, we could not directly use the plate motions. If paleomagnetic data were available, we were able to use them. But in most cases, they were not available and we could not determine their detailed positions in the ocean. We could only determine the pelagic environment in an ocean that faces an orogenic belt. In cases where greenstones or ophiolites had superplume affinities or oceanic plateau affinities and the orogenic belts faced the Pacific Ocean, they could be located in the Pacific Superplume region at their eruption age, based on the analogy that Cretaceous oceanic plateaus were generated in the Pacific Superplume region.

3 RECONSTRUCTIONS

3.1 From 200 Ma to the present

3.1.1 Continental domain

In this period, the history of continents involved the breakup of the supercontinent Pangea and the redistribution of the fragments (e.g., Ford and Golonka, 2003; Golonka et al., 2003, and references therein). Rifting of Pangea was initiated in the Early Triassic. The drift-rift transition occurred at ∼200 and ∼185 Ma in the southeastern US and maritime Canada, respectively. The start of seafloor spreading in the central Atlantic is dated as 175 Ma. The breakup of Africa from India/Antarctica took place in the period 198–173 Ma. The initial opening of South Atlantic between Africa and South America was at 130 Ma. The Central Atlantic Ocean propagated towards the North Atlantic and the onset of seafloor spreading of Rockall Trough started at ∼95 Ma. The separation of Madagascar/India from Africa began at ∼180 Ma and was stable relative to Africa by 112 Ma (Coffin and Rabinowitz, 1988). The breakup of Greater India from Australia is dated as 136 Ma (Müller et al., 1998). The beginning of separation of India from Antarctica and from Madagascar occurred at ∼134 Ma

and at ~88 Ma, respectively (Ramana et al., 2001; Storey et al., 1997). Seafloor spreading at 85 Ma led to the separation of Australia from Antarctica (Norvick and Smith, 2001). The Labrador Sea started to open at 62 Ma (Saunders et al., 1997). South America began to migrate away from Antarctica at ~50 Ma (Livermore et al., 2005).

The extrusion of much continental flood basalt occurred in this period; the Columbia River basalts at 6–17 Ma (Baksi, 1989; Tolan et al., 1989), Ethiopian and Yemen Traps at 30 Ma (Hofmann et al., 1997), North Atlantic Volcanic Province (NAVP) at 60 ± 1 Ma (Eldholm and Grue, 1994), Deccan Traps ~66 Ma (e.g., Baksi, 1994), Madagascar basalt at 88 Ma (Storey et al., 1995), Rajmahal basalt at 116 Ma (Pringle et al., 1994), Paraná-Etendeka basalts at 138–131 Ma (Stewart et al., 1996), Karoo-Ferrar basalts at ~180 Ma (e.g., Marsh et al., 1997), and the Central Atlantic Magmatic Province (CAMP) at 197–201 Ma (Marzoli et al., 1999a,b). The age and distribution of NAVP, the Madagascar, Rajmahal, Paraná-Etendeka and Karoo-Ferrar basalts and the CAMP indicate the initial stage of opening or breakup of the North Atlantic Ocean, Madagascar/India, India/Antarctica, South Atlantic Ocean, Africa/Antarctica, Central Atlantic Ocean, respectively. Except NAVP, these LIPs were generated directly or nearly on the African low seismic velocity area in the lower mantle (Fig. 4). The main breakup event of Pangea occurred in the African Superplume region. Ultramafic lamprophyres in the Ferrar igneous province have a HIMU-signature (Riley et al., 2003), suggesting that breakup of Pangea was controlled by upwelling of the lower mantle.

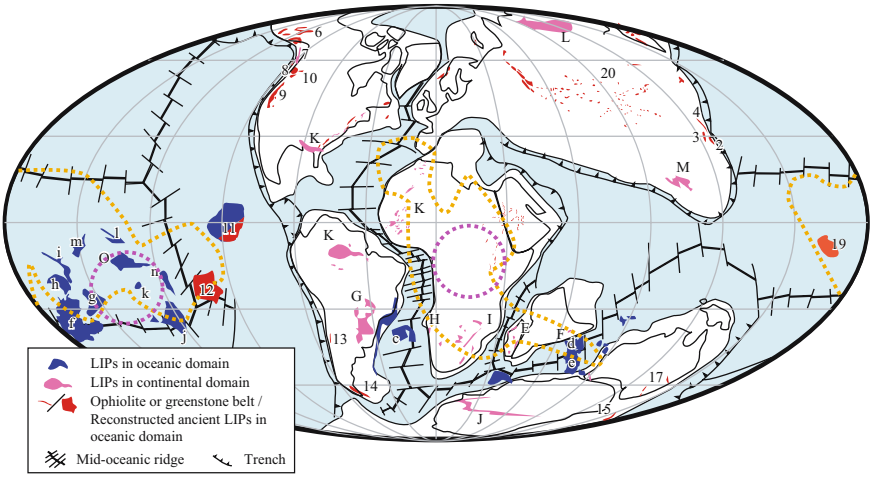

Figure 4. Reconstructed paleogeographic maps at ca. 90 Ma. The distribution of continents is referred to Scotese (2004). Alphabets of LIPs and numbers of ophiolites or greenstone belts are shown as Figure 2. Although Sorachi-Yezo belt (4) and Iratsu massif (2) is generated in superplume region at ca. 150 Ma, they were rapidly transported to subduction zone on Izanagi plate and had already been accreted before 90 Ma.

3.1.2 Oceanic domain

Oceanic plateaus, oceanic floor flood basalts, and aseismic ridges in this period are widely dispersed in the world's oceans. Major examples are: Iceland at 0–15 Ma (McDougall et al., 1984), Walvis Ridge at 79–30 Ma and Rio Grande Plateau at 89 Ma (O'Connor and Duncan, 1990) in the Atlantic Ocean, Broken Ridge at 94–95 Ma, Kerguelen Plateau at 118–34 Ma (Duncan, 2002) in the Indian Ocean, Ontong Java Plateau at 122 and 90 Ma (Mahoney et al., 1993), Nauru Basin at 110.8 Ma (Castillo et al., 1994), East Mariana Basin and Pigafetta Basin at 114.6–126.1 Ma (Pringle, 1992), Manihiki Plateau at 91–114 Ma (Lanphere and Dalrymple, 1976), Magellan Rise at ∼135 Ma (Winterer et al., 1973), Hess Rise at 99–112 Ma (Kroenke and Nemoto, 1982) and Shatsky Rise at 126–150 Ma (Nakanishi et al., 1989) in the Pacific Ocean.

Most oceanic LIPs in the Atlantic and Indian Oceans have a ridge-like geomorphology and a long active time-span, or are related to continental flood basalts by hot spot tracks; e.g., NAVP and Iceland, Paraná-Etendeka basalt and Walvis Ridge-Rio Grande Plateau, and Rajmahal basalt and Kerguelen Plateau-Broken Ridge-Ninetyeast Ridge (Morgan, 1981; Richards et al., 1989). Although some of those in the Pacific have the above-mentioned characteristics, most have short active life spans. Their eruption ages concentrate in the Jurassic-Cretaceous (80–150 Ma) and their paleopositions in the center of the Pacific Superplume region at their generation age (Fig. 4; Larson, 1991a). Furthermore, western Pacific seamounts have non-sequential, synchronous ages and non-concordant chain with the Pacific plate motion (e.g., Line Islands at 81–86 and 68–73 Ma, Davis et al., 2002; Mid-Pacific Mountains at 117–132 Ma, Smoot, 1999), and were derived from the Pacific Superplume along preexisting linear weaknesses in the lithosphere. In this period, the relevant part of the Pacific plate was divided into several micro-plates (Nakanishi and Winterer, 1998) and the Shatsky Rise was generated by propagation of a ridge-ridge-ridge (RRR) triple junction (Nakanishi et al., 1999). These lines of evidence support the idea that mantle upwelling took place.

The Resurrection Peninsula and Knight Island Ophiolites from the Orca Group in southern Alaska contain pillow basalts interbedded with terrigenous sediments and sheeted dykes (Lytwyn et al., 1997). The Resurrection Peninsula Ophiolite is dated as 57 ± 1 Ma by the zircon U-Pb method on intruded plagiogranite. The basalts commonly have plagioclase phenocrysts, clinopyroxene microphenocrysts, and olivine phenocrysts, but have flat REE patterns and transitional-type MORB-like geochemical signatures. These ophiolites were generated at a trench-trench-ridge (TTR) triple junction and are relicts of the subduction of the Kula-Farallon ridge.

Mélange units containing greenstones are common throughout the Shimanto Supergroup in the Ryukyu Islands and southwestern Japan. The greenstones from some formations (Naze Formation, Makimine Formation, Okitsu Mélange, Mugi Formation, Ryujin Formation, and Inui Group) have closely related shales and lack bedded cherts (Kiminami et al., 1994). Radiolarian assemblages from the shales indicate Cenomanian-Turonian, Santonian-Middle Campanian, Coniacian-Campanian, Campanian-Early Maestrichtian, Late Campanian-Maestrichtian, and

Late Maestrichtian-earliest Paleocene ages for the Naze Formation, Makimine Formation, Okitsu Melange, Mugi Formation, Ryujin Formation, and Inui Group, respectively. They all have MORB-like geochemical features, and were generated at a TTR triple junction and are relicts of the subduction of the Kula-Pacific ridge on the basis of these characteristics. The ridge motions by plate reconstructions (Maruyama and Seno, 1986) are consistent with the evidence that the greenstones become younger eastwards (Kiminami et al., 1994).

In New Caledonia in the southwestern Pacific one of the largest ophiolites of the world belongs to the Ophiolitique Nappe, the Poya Terrane and Pouebo Terrane (Cluzel et al., 2001). In the Poya Terrane pillowed and massive basalts, dolerites, and fine-grained gabbros are interbedded with or covered by abyssal argillite and chert. The most common radiolaria extracted from the sedimentary rocks indicate an Upper Cretaceous (Campanian) age. An Upper Paleogene fauna has also been recovered from some localities. Due to the absence of terrigenous materials, it is inferred that the ophiolite was accreted in an intra-oceanic environment. The Poya Terrane in general was metamorphosed in the greenschist facies interpreted as ocean floor metamorphism. However, because the terrane is severely disrupted, the primary thermal structure of the crust cannot be reconstructed. The volcanic rocks from the Poya Terrane are divided into three types on the basis of their REE patterns. An "undepleted type" has a flat REE pattern and contains augite and plagioclase phenocrysts. A "depleted type" has a slightly depleted REE pattern and Nb depletion and contains augite microphenocrysts. Nd isotopic variations of "undepleted" and "depleted" types suggest mixing between DM and EM2 sources. Synthesizing the features above, "undepleted" and "depleted" types are inferred to have been generated in a plume-enhanced marginal basin. The third REE type is an alkaline volcanic rock that has highly enriched REE patterns, is associated with micritic interpillow sediments, and has pinkish Al and Ti-enriched diopside, plagioclase and Fe-Ti oxides microphenocrysts. It is interpreted to have erupted as a seamount in the basin that provided the other types of volcanic rocks. The faunas recovered from micritic interpillowed materials indicate an Upper Paleocene (56–59 Ma) age, which indicates this is the youngest of the terranes and is consistent with the interpretation of the tectonic setting. The mafic rocks from the Pouebo Terrane occur in a metamorphosed ophiolitic mélange, and have similar geochemical features to those of the Poya Terrane and to island arc tholeiites with a slightly enriched REE pattern and Nb depletion. The protoliths seem to be derived from the reworked Poya and island arc terranes. The Ophiolitique Nappe is underthrusted by the Poya and Pouebo Terranes and is mainly composed of harzburgite and dunite. This ultramafic allochthon is extremely depleted and cannot have been in equilibrium with a melt of MORB composition (Eissen et al., 1998). The Ophiolitique Nappe was the basement on which, not the Poya Terrane, but the arc (Loyalty Arc) was built (Cluzel et al., 2001).

The Tangihua Ophiolite Complex, informally known as the Northland Ophiolite, is situated in the north of North Island, New Zealand. It consists of basaltic pillow and massive lavas, sheeted dykes, plutonic gabbro, diorite and plagiogranite, cumulate layered ultramafic rocks and gabbros, harzburgites and lherzolites (Malpas et al.,

1992). The lavas are intercalated with siliceous mudstone and micritic limestone. Intercalated and interpillowed sedimentary rocks have macro- and micro-faunas with an age ranging from mid-Cretaceous to Paleocene (Brook et al., 1988). Basalts contain phenocrysts of plagioclase, clinopyroxene, orthopyroxene, and rare magnetites and titanites. Olivine-rich and hornblende-bearing basalts are rare (Nicholson et al., 2000). Most lavas have a slightly LREE-depleted REE pattern and negative Nb anomalies. Several lavas have a LREE-enriched REE pattern. The Tangihua Ophiolite was generated in an arc and a back-arc (Nicholson et al., 2000).

The thick oceanic crust (up to 15–20 km) of the Caribbean plate has bulk Ar-Ar ages of ca. 90 Ma and 75 Ma (Sinton et al., 1998). It has mostly REE patterns that range from slightly LREE-depleted through flat to slightly LREE-enriched; but a few are OIB-like and LREE-enriched (Kerr et al., 1997b; Sinton et al., 1998). Cretaceous lavas crop out on islands in the Caribbean Sea (Aruba, Curacao, Trinidad, Hispaniola, Jamaica and Cuba), in the Coastal borderlands of Venezuela, the Pacific coast of Costa Rica, the Azuero and Sona peninsulas and Caribbean coasts of Panama, and in the Central and Western Cordillera of western Colombia and Ecuador (Kerr et al., 1997b and references therein). They mostly have bulk Ar-Ar ages of ca. 90 Ma and 75 Ma that are coeval with the Caribbean plate (e.g., Sinton et al., 1998). Their REE and isotopic compositional diversity are similar to that of the Caribbean plate (e.g., Kerr et al., 1997a; Sinton et al., 1998; Thompson et al., 2003). The contemporaneity and geochemical similarity between the Caribbean Plate and the Cretaceous lavas that crop out within and around the Caribbean Sea and in Western and Central Cordillera suggest a genetic derivation. Moreover, on the island of Curacao and in the Central Cordillera (Kerr et al., 1996b, 1997a) picritic lavas belong to the Caribbean Plateau (e.g., Kerr and Tarney, 2005). The isotopic signature of the Caribbean Plateau basalts shows that they were generated in the Galapagos hotspot (Thompson et al., 2003). This is consistent with paleomagnetic data that indicate derivation from near-equatorial latitudes (Acton et al., 2000). Radiolarian species in chert beds exposed on the islands of the northern Caribbean margin indicate a Pacific rather than a Caribbean/Atlantic origin (Montgomery et al., 1994). The Caribbean Plateau was generated at the present-day Galapagos hotspot.

Lavas coeval with the Caribbean Plateau occur on Gorgona Island and at Serrania de Baudo on the Pacific coast of Colombia, and at Pinon and Pedernales-Esmeraldas in Ecuador (Kerr et al., 1997a; Sinton et al., 1998). Gorgona Island is well known for its unique occurrence of Phanerozoic komatiite. Although most coastal lavas are geochemically similar to those of the Caribbean Plateau, komatiites, picrites and basalts from Gorgona have more diverse REE patterns that range from strongly LREE-depleted to LREE-enriched (Kerr et al., 1996a, 1997a). Depleted lavas from Gorgona are isotopically distinguishable from those of the Caribbean Plateau (Thompson et al., 2003). The coastal lavas are tectonically separated from the Western Cordillera by island arcs (Kerr et al., 2002; Kerr and Tarney, 2005). Although the Gorgona and coastal lavas have been regarded as a part of the Caribbean Plateau, it has been suggested that these are part of another plateau termed the Gorgona Plateau (Kerr et al., 2002; Kerr and Tarney, 2005). The accretion ages are critical to settle the controversy.

On Gorgona Island middle Eocene marine sedimentary rocks occur in a fault-bounded block in contrast to Miocene and Oligocene unconformable deposits on lavas without tectonic disturbance (Kerr and Tarney, 2005); this suggests that the accretion age was Late Eocene. Tonalite batholiths from the island of Aruba in the Caribbean Sea have a biotite Ar-Ar age of 85–82 Ma (White et al., 1999), indicating Late Cretaceous accretion of the Caribbean Plateau (Kerr and Tarney, 2005). Paleomagnetic data for Gorgona Island indicate a provenance latitude of ~26°S (MacDonald et al., 1997). This is consistent with a longer duration of migration of the Gorgona Plateau compared with that of the Caribbean. Kerr and Tarney (2005) proposed that the Gorgona Plateau formed at the site of the present-day Sala y Gomez hotspot.

The East Sulawesi Ophiolite, Indonesia, has a crust with a minimum thickness of 8 km (Kadarusman et al., 2004). The most common basalts are aphyric; and minor porphyritic basalts have less olivine phenocrysts. Mineral chemistry of cumulate rocks clearly cannot indicate that the rocks are derived from an arc setting, although the geochemical features of the basalts indicate their suprasubduction origin. On the basis of the petrological and mineral chemical data, Kadarusman et al. (2004) suggested that the rocks were generated in an oceanic plateau. K-Ar dating of underlying mélange and metamorphic sole indicates it was generated at 138 Ma and emplaced before 28 Ma (Parkinson, 1998). The plateau can be tracked back to near the Pacific Superplume region at its formation age (Kadarusman et al., 2004).

The Iratsu and Higashi-Akaishi bodies that contain the highest grade rocks of the Sanbagawa metamorphic belt in southwestern Japan are composed of ultramafic rocks, eclogitic metabasites with a basalt-gabbro origin, metacarbonate, metachert and pelitic gneiss in ascending order (Maruyama et al., 2001; Terabayashi et al., 2005). The bodies are separated from their surrounding schists on the top by a roof thrust and on the bottom by a floor thrust. They have a duplex structure composed of four horses. The reconstructed OPS of the bodies suggests that they were derived from a huge oceanic plateau covered by pelagic limestone with minor chert on its flank (Maruyama et al., 2001; Kugimiya and Takasu, 2002). Metagabbros contain relics of high-pressure (i.e., garnet-bearing) granulite-facies and subsequent eclogite-facies metamorphism (Yokoyama, 1980). The petrological thickness of the plateau must have exceeded 30 km because of the occurrence of the relict high-pressure granulites in the lower horizons of the reconstructed stratigraphy. The Mikabu greenstone belt that extends for about 800 km along the southern margin of the Sanbagawa belt is mainly composed of mafic volcanic rocks and ultramafic-mafic cumulates (e.g., Ozawa et al., 1997). The Mikabu greenstones also underwent subduction-related high-P/T metamorphism, and are regarded as the low-grade part of the Sanbagawa belt (e.g., Banno and Sakai, 1989; Suzuki and Ishizuka, 1998). Their geology and petrochemistry including a HIMU signature (high-Nb/Zr and Nb/Y ratio; Ozawa et al., 1999) indicate that the Mikabu greenstones were derived from a seamount chain and/or oceanic plateau (Isozaki et al., 1990; Ozawa et al., 1999; Uesugi and Arai, 1999); i.e., they formed by superplume or plume activity. K-Ar dating of igneous amphiboles from the Mikabu gabbros (Ozawa et al., 1997), and U-Pb dating for zircons (inherited cores) from the Sanbagawa eclogites (Okamoto et al., 2004) combined

with microfossils from pelagic sediments associated with the greenstones indicate the Sanbagawa and Mikabu protoliths have eruption ages of 142–153 Ma (Sanbagawa: Isozaki and Itaya, 1990; Mikabu: Sakakibara et al., 1993). Metamorphic zircons from the Sanbagawa eclogites have U-Pb ages of 110–120 Ma; this points to the accretion age (Okamoto et al., 2004).

Greenstones from the Sorachi-Yezo belt in central Hokkaido, northern Japan have N-MORB- to E-MORB- and OIB-like geochemical features (Sakakibara et al., 1999; Nagahashi and Miyashita, 2002). Some OIB-like greenstones have high Nb/Y and Nb/Zr ratios (Sakakibara et al., 1999) and were generated from heterogeneous sources in an oceanic plateau (Kimura et al., 1994; Sakakibara et al., 1999). The radiolarian age of chert xenoliths in lavas is Latest Jurassic (ca. 150 Ma) and is regarded as close to the time of eruption (Sakakibara et al., 1999). Radiolaria from black shale in the top layer of the OPS including the Plateau indicate that the emplacement age was Barremian (Sakakibara et al., 1999). This oceanic plateau can be tracked back to the Pacific Superplume region (Kimura et al., 1994).

The Josephine Ophiolite in northern California and southern Oregon, US, contains pillow lavas overlain conformably by thin chert and thick turbidite and a sheeted dyke complex (Saleeby et al., 1982; Harper, 1984). Plagiogranite pods in gabbro-diorite and between sheeted dykes, and a dacite dyke that cuts both lavas and sediments have zircon U-Pb ages of 157 and 151 Ma, respectively (Saleeby et al., 1982). The former is regarded as the generation age and the latter the age of emplacement; the Josephine Ophiolite had a short time interval from generation to emplacement. Because the turbidites include andesitic clastics, the Josephine ophiolite is thought to have formed in proximity to an island arc (Saleeby et al., 1982; Harper, 1984). A marginal basin origin is indicated by earlier clinopyroxene crystallization based on the phenocryst assemblage of the lavas and the occurrence of orthopyroxene in cumulates (Harper, 1984). The trace element patterns of the lavas correspond to those from MORB to island arc tholeiite. The fact that the highest grade of hydrothermal metamorphism is amphibolite facies in cumulates indicates a relatively thin crust. We agree with Saleeby et al. (1982) and Harper (1984) that the above-mentioned data indicate that the Josephine Ophiolite was generated during the opening of a marginal basin. The Devils Elbow Ophiolite in western California has similar stratigraphic and geochemical features as the Josephine ophiolite and is regarded as its southern continuation; its zircon U-Pb age is 164 Ma (Wright and Wyld, 1986; Wyld and Wright, 1988). The marginal basin that generated the Josephine Ophiolite began to open by this time.

The Coast Range Ophiolite that crops out in scattered localities over a 700-km-long segment in western California contains two rock units. One is associated with minor felsic igneous rocks and shows island arc geochemical features and a zircon U-Pb age of 160–170 Ma (Shervais and Kimbrough, 1985). The other is a mélange with a serpentinite matrix and has MORB or seamount geochemical features and a Tuthonian radiolarian fauna in chert blocks (Shervais and Kimbrough, 1985). The first unit was generated in an island arc, and the second in a seamount. The Great Valley Group that overlies the Coast Range Ophiolite contains greenstones that have

similar geochemical features and radiolarian ages (MacPherson and Phipps, 1988), and seems to have an origin similar to the Coast Range Ophiolite.

Although many ophiolites and greenstones were generated in convergent regions, there are many ancient plateaus in accretionary prisms in circum-Pacific orogenic belts; the Caribbean Plateau, Gorgona Plateau, East Slawesi Ophiolite, Iratsu massif and Sorachi-Yezo belt. The eruption ages of these plateaus are dated as 75–150 Ma that is close to the peak age of the Cretaceous plateaus in the western Pacific. Considering their emplacement ages and durations of migration, the birth-place of these plateaus was directly or nearly on the Pacific Superplume region (Fig. 4). This indicates that the Pacific Superplume contribution to the Cretaceous pulse was much higher than previously estimated.

3.2 From 550 to 200 Ma

3.2.1 Continental domain

In this period, the history of continents was dominated by the amalgamation of the supercontinent Pangea (e.g., Ford and Golonka, 2003; Golonka et al., 2003; Windley, 1995, and references therein). The (semi-) supercontinent Gondwana and the three major cratons of Baltica (northeastern Europe), Laurentia (North America including Greenland, northern Scotland and northern Ireland) and Siberia were dispersed in Cambrian (Fig. 5). Laurentia collided with Baltica in the Silurian (East Greenland Caledonian and Scandian orogenies). The suture of Laurentia with Avalonia that had departed from the northern margin of Gondwana also formed at this time (Acadian

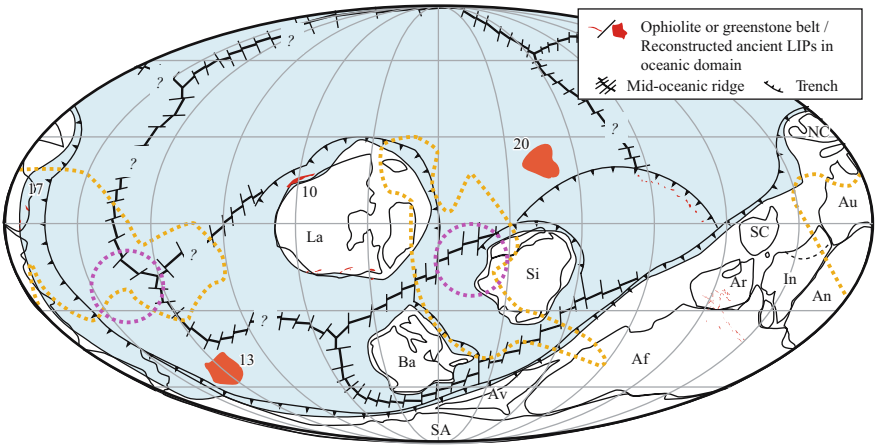

Figure 5. Reconstructed paleogeographic maps at ca. 500 Ma. The distribution of continents is refered to Scotese (2004). Numbers of ophiolites or greenstone belts are shown as Figure 2. Af = Africa; Ar = Arabia; An = Antarctica; Au = Australia; Av = Avalonia; Ba = Baltica; In = India; La = Laurentia; NC = North China; SA = South America; SC = South China; Si = Siberia.

orogen). A series of collisions between Laurentia, Baltica and Avalonia resulted in closure of the Iapetus Ocean and formation of Laurussia. Prior to these collisions, Pacific-type orogens developed in the Cambrian (e.g., Penobscotian and Finnmarkian orogenies). Laurussia collided with the western and central European blocks from the Devonian (Hercynian/Variscan orogen). Meanwhile, the most extensive juvenile additions to the crust in the Phanerozoic took place around the western, eastern and southern margins (present-day coordinates) of Siberia, and involved continental fragments separated from the northern margin of Gondwana (the Central Asian Orogenic Belt, Jahn et al., 2000, 2004). The Kazakhstan block that mainly consists of Neoproterozoic and early Phanerozoic juvenile crusts (Heinhorst et al., 2000) converged with Siberia in the Early Carboniferous. The collision of Kazakhstan/Siberia with Laurussia occurred in the Late Carboniferous (Uralian orogen) and resulted in the formation of Laurasia that became a northern part of Pangea. The final formation of Pangea was caused by the collision of Laurasia and Gondwana in Late Carboniferous-Early Permian time (Alleghenian and West African orogens).

The Pacific Ocean has been closing along its eastern (Cordilleran, western North America) and western margins (Tasmanide, Western Australia) since the Cambrian (Fig. 5). The Paleo- and Neo-Tethyan Oceans developed as Indian-type oceans that have one-side subduction (Figs. 6 and 7). These oceans transported the continental fragments separated from the Gondwana margin to Laurentia, Baltica and Siberia. Laurentia was subducted along both its eastern and western sides and a V-shaped subduction zone, like that in the present-day Western Pacific, was formed around

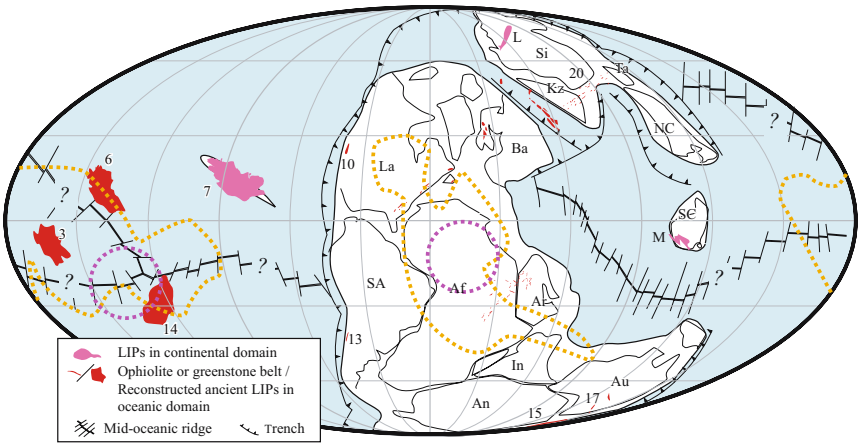

Figure 6. Reconstructed paleogeographic maps at ca. 250 Ma. The distribution of continents is mainly refered to Scotese (2004) but we divided Kazakhstan from Baltica because final event of Uralian orogeny occurred during the Triassic and Early Jurassic (Golonka et al., 2003). Alphabets of LIPs and numbers of ophiolites or greenstone belts are shown as Figure 2. Af = Africa; Ar = Arabia; An = Antarctica; Au = Australia; Ba = Baltica; In = India; Kz = Kazakhstan; La = Laurentia; NC = North China; SA = South America; SC = South China; Si = Siberia; Ta = Tarim.

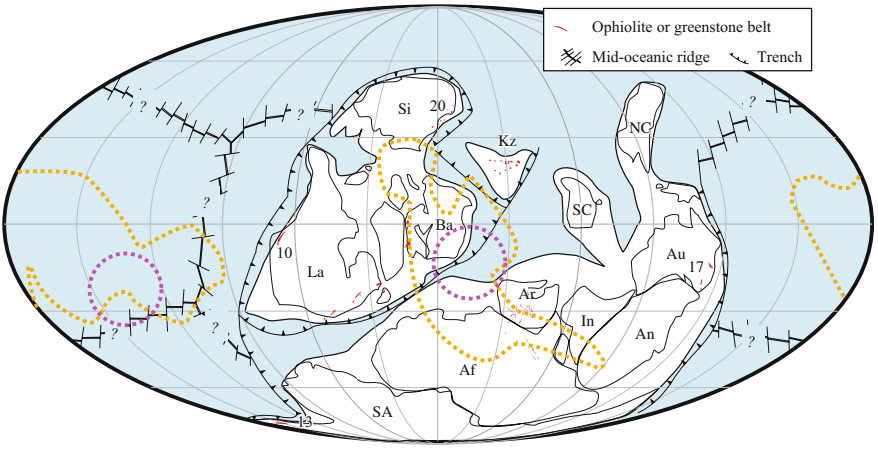

Figure 7. Reconstructed paleogeographic maps at ca. 400 Ma. The distribution of continents is mainly refered to Scotese (2004) but we divided Laurentia from Africa because Alleghenian and Western African orogen was developed during Late Carboneferous and Earky Permian (Ford and Golonka, 2003). Numbers of ophiolites or greenstone belts are shown as Figure 2. Af = Africa; Ar = Arabia; An = Antarctica; Au = Australia; Ba = Baltica; In = India; Kz = Kazakhstan; La = Laurentia; NC = North China; SA = South America; SC = South China; Si = Siberia.

this craton. This Paleozoic plate conversion and the resultant formation of Laurussia occurred in the African Superplume region (Fig. 7).

Continental flood basalts erupted in two regions at the Permian-Triassic boundary; the Siberian Traps at 251.2 ± 0.3 Ma (Kamo et al., 1996), and the Emeishan flood basalts in South China at 251–253 Ma (Lo et al., 2002). These differ from the Mesozoic continental flood basalts; they were generated far from superplume regions (Fig. 6), and failed to develop to continental breakup (Courtillot et al., 1999).

3.2.2 Oceanic domain

A large Triassic greenstone belt in the Wrangellia Terrane extends from Vancouver Island in British Columbia to southern Alaska. It consists of subaerial flows, pillow basalts, but no sheeted dykes and is overlain by cherts and middle Ladinian limestones and by late Karnian and early Norian limestones (Jones et al., 1977). The thickness of this Triassic greenstone is up to ~7000 m (Lassiter et al., 1995). It overlies Pennsylvanian to early Permian volcanics and sedimentary rocks belonging to an island arc (Jones et al., 1977). The greenstones have an E-MORB-like geochemical signature (Davis and Plafker, 1984) but suffer isotopically from crustal contamination (Lassiter et al., 1995). These geologic and geochemical features indicate that the Triassic greenstones in the Wrangellia Terrane were flood basalts on top of an island arc.

In a low-grade metamorphic complex in the Andes of Aysén, southern Chile pillow basalts from the Chonos metamorphic complex contain turbiditic pelitc-psammitic schist intercalations (Hervré et al., 1999). The deposition age of the turbidites is Late

Triassic. The basalts have a phenocryst assemblage of clinopyroxene and plagioclase and E-MORB-like geochemical features (Hervé et al., 1999). Although geochemical, geologic and geochronological evidence is minor, this complex may have been derived from an oceanic plateau setting. Paleozoic pillow basalts from the Eastern Andes metamorphic complex occur as blocks together with marbles in turbiditic sediments (Hervé et al., 1999). They are correlated with the Late Devonian Bahia de la Lancha formation in Argentina. The basalts have small phenocrysts of clinopyroxene and plagioclase, enriched REE patterns and high Nb/Y ratios. Their Nb/Y ratios are comparable with those in Polynesian basalts. We consider the basalts are OIB related to a superplume.

The Yakuno Ophiolite in Southwest Japan contains plagiogranite with a zircon U-Pb age of 282–285 Ma (Herzig et al., 1997). Associated amphibolites have Permian K-Ar and Rb-Sr ages that date the time of low-pressure metamorphism prior to emplacement (Ishiwatari, 1985b). Basaltic pillow lavas are intercalated with black shales and felsic volcanics; sheeted dykes are absent (Ishiwatari, 1985a,b). The basalts are mostly aphyric, although olivine and plagioclase phenocrysts (both are pseudmorphed) are present. The chemistry of whole rocks, relict clinopyroxene, and relict chromian spinel all indicates a tholeiitic affinity. Downward increase of the metamorphic grade up to the pyroxene-granulite facies indicates that the oceanic crust was unusually thick. Although Ishiwatari (1985a) suggested the ophiolite was derived from a small oceanic basin like the Black Sea, it is more likely that it was an oceanic plateau in origin (Isozaki, 1997).

Greenstones from the Angayucham Terrane, central Alaska are overlain by thin chert beds (Pallister et al., 1989). The radiolaria from inter-pillowed chert points to a Mississippian deposition age (Barker et al., 1988). The greenstones are E-MORB-like tholeiites (Barker et al., 1988; Pallister et al., 1989). According to the geologic and geochemical data, these rocks are an oceanic plateau in origin. Subsequently, the plateau became occur according to radiolarian ages and finally arrived at the Brooks Range in Alaska in the Middle Jurassic (Pallister et al., 1989).

The Dun Mountain Ophiolite has a length of >1100 km in the South Island, New Zealand. The igneous rocks are divided into three: 1) a lower sequence of olivine-phyric pillow lavas and autobrecciated flows and comagmatic intrusives, 2) an upper sequence of massive and brecciated, predominantly aphyric, augite and Fe-Ti oxide-bearing basaltic sheeted flows, 3) a suite of cross-cutting (non-sheeted) mafic dykes and small irregular plutons, layered ultramafics and gabbroic cumulates, isotropic gabbros, and abundant plagiogranites dykes and plutons (Sivell and McCulloch, 2000). Plagiogranite has a zircon U-Pb age of 275–285 Ma (Kimbrough et al., 1992). Mafic dykes and plagiogranites from the suite have a Sm-Nd bulk isochron age of 278 ± 4 Ma (Sivell and McCulloch, 2000), while the upper sequence has a Sm-Nd bulk isochron age of 308 ± 12 Ma on basalt and related ferrogabbro. The Dun Mountain Ophiolite lacks thick pelagic chert but has voluminous terrigenous sediments, although the upper sequence is conformably overlain by red cherts, Fe-Mn-rich nodular encrustations, red mudstones and altered hyaloclastites, and thick turbidite argillites (Sivell, 2002). Lavas from the lower sequence are typically olivine-phyric

and have LREE-enriched REE patterns, high Nb contents and enriched Nd isotopic compositions. Massive lava flows from the upper sequence have LREE-depleted REE patterns, negative Nb anomalies and slightly depleted Nd isotopic compositions. A suite of dykes and plutons have a LREE-depleted REE pattern, a negative Nb anomaly and a depleted Nd isotopic composition (Malpas et al., 1994; Sano et al., 1997; Sivell and McCulloch, 2000). The lower and upper sequences and the suite of dykes and plutons are similar in geochemistry to OIB, back-arc basin basalt, and island arc tholeiite, respectively. Although Malpas et al. (1994) considered that lavas from the lower sequence formed in a seamount in a mid-ocean, Sivell and McCulloch (2000) concluded that together with the basalts they were akin to back-arc basin basalts and favored generation in a seamount in a back-arc basin. Dykes and plutons represent incipient arc magma intruding preexisting back-arc-basin crust at an initial subduction (Sivell and McCulloch, 2000).

Cambrian ophiolites occur throughout the Tasmanides of eastern Australia. Ophiolites in the Tyennan and Delamerian orogens near the western margin of the Tasmanides have a zircon U-Pb age of 514 Ma on tonalite and 524 Ma on leucogabbro (Black et al., 1997; Maher et al., 1997). Lavas in the Tyennan orogen are pillowed or massive low-Ti basalts and boninites and cumulates are orthopyroxene-rich (Crawford and Berry, 1992). The basalts have a LREE-depleted REE pattern and low Ti, Nb, and Zr contents. Mafic-ultramafic complexes of the Dimboola subzone in the Delamerian orogen have petrological and geochemical characteristics similar to those of the Tyennan orogen (Maher et al., 1997). The Lachlan orogen that occupies the central Tasmanides has two major ophiolitic belts; Heathcote and Mount Wellingston. The Heathcote belt contains a conformable sequence of basalt, chert-shale-volcanoclastic sandstone, and quartz-rich turbidite, within which tuffeceous litherenite has a zircon U-Pb age of 503 Ma (Spaggiari et al., 2003). Volcanic rocks consist of basalts, boninites and andesites; the basalts have flat REE patterns and geochemical characteristics between MORB and arc tholeiite (Crawford and Keays, 1987). The Mount Wellingston belt has a zircon U-Pb age of 502 Ma from hornblende gabbro (Spaggiari et al., 2003). Volcanic rocks are basalts and boninites. The pillow basalts are conformably overlain by and interbedded with chert and silicified black shale, which in turn is conformably overlain by turbidite. Basalts have flat REE patterns and geochemical characteristics between MORB and arc tholeiite and are similar to those in the Heathcote Belts (Crawford and Keays, 1987). The New England orogen that is situated in the eastern Tasmanides has Neoproterozoic and Cambrian ophiolites. The Marlborough block consists of dominant serpentinized harzburgite and minor dunite, pyroxenite, gabbro, and mafic and felsic intrusive rocks (Bruce et al., 2000). Basalts have depleted MORB-like geochemical and isotopic signatures and a whole-rock Sm-Nd isochron age of 562 Ma. Ophiolitic mélange from the Peel-Manning Fault system contains basalts that have geochemical affinities with MORB to island-arc basalt, and lower-Ti and high-Mg island-arc- or fore-arc-basalt signatures (Yang and Seccombe, 1997). Plagiogranite blocks in a serpentinite matrix have zircon U-Pb ages of 530, 509, and 535 Ma (Aitchison et al., 1992; Aitchison and Ireland, 1995). These are suprasubduction zone ophiolites that developed along the

East Gondwana active margin from the Latest Neoproterozoic to the Late Cambrian (Crawford and Berry, 1992; Spaggiari et al., 2003).

The Wrangellia Terrane comprises a flood basalt erupted on an island-arc basement. According to paleomagnetic data, the terrane was positioned somewhere in the eastern Pacific Ocean and detached from the eastern margin of Laurentia at a paleolatitude of 10°N–20°N in the Late Triassic (Butler et al., 1997). The flood basalts were erupted near the Pacific Superplume region. The Permian Angayucham Terrane and Yakuno Ophiolite were regarded as the remnants of an oceanic plateau. Although there is little supporting evidence, the basalts from Chonos metamorphic belt might also have formed in an oceanic plateau. These generation ages are nearly coeval with those of the Wrangellia Terrane (230–290 Ma). Although there are no available paleomagnetic data for these greenstones and ophiolite, by comparing their data with those from the Cretaceous oceanic plateaus in western Pacific, it could be concluded that they were generated in the region of the Pacific Superplume (Fig. 6).

3.3 From 750 to 550 Ma

3.3.1 Continental domain

In the period from 550 to 750 Ma the supercontinent Rodinia brokeup and this led to the formation of the (semi-) supercontinent Gondwana (Hoffman, 1991; Dalziel, 1992). The formation of Gondwana was likely caused by a rapid fan-like closure of the Mozambique Ocean that was present between Eastern and Western Gondwana, and it was dramatically completed by the collisional 550–500 Ma Mozambique orogeny that represents the final event of the Pan-African orogen (Dalziel, 1992; the "Inside-out model" by Hoffman, 1991). However, recent geochronological data require us to revise our ideas about the distribution of the Pan-African orogen and the formation model of Gondwana. One of the important points of the previous model was that Eastern Gondwana was a stable large continent in the period concerned in East Antarctica that constitutes the core of Eastern Gondwana. Pan-African orogens have recently been subdivided into three provinces (Shiraishi et al., 1994; Fitzsimons, 2000). According to their ages, Eastern Gondwana was not present until 530 Ma (Meert, 2003). The qualitative and quantitative geologic and geochronological data from the Pan-African orogens in the African and South American continents revealed that the formation of Western Gondwana was not completed until 520 Ma (e.g., Campos Neto, 2000). This refers to the idea that Gondwana was formed by the collision of several cratons in sequence rather than by a simple collision between two large continents. This mode of continental amalgamation is comparable with that of Laurasia in the Phanerozoic.

Did Gondwana include Laurentia or was there are a Latest Proterozoic supercontinent termed Pannotia (Dalziel, 1997)? This question is related to the time of the opening of the Iapetus Ocean. The remnants of the opening stages of the Iapetus Ocean in the Laurentia, Baltica, and Amazonia cratons that surround the ocean are dated as ca. 600 Ma (Hoffman, 1989; Svenningsen, 2001). This age indicates that the

birth of the Iapetus Ocean was followed by the completion of Gondwana formation. The Baltica and Siberia cratons also departed from Gondwana. Therefore, we regard Gondwana not as a supercontinent but as a semi-supercontinent.

The breakup of Rodinia and the opening of the Pacific Ocean occurred at ca. 750 Ma (Fig. 8). The initial stage is represented by dyke swarms and associated volcanism; the Gairdner dyke swarm in central Australia at 827 ± 6 Ma (Wingate et al., 1998), the Amata dyke swarm in south-central Australia at 824 ± 4 Ma (Sun and Sheraton, 1996), the Mundine Well dyke swarm in northwestern Australia at 755 ± 3 Ma (Wingate and Giddings, 2000), the Sanfang mafic intrusive in South China at 828 ± 7 Ma (Li et al., 1999), the Richtersveld Igneous Complex in eastern South Africa at 833 ± 2 Ma (Frimmel et al., 2001), the Gunbarrel mafic magmatic event in eastern Laurentia at 780 ± 1 Ma (Harlan et al., 2003), and the Franklin dyke swarm at $723 + 4/-2$ Ma in northern Laurentia (Heaman et al., 1992). According to the reconstruction of continental distributions by the PALEOMAP project (Scotese, 2004), these events occurred in today's Pacific Superplume region (Fig. 8). In the period from 750 to 650 Ma, Rodinia was almost surrounded by Pacific-type orogenic belts. The Cadomian, Avalonian, Timanian, and Baikalian orogens developed along the margin of Western Africa, Amazonia, Baltica, and Siberia, respectively (e.g., Egal et al., 1996; Doig et al., 1993; Kuzmichev et al., 2001; Scarrow et al., 2001;

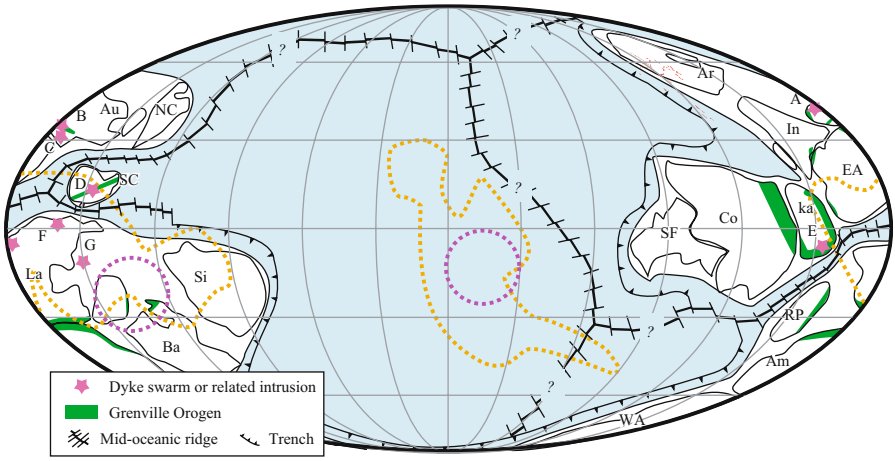

Figure 8. Reconstructed paleogeographic maps at ca. 750 Ma. The distribution of continents is mainly refered to Scotese (2004) but the South China was positioned on the basis of the reconstruction of Li and Powell (2001). According to the age of the Richtersveld Igneous Complex (Frimmel et al., 2001), Kalahari was separated from the Rodinia. The distribution of Grenville orogen is modified after Hoffman (1991). A = Mundine Well dyke swarm; B = Amata dyke swarm; C = Gairdner dyke swarm; D = Sanfang mafic intrusive; E = Richtersveld Igneous Complex; F = Gunbarrel mafic magmatic event; G = Franklin dyke swarm. Am = Amazonia; Ar = Arabia; Au = Australia; Ba = Baltica; Co = Congo; EA = East Antarctica; In = India; Ka = Kalahari; La = Laurentia; NC = North China; RP = Rio de la Plata; SC = South China; SF= Sao Francisco; Si = Siberia; WA = West Africa.

Khain et al., 2003). The early stage of the Pan-African orogen developed around the Sao Francisco-Congo craton (e.g., Campos Netro, 2000; Pimentel et al., 1991), and the extensive juvenile crust of the Nubian-Arabian shield was formed (Stein and Goldstein, 1996).

3.3.2 Oceanic domain

The Trinity Ophiolite that formed from the Cambrian to the Silurian is situated in eastern Klamath, northern California in western North America. In the Lovers Leap-South China Mountain area plagiogranite has a zircon U-Pb age of 565–570 Ma (Wallin et al., 1988). Lavas consist of basalt, andesite, and dacite, all of which have plagioclase and clinopyroxene phenocrysts, and orthopyroxene is present in a few andesites (Brouxel et al., 1989). Hornblende phenocrysts occur in dacitic andesites and dacites. The lavas are divided into two types based on their geochemical features. One is low-K tholeiite with a depleted REE pattern and the other is calc-alkaline with an enriched REE pattern. The calc-alkaline rocks are conformably overlain by Ordovician limestones. Both low-K tholeiite and calc-alkaline rocks have negative Nb anomalies (Brouxel et al., 1989). Well-developed sheeted dykes are absent (Lindsley-Griffin, 1994). Pegmatitic trondhjemite dykes that intrude gabbro have a zircon U-Pb age of 412 Ma (Wallin et al., 1988). In the Dunsmuir area a complete ophiolitic succession is present. Nd isotopic ratios measured on basalt, plagiogranite, isotropic gabbro, cumulate layered gabbro, and gabbroic pegmatite plot on 452 ± 40 Ma isochron (Brouxel and Lapierre, 1988). The peridotite layer has unusually large amounts of lherzolite (Brouxel and Lapierre, 1988) and some lherzolites and harzburgites have high plagioclase contents (Lindsley-Griffin, 1994). A sheeted dyke complex (Brouxel and Lapierre, 1988) occurs with predominant basaltic pillow lavas that are unconformably overlain by Carboniferous sandstone and shale. The basalts are divided into three types based on their petrography; plagioclase-porphyritic basalts with rare clinopyroxenes, intersertal basalts with clinopyroxene microphenocrysts and plagioclase laths, and subaphyric basalts with clinopyroxene microlites (Brouxel et al., 1989). The lavas of these basalts have depleted REE patterns and negative Nb anomalies (Brouxel et al., 1989). In the Redding area massive and pillowed flows are overlain by rhyolites, and are unconformably overlain by Early Devonian shales and limestones (Brouxel et al., 1988). The flows consist of basalts and andesites that are highly porphyritic with plagioclase, olivine and clinopyroxene phenocrysts (Brouxel et al., 1989). The basalts and andesites show a significant geochemical heterogeneity that is indicated by variable REE patterns that range from moderately depleted to strongly enriched (Brouxel et al., 1988), and they have negative Nb anomalies (Brouxel et al., 1989). High-Mg andesites have $SiO_2 \geq 55\%$, $MgO \geq 7\%$, and flat REE patterns (Brouxel et al., 1988). The above geochemical characteristics suggest that the Trinity Ophiolite was generated in an island arc-marginal basin (Brouxel and Lapierre, 1988; Brouxel et al., 1988, 1989).

A highly deformed mafic-ultramafic complex is situated in the southwestern margin of the Precordillera of Argentina. It is divided into three tectonic units; a gabbro, microgabbro, and diabase unit (massive diabase), an ultramafic and layered gabbro

complex that intrudes quartzofelspathic gneiss (ultramafic-layered complex), and metasedimentary rocks with interlayered mafic flows and sills. Based on geochemistry, metamorphism and geochronology, these units are unrelated to each other and cannot represent a fragmented single ophiolite (Davis et al., 2000). The massive diabase unit consists of gabbro to diabase bodies with small plagiogranite and sheeted half dykes with pillow lavas. Sedimentary rocks are not associated with pillow lavas (Gregori and Bjerg, 1997; Davis et al., 2000). This unit has a zircon U-Pb age of 576 ± 17 Ma from microgabbro (Davis et al., 2000). The lavas and dykes have REE patterns that range from flat through slightly LREE-enriched to enriched patterns and no negative Nb anomaly (Gregori and Bjerg, 1997). These were interpreted to form at a mid-oceanic ridge associated with a plume (Gregori and Bjerg, 1997) or at a well-developed rift (Davis et al., 2000). But the geochemical signature of the massive diabase unit is also similar to that of an oceanic plateau. Present-day western margin of South America was faced to the Pacific Ocean in this period. Therefore, it is possible that the massive diabase unit in the southwestern margin of the Precordillera was generated at the Pacific Superplume region.

A Cambrian accretionary complex in the Gorny Altai Mountains in southern Siberia continues in the Altai Range through Mongolia to China. The accretionary complex is composed of limestone, greenstone, sandstone and mudstone (Buslov et al., 1993; Buslov and Watanabe, 1996). The Baratal limestone in the Kurai area has a $^{207}Pb/^{206}Pb$ bulk isochron age of 598 ± 25 Ma, and has a primary stratigraphy made-up of massive limestone and limestone breccia that conformably overlies basaltic greenstones (Uchio et al., 2004). Some limestones contain stromatolites and ooids that suggest a shallow-marine environment. Some limestone breccias contain clasts of micritic limestone, greenstone and chert, and are poorly sorted and thinly bedded, suggesting that they formed as gravity-flow (debris flow) deposits. In addition, laminated limestone and bedded micritic limestone are associated with the limestone breccias. The absence of coarse-grained terrigenous clastics indicates that all the limestones were deposited in a mid-oceanic environment distant from a continental source. The Baratal limestone is interpreted as a paleoseamount limestone that accumulated on MORB- and OIB-type basaltic greenstones (Buslov et al., 1993). Most of the greenstones have phenocrysts of clinopyroxene and plagioclase. The above evidence suggests that the limestones accumulated on the slope or at the base of a slope of a paleo-seamount or plateau (Dobretsov et al., 2004; Uchio et al., 2004).

A Precordilleran ophiolite in Argentina might be a fragment of an ancient oceanic plateau. The greenstones in the Gorny Altai area of southern Russia have an oceanic plateau affinity. Although the Central Asian Orogenic Belt that includes the Gorny-Altai region faced the Tethyan Ocean, the accretionary prism developed along an oceanic island arc and could have faced the Pacific Ocean (Fig. 5). The oceanic plateau might have formed in the Pacific Superplume region. Their ages are nearly coincident (ca. 580–600 Ma). While there are no available paleomagnetic data for these ophiolite greenstone belt, by comparing them with the Cretaceous pulse, we can conclude they were generated in the Pacific Superplume region.

4 DISCUSSION

4.1 The reconstruction of rodinia and initial opening of the pacific ocean

Our reconstructions and discussion are tentatively based on the PALEOMAP project maps (Scotese, 2004) but the continental arrangement of Rodinia has not yet reached a consensus; thus it is necessary to consider other reconstructions. Although many papers concerned with Rodinia have been published since the proposal by Hoffman (1991) and Dalziel (1991), due to space limitations we keep this review to a minimum so as to extract the essence of the consensus and arguments.

Because of the presence of Grenvillian-age orogens within the cratons, the connections between Baltica, Amazonia, and Rio de La Plata with Laurentia are broadly accepted. It is also widely accepted that Siberia was connected to northern Laurentia, but there has been little agreement on the geometry of the fit due to a lack of decisive paleomagnetic or geochronological data. Kravchinsky et al. (2001) pointed out that the Siberian platform, composed of the Anabar, Angara and Aldan blocks, might not have been fully amalgamated by Late Proterozoic to Early Cambrian time.

To explain the paleoposition of East Gondwana (Antarctica, Australia and India) against Laurentia in Rodinia, three models have been proposed: (1) East Antarctica (Transantarctic Mountains) was connected with the southwestern coast of Laurentia. This is based on correlations of Grenville-age orogens and Precambrian-Paleozoic sedimentary rocks (the SWEAT model: Moores, 1991; Dalziel, 1991; Hoffman, 1991; Young, 1992), and the idea that South China was placed among Australia and Laurentia-Siberia (Li and Powell, 2001). Powell et al. (1993) argued against the validity of the SWEAT model with APWPs for both East Gondwana (mainly from Australia and partly from India) and Laurentia, and Li (2000) and Wingate and Giddings (2000) supported this idea from the viewpoint of the APWPs for western Australia and Laurentia. (2) A suture along the eastern coast of India, the eastern coast of East Antarctica and the central-southwestern part of Australia continued into the Grenville orogen through the southern end of Laurentia, and Australia was connected with western Laurentia (the AUSWUS model: Karlstrom et al., 1999, 2001; Burrett and Berry, 2000). In this model South China was separated by small oceans from Australia and Siberia (Condie, 2003). Karlstrom et al. (2001) suggested that the AUSWUS model provided a better fit of paleomagnetic data (APWP) than the SWEAT model. (3) A model with the Australia-Mexico connection (AUSMEX), inferred from ca. 1070-Ma paleopoles from Australia with a high-stability paleomagnetic remanence (Wingate et al., 2002). On the other hand, from zircon U-Pb data and geologic correlations Fitzsimons (2000) and Boger et al. (2001) suggested that East Antarctica should be separated into two or three provinces with a Grenville-age by Pan-African orogens. In addition, Powell and Pisarevsky (2002) pointed out that India lay near the pole, whereas Australia was at a low latitude at 810 Ma, and final amalgamation of East Gondwana was not complete until the Early Cambrian. Considering these suggestions, Pisarevsky et al. (2003) proposed a new reconstruction of Rodinia at 990 Ma, in which the AUSMEX model was adopted, and India was

excluded from Rodinia. However, the AUSWUS and AUSMEX models suggest that up to 10,000-km of Late Proterozoic rift margins in northern Australia and western Laurentia need to be matched with other continental blocks within any proposed Rodinia. As for the paleoposition of India, Radhakrishna and Joseph (1996) placed India near the equator at ca. 1000 Ma, suggesting a Late Proterozoic East Gondwana as before. On the other hand, Pisarevsky et al. (2003) disproved of this reconstruction due to the inconsistency between paleopoles of India and Australia at ca. 1070 Ma, although the APWPs of India from 1100 to 800 Ma were not available.

The recent accumulation of more precise paleomagnetic and geochronological data has provided several constraints and new models for Late Proterozoic reconstructions; however the controversy about East Gondwana and Rodinia has become more complicated. Each model has both advantages and disadvantages. At present, although it is still difficult to evaluate the validity of the recent reconstruction models, it can be emphasized that Laurentia was positioned in the center of Rodinia in all versions.

Figure 9 shows various models for the opening of the Pacific Ocean. The timing and distribution of rift systems depends not only on the age and dispersal of dyke swarm, but also on the arrangement of continents. Maruyama (1994) first proposed that the Pacific Superplume generated the Paleo-Pacific Ocean at 600–700 Ma on the basis that the paleolatitude of the RRR triple junction that was at ca. 20°S, corresponding to the active region of the present Pacific Superplume, and to the paleoposition of the Pacific superplume at the RRR triple junctions between western Laurentia, Australia and South China, and between the northern Laurentia, South China and Siberia (Fig. 9a). Li et al. (1999) and Li and Powell (2001) showed a similar triple

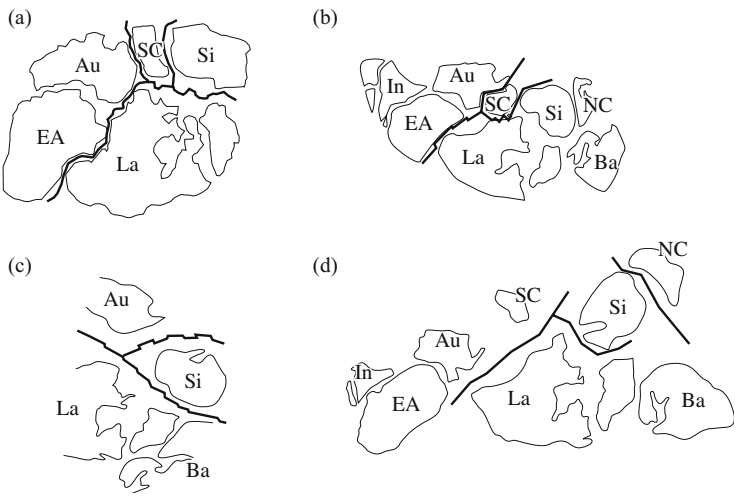

Figure 9. Paleogeographic reconstruction models of the supercontinent Rodinia. (a) After Maruyama (1994); (b) Li and Powell (2001); (c) Dobretsov et al. (2002); (d) after Condie (2003). Bold lines show rifts. Abbreviations of name of cratons are explained as in Figure 8.

junction at ca. 760 Ma, and suggested a mantle plume beneath South China (Fig. 9b). Dobretsov et al. (2003) provided stepwise rifting from 950–800 Ma between Australia and Siberia through 750–700 Ma rifting between Siberia and Laurentia and finally to an RRR triple junction between the three cratons (Fig. 9c). Condie (2003) produced a different model based on the AUSWUS model from other reconstructions based on the SWEAT model (Fig. 9d). But this also has a RRR triple junction at the opening of the Pacific Ocean. The RRR triple junctions are recognized in all reconstructions although the defining cratons differ from one to another. Using the analogy of the African rift system, an RRR triple junction is the expression of continental rift caused by plume upwelling (see summary by White and McKenzie, 1989). The paleolatitudes of RRR triple junctions vary from 30°N to 20°S. Because the uncertainty of paleolatitude estimation is up to 30° in this period (Scotese, 2004), the positions are roughly in agreement in the equatorial area. Although, in principle, paleolongtitude is not defined only by paleomagnetism, the reconstructed Rodinia of the PALEOMAP project at 750 Ma is in the Pacific Superplume region. According to the paleopole data of Weil et al. (1998, 2004), Laurentia occupying the central part of Rodinia moved to the south by ∼20° at ca. 800 Ma from the position at 750 Ma. This means that the initial rifting of Rodinia occurred in the Pacific Superplume region.

4.2 Comparison of the Pacific superplume with the African superplume

Associated with extensive flood basalt volcanism, the dispersal of Pangea occurred at 80–200 Ma on the African seismic lower velocity zone in the lower mantle that exists today. The relation of continental breakup with plume initiation has been mentioned by previous workers on the basis of analogue experiments of mantle convection and hot spot tracks (e.g., Morgan, 1981; Richards et al., 1989). Richards et al. (1989) suggested that a number of new mantle plumes were formed in this period. These are essentially independent and have no relation with one another. Each plume head generated flood basalts, subsequently plume tail activities left hot spot tracks. The model needs a number of narrow conduits from the core-mantle boundary, but it is not consistent with recent mantle tomographic images with higer resolution (e.g., Zhao, 2004). The seismic observations make us infer that the continental fragmentation was caused by cognate plume upwellings rooted in the upwelling lower mantle. This view is similar to the hotspot image provided by Courtillot et al. (2003). In analogy with Pangea, the fragmentation of Rodinia at 720–830 Ma arose in the Pacific. The breakup of a supercontinent is caused by superplume activity.

Dalziel et al. (2000) insisted that Pangea was fragmented by a preexisting plume. But the present position of the African superplume overlaps in paleo-latitude with the region where the 300–500 Ma orogens have been present. Pangea was formed by extensive collision-amalgamation processes around Laurentia after Pacific-type orogens were developed in the region. The eastern and western Laurentian margins underwent subduction both from the Pacific and Iapetus Oceans with the resultant formation of V-shaped Pacific-type orogens. This means that mantle downwelling rather than plume upwelling was provided by cold subducted slabs and is not consistent

with the model of Dalziel et al. (2000). During the formation of Rodinia, a large amount of oceanic lithosphere would have been subducted beneath proto-Rodinia along V-shaped paleo-trenches of the proto-Grenville orogens that were positioned on the Pacific Superplume region. These correlations suggest that the birth of a superplume was related to the formation processes of supercontinents, which include the Pacific-type orogeny along V-shaped subduction zones and the resultant collage of island arcs. The concentration of oceanic plate subduction during the formation process of a supercontinent could have greatly accelerated to create physical instabilities and chemical heterogeneities in the deep mantle, either or both of which must be deeply concerned with the birth of a superplume. There is no viable model with a consensus, however the transportation of oceanic lithosphere into the deep mantle most likely played an essential role in the birth of a superplume.

4.3 Superplume pulse

Cretaceous oceanic plateaus are widespread in the present western Pacific (e.g., Ontong Java Plateau, Manihiki Plateau, Hess Rise), and most formed at 75–150 Ma. In addition, the accreted fragments of oceanic plateaus in circum-Pacific orogens are coeval (Table 3). They can be traced back and found to be concentrated in the present active region of the Pacific Superplume (Fig. 4; Suzuki et al., 2000). This suggests that a large amount of igneous rocks (10.7×10^6 km^2 and 19.1×10^7 km^3) was formed in the Cretaceous by superplume activity. It is larger than the Australian continent (7.6×10^6 km^2).

In the mid-Cretaceous, most global changes of the surface environment can be comprehensively explained by the activities of the Pacific Superplume (Larson, 1991a,b); the Cretaceous global transgression was caused by a rise of sea level due to increasing spreading rates of mid-oceanic ridges, and the resultant young oceanic lithosphere was related to the Pacific Superplume activity. Cretaceous global warming also resulted from increasing rates of degassing by an extensive volcanism related to the superplume activity. In our estimation, the total amount of CO_2 derived from magmatism at that time is 2.8×10^{21} g, where the CO_2 contents in plateau basalt was assumed to be 0.5 wt% (Johnson et al., 1994). Kerrick and Caldeira (1993) concluded that over a 1-million-year period, excess CO_2 degassing of $>0.5 \times 10^{18}$ mol would be required to produce notable grobal warming. The degassing rate of CO_2 deduced from our composite volcano (0.82 10^{18} mol/m.y.) suggests a significant impact for Cretaceous global warming. In addition, excess CO_2 could be expelled by increasing spreading rate of mid-oceanic ridge (Larson, 1991a) and the coinciding formation of vast granite batholith in circum-Pacific belts (e.g., Wu et al., 2005).

From our review of circum-Pacific ophiolites and greenstone belts we infer that events such as the Cretaceous pulse occurred at 230–280 and 580–600 Ma, after the birth of the Pacific Ocean. Recent knowledge from ultrahigh-pressure experiments enables us to speculate with the following model for the active volcanism in the Pacific (Fig. 10). Phase relations in a mantle peridotite system (Zhang and Herzberg, 1994;

Table 3. Summary of the Cretaceous LIPs and their accreted fragments in the Pacific Ocean

Name	Age (Ma)	Area (10^5 km^2)	Volume (10^6 km^3)	Reference (age)	Reference (volume)
Ontong java plateau	90, 122	16	53	Mahoney et al., 1993	Richardson et al., 2000
Nauru basin	110.8	18	0.9	Castillo et al., 1994	Eldholm and coffin, 2000
East mariana basin	114.6	5	0.25	Pringle, 1992	Coffin, Eldholm, 1994
Pigafetta basin	126.1				
Manihiki plateau	91–114	8	8.8	Lanphere and Dalymple, 1976	Eldholm and coffin, 2000
Magellan rise	~135	5	1.8	Winterer et al., 1973	Eldholm and coffin, 2000
Hess rise	99–112	8	9.1	Kroenke and Nemoto, 1982	Eldholm and coffin, 2000
Shatsky rise	126–150	2	2.5	Nakanishi et al., 1989	Eldholm and coffin, 2000
Line islands	68–73, 81–86	-	5	Davis et al., 2002	Larson, 1991a
Mid-pacific mountain	117–132	-	22	Smoot, 1999	Larson, 1991a
Caribbean plateau	75, 90	11	4.5	Sinton et al., 1998	Eldholm and coffin, 2000
Caribbean plateau (accreted part)	75, 90	13*	26^+	Sinton et al., 1998	-
Gorgona plateau	75, 90	13*	26^+	Sinton et al., 1998	-
East slawesi ophiolite	138	2.5*	5^+	Parkinson, 1998	-
Iratsu massif	142–153	5*	10^+	e.g., Ozawa et al., 1997	-
Sorachi-Yezo belt	150	8*	16^+	Sakakibara et al., 1997	-
Total		107	191		

* Estimated by assuming oceanic plateau is circle which have the diameter equall to overall length of ophiolite or greenstone belts.
$^+$ Estimated by assuming crustal thickness is 20 km.

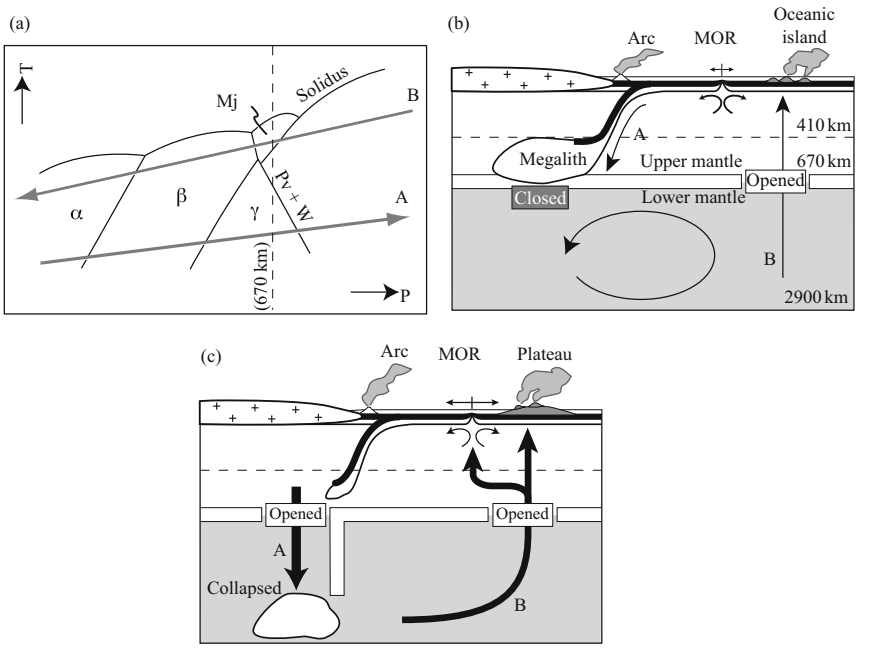

Figure 10. Cartoons showing Cretaceous plate tectonics and a superplume in the Pacific. (a) Schematic phase diagram of mantle peridotite in P-T space (modified after Zhang and Herzberg, 1994; Hirose, 2002) with subduction zone geotherm A and plume geotherm B. The plume geotherm passes the majorite/perovskite transition curve with a positive slope, suggesting that mantle upwelling can be accelerated at ca. 670-km depth to transport fertile lower mantle materials to the upper mantle (See also Kumazawa and Maruyama, 1994). (b) Schematic cross-section showing mantle convection and its related volcanism at a normal stage. (c) Schematic cross-section showing whole-mantle convection and the resultant activated volcanism at a pulse stage. A collapsed megalith accelerates a single-layered convection at a whole-mantle scale.

Hirose, 2002) suggest that a plume geotherm passes the majorite/perovskite transition curve with a positive slope indicating that mantle upwelling can be accelerated at ca. 670-km depth to transport fertile lower mantle materials to the upper mantle (Fig. 10a). Within-plate volcanism related to mantle upwelling indicates that a window between the upper and lower mantle was opened in the Pacific. However, mantle convection at normal times is double-layered and mantle materials are independently circulated within the upper and lower mantles (Fig. 10b). The downwelling beneath a subduction zone due to plate subduction in the circum-Pacific was stopped at 670-km depth by a negative Clausius-Clapeyron slope along the cold geotherm along a subducting plate, resulting in the formation of a megalith (e.g., Irifune and Ringwood, 1993). Subsequently, the megalith collapsed down to the lower mantle, and accelerated a single-layered convection on a whole-mantle scale (Fig. 10c); the resultant mantle upwelling activated episodically. The hot geotherm passes the

majorite/perovskite transition curve with a positive slope, suggesting that mantle upwelling can be accelerated at ca. 670-km depth. As a result, material- and heat-supply from the lower to the upper mantle through the window activated volcanism both at the mid-oceanic ridge and within the plate. The episodic events were not derived from the initiation of a number of plumes (e.g., Richards et al., 1991) but from the pulse of a superplume at a preexisting thermal window.

5 CONCLUSIONS

In summary, the most probable history of the Pacific Ocean and Superplume is as follows. The Pacific Ocean was born by the breakup of the supercontinent Rodinia at ca. 750 Ma. It was derived from the birth of Pacific Superplume. At ca. 550 Ma subduction zones began to develop along the Pacific margin in both eastern Gondwana and western Laurentia. The Pacific Ocean passed through the superocean stage (only one continent and one ocean existed on the earth) from ca. 230 to ca. 180 Ma. These are coincident with the formation of the supercontinent Pangea and the birth of the Atlantic Ocean, respectively. Including circum-Pacific ophiolites and greenstone belts, there were three superplume pulse events (80–150 Ma, 230–300 Ma and 580–600 Ma).

Comparing the Pacific Superplume with the African Superplume, the common relation of a superplume with the surface of the solid earth is as follows. The birth of a superplume arises from the breakup of a supercontinent accompanied by the eruption of continental flood basalts. Prior to this, the formation of a supercontinent occurs in a pre-superplume region. A V-shaped double subduction zone enables the transportation of a vast amount of cold slab into the mantle. This greatly accelerates and creates physical instabilities and chemical heterogeneities in the deep mantle, either or both of which must be deeply concerned with the birth of a superplume. Once a superplume is formed, it behaves as a thermal window. It gives rise to oceanic islands and seamounts in a calm period and oceanic plateaus and oceanic flood basalt in a pulse period.

ACKNOWLEDGEMENTS

Soichi Omori and Kouki Kitajima gave helpful advice that improved our manuscript and Shuji Rino and Shio Watanabe helped draw Figure 1; we express our sincere gratitude to them. This study was supported by a project on Whole Earth Dynamics from the Science and Technology Agency of Japan.

REFERENCES

Acton, G.D., B. Galbun, and J.W. King (2000) Paleolatitude of the Caribbean plate since the Late Cretaceous. *Proc. ODP Sci. Results*, 165, 149–173.

Aitchison, J.C., and T.R. Ireland (1995) Age profile of ophiolitic rocks across the Late Paleozoic New England Orogen, New South Wales: Implications for tectonic models. *Aust. J. Earth Sci.*, 42, 11–23.

Aitchison, J.C., T.R. Ireland, M.C. Blake Jr., and P.G. Flood (1992) 530 Ma age for ophiolite from the New England Orogen: Oldest rocks known from eastern Australia. *Geology*, 20, 125–128.

Baksi, A.K. (1989) Reevaluation of the timing and duration of the extrusion of the Imnaha, Picture Gorge and Grande Ronde Basalts, Columbia River Basalt Group. In Reidel, S.P., and P.R. Hooper (eds.) Volcanism and Tectonism in the Columbia River Flood Basalt Province, Special Paper, vol. 239, Geological Society of America, Boulder, Colorado, US, pp. 105–112.

Baksi, A.K. (1994) Geochronological studies on whole-rock basalts. Deccan Traps, India; evaluation of the timing of volcanism relative to the K-T boundary. *Earth Planet. Sci. Lett.*, 121, 43–56.

Banno, S., and C. Sakai (1989) Geology and metamorphic evolution of the Sanbagawa metamorphic belt, Japan. In Daly, J.S., R.A. Cliff, and B.W.D. Yardley (eds.) Evolution of Metamorphic Belts, Special Publication, vol. 43, Geological Society, London, pp. 519–532.

Barker, F., D.L. Jones, J.R. Budahn, and P.J. Coney (1988) Ocean Plateau-Seamount Origin of Basaltic Rocks, Angayucham Terrane, central Alaska. *J. Geo.*, 96, 368–374.

Black, L.P., D.B. Seymour, K.D. Corbett, S.E. Cox, J.L. Everard, G.R. Green, M.P. McClenaghan, J. Pemberton, D.B. Seymour, J.E. Streit, J. Taheri, and N.J. Turner (1997) *Dating Tasmania's Oldest Geological Events. AGSO Record, 1997/5*.

Boger, S.D., C.J.L. Wilson, and C.M. Fanning (2001) Early Paleozoic tectonism within the East Antarctic craton: The final suture between east and west Gondwana? *Geology*, 29, 463–466.

Brook, F.J., M.J. Isaac, and B.W. Hayward (1988) Geology of autochthonous and allochthonous strata in the Omahua area, northern New Zealand. *New Zealand Geological Survey Record*, 32, 40.

Brouxel, M., and H. Lapierre (1988) Geochemical study of an early Paleozoic island-arc-back-arc basin system. Part 1: The Trinity Ophiolite (northern California). *Geol. Soc. Am. Bull.*, 100, 1111–1119.

Brouxel, M., H. Lapierre, A. Michard, and F. Albalede (1988) Geochemical study of an early Paleozoic island-arc-back-arc basin system. Part 2: Eastern Klamath, early to middle Paleozoic island-arc volcanic rocks (northern California). *Geol. Soc. Am. Bull.*, 100, 1120–1130.

Brouxel, M., C. Lecuyer, and H. Lapierre (1989) Diversity of magma types in a lower Paleozoic island arc-marginal basin system (Eastern Klamath Mountains, California, USA). *Chemical Geology*, 77, 251–264.

Bruce, M.C., Y. Niu, T.A. Harbort, and R.J. Holcombe (2000) Petrological, Geochemical and Geochronological evidence for a Neoproterozoic ocean basin recorded in the Marlborough terrane of the northern New England Fold Belt. *Aust. J. Earth Sci.*, 47, 1053–1064.

Burrett, C., and R. Berry (2000) Proterozoic Australia-western Unites States (AUSWUS) fit between Laurentia and Australia. *Geology*, 28, 103–106.

Buslov, M.M., N.A. Berzin, N.L. Dobretsov, and V.A. Simonov (1993) Geology and Tectonics of Gorny Altai: Guidebook for post-symposium excursion. *The 4th international symposium of the IGCP project 283 Geodynamic evolution of the Paleoasian ocean*, Russian Academy of Sciences, Siberian branch, United Institute of Geology, Geophysics and Mineralogy, Novosibirsk, p. 122.

Buslov, M.M., and T. Watanabe (1996) Intrasubduction collision and its role in the evolution of an accretionary wedge: The Kurai zone of Gorny Altai, Central Asia. *Russian Geol. Geophys.*, 36, 83–94.

Butler, R.F., G.E. Gehrels, and D.R. Bazard (1997) Paleomagnetism of Paleozoic strata of the Alexander terrane, southeastern Alaska. *Geol. Soc. Am. Bull.*, 109, 1372–1388.

Campos Neto, M.C. (2000) Orogenic system from Southwestern Gondwana: An approach to Brasiliano-Pan-African cycle and orogenic collage in southeastern Brazil. In Cordani, U.G., E.J. Milani, A. Thomaz Filho, and D.A. Campos (eds.) Tectonic Evolution of South America, Proceedings of the Thirty-first International Geological Congress, Rio de Janeiro, Brazil, pp. 335–365.

Castillo, P.R., M.S. Pringle, and R.W. Carlson (1994) East Mariana Basin tholeiites: Cretaceous intraplate basalts or rift basalts related to the Ontong Java Plume? *Earth Planet. Sci. Lett.*, 123, 139–154.

Cluzel, D., J.C. Aitchison, and C. Picard (2001) Tectonic accretion and underplating of mafic terranes in the Late Eocene intraoceanic fore-arc of New Caledonia (Southwest Pacific): Geodynamic implications. *Tectonophysics*, 340, 23–59.

Coffin, M.F., and O. Eldholm (1994) Large igneous provinces: Crustal structure, dimensions, and external consequences. *Rev. Geophys.*, 32, 1–36.

Coffin, M.F., and P.D. Rabinowitz (1988) *Evolution of the conjugate East African-Madagascan margins and the western Somali Basin,* Special Paper, vol. 226, p. 78, Geological Society of America, Boulder, Colorado.

Condie, K.C. (2003) Supercontinents, superplumes and continental growth: The Neoproterozoic record. In Yoshida, M., B.F. Windley, and S. Dasgupta (eds.) Proterozoic East Gondwana: Super Continent Assembly and Break-up, Special Publication, vol. 206, Geological Society, London, pp. 1–21.

Courtillot, V., A. Davaille, J. Besse, and J. Stock (2003) Three distinct types of hotspots in the Earth's mantle. *Earth Planet. Sci. Lett.*, 205, 295–308.

Courtillot, V., C. Jaupart, I. Manighetti, P. Tapponnier, and J. Besse (2003) On causal links between flood basalts and continental breakup. *Earth Planet. Sci. Lett.*, 166, 177–195.

Crawford, A.J., and R.F. Berry (1992) Tectonic implications of Late Proterozoic-Early Paleozoic igneous rock associations in western Tasmania. *Tectonophysics*, 214, 37–56.

Crawford, A.J., and R.R. Keays (1987) Petrogenesis of Victorian Cambrian tholeiites and implications for the origin of associated boninites. *J. Petrol.*, 28, 1075–1109.

Dalziel, I.W.D. (1991) Pacific margins of Laurentia and East Antarctica-Australia as a conjugate rift pair: Evidence and implications for an Eocambrian supercontinent. *Geology*, 19, 598–601.

Dalziel, I.W.D. (1992) Antarctica; A tale of two supercontinents? *Annu. Rev. Earth Planet. Sci.*, 20, 501–526.

Dalziel, I.W.D. (1997) Neoproterozoic-Paleozoic geography and tectonics: Review, hypothesis, environmental speculation. *Geol. Soc. Am. Bull.*, 109, 16–42.

Dalziel, I.W.D., L.A. Lawver, and J.B. Murphy (2000) Plumes, orogenesis, and supercontinental fragmentation. *Earth Planet. Sci. Lett.*, 178, 1–11.

Davis, A.S., L.B. Gray, D.A. Clague, and J.R. Hein (2002) The Line Islands revisited: New $^{40}Ar/^{39}Ar$ geochronologic evidence for episodes of volcanism due to lithospheric extension. *Geochem. Geophys. Geosyst.*, 3, doi:10.1029/2001GC000190.

Davis, A., and G. Plafker (1984) Comparative geochemistry and petrology of Triassic basaltic rocks from the Taku terrane on the Chilkat Peninsula and Wrangellia. *Can. J. Earth Sci.*, 22, 183–194.

Davis, J.S., S.M. Roeske, W.C. McClelland, and S.M. Kay (2000) Mafic and ultramafic crustal fragments of the southwestern Precordillera terrane and their bearing on tectonic models of the early Paleozoic in western Argentina. *Geology*, 28, 171–174.

Dobretsov, N.L., M.M. Buslov, and Y. Uchio (2004) Fragments of oceanic islands in accretion–collision areas of Gorny Altai and Salair, southern Siberia, Russia: Early stages of continental crustal growth of the Siberian continent in Vendian–Early Cambrian time. *J. Southeast Asian Earth Sci.*, 23, 673–690.

Dobretsov, N.L., M.M. Buslov, and V.A. Vernikovsky (2003) Neoproterozoic to Early Ordovician evolution of the Paleo-Asian Ocean: Implication to the breakup of Rodinia. *Gondwana Research*, 6, 143–159.

Doig, R., J.B. Murphy, and R.D. Nance (1993) Tectonic significance of the Late Proterozoic Economy River Gneiss, Cobequid Highlands, Avalon composite terrane, Nova Scotia. *Can. J. Earth Sci.*, 30, 474–479.

Duncan, R.A. (2002) A Time frame for construction of the Kergueln Plateau and Broken Ridge. *J. Petrol.*, 43, 1109–1119.

Dziewonski, A.M. (1984) Mapping the lower mantle: Determination of lateral heterogeneity in P velocity up to degree and order 6. *J. Geophys. Res.*, 89, 5929–5952.

Dziewonski, A.M., and J.H.Woodhouse (1987) Global images of the Earth's interior. *Science*, 236, 37–48.

Egal, E., C. Guerrot, D. Le Goff, D. Thieblemont, and J. Chantraine (1996) The Cadomian orogeny revisited in northern France. In Nance, R.D., and M.D. Thompson (eds.) Avalonian and Related Peri-Gondwanan Terranes of the Circum-North Atlantic, Special Paper, vol. 304, Geological Society of America, Boulder, Colorado, pp. 281–318.

Eissen, J.-P., A.J. Crawford, J. Cotten, S. Meffre, H. Bellon, and M. Delaune (1998) Geochemistry and tectonic significance of basalts in the Poya Terrane, New Caledonia. *Tectonophysics*, 284, 203–219.

Eldholm, O., and M.F. Coffin (2000) Large igneous provinces and plate tectonics. In Richards, M.A., R.G. Gordon, and R.D. Van der Hilst (eds.) The History and Dynamics of Global Plate Motions, Geophysical Monograph Series, vol. 121, American Geophysical Union, Washington, D.C., pp. 309–326.

Eldholm, O., and K. Grue (1994) North Atlantic volcanic margins: Dimensions and production rates. *J. Geophys. Res.*, 99, 2955–2968.

Engebretson, D.C., A. Cox, and R.G. Gordon (1985) In Boulder, C.O. (ed.) Relative Motions between Oceanic and Continental Plates in the Pacific Basins, Geological Society of America, Special Paper, 206, p. 59.

Fitzsimons, I.C.W. (2000) Grenville-age basement provinces in East Antarctica: Evidence for three separate collisional orogens. *Geology*, 28, 879–882.

Ford, D., and J. Golonka (2003) Phanerozoic paleogeography, paleoenvironment and lithofacies maps of the circum-Atlantic margins. *Marine and Petroleum Geology*, 20, 249–285.

Frimmel, H.E., R.E. Zartman, and A. Späth (2001) The Richtersveld igneous complex, South Africa: U-Pb zircon and geochemical evidence for the beginning of Neoproterozoic continental breakup. *J. Geol.*, 109, 493–508.

Fukao, Y. (1992) Seismic tomogram of the Earth's mantle: Geodynamic implications. *Science*, 258, 625–630.

Golonka, J., N.Y. Bocharova, D. Ford, M.E. Edrich, J. Bednarczyk, and J. Wildharber (2003) Paleozoic reconstructions and basins development of the Arctic. *Marine and Petroleum Geology*, 20, 211–248.

Gregori, D.G., and E.A. Bjerg (1997) New evidence on the nature of the Frontal Cordillera Ophiolitic Belt—Argentina. *Journal of South American Earth Sciences*, 10, 147–155.

Harlan, S.S., L. Heaman, A.N. LeCheminant, and W.R. Premo (2003) Gunbarrel mafic magmatic event: A key 780 Ma time marker for Rodinia plate reconstructions. *Geology*, 31, 1053–1056.

Gregoire, M., N. Mattieli, C. Nicollet, J.Y. Cottin, H. Leyrit, D. Weis, N. Shimizu, and A. Giret (1994) Oceanic mafic granulite xenoliths from the Kerguelen archipelago. *Nature*, 367, 360–363.

Harper, G.D. (1984) A review of hemipelagic and flysch sedimentation associated with the Josephine ophiolite, California. *Ofioliti*, 19, 397–411.

Heaman, L.M., A.N. LeCheminant, and A.H. Rainbird (1992) Nature and timing of Franklin igneous events, Canada: Implications for a late Proterozoic mantle plume and the break-up of Laurentia. *Earth Planet. Sci. Lett.*, 109, 117–131.

Heinhorst, J., B. Lehmann, P. Ermolov, V. Serykh, and S. Zhurutin (2000) Paleozoic crustal growth and metakkogeny of the Central Asia: Evidence from magmatic-hydrothermal ore system of Central Kazakhstan. *Tectonophysics*, 328, 69–87.

Hervé, F., L. Aguirre, V. Sepulveda, and D. Morata (1999) Contrasting geochemistry and metamorphism of pillow basalts in metamorphic complexes from Aysén, S. Chile. *Journal of South American Earth Sciences*, 12, 379–388.

Herzig, C.T., D.L. Kimbrough, and Y. Hayasaka (1997) Early Permian zircon uranium-lead ages for plagiogranites in the Yakuno ophiolite, Asago distinct, southwest Japan. *The Island Arc*, 6, 396–403.

Hill R.I. (1991) Starting plumes and continental break-up. *Earth Planet. Sci. Lett.*, 104, 398–416.

Hirose, K. (2002) Phase transitions in pyrolitic mantle around 670-km depth: Implications for upwelling of plumes from the lower mantle. *J. Geophys. Res.*, 107, doi:10.1029/2001JB000597.

Hoffman, P.F. (1989) Precambrian geology and tectonic history of North America. In Bally, A.W., and A.R. Palmer (eds.) The Geology of North America-An Overview, Geological Society of America, Boulder, Colorado, USA, pp. 447–512.

Hoffman, P.F. (1991) Did the breakout of Laurentia turn Gondwanaland inside-out? *Science*, 252, 1409–1412.

Hofmann, C., V. Courtillot, G. Féraud, P. Rochette, G.Yirgu, E. Ketefo, and R. Pik (1997) Timing of the Ethiopian flood basalt event and implications for plume birth and global change. *Nature*, 389, 838–841.

Irifune, T., and A.E. Ringwood (1993) Phase relationships in subducted oceanic crust and buoyancy relationships at depths of 600–800 km in the mantle. *Earth Planet. Sci. Lett.*, 117, 101–110.

Ishiwatari, A. (1985a) Igneous petrogenesis of the Yakuno ophiolite (Japan) in the context of the diversity of ophiolites. *Contrib. Mineral. Petrol.*, 89, 155–167.

Ishiwatari, A. (1985b) Granulite-facies metacumulates of the Yakuno ophiolite, Japan: Evidence for unusually thick oceanic crust. *J. Petrol.*, 26, 1–30.

Ishizuka, H., and S. Suzuki (1995) Ophiolite metamorphism and ocean-floor metamorphism. *J. Geog.*, 104, 350–360 (in Japanese with English abstract).

Isozaki, Y. (1997) Contrasting two types of orogen in Permo-Triassic Japan: Accretionary versus collisional. *The Island Arc*, 6, 2–24.

Isozaki, Y., and T. Itaya (1990) Chronology of Sanbagawa metamorphism. *J. Metamo. Geol.*, 8, 401–411.

Isozaki, Y., S. Maruyama, and F. Furuoka (1990) Accreted oceanic materials in Japan. *Tectonophysics*, 181, 179–205.

Jahn, B.-M., W.L. Griffin, and B.F. Windley (eds) (2000) Continental growth in the Phanerozoic: Evidence from Central Asian Orogenic Belt. *Tectonophysics*, 328, 1–227.

Jahn, B.-M., B.F. Windley, B. Natal'in, and N. Dobretsov (eds) (2004) Phanerozoic continental growth in Central Asia. *J. Southeast Asian Earth Sci.*, 23, 599–815.

Johnson, M.C., A.T. Anderson Jr., and M.J. Rutherford (1997) Pre-eruptive volatile contents of magmas. In Carroll, M.R., and J.R. Holloway (eds.) Volatiles in Magmas, Reviews in Mineralogy, vol. 30, Mineralogical Society of America, Washington, D.C., pp. 281–330.

Jones, D.L., N.J. Silberling, and J. Hillhouse (1977) Wrangellia—a displaced terrane in northwestern North America. *Can. J. Earth Sci.*, 14, 2565–2577.

Kadarusman, A., S. Miyashita, S. Maruyama, C.D. Parkinson, and A. Ishikawa (2004) Petrology, geochemistry and paleogeographic reconstruction of the East Sulawesi Ophiolite, Indonesia. *Tectonophysics*, 392, 55–83.

Kamo, S.L., G.K. Czamanske, and T.E. Krogh (1996) A minimum U-Pb age for Siberian flood-basalt volcanism. *Geochim. Cosmochim. Acta*, 60, 3505–3511.

Karlstrom, K.E., K.-I. Åhäll, S. Stephen, S.S. Harlan, M.L. Williams, J. McLelland, and J.W. Geissman (2001) Long-lived (1.8–1.0 Ga) convergent orogen in southern Laurentia, its extensions to Australia and Baltica, and implications for refining Rodinia. *Precambrian Res.*, 111, 5–30.

Karlstrom, K.E., S.S. Harlan, M.L. Williams, J. McLelland, J.W. Geissman, and K.-I. Åhäll (1999) Refining Rodinia: Geologic evidence for the Australian-western US connection in the Proterozoic. *GSA Today*, 9, 1–7.

Kerr, A.C., J.A. Aspden, J. Tarney, and L.F. Pilatasig (2002) The nature and provenance of accreted oceanic terranes in western Ecuador: Geochemical and tectonic constraints. *J. Geol. Soc. London*, 159, 577–594.

Kerr, A.C., G.F. Marriner, N.T. Arndt, J. Tarney, A. Nivia, A.D. Saunders, and R.A. Duncan (1996b) The petrogenesis of Gorgona komatiites, picrites and basalts: New field, petrographic and geochemical constraints. *Lithos*, 37, 245–260.

Kerr, A.C., G.F. Marriner, J. Tarney, A. Nivia, A.D. Saunders, M.F. Thirlwall, and C. Sinton (1997a) Elemental and isotopic constraints on the petrogenesis and original tectonic setting of Cretaceous basaltic terranes in western Colombia. *J. Petrol.*, 38, 667–702.

Kerr, A.C., and J. Tarney (2005) Tectonic evolution of the Caribbean and northwestern South America: The case for accretion of two Late Cretaceous oceanic plateaus. *Geology*, 33, 269–272.

Kerr, A.C., J. Tarney, G.F. Marriner, G.T. Klaver, A.D. Saunders, and M.F. Thirlwall (1996a) The geochemistry and petrogenesis of the late-Cretaceous picrites and basalts of Curacao, Netherlands Antilles: A remnant of an oceanic plateau. *Contrib. Mineral. Petrol.*, 124, 29–43.

Kerr, A.C., J. Tarney, G.F. Marriner, A. Nivia, and A.D. Saunders (1997b) The Caribbean-Colombian Cretaceous Igneous Province: The internal anatomy of an oceanic plateau. In Mahoney, J.J., and M.F. Coffin (eds.) Large Igneous Provinces; Continental, Oceanic, and Planetary Flood Volcanism, Geophysical Monograph Series, vol. 100, American Geophysical Union, Washington, D.C., pp. 123–144.

Kerrick, D.M., and K. Caldeira (1993) Paleoatmospheric consequences of CO_2 released during early Cenozoic regional metamorphism in the Tethyan orogen. *Chem. Geol.*, 108, 201–230.

Khain, E.V., E.V. Bibikova, E.B. Salnilkova, A. Kröner, A.S. Gibsher, A.N. Dienko, K.E. Degtyarev, and A.A. Fedotova (2003) The Paleo-Asian ocean in the Neoproterozoic and early Paleozoic: New geochronologic data and palaeotectonic reconstructions. *Precambrian Res.*, 122, 329–358.

Kimbrough, D.L., J.M. Mattinson, D.S. Coombs, C.A. Landis, and M.R. Johnson (1992) Uranium-lead ages from the Dun Mountain Ophiolite Belt and Brook Street terrane, South Island, New Zealand. *Geol. Soc. Am. Bull.*, 104, 429–443.

Kiminami, K., S. Miyashita, and K. Kawabata (1994) Ridge collision and in-situ greenstones in accretionary complex: An example from the Late Cretaceous Ryukyu Island and southwest Japan margin. *The Island Arc*, 3, 103–111.

Kimura, G., M. Sakakibara, and M. Okamura (1994) Plumes in central Panthalassa? Deductions from accreted oceanic fragments in Japan. *Tectonics*, 13, 905–916.

Kravchinsky, V.A., K.M. Konstantinov, and J.-P. Cogne (2001) Palaeomagnetic study of Vendian and Early Cambrian rocks of South Siberia and Central Mongolia: Was the Siberian platform assembled at this time? *Precambrian Res.*, 110, 61–92.

Kroenke, L.W., and K. Nemoto (1982) Marine geology of the Hess Rise 2. Basement Morphology, Sediment thickness, and structural geology. *J. Geophys. Res.*, 87, 9259–9278.

Kugimiya, Y., and A. Takasu (2002) Geology of the Western Iratsu mass within the tectonic melange zone in the Sambagawa metamorphic belt, Besshi district, central Shikoku, Japan. *J. Geol. Soc. Jpn.*, 108, 644–662 (In Japanese with English abstract).

Kumazawa, M., and S. Maruyama (1994) Whole Earth tectonics. *J. Geol. Soc. Jpn.*, 100, 81–102.

Kuzmichev, A.B., E.V. Bibikova, and D.Z. Zhuravlev (2001) Neoproterozoic (~800 Ma) orogeny in the Tuva-Mongolia Massif (Siberia): Island arc-continent collision at the northeast Rodinia margin. *Precambrian Res.*, 110, 109–126.

Lanphere, M.A., and G.B. Dalrymple (1976) K-Ar ages of basalts from DSDP Leg33: Sites 315 (Line Islands) and 317 (Manihiki Plateau). *Initial Report of the Deep Sea Drilling Project*, 33, 649–654.

Larson, R.L. (1991a) Latest pulse of Earth: Evidence for a mid-Cretaceous superplume. *Geology*, 19, 547–550.

Larson, R.L. (1991b) Geological consequences of superplumes. *Geology*, 19, 963–966.

Lassiter, J.C., D.J. DePaolo, and J.J. Mahoney (1995) Geochemistry of the Wrangellia Flood Basalt Province: Implications for the role of continental and oceanic lithosphere in flood basalt genesis. *J. Petrol.*, 36, 983–1009.

Li, Z.X. (2000) New palaeomagnetic results from the 'cap dolomite' of the Neoproterozoic Walsh tillite, northwestern Australia. *Precambrian Res.*, 100, 359–370.

Li, Z.X., X.H. Li, P.D. Kinny, and J. Wang (1999) The breakup of Rodinia: Did it start with a mantle plume beneath South China? *Earth Planet. Sci. Lett.*, 173, 171–181.

Li, Z.X., and C.McA. Powell (2001) An outline of the paleogeographic evolution of the Australasian region since the beginning of the Neoproterozoic. *Earth Sci. Rev.*, 53, 237–277.

Lindsley-Griffin, N. (1994) The Cambrian Trinity ophiolite and related rocks of the Lower Paleozoic Trinity complex, northern California, USA. In Ishiwatari, A., J. Malpas, and H. Ishizuka (eds.) Proceedings of the 29th IGC Ophiolite Symposium, Circum-Pacific Ophiolites, VSP International Science Publishers, Netherlands, pp. 47–68.

Liou, J.G., S. Maruyama, X. Wang, and S. Graham (1990) Precambrian blueschist terranes of the world. *Tectonophysics*, 181, 97–111.

Livermore, R., A. Nankivell, G. Eagles, and P. Morris (2005) Paleogene opening of Drake Passage. *Earth Planet. Sci. Lett.*, 236, 459–470.

Lo, C.-H., S.-L. Chung, T.-Y. Lee, and G. Wu (2002) Age of the Emeishan flood magmatism and relations to Permian-Triassic boundary events. *Earth Planet. Sci. lett.*, 198, 449–458.

Lytwyn, J., J. Casey, S. Gilbert, and T. Kusky (1997) Arc-like mid-ocean ridge basalt formed seaward of a trench-forearc system just prior to ridge subduction: An example from subaccreted ophiolites in southern Alaska. *J. Geophys. Res.*, 102, 10225–10243.

MacDonald, W.D., J.J. Estrada, and G. Humberto (1997) Paleoplate affiliations of volcanic accretionary terranes of the northern Andes. *Geological Society of America Abstract with Program*, 29, 245.

MacPherson, G.J., and S.P. Phipps (1988) Geochemistry and petrology of mafic volcanic rocks from olistostromes in the basal Great Valley Group, northern California Coast Ranges. *Geol. Soc. of Am. Bull.*, 100, 1770–1779.

Maher, S., D.H. Moore, A.J. Crawford, R. Twyford, and C.M. Fanning (1997) Test Drilling of the Southern Margin of the Murray Basin. *Victorian Initiative for Minerals and Petroleum Report*, 52, 275.

Mahoney, J.J., M. Storey, R.A. Duncan, K.J. Spencer, and M. Pringle (1993) Geochemistry and geochronology of the Ontong Java Plateau. In Pringle, M., W. Sager, W. Sliter, and S. Stein (eds.) The Mesozoic Pacific. Geology, Tectonics, and Volcanism, Geophysical Monograph Series, vol. 77, American Geophysical Union, Washington, D.C., pp. 233–261.

Malpas, J., I.E.M. Smith, and D. Williams (1994) Comparative genesis and tectonic setting of ophiolitic rocks of the South and North Islands of New Zealand. In Ishiwatari, A., J. Malpas, and H. Ishizuka (eds.) Proceedings of the 29th IGC Ophiolite Symposium, Circum-Pacific Ophiolites, VSP International Science Publishers, Netherlands, pp. 29–46.

Malpas, J., K.B. Spörli, P.M. Black, and I.E.M. Smith (1992) Northland ophiolite, New Zealand, and implications for plate-tectonic evolution of the southwest Pacific. *Geology*, 20, 149–152.

Mann, P., and A. Taira (2004) Global tectonic significance of the Solomon Island and Ontong Java plateau convergent zone. *Tectonophysics*, 389, 137–190.

Marsh, J.S., P.R. Hooper, J. Rehacek, R.A. Duncan, and A.R. Duncan (1997) Stratigraphy and age of Karoo basalts of Lesotho and implications for correlations within the Karoo Igneous Province. In Mahoney, J.J., and M.F. Coffin (eds.) Large Igneous Provinces; Continental, Oceanic, and Planetary Flood Volcanism, Geophysical Monograph Series, vol. 100, American Geophysical Union, Washington, D.C., pp. 247–272.

Maruyama, S. (1994) Plume tectonics. *J. Geol. Soc. Jpn.*, 100, 24–49.

Maruyama, S. (1997) Pacific-type orogeny revised: Miyashiro-type orogeny proposed. *The Island Arc*, 6, 91–120.

Maruyama, S., Y. Kaneko, T. Ota, M. Terabayashi, H. Yamamoto, I. Katayama, K. Okamoto, T. Komiya, H. Ozawa, R. Anma, A. Ishikawa, J.G. Liou, and B.F. Windley (2001) A speculation of Sanbagawa metamorphism; from accretion at trench through deep subduction to the surface exposure. *Abstracts in UHPM Workshop 2001 at Waseda University, Fluid/Slab/Mantle Interactions and Ultrahigh-P Minerals*, Tokyo, 243–246.

Maruyama, S., J.G. Liou, and M. Terabayashi (1996) Blueschists and Eclogites of the World and Their Exhumation. *Internat. Geol. Rev.*, 38, 485–594.

Maruyama, S., and T. Seno (1986) Orogeny and relative plate motions: Example of the Japanese Islands. *Tectonophysics*, 127, 305–329.

Marzoli, A., L. Melluso, V. Morra, P.R. Renne, I. Sgrosso, M. D'Antonio, L. Duarte, E.A.A. Morais, E.A.A. Morais, and G. Ricci (1999a) Geochronology and petrology of cretaceous basaltic magmatism in the Kwanza Basin (western Angola), and relationships with the Paraná-Etendeka flood basalt province. *J. Geodynam.*, 28, 341–356.

Marzoli, A., P.R. Renne, E.M. Piccirillo, M. Ernesto, G. Bellieni, and A. De Min (1999b) Extensive 200 million year old continental flood basalts of the central Atlantic magmatism province. *Science*, 284, 616–618.

Matsuda, T., and Y. Isozaki (1991) Well-documented travel history of Mesozoic pelagic chert, from mid-oceanic ridge to subduction zone. *Tectonics*, 10, 475–499.

McDougall, I., L. Kristjansson, and K. Saemundsson (1984) Magnetostratigraphy and geochronology of NW-Iceland. *J. Geophys. Res.*, 89, 7029–7060.

Meert, J.G. (2003) A synopsis of events related to the assembly of eastern Gondwana. *Tectonophysics*, 362, 1–40.

Montogomery, H., E.A.J. Pessagno, J.F. Lewis, and J. Schellekens (1994) Paleogeography of Jurassic fragments in the Caribbean. *Tectonics*, 13, 725–732.

Moores, E.M. (1991) Southwest US—East Antarctic (SWEAT) connection: A hypothesis. *Geology*, 19, 425–428.

Morgan, W.J. (1981) Hot spot tracks and the opening of the Atlantic and Indian oceans: The oceanic lithosphere. In Emiliani, C. (ed.) The Sea-Ideas and Observations on Progress in the Study of the Seas, vol. 7, Wiley Interscience, New York, pp. 443–487.

Müller, R.D., D. Mihut, and S. Baldwin (1998) A new kinematic model for the formation and evolution of the West and Northwest Australian margin. In Purcell, P.G., and R.R. Purcell (eds.) The Sedimentary Basins of Western Australia, vol. 2, Proceedings of Petroleum Exploration Society of Australia Symposium, Perth, pp. 55–72.

Nagahashi, T., and S. Miyashita, (2002) Petrology of the greenstones of the Lower Sorachi Group in the Sorachi-Yezo Belt, central Hokkaido, Japan, with special reference to discrimination between oceanic plateau basalts and mid-oceanic ridge basalts. *The Island Arc*, 11, 122–141.

Nakanishi, M., W.W. Sager, and A. Klaus (1999) Magnetic lineations within Shatsky Rise, northwest Pacific Ocean: Implication for hot spot-triple junction interaction and oceanic plateau formation. *J. Geophys. Res.*, 104, 7539–7556.

Nakanishi, M., K. Tamaki, and K. Kobayashi (1989) Mesozoic magnetic anomaly lineations and seafloor spreading history of the northwestern Pacific. *J. Geophys. Res.*, 94, 15437–15462.

Nakanishi, M., and E.L. Winterer (1998) Tectonic history of the Pacific-Farallon-Phoenix triple junction from Late Jurassic to Early Cretaceous: An abandoned Mesozoic spreading system in the central Pacific basin. *J. Geophys. Res.*, 103, 12453–12468.

Neal, C.R., J.J. Mahoney, L.W. Kroenke, R.A. Duncan, and M.G. Petterson (1997) The Ontong Java Plateau. In Mahoney, J.J., and M.F. Coffin (eds.) Large Igneous Provinces; Continental, Oceanic, and Planetary Flood Volcanism, Geophysical Monograph Series, vol. 100, American Geophysical Union, Washington, D.C., pp. 183–216.

Nicholson, K.N., P.M. Black, and C. Picard (2000) Geochemistry and tectonic significance of the Tangihua Ophiolite Complex, New Zealand. *Tectonophysics*, 321, 1–15.

Norvick, M.S., and M.A. Smith (2001) Mapping the plate tectonic reconstruction of southern and south-eastern Australia and implications for petroleum systems. *Australian Petroleum Production and Exploration Association Journal*, 41, 15–35.

O'Connor, J.M., and R.A. Duncan (1990) Evolution of the Walvis Ridge-Rio Grande Rise hot spot system: Implications for African and South American plate motions over plumes. *J. Geophys. Res.*, 95, 17475–17502.

Okamoto, K., H. Shinjoe, I. Katayama, K. Terada, Y. Sano, and S. Johnson (2004) SHRIMP U-Pb dating of quartz-bearing eclogite from the Sanbagawa belt, south-west Japan: Implications for metamorphic evolution if subducted protolith. *Terra Nova*, 16, 81–89.

Ozawa, H., S. Motoyama, S. Inoue, Y. Kato, and M. Murata (1999) Petrology of basic volcanics of the Mikabu greenstone complex in the eastern Shikoku. *Mem. Geol. Soc. Jpn.*, 52, 217–228 (in Japanese with English abstract).

Ozawa, H., M. Murata, H. Nishimura, and T. Itaya (1997) Petrological feature and dating of igneous rocks of the Mikabu belt. *Bull. Volcanol. Soc. Jpn.*, 42, S231–237 (in Japanese with English abstract).

Pallister, J.S., J.R. Budahn, and B.L. Murchy (1989) Pillow basalts of the Angayucham Terrane; oceanic plateau and island crust accreted to the Brooks Range. *J. Geophys. Res.*, 94, 15901–15923.

Parkinson, C.D. (1998) Emplacement of the East Sulawesi Ophiolite: Evidence from subophiolite metamorphic rocks. *J. Southeast. Asian Earth Sci.*, 6, 1–16.

Pimentel, M.M., L. Heaman, and R.A. Fuck (1991) U-Pb zircon and sphene geochronology of Late Proterozoic volcanic arc rock units from southwestern Goiás, central Brazil. *Journal of South American Earth Sciences*, 4, 329–339.

Pisarevsky, S.A., M.T.D. Wingate, C.McA. Powell, S. Johnson, and D.A.D. Evans (2003) Models of Rodinia assembly and fragmentation. In Yoshida, M., B.F. Windley, and S. Dasgupta (eds.) Models of Rodinia assembly and fragmentation, Special Publications, vol. 206, Geological Society, London, pp. 35–55.

Powell, C.McA., Z.X. Li, M.W. McElhinny, J.G. Meert, and J.K. Park (1993) Paleomagnetic constraints on timing of the Neoproterozoic breakup of Rodinia and Cambrian formation of Gondwana. *Geology*, 21, 889–892.

Powell, C.McA., and S.A. Pisarevsky (2002) Late Neoproterozoic assembly of East Gondwanaland. *Geology*, 30, 3–6.

Pringle, M.S. (1992) Radiometric ages of basaltic basement recovered at Sites 800, 801 and 802, ODP Leg 129, western Pacific Ocean. *Proc. ODP Sci. Results*, 129, 389–404.

Pringle, M.S., M. Storey, and J. Wijbrans (1994) $^{40}Ar/^{39}Ar$ geochronology of Mid-Cretaceous Indian Ocean basalts: Constraints on the origin of the large flood basalt provinces. EOS Transactions, American Geophysical Union, 75, Fall Meeting Supplement, abstract, p. 728.

Radhakrishna, T., and M. Joseph (1996) Proterozoic paleomagnetism of the mafic dyke swarms in the high-grade region of southern India. *Precambrian Res.*, 76, 31–46.

Ramana, M.V., T. Ramprasad, and M. Desa (2001) Seafloor spreading magnetic anomalies in the Enderby Basin, East Antarctica. *Earth Planet. Sci. Lett.*, 191, 241–255.

Richards, M.A., R.A. Duncan, and V.E. Courtillot (1989) Flood basalts and hot-spot tracks; plume heads and tails. *Science*, 246, 103–107.

Richards, M.A., D.L. Jones, R.A. Duncan, and D.J. Depaolo (1991) A mantle plume initiation model for the Wrangellia Flood Basalt and other oceanic plateau. *Science*, 254, 263–267.

Richardson, W.P., E.A. Okal, and S. Van der Lee (2000) Rayleigh-wave tomography of the Ontong-Java Plateau. *Phys. Earth Planet. Inter.*, 118, 29–51.

Riley, T.R., P.T. Leat, B.C. Storey, I.J. Parkinson, and I.L. Millar (2003) Ultramafic lamprophyres of the Ferrar large igneous province: Evidence for a HIMU mantle component. *Lithos*, 66, 63–76.

Ringwood, A.E. (1975) Composition and Petrology of the Earth's mantle, McGraw-Hill, New York, p. 618.

Rollinson, H. (1993) Using Geochemical Data: Evaluation, Presentation, Interpretation, Longman, UK, p. 352.

Ruffman A., and J.D. Greenough (1990) The Weekend dykes, a newly recognized mafic dyke swarm on the eastern shore of Nova Scotia, Canada. *Can. J. Earth Sci.*, 27, 644–648.

Sakakibara, M., R.S. Hori, G. Kimura, M. Ikeda, T. Moumoto, and H. Kato (1999) The age of magmatism and petrochemical characteristics of the Sorachi plateau reconstructed in Cretaceous accretionary complex, central Hokkaido, Japan. *Mem. Geol. Soc. Jpn.*, 52, 1–15 (in Japanese with English abstract).

Sakakibara, M., R.S. Hori, and T. Murakami (1993) Evidence from the radiolarian chert xenoliths for post-Jurassic volcanism of the Mikabu greenrocks, Okuki area, western Shikoku, Japan. *J. Geol. Soc. Jpn.*, 99, 831–833.

Saleeby, J.B., G.D. Harper, A.W. Snoke, and W.D. Sharp (1982) Time relations and structural-stratigraphic patterns in ophiolite accretion, West Central Klamath Mountains, California. *J. Geophys. Res.*, 87, 3831–3848.

Sano, S., K. Tazaki, Y. Koide, T. Nagao, T. Watanabe, and Y. Kawachi (1997) Geochemistry of dike rocks in Dun Mountain Ophiolite, Nelson, New Zealand. *N.Z. J. Geol. Geophys.*, 40, 127–136.

Saunders, A.D., J.G. Fitton, A.C. Kerr, M.J. Norry, and R.W. Kent (1997) The North Atlantic igneous province. In Mahoney, J.J., and M.F. Coffin (eds.) Large Igneous Provinces; Continental, Oceanic, and Planetary Flood Volcanism, Geophysical Monograph Series, vol. 100, American Geophysical Union, Washington, D.C., pp. 45–93.

Scarrow, J.H., V. Pease, C. Fleutelot, and V. Dushin (2001) The late Neoproterozoic Enganepe ophiolite, Polar Urals, Russia: An extension of the Cadomian arc? *Precambrian Res.*, 110, 255–275.

Scotese, C.R. (2004) A continental drift flipbook. *J. Geol.*, 112, 729–741.

Shervais, J.W., and D.L. Kimbrough (1985) Geochemical evidence for the tectonic setting of the Coast Range ophiolite: A composite island arc- oceanic crust terrane in western California. *Geology*, 13, 35–38.

Shiraishi, K., Y. Motoyoshi, Y. Nakai, D.J. Ellis, Y. Hiroi, and C.M. Fanning (1994) Cambrian orogenic belt in East Antarctica and Sri Lanka: Implications for Gondwana assembly. *J. Geol.*, 102, 47–65.

Sinton, C.W., R.A. Duncan, M. Storey, J. Lewis, and J.J. Estrada (1998) An oceanic flood basalt province within the Caribbean plate. *Earth Planet. Sci. Lett.*, 155, 221–235.

Sivell, W.J. (2002) Geochemistry and Nd-isotope systematics of chemical and terrigenous sediments from the Dun Mountain Ophiolite, New Zealand. *N.Z. J. Geol. & Geophys.*, 45, 427–451.

Sivell, W.J., and M.T. McCulloch (2000) Reassessment of the origin of the Dun Mountain Ophiolite, New Zealand: Nd-isotopic and geochemical evolution of magma suites. *N.Z. J. Geol. & Geophys.*, 43, 133–146.

Smoot, N.C. (1999) Orthogonal intersections of megatrends in the Western Pacific ocean basin: A case study of the Mid-Pacific mountains. *Geomorphology*, 30, 323–356.

Spaggiari, C.V., D.R. Gray, and D.A. Foster (2003) Tethyan- and Cordilleran-type ophiolites of eastern Australia: Implications for the evolution of the Tasmanides. In Dilek, Y., and P.T. Robinson (eds.) Ophiolites in Earth History, Special Publications, vol. 218, Geological Society, London, pp. 517–539.

Stein, M., and S.L. Goldstein (1996) From plume head to continental lithosphere in the Arabian-Nubian shield. *Nature*, 382, 773–778.

Stewart, K., S. Turner, S. Kelley, C.J. Hawkesworth, L. Kirstein, and M.S.M. Mantonavi (1996) 3-D ^{40}Ar-^{39}Ar geochronology in the Palaná flood basalt province. *Earth Planet. Sci. Lett.*, 143, 95–110.

Storey, M., J.J. Mahoney, and A.D. Saunders (1997) Cretaceous basalts in Madagascar and the transition between plume and continental lithosphere mantle source. In Mahoney, J.J., and M.F. Coffin (eds.) Large Igneous Provinces; Continental, Oceanic, and Planetary Flood Volcanism, Geophysical Monograph Series, vol. 100, American Geophysical Union, Washington, D.C., pp. 95–122.

Storey, M., J.J. Mahoney, A.D. Saunders, R.A. Duncan, S.P. Kelley, and M.F. Coffin (1995) Timing of hot-spot related volcanism and the breakup of Madagascar and India. *Science*, 267, 852–855.

Sun, S.-S., and W.F. McDonough (1989) Chemical and isotopic systematics of oceanic basalts; implications for mantle composition and processes. In Saunders A.D., and M.J. Norry (eds.) Magmatism in the Ocean Basins, Special Publication, vol. 42, Geological Society, London, UK, pp. 313–345.

Sun, S.-S., and J.W. Sheraton (1996) Geochemical and isotopic evolution. In Glikson, A.Y., A.J. Stewart, C.G. Ballhaus, G.L. Clarke, E.H.J. Feeken, J.H. Leven, J.W. Sheraton, and S.-S. Sun (eds.) Geology of the western Musgrave Block, central Australia, with particular reference to the mafic-ultramafic Giles Complex, Australian Geological Survey Organization Bulletin, 239, pp. 135–143.

Suzuki, S., and H. Ishizuka (1998) Low-grade metamorphism of the Mikabu and northern Chichibu belts in central Shikoku, SW Japan: Implications for the areal extent of the Sanbagawa low-grade metamorphism. *J. Metamor. Geol.*, 16, 107–116.

Suzuki, N., A. Kadarusman, and S. Maruyama (2000) Gossira continent: A new name of composite volcanoes formed at South Pacific Superplume during the Cretaceous. Eos Transaction, 81, 48, AGU Fall Meeting Supply, Abstract, V62B–33.

Svenningsen, O.M. (2001) Onset of seafloor spreading in the Iapetus ocean at 608 Ma: Precise age of the Sarek Dyke Swarm, northern Swedish Caledonides. *Precambrian Res.*, 110, 241–254.

Tatsumi, Y., H. Shinjoe, H. Ishizuka, W.W. Sager, and A. Klaus (1998) Geochemical evidence for a mid-Cretaceous superplume. *Geology*, 26, 151–154.

Tejada, M.L.G., J.J. Mahoney, R.A. Duncan, and M.P. Hawkins (1996) Age and geochemistry of basement and alkalic rocks of Malaita and Santa Isabel, Solomon Islands, southern margin of Ontong Java Plateau. *J. Petrol.*, 37, 361–369.

Terabayashi, M., K. Okamoto, H. Yamamoto, Y. Kaneko, T. Ota, S. Maruyama, I. Katayama, T. Komiya, A. Ishikawa, R. Anma, H. Ozawa, B.F. Windley, and J.G. Liou (2005) Accretionary complex origin of the mafic-ultramafic bodies of the Sanbagawa belt, Central Shikoku, Japan. *Intl. Geol. Rev.*, 47, 1058–1073.

Thompson, P.M.E., P.D. Kempton, R.V. White, A.C. Kerr, J. Tarney, A.D. Saunders, J.G. Fitton, and A. McBirney (2003) Hf-Nd isotopic constraints on the origin of the Cretaceous Caribbean plateau and its relationship to the Galapagos plume. *Earth Planet. Sci. Lett.*, 217, 59–75.

Tolan, T.L., S.P. Reidel, M.H. Beeson, J.L. Anderson, K.R. Fecht, and D.A. Swanson (1989) Revisions to the estimates of the aerial extent and volume of the Columbia River Basalt Group. In Reidel, S.P., and P.R. Hooper (eds.) Volcanism and Tectonism in the Columbia River Flood Basalt Province, Special Paper, vol. 239, Geological Society of America, Boulder, Colorado, pp. 1–20.

Uchio, Y., Y. Isozaki, T. Ota, A. Utsunomiya, M.M. Buslov, and S. Maruyama (2004) The oldest mid-oceanic carbonate buildup complex: Setting and lithofacies of the Vendian (Late Neoproterozoic) Baratal limestone in the Gorny Altai Mountains, Siberia. *Proc. Jpn. Acad.*, 80(B), 422–428.

Uesugi, J., and S. Arai (1999) The Shiokawa peridotite mass in the Mikabu belt, central Japan, as a cumulate from intra-plate tholeiite. *Mem. Geol. Soc. Jpn.*, 52, 229–242 (in Japanese with English abstract).

Wallin, E.T., J.M. Mattinson, and A.W. Potter (1988) Early Paleozoic magnetic events in the eastern Klamath Mountains, northern California. *Geology*, 16, 144–148.

Weil, A.B., J.W. Geissman, and R. Van der Voo (2004) Paleomagnetism of the Neoproterozoic Chuar Group, Grand Canyon Supergroup, Arizona: Implications for Laurentia's Neoproterozoic APWP and Rodinia break-up. *Precambrian Res.*, 129, 71–92.

Weil, A.B., R. Van der Voo, C.M. Niocaill, and J.G. Meert (1998) The Proterozoic supercontinent Rodinia: Paleomagnetically derived reconstructions for 1100 to 800 Ma. *Earth Planet. Sci. Lett.*, 154, 13–24.

White, R., and D. McKenzie (1989) Magmatism at rift zones: The generation of volcanic continental margins and flood basalts. *J. Geophys. Res.*, 94, 7685–7729.

White, R.V., J. Tarney, A.C. Kerr, A.D. Saunders, P.D. Kempton, M.S. Pringle, and G.T. Klaver (1999) Modification of an oceanic plateau, Aruba, Dutch Caribbean: Implications of the generation of continental crust. *Lithos*, 46, 43–68.

Wilson, M. (1989) Igneous petrogenesis: A global tectonic approach, Chapman and Hall, London, p. 466.

Windley, B.F. (1995) The Evolving Continents 3rd Ed., John Wiley, Chichester, p. 526.

Wingate, M.T.D., I.H. Campbell, W. Compston, and G.M. Gibson (1998) Ion microprobe U-Pb ages for Neoproterozoic-basaltic magmatism in south-central Australia and implications for the breakup of Rodinia. *Precambrian Res.*, 87, 135–159.

Wingate, M.T.D., and J.W. Giddings (2000) Age and paleomagnetism of the Mundine Well dyke swarm, Western Australia: Implications for an Australia-Laurentia connection at 755 Ma. *Precambrian Res.*, 100, 335–357.

Wingate, M.T.G., S.A. Pisarevsly, and D.A.D. Evans (2002) Rodinia connections between Australia and Laurentia: No SWEAT, no AUSWUS? *Terra Nova*, 14, 121–128.

Winterer, E.L., J.I. Ewing, R.G. Douglas, R.D. Jarrard, Y. Lancelot, R.M. Moberly, T.C. Moore, P.H. Roth, and S.O. Schlanger (eds.) (1973) *Leg 17: Honolulu to Hawaii, Initial Report of the Deep Sea Drilling Project*, 17, p. 930.

Woodhouse, J.H., and A.M. Dziewonski (1984) Mapping the upper mantle: Three-dimensional modeling of Earth structure by inversion of seismic waveforms. *J. Geophys. Res.*, 89, 5953–5986.

Wright, J.E., and S.J. Wyld (1986) Significance of xenocrystic Precambrian zircon contained within the southern continuation of the Josephine ophiolite: Devils Elbow ophiolite remnant, Klamath Mountains, northern California. *Geology*, 14, 671–674.

Wu, F.-Y., J.-Q. Lin, S.A. Wide, X.'O. Zhang, and J.-H. Yang (2005) Nature and significance of the Early Cretaceous giant igneous event in eastern China. *Earth Planet. Sci. Lett.*, 233, 103–119.

Wyld, S.J., and J.E. Wright (1988) The Devils Elbow ophiolite remnant and overlying Galice Formation: New constraints on the Middle to Late Jurassic evolution of Klamath Mountains, California. *Geol. Soc. Am. Bull.*, 100, 29–44.

Yang, K., and P.K. Seccombe (1997) Geochemistry of the mafic and ultramafic complexes of the northern Great Serpentinite Belt, New South Wales: Implications for first stage melting. In Ashley, P.M., and P.G. Flood (eds.) Tectonics and Metallogenesis of the New England Orogen, Special Publication, vol. 19, Geological Society of Australia, Sydney, pp. 197–217.

Yokoyama, K. (1980) Nikubuchi peridotite body in the Sanbagawa metamorphic belt; thermal history of the 'Al-pyroxene-rich suite' peridotite body in high pressure metamorphic terrain. *Contrib. Mineral. Petrol.*, 73, 1–13.

Young, G.M. (1992) Late Proterozoic stratigraphy and the Canada-Australia connection. *Geology*, 20, 215–218.

Zhang, J., and C.T. Herzberg (1994) Melting experiments on anhydrous peridotite KLB-1 from 5.0 to 22.5 Gpa. *J. Geophys. Res.*, 99, 17729–17742.

Zhao, D. (2004) Global tomographic images of mantle plumes and subducting slabs: Insight into deep Earth dynamics. *Phys. Earth Planet. Inter.*, 146, 3–34.

Zindler, A., and S.R. Hart (1986) Chemical geodynamics. *Annu. Rev. Earth Planet. Sci.*, 14, 493–571.

CHAPTER 14

PLUME WINTER SCENARIO FOR BIOSPHERE CATASTROPHE: THE PERMO-TRIASSIC BOUNDARY CASE

YUKIO ISOZAKI

Department of Earth Science and Astronomy, The University of Tokyo, Komaba, Meguro, Tokyo 153-8902 Japan;
E-mail: isozaki@chianti.c.u-tokyo.ac.jp

Abstract
The Permo-Triassic boundary (P-TB) interval is unique in having experienced three unusual geologic phenomena on a global scale that had never occurred in the rest of the Phanerozoic, viz., 1) the greatest mass extinction, 2) development of superanoxia (nearly 20 million year-long anoxia), and 3) initial breakup of the supercontinent Pangea. The so-called end-Paleozoic mass extinction was double-phased, one at the Guadalupian-Lopingian boundary (G-LB; ca. 260 Ma) and the other at the Changhsingian/Induan boundary (P-TB *sensu stricto*; ca. 252 Ma). The coincidence in timing between the G-LB mass extinction, the onset of superanoxia, and the probable initial rifting of Pangea strongly suggests their causal link. This article reviews current understanding of the end-Paleozoic event, and proposes a possible scenario to explain these three unique geological phenomena in a cause–effect context. Violent volcanism is favored by many on the basis of the apparent coincidence in timing between the two Late Permian mass extinctions and the volcanism of continental flood basalts (CFB). However, the only available material-based evidence for putative violent volcanism is the felsic tuffs in the Upper Permian in South China and Japan that appear inconsistent with the CFB link. The end-Paleozoic global environmental change was likely triggered by the episodic activity of a mantle plume, not through basaltic but rhyo-dacitic volcanism. The felsic nature of the volcanism suggests not only highly explosive eruption but also extensive delivery of air-borne ash. Alkaline magmatism derived directly from a mantle plume, may have played an important role both in the G-LB and P-TB extinction-relevant environmental turmoils. The "Plume Winter" scenario is proposed here to explain the unique geological phenomena of the end-Paleozoic event. When a plume head hits the bottom of a pre-existing continental lithosphere, alkaline volcanism of felsic to intermediate composition, often accompanying kimberlite/carbonatite, occurs in a highly explosive manner prior to a voluminous CFB eruption in a later stage. The violent volcanism directly causes 1) extensive ash fall, 2) formation of a dust/aerosol-screen in the stratosphere, and 3) acid rain, and these are followed by severe destruction of the photosynthesis-supported global food web both on land and in sea through 4) less insolation and 5) low temperature. A sharp decline or cessation of the primary production may have triggered cascaded extinctions of marine and terrestrial

D. A. Yuen et al. (eds.), Superplumes, 409–440.
© 2007 *Springer.*

heterotrophic animals. In the aftermath, increase in atmospheric CO_2 by volcanism drives global warming, prolonged anoxia, and delayed biotic recovery. "Plume Winter" initiated by the uprising African superplume may have caused the end-Paleozoic double-phased mass extinction and the superanoxia. The G-LB event appears to have been more important than that at P-TB, because everything geologically significant started at that time, viz. the initial breakup of Pangea, mass extinction, and superanoxia. This is also supported by the remarkable turning point of the Phanerozoic in the global sea level, initial $^{87}Sr/^{86}Sr$ ratio of seawater, and geomagnetic field behavior. The major re-organization of the mantle plume structure from the Pacific to the Atlantic regimes corresponds to the largest turning point in the Phanerozoic history of life from the Paleozoic to the Mesozoic-Modern regime.

1 INTRODUCTION

In the last one ninth of Earth's history, the Phanerozoic (ca. 542 million years), five major mass extinction events occurred at the end-Ordovician, Late Devonian, end-Permian, end-Triassic, and end-Cretaceous (Sepkoski, 1984; Hallam and Wignall, 1997). As each event was unique in character, it seems unlikely that there was only one common cause that drove all the five extinction events. An extraterrestrial cause has only been proved reliably for the end-Cretaceous (K-T boundary) event (Alvarez, 1997). Although a similar K-T boundary-style impact was claimed for the Late Devonian, end-Permian, and end-Triassic events, none of these has been supported by convincing evidence. This definitely suggests that there were other causes, in particular those related to terrestrial processes.

Among the big five mass extinctions, the end-Permian (=Permo-Triassic boundary or P-TB; ca. 252 Ma) event is outstanding because it marks the greatest divide in Phanerozoic biosphere history, i.e., the irreversible change from the Paleozoic to the Mesozoic-Modern regime (Sepkoski, 1984). We can recognize three distinct global geologic phenomena that occurred uniquely at the P-TB time; i.e., 1) the largest mass extinction, 2) superanoxia, and 3) the initial breakup of the Pangea supercontinent. All these three geological events are unique to the P-TB as they have never been recorded as having happened in the rest of the Phanerozoic. Judging from their global nature, such uniqueness potentially suggests that these three phenomena occurred at the same time not by accident but in a tight cause–effect link(s), probably through terrestrial processes.

This chapter reviews the current understanding of the P-TB event, focusing on the above-mentioned three distinct and unusual geological phenomena, and discusses their possible cause–effect link in a new volcanism-triggered scenario named the "Plume Winter". In contrast to the Phanerozoic era, Precambrian time appears to provide little or no information on mass extinctions, owing to the scarcity of the fossil record; however, the current approach, assuming Earth-bound and mantle plume-related mechanisms of mass extinction, may open a new window into the *Terra incognita*.

2 P-TB EVENT

The greatest mass extinction in the Phanerozoic was at the Permo-Triassic boundary (P-TB), at a time when many marine and terrestrial biotas were terminated (e.g., Sepkoski, 1984; Erwin, 1993; Benton, 1985; Visscher et al., 1996). Despite the variety of hypotheses and ideas proposed in the last 100 years by many researchers, the ultimate cause of the P-TB mass extinction has not yet been identified (e.g., Hallam and Wignall, 1997; Erwin et al., 2002; Bottjer, 2004). Following research on the K-T boundary, similar evidence for an extraterrestrial impact such as an Ir anomaly was claimed for the P-TB event, but all efforts to produce similar data failed totally (Clark et al., 1986; Zhou and Kyte, 1988). Likewise, a recently reported ^{3}He anomaly from the P-TB (Becker et al., 2001) is not convincing because of poor analytical procedures that violated the double-blind test protocol (Farley et al., 2005). In addition, an analyzed sample from Japan was obviously taken not from the P-TB horizon but from the Upper Permian interval (Isozaki, 2001). Even concerning a possible *bona fide* P-TB sample from South China, Kaiho et al. (2001) reported more data to support an extraterrestrial impact but these are criticized to be equivocal by Koeberl et al. (2002). The notion that the "Bedout" impact off Western Australia caused the P-TB extinction (Becker et al., 2004) was immediately questioned by Wignall et al. (2004) and Renne et al. (2004). A P-TB impact in the southern hemisphere sounds unrealistic because Paleozoic radiolarians became completely extinct in the northern hemisphere at the P-TB, whereas they survived solely in the southern hemisphere off New Zealand (Takemura et al., 2003). Judging from such long-term intense efforts in search of extraterrestrial signatures and from the barren results so far, it seems likely at present that there is no convincing evidence to support extraterrestrial impact at the P-TB.

By assuming no planetary impact, we may look for a more reasonable cause for the P-TB catastrophe within our own planet. Besides the greatest mass extinction in the Phanerozoic, the P-TB interval is characterized by two other unusual geologic events of global significance, i.e., the development of extraordinarily long-lasting oxygen-depleted condition called superanoxia (Isozaki, 1994, 1997), and the initial breakup of the supercontinent Pangea. As these two events never occurred together at any other time in the Phanerozoic except for at the P-TB, their apparent coincidence in timing with the greatest mass extinction of the Phanerozoic strongly suggests a potential cause–effect relationship (Fig. 1). Thus the ultimate cause of the P-TB event may be better sought by establishing possible viable link between these three unusual global phenomena of the Phanerozoic.

2.1 Extinction

The P-TB mass extinction has long been regarded as the most outstanding biological turnover event in the Phanerozoic, when nearly 90% of marine invertebrate species and a comparable diversity of land biota were terminated (e.g., Sepkoski, 1984; Labandeira and Sepkoski, 1992; Erwin, 1993; Benton, 1985; Visscher et al., 1996; Hallam and Wignall, 1997; Fig. 2a). The severity of the mass extinction is

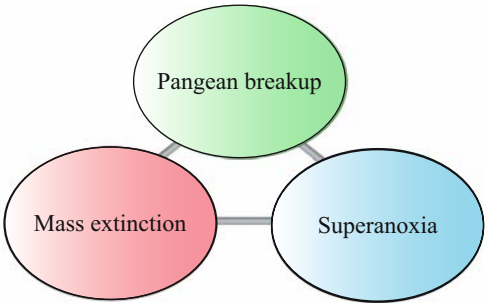

Figure 1. Schematic diagram showing three unusual geologic phenomena of global context that make the Permian-Triassic boundary (P-TB) event unique in the Phanerozoic. The main goal of the current P-TB study is to establish possible cause–effect relationships among these three global geologic phenomena unique to the P-TB.

biostratigraphically documented in various P-TB sections around Pangea including South China (Zhao et al., 1981; Yin, 1996; Yin et al., 2001), the Tethyan domain of the Middle East and Europe (e.g., Iranian-Japanese Research Group, 1981; Pakistani-Japanese Research Group, 1985; Holser and Schoenlaub, 1991; Cirilli et al., 1998), Laurentia of Greenland (e.g., Looy et al., 2001), and South Africa plus Australia in Gondwana (e.g., MacLeod et al., 2000; Retallack et al., 2003; Thomas et al., 2004). In particular in the Global Stratotype Section and Point (GSSP) of the P-TB at Meishan, South China, the sharp termination of more than 150 species is well-documented (Yang et al., 1991; Jin et al., 2000). In addition, even in the middle of the superocean Panthalassa, the extinction of Paleozoic radiolarians, fusulines, and rugose corals was detected in mid-oceanic deep-sea chert and shallow marine atoll carbonates (Isozaki, 1994, 1997, 2007; Koike, 1996). Thus the P-TB mass extinction was a global occurrence, affecting both Pangea and Panthalassa from low- to high-latitudes.

The main extinction timing of the P-TB is chronologically constrained at 252.6 Ma by the latest sophisticated dating techniques (Mundil et al., 2004), although the tempo and duration of the main pulse are not yet clarified. In addition, chemostratigraphic analyses have identified a sharp negative shift in stable carbon isotope ratios across the P-TB in almost all P-TB sections across the world (e.g., Holser et al., 1989; Baud et al., 1989; Yin, 1996; Musashi et al., 2001), indicating that the carbon cycle in the ocean-atmosphere was significantly perturbed at the P-TB on a global scale, probably coupled with a change in global bio-productivity. The post-extinction recovery was considerably delayed both in the biodiversity and complexity of the ecosystem compared with other major extinctions of the Phanerozoic (Bottjer, 2004), as clearly demonstrated by low-diversity fauna, a secular change in ichnofabric (Schubert and Bottjer, 1995; Twitchett, 1999) and the development of a "reef gap" (Stanley, 1988).

Recent results suggest that the end-Permian mass extinction was double-phased; the first extinction at the Guadalupian-Lopingian boundary (G-LB, Middle-Upper Permian boundary) and the second at the Lopingian-Induan boundary (P-TB *sensu*

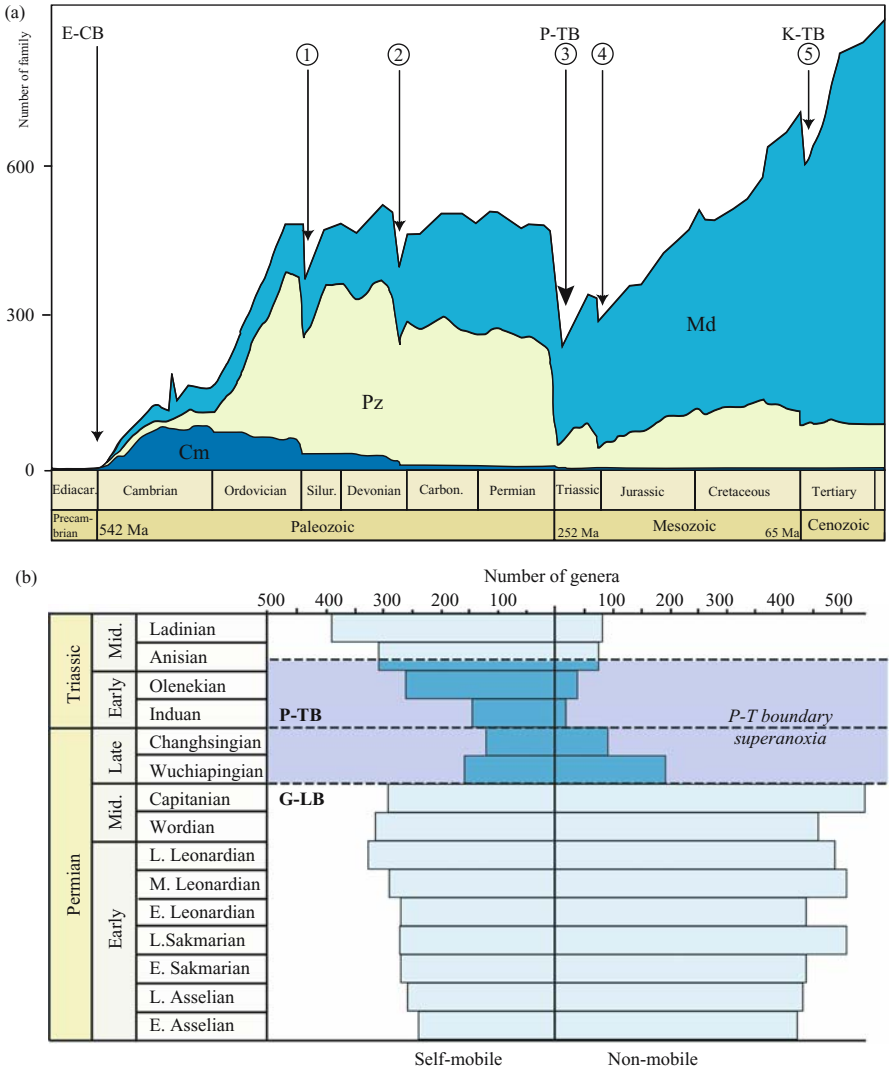

Figure 2. Secular change in biodiversity in the Phanerozoic (A: modified from Sepkoski, 1984) and across the P-TB (B: modified from Knoll et al., 1996). a: The P-TB mass extinction represents the greatest in the Phanerozoic but it is in fact composed of two distinct extinction events; i.e., the Guadalupian-Lopingian boundary (G-LB) event and the Changhsingian/Induan boundary (P-TB *sensu stricto*) event, that occurred in a relatively short time interval less than 10 million years. b: An overall bottleneck pattern in biodiversity is clearly observed across the P-TB in general, however, the most severe extinction occurred first at the G-LB, preferentially terminating bottom-dwellers (sessile benthos) with passive respiratory systems, prior to the P-TB. The prominent end-Paleozoic extinction was a combined consequence of the two distinct extinction events.

stricto). Since Stanley and Yang (1994) and Jin et al. (1994) pointed out the double-phased nature of the end-Permian extinction based on data from South China, the significance of the G-LB extinction event has become more apparent (Fig. 2b). Biostratigraphical research on coeval mid-oceanic deep-sea cherts and shallow marine atoll carbonates has confirmed that the double-phased faunal turnover occurred in radiolarians and fusulines in mid-Panthalassa as well as in peri-Pangean shelf sediments (Isozaki, 2007; Ota and Isozaki, 2006). Noteworthy is the same magnitude of extinction (extinction rate nearly 90% at species level) in the two events and a relatively short time interval between them, less than 10 million years. Thus the responsible global environmental change should have also been double-phased to account for the independent two mass extinctions. The devastating diversity-loss of the Paleozoic biota at the P-TB was probably due to the fact that the two large events occurred in a back-to-back manner in a short interval that did not allow enough time for the biosphere to recover to the pre-existing level in the Permian (Stanley and Yang, 1994; Isozaki, 2007). With a long-term viewpoint of Phanerozoic evolutionary history, therefore, the drastic change from the Paleozoic to the Mesozoic-Modern regime most likely started not at the P-TB *per se* but probably at the G-LB, viz. nearly 10 million years earlier than previously believed.

2.2 Superanoxia

Detailed stratigraphical studies of accreted mid-oceanic deep-sea cherts in Japan and British Columbia (Fig. 3a) have demonstrated that a long-term oxygen-depleted condition (oceanic anoxia) occurred in the Late Permian to Middle Triassic (Isozaki, 1994, 1997). This unique geological phenomenon, named superanoxia, lasted for an unusually long period during the Lopingian (Late Permian), Induan-Olenekian (Early Triassic) and early-middle Anisian (Middle Triassic) (Fig. 3b). According to the latest geologic timescale (Gradstein et al., 2004), this superanoxic interval ranged for ca. 20 million years from 260 to 240 Ma.

The secular change in the oceanic redox state was first detected in the sensitive switch of Fe-bearing minerals in deep-sea chert; i.e., hematite in oxic vs. pyrite in reduced conditions, as reflected in chert color (red vs. gray). The symmetrical pattern in redox state across the P-TB was confirmed by various geochemical analyses utilizing rare earth element abundances, Mössbauer spectroscopy, and trace element abundances (Kakuwa, 1996; Kato et al., 2002; Matsuo et al., 2003; Xia et al., 2004). Some sulfur isotope and organic geochemical analyses suggested the existence of a short-term oxic spike within this superanoxic period (Kajiwara et al., 1994; Suzuki et al., 1998), but this idea was later criticized (Wignall and Twitchett, 2002). During the P-TB superanoxia, deep-sea sediments became enriched both in pyrite and organic carbon, suggesting an anoxic and even euxinic condition mostly in the superocean (Isozaki, 1997) except for some areas in the southern hemisphere (Takemura et al., 2003). At the P-TB in the midst of the superanoxia, Paleozoic radiolarians became extinct particularly in the northern hemisphere. As radiolarians were the main representative plankton in the Paleozoic, their extinction most likely led to a major reorganization of the global bio-productivity and marine food web system. These

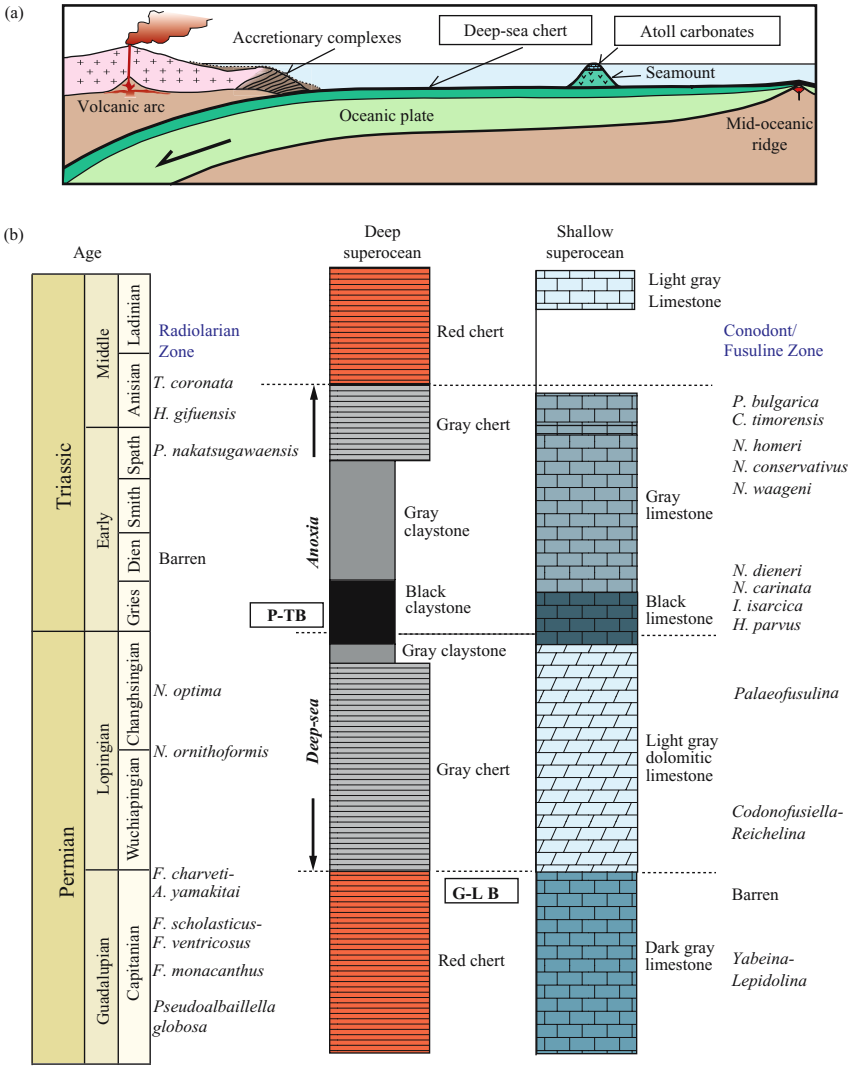

Figure 3. Schematic diagram showing the primary depositional sites of deep-sea pelagic cherts and mid-oceanic atoll carbonates in a simplified ridge-trench transect (a), and the composite stratigraphic columns of the Permian-Triassic deep-sea cherts and shallow-marine paleo-atoll carbonates deposited in the mid-Panthalassa (a: simplified from Isozaki et al., 1990; b: modified from Isozaki, 2007). Pre-Jurassic mid-oceanic records can be obtained solely from ancient oceanic rocks contained in subduction-accretion complexes formed along the ancient active continental margin because all pre-Jurassic seafloors had completely disappeared from the Earth's surface by the successive plate tectonics-driven subduction processes (a). The Jurassic accretionary complex in Japan contains numerous exotic blocks of the Permo-Triassic deep-sea chert and atoll carbonates of mid-oceanic origin, and some retain coherent primary stratigraphy across the G-LB and P-TB (b). These oceanic rocks are biostratigraphically tuned in high resolution by microfossils (fusulines, conodonts, and radiolarians). Three horizons, i.e., G-LB, P-TB, and

relations suggest that the oceanography of Panthalassa was drastically perturbed on a global scale, coupled with large changes in environment and biota *per se*. Such an anomaly in ocean is clearly reflected in the unusual deposition of anachronistic (Precambrian-like) aragonite precipitates during the Early Triassic (e.g., Schubert and Bottjer, 1992; Woods et al., 1999).

The superanoxia probably culminated at the P-TB, because the P-TB interval is centered by a unique, jet black, carbonaceous/pyritiferous siliceous shale (probably of the Griesbachian age; Yamakita et al., 1999) within a deep-sea chert succession (Fig. 3b). Moreover, shallow marine sequences recorded a short-term anoxia in the lowermost Triassic (e.g., Wignall and Hallam, 1992; Grice et al., 2005). These observations indicate that anoxic waters may have originated in the deep-sea in the Late Permian, invaded shallow-sea including continental shelves across the P-TB, and finally retreated to the deep-sea in the early Middle Triassic (Isozaki, 1996, 1997; Fig. 4).

Noteworthy is the timing of onset and disappearance of the superanoxia, because it coincided with major changes in biological diversity in the Late Permian and Middle Triassic (Fig. 3). The superanoxia started at the G-LB when the first mass extinction occurred. In contrast, the superanoxia started to wane in the late Olenekian to early Anisian by showing a fluctuation in redox, and finally it completely disappeared in the middle Anisian. This timing corresponds precisely with that of the full recovery of biodiversity, in particular, the re-appearance of reef complexes after a nearly 10 million-year gap (Stanley, 1988). These coincidences in timing suggest a causal link between the redox change in the superocean and the biodiversity.

2.3 Pangean breakup

Ever since Valentine and Moores (1970) and Schopf (1974) pointed out the sharp correlation between continent distribution pattern and secular change in biotic diversity in the Phanerozoic (amazingly just 5 years after the formulation of modern plate tectonics), the link between solid Earth processes and the biosphere crisis has attracted considerable interests from numerous geologists. Since 2.7 Ga, the formation and breakup of supercontinents have taken place at least 4 or 5 times (e.g., Hoffman, 1991; Dalziel, 1995; Rogers and Santosh, 2004). Late Paleozoic to early Mesozoic Pangea was the only supercontinent that appeared in the Phanerozoic. During the Late Carboniferous, two large continents, Gondwana and Laurasia, merged to form Pangea by closing an intervening ocean that corresponds to the western part of Tethys.

Figure 3. (*Continued*) mid-Anisian, are particularly noteworthy in correlation because synchronous phenomena are observed between the deep-sea chert and shallow marine carbonates. Faunal turnover both at the G-LB and P-TB is clearly detected in the deep-sea chert with radiolarians and in the atoll carbonates with fusulines. These two pulses in biodiversity change indicate that the relevant environmental change were of global in context. The onset of the ca. 20 million year-long deep-sea anoxia (superanoxia; Isozaki, 1994) apparently coincides with the G-LB event, whereas the superanoxia disappeared in the Anisian (Middle Triassic) at the time of full recovery in reef development and in global biodiversity. It is noteworthy that the P-TB event occurred in the climax of the superanoxic period.

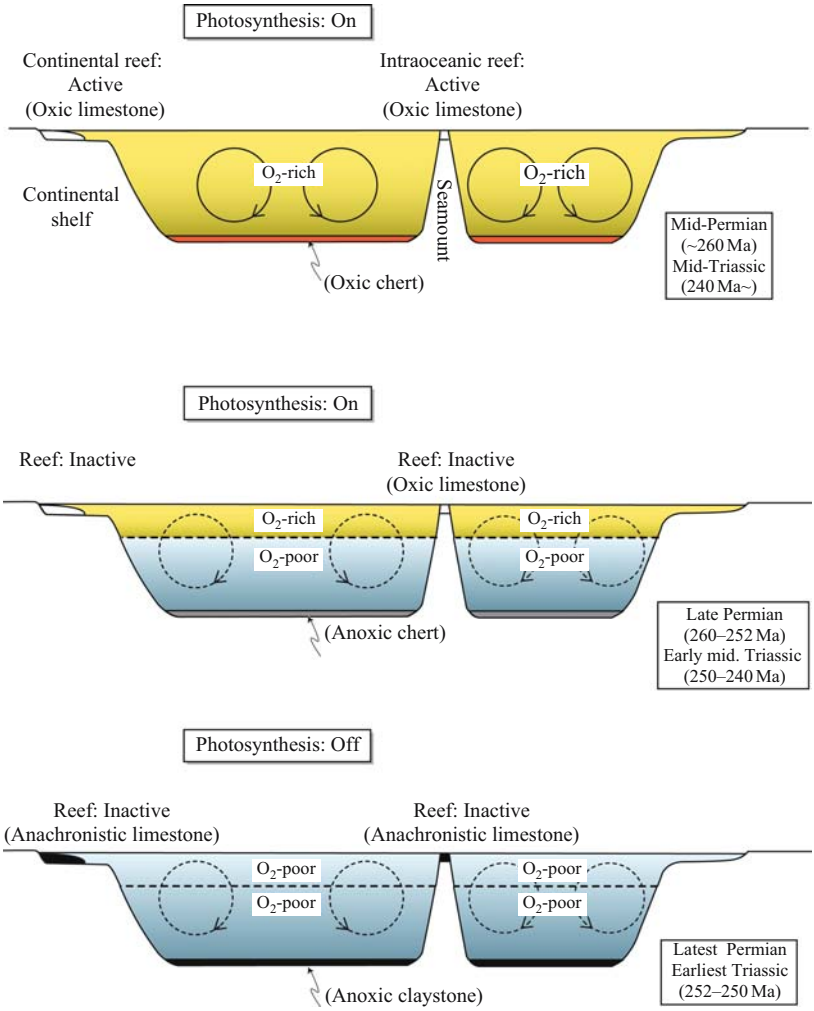

Figure 4. Schematic diagram of three modes of the superocean Panthalassa, showing the waxing and waning of the P-TB superanoxia (modified from Isozaki, 1996). The development of the superanoxia was monitored in three distinct lithofacies; continental shelf carbonates, mid-oceanic atoll carbonates, and deep-sea cherts. Top: Before the G-LB (ca. 260 Ma) and after the mid-Anisian (ca. 240 Ma), the whole superocean was healthy with oxygenated waters both in surface and bottom under effective oceanic circulation/mixing and resultant deep-sea ventilation. Middle: In the Late Permian (ca. 260–252 Ma) and most of the Early Triassic (ca. 250–240 Ma), deep superocean was anoxic while its shallow part remained oxygenated with active photosynthesis on surface. Bottom: Across the P-TB (ca. 252–250 Ma), the shallow superocean was also involved in the anoxia. In such an extreme condition, the global photosynthesis was likely shut down or considerably suppressed to drive the surface water anoxic regardless of oceanic circulation. This symmetric mode change during the 20 million year-long interval across the P-TB suggests that prolonged Earth-bound processes were responsible for the end-Paleozoic event rather than short-term episodic causes such as bolide impact and sudden methane release.

This supercontinent existed for nearly 100 million years until it broke apart in the Late Triassic by the opening of the new Atlantic Ocean. Concerning a possible connection of Pangea to the P-TB mass extinction and superanoxia, its breakup appears more important than its assembly.

In general, continental breakup is regarded as a consequence of episodic activity of large mantle plumes (e.g., Maruyama, 1994; Ernst and Buchan, 2003). Particularly noteworthy is an extraordinarily large plume over 1000 km in diameter (a superplume) that represents the largest flow of material and of energy from the interior to the surface of the planet Earth. When the head of a superplume reaches the base of the overlying lithosphere, decompressional partial melting of mantle peridotite occurs in association with large-scale melting of pre-existing crustal rocks to generate extensive magmatism that results in formation of a large igneous province (LIP), one consequence of which is continental flood basalt (CFB) (or plateau basalt).

The main phase of Pangean breakup gave rise to the opening of the Atlantic Ocean in the Early Jurassic. A series of mantle plumes aligned in a N–S direction was responsible for the opening of this new ocean, and the remnants of the plumes are now observed as the voluminous volcanic rocks and dyke swarms in the Central Atlantic Magmatic Province (CAMP) along both sides of the Atlantic margins (Marzoli et al., 1999) (Fig. 5a). Prior to the opening of a new ocean, the breakup of a supercontinent was expressed by an initial rifting stage, in which the pre-existing continental crust is attenuated in an extensional tectonic regime induced by an uprising superplume. The development of the Late Triassic Newark rift basins coupled with the frequent intrusion of the Palisade Sills in the eastern USA represents direct consequences of such extensional tectonics associated with the continental breakup.

The above-mentioned volcanism and rift-related geological features are, however, obviously too young to be responsible for the P-TB extinction. The breakup of the supercontinent did not start from a single plume, because there are more plume remnants in the rest of Pangea that are much older. These include CFB of the Siberian Traps in Siberia, the Emeishan Traps in South China, the Panjal Traps in India, and alkaline volcanic rocks/intrusions in Oman, W. Australia, and Norway (Fig. 5b). Their contemporaneity with the proximal ages of the P-TB and G-LB extinctions have led many geologists to discuss possible causal links between the CFB volcanism and the mass extinction, and putative plume-generated large-scale volcanism is often regarded as the ultimate cause of the biggest mass extinction of the Phanerozoic (e.g., Renne and Basu, 1991; Campbell et al., 1992; Veevers and Tewari, 1995; Chung et al., 1998; Courtillot, 1999). In contrast, plate tectonic-driven (subduction- and ridge-related) magmatism occurred almost at a steady state throughout the entire Phanerozoic, thus had nothing to do with rare and unique geologic events that gave rise to major mass extinctions.

The secular change in initial $^{87}Sr/^{86}Sr$ isotope ratio of marine carbonates reflects that of contemporary seawater. The Phanerozoic $^{87}Sr/^{86}Sr$ curve (Fig. 6; Veizer, 2003; McArthur and Howarth, 2004) clearly demonstrates that the input of continental material into the oceans was suppressed most at the G-LB to give rise to the lowest initial $^{87}Sr/^{86}Sr$ ratio of the Paleozoic, probably implying the zenith (maximum assembly)

(a) Plume-related volcanism in the Triassic and Jurassic (200–170 Ma) (CAMP domain)

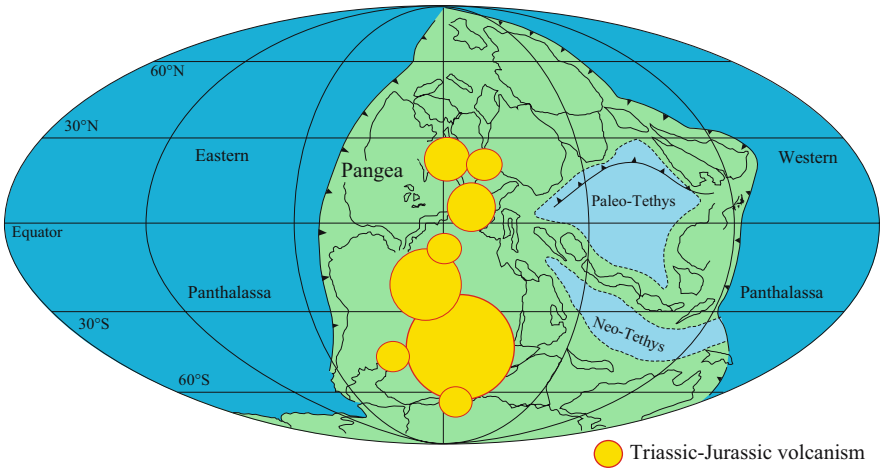

(b) Plume-related alkaline volcanism in the Late Permian (260–250 Ma)

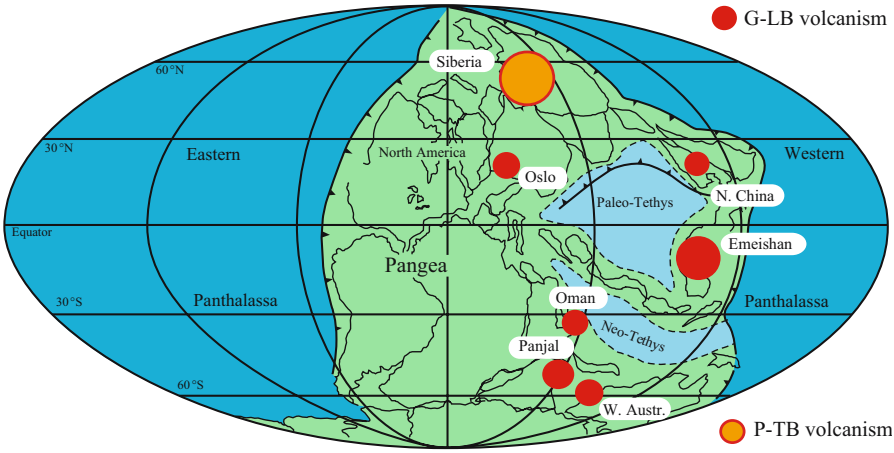

Figure 5. The mantle plume-derived large igneous provinces (LIPs) and relevant alkaline intrusions emplaced during the breakup of the supercontinent Pangea (base map from Scotese and Langford, 1995). a: The Triassic to Jurassic LIPs relevant to the opening of the Atlantic ocean (Central Atlantic Magmatic Province; CAMP; Maruyama, 1994); b: The Late Permian LIPs and major alkaline complexes including the continental flood basalts of Siberian (Russia), Emeishan (South China/Vietnam), and Panjal (India) Traps. The alkaline intrusive complexes, comprising syenite, nephelinite, lamproite etc., probably formed in relation with rifting under extensional tectonic regime. Two distinct phases of plume activity are recognized in the Pangea domain, one in the Late Permian and the other in the Triassic-Jurassic. It is noteworthy that the area of plume impingement shifted from the eastern half of Pangea in the Permian (b) to the western half in the Triassic-Jurassic (a). This apparent shift in activity center may have reflected heterogeneous conditions of the mantle beneath Pangea, or major morphological change of the superplume such as branching into several secondary plumes at the mantle transition zone ca. 400–660 km deep.

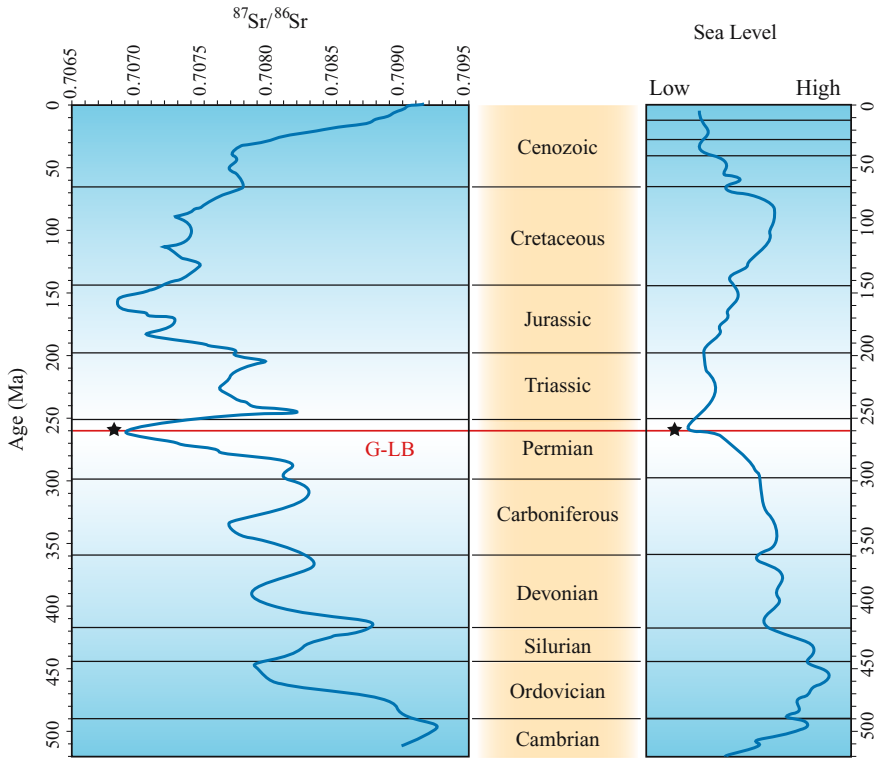

Figure 6. Phanerozoic secular change of initial $^{87}Sr/^{86}Sr$ isotope ratio of seawater (McArthur and Howarth, 2004) and relevant sea level change (modified from Hallam, 1992; Hallam and Wignall, 1999; Tong et al., 1999). Note that both the lowest value of $^{87}Sr/^{86}Sr$ ratio and the lowest sea-level of the Phanerozoic occurred not at the P-TB but around the G-LB. During the Pangean assembly in the Carboniferous to Middle Permian, continental drainage systems shrunk in total to decrease terrigenous supply to the superocean, thus to lower the seawater $^{87}Sr/^{86}Sr$ ratio. As triggered by the initial plume impingement beneath Pangea at the G-LB, the initial rifting in the eastern Pangea opened new drainage systems to put continental material with high $^{87}Sr/^{86}Sr$ ratio into the superocean. Plume-related excess input of volcanogenic CO_2 to atmosphere may have started global warming and sea-level rise toward the Mesozoic. The G-LB event rather than the P-TB event potentially marks the critical turning point from the Paleozoic to Mesozoic regime in various geological aspects.

of Pangea caused by the closure of pre-existing small oceans between continental blocks. In turn, in the Late Permian, the initial $^{87}Sr/^{86}Sr$ ratio started to increase rapidly, suggesting that the supply of weathered continental material to the oceans revived probably by continental rifting and the appearance of new intracontinental drainage systems. Thus the initial breakup of Pangea likely started not in the Early Triassic but already at the time of the G-LB in the Permian, considerably before the opening of the Atlantic in the Jurassic.

3 ENIGMA OF THE LATE PERMIAN VOLCANISM

Concerning a possible link between the large-scale volcanism and the P-TB and G-LB mass extinctions, most previous discussions have focused on the apparent chronological coincidence between the mass extinctions and CFB volcanism. This type of approach may suggest a possible causal link; however, it cannot establish its validity without other independent geological hard evidence, as in the case of the early K-TB controversy in which geochronological data alone were unable to determine whether volcanism or extraterrestrial impact was responsible for the extinction. Thus we must examine material-based geological evidence in various P-TB sections that can link volcanism to biospheric perturbation including extinction. The occurrence of tuff bed at the P-TB and G-LB horizons (Fig. 7) provides promising information for this approach, because they represent sole direct results of volcanism identified at the extinction horizons.

3.1 P-TB tuffs

The P-TB sections in South China contain remarkable evidence of volcanism adjacent to the mass extinction horizon in more than 35 sections including the GSSP at Meishan in Zhejian (e.g., Yin et al., 1993; Yang et al., 1991; Li et al., 1991). In the Meishan section, the top of Bed 24, marking the main extinction horizon, is directly overlain by an altered tuff (Bed 25, Fig. 7c). Also in the well-studied Shangsi section in Sichuan, several altered tuff beds occur around the P-TB (Li et al., 1989; Mundil et al., 2004). The P-TB tuffs have 1) euhedral phenocrysts, such as β-quartz, zircon and apatite, 2) pumice and/or glass shards, and sometimes show 3) porphyritic texture, suggesting that they were derived from explosive magma of felsic to intermediate composition (Yin et al., 1993). In the Chaotian section in Sichuan, 11 felsic tuff beds are concentrated within the 3 m-thick P-TB interval, suggesting a link between the violent volcanism and extinction-relevant environmental change (Isozaki et al., 2004, 2007b in press). Judging from the widespread occurrence of P-TB felsic tuff beds extending from Zhejian through Sichuan to Guangxi provinces (Figs. 7b–d), a remarkably large volcanic explosion likely caused the whole of South China to be covered with volcanic ash around the time of the P-TB, although the source volcano(s) has not yet been located. The so-called P-TB clay beds in Iran, Transcaucasia, and the Alps (Yin et al., 1993), and rhyo-dacitic tuff in Oman and Primorye in Russia (Rabu et al., 1990; Zakharov et al., 1995) should be re-examined in more detail.

3.2 G-LB tuff

A remarkable tuff bed characterizes the G-LB sections in South China. In contrast to the P-TB tuff beds, the G-LB tuff forms only one bed but is much thicker, 1–2 m (Fig. 7a). The G-LB tuff in South China was previously called the Wangpo bed (Lu, 1956; Li et al., 1991) and regarded as a terrigenous claystone until Isozaki and Ota

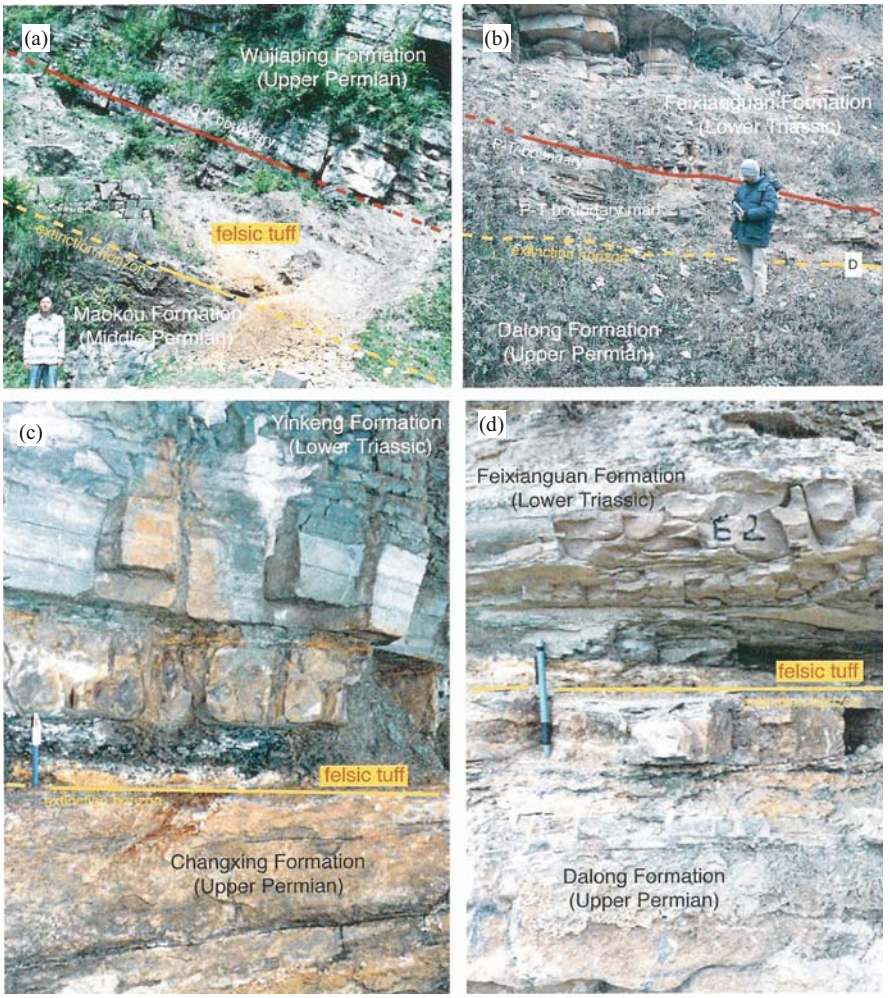

Figure 7. Field occurrence of the G-LB and P-TB felsic (rhyo-dacitic) tuffs in South China. a: G-LB tuff (2 meter thick; locally called the Wangpo bed) at Chaotian in northern Sichuan, b, d: P-TB tuff at Chaotian (Bed E1) (refer to Isozaki et al., 2004, 2007b in press), c: P-TB tuff (Bed 25) at Meishan in Zhejiang (refer to Yin et al., 1993, 2001). The abundant occurrence of zircon, β-quartz, and apatite phenocrysts suggests their origin from felsic alkaline magmatism rather than flood basalts (Siberian and Emeishan Traps). These boundary tuff beds occur mostly throughout South China, suggesting an extensive coverage of air-fall ash and a great magnitude and violent nature of source volcanisms.

(2001) pointed out its volcanogenic nature. This is an altered tuff (weathered into soft clay) that contains abundant euhedral phenocrysts such as β-quartz, plagioclase, zircon and apatite, suggesting that the source magma had a felsic to intermediate composition. According to this unique tuff within carbonate-dominant Permian sequence,

the Wangpo bed serves as a significant marker throughout South China, recognized in many sections (including its type locality in Lianshan, Shaanxi), in Chaotian, Shangsi, Emei-Ebian, Huaying (Sichuan), and Zhonghuopu (Hunan) (Li et al., 1991; Isozaki et al., 2004). It covers an area of nearly 1000 km N–S and 500 km E–W. Its regional extent within south China and its thickness of over 1 m require that the source volcano(s) was of enormous size, and that it was an explosive eruption with a felsic to intermediate composition.

Furthermore, Isozaki and Ota (2001) and Isozaki et al. (2004) pointed out the correlation between the mid-oceanic tuff beds and the Wangpo bed in South China. The occurrence of air-borne rhyo-dacitic tuff beds in mid-oceanic carbonate buildups further supports the large magnitude of the G-LB volcanism (Isozaki, 2007). As these rocks in Japan form exotic blocks secondarily incorporated in the Jurassic accretionary complexes, their primary sites of deposition were in the middle of the superocean Panthalassa off South China, probably over 3000 km to the east. The felsic volcanic ash was deposited in the mid-Panthalassa domain, at least in its western half, at the time of G-LB. In addition, the Upper Permian accretionary complex in Japan also contains G-LB rhyo-dacitic tuffs (tuff and tuffaceous mudstone; Nishimura et al., 1989); the felsic tuffs were deposited in a hemipelagic domain in western Panthalassa off Permian Japan (= South China) and were accreted to the Japan margin in the latest Permian. Their total thickness is over 100 m, though diluted by mud, that is much greater than that in the Jurassic complex, probably reflecting proximity to its source (Isozaki, 2007). Judging from such a difference in thickness, the relevant ash probably came from somewhere to the west of Panthalassa. It seems likely that western Panthalassa, together with South China, was extensively covered by air-borne ash of felsic composition at the G-LB. An extremely large, highly explosive felsic volcano(s) in western Pangea can explain both the long-distance delivery and huge volume of tuffaceous material in South China and western Panthalassa.

3.3 Volcanism at extinction boundaries: felsic vs. mafic

Based on their chronological coincidence, CFB are often regarded as the ultimate cause of the mass extinction (e.g., Courtillot, 1999; Ernst and Buchan, 2003; Wignall, 2001). For the P-TB and G-LB extinctions, the Siberian Traps and Emeishan/Panjal Traps (Fig. 5b) are nominated as the most popular candidates, respectively (e.g., Renne and Basu, 1991; Campbell et al., 1992; Chung et al., 1998).

Concerning the P-TB event, the Siberian Traps in Siberia (Fig. 5b) have the largest total volume and flow area of any CFB of ancient LIPs (e.g., Reichow et al., 2002; Saunders et al., 2005). By assuming the apparent coincidence in timing between the extinction and CFB, possible scenarios have been proposed to explain the volcanogenic catastrophe through aerosol-derived acid rain and/or volcanic gas-driven global warming (e.g., Campbell et al., 1992; Veevers and Tewali, 1995; Kozur, 1998; Racki and Wignall, 2005).

Although its initial eruption age has been controversial, it has recently been constrained to 251.7 ± 0.4 Ma by the latest U-Pb technique (Kamo et al., 2003). The age

of the P-TB extinction is dated as 252.4 ± 0.3 Ma at Meishan or 252.6 ± 0.2 Ma at Shangsi (Mundil et al., 2004). Comparing the ages of extinction and CFB volcanism, we admit that there is still an appreciable gap between the two events with respect to the error range, and that the extinction apparently predates the volcanism by 1–2 m.y.

For the cause of the G-LB extinction, the Emeishan Traps in western South China and the Panjal Traps in northern India (Fig. 5b) are likewise favored by many because of their apparent coincidence in timing (e.g., Chung et al., 1998; Zhou et al., 2002; Ali et al., 2002). Recent dating results of the Emeishan Traps identified the main eruption age at 256–259 Ma (Zhou et al., 2002), whereas age constraints for the Panjal Traps are not enough for precise correlation. The age of the G-LB mass extinction has not been tightly constrained yet but an age of 260.4 ± 0.7 Ma is proposed in the latest time scale (Gradstein et al., 2004). Like the P-TB case, the trap volcanism apparently postdates the mass extinction; it may thus not be the main cause. This age gap may become greater because the G-LB horizon is defined by the first appearance datum (FAD) of a new fossil taxon that belongs to the Lopingian (Upper Permian) fauna. The main extinction horizon of the Guadalupian (Middle Permian) fauna is located at a relatively low horizon below a post-extinction barren interval (e.g., Ota and Isozaki, 2006).

In all previous discussions on possible cause–effect relationships, the absence of material-based hard evidence that directly links the two independent events, i.e., extinction and CFB volcanism, remains a major obstacle regardless of the credibility of coincidence in mutual timing. In addition, the basaltic geochemistry of these CFB examples can explain neither the violent explosive eruption nor the felsic nature of the P-TB and G-LB tuffs. In fact, some andesitic basalt and rhyolite units occur in the CFBs, but they are confined not to the basal parts of the traps but to the middle-upper part (e.g., Xu et al., 2001) and they are too small in volume to account for the entire coverage of the above-mentioned regional tephra. Thus andesitic basalt and rhyolite units within the traps are not the likely source of the felsic tuffs at both the P-T and G-L extinction boundaries. The boundary tuffs in South China and Panthalassa represent the only available hard evidence that can link volcanism with the two major mass extinctions; therefore, their unique felsic nature needs a more detailed scrutiny.

4 ALKALI MAGMATISM

To seek a possible link between large-scale felsic volcanism and Pangean breakup, unique alkaline magmatism is the focus of this section. The breakup of a supercontinent is likely related to mantle plume activity (e.g., Maruyama, 1994; Ernst and Buchan, 2003) that often leaves relevant LIPs associated with extensional tectonic features. LIPs in mid-continental rifts or rifted continental margins are mainly composed of CFB that are often associated with alkaline igneous rocks.

Modern and ancient alkaline igneous suites in large, ring-shaped intrusive complexes show a great variety of rock types; e.g., nepheline syenite, phonolite, nephelinite, ijolite, and lamproite. Such a wide diversity in alkaline rocks, from ultramafic to felsic composition, is generally explained in terms of magmatic interaction between mantle-derived primordial magma and pre-existing, already differentiated lithospheric rocks (e.g., Sorensen, 1974; Bell, 1989).

As mentioned above, the putative G-LB and P-TB felsic volcanisms were unusually large-scale and quite distinct from plate tectonic-driven volcanism along island arcs and mid-oceanic ridges. Volcanism in arcs and ridges continuously maintains its activity as long as plate tectonics is in operation, thus such continuous volcanism probably has nothing to do with rare and catastrophic events like major mass extinctions that occurred only five times in the ca. 550 million year-long Phanerozoic. The other possible felsic magma source exists solely at a hotspot, in particular that located on the continental lithosphere, where a mantle plume differentiates magma into various compositions. Therefore, the episodic felsic volcanism at the G-LB and P-TB were likely related to alkaline volcanism induced by non-steady-state or non-plate-tectonic magmatism associated with a mantle plume.

In this regard, the common occurrence of apatite phenocrysts both in the G-LB and P-TB tuffs (Isozaki et al., 2004, 2007b in press; Yin et al., 1993) is noteworthy because apatite commonly occurs in alkaline rocks reflecting the enrichment of phosphorous in alkaline magma. This positively suggests that felsic to intermediate magmatism of the alkaline rock series was involved in the two boundary events.

In South China, major Permian intrusive complexes are composed of syenite, essexite, and alkali gabbro. For example, the kilometer-size Baima, Maomaogou and Panzhihua intrusive complexes in southern Sichuan are composed of nepheline syenite, including some up to 10 km × 20 km (Co-operative Geological Research Group of Japan and China in the Panxi Region, 1986), and were dated as 252–255 Ma (Lo et al., 2002). They may represent the source of the latest Permian felsic tuffs, although their effusive counterparts have not so far been recognized, probably owing to surface erosion. The occurrence of such large-scale alkaline complexes in the vicinity of the Emeishan CFB in South China suggests that at least one plume head (not necessarily a superplume but probably a smaller branched secondary plume) has impinged beneath South China in the Late Permian.

The occurrence of thick felsic tuffs in uppermost Permian shelf sediments in Primorye (Zakharov et al., 1995) suggests that similar violent volcanism affected Far East Russia around the P-TB timing. The ring-shaped Maimecha-Kotui alkaline-ultramafic complex (253 Ma) in Siberia is likely a remnant of such alkaline magmatism induced by a mantle plume (Basiliev and Zolotukhin, 1995); however, no effusive counterparts of felsic to intermediate composition are known. More work is needed from high-resolution volcanic stratigraphy coupled with geochronology in regions with contemporary CFBs, such as South China, Siberia, and northern India. Also in the rest of the world, similar alkaline intrusive complexes of similar age to the P-TB and G-LB should be checked in this regard. Possible candidates of such Permian alkaline intrusives include those in southern Norway, Oman, and W. Australia

(Neumann et al., 1992; Rabu et al., 1990; Le Maitre, 1975; Veevers and Tewari, 1995; Fig. 5b).

Among these alkaline rocks, although not so large in extent, some have highly distinctive composition, such as carbonatite and kimberlite. Carbonatite commonly occurs in close association with the above-mentioned alkaline silicate rocks in large intrusive bodies (Bell, 2001). Recently the occurrence of Permo-Triassic carbonatites was reported in North China, Tarim, and the North/South China border (Yang and Woolley, 2006). Kimberlite is another diagnostic rock in the alkaline suite. Besides its diamondiferous nature, kimberlite has a unique mode of occurrence as a diatreme or a pipe that is generally regarded to have formed through a highly explosive eruption, in accordance with the high content of its volatile components (Mitchell, 1991). Alkaline volcanism, sometimes accompanying kimberlite and carbonatite in the early stage, may drive violent eruptions (Bell, 2001) because the relevant magmas can carry huge amounts of a gas phase. Carbonatites occur preponderantly in North China and Tarim, probably reflecting the development of an Archean tectosphere (continental keel) enriched in carbon.

Isozaki (2000, 2001) speculated that such a highly explosive eruption by rapidly ascending kimberlite from the deep mantle rather than CFB *per se*, may have caused the remarkable biospheric perturbation at the P-TB. From a theoretical viewpoint, Morgan et al. (2004) recently proposed a similar interpretation (Verneshot hypothesis) to explain a possible general link between plume activity and mass extinction. Alkaline magmatism, in particular from a kimberlitic eruption, may represent a precursor of plume-related magmatism prior to the main eruption of CFB as suggested from the mode of occurrence of kimberlite with respect to CFB (e.g., kimberlite pipe fields were buried under CFB in Deccan and Siberia) and from pressure-temperature conditions in the subcontinental mantle capable of generating a carbon-rich magma (e.g., Morgan et al., 2004).

I emphasize here that both the G-LB and P-TB biospheric turnovers were probably triggered not by CFBs but by violent alkaline magmatism possibly including kimberlite/carbonatite intrusions, and that all this volcanism was essentially driven by the impingement of a superplume beneath the supercontinent Pangea. To date, however, such a link between kimberlite eruption and mass extinction has not yet been proven in any mass extinction event of the Phanerozoic on the basis of substantiated evidence. Neither kimberlite nor carbonatite can form felsic tuffs at the extinction boundary horizons, probably because they usually do not leave large amounts of lava/pyroclastics and tuffs. In this respect, kimberlite/carbonatite eruption alone cannot explain the extensive delivery of felsic ash at the boundaries, and the nature of the contemporary alkaline volcanism should be further clarified.

5 PLUME WINTER: A POSSIBLE SCENARIO

In order to explain the felsic tuffs closely associated with the G-LB and P-TB mass extinction horizons, the possible scenario of a “Plume Winter” was proposed by Isozaki (2000, 2001). This may sound similar to the recent popular idea of

linking CFB and mass extinction at both the G-LB and P-TB (e.g., Courtillot, 1999; Wignall, 2001; Racki and Wignall, 2005). However in the "Plume Winter" hypothesis, the emphasis is placed not on CFB basalt but on alkaline magmatism (including carbonatite/kimberlite) and its effect on the biosphere.

The scenario is simple and straightforward, if we assume plume-induced violent volcanism was the cause of the biospheric perturbation (Figs. 8, 9). When a plume head impinged at the lithosphere/asthenosphere boundary beneath the supercontinent Pangea, mantle-derived primordial magmas induced melting/metasomatism of pre-existing continental lithosphere to generate diverse magmas with alkaline signatures. Partial melting in shallow crustal levels gave rise to highly explosive alkaline volcanism of felsic to intermediate composition prior to the eruption of voluminous CFB. The alkaline lavas may have been associated with kimberlite/carbonatite, highly enriched in volatile components, such as CO_2 and SO_2, particularly in the early stage. As they were transported rapidly to the surface, they generated extraordinary large explosive eruptions. In domains above plumes, swarms of kimberlite/carbonatite may have become activated to leave a profound impact on the surface environment, although each intrusion or diatreme/pipe was small.

Such violent volcanism might directly cause 1) delivery of air-borne ash of felsic-intermediate nature over extensive areas, 2) formation of a dust/aerosol-screen in the stratosphere, and 3) input of CO_2 and SO_2 to the atmosphere. These phenomena would be followed by 4) decrease in insolation on the Earth's surface, 5) lowering of the surface temperature, and 6) pouring of acid rain; these were all critical for maintaining a pre-existing food web system in the biosphere. In particular, the combination of dim light, coldness, and highly acidic surface water may have severely destroyed the photosynthesis-driven primary productivity on both land and sea that formed the base of the food web on a global scale. A sharp decline or even temporary cessation of the primary production may have triggered cascaded extinctions of marine and terrestrial heterotrophic animals, firstly herbivorous, then carnivorous. Possible kill mechanisms include also volcanogenic heavy metal poisoning and volcanic gas-induced troubles in respiratory/circulatory or nerve systems in biota, in particular for those dependent on O_2 respiration. The deep-sea oxygen depletion may have been triggered by a temporary crash of photosynthesis rather than sluggish oceanic circulation as suggested by many (e.g., Hotinski et al., 2001). The following alkaline magmatism of the main phase delivered a large quantity of air-borne felsic ash, and CFB in the later stage added huge amount of CO_2 to turn the environment into a global warming trend that not merely enhanced the deep-sea anoxia by slow oceanic circulation but also delayed the biotic recovery.

The greatness of the end-Permian biospheric crisis is regarded as the combined consequence of two independent events, one at the G-LB (ca. 260 Ma) and the other at the P-TB (ca. 252 Ma), that occurred in a relatively short time interval of less than 10 million years (Stanley and Yang, 1994). The two end-Paleozoic mass extinctions likely occurred in two episodes of "Plume Winter" related to two independent activity-highs of mantle plume (Fig. 10). Nearly 8–10 million years after the initial development of deep-sea anoxia, by invading shallow marine environments on the

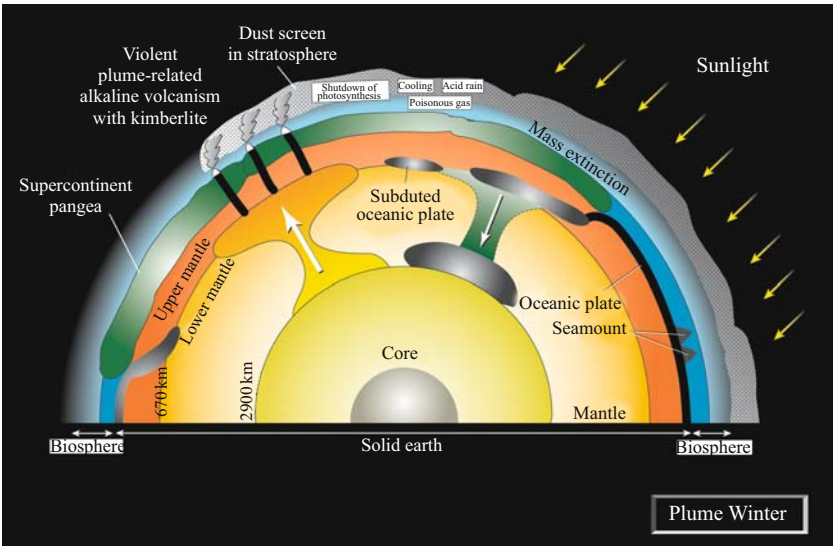

Figure 8. Schematic diagram of the "Plume Winter" scenario. The ascent of a superplume beneath the supercontinent Pangea was the most likely ultimate cause of the double-phased mass extinction at the G-LB and P-TB, as a mantle superplume represents the largest flow of material and of energy within the planet Earth. Up-rising hot plumes paired with a down-going cold plume form a large-scale whole-mantle convection cell; however, their behavior is not smooth/continuous but intermittent as paced in the mantle transition zone (ca. 400–660 km deep). Break-up of a supercontinent is intimately linked to the impingement of a superplume-head at the base of a supercontinental lithosphere. Prior to the final breakup of a supercontinent coupled with opening a new ocean, the initial stage of rifting is characterized by precursory alkaline magmatism that includes kimberlite/carbonatite enriched in volatile components. High temperature alkaline magma generated in the upper mantle re-melts pre-existing lower crust of a supercontinent to generate felsic to intermediate, alkaline magmatism before the outpouring of continental flood basalt (CFB) in a later stage of rifting. An extraordinarily explosive volcanism in the earlier stage of such plume-induced magmatism may cause various unusual impacts on the surface environments, in particular on the biosphere. Direct volcanogenic deterioration includes formation of a dust/aerosol screen in the stratosphere, gas poisoning, lowering of surface temperature, and acid rain. Among everything else, the shutdown of sunlight and global cooling by the dust/aerosol screen appear the most significant because the cessation of photosynthesis on a global scale is critical in maintaining bio-productivity. A short-time darkness and coldness can halt photosynthesis on a global scale and disorganize the pre-existing food web. Increase of atmospheric CO_2 by alkaline magmatism and later CFB causes global warming to drive prolonged anoxia and the delayed recovery of biodiversity. In the case of the Paleozoic-Mesozoic transition, the African superplume, probably its secondary branched plumes, ascended beneath Pangea in two phases, i.e., at the G-LB and P-TB, driving two episodes of "Plume Winter".

peri-Pangean continental shelves with oxygen-depleted water, the superanoxia likely culminated at the time of P-TB when the second "Plume Winter" (Plume Winter II) occurred.

From a long-term viewpoint, the G-LB event (Plume Winter I) appears more important than that at the P-TB (Plume Winter II) (Fig. 10) because all the global geological

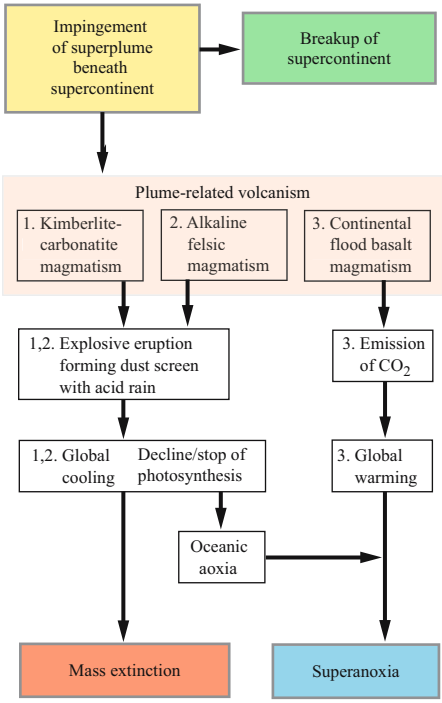

Figure 9. Flow chart of the end-Paleozoic "Plume Winter" scenario. The impingement of the African superplume head beneath the supercontinent Pangea caused the three unique geological phenomena at the Paleozoic/Mesozoic transition, viz. the initial breakup of Pangea, the development of superanoxia, and the greatest mass extinction of the Phanerozoic (Fig. 1). The key process that linked these global geological phenomena unique to the P-TB was extraordinarily violent volcanism induced by the superplume. Plume-related magmatism was three-fold; i.e., 1) precursory kimberlite/carbonatite, 2) alkaline felsic-intermediate volcanism, and 3) continental flood basalt. The former two were responsible for the mass killing through explosive eruptions forming dust/aerosol screen, while the latter for the prolonged anoxia and delayed recovery through global warming.

phenomena, including the superanoxia and decline in biodiversity, started at the time of G-LB as emphasized by Isozaki (1997). It is also noteworthy that the plume activity related to the Pangean breakup became apparent for the first time not in the Triassic-Jurassic time but already in the late Middle Permian. The following independent lines of evidence support this view. The secular changes in the global sea-level curve (Hallam and Wignall, 1999; Tong et al., 1999) and in the initial $^{87}Sr/^{86}Sr$ isotope ratio (Veizer, 2003; McArthur and Howarth, 2004) clearly show a sharp turning point around the G-LB (Fig. 6). Both signatures are regarded as reflecting the beginning of a new plume activity at the Earth's surface at the time of the G-LB. Global sea level hit its lowest level in the Phanerozoic around the G-LB, and then started to rise almost uni-directionally in the Late Permian and Mesozoic (Hallam and Wignall,

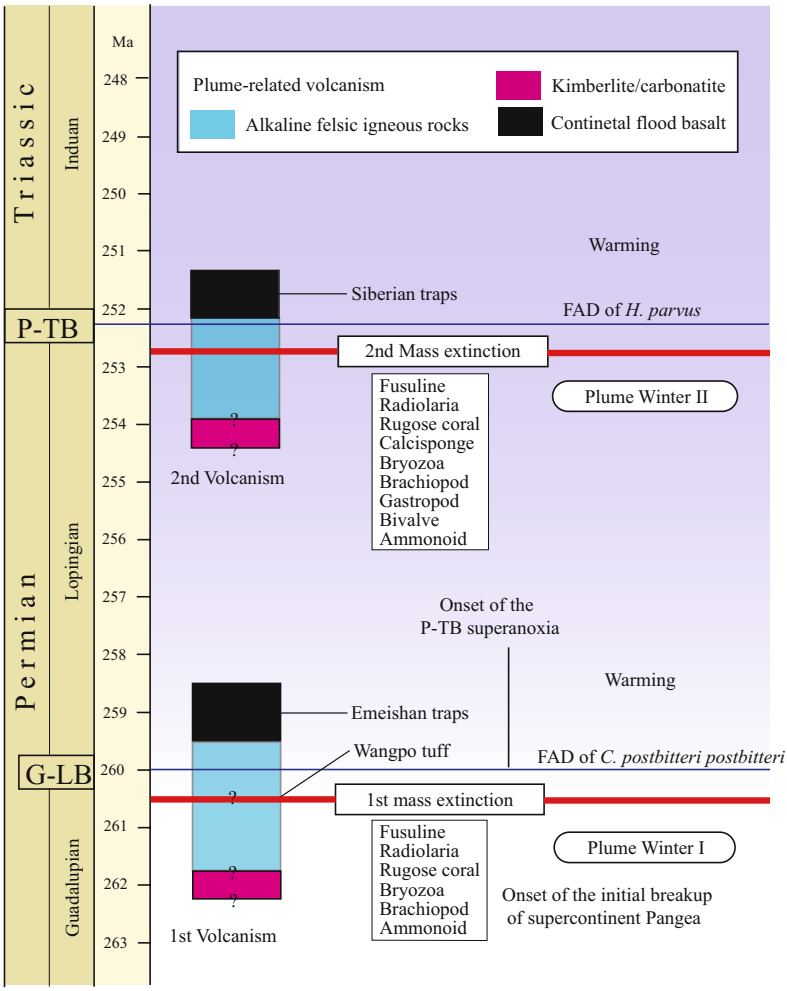

Figure 10. Schematic timetable of the end-Paleozoic global events with two episodes of "Plume Winter". The double-phased mass extinction corresponds to the double-phased plume-generated explosive volcanism of alkaline nature. Each event was large enough to change the surface environment and to terminate various animals on land and in sea; nonetheless, the greatest magnitude of the terminal Paleozoic extinction was achieved by two "Plume Winter" episodes occurring within a relatively short time interval (less than 10 million years) that did not allow full biotic recovery after the first event. Note that the mass extinction predated the CFB volcanism in both the G-LB and P-TB cases.

1999). A short-term cool period was newly detected by stable carbon isotope analysis of marine carbonates in uppermost Middle Permian atoll limestone in the low latitude domain of Panthalassa (Isozaki et al., 2007a) in accordance with the low sea-level, and this appears to have been coeval with the claimed "Plume Winter I".

On the other hand, the initial $^{87}Sr/^{86}Sr$ ratio also hit a low in the uppermost Middle Permian and started to rise rapidly and uni-directionally in the Late Permian and Triassic (Fig. 6; e.g., Veizer, 2003; McArthur & Howarth, 2004; Fukui et al., 2005). Low $^{87}Sr/^{86}Sr$ values of seawater usually suggest a high stand of sea-level due to lesser erosion on continents and resultant lesser flux of continental crust-derived material enriched with radiogenic ^{87}Sr into oceans. In this context, the low $^{87}Sr/^{86}Sr$ values and low sea-level detected around the G-LB apparently contradict each other. However, this probably reflects the unique paleogeography at the initial breakup of the supercontinent around the G-LB that has controlled the drainage systems on Pangea. During most of the Early-Middle Permian when major continental blocks merged, nearly a half of the pre-existing river systems became highly restricted within Pangea, losing direct passage to the superocean, and this resulted in lowering the seawater $^{87}Sr/^{86}Sr$ ratio to the Paleozoic minimum (Fig. 6). In turn, the plume-driven initial rifting of Pangea around the G-LB gave rise to rift-related new drainage systems connected to the superocean for the first time since the mid-Carboniferous, and this forced the $^{87}Sr/^{86}Sr$ ratio of the global seawater to start increasing.

Moreover, it is also worth noting that the magnetostratigraphic records demonstrate a clear mode change around the basal Capitanian (ca. 265 Ma; Late Guadalupian) immediately before the G-LB, from the long-term Kiaman Reverse superchron (throughout the Late Carboniferous and Early-Middle Permian) to the Permian-Triassic Mixed superchron with frequent polarity change (in the Late Permian and Early Triassic) (Fig. 11; Haag and Heller, 1991; Heller et al., 1995; Jin et al., 1997; Gradstein et al., 2004). This remarkable change called the Illawarra Reversal (Menning, 2000) probably reflects the appearance of thermal instability at the 2900 km-deep mantle/core boundary after a 60-m.y. long stable period, probably by the landing of a cold megalith (= cold plume or chunk of subducted slabs) onto the mantle/core boundary (Fig. 8). This may have affected the state of geodynamo by heat transfer from the core and initiated a superplume. The time lag between the Illawarra Reversal and the G-LB event is ca. 5 million years or less according to the timescale of Gradstein et al. (2004), and this may represent the travel time of a plume head from the lower mantle to the upper mantle above the 660 km-deep discontinuity. Judging from an estimated ascending rate of a mantle plume (several 10 cm/year), this time lag appears reasonable on the order of magnitude (M. Ogawa, personal communication). In contrast, the secondary plumes that affected the biosphere twice (at the G-LB and P-TB) were originated from the mantle transition zone (ca. 400–660 km deep) and did not cause any significant change on the core/mantle boundary and of the geodynamo in the outer core (Fig. 11).

This "Plume Winter" scenario (Figs. 8, 9) can thus reasonably explain not only the three major geological phenomena 1) the greatest mass extinction, 2) superanoxia, and 3) breakup of a supercontinent that occurred uniquely at the Paleozoic-Mesozoic transition (Fig. 1) but also the long-term changes in sea level, seawater $^{87}Sr/^{86}Sr$ ratio, and geomagnetic field behavior (Figs. 6, 11).

After the second episode (Plume Winter II), the accumulated atmospheric CO_2 and additional methane from clathrates may explain the global warming and sea-level

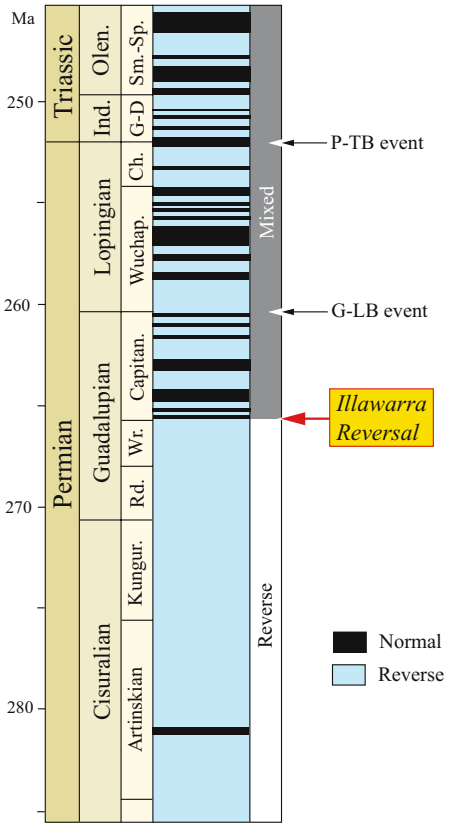

Figure 11. Geomagnetic field behavior in the Permian to Early Triassic and its possible link to the mass extinction events at the P-TB and G-LB (modified from Gradstein et al., 2004). A major change in geomagnetic filed behavior (Illawarra Reversal) occurred in the early Capitanian (Late Guadalupian) immediately before the G-LB event, from the long-term Kiaman Reverse superchron to the Permian-Triassic Mixed superchron with frequent fluctuation. This represents the most prominent marker in magnetostratigraphic correlation of the Late Paleozoic, suggesting that a cold megalith landed on the mantle/core boundary and a superplume was launched from the lower mantle in association with instability at the mantle/core boundary, changing the mode of geodynamo. The time lag between the Illawarra Reversal and the G-LB extinction event (ca. 5 million years or less) may represent a travel time of a superplume from the lower to upper mantle.

rise in the Early Triassic (e.g., Retallack, 1999; Hallam and Wignall, 1999). The global warming by excess greenhouse CO_2 may have accelerated the environmental deterioration and drove the prolonged deep-sea anoxia (Isozaki, 1994) and delayed recovery of biospheric structure until the Middle Triassic (Bottjer, 2004; Stanley, 1988), however, all these occurred in the Early Triassic nearly 10 million years after the first event at the time of the G-LB, just representing the aftermath of the double-phased “Plume Winter” episode.

6 CONCLUSIONS

The breakup of the supercontinent Pangea gave rise to the opening of the Atlantic and Indian oceans. Plural plumes became activated successively in the latest Paleozoic to Early Mesozoic, and rifted apart the pre-existing continental lithosphere to accommodate space for the new oceans, and the rifted continental margins of which are marked by LIPs and radial dike swarms. All these plumes activated beneath Pangea, including those at G-LB and P-TB, probably represent secondary plumes that branched off from a superplume in the mantle transition zone (Maruyama, 1994). Judging from the analyses of modern-day topography of Africa and of global seismic tomography (e.g., Fukao et al., 1994; Zhao, 2007 this volume), the main superplume responsible for the breakup of Pangea was located beneath Africa. Thus the G-LB and P-TB plumes mark the first impingement of the African superplume beneath the Pangean continental lithosphere. In addition to the widely known LIPs of Siberia, Emeishan and Panjal, more remnants of coeval branched plumes may be detected. It is noteworthy that the Late Permian LIPs were concentrated in the eastern half of Pangea, whereas the Triassic-Jurassic ones of CAMP domain in the western half (Fig. 5). This apparent shift of activity-center during a 100 million year interval may reflect a secular change in the behavior of the African superplume with respect to mantle heterogeneity or to change in plume geometry in the mantle transition zone.

This is in sharp contrast with the much older Pacific opening that occurred at nearly 700–750 Ma when the supercontinent Rodinia broke up (e.g., Hoffman, 1991; Dalziel, 1995). Remnants of this superplume can be recognized not only in the LIPs on former rifted continental margins but also in the modern southern Pacific, i.e., the Pacific superswell, over 2000 km in diameter, featuring plural hotspots (McNutt and Judge, 1990).

Thus with a long-term viewpoint, a major reorganization in mantle regime corresponds to the Wilson cycle in crustal plate tectonics. The Phanerozoic mantle regime is divided into two periods; earlier one controlled by the Pacific superplume and the later one by the African superplume, and these two correspond to the expanding period of the Pacific Ocean (late Neoproterozoic to Paleozoic) and that of the Atlantic–Indian ocean (Mesozoic to the present), respectively. In this context, the P-TB, previously recognized solely as a time of major reorganization of biota from the Paleozoic to the Mesozoic-Modern regime, in fact corresponds to the time of major re-organization of the mantle regime.

As summarized above, the end-Paleozoic mass extinction, i.e., the largest biospheric turnover in the Phanerozoic, occurred in the middle of global re-organization of the planet's interior. In the Precambrian, there should have been several major extinction events driven by similar causes; however, the rare occurrence of fossils, microbial remains in particular, has hampered detailed documentation of such unidentified cryptic extinction events. Nonetheless our curiosity is stimulated by the apparent coincidence in timing between the Neoproterozoic snowball Earth event (Kirschvink, 1992; Hoffman and Schrag, 2002) and the breakup of the supercontinent Rodinia (Hoffman, 1991), or that between the Paleoproterozoic snowball Earth

(Kirschvink et al., 2000) and the breakup of Neoarchean (super-)continent including Kenoria (Arctica) and/or Ur (e.g., Rogers and Santosh, 2004). A precise understanding of the Phanerozoic mass extinction events, in particular their cause–effect, will open a new window to look into the mysterious Precambrian biosphere and its evolution.

ACKNOWLEDGEMENTS

The author greatly appreciates constructive discussions with Shigenori Maruyama (Tokyo Inst. Tech.), Masaki Ogawa (Univ. Tokyo), language check by Brian Windley (Leicester Univ.), and help in drafting figures by Shio Watanabe.

REFERENCES

Ali, J.R., G.M. Thompson, X.Y. Song, and Y.L. Wang (2002) Emeishan basalts (SW China) and the 'end-Guadalupian' crisis: Magnetobiostratigraphic constraints. *J. Geol. Soc., London*, 159, 21–29.

Alvarez, W. (1997) *T. rex* and the Crater of Doom, Princeton Univ. Press, Princeton.

Basiliev, Y.R., and V.V. Zolotukhin (1995) The Maimecha-Kotui alkaline-ultramafic province of the northern Siberian platform, Russia. *Episodes*, 18, 155–164.

Basu, A.R., R.J. Poreda, P.R. Renne, F. Teichmann, Y.R. Vasiliev, N.V. Sobolev, and B.D. Turrin (1995) High-^{3}He plume origin and temporal-spatial evolution of the Siberian flood basalts. *Science*, 269, 822–825.

Baud, A., M. Magaritz, and W.T. Holser (1989) Permian-Triassic of the Tethys: Carbon isotope studies. *Geol. Rundschau*, 78, 649–677.

Becker, L., R.J. Poreda, A.R. Basu, K.O. Pope, T.M. Harrison, C. Nicholson, and R. Iasky (2004) Bedout: A possible end-Permian impact crater offshore of northwestern Australia. *Science*, 304, 1469–1474.

Becker, L., R.J. Poreda, A.G. Hunt, T.E. Bunch, and M. Rampino (2001) Impact event at the Permian-Triassic boundary: Evidence from extraterrestrial noble gases in fulleranes. *Science*, 291, 1530–1533.

Bell, K. (1989) Carbonatites: Genesis and Evolution, Unwin Hyman, London.

Bell, K. (2001) Carbonatites: Relationships to mantle-plume activity. In Ernst, R.E., and K.L. Buchan (eds.) Mantle Plumes: Their Identification Through Time, *Geol. Soc. Am. Special Paper*, 352, pp. 267–290.

Benton, M.J. (1985) Mass extinction of non-marine tetrapods. *Nature*, 316, 811–814.

Bottjer, D. (2004) The beginning of the Mesozoic: 70 million years of environmental stress and extinction. In Taylor, P.D. (ed.) Extinctions in the History of Life, Cambridge Univ. Press, Cambridge, pp. 99–118.

Campbell, I., G.K. Czamanske, V.A. Fedorenko, R.I. Hill, and V. Stepanov (1992) Synchronism of the Siberian traps and the Permian-Triassic boundary. *Science*, 258, 1760–1763.

Chung, S.L., B.M. Jahn, G.Y. Wu, C.H. Lo, and B.L. Cong (1998) The Emeishan flood basalt in SW China: A mantle plume initiation model and its connection with continental breakup and mass extinction at the Permian-Triassic boundary. *Am. Geophys. Union Geodynamic Ser.*, 27, 47–58.

Cirilli, S., C.P. Radrizzani, M. Ponton, and S. Radrizzani (1998) Stratigraphical and palaeoenvironmental analysis of the Permian-Triassic transition in the Badia Valley (Southern Alps, Italy). *Paleogeogr. Paleoclimat. Paleoecol.*, 138, 85–113.

Clark, D.L., C.Y. Wang, C.J. Orth, and J.S. Gilmore (1986) Conodont survival and low iridium abundances across the Permian-Triassic boundary in South China. *Science*, 233, 984–986.

Co-operative Geological Research Group of Japan and China in the Panxi Region (1986) Geology of the Panxi region, Sichuan province, southwest China, Yamaguchi Univ., Yamaguchi, 340p.

Courtillot, V.E. (1999) Evolutionary Catastrophe. The Science of Mass Extinction, Cambridge Univ. Press, Cambridge, 173p.

Dalziel, I. (1995) Earth before Pangea. *Scientific American*, 1995-1, 38–43.

Ernst, R.E., and K.L. Buchan (2003) Recognizing mantle plume and the geological record. *Ann. Rev. Earth Planet. Sci.*, 31, 469–523.

Erwin, D.H. (1993) The Great Paleozoic Crisis: Life and Death in the Permian. Columbia Univ. Press, New York, 327p.

Erwin, D.H., S.A. Bowring, and Y.G. Jin (2002) End-Permian mass extinctions: A review. *Geol. Soc. Amer. Spec. Pap.*, 356, 363–383.

Farley, K.A., P. Ward, G. Garrison, and S. Mukhopadhyay (2005) Absence of extraterrestrial ^{3}He in Permian-Triassic age sedimentary rocks. *Earth Planet. Sci. Lett.*, 240, 265–275.

Fukao, Y., S. Maruyama, M. Obayashi, and H. Inoue (1994) Geologic implication of the whole mantle P-wave tomography. *J. Geol. Soc. Jpn.*, 100, 4–23.

Fukui, M., T. Kani, H. Nohda, and Y. Isozaki (2005) Pb-Pb isochron age and Sr isotope study for the Middle-Upper Permian limestone in the Kamura area in Kyushu, Japan. Abst. Amer. Geophys. Union, V41F-1526.

Gradstein, F., J. Ogg, and A. Smith (2004) Geologic Timescale, Cambridge Univ. Press, Cambridge, 589p.

Grice, K., C. Cao, G.D. Love, M.E. Böttcher, R.J. Twitchett, E. Grosjean, R.E. Summons, S.C. Turgeon, W. Dunning, and Y.G. Jin (2005) Photic zone euxinia during the Permian-Triassic superanoxic event. *Science*, 307, 706–709.

Haag, M., and F. Heller (1991) Late Permian to Early Triassic magnetostratigraphy. *Earth Planet. Sci. Lett.*, 107, 42–54.

Hallam, A. (1992) Phanerozoic Sea-level Changes, Columbia Univ. Press, New York, 266p.

Hallam, A., and R. Wignall (1997) Mass Extinctions and their Aftermath, Oxford Univ. Press, Oxford, 320p.

Hallam, A., and P. Wignall (1999) Mass extinctions and sea-level changes. *Earth-Sci. Review*, 48, 217–250.

Heller, F., H.H. Chen, J. Dobson, and M. Haag (1995) Permian-Triassic magnetostratigraphy—new results from South China. *Phys. Earth Planet Inter.*, 89, 281–295.

Hoffman, P.F. (1991) Did the breakout of Laurentia turn Gondwanaland inside-out? *Science*, 252, 1409–1412.

Hoffman, P.F., and D.P. Schrag (2002) The snowball Earth hypothesis: Testing the limits of global change. *Terra Nova*, 14, 129–155.

Holser, W.T., H.P. Schönlaub, M. Attrep Jr., and 12 others (1989) A unique geochemical record at the Permian/Triassic boundary. *Nature*, 337 39–44.

Holser, W.T., and H.P. Schönlaub (eds.) (1991) The Permian-Triassic boundary in the Carnic Alps of Austria (Gartnerkofel region). *Abhandl. Geol. Bundesanst.*, 45, 1–232.

Hotinski, R.M., K.L. Bice, L.R. Kump, R.G. Najjar, and M.A. Arthur (2001) Ocean stagnation and end-Permian anoxia. *Geology*, 29, 7–10.

Iranian-Japanese Research Group (1981) The Permian and the Lower Triassic Systems in Abadeh region, central Iran. *Memoir, Fac. Sci. Kyoto Univ., ser. Geol. Mineral.*, 47(2) 61–133.

Isozaki, Y. (1994) Superanoxia across the Permo-Triassic boundary: Record in accreted deep-sea pelagic chert in Japan. In Embry, A.F., B. Beauchamp, and D.J. Glass (eds.) Pangea: Global Environments and Resources. *Mem. Canad. Soc. Petrol. Geol.* 17, 805–812.

Isozaki, Y. (1996) P-T Boundary Superanoxia and oceanic stratification in Panthalassa. In Noda, H., and K. Sashida (eds.) Prof. H. Igo Commemorative Volume on Geology and Paleontology of Japan and Southeast Asia. Gakujutu-Tosho Publ., Tokyo 29–41.

Isozaki, Y. (1997) Permo-Triassic boundary superanoxia and stratified superocean: Records from lost deep sea. *Science*, 276, 235–238.

Isozaki, Y. (2000) Plume winter: A scenario for the greatest biosphere catastrophe across the Permo-Triassic boundary. Abstr. 31th Int. Geol. Congr., 1.9–16.

Isozaki, Y. (2001) An extraterrestrial impact at the Permian-Triassic boundary? *Science*, 293, 2343a.

Isozaki, Y. (2001) Plume Winter scenario for the Permo-Triassic boundary mass extinction. *PaleoBios* 21 (Supplement no. 2) 70–71.

Isozaki, Y. (2007) Guadalupian-Lopingian boundary event in mid-Panthalassa: Correlation of accreted deep-sea chert and mid-oceanic atoll carbonate. In T. Wong (ed.), Proc. XVIth Congress of Carboniferous and Permian stratigraphy in Utrecht 2003, 21–34, Royal. Netherlands National Academy of Arts and Sciences, Amsterdam.

Isozaki, Y., H. Kawahata, and A. Ota (2007a) A unique carbon isotope record across the Guadalupian-Lopingian (Middle-Upper Permian) boundary in mid-oceanic paleoatoll carbonates: The high-productivity "Kamura event" and its collapse in mid-superocean. *Global Planetary Change*, 55, 21–38.

Isozaki, Y., S. Maruyama, and F. Furuoka (1990) Accreted oceanic material in Japan. *Tectonophysics*, 181, 179–205.

Isozaki, Y., and A. Ota (2001) Middle/Upper Permian (Maokouan/Wuchiapingian) boundary in mid-oceanic paleo-atoll limestone in Kamura and Akasaka, Japan. *Proc. Japan Acad.*, 77B, 104–109.

Isozaki, Y., N. Shimizu, J.X. Yao, Z.S. Ji, and T. Matsuda (2007b) End-Permian extinction and volcanism-induced environmental stress: The Permian-Triassic boundary interval of lower-slope facies at Chaotian, South China. *Paleogeogr. Paleoclim. Paleoecol.*, in press.

Isozaki, Y., J.X. Yao, T. Matsuda, H. Sakai, Z.S. Ji, N. Shimizu, N. Kobayashi, H. Kawahata, H. Nishi, M. Takano, and T. Kubo (2004) Stratigraphy of the Middle-Upper Permian and lowermost Triassic at Chaotian, Sichuan, China. *Proc. Japan Acad.*, 80B, 10–16.

Jin, Y.G., Y. Wang, W. Wang, Q.H. Shang, C.Q. Cao, and D.H. Erwin (2000) Pattern of marine mass extinction near the Permian-Triassic boundary in South China. *Science*, 289, 432–436.

Jin, Y.G., B.R. Wardlaw, B.F. Glenister, and G.V. Kotlyar (1997) Permian chronostratigraphic subdivisions. *Episodes*, 20, 10–15.

Jin, Y.G., J. Zhang, and Q.H. Shang (1994) Two phases of the end-Permian mass extinction. In Embry, A.F., B. Beauchamp, and D.J. Glass (eds.) Pangea: Global Environments and Resources. *Mem. Canad. Soc. Petrol. Geol.*, 17, 813–822.

Kaiho, K., Y. Kajiwara, T. Nakano, Y. Miura, H. Kawahata, K. Tazaki, M. Ueshima, Z.Q. Chen, and G.R. Shi (2001) End-Permian catastrophe by a bolide impact: Evidence of a gigantic release of sulfur from the mantle. *Geology*, 29, 815–818.

Kajiwara, Y., S. Yamakita, K. Ishida, H. Ishiga, and A. Imai (1994) Development of a largely anoxic stratified ocean and its temporary massive mixing at the Permian/Triassic boundary supported by the sulfur isotopic record. *Paleogeogr. Paleoclim. Paleoecol.*, 111, 367–379.

Kakuwa, Y. (1996) Permian-Triassic mass extinction event recorded in bedded chert sequence in southwest Japan. *Paleogeogr. Paleoclim. Paleoecol.*, 121, 35–51.

Kamo, S.L., G.K. Czamanske, Y. Amelin, V.A. Fedorenko, D.W. Davis, and V.R. Trofimov (2003) Rapid eruption of Siberian flood-volcanic rocks and evidence for coincidence with the Permian-Triassic boundary and mass extinction at 251 Ma. *Earth Planet. Sci. Lett.*, 214, 75–91.

Kato, Y., K. Nakao, and Y. Isozaki (2002) Geochemistry of Late Permian to Early Triassic pelagic cherts from southwest Japan: Implications for an oceanic redox change. *Chem. Geol.*, 182, 15–34.

Kirschvink, J.L. (1992) Late Proterozoic low-latitude global glaciation: The Snowball Earth. In Schopf, J.W., and C. Klein (eds.) The Proterozoic Biosphere, Cambridge Univ. Press, Cambridge, pp. 51–52.

Kirschvink, J.L., E.J. Gaidos, L.E. Bertani, N.J. Beukes, J. Gutzmer, L.N. Maepa, and R.E. Steinberger (2000) Paleoproterozoic Snowball Earth: Extreme climatic and geochemical global change and its biological consequences. *Proc. Natl. Acad. Sci., USA*, 97, 1400–1405.

Knoll, A.H., R.K. Bambach, D.E. Canfield, and J.P. Grotzinger (1996) Comparative Earth history and Late Permian mass extinction. *Science*, 273, 452–457.

Koeberl, C., I. Gilmour, W.U. Reimond, P. Claeys, and B. Ivanov (2002) End-Permian catastrophe by bolide impact: Evidence of a gigantic release of sulfur from the mantle: Comment and reply. *Geology*, 30, 855–856.

Koike, T. (1996) The first occurrence of Griesbachian conodonts in Japan. *Trans. Palaeont. Soc. Japan, New Series*, 181, 337–346.

Kozur, H. (1998) Some aspects of the Permian-Triassic boundary (PTB) and of the possible causes for the biotic crisis around this boundary. *Palaeogeogr. Palaeoclim. Palaeoecol.*, 143, 227–272.

Labandeira, C.C., and J.J. Sepkoski (1992) Insect diversity in the fossil record. *Science*, 261, 310–315.

Le Maitre, R.W. (1975) Volcanic rocks from EDEL no. 1 petroleum exploration well, offshore Carnavon basin, Western Australia. *J. Geol. Soc. Australia*, 22, 167–174.

Li, Z.S., L.P. Zhan, J.Y. Dai, R.G. Jin, X.F. Zhu, J.H. Zhang, H.Q. Huang, D.Y. Xu, Z. Yan, and H.M. Li (1997) Study on the Permian-Triassic Biostratigraphy and Event Stratigraphy of Northern

Sichuan and Southern Shaanxi. Geological Publishing House, Beijing (1989) 435p. (in Chinese with English abstract).

Li, Z.S., L.P. Zhan, J.X. Yao, and Y.Q. Zhou (1991) On the Permian-Triassic events in South China—probe into the end-Permian abrupt extinction and its possible causes. *Proc. Shallow Tethys (Sendai)*, 3, 371–385.

Lo, C.H., S.L. Chung, T.Y. Lee, and G.Y. Wu (2002) Age of the Emeishan flood magmatism and relations to Permian-Triassic boundary events. *Earth Planet. Sci. Lett.*, 198, 449–458.

Looy, C.V., R.J. Twitchett, D.L. Dilcher, J.H.A. van Konijinenburg-van Cittert, and H. Visscher (2001) Life in the end-Permian dead zone. *Proc. Nat. Acad. Sci. USA*, 98, 7879–7883.

Lu, Y.H. (1956) The Permian of Liangshan and its bearing on the classification and correlation of the Permian rocks of South China. *Scientia Sinica*, 5, 733–761.

MacLeod, K.G., R.M.H. Smith, P.L. Koch, and P.D. Ward (2000) Timing of mammal-like reptile extinctions across the Permian-Triassic boundary in South Africa. *Geology*, 28, 227–230.

Maruyama, S. (1994) Plume tectonics. *J. Geol. Soc. Jpn.*, 100, 24–49.

Marzoli, A., P.R. Renne, E.M. Piccirillo, M. Ernesto, G. Bellieni, and A. De Min (1999) Extensive 200 million-year-old continental flood basalts of the Central Atlantic Magmatic Province. *Science*, 284, 616–618.

Matsuo, M., K. Kubo, and Y. Isozaki (2003) Mössbauer spectroscopic study on characterization of iron in the Permian to Triassic deep-sea chert from Japan. *Hyperfine Interact. (C)*, 5, 435–438.

McArthur, J.M., and R.J. Howarth (2004) Strontium isotope stratigraphy. In Gradstein, F., J. Ogg, and A. Smith (eds.) Geologic Timescale, 2004. Cambridge Univ. Press, Cambridge, pp. 96–105.

McNutt, M.K., A.V. Judge (1990) The superswell and mantle dynamics beneath the South Pacific. *Science*, 248, 969–975.

Menning, M. (2000) Magnetostratigraphic results from the Middle Permian Type section, Guadalupe mountains, West Texas. *Permophiles*, 37, 16.

Mitchell, R.H. (1991) Kimberlites and lamproites: Primary sources of diamond. *Geosci. Canada*, 18, 1–16.

Morgan, J.P., T.J. Reston, and C.R. Ranero (2004) Contemporaneous mass extinctions, continental flood basalts, and 'impact signals': Are mantle plume-induced lithospheric gas explosions the causal link? *Earth Planet. Sci. Lett.*, 217, 263–284.

Mundil, R., K.R. Ludwig, I. Metcalf, and P. Renne (2004) Age and timing of the Permian mass extinction. *Science*, 305, 1760–1763.

Musashi, M., Y. Isozaki, T. Koike, and R. Kreulen (2001) Stable carbon isotope signature in mid-Panthalassa shallow-water carbonates across the Permo-Triassic boundary: Evidence for ^{13}C-depleted ocean. *Earth Planet. Sci. Lett.*, 196, 9–20.

Neumann, E.R., K.H. Olsen, W.S. Baldridge, and B. Sundvoll (1992) The Oslo rift: A review. *Tectonophysics*, 208, 1–18.

Nishimura, Y., T. Itaya, Y. Isozaki, and A. Kameya (1989) Depositional age and metamorphic history of 220 Ma high P/T type metamorphic rocks: An example of the Niishiki-cho area, Yamaguchi prefecture, Southwest Japan. *Mem. Geol. Soc. Jpn.*, 33, 143–166 (in Japanese with English abstract).

Ota, A., and Y. Isozaki (2006) Fusuline biotic turnover across the Guadalupian-Lopingian (Middle-Upper Permian) boundary in mid-oceanic carbonate buildups: Biostratigraphy of accreted limestone in Japan. *J. Asian Earth Sci.*, 26, 353–368.

Pakistani-Japanese Research Group Permian and Triassic Systems in the Salt Range and Surghar Range Pakistan (1985). In Nakazawa, K., and J.M. Dickins (eds.) The Tethys: Her Paleogeography and Paleobiogeography from Paleozoic to Mesozoic, Tokai Univ. Press, Tokyo, pp. 221–312.

Rabu, D., J. Le Metour, F. Bechennec, M. Beurrier, M. Villey, and C. Bourdillon-Jeudy de Grissac (1990) Sedimentary aspects of the Eo-Alpine cycle on the northeast edge of the Arabian Platform (Oman Mountains). In Robertson, A.H.F., M.P. Searle, and A.C. Ries (eds.) The Geology and Tectonics of the Oman Region. *Geol. Soc. Spec. Publ.*, 49, 49–68.

Racki, G., and P. Wignall (2005) Late Permian double-phased mass extinction and volcanism: An oceanographic perspective. In Over, D.J., J.R. Morrow, and P.B. Wignall (eds.) Understanding Late Devonian

and Permian-Triassic Biotic and Climatic Events: Towards an Integrated Approach, Cambridge Univ. Press, Cambridge, pp. 263–297.

Reichow, M.K., A.D. Saunders, R.V. White, M.S. Pringle, A.I. Al'Mukhamedov, A. Medvedev, and N. Korda (2002) $^{40}Ar/^{39}Ar$ dates from the West Siberian Basin: Siberian flood basalt province doubled. *Science*, 296, 1846–1849.

Renne, P.R., and A.R. Basu (1991) Rapid eruption of the Siberian Traps flood basalts at the Permo-Triassic boundary. *Science*, 253, 176–179.

Renne, P.R., H.J. Melosh, K. Farley, W.U. Reimold, C. Loeberl, M.R. Rampino, S.P. Kelly, and B.A. Ivanov (2004) Is Bedout an impact crater? Take 2. *Science*, 306, 610–611.

Retallack, G.J. (1999) Postapocalyptic greenhouse paleoclimate revealed by earliest Triassic paleosols in the Sydney Basin, Australia. *Geol. Soc. Amer. Bull.*, 111, 52–70.

Retallack, G.J., R.M.H. Smith, and P.D. Ward (2003) Vertebrate extinction across Permian-Triassic boundary in Karoo Basin, South Africa. *Geol Soc. Amer. Bull.*, 115, 1133–1152.

Rogers, J.J.W., and M. Santosh (2004) Continents and Supercontinents. Oxford Univ. Press, Oxford, 289p.

Saunders, A.D., R.W. England, M.K. Reichow, and R.V. White (2005) A mantle plume origin for the Siberian traps: Uplift and extension in the West Siberian basin, Russia. *Lithos*, 79, 407–424.

Schopf, T.J.M. (1974) Permo-Triassic extinctions: Relation to sea-floor spreading. *J. Geol.*, 82, 129–143.

Schubert, J.K., and D.J. Bottjer (1992) Early Triassic stromatolites as post-mass extinction disaster forms. *Geology*, 20, 883–886.

Schubert, J.K., and D.J. Bottjer (1992) Aftermath of the Permian-Triassic mass extinction event: Paleoecology of Lower Triassic carbonates in the western USA. *Paleogeogr. Paleoclim. Paleoecol.*, 116, 1–39.

Scotese, C.R., and R.P. Langford (1995) Pangea and the Paleogeography of the Permian. In Scholle, A., T.M. Peryt, and D.A. Ulmer-Scholle (eds.) The Permian of Northern Pangea, Vol. 1, Springer, Berlin, pp. 3–19.

Sepkoski, Jr., J.J. (1984) A kinetic model of Phanerozoic taxonomic diversity. III. Post-Paleozoic families and mass extinctions. *Paleobiology*, 10, 246–267.

Sorensen, H. (1974) The Alkaline Rocks, Wiley, London, 622p.

Stanley, Jr., G.D. (1988) The history of early Mesozoic reef communities: A three step process. *Palaios*, 3, 170–183.

Stanley, S.M., and X. Yang (1995) A double mass extinction at the end of the Paleozoic era. *Science*, 266, 1340–1344.

Suzuki, N., K. Ishida, Y. Shinomiya, and H. Ishiga (1998) High productivity in the earliest Triassic ocean: Black shales, southwest Japan. *Paleogeogr. Paleoclim. Paleoecol.*, 141, 53–65.

Takemura, A., M. Sakai, S. Yamakita, and 15 others (2003) Early Triassic radiolarians from Arrow Rocks in the Waipapa terrane, Northern Island, New Zealand. Abstr. InterRad, Univ. Lausanne, 64.

Thomas, B.M., R.J. Willink, K. Grice, R.J. Twitchett, R.R. Purcell, N.W. Archbold, A.D. George, S. Tye, R. Alexander, C.B. Fostre, and C.J. Barber (2004) A unique Permian-Triassic boundary section from Western Australia. *Austral. J. Earth Sci.*, 51, 423–431.

Tong, J.N., H.F. Yin, and K.X. Zhang (1999) Permian and Triassic sequence stratigraphy and sea level changes of eastern Yangtze platform. *J. China Univ. Geosci.*, 10, 161–169.

Twitchett, R.J. (1999) Paleoenvironments and faunal recovery after the end-Permian mass extinction. *Paleogeogr. Paleoclim. Paleoecol.*, 154, 27–37.

Valentine, J.W., and E.M. Moores (1970) Plate-tectonic regulation of faunal diversity and sea level: A model. *Nature*, 228, 657–659.

Veevers, J.J., and R.C. Tewali (1995) Permian-Carboniferous and Permian-Triassic magmatism in the rift zone bordering the Tethyan margin of southern Pangea. *Geology*, 23, 467–470.

Veizer, J. (2003) Isotopic evolution of seawater on geological time scales: Sedimentological perspective. In Lentz, D.R. (ed.) Geochemistry of sediments and sedimentary rocks. *Geol. Assoc. Canada, GeoText*, 4, 53–68.

Visscher, H., H. Brinkhuis, D.L. Dilcher, W.C. Elsik, Y. Eshet, C. Looy, M.R. Rampino, and A. Traverse (1996) The terminal Paleozoic fungal event: Evidence of terrestrial ecosystem destabilization and collapse. *Proc. Nat. Acad. Sci. USA*, 93, 2155–2158.

Wignall, P. (2001) Large igneous provinces and mass extinctions. *Earth-Sci. Review*, 53, 1–33.

Wignall, P., and A. Hallam (1992) Anoxia as a cause of the Permian/Triassic mass extinction: Facies evidence from northern Italy and the western United States. *Palaeogeogr. Palaeoclim. Palaeoecol.*, 93, 21–46.

Wignall, P., B. Thomas, R. Willink, and J. Watling (2004) Is Bedout an impact crater? Take 1. *Science*, 306, 609–610.

Wignall, P., and R. Twitchett (2002) Extent, duration and nature of the Permian-Triassic superanoxic event. *Geol. Soc. Amer. Spec. Pap.*, 356, 395–413.

Woods, A.D., D.J. Bottjer, M. Mutti, and J. Morrison (1999) Lower Triassic large sea-floor carbonate cements: Their origin and a mechanism for the prolonged biotic recovery from the end-Permian mass extinction. *Geology*, 27, 645–648.

Xia, W.C., N. Zhang, G.Q. Wang, and Y. Kakuwa (2004) Pelagic radiolarian and conodont biozonation in the Permo-Triassic boundary interval and correlation to the Meishan GSSP. *Micropaleontology*, 50(1), 27–44.

Xu, Y.G., S.L. Chung, B.M. Jahn, and G.Y. Wu (2001) Petrologic and geochemical constraints on the petrogenesis of Permian–Triassic Emeishan flood basalts in southwestern China. *Lithos*, 58, 145–168.

Yamakita, S., N. Kadota, T. Kato, R. Tada, S. Ogihara, E. Tajika, and Y. Hamada (1999) Confirmation of the Permian/Triassic boundary in deep-sea sedimentary rocks; earliest Triassic conodonts from black carbonaceous claystone of the Ubara section in the Tamba belt, Southwest Japan. *J. Geol. Soc. Jpn.*, 105, 895–898.

Yang, Z.M., and A. Woolley (2006) Carbonatites in China: A review. *J. Asian Earth Sci.*, 27, 559–575.

Yang, Z.Y., S.B. Wu, H.F. Yin, G.R. Xu, and K.X. Zhang (1991) Permo-Triassic events of South China. *Geol. Publ. House*, Beijing (in Chinese with English abstract).

Yin, H.F. (ed.) (1996) The Palaeozoic-Mesozoic boundary: Candidate of the Global Stratotype Section and Point of the Permian-Triassic Boundary, China Univ. Geosci. Press, Wuhan, 137p.

Yin, H.F., S.J. Huang, K.X. Zhang, H.J. Hansen, F.Q. Yang, M.H. Ding, and X.M. Bie (1993) The effect of volcanism on the Permo-Triassic mass extinction in South China. In Sweet, W.C., Z.Y. Yang, J.M. Dickins, and H.F. Yin (eds.) Permo-Triassic events in the eastern Tethys, Cambridge Univ. Press, Cambridge, pp. 146–157.

Yin, H.F., K.X. Zhang, J.N. Tong, Z.Y. Yang, and S.B. Wu (2001) The global stratotype section and point (GSSP) of the Permian-Triassic boundary. *Episodes*, 24, 102–114.

Zakharov, Y.D., G.V. Kotlyar, and A.V. Oleinikov (1995) Late Dorashamian (Late Changxingian) invertberates of the Far East and Permian to Triassic volcanism in the western Circumpacific. *Geol. Pacific Ocean*, 12, 47–60.

Zhao, D.P. (2007) Multiscale seismic tomography of mantle plumes. In Yuen, D.A., S. Maruyama, S. Karato, and B.F. Windley (eds.) Superplumes: Beyond Plate Tectonics, Springer, Dordrecht, pp. 7–30.

Zhao, J.K., J.Z. Sheng, Z.Q. Yao, X.L. Liang, C.Z. Chen, L. Rui, and Z.T. Liao (1981) The Changhsingian and Permian-Triassic boundary of South China. *Bull. Nanjing Inst. Geol. Paleont., Acad. Sinica*, 2, 1–85 (in Chinese with English abstract).

Zhou, L., and F.T. Kyte (1988) The Permian-Triassic boundary event: A geochemical study of three Chinese sections. *Earth Planet. Sci. Lett.*, 90, 411–421.

Zhou, M.F., J. Malpas, X.Y. Song, and 5 others (2002) A temporal link between the Emeishan large igneous province (SW China) and the end-Guadalupian mass extinction. *Earth Planet. Sci. Lett.*, 196, 113–122.

CHAPTER 15

DYNAMICS OF PLUMES AND SUPERPLUMES THROUGH TIME

SHIGENORI MARUYAMA[1], DAVID A. YUEN[2], AND BRIAN F. WINDLEY[3]

[1]*Department of Earth and Planetary Sciences, Tokyo Institute of Technology, O-okayama 2-12-1, Tokyo, Japan;*
E-mail: smaruyam@geo.titech.ac.jp

[2]*Department of Geology and Geophysics and Minnesota Supercomputing Institute, Univ. Minnesota, Minneapolis, Minnesota 55455, USA*

[3]*Department of Geology, University of Leicester, Leicester, UK*

Abstract

The thermal structure of the solid Earth was estimated from the phase diagrams of MORB and pyrolite combined with seismic discontinuity planes at 410–660 km, thickness of the D″ layers, and distribution of the ultra-low velocity zone (ULVZ). The result clearly shows the presence of two major superplumes and one cold super-downwelling. A temperature difference at the core-mantle boundary layer reaches an average of 1500 K, strongly indicating that the driving force of mantle convection is core heat that generates superplumes as a main engine to drive the mantle dynamics. Superplumes cause the breakup of supercontinents and control plate tectonics, until subduction zones develop at the ocean margins.

The major driving force of whole Earth dynamics is derived from a superplume that transports core heat to planetary space. Plume tectonics dominates in the mantle, except for the uppermost part where plate tectonics operates, but only independently if a slab-pull force is generated.

Comparison of the thermal structure combined with seismic tomography under the western Pacific, Asia, Africa, and the Pacific leads us to speculate on the mechanism of the formation of a superplume. A mantle made extremely cold by extensive subduction during the formation of a supercontinent is transformed into the hottest mantle triggered by the exothermic reaction of perovskite to post-perovskite (pPV) underneath the supercontinent over several 100 million years. The fuel to develop a superplume is recycled MORB at the CMB that partially melts to sink down to form an anti-crust and a buoyant andesitic restite to promote a rising plume. When all recycled MORB slabs are spent, it is the time of the demise of a superplume.

We propose here that mantle dynamics evolved from double-layer convection in the Archean to episodic whole mantle convection thereafter. This change was due to the widespread occurrence of majorite (Mj) instead of ringwoodite in the MBL in the Archean and *vice versa* thereafter. During the transition period mantle overturn occurred at 2.8–2.7 Ga, and probably at 2.3 Ga, when pPV was born at the CMB to initiate a new superplume-supercontinent cycle that lasted until now. The return-flow by the subduction of seawater into the mantle began at 0.75 Ga causing the sea-level to drop. Through the

D. A. Yuen et al. (eds.), Superplumes, 441–502.
© 2007 *Springer.*

extensive surface erosion of the continental landmass, the surface environment of the Earth drastically changed making it possible that the large multi-cellular animals appeared to evolve in the Phanerozoic.

1 INTRODUCTION

In spite of the remarkable progress in understanding mantle dynamics by seismic tomography (Dziewonski, 1984; Fukao, 1992; Fukao et al., 1994; van der Hilst et al., 1997; Grand et al., 1997), the presence or absence of superplumes is still debated. However, recent investigations by more than eight different groups of researchers have confirmed their existence (see summary by Zhao, 2007 this issue).

An ULVZ, in which there is a 30% reduction of S-wave velocity, occurs locally in the central bottom portion of the superplume, whereas it is absent in the colder circum-Pacific and Tethyan D″ layers (Garnero and Helmberger, 1998; Garnero, 2004; Garnero et al., 2007 this issue). As a result of experimental documentation of the stable occurrence of pPV at CMB depth range (Murakami et al., 2004), the velocity jump at the top of the D″ layer can be interpreted as a phase change from PV to pPV (e.g., Nakagawa and Tackley, 2004a,b; Matyska and Yuen, 2005). Moreover, the anisotropy of the D″ layer can be explained by the elastic properties of pPV (e.g., Oganov and Ono, 2004; Wentzcovitch et al., 2006).

The margin of a superplume may be defined precisely by a steep lateral velocity gradient (Ni et al., 2002; To et al., 2006). The thickness of the D″ layer can be mapped regionally (Wysession et al., 1998), and the top and bottom boundaries of the D″ layer have been measured seismologically, e.g., the positive and negative velocity jumps respectively (Hernlund et al., 2005), which may be related to the stability relations of pPV to PV at the CMB (Murakami et al., 2004; Ono and Oganov, 2005). Moreover, improved S- and P-wave tomographic images specifically right above the CMB are now available, and the seismic definition of superplume seems to be settled (Romanowicz and Gun, 2002; Zhao, 2004).

The geophysical structure of the mantle reflects the composition and thermal state of the Earth. The phase diagrams of MORB and pyrolite mantle have recently been completed over the whole mantle depth. Applying these to seismic observations promotes our understanding of solid Earth dynamics.

We summarize all these findings in order to develop a self-consistent model for the thermal history of the solid Earth. Combining recent research progress on subduction history with seismic tomographic images above the CMB, we propose a mechanism of the formation of a superplume. Superplume, supercontinent and pPV are all key components of the Earth (Maruyama et al., 2007).

Present-day mantle dynamics do not behave as they did in the past, because of an ancient higher mantle temperature, lower viscosity, absence of post-perovskite, widespread occurrence of majorite, and a thin layer of ringwoodite. Finally, we review

Table 1. Acronyms used in the text and figures

DAC	Diamond anvil cell
WPTZ	Western Pacific triangular zone
MBL	Mantle boundary layer or mid-mantle boundary layer
CMB	Core-mantle boundary
ICB	Inner core boundary
ULVZ	Ultra-low velocity zone
MORB	Mid-oceanic ridge basalt
AMORB	Archean mid-oceanic ridge basalt
OIB	Ocean island basalt
BABB	Back arc basin basalt
TTG	Tonalite-trondhjemite-granodiorite
EPR	East Pacific rise
LILE	Large ion lithophile elements
REE	Rare earth element
CAS	CaAl-rich silicate
Pv	Perovskite
pPV	Post-perovskite
Ca-Pev	Calcium perovskite
Mg-Pv	Magnesium perovskite
Mj	Majorite
Mw	Magnesio- wüstite
RRR	Ridge-ridge-ridge triple junction

the recent data on these topics, and use them to build a speculative and evolutionary model of mantle dynamics through time.

Abbreviations used in this paper are summarized in Table 1.

2 PHASE DIAGRAMS OF MORB AND PYROLITE

The MORB and Pyrolite systems have recently been well-investigated over a wide P-T range, especially due to the development of multi-anvil and DAC (diamond anvil cell) facilities that cover almost the entire region of the mantle from top to bottom. Figure 1 summarizes the critical reactions, indicating those that define the mid-mantle boundary layer (MBL) and the D″ layer, and it also shows the solidus for MORB and pyrolite.

The pressure scale remains unsolved for the ultrahigh-pressure regions, and thus there is a continuous debate about the resolution. However, the Earth itself serves as a potential pressure scale. The 660 km depth temperature is fixed at 1600°C, as an adiabatic extrapolation from the MORB potential temperature (McKenzie and Bickle, 1988). The temperature of the CMB depth is assumed to be ca. 3800 K, because of the presence of partial melts, presumably derived from recycled MORB rather than from the slab peridotite which has a solidus that is 200 K higher than that of MORB (Fig. 1). Another constraint of the CMB temperature is an adiabatic extrapolation from the inner core/outer core boundary that indicates a temperature at the CMB of ca. 4000 K (Anderson, 2003). This value may be lower by 500 degrees, because

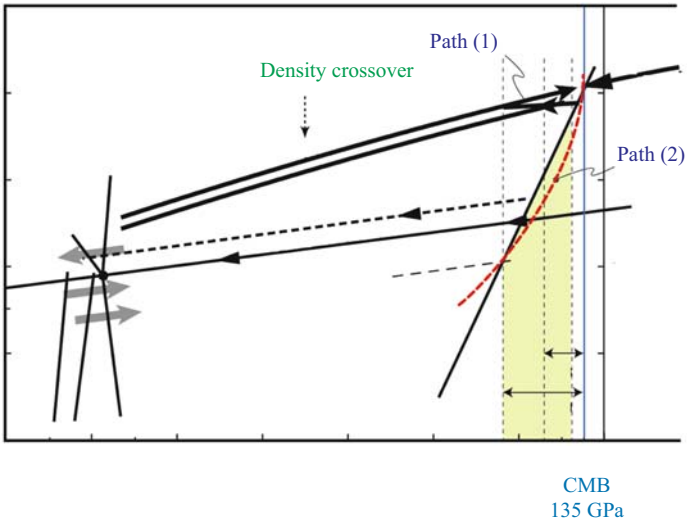

Figure 1. Phase diagrams of MORB and pyrolite compiled after Hirose et al. (1999), Hirose and Fei (2002), Hirose (2002, 2007), and Murakami et al. (2004). Adiabats of modern MORB, Archean MORB (AMORB) and the core are shown. Note the narrow stability field of majorite in the MgO-FeO-SiO_2 system. Path (1) shows that an adiabatic-rising plume hits the pyrolite or MORB solidus, then the melt sinks down to the bottom of the mantle to form a ULVZ. The point of density crossover is after Ohtani and Maeda (2001). Path (2) shows the estimated geotherm across the D″ layer (Hernlund et al., 2005). Abbreviations are from Table 1. The thickness of the D″ layer and the slope of the pPV/PV phase-change curve are also shown.

of the large uncertainties in the pressure scales and other themodynamic error estimates.

The boundary at 410 km depth is assumed to be the phase change of olivine to wadsleyite, the 660 km depth boundary is marked by the breakdown reaction of ringwoodite to perovskite + wüstite, and the top of the D″ layer is assumed to be the polymorphic phase change from perovskite to post-perovskite (Murakami et al., 2004). Seismologists have long measured seismic discontinuities at these boundaries that have been used to estimate the temperature distribution in the solid Earth.

Moreover, we emphasize the narrow high-T stability field of majorite in the lowermost pressure region in the upper mantle (Fig. 1). Majorite occupies about 70 modal % of pyrolite at this depth range, but is stable only above T = 1800°C. $MgSiO_3$ polymorphs such as perovskite, majorite, enstatite, clinoenstatite, ilmenite, and orthoenstatite form several invariant points in P-T space above 26 Gpa, one of which occurs at ca. 25–26 GPa and T = 1800°C from which radiate three univariant lines, majorite/perovskite, ilmenite/perovskite, and majorite/ilmenite. The majorite/perovskite univariant line crosscuts the reaction, ringwoodite = perovskite + wüstite (Fig. 1). It is for this reason that a plume rising above this invariant point does not pass the reaction with a negative Clapeyron slope; instead, perovskite transforms to majorite with a steep positive Clapeyron slope with a

large volume change. On the lower pressure side near the solidus of MORB, the reaction majorite + wüstite leads wadsleyite. This reaction must have a much gentler Clapeyron slope than that of ringwoodite = perovskite + wüstite at low-T side. This reaction should be present under the hot rising plume at the boundary between the lower and upper mantle. We emphasize that the ΔV is large in both majorite/perovskite and ringwoodite breakdown reactions, but not in the case of ringwoodite = perovskite + wüstite (Hirose, 2002). But ringwoodite is not stable on the higher-T side at >1900°C and >600 km depth, where wadsleyite is stable leading to the reaction to form majorite + wüstite with a considerable change of ΔV (Fig. 14). This is critical in the discussion of Archean mantle convection.

Polymorphic transformation of perovskite to post-perovskite (Murakami et al., 2004) occurs at the depth of the CMB. Due to the absence of an absolute pressure-scale at this depth, and due to the difficulty of controlling temperature, the Clapeyron slope of this transformation has a large error bar. The first principles calculation of the Clapeyron slope is: it ranges from 4.0 to 10.0 depending on the equations employed (Oganov and Ono, 2004; Tsuchiya et al., 2004). Although the results differ between authors, there are some general agreements such as (1) the slope passes at ca. 4000 K at the CMB pressure (135 Gpa) (Hirose et al., 1999; Hirose, 2007), and (2) the slope indicates around 7.5 MPa/K (Tsuchiya et al., 2004). The average temperature estimated for the thickness of the MBL ranges from 2073 K (1800°C) for a rising superplume to 1573 K (1300°C) for the WPTZ (Fig. 2). If low-T stagnant slabs at the MBL in the WPTZ fall down to the bottom of the CMB, as observed in the D″ layer below the WPTZ (e.g., Zhao, 2004), then the T must be higher than the adiabatically extrapolated value, with a rate of increase of ca. 50 K/100 km. The thickest D″ layer, which is up to 350 km thick (Wysession et al., 1998), has a minimum value of 2000 K at its top. Accordingly, the Clapeyron slope has a value of 9.0 MPa/K (Fig. 1).

3 THERMAL STRUCTURE OF THE EARTH

In spite of the possible presence of large-scale compositional variations in the solid Earth, the T variation can be estimated from the polymorphic phase relations mentioned above, combined with the regional variation of topography of the seismic reflection surface of the mantle transition zone, the thickness of the D″ layer, and the presence or absence of ULVZ right above the CMB.

3.1 Upper mantle <410 km

S-wave tomographic images by Zhang and Tanimoto (1991) and Grand (2002) clearly demonstrated that a curtain-like upwelling continues down to a depth of 200–300 km under a mid-oceanic ridge. The improved P-wave whole mantle tomography by Zhao (2004) suggests a much deeper continuation down to 410 km depth from which the curtain-flow rises up. The composition of MORB is very homogeneous, regardless of the spreading rate, the thickness of MORB crust, and the particular ocean. The potential temperature of the MORB source mantle is ca. 1300°C (McKenzie and

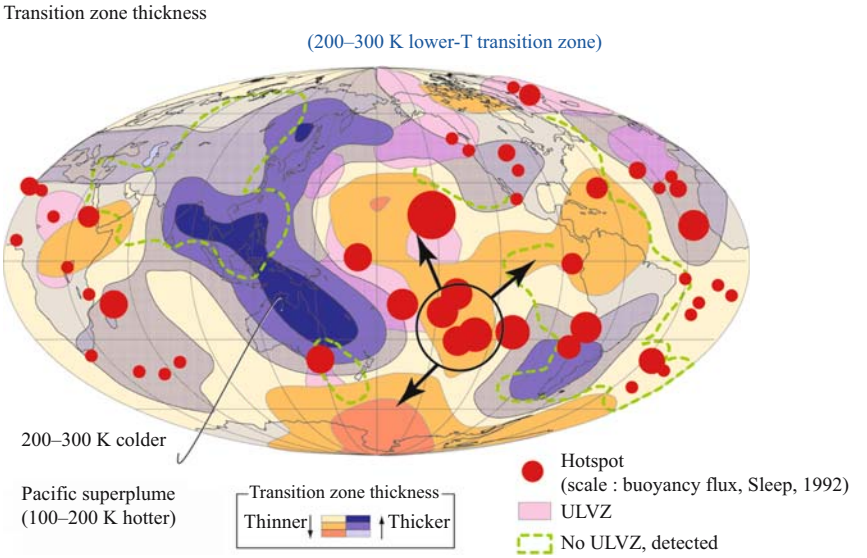

Figure 2. The thermal structure of the MBL estimated by the thickness of the MBL combined with the phase diagram. The thickness of the MBL (410–660 km) mapped by Shearer and Flanagan (1999) was transferred to a T variation by Maruyama et al. (2001). Note that the super-upwells in the central Pacific and Africa are 100–200 K higher, and the circum-Pacific lithospheric graveyards are 200–300 K colder than the standard area.

Bickle, 1988), indicating a homogeneous mantle temperature at 660 km depth of about 1600°C, which is extrapolated adiabatically by using the potential temperature of a MORB source mantle.

An OIB source mantle temperature (see review by Kogiso, 2007 this issue) reaches 100–200 K higher than that of MORB, suggesting that most OIB plumes are derived from plumes from the lower mantle.

Komiya and Maruyama (2007) demonstrated that the temperature and water content in the western Pacific region are 60 K lower and one order of magnitude higher in the source mantle, compared with a MORB-source mantle.

3.2 Mid-mantle boundary layer (MBL) (410–660 km)

Here, we estimate the temperature distribution of the MBL under the western Pacific triangular zone (Kamchatska-New Zealand-Tibet area, hereafter WPTZ), combining the phase diagram of pyrolite mantle with topography of the MBL measured by Flanagan and Shearer (1998).

Because the MBL thickness is defined by the phase transformation of olivine to wadsleyite with a positive Clapeyron slope at around 410 km depth, and ringwoodite to perovskite+wüstite with a negative Clapeyron slope at about 660 km depth (Ito and Takahashi, 1989), the thickness of the MBL is a function of temperature (Fig. 1).

Multi-anvil experiments for these phase transformations have been performed independently in several laboratories to satisfy the curves reproduced in Figure 1, although the pressure-scale has not yet been fully resolved. Despite the lack of consensus on the pressure-scale, the thickness of the MBL is an appropriate tool to measure the temperature difference, reflecting the relative temperature on a global scale. At the standard state, the thickness of the MBL is $660 - 410 = 250$ km, and the departure of 25 km corresponds to 300 K.

Flanagan and Shearer (1998) showed the global variation of thickness of the MBL. Their data can be expressed by the relative temperature variation (Fig. 2). The result clearly supports the idea that the western Pacific has the coldest MBL in the world, 200–300 K colder than the standard conditions of the MBL. This is consistent with a 60 K lower temperature at 30 km depth (Komiya and Maruyama, 2007), and with 600 m deeper ocean basins due to underlying cold mantle reported by Park et al. (1990).

In contrast, in the central Pacific and Africa, the MBLs are 100–200 K higher than the standard MBL (Fig. 2). These regions correspond to the Pacific and African superplumes as clearly defined by P- and S-wave tomographies by eight different research schools worldwide (Fukao et al., 1994; Su and Dziewonski, 1997, van der Hilst et al., 1997, Ritsema et al., 1999; Masters et al., 2000; Romanowicz and Gung, 2002; Grand, 2002; Zhao, 2004). These two mantle upwellings are the major mantle convections on a global scale, paired with a cold down-welling in the WPTZ (Maruyama, 1994). .

3.3 Mantle temperature at the CMB

Using the phase diagram of perovskite transformation, the depth of the top of the D″ layer can be translated to temperature, following Wysession et al. (1998) who demonstrated the regional distribution of thickness of the D″ layer by S- and P-waves (Fig. 3). The result shows that the bottom of the WPTZ is the coldest over the world, reaching 2000 K. There exists about 2000 K temperature rise across the 350 km-thick D″ layer, because the bottom of the mantle can reach as high as 4000 K. A thin layer near the bottom should be in the stability field of perovskite again, and this has been confirmed seismologically by a velocity jump (Hernlund et al., 2005).

In both Pacific and African superplumes, there are no regions in which post-perovskite is stable, i.e., the D″ layer is absent (Fig. 3). The boundaries defining the margins of the superplume are sharp, as well documented recently by a steep velocity gradient near the margin of both superplumes (Thorn et al., 2004; To et al., 2005). There are no constraints on drawing isotherms by phase transformation within a superplume region.

3.4 Distribution of the ULVZ at the bottom of the CMB

The distribution of the ultra-low velocity zone (ULVZ) defined as a region with 30% reduction of S-wave velocity (Helmberger et al., 2000), has been mapped on a global

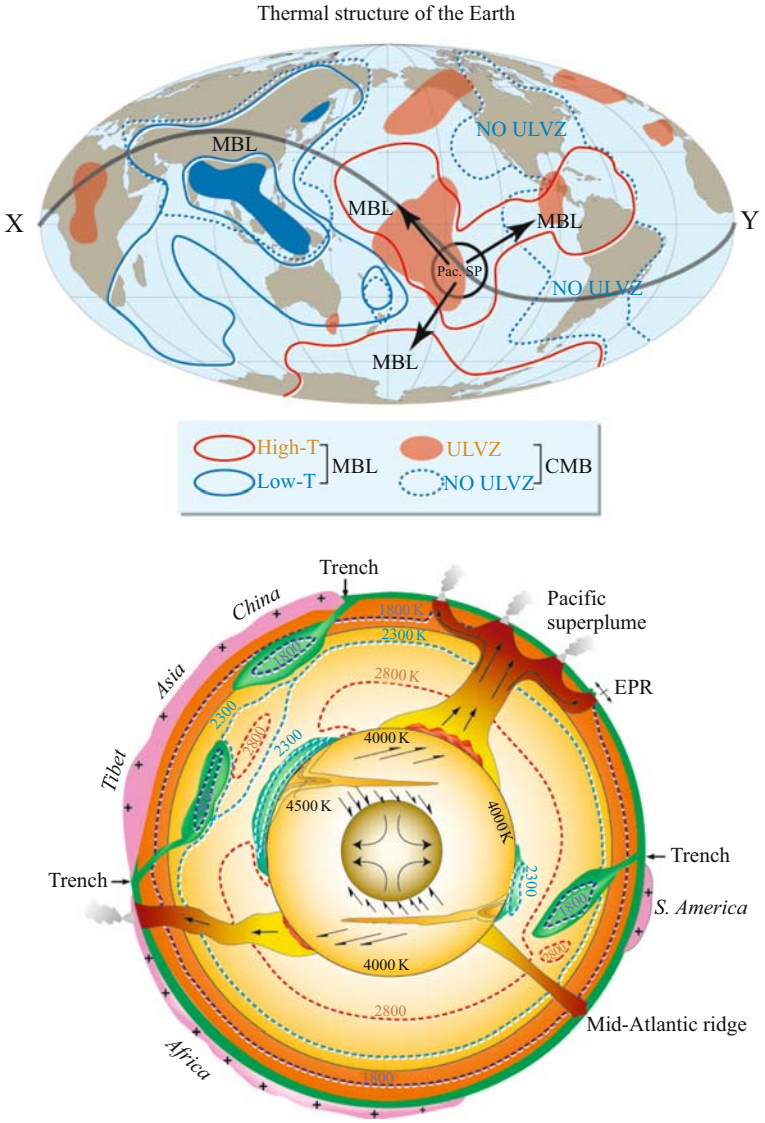

Figure 3. The thermal structure of the Earth in a plain view (above) and a cross-section along X-Y (below). Three data sets of thickness of MBL, thickness of the D″ layer (Wysession et al., 1998), and the global distribution (presence or absence) of ULVZ (Helmberger et al., 2000; Garnero, 2000; Lay and Garnero, 2004) are used, combined with phase diagrams to draw the thermal structure of the Earth. Using the detailed distribution of the thickness of the D″ layer, the thermal structure along X-Y is drawn (below). In both diagrams the WPTZ is the coldest mantle from top to bottom, and the superplume regions are the hottest in the whole mantle depth range. The topmost core is 4000 K everywhere. Cold spots on the CMB drive a downwelling dynamo-flow in the outer core. The coldest spot under the WPTZ causes downwellings to cool the solid inner core and a preferential growth of the equatorial inner core by precipitation-accumulation

scale, although not yet completely (Garnero, 2004). A major contrast is present, in that the absence of an ULVZ is restricted to the circum-Pacific and the Tethyan slab graveyards, whereas a major ULVZ is present in both Pacific and African superplume regions (Fig. 3). Using an extrapolated solidus at 135 GPa, ca. 4000 K is obtained for the T of the ULVZ right above the CMB (Fig. 3). The thickness of the ULVZ is up to 10 km (Garnero et al., 2007).

These four independent observations all confirm that the WPTZ is the coldest region from the surface to the bottom of the mantle, whereas the central Pacific and African regions have the hottest oceanic and subcontinental mantle, indicating that there are three major flows of mantle convection on a global scale (Fig. 3).

3.5 Thermal structure of the Earth

The estimated thermal structure of the Earth is shown in Figure 3. Temperature estimates at different depths consistently indicate that the vertical mantle flow dominates. Under the southern Pacific and Africa, the highest temperature CMB continues upward all the way to the surface. In the western Pacific to Himalayan region, a cold CMB continues through the MBL to the surface; apparently contradictory processes of active volcanism, associated deformation, seismicity, and formation of back-arc basins, are all due to the high-water content. Collision of India and subsequent indentation into Asia over 2000 km was probably made possible by hydro-softening of the lithosphere and underlying mantle due to the addition of water. Collision may have played a subordinate role in the deformation of East Asia, and it is unrelated to active volcanism in the WPTZ.

A cross-section of the Earth is shown Figure 3 with two superplumes and one downflow in the western Pacific. The estimated thermal structure is shown in Figure 3, where isotherms of 1800, 2300, 2800 and 4000 K are delineated. A stagnant slab forming a megalith would have the coldest core in the MBL, which at its coldest would reach 1800 K, presumably the same as the huge blob in the middle-lower mantle under middle to South America. In general, the circum-Pacific and Tethyan regions have a low-T. Locally overturned regions are present in Asia and S. America.

In contrast, two large, hot regions, are present which from top to bottom are high-T, corresponding to the two superplumes. The Pacific superplume extends nearly vertically to the surface, whereas the African superplume tilts 45 degree northwards.

The highest T gradient is observed between the mantle and the core, forming the core/mantle boundary layer. The cold spot on the CMB, under Asia, may eject a

---

Figure 3. (*Continued*) of Fe-Ni crystals, whereas the residual liquids become less dense, owing to enrichment of light elements. The residual buoyant dynamo-flows rise up to the root of the Pacific superplume. Enriched light elements in the upwellings in the outer core may escape from the outer core to the mantle, and drive a superplume as a huge stable pipe to connect with the surface of the Earth over 1.0 Ga. Another cold spot derived from a S. American downflow causes similar dynamics against the inner core and the African superplume. Tectonites in the solid inner core may similarly be formed under the differential stress field to yield the preferred orientation of metallic phases.

columnar dynamo down-flow that cools the equatorial inner core, and expands the inner core by the accumulation of crystallized solids in it. The remaining flows, enriched in light elements turn up at the root of the Pacific superplume. As a source of buoyancy, these light elements may enter the mantle to drive a superplume. For the African superplume a similar mechanism may work from the cold spot that originated by downflow under S. America (Fig. 3).

3.6 Major convection pattern in the present-day Earth's mantle

The Pacific superswell (McNutt and Judge, 1990; DeLaughter et al., 2005) is a huge bulge 3000 km across that stands 300 m high from the surrounding ocean-floor. On it there are four hotspots suggesting multiple rising mantle plumes underneath. A second superswell under Africa is defined by combined with P-wave and S-wave whole mantle tomography. The terms Pacific and African superplumes are now established in the geological literature, since the first proposal by Maruyama (1994).

If super-upwelling is present, then down-welling is necessary to balance the material circulation. The process of down-welling mantle flow in the lower mantle is not simple, because of the phase transformation at 660 km depth, where ringwoodite breaks down to form perovskite and wüstite, with a negative Clapeyron slope (Ito and Takahashi, 1989). Moreover, mantle viscosity changes drastically at this boundary, with about 1–2 orders of magnitude difference between the upper and lower zones. As clearly documented in high-resolution whole mantle tomography, the subducted curtain-like lithosphere becomes stagnant at the 660 km depth barrier, and changes shape from plate-let or curtain-like to blob-shape (Fukao et al., 2001; Zhao, 2004). Any cold-anomalies in the lower mantle exhibit blob-shapes that are separated and isolated from the shallower high-V anomalies, indicating the origin of once-stagnant slabs at the 660 km depth barrier.

The distribution of high-V anomalies is restricted to the circum-Pacific and Tethyan domains over the world (Fukao et al., 1994, 2001; Zhao, 2004), and is consistent with the subduction history of the Earth back to 180 Ma (Fig. 3) strongly indicating that the high-V anomaly is the subducted lithosphere. There is a stronger high-V anomaly, both in intensity and size, within the mantle. This anomaly occurs in the western Pacific and East Asia (Fig. 3), and coincides with the circum-Pacific subduction zone that meets with the Tethyan domain, forming an overlapping subduction zone on a mega-scale. Maruyama (1994) named this zone a super-downwelling zone, or Asian cold superplume. Cold superplume does not mean lower temperature upwelling, but it denotes downwelling according to the definition of Maruyama (1994). We emphasize that both rising and falling mantle flow should be termed plumes, although most geologists recognize plumes as a rising feature, and therefore the term cold plume might give the impression of a low-T rising plume, although in fact it is a descending (downwelling) plume.

Thus, we believe that there is sufficient evidence for proposing the presence of one super-downwelling in the WPTZ, paired with two superplumes on the Earth,

and these represent the major convection pattern of the Earth's mantle (See Fig. 1 in Section 2).

3.7 Two major boundary layers and radiogenic elements in the core

Figure 3 shows that several steep geothermal gradients are present in the Earth. The best-known example is the surface boundary layer that comprises ca. 100 km-thick lithosphere; although not shown in the figure, it is listed as a background framework. The temperature difference between the top and bottom is ca. 800–1000 K.

Compared with this difference, the 250 km-thick MBL indicates a temperature of 200–300 K for several 100 km; it reaches a maximum of 600 K locally in subduction zones, e.g., between the center of a slab and the surrounding mantle at 660 km depth.

The largest temperature gradient occurs at the CMB, where the maximum temperature difference reaches 2000 K at the CMB underneath Asia, below and above the 350 km thick D″ layer.

Thus, the solid Earth contains the following zones. The highest temperature of the outer core is around 4000 K at its top, and the inner core/outer core boundary presumably has a temperature of 5000 K (Anderson, 2003). The cold lower mantle caps the hot outer core with a maximum temperature difference of 2000 K, and the cooled lithosphere caps the hot mantle. Moreover, the size of the core is only 1/8 of that of the Earth, too small to play a role as a heat source to drive the Earth for over 4.56 Ga. These relationships suggest that a radiogenic heat source must be present in the outer core. Considerable quantities of K and Al (light elements), U and Th (heavy elements) have been experimentally confirmed in Fe melts at the CMB pressure and elevated temperature (Hirao et al., 2005).

4 SUBDUCTION CONTROLS THERMAL STRUCTURE

As clearly documented in the thermal structure of the Earth, the isotherm distribution in the solid Earth is not homogeneous and concentric. In this section we discuss the controlling factor of the thermal structure of the Earth based on the history of subduction back to ca. 1.0 Ga.

4.1 Slab graveyards

Subduction history back to 180 Ma (Engebretson et al., 1985; Lithgow-Bertelloni and Richards, 1998) can explain the thermal structure of the Earth, and in particular the presence of cold mantle along the circum-Pacific to Tethyan domain, and of hot regions in the center of the Pacific and Africa (Fig. 4). Tomographic images by P- and S-waves clearly support the above idea, showing stagnant slabs at the MBL depth and in the lower mantle underneath the circum-Pacific and Tethyan domains (e.g., Zhao, 2007 this issue).

But the tomographic images at the CMB (2600–2900 km) show no correlation between the history of subduction back to 180 Ma. For example, several

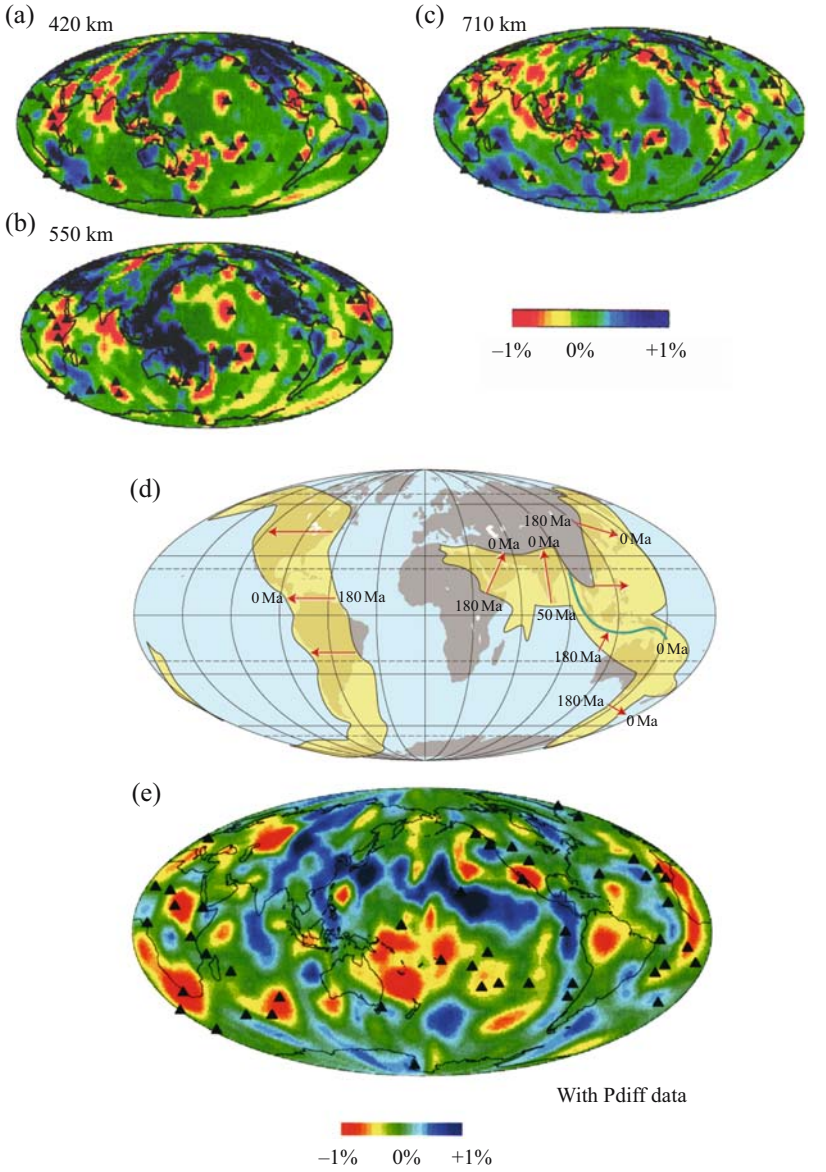

Figure 4. P-wave tomographic images at 420 km, 550 km, 710 km depth, and the base of the mantle (after Zhao, 2004). Note (1) that a high-V anomaly is present predominantly along the circum-Pacific and the Tethyan subduction zones in the MBL; and (2) the calculated slab graveyard created in the last 180 Ma matches well the observed high-V anomaly in the MBL. But the high-V anomaly on the CMB does not coincide with the slab graveyards back to 180 Ma, although they overlap to some extent. The high-V anomalies in the Pacific, India, Antarctica and Africa suggest the presence of slab graveyards much older than 180 Ma.

high-V anomalies are present even within the Pacific ocean and under Africa and its surrounding regions (Fig. 4).

In the paleogeographic map for 180 Ma, before the opening of the Atlantic and Indian Oceans, a wide ocean called the Panthalassan Sea was present in the present Pacific Ocean. Since then, the size of the Ocean has decreased to become the Pacific Ocean. During this period no subduction zones developed within the Pacific, except minor ones off Alaska. Therefore, we cannot interpret the cold anomaly right above the CMB in the central Pacific Ocean.

Similarly, we cannot explain cold anomalies on the CMB in the Indian and Atlantic Oceans. To understand these, we must turn to the subduction history back to the time of Pangea formation, and even further back to the time of Rodinia formation. In the following, we briefly describe the geologic history of (1) WPTZ, (2) Laurasia, (3) Gondwana, and (4) Rodinia (Fig. 5).

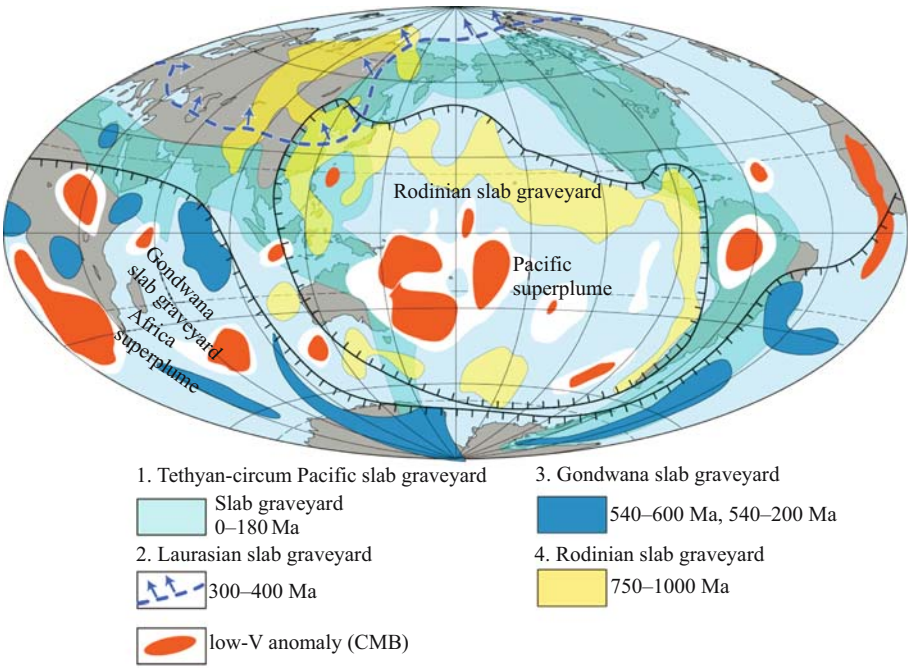

Figure 5. Speculative slab graveyards on the CMB as estimated from P-wave whole mantle tomography by Zhao (2004). The green region shows the calculated slab graveyards during the last 180 Ma along the circum-Pacific and Tethyan subduction zones. The Laurasian slab graveyard is shown by the encircled blue broken line. The Gondwana slab graveyard remains under Africa, the Indian Ocean, S. Atlantic, and Antarctica shown in blue. A Rodinia slab graveyard remains in the Pacific Ocean, sporadically surrounding the Pacific superplume. The definitions of a slab graveyard are based on the paleo-positions of supercontinents. We point out here the concentric structure of the Pacific superplume, suggesting that the Pacific superplume has evolved from the slab graveyard.

4.2 Western Pacific Triangular Zone (WPTZ)

The WPTZ marks the frontier of a future supercontinent. The western Pacific is a domain characterized by a double subduction zone, a N-S trending trench where the old 100–200 Ma Pacific lithosphere is subducting, and an EW-trending Java-Sumatra trench where the Jurassic to Eocene Indo-Australian plate is being subducted. The two subduction zones carry double the amount of cold slabs into the deep mantle to refrigerate the surrounding mantle in the western Pacific to eastern Asia (see details later, Fig. 17). The major characteristics of the WPTZ are as follows.

The upper mantle is very low in temperature, about 200–300 K lower compared to the standard MBL depth (Fig. 2). Hydrous plumes originating from 410 km have been well-documented by high-resolution P-wave tomography (Zhao, 2004). Several active volcanoes stand right above those plumes documented by tomography. In spite of its low-temperature mantle, the WPTZ is a most active area of volcanism, seismicity, deformation, and mountain building along the boundaries of its microplates. The WPTZ is bordered by abundant Cenozoic back-arc and marginal basins, and was intruded in the Cenozoic by abundant strongly alkaline basalts (Smith, 1998).

The MBL contains the most spectacular stagnant slabs that extend for over 2000 km from the Japan trench to deep-inside Eastern Asia (Zhao 2004, 2007; Zhao et al., 2007) (Fig. 4). The total amount of slabs present are the total that was subducted during the last 20 Ma, if the MBL is composed of three layers of about 80 km thick slabs. Slabs older than 20 Ma must have collapsed to flow down to the bottom of the CMB that is now seen as a 1000 km-thick high-V anomaly right above the CMB or as a few blobs in the upper half of the lower mantle (Zhao, 2004).

Summarizing the characteristics of the WPTZ: (1) there is no ULVZ right above the CMB, (2) a D″ layer, about 350 km thick, is common in addition to a thick high-V anomaly above the D″ layer, (3) no plumes, and an absence of a low-V anomaly right above the CMB.

4.3 Laurasian slab-graveyard

Before the formation of Laurasia (Paleoasia) extensive subduction of oceanic lithosphere must have occurred underneath Asia. More than seven continents including Siberia, N. China, S. China, Indochina, Tarim, Kazakhstan, and Baltica (Russian platform) finally collided in the period 300–200 Ma. Thereafter, along the southern margin, small continental fragments in Indonesia, Tibet (the Lhasa block), India, Saudi-Arabia, Turkey and others collided against Asia after 100 Ma, and the collisions continue to the present. For example, at 50 Ma, the Indian continent started to collide at the site near the southern end of India, and to indent to the north for over 2000 km. Slab graveyards can be well-observed under the Indian continent, reflecting the original site of the trench line (Fukao et al., 1994).

To complete the northern half of the supercontinent Pangea, extensive subduction must have occurred, and thus a slab graveyard must be present under Asia. In the eastern part of the suture between Siberia and N. China, a high-speed anomaly is

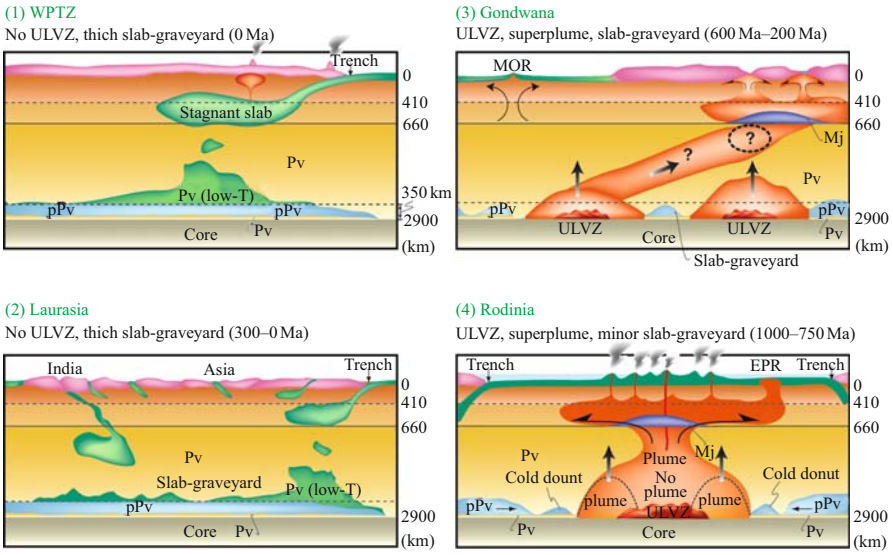

Figure 6. Comparison of mantle structure: (1) the WPTZ (frontier of a future supercontinent), (2) Laurasian D″ layer (northern half of Pangea formed at ca. 300 Ma), (3) Gondwana (formed as a semi-supercontinent at ca. 540 Ma), and (4) Rodinia (a supercontinent formed at ca. 750 Ma). The change from (1) to (4) demonstrates the sequential variation of the Wilson Cycle or supercontinent cycle. In the first two there are no superplumes, but the last two contain superplumes at different stages of evolution. We emphasize here the evolutionary change of the mantle from the coldest (type 1) to the hottest (type 4) through time.

present in the upper to lower mantle, suggesting that not all slabs descended down to the CMB.

We emphasize that (1) the presence of high-V anomalies on the CMB under Asia in general, now seen as a high-V anomaly above the CMB, (2) no ULVZ and no plumes; instead the presence of a thick D″layer (350 km), and (4) no stagnant slabs in the MBL under the central portion of Asia (Laurasia) (Fig. 6).

4.4 Gondwana slab-graveyard

Gondwana was formed in the period from 750 to 500 Ma by the extensive collision and amalgamation of more than ten continents including W. Africa, Congo, Amazonia, San Francisco craton, S. India, Madagascar, N. Africa-Saudi Arabia, and the Arabian-Nubian shield: of a composite terrane of juvenile arcs, and some blocks in Antarctica. Through these orogenic events, oceanic plates between the continents must have been subducted under Gondwana. Thereafter, continuous subduction along the west and south of the semi-supercontinent of Gondwana must have carried down many slabs beneath it. Some of these still remain immediately above the CMB under Africa, the S. Atlantic Ocean, India, the Indian Ocean and Antarctica (Figs. 4 and 5).

Stagnant slabs are absent in the MBL in the mantle under the former site of Gondwana, but they are locally present right above the CMB. In contrast to the mantle under Asia and the WPTZ, plumes were derived from the CMB; one such is the African superplume where an ULVZ is present above the CMB (Fig. 6).

The African superplume is different in shape from the Pacific superplume. The African superplume is bending northwards, whereas the Pacific superplume is rising vertically (Ritsema et al., 1999; Romanovicz and Gung, 2002; Zhao, 2004). This difference may be explained by their different convection patterns: the Pacific superplume is surrounded by the circum-Pacific down-flow, but there is no down-flow around the African superplume region (Zhao, 2004; Ni and Helmberger, 2003).

4.5 Rodinia slab-graveyard

Before the opening of the Pacific Ocean, the supercontinent Rodinia covered the entire region of the present-day Pacific Ocean. A ca. 750 Ma Pacific superplume was born that broke-up Rodinia and created the Pacific Ocean. After its inception the Ocean widened with time until at ca. 500–450 Ma its passive continental margins became active margins. Since then, the Pacific Ocean has decreased in size until now (Maruyama, 1994; Maruyama et al., 1996).

To form the supercontinent Rodinia, extensive subduction must have taken place, to transport huge amounts of oceanic lithosphere into the deep mantle below Rodinia, which must have been largely transformed to a normal or high-T mantle by heating from the outer core through the CMB. As expected, the world's largest superplume occupies the lower center of the Pacific Ocean (Fig. 6). The world largest ULVZ is present right below the low-V anomaly and right above the CMB. Also, note the concentric isotherms around the margin of the ULVZ (about 3800 K), surrounded by a steep velocity gradient and a high-V zone, giving rise to a so-called "cold donut." In the center of the superplume there is no low-V anomaly, because of the compositional anomaly created by recycled MORBs and consumed by the highest-T in the center. There is no D″ layer on the CMB in the Pacific superplume.

We emphasize the high-V velocity anomaly that forms a cold-donut around the Pacific superplume (Maruyama et al., 2007). These cold anomalies within the Pacific Ocean cannot be explained by subduction after 500 Ma; rather they are the remnants of the Rodinia slab-graveyard (Fig. 6).

5 MECHANISM TO FORM A SUPERPLUME

5.1 Sequential change of mantle in relation to supercontinent, superplume and pPV

As mentioned above, four examples describe the sequential changes of the mantle through time according to the Wilson cycle or supercontinent cycle. These illustrate the different stages of evolution: (1) the frontier of a future supercontinent, (2) the center of a future supercontinent nucleated at ca. 300 Ma ago, (3) 200 m.y. after Pangea breakup, and 500–600 Ma after the formation of the semi-supercontinent

Gondwana, and (4) the demise of the Pacific Ocean and the end of the superocean, Sea of Panthalassa. The superplume played a major role in mantle convection in the center of the Pacific Ocean. There were no superplumes in stages (1) and (2), when thick slab graveyards were formed, together with a thick D″ layer. On the other hand, a superplume and ULVZ were present in stages (3) and (4), when there was no D″ layer. The present Pacific superplume is in a more advanced stage of development than the African superplume.

One of the most important observations, in comparison with the above four examples, is the fact that the coldest mantle is transformed into the hottest mantle in a time interval of ca. 1 b.y. This is one of the puzzling aspects of the supercontinent cycle. The concept of a thermal blanket was not able to explain the fact that the subcontinental mantle is colder than that of the oceanic mantle, as well documented by mantle-xenoliths (e.g., Kawasaki, 2006).

5.2 How to form a superplume: a model

We can interpret the observation that the coldest mantle changes to the hottest mantle underneath a supercontinent, if we employ the exothermic heat transfer caused by pPV that is preferentially stable under low-T conditions (Fig. 7). Nakagawa and Tackley (2004a,b) calculated the exothermic phase transformation of pPV to PV at the CMB, and demonstrated how it affected the transfer of core heat to the whole mantle. If the reaction has a negative Clapeyron slope, a large thermal gradient is formed at the CMB (Fig. 7a). If the reaction has a positive slope, as in the case of pPV/PV, a number of small plumes can be formed on the CMB that transfer effectively the core heat to the mantle. Moreover, if the Clapeyron slope is as large as 9 MPa/K, the mantle temperature rises by around 200 K in the whole mantle, except at the top and bottom thermal boundary layers (Fig. 7b).

When a supercontinent is formed by extensive collision and amalgamation of continents through time (stage 1), the once stagnant slabs at the MBL accumulate on the CMB, first under the center of a supercontinent, and then they migrate to the margins of the supercontinent (stage 2). The oceanic slabs that have dropped down to the CMB are cold enough to stabilize pPV, which is transformed to PV by heating from the outer core. Perovskite appears from the transformation of pPV on the bottom of the D″ layer, to form a sandwich-shaped pPV-bearing lens in the D″ layer under the supercontinent. The recycled MORB slabs in the D″ layer right above the CMB partially melt when the temperature reaches 3800 K, to form a dense Fe-rich silicate melt which sinks down to develop an anti-crust on the bottom of the mantle. The remaining andesitic restite derived from partial melting of the recycled MORB would be buoyant, and so rises up to form a small-scale plume, first in the center of the slab graveyard (stage 2).

Small chemically driven plumes collide and coalesce to form a bigger plume by attraction, and finally a superplume with a size of the scale of 1000 km develops, through upward migration. The migration of plumes formed at the CMB carries heat upwards; hence the bigger plumes at shallower levels have higher-T than the

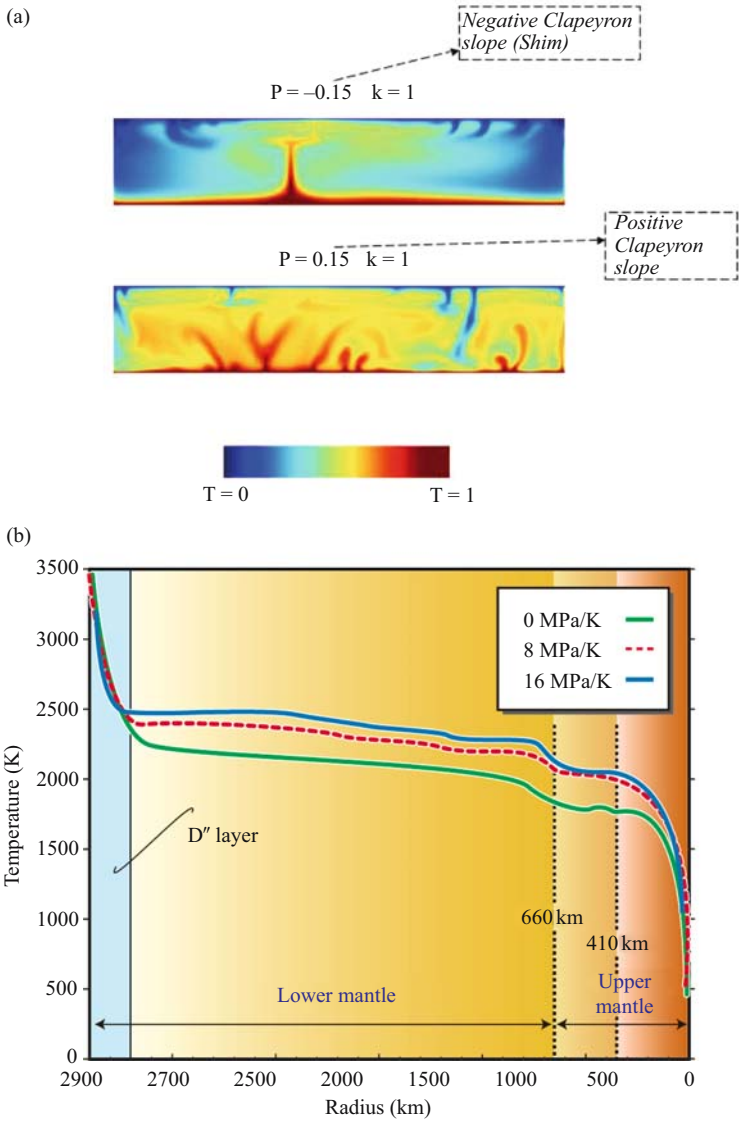

Figure 7. Numerical simulation of mantle convection with or without pPV on the CMB after Nakagwa and Tackley (2004a). Top figure: Mantle convection with the endothermic phase transformation at the CMB (above), and the exothermic phase transformation (below, in the case of pPV). A number of small plumes can be formed in the latter and a single large plume is formed in the former. Bottom figure: Effects of Clapeyron slope. Compared to the case where there is no phase transformation at the CMB (0 MPa/K), a PV/pPV phase transformation with a slope of 9 MPa/K increases the mantle temperature not only in the lower but also in the upper mantle by about 200 K, except in the 200–300 km-thick boundary layers on the top and bottom of the mantle.

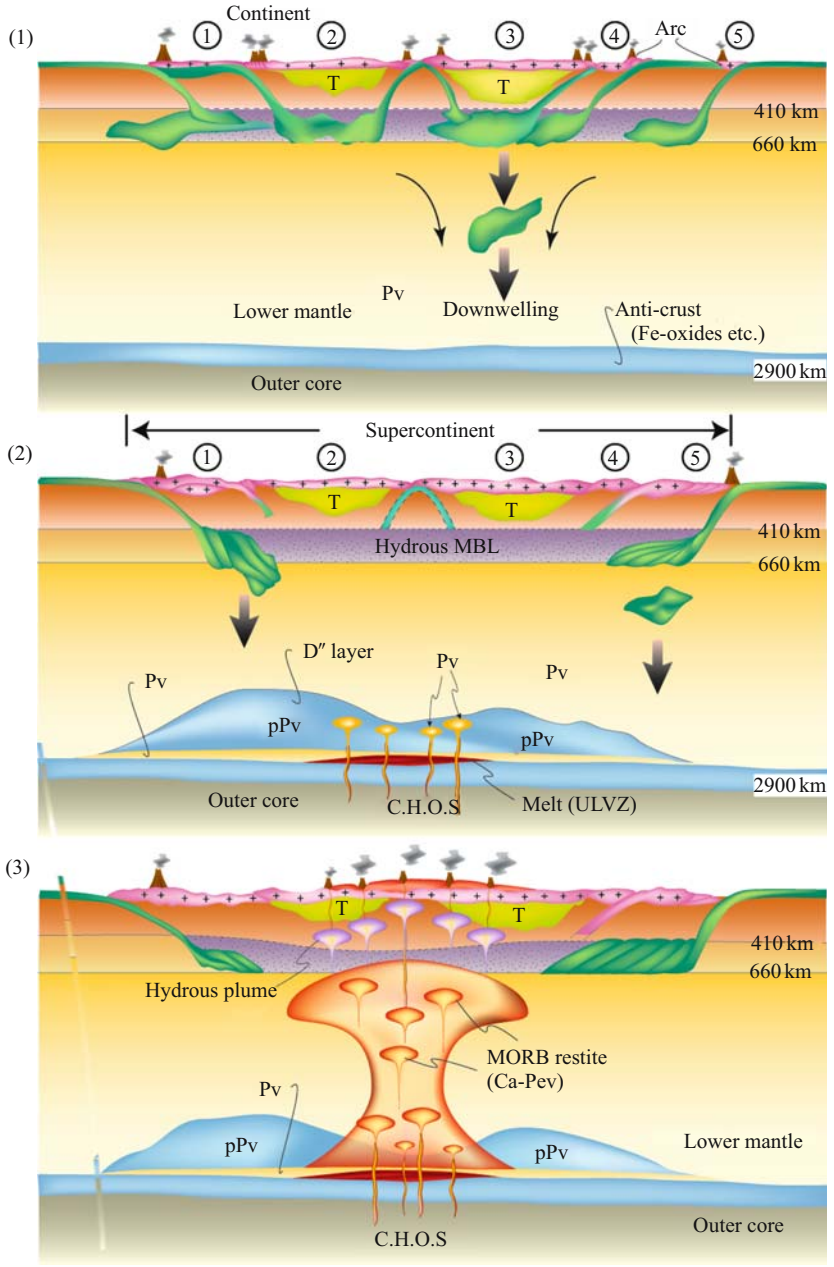

Figure 8. A possible mechanism of the creation of a superplume at the CMB from the accumulated slabs right above the CMB and underneath the center of a supercontinent. The coldest mantle is transformed into the hottest mantle by the action of pPV at the CMB and by the partial melting of recycled MORBs in

surrounding mantle. A superplume as a cluster of small plumes may develop more effectively, if light elements from the outer core are supplied through the high-T window on the CMB (stage 3). When a high-T superplume reaches the 660 km boundary, it warms up the hydrous MBL to break down hydrous ringwoodite and wadleyite, which radiates out water-enriched, buoyant magma at 410 km depth. If carbonate-rich peridotite is present, kimberlite-carbonatite magma flushes up along the rifted faults in the fragmenting supercontinent.

Once the D″ layer is depleted in the recycled MORB components, it cannot generate any more plumes, in spite of its high temperature. With time, the birth place of a plume would therefore move from the center to the periphery of the superplume, leaving behind Mg-perovskite-enriched mantle, and melt in the D″ layer (Fig. 8).

6 PETROLOGIC STRUCTURE OF THE PACIFIC SUPERPLUME

The thermal structure of the Earth clearly demonstrates that the mantle under the Pacific Ocean exhibits a concentric thermal structure, high at the center surrounded by a low-T region where the slab-graveyard is concentrated. The center of the superplume stands above the ULVZ, about 2000 km across, has a temperature about 3500 K, and is surrounded by a low-V region defined as a superplume ca. 3000 km across. The superplume is bound by a steep velocity gradient zone, and rimmed by the high-Vp region (Zhao, 2004). The central core of the Pacific superplume is characterized not by the low-Vp region, but by intermediate Vp and Vs velocities, in spite of the presence of an ULVZ right below the thermal boundary layer. This suggests a compositional difference between the central and surrounding regions.

The thermal boundary layer of the Pacific superplume is composed of five plumes (Fig. 9), all of which stand above the ULVZ, except for French-Polynesia that occurs near the margin. Between the superplume and the Rodinia slab-graveyard, labeled as a cold donut in Figure 9, there is a 1000–2000 km-wide medium-transition zone.

From the center to the cold donut, temperature should decrease concentrically, reflecting the concentric thermal structure. If so, the petrologic structure of the Pacific superplume can be drawn (Fig. 10), assuming that the original D″ layer was enriched in subducted slabs with recycled MORB crust.

Figure 8. (*Continued*) the slab graveyard. (1) The top figure shows the formation of a supercontinent by successive collision and amalgamation of continents around a nuclei of continents. By this process many subducted slabs become stagnant at the MBL, and finely they accumulate on the CMB. (2) The selective accumulation of cold slabs on the CMB develops pPV in the D″ layer. The colder it is, a thicker D″ layer is developed. The earlier developed slab graveyard under the center of a supercontinent is warmed up to partially melt the recycled MORB slabs, when T reaches 3800 K. The melt is dense and sinks down to develop an anti-crust, whereas the restite arises to generate small plumes. The resultant change of thermal structure reduces the thickness of the D″ layer. (3) With time, the small plumes coalesce into a bigger plume by amalgamation due to attraction and collision, and finally a superplume is created. When a superplume reaches the supercontinent, rifting begins with explosive kimberlite-carbonatite magmatism, to be followed by flood basalt extrusion.

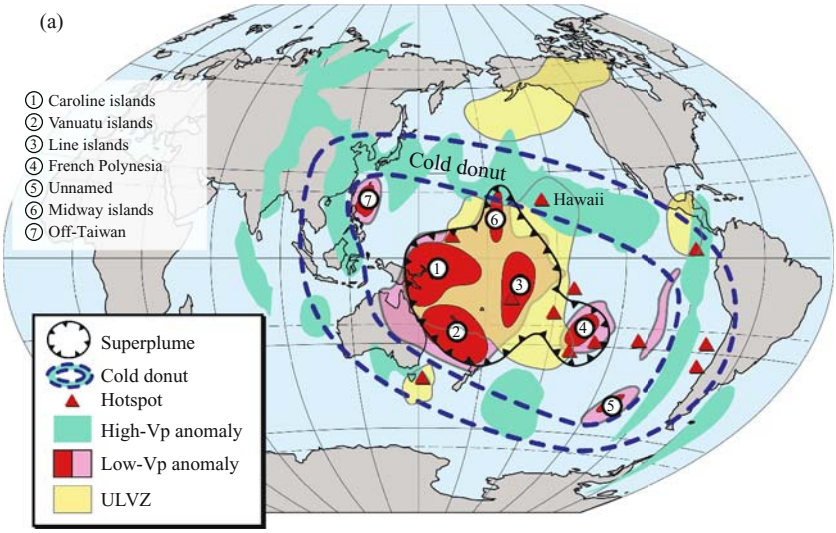

Figure 9. The structure of the Pacific superplume as a cluster of four independent plumes originating on the CMB, outlined after Zhao (2004). Between these plumes identified by low-V anomalies, a high-V region is present near the center of the superplume. Note the coincidence of the ULVZ below the superplume. A cold donut presumably derived from slab graveyards surrounds the Pacific superplume. An approximately EW cross-section is shown schematically in Figure 10.

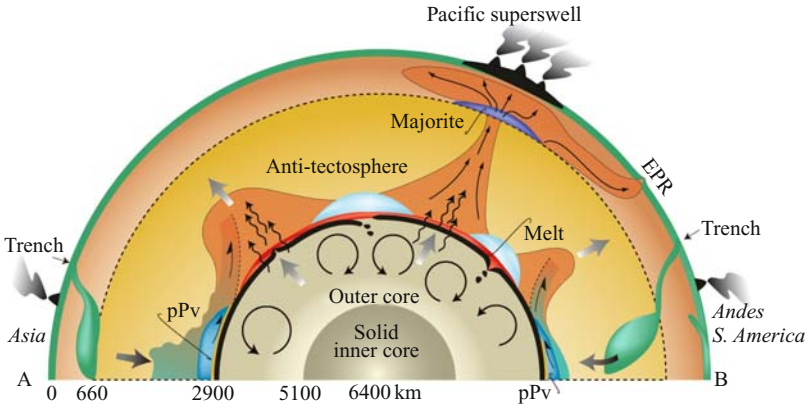

Figure 10. An EW cross-section of the Pacific superplume to show its petro-chemical structure and dynamics. The old center of the superplume may have lost its recycled MORB component. Instead, it is enriched in Mg-PV that is defined as an anti-tectosphere, defined below. See text for the details.

The center of the Pacific superplume, if originally enriched in slabs with MORB crusts, and the presence of an ULVZ indicates that recycled MORB crust must have partially melted earlier than slab peridotite, because the solidus of MORB is ca. 200 K lower than that of pyrolitic peridotite, and so produces an FeO-rich melt (Fig. 1). If the temperature is higher than the solidus of pyrolitic peridotite right above the ULVZ, pyrolite must also have partially melted, shifting the residual solid composition towards the MgO-rich side and increasing FeO in the melt. MORB components as well as surrounding mantle peridotite must be depleted in the central region. The depleted nature of the mantle in the center of superplume would explain different P- and S-wave signatures, and P/S ratios (see tomographic images summarized by Garnero et al., 2007 this volume). This may explain the absence of plumes in the center.

Away from the center, the low-Vp region, defined as plume-enriched, is shown in Figure 12, as a cluster of small-scale plumes, each of which is speculated to be a restite enriched in Ca-perovskite, Ca-Al silicate and a SiO_2 phase after the release of a dense Fe-rich melt (Hirose et al., 2004). Because the melt is dense, it moves down to the bottom of the CMB, to form the ULVZ (Garnero et al., 2007 this volume), and the residual solid must rise by its chemical buoyancy. Note the size of plumes in the first stage that range from km to several tens of km near the CMB. If a plume were larger than these values, it would be swallowed up to make a bigger plume by size-dependent buoyancy differences. Moreover, plumes rising up side by side, would be attracted to combine together to grow a bigger plume. Thus, the number of small plumes decreases with height and with time (Fig. 10). The cluster of small-scale plumes represents those plumes detected by P- and S-wave tomography with a spatial resolution of several hundred kilometers.

A steep velocity gradient is observed along the margins of a superplume. This region reflects the steep temperature gradient, as suggested by the rapid decrease in thickness of the D″ layer on a plan view (Fig. 11). A thick layer enriched in pPV and a recycled MORB component is 350 km thick, suddenly decreases towards the superplume and is absent within the superplume. The center of the thick D″ layer may be as cold as 2000 K. Near the CMB below the D″ layer, the temperature reaches 4000–3500 K, where PV is stable, as supported by the velocity jump (Hernlund et al., 2005). No plumes are present in this cold region.

An ULVZ is present on the bottom of the mantle. If this is Fe-rich silicate melt, and is separated from the liquid core, the solid interface in-between may be a metasomatized mixture of metallic phases and Fe-silicates (Jeanloz and Williams, 1998). Between the lower interface termed the lower anti-crust, and the overlying solidified part of the forming ULVZ, there is a thin ($<$10 km, after Garnero et al., 2007 this issue) lens-shaped zone. Accordingly, the lower anti-crust is sandwiched between two melt layers. Anti-crust, as used in this paper, is defined as fractionated partial melt derived from mantle peridotite on the bottom of the mantle. If it is derived from recycled MORB, it is enriched in Fe silicates. If it is derived from cooled Fe-melts at the interface between the outer core and the mantle, it is composed of a mixture of Fe silicates and Fe metallic phases. Immediately after the consolidation of the magma

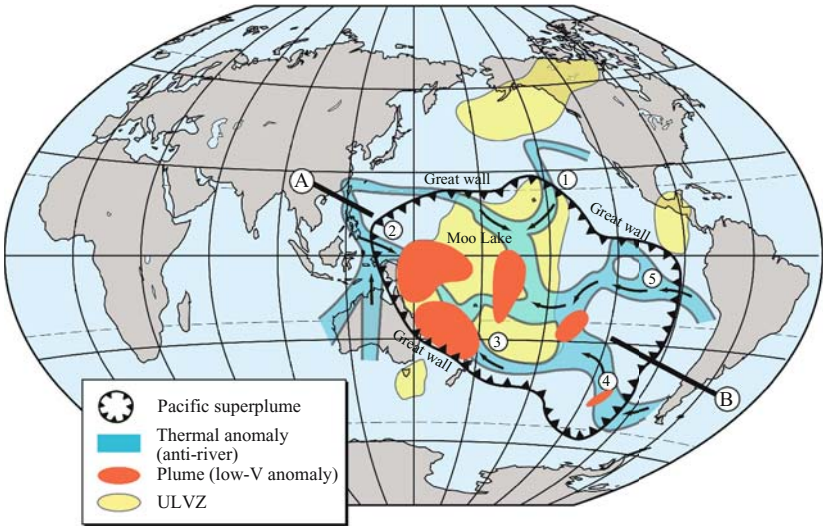

Figure 11. The geography of the Pacific superplume near the CMB. (a) Distribution of the thermal anomaly calculated after Trampert et al. (2004). The network of these anomalies may indicate the lateral flow of partial melt, mimicking river drainage systems at the bottom of the mantle. The arrows represent the directions of river flow towards the lake named "Moo". All the rivers meet at Moo Lake in the center of the Pacific superplume. The numbers 1–5 correspond to the names defined as anti-rivers on the CMB (see text for details). Note that the site of the rising plumes tends to coincide with the junctions of the anti-rivers. A steep velocity gradient is present on the margin of the superplume, named the Great Wall. (b) A cross-section along A-B in Figure 11-a, where convection cells right below the thermal anomaly on the CMB are shown schematically in the outer core. Note the global material circulation driven by the Pacific superplume, and the material fractionation on the bottom of the mantle that yields anti-crust and anti-tectosphere (defined below).

ocean, when the Earth formed at 4.56 Ga, a proto-anticrust may have formed on the bottom of the mantle, and that may be present in the D″ layer.

The high temperature metallic liquid rises up underneath the center of the superplume where the temperature is highest, compared with the surrounding regions. A decompressional rise would freeze the metallic liquid to make a thin solid layer of lower anti-crust that would move horizontally away from the center. The lower anti-crust moves smoothly underneath the superplume, because it is sandwiched between two liquid layers, but it may be stacked at the margin of superplume, where the melt disappears on the top boundary.

The anti-crust can develop on the bottom of the mantle by growing Fe-silicates formed by partial melting of recycled MORB in the upper half of the anti-crust, while the lower half is formed by metasomatic solidification of metallic liquid and Fe-silicates in the upper crust. Along the margins of the superplume, stacking and accretion of the siderosphere occurs by subhorizontal movement of the lower anti-crust. The siderosphere is defined in this paper to be the solidified metallic portion on

the top of the outer core, similar to the lithosphere on the top of the mantle. For the upper anti-crust, the opposite sense of shear modifies its structure (Fig. 10). Although the deformation proceeds in a ductile, rather than brittle, manner due to its high temperature, the thickness of the anti-crust may suddenly increase at the margins of the superplume, due to the absence of an ULVZ (melt). If this is correct, the outer surface of the outer core is not perfectly spherical, and this could be the cause of the irregular pattern of dynamo convection.

7 ANTI-PLATE TECTONICS ON THE CMB

In this section we summarize the characteristic tectonic processes operating at the CMB, and propose the existence of an "anti-crust" generated through "anti-plate tectonics" at the bottom of the mantle. The chemistry of the anti-crust markedly contrasts with that of the continental crust overlying the mantle. Both the crust and the anti-crust must have increased in volume through geologic time, presumably in close relation to the geochemical reservoirs of the Earth.

7.1 Topography of the Pacific superplume

Topographic aspects of the Pacific superplume are briefly summarized in this section in addition to some aspects of mega-structure mentioned in the previous section. An ULVZ (Lay et al., 1998) is present within the Pacific superplume right above the CMB (Fig. 11a). Trampert et al. (2004) calculated that the D″ temperature anomaly immediately above the CMB is focused into a series of networks, which suggests the possible distribution of Fe-rich horizontal melt-flow (Fig. 11a). Melt should flow from topographically higher to lower regions, and settle in a "lake" of the ULVZ right above the CMB. The thickest melt region should correspond to the highest T region at the center of Pacific superplume in which the first rising plume originated at 750 Ma. Five major "streams" meet at the center of the Pacific superplume, presumably transporting partial melt to the lake. We name these rivers, from the north in a counterclockwise direction, as the anti-rivers: (1) Hawaii-Line islands, (2) Solomon-Vanuatu-Samoa islands, (3)Vanuatu-New Zealand, (4) Off central-Chile, and (5) the area to the south of the Galapagos islands. The confluence of all these anti-rivers is named as the Moo Lake (Fig. 11a). The counterpart lake, called Atlantis, may be present beneath the African superplume; these two names derive from the Greek mythology of "lost continents".

Underneath an anti-river and within a few hundreds kilometers distance of it, rising plumes may be present in the outer core (Trampert et al., 2004). Therefore, the network pattern of the D″ temperature anomaly suggests a convection pattern of rising plumes in the liquid outer core. The convection cells in the core are about 1000 km across (Fig. 11b).

We show an east-west section that crosscuts the Pacific superplume to illustrate the CMB tectonics (Fig. 13b). The major convection right below the center of the Pacific superplume is shown within the liquid outer core. The topmost portion of

the rising convection is quenched at the CMB, leading to the formation of a thin solid layer composed of metallic phases similar to a lithospheric plate at the topmost part of the Earth. We coin the term "siderosphere" for this layer, above which is the FeO-rich Moo Lake. The siderosphere is bounded on the top by a melt zone and on the bottom by a liquid zone, and is hence characterized by horizontal mobility just like the lithosphere in the outer shell of the Earth. Many smaller-scale convection cells may also be associated with the overlying iron-silicate melt rivers, which transport volatile components such as C, H, O, S and the common lithophile elements of Si and Mg. We term them "anti-hotspots" at the CMB that penetrate the siderosphere and originate in the core.

From the top of the Moo Lake, Fe-silicates may gradually grow downwards to increase the volume of the anti-crust. Towards the extremity of the Moo Lake, a consuming anti-plate boundary appears, which generates anti-orogenic belts by thrust tectonics. This is partly due to the absence of partial melt above the CMB. The thickness of the anti-orogen may be larger at this boundary through the duplication of anti-crust composed of more metallic lower crust and Fe-silicate above (Fig. 11b).

A steep geothermal gradient on the boundary of the Pacific superplume corresponds to a steep cliff termed herein the "Great Wall" (Fig. 11a). This in turn corresponds to the boundary between pPV above and PV below. The P-wave velocity jump has been well documented at the thick sandwiched pPV layer, redefined in the strict sense as the D″ layer. The thick D″ layer suddenly thins out into the superplume region. Abundant recycled MORB slabs are present in the thick D″ layer with a low-T core in the middle of the D″ layer and their volume decreases inwards into the superplume, because partial melting proceeds in that direction, due to an inward increase in T. The resultant dense melt moves downwards forming the anti-rivers, whereas the residual solid rises up producing small chemical plumes enriched in Ca-perovskite, Ca-Al silicate, and a SiO_2 phase. Collision of these chemical plumes generates a larger plume by amalgamation, and the larger plume rises up faster and chases the smaller ones. The larger plumes thus become even larger by swallowing up the smaller plumes. Finally, this results in a huge plume developed on the top of the peripheral part of the superplume, as a high-T and compositionally different superplume from the surrounding mantle. A superplume is thus a cluster of plumes compositionally and thermally different from the surrounding mantle.

In the center of the superplume recycled MORB may be absent, due to the inability to yield andesitic plumes through time. Instead, residual phases such as Mg-perovskite may predominate.

7.2 Anti-crust: another continental crust at the bottom of the mantle

According to multi-anvil melting experiments of MORB under conditions of the uppermost lower mantle performed at 25–27 Gpa and T = 2400–2530°C (Hirose et al., 1999, 2004), a partial melt generated by 43% melting has a composition characterized by an FeO-rich silicate melt and an andesitic residual solid composed of Ca-perovskite + CAS (CaAl-rich silicate) + SiO_2 phase (stishovite). Under the

conditions of the CMB, the melt is presumably denser than the solid residue, due to the high-FeO composition of the melt, suggesting compositional separation. Ohtani and Maeda (2001) measured the depth of density crossover in the pyrolite system to be 70 Gpa in the middle of the lower mantle (Fig. 1). It is important to note here that the density crossover is very sensitive to the FeO content of the host rocks. If the source material is recycled MORB, the partial melt would sink to the CMB (Ohtani and Maeda, 2001).

However, melt formation can be possible only near the top and bottom of the mantle, because the solidus is close to the postulated geotherm only near the top of the mantle called the boundary layer, and again at the boundary layer of the core. This is a consequence of the presence of the boundary layers that cover the high-T mantle (1300°C mantle potential T) near the surface (room temperature), and the high-T at the core-mantle boundary (4000 K), above which only a 2000 K warm mantle is present. Hence a steep T-gradient is present in both regions, and the solidus is close to the geotherm.

In both regions, partial melt can be formed through the melting of basalts which are supplied by lithosphere that is produced at a mid-oceanic ridge (Fig. 12). The tectonic regime is very similar in both regions: horizontal movement followed by subduction of low-T slabs from trench to deep mantle, and the stagnation and drop of slabs at the MBL on their way to the bottom of the mantle. These cold-slab aggregates enriched in MORB crust move horizontally, right above the CMB, thereafter to finally

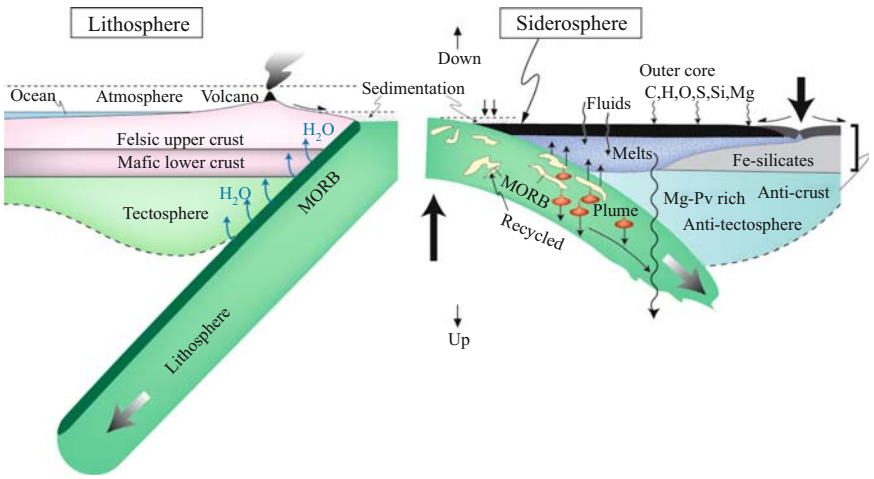

Figure 12. A schematic illustration of anti-plate tectonics on the bottom of the mantle (right). For comparison, plate tectonics is shown to form the continental crust (left). Note the upside-down nature of the right figure, which makes it easy to understand the similarity between the two processes on the top and bottom of the mantle. The similarity is summarized as: (1) horizontal movement, (2) role of fluids, water vs light elements in the core, (3) dual compositional layers in the crust, (4) role of MORB crust in chemical fractionation, and (5) sedimentation. See the details in the text.

rise up obliquely, or "subduct" if we consider the schematic illustration given in Figure 12 upside down. The released partial melt increases the volume of the anti-crust with time. Compared with the rate of subduction on the surface of the Earth, the "subduction" of the bottom layer is rapid, almost four times faster. This is because the circumference of the surface layer is larger than that of the bottom layer by about four times. The subducted slab aggregates supplied from the low-T, thick D″ layer finally rose up as chemical plumes and plume clusters from the superplume region, with the gravitationally stable mantle remaining in the center of the superplume enriched in Mg-perovskite. This dense peridotite, presumably with Ca-perovskite, corresponds to the tectosphere in the surface layer outlined by Jordan (1988). We name this 'anti-tectosphere'.

The partial melt derived from recycled MORB at the CMB accumulates at the bottom of the CMB to grow an anti-crust. Simultaneously, another anti-crust that is compositionally different forms under the superplume, through the cooling of uprising liquid metallic core. Thus, the anti-crust is composed of a lower metallic crust and an upper Fe-rich silicate crust. This is very similar to the growth process on the outer layer of the Earth involving subduction of lithosphere to yield a partial melt of felsic magma (TTG) caused by subducting MORB crust, the mafic lower crust, and by addition of water released from subducting slabs (Fig. 12). Slab melting may have been a predominant process in the hot Archean Earth as shown by the REE geochemistry of TTG rocks by Brown (1979) and Martin (1986), and less common in the Phanerozoic. The double layer structure proposed above is similar to the compositional structure of the continental crust, composed of mafic lower and felsic upper crusts.

With time the continental crust at the surface has grown, occupying one third of the globe's surface, and it reached an average thickness of 35 km after 4.6 Ga of evolution with large pulses of crustal formation at 2.7 Ga and 2.0 Ga (Rino et al., 2004). Although highly speculative, by analogy with these episodic events on the surface of the Earth, we propose that the growth history of the anti-crust may also have followed a similar sequence.

8 PLATE TECTONICS VS SUPERPLUME DYNAMICS

In this section, we will show that superplume dynamics is a tectonic paradigm independent of plate tectonics. Plate tectonics is restricted to the upper mantle, where horizontal movement of lithosphere dominates, but not in the lower mantle where vertical movement of cold blobs or plumes dominates. A superplume is centered in plume tectonics in the lower mantle. Immediately above the CMB, anti-plate tectonics plays a key role in fractionating mantle to create anti-crust, which is an equivalent of continental crust formed by a subducting slab in the surface layer of the Earth.

Thus, the solid Earth is driven by two plate-tectonic systems at the top and bottom of the mantle separated by a plume tectonics domain in between. The driving force of plates has long been regarded to be predominantly by slab-pull at a consuming plate boundary with a subordinate role of ridge push at a divergent plate boundary.

A slab-pull force is made by cooling of lithosphere, and leads to the idea that cooling is a major cause of plate tectonics (e.g., Anderson, 2005).

Yet, a new paradigm of whole Earth dynamics suggests a different view as follows. Anti-plate tectonics is driven by a strong vertical flow driven by superplumes. A major energy flow moves to the surface from the D″ layer through a superplume, because the temperature of the outer core is 1500 K higher than that of the overlying mantle, and it heats up the mantle to create a superplume. This clearly indicates that superplumes control the Earth's dynamic and that plate tectonics is a subordinate element in the whole Earth system driven by superplumes.

Material fractionation is due to melt formation and removal towards the top and bottom of the mantle. This is due to the presence of boundary layers, i.e., lithosphere and D″ layer, from which two different continents have grown through time.

Between the two regions of plate tectonics at the top and bottom of the mantle, plume tectonics causes vertical material transportation. This flow is, however, discontinuous because of the presence of a thermal boundary layer at 660 km depth.

8.1 660 km depth dynamics

The MBL is a boundary layer which exhibits $\Delta T = 200$–300 K under a subduction zone, and $\Delta T = 100$–200 K under a rising plume (Fig. 2).

Due to the presence of a phase change reaction with a negative Clapeyron slope, and a viscosity drop at this boundary, a subducted slab cannot penetrate through the 660 km boundary; this was first predicted by Ringwood (1982) who named a stagnant slab a "megalith" (Ringwood and Irifune, 1988).

The stagnant slabs were later identified by the development of tomography under eastern Asia by Fukao (1992). Where a slab penetrates into the lower mantle, a huge blob-shaped mass is present, clearly demonstrating that the mass was once stagnant at 660 km depth (Fukao et al., 2001; Zhao, 2004).

The collapse mechanism of a once-stagnant slab is controlled by the following parameters: (1) a lower mantle more viscous by 1–2 orders of magnitude than the upper mantle, (2) a viscosity drop due to recrystallization at 660 km from coarse-grained ringwoodite to fine-grained perovskite plus wüstite, (3) positive buoyancy in the center of the slab due to the above phase change that has a negative Clapeyron slope, and (4) the size of the stagnant slab that may create negative buoyancy due to its cold temperature.

Honda et al. (1993) were the first to simulate by numerical modeling the avalanche of once-stagnant slabs at 660 km depth. The best-documented geological example is the Cretaceous event first pointed out by Larson (1991) who used the term "superplume", regardless of its size, for the extremely active plume event in the Cretaceous. The term pulse is used here to describe a transient disturbance by a superplume of the mantle operating system. A superplume pulse event is the result of the flushing of stagnant slabs through the 660 km barrier on a huge scale, as described by Honda et al. (1993), Maruyama (1994), Larson and Kincaid (1996) and Condie (1998).

A superplume pulse or pulsation causes an episodic mantle event that is different from a normal period of double-layered mantle convection. The pulsation of superplumes occurred every 100–200 m.y. giving rise to geologically well-recognized events such as ophiolite pulses. Episodic whole-mantle convection triggers a pulsation. A superplume is active in a geologically restricted time, controlled by the amount of recycled MORB under a supercontinent (for details see Utsunomiya et al., 2006 in this volume). This implies that a superplume has a life-time from birth to demise. The birth of a superplume is an event that commonly coincides with the break-up of a supercontinent (Maruyama et al., 2001). The most extensive superplume event is a mantle overturn that can change whole-mantle convection to double-layered convection (Breuer and Spohn, 1995) and that may take place in a time-scale of billions of years (Maruyama et al., 2001). Accordingly, the behavior of the mantle may be classified into four hierarchical ranks: (1) normal period (2) pulse period (3) the birth of a superplume, and (4) mantle overturn (Fig. 13).

8.2 Role of the MBL in the upwelling

If a rising plume hits the ringwoodite breakdown reaction, it may not be able to penetrate through the 660 km barrier. However, if the ringwoodite breakdown reaction is cut by another reaction with a positive Clapeyron slope at an elevated temperature in P-T space, and if the rising plume cuts this reaction line, the plume will accelerate to penetrate through the boundary. This is the case of majorite that is stable on the

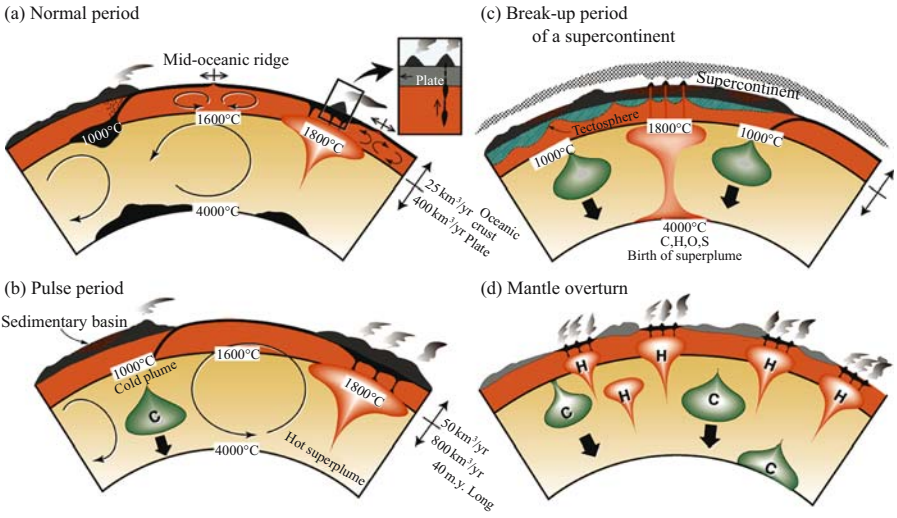

Figure 13. The hierarchy of mantle dynamics: (a) normal period, (b) pulse period, (c) the birth of a superplume, and (d) mantle overturn (after Maruyama et al., 2001). The impact by these events on the surface environment depends on their type, e.g., type (3) leads to mass extinctions; type (4) is the strongest.

high-temperature side at 660 km depth. The stability field of majorite on the high-temperature side close to the pyrolite solidus has been experimentally determined with multi-anvil apparatus (Hirose, 2002). This supports the idea that a plume rising from the lower mantle will not be stagnant, i.e., stop at the 660 km boundary. This can explain the observation that most S- and P-wave global tomography or focused tomography of plumes at 660 km depth in most places worldwide never shows the clear stagnant shape.

However, another important reaction of ringwoodite = majorite+wüstite that has a negative Clapeyron slope is present after the rising plume passes the majorite stability field (Fig. 14). This reaction occurs slightly above the 660 km discontinuity plane.

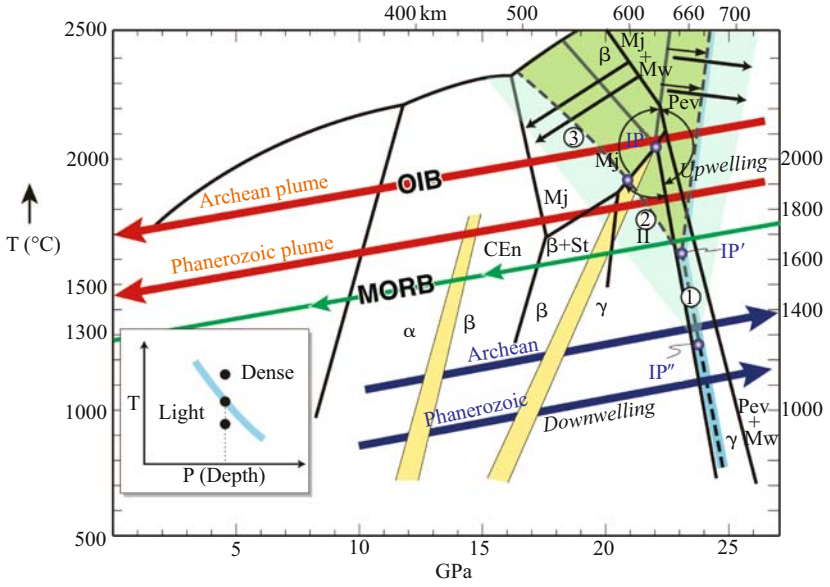

Figure 14. A phase diagram of pyrolite in the upper mantle. The Mg_2SiO_4 phase transforms from olivine (α), wadsleyite (β), and ringwoodite (γ) depending on pressure, with a narrow transition depth range shown in yellow. A subduction zone geotherm and mantle upwelling are schematically shown with blue and red arrows respectively, for Phanerozoic and Archean time in comparison with the modern MORB adiabat (green). Ringwoodite breaks down to prerovskite + magnesiowüstite with a negative Clapeyron slope, which causes stagnant slabs at 660 km depth. This curve bends at IP′ (23 Gpa and 1600°C) to the much lower pressure side with a far more gentle slope. Majorite ($MgSiO_3$) has a wide wedge-shaped stability field above the IP′ point bordered on the high-P side by a steep positive curve of majorite-perovskite with a large ΔV. Due to the polymorphic transformation from PV to Mj a rising plume is promoted that penetrates the 660 km boundary; thereafter it may be stagnant at 600 km due to the ringwoodite breakdown reaction. If the plume T is higher than that of a Phanerozoic plume, a wadsleyite breakdown reaction intersects with the plume adiabat. The ΔV of this reaction is much larger than that of the ringwoodite breakdown reaction, hence much more difficult to penetrate through the boundary. Under the higher-T conditions in the Archean the stability field of ringwoodite was small; instead majorite had a wide stability range in the MBL. The small inset figure on the lower left shows the principle of a stagnant slab at 660 km depth.

In a strict sense there are two major boundaries in a high-geothermal region, one at the majorite/perovskite polymorphic transformation and another at the ringwoodite breakdown reaction. The modal volume % amounts to 40% $MgSiO_3$ phase and 60% ringwoodite in this P-T region, hence both boundaries should be seismologically detectable. The branching shape of the Pacific superplume at the depth of the MBL (Fig. 2) may reflect the role of majorite, although a detailed seismological study has not yet been completed.

The major cause of the stagnant shape of a rising plume is the degree of the negative Clapeyron slope and ΔV of the reaction. The largest ΔV and most gentle slope is provided by the wadsleyite breakdown reaction among the three reactions, in ascending order of temperature, (1) ringwoodite = Pv + Mw, (2) ringwoodite = Mj + Mw, and (3) wadsleyite = Mj + Mw (Fig. 16). Reaction (2) has a narrow P-T range, and if the rising plume is locally hotter, it may hit reaction (3) to be stagnant above 600 km depth. If the T is slightly lower, it may penetrate through the boundary by reaction (2) below 600 km depth. These petrological inferences may well explain the shape of the Pacific superplume in the MBL, i.e., absence of a deformational shape of the plume at 660 km depth, but branching on the bottom of the MBL into three different horizontal directions (Fig. 2).

8.3 The MBL in the Archean

In the Archean a hotter mantle majorite was probably stable over a wider pressure range than in the modern mantle, because the temperature of the MORB source mantle was c. 200 K higher than today (Komiya, this volume). Moreover, the fact that the composition of the Archaean mantle was ca. 2 wt% richer in FeO than today's mantle (Komiya, this volume) would have enlarged the majorite stability field towards the higher and lower temperature sides and towards the lower-pressure side (Fig. 14). Note the invariant point of IP″ located at 660 km and 1200–1300°C in Figure 16. Even in the modern MORB adiabat, the stability field of majorite is 150 km thick, if the peridotite is FeO-rich, as in the Archean MBL. Majorite is not stable in a modern subduction environment, but it may have been present in the Archean (Fig. 14).

Along the Archean geotherm the mineralogical and modal change of mantle peridotite via depth is shown in Figure 17. The FeO-rich Archean mantle (case of Archean 2) has a wide stability field of majorite (80%) in the MBL (520–710 km depth range) in the mantle upwelling zone, where ringwoodite has no stability field. In contrast, in a subduction zone environment, majorite has a narrow stability range from 650 to 670 km depth, and instead ringwoodite is predominant (Fig. 15).

This presumably caused the double-layered mantle convection in the Archean, because the majorite-producing reaction by consumption of wadsleyite would have had a more gentle Clapeyron slope than ringwoodite breakdown reaction to yield perovskite + Mw, as at present (Fig. 14).

Another characteristic feature of the Archean Earth was a thicker MORB crust (20 km) than today (6 km) and a thinner lithosphere (40 km at 50 Ma) than today (60 km at 50 Ma) (Komiya, this volume). This difference would have promoted the

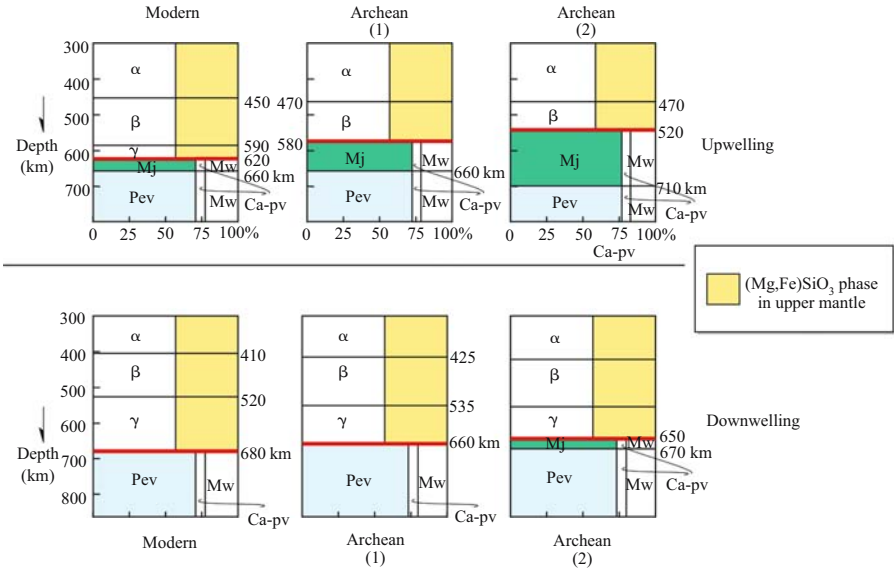

Figure 15. The mineralogical and the modal change of peridotite with depth along Phanerozoic and Archean geotherms. Geotherms are from Figure 16. Three representative modal changes are shown in the Modern, Archean (1) and Archean (2) in the depth range from 300 to 800 km. Note the systematic difference in mineralogy between the majorite-enriched Archean and the ringwoodite-enriched Phanerozoic mantle. Archean (1) assumes the same chemical composition of peridotite as the modern one. Two different reactions with negative Clapeyron slopes are shown by red lines. The MBL is marked in green and blue.

selective segregation of MORB crust into the MBL and so the MORB component in the MBL would have accumulated with time, because the density of MORB is smaller than that of slab peridotite in the MBL depth range (Fig. 16). These recycled MORB or garnet pyroxenites were residues of TTG melt extraction after slab melting, and would have played a critical role in the generation of flood basalts when the mantle overturned at 2.8–2.7 Ga, as discussed later.

8.4 The MBL as a huge water storage tank

As the mantle cooled with time, the stability field of majorite in the MBL was progressively reduced, whereas the stability field of dense hydrous silicates would have enlarged with time. If the temperature at 150–200 km depth (ca. 5.5 GPa) decreased 550°C (the choking point of Kawamoto, 2004), then surface water must have moved down to 410 km along subduction zones (Ohtani et al., 2004). Considering past subduction zone geotherms, this most likely occurred at some time around 600 Ma (Maruyama and Liou, 2005). This topic is reviewed by Omori and Komabayashi (2007) in Part II of this book.

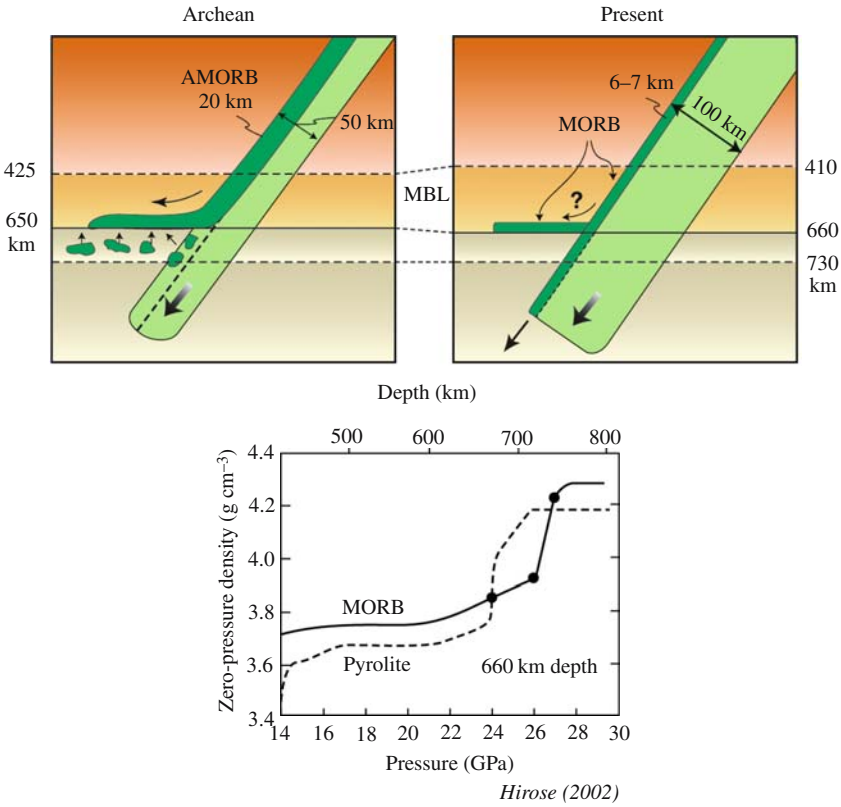

Figure 16. The more effective segregation of MORB crust in the Archean MBL, compared with that of the present MBL. The density profile of MORB vs peridotite in the pressure range of 14–30 GPa is after Hirose (2002). The thicker Archean MORB crust (15–20 km) in spite of a thinner lithosphere (c. 40 km at a given age, e.g., 50 Ma), compared with the modern Earth, tends to promote the segregation and accumulation of the MORB crust (Karato, 1997) specifically in the Archean MBL.

Whether or not the density crossover of melt against surrounding mantle occurs at 410 km depth has been hotly debated since Ohtani et al. (1998). Recently Bercovic and Karato (2003) suggested that ubiquitous melt occurs at 410 km depth not only under a subduction zone but also under a rising plume, and that the melt works as a filter to alter the penetrating flow from below or above. UHP experiments that estimate the density crossover at the MBL depth support the idea, but only if water is deficient (Matsukage et al., 2005; Sakamaki et al., 2006). There is, however, no strong evidence to support this idea at least in the western Pacific, because above 410 km depth electrical conductivity is one order of magnitude higher than that of the Pacific standard area, indicating a higher water content

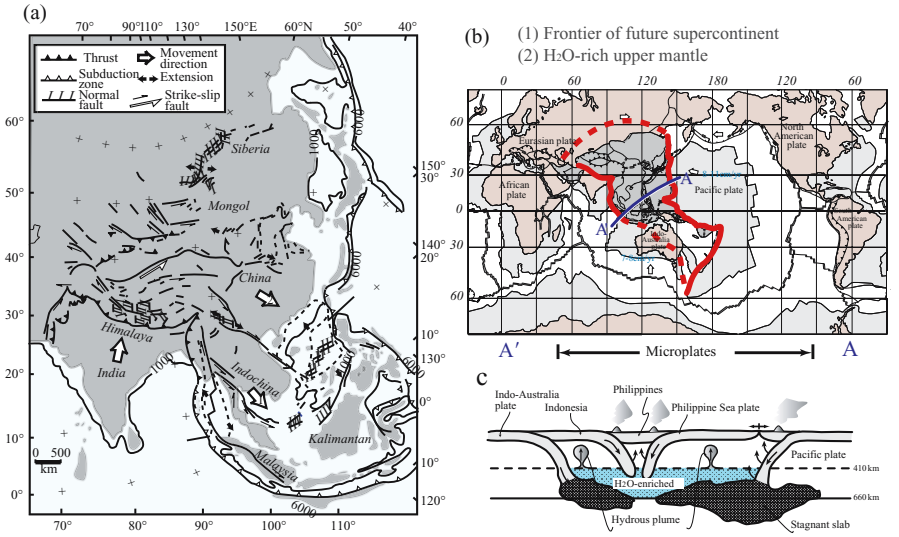

Figure 17. The WPTZ is the entrance window of water carried into the deep mantle by double-sided subduction. The WPTZ is characterized by numerous microplates in the continent and ocean, and by active volcanism. The cross-section along A-A′ shows water-rich MBL and hydrous plumes originating at 410 km depth. Active deformation, which is most extensive in the WPTZ, has been interpreted to be a result of the indentation of India into Asia (top figure by Tapponnier et al., 1982). However, the active deformation of the WPTZ is more likely to be due primarily to a high-water content in the underlying MBL supplied by double-sided subduction; the Indian collision played at most a subordinate role. An upper mantle softened by water made it possible for the Indian continent to indent some 2000 km northwards into Asia (top figure).

(Ichiki et al., 2006; Hae et al., 2006). The higher water content increases melt buoyancy.

Field observations in the western Pacific are the key to confirming the filtering model of Bercovici and Karato (2003). The WPTZ is the zone where water enters into the deep mantle by double-sided subduction (Fig. 17). On the eastern side the old Pacific plate was subducting under the WPTZ, while from the south the Jurassic to Eocene Indo-Australian plate was subducting northwards. These subduction zones transported hydrous silicates trapped in hydrated oceanic lithosphere along transform faults and in curved normal faults developed on the trench-outer wall.

The WPTZ is characterized by a MBL temperature that is 200–300 K lower than that of standard mantle (Fig. 3) due to the cooling effects of double-sided subduction, and this process led to refrigeration. The temperature of the source mantle of back-arc basin basalts is 60 K lower than that of MORB source mantle, while the water content of the source mantle is 0.2 wt%, which is about 10 times more than that of MORB source mantle (Komiya and Maruyama, 2007). Moreover, the measured

electrical conductivity above 410 km clearly demonstrates the presence of water-rich mantle, in contrast to the underlying MBL and other areas in the Pacific (Ichiki et al., 2006).

In spite of having the lowest temperature mantle in the world, the WPTZ is the most active volcanic zone that has numerous island arcs (22 arcs among the world's 34 arcs), opened back-arc basins and small ocean basins, and continental hot regions (e.g., Miyashiro, 1986; Smith, 1998; Fan and Hooper, 1991). Moreover, the WPTZ is a most active zone of deformation that is still on-going; it is characterized by the presence of numerous microplates, by the fragmentation of continents, and by strike-slip movements on faults. Active deformation, seismicity, continental fragmentation (Molnar and Tapponnier, 1975) (Fig. 17a), and the formation of magma (Flower et al., 1998) can all be interpreted as a result of the high content of water transported to the MBL by double-sided subduction. In conclusion, water and water-rich magmas never stay at 410 km depth due to the density-crossover; in general they rise up to cause active mantle dynamics in the WPTZ, in spite of the 200–300 K lower temperature of the MBL.

Seismic observations in the western Pacific definitely do not support the idea of a ubiquitous melt layer at 410 km depth (Kato and Jordan, 1999). Instead, P-wave tomography clearly demonstrates the presence of plumes originating at 410 km depth right below active volcanoes in eastern China (Zhao, 2004). These observations suggest the ubiquitous occurrence of H_2O-rich fluids above 410 km, which cause: (1) a lower viscosity (Karato and Jung, 1998), (2) a lower melting temperature (Iwamori, 1998), and (3) hydro-softening of the lithosphere.

9 MANTLE DYNAMICS THROUGH TIME

In this section we will discuss the basic principles of the thermal history of the Earth; firstly to predict the geological change in tectonic style through time, and secondly, to review the geologic record of mantle convection in order to test ideas on the secular evolution of mantle dynamics.

Geologic time is divided into four Eras, Hadean (4.56–4.0 Ga), Archean (4.0–2.5 Ga), Proterozoic (2.5–0.6 Ga) and Phanerozoic (0.6 Ga-present). The Hadean is the Era with no extant geologic record, except for some 4.4–4.2 Ga detrital zircons found in Proterozoic river sediments in W. Australia (Wilde et al., 2001), and for one 4.2 Ga xenocrystic zircon *in situ* in the Acasta Gneisses of NW Canada (Iizuka et al., 2006). The mystery of why no rocks of this Era remain on the Earth has been much debated and is not well understood. One hypothesis assumes that there was no continental crust, oceans or plate tectonics until 4.0 Ga due to active convection, because a thick hot CO_2-enriched primordial atmosphere prohibited rapid cooling as in present-day Venus. However, the theory of planetary formation does not support this interpretation, because the calculated cooling rate is too fast to have a primordial ocean, at least less than 100 m.y. after the planetary formation. Moreover, the heavy meteorite bombardment that deformed the Earth must have been very short, of the order of 10 m.y. and at most 100 m.y. (e.g., Abe and Matsui, 1985).

The second model assumes firstly the existence of extensive continental crust throughout most of the Hadean Earth, and secondly the operation of plate tectonics that was responsible for the generation of that continental crust. This vast primordial continental crust was melted by the heavy bombardment that peaked at 4.0 Ga. A new magma ocean was made by this event. This scenario has come from the following idea.

An extremely high cratering rate on the Moon immediately before 3.8 Ga suggests a possible scenario according to which the primordial continental crust formed after the consolidation of a magma ocean at 4.56 Ga on the Earth, and it may have re-melted extensively at around 4.0 Ga. Before this heavy bombardment, plate tectonics began to form primordial granitic crust around anorthositic proto-continents until 4.0 Ga. A new theory has come to explain this scenario according to which planetesimals in the Kuiper belt were transported to the inner terrestrial planets including the Earth at about 4.0 Ga, by the resonant interaction between Jupiter and Saturn. These planetesimals destroyed the primordial continental crust to reproduce the shallow magma ocean (Tsiganis et al., 2005).

The thermal history of the Earth is briefly summarized below. Immediately after the formation of the Earth by the extensive collision and amalgamation of planetesimals at 4.56 Ga, the early Earth must have been completely molten even in the center, if a giant impact occurred to form the Moon (e.g., Ida et al., 1997). The Earth started its history from a totally molten state by cooling. Before 4.0 Ga, a primordial ocean was born to initiate plate tectonics. Then, a second heavy bombardment re-melted the primary continental crust by the resonance of Jupiter and Saturn that transported a number of planetesimals to the Earth from the Kuiper belt.

Since then, the Earth has cooled down through time with episodic thermal events according to inevitable mechanisms within the solid Earth portrayed in Figure 20. Mantle evolution in the last 4.0 Ga may be classified by the following four events, (1) double-layered mantle convection in the Archean, (2) mantle overturn at 2.8–2.7 Ga, and subsequent episodic whole-mantle convection, (3) birth of pPV at 2.3 Ga on the CMB, and (4) initiation of the return-flow of seawater into the mantle at 0.75 Ga (Fig. 18).

9.1 Double-layered mantle convection in the Archean

In the Archean MBL region, majorite would have occupied a wide stability field in a regime with a high Rayleigh number due to higher-temperature than today, and with a more gentle Clapeyron slope for the wadsleyite breakdown reaction to yield majorite + wüstite than that of the reaction ringwoodite = perovskite + wüstite in the Archean MBL (Figs. 14 and 15). Instead, ringwoodite may have not been present in the Archean MBL, or it had a narrow stability field in deep subduction zones, if present (Fig. 19). This caused Archean mantle convection to have a double-layered mode.

The Archean MORB potential temperature estimated by Komiya (2004), and Komiya et al. (2002b, 2004) was 150–200 K higher than today and 300 K higher for OIB magma in the Archean. Moreover, 2 wt% higher FeO in the mantle in the

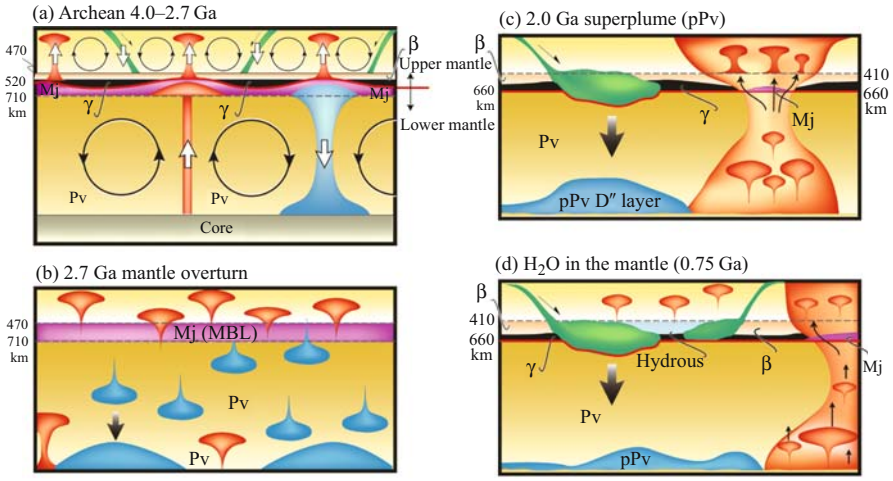

Figure 18. The evolution of mantle convection through time after 4.0 Ga. (a) double-layered in the Archean, (b) mantle overturn at 2.8–2.7 Ga that caused the Earth to be covered by around two to three kilometer-thick basalts, (c) birth of pPV on the CMB at ca. 2.3 Ga, and (d) return-flow of seawater into the mantle at 0.75 Ga.

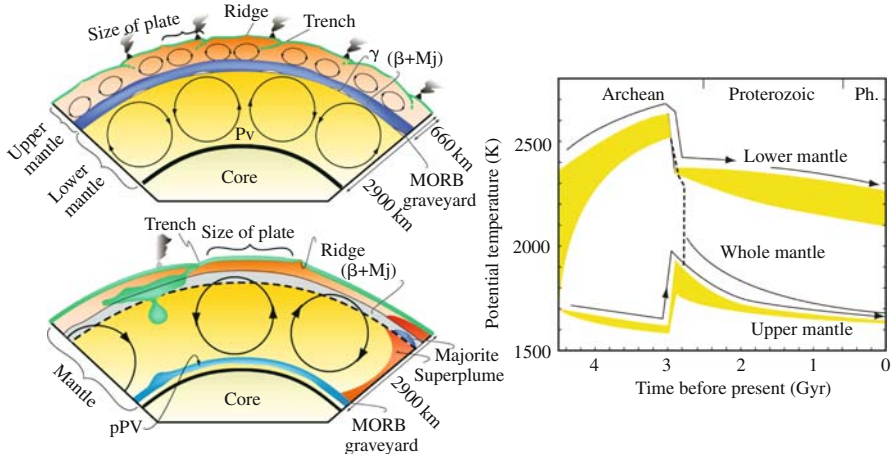

Figure 19. Archean double-layered mantle convection was due to the widespread occurrence of majorite in the MBL, and to a higher mantle temperature than today. And an FeO-rich Archean mantle promoted a wider stability field of majorite than today. The double-layered mode must have changed, preseumably at 2.8–2.7 Ga during a mantle overturn event. The widespread occurrence of flood basalts over most pre-2.8 Ga cratons supports this idea (see Komiya, this volume).

Archean than today must have caused majorite to have a wider stability field in the MBL in the Archean, which promoted double-layered mantle convection (Fig. 15).

The thermal gradient in the MBL of the modern Earth is 200–300 K under a subduction zone and 100–200 K under rising plumes. But if the convection were double-layered, the thermal gradient must have been large in the Archean, when a high-T mantle plume would originate easily at 470 km depth (Fig. 15). The top and bottom of the MBL including their mineralogy, were different in the Archean compared with the modern Earth. If we define the MBL as a zone in which wadsleyite and majorite are stable in the high-T region, it ranges from 470 to 710 km depth. On the other hand, under a cold region such as a deep subduction zone, the MBL ranges from 425 to 670 km, where wadsleyite, ringwoodite and majorite are stable.

There is another definition of the Archean MBL. The most critical physical reason for the definition of the boundary between the upper and lower mantle in the modern Earth is derived from the ringwoodite breakdown reaction with its negative Clapeyron slope. In the Archean, the reaction was different from this curve, because the wadsleyite breakdown reaction was present. If we adopt this curve with its negative Clapeyron slope for the definition, the Archean MBL must have occurred at 520 km depth with a thick majorite layer of ca. 190 km in the hot region. On the other hand, the boundary reaction under a deep subduction zone would have been at 650 km depth (Fig. 15). Thus the boundary between the upper and lower mantle in the Archean was variable, ranging from 520 to 650 km depending on the T.

In the Archean plumes radiating from a depth of 470 km may have had a big head and slender tail, and have generated komatiitic lava flows in a hotspot island in a regime with smaller plates on the surface than today. The Archean Earth may have been covered by about 400 microplates about 700 km across and full of intra-oceanic island arcs (Komiya et al., 1999). The modern analog is the western Pacific, where similar dynamic plate boundary processes are on-going, presumably with a mantle viscosity similar to that in the Archean on account of its higher water content.

With time, collision and amalgamation of immature island arcs caused the growth of continents. These processes are best documented in N. America where a primitive composite continent formed at ca. 1.9–1.8 Ga (Hoffman, 1989). The N. American united continent was over 3000 km across, as seen today, because N. America combined with Baltica is still 3000 km across. This continent is called Laurentia (Hoffman, 1989). The length of an orogenic belt was less than 700 km in the Archean, and a continent was less than 700 km across before 2.7 Ga, but grew to more than 3000 km across after 1.8 Ga. N. America combined with Greenland and the northern British Isles made up Laurentia, which was combined with Baltica. This large continent named Laurussia was half the size of the Pangea supercontinent (Hoffman, 1989). These observations support the idea of a change in the size of plates at sometime after 2.7 Ga and before 1.8 Ga. This presumably reflects the change in size of mantle convection, which in turn was related to a change in mantle convection from double-layered to episodic whole-mantle during the transitional period of 2.7–1.8 Ga.

According to Christensen and Yuen (1985), whole-mantle or double-layered convection is controlled by the Clapeyron slope of a phase change and density difference.

As mentioned above, in Archean time the MORB source mantle was 150–200 K higher, and the OIB source mantle (MBL) was around 300 K higher than today. These relations led to the predominant occurrence of majorite at the bottom of the MBL instead of ringwoodite, particularly in an FeO-rich Archean mantle (see summary by Komiya, this issue), and they also led to a more gentle negative Clapeyron slope than that of the breakdown reaction of ringwoodite to yield majorite + wüstite; all these relationships strongly suggest double-layered convection in the Archean.

One of the critical observations is the presence of restricted occurrence of Al-depleted komatiite which geochemistry strongly supports the dominant occurrence of majorite in the source mantle (Ohtani, 1983; Herzberg et al., 1988; Walter, 1998).

9.2 Mantle overturn at 2.7 Ga, and subsequent episodic whole-mantle convection

Because double-layered convection continued for a long time throughout the Archean (one-third of Earth history), the upper mantle, being separated from the lower mantle, would have been isolated without any input of hot and fertile material from below. This caused effective cooling of the Archean upper mantle through time, leading to eventual catastrophic mantle overturn, because heat loss in the upper mantle by plate tectonics leads to cooling with recycled MORB dominant on the bottom of the MBL. In contrast, the topmost lower mantle would have heated up by radiogenic decay of K, U and Th that was more effective in the Early Earth, and eventually this brought about a density overturn between the upper mantle and the topmost lower mantle.

Numerical simulation supports this idea, and the calculation suggests that the time-span for an overturn is ca. 100 m.y. (Breuyer and Spohn, 1995). Geologic records reviewed by Komiya (this volume) indicate that the Earth was covered by about 2000–3000 m (as stated before)-thick flood basalts in the period 2.8–2.7 Ga over at least 35 small Archean continental fragments that were largely composed of composite island arcs. These observations suggest that the Earth was covered on a global scale by flood basalts on both continents and oceans at this time. Although most records from the oceans have been lost by later subduction, there are some preserved relicts of Pacific-type accretionary orogens. We point out that the formation of 2.7–2.8 Ga global-scale flood basalts was immediately after a period of minimum world magmatism (Fig. 20), as shown by Komiya (this volume).

9.3 Birth of post-perovskite at the CMB and the birth of superplumes

The continental growth curve has been one of the most important conceptual constructions on the water-covered planet of the Earth. Several different views and estimates have been proposed; (1) 120% of continental crust had already been formed before 4.0 Ga, and decreased thereafter, based on thermal consideration of Earth history, (2) steady-state growth through time, (3) episodic growth due to the evolution of mantle convection (see summary by Reymer and Schubert, 1984). Among these, one of the most widely accepted has been the idea that early growth was so rapid that

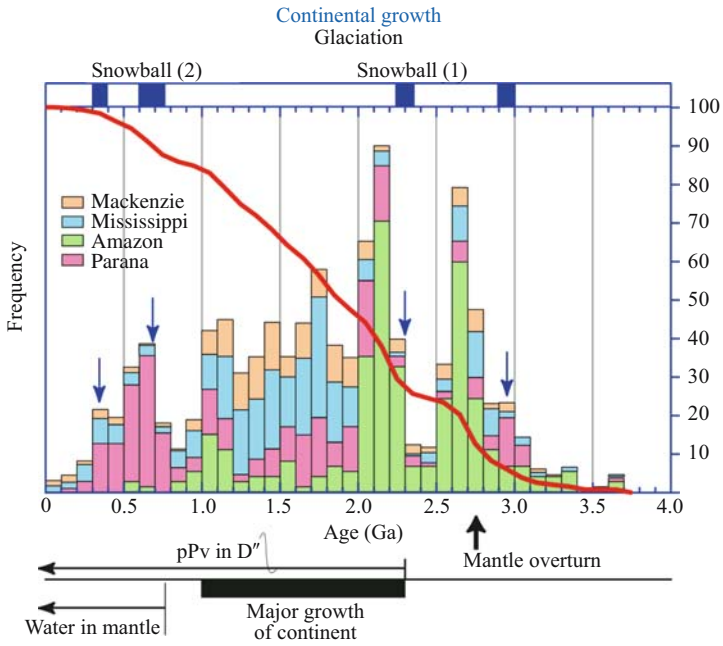

Figure 20. Birth of pPV at the CMB at ca. 2.3 Ga. The growth curve of the continental crust inferred from the age population of river-mouth zircons is after Rino et al. (2004). Note the rapid growth of the crust after 2.3 Ga (25%) until 1.0 Ga (85%). This may be caused by the birth of pPV on the CMB.

about 80% of continental crust was produced by the latest Archean (Reymer and Schubert, 1984).

Regardless of any hypothesis, an estimate of crustal growth rate has been made using the age of river-mouth zircons, starting from N. America, S. America, East-Central Asia, and Africa by the Titech Group, Japan (Rino et al., 2004). In contrast to the generally agreed ideas mentioned above that the main growth was in the Archean, the river data (Fig. 20) show that the major period of continental growth was in the Proterozoic, when ca. 60% of continental crust was produced in the period from 2.3 Ga to 1.0 Ga. How can we interpret this unusual result in the framework of a cooling Earth? The answer comes from the discovery of post-perovskite (pPV).

The birth of pPV at the bottom of the mantle in the early Proterozoic may explain the new river-zircon continental growth curve, because the pPV/PV transition curve has a positive Clapeyron curve of 9.0 MPa/K (Fig. 1). This causes a huge temperature increase in the whole mantle of about 100–200 K (Nakagawa and Tackley, 2004b). Please note that the post-perovskite is not a high-T mineral which was stable in the Archean. It takes time to bear the post-perovskite at CMB through the cooling history of the Earth. Once appeared, the pPV transports the core heat more extensively than before, hence more active mantle convection and plate tectonics on the surface

of the Earth. If we know the continental growth curve, it must not be the simple and gradual decreasing curve. Instead, it may be the one with a rapid growth promoted by the birth of pPV after the early gradual growth. The estimated continental growth curve by the river-mouth zircon (Fig. 20) suggests that the birth of pPVmay be 2.3 Ga.

The trigger for the birth of pPV may be related to the mantle overturn at 2.3 Ga, because if it happened, the cold stagnant slabs in the MBL would have effectively cooled the CMB. A cold avalanche at the CMB would have made pPV stable in the D″ layer by 2.0 Ga.

9.4 Initiation of the return-flow of seawater into the mantle

When the Earth was born by extensive collision of planetesimals with a final giant impact, the layered compositional separation of core, mantle and primordial atmosphere was completed. The high-temperature atmosphere was cooled down, and the ocean was born. The H_2O component originally trapped inside hydrous minerals within planetesimals and early primitive Earth must have moved from the inside to the surface of the Earth to form a high-T primordial atmosphere. After the consolidation of a magma ocean, wet komatiitic magmas transported water in the MBL to the surface. However, the surface water had to return to the inside of the Earth by subduction of a cool lithosphere a long time after her birth.

The stability field of dense hydrous silicates has been experimentally and thermodynamically well constrained, as summarized by Komabayashi et al. (2005) (see Figure 3 of Part II). The MBL is a huge water tank in which 5–6 times of the volume of the present ocean can be stored as crystalline water in hydrous silicates. Hydrous slabs transport surface water into the MBL only if the slab temperature is below 550°C at 150–160 km depth (Fig. 3 in Part II). To find out when subduction zones cooled down enough to this critical temperature, the P-T changes in regional metamorphic belts provide the only meaningful data set. According to the extensive compilation of blueschists and eclogites worldwide by Maruyama et al. (1996) and Komiya et al. (2002a), P-T conditions gradually changed through time since the Archean, and specifically after 750 Ma, when temperature decreased quickly enabling blueschists to first appear on the Earth. The first appearance of ultrahigh-pressure eclogite was in S. America around 640 Ma (Maruyama et al., 1996; Maruyama and Liou, 2005).

Recent investigations show that hydration into the center of subducting old lithospheric slabs was a common phenomenon that enabled double-seismic planes and deep earthquakes to be triggered by dehydration reactions (see Omori and Komabayashi, 2007 this volume).

If water transportation into the MBL began after 750 Ma, surface water must have decreased since then, and mantle wedges should be more extensively hydrated. The hydration fronts along subduction zones migrated downward, and as a result serpentinized mantle wedges were pushed up the hanging wall of continental margins to increase the landmass above sea level. Decrease of surface seawater also dropped

the sea level. The increased landmass caused the erosion of mountains and the transport of sediments to the ocean, where diagenesis consumed atmospheric CO_2 more effectively than before. This may have been the major cause of the Sturtian snowball Earth near 750 Ma. At the same time, the increased sediments buried organic matter and that caused a rapid increase of free oxygen in the atmosphere (see more details in Maruyama and Liou, 2005). Thus, the surface environment must have changed drastically, because the Earth's landmass would reduce from 30% to 10%, if the sea level was 200–300 m higher than at present (Maruyama and Isozaki, 1998; Maruyama et al., 2001; Maruyama and Liou, 2005).

If this happened, then what kinds of change in mantle dynamics would be expected? They are: (1) a drastic change in local mantle viscosity, (2) a drastic drop of melting T in a localized wet mantle, and (3) hydro-weakening of the lithosphere.

At 1.0 Ga, the supercontinent Rodinia was formed, and did not rift until 750 Ma. After a long cessation or slow-down of plate tectonic activity, as seen in Figure 20, the rifting started of Rodinia that was separated into several continents by 600 Ma. Thereafter, formation of the semi-supercontinent of Gondwana was completed in a short time of less than 100 m.y. It took about twice that time for the next supercontinent cycle from Gondwana (540 Ma) to Pangea (250 Ma). This may have been caused by the introduction into the mantle of water that promoted active convection by lowering viscosity, partial melting and the melting point (Fig. 21, Maruyama and Liou, 2005).

Breakup of the supercontinent Rodinia after the long cessation of magmatism at 750–600 Ma, more rapid continental dispersion, and more active plate tectonics, were all related to water transportation into the mantle. More active mantle dynamics may have been the reason why the snowball Earth was melted by the increased magmatic CO_2 in the atmosphere (Maruyama and Liou, 2005).

10 DISCUSSION

10.1 Superplume, presence or absence

Since the huge low-velocity P-wave anomaly in the deep Pacific mantle was demonstrated by Fukao (1992), a debate has taken place on whether or not there is a superplume (Maruyama, 1994; Fukao et al., 1994). The term superplume was proposed by Larson (1991), but his definition was different from that which we now use. Larson (1991) defined it as a collection of extraordinary active plumes in the Cretaceous when not only plumes but also mid-oceanic ridges in the Pacific were active from 120 to 80 Ma. Following Larson (1991), Campbell and Griffiths (1990, 1992) used the terms superplume and plume tectonics. However, they considered a plume to have a high-T, and hence a skinny shape with a big head that was a potential source of a hotspot. When a gigantic superplume was proposed, most geophysicists doubted its presence, because its extreme buoyancy would have made it unstable gravitationally, although the temperature difference between a superplume and its surrounding mantle was estimated to be as small as 50 K (Fukao et al.,1994).

Since that time, more than eight different research groups studying whole-mantle tomography by P-waves or S-waves have tested the possible presence of a superplume, and have confirmed it. Consequently, the main purpose has shifted to define the margins of the Pacific superplume (e.g., Ni et al., 2002; To et al., 2005).

10.2 Entity of the superplume, T or X

The entity of the superplume is the next important target, which is to determine whether it is a temperature anomaly, a compositional anomaly, or both. Numerical simulations suggest that the temperature anomaly is about 200–300 K higher for a plume in general (e.g., see summary by Coffin and Eldholm, 1994). In these simulations, plumes always show a characteristic shape with a big head and thin tail, because of the high-temperature. Nevertheless, no tomographic images show the presence of such a high-T plume shape, although the spatial resolution is still not enough to document the details.

Recently, petrologists have started to realize that the plume source contains abundant recycled MORB materials, and the source mantle seems to have a slightly higher-T than the surrounding mantle, say 50–100 K, enough to create the huge

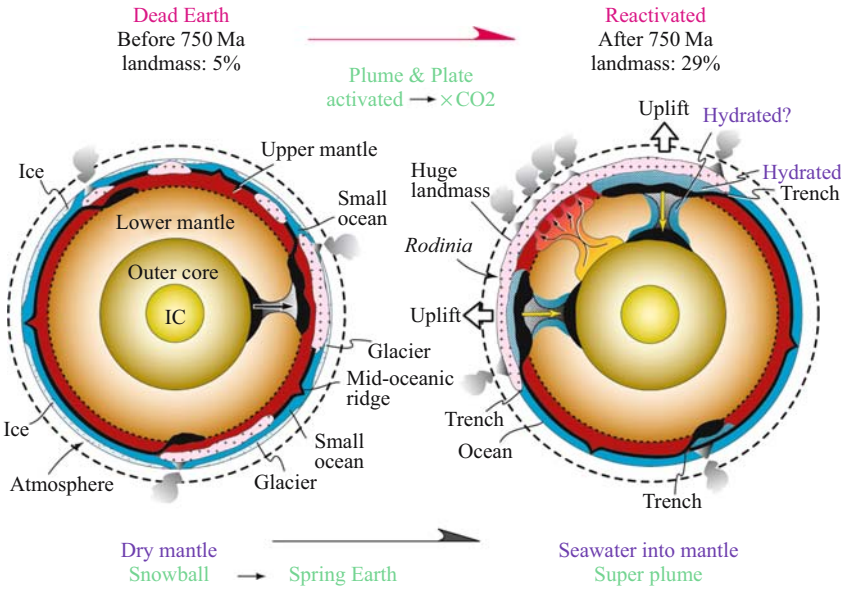

Figure 21. Initiation of the return-flow of seawater into the mantle at 750 Ma. The Earth's dynamics were drastically different before and after this time. A dead Earth (left) was reactivated to become a spring Earth (right). The drastic viscosity drop due to water infiltration promoted mantle convection to break up the supercontinent Rodninia, and to cause more active plate tectonics than before. The lowering melting temperature activated magmatism to transport mantle CO_2 into the atmosphere, and melted glaciers by the greenhouse effect.

amounts of melt, which can easily explain the sporadic occurrence of hotspot tracks in the oceans such as the Hawaiian islands (see details by Kogiso, 2007 this volume). However, if a rising plume includes recycled MORBs, that MORB must be depleted in a SiO_2 phase to reduce the density of the rising plume in the upper mantle. This may be explained by subduction zone metasomatism, where dehydrated fluids are enriched not only in water but also SiO_2.

Metasomatized and SiO_2-depleted MORB can be segregated in the MBL during the process to be stagnant and during recrystallization through a phase change at 660 km depth (Karato, 1997). The MORB crust is buoyant immediately below 660 km depth (Ringwood and Irifune, 1988), supporting the idea of selective accumulation of MORB crusts in the MBL. Moreover, the P- and S-wave velocities of the MBL suggest that the bulk chemistry is enriched in MORB rather than in pyrolite (Nishihara and Takahashi, 2001).

Thus, if this idea is correct, the temperature of a plume must be only 50–100 K higher than that of the surrounding mantle, and cannot be of the order of 200–300 K as suggested by numerical simulations. From temperature estimates using the thickness of the MBL as shown in Figure 2, the temperature of the MBL of the Pacific and African superplumes is 100–200 K higher than that of standard MBL mantle, reflecting a 400–500 km spatial resolution. Suetsugu et al. (2004) measured the MBL thickness of the Pacific superplume using new seismic stations on the French Polynesia islands, and they concluded that the thickness is of the order of 20–25 km, suggesting a 200–300 K higher temperature in a spatial resolution of 200–300 km. In conclusion, a superplume is certainly enriched in recycled metasomatized MORB crusts, a plume itself has a high-temperature of the order of 100–200 K in a 400–500 km scale, and the temperature is 200–300 K higher in the center of the plume in a 200–300 km scale; hence the plume material must include considerable amounts of lower mantle.

10.3 Mechanism to produce a superplume

The mechanism to create a superplume has been debated since the first proposal for a superplume in 1994. The most fundamental mechanism is to produce a plume and superplume from the top of the boundary layer immediately above the CMB. A high-T plume can be easily explained by this mechanism, but not a superplume. Yuen et al. (1996, 1998, 1999) introduced the idea of radiative heat transfer by wüstite to effectively heat up the bottom of the mantle. The result shows numbers of small plumes that stand up above the CMB, suggesting a plume cluster as an entity of a superplume (Matyska and Yuen, 2005). Reviewing numerical and seismological observations of a superplume, Schubert et al. (2004) concluded a superplume is a cluster of small-scale plumes.

Instead of a boundary layer origin for a superplume, Kellogg et al. (1999) proposed a mid-mantle origin, speculating that the vertical difference in P-wave velocity structure is the compositional variation remaining from the primordial mantle in the lower half

of the lower mantle, from the top of which a superplume appears with a mid-mantle origin. In this scenario, a huge low-V anomaly right above the CMB is regarded as a compositional anomaly without a thermal anomaly.

Since the discovery of pPV above the CMB, the phase change of PV/pPV with its positive Clapeyron slope has been considered to originate a superplume. Nakagawa and Tackley (2004a,b) simulated the effect of this phase change and concluded that numbers of small plumes can generate at the CMB to form a superplume as a cluster of plumes, and that the temperature of the upper and lower mantle rises about 100–200 K depending on the angle of the Clapeyron slope.

In terms of seismological evidence, a velocity jump across the D″ layer, about a 1% positive jump followed by a negative jump across the D″ layer from top to bottom, was observed suggesting a sandwich structure with a core of pPV wrapped by PV (Hernlund et al., 2005). In this case, the bottom thin layer of PV is buoyant against overlying pPV, to yield a gravitational instability that develops a plume at the CMB (Hernlund et al., 2005). If this is correct, plumes must appear at any place where the sandwich structure is present.

From a geological viewpoint, Maruyama et al. (2007) emphasized that a superplume never develops anywhere on the CMB; instead a superplume can only be born at the breakup of a supercontinent, and it has a lifetime of <1 b.y. Accordingly, this creates the following two critical constraints. First, a superplume is born under a supercontinent, where the mantle must be the coldest and enriched in recycled MORB crusts. Second, the coldest mantle must change to the hottest after several hundred million years. This enigma can be interpreted only by introducing pPV at the CMB, and the recycled MORBs as a fuel for the superplume. When all the MORB slabs are spent, it is the time of demise of the superplume. A partial melt of the recycled MORB develops into an anti-crust, whereas an andesitic restite rises up to create plumes, and finally a superplume develops from a cluster of plumes. Because of their extremely long wavelengths, superplumes may also influence the rotation of the Earth and cause significant polar wandering (Greff-Leftz, 2004). This can be influential in causing climatic changes and has an important impact on the environment, such as life evolution.

10.4 Classification of plumes and superplumes

Plumes originate at a boundary layer as a result of Taylor instability. Within the solid Earth, several boundary layers are present; at 2900 km depth at the pPV/PV reaction, at 660 km and 410 km depths. Therefore, theoretically, plumes can be classified into four groups, based on their depth of origin (Fig. 22) (Yuen et al., 1998; Cserepes and Yuen, 2000). Recent tomographic images are available to test this classification. A superplume can be well demonstrated to be derived from the CMB. In the western Pacific region, plumes originating from 410 km depth right below active intracontinental volcanoes have been demonstrated by improved P-wave tomographic images (Zhao et al., 2004).

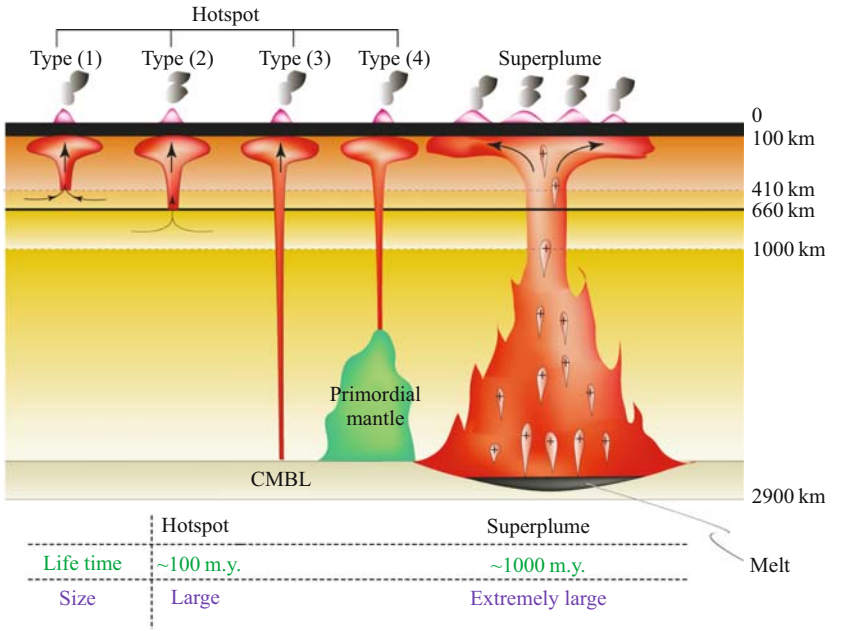

Figure 22. The classification of plumes, modified after Cserepes and Yuen (2000). Hotspots with four different depth origins are shown on the left. Type (4) is a mid-mantle plume derived from primordial mantle (Kellogg et al., 1999). A superplume has an extraordinary size and acts as an engine to drive the Earth's dynamics; its lifetime spans 1.0 Ga, and it may have formed from a cluster of plumes.

Plumes starting at 660 km depth may be present off the NE Japanese arc. Under a thick oceanic plateau on the ca. 100 Ma Pacific plate, a P-wave low-V anomaly is clearly observed in the upper mantle and topmost lower mantle (Zhao, 2004). 5.9 Ma (Ar-Ar age) alkaline basalts have been dredged on this plateau (Hirano et al., 2001). This plume may have formed in relation to the fate of stagnant slabs at 660 km depth and their replacement by a local overturn at 20–30 Ma when Japan Sea opened.

On the other hand, plumes may be classified according to their size and shape. A superplume is different from a normal plume in its size. Pacific and African superplumes are now confirmed, and they are different from Iceland, Hawaii and other plumes in their size. The African superplume seems to be bent about 45 degrees northwards, whereas the Pacific superplume stands up vertically. This difference may be due to their different evolution. In the Pacific, the superplume is surrounded by a circum-Pacific down-welling on the margin of the ocean, but the African superplume is not surrounded by a subduction zone except on the northern margin of the Indian ocean.

High-T plumes must be different in shape from low-T ones, but a classification has not yet been undertaken.

10.5 Role of majorite in modifying the dynamics of mantle upwelling, and its role in the Archean

The role of majorite in mantle dynamics has not been well appreciated. One of the reasons for this is its narrow stability field in the pyrolite system. Majorite is not an important mineral for cold regions such as subduction zones, but it is critical for the high-T region of a rising plume, as discussed in this section. The Pacific superplume is bent horizontally in the MBL, branching into three directions after penetrating the 660 km boundary. This may be interpreted by the influential role of majorite, as discussed in the previous section.

Majorite has a wide stability field if the mantle temperature was higher than at present, and thus particularly in Archean time. Moreover, if the mantle was more FeO-rich than the present-day mantle, as in the Archean, the stability field of majorite would expand considerably towards the lower pressure side, although this has not yet been determined quantitatively in the laboratory. In the Archean, majorite would have been an omnipresent mineral in the MBL, but at present it is restricted to the zone above rising plumes. The ubiquitous occurrence of majorite may be the main reason for the double-layered mantle convection in the Archean.

10.6 Geochemical reservoir of OIB and its geochemical characteristics

It has long been considered by geochemists that there are primordial areas in the lower mantle that create a geochemical reservoir with primitive characteristics, shown by primitive $^{3}He/^{4}He$ and Re-Os isotopes. Kellogg et al. (1999) considered that the lower half of the lower mantle may be the primordial mantle from which a superplume originates.

We suggest that there are no primordial mantle reservoirs in any part of the present mantle. Instead, the lower mantle must have fractionated more extensively than the top of the mantle to produce an anti-crust, because the bottom of the mantle must have been heated more extensively to be compositionally fractionated than the top of the mantle through geologic time. Hence, we predict that the volume of anti-crust on the bottom of the mantle may be larger than the total volume of continental crust on the Earth. Moreover, an anti-tectosphere may be present in most places in the deep mantle just above the D″ layer, although the detailed geography has yet to be clarified.

Primordial geochemical characteristics may be derived directly from the outer core through a superplume.

The temperature of the OIB source mantle can be estimated by petrochemical comparison of primary basalts with high-pressure experiments with different bulk chemical compositions (see a review by Kogiso, 2007 this volume). The estimated temperature of the source mantle of a superplume is 200–300 K higher than 1600°C at 660 km depth, derived from the MORB potential temperature (see review by Utsunomiya et al., 2007 this volume). This is consistent with geophysical estimates, using the global thickness variation of the MBL mentioned above. If the temperature

estimate is higher than 1600°C at 660 km depth, the origin of OIB source must be in the lower mantle, or at least in the MBL, where a large temperature gradient up to 300 K is present.

As illustrated by tomographic images, a superplume must retain geochemical characteristics of its CMB origin. One of the most characteristic signatures has long been considered to be the HIMU isotopic anomaly, which has been considered to be derived from recycled pelagic sediments (e.g., Kogiso et al., 1997). However, Hirose et al. (2004) have produced a more probable, new interpretation.

If partial melting of the source occurs in the lower mantle, the behavior of incompatible elements is opposite of that in the upper mantle. In the upper mantle, incompatible elements such as K, Rb, Sr and REE enter into melts, because olivine and orthopyroxene remain in residual solid phases. In contrast, under lower mantle conditions, Ca-perovskite remains as a residual phase containing incompatible elements (Hirose et al., 2004). Chemical plumes generated as a restite of partially melted recycled MORB, rise up to enter the MBL, where Ca-perovskite reacts to transfer those incompatible elements to majorite, Ca-Al phases and hydrous ringwoodite or wadsleyite. These minerals are not stable anymore in shallower than 410 km depth, from which jet-like plumes radiate with melts enriched in incompatible elements. Dense hydrous magnesium silicates including wadsleyite may be the potential container of incompatible elements in the MBL.

If a superplume derived from the CMB is melted on its way to the MBL, the fate of the melt is discussed here. Ohtani and Maeda (2001) measured the density crossover of melt against surrounding mantle in lower mantle conditions, and concluded that ca. 70 Gpa is the crossover depth, below which melt must sink to the CMB. Melts below 1800 km depth cannot rise to the surface.

In the Archean double-layered regime of mantle convection, a large temperature gradient is expected in the MBL, OIB magma radiating from 410 km depth, showing komatiitic geochemical signatures. This high-T komatiite is an Al-depleted type that is known to occur only before 3.5 Ga (see a review by Komiya, this issue). Al-enriched komatiite is common in the late Archean and early-middle Proterozoic and less common in the Phanerozoic. The youngest komatiite is from the Cretaceous Gorgona islands off Columbia. Alkaline basalts began to appear as OIB magmas after 2.7 Ga, and are very common in the Phanerozoic. This petrochemical secular trend of OIB magma roughly corresponds to the secular change of the much smaller ΔT in the MBL through time.

10.7 Mantle convection through time

The changing style of mantle convection through geologic time must be one of the most critical features of an evolving terrestrial planet. With cooling, what would be the expected sequential change of the mantle? This has not been systematically considered until now. We propose the following sequence of events. First, after consolidation of the magma ocean, majorite occupied a wide stability field in the MBL, and played a critical role in double-layered mantle convection in the early Earth (Fig. 20).

Second is the inevitable result of a mantle overturn that took 100 m.y. at 2.8 Ga, after which episodic whole-mantle convection prevailed.

When the CMB cooled down enough to make pPV stable, a new style of mantle convection started. A superplume appeared to enter a new stage of mantle dynamics. A trinity of supercontinent, superplume and pPV has controlled the cooling history of the Earth since 2.3 Ga.

The final catastrophic event was the initiation of return-flow of seawater into the MBL at 750 Ma. This drastically changed mantle dynamics, and the Earth entered Phanerozoic time which started from the deglaciation of the snowball Earth caused by this mantle hydration event. Specifically, a drastic change occurred in the surface environment of the Earth, as a result of the emergence of a huge landmass like today. This drastic change caused the extensive erosion of mountain belts and the transport of huge amounts of sediment into the ocean, and atmospheric oxygen increased as a mirror effect of buried organic matter in the sediments. The increased oxygen, and seawater enriched in nutrients such as CaO and P_2O_5 caused the birth of large multicellular animals. A strong ozone barrier was created from the increased free oxygen that accumulated in the atmosphere by Ordovician time, when the first plants evolved on land and conquered the new frontier together with animals (Maruyama et al., 2001; Maruyama and Liou, 2005).

10.8 Earth system, and its evolution

The Earth is composed of six sub-systems as mentioned on the cover of this book. The Earth behaves as a system through the interaction of subsystems. The surface of the Earth is driven by the selective heating of the equatorial ocean by the Sun, whereas the solid Earth is driven by a superplume transporting heat energy from the core. H_2O acts as a chemical agent to drive the surface environment, transferring solar energy from the equator to the polar regions. In contrast, the lithosphere capped by MORB crust acts as a chemical agent to drive mantle dynamics. MORB partially melts to yield continental crust on the top of the mantle, and anticrust at the bottom of the mantle, and this has chemically fractionated the mantle through time.

Since its birth the Earth system itself has also evolved through geologic time. The Archean planet was different from the modern Earth, as mentioned above. The change in style followed mineralogical evolution of the mantle. The Archean mantle was separated into two regions, the upper and lower, by the majorite-dominated MBL. The upper mantle acted as a thermal blanket that kept the Earth's surface habitable until 2.8 Ga, when catastrophic mantle overturn took place, and continued for over 100 m.y. In this period, the mantle behaved as one system.

The time of formation of the solid inner core is still debated. The birth of the solid inner core was once considered to be at 2.8 Ga, based on the rapid increase of magnetic intensity (Hale, 1987). But recent extensive measurements of mid-Archean paleomagnetism suggest a much earlier time, before 3.5 Ga (Yoshihara et al., 2003,

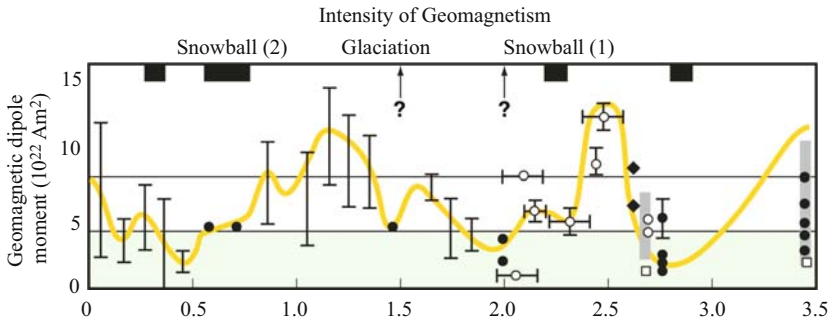

Figure 23. The secular change of geomagnetic intensity through geologic time, compiled after Kohno and Tanaka (1995) and Yoshihara et al. (2003). Note the half billion to one billion year time variation, e.g., from 2.8 to 2.0 Ga, from 2.0 to 0.5 Ga, and from 0.5 Ga to the present. Also note the correlation between the glaciation (solid bar on the top) and weak geomagnetic intensity. When the intensity decreased to less than ca. 50% of the present-day value of 8×10^{22} Am^2, glaciation occurred, except at 2.0–1.8 Ga. The Proterozoic was a time of extreme conditions on the surface with two periods of snowball glaciation, and on the core with the most active geomagnetism through time. Moreover, the most active production of the continental crust was at this time (Fig. 20).

Fig. 23). Magnetic intensity also controls the Earth's system, particularly the surface environment, contributing to the albedo effect by cloud formation (Gallet et al., 2005), although the details are not yet fully understood. The widespread occurrence of stromatolites over the world since 2.7 Ga may be due to the increase in intensity of geomagnetism at this time. Empirically, the magnetic intensity seems to be co-related to the surface temperature of the Earth. When the intensity decreased to a level lower than 50% of the present value, the Earth was covered globally by snowball ice (Fig. 23).

After the birth of pPV on the CMB, the Earth system has been extensively modified. Average mantle temperature increased 100–200 K in both the upper and lower mantle. These values are very significant, if we realize that the difference in MORB source mantle temperature between the Archean and the present is only 200 K (Komiya, this issue). After 2.3 Ga the mantle was stimulated to be more active than before by the birth of pPV on the CMB. The heterogeneous distribution of pPV on the CMB caused the subsequent supercontinent-superplume cycle. Light elements in the outer core were moved through a superplume to the gravitationally stable surface. As a result, continental growth effectively proceeded by the appearance of pPV on the CMB, and presumably on the bottom of the mantle to increase the anti-crust. 60% of the present continental crust was produced in the 1.3 b.y. period from 2.3 to 1.0 Ga (Fig. 20).

Initiation of the return-flow of seawater into the mantle drastically changed the mantle dynamics, from a dead Earth to a spring Earth, and it reactivated the mantle to deglaciate the snowball surface of the Earth in the period 750–600 Ma. The Pacific superplume was born during the breakup of the Rodinia supercontinent, to open a

new ocean in which large multi-cellular animals were born in new nutrient-enriched (especially P) seawater environments in the center of the supercontinent. Above all, the surface environmental change was drastic, triggered by the return-flow of seawater into the mantle.

A supercontinent cycle is the result of a double-sided subduction system that leads to the formation of the coldest, but water-enriched, upper mantle in the front of a future supercontinent such as the present-day WPTZ. The mantle of the WPTZ resembles that in the Archean, presumably due to similar mantle viscosity caused by water.

10.9 Functions to keep the Earth habitable

The Earth has been habitable for over 4.0 Ga, in spite of a gradual increase in solar luminosity since her birth. To compensate for increased energy input from the Sun, the amount of greenhouse gases have changed with time. Above all, the greenhouse effect has long been believed to be the major cause, in spite of an insufficient data set. In this scenario, the Archean atmosphere should have been enriched in CO_2 and/or CH_4. However, the observed geological data and the calculation of greenhouse point to a different conclusion (Shaviv and Veizer, 2003). The Earth's surface environment has not gradually cooled, or been constant, as the well-documented repeated occurrence of snowball Earth conditions indicate. In the following, the role of the solid Earth is discussed.

The temperature history of: (1) the Earth's surface, (2) the upper mantle at 660 km depth, (3) the CMB, and (4) the ICB (inner core boundary) over 4.6 Ga is summarized in Figure 23. The Earth's surface has been covered by ice sheets several times, first at 3.0 Ga, followed by 2.3 Ga, and again at 0.75 Ga and 0.63 Ga. In the Phanerozoic, periodic glaciation attacked the Earth four times (Fig. 24).

The solid Earth has a mechanism to extrude internal heat economically to the surface as mentioned before (Fig. 13). To examine this process, the measured temperature of the MORB source mantle at a given age is reviewed in Figure 25, following Komiya (2004). The temperature is extrapolated to that at 660 km depth, using the mantle adiabat of 50 K/100 km. Broadly speaking, the upper mantle temperature seems to have gradually decreased through time, although the change is as small as 200 K over 3.8 Ga. Moreover, several pulse events occurred probably in the late Archean to early Proterozoic to increase mantle temperature, as documented by the common occurrence of Al-enriched komatiitic volcanism.

The temperature at the CMB seems to be difficult to estimate, even with our present knowledge of the pPV transition. The temperature at the top of the D″ layer can be estimated to be 3100 K, assuming the D″ layer has an average thickness of 175 km. Based on the speculation of rapid growth of the continental crust caused by the birth of pPV at the CMB, coincident with the first supercontinent and the first superplume, the temperature decreased to 4000 K at 2.3 Ga. If so, the temperature of the top of D″ layer decreased 1000 K during the last 2.3 Ga. This value is very large compared with the value of 200 K for the MORB-source mantle during the last 3.8 Ga. This may be due to the role of pPV that has a second power of the phase change to transfer the

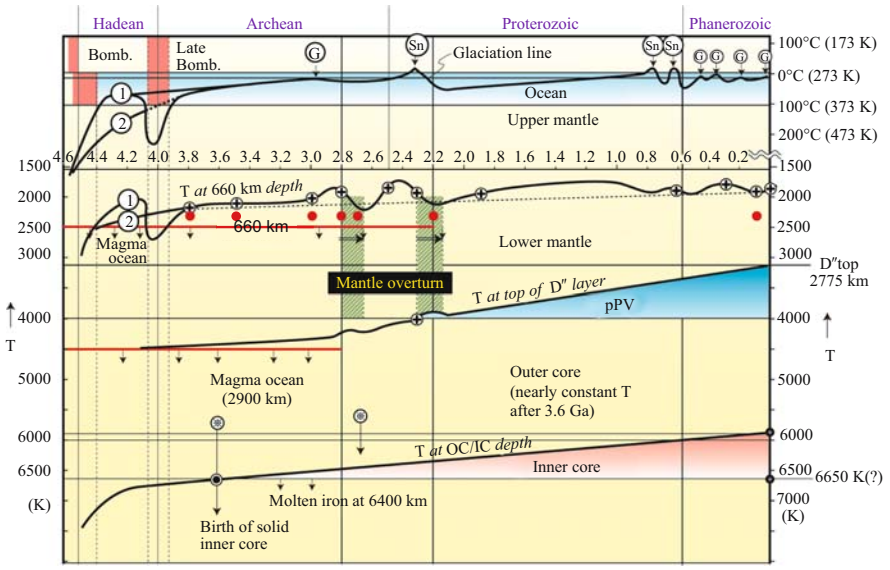

Figure 24. Thermal history of the Earth through 4.6 Ga, shown as temperature change at the surface (1), the upper mantle (2), the lower mantle (3), and the core (4). The data source is shown in the text. The surface temperature was estimated by the presence of tillite at a given geologic age. Sn and G refer to snowball and glacial periods. The present-day average T of the surface of the Earth is 20°C, glaciers are developed in both polar regions, and are used as a reference line for the appearance or absence of a glacial period. There are no constraints for Hadean time; two speculative possibilities are: (1) a thick greenhouse gas enriched in CO_2, hence no ocean, or (2) the presence of a primordial ocean that evaporated at ca. 4.0 Ga during the heavy bombardments. The temperature of the upper mantle is after Komiya et al. (1999, 2002, 2004). Note the slight average decrease of about 150–200 K since 3.8 Ga. Komatiitic OIB magmas are shown by red dots. The high-T maximum is given by the solidus at 660 km depth. The temperature of the bottom of the lower mantle is given by the phase transformation of pPV/PV. The time of birth of pPV at the bottom of the mantle is estimated to be at 2.3 Ga. The high-T limit of the CMB is given by the solidus at 2900 km depth. Note the slow cooling until 2.3 Ga, followed by rapid cooling. On the other hand, note that fast cooling of the core in Hadean to Archean time was followed by slower cooling in the Proterozoic to Phanerozoic. The time of birth of the solid inner core is speculated to be at either 3.6 Ga or 2.7 Ga (asterisk). The core temperature T is given for the growing surface of solid inner core. Once the solid inner core was formed, the outer core must have stayed at nearly constant T.

core heat. Without pPV, the boundary layer right above the CMB transfers the core heat only by diffusion (first power), but can transport the core heat more effectively by an exothermic phase change (second power) after the birth of pPV in addition to the first power.

A magma ocean must have consolidated by 3.8 Ga. Hence the high-temperature limit at the CMB is 4400 K at 3.8 Ga. This constraint gives a temperature decrease of less than 400 K from 3.8 Ga to 2.3 Ga at the CMB, which is very small, compared to 1000 K during the last 2.3 Ga. This suggests the viability of double-layered convection in the Archean, when the upper mantle behaved as a thermal blanket.

The temperature at the boundary between the inner and outer core is particularly difficult to estimate even now. 5850 K is the value recommended by Anderson (2003). Assuming the birth of the solid inner core was some time between 3.8 and 3.5 Ga, as inferred by the strong geomagnetism recorded in 3.5 Ga volcanic rocks (Fig. 24), the temperature at the ICB was 6650 K at 3.5 Ga, suggesting that the temperature decrease reached 800 K during the 3.5 b.y. The T decrease of the liquid outer core after the birth of the solid inner core seems to be only 200 K, if we assume the same mantle adiabat of 50 K/100 km. This supports the idea of T being internally buffered by the growing solid inner core.

One important conclusion is the contrasting cooling history between the lower mantle (CMB) and the upper mantle. The temperature of the upper mantle seems to have been nearly constant, whereas the lower mantle temperature has decreased drastically since 2.3 Ga, but not in the Archean. The Archean lowermost mantle is restricted to be lower than the solidus T of 4500 K (see Fig. 1). This gives a highest-T limit of the CMB, and hence giving a cooling rate of only 500 K from 4.0 to 2.3 Ga. On the other hand, the rate reaches 1500 K from 2.3 Ga to the present (Fig. 24).

This strongly indicates that an internally buffered system is present within the solid mantle. That is, the double-layered mantle convection in the Archean was followed by a mantle overturn at 2.8–2.7 Ga, by the birth of pPV at 2.3–2.2 Ga which transferred core heat to the surface more effectively than before, and finally by the return-flow of seawater into the mantle after 0.75 Ga.

These sequential and relayed drastic changes were the most critical processes that kept the Earth habitable. If these had not been sequentially ordered, the surface of the Earth would have been frozen for a long time which would not have enabled life to evolve to large multi-cellular animals such as one seen today.

10.10 Driving force of mantle dynamics

In this section, we discuss the driving force of mantle dynamics. In the framework of plate tectonics, the cooling of the lithosphere has been suggested as the main driving force to yield a recycled lithosphere on a global scale (Forsyth and Uyeda, 1975; Richardson et al., 1976; Anderson, 2005). A large slab-pull force causes faster plate movements in the Pacific and Indian oceans, compared with the Atlantic and African regions where ridge push force derived from the rising plume is in operation, but where the speed of plate divergence is very slow. Thus, the so-called “table cloth” theory was born to drive plate tectonics.

However, if the Pacific MORB-source mantle is supplied with more fertile and higher-T material by the Pacific superplume from the lower mantle through a larger window in the MBL that is not possible in the Atlantic, then the above reasoning changes. Moreover, the mid-Atlantic ridge has been anchored by mantle plumes as in Iceland with an origin in the lower mantle, presumably originating at the CMB. The African rift systems are also anchored by the African superplume. These observations suggest that superficial plate tectonics is controlled by plume dynamics in these regions, although both Indian and Pacific domains are different.

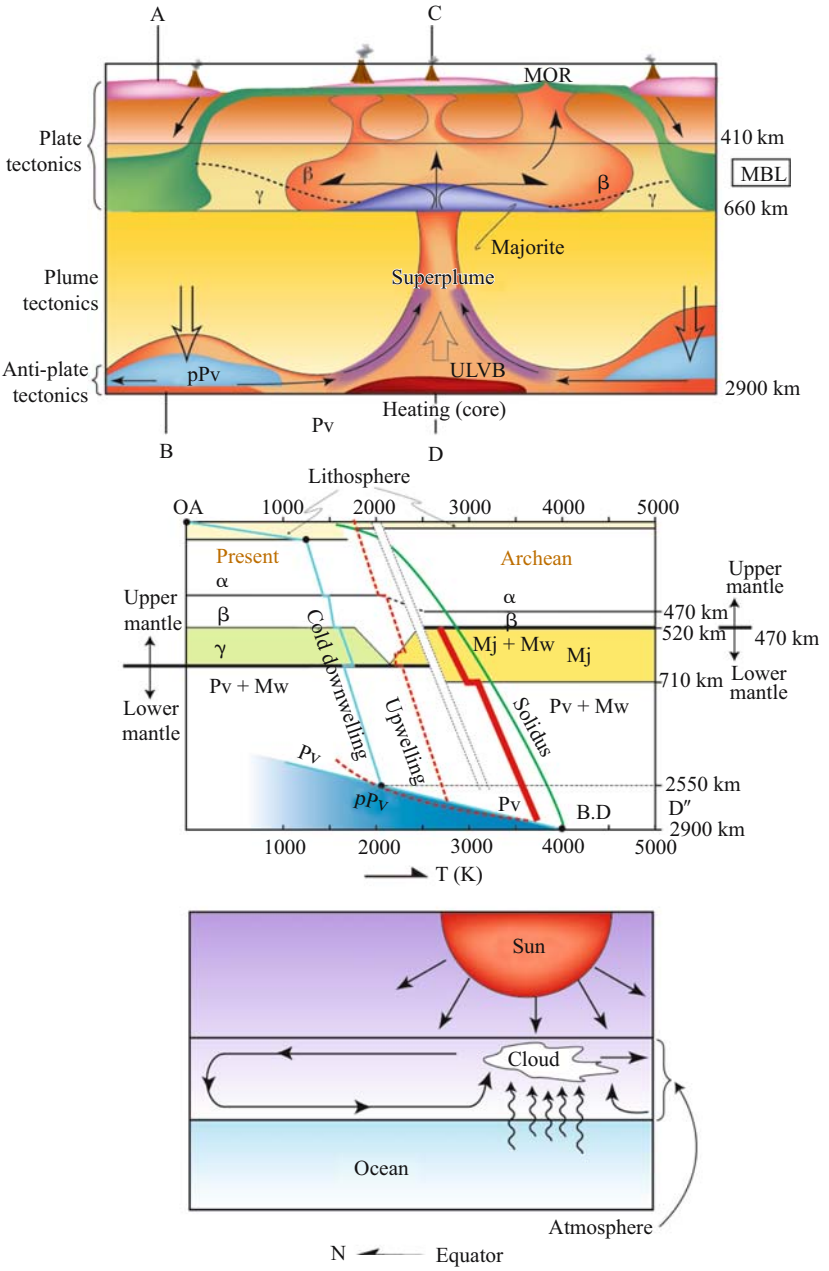

Figure 25. The driving force of mantle dynamics of the Earth. Heating at the bottom of the mantle, and cooling from the top of the mantle are coupled to transfer the internal heat of the planet to planetary space. A major agent in driving this system is a superplume driven by recycled MORB crust and pPV above the

The most critical discovery is the large temperature difference between the outer core (4000 K) and the bottom of the mantle (2000 K minimum at the top of the D″ layer), strongly indicating that heating of the low-T mantle by the core is the major force that drives mantle convection in the present Earth. The major evacuation of core heat is channeled into the superplume.

The fuel for the superplume dynamics is the recycled MORB, and also light elements from the outer core, both producing chemical buoyancy to drive superplume convection after pPV transforms the coldest mantle to a normal-T mantle with time, as the recycled MORB would partially melt at 200 K below the solidus of slab peridotite at 4000 K. Note that a dense melt concentrates radiogenic elements such as U, K, and Th that enter the anti-crust on the CMB. If so, anti-crust may play a significant role as a heat source, in addition to those elements in the outer core. When a superplume loses recycled MORB at the CMB, it marks the time of demise of the superplume.

However, the core is very small, 1/8 volume of the whole solid Earth, and hence it seems to be difficult to maintain a high-T to drive mantle dynamics over the past 4.6 Ga only from the initial total heat when the Earth was formed. This suggests the presence of radiogenic elements in the core, although it is necessary to calculate quantitatively the role of radiogenic elements.

A rising superplume breaks up a supercontinent, disperses continents, and supplies fertile materials into the MORB source mantle. This means that a superplume controls plate tectonics on the surface until subduction zones develop on the ocean margins. Although a slab-pull force promotes faster and passive spreading at a mid-oceanic ridge, active plumes, rising from the lower mantle and driven by core heat, supply the fertile and high-T materials to the upper mantle thus driving plate tectonics.

The best analogy to explain this process is the climate system at the surface of the Earth (Fig. 25). Solar energy differentially heats up the equatorial ocean to evaporate seawater that rises into the atmosphere to form clouds in the convective sphere. These clouds migrate from the equator to the polar regions, and are cooled, so they flow down to the surface. Thus, in the pattern of atmospheric circulation, the most essential driving force is solar energy. Cooling alone, without the Sun, could not produce the present climate system. Heating the equatorial ocean by the Sun corresponds to the superplume heated by the outer core. A convecting atmosphere enriched in water corresponds to a convecting lithosphere capped by MORB. Circulating MORB plays a key role in the chemical fractionation of the mantle through time that formed two continents at the top and bottom of the mantle.

Figure 25. (*Continued*) CMB and by the buoyancy force of light elements derived from the outer core (top). The thermal profile of the mantle along A-B and C-D in the top figure is for both the modern and Archean Earth (middle). Note the contrasting mineralogy between both periods. Also note the contrasting difference between two geotherms in both periods. The best analogy of mantle dynamics is the climate on the surface driven by the Sun (c).

ACKNOWLEDGEMENTS

S. Maruyama thanks his colleagues including K. Hirose, T. Komiya, T. Kogiso, and S. Omori. Special thanks go to D. Zhao at Ehime Univ. for permission to use his P-wave tomographic images of the whole mantle, and to M. Kumazawa and K. Nakazawa for continuous discussions and encouragement of this work. D.A. Yuen is grateful for the support given to him by the National Science Foundation's CSEDI and ITER programs.

REFERENCES

Abe, Y., and T. Matsui (1985) The formation of an impact-generated H_2O atmosphere and its implications for the thermal history of the Earth. *J. Geophy. Res.*, 90, suppl., C545–C559.

Anderson, O.L. (2003) The three dimensional phase diagram of iron. In Dehart, V. et al. (eds.) "Earth's Core; Dynamics, Structure and Rotation", Geodynamic Series, 31, AGU, 83–103.

Anderson, D.L (2005) Scoring hotspots: The plume and plate paradigms. In Foulger, G.R. et al. (eds.) "Plates, Plumes, and Paradigms", Special Pap. 388, GSA, 31–54.

Bercovici, D., and S. Karato (2003) Whole-mantle convection and the transition-zone water filter. *Nature*, 425, 39–44.

Breuer, D., and T. Spohn (1995) Possible flush instability in mantle convection at the Archean-Proterozoic transition. *Nature*, 378, 608–610.

Brown, G.C. (1979) The changing pattern of batholith emplacement during earth history. In Atherton, M.P., and J. Tarney (eds.) In "Origin of Granite Batholiths", Shiva, Nantwich, UK, pp. 106–115.

Campbell, I.H., and R.W. Griffiths (1990) Implications of mantle plume structure for the evolution of flood basalts. *Earth Planet. Sci. Lett.*, 99, 79–93.

Campbell, I.H., and R.W. Griffiths (1992) The changing nature of mantle hot spots through time. *J. Geol.*, 92, 497–523.

Christensen, U.R., and D.A. Yuen (1985) Layered convection induced by phase transitions. *J. Geophys. Res.*, 90, 10291–10300.

Coffin, M.F., and O. Eldholm (1994) Large igneous provinces: Crustal structure, dimensions and external consequences. *Rev. Geophys.*, 31, 1–36.

Condie, K.C. (1998) Episodic continental growth and supercontinents: A mantle avalanche connection? *Earth Planet. Sci. Lett.*, 163, 97–108.

Cserepes, L., and D.A. Yuen (2000) On the possibility of a second kind of mantle plume. *Earth Planet. Sci. Lett.*, 183, 61–71.

DeLaughter, J.E., C.A. Stein, and S. Stein (2005) A view from the swells. In Foulger, G.R., J.H. Natland, D.C. Presnall, and D.L. Anderson (eds.) "Plates, Plumes and Paradigms", Geol. Soc. Am., Sp. Paper, 338, 257–278.

Dziewonski, A. (1984) Mapping the lower mantle; determination of lateral heterogeneity in P velocity up to degree order 6. *J. Geophys. Res.*, 89, 5929–5952.

Engebretson, D., A. Cox, and R.G. Gordon (1985) Relative plate motions between oceanic and continental plates in the Pacific basin. Geol. Soc. Am., Sp. Paper, 206, 59pp.

Fan, Q.C., and P.R. Hooper (1991) The Cenozoic basaltic rocks of eastern China: Petrology and chemical composition. *J. Petrol.*, 32, 765–810.

Flanagan, M., and P. Shearer (1998) Global mapping of tomography on transition zone velocity discontinuities by stacking SS precursors. *J. Geophys. Res.*, 103, 2673–2692.

Flower, M., K. Tamaki, and N. Hoang (1998) Mantle extrusion: A model for dispersed volcanism and DUPAL-like asthenosphere in East Asia and the Western Pacific. In Flower, M.F.J, S.L. Chung, C.H. Lo, and T.Y. Lee (eds.) " Mantle Dynamics and Plate Interactions in East Asia", Geodynamics Series Vol. 27, Am. Geophys. Union, Washington DC, 67–88.

Forsyth, D., and S. Uyeda (1975) On the relative importance of the driving forces of plate motions. *Geophys. J. R. Astron. Soc.*, 43, 163–200.

Fukao, Y. (1992) Seismic tomogram of the Earth's mantle: Geodynamic implications. *Science*, 258, 625–630.

Fukao, Y., S. Maruyama, M. Obayashi, and H. Inoue (1994) Geologic implication of the whole mantle P-wave tomography. *J. Geol. Soc., Jpn.*, 100, 4–23.

Fukao, Y., S. Wildiyantoro, and M. Obayashi (2001) Stagnant slabs in the upper and lower mantle transition region. *Rev. Geophys.*, 39, 291–323.

Gallet, Y., A. Gnenevey, and F. Fluteau (2005) Does Earth's magnetic field secular variation control centennial climate change? *Earth Planet. Sci. Lett.*, 236, 339–347.

Garnero, E.J., and D.V. Helmberger (1998) Further structural constraints and uncertainties of a thin laterally varying ultralow-velocity layer at the base of the mantle. *J. Geophys. Res.*, 103, 12495–12505.

Garnero, E.J. (2000) Heterogeneity of the lowest mantle. *Ann. Rev. Earth Planet. Sci.*, 28, 509–537.

Garnero, E.J. (2004) A new paradigm for Earth's core-mantle boundary. *Science*, 304, doi: 10.1126/science, 1097849.

Garnero, E.J., M.S. Thorne, A. McNamara, and S. Rost (2007) Fine-scale ultra-low velocity zone layering at the core-mantle boundary and superplumes. In Yuen, D.A., S. Maruyama, S. Karato, and B.F. Windley (eds.) Superplumes: Beyond Plate Tectonics, Springer, Dordrecht, pp. 139–158.

Grand, S.P., R.D. van der Hilst, and S. Widiyantoro (1997) Global seismic tomography: A snapshot of convection in the Earth. *GSA Today*, 7, 1–7.

Grand, S.P. (2002) Mantle shear-wave tomography and the fate of subducted slabs. *Philos. Trans. R. Soc. Lond. A*, 360, 2475–2491.

Greff-Leftz, A. (2004) Upwelling plumes, superswells and true polar wander. *Geophys. J. Int.*, 159, 1125–1137.

Hae, R., E. Ohtani, T. Kubo, T. Koyama, and H. Utada (2006) Hydrogen diffusivity in wadsleyite and water distribution in the mantle transition zone. *Earth Planet. Sci. Lett.*, 243, 141–148.

Hale, C.J. (1987) Paleomagnetic data suggest link between the Archean-Proterozoic boundary and inner-core nucleation. *Nature*, 338, 496–499.

Helmberger, D., S. Ni, I.L. Wen, and J. Ritsema (2000) Seismic evidence for ultralow-velocity zones beneath Africa and eastern Atlantic. *J. Geophys. Res.*, 105, B10, 23865–23878.

Hernlund, J.W., C. Thomas, and P.J. Tackley (2005) A doubling of the post-perovskite phase boundary and structure of the Earth's lowermost mantle. *Nature*, 434, 882–886.

Herzberg, C., M. Feigenson, C. Skuba, and E. Ohtani (1988) Majorite fractionation recorded in the geochemistry of peridotites from South Africa. *Nature*, 332, 823–826.

Hirano, N., Y. Ogawa, and K. Kawamura (2001) A new type of intra-plate volcanism; young alkali-basalts discovered from the subducting Pacific Plate, Northern Japan Trench. *Geophys. Res. Lett.*, 28, 2719–2722.

Hirao, N., E. Ohtani, N. Kondo, Endo, T. Kubo, T. Suzuki, A. Yasuhara, and T. Kikegawa (2005) Partitioning of potassium between iron and silicate at high pressure and temperature. EOS, abst., MR 13A-0067.

Hirose, K., Y. Fei, Y. Ma, and H. Mao (1999) The fate of subducted basaltic crust in the Earth's lower mantle. *Nature*, 397, 53–56.

Hirose, K. (2002) Phase transitions in pyrolitic mantle around 670 km depth: Implication for the upwelling of plumes from the lower mantle. *J. Geophys. Res.*, 107, doi:10.1029/2001JB000597.

Hirose, K., and Y. Fei (2002) Subsolidus and melting phase relations of basaltic composition in the uppermost lower mantle. *Geochim. Cosmochim. Acta*, 66, 2099–2108.

Hirose, K., N. Shimizu, W. van Westrenen, and Y. Fei (2004) Trace element partitioning in Earth's lower mantle and implications for geochemical consequences of partial melting at the core-mantle boundary. *Phys. Earth Planet. Inter.*, 146, 249–260.

Hirose, K. (2007) Post-perovskite transformation and the nature of D″ layer. In Yuen, D.A., S. Maruyama, S. Karato, and B.F. Windley (eds.) Superplumes: Beyond Plate Tectonics, Springer, Dordrecht, pp. 69–82.

Hoffman, P.F. (1989) United plates of North America, the birth of craton: Early Proterozoic assembly and growth of Laurentia. *Ann. Rev. Earth Planet. Sci.*, 16, 543–603.

Honda, S., S. Balachander, D.A. Yuen, and R. Reuteler, (1993) Three-dimensional mantle dynamics with an endothermic phase transition. *Science*, 259, 1308–1311.

Ichiki, M., K. Baba, M. Obayashi, and H. Utada (2006) Water content and geotherm in the upper mantle above the stagnant slab: Implication of electrical conductivity and seismic P-wave velocity models. *Phys. Earth Planet. Inter.*, 155, 1–15.

Ida, S., R.M. Canup, and G.R. Stewart (1997) Lunar accretion from an impact-generated disk. *Nature*, 389, 353–357.

Iizuka, T., K. Horie, T. Komiya, S. Maruyama, T. Hirata, H. Hidaka, and B.F. Windley (2006) 4.2 Ga zircon xenocryst in an Acasta gneiss from northwestern Canada: Evidence for early continental crust. *Geology*, 34, 245–248.

Ito, E., and E. Takahashi (1989) Postspinel transformations in the system Mg_2SiO_4-Fe_2SiO_4 and some geophysical implications. *J. Geophys. Res.*, 94, 10637–10646.

Iwamori, H. (1998) Transportation of H_2O and melting in subduction zone. *Earth Planet. Sci. Lett.*, 160, 65–80.

Jeanloz, R., and Q. Willimas (1998) The core-mantle boundary region. *Rev. Mineral.*, 37, 241–259.

Jordan, T. (1988) Structure and formation of the continental tectosphere. *J. Petrol.*, Special Lithosphere Issue, 11–37.

Karato, S. (1997) On the separation of crustal component from subducted oceanic lithosphere at the 660 km discontinuity. *Phys. Earth Planet. Inter.*, 99, 103–111.

Karato, S., and H. Jung (1998) Water, partial melting and the origin of the seismic low velocity and high attenuation zone in the upper mantle. *Earth Planet. Sci. Lett.*, 157, 193–207.

Kato, M., and T.H. Jordan (1999) Seismic structure of the upper mantle beneath the western Philippine Sea. *Phys. Earth Planet. Inter.*, 110, 263–283.

Kawamoto, T. (2004) Hydrous phase stability and partial melt chemistry in H_2O saturated KLB-1 peridotite up to the uppermost lower mantle conditions. *Phys. Earth Planet. Inter.*, 143–144, 387–395.

Kawasaki, T. (2006) "Thermodynamics in Petrology", Kyoritsu Pub., 266pp (in Japanese).

Kellogg, L.H., B.H. Hager, and van der Hilst (1999) Compositional stratification in the deep mantle. *Science*, 283, 1881–1884.

Kogiso, T. (2007) A geochemical and petrological view of mantle plume. In Yuen, D.A., S. Maruyama, S. Karato, and B.F. Windley (eds.) Superplumes: Beyond Plate Tectonics, Springer, Dordrecht, pp. 165–186.

Kogiso, T., Y. Tatsumi, and S. Nakano (1997) Trace element transport during dehydration processes in the subducted oceanic crust: 1. Experiments and implications for the origin of ocean island basalts. *Earth Planet. Sci. Lett.*, 148, 193–205.

Kohno, M., and H. Tanaka (1995) Intensity of the geomagnetic field in geologic time: A statistical study. In Yukutake, T. (ed.) "The Earth's Central Part: Its Structure and Dynamics", Terra Scientific Publishing Company, Tokyo, pp. 75–94.

Komabayashi, T., S. Omori, and S. Maruyama (2005) Experimental and theoretical study of stability of dense hydrous magnesium silicates in the deep mantle. *Phys. Earth Planet. Inter.*, 153, 191–209.

Komiya, T. (2004) Material circulation model including chemical differentiation within the mantle and secular variation of temperature and composition of mantle. *Phys. Earth Planet. Inter.*, 146, 333–367.

Komiya, T., and S. Maruyama (2007) A very hydrous mantle under the western Pacific region: Implications for formation of marginal basins and style of Archean plate tectonics. *Gondwana Research*, 11, 130–145.

Komiya, T., S. Maruyama, S. Nohda, T. Matsuda, M. Hayashi, and S. Okamoto (1999) Plate tectonics at 3.8–3.7 Ga; Field evidence from the Isua accretionary complex, southern West Greenland. *J. Geol.*, 107, 515–554.

Komiya, T., M. Hayashi, S. Maruyama, and H. Yurimoto (2002a) Intermediate-P/T type Archean metamorphism of the Isua supracrustal belt: Implications for secular change of geothermal gradients at subduction zones and for Archean plate tectonics. *Am. J. Sci.*, 302, 804–826.

Komiya, T., S. Maruyama, T. Hirata, and H. Yurimoto (2002b) Petrology and geochemistry of MORB and OIB in the mid-Archean North Pole region, Pilbara craton, Western Australia:

Implications for the composition and temperature of the upper mantle at 3.5 Ga. *Inter. Geol. Rev.*, 44, 988–1016.

Komiya, T., S. Maruyama, T. Hirata, H. Yurimoto, and S. Nohda (2004) Geochemistry of the oldest MORB and OIB in the Isua supracrustal belt (3.8 Ga), southern West Greenland: Implications for the composition and temperature of early Archean upper mantle. *The Island Arc*, 13, 47–72.

Larson, R.L. (1991) Geological consequences of superplumes. *Geology*, 19, 963–966.

Larson, R.L., and C. Kincaid (1996) Onset of mid-Cretaceous volcanism by elevation of the 670 km thermal boundary layer. *Geology*, 24, 551–554.

Lay, T., Q. Williams, and E.J. Garnero (1998) The core-mantle boundary layer and deep Earth dynamics. *Nature*, 392, 461–468.

Lay, T., and E.J. Garrnero (2004) Core-mantle boundary structures and processes. In Hawkesworth, C.J., and S. Sparks (eds.) "State of the Planet", Geophysical Monograph 150, American Geophysical Union, Washington D.C., 25–41.

Lithgow-Bertelloni, C., and M.A. Richards (1998) The dynamics of Cenozoic and Mesozoic plate motions. *Rev. Geophys.*, 36, 27–78.

Martin, H. (1986) Effect of steeper Archean geothermal gradient on geochemistry of subduction-zone magmas. *Geology*, 14, 753–756.

Maruyama, S. (1994) Plume tectonics. *Geol. Soc. Jpn.*, 100, 24–49.

Maruyama, S., and Y. Isozaki (1998) History of Life and the Earth, Iwanami-shoten, 275pp (in Japanese).

Maruyama, S., and J.G. Liou (2005) From snowball to Phanerozoic Earth. *Inter. Geol. Rev.*, 47, 775–791.

Maruyama, S., and J.G. Liou (1997) Initiation of ultrahigh-pressure metamorphism and its significance on the Proterozoic-Phanerozoic boundary. *The Island Arc*, 7, 6–35.

Maruyama, S., J.G. Liou, and M. Terabayashi (1996) Blueschists and eclogites of the world, and their exhumation. *Inter. Geol. Rev.*, 38, 485–594.

Maruyama, S., M. Santosh, and D. Zhao (2007) Superplume, supercontinent, and post-perovskite; Mantle dynamics and anti-plate tectonics on the core-mantle boundary. *Gondwana Research*, 11, 7–37.

Maruyama, S., S. Nakashima, Y. Isozaki, and B.F. Windley (2001) History of the Earth and life. In Nakashima, S. et al. (eds.) "Geochemistry and Origin of Life", Universal Academic Press, Tokyo, 285–325.

Masters, G., G. Laske, H. Bolton, and A.M. Dziewonski (2000) The relative behavior of shear velocity, bulk sound speed, and compressional velocity in the mantle: Implications for chemical and thermal structure in Earth's deep mantle. In Karato, S. et al. (eds.) Mineral Physics and Tomography from the Atomic to the Global Scale, Washington D.C., pp. 63–87.

Matsukage, K.N., Z. Jing, and S. Karato (2005) Density of hydrous silicate melt at the conditions of the Earth's deep upper mantle. *Nature*, 438, 488–491.

Matyska, C., and D.A. Yuen (2005) The importance of radiative heat transfer on superplumes in the lower mantle with the new post-perovskite phase change. *Earth Planet. Sci. Lett.*, 234, 71–81.

McKenzie, D., and M.J. Bickle (1988) The volume and composition of melt generated by extension of lithosphere. *J. Petrol.*, 29, 625–649.

McNutt, M.K., and A.V. Judge (1990) The superswell and mantle dynamics beneath the South Pacific. *Science*, 248, 969–975.

McMenamin, M.A.S., and D.L.S. McMenamin (1990) The emergence of animals: The Cambrian breakthrough. New York, Columbia University Press.

Miyashiro, A. (1986) Hot regions and the origin of marginal basins in the western Pacific. *Tectonophysics*, 122, 195–216.

Molnar, P., and P. Tapponnier (1975) Cenozoic tectonics of Asia: Effects of a continental collision. *Science*, 189, 419–426.

Murakami, M., K. Hirose, K. Kawamura, K. Sata, and Y. Ohishi (2004) Post-perovskite phase transition in $MgSiO_3$. *Science*, 304, 855–858.

Nakagawa, T., and P.J. Tackley (2004a) Effects of thermo-chemical mantle convection on the thermal evolution of the Earth's core. *Earth Planet. Sci. Lett.*, 220, 107–119.

Nakagawa, T., and P.J. Tackley (2004b) Effects of a perovskite-post perovskite phase change near core-mantle boundary in compressible mantle convection. *Geophys. Res. Lett.*, 31, L16611.

Ni, S., E. Tan, M. Gurnis, and D.V. Hemberger (2002) Sharp sides to the African superplume. *Science*, 296, 1850–1852.

Ni, S., and D.V. Helmberger (2003) Seismological constraints on the South African superplume; could be the oldest distinct structure on Earth. *Earth Planet. Sci. Lett.*, 206, 119–131.

Nishihara, Y., and E. Takahashi (2001) Phase relation and physical properties of an Al-depleted komatiite to 23 Gpa. *Earth Planet. Sci. Lett.*, 190, 65–77.

Oganov, A.R., and S. Ono (2004) Theoretical and experimental evidence for a post-perovskite phase of $MgSiO_3$ in Earth's D″ layer. *Nature*, 430, 445–448.

Ohtani, E. (1983) Melting temperature distribution and fractionation in the lower mantle. *Phys. Earth Planet. Inter.*, 33, 12–25.

Ohtani, E., A. Suzuki, and T. Kato (1998) Flotation of olivine and diamond in mantle melt at high-pressure: Implications for fractionation in the deep mantle and ultra-deep origin of diamond. In Manghnani, M.H., and T. Yagi (eds.) "Properties of Earth and Planetary Materials at High pressure and Temperature" *Geophys. Monogr.*, 101, AGU, 227–239.

Ohtani, E., and M. Maeda (2001) Density of basaltic melt at high pressure and stability of the melt at the base of the lower mantle. *Earth Planet. Sci. Lett.*, 193, 69–75.

Ohtani, E., K. Litasov, T. Hosoya, T. Kubo, and T. Kondo (2004) Water transport into the deep mantle and formation of a hydrous mantle transition zone. *Phys. Earth Planet. Inter.*, 143, 255–269.

Omori, S., and T. Komabayashi (2007) Subduction zone: The water channel to the mantle. In Yuen, D.A., S. Maruyama, S. Karato, and B.F. Windley (eds.) Superplumes: Beyond Plate Tectonics, Springer, Dordrecht, pp. 113–138.

Ono, S., and A.R. Oganov (2005) *In situ* observations of phase transition between perovskite and $CaIrO_3$-type phase in $MgSiO_3$ and pyrolitic mantle composition. *Earth Planet. Sci. Lett.*, 236, 914–932.

Park, C.-H., K. Tamaki, and K. Kobayashi (1990) Age-depth correlation of the Philippine Sea back-arc basins and other marginal basins in the world. *Tectonophys.*, 181, 351–371.

Reymer, A., and G. Schubert (1984) Phanerozoic addition rates to the continental crust and crustal growth. *Tectonics*, 3, 63–77.

Richardson, R.M., S.C. Solomon, and N.H. Sleep (1976) Intraplate stress as an indicator of plate tectonic driving forces. *J. Geophys. Res.*, 81, 1847–1856.

Ringwood, A.E. (1982) Phase transformations and differentiation in subducted lithosphere: Implications for mantle dynamics, basalt petrogenesis, and crustal evolution. *J. Geology*, 90, 611–643.

Ringwood, A.E., and T. Irifune (1988) Nature of the 650-km seismic discontinuity: Implications for mantle dynamics and differentiation. *Nature*, 352, 131–136.

Rino, S., T. Komiya, B.F. Windley, S. Katayama, A. Motoki, and T. Hirata (2004) Major episodic increases of continental crustal growth determined from zircon ages of river sands; implications for mantle overturns in the Early Precambrian. *Phys. Earth Planet. Inter.*, 146, 369–394.

Ritsema, J., H.J. van Heijst, and J.H. Woodhouse (1999) Complex shear wave velocity structure imaged beneath Africa and Iceland. *Science*, 286, 131–136.

Romanovicz, B., and Y.C. Gung (2002) Superplume from core-mantle boundary to the lithosphere: Implications for the heat flux. *Science*, 296, 513–516.

Sakamaki, T., A. Suzuki, and E. Ohtani (2006) Stability of hydrous melt at the bottom of the Earth's upper mantle. *Nature*, 439, 192–194.

Schubert, G., G. Masters, P. Olson, and P.J. Tackley (2004) Superplume or plume clusters? *Phys. Earth Planet. Inter.*, 146, 147–1262.

Shaviv, N.J., and J. Veizer (2003) Celestrial driver of Phanenrozoic climate? *GSA Today*, 13, 4–10.

Suetsugu, D., T. Saita, H. Takenaka, and F. Niu (2004) Thickness of mantle transition zone beneath the south Pacific as inferred from analyses of ScS reverberated and Ps converted waves. *PEPI*, 146, 3–34.

Smith, A.D. (1998) The geodynamic significance of the DUPAL anomaly in Asia. In Flower, M.F.J., S.L. Chung, C.H. Lo, and T.Y. Lee (eds.), "Mantle Dynamics and Plate Interactions in East Asia", Geodynamics Series Vol. 27, Amer. Geophys. Union, Washington DC, 89–105.

Su, W.J., and A.M. Dziewonski (1997) Simultaneous inversion for 3D variations in shear and bulk velocity in the mantle. *Phys. Earth Planet. Inter.*, 100, 135–156l.

Tapponnier, P., G. Peltzer, A.Y. Le Dain, R. Armijo, and P. Cobbold (1982) Propagating extrusion tectonics in Asia: New insights from simple experiments with plasticine. *Geology*, 7, 611–616.

Thorn, M.S., E.J. Garnero, and S.P. Grand (2004) Geographic correlation between hot spots and deep mantle lateral shear-wave velocity gradients. *Phys. Earth Planet. Inter.*, 146, 47–63.

To, A., T.B. Ramanowicz, Y. Capdeville, and N. Takeuchi (2005) 3D effects of sharp boundaries at the borders of the African and Pacific Superplumes: Observation and modeling. *Earth Planet. Sci. Lett.*, 233, 137–153.

Trampert, J., F. Deschamps, J. Resovsky, and D.A. Yuen (2004) Probabilistic tomography maps and chemical heterogeneities throughout the mantle. *Science*, 306, 853–856.

Tsiganis, K., A. Morbidelli, and H.F. Levison (2005) Origin of the orbital architechture of the giant planets of the solar system. *Nature*, 435, 459–461.

Tsuchiya, T., J. Tsuchiya, K. Umemoto, and R.M. Wentzcovitch (2004) Phase transition in $MgSiO_3$ perovskite in the earth's lower mantle. *Earth Planet. Sci. Lett.*, 224, 241–248.

Utsunomia, A., T. Ota, B.F. Windley, N. Suzuki, Y. Uchio, K. Munakata, and S. Maruyama (2007) History of the Pacific superplume: Implications for Pacific paleogeography since the Late Proterozoic. In Yuen, D.A., S. Maruyama, S. Karato, and B.F. Windley (eds.) Superplumes: Beyond Plate Tectonics, Springer, Dordrecht, pp. 363–408.

van der Hilst, R.D., S. Widiyantoro, and E.R. Engdahl (1997) Evidence for deep mantle circulation from global tomography. *Nature*, 386, 578–584.

Walter, M.J. (1998) Melting of garnet peridotite and the origin of komatiite and depleted lithosphere. *J. Petrol.*, 39, 29–60.

Wentzcovitch, R.M., T. Tsuchiya, and J. Tsuchiya (2006) $MgSiO_3$ postperovskite at D'' conditions. Proceedings of the National Academy of Sciences of the United States of America, 103, No.3, 543–546.

Wilde, S.A., J.W. Valley, W.H. Peck, and C.M. Graham (2001) Evidence from detrital zircons for the existence of continental crust and oceans on the Earth 4.4 Gyr ago. *Nature*, 409, 175–178.

Wysession, M.E., T. Lay, J. Revenaugh, Q. Williams, E.J. Garnero, R. Jeanloz, and L.H. Kellogg (1998) The D'' discontinuity and its implications. In Gurnis, M.E., and others (eds.) "The Core-mantle Boundary Region", Geodynamic Series, pp. 273–297.

Yoshihara, A., T. Hatakeyama, I. Sumita, and Y. Hamano (2002) The Earth history and geomagnetism, with a special reference to the Archean geomagnetis m. In Kumazawa, M. et al. (eds.) "Decoding the Earth's Evolution", Univ. Tokyo Press, pp. 363–389 (in Japanese).

Yuen, D.A., L. Cserepes, and B.A. Schroeder (1998) Mesoscale structure in the transition zone: Dynamical consequences of boundary layer activities. *Earth Planet Space*, 50, 1035–1045.

Yuen, D.A., S. Balachandar, and U. Hansen (1999) Modeling mantle convection: A significant challenge. In Kerr, R., and P. Fox (eds.) "Geophysical Fluid Dynamics", Gordon and Breach Inc., Chapter 13, pp. 259–295.

Yuen, D.A., O. Cadek, P. van Keken, D.M. Reuteler, H. Kyvalova, and B.A. Schroeder (1996) Combined results from mineral physics, tomography and mantle convection, and their implications on global geodynamics. In Boschi, et al. (eds.) "Seimic Modelling of Earth Structure" Editrice Compositori, Bologna, Italy, pp. 463–506.

Zhang, Y.-S., and T. Tanimoto (1991) Global Love wave phase velocity variation and its significance to plate tectonics. *Phys. Earth Planet. Inter.*, 66, 160–202.

Zhao, D. (2004) Global tomographic images of mantle plumes and subducting slabs: Insight into deep earth dynamics. *Phys. Earth Planet. Inter.*, 146, 3–34.

Zhao, D. (2007) Multiscale seismic tomography of mantle plumes and subducting slabs. In Yuen, D.A., S. Maruyama, S. Karato, and B.F. Windley (eds.) Superplumes: Beyond Plate Tectonics, Springer, Dordrecht, pp. 7–30.

Zhao, D., S. Maruyama, and S. Omori (2007) Tomographic images in the western Pacific and their implications for mantle dynamics. *Gondwana Research*, 11, 120–131.

PART VI

PLUMES AND SUPERPLUMES ON MARS AND VENUS

INTRODUCTION

In this Part, we focus on superplumes on the other terrestrial planets, Mars and Venus. No superplumes have been identified on Venus, where numbers of plumes with a maximum of 2000 km across are found on the equatorial region; a sole superplume is present on Mars (Fig. 1). The absence of superplumes on Venus may be explained by the absence of post-perovskite on the CMB, owing to the smaller size of Venus compared with the Earth.

Baker, V. et al. review the geology of Mars, and point out the presence of a superplume on the Tharsis region. The tharsis superplume may have been born ca. 4.0 Ga

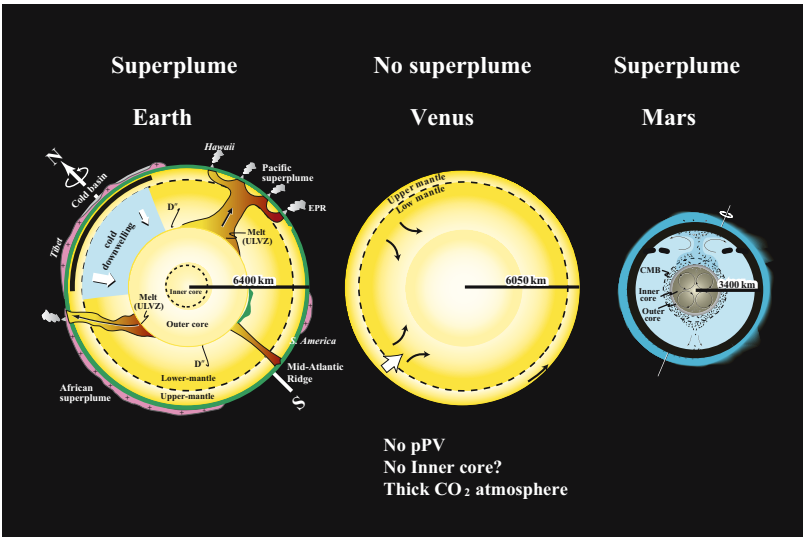

Figure 1. Plumes and superplumes on Venus, Earth and Mars. The absence of post-perovskite on Venus, and the presence of phase change with a negative Clapeyron slope near CMB on Mars and positive Clapeyron slope on Earth are the critical differences resulting in whether or not a superplume is born. The role of water in mantle made Mars superplume active even after plate tectonics on Mars had stopped.

D. A. Yuen et al. (eds.), Superplumes, 505–506.
© 2007 *Springer.*

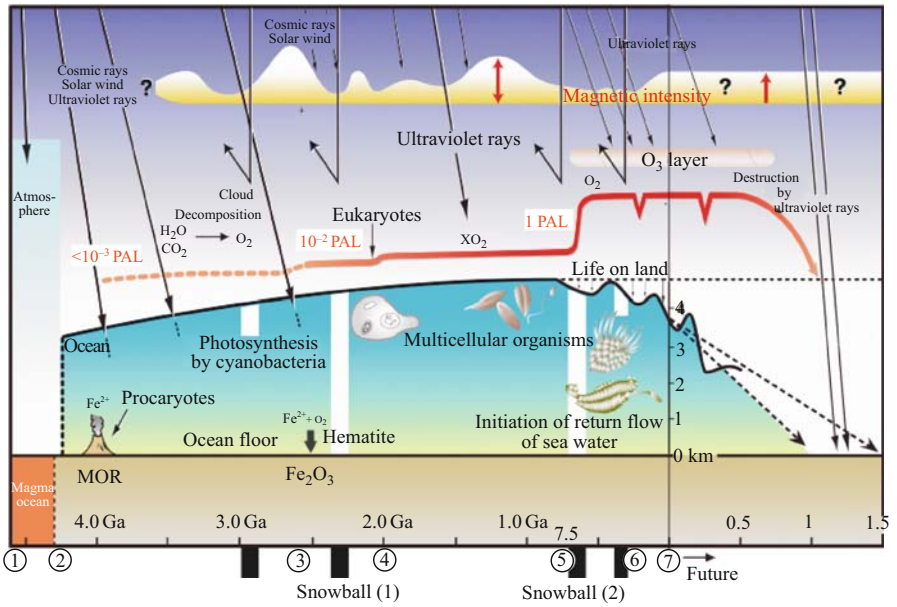

Figure 2. The history of the Earth and Life and their future (Maruyama et al., 2001). Compared with those on Mars and Venus, the Earth has been habitable through the past 4.0 Gyr, buffered by the solid Earth dynamics. The surface ocean will disappear ca. 1.0–1.5 Gyr after the present, which will be the end of life. The controlling factors for the habitable planet are discussed in the text, and may be fully clarified in the near future, and offer a critical point of view from which to search the extra-solar planets.

by the double-sided subduction zone by which large amounts of surface water moved down into mantle transition zone on Mars. The hydrated mantle transition zone is presumably a major reason why the Tharsis superplume has been episodically active for a long time until 300 Ma at least (Fig. 2).

Dohm et al. summarize the detailed magmatic events on the Tharsis superplume: five events from 4.0 Ga to the present, based on the surface geology revealed by detailed photos of Mars.

Ernst et al. review the plumes on Venus, comparing them with plumes on the Earth through time. The plumes on Venus are well expressed on the surface. Numbers of plumes and plume clusters are present and aligned on the equatorial region, forming various topographic features such as coronae or large volcanoes with a maximum of 1000 km across.

REFERENCE

Maruyama, S., S. Nakashima, Y. Isozaki, and B.F. Windley (2001) History of the Earth and life. In Nakashima, S. et al. (eds.) Geochemistry and the Origin of Life, Universal Academic Press, Tokyo, pp. 285–325.

CHAPTER 16

THARSIS SUPERPLUME AND THE GEOLOGICAL EVOLUTION OF EARLY MARS

VICTOR R. BAKER[1], SHIGENORI MARUYAMA[2], AND JAMES M. DOHM[1]

[1] *Department of Hydrology and Water Resources (and The Lunar and Planetary Laboratory), The University of Arizona, Tucson, Arizona 85721-0011 USA;*
E-mail: baker@hwr.arizona.edu

[2] *Department of Earth and Planetary Sciences, Tokyo Institute of Technology, Meguro-ku 152-8551, Japan*

Abstract
Anomalous aspects of Martian geology are explained by a theory that incorporates the onset and termination of a core dynamo, associated with an early regime of plate tectonics during the first few hundred million years of the planet's history. Rapid accretion of thickened continental crust, as modified by concurrent high impacting rates, volcanism, and denudation, ultimately resulted in the southern highlands. Following cessation of the dynamo, the plate-tectonic regime terminated with zones of focused subduction in the Tharsis and Elysium areas. The resulting high concentration of water and other volatiles in the Martian deep mantle led to the Tharsis and Elysium superplumes, the long-term persistence of which is responsible for much of the volcanism, tectonism, water outbursts, and climate change that mark the subsequent, 4-billion-year geological history of Mars.

1 INTRODUCTION

Recent confirmation of large quantities of near-surface water (ice) (Boynton et al., 2002) shows that Mars, like Earth, is a water-rich terrestrial planet. Although this fact has long been obvious from geomorphological evidence (Baker, 1982), it proved difficult to reconcile with prevailing theories of Martian geochemistry and geophysics (e.g., Carr, 1996). Nevertheless, physical theory holds that terrestrial planets should evolve through progressive dynamical stages, including accretion, differentiation, and tectonics (Kaula, 1975), and through various modes of mantle convection, including those associated with magma ocean, plate tectonic, and stagnant-lid processes (Sleep, 2000). The Earth's surface and geological history exemplify these processes,

D. A. Yuen et al. (eds.), Superplumes, 507–522.
© 2007 *Springer.*

particularly with regard to plate tectonics and superplume activity (Maruyama, 1994). Similar processes may also explain the geophysical character and geological history of Mars, as proposed by Baker et al. (2002), who revised and extended a previous model that invoked plate-tectonic processes to explain the origin of the highlands/lowlands topographic dichotomy on Mars (Sleep, 1994). Building upon critical insights gained from study of data returned by recent planetary missions, this new conceptual geological model invokes Earth-like volcanism and tectonics, combined with volatile release and sequestering, processes that were exceptionally intense very early in Martian history. Because of Mars' smaller planetary radius (Zuber, 2001), rates of planetary heating and subsequent cooling were much faster than on Earth. Concurrent with core evolution, these processes led to the development of major superplumes at Tharsis and Elysium. The latter then dominated subsequent geological activity, notably through the episodic disruption (Baker et al., 1991) of the cold, dry climate that prevailed on Mars after cessation of the heavy bombardment phase of impacting.

2 MARS ANOMALIES

A successful theory for Martian planetary evolution needs to account for many seemingly anomalous observations that cannot be reconciled with current understanding. Many of these anomalies derive from the discoveries made by the most recent planetary missions. For example, the Martian crust shows major variations from thin beneath the northern plains (∼30 km) to thick (∼60 km) beneath the southern highlands and Tharsis (Zuber et al., 2000). The origin of the great hemispheric dichotomy between the low-lying northern plains and the elevated southern highlands has long been the subject of unresolved multiple hypotheses, including mantle convection associated with core formation (Wise et al., 1979), a colossal impact that formed a basin in the north polar region (Wilhelms and Squyres, 1984), extensive southward erosional retreat of the heavily cratered highland plateau (Scott, 1978; Hiller, 1979), and plate tectonics (Sleep, 1994). Andesitic compositions characterize the surface materials overlying the relatively thin crust of the low-lying northern plains, while basaltic surface materials overlie the much thicker highland crust (Bandfield et al., 2000). These data can be consistently explained by having both igneous rock types forming in a hydrous fractional crystallization series typical of terrestrial subduction zone settings (McSween et al., 2003). In contrast, the basalt compositions of the SNC (Mars-derived) meteorites are consistent with dry fractional crystallization, and probably represent relatively young surficial lavas derived from upper mantle sources that are depleted in volatiles. Recent identification in highland areas of local, deep crustal rocks of likely granitic composition (Bandfield et al., 2004) provide another tantalizing clue, suggesting that the silica-rich surface materials on the northern plains could be derived from deep highland sources.

Linear crustal magnetization anomalies of surprisingly great intensity occur in portions of Mars' southern highlands (Connerney et al., 1999). The responsible remnant magnetization of crustal rocks implies that the Martian dynamo shut off during the Noachian Epoch, about 4 billion years ago (Acuna et al., 1999). This transition may

be associated with greatly reduced heat flow, as commonly calculated by thermal evolution models (Spohn et al., 2001). However, episodic volcanism and related tectonism persisted through subsequent Martian history, and are notably concentrated at Tharsis (Anderson et al., 2001).

Straddling the planetary dichotomy between the northern plains and the southern highlands, Tharsis is an immense pile of volcanic crustal mass for which a plume origin has been proposed on geological grounds (Mege and Masson, 1996). The major phase transition at the base of the Martian mantle was proposed as the key to initiating a single, stable plume beneath Tharsis (Harder and Christensen, 1996). However, this mechanism fails to account for the remarkable apparent stability of the plume, its specific location, and its persistence in time, long after the apparent reduced heat flow from the core that is indicated by the early cessation of the dynamo. Volcanism and tectonism became concentrated at Tharsis and Elysium, episodically operating through most of Martian history, extending from the later Noachian to the present (Anderson et al., 2001; Fairén et al., 2003).

The usual model applied to the long-term movement of subpermafrost groundwater on Mars (Carr, 1996; Clifford, 1993) presumes that the crust consists of blocky, porous "megaregolith" formed during the heavy bombardment by the intense fracturing of basement and overlain by interbedded crater ejecta and lava flows. However, recently acquired data show that the upper crust of Mars is extensively layered to depths of several kilometers, probably with both sedimentary and volcanic rocks that reflect a long period of large-scale erosion and deposition within what is now, the ancient heavily cratered terrain (Malin and Edgett, 2000a, 2001). This early phase of sedimentation probably coincides with an early history of extensive fluvial denudation (Craddock and Howard, 2002) and/or volcanic activity contemporaneous with the crater heavy bombardment. Although this relatively intense erosion terminated by the end of the heavy bombardment, immense volumes of water were episodically released from the Mars subsurface through outflow channels during subsequent Martian history (Baker et al., 1991). The water was delivered to the northern plains, where phenomenal topographic smoothness is consistent with the sedimentation (Head et al., 1999).

Evidence for a northern plains "ocean" was originally recognized in studies of landforms on Viking imagery (Jons, 1985; Lucchitta et al., 1986; Parker et al., 1989; Gulick and Baker, 1990), but this "ocean" was transient and episodic, having its origin in the immense discharges of water delivered by the outflow channels from the Tharsis area and southern highlands in Hesperian and Amazonian time (Baker et al., 1991). Viking-based geological mapping investigations also noted the possible existence of large lake bodies during this same time period (Scott et al., 1995). Data from the Mars Global Surveyor mission's Mars Orbiter Laser Altimeter confirm the remarkable smoothness of the northern plains as well as other features that seem best explained by extensive ponding of water relatively late in Martian history (Head et al., 1999). While this morphological evidence shows the long-term importance of water in later Martian history, there are also strong indications that an early (Noachian) ocean was an essential component of Mars' hydrological cycle. This very

ancient ocean may explain the loss of CO_2 from an early dense atmosphere through surface weathering and associated formation of carbonate rocks (Schaefer, 1993). Alternatively, the early ocean may have been acidic (Fairén et al., 2004), such that CO_2 would have remained in the early atmosphere, with much of it subsequently lost to space. The recent discovery of extensive sulfate salts on the Martian surface (Kerr, 2004a) is consistent with the acidic ocean. SO_2 and water generated from the volcanism and flood outbursts may also have produced the acid conditions that led to extensive sulfate salt emplacement on the Mars surface (Moore, 2004).

Remarkably, water-related activity on Mars persisted up to nearly the present day, as documented by extensive evidence of very recent hillslope gullies (Malin and Edgett, 2000b), glaciers (Kargel, 2004), outlflow channels (Berman and Hartmann, 2002; Burr et al., 2002), and related phenomena (Baker, 2001). However, the apparent lack of carbonate exposures (Christensen et al., 2001a), and the extensive presence of unaltered feldspar and pyroxene in relatively unweathered basalt outcrops (Christensen, 2000), both seem inconsistent with recent and past aqueous activity. In contrast, extensive, ancient hematite mineralization is best explained by aqueous processes, either ponding or hydrothermal alteration (Christensen et al., 2001b), and exciting new data from the Opportunity Landing Site provides strong evidence for ponded surface water during the early history of Mars (Kerr, 2004a).

Associated with the aqueous activity, there may have been a Martian biosphere (McKay et al., 1996). The recent discovery of small amounts of methane in the Martian atmosphere (Kerr, 2004b) opens up very intriguing scenarios. The methane could be derived from a deep biosphere of methanogens in the Martian groundwater. Alternatively the methane could derive from very recent volcanism. (The residence time for methane in the Martian atmosphere is on the order of 10^2 years.) Clearly, the long-term history of Martian water, both surface and subsurface, is central to nearly all the unanswered questions and anomalies.

3 ACCRETION, CORE EVOLUTION, AND PLATE TECTONICS

Mars probably initially accreted from water-rich planetesimals, then very rapidly differentiated to a liquid metallic core and solid mantle (Halliday et al., 2001), degassing a steam atmosphere rich in CO_2 and H_2O. Early Mars probably had a magma ocean, though its relatively smaller size than Earth greatly influenced the separation of refractory and volatile elements for the two evolving planets (Agee, 2004; Rubie et al., 2004). The magma ocean that formed between the intense greenhouse and the hot planetary interior initially developed a solid lid that would frequently founder back into the interior of the ocean (Abe, 1997). As the planet and its atmosphere cooled, the latter condensed to form a liquid water ocean over this solid lid, which enlarged downward over the freezing magma ocean (Fig. 1). Plate tectonics was initiated when such a lid was able to subduct (Sleep, 2000). Hydration of the young crust under the primordial ocean was probably critical to initiation of the subduction process (Reese et al., 1998), promoting it through a process of hydrosoftening where subduction beneath a liquid-water ocean was initiated by localized plastic yielding and a double

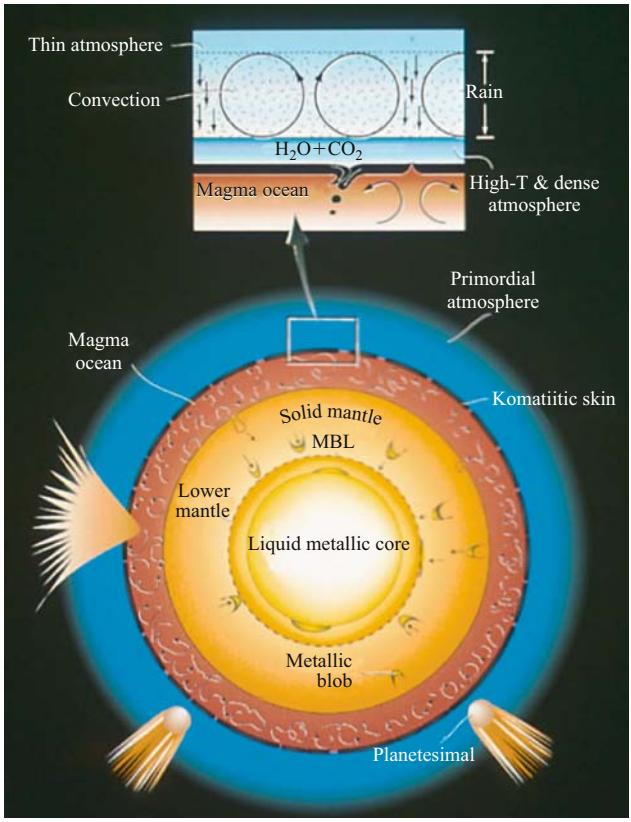

Figure 1. Schematic cross section through Mars shortly after accretion, showing differentiation, probably very rapid, to a metallic core, a mantle boundary layer (MBL) of high-pressure silicate mineral phases, upper mantle, magma ocean, thin komatiitic crust, and very hot convecting steam atmosphere (inset). Iron-rich metallic blobs are shown descending from the magma ocean and through the developing mantle in a process that generates the liquid metallic core.

feedback mechanism (thermo-elastic-rheological) that was promoted by water lubrication (Regenauer-Lieb et al., 2001). The transition from magma ocean processes to plate tectonics may have occurred relatively rapidly on Mars because of that planet's more rapid thermal evolution in comparison to Earth.

Calculations for the effect of reduced Martian gravity (0.3795 that of Earth) show that, in comparison to Earth, for similar thermal conditions: (1) Martian oceanic crust produced in sea-floor spreading was considerably thicker; (2) it spread much more rapidly; and (3) the hydrothermally altered zone of oceanic crust was much thicker (Sleep, 1994). Thus, the combination of mid-oceanic rifting, relatively rapid sea-floor spreading, and efficient subduction will be especially effective at injecting hydrothermally emplaced water, carbonates, and sulfates of the upper oceanic crust

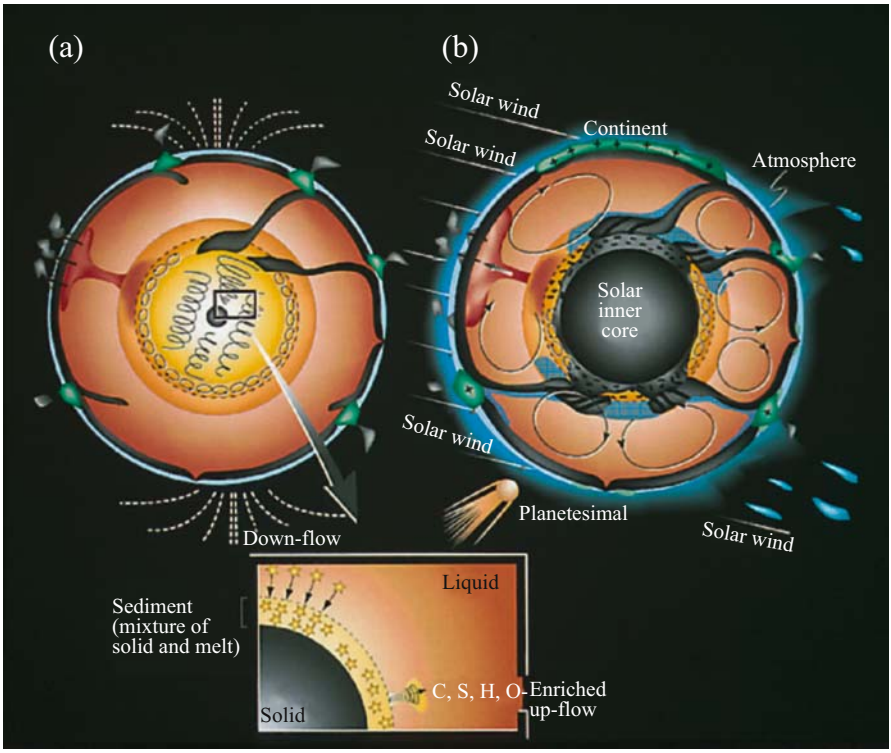

Figure 2. (a) Possible scenario for the initiation of the Martian core dynamo during the period of the early heavy bombardment. The inset detail shows how siderophile elements in the outer liquid core (yellow stars) move to the lowermost portions of the fluid core and chemical convection is promoted as light elements (C, S, H, O) are expelled from the solidifying inner core. The resulting dynamo continued for few hundred million years during a time of rapid accretion of thickened continental crust. The early Noachian ocean that promoted the warm, wet surface conditions conducive to rapid denudation was progressively depleted by the return of seawater through subduction of hydrated oceanic curst (shown as a dark layer of surface material intruding into the planetary interior). (b) The core dynamo stopped during the heavy bombardment, while plate tectonics continued, when the inner core grew so large that its internal convection could no longer sustain the dynamo.

into the Martian mantle. If plate tectonics was indeed present on early Mars, subduction of a thick carbonate layer formed by ridge hydrothermal metamorphism would have transported CO_2 into the mantle (Kitajima et al., 2001), thereby sequestering the CO_2 that otherwise would comprise carbonate rocks. The subduction of hydrated lithosphere led to dehydration reactions that lowered melting temperatures in the portions of the asthenosphere lying above the subducting slab. As on Earth (Campbell and Taylor, 1983), this process was able to generate calc-alkaline rocks, including andesites. In our conceptual model these silicic rocks were initially associated with arc volcanism.

If, as argued above, plate tectonics occurred on early Mars, the resulting high surface heat flux would have led to convection in the developing liquid core and the initiation of a dynamo (Nimmo and Stevenson, 2000). Additionally, a spot-cooling effect would have been produced by the impingement of subducted, hydrated slabs above the density-stratified molten core. This process promoted the growth of a solid inner core and drove chemical convection in the molten outer core (Fig. 2, inset detail). The latter process occurred because the solubility of light elements in solid iron decreases with increasing pressure (O'Neill et al., 1998). Continued evolution of the core produced a remarkably strong dynamo and consequent magnetosphere, the latter providing a shielding effect in regard to the solar wind and high-energy particles from space.

4 INFERRED EARLY CRUSTAL EVOLUTION

Extremely rapid plate motion and subduction will result in (a) very fast accretion of thickened "continental" crust, and (b) removal of the ocean water to the mantle boundary layer over the cooling and solidifying core (Fig. 2). Unusually large oceanic plateaus, generated over local mantle plumes, will also be accreted to the evolving Mars "continent", or "continents". The rocks in these assemblages are highly susceptible to very strong remnant magnetization. The presence of single-domain magnetite crystals in Martian meteorite ALH84001 (Weiss et al., 2001), a possible biomarker(Thomas-Keptra et al., 2001), provides an important indicator of mineralization appropriate to very strong remnant magnetization. Magnetic minerals in dikes may also be important (Nimmo, 2000). Very strong remnant magnetism is also reported from Icelandic basalts (Kristjansson and Johanesson, 1999). Their incorporation into the accreting continental terrains would result in the observed prominent magnetic anomalies of the Martian highlands. Immense hematite deposits could also have been emplaced in association with large igneous provinces, as hypothesized for the early Earth (Barley et al., 1997). These could be parts of terrains accreted to the evolving Martian continental crust, or they could be associated with basins formed on the continental margins. The oxygen for hematite formation could have been derived from photosynthesis, which would become possible by the birth of a strong magnetosphere, thereby protecting the near-surface environment for early life.

The period of rapid continental crustal accretion would have to occur in the first several hundred million years of Martian history (the earliest Noachian Epoch). This period was also probably a time of extensive erosion and formation of sediments, associated with a relatively dense, water-rich atmosphere. Relatively high denudation rates for the ancient highlands in early Noachian time were recognized from Viking imagery (Craddock and Maxwell, 1990, 1993). The Mars Obiter Camera (MOC) of the Mars Global Surveyor Mission provided striking new data (Malin and Edgett, 2000a, 2001) showing that the ancient Martian crust is intensively layered to considerable depths (in contrast to the lunar "megaregolith" model; Carr, 1996). The layering is caused by sedimentary rocks formed by intense denudation during the period of heavy bombardment (Malin and Edgett, 2000a, 2001). MOC imagery

shows that the Martian highlands do not consist of an initially lunar-like surface that was subsequently modified by fluvial and other processes. Instead, cratering, erosion, and deposition of layered materials probably all occurred contemporaneously, leading to a complex interbedding of lava flows, igneous intrusions, sediments, buried craterforms, and erosional unconformities (Malin and Edgett, 2000a, 2001). Add to this scenario the constructional process of continental accretion, plus the effects of large basin-forming impacts (Hellas and Argyre), and one can explain key aspects of the highlands crustal thickness and magnetic anomaly patterns.

Continued planetary cooling and core solidification terminated the dynamo while plate tectonics continued (Fig. 2b), as predicted by the ultrahigh-pressure experiments on the Fe-FeO-FeS system at the core-mantle boundary pressure of 28 Gpa (Boehler, 1996). The frozen temperature of core at CMB ranges from 2400 K (pure iron) to 1850 K (saturated in S), which is even higher in temperature than that of modern

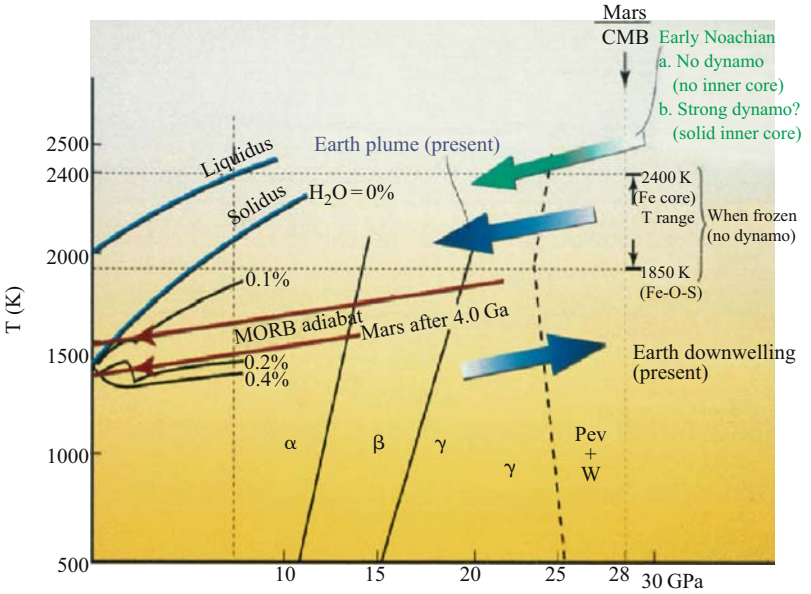

Figure 3. Temperature estimates for the Martian mantle. Because of its relatively high temperature, the early Noachian mantle would have generated extensive magmatism by rising plumes and mantle upwelling under mid-oceanic ridges. This process would continue even after the core nearly all solidified, as shown by the temperature estimate for the topmost core when frozen. Note that the rising hydrous plume (arrow) generates extensive melting even though the mantle adiabat cannot cross the dry solidus for mantle rock. This causes extensive magmatism observed in the Tharsis region, below which the mantle was enriched in water. The KLB-1 peridotite dry solidus and liquidus, and the wet solidus with 0.1, 0.2, and 0.4 weight percent water, are redrawn from a summary by Iwamori (1998). Stability fields of Mg_2SiO_4 are also shown, and abbreviated as alpha, beta, and gamma. The breakdown reaction of gamma (ringwoodite) leading to + wurstite is illustrated by the broken line. At higher temperatures than 1900 K, the reaction is replaced by a curve with positive slope for majorite.

MORB with a 1570 K mantle potential temperature (Fig. 3) (McKenzie and Bickle, 1988). This implies that Mars plate tectonics must have operated to form thicker MOR crust than 18 km when the core was frozen. The last remnant of oceanic crust, the area now beneath the northern plains, shows no magnetic lineations (Connerney et al., 1999), but it is marked by large impact basins that were likely emplaced during the later part of the heavy bombardment (Frey et al., 2002).

5 TERMINATION OF PLATE TECTONICS

Also during this time (earliest Noachian), when the effects of the dynamo and magnetosphere were declining and plate tectonics continued, we propose that the linear zone of subduction between the oceanic northern plains and the "continental" southern highlands became deformed into a loop or bight at Tharsis. A speculative possibility is that this might occur as the antipodal effect of impact basin formation (Watts et al., 1991), with the very ancient impact located in the Arabia region (Dohm et al., 2004). Alternatively, the direct effect of a very large impact on the Mantle at Tharis itself may have induced a local convective regime that led to the changes (Reese et al., 2002). Either way, the result could have been a plate boundary analogous to that now occurring in southeast Asia and the western Pacific, where double-sided subduction zones are currently transporting unusual quantities of water to Earth's upper mantle (T. Komiya, written communication). In analogous fashion to Earth, a high concentration of water-rich oceanic crust could be conveyed to the mantle boundary layer beneath Tharsis by this process.

Preliminary calculations (Sleep, 1994) showed that the equivalent of a Martian ocean, 130 m of water spread over the whole planet, could be transferred to the local Martian mantle beneath Tharsis by subduction processes. On a much smaller scale, but in an analogous manner and later in time of formation, the plate boundary in the area that is now Elysium may also have been initiated by the antipodal effects of the late-heavy-bombardment Argyre impact basin, or more directly by an impact at Elysium itself.

Early to middle Noachian Martian plate tectonics is consistent with a preliminary synthesis of published Viking-based information generated by regional mapping. Relevant observations include the geological and structural histories of the Thaumasia and Coprates mountain ranges, which partly form the eastern and southern margins of the Thaumasia Plateau (Dohm et al., 2001a) and the southeastern margin of the Tharsis magmatic complex (Dohm et al., 2001b). There are also numerous linear structures in the southern hemisphere that are tens to thousands of kilometers long and appear to result from contractional deformation by thrust faulting (Schultz and Tanaka, 1994). These macrostructures (Fairén and Dohm, 2004) (a) occur among highly degraded promontories, interpreted to be silica-rich magmatic intrusives or volcanic constructs (Dohm and Tanaka, 1999), and (b) form the margins of elongated basins, plateaus, and "banded" zones of anomalous magnetism, as in Terra Cimmeria and Terra Sirenum (Connerney et al., 1999). All these relationships can be interpreted as the faulted boundaries of accreted terranes (Fairén et al., 2002), an explanation that is consistent with other relationships described in this paper.

6 THE THARSIS SUPERPLUME

According to the currently accepted time scale (Hartmann and Neukum, 2001), the plate tectonic phase for Mars could have lasted as long as 500 million years, approximately the same duration as Earth's Phanerozoic era. As plate tectonics terminated in the cooled Mars, perhaps about 4 billion years ago, it would have been replaced by stagnant-lid convection and associated episodic plume activity on a one-plate planet. Water, carbonates, and sulfates had been largely conveyed to the mantle boundary layer, immediately above the more slowly cooling solid core. The surface was now cold and dry, but the seeds of its episodic transformation had been sown into the deep mantle. The water in the mantle produced decreased melting temperatures and viscosities above those preferential zones most enriched in water because of the double-sided convection that terminated the plate-tectonic phase (Fig. 4). The conductive heating from the underlying core would have led to breakdown reactions of hydrous beta and gamma mineral phases to liberate free water in hydrous plumes. The recycled MORB crusts within the plumes became a potential source of flood basalts, and, by their heterogeneous distribution, they caused episodic magma ascent and volcanism. Moreover, the presence of a lower mantle on Mars may have acted as a thermal boundary layer to further induce episodicity of Tharsis magmatism.

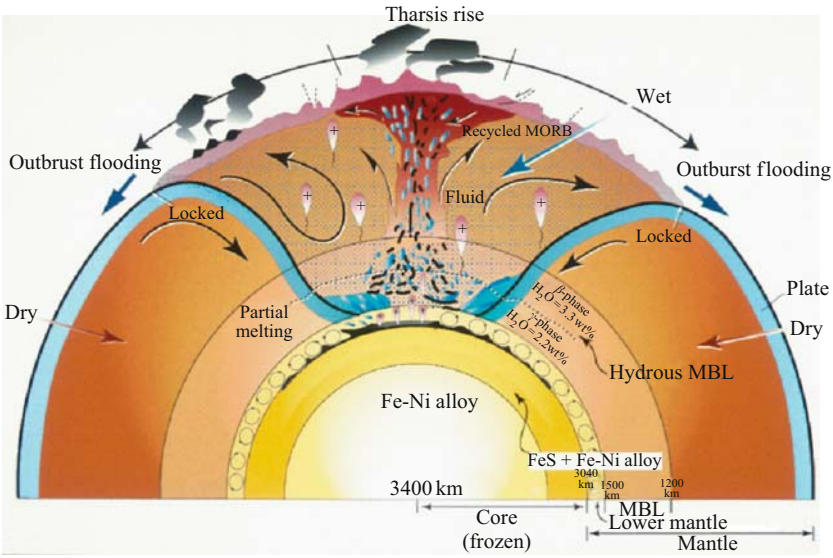

Figure 4. Hypothetical initiation of the Tharsis superplume by focused subduction, delivering huge amounts of water-rich oceanic crust to the local MBL. Massive basaltic volcanism at Tharsis is associated with temporary outgassing to water to enhance the atmosphere, and to produce huge outburst floods of water, episodically replenishing the northern plains "ocean".

Collectively, the above-described phenomena constitute the Tharsis superplume, (Fig. 4) initially leading to immense outpourings of basaltic lava during the late Noachian (Dohm et al., 2001b; Phillips et al., 2001). At declining rates, lavas continued to emerge throughout Martian history. Further evidence for this scenario is found in the SNC Martian meteorites most of which represent basalts with crystallization ages between 0.15 and 1.3 Ga (Nyquist et al., 2001). These basalts derived from magmas that were water-rich (McSween et al., 2001). Moreover, their oxidized state relative to the ancient, primordial Mars sample provided by meteorite ALH84001 (Warren and Kallemeyn, 1996) may indicate derivation from a relatively hydrous, recycled source region, as would be expected in this scenario.

Beginning in the later Noachian, the magma-driven structural landform complexes of the Tharsis superplume became the sites of immense outflows of water (Dohm et al., 2001c). Possibly associated with the downwelling of the subducting plates, a huge sedimentary basin developed at Tharsis during its early history (Dohm et al., 2001b). This would have been analogous in timing and association to the megabasins characterizing the early development of terrestrial superplumes (Maruyama, 1994; Irvine, 1989). Also similar to Earth, parts of the Tharsis basin were subsequently inverted by magmatic-driven uplifts (Dohm et al., 1998; Anderson et al., 2001), probably related to later upwelling of the superplume. The formation of Valles Marineris exposed the 10-km thick pile of lavas (McEwen et al., 1999), and probable interfingering sediments (Malin and Edgett, 2001), that comprise the fill of the ancient basin.

The outburst floods eroded into the deep andesitic crust of the highlands, delivering the resulting sediments to blanket the oceanic crust of the northern lowlands with a thin andesitic cover, while the highlands were mantled by the products of younger, plume-related basaltic lavas, thereby explaining the observed surface compositions (Bandfield et al., 2000). Although considerable CO_2, H_2O and SO_2 were temporarily delivered to the atmosphere in episodic outbursts (Baker et al., 1991), these were subsequently trapped in the near-surface permafrost zone as ground ice and gas hydrates (Baker, 2001). The episodes of climate change were sufficiently infrequent and of such short duration to have not produce appreciable weathering of basalt rock outcrops. Any remaining atmosphere was progressively altered by the long-term action of the solar wind, unconstrained by effects of a magnetosphere. Extant Martian life, which enjoyed earlier phases of near-surface activity, is probably confined to a subsurface zone beneath the permafrost and possible "windows" at local zones of hydrothermal activity (Fisk and Giovannoni, 1999).

7 DISCUSSION AND CONCLUSIONS

If, as we propose, Mars developed a temporary, very ancient phase of plate tectonics (PT) (Baker et al., 2002), this would have had the following characteristics and consequences: (a) PT was a natural consequence of the progressive decline in heat flow (Sleep, 2000) and the evolution of the core (Nimmo and Stevenson, 2000).

(b) It occurred during the early part of the extremely intense heavy bombardment, not in later Martian history, as proposed by Sleep (1994). (c) It was associated with a remarkably intense core dynamo and consequent magnetosphere, leading to intensely magnetized oceanic plateaus that accreted to proto-continental terrains now in evidence as the linear anomalies of remnant magnetism in the Martian southern highlands (Fairén et al., 2002). (d) It conveyed, via subduction, water, carbon dioxide, and sulfates to the core-mantle boundary zone, thereby depleting the reservoir of these materials from the surface to the upper mantle. (e) Its whole-mantle subduction processes cooled the evolving core, thereby terminating the dynamo during the heavy bombardment, prior to 4.0 Ga. (f) After at most a few 10^8 years, PT ended with focused subduction, perhaps localized by late bombardment mega-impact structures, and also generating the observed planetary dichotomy. The focused subduction led to the Tharsis superplume, with its massive late Noachian volcanism (Phillips et al., 2001), with magmas derived from the hydrated zone of the lower mantle, in analogous manner to Earth-like superplumes (Maruyama, 1994). Episodic and long-term associated volcanic, tectonic, and hydrologic activity (decreasing in magnitude to the present day) can then be readily explained as direct consequences of the above scenario.

Volatile-rich magmas (McSween et al., 2001) that emerged during post-PT, post-heavy-bombardment Martian history were probably derived from the deep-mantle reservoir that had been charged by very early subduction processes. In later Mars history, water delivered to the surface by volcanism eventually concentrated as ground ice and ground water in the near-surface crust, where it is still present (Boynton et al., 2002). This water was episodically returned to the surface by outflow channel activity and valleys, temporarily constituting a northern plains "ocean" (Baker et al., 1991; Fairén et al., 2003). The various channels are cut into the deeper silicic crust of the highlands, which was partly derived from ancient PT-accretionary processes (Fairén et al., 2002). The silicic sediments were delivered as a sedimentary cover to the northern plains, while the highlands and Tharsis became mantled by relatively young, volatile-poor basalts, derived from the more depleted upper mantle. The Martian surface has remained predominantly cold and dry since at least the late Noachian, but its very recent water-related episode and discrete past episodes reflect short-term excursions that can be explained as natural consequences of the ancient legacy of a very early aqueous history and associated plate tectonics.

The foregoing holds that Mars, like Earth, is characterized by long-term cycles of water and rock (igneous, metamorphic, and sedimentary). These cyclic processes are intimately tied to the evolution of the planetary lithosphere, atmosphere, and hydrosphere. However, the thermal evolution of Mars was much faster than that of Earth. Mars experienced and completed its plate-tectonic phase during the heavy bombardment, while Earth remains in that planetary evolutionary phase. Thus, the theory strongly follows the insight (Sleep, 1994, 2000) that the phenomenon of plate tectonics is not exhausted by a planetary sample of one, but rather that it is a natural consequence of the more general evolutionary sequence of a water-rich terrestrial

planet. Clearly our conceptual model needs further elaboration for its many components, plus further "testing" in terms of its many consequences, consistent with the planetary geological history, internal coherence, and with new data from on-going missions.

ACKNOWLEDGEMENTS

We thank G. Komatsu for helpful comments. The illustrations were prepared by Shio Watanabe. V.R.B. and J.M.D. received partial support from NASA grant NAG-5-9790.

REFERENCES

Abe, Y. (1997) Thermal and chemical evolution of the terrestrial magma ocean. *Phys. Earth Planet. Inter.*, 100, 27–39.

Acuna, M.H. et al. (1999) Global distribution of crustal magnetization discovered by the Mars Global Surveyor MAG/ER experiment. *Science*, 284, 790–793.

Agee, C.B. (2004) Earth science: Hot metal. *Nature*, 429, 33–35.

Anderson, R.C., J.M. Dohm, M.P. Golombek, A.F.C. Haldemann, B.J. Franklin, K.L. Tanaka, J. Lias, and B. Peer (2001) Primary centers and secondary concentrations of tectonic activity through time for the western hemisphere of Mars. *J. Geophys. Res.*, 106, 20563–20585.

Baker, V.R. (1982) The Channels of Mars, University of Texas Press, Austin, Texas, pp. 1–198.

Baker, V.R. (2001) Water and the Martian landscape. *Nature*, 412, 228–236.

Baker, V.R., S. Maruyama, and J.M. Dohm (2002) A theory of plate tectonics and subsequent long-term superplume activity on Mars. In International Workshop: Role of superplumes in the Earth system, Tokyo Inst. of Technology, Tokyo, Japan, pp. 312–316. (Published in the journal *Electronic Geosciences*, 8, on the web at http://194.94.42.12/licensed_materials/10069/free/conferen/superplu/index.html

Baker, V.R., R.G. Strom, V.C. Gulick, J.S. Kargel, G. Komatsu, and V.S. Kale (1991) Ancient oceans, ice sheets and the hydrological cycle on Mars. *Nature*, 352, 589–594.

Bandfield, J.L., P.R. Christensen, V.E. Hamilton, and H.Y. McSween, Jr. (2004) Identification of a Quartz and Na-Feldspar Surface Mineralogy in Syrtis Major. Lunar Planet. Sci. Conf. XXXV, Abstract 1449.

Bandfield, J.L., V.H. Hamilton, and P.R. Christensen (2000) A global view of Martian surface composition from MGS-TES. *Science*, 287, 1626–1630.

Barley, M.E., A.L. Pickard, and P.J. Sylvester (1997) Emplacement of a large igneous province as a possible cause of banded iron formation 2.45 billion years ago. *Nature*, 385, 55–58.

Berman, D.C., and W.K. Hartmann (2002) Recent fluvial, volcanic, and tectonic activity on the Cerberus Plains of Mars. *Icarus*, 159, 1–17.

Boehler, R. (1996) Melting temperature of the Earth's mantle and core: Earth's thermal Structure. *Annu. Rev. Earth Planet. Sci.*, 24, 15–40.

Boynton, W.V. et al. (2002) Distribution of hydrogen in the near surface of Mars: Evidence for subsurface ice deposits. *Science*, 297, 81–85.

Burr, D.M., J.A. Grier, A.S. McEwen, and L.P. Keszthelyi (2002) Repeated aqueous flooding from the Cerberus Fossae: Evidence for very recently extant, deep ground- water on Mars. *Icarus*, 159, 53–73.

Campbell, I.K., and S.R. Taylor (1983) No water, no granites–no oceans, no continents. *Geophys. Res. Lett.*, 10, 1061–1064.

Carr, M.H. (1996) Water on Mars, Oxford University Press, New York, pp. 1–229.

Christensen, P.R. et al. (2000) Identification of a basaltic component of the Martian surface from Thermal Emission Spectrometer data. *J. Geophys. Res.*, 105, 9609–9621.

Christensen, P.R. et al. (2001a) Mars Global Surveyor Thermal Emission Spectrometer experiment: Investigation, description and surface science results. *J. Geophys. Res.*, 106, 23823–23871.

Christensen, P.R. et al. (2001b) Global mapping of Martian hematite mineral deposits: Remnants of water-driven processes on Mars. *J. Geophys. Res.*, 106, 23873–23885.

Clifford, S.M. (1993) A model for the hydrologic and climate behavior of water on Mars. *J. Geophys. Res.*, 98, 10973–11016.

Connerney, J.E.P. et al. (1999) Magnetic lineations in the ancient crust of Mars. *Science*, 284, 794–798.

Craddock, R.A., and A.D. Howard (2002) The case for rainfall on a warm, wet early Mars. *J. Geophys. Res.*, 107, doi:10.1029/2001JE001505.

Craddock, R.A., and T.A. Maxwell (1990) Resurfacing of the Martian highlands in the Amenthes and Tyrrhena region. *J. Geophys. Res.*, 95, 14265–14780.

Craddock, R.A., and T.A. Maxwell (1993) Geomorphic evolution of the Martian highlands through ancient fluvial processes. *J. Geophys. Res.*, 98, 3453–3468.

Dohm, J.M., R.C. Anderson, and K.L. Tanaka (1998) Digital structural mapping of Mars. *Astron. & Geophys.*, 39, 3.20–3.22.

Dohm, J.M., and K.L. Tanaka (1999) Geology of the Thaumasia region, Mars: Plateau development, valley origins, and magmatic evolution. *Planet. Space Sci.*, 47, 411–431.

Dohm, J.M., K.L. Tanaka, and T.M. Hare (2001a) Geologic map of the Thaumasia region of Mars. *US Geol. Survey Map* I-2650.

Dohm, J.M. et al. (2001b) Ancient drainage basin of the Tharsis region, Mars: Potential source for outflow channel systems and putative oceans or paleolakes. *J. Geophys. Res.*, 106, 32943–32958.

Dohm, J.M. et al. (2001c) Latent activity for western Tharsis, Mars: Significant flood record exposed. *J. Geophys. Res.*, 102, 12301–12314.

Dohm, J.M. et al. (2004) Ancient giant basin/aquifer system in the Arabia region, Mars. *Lunar Planet. Sci. Conf.* XXXV, Abstract 1209.

Fairén, A.G., and J.M. Dohm (2004) Age and origin of the lowlands of Mars. *Icarus*, 169, 277–284.

Fairén, A.G., J.M. Dohm, V.R. Baker, M.A. de Pablo, J. Ruiz, J.C. Ferris, and R.C. Anderson (2003) Episodic flood inundations of the northern plains of Mars. *Icarus*, 165, 53–67.

Fairén, A.G., D. Fernández-Remolar, J.M. Dohm, V.R. Baker, and R. Amils (2004) Inhibition of carbonate synthesis in acidic oceans on early Mars. *Nature*, 431, 423–426.

Fairén, A.G., J. Ruiz, and F. Angula (2002) An origin for the linear magnetic anomalies on Mars through accretion of terranes: Implications for dynamo timing. *Icarus*, 160, 220–223.

Fisk, M.R., and S.J. Giovannoni (1999) Source of nutrients and energy for a deep biosphere on Mars. *J. Geophys. Res.*, 104, 11805–11815.

Frey, H.V., J.H. Roark, K.M. Shockey, E.L. Frey, and S.E.H. Sakimoto (2002) Ancient lowlands on Mars. *Geophys. Res. Lett.*, 29, doi:10.1029/2001GL013832.

Gulick, V.C., and V.R. Baker (1990) Origin and evolution of valleys on Martian volcanoes. *J. Geophys. Res.*, 95, 14325–14344.

Halliday A.N. et al. (2001) Accretion, composition and early differentiation of Mars. *Space Sci. Rev.*, 96, 197–230.

Harder, H., and U.R. Christensen (1996) A one-plume model of Martian mantle convection. *Nature*, 380, 507–509.

Hartmann, W.K., and G. Neukum (2001) Cratering chronology and the evolution of Mars. *Space Sci. Rev.*, 96, 165–194.

Head III, J.W. et al. (1999) Possible ancient oceans on Mars: Evidence from Mars Orbiter Laser Altimeter data. *Science*, 286, 2134–2137.

Hiller, K. (1979) Geologic map of the Amenthes Quadrangle, Mars. *U.S. Geol. Sur. Map*, I-1110.

Irvine, T.N. (1989) A global convection framework: Concepts of symmetry, stratification and system in the Earth's dynamic structure. *Econ. Geol.*, 84, 2059–2114.

Iwamori, S. (1998) Transportation of H_2O and melting in subduction zones. *Earth Planet. Sci. Lett.*, 160, 65–80.

Jons, H.P. (1985) Late sedimentation and late sediments in the northern lowlands of Mars. *Lunar Planet. Sci.*, 16, 414–415.
Kargel, J.S. (2004) Mars: A Warmer Wetter Planet, Springer, London, pp. 1–557.
Kaula, W.M. (1975) The seven ages of a planet. *Icarus*, 26, 1–15.
Kerr, R.A. (2004a) A wet early Mars seen in salty deposits. *Science*, 303, 1450.
Kerr, R.A. (2004b) Life or volcanic belching on Mars. *Science*, 303, 1953.
Kitajima, K. et al. (2001) Seafloor hydrothermal alteration of an Archaean mid-ocean ridge. *J. Metamorphic Geol.*, 19, 581–597.
Kristjansson, L., and H. Johanesson (1999) Secular variation and reversals in a composite 2.5 km thick lava section in central western Iceland. *Earth Planets Space*, 51, 261.
Lucchitta, B.K., H.M. Ferguson, and C. Summers (1986) Sedimentary deposits in the northern lowland plains, Mars. *J. Geophys. Res.*, 91, E166–E174.
Malin, M.C., and K.S. Edgett (2000a) Sedimentary rocks of early Mars. *Science*, 290, 1927–1937.
Malin, M.C., and K.S. Edgett (2000b) Evidence for recent groundwater seepage and surface runoff on Mars. *Science*, 288, 2330–2335.
Malin, M.C., and K.S. Edgett (2001) Mars Global Surveyor Orbiter Camera: Inter-planetary cruise through primary mission. *J. Geophys. Res.*, 106, 23429–23570.
Maruyama, S. (1994) Plume tectonics. *J. Geol. Soc. Jpn.*, 100, 24–49.
McEwen, A.S., M.C. Malin, M.H. Carr, and W.K. Hartmann (1999) Voluminous volcanism on early Mars revealed in Valles Marineris. *Nature*, 397, 584–586.
McKay, D.S. et al. (1996) Search for past life on Mars: Possible relic biogenic activity in Martian meteorite ALH84001. *Science*, 273, 924–930.
McKenzie, D.P., and M.J. Bickle (1988) The volume and composition of melt generated by extension of the lithosphere. *J. Petrol.*, 29, 625–679.
McSween, H.Y., Jr. et al. (2001) Geochemical evidence for magmatic water within Mars from pyroxenes in the Shergotty meteorite. *Nature*, 409, 487–490.
McSween, H.Y., Jr., T.L. Grove, and M.B. Wyatt (2003) Constaints on the composition and petrogenesis of the Martian crust. *J. Geophys. Res.*, 108, doi:10.1029/2003JE002175.
Mege, D., and P. Masson (1996) A plume tectonics model for the Tharsis province, Mars. *Planet. Space Sci.* 44, 1499–1546.
Moore, J.M. (2004) Mars: Blueberry fields for ever. *Nature*, 428, 711–712.
Nimmo, F. (2000) Dike intrusion as a possible cause of linear Martian magnetic anomalies. *Geology*, 28, 391–394.
Nimmo, F., and D.J. Stevenson (2000) Influence of early plate tectonics on the thermal evolution and magnetic field of Mars. *J. Geophys. Res.*, 105, 11969–11979.
Nyquist, L.E. et al. (2001) Ages and geologic histories of Martian meteorites. *Space Sci. Rev.*, 96, 105–164.
O'Neill, H., D. Canil, and D.C. Rubie (1998) Oxide-metal equilibria to 2500°C and 25 Gpa: Implications for core formation and the light component of the Earth's core. *J. Geophys. Res.*, 103, 12239–12248.
Parker, T.J., R.S. Saunders, and D.M. Schneeberger (1989) Transitional morphology in the west Deuteronilus Mensae region of Mars: Implications for the modification of the lowland/upland boundary. *Icarus*, 82, 111–145.
Phillips, R.J. et al. (2001) Ancient geodynamics and global change hydrology on Mars. *Science*, 291, 2587–2591.
Reese, C.C., V.S. Solomatov, and L.-N. Moresi (1998) Heat transport efficiency for stagnant lid convection with dislocation viscosity: Application to Mars and Venus. *J. Geophys. Res.*, 103, 13643–13657.
Reese, C.C., V.S. Solomatov, and J.R. Baumgardner (2002) Survival of impact-induced thermal anomalies in the Martian mantle. *J. Geophys. Res.*, 107(E7), 5054, doi:10.1029/2000JE001474.
Regenauer-Lieb, K., D.A. Yuen, and J. Branlund (2001) The initiation of subduction: Criticality by addition of water? *Science*, 294, 578–580.
Rubie, D.C., C.K. Gessmann, and D.J. Frost (2004) Partitioning of oxygen during core formation on the Earth and Mars. *Nature*, 429, 58–61.
Schaefer, M.W. (1993) Aqueous geochemistry on early Mars. *Geochim. Cosmochim. Acta.*, 57, 4619–4625.

Schultz, R.A., and K.L. Tanaka (1994) Lithospheric-scale buckling and thrust structures on Mars: The Coprates rise and south Tharsis ridge belt. *J. Geophys. Res*., 99, 8371–8385.

Scott, D.H. (1978) Mars, highlands-lowlands: Viking contribution to Mariner relative age studies. *Icarus*, 34, 479–485.

Scott, D.H., J.M. Dohm, and J.W. Rice (1995) Map of Mars showing channels and possible paleolake basins. US Geol. Survey Map I-2461.

Sleep, N.H. (1994) Martian plate tectonics. *J. Geophys. Res.*, 99, 5639–5655.

Sleep, N.H. (2000) Evolution of the mode of convection within terrestrial planets. *J. Geophys. Res.*, 105, 17563–17578.

Spohn, T. et al. (2001) Geophysical constraints on the evolution of Mars. *Space Sci. Rev.*, 96, 231–262.

Thomas-Keptra, K.L. et al. (2001) Truncated hexa-octahedral magnetite crystals in ALH84001: Presumptive biosignatures. *Proc. Natl. Acad Sci. USA*, 98, 2164–2169.

Warren, P.H., and G.W. Kallemeyn (1996) Siderophile trace elements in ALH84001, other SNC meteorites and eucrites: Evidence of heterogeneity, possibly time linked, in the mantle of Mars. *Meteroritics Plan. Sci.*, 31, 97–105.

Watts, A.W., R. Greeley, and H.J. Melosh (1991) The formation of terrains antipodal to major impacts. *Icarus*, 93, 159–168.

Weiss, B.P. et al. (2001) Records of an ancient Martian magnetic field in ALH84001. *Lunar Planet. Sci. Conf.* XXXII, Abstract 1244.

Wilhelms, D.E., and S.W. Squyres (1984) The martian hemispheric dichotomy may be due to a giant impact. *Nature*, 309, 138–140.

Wise, D.U., M.P. Golombek, and G.E. McGill (1979) Tharsis province of Mars: Geologic sequence, geometry, and a deformation mechanism. *Icarus*, 38, 456–472.

Zuber, M.T. (2001) The crust and mantle of Mars. *Nature*, 412, 220–227.

Zuber, M.T. et al. (2000) Internal structure and early thermal evolution of Mars from Mars Global Surveyor topography and gravity. *Science*, 287, 1788–1793.

CHAPTER 17

TRAITS AND EVOLUTION OF THE THARSIS SUPERPLUME, MARS

JAMES M. DOHM[1], VICTOR R. BAKER[1], SHIGENORI MARUYAMA[2], AND ROBERT C. ANDERSON[3]

[1] *Department of Hydrology and Water Resources (and The Lunar and Planetary Laboratory), The University of Arizona, Tucson, Arizona 85721-0011, USA;*
E-mail: jmd@hwr.arizona.edu

[2] *Department of Earth and Planetary Sciences, Tokyo Institute of Technology, Meguro-ku 152-8551, Japan;*

[3] *Jet Propulsion Laboratory, California Institute of Technology, Pasadena, California 91109, USA*

Abstract
When compared to the previous explanations that attempt to explain the long-lived internal heat engine of Tharsis, Mars (e.g., >3 Ga), the Tharsis Superplume hypothesis provides a cohesive explanation for the evolution of the magmatic complex and forms a sound basis for further productive inquiry. Contributors to its formation and long-term, pulsating evolution may include: (1) extremely ancient plate tectonism (Baker et al., this volume), (2) an extremely ancient giant impact in the Arabia Terra region, which is located nearly antipodal to the superplume (Dohm et al., 2004), and (3) later smaller impacts (e.g., Hellas and Isidis) when compared to the putative Arabia impact with a primary basin estimated to be at least 3000 km in diameter. The extensive geological and paleohydrological records of the Tharsis Superplume presented here, which includes extremely long-lived magma and liquid and frozen water interactions in the subsurface and the surface, have tremendous implications concerning future missions to Mars that will unfold the potential astrobiological information that awaits discovery.

1 INTRODUCTION

Viking-based geological and geophysical investigations and recent acquisition of high-resolution topography, imagery, and geophysical data reveal an active and varied martian geological history (Baker, 2001). Whereas Earth has protracted periods of high erosion rates and well-documented, sustained plate tectonism, Mars comprises geologic terrains that archive substantial stratigraphic, magmatic, paleotectonic, and

D. A. Yuen et al. (eds.), Superplumes, 523–536.
© 2007 *Springer.*

paleoerosional information potentially further back than 4 ga (Hartmann, 1978; Neukum and Hiller, 1981). Similar to Earth, however, the stratigraphic, paleotectonic, and paleoerosional information of Mars, compiled by planetary geologists through numerous mapping investigations at global to local scales, demonstrate that magmatic-driven processes, including plume-driven tectonism, dominate the dynamic geologic history. This is best exemplified at Tharsis and the surrounding regions (e.g., Scott and Tanaka, 1986; Mege and Masson, 1996), where five major stages of pulse-like geologic activity resulted in the formation of a magmatic complex (Dohm and Tanaka, 1999; Dohm et al., 2000, 2001a–c; Anderson et al., 2001a) (Figs. 1 and 2). The resulting Tharsis magmatic complex exhibits topography, structure, geomorphic expression, and geophysical traits that are similar to the expression of Earth's

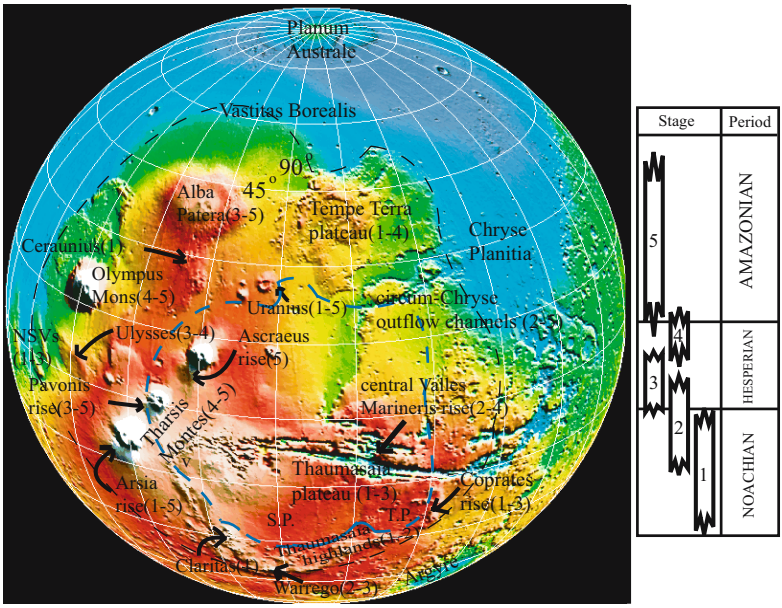

Figure 1. MOLA shaded relief map (courtesy of the MOLA team) showing features of interest and their relative stage of Tharsis Superplume evolution, which includes northwestern slope valleys (NSVs) and circum-Chryse outflow channel systems (northwest and northeast watersheds of Tharsis, respectively), Tharsis Montes, Olympus Mons, and Alba Patera shield volcanoes, centers of magmatic-driven tectonic activity (Claritas, Ceraunius, Warrego, Syria Planum, and central Valles Marineris rise), Tempe Terra and Thaumasia igneous plateaus, ancient mountain ranges, Thaumasia Highlands and Coprates rise, Argyre impact basin, and parts of the northern plains (Chryse Planitia, Vastitas Borealis, and Planum Australe). The five major stages of Tharsis Superplume activity (stages 1–5 after Dohm and Tanaka, 1999; Dohm et al., 2001a) correspond to the geologic periods of Scott and Tanaka (1986). Also shown is the estimated extent of the Tharsis Superplume (black dashed line), which encompasses a total surface area of approximately 2×10^7 km^2 compared to the largest terrestrial igneous plateau, Ontong-Java, which encompasses a total surface area of approximately 2×10^6 km^2, and the Europe-sized Tharsis Noachian drainage basin/aquifer system (blue dashed line) of Dohm et al. (2001b), which is considered to be the primary source of water for the NSVs and circum-Chryse outflow channel systems.

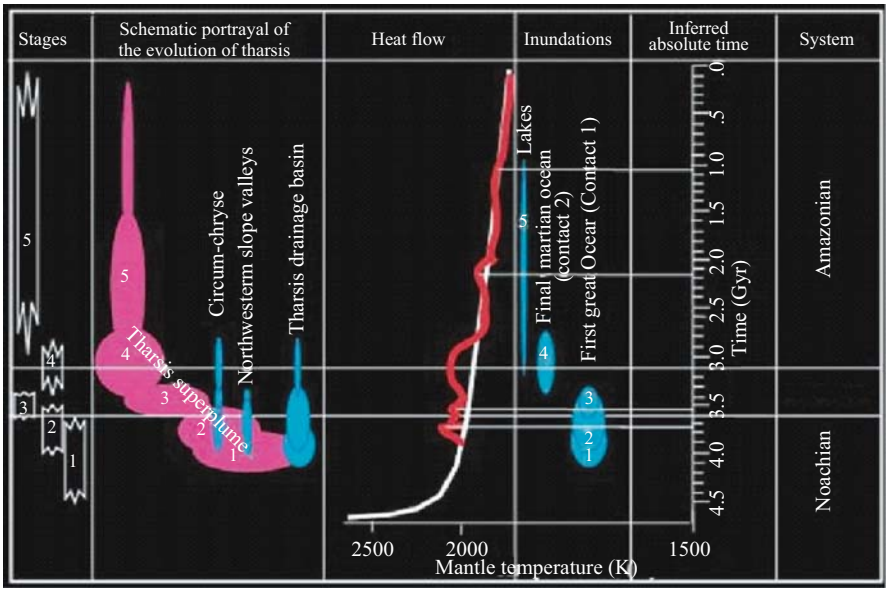

Figure 2. Chart comparing the evolutional stages of geologic activity in the Tharsis Superplume (similar to Fig. 1), which includes circum-Chryse, NSVs, and Tharsis drainage basin/aquifer system (Dohm et al., 2001b), with: (1) heat flow; note the maximum effective heat flow from the core to lithosphere in the Early and Middle Noachian (white line) and non-steady-state decline in subjective heat flow extending from Middle Noachian to present (red line) compared to proposed steady-state decline in mantle temperature with time (white line; Schubert et al., 1992) based on published geologic information (e.g., Dohm and Tanaka, 1999; Dohm et al., 2001a–c; Anderson et al., 2001a; Baker et al., 2002; Fairén et al., 2003), (2) hypothesized Tharsis-triggered inundations in the northern plains ranging from oceans to lakes (Fairén et al., 2003), (3) inferred absolute time (Hartmann and Neukum, 2001), and (4) System information of Scott and Tanaka (1986). Sizes of solid areas are roughly proportional to degree of exposed activity.

superplumes (Maruyama, 1994; Maruyama et al., 2001; Dohm et al., 2001d; Baker et al., 2001; Li et al., 2003), referred to hereafter as the Tharsis Superplume. Partly due to relatively low, long-term erosion rates on Mars since its formation (except during transient climatic perturbations; Baker et al., 1991), Tharsis represents the solar system's prime example of a superplume (for additional information on how the Tharsis Superplume fits in the hypothesized geologic evolution of Mars, see Baker et al., this volume).

2 DISTINCTIVE TRAITS OF THE THARSIS SUPERPLUME

The Tharsis Superplume displays the following characteristics:

- Distinct episodes of intensive early magmatic/tectonic activity that declines with time, including development of local and regional centers of tectonic activity of

varying age, size, and duration of formation (Anderson et al., 2001a). Most of these centers are interpreted to be the sites of plume-related activity, including uplift, extensional and contractional tectonism, dike emplacement, volcanism, and hydrothermal activity (e.g., Dohm et al., 2001b), and some that may have triggered: (a) outflow events (Dohm et al., 2001c), (b) ponding resulting from the outflows to form oceans (e.g., Jons, 1985; Parker et al., 1989; Baker et al., 1991; Fairén et al., 2003) and/or lakes (Scott et al., 1995), (c) glaciers and ice sheets, especially in the northern and southern hemispheres (e.g., Kargel and Strom, 1992; Baker, 2001), and (d) short-lived climatological perturbations on the order of tens of thousands of years (Baker et al., 1991),

- Fault and rift systems of varying extent and relative age of formation, including vast canyon systems of Valles Marineris, interpreted to be the site of a lithospheric zone of weakness, vertical uplift related to plume manifestation (e.g., Dohm et al., 1998, 2001b), rotation of the Thaumasia crustal block (e.g., Maruyama et al., 2001; Dohm et al., 2001d; Baker et al., 2001), and/or extremely ancient plate tectonism (Baker et al., 2002; Dohm et al., 2002; Fairén et al., 2002; Fairén and Dohm, 2004),
- A suite of diagnostic landforms, including volcanic constructs of diverse sizes and shapes and extensive lava flow fields (e.g., Scott et al., 1986), large igneous plateaus (Frey and Grant, 1990; Dohm et al., 2001a), canyon systems (Witbeck et al., 1991; Lucchitta et al., 1992), putative ash-flow and air-fall deposits (e.g., Malin, 1979), systems of radial faults and circumferential systems of wrinkle ridges and fold belts (Schultz and Tanaka, 1994) centered about local and regional centers of magmatic-driven activity (Anderson et al., 2001a), and catastrophic outflow channels (e.g., Scott and Tanaka, 1986; Dohm et al., 2001c),
- Early explosive activity transitioning into more concentrated, volcano and fissure-fed eruptions, as documented in the Thaumasia region and elsewhere (Dohm and Tanaka, 1999; Dohm et al., 2001a,b),
- Early basin formation (Dohm et al., 2001b).

3 EVOLUTION OF THE THARSIS SUPERPLUME

This summary provides an interpretive geologic history of the Tharsis Superplume based on topographic, stratigraphic, paleoerosional, and paleotectonic information compiled from the work of numerous investigators. Key information used in this construction includes the spatial and temporal relations among shield volcanoes, igneous plateaus, magmatic-driven centers of tectonic activity, fault and rift systems, and lava flow fields (see Figs. 1 and 2). Stage information is based on Dohm and Tanaka (1999) and Dohm et al. (2001a) and roughly corresponds to the martian stratigraphic scheme (Tanaka, 1986); there is overlap among the stages to account for overlapping stratigraphic positions of published map units and crater count statistical error. Figures 3–7 are 3-D visual appearances that portray each of the five major

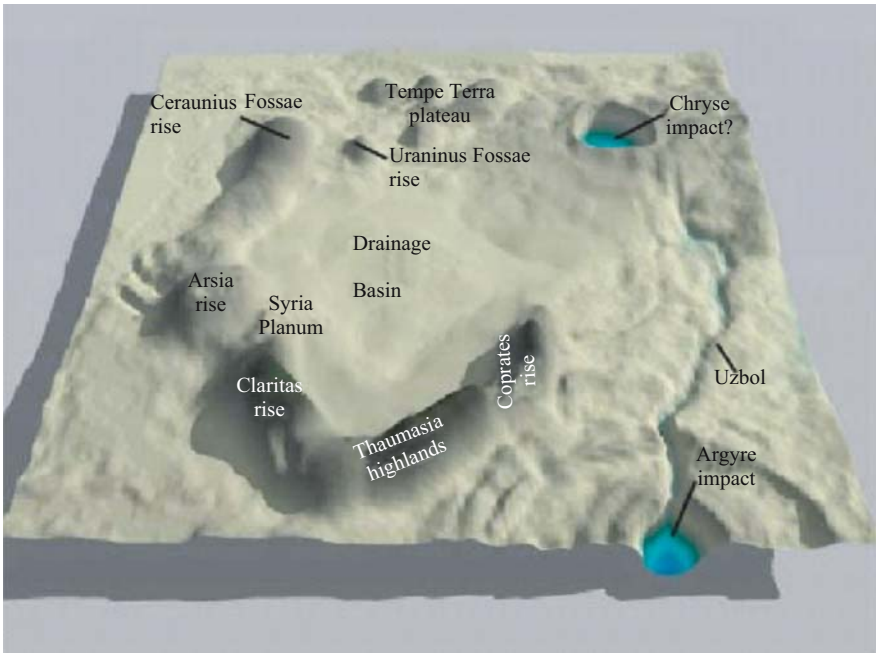

Figure 3. 3-D portrayal of the major geologic features of the Tharsis Superplume during the Early into Middle Noachian Period (part of stage 1), including the drainage basin. Significant highlights include: (1) drainage basin, (2) distinct mountain ranges of Coprates rise, Thaumasia highlands, and multi-ringed structures of the Argyre impact basin (the Charitum and Nereidum Montes), (3) incipient Ceraunis Fossae, Claritas, and Arsia rises, Syria Planum, and Tempe plateau, (4) absence of highland-lowland boundary (further to the north outside of the scene; interpreted to be partly the result of Early into Middle Noachian plate tectonism (Baker et al., 2002; Dohm et al., 2002; Fairén et al., 2002; Fairén and Dohm, 2004), Valles Marineris, circum-Chryse outflow channel systems, and Thaumasia plateau, (5) distinct Argyre and putative Chryse impact basins, and (6) Uzboi Vallis.

stages of activity through time (until present-day MOLA topography) for the Tharsis Superplume. We emphasize that these illustrations are qualitative at this point. They represent a working hypothesis, based on our interpretation of the geologic mapping and analyses and synthesis of published map information, that should be tested with quantitative data as these become more available in formats that can be related to the geology. We also emphasize that the thicknesses and areal extent of features/materials are approximated, because geologic histories for Mars are established through photogeologic mapping and relative-age determination of surfaces and structures. Paleotopographic reconstructions are difficult even on Earth, for which much richer tools are available when analyzing the geologic record, including field mapping and the absolute dating of rocks.

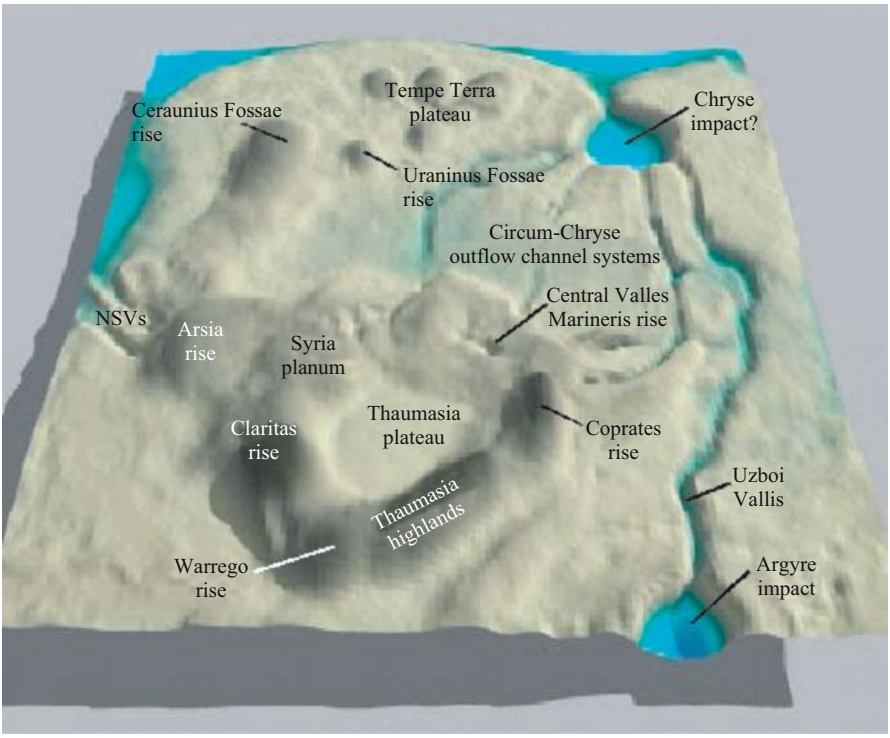

Figure 4. 3-D portrayal of the major geologic features of the Tharsis Superplume during stages 2 and 3 (Late Noachian-Early Hesperian). Significant highlights include: (1) more prominent Warrego and Arsia rises when compared to Figure 3, (2) uplift and incipient trough development at central Valles Marineris, (3) incipient development of Thuamasia igneous plateau and growth of Syria Planum, (4) the highland-lowland boundary and significant modification of the putative Chyrse impact basin, (5) significant modification of the Tharsis basin, (6) more defined NSVs and Uzboi Vallis, and (7) early development of the circum-Chryse outflow channels.

3.1 Early to middle Noachian, part of stage 1 (Figs. 1 and 3)

The greatest percentage of faults preserved in Noachian materials of the western hemisphere originate near the central part of the Claritas rise. This region is marked by an enormous rift system and highly-deformed promontories interpreted to belong to a basement complex. The Claritas rise is a center of activity representing a region of broad magmatic-driven uplift and associated volcanism and tectonism. However, it is difficult to determine whether this Noachian center, which corresponds to a circular magnetic anomaly (e.g., Acuna et al., 1999), marks pre-Tharsis activity (suggesting that Tharsis largely post-dates the dynamo terminus) or incipient Tharsis Superplume activity (suggesting that Tharsis initiated during the Magnetosphere). This is largely due to the strain history recorded in the western equatorial region

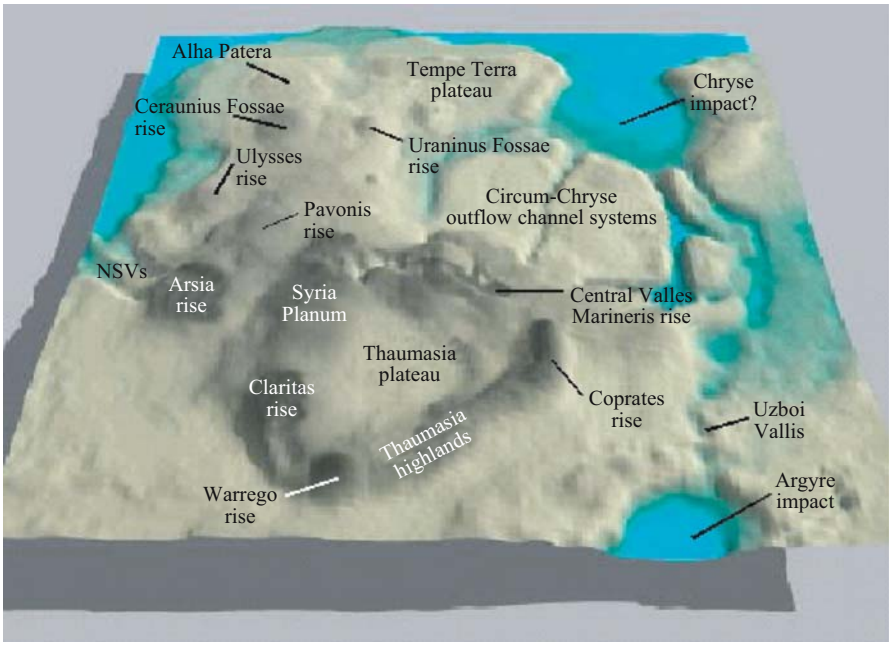

Figure 5. 3-D portrayal of the major geologic features of the Tharsis Superplume during stage 3 (Early Hesperian). When compared to stage 2 (Fig. 4), significant highlights include: (1) continued growth of Tharsis Montes drainage divide, Syria Planum, and Tempe igneous plateau, (2) incipient activity (pre-Tharsis Montes activity) in the Pavonis Mons and Alba and Ulysses Paterae regions, (3) additional development of the circum-Chryse system of outflow channels, the NSVs, and Valles Marineris, and (4) continued southerly retreat of the highland-lowland boundary.

(Scott and Dohm, 1990, 1997; Anderson et al., 2001a), which is complicated by later development of younger prominent centers of activity such as Syria Planum and Alba Patera (Anderson et al., 2004). In addition to the Claritas rise, magmatic-driven tectonic activity is also identified for the Tempe igneous plateau and pre-Tharsis Montes rises: Uranius, Ceraunius, and Arsia SW. Uncertainty exists in the commencement of ancient local and regional centers of magmatic-related activity. Syria Planum and Arsia rise, for example, most likely began as local centers of activity during the Middle Noachian with substantial growth, perhaps episodically, through the Hesperian and possibly into the Amazonian Periods. The Noachian magmatic activity mostly occurs along large fracture/fault zones, many of which may represent large dislocations in the martian crust/lithosphere (Scott and Dohm, 1997). Such dislocations may be the result of the Tharis Superplume development, plate or block boundaries formed during the period of high heat flow (e.g., Schubert et al., 1992; Sleep, 1994), large impacts (e.g., Scott and Tanaka, 1986), and/or extremely ancient plate tectonism (Baker et al., 2002; Dohm et al., 2002; Fairén et al., 2002;

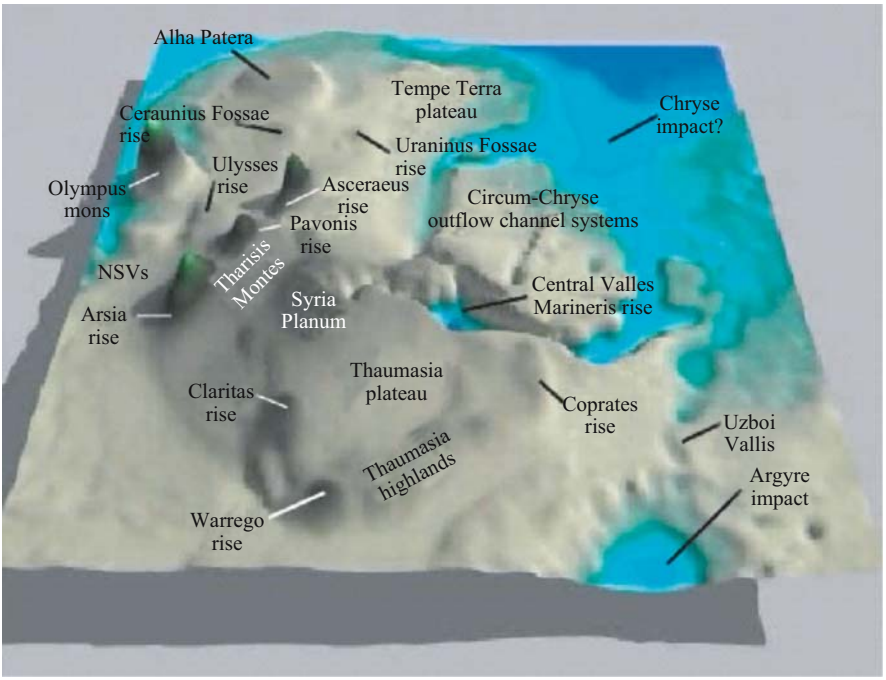

Figure 6. 3-D portrayal of the major geologic features of the Tharsis Superplume during stages 4 and 5 (Late Hesperian-Early Amazonian). When compared to stage 3 (Figure 5), significant highlights include: (1) development of Olympus Mons and the Tharsis Montes shield volcanoes, (2) the emplacement of voluminous sheet lavas centered at the large shield volcanoes and at Syria Planum, (3) significant growth of Alba Patera, (4) significant circum-Chryse outflow channel and Valles Marineris development possibly related to yet another pulse of magmatic activity at Tharsis Montes, Syria Planum, and the central part of Valles Marineris, and (5) continued southerly retreat of the highland-lowland boundary.

Fairén and Dohm, 2004) that represents an earlier phase of Mars geological evolution (Baker et al., this volume). Plate tectonism and Tharsis Superplume activity help explain the prominent landforms (Thaumasia Highlands and Coprates rise mountain ranges) that record complex basement structural fabrics (Dohm et al., 2001a) and distinct magnetic signatures (Acuna et al., 1999; Connerney et al., 2005); the recorded histories of the mountain ranges indicate that they formed prior to the onset of the Tharsis Superplume and were subsequently modified by Superplume-related activity (e.g., vertical uplift, in places, and contractional and extensional tectonism that reactivated existing basement structures and formed fractures, faults, and rift systems).

Broad rises, the distinct rugged Thaumasia Highlands and Coprates rise mountain ranges, and the putative Chyrse impact basin (marked by a highly degraded ridge in the MOLA topography), partly form the margin of the proposed enormous

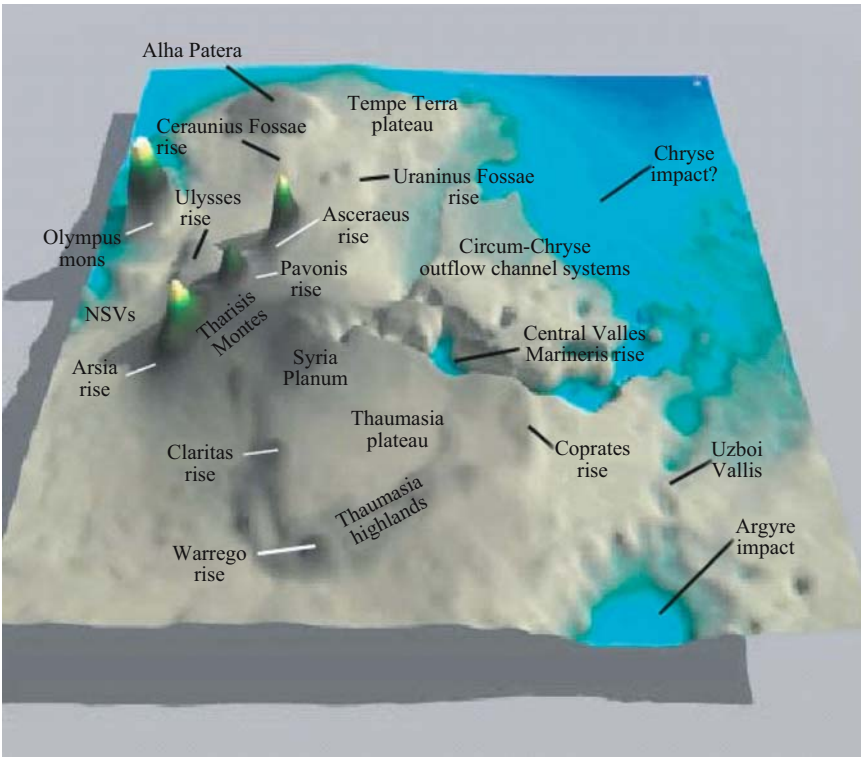

Figure 7. 3-D portrayal of the present-day major geologic features of the Tharsis Superplume using Mars Global Surveyor MOLA data (stage 5—Amazonian).

Noachian drainage basin (Dohm et al., 2001b). The development of the highland-lowland boundary sometime during the Noachian may have resulted in a substantially different paleohydrologic regime in Chryse Planitia region, including an enhanced hydraulic gradient.

3.2 Late Noachian to early Hesperian, stages 2 and 3 (Figs. 1 and 4)

In addition to continued growth of the Arsia rise (pre-Tharsis Montes shied volcanoes), centers of magmatic-driven tectonic activity and possible associated volcanic eruptions and hydrothermal activity are identified near the central part of Valles Marineris, Syria Planum, and the source region of Warrego Valles. Numerous faults, for example, are radial to or concentric about the central part of Valles Marineris, representing a broad center of magmatic-driven uplift along a large crustal/lithospheric dislocation (Dohm et al., 1998; Dohm et al., 2001b; Anderson et al., 2001a). Similar to the central part of Valles Marineris, Syria Planum is also a site of long-lived (Noachian

through at least Late Hesperian) magmatic/tectonic activity, which includes domal uplift and associated radial and concentric faulting, but at a much larger scale and longer duration than is recognized at the central part of Valles Marineris (Dohm et al., 2001b; Anderson et al., 2004).

Magmatic-related activity such as doming underlying Arsia Mons and at Syria Planum and central Valles Marineris may be genetically associated with the early development of the circum-Chryse outflow channel systems (e.g., Dohm et al., 1998; McKenzie and Nimmo, 1999; Dohm et al., 2001b, c; Komatsu et al., 2004), as well as the formation of the northwestern slope valleys (NSVs; Dohm et al., 2001c), located on the opposite side of the Tharsis rise from the circum-Chryse system of outflow channels, several thousands of kilometers to the west. In addition, the source region of Warrego Valles has been interpreted to be a site of intrusive-related doming and tectonic and hydrothermal activity resulting in the formation of well-defined valley networks of Warrego Valles (Gulick, 1993; Dohm and Tanaka, 1999; Dohm et al., 2001a).

The Thaumasia plateau uplift also occurred during this time (Dohm and Tanaka, 1999; Dohm et al., 2001a). The plateau uplift and local/regional centers of magmatic activity largely modified the paleotopography of the Tharsis Superplume region. These activities resulted in the masking of the Tharsis basin, releasing catastrophic floods that led to the early formation of the circum-Chryse system of outflow channels (e.g., Rotto and Tanaka, 1995; Nelson and Greeley, 1999) and the NSVs. This probably drove volatiles (e.g., groundwater) from uplifted regions such as the central part of Valles Marineris and Syria Planum into nearby topographic lows (e.g., Dohm et al., 2000b; Barlow et al., 2001). The time of initial formation of these outflow channel systems is uncertain. For example, lava flows sourcing from stages 2–3 centers of activity (e.g., Syria Planum and Pavonis; Anderson et al., 2001a) may have partly infilled and followed paleovalleys associated with early development of the large outflow channel systems resulting in an inversion of topography (lava ridges/mesas resulting from subsequent erosion of less competent brecciated surrounding materials, as observed on Earth; e.g., Holm, 2001). Later episodes of magmatic-triggered flooding may have formed new valleys or may have followed paleovalleys. Also during this time, extensive, older, ridged plains materials (Dohm and Tanaka, 1999) and intercrater materials were emplaced in topographically low areas. Some intercrater materials may be the result of phreatomagmatic explosions, such as in the Valles Marineris region where magma/water/water-ice interactions have been proposed (e.g., Komatsu et al., 2004).

3.3 Early Hesperian, stage 3 (Figs. 1 and 5)

Continued magmatic/tectonic activity is identified at Arsia-SW rise (continued growth of Tharsis rise drainage divide), Syria Planum, and Tempe igneous plateau. Incipient activity (pre-Tharsis Montes activity) is also recognized in the Pavonis Mons (Plescia and Saunders, 1982; Anderson et al., 2001a) and Alba and Ulysses Paterae regions.

Also during the Early Hesperian Period, additional development is recorded for the circum-Chryse system of outflow channels and at the NSVs, possibly related to another pulse of magmatic activity at Arsia-SW dome, Syria Planum, and the central part of Valles Marineris. Extensive, younger, ridged plains materials were emplaced in topographic lows.

3.4 Late Hesperian to early Amazonian, stages 4 and 5 (Figs. 1 and 6)

Significant effusive volcanic activity is recorded during the Late Hesperian and Early Amazonian, including the development of Olympus Mons and the Tharsis Montes shield volcanoes. Also emplaced were voluminous sheet lavas centered at the large shield volcanoes and at Syria Planum. Lava flows centered at Arsia Mons, for example, may extend to the northwest as far as the NSVs embaying the gigantic northwest-trending promontories and partly infilling the system of valleys (Zimbelman et al., 2000).

A significant transition from magmatic-tectonic activity to volcanic activity is observed at the major centers of activity, notably at Syria Planum (Dohm and Tanaka, 1999; Dohm et al., 2001a). The final appearance of large-scale tectonism for the western hemisphere is associated with the dominant center of tectonic activity, Alba Patera (Anderson et al., 2001a, 2004). Significant outflow channel formation also occurred in the circum-Chryse system of outflow channels during the Late Hesperian and into the Early Amazonian. This may be related to yet another pulse of magmatic activity at Tharsis Montes, Syria Planum, and the central part of Valles Marineris, which is consistent with the driving mechanism in the MEGAOUTFLO hypothesis (Baker et al., 1991, 2000).

3.5 Amazonian, stage 5 (Figs. 1 and 7)

Evidence for continued growth of Olympus Mons and the Tharsis Montes shield volcanoes is identified during this geologic period. Isolated occurrences of magmatic/tectonic activity appear to be associated with continued construction of the Tharsis Montes shield volcanoes and Olympus Mons (Anderson et al., 2001a). Other than minor graben formation associated with the final stages of Alba Patera, these local volcanic sources may represent late-stage pulses of magmatic-tectonic activity in the Tharsis region. The Tharsis Superplume appears to not have reached its cooling threshold, and elevated heat flow and continued activity may continue well into the future (Dohm et al., 2001b; Anderson et al., 2001b).

ACKNOWLEDGEMENTS

The illustrations were prepared with significant help from Trent M. Hare of the U.S. Geological Survey, Flagstaff. V.R.B. and J.M.D. received partial support from NASA grant NAG-5-9790.

REFERENCES

Acuna, M.H. et al. (1999) Global distribution of crustal magnetization discovered by the Mars Global Surveyor MAG/ER experiment. *Science*, 284, 790–793.

Anderson, R.C., J.M. Dohm, M.P. Golombek, A.F.C. Haldemann, B.J. Franklin, K.L. Tanaka, J. Lias, and B. Peer (2001a) Primary centers and secondary concentrations of tectonic activity through time for the western hemisphere of Mars. *J. Geophys. Res.*, 106, 20563–20585.

Anderson, R.C., J.M. Dohm, M.P. Golombek, V.R. Baker, J.C. Ferris, and T.M. Hare (2001b) Amazonian faulting: Is Mars tectonically active today? *Lunar Planet. Sci. Conf.* [CD-ROM], XXXII, Abstract 2130.

Anderson, R.C., J.M. Dohm, A.F.C. Haldemann, T.M. Hare, and V.R. Baker (2004) Tectonic histories between Alba Patera and Syria Planum, Mars, Mars. *Icarus*, 171, 31–38.

Baker, V.R. (2001) Water and the Martian landscape. *Nature*, 412, 228–236.

Baker, V.R., S. Maruyama, and J.M. Dohm (2001) Tharsis superplume (3): Implications on the role of water, environmental change and life. *Geol. Soc. America Abstracts with Programs*, 33(7), A432.

Baker, V.R., S. Maruyama, and J.M. Dohm (2002) A theory of plate tectonics and subsequent long-term superplume activity on Mars. In International Workshop: Role of Superplumes in the Earth System, Tokyo Inst. of Technology, Tokyo, Japan, pp. 312–316. (Published in the journal *Electronic Geosciences*, 8, on the web at http://194.94.42.12/licensed_materials/10069/free/conferen/superplu/index.html)

Baker, V.R., R.G. Strom, J.M. Dohm, V.C. Gulick, J.S. Kargel, G. Komatsu, G.G. Ori, and J.W. Rice Jr. (2000) Mars' Oceanus Borealis, ancient glaciers, and the MEGAOUTFLO hypothesis. *Lunar Planet. Sci. Conf.* [CD-ROM], XXXI, Abstract 1863.

Baker, V.R., R.G. Strom, V.C. Gulick, J.S. Kargel, G. Komatsu, and V.S. Kale (1991) Ancient oceans, ice sheets and the hydrological cycle on Mars. *Nature*, 352, 589–594.

Barlow N.G., J. Koroshetz, and J.M. Dohm (2001) Variations in the onset diameter for Martian layered ejecta morphologies and their implications for subsurface volatile reservoirs. *Geophys. Res. Lett.*, 28, 3095–3099.

Connerney, J.E.P., M.H. Acuña, N.F. Ness, G. Kletetschka, D.L. Mitchell, R.P. Lin, and H. Reme (2005) Tectonic implications of Mars crustal magnetism. *Science*, 102, 14970–14975.

Dohm, J.M., R.C. Anderson, and K.L. Tanaka (1998) Digital structural mapping of Mars. *Astron. & Geophys.*, 39, 3.20–3.22.

Dohm, J.M., R.C. Anderson, V.R. Baker, R.G. Strom, G. Komatsu, and T.M. Hare (2000) Pulses of magmatic activity through time: Potential triggers for climatic variations on Mars. *Lunar Planet. Sci. Conf.* [CD-ROM], XXXI, Abstract 1632.

Dohm, J.M., and K.L. Tanaka (1999) Geology of the Thaumasia region, Mars: Plateau development, valley origins, and magmatic evolution. *Planet. Space Sci.*, 47, 411–431.

Dohm, J.M., K.L. Tanaka, and T.M. Hare (2001a) Geologic map of the Thaumasia region of Mars. *US Geol. Survey Map* I-2650 (1: 5,000,000).

Dohm, J.M. et al. (2001b) Ancient drainage basin of the Tharsis region, Mars: Potential source for outflow channel systems and putative oceans or paleolakes. *J. Geophys. Res.*, 106, 32943–32958.

Dohm, J.M. et al. (2001c) Latent activity for western Tharsis, Mars: Significant flood record exposed. *J. Geophys. Res.*, 102, 12301–12314.

Dohm, J.M., S. Maruyama, V.R. Baker, R.C. Anderson, and J.C. Ferris (2001d) Earth-like evolution of the Tharsis Magmatic Complex: Traits of a Terrestrial Superplume (2), *Geol. Soc. America Abstracts with Programs*, 33(7), A309.

Dohm, J.M., N.G. Barlow, J.P. Williams, V.R. Baker, R.C. Anderson, W.V. Boynton, A.G. Fairén, and T.M. Hare (2004) Ancient giant basin/aquifer system in the Arabia region, Mars. *Lunar Planet. Sci. Conf.* [CD-ROM], XXXV, Abstract 1209.

Fairén, A.G., and J.M. Dohm (2004) Age and origin of the lowlands of Mars. *Icarus*, 169, 277–284.

Fairén, A.G., J. Ruiz, and F. Angula (2002) An origin for the linear magnetic anomalies on Mars through accretion of terranes: Implications for dynamo timing. *Icarus*, 160, 220–223.

Fairén, A.G., J.M. Dohm, V.R. Baker, M.A. de Pablo, J. Ruiz, J.C. Ferris, and R.C. Anderson (2003) Episodic flood inundations of the northern plains of Mars. *Icarus*, 165, 53–67.

Frey, H., and T.D. Grant (1990) Resurfacing history of Tempe Terra and surroundings. *J. Geophys. Res.*, 95, 14249–14263.

Gulick, V.C. (1993) Magmatic intrusions and hydrothermal systems: Implications for the → formation of small Martian valleys. Ph.D. Thesis, Univ. of Arizona, Tucson, Arizona.

Hartmann, W.K. (1978) Martian cratering V: Toward an empirical Martian chronology, and its implications. *Geophys. Res. Lett.*, 5, 450–452.

Hartmann, W.K., and G. Neukum (2001) Cratering chronology and the evolution of Mars. *Space Sci. Rev.*, 96, 165–194.

Holm, R.F. (2001) Cenozoic paleogeography of the central Mogollon Rim–southern Colorado Plateau region, Arizona, revealed by Tertiary gravel deposits, Oligocene to Pleistocene lava flows, and incised streams. *GSA Bulletin*, 113, 1467–1485.

Jons, H.P. (1985) Late sedimentation and late sediments in the northern lowlands of Mars. *Lunar Planet. Sci.* 16, 414–415.

Kargel, J.S., and R.G. Strom (1992) Ancient glaciation on Mars. *Geology*, 20, 3–7.

Komatsu, G., J.M. Dohm, and T.M. Hare (2004) Hydrogeologic processes of large-scale tectonomagmatic complexes in Mongolia-southern Siberia and on Mars. *Geology*, 32, 325–328.

Li, Z.X., X.H. Li, P.D. Kinny, J. Wang, S. Zhang, and H. Zhou (2003) Geochronology of Neoproterozoic syn-rift magmatism in the Yangtze Craton, South China and correlations with other continents: Evidence for a mantle superplume that broke up Rodinia. Precambrian Res., 122, 85–109.

Lucchitta, B.K., A.S. McEwen, G.D. Clow, P.E. Geissler, R.B. Singer, R.A. Schultz, and S.W. Squyres (1992) The canyon system on Mars. In *Mars*, Univ. of Ariz. Press, Tucson, pp. 453–492.

Malin, M.C. (1979) Mars: Evidence of indurated deposits of fine materials, *NASA Conf., Pub.*, 2072, 54.

Maruyama, S. (1994) Plume tectonics. *J. Geol. Soc. Jpn.*, 100, 24–49.

Maruyama, S., J.M. Dohm, and V.R. Baker (2001) Tharsis superplume (1): Why superplume? *Geol. Soc. Am. Abstracts with Programs*, 33(7), A310.

McKenzie, D., and F. Nimmo (1999) The generation of Martian floods by the melting of ground ice above dykes. *Nature*, 397, 231–233.

Mege, D., and P. Masson (1996) A plume tectonics model for the Tharsis province, Mars. *Planet. Space Sci.* 44, 1499–1546.

Nelson, D. M., and R. Greeley (1999) Geology of Xanthe Terra outflow channels and the Mars Pathfinder landing site. *J. Geophys. Res.*, 104, 8653–8669.

Neukum, G., and K. Hiller (1981) Martian ages. *J. Geophys. Res.*, 86, 1381–1387.

Parker, T.J., R.S. Saunders, and D.M. Schneeberger (1989) Transitional morphology in the west Deuteronilus Mensae region of Mars: Implications for the modification of the lowland/upland boundary. *Icarus*, 82, 111–145.

Plescia, J.B., and R.S. Saunders (1982) Tectonic history of the Tharsis region, Mars. *J. Geophys. Res.*, 87, 9775–9791.

Rotto, S.L., and K.L. Tanaka (1995) Geologic/geomorphologic map of the Chryse Planitia region of Mars. *US Geol. Survey Map* I-2441 (1:5,000,000).

Schubert, G., S.C. Solomon, D.L. Turcotte, M.J. Drake, N.H. Sleep (1992) Origin and thermal evolution of Mars. In Kieffer, H.H., B.M. Jakosky, C.W. Snyder, and M.S. Matthews (eds.) Mars, Univ. of Arizona Press, Tucson, pp. 147–183.

Schultz, R.A., and K.L. Tanaka (1994) Lithospheric-scale buckling and thrust structures on Mars: The Coprates rise and south Tharsis ridge belt. *J. Geophys. Res*., 99, 8371–8385.

Scott, D.H., and J.M. Dohm (1990) Faults and ridges: Historical development in Tempe Terra and Ulysses Patera regions of Mars. In *Proc. of the 20th Lunar Planet. Sci. Conf.*, pp. 503–513.

Scott, D.H., and J.M. Dohm (1997) Mars: Structural geology and tectonics. In Shirley, J.H., and R.W. Fairbridge (eds.) Encyclopedia of Planetary Sciences, Van Nostrand Reinhold, New York, p. 990.

Scott, D.H., and K.L. Tanaka (1986) Geologic map of the western equatorial region of Mars, *US Geol. Survey Map* I-1802-A (1:15,000,000).

Scott, D.H., J.M. Dohm, and J.W. Rice (1995) Map of Mars showing channels and possible paleolake basins. *US Geol. Survey Map* I-2461 (1:30,000,000).

Sleep, N.H. (1994) Martian plate tectonics. *J. Geophys. Res.*, 99, 5639–5655.

Tanaka, K.L. (1986) The stratigraphy of Mars. *Proc. of the 17th Lunar Planet. Sci. Conf.*, in *J. Geophys. Res. pt. 1*, 91, E139–E158.

Witbeck, N.E., K.L. Tanaka, and D.H. Scott (1991) Geologic map of the Valles Marineris region, Mars (east half and west half). *US Geol. Survey Map* I-2010 (1:2,000,000).

Zimbelman, J.R., S.E.H. Sakimoto, and H. Frey (2000) Evidence for a fluvial contribution to the complex story of the Medusae Fossae Formation on Mars. *Geol. Soc. Am. An. Meeting*, Abstract 50423.

CHAPTER 18

PLUMES AND PLUME CLUSTERS ON EARTH AND VENUS: EVIDENCE FROM LARGE IGNEOUS PROVINCES (LIPS)

RICHARD E. ERNST[1], K.L. BUCHAN, AND D.W. DESNOYERS

Geological Survey of Canada, 601 Booth Street, Ottawa, Ontario K1A 0E8
[1]*Now at Ernst Geosciences, 43 Margrave Avenue, Ottawa, Canada K1T 3Y2; and Department of Earth Sciences, Carleton University, Ottawa, Canada K1S 5B6;*
E-mail: richard.ernst@ernstgeosciences.com

Abstract

The record of Large Igneous Provinces (LIPs) is used to characterize and evaluate plume concepts as applied to Earth and Venus. Conclusions regarding the terrestrial record are that: (1) plumes of deep mantle origin are frequent, occurring on average once every 10–20 Myr since the end of the Archean, and (2) plumes occur both singly and in clusters, the latter sometimes called superplumes or superplume events. The most convincing plume clusters are found in the young record, where LIPs are spatially associated with two regional geoid highs, in the Pacific and Africa. The identification of older plume clusters is complicated by uncertain plate reconstructions, the difficulty of recognizing ancient regional geoid highs and lower mantle seismic anomalies. The best candidates for pre-Mesozoic plume clusters are spatial clusters of LIPs in which activity is synchronous, or in which activity is linked to supercontinent breakup. Similarly on Venus, there are several categories of LIPs which can be linked to mantle plumes. The most prominent are the large volcanoes (100–1000 km in diameter); over 168 are recognized. These volcanoes are thought to be the product of individual mantle plumes, particularly those which are associated with geoid and topographic highs and triple junction rifting. Giant radiating graben systems (the surface expression of giant radiating dyke swarms) are potentially even more common than large volcanoes and may augment the record of plumes; several hundred are recognized. In addition, more than 500 circular volcano-tectonic features termed coronae occur as isolated features, in local clusters with other coronae and volcanoes, or concentrated along rift zones. At least ten clusters of volcanoes and coronae, most associated with topographic swells, are identified.

D. A. Yuen et al. (eds.), Superplumes, 537–562.
© 2007 *Springer.*

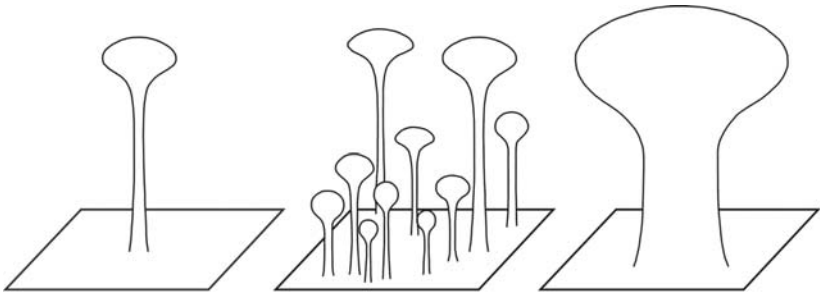

Figure 1. Plumes, plume clusters and superplumes events (modified after Schubert et al., 2004). The heads of hypothetical superplumes would have a scale of several 1000 to 10,000 km, while the heads of the individual plumes would range from 100 to 2000 km.

1 INTRODUCTION

Mantle plumes are important in the magmatic and tectonic history for both Earth and Venus, where they can be linked with broad regional domal uplift and triple junction rifting (e.g., for Earth: Burke and Dewey, 1973; White and McKenzie, 1989; Campbell et al., 1989; Cox, 1989; Griffiths and Campbell, 1991; Hill, 1991; Maruyama, 1994; Campbell, 1998, 2001; Condie, 2001; Şengör, 2001; Şengör and Natal'in 2001; Ernst and Buchan, 2001, 2003; Courtillot et al., 2003; and for Venus: Head et al., 1992; Hansen et al., 1997; Nimmo and McKenzie, 1998; Ernst and Desnoyers, 2004). However, their expression differs and is complementary on the two planets given the absence of plate tectonics and surface erosion on Venus. In this review, we use the LIP record of Earth and Venus in order to develop insights into the nature of plumes, plume clusters, and superplumes (Fig. 1). One important conclusion is that proposed examples of the latter, superplumes, are probably better characterized as plume clusters.

2 LARGE IGNEOUS PROVINCES (LIPS) ON EARTH

Earth history is punctuated by numerous periods during which large volumes of mafic magma were emplaced (Fig. 2). Such magmas are termed as LIPs if they are not generated by a "normal" spreading ridge or by subduction. Strictly speaking LIPs consist of continental flood basalts, volcanic rifted margins, oceanic plateaus, ocean basin flood basalts, submarine ridges, and seamount chains (Coffin and Eldholm, 1994, 2001) and their feeder systems (Ernst and Buchan, 1997, 2001). However, in typical usage, the term LIPs is usually restricted to the first four types; these are characteristically of short duration (<10 Myr) and are sometimes termed "transient" LIPs to distinguish them from longer duration submarine ridges and seamount chains (Coffin and Eldholm, 2001). In this paper we focus on the "transient" LIPs, for which we will simply use the term "LIPs".

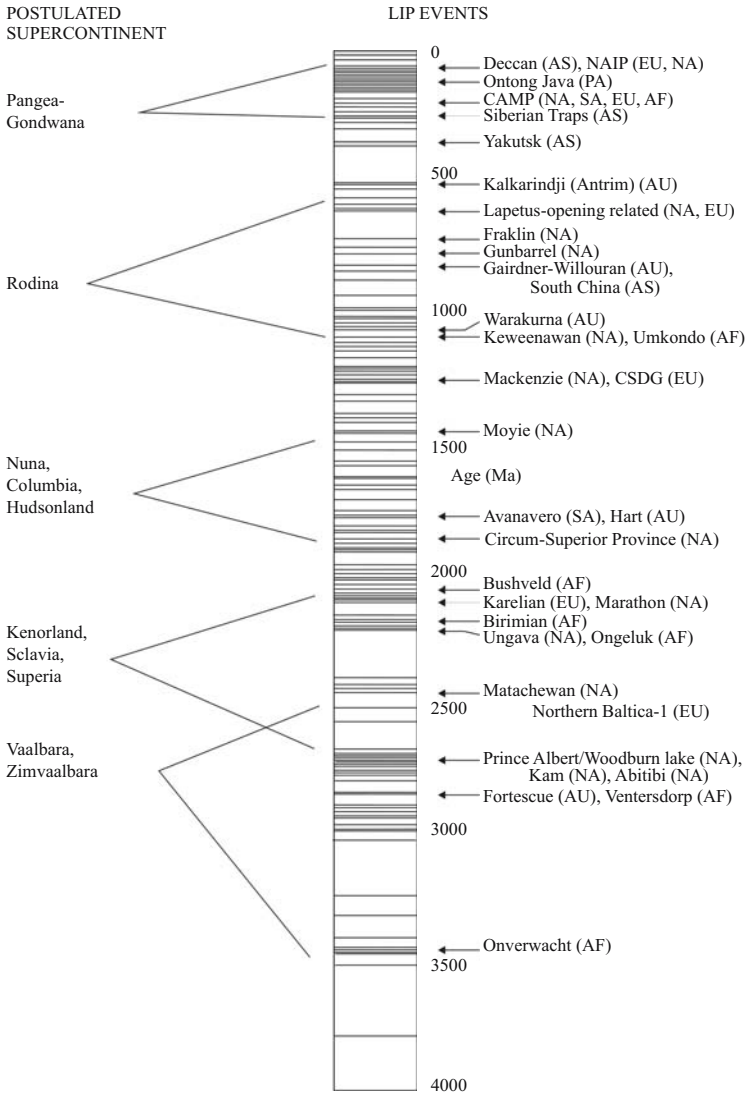

Figure 2. Age spectrum (bar code) of large igneous provinces through time. After Figs. 2b and 3b, respectively in Ernst and Buchan (2001, 2002). Includes events rated as "well-established and probable plume head mafic magmatic events" according to criteria in Ernst and Buchan (2001). Selected events are labeled at the starting age of the main pulse. Locations for events are indicated as follows: NA is North America, SA is South America, EU is Europe, AF is Africa, AS is Asia, AU is Australia, and PA is Pacific Ocean. Event names are mostly after Ernst and Buchan (2001). Exceptions include the 615–550 Ma Iapetus-related (Puffer (2002), the 1076 Ma Warakurna (Wingate et al., 2004), and 1880–1860 Ma Circum-Superior Province (see http://www.largeigneousprovinces.org/May.html) events. Names and approximate durations of proposed supercontinents are given on the left hand side of the diagram, and are after Pesonen et al. (2003) and Bleeker (2004).

The size criterion for LIPs is debated. We use the original criterion of an areal extent of at least 100,000 km^2 (Coffin and Eldholm, 1994, 2001; Ernst and Buchan, 2001; Ernst et al., 2005). Note, however that others, such as Courtillot and Renne (2003), prefer a more restrictive criterion of an areal extent of 1 Mkm^2, with a volume of 1 Mkm^3. It should be noted that the size of most LIPs is 'growing' as a vast 'reservoir' of previously uncharacterized igneous units are gradually dated and correlated with known LIPs or define new LIPs (e.g., Ernst and Buchan, 2005).

The expression of LIPs varies through Earth history (Ernst et al., 2005). LIPs of Mesozoic and Cenozoic age are typically the best preserved and consist mainly of flood basalts. Those of Paleozoic and Proterozoic age are often more deeply eroded, and comprise flood basalt remnants and an underlying plumbing system of giant dyke swarms, sill provinces and layered intrusions. In the Archean, the most promising LIP candidates are greenstone belts of the tholeiite–komatiite association. Many LIPs have been linked to regional-scale uplift, continental rifting and breakup, and climatic crises. They can be used as precisely dated time markers in the stratigraphic record, and represent a key target for Ni-Cu-PGE and Fe-Ti-V exploration.

LIPs are the key tool for recognizing the presence of mantle plumes in the geological record. Many are linked to partial melting of the plume head, and seamount chains have been interpreted as hotspots linked to the protracted activity generated by a plume tail (e.g., Morgan 1981; Duncan and Richards, 1991). Alternative models for LIP origin may be applicable in some cases (Foulger et al., 2005): decompression melting associated with the onset of rifting above hot mantle (White and McKenzie, 1989), convection between thick and adjacent thin lithosphere (edge-convection) bringing hot mantle to shallower levels where it melts by decompression (e.g., Anderson, 1995, 1998; King and Anderson, 1998; Foulger and Natland, 2003); delamination (Elkins-Tanton and Hager, 2000), hot sheet/ hot lines in the mantle (e.g., Al-Kindi et al., 2003), melting in a back-arc extensional environment (e.g., Rivers and Corrigan, 2000), overriding of a spreading ridge (e.g., Gower and Krogh, 2002), and meteorite impact (e.g., Jones et al., 2002; Ingle and Coffin, 2004; Reese et al., 2004). Some hybrid models are plausible. For instance, some LIPs are associated with two magmatic pulses separated by several million years or more (Campbell, 1998; Courtillot and Renne, 2003; Ernst et al., 2005). The first may be linked to a plume head arrival and the second to onset of rifting above mantle with elevated temperatures (i.e., rift-melting model of White and McKenzie, 1989).

There are important caveats related to using the LIP record for interpreting the nature and distribution of plumes and plume clusters:

(1) LIPs occur with an average frequency (since the Archean) of at least one every 20 Myr, and perhaps as often as one every 10 Myr (Ernst and Buchan, 2001, 2002). However, the average spacing between events may approach 30 Myr given that many LIPs are synchronous (e.g., Dobretsov, 2005). The once-per-10-Myr rate applies if the current rate of occurrence of oceanic plateaus in the < 200 Ma record (Coffin and Eldholm, 2001) can be extrapolated to the older record. Because of the high frequency of events, assessing a genetic link between synchronous events is problematic. Furthermore, even if coeval events are regionally grouped, can

we assume that they belong to the same deep-seated event? Given a modeled minimum nucleation spacing of 265 km for plumes originating from D″ in the deep mantle (Schubert et al., 2004), we calculate a spacing at the Earth's surface of 485 km. Therefore, LIPs can be quite closely spaced and yet represent independent upwellings.

(2) Continental reconstructions prior to 400 Ma are poorly known (e.g., Buchan et al., 2001). Therefore, assessing proximity of events in the older record is commonly difficult. There are at least 35 times since the Archean during which intraplate mafic magmatic events of the same age occur on more than one block (Ernst and Buchan, 2002). However, until Precambrian (and early Proterozoic) reconstructions are better determined it will remain unknown which represent single fragmented LIPs derived from single plumes, and which represent LIP clusters derived from plume clusters.

(3) Even the size of events on individual continental blocks is often uncertain (see varying estimates for some events in Fig. 3). Many mafic and ultramafic magmatic units remain undated, and ongoing dating programs can reveal dramatic new extensions of known LIPs and identification of new LIPs. For example,

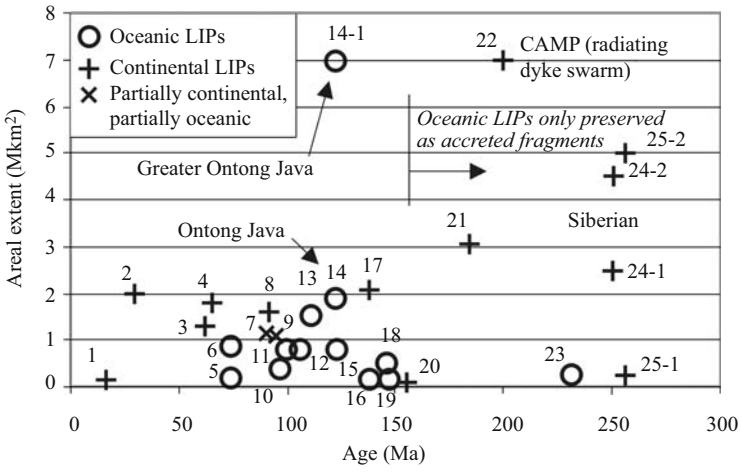

Figure 3. Comparison of age vs. estimated original size of LIPs since 258 Myr. (1) Columbia River, (2) Afar ("Ethiopian and Yemen Traps"), (3) North Atlantic Igneous Province ("Brito-Arctic Province"), (4) Deccan, (5) Maud Rise, (6) Sierra Leone Rise, (7) CCCIP (Colombia-Caribbean), (8) Madagascar, (9) HALIP (High Arctic Large Igneous Province; includes Alpha Ridge), (10) Wallaby Plateau, (11) Hess Rise, (12) Hikurangi Plateau, (13) Kerguelen, (14) Ontong Java, (14-1) Greater Ontong Java, (15) Manihiki Plateau, (16) Gascoyne Margin, (17) Paraná-Etendeka, (18) Magellan Rise, (19) Shatsky Rise, (20) Argo Basin, (21) Karoo-Ferrar, (22) CAMP (Central Atlantic Magmatic Province, (23) Wrangellia, (24-1, 24-2) Siberian, and (25) Emeishan. Sizes for most events after Ernst and Buchan (2001) and Coffin and Eldholm (2001). Exceptions include: event 9 measured from Figure 1 in Maher (2001), event 14-1 measured from Figure in Ingle and Coffin (2004), event 23 measured from map in Buchan and Ernst (2004), event 24-1 after Courtillot and Renne (2003), event 24-2 after Saunders et al. (2005), and event 25-2, a maximum estimate, see Courtillot and Renne (2003). Age for Hikurangi Plateau (event 12) is approximate.

recent Ar-Ar dating of basalts underlying the West Siberian basin (Reichow et al., 2002, 2005) has dramatically increased the known size of the Siberian LIP event. Previously, Courtillot and Renne (2003) estimated the original areal extent at >4 Mkm^2 and volume at >3 Mkm^3. Taking account of the volcanic and intrusive components within the West Siberian basin, the Altai Sayan fold belt and other regions as well, Dobretsov et al. (2005) suggested that the volume of magma associated with the Siberian and similar-aged Emeishan LIPs may have exceeded 16 Mkm^3.

To address points 2 and 3 above, the LIPs Commission (www.largeigneousprovinces.org) has proposed a multi-year research agenda to improve the pre-Mesozoic LIP database through a concerted program of high-precision (U-Pb and Ar-Ar) geochronology integrated with paleomagnetism and geochemistry (Ernst et al., 2005). A similar program has been proposed for Canada (Bleeker, 2004). Such studies, carried out on a large number of mafic units (dyke swarms, sills, layered intrusions and volcanics), and related felsic units, would allow a much better understanding of the age, duration and extent of LIP events and, in particular, the correlation of events between continental blocks through improved reconstructions. The value of such integrated programs of high-precision dating, paleomagnetism and geochemistry has been demonstrated through work at the Geological Survey of Canada (Buchan et al., 1996, 2000, 2001), and at the Tectonics Special Research Centre based at the University of Western Australia (www.tsrc.uwa.edu.au) in its mission of "discovering the supercontinents of which Australia has been part in the past 3000 million years".

3 PLUMES ON EARTH

The LIP record confirms the importance of both individual plumes, and plume clusters. However, the existence of extra-large single plumes (superplumes) is not supported by the LIP record. This point is discussed first with reference to the "greatest" LIP on earth, the Ontong Java event.

3.1 Largest LIP event on Earth: Ontong Java

In terms of volume (but not in terms of areal extent), the largest known LIP is "the greater Ontong Java" event (122 Ma) (Fig. 3). A volume of 58 Mkm^3 is inferred for this event, which consists of Ontong Java (44 Mkm^3, Coffin and Eldholm, 2001) and adjacent flood basin LIPs including the Nauru, East Mariana, and Pigafetta basins that are thought to be fed by Ontong Java (Ingle and Coffin, 2004). An even larger size of about 70 Mkm^3 applies if Ontong Java, Manihiki Plateau, and Hikurangi Plateau were originally a single plateau that broke up (Taylor, 2006). However, the analysis of Courtillot and Renne (2003) revealed that most of the volume of Ontong Java resides in its intrusive component, whereas the volcanic portion of Ontong Java is only 6 Mkm^3, marginally larger than the maximum values quoted for continental LIPs.

Table 1. Regional plume clusters and their separation distances

Age	LIP events and their separation distances
90 Ma	Caribbean and Gorgona = 4300 km
122 Ma	Ontong Java and Manihiki = 3000 km (see note)
138–130 Ma	Parana-Etendeka and Equatorial Circum-Atlantic = 2500 km
183 Ma	Karoo-Ferrar
	Lower Limpopo and Lower Zambesi = 800 km
	Lower Limpopo and Dufek = 1900 km
	Lower Limpopo and Weddell sea = 1100 km
	Lower Zambesi and Weddell sea = 1600 km
	Lower Zambesi and Dufek = 2200 km
	Weddell sea and Dufek = 900 km
1280–1265 Ma	Mackenzie and Nain/Harp-CSDC
	Mackenzie and Nain/Harp = 3100 km
	Nain/Harp and CSDC = 2000 km
	Mackenzie and CSDC = 5000 km

Note: Recent publication (Taylor, 2006) suggests that Ontong Java, Manihiki Plateau and Hikurangi Plateau were originally emplaced as a single LIP that subsequently broke up. The 90 Ma events are described in Kerr and Tarney (2005), and the distance between plumes at initiation was measured from Figure 3 in Kerr and Tarney (2005); the other examples are from Table 2 in Ernst and Buchan (2002). We only includes events that are $\leq$ 5000 km apart. The distance between plumes is taken as the distance between their centres. In some cases the plume centre is known based on a radiating dyke swarm. In other cases, the plume centre is assumed to lie at the centre of the LIP, e.g., for oceanic plateaus, and for the CDSC (Central Scandinavian Dolerite Complex) in Baltica. Nain/Harp plume centre is assumed to be in the Gardar Province of Greenland.

Furthermore, it follows from their analysis that the intrusive component of continental LIPs is much larger than typically recognized, perhaps approaching the Ontong Java scale. The intrusive component of continental LIPs consists of the plumbing system of dykes, sills, and layered intrusion and also underplated crust produced during the event. Its size is difficult to quantify.

3.2 Plume clusters on Earth

The archetype "superplumes" are those linked with the low velocity regions of the lower mantle and two geoid highs on the Earth: in the Pacific and Africa (e.g., Crough and Jurdy, 1980; Duncan and Richards, 1991; McNutt, 1998; Davies, 1999). They are associated with present-day clusters of hotspots, which in detail are linked with deep mantle lateral shear-wave velocity gradients (Thorne et al., 2004). These "superplumes" are also linked with the backtracked positions of LIPs interpreted to mark plume head events (Burke and Torsvik, 2004). The correlation between LIPs and geoid highs indicates that the low-velocity regions in the deep mantle have been relatively stationary with respect to the Earth's spin-axis and the core since the early Jurassic. A more recent seismic and dynamic analysis indicates that each of the two regional upwellings must be marked by a cluster of plumes rather than a single

Table 2. Plume clusters (with a range of ages) associated with breakup

Age	LIP name	Breakup/ rifting event	No. of plumes involved	Key reference
130–90 Ma	HALIP (High Arctic LIP)	Opening of Amerasian Basin	2 plumes	Maher et al. (2001); Buchan & Ernst (2006)
200–65 Ma	Karoo-Ferrar (183 Ma), Parana-Etendeka (133 Ma), Madagascar (90 Ma), Deccan (65 Ma),	Gondwana breakup	>4 plumes	Storey (1995)
825–720 Ma	South China (825 Ma), Gunbarrallel (780 Ma); Mundine Well (755 Ma), Franklin (720 Ma)	Rodinia breakup	>4 plumes	Li et al. (2003); Li et al. (2006)
615–555 Ma	Central Iapetus includes: Long Range (615 Ma), Grenville-Rideau (590 Ma), Sept Ilse and Catoctin (560 Ma)	Iapetus Margin of Laurentia	≥2 plumes	Puffer (2002); Ernst and Buchan (1997)
2510–2445 Ma	Matachewan, Mistassini	SW margin of Superior Province, Canada and northern margin of Baltica	≥2 plumes	e.g., Ernst and Buchan (2002)

broad upwelling (plume) 10,000 km across as is conventionally interpreted (Fig. 1; Schubert et al., 2004). Therefore, these may be better termed "plume clusters" than "superplumes".

How do we recognize plume clusters in the older record, particularly in the absence of corroborating evidence for a linked origin in the form of a regional (10,000 km scale) geoid high, topographic high, or deep mantle seismic anomaly? It is particularly difficult to recognize spatial groupings of related LIPs given the dense spectrum of events (e.g., averaging at least 1 per 20–30 Myr), and given the uncertainty of pre-400 Ma plate reconstructions (as discussed earlier). However, two categories of LIPs in the pre-Mesozoic record are plausible plume clusters (Ernst and Buchan, 2002): regional clusters of identically-aged LIPs (Table 1), and LIPs that have a range of ages, but which are spatially linked to supercontinent breakup (Table 2).

A key question in the latter case is whether this apparent association of clusters of LIPs (and plumes) with major (e.g., supercontinent) breakup events is real. It is alternatively possible that plumes arriving randomly beneath continents experiencing extensional plate stresses will produce more dramatic LIPs and more frequently lead to breakup, whereas those arriving into orogenic settings will have less dramatic expression. For instance the ca. 1100 Ma Keweenawan plume produced magmatism concentrated in the mid-continent rift of North America, but did not lead to ocean

opening because of coeval convergence during the nearby Grenville orogeny (e.g., Manson and Halls, 1997; Hanson et al., 2004).

In Figure 2, the ages of LIPs are compared with the ages of postulated supercontinents. Although the timing of assembly and breakup of most of the supercontinents is speculative, Figure 2 indicates no obvious correlation between the frequency of LIPs and supercontinent breakup.

4 PLUMES AND PLUME CLUSTERS ON VENUS

4.1 Importance of plumes on Venus

Given the limitations of the terrestrial record for identifying and characterizing plume and plume cluster events, we explore whether Venus can provide some insights. Mantle plumes are important in the magmatic and tectonic history of Venus (e.g., Head et al., 1992; Price and Suppe, 1994, 1995; Hansen et al., 1997; Head and Coffin, 1997; McKinnon et al., 1997; Basilevsky and Head, 2002; Ernst and Desnoyers, 2004). However, in contrast to the Earth, Venus has no observed record of plate tectonics, a low degree of surface erosion, and an apparently short period of formation of the present planetary surface. The absence of plate tectonics indicates that all magmatism is "intraplate", and is generated beneath a stagnant lithospheric lid. A low degree of surface erosion preserves the surface structures and short-wavelength topography. The short duration of preserved magmatic activity suggests a global resurfacing event.

It should also be noted that whereas Venus can provide important lessons for understanding mantle plumes on the Earth, it is possible that some distinctive differences may complicate the comparison of Venus with Earth. For instance, the viscosity contrast across the Venusian mantle may have been less than that of the Earth (e.g., Jellinek et al., 2002), and the overall Venusian mantle viscosity may have been higher owing to planetary loss of water (e.g., Nimmo and McKenzie, 1996; Arkani-Hamed, 1996; Moore and Schubert, 1997).

4.2 LIP record of Venus

Main magmatic elements on Venus include (Tables 3 and 4; Figs. 4–6): (a) individual volcanoes; those with diameters between 100 and 1000 km can be correlated with plumes (e.g., Head et al., 1992; Herrick, 1999; Stofan et al., 1995; Crumpler and Aubele, 2000); (b) annular structures termed coronae (and arachnoids) with diameters averaging 300 km, but ranging up to 2600 km which appear to lack terrestrial analogues, but are arguably related to plumes or diapirs (Janes et al., 1992; Herrick, 1999; Crumpler and Aubele, 2000; Stofan et al., 2001; Johnson and Richards, 2003; Hoogenboom et al., 2005) (c) radiating graben-fissure systems extending up to 2000 km from their foci, some of which are purely uplift related while others mark the plumbing system (dyke swarms) of plumes (Grosfils and Head, 1994; Ernst et al., 2003); (d) lava flow fields of scale comparable to terrestrial flood basalts (Crumpler and Aubele, 2000; Magee and Head, 2001); (e) regions of small shield volcanoes

Table 3. Classes of magmatic/tectonic features on Venus (modified from Ernst and Desnoyers, 2004)

Feature type	Number of features	Size of features	Distribution	Possible tectono-magmatic setting
Volcanoes				
Large volcanoes (>100 km in diameter)	168 [1]	defined as ≥100 km diam.; max. 1000 km diam.; 60 ≥ 500 km diam. [1]	Located on volcanic rises, along chasmata and in the plains. Sometimes clustered, sometimes as isolated features.	Major plumes/hotspots
Intermediate volcanoes (100–20 km in diameter)	289 [1]	defined as <100 ≥ 20 km in diam. [1]		Plumes/hotspots?
Shield fields	647 [1]	mean: 50–350 km mode: 100–150 km; max.: 1200 × 300 km [1]	Widely distributed within a global stratigraphic unit [6]. Regionally clustered and diachronous on a global scale in part post-dating regional plains volcanism [7]; local clusters associated with individual coronae (e.g. [1]).	Shallow mantle sources
Circular structures				
Coronae	473 (including 265 arachnoid subclass) [1] 513 type 1 and type 2 ('stealth' coronae) [1a] 96 [1b]	Arachnoid subclass: most: <200 km diam. max.: 280 km diam. [1] Other coronae: most: 200–250 km diam. max.: 1000 km diam. 18 ≥ 500 km diam. [1]; Note Artemis (with 2600 km diam.) not included in [1]	Distributed along rifts (chasmata), clustered in volcanic rises, or occurring as isolated features in the plains	Transient plumes (thermals) or diapirs or subsurface intrusions
Calderae	97 [1]	Most: 60–80 km diam.; max.: 225 × 150 km diam. [1]		Subsurface intrusions

Flows				
Flow fields	208; including 81 giant flow fields [4]	Defined: >50,000 sq. km; max.: 1,630,000 sq. km; 140 > 100,000 sq. km; 81 giant flow fields = flow length >500 km [4]	Associated with both volcanoes and coronae	= Large Igneous Provinces (LIPs)
Canali		Up to 6800 km long [8]		Low viscotiy lava flows: komatiite, carbonatite, or sulphur rich
Radiating graben-fissure systems			Associated with volcanoes, arachnoids and coronae	Largest are giant radiating dyke swarms derived from mantle plumes
Global reconnaissance survey at C1-MIDR scale	163 in global C1-MIDR study [2]	Range: 40 to >2000 km radius mean: 325 km radius [2]		
Detailed local study at FMAP-scale	34 in regional FMAP study [3]	15 ≥ 300 km radius [3] 8 ≥ 1000 km radius [3]	Area of detailed study bounded by 264–312°E and 24–60°N	
Radial fracture centers also termed novae	64 [1]	Range: 50–300 km diam. [1]		
Arachnoids: subset having radiating graben	Minor portion of arachnoid population [1b]			

(*Continued*)

Table 3. (*Continued*)

Feature type	Number of features	Size of features	Distribution	Possible tectono-magmatic setting
Radiating ridge systems				
Arachnoid: subset with radiating ridges	Majority of arachnoid population [1b]			??
Crustal plateaus (tesserae)				
Regional uplifts of 'basement' tesserae terrain [5]	7	1600–2500 km in diameter		Upwelling or downwelling
Groupings of events				
Clusters of Volcanic Features	9		Usually associated with topographic and geoid highs	Plume cluster (superplume event)
Volcanic Rises: volcano, corona, and rift dominated types				
Linear distributions			Mainly along Parga Chasma and Hecate Chasma	Rift-related

[1] Crumpler and Aubele (2000); [1a] Stofan et al. (2001), Glaze et al. (2002); [1b] Kostama and Aittola (2001), Aittola and Kostama (2002); [2] Grosfils and Head (1994); Grosfils (1996); [3] Ernst et al. (2003); [4] Magee and Head (2001); [5] Hansen et al. (1999); [6] Basilevsky and Head (1998, 2002), Ivanov and Head (2004); [7] Addington (2001); [8] Baker et al. (1997), Williams-Jones et al. (1998); [9] Ernst and Desnoyers (2004).

Table 4. Clusters of volcanic activity on Venus marking plume clusters (modified after Ernst and Desnoyers, 2004)

Clusters	Location (lat.-long)	Characteristics
Volcanic rises: rift dominated type		
Atla Regio diameter: 1200–1600 km	00°N, 200°E (BAT region)	Apparent depth of compensation: 175 km [1] Topographic rise: swell height 2.5 km [1] Central volcanoes: 7 volcanic centers, most importantly Maat and Ozza Mons. Sapas Mons is to the west, but still within the geoid high Triple junction rifting: Hecate, Parga, Dali/Diane chasmata
Beta Regio diameter: 1900–2500 km	25°N, 280°E (BAT region)	Apparent depth of compensation: 225 km [1] Topographic rise: swell height 2.1 km [1] Central volcano: Theia Mons Triple junction rifting: Devana Chasma (two arms) and Žverine Chasma (eastern end of Hecate chasmata)
Volcanic rises: volcano dominated type		
Imdr Regio diameter: 1200–1400 km	40°S, 020°E	Apparent depth of compensation: 260 km [1] Topographic rise: swell height 1.6 km [1] Central volcano: unnamed volcano; no associated coronae
Western Eistla Regio diameter: 2000–2400 km	25°N, 355°E (Eistla region)	Apparent depth of compensation: 200 km [1] Topographic rise: swell height 1.8 km [1] Central volcanoes: two major shield volcanoes (Sif Mons, Gula Mons), several smaller edifices and two coronae on its northern flank
Dione Regio	40°S, 325°E	Apparent depth of compensation: 130 km [1] Topographic rise: swell height 0.5 km [1] Central volcanoes: Ushas, Innini, and Hathor Mons; no associated coronae
Bell Regio diameter: 1100–1400 km	30°N, 50°E (Eistla region)	Apparent depth of compensation: 125 km [1] Topographic rise: swell height 1.2 km [1] Central volcano: Tepev Mons, Nefertiti "two major shields and a corona"
Themis Regio diameter: 1650–2300 km	40°S, 285°E (BAT region)	Apparent depth of compensation: 100 km [1] Topographic rise: swell height 1.5 km [1] Coronae: five major coronae and lies at the southeast end of the Parga Chasma corona chain"
Laufey Regio diameter: 1000–2000 km	05°N, 310°E	Apparent depth of compensation: 32–74 km [5] Topographic rise: swell height 0.5 km [5] Dominated by two large volcanoes Var and Atanua Montes, and numerous coronae [5]
Volcanic rises: corona dominated type		
Central Eistla Regio diameter: 1000–1400 km	10°N, 15°E (Eistla region)	Apparent depth of compensation: 120 km [1] Topographic rise: swell height 1.0 km [1] Volcanoes: dominated by three coronae including Sappho corona.
Eastern Eistla Regio diameter: 1600–1800 km	15°N, 45°E (Eistla region)	Apparent depth of compensation: 65 km [1], 75 km [2] Topographic rise: swell height 1.0 km [1] Cluster of about 12 coronae. Includes four main coronae, the largest of which is Pavlova Corona

(*Continued*)

Table 4. (*Continued*)

Clusters	Location (lat.-long)	Characteristics
Arachnoid clusters		
Bereghinya Planitia	45°N, 15°E (Eistla region)	At least 10 arachnoids [3]
Ganiki Planitia	45°N, 190°E	5 arachnoids [3]
Clusters lacking a distinct topographic swell		
Mnemosyne Regio	70°N, 270°E	A corona cluster that lacks a distinct swell [1,4]

[1] Stofan et al. (1995); [2] Schubert et al. (1994); [3] Kostama (2002); [4] Stofan and Head (1990); [5] Brian et al. (2004).

representing shallow source melting (Addington, 2001; Ivanov and Head, 2004), and (f) canali which consist of narrow sinuous flows that extend up to 6800 km (e.g., Baker et al., 1997), recently revised to 7100 km (Blinova et al., 2004). These are superimposed on an earlier history of plains volcanism and earlier tessarae formation (deformed terrains). Basaltic compositions dominate.

As noted by Head and Coffin (1997, p. 429), "two units that could be interpreted as LIP-related [are] the ridged plains, where large-scale sinuous channel-type emplacement occurred, and the smooth/lobate plains, where flood-basalt-like provinces were produced, often in conjunction with rift zones." In addition, individual volcanoes that are greater than 500 km in diameter (60 examples), radiating graben systems of similar extent, giant lava flow fields (140 having size $> 100{,}000$ km^3), and some of the larger coronae also classify as LIPs based on scale (Ernst and Desnoyers, 2004).

4.3 Individual plumes on Venus

Based on the record summarized in Table 3 we conclude that the maximum size of plumes on Venus is similar to that inferred for Earth (e.g., Ernst and Desnoyers, 2004). The topographic rises such as Atla and Beta Regio with their triple-junction rifting and central volcanoes are about 2000 km across. These young volcanoes in the Beta-Atla-Themis (BAT) region (Fig. 5) are of similar areal extent to the largest individual plumes identified on Earth such as the 122 Ma Ontong Java, 200 Ma Central Atlantic Magmatic Province, and 1267 Ma Mackenzie (Ernst and Buchan, 2002) and also with the smaller but exceptionally well characterized 258 Ma Emeishan of China (Xu et al., 2004). In addition, they correspond to the inferred size of a plume that originates at the base of the mantle and flattens against the lithosphere (e.g., Griffiths and Campbell, 1991).

There are also numerous large (>100 km) isolated volcanoes on Venus outside the BAT region which are not associated with topographic swells or geoid highs or rifts. However, these isolated volcanoes are the same sizes and can have associated radiating graben systems of the same areal extent as those younger volcanoes in

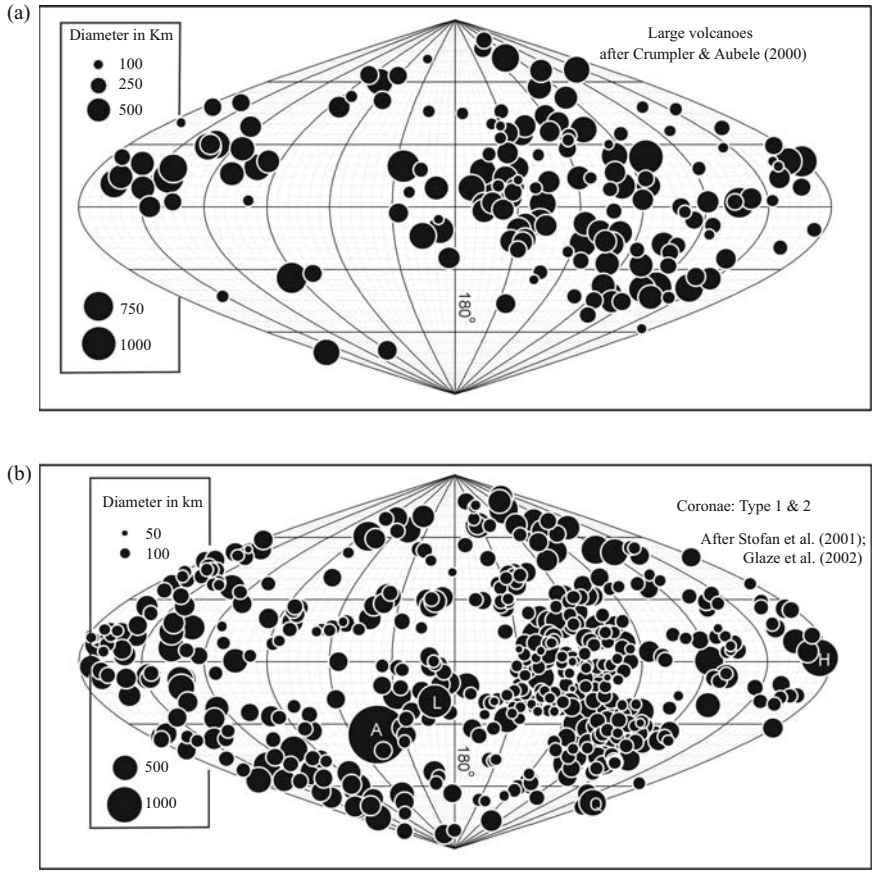

Figure 4. (a) Distribution of large volcanoes on Venus. Displayed in a sinusoidal projection with a central meridian of 180°. Extracted from catalogue of Crumpler and Aubele (2000). Symbol size is greater than the actual feature size; this was done to allow a greater dynamic range in symbol size, so as to better display the range in feature size. (b) Distribution of coronae on Venus. Displayed in a sinusoidal projection with a central meridian of 180° after Stofan et al. (2001) as modified in Glaze et al. (2002), and includes both Type 1 and 2 coronae. A is Artemis, F is Fatua, H is Heng-O, L is Latona, and Q is Quetzalpetlatl. As in part (a), symbol sizes were exaggerated to better display the range in feature sizes.

the BAT region. It is proposed that the isolated volcanoes represent older plume centres whose associated topographic swell and geoid anomaly have disappeared as the thermal anomaly faded over 10 s to 100 s of millions of years and as the associated rifts were flooded by lava (see discussion in Ernst and Desnoyers, 2004).

As noted above, individual volcanoes on Venus can be up to 1000 km in diameter, substantially larger any volcanoes observed on Earth. Owing to the absence of plate tectonics, plumes remain underneath the same region of lithosphere through both their plume head and plume tail stages. Thus the greater size of volcanoes on Venus

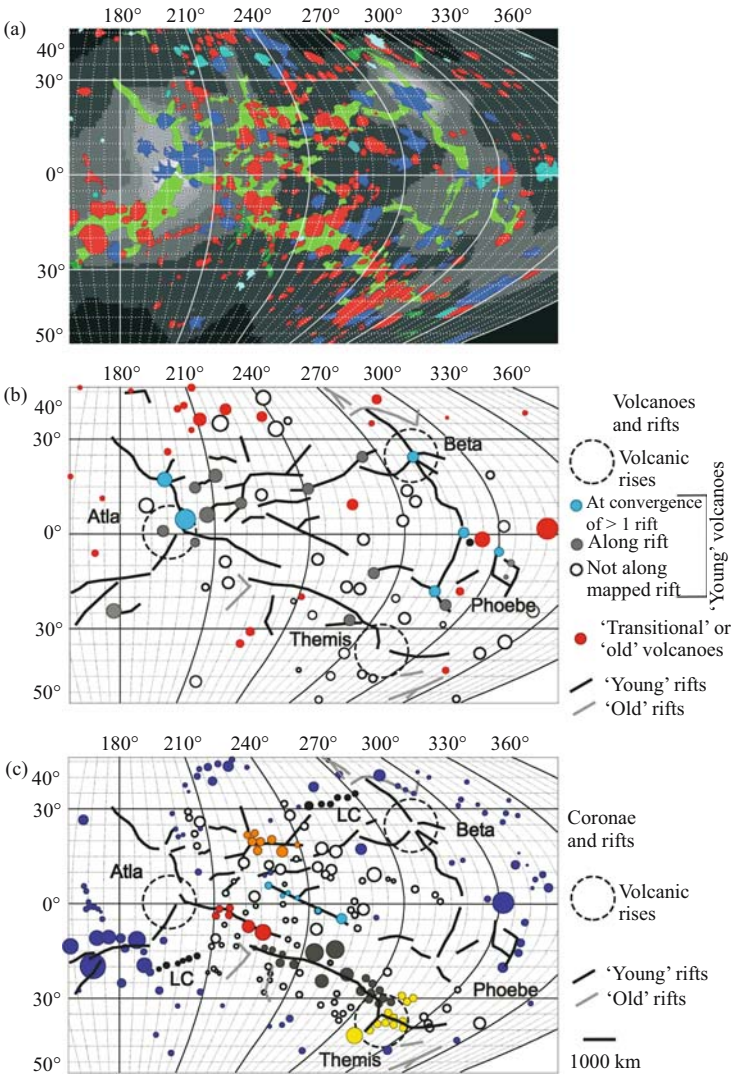

Figure 5. Distribution of volcanoes, coronae (including arachnoids) and young rifts in the BAT (Beta-Atla-Themis region). (a) Mapped distribution of geological features superimposed on geoid, from Herrick (1999) which is after Price (1995) and Price and Suppe (1995). Coronae are red, rifts are green, and volcanoes are blue (those in dark blue are "young" while those in light blue are "transitional" to "old" in age, based on a Basilevsky and Head (2000). (b) Generalized distribution of volcanoes and rifts. (c) Generalized distribution of coronae and rifts. Regional rises located with large circles. Separation of rifts into "young" and "old", and separation of volcanoes into "young" and "transitional/old" is based on Plate 1 in Basilevsky and Head (2000). Symbol size = approximately the minimum dimension of the feature. Sinusoidal projection with a central meridian of 180°. Thin latitude and longitude lines are spaced at 5° intervals. Thick lines are at 30° intervals. LC = lines of coronae not associated with a mapped rift. Hecate Chasma connects Atla and Beta, and Parga Chasma connects Atla and Themis.

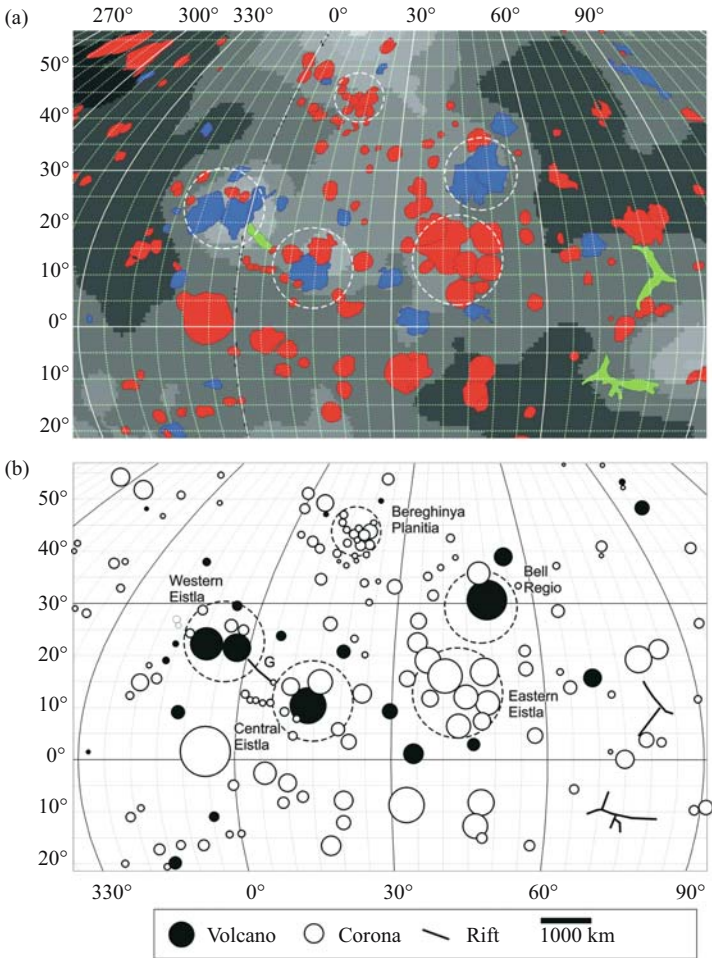

Figure 6. Distribution of volcanoes, coronae (including arachnoids) and young rifts in the Eistla region. (a) Mapped distribution of features from Herrick (1999) which is after Price (1995) and Price and Suppe (1995). Coronae are red, rifts are green, and volcanoes are blue. (b) Generalized geology. Symbol size = approximately the minimum dimension of the feature. Sinusoidal projection with a central meridian of 40°. Thin latitude and longitude lines are spaced at 5° intervals. Thick lines are at 30° intervals.

may result from the combination of superposition of plume head and plume tail magmatism. Additional reasons that Venusian volcanoes are broader (and not as high) as those on Earth are discussed in Head and Coffin (1997).

The largest coronae on Venus (Ivanov and Head, 2003), which include the 2600 km diameter Artemis, 900 km diameter Heng-O, and 800 km diameter Quetzalpetlatl coronae (Fig. 4), suggest that the associated plumes are of broadly similar maximum size. Thus the plume record for Venus provides no evidence for individual plumes

larger than those consistent with models for "normal" plume ascent from the deep mantle.

Herrick et al. (2005) explored the link between coronae and large volcanoes, and concluded that there are constructs which have the characteristics of each. Thirteen of twenty nine large volcanoes studied had a central depression (typically 150 km wide and 500 m deep) rather than a domical topographic expression. They suggested that "the central depressions are probably … the result of a corona-like sagging of a previously domical volcano". It can be concluded that volcanoes and coronae represent a spectrum of processes rather than two distinct classes of events.

4.4 Plume cluster

The best candidate for a plume cluster event on Venus is in the Beta-Atla-Themis (BAT) region (Figs. 4 and 5). This is an area with concentrated magmatic activity and an associated geoid high. Furthermore, the scale of the BAT region, almost 10,000 km across, is similar to the scale inferred for the African and Pacific plume cluster/superplume events on Earth. A second area, the Eistla region also exhibits anomalous volcanism (Figs. 4 and 6). Gravitationally uncompensated coronae (indicating their young age), are concentrated in both regions, but particularly in the BAT region (Johnson and Solomon, 2002).

Within these two broad regions and elsewhere on the planet there are 10 local clusters of volcanoes and coronae. Most are associated with local topographic rises, and geoid highs (Table 3).

4.5 Regional clusters associated with rifts on Venus

The preferential clustering of coronae along the prominent triple junction rift systems of Venus is remarkable (Fig. 5). As shown by the analysis of Magee and Head (2001) many lava flow fields are associated with such coronae, demonstrating that significant LIP magmatism is associated with the rift systems on Venus.

There are also linear distributions of coronae which are not associated with a specific mapped rift (labelled "LC" in Fig. 5). Perhaps these mark older rifts that are obscured by younger lava flows.

4.6 Global event on Venus

An additional characteristic of the magmatic (LIP) record on Venus is the possibility of global flooding in a short period of time. Based on the globally uniform abundance of impact craters, the entire planet was initially inferred to have been resurfaced between 500 and 300 Ma ago (Phillips et al., 1992; Schaber et al., 1992; Strom et al., 1994; Herrick, 1994; Herrick et al., 1995; Price and Suppe, 1995; Price et al., 1996; Head and Coffin, 1997) in an interval perhaps as short as 10 Myr (Strom et al., 1994). The timing of this period of dramatic resurfacing was changed based on a new estimate for the mean surface age of 750 Ma (McKinnon et al., 1997).

However, it is also possible that the period of resurfacing was not as short-lived as generally viewed. The revised mean-surface age with its uncertainties, T = 750 + 250/−450 Ma (McKinnon et al., 1997), and the ages relative to T for different units on Venus, ranging from (1.47 ± 0.46) T for tessarae units to (0.27 ± 0.39) T for the youngest rifts, (Basilevsky and Head, 2002) can lead to new estimates for the age and duration of resurfacing (Ernst and Desnoyers, 2004). Using extreme values and the maximum uncertainties leads to a maximum estimate for resurfacing between about 2000 Ma-Present. However, using mean values leads to a more conservative estimate of resurfacing between 1100 and 200 Ma.

Most resurfacing is associated with the plains units which cover 80% of the surface area of Venus or about 368 Mkm^2. Their inferred volume (assuming an average plains thickness of 2.5 km) is about 920 Mkm^3 (Head and Coffin, 1997). The magmatism responsible for flooding the Venusian plains would therefore be equivalent to about 16 plumes of the scale of the largest LIP on Earth (Greater Ontong Java, 58 Mkm^3). It would be equivalent to 184 of the largest continental LIPs (estimated to be about 5 Mkm^3 in volume; a number that must be an underestimate given the difficulties of quantifying both intrusive and underplate components; see earlier discussion). Based on the terrestrial LIP record (Coffin and Eldholm, 2001; Ernst and Buchan, 2002) the time required for Venus resurfacing would range from 160 to 1840 Myr (using the terrestrial rate of one plume per 10 Myr), or from 320 to 3680 Myr (using the rate of one plume per 20 Myr).

Therefore, using plausible terrestrial values of one 5 Mkm^3 LIP produced every 10 Myr, resurfacing could be accomplished within 1840 Myr, which is close to the maximum estimate of resurfacing (2000 Ma-Present, as discussed above). So it is just possible that the global resurfacing of Venus could be accomplished by a normal terrestrial rate of plume head generated magmatism. However, a "normal" terrestrial rate of plume production would be totally insufficient using the more conservative estimate of Venus resurfacing between 1100 and 200 Ma.

An alternative is that the plains were resurfaced by a thin volcanic 'veil' derived from widespread volcanism of small (1–15 km diameter) volcanoes (Hansen and Bleamaster, 2002). In this case the volume of resurfacing would be greatly reduced, and catastrophic resurfacing would not be required. Therefore, it will be important to map the thickness of the plains units, a number which well help resolve the debate on the nature, scale and duration of the resurfacing event on Venus.

5 DISCUSSION AND CONCLUSIONS

Based on the LIP record we have inferred that plumes occur at an average rate of one per 10–20 Myr (with an average spacing of perhaps 1 per 30 Myr) on Earth and are also very common on Venus. Both planets exhibit clusters of plumes associated with geoid highs that we prefer to term "plume clusters" (Ernst and Buchan, 2002) but which have also been termed "superplume events" (Condie, 2001). We now focus on a key unresolved question for future work that applies to both Earth and Venus.

5.1 Development of criteria to recognize regional clusters through time

On Earth plume clusters are located in the Pacific and under Africa, and are recognized by the association of hotspots (marking plume stalks) and back-tracked LIPs with geoid highs and deep mantle shear wave velocity gradients (Thorne et al., 2004). On Venus they are located in the BAT (Beta-Atla-Themis) and Eistla regions, and are recognized by the clustering of volcanoes and coronae with regional geoid highs.

A key frontier question is how to recognize plume clusters in the older record of both planets. On Earth the problem is the lack of reliable reconstructions older than about 400 Myr which complicates the recognition of spatial clusters. Also geoid highs and deep mantle seismic anomalies are the key to linking spatially-clustered plumes, but there are no obvious criteria for recognizing paleogeoid highs, or fossil deep mantle seismic anomalies. On Venus, there is no plate tectonics, which simplifies the recognition of LIP clusters. However, because the planet has been "recently" resurfaced, only the youngest LIP clusters are preserved.

On Earth, there are two provisional approaches to recognizing older plume clusters: (1) spatial clusters (distributed over an area with a diameter of 10,000 km) consisting of coeval LIP events, and (2) spatial clusters with a range of ages, but which are clearly associated with continental breakup. On Venus the link with triple junction rifting is a key to the recognition of plume clusters in the BAT and Eistla regions. In the older record of Venus, there may be cryptic (flooded) rifts marked by lines of coronae (Fig. 5) (Ernst and Desnoyers, 2004) which may help in the identification of triple junction rifting and older plume clusters.

ACKNOWLEDGEMENTS

We appreciate the reviews of Simon Hanmer and Vic Baker, and also discussions with Wouter Bleeker on the topics of plumes and large igneous provinces.

REFERENCES

Addington, E.A. (2001) A stratigraphic study of small volcano clusters on Venus. *Icarus*, 149, 16–36.

Aittola, M., and V.-P. Kostama (2002) Chronology of the formation process of Venusian novae and the associated coronae. *J. Geophys. Res.*, 107(E11), 5112, doi:10.1029/2001JE001528, 26p.

Al-Kindi, S., N. White, M. Sinha, R. England, R. Tiley (2003) Crustal trace of a hot convective sheet. *Geology*, 31(3), 207–210.

Anderson, D.L. (1995) Lithosphere, asthenosphere, and perisphere. *Rev. Geophys.*, 33, 19–41.

Anderson, D.L. (1998) The EDGES of the mantle. In Gurnis M., M.E. Wysession, E. Knittle, and B.A. Buffett (eds.) The Core-Mantle Boundary Region, Am. Geophys. Union, Geodynamics Series, 28, 255–271.

Arkani-Hamed, J. (1996) Analysis and interpretation of the surface topography and gravvitational potential of Venus. *J. Geophys. Res.*, 101(E2), 4711–4724.

Baker, V.R., G. Komatsu, V.C. Gulick, and T.J. Parker (1997) Channels and Valleys. In Bougher, S.W., D.M. Hunter, and R.J. Phillips (eds.) Venus II: Geology, Geophysics, Atmosphere and Solar Wind Environment, Univer. of Arizona Press, Tuscon, pp. 757–793.

Basilevsky, A.T., and J.W. Head (1998) The geologic history of Venus: A stratigraphic view. *J. Geophys. Res.*, 103, 8531–8544.

Basilevsky, A.T., and J.W. Head (2000) Rifts and large volcanoes on Venus: Global assessment of their age relations with regional plains. *J. Geophys. Res.*, 105, 24583–24611.

Basilevsky, A.T., and J.W. Head (2002) Venus: Timing and rates of geologic activity. *Geology*, 30, 1015–1018.

Bleeker, W. (2004) Taking the pulse of planet Earth: A proposal for a new multi-disciplinary flagship project in Canadian solid Earth sciences. *Geoscience Canada*, 31(4), 179–190.

Blinova, A.I., R.E. Ernst, K. Bell, and D.W. Desnoyers (2004) Venusian canali: In search of 'stops' and 'starts' (2004) 40th Microsymposium sponsored by the Vernadsky Institute and Brown University, Moscow Russia 10–13 October 2004.

Brian, A.W., E.R. Stofan, J.E. Guest, and S.E. Smrekar (2004) Laufey Regio: A newly discovered topographic rise on Venus. *J. Geophys. Res.*, 109, E07002, doi: 10.1029/2002JE002010, 20p.

Buchan, K.L., and R.E. Ernst (2004) Diabase dyke swarms and related units in Canada and adjacent regions. Geol. Surv. Can. map 2022A (1:5,000,000 Map and accompanying booklet).

Buchan, K.L., and R.E. Ernst (2006) Giant dyke swarms and the reconstruction of the Canadian Arctic islands, Greenland, Svalbard and Franz Josef Land. In Hanski, E., S. Mertanen, T. Rämö, and J. Vuollo (eds.) Dyke Swarms: Time Markers of Crustal Evolution, A.A. Balkema, Rotterdam, pp. 27–48.

Buchan, K.L., H.C. Halls, and J.K. Mortensen (1996) Paleomagnetism, U-Pb geochronology, and geochemistry of Marathon dykes, Superior Province, and comparison with the Fort Frances swarm. *Can. J. Earth Sci.*, 33, 1583–1595.

Buchan, K.L., S. Mertanen, R.G. Park, L. Pesonen, S.-Å. Elming, N. Abrahamsen, and G. Bylund (2000) Comparing the drift of Laurentia and Baltica in the Proterozoic: The importance of key paleomagnetic poles. *Tectonophysics*, 319, 167–198.

Buchan, K., R. Ernst, M. Hamilton, S. Mertanen, L.J. Pesonen, and S.-Å. Elming (2001) Rodinia: The evidence from integrated paleomagnetism and U-Pb geochronology. *Precambrian Res.*, 110, 9–32.

Burke, K., and J. Dewey (1973) Plume-generated triple junctions: Key indicators in applying plate tectonics to old rocks. *J. Geol.*, 81, 406–433.

Burke, K., and T.H. Torsvik (2004) Derivation of large igneous provinces of the past 200 million years from long-term heterogeneities in the deep mantle. *Earth Planet. Sci. Lett.*, 227(3–4), 531–538.

Campbell, I.H. (1998) The mantle's chemical structure: Insights from the melting products of mantle plumes. In Jackson I.N.S. (ed.) The Earth's Mantle: Composition, Structure and Evolution, Cambridge Univ. Press, New York, pp. 259–310.

Campbell, I.H. (2001) Identification of ancient mantle plumes. In Ernst, R.E., and K.L. Buchan (eds.) Mantle Plumes: Their Identification Through Time, Geological Society of America Special Paper 352, pp. 5–21.

Campbell, I.H., R.W. Griffiths, and R.I. Hill (1989) Melting in an Archaean mantle plume: Heads it's basalts, tails it's komatiites. *Nature*, 339, 697–699.

Coffin, M.F., and O. Eldholm (1994) Large igneous provinces: Crustal structure, dimensions and external consequences. *Rev. Geophys.*, 32, 1–36.

Coffin, M.F., and O. Eldholm (2001) Large igneous provinces: Progenitors of some ophiolites? In Ernst, R.E., and K.L. Buchan (eds.) Mantle Plumes: Their Identification Through Time, Geological Society of America Special Paper 352, pp. 59–70.

Condie, K.C. (2001) Mantle Plumes and Their Record in Earth History, Cambridge University Press, 306p.

Courtillot, V.E., and P.R. Renne (2003) On the ages of flood basalt events. *C.R. Geoscience*, 335, 113–140.

Courtillot, V., A. Davaille, J. Besse, and J. Stock (2003) Three distinct types of hotspots in the Earth's mantle. *Earth Planet. Sci. Lett.*, 205, 295–308.

Cox, K.G. (1989) The role of mantle plumes in the development of continental drainage patterns. *Nature*, 342, 873–877.

Crough, S.T., and D.M. Jurdy (1980) Subducted lithosphere, hot spots and the geoid. *Earth Planet. Sci. Lett.*, 48, 15–22.

Crumpler, L.S., and J.C. Aubele (2000) Volcanism on venus. In Sigurdsson, H. (ed.) Encyclopedia of Volcanoes, Academic Press, San Diego, pp. 727–769.

Davies, G.F. (1999) Dynamic Earth: Plates, Plumes, and Mantle Convection, Cambridge University Press, Cambridge, U.K., 458p.

Dobretsov, N.L. (2005) 250 Ma large igneous provinces of Asia: Siberian and Emeishan traps (plateau basalts) and associated granitoids. *Russian Geology and Geophysics*, 46(9), 870–890.

Dobretsov, N.L., A.G. Vladimirov, and N.N. Kruk (2005) Permian-Triassic magmatism in the Altai-Sayan fold system as a reflection of the Siberian superplume. *Doklady Earth Sciences (English)*, 400(1), 40–43.

Duncan, R.A., and M.A. Richards (1991) Hotspots, mantle plumes, flood basalts, and true polar wander. *Rev. Geophys.*, 29, 31–50.

Elkins-Tanton, L. T., and B.H. Hager (2000) Melt intrusion as a trigger for lithospheric foundering and the eruption of the Siberian flood basalts. *Geophys. Res. Lett.*, 27, 3937–3940.

Elliot, D.H., and T.H. Fleming (2000) Weddell triple junction: The principal focus of Ferrar and Karoo magmatism during the initial breakup of Gondwana. *Geology*, 28, 539–542.

Ernst, R.E., and K.L. Buchan (1997) Giant raditing dyke swarms: Their use in identifying pre-Mesozoic Large igneous provinces and mantle plumes. In Mahoney, J.J., and M.F. Coffin (eds.) Large Igneous Provinces: Continental, Oceanic, and Planetary Flood Volcanism, Am. Geophys. Union, Geophys. Monogr., 100, pp. 297–333.

Ernst, R.E., and K.L. Buchan (2001) Large mafic magmatic events through time and links to mantle-plume heads. In Ernst, R.E., and K.L. Buchan (eds.) Mantle Plumes: Their Identification Through Time. Special Paper 352, Geological Society of America, Boulder CO, pp. 483–575.

Ernst, R.E., and K.L. Buchan (2002) Maximum size and distribution in time and space of mantle plumes: Evidence from large igneous provinces. In Condie, K.C., D. Abbot, and D.J. Des Marais (eds.) Super-plume Events in Earth's History: Causes and Effects, J. Geodynamics (Special Issue) 34, 309–342 [Erratum, J. Geodynamics 2002, 34: 711–714].

Ernst, R.E., and K.L. Buchan (2003) Recognizing mantle plumes in the geological record. *Ann. Rev. Earth Planet. Sci.*, 31, 469–523.

Ernst, R.E., K.L. Buchan, and I.H. Campbell (2005) Frontiers in Large Igneous Province research. *Lithos*, 79, 271–297.

Ernst, R.E., and D.W. Desnoyers (2004) Lessons from Venus for understanding mantle plumes on Earth. *Phys. Earth Planet. Inter.*, 146, 195–229 [Corrigendum 2005, 149: 371].

Ernst, R.E., D.W. Desnoyers, J.W. Head, and E.B. Grosfils (2003) Graben-fissure systems in Guinevere Planitia and Beta Regio (264–312°E, 24–60°N), Venus, and implications for regional stratigraphy and mantle plumes/diapirs. *Icarus*, 164, 282–316.

Foulger, G.R., and J.H. Natland (2003) Is "hotspot" volcanism a consequence of plate tectonics? *Science*, 300, 921–922.

Foulger G.R., J.H. Natland, D.C. Presnall, and D.L. Anderson (eds.) (2005) Plates, Plumes and Paradigms, Geological Society of America Special Paper 388, 881p.

Glaze, L.S., E.R. Stofan, S.E. Smrekar, and S.M. Baloga (2002) Insights into corona formation through statistical analyses. *J. Geophys. Res.*, 107(E12), 5135, doi:10.1029/2002JE001904.

Gower, C.F., and T.E. Krogh (2002) A U-Pb geochronological review of the Proterozoic history of the eastern Grenville Province. *Can. J. Earth Sci.*, 39, 795–829.

Griffiths, R.W., and I.H. Campbell (1991) Interaction of mantle plume heads with the Earth's surface and onset of small-scale convection. *J. Geophys. Res.*, 96, 18295–18310.

Grosfils, E.B. (1996) The emplacement of giant radiating dike swarms on Venus: Implications for magma stalling and reservoir formation, the origin of shallow stress fields and the recent geologic history of the planet. PhD. Thesis, Brown University, 221pp.

Grosfils, E.B., and J.W. Head (1994) The global distribution of giant radiating dike swarms on Venus: Implications for the global stress state. *Geophys. Res. Lett.*, 21, 701–704.

Hansen, V.L., and L.F. Bleamaster, III (2002) Distributed point source volcanism: A mechanism for 'regional plains' resurfacing, Venus. *Lunar Planet. Sci.* XXXIII, Abstract no. 1061, Lunar and Planetary Institute, Houston, Texas (CD-ROM).

Hansen, V.L., B.K. Banks, and R.R. Ghent (1999) Tessera terrain and crustal plateaus, Venus. *Geology*, 27, 1071–1074.

Hansen, V.L., J.J. Willis, and W.B. Banerdt (1997) Tectonic overview and synthesis. In Bougher, S.W., D.M. Hunten, and R.J. Phillips (eds.) Venus II: Geology, Geophysics, Atmosphere, and Solar Wind Environment, Univ. of Arizona Press, Tucson, Arizona, pp. 797–844.

Hanson, R.E., J.L. Crowley, S.A. Bowring, J. Ramezani, W.A. Gose, I.W.D. Dalziel, J.A. Pancake, E.K. Seidel, T.G. Blenkinsop, and J. Mukwakwami (2004) Coeval large-scale magmatism in the Kalahari and Laurentian cratons during Rodinia assembly. *Science*, 304, 1126–1129.

Head, J.W., and M.F. Coffin (1997) Large Igneous Provinces: A planetary perspective. In Mahoney, J.J., and M.F. Coffin (eds.) Large Igneous Provinces: Continental, Oceanic and Planetary Flood Volcanism, American Geophys. Union, Geophys. Monograph, 100, pp. 411–438.

Head, J.W., L.S. Crumpler, J.C. Aubele, J.E. Guest, and R.S. Saunders (1992) Venus volcanism: Classification of volcanic features and structures, associations, and global distribution from Magellan data. *J. Geophys. Res.*, 97, 13153–13197.

Herrick, R.R. (1994) Resurfacing history of Venus. *Geology*, 22, 703–706.

Herrick, R.R. (1999) Small mantle upwellings are pervasive on Venus and Earth. *Geophys. Res. Lett.*, 26, 803–806.

Herrick, R.R., J. Dufek, and P.J. McGovern (2005) Evolution of large shield volcanoes on Venus. *J. Geophys. Res.*, 110, E01002, doi:10.1029/2004JE002283, 19p.

Herrick, R.R., N. Izenberg, and R.J. Phillips (1995) Comment on "The global resurfacing of Venus" by R.G. Strom, G.G. Schaber, and D.D. Dawson. *J. Geophys. Res.*, 100, 12255–12259.

Hill, R.I. (1991) Starting plumes and continental break-up. *Earth Planet. Sci. Lett.*, 104, 398–416.

Hoogenboom, T., S.E. Smrekar, F.S. Anderson, and G. Houseman (2004) Admittance survey of type 1 coronae on Venus. *J. Geophys. Res.*, 109(E3), E03002, doi:10.1029/2003JE002171.

Ingle, S., and M.F. Coffin (2004) Impact origin for the greater Ontong Java Plateau? *Earth Planet. Sci. Lett.*, 218, 123–134.

Ivanov, M.A., and J.W. Head (2003) Evolution of three largest coronae on Venue, Heng-O, Quetzalpetlatl, and Artemis: Preliminary results. *Lunar Planet. Sci.* XXXIV, Abstract no. 1188, Lunar and Planetary Institute, Houston, Texas (CD-ROM).

Ivanov, M.A., and J.W. Head (2004) Stratigraphy of small shield volcanoes on Venus: Criteria for determing stratigraphic relationships and assessment of relative age and temporal abundance. *J. Geophys. Res.*, 109, E10001, doi:10.1029/2004JE002252, 32p.

Janes, D.M., S.W. Squyres, D.L. Bindshadler, G. Baer, G. Schubert V.L. Sharpton, and E.R. Stofan (1992) Geophysical models for the formation and evolution of coronae on Venus. *J. Geophys. Res.*, 97, 16055–16067.

Jellinek, A.M., A. Lenardic, and M. Manga (2002) The influence of interior mantle temperature on the structure of plumes: Heads for Venus, tails for the Earth. *Geophys. Res. Lett.*, 29(11), 1532, doi:10.1029/2001GL014624.

Johnson, C.L., and M.A. Richards (2003) A conceptual model for the relationship between coronae and large-scale mantle dynamics on Venus. *J. Geophys. Res.*, 108(E6), 5058, doi:10.1029/2002JE001962, 18p.

Johnson, C.L., and S.C. Solomon (2002) A global characterization of the gravity signatures of coronae on Venus. *Lunar Planet. Sci.* XXXIII, Abstract no. 1952, Lunar and Planetary Institute, Houston (CD-ROM).

Jones, A.P., G.D. Price, N.J. Pricea, P.S. DeCarli, and R.A. Clegg (2002) Impact induced melting and the development of large igneous provinces. *Earth Planet. Sci. Lett.*, 202, 551–561.

Kerr, A.C., and J. Tarney (2005) Tectonic evolution of the Caribbean and northwestern South America: The case for accretion of two Late Cretaceous oceanic plateaus. *Geology*, 33(4), 269–272.

King, S.D., and D.L. Anderson (1998) Edge-driven convection. *Earth Planet. Sci. Lett.*, 160, 289–296.

Kostama, V.-P. (2002) The four arachnoid groups of Venus. In *Lunar Planet. Sci.* XXXIII, Abstract no. 1115, Lunar and Planetary Institute, Houston USA (CD-ROM).

Kostama, V.-P., and M. Aittola (2001) The global distribution and altimetry of Venusian arachnoids, nove and coronae. In *Lunar Planet. Sci.* XXXII, Abstract No. 1185, Lunar and Planetary Institute, Houston (CD-ROM).[http://cc.oulu.fi/tati/JR/Venus/volcanotectonics/catalogue.html]

Li, Z.X., S.V. Bogdanova, A.S. Collins, A. Davidson, B. De Waele, R.E. Ernst, I.C.W. Fitzsimons, R.A. Fuck, D.P. Gladkochub, J. Jacobs, K.E. Karlstrom, S. Lu, L.M. Natapov, V. Pease, S.A. Pisarevsky, K. Thrane, and V. Vernikovsky (2006) Assembly, configuration, and break-up history of Rodinia: A synthesis. Precambrian Geology, special issue (accepted).

Li, Z.X., X.H. Li, P.D. Kinny, J. Wang, S. Zhang, and H. Zhou (2003) Geochronology of Neoproterozoic syn-rift magmatism in the Yangtze Craton, South China and correlations with other continents: Evidence for a mantle superplume that broke up Rodinia. *Precambrian Res.*, 122(1–4), 85–109.

Magee, K.P., and J.W. Head (2001) Large flow fields on Venus: Implications for plumes, rift associations, and resurfacing. In Ernst, R.E., and K.L. Buchan (eds.) Mantle Plumes: Their Identification Through Time, Geol. Soc. America Special Paper 352, pp. 81–101.

Maher, H.D. (2001) Manifestations of the Cretaceous High Arctic Large Igneous Province in Svalbard. *J. Geol.*, 109, 91–104.

Manson, M.L., and H.C. Halls (1997) Proterozoic reactivation of the southern Superior Province and its role in the evolution of the Midcontinent rift. *Can. J. Earth Sci.*, 34, 562–575.

Maruyama, S. (1994) Plume tectonics. *J. Geol. Soc. Jpn.*, 100, 24–49.

McKinnon, W.B., K.J. Zahnle, B.A. Ivanov, and H.J. Melosh (1997) Cratering on Venus: Models and observations. In Bougher, S.W., D.M. Hunten, and R.J. Phillips (eds.) Venus II: Geology, Geophysics, Atmosphere, and Solar Wind Environment, Univ. of Arizona Press, Tucson, Arizona, pp. 969–1014.

McNutt, M.K. (1998) Superswells. *Rev. Geophys.*, 36, 211–244.

Moore, W.B., and G. Schubert (1997) Venusian crustal and lithospheric properties from nonlinear regressions of highland geoid and topography. *Icarus*, 128, 415–428.

Morgan, W.J. (1981) Hotspot tracks and the opening of the Atlantic and Indian Oceans. In Emiliani, C. (ed.) The Sea, Volume 7: Wiley Interscience, New York, pp. 443–475.

Nimmo, F., and D. McKenzie (1996) Modelling plume-related uplift, gravity and melting on Venus. *Earth Planet. Sci. Lett.*, 145, 109–123.

Nimmo, F., and D. McKenzie (1998) Volcanism and tectonics on Venus. *Ann. Rev. Earth Planet. Sci.*, 26, 23–51.

Pesonen, L.J., S.-Å. Elming, S. Mertanen, S. Pisarevsky, M.S. D'Agrella-Filho, J.G. Meert, P.W. Schmidt, N. Abrahamsen, and G. Bylund (2003) Palaeomagnetic configuration of continents during the Protoeroizc. *Tectonophysics*, 375, 289–324.

Phillips, R.J., R.F. Raubertas, R.E. Arvidson, I.C. Sarkar, R.R. Herrick, N. Izenberg, and R.E. Grimm (1992) Impact craters and Venus resurfacing history. *J. Geophys. Res.*, 97, 15923–15948.

Price, M. (1995) Tectonic and Volcanic Map of Venus, Dept. of Geol. Sci., Princeton Univ., Princeton, NJ.

Price, M., and J. Suppe (1994) Young volcanism and rifting on Venus. *Nature*, 72, 756–759.

Price, M., and J. Suppe (1995) Constraints on the resurfacing history of Venus from the hypsometry and distribution of volcanism, tectonism, and impact craters. *Earth Moon Planets*, 71, 99–145.

Price, M.H., G. Watson, J. Suppe, and C. Brankman (1996) Dating volcanism and rifting on Venus using impact crater densities. *J. Geophys. Res.*, 101, 4657–4671.

Prokoph, A., R.E. Ernst, and K.L. Buchan (2004) Time-series analysis of large igneous provinces: 3500 Ma to present. *J. Geol.*, 112, 1–22.

Puffer, J.H. (2002) A Late Neoproterozoic eastern Laurentian superplume; location, size, chemical composition, and environmental impact. *Am. J. Sci.*, 302(1), 1–27.

Reese, C.C., V.S. Solomatov, J.R. Baumgardner, D.R. Stegman, and A.V. Vezolainen (2004) Magmatic evolution of impact-induced Martian mantle plumes and the origin of Tharsis. *J. Geophys. Res.*, 109, E08009, doi:10.1029/2003JE002222, 10p.

Reichow, M.K., A.D. Saunders, R.V. White, M.S. Pringle, A.I. Al-Mukhamedov, A.I. Medvedev, and N.P. Kirda (2002) $^{40}Ar/^{39}Ar$ dates from the West Siberian Basin: Siberian flood basalt province doubled. *Science*, 296, 1846–1849.

Reichow, M.K., A.D. Saunders, R.V. White, A.I. Al'Mukhamedov, A.Ya. Medvedev (2005) Geochemistry and petrogenesis of basalts from the West Siberian Basin: An extension of the Permo-Triassic Siberian Traps, Russia. *Lithos*, 79, 425–452.

Rivers, T., and D. Corrigan (2000) Convergent margin on southeastern Laurentia during the Mesoproterozoic: Tectonic implications. *Can. J. Earth Sci.*, 37, 359–383.

Saunders, A.D., R.W. England, M.K. Reichow, and R.V. White (2005) A mantle plume origin for the Siberian traps: Uplift and extension in the West Siberian Basin, Russia. *Lithos*, 79, 407–424.

Schaber, G.G., R.G. Strom, H.J. Moore, L.A. Soderblom, R.L. Kirk, D.J. Chadwick, D.D. Dawson, L.R. Gaddis, J.M. Boyce, and J. Russell (1992) Geology and distribution of impact craters on Venus: What are they telling us? *J. Geophys. Res.*, 97, 13257–13301.

Schubert, G., G. Masters, P. Olson, and P. Tackley (2004) Superplumes or plume clusters? *Phys. Earth Planet. Inter.*, 146, 147–162.

Schubert, G., W.B. Moore, and D.T. Sandwell (1994) Gravity over coronae and chasmata on Venus. *Icarus*, 112, 130–146.

Şengör, A.M.C. (2001) Elevation as indicator of mantle-plume activity. In Ernst, R.E., and K.L. Buchan (eds.) Mantle Plumes: Their Identification Through Time, Geol. Soc. America Spec. Paper 352, pp. 183–225.

Şengör, A.M.C., and B.A. Natal'in (2001) Rifts of the world. In Ernst, R.E., and K.L. Buchan (eds.) Mantle Plumes: Their Identification Through Time, Geol. Soc. America Spec. Paper 352, pp. 389–482.

Stein, M., and A.W. Hofmann (1994) Mantle plumes and episodic crustal growth. *Nature*, 372, 63–68.

Stofan, E.R., and J.W. Head (1990) Coronae of Mnemosyne Regio: Morphology and origin. *Icarus*, 83, 216–243.

Stofan, E.R., S.E. Smrekar, D.L. Bindschadler, and D.A. Senske (1995) Large topographic rises on Venus: Implications for mantle upwelling. *J. Geophys. Res.*, 100, 23317–23327.

Stofan, E.R., S.E. Smrekar, S.W. Tapper, J.E. Guest, and P.M. Grinrod (2001) Preliminary analysis of an expanded corona database for Venus. *Geophys. Res. Lett.*, 28, 4267–4270.

Storey, B.C. (1995) The role of mantle plumes in continental breakup: Case histories from Gondwanaland. *Nature*, 377, 301–308.

Strom, R.G., G.G. Schaber, and D.D. Dawson (1994) The global resurfacing of Venus. *J. Geophys. Res.*, 99, 10899–10926.

Taylor, B. (2006) The single largest oceanic plateau: Ontong Java–Manihiki–Hikurangi. *Earth Planet. Sci. Lett.*, 241, 372–380.

Thorne, M.S., E.J. Garnero, and S.P. Grand (2004) Geographic correlation between hotspots and deep mantle lateral shear-wave velocity gradients. *Phys. Earth Planet. Int.*, 146, 47–63.

White, R.S., and D.P. McKenzie (1989) Magmatism at rift zones: The generation of volcanic continental margins and flood basalts. *J. Geophys. Res.*, 94, 7685–7729.

Williams-Jones, G., A.E. Williams-Jones, and J. Stix (1998) The nature and origin of Venusian. *Can. J. Geophys. Res.*, 103, 8545–8555.

Wingate, M.T.D., F. Franco, and P.A. Morris (2004) Warakurna large igneous province: A new Mesoproterozoic large igneous province in west-central Australia. *Geology*, 32(2), 105–108.

Xu, Y.-G, B. He, S.-L. Chung, M.A. Menzies, and F.A. Frey (2004) Geologic, geochemical, and geophysical consequences of plume involvement in the Emeishan flood-basalt province. *Geology*, 32(10), 917–920.

Yarmolyuk, V.V., V.I. Kovalenko, and M.I. Kuzmin (2000) North Asian superplume activity in the Phanerozoic: Magmatism and geodynamics. *Geotectonics*, 34(5), 343–366.

INDEX